SF2A 2014
J. Ballet, F. Bournaud, F. Martins, R. Monier and C. Reylé (eds)

Proceedings of the annual meeting of the French Society of Astronomy & Astrophysics

Paris, June 3-6, 2014

Credits: Christine Toutain. ESA/Herschel space observatory/AIM PH. André et al. Orion A

Contents

Foreword

The 2014 annual meeting of the French Society of Astronomy and Astrophysics (Société Française d'Astronomie et d'Astrophysique – SF2A) was hosted by the "Astrophysique Instrumentation et Modélisation" laboratory from June 3 to 6, in Paris. These "Journées" gathered about 365 professional astronomers and astrophysicists, who participated to plenary sessions organized by the SF2A and to workshops organized by the scientific committees of the "National Programs" and "Actions Spécifiques" of INSU-CNRS, several of them in collaboration with our special guest, the Sociedade Portuguesa de Astronomia (Portugal).

During the plenary sessions excellent scientific reviews were presented on outstanding scientific results obtained recently by our community. Also, general interest talks led to topical discussions on scientific projects (e.g. at CFHT as presented by D. Simons) as well as on the organization and the future of french astronomical research in the international environment. In particular, the latest news on the reform of the International Astronomical Union was introduced by the General Secretary T. Montmerle, D. Mourard provided the community with information of the Institut National des Sciences de l'Univers (INSU-CNRS), and F. Casoli presented a review of the current and future activities of the Centre National d'Etudes Spatiales (CNES).

This year twelve scientific workshops were organized on topical subjects, and one additional session was devoted to outreach and communication in astronomy. A users' meeting of the national two meter telescopes (TBL and OHP/T193) was also scheduled.

A large number of SF2A members attended the General Assembly where the annual activity and financial reports of our Society were presented by the president and treasurer of the SF2A Council, C.Reylé and S.Boissier. The 2014 SF2A "Thesis Prize" was presented to E. Huby by G. Perrin (Paris Observatory). The 2014 SF2A prize "Jeune Chercheur" was presented to E. Hugot by D. Rouan (Paris Observatory), and the 2014 prize "Jeune Enseignant-Chercheur" was presented to F. Lique by P. Encrenaz (Paris Observatory). We warmly thank the sponsors of these prizes, EdP Sciences, the HP company and the Exelis company for their continuing interest in our science and support to our Society. Following the award ceremony an excellent cocktail was served in the buildings of the Sorbonne University.

Along the Journées a number of social, outreach, and cultural events were organized. The SF2A Prize "Découvrir l'Univers" sponsored by EdP Sciences and Bayard Jeunesse aimed at promoting astronomy among children and young students. The award ceremony was held in the Cité des Sciences in La Villette. A movie session was offered by the planetarium to all the laureates. P.-A. Duc and A. Brahic gave two public conferences during the week.

We wish to thank the INSU-CNRS, the laboratoire Astrophysique Instrumentation et Modélisation, as well as the CNES, the CEA/DSM/IRFU, and the National Programs and Actions Spécifiques of INSU-CNRS for their financial and organisational support. We are extremely grateful to the University Paris-Diderot for hosting the Journées.

We warmly thank the members of the Local Organizing Committee: the chair, J. Ballet, and the team J.M. Bonnet-Bidaud, P. Bouchet, F. Bournaud, Ph. Briet, P.-A. Duc, D. Gilles, M. González, P.-O Lagage, S. Rodriguez, C. Toutain, H. Triou. Their outstanding work and their generous contributions were absolutely crucial for making the "Journées" such a success. Thanks also to SF2A board and council for its active contribution, and to the editors of these proceedings.

Céline Reylé Présidente de la SF2A

List of participants

ACEBRON Ana
ACERO Fabio
ALECIAN Evelyne
ALEXANDROVA Olga
ALI-DIB Mohamad
ALLARD France
ALVAN Lucie
AMARD Louis
ANDRE Nicolas
ARENOU Frédéric
ARLOT Jean-Eudes
ARNAUD Monique
ASCASO Begoña
AUCLAIR-DESROTOUR Pierre
AUGEREAU Jean-Charles
AUSSEL Herve
AYDI Elias
BACMANN Aurore
BAILLIÉ Kévin
BALANÇA Christian
BALLET Jean
BARBAN Caroline
BARBOT Armand
BAUDIN Frédéric
BAUDINO Jean-Loup
BAZIN Cyrille
BECK Paul
BENISTY Myriam
BERNARD Anaïs
BERTONE Stefano
BEURET Maxime
BÉZARD Bruno
BIVER Nicolas
BLAZERE Aurore
BOCKELEE-MORVAN Dominique
BOHM Torsten
BOISSE Isabelle
BOISSIER Samuel
BOISSIER Jeremie
BOISSON Catherine
BOLMONT Emeline
BONIFACIO Piercarlo
BONNACIEUX Etienne
BONTEMPS Sylvain
BOONE Frédéric

BORG Janet
BORGNIET Simon
BOUCHET Patrice
BOURET Jean-Claude
BOURGOIN Adrien
BOURNAUD Frederic
BOURRIER Vincent
BRAINE Jonathan
BREITFELDER Joanne
BRIOT Danielle
BRUGGER Bastien
CABANAC Rémi
CABRIT Sylvie
CAMBRESY Laurent
CANTALLOUBE Faustine
CAPITAINE Nicole
CARDOSO Jean-François
CASOLI Fabienne
CASSAN Arnaud
CATALA Claude
CAVALIÉ Thibault
CECCARELLI Cecilia
CEILLIER Tugdual
CHALLOUF Mounir
CHAMBRAUD Pascal
CHARBONNEL Corinne
CHARDIN Jonathan
CHARNOZ Sebastien
CHATY Sylvain
CHAUVIN Gaël
CHEMIN Laurent
CHEVANCE Mélanie
CHIEZE Jean-Pierre
CLARET Arnaud
CLAVEL Maïca
CLÉNET Yann
COLAS François
COLL Patrice
COLLIN-ZAHN Suzy
COMBES Francoise
CORBEL Stéphane
COTTALORDA Erik
COURTIN Régis
COUSIN Morgane
CREEVEY Orlagh
CRIDA Aurélien
CRIFO Françoise
CUELLO Nicolas
CUILLANDRE Jean-Charles
DAIGNE Frédéric
DALLIER Richard
DAMIANI Cilia
DANIELSKI Camilla
DEGRANGE Bernard
DELFOSSE Xavier

DELORME Yan
DENIS Loic
DERRIERE Sebastien
DEVOST Daniel
DI FOLCO Emmanuel
DI MATTEO Paola
DOLE Herve
DOUSPIS Marian
DRAPPEAU Samia
DUBERNET Marie-Lise
DUBOIS Yohan
DUBUS Guillaume
DUC Pierre-Alain
DUCOURANT Christine
DURRET Florence
DURRIVE Jean-Baptiste
DUTREY Anne
EGRET Daniel
EISENHAUER Frank
EL MELLAH Ileyk
ENGEL Céline
EPCHTEIN Nicolas
FAHED Rémi
FARAMAZ Virginie
FARES Rim
FAURE Carole
FAUROBERT Marianne
FEAUTRIER Nicole
FOGLIZZO Thierry
FONTAINE Dominique
FONTAINE Gerard
FORGET Francois
FORNASIER Sonia
FREUNDLICH Jonathan
FRUET Guillaume
GARGAUD Muriel
GARNIER William
GAVAZZI Raphael
GERARD Eric
GERIN Maryvonne
GIEBELS Berrie
GILLES Dominique
GILLET Nicolas
GIRAUD-HÉRAUD Yannick
GLANZ Georges
GOMEZ Ana
GONNEAU Anaïs
GONZALEZ Jean-François
GONZALEZ Matthias
GöTZ Diego
GOURGOULHON Eric
GRANDCLEMENT Philippe
GRANDIN Maxime
GRATIER Pierre
GRIESSMEIER Jean-Mathias

GROULD Marion
GUENEL Mathieu
GUERIN Frédéric
GUILET Jérôme
GUILLARD Pierre
GUILLEMOT Lucas
GUILLOTEAU Stéphane
HADID Lina
HALBWACHS Jean-Louis
HALLÉ Anaëlle
HAUBOIS Xavier
HAYWOOD Misha
HÉBRARD Elodie
HÉBRARD Guillaume
HERVE Anthony
HESTROFFER Daniel
HEYDARI-MALAYERI Mohammad
HILL Vanessa
HOSSEINI-KAZERONI Rémi
HUE Vincent
HUERTAS-COMPANY Marc
HUGOT Emmanuel
IBATA Rodrigo
IRINA Kovalenko
ISSAUTIER Karine
JEAN-BAPTISTE Ingrid
JOãO Fernandes
KATZ David
KERVELLA Pierre
KIEFER Flavien
KILBINGER Martin
KILICOGLU Tolgahan
KLEIN Karl-Ludwig
KNöDLSEDER Jürgen
KOECHLIN Laurent
KORDOPATIS Georges
KOUTCHMY Serge
KRAL Quentin
KRALJIC Katarina
KRETZSCHMAR Matthieu
KRIPS Melanie
LACHAUD Cyril
LACOUR Sylvestre
LADJELATE Bilal
LAGACHE Guilaine
LAGAGE Pierre-Olivier
LAGARDE Nadège
LALLEMENT Rosine
LANGER Mathieu
LANCON Ariane
LAPORTE Nicolas
LAROUR Jean
LAVIE Baptiste
LE BERTRE Thibaut
LE BOUQUIN Jean-Baptiste

LE CHAT Gaétan
LE COZ Sandra
LE FLOCH Bertrand
LE GAL Romane
LE PENNEC Maëlle
LE PONCIN-LAFITTE Christophe
LE SERGEANT D'HENDECOURT Louis
LEBRETON Yveline
LEBRETON Jérémy
LEFEVRE Charlène
LELEU Adrien
LELLOUCH Emmanuel
LEMASLE Bertrand
LEMOINE Martin
LESTRADE Jean-Francois
LE VAN SUU Auguste
LICITRA Rossella
LIGI ROXANNE
LION Sonny
LIQUE François
LOH Alan
LOPES Ilidio
LOPEZ SEPULCRE Ana
LOUVET Fabien
LUZ David
MACHADO Pedro
MAGGI Pierre
MALBET Fabien
MALZAC Julien
MAMON Gary
MARET Sébastien
MARIN Frédéric
MARQUES Miguel
MARSHALL Douglas
MARTIN Pierrick
MARTIN Nicolas
MARTINET Nicolas
MARTINS Fabrice
MARTRAIRE Diane
MATHIS Stéphane
MATHUR Savita
MATTER Alexis
MEI Simona
MELCHIOR Anne-Laure
MELIANI Zakaria
MICHEL Eric
MIROUH Giovanni
MOCHKOVITCH Robert
MODICA Paola
MOITINHO André
MONCEAU-BAROUX Rémi
MONIER Richard
MONTARGÈS Miguel
MONTMERLE Thierry
MORENO Raphael

MOSSER Benoît
MOUCHET Martine
MOURARD Denis
MUGNIER Laurent
NARDETTO Nicolas
NEINER Coralie
NESVADBA Nicole
NOVAK Jerome
OCVIRK Pierre
OLIVIER Marc
ORIEUX François
PAGANI Laurent
PAUMARD Thibaut
PERALTA Raphaël
PEROUX Celine
PERRAUT Karine
PERRONE Denise
PETIT Pascal
PETY Jérôme
PICHON Christophe
PIGNATALE Francesco Cristiano
PINTO Rui
PIRON Frédéric
PRUNET Simon
RAICHOOR Anand
RAJPUROHIT Arvind
RANC Clément
RAPIN William
RAYNAUD Raphaël
RECIO-BLANCO Alejandra
RÉVILLE Victor
REYLÉ Céline
RIEUTORD Michel
ROBERT Francois
ROBIN Annie
ROCCA VOLMERANGE Brigitte
RODRIGUEZ Sebastien
ROGER Thibaut
ROOS Orianne
ROUAN Daniel
ROYER Frédéric
SAHAL-BRÉCHOT Sylvie
SAKR Ziad
SALABERT David
SALOME Quentin
SALOMÉ Philippe
SALOMON Jean-Baptiste
SAMADI Réza
SANTERNE Alexandre
SCHANNE Stéphane
SCHüSSLER Fabian
SERVILLAT Mathieu
SIMONS Doug
SINGH Raj Laxmi
SNAITH Owain

SOMÉ Claire
SOTIRIADIS Sotiris
SOUBIRAN Caroline
SOUCAIL Geneviève
SOULAIN Anthony
SOULEZ Ferreol
STEHLE Chantal
STOLARCZYK Thierry
STRUGAREK Antoine
SULIS Sophia
TAILLIFET Esther
TALLON Michel
TCHANG-BRILLET Lydia
THUILLOT William
TOULI-LEBRETON Dimitra
TREBITSCH Maxime
TREMBLIN Pascal
TRIOU Henri
TUCKEY Phillip
TURCK-CHIEZE Sylvaine
TURCO-LIVERI Robert
TURON Catherine
VALDIVIA Valeska
VAN ELEWYCK Veronique
VAN ZUILEN Mark
VANGIONI Elisabeth
VARNIERE Peggy
VAUCLAIR Sylvie
VAUPRÉ Solenn
VENOT Olivia
VETOIS Jacques
VIBERT Didier
VILMER Nicole
VINCENT Frédéric
VRARD Mathieu
VUILLAUME Thomas
WANG Shaobo
WESTALL Frances
WIEDNER Martina
WIESENFELD Laurent
WOLF Peter
YUE Dong
ZABOROV Dmitry
ZAHN Jean-Paul
ZARKA Philippe

Session SF2A

Session Plénière

SF2A 2014
J. Ballet, F. Bournaud, F. Martins, R. Monier and C. Reylé (eds)

COMPLEX ORGANIC MOLECULES AND STAR FORMATION

A. Bacmann[1] and A. Faure[1]

Abstract. Star forming regions are characterised by the presence of a wealth of chemical species. For the past two to three decades, ever more complex organic species have been detected in the hot cores of protostars. The evolution of these molecules in the course of the star forming process is still uncertain, but it is likely that they are partially incorporated into protoplanetary disks and then into planetesimals and the small bodies of planetary systems. The complex organic molecules seen in star forming regions are particularly interesting since they probably make up building blocks for prebiotic chemistry. Recently we showed that these species were also present in the cold gas in prestellar cores, which represent the very first stages of star formation. These detections question the models which were until now accepted to account for the presence of complex organic molecules in star forming regions. In this article, we shortly review our current understanding of complex organic molecule formation in the early stages of star formation, in hot and cold cores alike and present new results on the formation of their likely precursor radicals.

Keywords: Stars: formation; Astrochemistry; ISM: molecules; ISM: abundances

1 Introduction

An important challenge in present day astrophysics is to understand the emergence of molecular complexity, from simple atoms and molecules to the richness of chemical species observed in the Solar System. During the low-mass star forming process, the interstellar gas evolves towards higher degrees of concentration and build up cores of denser matter. Some of these gravitationally bound cores, called prestellar cores, collapse under their own gravity and form one or several protostar(s). Protostars are still deeply embedded within their parent envelope and are in the process of accreting most of their mass. It is believed that even at a very young stage, they are surrounded by a disk, which becomes the birth place of planetesimals, (exo)planets, asteroids and cometary bodies in the later phases of the process, when the surrounding envelope has been either accreted or dispersed. During the star formation process, molecules present in the interstellar gas can therefore be formed, destroyed, or incorporated at the various stages, and it is therefore possible that part of the chemical species and molecular complexity that are seen nowadays on planets like the Earth are inherited from earlier phases and the interstellar medium.

Like in chemical science, organic molecules are defined in astrochemistry as molecules containing the atoms C, H, O or N. The definition of a complex molecule however is a lot more humble applied to the interstellar medium than to chemistry on Earth. Herbst & van Dishoeck (2009) suggested that molecules with 6 atoms can be considered as complex. In the interstellar medium, highly unsaturated molecules (carbon chains, cyanopolyynes) have long been observed, but more saturated, terrestrial like complex organic molecules are also found. These latter species typically include formamide NH_2CHO, acetaldehyde CH_3CHO, ethanol CH_3CH_2OH, dimethyl ether CH_3OCH_3, methyl formate CH_3OCHO or methanol CH_3OH. They currently draw much attention, as they are believed to be the building blocks for prebiotic chemistry. It is therefore of high interest to investigate where they are found in space and under which conditions, how they are formed, and how they evolve. In what follows, we will only concentrate on these terrestrial saturated molecules.

[1] Univ. Grenoble Alpes, CNRS, IPAG, F-38000 Grenoble, France

2 Complex organic molecules in the early phases of star formation

2.1 Observations of complex organic molecules

Complex organic molecules (hereafter COMs) have long been detected in the interstellar medium. The first detections date back to the 1970s, where molecules like acetaldehyde (Gottlieb 1973) or methyl formate (Brown et al. 1975) were seen towards the hot molecule-rich regions of Sgr B2 and Orion, where massive stars are forming. A decade later, spectral surveys in the millimeter range revealed that hot cores of massive star forming regions were characterized by the presence of a large variety of COMs (e.g. Sutton et al. 1985; Blake et al. 1987; Cummins et al. 1986). Continuous progress in the sensitivity of millimeter wave telescopes have led to an increase in the number of species detected in the interstellar medium. Whereas about 50 species had been detected in 1980, the inventory reaches over 180 species 35 years later, and molecules with up to 13 atoms have been detected (not including PAHs and fullerenes).

Spectral surveys in low-mass star forming regions have revealed a similar complex organics composition as in high-mass hot cores (van Dishoeck et al. 1995; Cazaux et al. 2003). Interferometric observations of low-mass protostars show that the COM emission originates from a compact region around the central source, corresponding to the area of warm dust and gas heated by the protostar, where ice mantles coating the grains have been evaporated (T$\sim$100 K). The resemblance with high-mass hot cores as far as contents and configuration are concerned led to the idea that COMs were characteristic of warm chemistry in young stellar objects.

2.2 Physical structure during the first stages of star formation and chemistry

In order to understand how molecules can form in low-mass star forming regions, it is necessary to determine the physical properties (density, temperature, UV radiation field, etc.) of the medium they are found in. The stage immediately before the protostar forms, the prestellar phase, is characterized by low temperatures (around 10 K), since there is no inner heating source, and moderate densities ($10^4 - 10^6\,\mathrm{cm}^{-3}$). The high extinction prevents interstellar UV radiation from penetrating inside the prestellar cores. As gravitational collapse proceeds, the density increases towards the centre of the object until it is high enough for a hydrostatic object to form. The newly-formed source heats up its surroundings, so that a temperature gradient is established between the outer envelope, where T is still around 10 K, towards the centre of the protostar. The hot core of the protostar is defined as the region where the temperature is above ~ 100 K.

The chemistry during these stages is largely influenced by the physical conditions. In cold pre-stellar cores, atoms and molecules present in the gas phase can stick to the dust grains upon collision with them. This opens up the possibility of grain surface chemistry, as the accreted atoms or simple molecules can react together to form more complex species. During the protostellar stage, two kinds of chemistry can take place: in the outer envelope, the conditions of density and temperatures are similar as in prestellar cores and the chemistry is also similar. As one approaches the protostar the density and temperature increase, and when the temperature reaches about 100 K in the hot core, ice mantles are evaporated in the gas-phase. The only chemistry which can take place is gas-phase chemistry, and since the central protostar emits UV, some photochemistry can be expected, as long as the opacities are not too large.

2.3 Complex organic molecule formation in hot cores

Two types of scenario have been invoked in order to account for the presence of COMs in protostellar hot cores. In the first scenario (e.g. Charnley et al. 1992), simple molecules and atoms are accreted during the prestellar phase (i.e. at 10 K) on the grains where they can be hydrogenated. After the protostar forms, the ices are evaporated above a temperature of 100 K, and the contents of the ice mantles are released into the gas-phase, where they can trigger new gas-phase reactions. For example, the methanol molecules formed in the ice mantle during the prestellar phase can be protonated by H_3^+ after they are desorbed, following: $CH_3OH + H_3^+ \rightarrow CH_3OH_2^+$. Protonated methanol $CH_3OH_2^+$ can then react with H_2CO and CH_3OH to form $HCOOCH_4^+$ (protonated methyl formate) and $CH_3OCH_4^+$ (protonated dimethyl ether), respectively. Upon dissociative recombination (i.e. the reaction of these positive ions with an electron), the protonated species can lose a proton to form $HCOOCH_3$ (methyl formate) and CH_3OCH_3 (dimethyl ether). Concerns that dissociative recombinations of large ions are inefficient to form COMs have emerged (e.g. Horn et al. 2004), as such energetic reactions most probably completely disrupt the parent ion into small fragments, and that the molecule obtained after the loss of a single proton is only a minor product (Geppert et al. 2006). Gas-phase scenarios are for this reason not currently favoured, but the issue is still debated, as all gas-phase chemical routes leading to COMs may not have been explored (Cole et al. 2012).

In the currently preferred second chemical scenario, COMs form entirely on grain surfaces (Garrod & Herbst 2006). During the prestellar phase, the chemistry does actually not differ from the previous scenario: simple atoms and molecules stick to the grains where they can be hydrogenated, even at temperatures as low as 10 K. The species present on the grains can be photodissociated by e.g. cosmic rays, thus giving rise to reactive radicals like HCO or CH_3O. Alternatively, these radicals, often intermediate products in the grain-surface hydrogenation of species like C or CO, can be trapped in the grain mantles and become unavailable for further hydrogenation (Taquet et al. 2012). When the protostar is formed and starts heating its surroundings, the gas and dust temperatures increase and heavy species become mobile on the grains (above $\sim$30 K). In particular, reactive radicals can diffuse on the surface and form more complex molecules (Garrod & Herbst 2006), following grain-surface routes like:

$$\mathrm{CH_3O + HCO \rightarrow CH_3OCHO}$$

$$\mathrm{CH_3 + CH_3O \rightarrow CH_3OCH_3}$$

Finally, those molecules as well as the whole contents of the ice mantle are evaporated into the gas-phase as the temperature keeps on rising (the temperatures at which it happens depends on the considered species, but above 100 K, all of the grain mantle should have desorbed).

3 Complex organic molecules in prestellar cores

As prestellar cores are the direct precursors of protostars studying their chemistry can bring valuable information on the initial conditions of protostellar chemistry. These sources are relatively simple in their structure: the density and temperature gradients are much shallower than in protostars, and they harbour no jet or outflow. Besides, they contain no inner energy source and their inner parts are well shielded from the interstellar radiation field (Av > 10), so that their inner temperatures are around (and often below) 10 K. Their chemistry is therefore dominated by barrierless ion-molecule reactions in the gas phase and accretion of species on the dust grains. Without thermal energy, only cosmic rays or secondary UVs induced by energetic electron collisions on H_2 molecules can help return some of the molecules into the gas phase.

In the view which prevailed until recently and which we highlighted in the previous section, complex organic molecules were not expected to be formed in prestellar cores, due to the very low temperatures precluding radical mobility on the grains. The exception to this is methanol, which is easily observed even in the very cold gas (Friberg et al. 1988; Tafalla et al. 2006). Methanol formation is thought to be inefficient in the gas-phase (as it results from the dissociative recombination of $CH_3OH_2^+$, in which the product branching ratio for CH_3OH is only 3% − Geppert et al. 2006), but it can form on grain surfaces by successive hydrogenations of CO on the grains. This mechanism has been shown in the laboratory to be efficient even at 10 K (Watanabe & Kouchi 2002). Unlike heavier species like e.g. HCO, H atoms are very mobile on grains at low temperatures and can scan the whole surface of the grains many times before they evaporate back to the gas phase (Tielens & Hagen 1982).

A search for terrestrial complex organic molecules in the prestellar core L1689B has shown the presence of several saturated O-bearing COMs: CH_3CHO, CH_3OCH_3, CH_3OCHO and CH_2CO (Bacmann et al. 2012). A spectral survey in the cold source B1-b carried out by Cernicharo et al. (2012) has revealed a similar richness in terrestrial organic molecules. The temperature in L1689B is close to 10 K (Redman et al. 2004), much lower than the temperature above which heavy radicals can diffuse on grain surfaces. The temperature in B1-b is also reported to be around 15 K by Cernicharo et al. (2012). These detections therefore cast doubts on the mechanisms previously proposed to explain the formation of COMs on grain surfaces. In any case, those mechanisms cannot apply to cold gas and prestellar cores.

4 How can COMs form at 10 K?

4.1 Grain surfaces

In prestellar cores, thermal energy is not sufficiently available to provide heavy radicals with enough mobility to diffuse on the grains, nor is it sufficient to desorb molecules from the grains back into the gas phase. However, molecules like CH_3OH which are believed to form solely on grain surfaces, are seen in the gas phase, so that other, non-thermal mechanisms which play a role in molecular desorption might also bring the needed energy to provide the mobility to the radicals. Cosmic ray impacts are likely candidates, as well as secondary UVs - which are by-products of cosmic ray impacts on H_2 molecules that get ionized and generate energetic electrons that excite H_2. Laboratory experiments (Gerakines et al. 1996) have shown that complex organic molecules can be formed at low temperatures by UV irradiation of methanol ices.

Quantitatively however, it is still uncertain whether these processes can reproduce the abundances of COMs observed in cold clouds. The parameters involved (cosmic ray spectrum in cores, energy deposited in the grains, energy available for diffusion and evaporation), remain very poorly constrained.

4.2 Gas phase

The detection of COMs in the cold gas has revived the interest for gas-phase formation mechanisms, and new chemical routes have been proposed by Vasyunin & Herbst (2013). Exothermic reactions between species on the grains can desorb species into the gas phase, including radicals. The desorbed species can then react together in the gas phase to form COMs or their protonated counterparts following various mechanisms: neutral-neutral reactions, protonation reactions, ion-molecule reactions. Vasyunin & Herbst (2013) suggest that radiative associations such as $CH_3O + CH_3 \rightarrow CH_3OCH_3 + h\nu$ as new possibilities to form COMs. The rate coefficients for these reactions have for the most part not been measured at 10 K and the efficiency of the concerned reactions is therefore uncertain. Another uncertainty factor comes from the reactive desorption efficiency, i.e. the yield of molecular desorption triggered by chemical reactions on the grains, which is unknown.

4.3 Comparison with observations

The gas-phase model of Vasyunin & Herbst (2013) gives the evolution with time of the abundances of several COMs detected in L1689B. The abundances of CH_3OCH_3 and CH_3CHO, which are around 10^{-10} in the source can be simultaneously reproduced by the model for an age of around 5 10^5 years, which is consistent with typical lifetimes of prestellar cores ($\sim 10^6$ years). In order to account for the abundance of these two species, an efficiency of 10% for the reactive desorption has to be assumed. With this rate however, the model overproduces the abundance of CH_3OH by nearly 2 orders of magnitude. For CH_3OCHO, the model cannot reproduce the observed abundance at any time by at least an order of magnitude. Although this model represents an improvement over previous attempts to account for gas-phase formation of COMs, many parameters/rate coefficients still need to be measured at 10 K in order to confirm whether the proposed new reactions are indeed efficient enough.

4.4 COM precursors

Radicals like HCO and CH_3O are believed to play an important role in the synthesis of complex organics. On grain-surfaces, they are intermediate products in the hydrogenation of CO leading to CH_3OH:

$$\mathrm{CO} \xrightarrow{\mathrm{H}} \mathrm{HCO} \xrightarrow{\mathrm{H}} \mathrm{H_2CO} \xrightarrow{\mathrm{H}} \mathrm{CH_3O} \xrightarrow{\mathrm{H}} \mathrm{CH_3OH}$$

In COM formation schemes like those of Garrod & Herbst (2006), HCO and CH_3O are direct precursors of species like CH_3OCHO of CH_3OCH_3. They might also be direct precursors of some COMs in the gas phase, as suggested by Vasyunin & Herbst (2013).

We have observed these two radicals in a sample of 8 prestellar cores from different star-forming regions (Bacmann & Faure 2015). Both species are widely present in the gas-phase of prestellar cores: HCO is detected in all the sources and CH_3O in half of them, as its lines are very weak. Spectra of HCO and CH_3O in the prestellar core L1689B are shown in Fig. 1. Absolute abundances vary by about one order of magnitude between the various sources, but the abundance ratios between the species are remarkably similar. We find that the abundance ratios HCO : H_2CO : CH_3O : CH_3OH are close to 10 : 100 : 1 : 100. Such ratios cannot be accounted for by the model of Vasyunin & Herbst (2013): in the model, the abundances of H_2CO and CH_3OH are similar only at steady-state, but at steady-state the CH_3OH, H_2CO and CH_3O abundances are one to two orders of magnitude higher than observed.

New laboratory experiments have recently shown that the neutral-neutral reaction $CH_3OH + OH \rightarrow CH_3O + H_2O$ accelerates when the temperature decreases from 200 K to about 50 K, and is fast despite having a barrier (Shan-

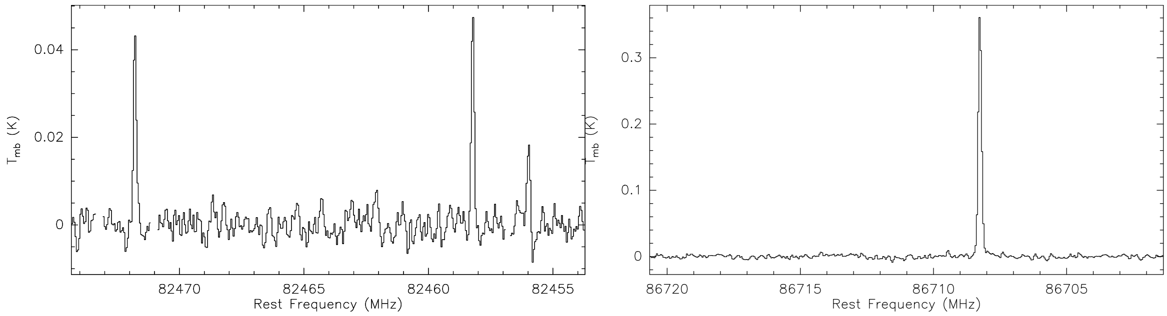

Fig. 1. Left: CH_3O spectrum in the core L1689B. **Right:** HCO spectrum in L1689B

non et al. 2014; Gómez-Martín et al. 2014). As OH is abundant in the interstellar medium (about $\sim 10^{-8}$ with respect to $H_2 -$ Crutcher 1979), this reaction may provide an efficient way to form CH_3O in the gas-phase. Assuming that CH_3O is formed in the gas phase by the above reaction and destroyed by reactions with proton donours such as H_3^+, we find that the abundance ratio $[CH_3O]/[CH_3OH]$ is 10^{-3} at steady-state, one order of magnitude below the observed abundance ratio. In order to derive this, we assumed that the reaction rate for the formation of CH_3O at 10 K is the value given by Gómez-Martín et al. (2014) ($k_{form} = 5\ 10^{-11}\,cm^3s^{-1}$) and that the reaction rate for its destruction is around $k_{destr} = 5\ 10^{-8}\,cm^3s^{-1}$. We have also assumed that the OH abundance is 10^{-8} with respect to H_2 (Crutcher 1979; Troland & Crutcher 2008), as is the proton donour abundance (Flower et al. 2005, 2006). Neutral-neutral reactions are therefore not fast enough to account for the CH_3O abundance in prestellar cores.

Faster formation routes for CH_3O can be provided by ion-molecule reactions with CH_3OH as a precursor. A likely formation pathway would be $CH_3OH + H_3^+ \rightarrow CH_3OH_2^+ + H_2$ followed by the dissociative recombination $CH_3OH_2^+ + e^- \rightarrow CH_3O + H_2$. The protonation of methanol can give several products and it is estimated that the branching ratio for protonated methanol $CH_3OH_2^+$ is about 25% (KIDA database). The dissociative recombination of protonated methanol also yields several products, and the branching ratio for CH_3O has been measured to be 6% (Geppert et al. 2006). Given these numbers and the measured reaction rate for the dissociative recombination, the abundance ratio estimated at steady-state is: $[CH_3O]/[CH_3OH] \sim 0.01$. This is consistent with the observed abundance ratio. Similar reactions between H_3^+ and H_2CO can account for the $[HCO]/[H_2CO]$ abundance ratio. Gas phase ion molecule processes seem able to account for the presence and abundances of the HCO and CH_3O in the gas phase. We stress however that our model relies on microphysics quantities, which for some of them have not been measured in the laboratory.

5 Conclusions

Star forming regions are rich in complex organic molecules from their earliest evolutionary stages. Terrestrial complex organic molecules, which were long believed to be characteristic of the warm/hot gas surrounding both low- and high-mass young stellar objects, are now being detected in the gas-phase of cold prestellar cores (T$\sim$ 10 K). These new detections pose a new challenge in regions where little thermal energy is available for chemical reactions on grain surfaces, and where external UV field do not penetrate because of the high visual extinctions. Grain-surfaces might still play a role in COM synthesis provided the energy necessary for radical formation/diffusion (and molecule desorption) either comes from photoprocesses (cosmic rays, secundary UV radiation) or has a chemical origin. Grain surface chemistry introduces many unconstrained parameters and reliable quantitative predictions are not yet available. Gas-phase chemical models have started including new reactions which leads to better agreements with the observations, although the suggested new processes have not been measured in the laboratory at the relevant temperatures. Finally, our new observations have shown that the abundances of HCO and CH_3O radicals, which are thought to be precursors of COMs, can be accounted for by pure gas-phase processes.

References

Bacmann, A., Taquet, V., Faure, A., Kahane, C., & Ceccarelli, C. 2012, Astronomy & Astrophysics, 541, L12

Blake, G. A., Sutton, E. C., Masson, C. R., & Phillips, T. G. 1987, Astrophysical Journal, 315, 621

Brown, R. D., Crofts, J. G., Godfrey, P. D., et al. 1975, Astrophysical Journal, 197, L29

Cazaux, S., Tielens, A. G. G. M., Ceccarelli, C., et al. 2003, The Astrophysical Journal, 593, L51

Cernicharo, J., Marcelino, N., Roueff, E., et al. 2012, The Astrophysical Journal Letters, 759, L43

Charnley, S. B., Tielens, A. G. G. M., & Millar, T. J. 1992, Astrophysical Journal, 399, L71

Cole, C. A., Wehres, N., Yang, Z., et al. 2012, The Astrophysical Journal Letters, 754, L5

Crutcher, R. M. 1979, Astrophysical Journal, 234, 881

Cummins, S. E., Linke, R. A., & Thaddeus, P. 1986, Astrophysical Journal Supplement Series (ISSN 0067-0049), 60, 819

Flower, D. R., Forêts, G. P. D., & Walmsley, C. M. 2005, Astronomy and Astrophysics, 436, 933

Flower, D. R., Forêts, G. P. D., & Walmsley, C. M. 2006, Astronomy and Astrophysics, 449, 621

Friberg, P., Hjalmarson, A., Madden, S. C., & Irvine, W. M. 1988, Astronomy and Astrophysics (ISSN 0004-6361), 195, 281

Garrod, R. T. & Herbst, E. 2006, Astronomy and Astrophysics, 457, 927

Geppert, W. D., Hamberg, M., Thomas, R. D., et al. 2006, Chemical Evolution of the Universe, 133, 177

Gerakines, P. A., Schutte, W. A., & Ehrenfreund, P. 1996, Astronomy and Astrophysics, 312, 289

Gómez-Martín, J., Caravan, R., Blitz, M., Heard, D., & Plane, J. 2014, J. Phys. Chem. A, 118, 2693

Gottlieb, C. A. 1973, Molecules in the Galactic Environment, 181

Herbst, E. & van Dishoeck, E. F. 2009, Annual Review of Astronomy & Astrophysics, 47, 427

Horn, A., Møllendal, H., Sekiguchi, O., et al. 2004, The Astrophysical Journal, 611, 605

Redman, M. P., Keto, E., Rawlings, J. M. C., & Williams, D. A. 2004, Monthly Notices of the Royal Astronomical Society, 352, 1365

Shannon, R. J., Cossou, C., Loison, J.-C., et al. 2014, eprint arXiv, 1406, 1363

Sutton, E. C., Blake, G. A., Masson, C. R., & Phillips, T. G. 1985, Astrophysical Journal Supplement Series (ISSN 0067-0049), 58, 341

Tafalla, M., Santiago-García, J., Myers, P. C., et al. 2006, Astronomy and Astrophysics, 455, 577

Taquet, V., Ceccarelli, C., & Kahane, C. 2012, Astronomy & Astrophysics, 538, 42

Tielens, A. G. G. M. & Hagen, W. 1982, Astronomy and Astrophysics, 114, 245, a&AA ID. AAA032.131.203

Troland, T. H. & Crutcher, R. M. 2008, The Astrophysical Journal, 680, 457

van Dishoeck, E. F., Blake, G. A., Jansen, D. J., & Groesbeck, T. D. 1995, Astrophysical Journal v.447, 447, 760

Vasyunin, A. I. & Herbst, E. 2013, The Astrophysical Journal, 769, 34

Watanabe, N. & Kouchi, A. 2002, The Astrophysical Journal, 571, L173

SF2A 2014
J. Ballet, F. Bournaud, F. Martins, R. Monier and C. Reylé (eds)

TRACING PDR PROPERTIES AND STRUCTURE IN THE CLOSEST MASSIVE LOW METALLICITY STAR-FORMING REGION: 30 DORADUS IN THE LMC

M. Chevance[1], S. Madden[1], V. Lebouteiller[1], L. Carlson[2], D. Cormier[3], F. Galliano[1], M.-Y. Lee[1] and R. Wu[4]

Abstract. More complete knowledge of galaxy evolution requires understanding the process of star formation and interaction between the interstellar radiation field and the ISM in galactic environments traversing a wide range of physical parameter space. Here we focus on the impact of star formation on the surrounding low metallicity ISM. Indeed, lowering the metal abundance, as is the case of some galaxies of the early universe, results in an overall lower galactic dust reservoir, hence, less shielding for the formation of the molecular gas necessary for star formation to proceed. A convenient laboratory to zoom into the various phases of the ISM to study the effects of low metallicity on the ISM properties, is our nearest neighbor, the Large Magellanic Cloud, which has a metallicity 1/2 that of solar. The goal is to construct a comprehensive, self-consistent picture of the density, radiation field, and ISM structure in the vicinity of one of the most massive star clusters in our local neighborhood, R136.

Keywords: ISM: individual objects (30 Doradus nebula) – Magellanic Clouds – ISM: structure

1 Introduction

We present *Herschel* spectroscopic data of 30 Doradus (hereafter 30Dor) in the Large Magellanic Cloud (LMC), one of the most active star forming region in our local universe. At a distance of only 50 kpc (Walker 2011), the LMC allows us to have a high spatial resolution view in a low metallicity environment ($\sim 1/2$ solar ; Rolleston et al. 2002; Pagel 2003). We investigate the consequences of reduced metallicity on the heating and cooling mechanisms of the gas, particularly in the photo-dissociation regions (PDRs) where the chemistry and thermal balance are regulated by far-ultraviolet photons (6eV$< h\nu <$13.6eV). In particular, the transition $C^+/C/CO$ can be altered from what we see in galactic regions (Kaufman et al. 1999) and the value of the conversion factor of CO to H_2, the X factor, can be affected. We interpret our observations of the 30Dor region with a PDR model to deduce the physical parameters and the structure of the gas around the massive stellar cluster R136.

2 Observations

2.1 PACS spectoscopy data

We have mapped the five fine structure lines, [CII] 157 μm, [NII] 122 μm, [OI] 63 μm, [OI] 145 μm and [OIII] 88 μm using the PACS spectrometer (Poglitsch et al. 2010) on board *Herschel*. These observations are part of the *Herschel* key program, SHINNING (P.I. E. Sturm), described in Madden et al. (2013), and OT2 (Indebetouw et al.). The different layers of the gas from the highly ionized medium near the star cluster R136, and deeper into the molecular gas can be identified in Fig. 1

The PACS array is composed of 5×5 spatial pixels, covering a total field of view of 47″. A region of approximately $4' \times 5'$ of 30Dor ($\sim$ 56 pc $\times$70 pc) was covered by *Herschel*, with a resolution of 9.5″ to 12″. The data reduction is done with the *Herschel* Interactive Processing Environment (HIPE) v12.0.0 (Ott 2010) from Level 0 to Level 1 and then with PACSman v3.61 (Lebouteiller et al. 2012) to fit the lines and make the maps.

[1] Laboratoire AIM, CEA Saclay, 91191 Gif-sur-Yvette, France
[2] Leiden Observatory, Leiden, Netherlands
[3] Institut für theoretische Astrophysik, Zentrum für Astronomie der Universität Heidelberg, D-69120 Heidelberg, Germany
[4] Department of Astronomy, Graduate School of Science, University of Tokyo, Tokyo, Japan

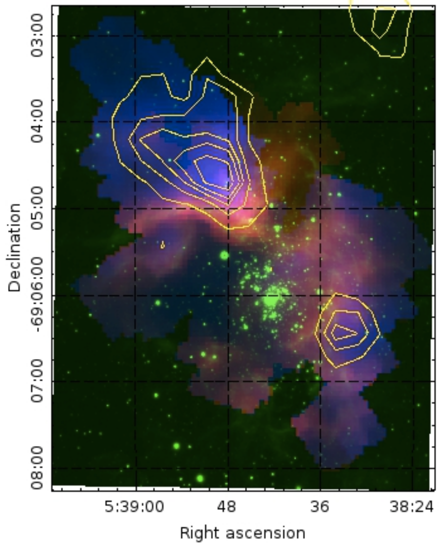

Fig. 1. Three-color image of the 30 Doradus nebula. Red: PACS [OIII] 88 μm. Blue: PACS [CII] 157 μm. Green: VISTA J band. Yellow contours: ^{12}CO(3-2) emission observed with ASTE (Minamidani et al. 2011).

As all of these tracers have different ionization energies and different critical densities, at this resolution we can distinguish different layers of the ionization and neutral structure. We note that the [OIII] emission is very extended, peaks closer to the star cluster than the [CII] emission and is everywhere brighter than [CII] 157 by a factor of 3 to 60. Both [OI] emission lines are PDR tracers and follow the emission of [CII]. The [NII] map is much smaller than the others since the line is very faint, often almost 10 times lower than [CII], but the signal to noise ratio is still larger than 6 everywhere on the map. All the maps are convolved to the resolution of PACS at 160 μm (12.3″), using the kernels from Aniano et al. (2011).

2.2 SPIRE FTS data

The SPIRE instrument includes an Imaging Fourier Transform Spectrometer (FTS) covering the 194-671 μm bandwidth. The [NII] 205 μm and [CI] 370 and 609 μm emission lines were observed in 30Dor with intermediate sampling. The data reduction is described in Lee et al. (in prep).

CO transitions from J = 4 − 3 to J = 13 − 12, also observed in 30Dor, are presented in Lee et al. (in prep).

2.3 Photometry data

PDR models explain the correlations observed between the energy emerging in the FIR cooling lines and the infrared continuum from dust. We use PACS and SPIRE photometry data to derive the total infrared luminosity. PACS and SPIRE maps of the Large Magellanic Cloud at 100, 160 250, 350 and 500 μm were first published in Meixner et al. (2013) as part of the HERITAGE project. We also use the *Spitzer* observations of 30Dor at 24 and 70 μm presented in Indebetouw et al. (2009) to construct the spectral energy distribution (SED).

We have applied the dust SED model of Galliano et al. (2011) to the *Spitzer* MIPS and *Herschel* PACS and SPIRE photometry to explain the observed continuum and to derive the L_{FIR}.

3 Tracing the PDRs

[NII] is a tracer of the low excitation diffuse gas. The critical densities for [NII] 122 μm and [NII] 205 μm are 310 cm^{-3} and 50 cm^{-3} respectively, making the ratio [NII] 122/[NII] 205 a good density tracer. We determine the density using the ratio of [NII] 122/[NII] 205 and the theoretical curve from Bernard-Salas et al. (2012) (Fig. 2). The calculated density ranges from 100 to 600 cm^{-3}. These values are consistent with the density calculated from the [SIII] 18/[SIII] 33 ratio, although this ratio is normally more sensitive to higher densities due to higher critical densities for the [SIII] lines ($n_{crit} = 1.5 \times 10^4$ cm^{-3} for [SiII] 18 μm and $n_{crit} = 4.1 \times 10^3$ cm^{-3} for [SiII] 33 μm).

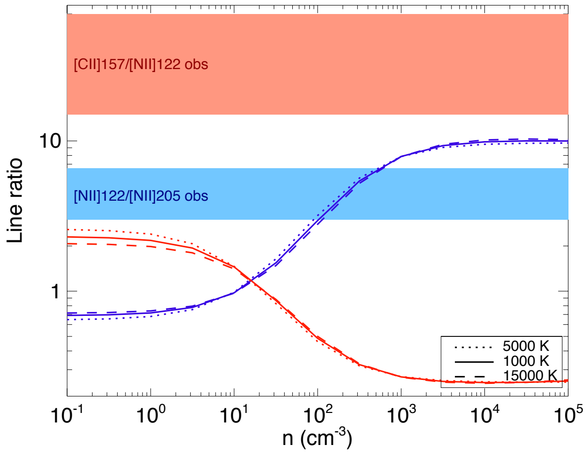

Fig. 2. Theoretical ratios [NII] 122 μm /[NII] 205 μm (blue) and [CII] 157 μm /[NII] 122 μm (red) at temperature 5000 K (dotted line), 10000 K (solid line) and 15000 K (dashed line). Blue and red areas indicate the observed values for the [NII] 122 μm /[NII] 205 μm and the [CII] 157 μm /[NII] 122 μm ratios respectively.

The range of density we find across 30Dor implies a theoretical ratio in the ionized gas of [CII] 157/[NII] 122 $\sim 0.3 - 0.5$ (Fig. 2). However, the observed ratio is significantly higher than this theoretical ratio in the ionized gas, indicating that most of [CII] is emitted in PDRs. At least 80% of the [CII] 157 is expected to be emitted from PDRs in this region. The [CII] emission can be considered a reliable tracer of the PDRs in 30Dor and used as a constraint for the PDR models.

4 PDR modeling

4.1 The Meudon PDR code

Tielens & Hollenbach (1985) showed that the emission from PDRs could be parametrized by the cloud density n and the strength of the UV radiation field illuminating the cloud G_{UV} (in units of the Habing Field, 1.6×10^{-3} ergs cm^{-2} s^{-1}). We use the Meudon PDR code (`http://pdr.obspm.fr/`), describe in Le Petit et al. (2006) to determine these two parameters, using the observational constraints described earlier. This model computes the atomic and molecular structure of interstellar clouds. It considers a 1D stationary plane parallel slab of gas and dust illuminated by a radiation field (from UV to radio) originating from one side of the cloud. The radiative transfer is solved in an iterative way at each point of the cloud as well as absorption by gas and dust and scattering and emission by dust.

We compute a grid of models with a density range from 10^2 to 10^5 cm^{-3} and an incident UV radiation field from 1 to 10^4 on one side (and fixed to 1 on the other side). We fixed the metallicity to half-solar and the total extinction of the cloud to $A_{V,tot} = 30$. We run a constant density model.

4.2 Results

Fig. 3 (left panel) presents the values of G_{UV} and n that reproduce the observed values for the ratios $\frac{[OI]145+[CII]157}{L_{FIR}}$, $\frac{[OI]145}{[CII]157}$, $\frac{[CI]370}{[CI]609}$ and $\frac{[OI]63}{[CII]157}$ for each of the $30'' \times 30''$ pixel of the map of 30Dor. The best solutions for the incident radiation field G_{UV} and the density n, are determined by the minimum of the χ^2 distribution: $\chi^2 = \sum_{i=1}^{N} \frac{D_i(x,y)-M_i}{\sigma_i(x,y)}$, where $D_i(x,y)$ is the observed value of the ratio i for a given pixel (x,y), $\sigma_i(x,y)$ is the uncertainty on this observed ratio and M_i is the value predicted by the model for the ratio i. N is the number of constrains (independent ratios) that are used. The best n and G_{UV} maps are presented on Fig. 3 (middle and right pannels).

The ratio $\frac{[OI]63}{[CII]157}$ is not used as a constraint with the other ratios, due to the fact that [OI] 63 μm can be optically thick (Tielens & Hollenbach 1985; Abel et al. 2007) or can be subject to absorption by cold gas on the line of sight (Liseau et al. 2006).

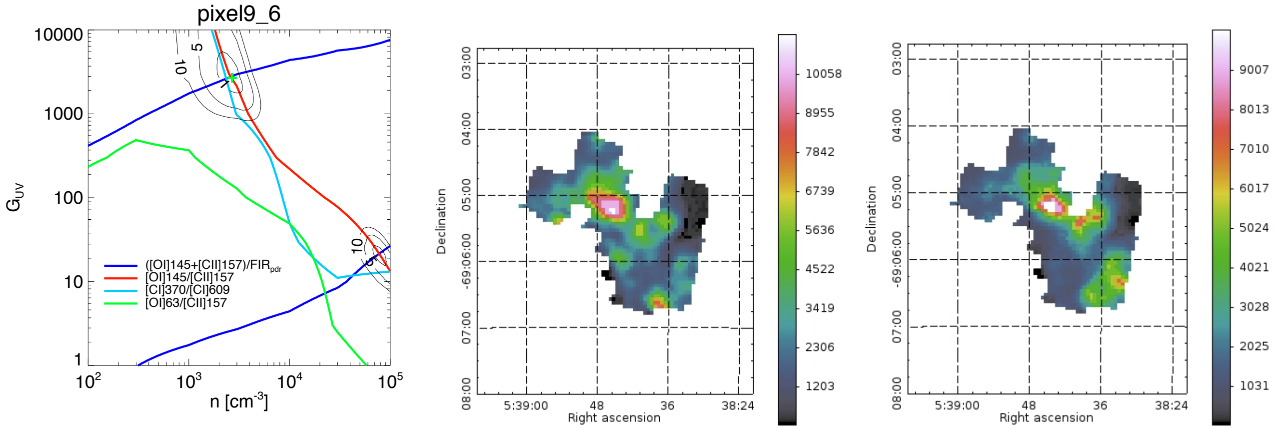

Fig. 3. Left: In colors, contour plot showing the sets of parameters G_{UV} and n able to reproduce the observed values of the ratios $\frac{[\text{OI}]145+[\text{CII}]157}{L_{FIR}}$ (dark blue), $\frac{[\text{OI}]145}{[\text{CII}]157}$ (red), $\frac{[\text{CI}]370}{[\text{CI}]609}$ (light blue) and $\frac{[\text{OI}]63}{[\text{CII}]157}$ (green). The black contours represent the values of the χ^2 . **Middle:** Best density map (in cm^{-3}) of the 30 Doradus region calculated from a chi square model, using ([OI]145+[CII]157)/ L_{FIR} and [OI]145/[CII]157 as constraints. **Right:** Same, for the incident radiation field G_{UV} (in units of the Habing field).

5 Conclusions

We used *Herschel* PACS and SPIRE observations to constrain a PDR model and determine the physical parameters of the gas in the 30 Doradus region in the LMC. We find a range of densities of $\sim 10^3 - 10^4$ cm and a range of incident radiation field $G_{UV} \sim 10^3 - 10^4$ with the Meudon PDR code.

We find that the ratios of lines that are not co-spatial (such as [CII]/[CI] or [CII]/CO) are not consistent with these solutions . For example, the observed values of the ratios [CII]/CO 1-0 and [CII]/CO 3-2 are much higher than the values predicted by the model. We can explain that by a lower total extinction of the cloud. This will be described in Chevance et al. (in prep).

References

Abel, N. P., Sarma, A. P., Troland, T. H., & Ferland, G. J. 2007, The Astrophysical Journal, 662, 1024

Aniano, G., Draine, B. T., Gordon, K., & Sandstrom, K. M. 2011, Publications of the Astronomical Society of the Pacific, 123, 1218

Bernard-Salas, J., Habart, E., Arab, H., et al. 2012, Astronomy & Astrophysics, 538, A37

Galliano, F., Hony, S., Bernard, J.-P., et al. 2011, Astronomy & Astrophysics, 536, A88

Indebetouw, R., de Messières, G. E., Madden, S. C., et al. 2009, The Astrophysical Journal, 694, 32

Kaufman, M. J., Wolfire, M. G., Hollenbach, D. J., & Luhman, M. L. 1999, ApJ, 527, 795

Le Petit, F., Nehme, C., Le Bourlot, J., & Roueff, E. 2006, The Astrophysical Journal Supplement Series, 164, 506

Lebouteiller, V., Cormier, D., Madden, S. C., et al. 2012, Astronomy & Astrophysics, 548, A91

Liseau, R., Justtanont, K., & Tielens, A. G. G. M. 2006, Astronomy and Astrophysics, 446, 561

Madden, S. C., Rémy-Ruyer, A., Galametz, M., et al. 2013, Publications of the Astronomical Society of the Pacific, 125, 600

Meixner, M., Panuzzo, P., Roman-Duval, J., et al. 2013, The Astronomical Journal, 146, 62

Ott, S. 2010, Astronomical Data Analysis Software and Systems XIX, 434, 139

Pagel, B. E. J. 2003, in Astronomical Society of the Pacific Conference Series, Vol. 304, CNO in the Universe, ed. C. Charbonnel, D. Schaerer, & G. Meynet, 187

Poglitsch, A., Waelkens, C., Geis, N., et al. 2010, Astronomy and Astrophysics, 518, L2

Rolleston, W. R. J., Trundle, C., & Dufton, P. L. 2002, Astronomy and Astrophysics, 396, 53

Tielens, a. G. G. M. & Hollenbach, D. J. 1985, The Astrophysical Journal

Walker, A. R. 2011, Astrophysics and Space Science, 341, 43

SF2A 2014
J. Ballet, F. Bournaud, F. Martins, R. Monier and C. Reylé (eds)

USING THE VIRTUAL OBSERVATORY: MULTI-INSTRUMENT, MULTI-WAVELENGTH STUDY OF HIGH-ENERGY SOURCES

S. Derrière[1], R. W. Goosmann[1], C. Bot[1] and F. Bonnarel[1]

Abstract. This paper presents a tutorial explaining the use of Virtual Observatory tools in high energy astrophysics. Most of the tools used in this paper were developed at the Strasbourg astronomical Data Center and we show how they can be applied to conduct a multi-instrument, multi-wavelength analysis of sources detected by the High Energy Stereoscopic System and the Fermi Large Area Telescope. The analysis involves queries of different data catalogs, selection and cross-correlation techniques on multi-waveband images, and the construction of high energy color-color plots and multi-wavelength spectra. The tutorial is publicly available on the website of the European Virtual Observatory project[*].

Keywords: Virtual Observatory, high energy astrophysics, data mining, H.E.S.S., Fermi-LAT

1 Introduction

The Virtual Observatory (VO) offers a vast set of tools[†] to explore archival observational data at almost all observable wavelengths. In this note, we illustrate the capacities of the VO in the gamma ray domain. We provide a step-by-step tutorial to walk the reader through the application of data mining tools as well as cross-matching procedures involving observational data from other wavebands. The user may explore how to...

- ...query astronomical catalogs in different gamma-ray bands using VO tools
- ...cross-correlate catalogs to find an object at different photon energy bands
- ...apply selection criteria when extracting sources from a catalog
- ...use the observational measures of the selected objects to explore possible correlations
- ...visualize astronomical images from the radio up to the high energy domain
- ...display spectral energy distributions obtained from different photometric data sets

2 Source catalogs in the H.E.S.S. and the Fermi-LAT energy bands

2.1 Exploring the gamma ray sky from the ground and from space

The *High Energy Stereoscopic System (H.E.S.S.)* is a ground-based gamma-ray observatory originally consisting of four optical Cherenkov telescopes. They are situated on top of the Gamsberg mountain in Namibia[‡] and detect air showers triggered by gamma ray photons in the energy range of 10s of GeV to 10s of TeV. The latest upgrade of the observatory came in summer 2012 when a fifth, larger telescope was added to constitute H.E.S.S. II.

[1] Observatoire Astronomique de Strasbourg, Université de Strasbourg, CNRS, UMR 7550, 11 rue de l'Université, 67000 Strasbourg, France
[*] http://www.euro-vo.org/?q=science/scientific-tutorials
[†] http://www.ivoa.net/astronomers/applications.html
[‡] http://www.mpi-hd.mpg.de/hfm/HESS

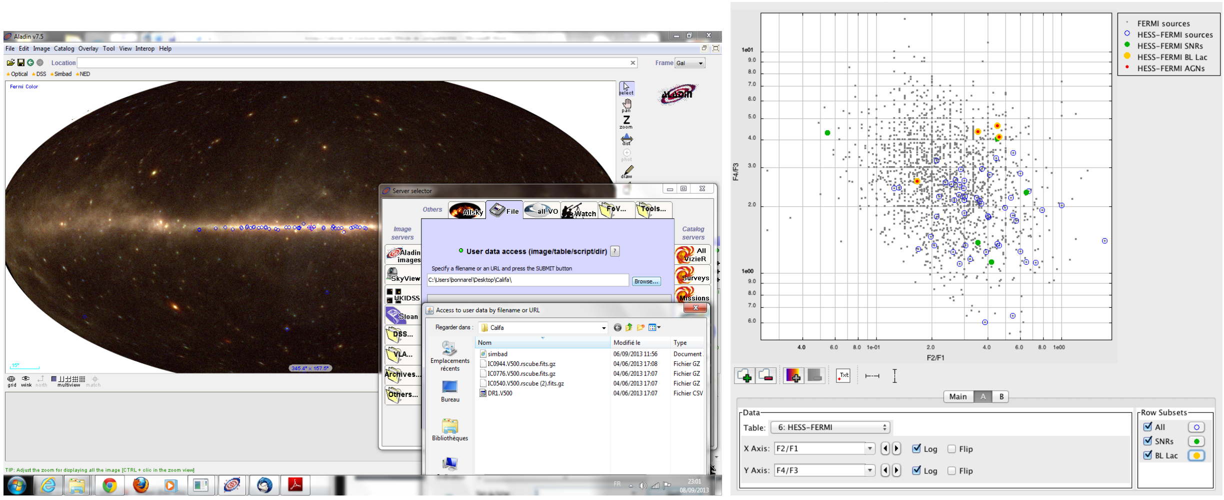

Fig. 1. Left: overlay of the H.E.S.S. source catalog and the second Fermi-LAT catalog in Aladin. Right: Cross-matching between the H.E.S.S. and Fermi-LAT catalogs and identification of individual source classes in a "high-energy color-color plot" in TOPCAT.

The *Fermi Gamma-ray Space Telescope* is a space-borne X-ray/gamma-ray observatory detecting sources in an energy range of 8 keV up to more than 300 GeV[§]. It carries two instruments, the *Glast burst monitor* reporting gamma ray bursts and the *Fermi Large Area Telescope (Fermi-LAT)* observing the transient gamma ray sky across a large field of view. The satellite was launched in 2008.

Both observatories are complementary in studying the non-thermal universe. Thermal heating processes can produce at maximum X-ray radiation up to a few keV. Beyond these photon energies, the radiation must be produced by nuclear processes or accelerated particles, for instance in shocks or magnetic reconnection events. The list of objects radiating in the gamma ray sky includes supernovae, pulsars, astrophysical jets in active galactic nuclei or X-ray binaries, gamma ray bursts, and our sun.

2.2 H.E.S.S., Fermi-LAT and the Virtual Observatory

For both *H.E.S.S.* and *Fermi-LAT*, public catalogs of observed sources have been compiled (Carrigan et al. 2013; Gasparrini et al. 2012) and can be queried with the help of VO tools. It is the ultimate goal of the VO to grant access to the whole body of astronomical observations at all wavebands. Therefore, a unifying and versatile data format was developed, the *VOTable* format (Ochsenbein et al. 2011). *VOTable* is an XML-based standard allowing to embed both tabular data and the corresponding metadata (e.g. column description) in a single file. Most VO-compliant data tools are able to understand and provide outputs in *VOTable* format. This way, the interoperability between different tools and wavebands can be assured.

The step-by-step tutorial summarized in the following sections makes great use of the *VOTable* format. We illustrate only the main steps, of which a complete and more detailed version can be found on the web[¶].

3 Cross-matching H.E.S.S. and Fermi-LAT to identify multi-wavelength sources

We start by investigating the H.E.S.S. source catalog looking for counterparts of the H.E.S.S. objects in the second Fermi-LAT catalog. The H.E.S.S. catalog is queried using the SIMBAD portal and the result is saved in a *VOTable*. The table can then be loaded into the Aladin tool (CDS 2011; Boch et al. 2011) dedicated to the analysis of astronomical images. In Aladin it is possible to project the list of H.E.S.S. sources onto the Fermi-LAT sky (see Fig. 1).

The 1873 Fermi-LAT sources are loaded in TOPCAT (Taylor 2011) by querying the VizieR catalogue service (Landais and Ochsenbein 2012). We broadcast the H.E.S.S. sources from Aladin to TOPCAT using the SAMP

[§]http://fermi.gsfc.nasa.gov
[¶]http://www.euro-vo.org/?q=science/scientific-tutorials

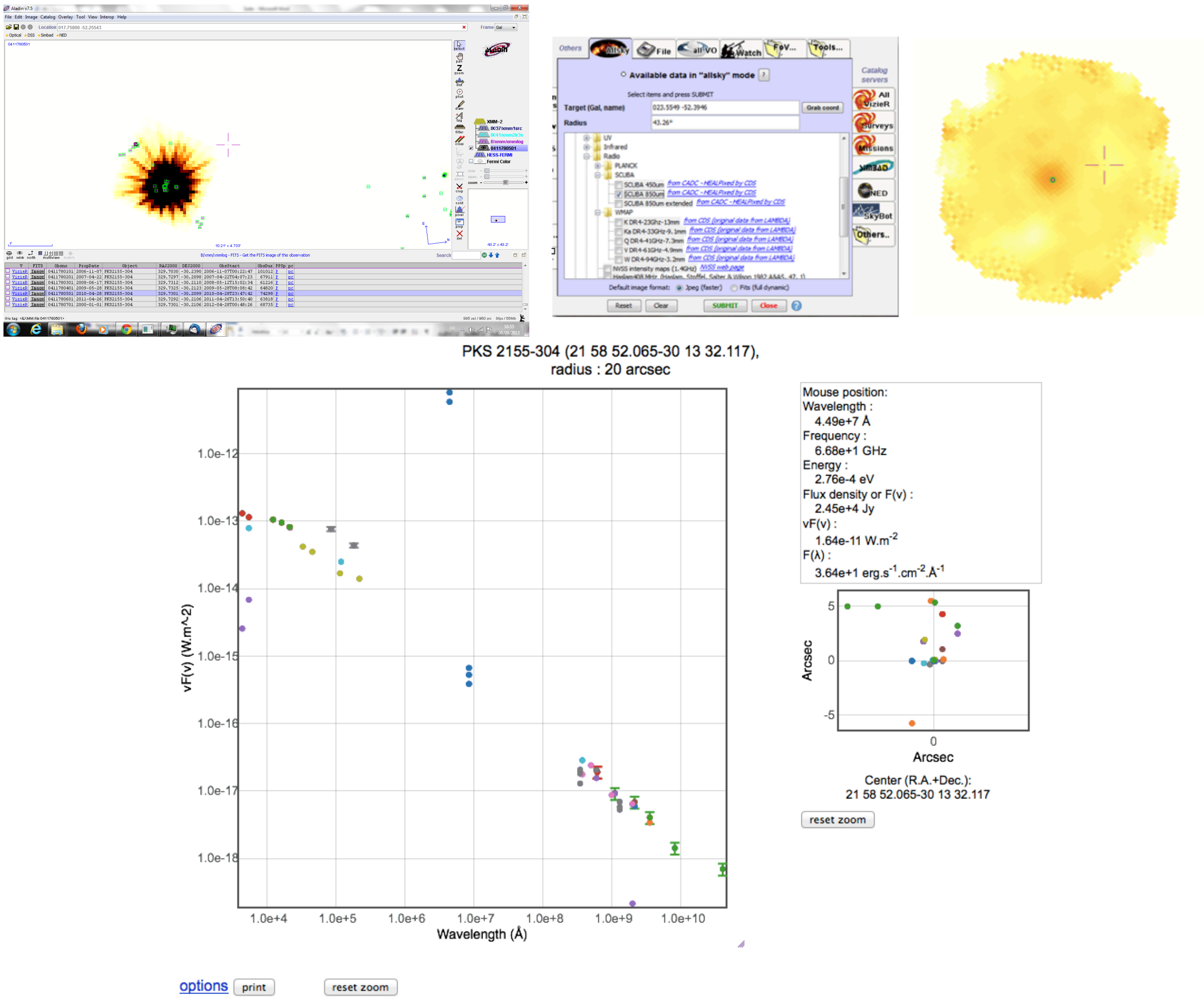

Fig. 2. Top left: X-ray image (0.2-12 keV) of PKS 2155-304 recovered from the XMM-Newton archive in Aladin. Top right: Analogous image from SCUBA in the sub-mm range (850 microns). Bottom: broad-band photometry data for PKS 2155-304 assembled using the VizieR photometry viewer widget.

protocol (Taylor et al. 2011). Next, we want to cross match both catalogs and possibly identify catalog entries describing the same source, at least when projected onto the plane of the sky. A difference in radial distance may exist but is unlikely given the relatively sparse distribution of H.E.S.S. and Fermi-LAT sources across the sky. The cross matching is carried out inside the VO tool TOPCAT assuming that a H.E.S.S. source and its supposed Fermi-LAT counterpart have an apparent angular distance of less then 1°. The cross matching establishes a new catalog that at the time of this writing contains 61 combined H.E.S.S. and Fermi-LAT sources. In the following we name this catalog *HESS-Fermi*.

The HESS-Fermi catalog still contains various types of sources. We want to classify them according to their overall gamma ray properties. In stellar astronomy, a convenient way to classify stars is to plot their colors against each other. Different stellar types then occur at defined regions of such a color-color diagram. We follow the equivalent approach for our HESS-Fermi sources by plotting different gamma ray flux ratios against each other. The "color-color" diagram to be computed involves the Fermi-LAT fluxes integrated over the following energy bands: 100 – 300 MeV (F1), 300 – 1000 MeV (F2), 1 – 3 GeV (F3), 3 – 10 GeV (F4). After constructing a plot of F4/F3 as a function of F2/F1 in log–log scale, the HESS table entries allow us to associate a type to each source (see Fig. 1, right). It turns out that the sources detected by both H.E.S.S. and Fermi-LAT preferentially populate the bottom-right corner of the color-color diagram. For now, the number of identified sources of a given type is too low to make a clear statement about its preferred locus on the plot.

Ackermann et al. (2011) have produced a catalogue of active galactic nuclei (AGNs), and we can identify sources from our HESS-Fermi catalog that are AGNs by matching their Fermi-LAT identifiers in TOPCAT. This yields 4 known AGNs in our sample, highlighted in the right panel of Fig. 1.

4 Constructing multi-wavelength images and spectra for the blazar PKS 2155-304

The remainder of the tutorial focuses on a particular object of the self-constructed Fermi-HESS catalog. PKS 2155-304 is a BL Lac object that is variable across a wide spectral range (see Abramowski et al. 2014, and references therein). BL Lac objects are AGNs launching magnetized, ballistic jets that are nearly aligned with the line of sight of the observer. The jet emission can be modeled as relativistically beamed synchrotron-self-Compton emission: the very hot electrons produce synchrotron emission that peaks in the radio band and then the very same electrons Comptonize the synchrotron photons and up-scatter them to gamma-rays and beyond.

The tutorial shows how to obtain multi-waveband imaging for PKS 2155-304 starting from the displayed catalog HESS-Fermi in Aladin. The interoperability of the VO tools allows the user to recover in a straightforward manner X-ray imaging data from XMM-Newton (Lumb et al. 2012) and a sub-mm image from SCUBA (Holland et al. 1998) by querying the respective data archives. The resulting images are given in Fig. 2 (top panel).

Aside from imaging at multiple wavebands, a photometry widget developed for the CDS portal allows to retrieve at once broad-band photometry data from many VizieR catalogues for a given object. Applying it on PKS 2155-304 we obtain a photometric "spectrum" of the source that reaches from the radio band all the way to the gamma ray range (see Fig. 2, bottom).

5 Summary and concluding remarks

We have briefly presented a tutorial illustrating the use of several VO tools in the context of gamma ray astronomy. The VO tools allow the user to efficiently mine data bases for images and spectra across all observed wave bands. The VO can thus be of great help when studying large ensembles of objects as well as for the in-depth exploration of an individual source.

The development of the VO tools is guided by the needs of the community. The Strasbourg Data Centre therefore is very grateful for feed-back and suggestions to improve and further develop the VO services.

References

Abramowski, A., Aharonian, F., Ait Benkhali, F., et al. 2014, arXiv:1409.0253

Ackermann, M., Ajello, M., Allafort, A. et al. 2011, ApJ, 743, 171

Boch, T., Oberto, A., Fernique, P. & Bonnarel, F. 2011, ADASS XX, Astronomical Society of the Pacific Conference Series, 442, 683

CDS 2011, Astrophysics Source Code Library, record ascl:1112.019

Carrigan, S., Brun, F., Chaves, R. C. G., et al. 2013, arXiv:1307.4868

Gasparrini, D., Cavazzuti, E., Cutini, S., et al. 2012, American Institute of Physics Conference Series, 1505, 478

Holland, W. S., Cunningham, C. R., Gear, W. K., et al. 1998, Proc. SPIE, 3357, 305

Landais, G. and Ochsenbein, F. 2012, ADASS XXI, Astronomical Society of the Pacific Conference Series, 461, 383

Lumb, D. H, Schartel, N., & Jansen, F. A 2012, arXiv:1202.1651

Ochsenbein, F., Williams, R., Davenhall, C. et al. 2011, arXiv:1110.0524O

Taylor, M. 2011, Astrophysics Source Code Library, record ascl:1101.010

Taylor, M., Boch, T., Fitzpatrick, M., et al. 2011, arXiv:1110.0528

SF2A 2014
J. Ballet, F. Bournaud, F. Martins, R. Monier and C. Reylé (eds)

SCIENTIFIC USE CASES FOR THE VIRTUAL ATOMIC AND MOLECULAR DATA CENTER

M.L Dubernet[1,2,3], J. Aboudarham[1,4], Y.A. Ba[1,2,3], M. Boiziot[5,6], S. Bottinelli[5,6], E. Caux[5,6], C. Endres[7], J.M. Glorian[5,6], F. Henry[4], L. Lamy[1,4], P. Le Sidaner[1], T. Möller[7], N. Moreau[1,2,3], C. Rénié[4], E. Roueff[1,2,3], P. Schilke[7], C. Vastel[5,6] and C.M. Zwölf[1,2,3]

Abstract. VAMDC Consortium is a worldwide consortium which federates interoperable Atomic and Molecular databases through an e-science infrastructure. The contained data are of the highest scientific quality and are crucial for many applications: astrophysics, atmospheric physics, fusion, plasma and lighting technologies, health, etc. In this paper we present astrophysical scientific use cases in relation to the use of the VAMDC e-infrastructure. Those will cover very different applications such as: (i) modeling the spectra of interstellar objects using the myXCLASS software tool implemented in the Common Astronomy Software Applications package (CASA) or using the CASSIS software tool, in its stand-alone version or implemented in the Herschel Interactive Processing Environment (HIPE); (ii) the use of Virtual Observatory tools accessing VAMDC databases; (iii) the access of VAMDC from the Paris solar BASS2000 portal; (iv) the combination of tools and database from the APIS service (Auroral Planetary Imaging and Spectroscopy); (v) combination of heterogeneous data for the application to the interstellar medium from the SPECTCOL tool.

Keywords: databases, software, atoms, molecules, solar physics, interstellar medium

1 Introduction

VAMDC(`http://www.vamdc.eu/`) (Dubernet et al. 2010) is a worldwide e-infrastructure which federates interoperable Atomic and Molecular databases. The contained data are of the highest scientific quality and are crucial for many applications: astrophysics, atmospheric physics, fusion, health, etc. In this paper we present astrophysical scientific use cases in relation to the use of the VAMDC e-infrastructure.

Those scientific science use cases reflect the strategy of the VAMDC Consortium towards users of atomic and molecular data. One objective consists in providing the scientific community with innovative tools for easily handling and processing results that are queried from the VAMDC interface portal (sect.2) or from standalone tools such as SPECTCOL(sect.3). Another strategy consists in porting the VAMDC capabilities and facilities into tools developed by institutes outside the consortium such as the SPECVIEW software (sect.4.1). This software is part of our main strategy of user software development as it can be used in many applications where visualisation of spectra is concerned, and for any type of users: researchers, education, business, outreach. In this paper we will present a science use case within the APIS service (sect. 4.2). A last objective consists in providing support so that external users can implement our VAMDC plugin in their software: this has been applied to the BASS2000 portal (sect.7), to the Cassis tool from IRAP (sect.r̃efcassis), and to the MyXCLASS interface for CASA (sect. 6).

[1] VO-PARIS Data Center, Observatoire de Paris, PSL Research University, 5 Place Janssen, 92195 Meudon, France
[2] LERMA, Observatoire de Paris, PSL Research University, CNRS, UMR8112, 5 Place Janssen, 92195 Meudon, France
[3] Sorbonne University, UPMC Univ Paris 06, CNRS, UMR8112, LERMA, 5 Place Janssen, 92195 Meudon, France
[4] LESIA, Observatoire de Paris, PSL Research University, UPMC Univ Paris 06, Univ. Paris Diderot, CNRS, UMR8109, 5 Place Janssen, 92195 Meudon, France
[5] Université de Toulouse, UPS-OMP, IRAP, F-31400 Toulouse, France
[6] CNRS, IRAP, 9 Av. Colonel Roche, BP 44346, F-31028 Toulouse Cedex 4, France
[7] I. Physikalisches Institut, Universität zu Köln, Zülpicher Straße 77, 50937 Köln, Germany

2 Link to Virtual Observatory Tools

A key element of the VAMDC infrastructure is the web portal (`http://portal.vamdc.eu`), that provides an unified way to query the VAMDC registered atomic and molecular databases. A request is built through a graphical user interface and sent to all the databases. They return data in a common XML format called XSAMS (`http://www.vamdc.eu/standards`).

The portal provides tools called "Processors" that can convert a XSAMS file into another format. The Processors called 'Molecular Spectroscopy XSAMS to HTML" and "Atomicxsams2HTML" display for, respectively molecular and atomic spectroscopic data, an HTML page where columns and lines can be selected. The selected data can be exported into 2 formats: a CSV table where column are separated by "," and a VOTable which is a Virtual Observatory (VO) standard used to exchange data among VO Tools.

The VOTable can be sent to any VO Tool launched on the users' desktop using the "send via SAMP" functionality of the processor. SAMP is another VO Standard (`http://www.ivoa.net/documents/SAMP/`) that allows several applications to exchange data directly, without the need to save and load a file locally.

In the example below, the file is sent to an application called TOPCAT (`http://www.star.bris.ac.uk/~mbt/topcat/`) which is dedicated to the visualisation of tabular data. All functionalities of TOPCAT can be used on the selected VAMDC data.

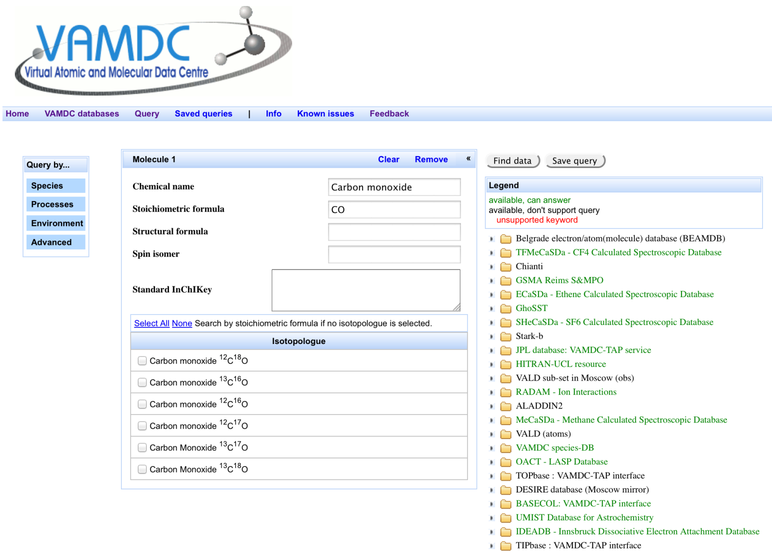

Fig. 1. VAMDC Portal:`http://portal.vamdc.eu`.

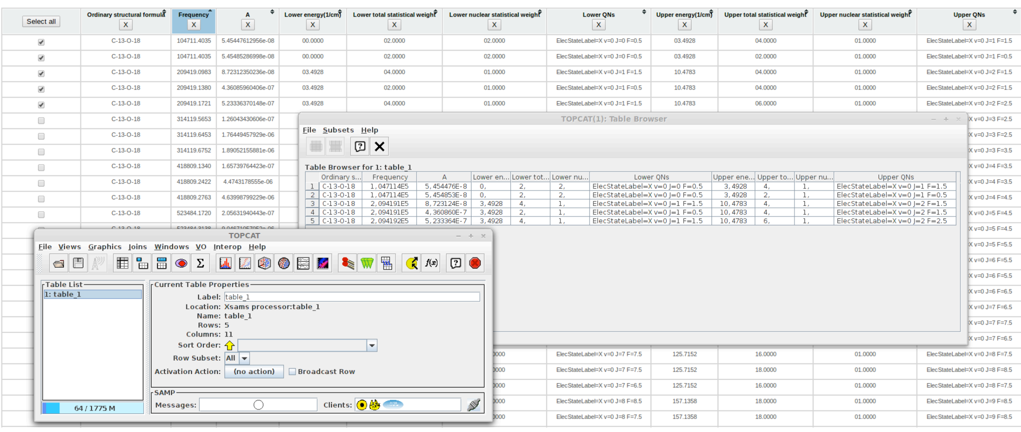

Fig. 2. Molecular data displayed by the processor and sent to TOPCAT VO Tool.

3 The Spectcol Tool

The aim of the client tool SPECTCOL (`http://www.vamdc.eu/software`) (Dubernet et al. 2012) is to associate spectroscopic data provided by spectroscopic databases with collisional data provided by collisional databases using the VAMDC technology.

The client tool interrogates the registries to find spectroscopic and collisional information about a molecule. It retrieves different possible sets of data from different databases. The user can associate sets of his own choice in order to create customized combination of spectroscopic and collisional data.

Indeed the usual difficulty met by astrophysical users is to combine collisional data from a database such as BASECOL Dubernet et al. (2013) (`http://basecol.obspm.fr`) with spectroscopic data coming from other native databases such as CDMS (`http://www.astro.uni-koeln.de/cdms`), JPL (`http://spec.jpl.nasa.gov/`) or any other spectroscopic databases. Combination of data implies the possibility to match molecular states that were very often described differently in JPL, CDMS and BASECOL, and this problem is now solved easily using VAMDC and SPECTCOL.

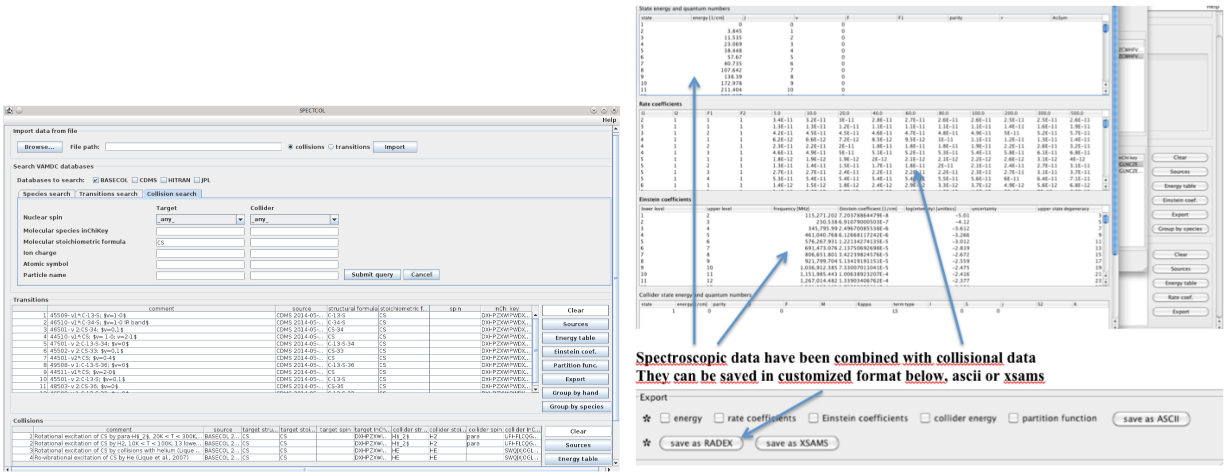

Fig. 3. Left: Spectcol Query Interface. **Right:** Spectcol output where matching has been done between spectroscopic data and collisional data.

4 Link within the APIS Service: Specview

4.1 *SPECVIEW*

Specview is a tool for 1-D spectral visualization and analysis of astronomical spectrograms from STScI (`http://www.stsci.edu/institute/software_hardware/specview/`). It is written in Java and thus can be run anywhere Java is supported. Specview is able to read all the Hubble Space Telescope spectral data formats, as well as data from several other instruments (such as IUE, FUSE, ISO, FORS and SDSS), preview spectra from MAST, and data from generic FITS and ASCII tables. It can also read data from Virtual Observatory servers, and read and write spectrogram data in Virtual Observatory SED format. It can also read files in the SPC Galactic format used in the chemistry field.

Specview can overplot spectral line identifications taken from a variety of line lists, including user-supplied lists. Its linelists' query form has been modified to include the VAMDC Query Module, called QueryBuilder (`http://www.vamdc.eu/developer`), thus providing the full capability of querying the VAMDC databases. In particular it allows to select finely the observed species and properties of linelists. Currently about 20 spectroscopic databases are inter-connected through VAMDC and accessible through VAMDC software and libraries.

4.2 *APIS*

The APIS service (Lamy et al. 2014) (for Auroral Planetary Imaging and Spectroscopy) is freely accessible at `http://apis.obspm.fr` since mid-2013. It consists of a high level database of auroral planetary observations (images and spectra) of the outer planets and their satellites taken by the Hubble Space Telescope in the Far-UV window from 1997 up to now, including more than 5000 individual observations. The APIS database is archived at VO-PARIS Data Center. Associated metadata are built along the standard Europlanet-Table Access Protocol (EPN-TAP) (Erard et al. 2014a), so that the data can be queried externally to APIS by VO portals such as VESPA)(`http://vespa.obspm.fr`) (Erard et al. 2014b), and be quickly and efficiently sorted out by a dedicated search interface (see left panel of Fig. 4). APIS finally proposes to interactively work with the data online, through VO tools, such as Aladin and Specview.

Both 1D and 2D spectra can be plotted online from APIS with Specview through a Simple Application Messaging Protocol (or SAMP) hub (see right panel of Fig. 4). As planetary aurorae result from the collisional excitation of the upper atmosphere by magnetospheric electrons, spectra of the outer planets provide a direct mean to probe the upper atmospheric composition, mainly populated by atomic and molecular hydrogen. Specview is able to retrieve transitions lines from VAMDC catalogues (H-Lya is provided by default with Specview, while H_2 lines can be retrieved from the SESAM database `http://sesam.obspm.fr`), and to superimpose them to the observations (see right panel of Fig. 4).

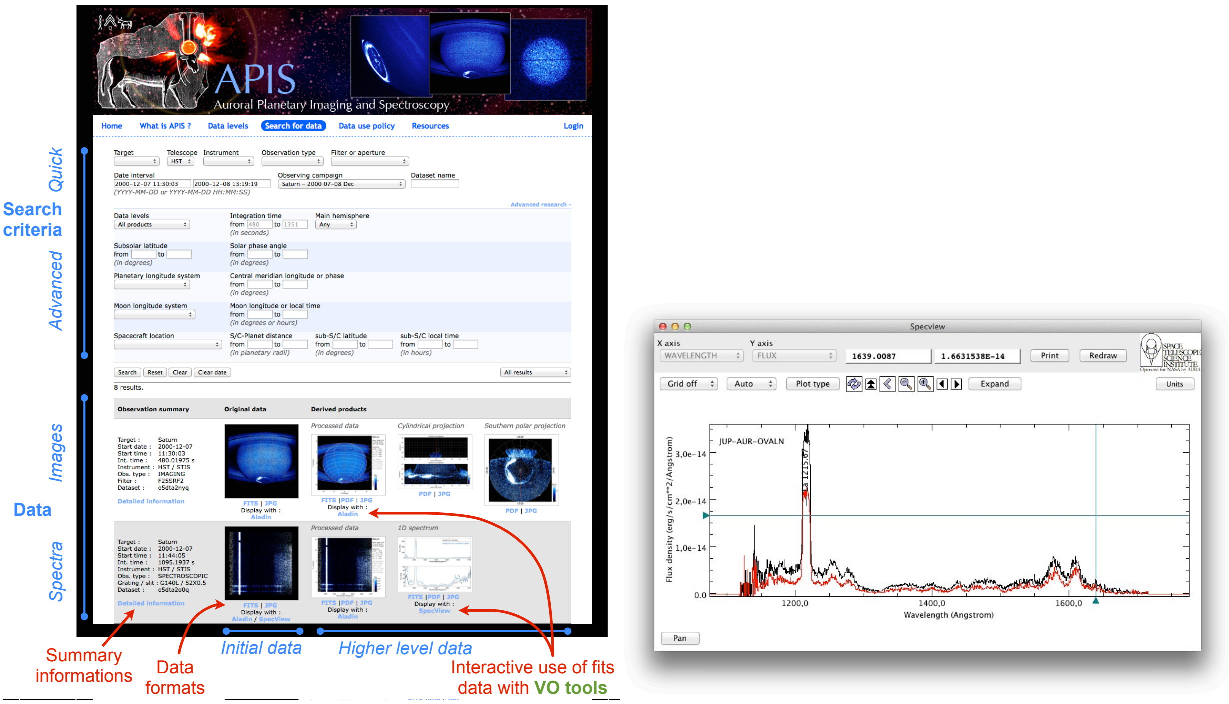

Fig. 4. Left: Example of data query with the APIS search interface. **Right:** Far-UV spectrum of Jupiter plotted with Specview. The H-Lya transition is marked by a vertical line.

5 Link from CASSIS Application

The CASSIS (Centre d'Analyse Scientifique de Spectres Instrumentaux et Synthétiques) software has been developed by CESR/IRAP since 2005 (`http://cassis.irap.omp.eu`). It allows to generate synthetic spectra to prepare astronomical observations or to compare with actual observations, provides the means to perform a quick line identification (necessary for large spectral surveys), and helps to determine the sources parameters (line width, column density, temperature, density, beam dilution) with LTE or non-LTE minimisation scripts or rotational diagram analysis when many transitions are available. CASSIS is available as a stand-alone application or as a plug-in of the Herschel Interactive Processing Environment (HIPE).

CASSIS uses the Single Spectral Access (SSA) Protocol to access the IVOA services in order to retrieve any spectra (Hubble, Corot, ISO, Pollux, etc) via our SSA module. Also CASSIS uses the SAMP messaging protocol that enables astronomy software tools to interoperate and communicate. CASSIS is able to retrieve informations on the spectroscopic data necessary for the modeling (LTE or non-LTE: see `http://cassis.irap.omp.eu/docs/RadiativeTransfer.pdf` for details) or identification from databases (CDMS, JPL) through the VAMDC

TAP protocol based on IVOA format. TAP provides virtual data and allows to plug in the query language VSS2 and the data model VAMDC-XSAMS (the latter being an output format)(`http://www.vamdc.eu/standards`).

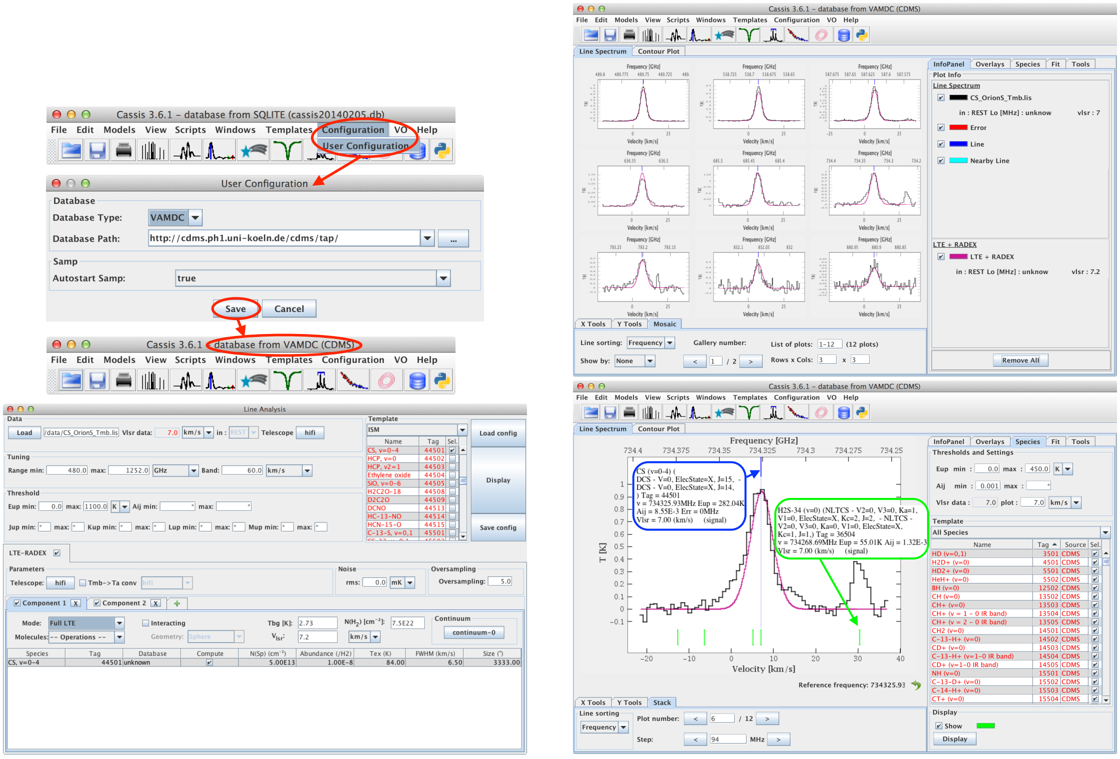

Fig. 5. Left: The top panels show how to change the user configuration in order to swap from a local SQLite database to the VAMDC database. The bottom panel is a snapshot of the Line Analysis module with parameters such that CASSIS will search all the CS transitions having an $E_{up} < 1100$ K, potentially present in the selected data file and will overlay an LTE model. The result is displayed in the figure to the right. **Right:** The top panel shows the result corresponding to the Line Analysis window (left panel). All the transitions found are displayed as a mosaic and clicking on one of the lines allows the user to zoom on it. The bottom panel shows a zoom of the 6th transition over which transitions (with $E_{up} < 450$ K and $A_{ij} > 10^{-3}$) from other species have been overlaid, allowing the identification of an $H_2{}^{34}S$ line next to the CS line (Herschel/HIFI data).

6 Link from myXCLASS Interface for CASA

Spectroscopic data as it is accessible via VAMDC is essential to model and analyze astronomical spectra. VAMDC has supported the development of a toolbox (`http://www.astro.uni-koeln.de/projects/schilke/myXCLASSInterface`) for the Common Astronomy Software Applications package (CASA) in order to include access to its databases. The toolbox contains the myXCLASS program, which is used to model astronomical spectra by solving the radiative transfer equation for an isothermal object in one dimension, whereas the finite source size and dust attenuation are considered as well.

The spectroscopic data, such as transition frequencies, state energies, Einstein A coefficients, degeneracies and partition functions, required for the modeling, is retrieved via the VAMDC infrastructure from the CDMS and the JPL catalogs, and then stored in a local database. Besides the access to the databases, the toolbox also includes the model optimizer package MAGIX Möller et al. (2013) (Modeling and Analysis Generic Interface for eXternal numeric codes). This optimizer helps to find the best description of the data using a given model, i.e., heps to find the parameter set that most closely reproduces the data.

A recent example, where the toolbox has been successfully used, is the analysis of spectra recorded towards the Sgr B2(M) cloud core which exhibits strong absorption features of gas located in the spiral arms of our galaxy. One of these spectra is shown in left panel of Fig. 6. It shows a spectrum of $^{36}ArH^+$ (1-0) (blue) recorded towards the star forming region SgrB2(M). The optimizer has been used to fit the spectrum (red) and to derive column densities and excitation temperatures as a function of relative velocity of the molecular gas. The derived column density per velocity as shown in the right hand side figure for the above example including other species provides important insights into the physical, chemical and structural composition of these objects Schilke et al. (2014).

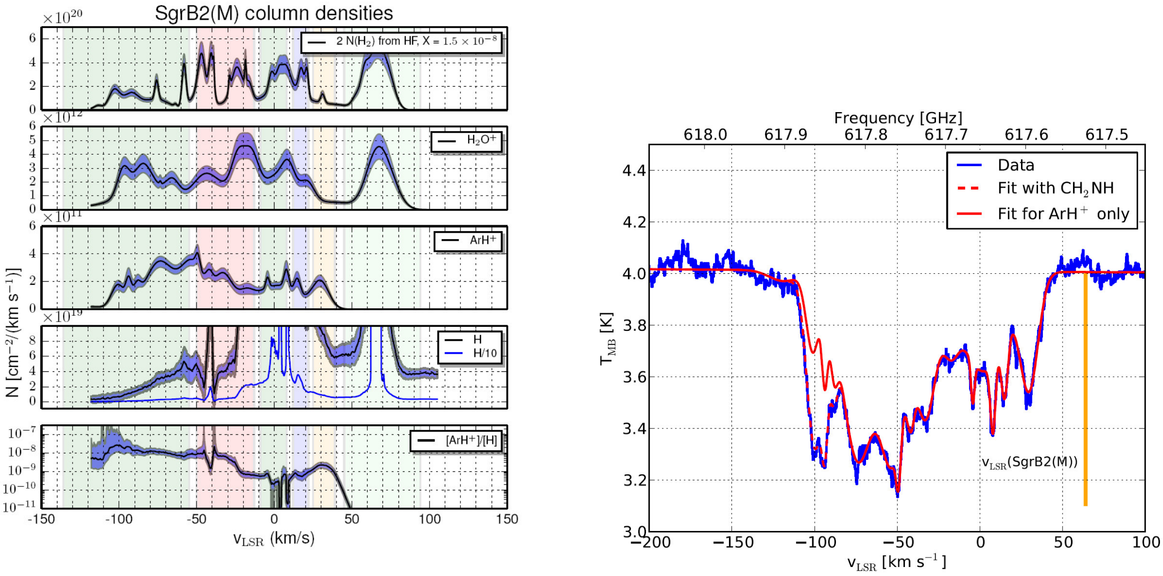

Fig. 6. Left: Spectrum of ^{36}ArH$^+$ (1-0) toward SgrB2(M) with fit including the H$_2$CNH line blending at -110 km s^{-1} as dashed red line, and fit ^{36}ArH$^+$ only in red. **Right:** Column density per km s^{-1} of HF, H$_2$O$^+$, ^{36}ArH$^+$, and H. The error estimate for ^{36}ArH$^+$ was done using the MAGIX Interval Nested Sampling algorithm. The uncertainty is marked by the blue shading around the curves.

7 Link from BASS2000 Portal

BASS2000 (`http:bass2000.obspm.fr`) provides access to a wide range of the Solar spectrum, from 67 nm to 5 400 nm. This spectrum is obtained from Curdt et al. (2001) for the UV part using SOHO/SUMER data; from Delbouille et al. (1972) for the visible part, using Kitt Peak National Observatory observations; from Delbouille et al. (1981) for the infrared part, also based on Kitt Peak observations. The visible part of the spectrum is very much used both for preparing and processing observations . Spectro-polarimeters take full advantage of the detailed knowledge of atomic data concerning the observed lines in order to be able to calculate local magnetic field. Therefore, Solar spectrum has been connected to VAMDC in order to provide directly useful information to the user. This helps for data processing, but also in order to prepare observations, for instance tagging atmospheric molecular lines, such as water, that may serve for wavelength calibration.

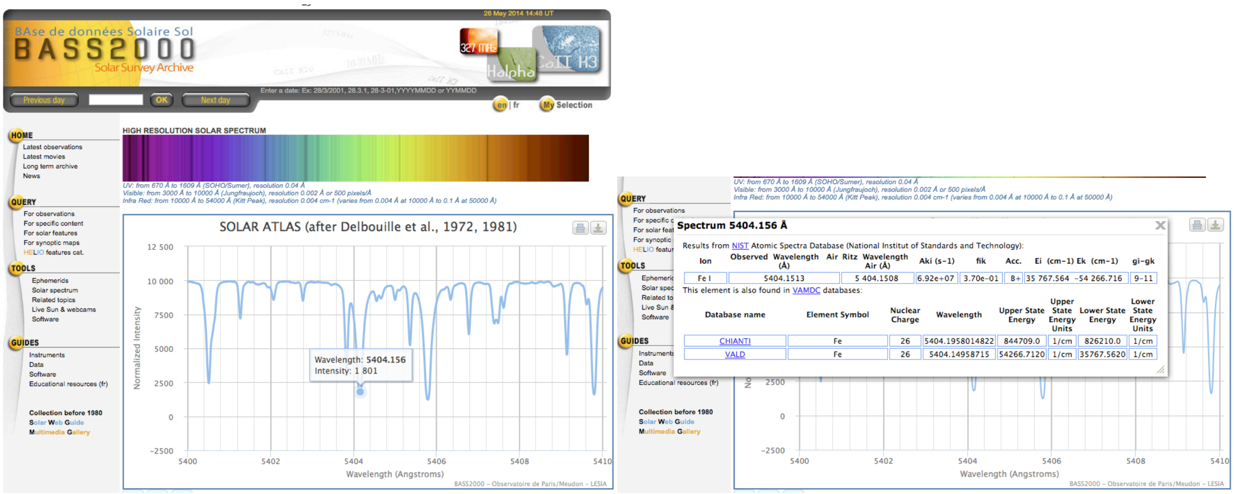

Fig. 7. Left: BASS2000 Solar spectrum gives directly wavelength and intensity of each spectral line. Those data are extracted from VAMDC databases using the VAMDC libraries. **Right:**When clicking on the solar spectrum, connection is made with VAMDC giving back information from adequate databases.

8 Conclusions

The VAMDC Consortium provides support for all those strategies: you can implement protocols that VAMDC has designed: see `http://www.vamdc.eu/standards`. You might want to save time and to use our libraries in Java or other languages: `http://www.vamdc.eu/developers`. You may need some tutorials: see `http://tutorial.vamdc.org`. You may need some help: send a mail to support@vamdc.eu. You may want to exchange: `http://forum.vamdc.org` and to create your own sub-topics. You may want that our services are improved, then contact the relevant people: `http://www.vamdc.eu/contact`.

The VAMDC Support has been provided through the SUP@VAMDC project funded under the “Combination of Coordination and Support Actions” Funding Scheme of The Seventh Framework Program. Call topic: INFRA-2012-3.3 Scientific Data Infrastructure. Grant Agreement number: 313284.

References

Curdt, W., Brekke, P. Feldman, U., et al. 2001, A&A, 375, 591

Delbouille, L., Neven, L., & Roland G. 1972, ‘Photometric atlas of the Solar spectrum from *lambda* 3000 to *lambda* 10000”, Publication de l’Observatoire de Liège

Delbouille, L., et al. 1981, ‘Photometric atlas of the Solar spectrum from 1850 to 10,000 cm^{-1},‘” Publication de l’Observatoire de Liège

Dubernet, M.L., et al. 2010, JQSRT, 111, 2151

Dubernet, M. L., Nenadovic, L., & Doronin, M. 2012, in ASP Conf. Ser., Vol. 461, ADASS XXI, ed. P. Ballester & D. Egret (San Francisco: ASP), 335

Dubernet, M.L., et al. 2013, A&A, 553, p A50

Erard, S., et al. 2014, “he EPN-TAP protocol for the Planetary Science Virtual Observatory,” Astronomy and Computing in pressarXiv:1407.5738.

Erard, S., et al. 2014, ‘Planetary Science Virtual Observatory architecture’, Astronomy and Computing in pressarXiv:1407.4886, doi:10.1016/j.ascom. 2014.07.005.

Lamy, L., et al. 2014, “The Auroral Planetary Imaging and Spectroscopy (APIS) service”, Astronomy and Computing, submitted to the special issue on Virtual Observatory.

Möller, T., et al. 2013, A&A, 549, A21

Schilke et al. 2014, A&A, 566, A29

SF2A 2014
J. Ballet, F. Bournaud, F. Martins, R. Monier and C. Reylé (eds)

PULSARS ALL ACROSS THE SPECTRUM

L. Guillemot[1]

Abstract. Pulsars, rotating magnetized neutron stars born in supernovae, are fascinating objects and their study finds applications in a wide range of physics and astrophysics. *Fermi* Large Area Telescope observations have shown that they form the main class of GeV gamma-ray sources in the Milky Way, and the detection of the Crab pulsar beyond 100 GeV by Cherenkov telescopes has opened a new window on their study at even more extreme energies. At the other end of the spectrum, radio observations over the last five years have doubled the number of known millisecond pulsars, those that rotate hundreds of times every second and that constitute unique gravity laboratories. Radio timing observations of an array of stable millisecond pulsars can also be used to search for low frequency gravitational waves from distant massive black hole binaries. I review recent results on pulsars and discuss future prospects for the study of these extreme objects, all across the spectrum.

Keywords: pulsars, pulsar timing, gamma rays, general relativity, gravitational waves

1 Introduction

Since the original discovery of a pulsar nearly fifty years ago (Hewish et al. 1968), more than 2300 of these fascinating objects have been observed, from radio observations in a vast majority of cases. Pulsars are rapidly-rotating neutron stars, thought to have radii of about 10 km and with measured masses of up to two solar masses (Antoniadis et al. 2013), making them the densest objects observable. They have large magnetic fields of $10^8 - 10^{15}$ G, and their magnetosphere is filled with plasma. Pulsars produce electromagnetic emission in the form of beams that are swept across the sky as they rotate, so that distant observers – provided that the emission is beamed toward them – see pulsars as periodic sources of emission. In fact, the periodicity of the observed emission, and the rate at which the period increases, give us a great deal of information about the pulsar responsible for the emission. Figure 1 shows the measured rotation periods P and their time derivatives $\dot{P} = dP/dt$ for currently known pulsars. Two main pulsar populations can easily be distinguished from this diagram: a category of about 2000 "normal" pulsars with $P \sim 0.1 - 1$ s in the upper right corner, and so-called "millisecond pulsars" (MSPs) in the lower left part of the plot, with rotation periods in the order of 1 ms and comparatively smaller values of $\dot{P}$. MSPs are thought to have acquired their low rotation periods by accretion of matter and thus transfer of angular momentum from a binary companion (Bisnovatyi-Kogan & Komberg 1974; Alpar et al. 1982). The values of P and $\dot{P}$ also inform us about the basic properties of pulsars: for instance, denoting I as the neutron star moment of inertia and $\Omega = 2\pi/P$ the angular velocity, the rotational kinetic energy $E_{\rm rot}$ is given by $\frac{1}{2}I\Omega^2$. Because pulsars slow down gradually, this energy budget varies at a rate $dE_{\rm rot}/dt = I\Omega\dot{\Omega} = -4\pi^2 I \frac{\dot{P}}{P^3}$. This quantity, noted $\dot{E}$, is called the "spin-down power" and traces the amount of energy loss that can go into electromagnetic radiation. In Section 2 we will see that pulsars with the highest $\dot{E}$ values are often detected as sources of high-energy radiation.

Pulsar observations find their applications in numerous fields of Physics and Astrophysics, from e.g. plasma physics and electrodynamics to tests of theories of Gravity, gravitational wave searches or studies of the neutron star equation of state, to name but a few examples. As in other fields of astronomy, one can study pulsars by recording and describing their temporal and spectral emission properties, at a given energy or across the electromagnetic spectrum to get complementary information. Figure 2 shows radio, X-ray and gamma-ray

[1] Laboratoire de Physique et Chimie de l'Environnement et de l'Espace – Université d'Orléans / CNRS, and Station de Radioastronomie de Nançay, Observatoire de Paris, CNRS / INSU

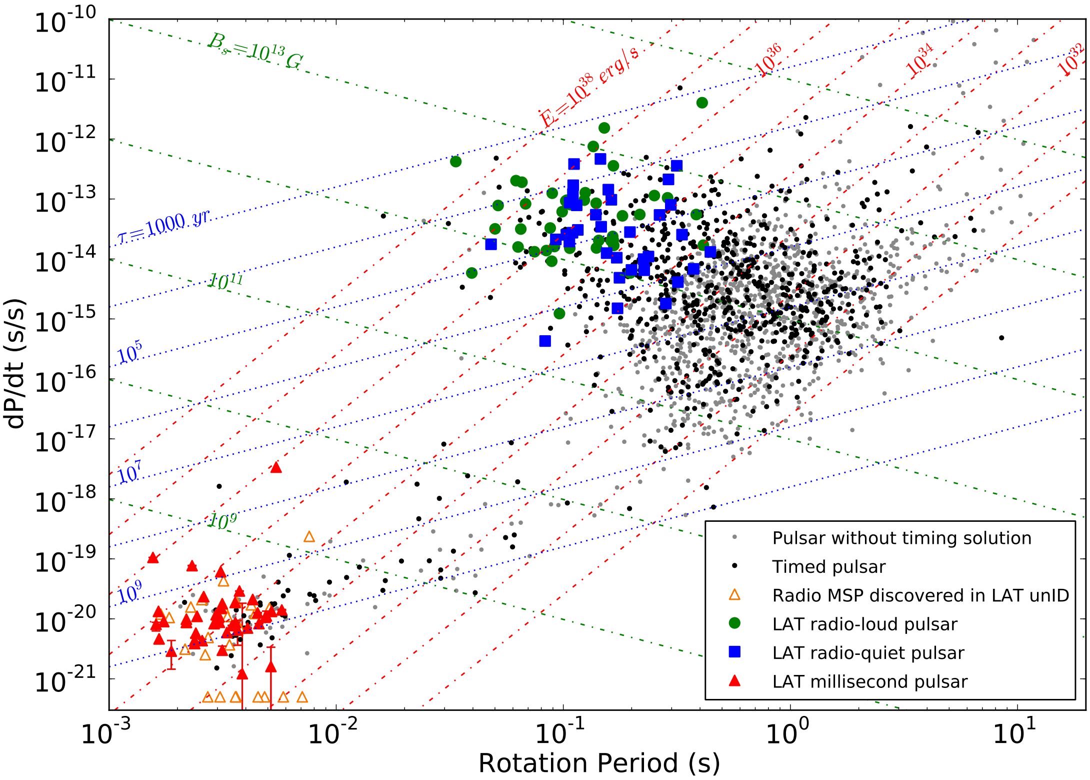

Fig. 1. Spin-down rate $\dot{P} = dP/dt$ versus rotation period P for known pulsars. Colored symbols (red triangles, blue squares and green circles) indicate pulsars detected by the *Fermi* LAT as pulsed sources of GeV gamma-ray emission. Also shown on this plot are lines of constant spin-down power $\dot{E}$, they are represented by the dashed red lines. Figure taken from Abdo et al. (2013), see this article for a complete description.

pulse profiles for the MSP B1821−24A in the globular cluster M28. Peak locations, multiplicities, shapes, and relative positions across the spectrum inform us about the physical mechanisms at play, and the geometry of the emission beams. Likewise, spectral measurements at different wavelengths give important clues about particle acceleration sites, physical processes involved, and emission energetics.

Another channel commonly used for studying pulsars is to do "pulsar timing". In pulsar timing, each rotation of a pulsar over a given time span (months to years or even more) is unambiguously accounted for, and the precise tracking of the pulsar's rotational phase enables sensitive measurements of phenomena affecting its rotation, binary motion, or perturbing the propagation of its signals through space. A detailed description of the technique and of its applications can be found in e.g. Lorimer & Kramer (2005). In practice, the technique gives its best results for MSPs, which are incredibly stable clocks. An illustration of the great stability of MSPs is shown in Figure 3: in this case, the root-mean-square (RMS) deviation of the differences between observed and predicted ticks from PSR J1909−3744 is smaller than 100 ns over five years! As a consequence, pulsar timing enables measurements of some physical quantities with fantastic precision. Examples of the applications of pulsar timing are given in Section 3.

The aim of these proceedings is not to give a full review of recent results of pulsar observations in different wavelength domains, but rather highlight some salient results and show some examples of the complementarity of multi-wavelength (or multi-energy) observations of pulsars.

2 Pulsars as sources of high-energy emission

The launch of the *Fermi* satellite in June 2008 marked the start of a new era in high-energy pulsar observations. Before the Large Area Telescope (LAT), main instrument on *Fermi*, started observing, fewer than ten pulsars

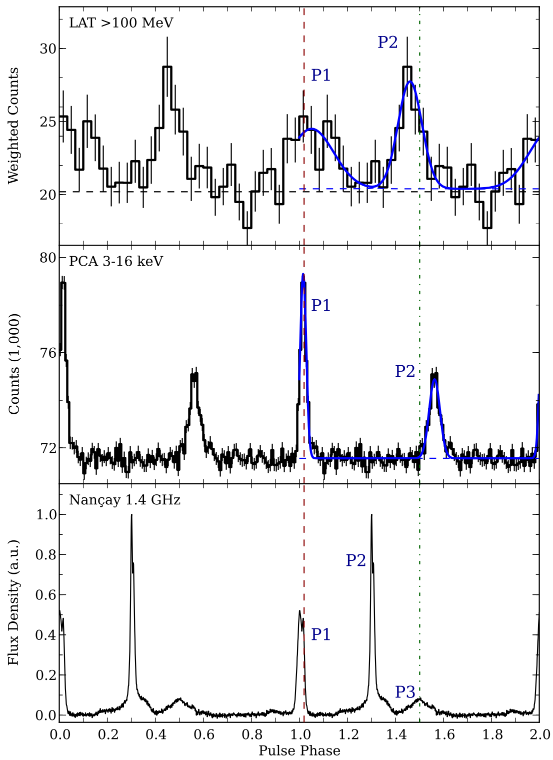

Fig. 2. Pulse profiles of PSR B1821−24A in the globular cluster M28, at different wavelengths. Bottom panel: 1.4 GHz Nançay profile. Middle panel: RXTE X-ray observation between 3 and 16 keV. Top panel: *Fermi* LAT gamma-ray observation above 0.1 GeV. Two full pulsar rotations are shown. See Johnson et al. (2013) for additional details on these profiles.

were known to emit GeV gamma rays. Attempts to understand the fundamental processes responsible for the high-energy emission from pulsars were thus confronted to a severe lack of observational data and of variety in the sample of known gamma-ray pulsars. The situation six years after the LAT began its observations of the GeV gamma-ray sky has changed dramatically, and the LAT has revolutionized our view of the gamma-ray pulsar population. As of September 2014, a total of 147 pulsars have been detected as pulsed sources of GeV gamma-ray emission, including more than 60 MSPs (all of them also detected as radio emitters), and the rest of normal pulsars, radio-loud or radio-quiet*. Figure 4 shows the locations of *Fermi* LAT detected pulsars on a map in Galactic coordinates, along with the locations of other known pulsars from the ATNF pulsar catalog† (Manchester et al. 2005). The pulsars were detected by either blind searching LAT sources for pulsations (e.g., Pletsch et al. 2013), or by folding the LAT photons at their apparent rotation periods as measured from supporting pulsar timing observations in the radio (see e.g., Guillemot et al. 2013; Ng et al. 2014). As the mission progresses, new gamma-ray pulsars continue to be detected (Hou et al. 2014), including less luminous pulsars or ones with broad gamma-ray pulses, making them difficult to distinguish from the background emission.

The second *Fermi* LAT catalog of gamma-ray pulsars (hereafter 2PC; Abdo et al. 2013) includes 117 gamma-ray pulsars detected using three years of LAT data, and represents the latest systematic effort to analyze and describe the properties of the population of GeV gamma-ray pulsars. A majority of 2PC pulsars have two gamma-ray peaks in their profiles, and with a few notable exceptions (e.g., Guillemot et al. 2012) the gamma-ray emission is separated from the radio emission, when present. Light curve modeling (e.g., Johnson et al. 2014) indicates that gamma-ray emission originates from the outer magnetosphere, in the form of fan-like beams

*See `https://confluence.slac.stanford.edu/display/GLAMCOG/Public+List+of+LAT-Detected+Gamma-Ray+Pulsars` for an up-to-date list of *Fermi* LAT detected pulsars.

†`http://www.atnf.csiro.au/people/pulsar/psrcat/`

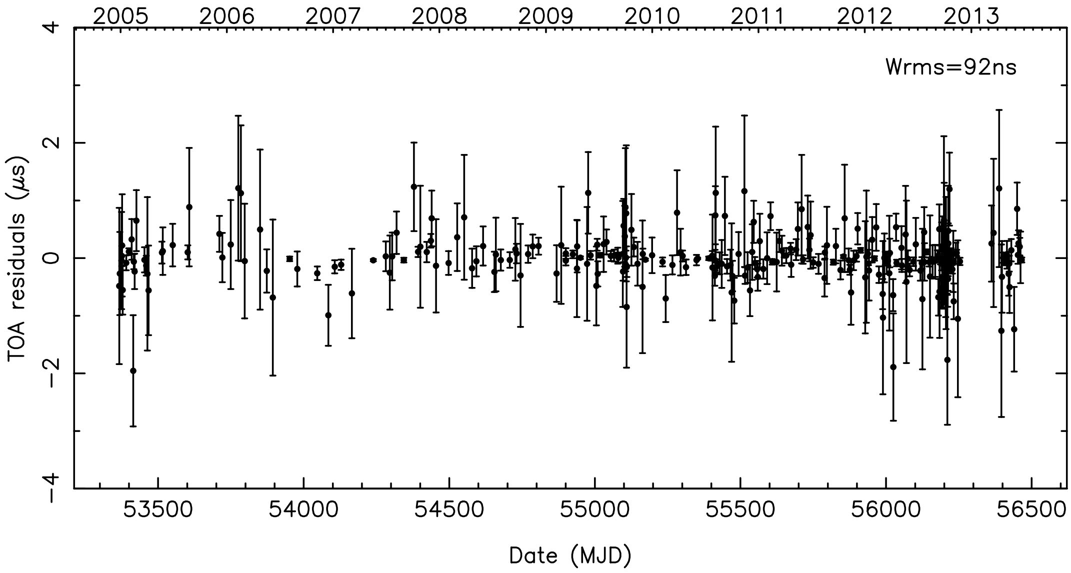

Fig. 3. Plot showing the difference between the observed times of arrival of radio pulses from the MSP J1909−3744 at the Nançay Radio Telescope and those predicted by a model (so-called "residuals"), as a function of time. The RMS of the residuals for the data shown in this plot is 92 ns.

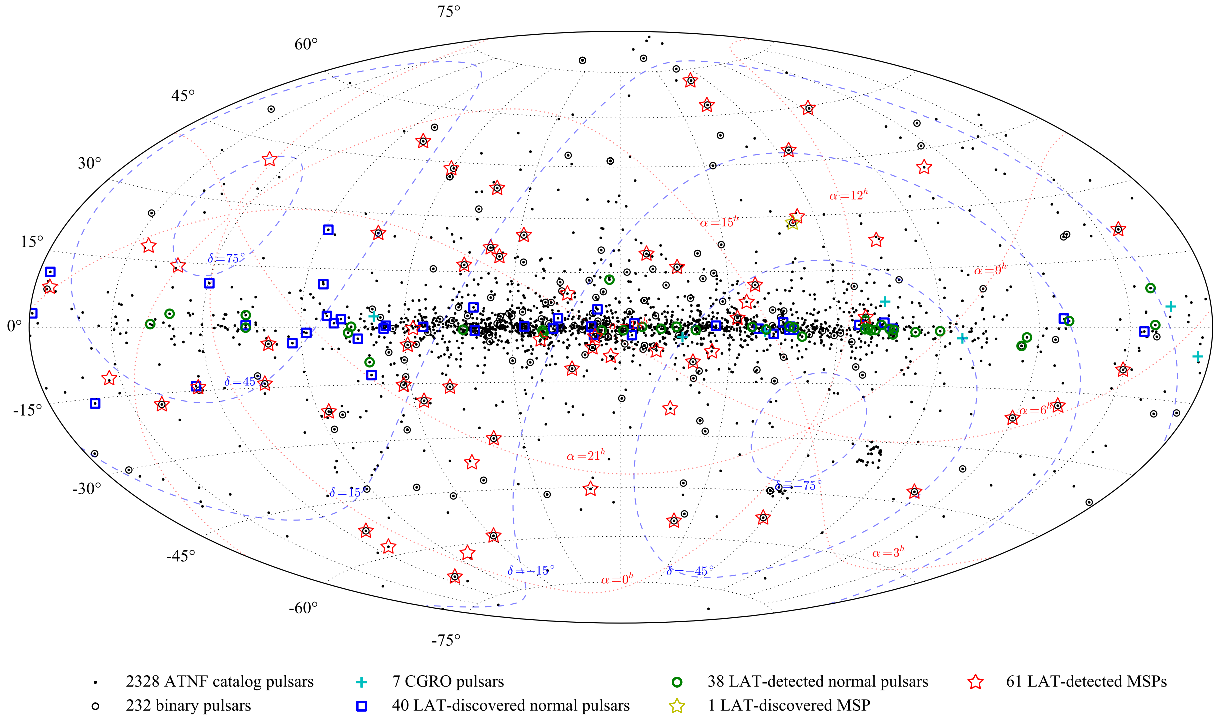

Fig. 4. Sky map in Galactic coordinates showing the locations of pulsars listed in the ATNF pulsar catalog, with pulsars detected as pulsed sources of gamma rays by the *Fermi* LAT represented as colored symbols. Lines of constant Right Ascension (respectively, Declination) are represented with red dotted lines (resp., blue dashed lines).

sweeping large portions of the sky. Spectral measurements also favor outer magnetospheric emission as opposed to gamma-ray emission from near the stellar surface: the spectra of most gamma-ray pulsars is indeed consistent with curvature radiation with no suppression caused by magnetic attenuation, as expected for emission produced away from the surface. Gamma-ray emission is only observed for high $\dot{E}$ pulsars (see Figure 1). Undetected pulsars with high $\dot{E}$ values could be too distant, leading to small gamma-ray fluxes, they can be embedded in regions of intense gamma-ray background emission, have broad gamma-ray emission profiles making them difficult to detect with commonly-used statistical tests (see Hou et al. 2014), or may simply not beam their gamma-ray emission in the direction of the Earth. On the other hand, LAT-detected pulsars have large gamma-ray efficiencies (ratio of the gamma-ray luminosity to the spin-down power $\dot{E}$) ranging from $\sim 1\%$ to 100%. Investigations of the photons with large energies also revealed that the LAT detects significant pulsations from 20 pulsars above 10 GeV, and from 12 pulsars above 25 GeV (Ackermann et al. 2013), confirming the very high energy detection of pulsations from the Crab pulsar by the MAGIC and VERITAS telescopes (Aliu et al. 2008; VERITAS Collaboration et al. 2011). Such high and very high energy detections of pulsars are important for understanding the fundamental processes at play in pulsar magnetospheres.

Another great success of the *Fermi* mission in terms of pulsar science is the discovery of many new gamma-ray sources with high energy emission properties similar to those of known gamma-ray pulsars, and that can be searched for pulsations either directly in the LAT data, or at other wavelengths. For example, optical and X-ray observations of the bright source with pulsar-like properties J1311.7−3429 from the 2FGL catalog of LAT sources (Romani 2012; Nolan et al. 2012) revealed a binary system with a 1.56-hr orbital period, and the partial constraints on the orbital parameters from this study allowed Pletsch et al. (2012) to discover the gamma-ray pulsations from the 2.5 ms pulsar J1311−3430 by blind searching the LAT data. J1311−3430 is the only example thus far of an MSP discovered by blind searching the LAT data. However, it is not yet the first example of a radio-quiet MSP, as Ray et al. (2013) detected weak radio pulsations from this object soon after its discovery. On the other hand, observations of *Fermi* LAT's previously unknown sources with pulsar-like emission properties in the radio domain have enabled the discovery of many new radio and gamma-ray MSPs (e.g., Ransom et al. 2011; Cognard et al. 2011; Barr et al. 2013): more than 60 as of today[‡], about 30% of the currently known population of Galactic disk MSPs. *Fermi* has therefore provided a vital contribution to the hunt for Galactic disk MSPs, and more MSPs will be found as new gamma-ray sources are discovered.

3 Science from timing observations of pulsars

As highlighted in the introduction, another common way of studying pulsars and their environment is through the so-called "pulsar timing" technique. In pulsar timing, times of arrival of pulses are recorded at a telescope and are used to count every single rotation of the pulsar. In this experiment, pulsars are therefore used as clocks, and perturbations in the "ticks" of these clocks allow us to measure and study many types of physical phenomena, especially if the pulsar belongs to a binary system (about 10% of known pulsars do).

A first famous example of a binary pulsar laboratory is the system formed by the 59-ms pulsar B1913+16 and its companion, also thought to be a neutron star but undetected as of now (Hulse & Taylor 1975). By timing B1913+16 in the radio, the discoverers rapidly came to the conclusion that the orbits of the stars in this system are not well represented by simple Keplerian orbits. In particular, the measurement of the decay of PSR B1913+16's orbit at a rate compatible with the predictions of Einstein's general relativity (GR) provided the very first evidence for the existence of gravitational waves. About ten years ago, the discovery of the double pulsar J0737−3039 (Burgay et al. 2003; Lyne et al. 2004), the unique case so far of a double neutron star system in which both objects are detected as radio pulsars, has provided pulsar astronomers with an even better laboratory for testing GR. The timing of the pulsars in this system allowed Kramer et al. (2006) to measure five post-Keplerian (PK) parameters (i.e., corrections to the Keplerian description of orbital motion), all of them for the fastest rotator in the binary, the 22-ms pulsar J0737−3039A: the advance of periastron in its orbit, the gravitational redshift parameter, the orbital period derivative, and two parameters describing the "Shapiro delay" induced by the deformation of space-time around its companion. By measuring the geodetic precession of the 2.8-s pulsar J0737−3039B, Breton et al. (2008) were able to determine a sixth PK parameter. Comparisons of the measured PK parameters in the double pulsar system with the expectations from GR have enabled the most precise tests of GR in the strong field regime done yet. In particular, the Shapiro delay parameter s measured by Kramer et al. (2006) agrees with the value predicted by GR at the 0.05% level. Recently, pulsar searches conducted with the Green Bank Telescope uncovered the 2.73-ms pulsar J0337+1715, a millisecond pulsar in a triple system with two other stars (Ransom et al. 2014). In this system, the radio MSP is in a short, 1.63-d orbit around a 0.20 $M_\odot$ white dwarf, and this inner binary system is itself in a wide,

[‡]See `http://astro.phys.wvu.edu/GalacticMSPs/GalacticMSPs.txt`

327.3-d orbit around a 0.41 $M_\odot$ companion, also white dwarf. PSR J0337+1715 is not the first case of a pulsar found to be in a triple system: PSR B1620−26 has a white dwarf companion and a Jupiter-mass companion (Thorsett et al. 1999), but in contrast with the latter system, the timing of PSR J0337+1715 reveals strong gravitational interactions between the three bodies in the system that need to be accounted for to properly model the pulsar's spin behavior. One promising application of the continued timing of PSR J0337+1715, when the effects affecting its motion are understood and well modeled, will be to test the strong equivalence principle (SEP) of GR: i.e., are the pulsar and the inner white dwarf falling in the gravitational field of the outer white in the same manner, in spite of their very different gravitational binding energies? If so, then alternative theories of gravity predicting such SEP violations will be ruled out by this experiment.

Another famous application of pulsar timing is the possibility to search for gravitational waves *directly*, with Pulsar Timing Arrays (e.g., Foster & Backer 1990). In a PTA experiment, the timing residuals of an array of very stable pulsars are analyzed jointly, to search for correlated perturbations tracing the passage of gravitational waves (GWs). Indeed, while pulsar rotation irregularities will induce timing residuals that are different between the pulsars, or other effects will affect the residuals of different pulsars identically (e.g., errors in the time standard), the phase and amplitude of residuals caused by gravitational waves is expected to depend on the pulsar directions with respect to the source. PTAs are sensitive to GWs with ultra-low frequencies of order $10^{-9} - 10^{-7}$ Hz. They are thus complementary to ground- and space-based GW detectors operating at much higher GW frequencies, such as LIGO and eLISA. Several collaborations have formed around the world, to search for GWs using the pulsar data recorded at different large radio telescopes. The Parkes Pulsar Timing Array (PPTA, Manchester et al. 2013) uses data from the Parkes radio telescope. The North American Nanohertz Observatory for Gravitational Waves (NanoGRAV, McLaughlin 2013) searches for GWs using pulsar timing data taken at the Green Bank and Arecibo radio telescopes. The European Pulsar Timing Array (EPTA, Kramer & Champion 2013) uses data from Jodrell Bank, Westerbork, Effelsberg, Nançay and Sardinia radio telescopes. Finally, the three collaborations form the International Pulsar Timing (IPTA, Manchester & IPTA 2013). Sources of GW emission that PTAs could be sensitive to are for instance supermassive black hole binaries or cosmological sources (cosmic strings, inflation era, etc.). A recent upper limit on a stochastic gravitational wave background is the one published by the PPTA collaboration (Shannon et al. 2013): by timing six highly stable pulsars for about 11 years, and assuming a slope of $-2/3$ for the red power spectrum induced by the GW background on the timing residuals, they placed a 95% upper limit on the characteristic strain h_c of 2.4×10^{-15}. Such a limit places useful constraints on the population of supermassive black hole binaries. The sensitivity of PTAs will continue to increase as more highly stable pulsars are discovered and added to PTAs, as the data sets get longer, as the timing precision on individual time of arrival measurements is improved (through e.g. instrumentation upgrades) and as sources of noise contaminating the timing data are understood and modeled better. By discovering many more highly stable MSPs and measuring times of arrival of radio pulses with much higher precision, future radio instruments such as the SKA[§] will increase the sensitivity of GW searches using PTAs dramatically.

4 Conclusions

In these proceedings I have reviewed some recent results from pulsar observations at different wavelengths. The list of examples chosen in the present document is far from exhaustive, yet it illustrates the importance of multi-wavelength observations of pulsars and the synergies that exist across the electromagnetic spectrum. The prospects for future pulsar observations are promising. With its enormous collecting area and frequency coverage, the SKA is expected to discovery many thousands to new radio pulsars (Smits et al. 2009), including hundreds in highly relativistic binaries allowing even more stringent tests of GR, and highly stable pulsars that can serve to search for GWs with PTAs. The SKA might also detect radio pulsars in compact orbits around the supermassive black hole at the center of the Milky Way, and the subsequent timing of these pulsars would then enable precise tests of the cosmic censorship conjecture and of the no-hair theorem (Liu et al. 2012). In a nearer future, observations with LOFAR[¶] or with NenuFAR[‖] will explore the very low radio frequency emission from pulsars and will be able to characterize the electron contents of the interstellar medium that induce strong dispersive delays at these low radio frequencies with unprecedented sensitivity. At the other end of the spectrum,

[§]Square Kilometre Array, see `https://www.skatelescope.org/`
[¶]Low-Frequency Array, `http://www.lofar.org/`
[‖]New Extension in Nançay Upgrading LOFAR, see `http://nenufar.obs-nancay.fr/?lang=en`

the *Fermi* LAT will detect more gamma-ray pulsars and find more sources in which to search for new radio pulsars, until the end of its activity. During the first half of the mission, the LAT has already demonstrated that pulsars constitute the dominant class of GeV gamma-ray sources in the Galaxy. The detection of pulsed emission above 10 and even 25 GeV for a number of pulsars, and the detection of Crab pulsations by Cherenkov telescopes at even more extreme energies have opened a new window on the study of pulsars and pulsar emission mechanisms in very high energy gamma rays. In this context, the advent of CTA**, the future ground-based very high energy gamma-ray observatory, is much anticipated.

I thank the scientific council of the Programme National Hautes Energies (PNHE) for inviting me to give this review on behalf of the PNHE.

References

Abdo, A. A., Ajello, M., Allafort, A., et al. 2013, ApJS, 208, 17
Ackermann, M., Ajello, M., Allafort, A., et al. 2013, ApJS, 209, 34
Aliu, E., Anderhub, H., Antonelli, L. A., et al. 2008, Science, 322, 1221
Alpar, M. A., Cheng, A. F., Ruderman, M. A., & Shaham, J. 1982, Nature, 300, 728
Antoniadis, J., Freire, P. C. C., Wex, N., et al. 2013, Science, 340, 448
Barr, E. D., Guillemot, L., Champion, D. J., et al. 2013, MNRAS, 429, 1633
Bisnovatyi-Kogan, G. S. & Komberg, B. V. 1974, Soviet Ast., 18, 217
Breton, R. P., Kaspi, V. M., Kramer, M., et al. 2008, Science, 321, 104
Burgay, M., D'Amico, N., Possenti, A., et al. 2003, Nature, 426, 531
Cognard, I., Guillemot, L., Johnson, T. J., et al. 2011, ApJ, 732, 47
Foster, R. S. & Backer, D. C. 1990, ApJ, 361, 300
Guillemot, L., Johnson, T. J., Venter, C., et al. 2012, ApJ, 744, 33
Guillemot, L., Kramer, M., Johnson, T. J., et al. 2013, ApJ, 768, 169
Hewish, A., Bell, S. J., Pilkington, J. D. H., Scott, P. F., & Collins, R. A. 1968, Nature, 217, 709
Hou, X., Smith, D. A., Guillemot, L., et al. 2014, A&A, 570, A44
Hulse, R. A. & Taylor, J. H. 1975, ApJ, 195, L51
Johnson, T. J., Guillemot, L., Kerr, M., et al. 2013, ApJ, 778, 106
Johnson, T. J., Venter, C., Harding, A. K., et al. 2014, ApJS, 213, 6
Kramer, M. & Champion, D. J. 2013, Classical and Quantum Gravity, 30, 224009
Kramer, M., Stairs, I. H., Manchester, R. N., et al. 2006, Science, 314, 97
Liu, K., Wex, N., Kramer, M., Cordes, J. M., & Lazio, T. J. W. 2012, ApJ, 747, 1
Lorimer, D. R. & Kramer, M. 2005, Handbook of Pulsar Astronomy, ed. Lorimer, D. R. & Kramer, M.
Lyne, A. G., Burgay, M., Kramer, M., et al. 2004, Science, 303, 1153
Manchester, R. N., Hobbs, G., Bailes, M., et al. 2013, PASA, 30, 17
Manchester, R. N., Hobbs, G. B., Teoh, A., & Hobbs, M. 2005, AJ, 129, 1993
Manchester, R. N. & IPTA. 2013, Classical and Quantum Gravity, 30, 224010
McLaughlin, M. A. 2013, Classical and Quantum Gravity, 30, 224008
Ng, C., Bailes, M., Bates, S. D., et al. 2014, MNRAS, 439, 1865
Nolan, P. L., Abdo, A. A., Ackermann, M., et al. 2012, ApJS, 199, 31
Pletsch, H. J., Guillemot, L., Allen, B., et al. 2013, ApJ, 779, L11
Pletsch, H. J., Guillemot, L., Fehrmann, H., et al. 2012, Science, 338, 1314
Ransom, S. M., Ray, P. S., Camilo, F., et al. 2011, ApJ, 727, L16
Ransom, S. M., Stairs, I. H., Archibald, A. M., et al. 2014, Nature, 505, 520
Ray, P. S., Ransom, S. M., Cheung, C. C., et al. 2013, ApJ, 763, L13
Romani, R. W. 2012, ApJ, 754, L25
Shannon, R. M., Ravi, V., Coles, W. A., et al. 2013, Science, 342, 334
Smits, R., Kramer, M., Stappers, B., et al. 2009, A&A, 493, 1161
Thorsett, S. E., Arzoumanian, Z., Camilo, F., & Lyne, A. G. 1999, ApJ, 523, 763
VERITAS Collaboration, Aliu, E., Arlen, T., et al. 2011, Science, 334, 69

**Cherenkov Telescope Array, `https://portal.cta-observatory.org/Pages/Home.aspx`

SF2A 2014
J. Ballet, F. Bournaud, F. Martins, R. Monier and C. Reylé (eds)

POSTCARD FROM GAIA

D. Katz[1]

Abstract. Nineteenth of December 2013 9h12 UTC, Gaia is launched from Kourou on a Soyouz-Frégat. Fourteenth of January 2014, Gaia is inserted on its orbit around the second Sun-Earth Lagrange point, 1.5 million kilometres beyond the Earth. The first months of the mission have been devoted to the commissioning of the satellite and its instruments and, since July, Gaia has entered the nominal mission phase. This presentation summarises the Gaia activities over the last months and presents the status of the mission at the beginning of the nominal phase.

Keywords: Surveys: Gaia.

1 Introduction

Gaia has been launched from Kourou on the 19^{th} of December 2013 at 9h12 UTC, by a Soyouz-Frégat. This success is the results of about 20 years of work during which several hundreds of people have been committed to the preparation of the Gaia mission. The ideas for a successor to Hipparcos have emerged in the first half of the 90s. In 2000, the Gaia mission was selected by the European Space Agency (ESA) as a cornerstone of its Horizon 2000+ space program. The next 13 years have been devoted to the definition of the technical design, then of the detailed technical design, building, assembly and ground-testing of the satellite. In 2006, and in parallel to the work on the spacecraft, a consortium has been charged by ESA to prepare and later operate the ground segment for the processing of the Gaia data. The Gaia Data Processing and Analysis Consortium (DPAC), today counts about 450 members from 25 different countries. The following pages present a tiny fraction of the work of the Gaia and DPAC people.

Gaia is orbiting around the second Lagrange point (L2) of the Sun-Earth system, about 1.5 million kilometres beyond the Earth. It has taken a little bit less than a month for Gaia to journey to L2. The insertion manoeuvre on the L2 orbit has been finalised on the 14^{th} of January 2014. Gaia is now repeatedly surveying the full celestial sphere for the 5 years of nominal mission and maybe for one or a few more years, if the fuel supply permits (which is currently the case). At the moment of the "Journées de la SF2A", June 2014, Gaia is at L2 since 5 months. These "Journées" offer an opportunity for a reminder of the Gaia science case and design (Sect. 2), for a presentation of the first news from the satellite (Sect. 3) and for an overview of the on-going ground-based activities connected to Gaia (Sect. 4).

2 Gaia in a few words

Gaia (Perryman et al. 2001; Lindegren 2010) is a full-sky survey mission. It is continuously and repeatedly observing the sky down to magnitude 20. This represents more than a billion sources. The bulk of them are stars from the Milky-Way, i.e. of the order of 1% of the total stellar content of our galaxy. In 5 years, Gaia will observe on average each source about 70 times (40 times for the RVS) with its 3 instruments: an astrometric instrument, a spectro-photometer and a medium resolution near infra-red spectrograph, the Radial Velocity Spectrometer or RVS. As successor of Hipparcos, Gaia will measure the position, trigonometric distances and proper motions of this billion sources. The spectrograph and spectro-photometer will complement the astrometric information with astrophysical parameters, e.g. radial velocities and stellar atmospheric parameters.

[1] GEPI, Observatoire de Paris, CNRS UMR 8111, Université Paris-Diderot, Université de recherche Paris Sciences & Lettres, 61 avenue de l'Observatoire, F-75014 Paris, France

2.1 Science case

Gaia will make a complete census of the celestial sources brighter than magnitude 20. This represents a large variety of objects and as a consequence the Gaia science case is very broad. The first science driver of Gaia is the study of our Galaxy, the Milky-Way: map its spatial, kinematical and chemical structure, reconstruct the history of the assembly of the stellar populations (inner and outer halo, thick and thin disk, bulge and bar), constrain the physical processes that drives the evolution of large spiral galaxies (turbulence, accretion, stellar mixing, dynamical resonances, etc...). Gaia is expected to provide distances with precisions better or equal to 10% for 150 millions stars (e.g. in zero extinction area, 10% precision on the parallax should be achieved for a 12 magnitude star located at 10 kpc).

Another important field of research for Gaia, is stellar physics. The direct measure of the distance will provide the absolute magnitude of the stars, which is a key parameter in stellar modelling. As a consequence, there will be a strong synergy between Gaia and the asteroseismology missions like, Kepler, Corot or the recently selected Plato mission. With 70 observations per source on average distributed over 5 years, Gaia will allow to study the time domain: variable stars, eruptive and cataclysmic variables, double and multiple stars (including the determination of stellar masses with precisions up to 1%). Gaia will provide information on the interstellar medium, in particular via a Diffuse Interstellar Band (DIB) located at 8620 Å and included in the RVS wavelength range. Gaia should detect extra-solar planets by spotting the (astrometric) reflex motion of the star due to the planetary companion(s). It should provide a census of Jupiter-like planets around bright stars within 200 parsecs, as well as masses for 2 000 to 5 000 planets with periods in the range 2 to 10 years.

In the solar system, Gaia should bring a factor 30 improvements on the orbits of small bodies, masses for about a hundred binary objects and shapes and dimensions for thousands of asteroids. By measuring the deflection of the light caused by the gravitational field of massive objects in the solar system (e.g. Jupiter), Gaia will provide tests of the theory of the general relativity. Gaia should also observe more than a million galaxies and 500 000 quasars. These later observations, performed in the optics, will allow for a direct link between Gaia's reference frame and the International Celestial Reference Frame (ICRF) defined in the radio domain. Gaia will spot some transient phenomenons which deserve a rapid ground-based follow-up and are interesting to observe without waiting for the publication of the catalogues. To allow for a rapid ground-based reaction, the DPAC will issue public science alerts. A typical case of science alerts are the super-novae. About 6 000 super-novae alerts are expected in 5 years, with 85% of SNe Ia and 30% discovered, and therefore observable, before maximum light.

2.2 Design

Gaia continuously surveys the sky with 2 telescopes. Their pupil areas are rectangular: 1.45×0.5 m. The 2 lines of sight are separated by 106.5 deg (hereafter referred to as the *basic angle*). The two fields of view, of 0.39×0.22 deg^2 each, are imaged on a single focal plane. It is made of 106 CCD detectors, for a total of about 1 billion pixels. The spatial resolution of a pixel is 59 mas by 177 mas.

Gaia payload's is made of 3 instruments. The astrometric instrument images the sky in a broad band G: [330, 1000] nm. Table 1 summarises the expected precisions (updated in July 2014 after the conclusion of the commissioning) on the end-of-mission parallaxes. This table is extracted from the Gaia *science performance* web page on the ESA Cosmos site, where a full detailed discussion of Gaia performances can be found: `http://www.cosmos.esa.int/web/gaia/science-performance`.

Table 1. Expected precision, as of July 2014, on the end-of-mission parallaxes. *"Bright stars"* corresponds to the V magnitude ranges 3 to 12 for B1V and G2V spectral types and 5 to 14 for M6V stars.

V	B1V	G2V	M6V
Bright stars	5-14 μas	5-14 μas	5-14 μas
15	26 μas	24 μas	9 μas
20	600 μas	540 μas	130 μas

The spectro-photometer (Jordi et al. 2010) is made of two prisms to disperse the light of the sources in two low resolution spectra, a blue spectrum [330, 680] nm and a red spectrum [640, 1050] nm. The spectral dispersion varies from 3 nm.pixel^{-1} at 330 nm to 27 nm.pixel^{-1} at 680 nm (for the blue channel) and from 7 nm.pixel^{-1} at 640 nm to 15 nm.pixel^{-1} at 1050 nm (for the red channel). The spectro-photometer provides the spectral energy distribution of the sources. For the stars, this allows to derive in particular their atmospheric parameters (effective temperature, surface gravity, metallicity) and mean alpha elements over iron ratio as well as to constrain the interstellar reddening.

The Radial Velocity Spectrometer (Katz et al. 2004; Katz 2009; Cropper & Katz 2011) is a medium resolution ($R = \lambda/\Delta\lambda = 11\ 500$) integral field near infra-red ([845, 872] nm) spectrograph. The RVS will record 40 epochs, on average, per source during the 5 years of the mission. The first objective of the spectrograph is the measure of the radial velocities down to about V=16 magnitude (for the redder stars). At the limiting magnitude, the end-of-mission precision on the mean radial velocity will be of the order of 15 km.s^{-1}. On the bright side (down to V=12-13), the expected end-of-mission precision is of the order of 1 km.s^{-1}. In addition to the radial velocity, the RVS will provide information on the stellar atmospheric parameters, on the abundance of the chemical species contained in its wavelength range (e.g. Si, Ti, Mg, N, S, Ne, C depending on the spectral type), on the interstellar reddening or on the rotational velocity.

In nominal observing mode, all the pixels are not transmitted to the ground, because this would largely exceed the antenna capabilities. Instead, "windows" around objects brighter than the limiting magnitude, are readout from the CCDs and telemetred to the Earth.

3 Postcard from L2

Gaia is orbiting around the second Lagrange point (L2) of the Sun-Earth system since the 14^{th} of January 2014. Mid-January, Gaia has started to record and transmit astrophysical data to the Earth. The data are received by the ESA Deep Space antenna in Cebreros (Spain), New Norcia (Australia) and Malargue (Argentina). They are then transmitted to the ESA and DPAC processing centers which have been successfully activated and process daily the incoming data. From January to June 2014, Gaia has collected a little bit more than 2 billion astrometric and spectro-photometric observations (representing respectively about 20 billion astrometric and 4 billion of spectro-photometric measures) and 500 million of spectroscopic observations (1.5 billion of RVS spectra)*. The volume of the raw scientific data is about 2.6 TB, while the processed data represent about 10 times more data, i.e. 25 TB.

The first months of the mission, December to July, have been devoted to the commissioning of the satellite and its instrument. This includes the adjustment of the satellite spin rate and the in-flight calibration of the micro propulsion system, the fine-tuning of the on-board software adjustable parameters, the focus of the telescope using mechanisms moving the M2 mirrors (Mora et al. 2014), the calibration of the CCDs, image quality, wavelength scale, instrument response and many other activities. Gaia has few calibration devices. The instruments are for a large part self-calibrated, i.e. calibrated using their own observations. For example, the RVS wavelength scale is calibrated from RVS spectra, measuring the location of reference lines in reference stars.

Figure 1 (top) shows an example of an RVS spectra of the star HIP86564. The "wings" on the left and right side, are produced by a filter which restrict the RVS wavelength range to [845, 872] nm (in order to limit the superposition of spectra, in particular in dense stellar areas). HIP86564 is a K star and its RVS spectrum is dominated by the strong lines of the Ca II triplet. Many other weaker lines are present in the spectrum. Four Fe and one Ti lines have been identified on the figure. HIP86564 is one of the reference stars, which has been used to calibrate the resolving power of the RVS by comparison to a library of ground-based spectra (assembled by DPAC members before launch in prevision of this task) convolved to a range of resolving power. This and other techniques†, have been used to find the best focus of the telescopes and optimise the image quality and the resolving power. Figure 1 (bottom) shows a spectrum of HIP86564 observed with the Narval@Pic-du-midi spectrograph. The Narval spectrum has been convolved to the nominal resolving power of the RVS, R = 11 500.

*One observation is made of 9 astrometric measures, 1blue and 1 red spectro-photometric measure and 3 RVS spectra

†e.g. the RVS resolving power has also been assessed by measure of the width of the cross-correlation function between RVS spectra and a mask. Dedicated methods have been used for the astrometric and spectro-photometric instrument.

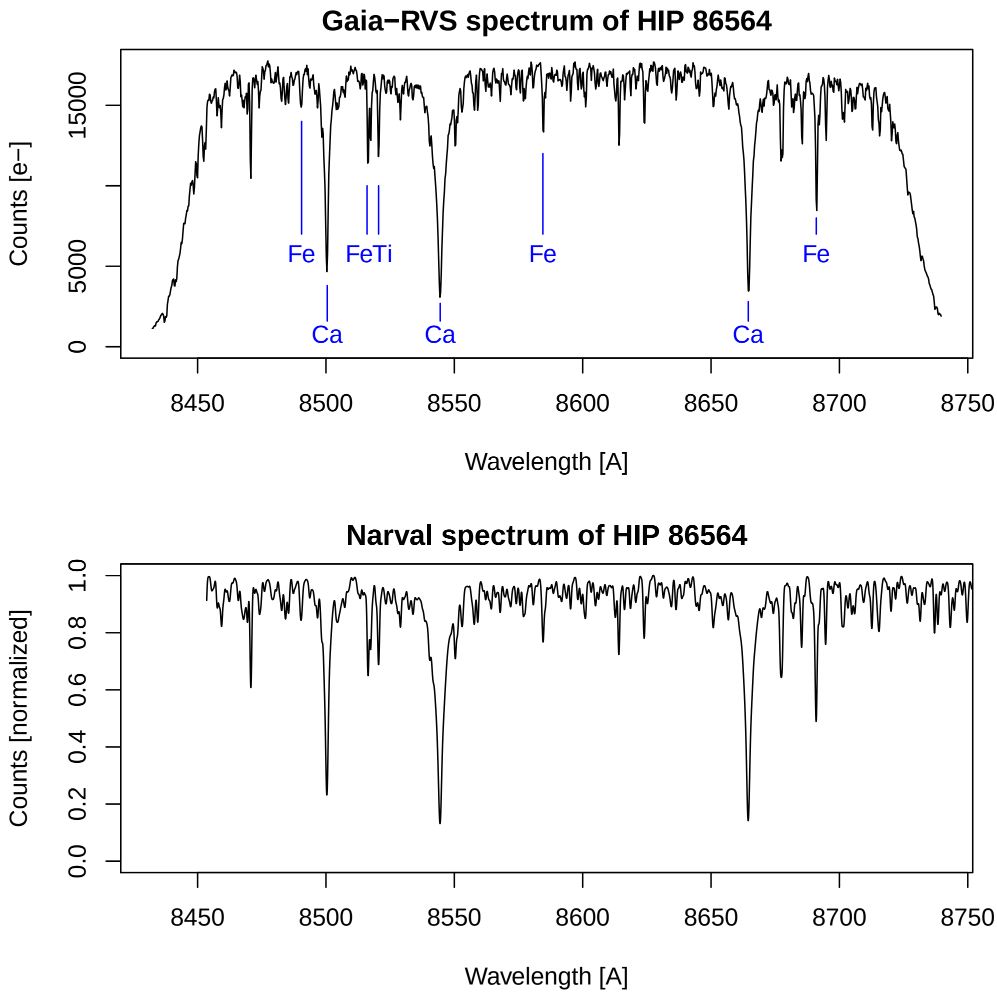

Fig. 1. Spectra of the star HIP86564, observed by the Gaia-RVS (top) and with the Narval spectrograph (bottom). The Narval spectrum has been convolved to the RVS nominal resolving power R = 11 500. Credits: ESA/Gaia/DPAC/Airbus DS/David Katz, Olivier Marchal and Caroline Soubiran.

At the start of the nominal mission phase, July 2014, Gaia works nominally, except for 3 issues that were identified during the commissioning:

- The level of straylight is higher than expected. This has a limited impact on the bright sources which remain much brighter than the underlying background. Faint sources, and in particular the faintest RVS targets, are more significantly impacted. To mitigate this problem, the on-board software and the RVS operating mode are revised. Since July, the RVS is operated in un-binned mode[‡]. It is also envisaged to reduce the surface of the windows read around each object in order to minimise the amount of background light recorded.

- The transmission of the mirror is slowly diminishing with time. This is caused by a small amount of water, trapped in the satellite, which deposits slowly, in particular, on some optical surfaces. The solution to recover the transmission is to briefly warm-up some mirrors and the focal plane which are equipped with heaters. This solution has been applied successfully during commissioning and could be repeated during the mission if needed.

[‡] The RVS used to be operated in 2 modes: an un-binned mode, called high resolution (HR), for the stars brighter than about V=11 and a binned mode, called low resolution (LR), in which the pixels were hardware-binned by samples of 3 pixels to minimise the total readout noise for the faint stars.

- The basic angle (i.e. the angle between the two lines of sight) is showing larger periodic variations than expected. Work is on-going to model and calibrate the effect.

4 Ground-based activities

4.1 *Ground-based processing*

The DPAC consortium includes several data processing centres (DPCs) in charge of different aspects of the processing[§]. In France, the Centre National d'Etudes Spatiales (CNES), is in charge of the processing of the spectroscopic data, of the asteroids, multiple systems, extra-galactic sources and of the classification and parameterisation of the sources. In particular the daily *routine* processing of the spectroscopic data should start soon. Figure 2 shows 3 spectra of the stars HIP117279 (K5 giant) recorded by 3 RVS CCDs during the same transit and processed at the CNES Toulouse centre. The spectroscopic pipeline (Katz et al. 2011) calibrates the RVS instrument, pre-processes, extracts, cleans and calibrates the spectra and derives their radial velocities (David et al. 2014). For HIP117279 the pipeline has derived a radial velocity of -49.1 km.s^{-1} (after barycentric correction), in good agreement (at this early stage) with the bibliographic radial velocity -50.1 km.s^{-1}.

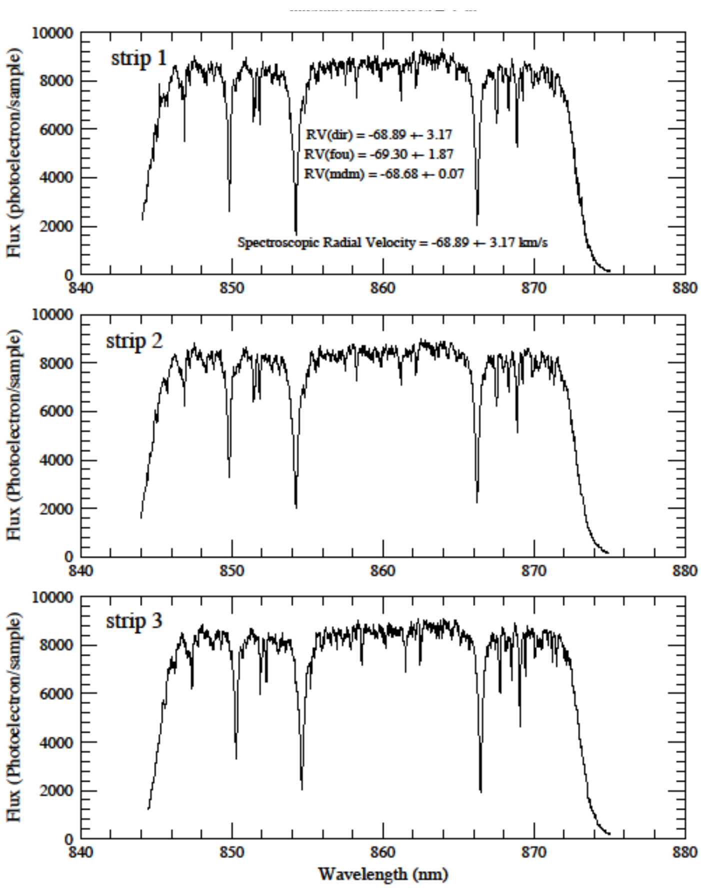

Fig. 2. Three RVS spectra of the star HIP 117279 processed at the CNES centre of Toulouse in September 2014. Credits: ESA/Gaia/DPAC/CNES/Yves Viala and Francoise Crifo.

The commissioning is completed and the nominal mission has started in July. The next important milestone will be the publication of the first intermediate catalogue, scheduled for the summer 2016. It should contain, the positions (α, δ) and G-magnitude for single stars as well as the proper motions and radial velocities for the Hipparcos stars. The second intermediate catalogue, scheduled early 2017, should contain the 5 astrometric parameters for single stars, integrated spectro-photometric bands and mean radial velocities for single stars. The

§for example: core and astrometric processing in ESAC (Spain), photometric processing in Cambridge (UK).

following intermediate catalogues will gradually provide more and more elaborated information with improved precision and accuracy until the final release currently scheduled in 2022. Detailed information can be found on the ESA Cosmos web site: `http://www.cosmos.esa.int/web/gaia/release`.

4.2 Ground-based observations

Several ground-based observing program are on-going in synergy with Gaia. They could be divided in two broad categories:

- The observations used for the calibration of Gaia and the processing of the data. Fall in this category, e.g. the observation of Gaia itself (the Ground-Based Optical Tracking - GBOT) necessary to achieve the best astrometric performance or the identification and characterisation of ground-based stable radial velocity standard stars (Crifo et al. 2010; Soubiran et al. 2013).
- The observations which will complement Gaia and maximise its scientific return: follow-up of Gaia detection of asteroids or of super-novae alerts, complementary spectroscopic surveys providing detailed chemical composition of bright stars and/or radial velocities beyond the RVS limiting magnitude. The Gaia-ESO Survey - GES (Randich et al. 2013), is a 300 nights survey on the VLT, aiming to collect about 100 000 Giraffe spectra and a few thousands UVES spectra.

Several projects of spectrograph with high multi-plexing will also provide ideal complement to Gaia. For the present/near future one can site: HERMES (Sheinis et al. 2014), MOONS (Cirasuolo et al. 2014), WEAVE (Dalton et al. 2014) or 4MOST (de Jong et al. 2014). For the next decade, the Maunakea Spectroscopic Explorer - MSE (Simons et al. 2014) is a very promising project. The concept is to upgrade the Canada-France-Hawaii telescope from the current 3.6 m telescope, to a 10 m telescope, to equip it with a wide field very large multiplexing low and high resolution spectrograph and to dedicate large fraction of the nights to spectroscopic surveys.

References

Cirasuolo, M., Afonso, J., Carollo, M., et al. 2014, in Society of Photo-Optical Instrumentation Engineers (SPIE) Conference Series, Vol. 9147, Society of Photo-Optical Instrumentation Engineers (SPIE) Conference Series

Crifo, F., Jasniewicz, G., Soubiran, C., et al. 2010, A&A, 524, A10

Cropper, M. & Katz, D. 2011, in EAS Publications Series, Vol. 45, EAS Publications Series, 181–188

Dalton, G., Trager, S., Abrams, D. C., et al. 2014, in Society of Photo-Optical Instrumentation Engineers (SPIE) Conference Series, Vol. 9147, Society of Photo-Optical Instrumentation Engineers (SPIE) Conference Series

David, M., Blomme, R., Frémat, Y., et al. 2014, A&A, 562, A97

de Jong, R. S., Barden, S., Bellido-Tirado, O., et al. 2014, in Society of Photo-Optical Instrumentation Engineers (SPIE) Conference Series, Vol. 9147, Society of Photo-Optical Instrumentation Engineers (SPIE) Conference Series

Jordi, C., Gebran, M., Carrasco, J. M., et al. 2010, A&A, 523, A48

Katz, D. 2009, in SF2A-2009: Proceedings of the Annual meeting of the French Society of Astronomy and Astrophysics, ed. M. Heydari-Malayeri, C. Reyl'E, & R. Samadi, 57

Katz, D., Cropper, M., Meynadier, F., et al. 2011, in EAS Publications Series, Vol. 45, EAS Publications Series, 189–194

Katz, D., Munari, U., Cropper, M., et al. 2004, MNRAS, 354, 1223

Lindegren, L. 2010, in IAU Symposium, Vol. 261, IAU Symposium, ed. S. A. Klioner, P. K. Seidelmann, & M. H. Soffel, 296–305

Mora, A., Biermann, M., Brown, A. G. A., et al. 2014, in Society of Photo-Optical Instrumentation Engineers (SPIE) Conference Series, Vol. 9143, Society of Photo-Optical Instrumentation Engineers (SPIE) Conference Series

Perryman, M. A. C., de Boer, K. S., Gilmore, G., et al. 2001, A&A, 369, 339

Randich, S., Gilmore, G., & Gaia-ESO Consortium. 2013, The Messenger, 154, 47

Sheinis, A., Barden, S., Birchall, M., et al. 2014, in Society of Photo-Optical Instrumentation Engineers (SPIE) Conference Series, Vol. 9147, Society of Photo-Optical Instrumentation Engineers (SPIE) Conference Series

Simons, D. A., Crampton, D., Côté, P., et al. 2014, in Society of Photo-Optical Instrumentation Engineers (SPIE) Conference Series, Vol. 9145, Society of Photo-Optical Instrumentation Engineers (SPIE) Conference Series

Soubiran, C., Jasniewicz, G., Chemin, L., et al. 2013, A&A, 552, A64

SF2A 2014
J. Ballet, F. Bournaud, F. Martins, R. Monier and C. Reylé (eds)

EXOCOMETS IN THE DISK OF TWO YOUNG A-TYPE STARS

F. Kiefer[1], A. Lecavelier des Etangs[1] and A. Vidal-Madjar[1]

Abstract. Optical spectra of the 20 Myrs old A-type stars β Pictoris and HD172555 have been collected between 2003 and 2011 with the HARPS instrument installed at the La Silla 3.6m telescope. In the two stellar absorption lines composing the Ca II doublet at 3950Å, we observed for these two targets narrow and doppler-shifted variable absorption features, which in the case of β Pictoris were known to occur since 1987. These transient signals are interpreted by the passage of orbiting evaporating bodies in front of the stellar disk, or transits of exocomets. We collected 493 individual detections of independent exocomets around β Pictoris allowing us to perform an unprecedented statistical studies of their physical properties (Kiefer et al. 2014a). Moreover, we report the detection of 4 transits of exocomets in front of the young A-type star HD172555; thus promoting this system as the second with simultaneous detection of exocomet transits in both lines of the Ca II doublet (Kiefer et al. 2014b).

Keywords: Exocomets, Beta Pictoris, HD172555

1 Introduction

The studies of young planetary systems, still forming or having yet formed planets, may unshade mysteries on the nature of our own Solar System as it was, 4.5 billion years ago. The system of the 20 Myrs old β Pictoris appears as a prototype for the young Solar System, and as such attracts a lot of attention since 30 years (Vidal-Madjar et al. 1998). This A5V star located at 19pc from Earth harbours plenty of features: a wide, warped and asymmetrical debris disk extending in both directions to more than 1000 AU from the star, an $8\,M_J$ planet β Pic b, and minor bodies such as comets, occasionnally grazing onto the star and producing the absorption signatures we are here reporting.

Several intriguing features of the β Pic disk find now explanations; among them, the asymmetry, possibly due to a clump produced by a collision between planetesimals at tenth of AU from the star (Dent et al. 2014, Telesco et al. 2005); the warp, compatible with the action of β Pic b on the disk (Mouillet et al. 1997); a stable gas disk at a couple of AU from the star standing still thanks to a braking effect due to a massive amount of carbon elements (Roberge et al. 2006); and the transient absorption in the stellar lines, identified as being due to exocomets (Ferlet et al. 1987, Beust et al. 1990, Vidal-Madjar et al. 1994). These all participate to build a comprehensive picture of this system, where planet formation happened in the same time as destructive collisions between planetesimals, where the dominating gravitationnal action of possibly the only massive planet present in that system, β Pic b, warps the disk from which it is born, and where icy bodies evaporate and replenish the disk in heavy elements such as carbon and oxygen (Lecavelier des Etangs et al. 1996).

Keeping in mind this picture of the system, the observation of exocomets orbiting close to β Pictoris does not look strange at all. In a system where planet formation comes with planetesimal destruction, some minor icy bodies of around 10 km size should form and undergo the influence of β Pic b to finally end up falling toward the star while evaporating plenty of gas and dust.

Until now, β Pictoris is the only known system with such a rich surroundings: planet, debris disk with various features and comets. However, we know that systems with debris disk are common (Booth et al. 2013, Morales et al. 2009, Plavchan et al. 2009, Roberge & Weinberger 2008), but we still lack detections of planets and comets in them. Planets are a challenge to find with the usual radial velocity and transit methods in young systems, mostly because the central star rotates fast and is often very active. However the recent development

[1] Institut d'Astrophysique de Paris, UMR 7095, 98bis Boulevard Arago, 75014 Paris

of direct imaging and interferometry already led to the evidence of the presence of planets aroung young stars (eg. Fomalhaut and Vega). But exocomets are even harder to observe. They are impossible to detect with direct imaging, since too faint. The only known method consists to observe narrow variable absorptions in the stellar spectrum. This requires the system to be seen edge-on, making it difficult to gather a large sample of exocomet-hosting young stars. Nevertheless, with luck and because the sample of stars with debris disk becomes larger and larger each year, several systems are seen edge-on and in some of them possible signatures of exocomets have been observed these last few years – such as HR10 (Lagrange-Henri et al. 1990), 49 Ceti (Welsh et al. 2013) and HD172555 (Kiefer et al. 2014b).

Among them, HD172555 is a very interesting system, and in some way resemble β Pictoris. It is roughly the same type (A7V) and the same age (12Myr); it harbours a dusty debris disk, although smaller; there is an intriguing excess of gas in the disk (Riviere-Marichalar et al. 2012); and a super-collision between planetesimals possibly occurred at 5 AU from the central star (Lisse et al. 2009). However, any planet has ever been discovered around it, in possible relation to the smallness of the disk, the super-collision, and the presence of a companion at 1000 AU.

In the first section, we report the detection of 493 exocomets passing in front of β Pictoris between 2003 and 2011 using archival data from the HARPS spectrograph (Kiefer et al. 2014a). The large size of this sample allowed us to conduct a statistical analysis of these objects. We discovered two families of exocomets orbiting β Pictoris. We show that they are physically distinct and thus differentiate by their origin. A first family, composed of aged comets depleted in volatile, is observed in an orbital evolution compatible with a mean-motion resonance mechanism induced by β Pic b. A second family, composed of fresher objects emitting volatiles 10 times more efficiently, roughly share a common orbit, compatible with the fragmentation of a bigger body, such as Shoemaker-Levy 9 or the Kreutz family in the Solar System.

In the second section, we report the detection of 4 exocomets passing in front of HD172555 using archival data collected with the HARPS spectrograph from 2004 to 2011 (Kiefer et al. 2014b). This is the second star after β Pictoris, around which we detect exocomets in both lines of the Ca II doublet. This allowed us to deduce the size of their cometary cloud and an estimation of their opacity.

2 The two families of exocomets in the disk of β Pictoris

Between 2003 and 2011, a total of 1106 optical spectra of β Pictoris have been collected with HARPS. As can be seen on Fig. 1, the Ca II doublet of β Pictoris presents at any time two main kind of features: a stable line centred at the star's radial velocity 21 km s^{-1}; and several narrow day-variable lines centred on radial velocities ranging from -150 to 200 km s^{-1}. The first kind of feature is the absorption line signature of a circumstellar gas disk seen edge-on, while the second kind of features is firmly identified to evaporating bodies, or exocomets, crossing the line of sight at different distances to the star (Beust et al. 1990, Ferlet et al. 1987).

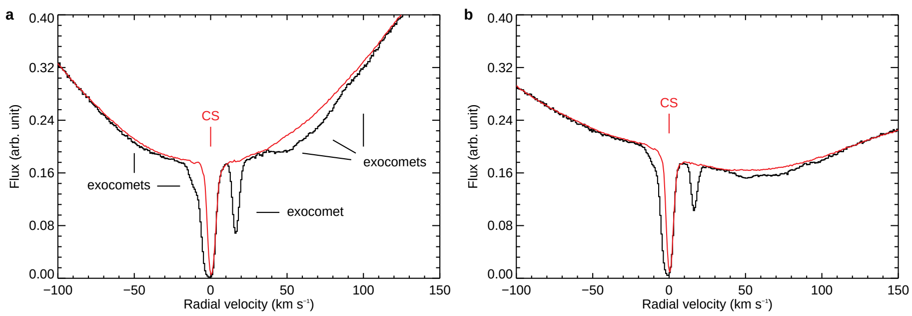

Fig. 1. This figure shows a typical spectrum of the Ca II doublet of β Pictoris obtained on 27 October 2009. **Left:** the Ca II-K line at 3934.66Å, with exocomets' transit signature identified; **right**: the simultaneously observed Ca II-H line at 3968.47Åwith the same signatures at the same velocities. The red line denote the reference spectrum derived from the data and CS indicates the stable circumstellar line. Radial velocities are given in the β Pic's rest frame. From Kiefer et al. 2014a.

The β Pic Ca II spectrum is observed to be stable on 30 min timescales. In order to limit any spurious spectral variability, while keeping track on variable comet's signatures, we resampled the 1106 HARPS spectra into 357 spectra separated by at least 10 min, averaging together all spectra collected in the same 10 min time interval. We then normalized each spectrum by the quiet reference spectrum, that we derived thanks to the large set of flux data points and depicted in red in Fig. 1. This led to normalized spectra showing exclusively features due to exocomets' transit. We fitted simultaneously each feature in the K and the H lines by a Gaussian depending on $p_{K,H}$ the K and H line depths, v_0 the central radial velocity, and Δv the linewidth FWHM,

$$p_{K,H}\, e^{4\ln 2 \frac{(v-v_0)^2}{\Delta v^2}} \quad \text{with} \quad p_K = \alpha e^{-A} \quad \text{and} \quad p_H = \alpha e^{-A/2}. \tag{2.1}$$

Because the depths of both Ca II K and H lines depend on the size (α) and the opacity (A) of the occulting cloud, and because we were able to probe both K and H lines in the same time, we could derive the size and the opacity of each detected cometary cloud. The size α measures the portion of the stellar disk occulted by the cometary cloud; it ranges between 0 and 1. In addition, we selected among all the detections a sample of 493 individual detections of independent exocomets. This allowed us to observe the presence of two clusters of detections: deep lines on one side (p_K>0.4) and shallow lines on the other side (p_K<0.4), as seen in Fig. 2 (left). The radial velocity and FWHM distributions of these two populations were clearly distinct. We could relate these observable quantities to physical quantities characterizing how the nuclei of the comets evaporate and which orbit they follow.

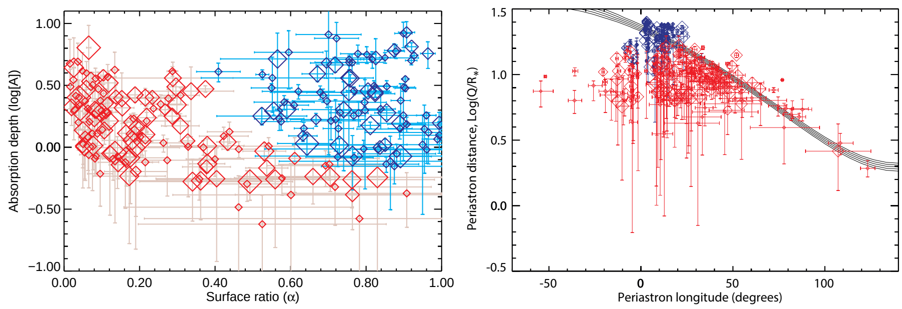

Fig. 2. Left: Diagram showing α, the portion of the star occulted by the cometary cloud, against $\log A$, a measure of the cloud's opacity for the 252 exocomets detected with α<1. Two clusters of data points are visible in this figure. They correspond, in blue, to the deep line population (p_H<0.4), and in red, to the shallow line population (p_K<0.4). The smallest data points correspond to data taken in 2003 and the largest data points to data taken in 2011. **Right:** This diagram shows the difference of distribution of exocomets' periastron distance with respect to periastron longitude between the two families. The black solid lines depict the expected evolution of orbits of small bodies in 4:1 mean-motion resonance with a jovian-mass planet at 5 AU from the central star. From Kiefer et al. 2014a.

Focusing on the exocomets occulting a portion of the star smaller than the stellar disk (α<1), we determined that the comets of the deep lines population, or population D, are ten times more efficient to reprocess incident stellar radiation into gas and dust evaporation than the comets of the shallow lines population, or population S. We also determined that the orbits of the population S exocomets follow a pattern compatible with a 4:1 mean-motion resonance mechanism with β Pic b (Beust & Morbidelli 1996, Thébault & Beust 2001); while the orbits of the population D exocomets scatter around a common orientation and periastron distance ($Q_D \simeq 18 \pm 4 R_\star$; $\varpi_D \simeq 7 \pm 8°$) as would happen in the case of the break-up of at least one bigger body (Fig. 2, right), much like the Kreuz Family in the Solar System. This is to be compared to the scattering of the orbits of population S with $Q_S \simeq 9 \pm 3 R_\star$ and $\varpi_S \simeq 22 \pm 25°$.

These results suggest that the two populations have distinct origin and therefore compose two distinct families of exocomets; one being a family of exhausted icy bodies that underwent a series of passage at close distance to the star, and the second being a family of fresher icy bodies possibly remnants of the fragmentation of one or a few bigger bodies.

3 Exocomets in the disk of HD172555

Between 2004 and 2011 a total of 129 spectra of HD172555 have been collected with HARPS, distributed on 22 nights of observations. The quiet Ca II spectrum of HD172555 is composed of two main features, an interstellar medium shallow absorption line at -19 km s^{-1}, and a central stable absorption line in both Ca II-K and Ca II-H lines. The first is identified to the G cloud of the local interstellar medium (ISM); while the second is identified to a circumstellar gas component, as for β Pic, yet shallower (Kiefer et al. 2014b). This is deduced from *i)* the lack of such absorption line in the Na I doublet at 5890Å, *ii)* the correspondance of the central radial velocity of this component to the redshift velocity of the star ($2\,\mathrm{km\,s^{-1}}$), and *iii)* any ISM component is expected at that redshift. The non-detection in Na I yields a 5-σ upper limit for the equivalent widths ratio of $EqW(\mathrm{Na\,I}\,D_2)/EqW(\mathrm{Ca\,II}\,K)<0.04$. This upper limit is much lower than typical values seen in the local interstellar medium where it is usually greater than 0.1 (see, e.g., Welsh et al. 2010). We thus concluded on the circumstellar nature of this feature.

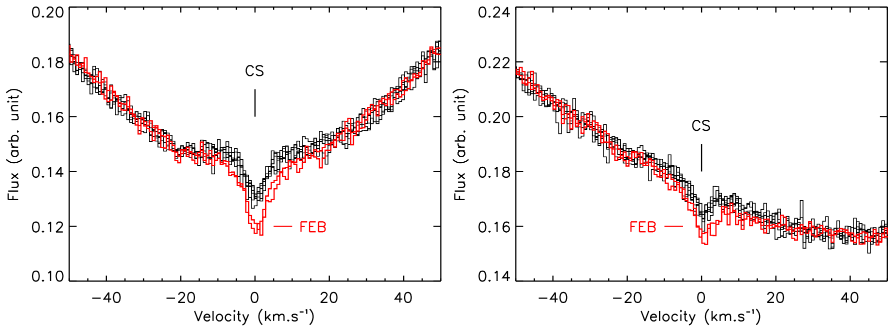

Fig. 3. Plot of HD172555 spectra of 2004. **Left:** the Ca II-K line; and **right:** the Ca II-H line. Two typical spectra on 22 September 2004 separated by a 6 minute-time interval (red lines) clearly show the presence of an additional absorption at the star's radial velocity in comparison to spectra obtained 100 days earlier (black lines). Velocities are given in the star's rest frame. From Kiefer et al. 2014b

But, transient events very similar to the variable absorption features of β Pic could also be observed on these spectra. As can be seen on Fig. 3, a significant narrow variable absorption is clearly detected in both Ca II-K and Ca II-H lines on the 22 September 2004 at the star's radial velocity. Three similar events were observed on 21 August 2005, 8 July 2010 and 11 July 2011. These are obviously due to the passage of occulting Ca^+ clouds in front of HD172555. Table 1 summarizes the properties of these occulting clouds that we derived by fitting the absorption lines, as for β Pic above.

Date (MJD)	Date (D/M/Y)	K line Depth	Velocity (km/s)	FWHM (km/s)	Surface Ratio α	Optical depth
53269.996	22/09/04	0.059 ± 0.003	0.35 ± 0.37	13.9 ± 0.9	≥ 0.9	0.061 ± 0.003
53270.134	22/09/04	0.072 ± 0.006	2.3 ± 0.5	19.5 ± 1.2	≥ 0.84	0.075 ± 0.006
53603.145	21/08/05	0.034 ± 0.004	13.5 ± 1.5	38.4 ± 9.7	$0.04^{+0.04}_{-0.01}$	1.69 ± 1.05
55385.285	08/07/10	0.029 ± 0.006	1.26 ± 1.07	$18.4^{+7.9}_{-10.1}$	≥ 0.024	≤ 10.3
55723.248	11/06/11	0.037 ± 0.002	-1.6 ± 0.5	22.5 ± 3.2	0.04 ± 0.01	1.90 ± 0.63
55723.280	11/06/11	0.032 ± 0.002	-2.44 ± 0.51	24.9 ± 3.3	0.04 ± 0.01	1.48 ± 0.51
55723.309	11/06/11	0.030 ± 0.003	-3.24 ± 0.73	24.2 ± 4.7	$0.04^{+0.02}_{-0.01}$	1.59 ± 0.78

Table 1. Table of the fit parameters with 1-sigma error bars. The upper and lower limits are given at the 1-sigma level. From Kiefer et al. 2014b.

Two types of clouds seem to be detected, if we compare the two most significant events (22/09/04 and 11/06/11): large and optically thin on one side, compared to small and opaque on the other side. There is no significant difference in the radial velocities, but the linewidth differ.

The fact that the measured surface ratio is well less than 1 for at least one of the most significant component, strongly suggests that we are witnessing the transit of cometary clouds in front of HD172555. The differences of the measured properties of these clouds can be explained as for β Pic's comet if the comets are detected at different distance to the star at the transit time. In this context, the similarity in radial velocities would be explained by different orientation of the respective orbits. This is usual observations on exocomets of β Pictoris.

4 Conclusions

The discovery of two families of exocomets orbiting β Pictoris leads to two main conclusions. First, the expected 4:1 mean-motion resonance mechanism induced by β Pic b dragging icy bodies towards the star is compatible with our observations. This indicates that if the planet is located at around 10 AU from the star, a reservoir of icy bodies exists at around 4 AU. This of course questions the origin of this 'belt' of icy planetesimals. The most straightforward answer would be that these bodies are the remnant of planet formation in the disk of β Pictoris. More investigations should be conducted on this question. Second, the observation of comets possibly originating from the break-up of a bigger bodies (like the Kreuz family in the solar system) and the emphasis of mean-motion resonance mechanism in the β Pic system, make this system even more similar to ours, and strengthen the identification of β Pic to a young solar system.

We also reported the discovery of exocomets orbiting the system of the young star HD172555, and the identification of a circumstellar gas disk feature. One of the main conclusions from these discovery is that the system should be seen almost edge-on. Morever, the system HD172555 appears then more and more similar to β Pictoris, in which the presence of a stable circumstellar gas disk can be explained by the evaporation of minor bodies, or comets. Since both features are detected around HD172555 it is tempting to invoke this relation to connect the presence of a circumstellar gas disk to the detection of exocomets. Future investigations will determine if this relation is real or not. Finally, the firm observation of exocomets in an other system brings hope to possibly observe exocomets in other young systems. Future observations of 30 young A-B type stars with HARPS are planned and will be dedicated to the search of exocomets.

References

Beust, H., Vidal-Madjar, A., Ferlet, R., & Lagrange-Henri, A. M. 1990, A&A, 236, 202

Beust, H., & Morbidelli, A. 1996, Icarus, 120, 358

Booth, M., Kennedy, G., Sibthorpe, B., et al. 2013, MNRAS, 428, 1263

Dent, W. R. F., Wyatt, M. C., Roberge, A., et al. 2014, Science, 343, 1490

Ferlet, R., Vidal-Madjar, A., & Hobbs, L. M. 1987, A&A, 185, 267

Kiefer, F., Lecavelier des Etangs, A., Augereau, J.-C., et al. 2014, A&A, 561, LL10

Kiefer, F., Lecavelier des Etangs, A., Boissier J., et al. 2014, Nature, 514, 462

Lagrange-Henri, A. M., Beust, H., Ferlet, R., Vidal-Madjar, A., & Hobbs, L. M. 1990, A&A, 227, L13

Lecavelier des Etangs, A., Vidal-Madjar, A., & Ferlet, R. 1996, A&A, 307, 542

Lisse, C. M., Chen, C. H., Wyatt, M. C., et al. 2009, ApJ, 701, 2019

Morales, F. Y., Werner, M. W., Bryden, G., et al. 2009, ApJ, 699, 1067

Mouillet, D., Larwood, J. D., Papaloizou, J. C. B., & Lagrange, A. M. 1997, MNRAS, 292, 896

Plavchan, P., Werner, M. W., Chen, C. H., et al. 2009, ApJ, 698, 1068

Riviere-Marichalar, P., Barrado, D., Augereau, J.-C., et al. 2012, A&A, 546, L8

Roberge, A., Feldman, P. D., Weinberger, A. J., Deleuil, M., & Bouret, J.-C. 2006, Nature, 441, 724

Roberge, A., & Weinberger, A. J. 2008, ApJ, 676, 509

Telesco, C. M., Fisher, R. S., Wyatt, M. C., et al. 2005, Nature, 433, 133

Thébault, P., & Beust, H. 2001, A&A, 376, 621

Vidal-Madjar, A., Lagrange-Henri, A.-M., Feldman, P. D., et al. 1994, A&A, 290, 245

Vidal-Madjar, A., Lecavelier des Etangs, A., & Ferlet, R. 1998, Planet. Space Sci., 46, 629

Welsh, B. Y., Lallement, R., Vergely, J.-L., & Raimond, S. 2010, A&A, 510, A54

Welsh, B. Y., & Montgomery, S. 2013, PASP, 125, 759

SF2A 2014
J. Ballet, F. Bournaud, F. Martins, R. Monier and C. Reylé (eds)

MAGNETOHYDRODYNAMICS AND SOLAR PHYSICS

Michel Rieutord[1]

Abstract. In this short review, I present some of the recent progresses on the pending questions of solar physics. These questions let us revisit the solar wind, the solar dynamo problem, the dynamics of the photosphere and finally have a glimpse at other solar type stars. Discussing the use of direct numerical simulations in solar physics, I show that the full numerical calculation of the flow in a single supergranule would require more electric power than the luminosity of the sun itself with present computer technology.

Keywords: solar physics, magnetohydrodynamics

1 Introduction

Studying the sun is motivated by many reasons. First, we would like to be able to explain to the street man, what is the sun, what has been its life until now, what will be its future, why it has permitted the appearance of life on Earth and whether it is unique or not in the Universe. These many reasons should be completed by the questions that stimulate astrophysicists in their quest of a full understanding of this celestial object. Indeed, the sun is also the closest star and it is a true self-operating physics laboratory where we can find conditions that cannot be reached on Earth.

Today the sun seems to be well-known: its fundamental parameters have been determined with some precision, not reached for any other star, and thanks to helioseismology, namely thanks to a careful interpretation of the frequencies of the tiny acoustic vibrations of the sun, we have also been able to check our calculations of its structure. It turns out that evolutionary models compare nicely to helioseismic models. Errors on basic thermodynamic quantities like temperature, density, pressure are around or less than 1% (Gough et al. 1996).

Of course the devil is in the details, and details are not missing on the sun. The first "big" detail is certainly its magnetic activity. If $\alpha - \Omega$ dynamo models allow us to retrieve the basic oscillation of the solar magnetic field, the understanding of irregularities of the cyle remains a challenge (Rieutord 2008). We understand that the cycle is strongly related to the differential rotation, but this feature of the dynamics of the sun still escapes a comprehensive view (although some numerical simulations can reproduce it – e.g. Brun & Toomre 2002). But among the challenges that the sun prompts to us, we should point out the origin of the supergranulation. This velocity feature has been known for more than fifty years (e.g. Rieutord & Rincon 2010), and we are still looking for the reasons of its existence. Last but not least, the problem of heating the sun's corona is still a pending challenge.

These questions are actually important for human activities. It is indeed observed that the magnetic activity of the sun is related to the irradiance of the Earth (see figure 1) and it is believed that the rather cooler climate that happened in Europe in the period 1645-1715 is actually a consequence of the vanishing solar activity during that period (the so-called Maunder minimum e.g. Ribes & Nesme-Ribes 1993 or Beer et al. 1998). Of course all the present space activities are dependent on the particle flux emitted by the sun and should be protected against the coronal mass ejection. However, the magnetic field of the magnetically active sun is also a shield that prevents, in part, the galactic cosmic rays from reaching the Earth. This is an everyday life concern for aircraft pilots who face the gamma ray bath due to these cosmic rays (e.g. O'Brien et al. 1996).

[1] Université de Toulouse; UPS-OMP; CNRS; IRAP; 14, avenue Edouard Belin, F-31400 Toulouse, France

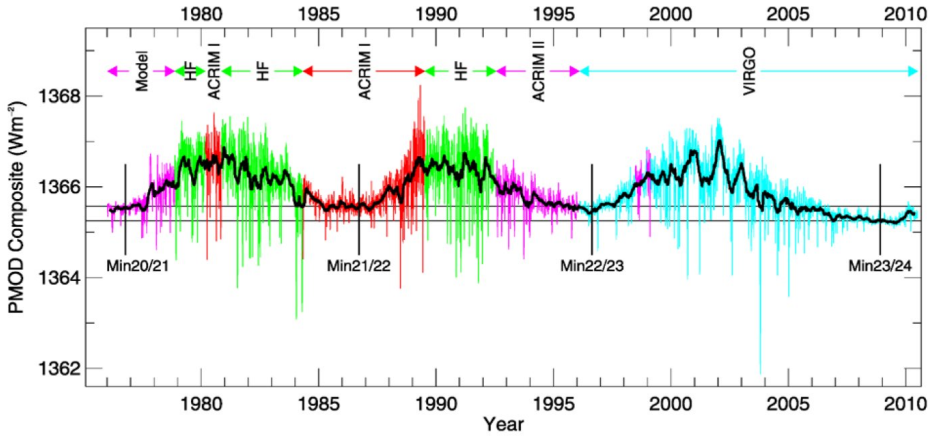

Fig. 1. Variation of the irradiance with time showing the imprint of the cycle (credit Fröhlich 2013).

2 The sun as a laboratory

The sun is a laboratory where we can observe matter in very extreme conditions compared to the terrestrial ones. In the old times, this allowed the discovery of helium by Janssen and Lockyer in 1868. More recently, the neutrinos oscillations have been discovered in the neutrinos emitted by the sun (e.g. Fukuda et al. 1998; Gough 2003). Yet, the sun is also a laboratory of giant size for studying turbulent fluid flows, or flows governed by magnetic fields, etc.

In particle physics, we are still looking for the theory that would unify, for instance, gravitation and the quantum world. In magnetohydrodynamics, the equations are well-know, namely,

$$\begin{cases} \rho\dfrac{D\vec{v}}{Dt} = -\vec{\nabla}P + \mu\Delta\vec{v} + \vec{j}\wedge\vec{B} \\ \\ \vec{\nabla}\cdot\vec{v} = 0 \\ \dfrac{\partial\vec{B}}{\partial t} = \overrightarrow{\mathrm{Rot}}(\vec{v}\wedge\vec{B}) - \overrightarrow{\mathrm{Rot}}(\eta\overrightarrow{\mathrm{Rot}}\vec{B}) \\ \vec{\nabla}\cdot\vec{B} = 0 \\ \rho\dfrac{De}{Dt} = \vec{\nabla}\cdot(\chi\vec{\nabla}T) - P\vec{\nabla}\cdot\vec{v} + \dfrac{\mu}{2}(\vec{\nabla}:\vec{v})^2 + \zeta(\vec{\nabla}\cdot\vec{v})^2 + \eta(\overrightarrow{\mathrm{Rot}}\vec{B})^2/\mu_0 \end{cases} \tag{2.1}$$

but their general solutions are still a dream.

2.1 Solving for the fluid flows

Solar flows are characterized by very large Reynolds numbers* typically above 10^{10}. Let us consider in more details the challenge of computing the evolution of a single solar granule from the sole fluid mechanics equation. With typical size of 1000 km, a typical velocity of 1 km/s and a typical kinematic viscosity of 10^{-3} m^2/s (e.g. Rieutord 2008), the Reynolds number is 10^{12}. The most energetic scale of the granule is of the size of the granule itself, namely 1000 km, and the scale at which viscosity smoothes velocity gradients is $\mathrm{Re}^{-3/4}$ smaller, namely 1 mm. It is therefore clear that numerical simulations will never reach such a resolution, at least for two reasons. First, it is useless: we are not interested in such details, and it is likely that such details are unimportant. Second, it is energetically impossible with present computer technology as we shall see now.

To include the smallest vortices, we need a grid mesh about ten times smaller than the dissipative structure, thus of size equal to 0.1 mm. Kolmogorov scaling law predicts that velocity amplitude decreases with the one third power of the scale. Hence, from 1000 km to 1 mm the velocity fluctuations have been reduced by a

*We recall that the Reynolds number of a flow is the ratio VL/ν where V is a typical velocity scale of the flow, L is a typical length scale of the flow and ν is the kinematic viscosity of the fluid.

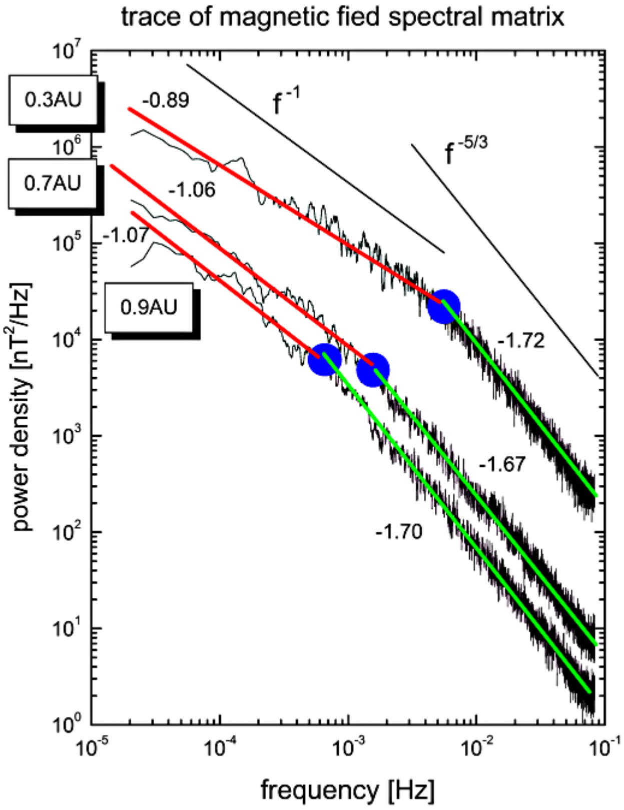

Fig. 2. Magnetic energy spectra as observed by Helios 2 in 1976 (from Bruno & Carbone 2005).

factor 10^3, thus to 1 m/s. Taking care of these velocities needs a time step of 10^{-4}s according to the Courant-Friedrichs-Lewy criterion ($\delta t \leq \delta x/V$). To summarize, we need a box of size 1000 km with a grid mesh of 0.1 mm, that is 10^{30} grid points. The time step needs to be not larger than 10^{-4} s, so as to follow the flow in real time.

As for the code, we take the PENCIL code as an example (Brandenburg & Dobler 2002). This code needs, typically, 80 floating-point operations per time step per grid point. Thus, just to follow the sun on one of its granule, we would need a calculator with that produces 8×10^{35} flops, a number to be compared with the present most powerful machine that produces 4×10^{16} flops. The difference is enormous, but the problem is that of the needed energy to run 8×10^{35} flops with present technology. Such technology indeed can produce 75 Gflops per watt. Hence, the power needed would be of order 10^{25} watts = 0.025 $L_\odot$ for a single granule! A single supergranule that contains a few hundred granules would need more than the power of the sun to be computed! Some colleagues mentioned to me the use of the quantum computer which may revolutionize the power needed for each flop, but it is not obvious that every algorithm will benefit from the efficiency of this computer.

The conclusion of this digression is that the modeling of the subgrid scales in turbulent flows remains a priority if we wish reasonable models of solar (and more generally of astrophysical) flows.

2.2 *Three kinds of flows*

As far as we know, turbulence modelling is not universal and therefore various and documented situations offer useful playgrounds to progress in our understanding of turbulent flows. As far as the sun is concerned, three regions may be observed and may lead to new guiding lines for turbulence modeling.

The first one may be the solar wind. This flow has been observed in situ by many space missions and celebrated spectra of the magnetic field fluctuations have been measured by Helios 2 (see Fig. 2). Such spectra are of interest because they guide us in the difficult problem of MHD turbulence. For instance, Iroshnikov (1964) and Kraichnan (1965) showed with phenomenological arguments, that the kinetic energy spectrum

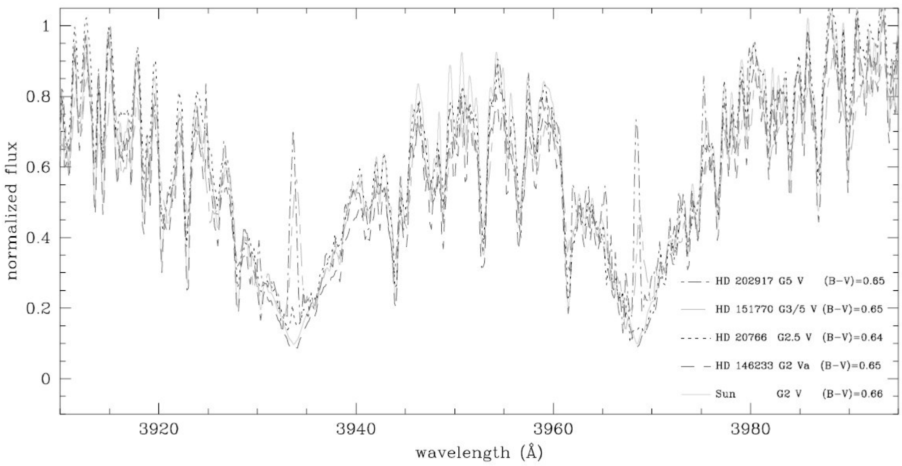

Fig. 3. The H and K absorption lines of Ca^+ for various solar-type stars (from Cincunegui & Mauas 2004). Note the thin emission line that arises in some stars right in the middle of the large absorption H and K lines.

should decrease like

$$E_k \propto k^{-3/2}$$

However this phenomenology was contested by Goldreich & Sridhar (1995) who showed that the anisotropy imposed by the magnetic field is crucial and therefore that $E_k \propto k_\perp^{-5/3}$, where $k_\perp$ is the wave vector component orthogonal to the mean-field.

Grappin & Müller (2010) and Grappin et al. (2014) have studied this problem through turbulence modelling in the spectral space using an incompressible and perfect (non-diffusive) fluid. The point was to determine the role of the various parameters that intervene in this problem. Among other things, they show that the nature of the spectrum, and therefore its exponent, depends on the intensity of the background magnetic field and on the correlation time of the large-scale forcing. They could compute the spectra for various relative angles of the wave and magnetic vectors, showing the presence of a $k^{-3/2}$ scaling spreading over a decade (Grappin et al. 2014).

Different conditions may be found at the sun's surface, in the photosphere. There, the magnetic and velocity fields can both be measured and spectra obtained (e.g. Rieutord & Rincon 2010), but most detailed observations are for the velocity fields, thanks to granule tracking (e.g. Rieutord et al. 2007). There too, various characteristics of turbulent flows can be measured. For instance Rieutord et al. (2008) have determined the first spectrum of surface flows describing supergranulation, while Rieutord et al. (2010) have shown that the supergranulation peak disappears when a magnetic pore is in the field. In this same study the spectra of intensity fluctuations have also been derived, showing among other results that the exponent describing the subgranular scale depends on the wavelength used for the observation. On the theoretical side, the main success has certainly been the simulation of the solar photosphere so as to reproduce the line profiles of various elements and deduce new constraints on the solar abundances (Nordlund et al. 2009).

In between the solar wind and the solar photosphere are the chromosphere and the corona. In these regions numerous questions are raised by MHD phenomena. We cannot avoid mentioning the still pending heating of the solar corona for which Alfvén (or magnetoacoustic) waves are serious candidates for carrying the energy. The recent result of López Ariste et al. (2013) on the dislocations observed in propagating MHD waves may both enlight the heating of the corona and the question of the flux of magnetic helicity at the sun's surface. Indeed, such dislocations may carry some magnetic helicity and therefore contribute to the global flux of magnetic helicity at the surface of the sun. We recall that magnetic helicity, namely

$$H_m = \int_{(V)} \vec{A} \cdot \vec{B} \, dV$$

is an invariant of ideal MHD if the boundary of the fluid does not let any magnetic flux going through (i.e. if $\vec{B} \cdot \vec{n} = 0$ on the boundary). This is typically an (approximate) invariant of coronal loops. But this is a quantity

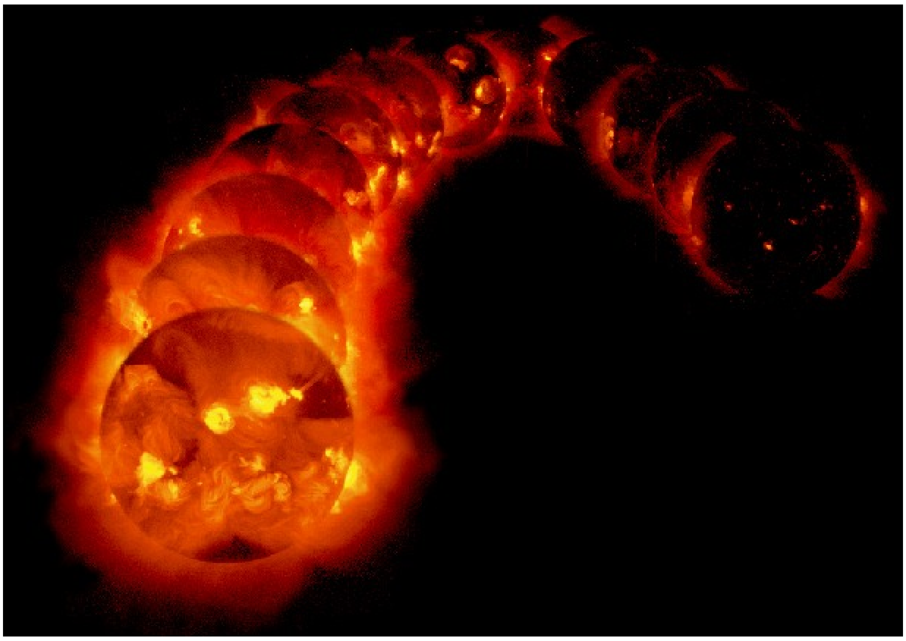

Fig. 4. The solar magnetic cycle as viewed in the X-rays by the satellite Yohkoh between 1991 and 2001.

that is important to measure so as to estimate its flux at the surface of the sun. Indeed, one of the recent results of numerical simulations of fluid dynamos is that saturation of the α-effect, the so-called α-quenching is affected by the magnetic helicity. If magnetic helicity cannot be expelled from the fluid domain, numerical simulations have shown that the α-effect is catastrophically quenched. At such a low level, this mechanism is no longer effective and would compromise the solar dynamo (Brandenburg & Subramanian 2005; Rieutord 2008). The sun manages to expell this helicity but the process is not well-known.

Hence, measuring the solar flux of magnetic helicity is crucial to put constraints on the solar dynamo. This is a difficult task that has been attempted by Dalmasse et al. (2014) for instance.

3 Moving to other stars

The sun itself shows only one example of a magnetically active star but astrophysicists would like a more general picture to appreciate, for instance, the effects of changing global parameters (mass, age, rotation, chemical composition, ...) on the magnetic activity.

A longstanding way of monitoring the magnetic activity of stars has been to measure the intensity of chromospheric lines, especially the H (396.85 nm) and K (393.368 nm) lines of the calcium ion Ca^+ (see figure 3). Understanding the magnetic activity of solar-like stars has become a crucial point for the detection of exo-planets because the magnetic activity raises the detection level of the radial velocity signature of a planet. As shown by Livingston et al. (2007), the emission inside the H & K line is quite nicely correlated to the solar cycle thus supporting the relevance of this index for monitoring the activity. Presumably, the emission line inside the large H & K absorption lines are coming from the chromosphere of the star but the process of this emission is not completely clear (Hall 2008).

Additional difficulties come from the modeling of the corona which is a region dominated by the magnetic fields. Global models of a corona like that of the sun are slowly emerging (Amari et al. 2013). These model are all the more welcome that the corona is the seat of the X-ray luminosity of solar-type stars. Such an emission is naturally another signature of the magnetic activity of stars. In X-rays the sun's luminosity is quite low, typically,

$$10^{-7}L_\odot \leq L_X \leq 10^{-6}L_\odot$$

but is varies with the cycle as nicely shown by the celebrated pictures obtained with the Yohkoh satellite (see figure 4). Since this X-ray emission is triggered by shock waves driven by flares in the corona of the stars, simulation of unstable magnetic configurations are an appropriate tool to investigate the energy released by the associated flows (Pinto et al. 2014).

4 Conclusion

Back to the sun we may conclude that our star is indeed a gigantic laboratory for MHD. There is a huge quantity of available data, but it is quite scattered (Rieutord 2012). From these data, constraints on various high Reynolds number flows may be derived. This is a detailed view of an active low mass star which should lead to understanding how such an activity influences the star's environment and further constraints the habitability problem.

References

Amari, T., Aly, J.-J., Canou, A., & Mikic, Z. 2013, A&A, 553, A43

Beer, J., Tobias, S., & Weiss, N. 1998, Solar Phys., 181, 237

Brandenburg, A. & Dobler, W. 2002, Computer Physics Communications, 147, 471

Brandenburg, A. & Subramanian, K. 2005, Phys. Reports, 417, 1

Brun, A. S. & Toomre, J. 2002, ApJ, 570, 865

Bruno, R. & Carbone, V. 2005, Living Reviews in Solar Physics, 2, 4

Cincunegui, C. & Mauas, P. J. D. 2004, A&A, 414, 699

Dalmasse, K., Pariat, E., Démoulin, P., & Aulanier, G. 2014, Sol. Phys., 289, 107

Fröhlich, C. 2013, Space Science Rev., 176, 237

Fukuda, Y., Hayakawa, T., Ichihara, E., et al. 1998, Physical Review Letters, 81, 1158

Goldreich, P. & Sridhar, S. 1995, ApJ, 438, 763

Gough, D. 2003, Ast. Space Sc., 285, 341

Gough, D. O., Kosovichev, A. G., Toomre, J., et al. 1996, Science, 272, 1296

Grappin, R. & Müller, W.-C. 2010, Phys. Rev. E, 82, 026406

Grappin, R., Müller, W.-C., Verdini, A., & Gürcan, Ö. 2014, ArXiv e-prints 1312.3459

Hall, J. C. 2008, Living Reviews in Solar Physics, 5, 2

Iroshnikov, P. S. 1964, Sov. Astron., 7, 566

Kraichnan, R. H. 1965, Phys. Fluids, 8, 1385

Livingston, W., Wallace, L., White, O. R., & Giampapa, M. S. 2007, ApJ, 657, 1137

López Ariste, A., Collados, M., & Khomenko, E. 2013, Phys. Rev. Lett., 111, 081103

Nordlund, Å., Stein, R. F., & Asplund, M. 2009, Living Reviews in Solar Physics, 6, 1

O'Brien, K., Friedberg, W., Sauer, H., & Smart, D. 1996, Environment International, 22, S9

Pinto, R. F., Vilmer, N., & Brun, A. S. 2014, ArXiv e-prints 1401.0916

Ribes, J. C. & Nesme-Ribes, E. 1993, A&A, 276, 549

Rieutord, M. 2008, C. R. Physique, 9, 757

Rieutord, M. 2012, in Astronomical Society of the Pacific Conference Series, Vol. 461, Astronomical Data Analysis Software and Systems XXI, ed. P. Ballester, D. Egret, & N. P. F. Lorente, 457

Rieutord, M., Meunier, N., Roudier, T., et al. 2008, A&A, 479, L17

Rieutord, M. & Rincon, F. 2010, Living Reviews in Solar Physics, 7, 1

Rieutord, M., Roudier, T., Rincon, F., et al. 2010, A&A, 512, A4

Rieutord, M., Roudier, T., Roques, S., & Ducottet, C. 2007, A&A, 471, 687

Session 01

Environnement planétaire et habitabilité: de la Terre primitive aux exoplanètes

SF2A 2014
J. Ballet, F. Bournaud, F. Martins, R. Monier and C. Reylé (eds)

A RADIATIVE-CONVECTIVE EQUILIBRIUM MODEL FOR YOUNG GIANT EXOPLANETS: APPLICATION TO GPI COMMISSIONING DATA

J.-L. Baudino [1], B. Bézard[1], A. Boccaletti[1], A.-M. Lagrange[2], M. Bonnefoy[2] and R. Galicher[1]

Abstract. We developed a radiative-convective equilibrium model for young giant exoplanets, in the context of direct imaging. Input parameters are the planet's surface gravity (g), effective temperature ($T_{\rm eff}$) and elemental composition. Under the additional assumption of thermochemical equilibrium, the model predicts the equilibrium temperature profile and mixing ratio profiles of the most important gases. Opacity sources include the H_2-He collision-induced absorption and molecular lines from H_2O, CO, CH_4, NH_3, VO, TiO, Na and K. Line opacity is modeled using k-correlated coefficients pre-calculated over a fixed pressure-temperature grid. Absorption by iron and silicate cloud particles is added above the expected condensation levels with a fixed scale height and a given optical depth at some reference wavelength. Model predictions are compared with the existing photometric and spectroscopic measurements of β Pictoris b and photometric data of HD95086 b recorded during GPI commissioning. This model was developed to interpret data of the instrument SPHERE at the VLT.

Keywords: radiative transfer, planets and satellites: atmospheres, planets and satellites: gaseous planets, stars: individual (β Pictoris), stars: individual (HD95086)

1 SPHERE

SPHERE (Spectro-Polarimetric High-contrast Exoplanet REsearch) is an instrument for the Very Large Telescope designed to study extra-solar planets by direct imaging. It is focused on spectroscopic and polarimetric characterization of giant planets. SPHERE combines extreme adaptive optics, coronography and spectroscopy, polarimetry and differential imaging.
We focus on young stars in the solar neighborhood to observe young planets just after their formation, thus having high temperature and self luminosity.

2 Model

We developed an atmospheric model based on radiative-convective equilibrium and thermochemical equilibrium. In this plane parallel model, the flux is thus constant with altitude and defined as $\pi F = \sigma {T_{\rm eff}}^4$.
The model includes absorption by eight molecular species and two different clouds. Molecular absorption is calculated using k-correlated coefficients computed on a grid of temperature profiles.
H_2O and CO: for water and carbon monoxide we used the HITEMP line list from Rothman et al. (2010).
CH_4: for methane we used line lists coming from Albert et al. (2009) , Boudon et al. (2006) , Daumont et al. (2013) and Campargue et al. (2012), and for CH_3D Nikitin et al. (2002), Nikitin et al. (2006) and Nikitin et al. (2013).
NH_3: for ammonia we used the Exomol line list from Yurchenko et al. (2011).
TiO and VO: for TiO and VO we used line lists coming from the website of B. Plez * (Plez (1998) with some

[1] LESIA, Observatoire de Paris, CNRS, UPMC, Université Paris-Diderot, 5 place Jules Janssen, F-92195 Meudon, France, jean-loup.baudino@obspm.fr
[2] UJF-Grenoble 1 / CNRS-INSU, Institut de Planétologie et d'astrophysique de Grenoble (IPAG) UMR 5274, Grenoble, F-38041, France
*`http://www.pages-perso-bertrand-plez.univ-montp2.fr/`

update since the publication).
Alkali Na and K: for alkali lines we used line lists from the NIST Atomic Spectra Database[†] with lineshape profiles from Burrows & Volobuyev (2003).
H_2-He CIA: for H_2-He, the collision-induced absorption coefficients were obtained from the website of A. Borysow [‡] (Borysow et al. (1988) Borysow et al. (1989) Borysow & Frommhold (1989) Borysow et al. (2001) Borysow (2002)). We considered absorption (and not scattering) by iron and silicate cloud particles, computed with the Mie theory for spherical particles, added above the expected condensation level with a fixed scale height and a given optical depth $\tau_{\rm ref}$ at some reference wavelength (1.2 μm).
The input parameters of the model are the effective temperature $T_{\rm eff}$, the acceleration of gravity g at 1 bar. The other set of free parameters is the optical depth of the silicate and iron clouds $\tau_{\rm ref}$, assuming the same column density, for the two species for a condensation pressure level of 1.0 bar, and the mean radius r of the cloud particles. Optical depths of the clouds are assumed to be proportional to the condensation pressure.
For output, the model then provides the radiative-convective equilibrium temperature profile $T(p)$, the corresponding vertical profiles of the absorbers at chemical equilibrium, and the spectrum at the resolution of the k-correlated coefficient distribution, i.e. 20 cm^{-1}.

We built some grids of surface spectra, corresponding to a range of $T_{\rm eff}$ and log(g) (Fig. 1). Each spectrum was computed for a radius equal to one Jupiter radius ($R_{\rm Jup}$) and a set of cloud parameters. We used the five grids (five sets of cloud parameters) defined in Appendix C of Bonnefoy et al. (2014).

For each set of observation and each synthetic planet in our grids, we selected the radius that minimizes the χ^2 between the Spectral Energy Distribution (SED) of the planet and the calculated spectrum, which is given by:

$$5\log_{10}(R) = -\frac{\sum(\frac{X_{\rm Observed}-X_{\rm Computed}}{\Delta X^2_{\rm Observed}})}{\sum(\frac{1}{\Delta X^2_{\rm Observed}})} \tag{2.1}$$

where R is the radius expressed in $R_{\rm Jup}$, $X_{\rm Observed}$ the observed apparent magnitudes bearing an uncertainty $\Delta X_{\rm Observed}$ and $X_{\rm Computed}$ magnitudes calculated at the distance of the planet from our model spectrum multiplied by the appropriate filter transmission. Then we multiplied our synthetic spectra by R^2 and computed the χ^2 between observed and calculated magnitudes.

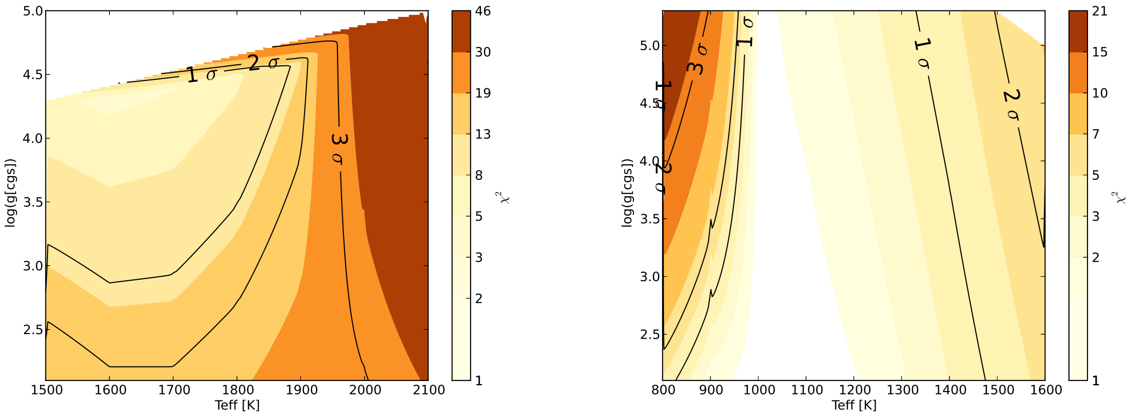

Fig. 1. Left: Example of grid for β Pictoris b SED with selection on radius and mass. **Right:** Example of grid for HD95086 b SED with selection on radius and mass.

We used the published age of the star and hot-start formation model from Spiegel & Burrows (2012) and classical core accretion formation model from Mordasini et al. (2012) to exclude synthetic planets with radius

[†]http://www.nist.gov/pml/data/atomspec.cfm/
[‡]http://www.astro.ku.dk/~aborysow/programs/

outside of the predicted ranges.
The mass is related to the radius R and the gravity g through the relation $g = \frac{GM}{R^2}$. In some cases, we made use of existing informations on the mass (e.g. through velocity measurements) to limit the range of allowed parameters R and g.

3 Planets

3.1 HD95086 b

In Galicher et al. (2014), we used apparent fluxes coming from NaCo and GPI (Gemini Planet Imager) observations in filters H, K1, L'.
To derive the planet parameters, we compared observations with BT-SETTL/Dusty/Cond models and our model.
Due to the lack of data it was difficult to obtain good constraints. In Galicher et al. (2014) we could still conclude that $T_{\rm eff} < 1500$ K and log(g[cgs])< 4.5 while with our model alone, we found $T_{\rm eff} = 1100 \pm 300$ K and no constraints on gravity.

3.2 β pictoris b

In Bonnefoy et al. (2014), we used observations coming from NaCo, NiCi, MagAO et GPI observations in filters Ys, J, $CH_{4_{S1\%}}$, H, Ks, L', NB4.05, M' and a J-band GPI spectrum (Figs. 2-3).
We begin to have a lot of data for the Spectral Energy Distribution (SED) of the planet and we have radial velocity measurements from Lagrange et al. (2012). With this last information, we can set a conservative upper limit on the mass of the planet of 25 $M_{\rm Jup}$.
We used either the SED alone or the normalized spectrum alone, and we considered upper limits on radius (2 $R_{\rm Jup}$) and mass (25 $M_{\rm Jup}$). In Bonnefoy et al. (2014), considering also other models BT-SETTL and Drift-PHOENIX, we derived $T_{\rm eff} = 1650 \pm 150$ K and log(g[cgs])< 3.7 for both cases, while, with our model alone we found 1650 ± 150 K and log(g[cgs])$= 3.7 \pm 0.9$.

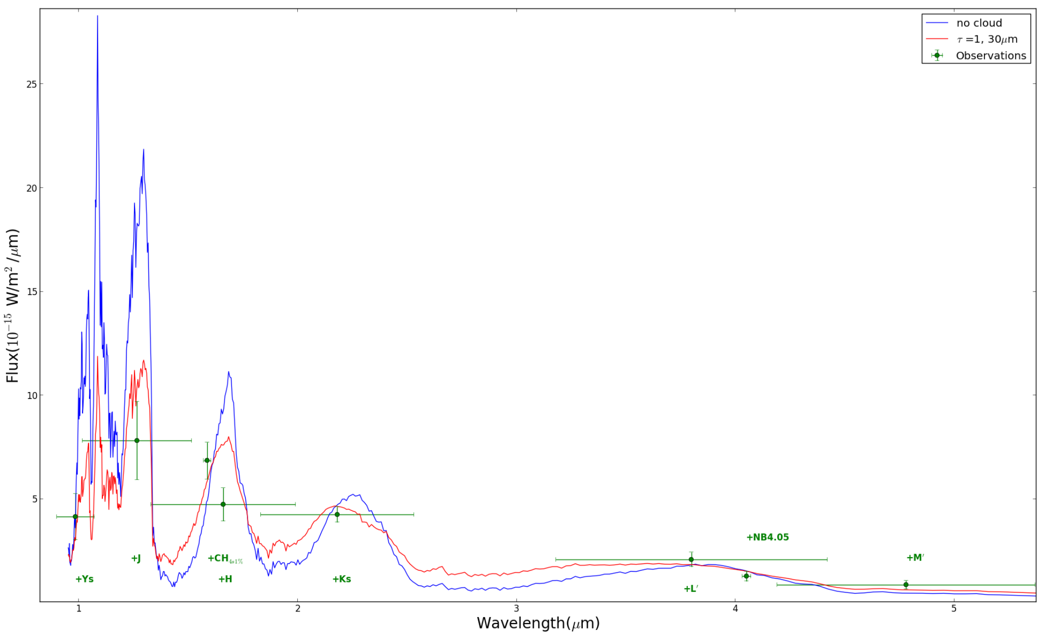

Fig. 2. SED of β Pictoris b (green dots) compared to the best fit models without clouds (blue) and with clouds (red).

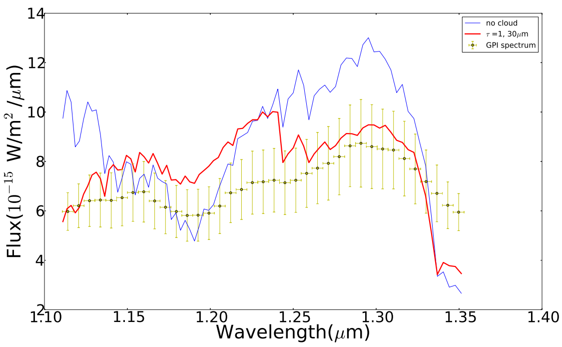

Fig. 3. J spectrum of β Pictoris b (yellow dots) compared to the best fit models without clouds (blue) and with clouds (red).

4 Conclusions and perspectives

We developed a very simple model that we compared with two sets of data. We derived constraints similar to those obtained from other models in the literature although our model is simpler.
We will obtain in a few months the first SPHERE data. Since the SF2A, we have updated our spectroscopic data for methane using the Exomol line list from Yurchenko & Tennyson (2014).
We begin to study the effect of metallicity on the derived parameters.

JLB PhD is funded by the LabEx Exploration Spatiale des Environnements Planétaires (ESEP) # 2011-LABX-030.

References

Albert, S., Bauerecker, S., Boudon, V., et al. 2009, Chemical Physics, 356, 131
Bonnefoy, M., Marleau, G.-D., Galicher, R., et al. 2014, A&A, 567, L9
Borysow , A., Jorgensen, U., & Fu, Y. 2001, J. Quant. Spec. Radiat. Transf., 68, 235
Borysow, A. 2002, A&A, 390, 779
Borysow, A. & Frommhold, L. 1989, ApJ, 341, 549
Borysow, A., Frommhold, L., & Moraldi, M. 1989, ApJ, 336, 495
Borysow, J., Frommhold, L., & Birnbaum, G. 1988, ApJ, 326, 509
Boudon, V., Rey, M., & Loëte, M. 2006, J. Quant. Spec. Radiat. Transf., 98, 394
Burrows, A. & Volobuyev, M. 2003, ApJ, 583, 985
Campargue, A., Wang, L., Mondelain, D., et al. 2012, Icarus, 219, 110
Daumont, L., Nikitin, A. V., Thomas, X., et al. 2013, J. Quant. Spec. Radiat. Transf., 116, 101
Galicher, R., Rameau, J., Bonnefoy, M., et al. 2014, A&A, 565, L4
Lagrange, A.-M., De Bondt, K., Meunier, N., et al. 2012, A&A, 542, A18
Mordasini, C., Alibert, Y., Georgy, C., et al. 2012, A&A, 547, A112
Nikitin, A., Brown, L. R., Féjard, L., Champion, J. P., & Tyuterev, V. G. 2002, Journal of Molecular Spectroscopy, 216, 225
Nikitin, A. V., Brown, L. R., Sung, K., et al. 2013, J. Quant. Spec. Radiat. Transf., 114, 1
Nikitin, A. V., Champion, J.-P., & Brown, L. R. 2006, Journal of Molecular Spectroscopy, 240, 14
Plez, B. 1998, A&A, 337, 495
Rothman, L. S., Gordon, I. E., Barber, R. J., et al. 2010, J. Quant. Spec. Radiat. Transf., 111, 2139
Spiegel, D. S. & Burrows, A. 2012, ApJ, 745, 174
Yurchenko, S. N., Barber, R. J., & Tennyson, J. 2011, MNRAS, 413, 1828
Yurchenko, S. N. & Tennyson, J. 2014, MNRAS, 440, 1649

SF2A 2014
J. Ballet, F. Bournaud, F. Martins, R. Monier and C. Reylé (eds)

THE JUNE 6 2012 TRANSIT OF VENUS: IMAGING AND SPECTROSCOPIC ANALYSIS OF THE UPPER ATMOSPHERE EMISSION

C. Bazin[1], X. Zhi[2], D. Valls-Gabaud[3], S. Koutchmy[1], P. Rocher[4], Z.Y. Zin[2], Y. Fu[2], L. Yang[2], G.Q. Liu[2], Z. Liu[2], K. Ji[5] and H. Goodarzi[6]

Abstract. In the context of transiting exoplanets, the last June 6, 2012 Venus transit was a unique opportunity to address important questions regarding its atmosphere. The transit of Venus is indeed a particular case of an Earth-like planet transit, and the inference one can make about the upper layers of its atmosphere can be applied to other exoplanets. To this aim, we designed a small spectrograph that we placed at the focus of the New Vacuum Solar Telescope of Yunnan Observatory in China (45 m focus and 1 m of aperture), coupled to a 4K×2K 14 bit CCD detector, to measure low-resolution optical spectra of the refracted, scattered and transmitted solar radiation in the upper layers of the planet. It covered the 385-780 nm range when Venus was over the disc, and 540-680 nm (including the O_2 terrestrial bands) during the 18 minutes-long egress. The Hα and He I D3 lines were recorded repeatedly. The atmospheric Lomonossov arc of Venus was simultaneously imaged using Hα and TiO filters, allowing us to check the slit position on the images of Venus and to locate the spectroscopic features on its disc. The spectra show the signature of the Northern Pole horn part; a second part was evidenced on the spectra taken near but outside the limb. We studied the O_2, H_2O and Hα line profiles searching for signatures arising from Venus and we compared the observed spectra with synthetic models. The spectroscopic dataset can now be used by a large community for discussing the properties of the upper atmosphere of Venus and the future detection of Venus-like exoplanets. Finally, the study is completed using a unique very high resolution deconvolved image of the arc and Venus silhouetted at the limb of the Sun, from the SOT of the Hinode space mission.

Keywords: Venus, transit, Lomonossov atmospheric arcs, Venus upper atmosphere, exoplanets

1 Introduction

On the occasion of the last 6 June 2012 Venus transit, we designed a spectrograph that we installed at the focus of the New Vacuum Solar Telescope of 1 meter-diameter and 45 meter of focal length at the Fuxian Lake site of Yunnan Observatory.

The goal of these observations was the study of the Lomonossov arc (L-arc) arising in the Venus atmosphere. In the 18th century, Lomonossov was the first who claimed to have observed the arc that he interpreted as an evidence of the Venus atmosphere), for analysing the transmitted, refracted, and reflected light of the Sun in the Venus upper atmosphere layers, which are badly known (see Russel et al. 2006; Tanga et al. 2011; Ehrenreich et al. 2011; Pasachoff et al. 2011). The Lomonossov arc occur when Venus crosses the solar limb. The context of this experiment is also that Venus can be considerered as a transiting exoplanet across the Sun, hence providing reference (optical) spectra when Venus-like transiting exoplanets will be found. In fact, no visible spectra existed or were obtained in the past Venus transits, and this was a unique opportunity and spectroscopic experiment ever attempted. We covered the full the visible range, from 380 nm to 780 nm, when Venus was transiting the solar disc. The slit of the spectrograph was placed across the Venus shadow, and 4 spectra per

[1] Institut d'Astrophysique de Paris, 98 bis Bd Arago, 75014 Paris, France
[2] Fuxian Solar Observatory, Yunnan Observatory, Chinese Academy of Sciences, Kunming, China
[3] LERMA, Observatoire de Paris, 61 Avenue de l'Observatoire, 75014 Paris, France
[4] IMCCE, Observatoire de Paris, 77 avenue Denfert-Rochereau, 75014 Paris, France
[5] Yunnan Key Laboratory of Computer Technology, Kunming, China
[6] Tabriz University, IR of Iran

second were recorded simultaneously with narrow-band Hα and TiO images. During the transit, we inserted a Rochon Calcite prism, to measure the polarisation in two orthogonal directions (see the optical configuration in Figure 1). We observed a high polarisation ratio and the data are still being analysed. We obtained 200 spectra over 70 nm-wide spectral intervals. In this contribution, we present a subset of our results, dealing with the O_2 line profiles along and outside the Lomonossov arc.

2 The Venus transit spectra and TiO 706 nm and Hα images

2.1 Spectrograph and optical setup

We used a Littrow spectrograph setup with two achromatic lenses for reducing the transverse aberrations. We placed before the spectrograph the usual "solar"-type imaging setup with a beam splitter cube, allowing us to have simultaneously the spectra, plus a channel in Hα (with a narrow-band filter) and channel for imaging in the TiO 706 nm filter to obtain near-IR images, see Figure 1. Further details of the configuration used are provided by Zhi et al. (2014).

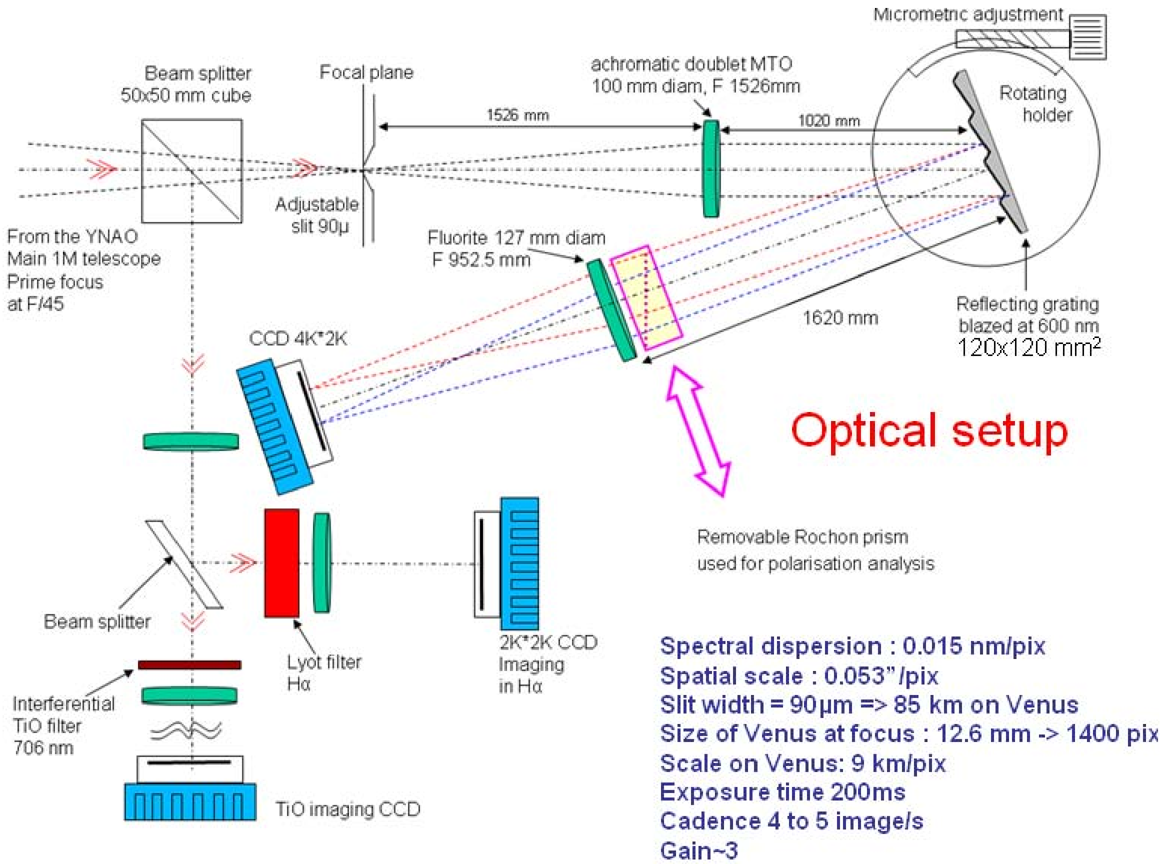

Fig. 1. Diagram of the optical setup after a cube beam splitter, including the Littrov spectrograph as a first channel, and the TiO 706 nm and Hα imaging channels in the reflected beam. We designed this setup for recording images and spectra simultaneously.

2.2 First visible spectra of the Lomonossov arc and O_2 line profiles analysis

Some 200 spectra with a 70 nm spectral range, covering the 380 nm to 780 nm interval, were successfully obtained during the egress phase of the transit of Venus.

As an example, we show a spectrum extracted from the sequence near Hα and the O_2 band. This spectrum (see Figure 2) was obtained when Venus was crossing the solar edge. Figure 2 also shows the Hα and TiO images obtained simultaneously, along with the position of the slit. The dark part of the spectrum is the shadow of Venus, and the bright continuum correspond to the Lomonossov arc.

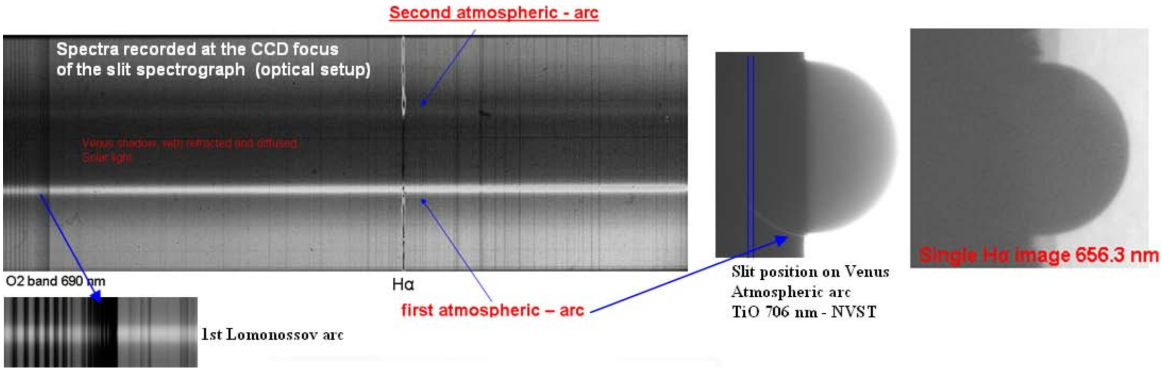

Fig. 2. *Left:* Two-dimensional spectrum in the O_2 bands and Hα region showing for the first time the spectra of the two Lomonossov arcs, (due to Mie scattering, see Ehrenreich et al. 2011). *Right:* the images in the Hα and TiO 706 nm bands and the position of the slit during the egress (when Venus crossed the solar limb at the end of the transit). Note the strong diffused light which makes the Venus disc not to be entirely dark, and the strong contribution of the chromospheric emission near the limb in the Hα image.

3 Discussion and conclusion

The adopted strategy for orienting the slit of the spectrograph was entirely successful. Two atmospheric horns corresponding to the Lomonossov arcs were observed, both photometrically and spectroscopically. The spectral range, exposure time, and the cadence were optimal. We observed the reddenning of the spectra, after analysing the intensity profiles in a more extended spectral domain.

The results presented here allowed us to disentangle the O_2 lines arising from the Earth atmosphere and those coming from the atmosphere of Venus. We note that there is a clear darkening followed by a brightening in the along the Lomonossov arc in the 688.8 to 688.9 nm O_2 line profile (see Figure 3).

The intensity profiles of Figure 3 give a better estimate of the gradients in the core (where the brightening occurs) and in the wings of this O_2 line as seen in absorption.

The collected data will be made publicly available and will be useful for analysis of Venus-type exoplanets, as the next Venus transit will not happen in 105 years (December 11, 2117). The database of level 2 spectra is in preparation and will be made publicly available.

CB and DVG warmly thank the hospitality of Fuxian Lake Observatory during the observations. We thank the entire NVST team from Fuxian Solar Observatory for the help provided to ensure the successful observations of the 2012 transit of Venus.

References

Ehrenreich, D., Vidal-Madjar, A., Widemann, T., Gronoff, G., Tanga, P., Barthélemy, M., Lilensten, J., Lecavelier des Etangs, A. and Arnold, L. 2011, A&A, 527, L2

Pasachoff, J.M., Schneider, G. and Widemann, T. 2011, AJ, 141, 112

Russell, C.T., Strangeway, R.J., Zhang, T.L. 2006, Planet. Space Sci., 54, 1344

Tanga, P., Widemann, T., Sicardy, B., Pasachoff, J., Arnaud, J., Comolli, L., Rondi, A., Rondi, S., and Suetterlin, P. 2011, Icarus, 218, 207

Xu, Z., Bazin, C., Valls-Gabaud, D., Koutchmy, S., Rocher, P., Jin, Z.Y., Fu, Y., Yang, L., Liu, G.Q., Liu, Z. and Ji, K. 2014, A&A Letters, submitted

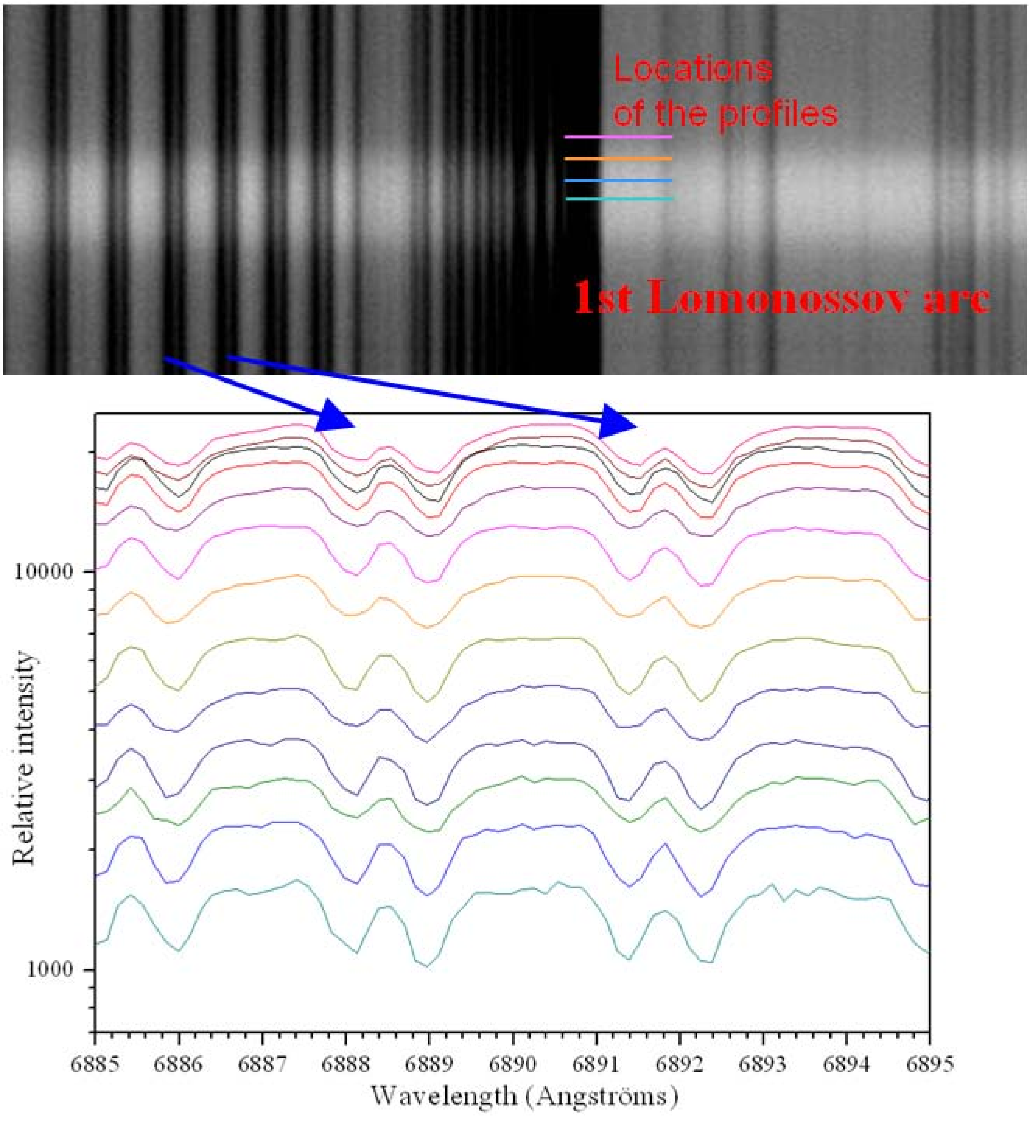

Fig. 3. Intensity profiles as a function of the wavelength in the O_2 terrestrial bands. The profiles are compared along and outside the Lomonossov arc to analyse the effects of the refracted, transmitted, and reflected solar light in the upper layers of the Venus atmosphere, and searching some O_2 line profiles signature. The distance between two consecutive radial cuts corresponds to 100 km on the Venus disc.

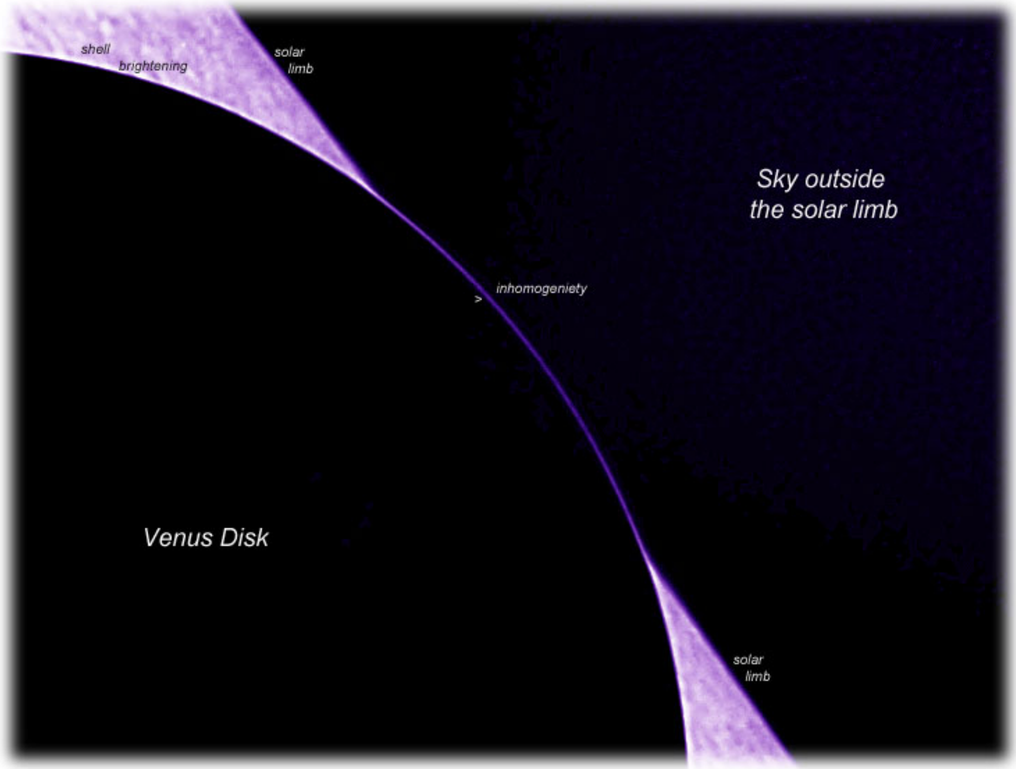

Fig. 4. The egress of Venus as observed by Hinode. The image has been processed and deconvolved, and note that no Gibbs effect is detected on the very narrow O II Lomonossov arc outside the solar disc. A narrow and faint brightening is seen around the disc of Venus, as seen in silhouette over the extreme solar limb.

SF2A 2014
J. Ballet, F. Bournaud, F. Martins, R. Monier and C. Reylé (eds)

DYNAMICS OF EXOPLANETARY SYSTEMS, LINKS TO THEIR HABITABILITY

E. Bolmont[1], S. N. Raymond[1] and F. Selsis[1]

Abstract. Our knowledge of planets' orbital dynamics, which was based on Solar System studies, has been challenged by the diversity of exoplanetary systems.

Around cool and ultra cool dwarfs, the influence of tides on the orbital and spin evolution of planets can strongly affect their climate and their capacity to host surface liquid water.

We illustrate the role of tides and dynamics with the extreme case of planets orbiting around brown dwarfs. In multiple planet systems, the eccentricity is excited by planet-planet interactions. Planets are therefore heated up from the inside by the tidally-induced friction. This process can heat a habitable zone planet to such a level that surface liquid water cannot exist.

We also talk about the newly discovered potentially habitable Earth-sized planet Kepler-186f. Given the poorly estimated age of the system, the planet could still be evolving towards synchronization and have a high obliquity or be pseudo-synchronized with a zero obliquity. These two configurations would have a different effect on the climate of this planet.

Keywords: Planets and satellites: atmospheres, Planets and satellites: dynamical evolution and stability, Planets and satellites: individual: Kepler-186f

1 Introduction

Since 1995 and the discovery of the first exoplanet orbiting a Sun-like star (Mayor & Queloz 1995), the number of detected exoplanets has been steadily increasing. With now almost 1500 confirmed exoplanets (`http://exoplanets.org/`) and around 20 of them good candidates to host surface liquid water (`http://phl.upr.edu/projects/habitable-exoplanets-catalog`), we enter in an fascinating age.

With the improvements made in exoplanet detection, we are able to detect planets less and less massive (or smaller and smaller) approaching the mass (or size) range of the Earth. We are now also able to probe the habitable zone of stars. We define here the habitable zone (HZ) as the region around a star where a planet with the right atmosphere can potentially sustain surface liquid water (Kasting et al. 1993; Selsis et al. 2007).

Most of the detected HZ planets are either too massive (radial velocity planets) or too large (transit planets) to be categorized unequivocally as terrestrial planets. For example, Kepler-22b, a 2.4 $R_\oplus$ planet could be either a mini-Neptune or a super-Earth (Borucki et al. 2012). However Quintana et al. (2014) reports the discovery of the first Earth-sized planet in the HZ of a low mass star: this planet has a radius only 10% bigger than Earth's. This planet is the closest we know to Earth, it is very likely rocky and can potentially host surface liquid water.

Unfortunately, being in the HZ of a star does not mean that the planet hosts surface liquid water. The presence of water depends on many different physical parameters and quantities. Not only does it depend on the characteristics of the atmosphere (pressure, temperature) and of its composition but also on the dynamics of the orbit of the planet. Indeed, the eccentricity of the orbit as well as the rotation period of the planet and its obliquity (the angle between the rotation axis and angular momentum vector) have an effect on the climate of a planet (the so-called Milankovitch cycles that govern the glaciation periods on Earth; Berger 1988). As all these quantities are influenced by tidal forces, one should take into account the tidal orbital evolution of the system in order to assess the potential of a planet to host water.

In Section 2, we describe how tides do influence the parameters affecting the climate of a planet. In Section 3, we study the evolution of planets around brown dwarfs which constitutes an extreme case of how dynamics and tides can impact a planet's climate. In Section 4, we study Kepler-186f, the first Earth-sized planet in the HZ of a cool star and discuss what can be said about its spin state. Finally, we conclude in Section 5.

[1] Univ. Bordeaux, LAB, UMR 5804, F-33270, Floirac, France
CNRS, LAB, UMR 5804, F-33270, Floirac, France

2 Tidal evolution

The tidal model used here is a re-derivation of the equilibrium tide model of Hut (1981) as done in Eggleton et al. (1998). We use the constant time lag model and consider non-coplanar situations as in Leconte et al. (2010).

Let us consider a system with N planets orbiting a star. In order to compute the correct tidal evolution of the system, one has to consider the tide raised by the star on each planet (called the planetary tide) but also the tide raised by each planet on the star (called the stellar tide). The planetary tide and stellar tide act on different quantities. Depending on the body considered and on its tidal dissipation factor (a quantity linked to the constant time lag), the tides act on different timescales.

2.1 Effect of the stellar tide

The force created by the stellar tide will influence the semi-major axis, eccentricity and inclination of the orbit of the planet. The resulting torque will impact the rotation rate of the star. As the mass of the star is usually much higher than that of the planet, the planet cannot distort the star significantly and the corresponding evolutions will occur on long timescales.

The semi-major axis evolution of the planet depends on the position of the planet with respect to the corotation radius, which is the orbital radius where the orbital period matches the star's rotation period. If the planet is inside the corotation radius, the planet migrates inwards and eventually falls on the star. If the planet is outside the corotation radius, it migrates outwards. The planet will affect the rotation rate of the star, however this effect is negligible in most cases. However, the rotation of a star can be significantly increased when a massive planet falls on it (Bolmont et al. 2012).

Unless the star is a very fast rotator, the stellar tide acts to decrease the eccentricity. When the star is a very fast rotator, a slingshot effect can lead to an increase of the eccentricity. The stellar tide acts to decrease the inclination of the planet: it brings back the orbital plane into the equatorial plane of the star.

2.2 Effect of the planetary tide

The force created by the planetary tide will influence the semi-major axis and eccentricity of the orbit of the planet. The resulting torque will impact the rotation rate of the planet: the rotation period and the obliquity. The star can distort the planet significantly and in particular the evolution of the spin will occur on short timescales.

Very quickly in the evolution of a circular orbit planet, the rotation will tend towards synchronization, which is a state for which the rotation period of the planet is equal to its orbital period. If the orbit is eccentric, the planet quickly reaches pseudo-synchronization, which means that its rotation tends to be synchronized with the orbital angular velocity at periastron (Hut 1981). The resulting rotation period is shorter than the orbital period. In the meantime, the obliquity of the planet quickly tends to zero.

On longer timescales, after the pseudo-synchronization state is reached, the planetary tide makes the eccentricity and semi-major axis of the planet decrease.

3 Planets around brown dwarfs

Planets around brown dwarfs are interesting to study for three reasons: the HZ is located close-in (Selsis et al. 2007; Andreeshchev & Scalo 2004), so planets in the HZ experience strong tidal interactions and these HZ planets are easy to detect (Belu et al. 2013; Triaud et al. 2013).

3.1 One planet system

Bolmont et al. (2011) investigated the influence of tides on the orbital evolution of single-planet systems orbiting brown dwarfs (BDs) of different masses. The BD tide, the tide created by the planet in the BD, makes the planets either fall on the BD or migrate slightly outwards (see Figure 1). Not taking this migration into account would over-evaluate the time a planet spends in the HZ (as was done in Andreeshchev & Scalo 2004). However Bolmont et al. (2011) showed that, despite this outward migration, planets around BDs more massive than $0.04\ M_\star$ could stay in the HZ up to a few gigayears.

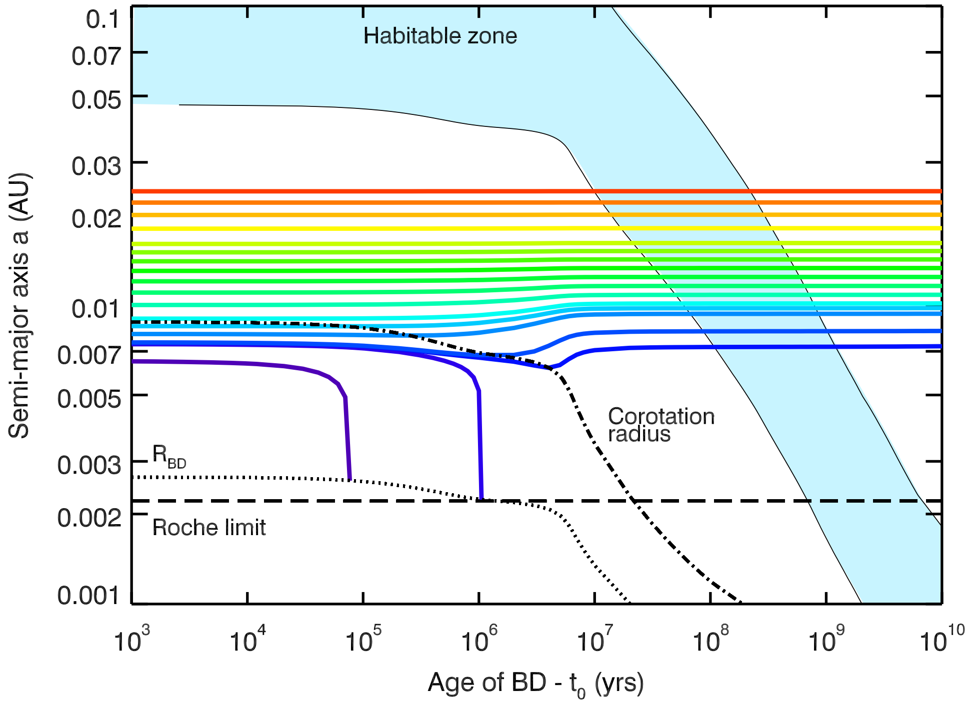

Fig. 1. Evolution of the orbital distance of an Earth-sized planet orbiting a BD of 0.04 $M_\star$. The colored lines correspond to the evolution for different initial orbital distances. The black dashed dotted line corresponds to the corotation radius, the dotted line corresponds to the BD's radius. The insolation HZ is also plotted (blue region). The thick dashed line corresponds to the Roche limit. t_0 is the initial time, named "time zero". It corresponds to the time of protoplanetary disk dispersal, taken here as 1 Myr (Bolmont et al. 2011).

Let us consider a single planet of 1 $M_\oplus$ orbiting a 0.04 $M_\star$ BD at 0.01 AU. It would reach the HZ about 100 Myr after the protoplanetary disk dispersal (Bolmont et al. 2011). A hundred million years is enough to erode the obliquity of the planet and bring it in pseudo-synchronization. If the eccentricity is very small the pseudo-synchronization rate is very similar to the synchronization rate (a difference of 3.5% for an eccentricity of 0.06 and of 0.1% for an eccentricity of 0.01). Therefore, when the planet reaches the HZ, it is likely to have a null obliquity and a synchronous rotation.

This means that this planet always shows the same side to the BD and that its poles receive very little light. This raises the problem of the possible existence of cold traps: i.e. regions on the planet where the temperature is constantly lower than 273 K and where all the water of the planet will condense (Joshi et al. 1997; Joshi 2003). In this configuration, night side and poles could be cold traps and although the planet is in the HZ, it would not be able to host surface liquid water. However, this situation is not completely hopeless, a dense enough atmosphere that would allow the repartition of heat around the whole planet could prevent cold traps from capturing the water content of the planet. Wordsworth et al. (2011) showed that Gliese 581 d (if it exists; Robertson et al. 2014) could have a habitable climate despite a synchronous rotation state.

3.2 *Multiple planet system*

The situation differs if the planet is part of a multiple planet system. Because of planet-planet interactions, eccentricity and obliquity do not tend to 0 but an equilibrium value which is the result of the competition between tidal damping and planet-planet excitation.

An extreme case of planet-planet excitation is the mean motion resonance (MMR). When two planets are in MMR, the ratio between their orbital periods is commensurable and the eccentricity is excited to higher levels. A close-by example is the 1:2:4 MMR between the 3 inner satellites of Jupiter (Io, Europa, Ganymede). This eccentricity excitation maintained by the resonance causes Io to experience an intense internal heating due to the stress it experiences on one orbit. This internal heating is estimated at about 3 W/m^2 (e.g., Spencer et al. 2000), which is about 40 times higher than the internal heat flux of Earth (about 0.08 W/m^2 and mainly due to radioactivity; e.g., Davies & Davies 2010). On Io this heat flux gives rise to intense volcanic activity. A tidally evolving planet in the HZ could be heated up and driven in a runaway greenhouse state (thus creating a "tidal Venus"; Barnes et al. 2013).

Let us consider the case of three Earth-sized planets orbiting just outside the corotation radius of a 0.08 $M_\star$ BD. We consider a) a BD with a tidal dissipation factor similar to hot Jupiters' (due to their likeliness in structure, we consider here that BDs and hot Jupiters have a similar dissipation factor Hansen 2010) and b) a BD with a tidal dissipation of ten times the dissipation of hot Jupiters.

In both cases, the planets experience a convergent outward migration but they will do so quicker in case b) than a). The difference in dissipation will lead to two dynamically different systems. As the migration is faster in case b) planets enter a MMR chain (1:2:4) after a few million years of evolution. However in case a), they stay outside of resonance. Figure 2 shows the evolution of such a system at an older age (1 Gyr), the HZ has shrunk and the two inner planets are now in the HZ. The eccentricities of the planets in case a) are relatively small < 0.07 but in case b) due to the MMR excitation, they can reach 0.15.

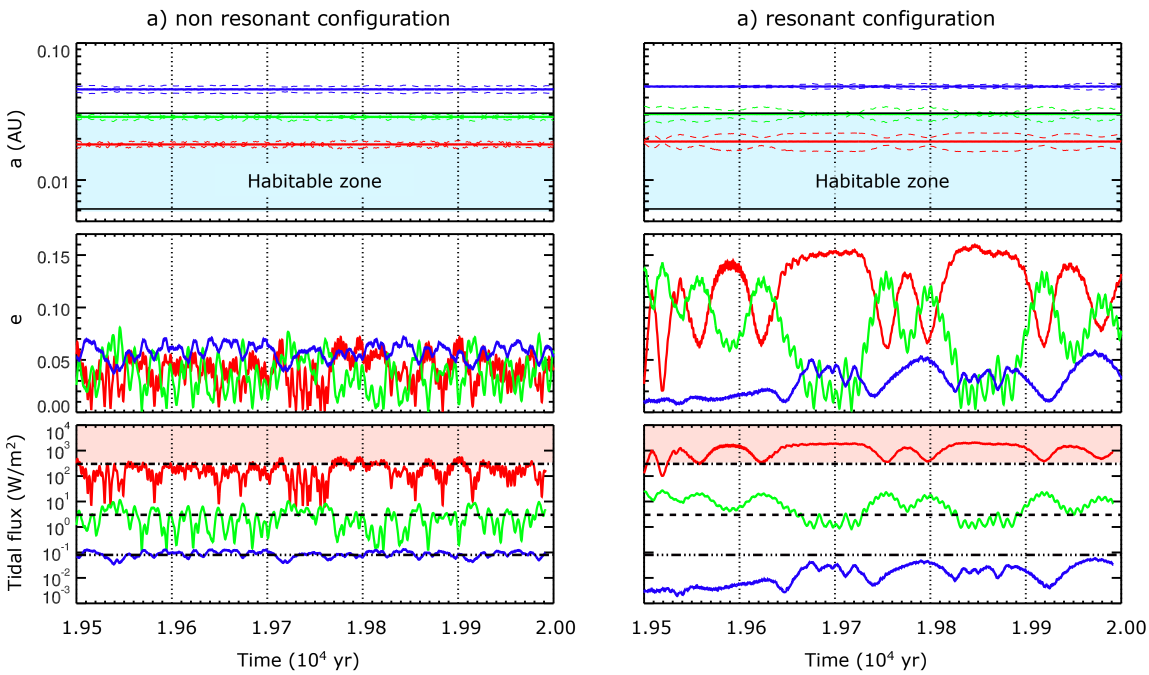

Fig. 2. Evolution of the orbital distance, eccentricity and tidal heat flux of three Earth-sized planets orbiting a BD of 0.08 $M_\star$ in a) a non-resonant configuration, b) a resonant configuration (1:2 MMR). Top graph: the full colored lines correspond to the semi-major axis evolution of the 3 planets, and the dashed lines correspond to their perihelion and aphelion distances. The blue shaded region is the HZ. Middle graph: eccentricity of the 3 planets. Bottom graph: the full colored lines correspond to the tidal heat flux of the 3 planets. The black dashed dotted line corresponds to 300 W/m^2, the dashed line corresponds to Io's heat flux and the dashed 3 dots line corresponds to Earth's heat flux. The shaded red region corresponds to where the heat flux is so high that the planet is in a runaway greenhouse state.

Figure 2 also shows the evolution of the tidal heat flux for each planet, compared to three values: the limit of runaway greenhouse 300 W/m^2 (Kopparapu et al. 2013)*, Io's tidal heat flux and Earth's heat flux.

In case a), the average tidal heat flux of the inner planet (red) is below the limit of 300 W/m^2 and sometimes exceeds this limit for a few 10 yr. If we consider that the tidal heat flux is the only heat source of the atmosphere of the planet (we neglect momentarily the insolation from the BD), we could say that most of the time the inner planet can have habitable conditions. Let us consider that this planet has oceans. When the tidal heat

*Note that this limit has been re-evaluated with 3D climate simulations at 375 W/m^2 by Leconte et al. (2013)

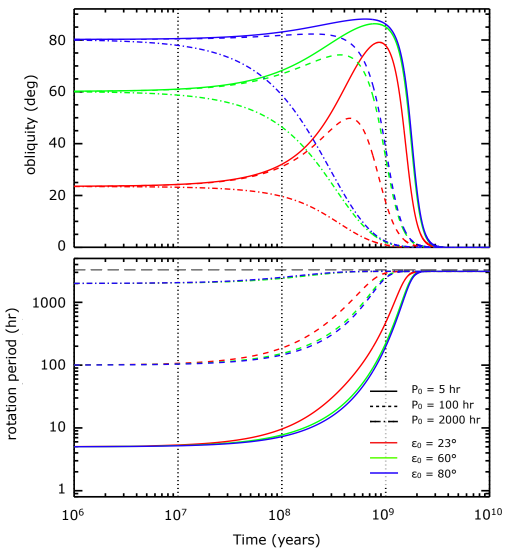

Fig. 3. Long-term evolution of the obliquity (top) and rotation period (bottom) of Kepler-186f (set $\mathcal{A}$). Each set of linestyle curves represents a different initial spin rate and each set of colored curves represents a different initial obliquity. The thick, black dashed line represents the pseudo-synchronous rotation which, for this zero-eccentricity example, is the 1:1 spin–orbit resonance. This Figure comes from Bolmont et al. (2014).

flux exceeds the runaway greenhouse limit, the oceans will start evaporating. However, for an Earth-like ocean, 10 years would not be enough to evaporate it all, so that the water reservoir would survive.

However, in case b), due to the excitation of the eccentricity of the orbits, the tidal heat flux of the inner planet always exceeds the runaway greenhouse limit. Thus, this HZ planet would be too hot to host surface liquid water.

The middle planet (in green) is on the outer edge of the HZ, and its tidal flux is relatively low (in average it is about Io's tidal flux). For case a), this planet could potentially have habitable conditions†. For case b), the planet spends some time around aphelion outside the insolation HZ and it has a tidal heat flux a bit superior to Io's in average. Without tidal heating, this planet could be too cold to be able to sustain a potential liquid water reservoir, however taking into account tidal heating will improve the conditions for habitability. One could imagine a more extreme case of a planet on an orbit completely outside the HZ but heated up by tides sufficiently to be able to host surface liquid water.

When assessing habitability of planets in the HZ of BDs, one should investigate if tides are strong enough to drive a runaway greenhouse. If the atmosphere receives an average flux ($\Phi_\star + \Phi_{\rm tides}$) lower than 300 W/m^2, the planet can sustain a liquid water reservoir, but if it receives an average flux higher than 300 W/m^2 the planet will be too hot to be able to sustain a liquid water reservoir.

4 Kepler-186

The planetary tide influences the rotation of the planet, which is an important parameter for climate studies. We take here the example of the planet Kepler-186f, the first Earth-sized planet in the HZ of a star (Quintana et al. 2014). Using the system parameters given in Bolmont et al. (2014), we compute the tidal evolution of the system and focus our attention on the fifth planet.

Contrary to the four inner planets, which quickly reach a pseudo-synchronous state and low obliquities (in $\lesssim 1$ Myr), the evolution timescale of the rotation of Kepler-186f is much longer. Figure 3 shows the evolution of obliquity and rotation period for Kepler-186f for different initial obliquities and rotation periods. The initial values are of course not known but N-body simulations of terrestrial accretion tend to produce planets with fast initial spins and isotropically distributed obliquities (Kokubo & Ida 2007).

Figure 3 shows that Kepler-186f's obliquity increases for all but the slowest initial spin rate. The obliquity increases for a few hundred megayears and this period is followed by a long, slow decay that lasts 2-3 Gyr (for the arbitrarily chosen range of initial spin rates and an Earth-like tidal dissipation). The equilibrium obliquity of the planet is very low, it does not feel the dynamical interactions of the four inner planet.

Given the estimated age of the system ($\gtrsim$4 Gyr according to Quintana et al. 2014), Kepler-186f could be in pseudo-synchronous rotation with a very small obliquity (see Fig. 3). But if the system is a bit younger

†We don't discuss here the influence of an intense volcanic activity on habitability (Hanslmeier 2012).

(1 Gyr), or if the planet dissipates less than what was assumed, Kepler-186f could have a faster rotation and a very high obliquity ($\lesssim 80$ degrees).

This would impact the climate of the planet: a non-negligible obliquity causes seasonal effects while a negligible obliquity causes a low insolation at the poles; the rotation has an impact on the heat transport in the atmosphere and if it is sufficiently close to the synchronous rotation, the night side could a cold trap. It is therefore necessary to consider all possible rotation states when assessing the climate and habitability of this planet.

5 Conclusions

The climate of a planet depends on many parameters. It depends on the atmospheric pressure, temperature and composition but also on astronomic quantities: orbital distance (insolation), eccentricity of the orbit (insolation, seasons), rotation of the planet (cold trap, heat redistribution), obliquity of the planet (cold trap, seasons), tidal heat flux (acting as an increase in insolation). The stellar tide influences the orbital distance and the eccentricity of the planet while the planetary tide influences all these quantities. There is therefore a very tight link between the dynamics of tidal evolution and the climate of a planet.

S. N. R. and F. S. acknowledge support from the Programme National de Planétologie (PNP).

References

Andreeshchev, A. & Scalo, J. 2004, in IAU Symposium, Vol. 213, Bioastronomy 2002: Life Among the Stars, ed. R. Norris & F. Stootman, 115

Barnes, R., Mullins, K., Goldblatt, C., et al. 2013, Astrobiology, 13, 225

Belu, A. R., Selsis, F., Raymond, S. N., et al. 2013, ApJ, 768, 125

Berger, A. 1988, Reviews of Geophysics, 26, 624

Bolmont, E., Raymond, S. N., & Leconte, J. 2011, A&A, 535, A94

Bolmont, E., Raymond, S. N., Leconte, J., & Matt, S. P. 2012, A&A, 544, A124

Bolmont, E., Raymond, S. N., von Paris, P., et al. 2014, ApJ, 793, 3

Borucki, W. J., Koch, D. G., Batalha, N., et al. 2012, ApJ, 745, 120

Davies, J. H. & Davies, D. R. 2010, Solid Earth, 1, 5

Eggleton, P. P., Kiseleva, L. G., & Hut, P. 1998, ApJ, 499, 853

Hansen, B. M. S. 2010, ApJ, 723, 285

Hanslmeier, A. 2012, Habitability and Cosmic Catastrophes, ed. A. Hanslmeier, S. Kempe, & J. Seckbach, 139–157

Hut, P. 1981, A&A, 99, 126

Joshi, M. 2003, Astrobiology, 3, 415

Joshi, M. M., Haberle, R. M., & Reynolds, R. T. 1997, Icarus, 129, 450

Kasting, J. F., Whitmire, D. P., & Reynolds, R. T. 1993, Icarus, 101, 108

Kokubo, E. & Ida, S. 2007, ApJ, 671, 2082

Kopparapu, R. K., Ramirez, R., Kasting, J. F., et al. 2013, ApJ, 765, 131

Leconte, J., Chabrier, G., Baraffe, I., & Levrard, B. 2010, A&A, 516, A64

Leconte, J., Forget, F., Charnay, B., Wordsworth, R., & Pottier, A. 2013, Nature, 504, 268

Mayor, M. & Queloz, D. 1995, Nature, 378, 355

Quintana, E. V., Barclay, T., Raymond, S. N., et al. 2014, Science, 344, 277

Robertson, P., Mahadevan, S., Endl, M., & Roy, A. 2014, Science, 345, 440

Selsis, F., Kasting, J. F., Levrard, B., et al. 2007, A&A, 476, 1373

Spencer, J. R., Jessup, K. L., McGrath, M. A., Ballester, G. E., & Yelle, R. 2000, Science, 288, 1208

Triaud, A. H. M. J., Gillon, M., Selsis, F., et al. 2013, ArXiv e-prints

Wordsworth, R. D., Forget, F., Selsis, F., et al. 2011, ApJ, 733, L48

SF2A 2014
J. Ballet, F. Bournaud, F. Martins, R. Monier and C. Reylé (eds)

WIND CIRCULATION REGIMES AT VENUS' CLOUD TOPS : GROUND-BASED DOPPLER VELOCIMETRY USING CFHT/ESPADONS AND COMPARISON WITH SIMULTANEOUS CLOUD TRACKING MEASUREMENTS USING VEX/VIRTIS

P. Machado[1], T. Widemann[1,2], D. Luz[3] and J. Peralta[4]

Abstract. We present new results based on ground-based Doppler spectroscopic measurements, obtained with the ESPaDOnS spectrograph at Canada-France-Hawaii telescope (CFHT) and simultaneous observations of velocity fields, obtained from space by the VIRTIS-M instrument on board the Venus Express spacecraft. These measurements are based on high-resolution spectra of Fraunhofer lines in the visible to NIR range (0.37-1.05 μm) acquired on Feb. 19-21, 2011 at a resolution of about 80,000, measuring Venus' winds at 70 km, using incoming solar radiation scattered by cloud top particles in the observer's direction (Widemann et al., 2007, 2008). The zonal wind field has been characterized by latitudinal bands, at a phase angle $\Phi = (68.7 \pm 0.3)^\circ$, between $+10^\circ$N and 60°S, by steps of 10°, and from $[\phi - \phi_E] = -50^\circ$ to sub-Earth longitude $\phi_E = 0^\circ$, by steps of 12°. From space, VIRTIS-M UV (0.38 μm) imaging exposures on the dayside were acquired simultaneously in orbit 1786, providing the first simultaneous cloud-tracking measurements with Doppler velocimetry. From the ground, we measured a zonal mean background velocity of $\overline{v}_z$ = (117.3 $\pm$ 18.0) m s^{-1} on Feb. 19, and $\overline{v}_z$ = (117.5 $\pm$ 14.5) m s^{-1} on Feb. 21. We detect an unambiguous poleward meridional flow on the morning dayside hemisphere of (18.8 $\pm$ 12.3) m s^{-1} on Feb. 19/21. Latitudinal variations of the zonal and meridional winds are further compared with the simultaneous VIRTIS data. We discuss temporal variability as well as its statistical significance (Machado et al., 2014).

Keywords: Venus, atmosphere; Atmospheres, dynamics; Spectroscopy.

1 Introduction

In a first approach Venus and Earth are similar planets: they accreted in the same proto-solar region and evolved out of the same initial densities, size, mass and bulk chemical composition (Svedhem et al. 2007); they both outgassed a thick initial atmosphere, allowing important cloud systems to develop (Bengtsson and Grinspoon 2013). A closer look, however, clearly evidences the drastic present differences between them.

The atmosphere of Venus in the upper cloud layer and lower mesosphere (65-85 km) is driven mainly by retrograde zonal circulation in cyclostrophic balance with the pressure gradient (Schubert et al. 1980). It is the site of significant variability of the flow, directly measured at both long and short timescales (Machado et al. 2012, 2014; Khatuntsev et al. 2013). This variability is likely coupled with variable horizontal distributions of dynamical tracers of the flow, such as water vapor, carbon monoxide and sulphur dioxide, for which different, and sometimes conflicting mixing ratios have been measured (de Bergh et al. 2006; Marcq et al. 2008; Bézard et al. 2009; Encrenaz et al. 2012; Chamberlain et al. 2013).

2 Observations and results

Background zonal wind circulation - We present in Table 1 the mean zonal wind velocities retrieved, under the assumption of a pure zonal one-wind system to data points acquired during sequences [1-6] (Feb. 19, 2011) and

[1] LESIA-Laboratoire d'Etudes Spatiales et d'Instrumentation en Astrophysique, Observatoire de Paris, France
[2] Université de Versailles-Saint-Quentin, France
[3] CAAUL-Centro de Astronomia e Astrofísica da Universidade de Lisboa, Portugal
[4] Instituto de Astrofísica de Andalucía, (CSIC), Spain

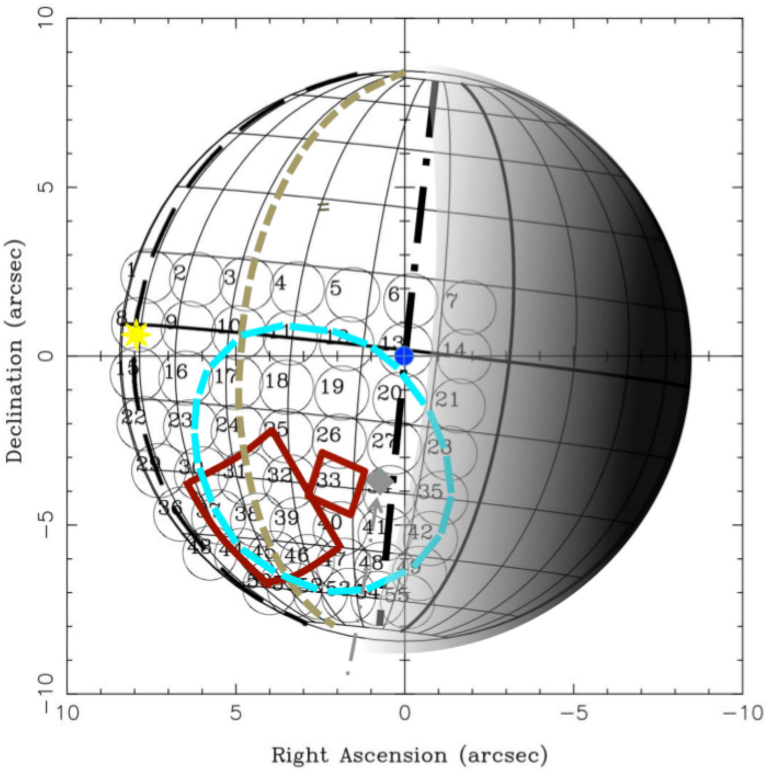

Fig. 1. Aspect and angular size of Venus as seen from Earth on Feb. 20, 2011 21h UTC, with superimposed Venus-Express instruments FOVs.

Date	Mean zonal wind (m s^{-1}) $\overline{v}_z$	reduced χ^2	2σ m s^{-1}	3σ m s^{-1}
19 Feb. 2011	117.3	1.16	$\pm$ 18.0	$\pm$27.0
21 Feb. 2011	117.5	2.12	$\pm$ 14.5	$\pm$ 21.5

Date	Meridional velocity (m s^{-1}) $\overline{v}_m$	reduced χ^2	2σ m s^{-1}	3σ m s^{-1}
19/21 Feb. 2011	18.8	1.38	$\pm$12.3	$\pm$19.6

Table 1. CFHT/ESPaDOnS mean zonal and mean meridional flow results. - (a) Mean zonal velocity $\overline{v}_z$ on Feb. 19 and Feb. 21, 2011 data. The 1-wind regime fit is applied to the entire probed region $v_{z,i}$ data points at latitudes 30° and 40° S (Feb. 19) and between latitudes 10° and 50° S (Feb. 21). Best-fit reduced χ^2 is indicated at 2σ and 3σ confidence. (b) Mean meridional wind velocity $\overline{v}_m$ fit along HPA meridian ($[\phi - \phi_E] = \Phi/2 \simeq$ -36°), obtained at 2σ and 3σ confidence level.

sequences [14-20] (Feb. 21, 2011), with the exception of points at the dayside limb facing east-sky and points with SZA $> \Phi = 68°$. The best-fit results for the two days of observations are self-consistent, with $\overline{v}_z$ = (117.3 $\pm$ 18.0) m s^{-1} on Feb. 19, and $\overline{v}_z$ = (117.5 $\pm$ 14.5) m s^{-1} on Feb. 21, respectively, with a good quality of fit (S_{min} = 1.16). Figures 2a,b present 1-parameter fit results for a pure zonal wind on Feb. 19, Feb. 21 observing sequences. The ESPaDOnS field-of-view (FOV) is represented to scale over the apparent Venus disk, and its projected size at disk center is indicated in Table 1. Zonal velocities retrieved at each offset position are weighed means of individual exposures.

Figure 3a shows all measurements for the zonal velocity at cloud tops as a function of latitude. The variability of $v_{z,i}$ in local time and $[\phi - \phi_E]$ longitude reflects the scatter of ESPaDOnS zonal velocities at each latitude of reference, as well as the time variability for data points acquired more than once during the day, *i.e.* at 40°

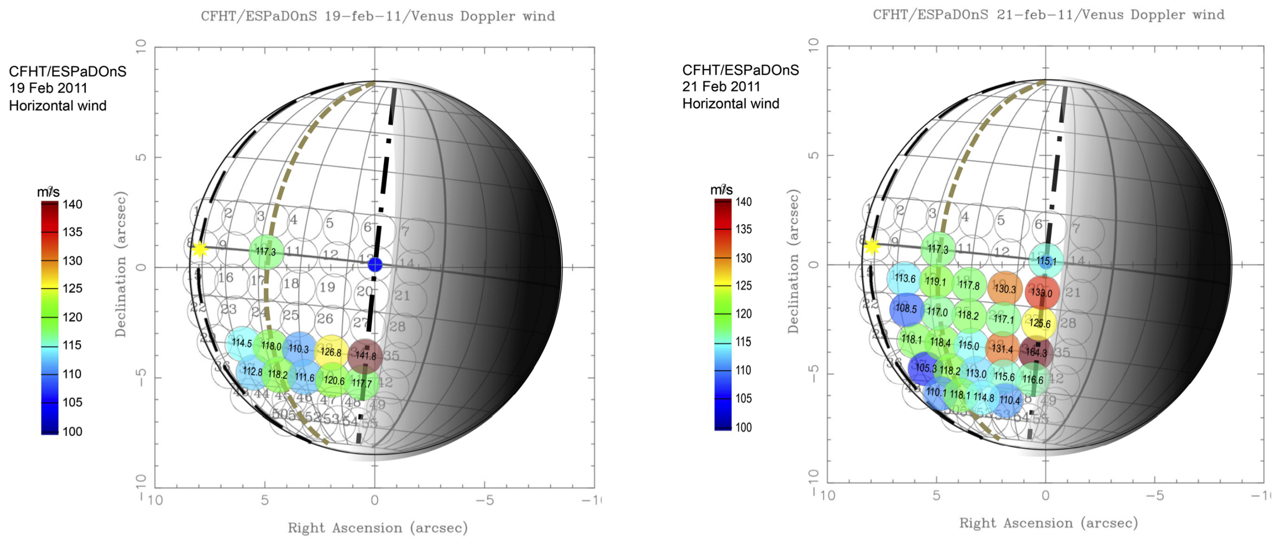

Fig. 2. Left: Results for day-averaged wind velocity $\overline{v}_{z,i}$ for observing sequences [1-6] (Feb. 19). $\overline{v}_{z,i}$ is the day-averaged zonal component at point i deprojected from line-of-sight day-averaged measurements $\overline{v}'_i$. Values are in m/s. Each point has a projected field of view of 574 km at Venus. **Right:** Results for Feb. 21, 2011 (sequences [14-21]). FOV is 582 km at Venus. Sub-solar, HPA, sub-terrestrial and morning terminator meridians are indicated as in Fig. 1.

and 50°S. Our mean zonal latitudinal profile is in general agreement with simultaneous as well as previous CT data. In the overlapping region between S lat. 20° and 50° we note an excellent agreement between $v_{z,i}$ and $v_{z,CT}$. Equatorward of 30°S we note a general excess of 10−15 m s^{-1} of the Doppler velocimetry results with respect to VIRTIS-M.

Figure 3b shows the comparison for the meridional circulation component. Results for cloud-tracking $v_{m,CT}$ of VIRTIS-M are compared to simultaneous $\overline{v}_m$ in CFHT/ESPaDOnS with a 1-wind fit to a pure meridional flow peaking at $\overline{v}_m = (18.8 \pm 12.3)$ m s^{-1} in Feb. 21 data. We note a good agreement between the two techniques at all latitudes where simultaneous measurements were performed. The meridional circulation found by Snchez-Lavega et al. (2008) and Moissl et al. (2009) displayed positive meridional velocities that increase from 0 m s^{-1} at the South pole to about 10 m s^{-1} at 55° S and then decrease to 0 m s^{-1} at low latitudes (Hueso et al. 2012). We observe a similar latitudinal profile for the pure meridional flow $\overline{v}_m = (18.8 \pm 12.3)$ m s^{-1} in Feb. 21 data. The upper cloud velocimetry in our data is therefore consistent with the poleward branch of a Hadley cell expected in global meridional circulation models. Our model flow $\overline{v}_m$ is assumed to vary sinusoidally with latitude through its de-projection coefficients (c_z), having zero velocity at equator and the poles, and a maximum velocity v$_m$ (positive for poleward motion) at lat 45°. The comparison between simultaneous velocity measurements with CFHT/ESPaDOnS ($\overline{v}_{z,i}$, $\overline{v}_m$) and VEx/VIRTIS ($v_{z,CT}$, $v_{m,CT}$) shows excellent agreement for both the zonal and meridional components of the global circulation, with minor differences equatorward of 30° S and significant temporal variations $v_{z,i} - \overline{v}_z$ to the mean zonal wind at 30° S.

ESPaDOnS measurements (green triangles) and simultaneous VIRTIS-M zonal velocity measurements the (red circles) show a good general agreement between the two methods. VIRTIS-M data have an uncertainty on individual motions of the tracked clouds of about 5 m s^{-1}, while ESPaDOnS individual measurement uncertainties $v_{z,i}$, due to additional on-sky calibration and data reduction have a final value of 10−12 m s^{-1}. The general latitudinal variation of the zonal wind field at cloud tops is in excellent agreement with previously published results of Snchez-Lavega et al. (2008); Moissl et al. (2009); Hueso et al. (2012), with zonal wind speed in the upper clouds at nearly constant speed from the equator down to 65°S followed by a steady decrease toward zero velocities at the pole. In our data the meridional shear of the wind between 60° and 80°S is -0.03 m s^{-1} km^{-1}.

Comparison between Cloud tracking (VIRTIS) and Doppler (ESPaDOnS)

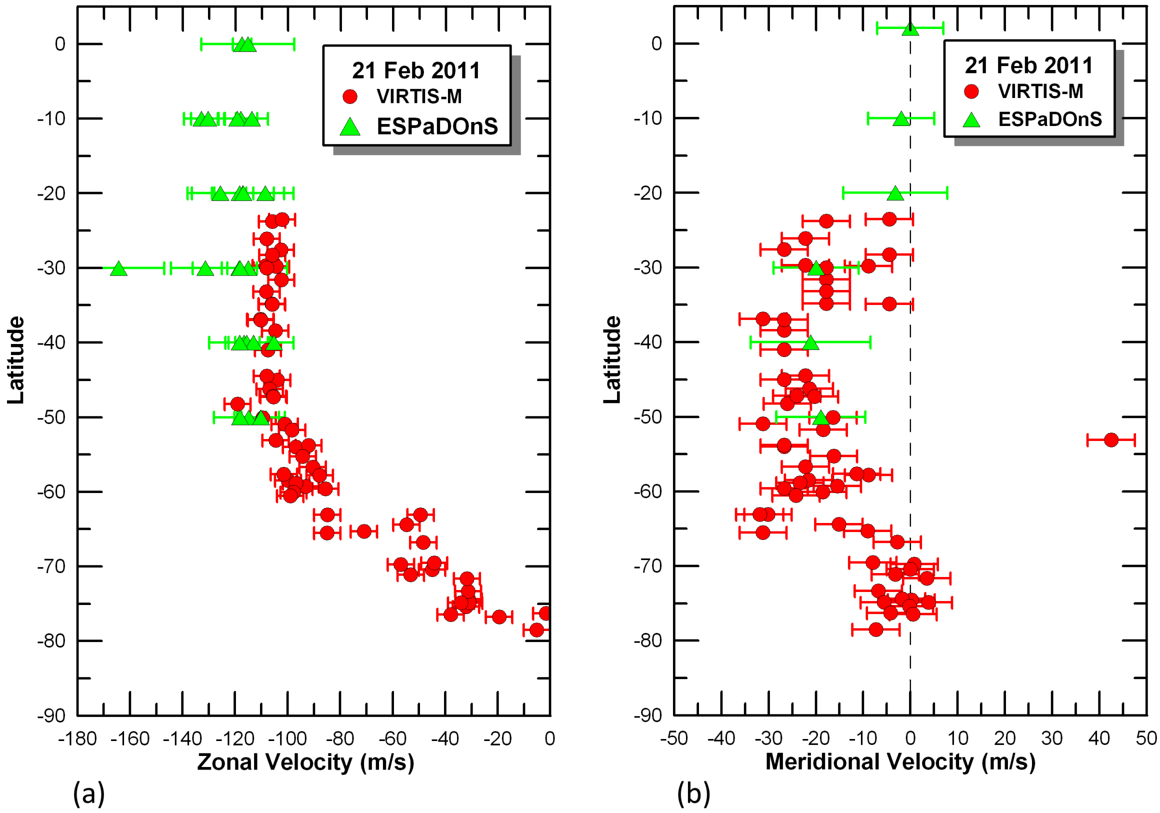

Fig. 3. Simultaneous cloud-tracking wind velocity measurements of VEx/VIRTIS-M (red dots) and CFHT/ESPaDOnS instantaneous Doppler winds (triangles, green in the online version) on February 21, 2011. For the two techniques horizontal velocity (x-axis) is plotted vs. latitude (y-axis) in m s^{-1}. (a) Cloud-tracking zonal component $v_{z,CT}$ plotted with Doppler zonal component $\overline{v}_{z,i}$. (b) Cloud tracking meridional component $v_{m,CT}$ plotted with Doppler meridional component $\overline{v}_{m,lat}$. CFHT/ESPaDOnS $\overline{v}_{z,i}$.

3 Conclusions

Winds can be measured from Venus Express orbit using cloud tracking at 45 and 70 km by both VIRTIS-M and VMC instruments (Markiewicz et al., 2007 ; Sanchez-Lavega et al., 2008 ; Hueso et al., 2012). However, winds derived in this manner are usually averaged over several days of observations and do not reflect instantaneous wind velocity and its significant variability at shorter time scales. In addition, cloud tracking is not able to measure wind fields above cloud level, where wind inferences have to rely on indirect hypothesis such as cyclostrophic balance.

The ground-based velocimetry technique has proven its reliability in constraining global wind circulation models, complementary of space-based measurements. Doppler retrievals in the visible are in good agreement with Venus-Express cloud tracking measurements within our confidence intervals, as was previously suggested (Widemann 2008, Machado 2012, Machado 2014). For the first time, simultaneous measurements were carried out and self-consistent results were obtained from space and ground-based observations. An unambiguous detection of poleward meridional circulation is reported on the morning dayside hemisphere, using optical Doppler velocimetry from the ground at CFHT.

In addition, we assessed the feasibility of day-to-day monitoring of short time-scale variability from the ground (although its significance remains essentially marginal at the 2-σ level). Establishing a reliable model of the circulation of Venus requires long-term as well as short-term averages to constrain both the mean circulation and eddy motions. Time-scale variations are expected to bring new constraints on Venus General Circulation Models at cloud top level, and we hope to develop further the technique's capability to track short-term variations in future observations. The present study also highlights the added value of coordinated studies from ground-based observatories and from spacecraft (Witasse et al. 2006; Lellouch and Witasse 2008; Machado et al. 2014).

The authors acknowledge funding from the European Union Seventh Framework Program (FP7) under grant agreement n°606798 (EuroVenus).

References

Bengtsson, L., and Grinspoon, D., Towards understanding the climate of Venus, (Vol. 11). Springer, 2013.

Bézard, B., Tsang, C., Carlson, R., Piccioni, G., Marcq, E., Drossart, P., Water vapour abundance near the surface of Venus from Venus Express/VIRTIS observations. J. Geophys. Res.-Planets 114, E00B39, 2009.

Chamberlain, S., Bailey, J., Crisp, D., Meadows, V., Ground-based Near Infrared Observations of Water Vapor in the Venus Troposphere, Icarus 222, 364-378, 2013.

de Bergh, C., Moroz, V., Taylor, F., Crisp, D., Bézard, B., Zasova, L., The composition of the atmosphere of Venus below 100 km altitude: An overview. Planet Space Sci. 54, 1389-1397, 2006.

Encrenaz, T., Greathouse, T. K., Roe, H., et al. HDO and SO2 thermal mapping on Venus: evidence for strong SO2 variability. Astronomy and Astrophysics, vol. 543, 2012.

Hueso, R., Peralta, J., Snchez-Lavega, A., Assessing the long-term variability of Venus winds at cloud level from VIRTIS-Venus Express, Icarus, volume 217, p. 585-598, 2012.

Khatuntsev, I.., Patsaeva, M., Titov, D., Ignatiev, N., Turin, A., Limaye, S., Markiewicz, W., Almeida, M., Roatsch, Th., Moissl, R., Cloud level winds from the Venus Express Monitoring Camera imaging, Icarus, Volume 226, p. 140-158, 2013.

Lellouch, E. and Witasse, O., A coordinated campaign of Venus ground-based observations and Venus Express measurements, Planetary and Space Science, volume 56, p. 1317-1319, 2008.

Machado, P., Luz, D. Widemann, T., Lellouch, E., Witasse, O, 2012, Characterizing the atmospheric dynamics of Venus from ground-based Doppler velocimetry, Icarus.

Machado, P., Widemann, T., Luz, D. and Peralta, J., 2014, Wind circulation regimes at Venus' cloud tops : Ground-based Doppler velocimetry using CFHT/ESPaDOnS and comparison with simultaneous cloud tracking measurements using VEx/VIRTIS in February 2011, Icarus, in press.

Marcq, E., Bezard, B., Drossart, P., Piccioni, G., Reess, J. M., Henry, F., A latitudinal survey of CO, OCS, H2O, and SO2 in the lower atmosphere of Venus: Spectroscopic studies using VIRTIS-H. Journal of Geophysical Research: Planets, 113(E5), 2008.

Markiewicz, W. et al., Venus Monitoring Camera for Venus Express, Planetary and Space Science, volume 55, p. 1701-1711, 2007.

Moissl, R. et al., Venus cloud top winds from tracking UV features in Venus Monitoring Camera, Jornal of Geophysical Research, volume 114, E00B31, 2009.

Snchez-Lavega, A., et al., Variable winds on Venus mapped in three dimensions, *Geophysical Research Letters*, volume 35, 2008.

Schubert, G. et al., Structure and circulation of the Venus atmosphere, J. Geophys. Res., 85, 8007 8025, doi:10.1029/JA085iA13p08007, 1980.

Svedhem, H.; Titov, D.; Taylor, F.; Witasse O., Venus as a more Earth-like planet, *Nature*, volume 450, p. 629-632, 2007.

Widemann, T. et al., New wind measurements in Venus lower mesosphere from visible spectroscopy, Planetary and Space Science, volume 55, p. 1741-1756, 2007.

Widemann, T. et al., Venus Doppler winds at cloud tops observed with ESPaDOnS at CFHT, Planetary and Space Science, volume 56, p. 1320-1334, 2008.

Witasse, O. et al., Overview of the coordinated ground-based observations of titan during the huygens mission. *Journal of Geophysical Research (Planets)*, 111:7, 2006.

SF2A 2014
J. Ballet, F. Bournaud, F. Martins, R. Monier and C. Reylé (eds)

EMULATING JWST EXOPLANET TRANSIT OBSERVATIONS IN A TESTBED LABORATORY EXPERIMENT

D. Touli[1], C. A. Beichman[1,2,3], G. Vasisht[2], R. Smith[4] and J. E. Krist[2]

Abstract. The transit technique is used for the detection and characterization of exoplanets. The combination of transit and radial velocity (RV) measurements gives information about a planet's radius and mass, respectively, leading to an estimate of the planets density (Borucki et al. 2011) and therefore to its composition and evolutionary history. Transit spectroscopy can provide information on atmospheric composition and structure (Fortney et al. 2013).

Spectroscopic observations of individual planets have revealed atomic and molecular species such as H2O, CO2 and CH4 in atmospheres of planets orbiting bright stars, e.g. (Deming et al. 2013). The transit observations require extremely precise photometry. For instance, Jupiter transit results to a 1% brightness decrease of a solar type star while the Earth causes only a 0.0084% decrease (84 ppm). Spectroscopic measurements require still greater precision <30ppm.

The Precision Projector Laboratory (PPL) is a collaboration between the Jet Propulsion Laboratory (JPL) and California Institute of Technology (Caltech) to characterize and validate detectors through emulation of science images. At PPL we have developed a testbed to project simulated spectra and other images onto a HgCdTe array in order to assess precision photometry for transits, weak lensing etc. for Explorer concepts like JWST, WFIRST, EUCLID.

In our controlled laboratory experiment, the goal is to demonstrate ability to extract weak transit spectra as expected for NIRCam, NIRIS and NIRSpec. Two lamps of variable intensity, along with spectral line and photometric simulation masks emulate the signals from a star-only, from a planet-only and finally, from a combination of a planet + star. Three masks have been used to simulate spectra in monochromatic light. These masks, which are fabricated at JPL, have a length of 1000 pixels and widths of 2 pixels, 10 pixels and 1 pixel to correspond respectively to the noted above JWST instruments (see Fig. 1. Left).

From many-hour long observing sequences, we obtain time series photometry with deliberate offsets introduced to test sensitivity to pointing jitter and other effects. We can modify the star-planet brightness contrast by factors up to 10^4:1. With cross correlation techniques we calculate positional shifts which are then used to decorrelate the effects of vertical and lateral offsets due to turbulence and instrumental vibrations on the photometry (see Fig. 1. Right).

Using Principal Component Analysis (PCA), we reject correlated temporal noise to achieve a precision lower than 50 ppm (Clanton et al. 2012). In our current work, after decorrelation of vertical and lateral offsets along with PCA, we achieve a precision of $\sim$20 ppm. To assess the photometric precision we use the Allan variance (Allan 1987). This statistical method is used to characterize noise and stability as it indicates shot noise limited performance.

Testbed experiments are ongoing to provide quantitative information on the achievable spectroscopic precision using realistic exoplanet spectra with the goal to define optimized data acquisition sequences for use, for example, with the James Webb Space Telescope.

Keywords: Exoplanet transits, spectroscopy, photometry, testbed, laboratory, detectors, simulation masks, data analysis

[1] Infrared Processing and Analysis Center, California Institute of Technology, Pasadena, CA 91125, USA, dtouli@ipac.caltech.edu
[2] Jet Propulsion Laboratory, California Institute of Technology, 4800 Oak Grove Dr., Pasadena, CA 91107, USA
[3] NASA Exoplanet Science Institute, California Institute of Technology, 770 S. Wilson Ave., Pasadena, CA 91125, USA
[4] Cahill Center for Astronomy and Astrophysics, California Institute of Technology, Pasadena, CA 91125, USA

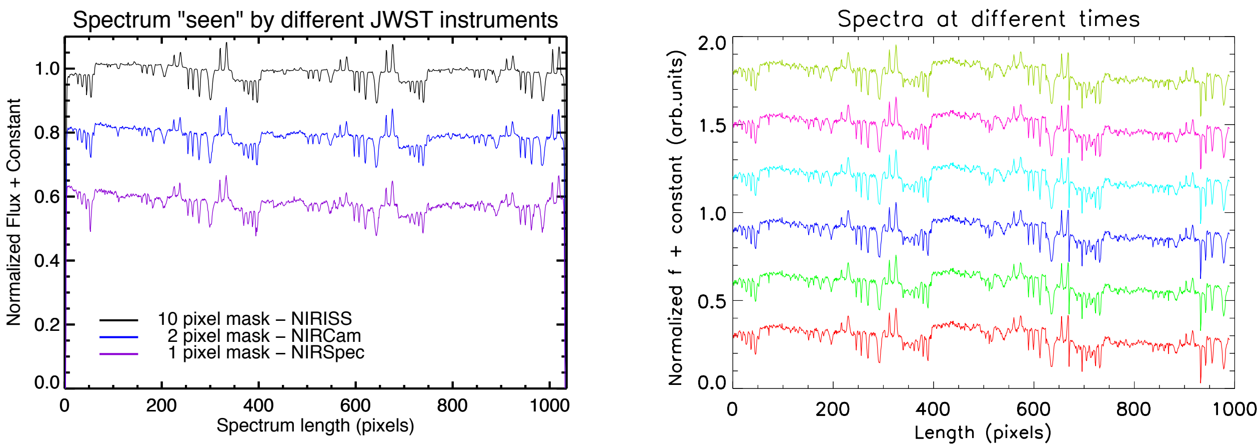

Fig. 1. Left: The detected spectrum, emulated by the three diferent masks which correspond respectively to the three following JWST instruments: NIRISS, NIRCam, NIRSpec. **Right:** Six of the synthetic spectra, produced by the 10-pixel width mask, at different times (shifted for clarity). The spectrum length is 1000 pixels. The features represent emission and absorption lines. After decorrelation of vertical and lateral offsets we achieve a precision <30 ppm.

References

Allan, D. W. 1987, IEEE-UFFC, 34, 647

Borucki, W. J., Koch, D. G., Basri, G., & et al. 2011, ApJ, 736, 19

Clanton, C., Beichman, C., Vasisht, G., & et al. 2012, PASP, 124, 700

Deming, D., Wilkins, A., McCullough, P., & et al. 2013, ApJ, 774, 95

Fortney, J. J., Mordasini, C., Nettelmann, N., & et al. 2013, ApJ, 775, 80

INFLUENCE OF DIFFERENT PARAMETERS ON THE CHEMICAL COMPOSITION OF WARM NEPTUNES

O. Venot[1], M. Agúndez[2], F. Selsis[3,4], M. Tessenyi[5] and L. Decin[1]

Abstract. We developed a 1D photo-thermochemical model to study the atmosphere of warm exoplanets. The chemical scheme used in this model is completely new in planetology and has been constructed in collaboration with specialists of combustion. It has been validated as a whole through experiments on a large range of temperature (300 - 2500 K) and pressure (1 mbar - 100 bar), allowing to study a wide variety of exoplanets. We have used this chemical model to study the atmosphere of two warm Neptunes, GJ3470b and GJ436b, and the influence of different parameters (vertical mixing, metallicity, temperature, . . .) on their chemical composition. We present here the results obtained in these studies.

Keywords: exoplanets; planetary systems; planets and satellites: atmospheres; planets and satellites: composition; planets and satellites: individual: GJ 3470b GJ 436b; astrochemistry

1 Introduction

Transit spectra have recently allowed us to characterise the atmosphere of the Neptune-sized planet like GJ 436b, GJ 3470b, or the super-Earth GJ 1214b, which orbit around M dwarf stars. These planets present interesting differences with respect to hot Jupiters. The first is because the host M dwarf star is smaller and cooler than a solar-type star, so the planet is less severely heated (even if the orbital distances in the range 0.01 – 0.04 AU are comparable to the ones of hot Jupiters). This results in planetary effective temperatures below 1000 K. Interestingly, it is around this temperature that a gaseous mixture at thermochemical equilibrium, with solar elemental abundances and at a pressure around 1 bar, shows a transition concerning the major carbon reservoir, either CO or CH_4 for temperatures above and below 1000 K, respectively (see Venot et al. 2014, their Fig. 1). In this regard it is interesting to note that transit spectra of GJ 436b indicates that its atmosphere is dominated by CO (Stevenson et al. 2010; Madhusudhan & Seager 2011; Knutson et al. 2011), whereas methane is predicted to be the major carbon reservoir at thermochemical equilibrium. However, such interpretation has been disputed by Beaulieu et al. (2011) based on a different analysis of transmission spectra. From a modelling point of view, Line et al. (2011), with a code considering thermochemical kinetics, vertical mixing, and photochemistry, concluded that CH_4 should be the major carbon-bearing molecule in GJ 436b's atmosphere.

A second important difference with respect to hot Jupiters is that (sub-)Neptune planets have a lower mass. Thus, they have a lower efficiency to retain light elements (Elkins-Tanton & Seager 2008), so we can expect their atmosphere to be enriched in heavy elements with respect to the solar composition. Previous photochemical studies dedicated to (sub-)Neptunes explored metallicities reasonably high (up to 50 × solar metallicity for Line et al. 2011; Miller-Ricci Kempton et al. 2012) but also extremely high (up to 10,000 × solar metallicity for Moses et al. 2013). In this study, we considered an enrichment in heavy elements between 1 and 100 × solar. Enrichment in heavy elements in the range 50-100 is extremely interesting because it corresponds to a change of the carbon reservoir (either CH_4 or CO) for pressures within 1 and 100 bar and temperatures within 1000 and 2000 K (see Venot et al. 2014, their Fig. 1). The deep atmospheric layers, with such high temperatures and pressures, can then contaminate most of the atmosphere due to the chemical quenching associated with vertical mixing (e.g. Prinn & Barshay 1977; Lewis & Fegley Jr 1984; Visscher & Moses 2011; Moses et al. 2011; Venot et al. 2012).

[1] Instituut voor Sterrenkunde, Katholieke Universiteit Leuven, Celestijnenlaan 200D, 3001 Leuven, Belgium
[2] Instituto de Ciencia de Materiales de Madrid, CSIC, C/Sor Juana Inés de la Cruz 3, 28049 Cantoblanco, Spain
[3] Univ. Bordeaux, LAB, UMR 5804, F-33270, Floirac, France
[4] CNRS, LAB, UMR 5804, F-33270, Floirac, France
[5] University College London, Department of Physics and Astronomy, Gower Street, London WC1E 6BT, UK

2 Chemical scheme

The first studies on hot Jupiters (Liang et al. 2003, 2004) used chemical schemes made originally for Jupiter or Saturn, so cold atmospheres in which endothermic processes happening only at high temperature were not included. Then, some improvements have been done, by adding exothermic reactions to these chemical schemes (i.e. Zahnle et al. 2009a,b; Line et al. 2010; Moses et al. 2011), but none of these studies discuss about the validation of the chemical network. In order to study correctly these hot exoplanets, we have developed a chemical scheme adapted to the high temperatures and pressures that are found in warm exoplanet atmospheres. Because such extreme conditions are also found in car engines, we have collaborated with specialists of combustion, working mainly for industrial purposes. We have implemented a chemical scheme new in planetology, that has been validated experimentally as a whole and not only for each individual reaction as it is often the case for chemical schemes used in planetology. This validation has been performed on a wide range of pressure and temperature (0.01 - 100 bar and 300-2500 K), allowing to explore a variety of atmospheric environments. The scheme includes 957 reversible and 6 irreversible reactions (so a total of 1920 reactions), involving 105 neutral species (molecule or radical). Helium is included in this mechanism and plays the role of third body in some reactions. It is available in the online database KIDA: KInetic Database for Astrochemistry* (Wakelam et al. 2012). More details about this chemical scheme and its experimental validation can be found in Venot et al. (2012).

Data used to model photolysis processes need also to be improved. Indeed, absorption cross sections, which are crucial to calculate photodissociation rates, are known only at ambiant and low temperature. In this view, we have measured the absorption cross section of CO_2 in the wavelength range [115-230] nm at temperatures up to 800K (Venot et al. 2013). Measurements of other molecules are now needed, and are currently in progress.

3 GJ 3470b

GJ 3470b is a transiting warm Neptune discovered by Bonfils et al. (2012). We used this planet as study-case to investigate the effect of temperature, vertical mixing, metallicity and UV irradiation on its atmospheric chemical composition. We explored the parameter space as explained in Table 1. The 17 models we have computed allowed us to frame the different compositions that are possible for this planet.

We were interested in the CH_4/CO ratio, which is a parameter quite controversial. Indeed, the identification of the C-bearing species from observations is still under debate for warm Neptunes such as GJ 436b (Stevenson et al. 2010; Madhusudhan & Seager 2011; Beaulieu et al. 2011). The results we obtained in this study show that the situation is also not simple from a chemical point of view. CH_4 may or may not be the major carbon reservoir, depending on the metallicity, the temperature, and the vertical mixing. Indeed, we found that in most of cases the CH_4/CO ratio is above 1, but CO can be more abundant in the case of a high metallicity ($> 100 \times$ solar) combined with an atmospheric temperature high too. These conditions are plausible, because an enrichment with respect to the solar elemental abundances can be expected for planets with a similar bulk composition as Uranus and Neptune. Because of similar physical properties, this result can be extrapolated to other warm (sub-)Neptunes, such as GJ 436b or GJ 1214b. Recently, a similar study has been carried out by Moses et al. (2013), who also find that a high metallicity could lead to a CH_4/CO ratio lower than 1 in GJ 436b. A very high metallicity ($100 \times$ solar metallicity) seems to be a solution to explore in order to interpret future observations, as it is very likely for these atmospheres.

The synthetic spectra we computed (see Venot et al. 2014, their Figs. 7 and 8) indicate that the brightness temperature, as well as the transit depth, vary significantly with the metallicity and the thermal profile, so future observations of GJ 3470b may be able to determine the metallicity and the temperature of this planet. Because of the strong opacities, spectra corresponding to high metallicity models ($100 \times$ solar) produce smaller features than low metallicity models ($1 \times$ solar). On the spectra corresponding to the primary transit, we found that the 3.3-to-4.7 μm ratio changes together with the CO/CH_4 ratio. Observations at these wavelengths are a possible way to constrain this ratio.

These results are presented in more details in Venot et al. (2014).

*http://kida.obs.u-bordeaux1.fr

Parameter	Range of values	Symbol
Metallicity	Solar ($\zeta = 1$)	ζ_1
	High ($\zeta = 100$)	ζ_{100}
Temperature	Warm atmosphere (+100 K)	T_{+100}
	Cool atmosphere (−100 K)	T_{-100}
Eddy diffusion coefficient	High (K_{zz} ×10)	$K_{zz}^{\times 10}$
	Low (K_{zz} ÷10)	$K_{zz}^{\div 10}$
Stellar UV flux	High irradiation (F_λ ×10)	$F_\lambda^{\times 10}$
	Low irradiation (F_λ ÷10)	$F_\lambda^{\div 10}$

Table 1. The parameter space of the model explored. All the parameters are changed with respect to the standard values showed in Venot et al. (2014) (their Figs. 3 and 4). The standard metallicity is 10 × solar ($\zeta = 10$).

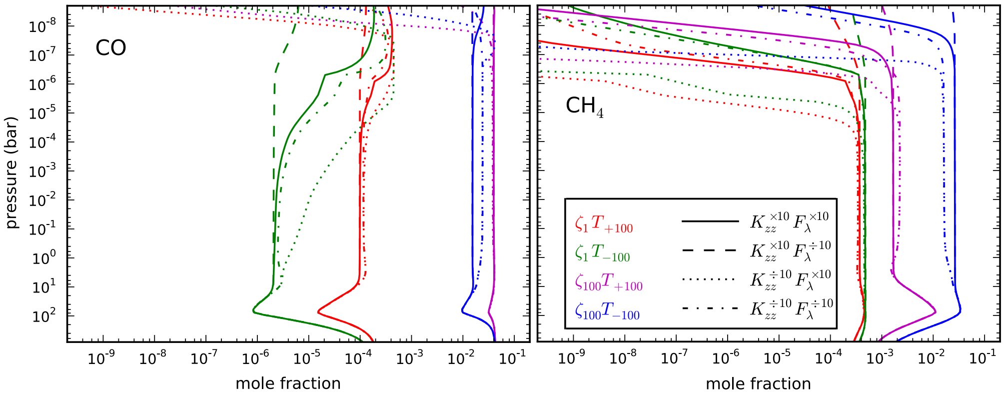

Fig. 1. Vertical abundance profiles of CO and CH_4 as calculated through each of the 16 models in which the space of metallicity, temperature, eddy diffusion coefficient, and stellar UV flux are explored. Each colour corresponds to a set of metallicity and temperature values and each line style to a set of eddy diffusion coefficients and stellar UV fluxes (see legend in the CH_4 panel and meaning of each symbol in Table 1.

4 GJ 436b

We did a study quite similar on GJ 436b, which is a warm Neptune with a high eccentricity (e = 0.16). Thus, the planet undergoes strong tidal forces. The dissipation of this energy in the planet depends on its internal composition and structure, which are both unknown. We have used a Constant Time Lag model to determine the range of internal temperatures that are possible for this planet. We found that the maximum internal temperature possible was 560 K. In our modelling, we considered 4 internal temperatures: 100, 240, 400, and 560 K. We have also explored the sensitivity of the atmospheric chemical composition to the metallicity by considering 3 cases: ζ = 1, 10, and 100 × solar metallicity.

As you see on Fig.2 (Left), the effect of the internal temperature is to heat the deep atmosphere (for a given pressure level, the hottest profile corresponds to the highest internal temperature), but the upper part of the thermal profiles (P less than ∼ 0.1 mbar), remains quasi identical whatever is the internal temperature. We have represented the equilibrium line CO/CH_4, to show that depending on the internal temperature and the metallicity, the thermal profiles do not cross this line at the same level pressure, and this has a great importance when considering quenching processes. Indeed, for the high metallicity cases, quenching happens for all the P-T profiles in a region where CO is the major C-bearing species, but for low metallicity cases, quenching can make either CO or CH_4 the major carbon reservoir, depending on the P-T profiles. For the three lower internal temperatures cases (T_{int}=100, 240, and 400 K) quenching happens where CH_4 is the C-bearing species, but for the highest internal temperature case (T_{int}=560 K), quenching happens where CO is more abundant than methane. This is then reverberated in all the atmosphere. As you see on Fig.2 (Right), except for the case ζ = 1 and T_{int}=100K, even if thermochemical equilibrium predicts that methane is the C-bearing species in the middle atmosphere ([10^{-1} - 10^{-7}] bar, area that can be probed by observations), because quenching happens deeper in the atmosphere, CO becomes the more abundant C-species in this part of the atmosphere.

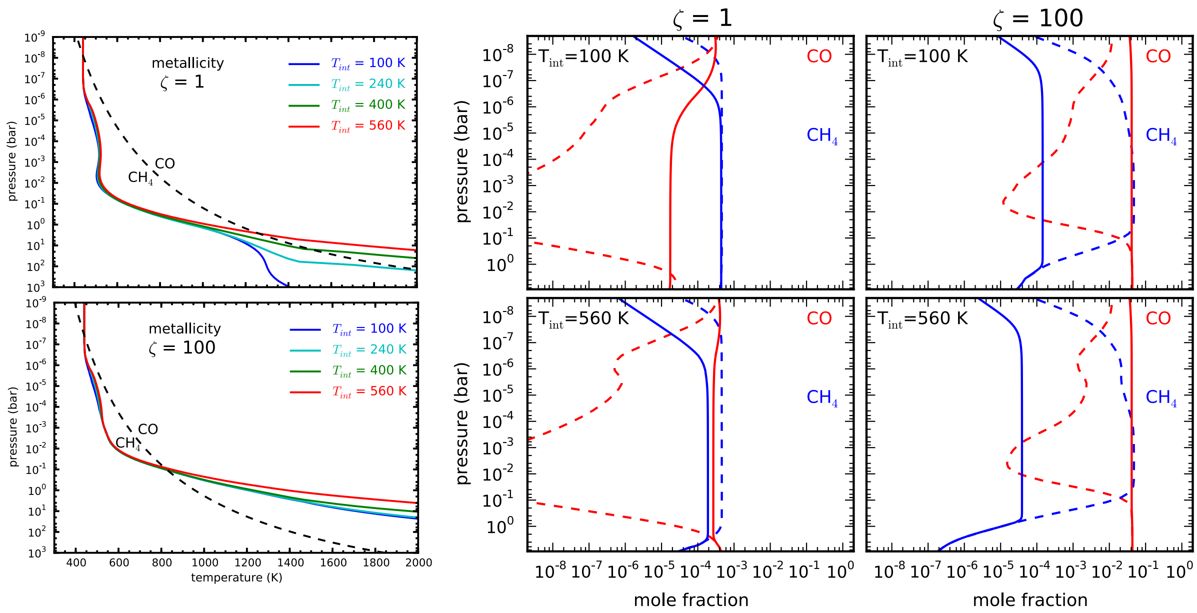

Fig. 2. Left: Thermal profiles corresponding to an atmosphere with a solar metallicity (*top*) and with a metallicity 100 × solar (*bottom*). Each colour corresponds to the internal temperature that varies from 100 to 560 K, corresponding to different factor of dissipation of the tidal heating. The equilibrium line CO/CH_4 is represented with a dashed line. **Right:** Abundance profiles of CO (red) and CH_4 (blue) for some selected cases. The thermochemical equilibrium is represented with a dashed line and the result of the chemical model with a full line.

We calculated synthetic spectra (see Agúndez et al. 2014, their Figs. 4 and 5) corresponding to the 12 cases we tested. Globally, their is a poor agreement with observation, but the transmission spectra measured by Knutson et al. (2011) seems to be consistent with models with a high metallicity and efficient tidal heating, which correspond to a methane-poor atmosphere. The relative variation of the transit depth in the 3.6 and 4.5 μm bands measured by Beaulieu et al. (2011), which suggests a high abundance of methane, cannot be reproduced by none of our models. The synthetic emission spectra is lower than observed during secondary eclipse, which suggests a warmer dayside atmosphere. This can be obtained by a more efficient tidal heating an/or a higher metallicity that could drive an inefficient daynight heat redistribution (Lewis et al. 2010).

More details about this study can be found in Agúndez et al. (2014).

5 Conclusions

Using a very robust chemical scheme developed especially for high temperatures, we have studied the chemical composition of two warm Neptunes: GJ 3470b and GJ 436b. We explored the space of the unknown parameters (metallicity, temperature, vertical mixing, UV flux, tidal heating) in order to constrain their atmospheric composition. We have seen that there is a combined effect of the metallicity, the temperature, and the vertical mixing on the chemical composition of these atmospheres. Indeed, because of quenching, the composition of the middle atmosphere can be affected by temperatures found much deeper than the observations. This can explain why we deduce from observation CO-rich atmospheres, whereas chemical equilibrium predicts that CH_4 should dominate this kind of atmospheres. We have also found that the eccentricity of a planet have an important influence on the chemical composition of an atmosphere. Indeed, strong tidal forces generate an important internal temperature that heat the deep atmosphere, allowing, because of quenching, to have a high CO/CH_4 ratio. This "carbon anomaly" depends on the temperature contrast between the probed layers, the quenching level, and the efficiency of the vertical mixing. To retrieve the elemental abundances of such atmospheres, self-consistent models that couple all these influences are needed.

O.V. acknowledges support from the KU Leuven IDO project IDO/10/2013 and from the FWO Postdoctoral Fellowship programme. M.A., and F.S. acknowledge support from the European Research Council (ERC Grant 209622: E$_3$ARTHs). Computer time for this study was provided by the computing facilities MCIA (Mésocentre de Calcul Intensif Aquitain) of the Université de Bordeaux and of the Université de Pau et des Pays de l'Adour.

References

Agúndez, M., Venot, O., Selsis, F., & Iro, N. 2014, ApJ, 781, 68
Beaulieu, J.-P., Tinetti, G., Kipping, D. M., et al. 2011, ApJ, 731, 16
Bonfils, X., Gillon, M., Udry, S., et al. 2012, A&A, 546, A27
Elkins-Tanton, L. T. & Seager, S. 2008, ApJ, 685, 1237
Knutson, H. A., Madhusudhan, N., Cowan, N. B., et al. 2011, ApJ, 735, 27
Lewis, J. S. & Fegley Jr, M. B. 1984, Space science reviews, 39, 163
Lewis, N. K., Showman, A. P., Fortney, J. J., et al. 2010, ApJ, 720, 344
Liang, M., Parkinson, C., Lee, A., Yung, Y., & Seager, S. 2003, ApJ, 596, L247
Liang, M., Seager, S., Parkinson, C., Lee, A., & Yung, Y. 2004, ApJ, 605, L61
Line, M., Liang, M., & Yung, Y. 2010, ApJ, 717, 496
Line, M., Vasisht, G., Chen, P., Angerhausen, D., & Yung, Y. 2011, ApJ, 738, 32
Madhusudhan, N. & Seager, S. 2011, ApJ, 729, 41
Miller-Ricci Kempton, E., Zahnle, K., & Fortney, J. J. 2012, ApJ, 745, 3
Moses, J., Visscher, C., Fortney, J., et al. 2011, ApJ, 737, 15
Moses, J. I., Line, M. R., Visscher, C., et al. 2013, ApJ, 777, 34
Prinn, R. G. & Barshay, S. S. 1977, Science, 198, 1031
Stevenson, K., Harrington, J., Nymeyer, S., et al. 2010, Nature, 464, 1161
Venot, O., Agúndez, M., Selsis, F., Tessenyi, M., & Iro, N. 2014, A&A, 562, A51
Venot, O., Fray, N., Bénilan, Y., et al. 2013, A&A, 551, A131
Venot, O., Hébrard, E., Agúndez, M., et al. 2012, A&A, 546, A43
Visscher, C. & Moses, J. I. 2011, ApJ, 738, 72
Wakelam, V., Herbst, E., Loison, J.-C., et al. 2012, The Astrophysical Journal Supplement Series, 199, 21
Zahnle, K., Marley, M., Freedman, R., Lodders, K., & Fortney, J. 2009a, The Astrophysical Journal Letters, 701, L20
Zahnle, K., Marley, M. S., & Fortney, J. J. 2009b, eprint arXiv:0911.0728

Session 02

Atelier général Hautes Energies

SF2A 2014
J. Ballet, F. Bournaud, F. Martins, R. Monier and C. Reylé (eds)

MODELING THE PROPAGATION OF SAGITTARIUS A*'S PAST ACTIVITY

M. Clavel[1,2], S. Soldi[1], R. Terrier[1], A. Goldwurm[1,2], M. R. Morris[3] and G. Ponti[4]

Abstract. The supermassive black hole Sgr A* has been active in the recent past and the echoes of its exceptionally luminous past outbursts are currently propagating through the Galactic center. The limited time baseline of the observations and missing information about the reflecting clouds are major limitations to the proper reconstruction of Sgr A*'s past lightcurve. In order to test several scenarios, we developed a simple model to derive the variations expected for the clouds' illumination as a function of the epoch and the duration of Sgr A*'s flares. Here, we present the results for a given set of parameters.

Keywords: Galactic center, diffuse X-rays, molecular clouds

1 Introduction

The supermassive black hole at the Galactic center, Sagittarius A*, is currently extremely faint but there are strong hints that it experienced a higher level of activity in the past (Ponti et al. 2013). In particular, its recent history can be reconstructed from the non-thermal emission emanating from the molecular clouds at the Galactic center. The hard X-ray radiation, presumably originating from Sgr A*, is indeed reflected through Compton scattering and photo-ionization, thereby creating an X-ray emission characterized by a hard continuum component and a strong Fe Kα line at 6.4 keV. The variation of this emission, induced by the propagation of the signal inside the central molecular zone (CMZ), has been detected from an increasing number of interstellar structures (Ponti et al. 2010; Terrier et al. 2010; Clavel et al. 2014a) and the detailed analysis of these variations has demonstrated that there were at least two short events now propagating through the inner regions of the Galaxy (Clavel et al. 2013). However, reconstructing the precise lightcurve of Sgr A* is very complex because the distribution of the clouds along the line of sight is barely known. In this work, we assume a given distribution for the CMZ and we investigate the timing properties of a single event propagating away from Sgr A*.

2 Simple model for the echo propagation

Modeling the propagation of an echo within the central molecular zone requires both a precise description of the matter distribution and detailed information about the incident radiation.

Matter distribution. So far, several models have been proposed to account for the 3D CMZ distribution, but there is no general consensus concerning the position and the internal structure of individual clouds. In our simulation, we decide to use a distribution of ellipsoidal and uniform-density clouds, which follows the twisted ring proposed by Molinari et al. (2011), as shown in Fig. 1.

Event propagation and illumination. We consider a single event originating at the position of Sgr A* and having a constant flux over 50 years. We show this event at different epochs in order to account for its propagation over time. At a given time, all the clouds illuminated by this event are along the same paraboloid, as first defined by Sunyaev & Churazov (1998) and represented in Fig. 1 (left). To determine the intensity of the Fe Kα emission line, projected onto the plane of the sky, we then integrate the illuminated material along the line of sight and follow Sunyaev & Churazov (1998, eq. 2) to derive the relative brightness of the illuminated structures (Fig. 1, right).

[1] AstroParticule et Cosmologie, Université Paris Diderot, 75013 Paris, France
[2] Service d'Astrophysique, CEA Saclay, 91191 Gif-sur-Yvette, France
[3] Department of Physics & Astronomy, University of California, Los Angeles, CA 90095, USA
[4] Max-Planck Institute for Extraterrestrial Physics, 85741 Garching, Germany

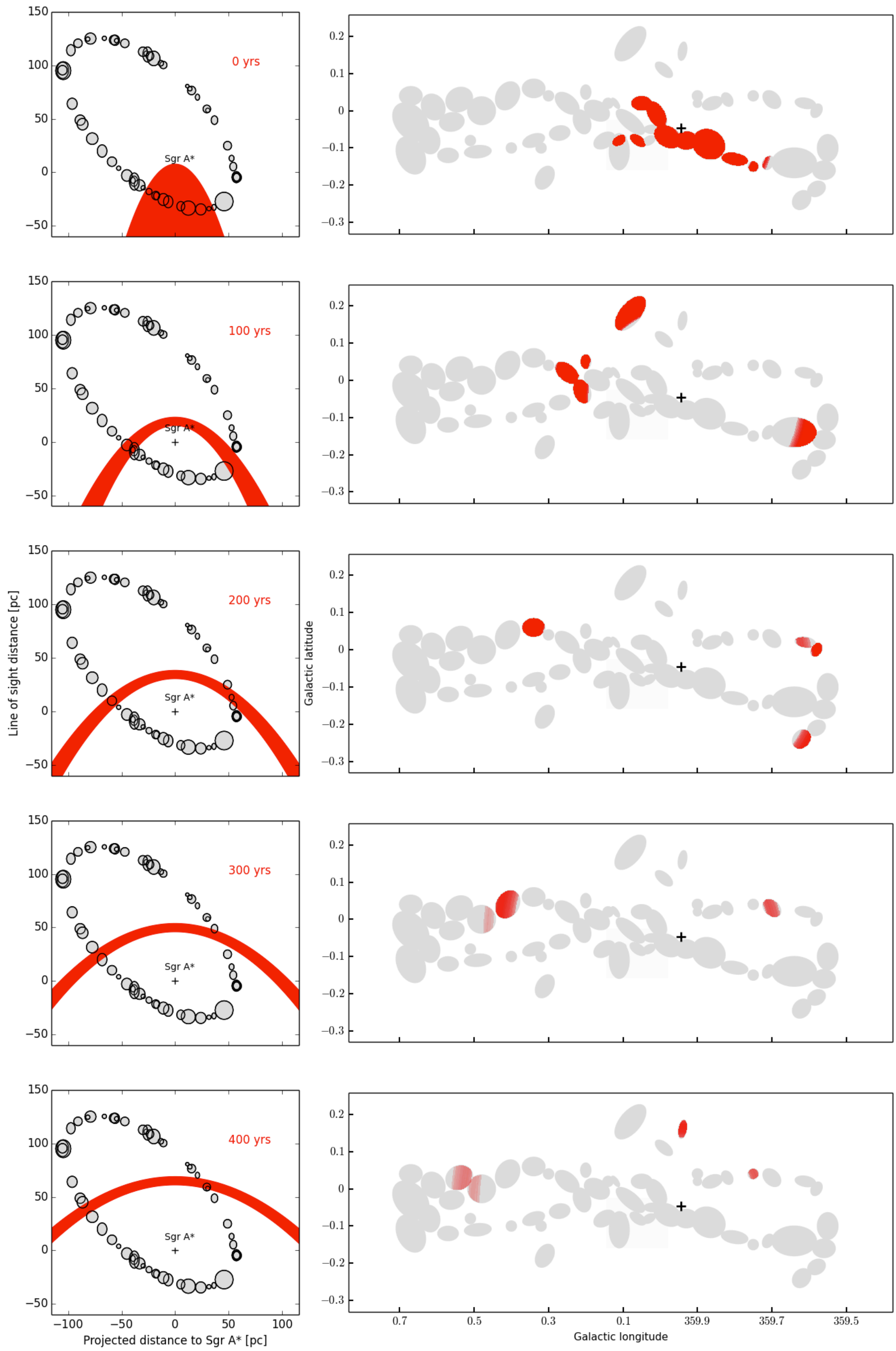

Fig. 1: Variations induced at the Galactic center by the reflection of a single past event of Sgr A*, assuming all the molecular clouds are distributed along the twisted ring proposed by Molinari et al. (2011). **Left:** Propagation of a 50-year duration event (in red) inside the molecular material (in grey) for ten different periods (spanning from 0 to 900 years after the end of the event). View from the Galactic North Pole. **Right:** See next page.

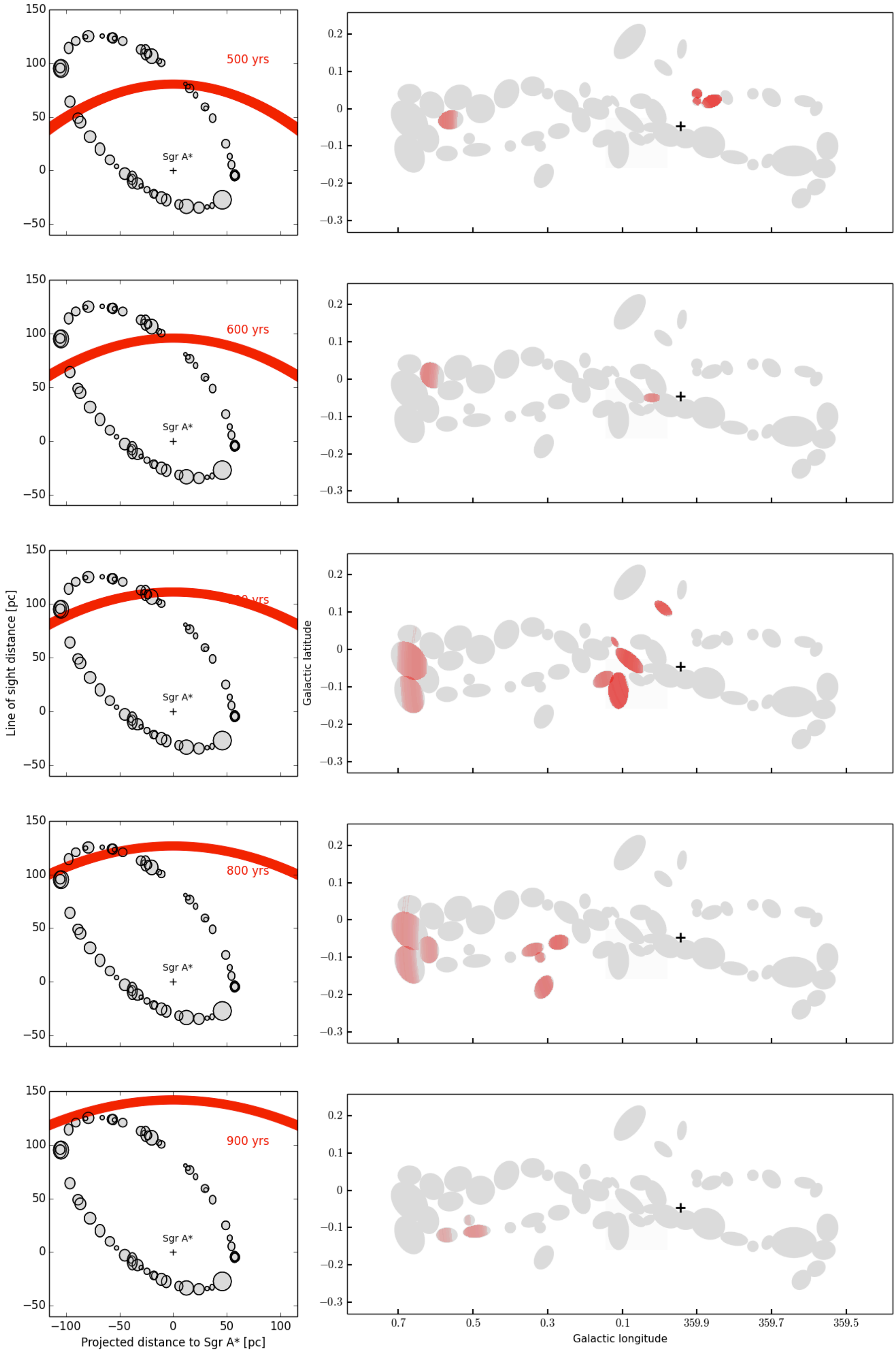

Fig. 1: (Continued). **Left:** See previous page. **Right:** Matter distribution projected onto the plane of the sky (in grey) and regions reflecting the past event at Sgr A* (in red). The strength of the red color indicates the intensity of the Fe Kα fluorescence line emission. The cross indicates the position of Sgr A*.

Predicted variability. As shown in Fig. 1, the echo will take about a thousand years to propagate entirely through the chosen cloud distribution, and it will illuminate very few clouds at any given time. As the event propagates through the matter distribution, it illuminates clouds that are, on average, more distant from Sgr A*, so the reflected flux is globally decreasing with time. Within a single cloud, the echo is likely to propagate away from Sgr A*. However, the global variation pattern seen in the plane of the sky is impossible to predict if the distribution along the line of sight is unknown. Indeed, clouds at the same projected distance (e.g. $l \sim 0.1^\circ$) can be illuminated after a short or a long delay, depending on whether they are in front or behind Sgr A*.

3 Comparison with the observations

An X-ray emission compatible with reflection is now observed from a large fraction of the CMZ. Furthermore, the regular X-ray monitoring of this region for the past fifteen years has allowed for detailed analyses of the spectral evolution of the molecular clouds. The main variations were detected from the dense molecular complexes. In particular, the systematic analysis performed on the Sgr A complex ($l \sim 0.1^\circ$) with an unprecedented spatial resolution, highlighted two distinct time behaviors that can only be explained by two distinct events of a few-year-duration propagating in this region (Clavel et al. 2014b). Thanks to a large survey, we are now extending this analysis to the entire CMZ (Soldi et al. 2014). We confirm the general decrease detected towards Sgr B ($l \sim 0.7^\circ$) and report, for the first time, a decreasing trend from Sgr C ($l \sim 359.6^\circ$). The variations observed in these two complexes are consistent with the reflection of short events, such as those detected in Sgr A.

Inputs from our model. Assuming that the matter distribution proposed by Molinari et al. (2011) is correct, at least three events are needed to account for the illumination of the bright molecular complexes. A recent event (less than 50 years) would explain one of the time behaviors detected in Sgr A, an earlier one (about 150 years) would account for the Sgr C emission and an even older one (about 700 years) would be responsible for both Sgr B and the second time behavior seen in Sgr A. Furthermore, the echo propagation away from Sgr A* is observed in several clouds of the Sgr A complex. However, a more precise comparison is not straightforward, mainly for two reasons. First, the fine details of the observed cloud lightcurves are partly due to the clouds' internal structure, which is poorly known and has not been modeled here. Second, the observations of the CMZ cover less than fifteen years, which means that the positional displacement of the wavefront in the data is smaller than the width of the event parabola in our simulation. Nevertheless, it seems difficult to reproduce with our simulation the rapidly decreasing trend we observe, since the event should continuously illuminate new clouds as it propagates away from Sgr A*.

4 Conclusions

The model we developed to better understand the timing properties of Sgr A*'s echoes at the Galactic center allows us to derive general properties about the illumination variations. However, the individual cloud comparison is highly dependent on the distribution chosen for the central molecular zone and is therefore not yet conclusive. Thus, to fully reconstruct Sgr A*'s past activity, a better 3D gas model and further observations will be needed in order to constrain both the individual cloud structures and the timing properties of the echoes.

References

Clavel, M., Soldi, S., Terrier, R., et al. 2014a, MNRAS, 443, L129

Clavel, M., Terrier, R., Goldwurm, A., et al. 2013, A&A, 558, A32

Clavel, M., Terrier, R., Goldwurm, A., et al. 2014b, in IAU Symposium, Vol. 303, IAU Symposium, ed. L. O. Sjouwerman, C. C. Lang, & J. Ott, 344–348

Molinari, S., Bally, J., Noriega-Crespo, A., et al. 2011, ApJ, 735, L33

Ponti, G., Morris, M. R., Terrier, R., & Goldwurm, A. 2013, in Advances in Solid State Physics, Vol. 34, Cosmic Rays in Star-Forming Environments, ed. D. F. Torres & O. Reimer, 331

Ponti, G., Terrier, R., Goldwurm, A., Belanger, G., & Trap, G. 2010, ApJ, 714, 732

Soldi, S., Clavel, M., Goldwurm, A., et al. 2014, in IAU Symposium, Vol. 303, IAU Symposium, ed. L. O. Sjouwerman, C. C. Lang, & J. Ott, 94–96

Sunyaev, R. & Churazov, E. 1998, MNRAS, 297, 1279

Terrier, R., Ponti, G., Bélanger, G., et al. 2010, ApJ, 719, 143

SF2A 2014
J. Ballet, F. Bournaud, F. Martins, R. Monier and C. Reylé (eds)

THE ROLE OF NEUTRON STAR MERGERS AND CORE COLLAPSE SUPERNOVAE IN R PROCESS NUCLEOSYNTHESIS

F. Daigne[1] and E. Vangioni[1]

Abstract. Recent IR/optical/UV observations and Gamma-ray burst rate determinations at high redshift have led to significant progress in establishing the cosmic evolution of the star formation rate density (SFRD). The SFRD is then used to predict the ionization history of the Universe, and the evolution of the cosmic chemical abundances, supernova rates, etc, as a function of the redshift z. These predictions are done in the framework of the hierarchical model for structure formation. In this context, we focus here our attention on the origin and evolution of a typical r process element: Europium, in two possible sites: core collapse supernovae (SNII) or Neutron Star Mergers (NSM). In the first scenario, there is only one parameter, the yield of Eu produced in these SNII. In the second one, there are three physical parameters, Eu yield, binary star fraction and time delay before the merger. The comparison of our results with available observations of Eu in stars at various metallicities strongly favors the NSM site for the r process. In addition, it allows to put a constraint on the time delay for mergers, which is typically 0.1-0.2 Gyr, and to make an independent prediction for the expected rate of mergers in the horizon of the adv Virgo/Ligo detectors, which we find typically to be of the order of 3 to 10 events per year for NS/NS and NS/BH mergers respectively.

Keywords: R process nucleosynthesis, neutron star mergers, supernovae, cosmic chemical evolution.

1 Introduction

The r-process, or rapid neutron-capture process, of stellar nucleosynthesis is invoked to explain the production of the stable neutron-rich nuclides heavier than iron. They are observed in stars of different metallicities, including in very low metalllicity stars (Roederer *et al.* 2014). However, despite a growing wealth of observational data (Francois *et al.* 2007; Ren *et al.* 2012; Roederer *et al.* 2012), and although increasingly better r-process models are developed with new astrophysical or nuclear physics ingredients, the astrophysical site of r-process is not clearly identified. Presently, two scenarios are considered. The first scenario (SNII site) is directly correlated to the global star formation rate (SFR). The second scenario, neutron star - neutron star and neutron star - black hole mergers (NSM) is from now on the favored site due to the new comprehensive nucleosynthesis analysis for ejecta of compact binaries (Goriely *et al.* 2011; Bauswein *et al.* 2013; Just *et al.* 2014).

2 Cosmic chemical evolution

We follow the cosmic chemical evolution using a semi-analytical model which reproduces the cosmic star formation rate in the cosmological context of hierarchical structure formation (standard Press-Schechter (PS) formalism, Press & Schechter 1974). Our model tracks baryons (i) in stars or their remnants within collapsed structures; (ii) in the gas within collapsed structures (the interstellar medium, ISM); (iii) in the gas outside of structures (the intergalactic medium, IGM). The model includes mass (baryon) exchange between the IGM and ISM (structure formation, galactic outflows), and between the ISM and the stellar component (star formation, stellar explosions). We assume the following cosmological parameters $\Omega_m = 0.27, \Omega_\Lambda = 0.73$ and $H_0 = 71$ km/s/Mpc (h = 0.71). This model allows to compute the evolution of many important quantities as a function of redshift, including stellar explosion rates and the cosmic abundances of several chemical elements. For details see Daigne *et al.* (2006); Rollinde *et al.* (2009).

[1] UPMC-CNRS, UMR7095, Institut d'Astrophysique de Paris, 75014 Paris, France

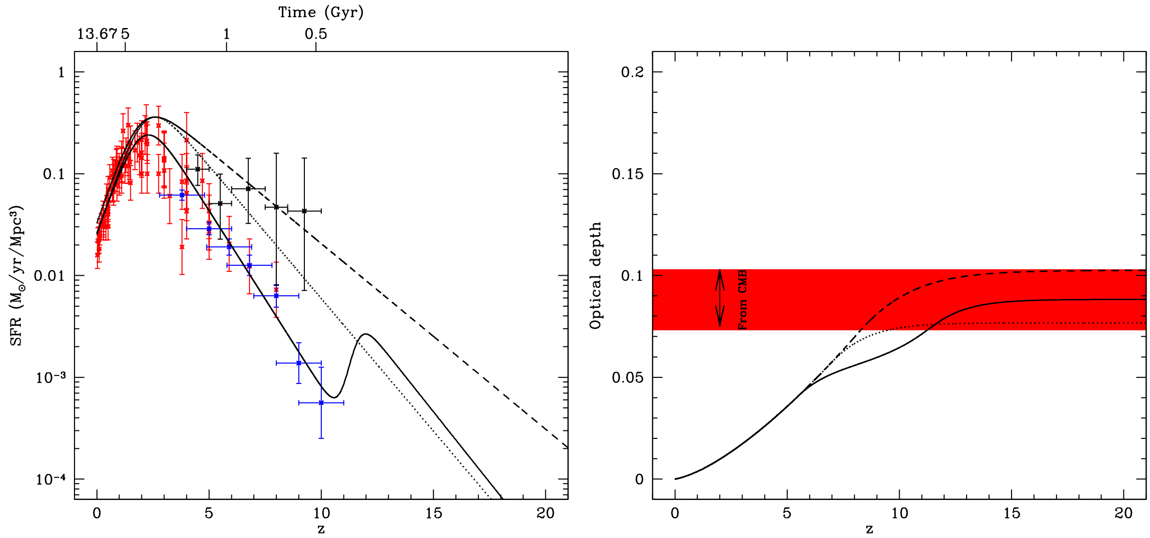

Fig. 1. Left: Cosmic SFR as a function of redshift for the three cases considered in our study (see text): SFR1, a standard SFR with a massive mode at high redshift (solid line); SFR2, a flattened standard SFR (dotted line); and SFR3, an extreme flattened standard SFR (dashed line). The observational constraints are also plotted (Behroozi *et al.* 2013, red points; Oesch *et al.* 2013a; Bouwens *et al.* 2014 and references therein, blue points; Kistler *et al.* 2013, black points). **Right:** For each of the three cases of SFR plotted on the left side (same line styles), the evolution of the Thomson optical depth due to free electrons in the IGM is plotted as a function of redshift. The constraint on this optical depth from CMB measurements is indicated by a red strip (WMAP9 results, Hinshaw *et al.* 2013).

In the following, we consider three distinct modes of star formation: (i) SFR1, a standard mode of Population II/I stars correlated to star forming galaxy observations (Behroozi *et al.* 2013; Oesch *et al.* 2013a; Bouwens *et al.* 2014), together with a more massive mode (Population III stars) at high redshift; (ii) SFR2, a flattened standard SFR; and (iii) SFR3, an extreme flattened standard SFR, correlated to recent measurements derived from the cosmic gamma ray burst rate (Kistler *et al.* 2013). In addition to these prescriptions for the formation rate, we adopt an IMF with a single Salpeter slope ($x = 1.35$), and a mass range 0.1-100 $M_\odot$ for the standard Pop II/I stars (SFR1-3) and 36-100 $M_\odot$ for the massive Pop III stars (SFR1). More details on these assumptions can be found in Vangioni *et al.* (2014a,b). These three cases are plotted on the left panel in Figure 1, together with the observational constraints cited above.

Predictions obtained with these three SFRD modes are compared with several observational constraints. We find a good agreement with the CMB constraint on the reionization of the IGM (see right panel in Figure 1); with the evolution of the rate of core-collapse and thermonuclear supernovae; with the evolution of the cosmic abundances of several chemical elements (C,O, Mg, Si, Fe) both in the ISM and the IGM. More details on the model and the comparison to observations can be found in (Daigne *et al.* 2006; Rollinde *et al.* 2009; Vangioni *et al.* 2014a,b). In this paper, we focus on the cosmic evolution of Europium, as a typical r process element.

3 Europium evolution: core collapse supernovae (SNII) vs mergers (NSM)

We compute the production of Eu, by assuming that it is produced either by core collapse supernovae (we assume a unique yield of 10^{-7} $M_\odot$ of Eu per explosion, for all progenitor masses and metallicities), or by NS/NS or NS/BH mergers. In the latter case, the model has three physical parameters: the Eu Yield (7 to 20 10^{-5} $M_\odot$, Just *et al.* 2014), the time delay between the formation of the neutron stars and the merger, and the fraction of neutron stars which are in a NS/NS or a NS/BH binary system leading to a merger (0.002).

We find that observations of Europium at [Fe/H] > -2.5 are well reproduced by both scenarios. On the other hand, the situation is very different at low metallicity, where the observed evolution of Europium clearly favors mergers as the main astrophysical site for the r process. Indeed, as shown in Figure 3, Eu is overproduced at high z/low metallicity in the core collapse supernova scenario, whereas the observed decrease of Eu/H for [Fe/H] < -2.5 is reproduced by mergers, due to the time delay between star formation and mergers, which is then constrained to be in the 0.1-0.2 Gyr range. This result depends on the iron yield from supernovae, and on the existence or not of the Pop III star mode at high redshift. If more iron is produced at early time (high redshift), the time delay is constrained to be shorter (see Figure 2). Note that the supernova scenario can be reconciled

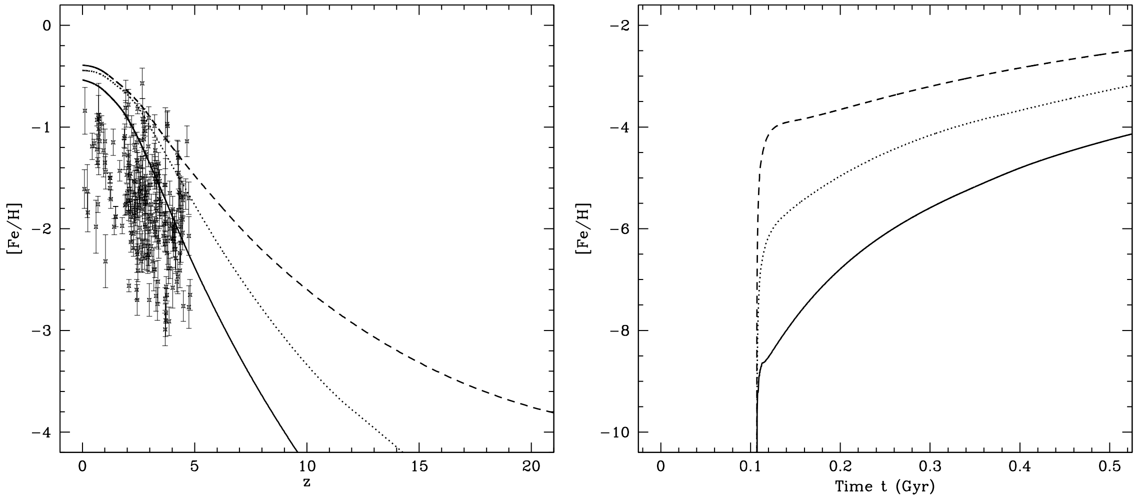

Fig. 2. Left: Iron evolution as a function of redshift z for the three SFR modes. Line styles are the same as in Figure 1. Measurements of the iron abundance in DLAs are also plotted (Rafelski *et al.* 2012). **Right:** Iron evolution as a function of time in the early Universe. Note that [Fe/H] can vary from -9 to -4, depending on the assumption for the SFRD.

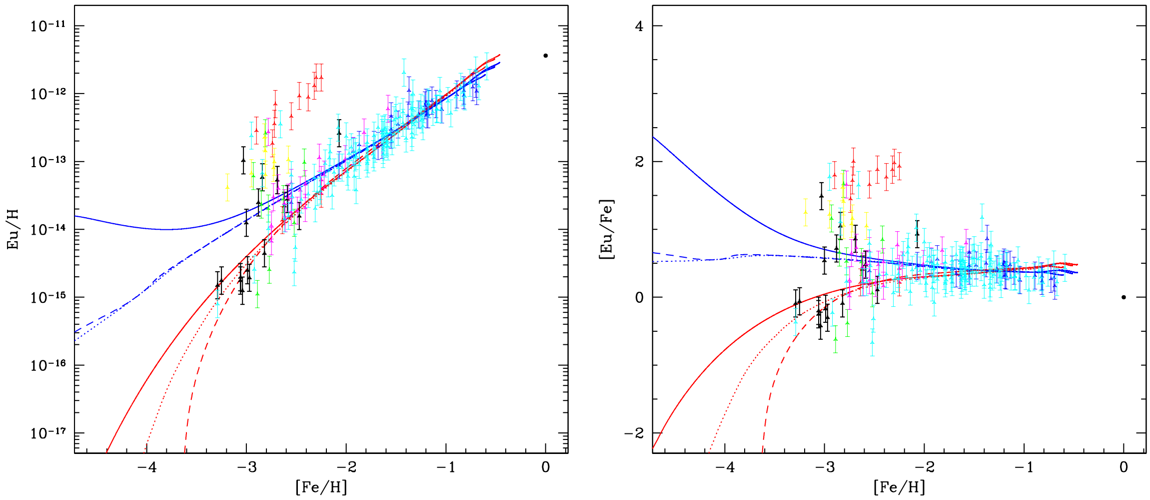

Fig. 3. Left: Evolution of Eu/H as a function of [Fe/H]. Blue lines represent the evolution of Eu in the SNII progenitor case, red lines represent the NSM progenitor case, for the three SFR modes (same line styles as in Figure 1). In the merger scenario, the time delay is adjusted to fit the observations, leading to 0.2, 0.15, 0.1 Gyr for the SFR1, SFR2, SFR3 modes, respectively. The other parameters are given in the text. **Right:** [Eu/Fe] vs [Fe/H] for the three considered SFR modes and for SNII (blue lines) and NSM (red lines) sites.

with observations if it is assumed that Eu is produced only when the progenitor star has a metallicity Z $> 10^{-4}$ $Z_{\odot}$. Unfortunately, Eu observations at very low metallicities are missing to further test our conclusions. In the future, we will consider also another element, Ba, for which observations at [Fe/H] $<$ -3 are available.

4 Conclusion

This work shows that the recent measurements of the Eu abundance in low metallicity stars leads to a cosmic evolution of this element which strongly favors NS/NS and NS/BH mergers as the main astrophysical site for the production of heavy elements by the r process. An interesting by-product of this study is the possibility to obtain an independent constraint on the merger rate in the Universe, thanks to the chemical evolution of r process elements. This is a key ingredient to predict detection rates by gravitational wave detectors. Our

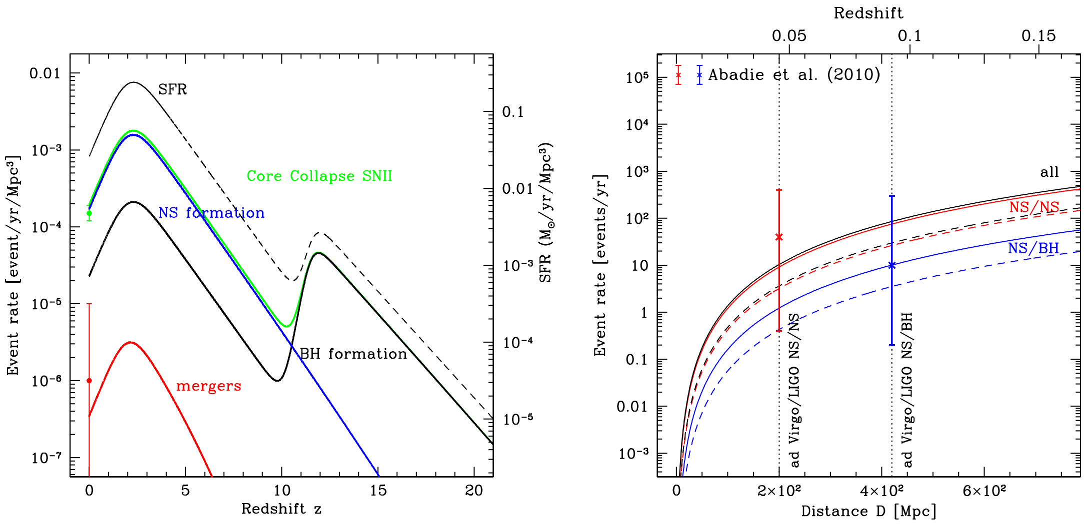

Fig. 4. Left: Star formation rate, birth rate of neutron stars (NS) and black holes (BH), core-collapse supernova rate (SNII), and NS/NS+NS/BH merger rate as a function of redshift, for the SFR1 mode. Green and red points represent the local SNII (Mattila *et al.* 2012) and merger (Abadie *et al.* 2010) rates, respectively. **Right:** integrated merger event rate (NS/NS, NS/BH and total) as a function of distance and redshift for the SFR1 mode. A comparison with Adv Virgo and Adv Ligo predictions is done (Abadie *et al.* 2010). Solid (resp. dashed) lines show the evolution with an Eu yield of 7 10^{-5} $M_\odot$ (resp. 2 10^{-4} $M_\odot$) and a fraction of mergers of 0.002 (resp. 0.0007). The time delay before coalescence is 0.2 Gyr in both cases.

result is plotted as a function of redshift in Figure 4, with a comparison to the predicted rates in the horizon of advanced Virgo/Ligo. The agreement is good with the mean values published by Abadie *et al.* (2010).

F.D. and E.V. acknowledge the Programme National Hautes Energies (PNHE) for financial support.

References

Abadie, J. *et al.* 2010, Cl.Qu.Gr., 27, 173001

Bauswein, A., Goriely, S. & Janka, H.T 2013, ApJ773, 78

Behroozi, P. S., Wechsler, R. H., & Conroy, C. 2013, ApJ, 770, 57

Bouwens, R. J. *et al.* 2014, arXiv 1403.4295

Daigne, F., Olive, K. A., Silk, J., Stoehr, F., & Vangioni, E. 2006, ApJ, 647, 773

Francois, P. *et al.* 2007, A&A, 476, 935

Goriely, S., Bauswein, A. & Janka, H.S. 2011, ApJL, 738, L32

Hinshaw, G., Larson, D., Komatsu, E. *et al.* 2013, ApJS, 208, 19

Just, O. *et al.* 2014, arXiv1406.2687

Kistler, M.D. *et al.* 2013, arXiv1305.1630

Mattila, S., Dahlen, T., Efstathiou, A. *et al.* 2012, ApJ, 756, 111

Oesch, P. A., Bouwens, R. J., Illingworth, G. D. *et al.* 2013a, ApJ, 773, 75

Oesch, P. A., Bouwens, R. J., Illingworth, G. D. *et al.* 2013b, arXiv:1309.2280

Press, W. H., & Schechter, P. 1974, ApJ, 187, 425

Rafelski, M. *et al.* 2012, ApJ, 755, 89

Ren, M. *et al.* 2012, ApJ, 755, 89

Roederer, I.U. *et al.* 2012, ApJS, 203, 27

Roederer, I.U. *et al.* 2014, accepted in ApJ, arXiv1402.4144

Rollinde, E., Vangioni, E., Maurin, D., Olive, K. A., Daigne, F., Silk, J., & Vincent, F. H. 2009, MNRAS, 398, 1782

Vangioni, E. *et al.* 2014a arXiv1409.2462

Vangioni, E. *et al.* 2014b submitted

SF2A 2014
J. Ballet, F. Bournaud, F. Martins, R. Monier and C. Reylé (eds)

SYMMETRY BREAKING BETWEEN SASI SPIRAL MODES

R. Kazeroni[1], J. Guilet[2] and T. Foglizzo[1]

Abstract. The accretion shock formed during the collapse of massive stars is subject to the Standing Accretion Shock Instability (SASI). Spiral modes of SASI can redistribute angular momentum and spin-up a neutron star born from a non-rotating progenitor. If the asymmetries in the progenitor are initially small, two counter-rotating spiral modes with similar amplitudes emerge. In the non-linear regime of SASI, the symmetry between these modes may be broken and a strong spiral mode dominates the dynamics. We study here the timescale for symmetry breaking in order to evaluate the favorable conditions leading to angular momentum redistribution by the SASI. We perform 2D numerical simulations of a simplified setup in cylindrical geometry. These simulations show that a symmetry breaking occurs only if the initial radius of the shock wave is large enough compared to the radius of the neutron star. Furthermore, in the regime where symmetry breaking occurs, we observe stochastic variations, which require a statistical approach. A path towards an analytical description of the timescale for symmetry breaking is proposed.

Keywords: hydrodynamics, instabilities, shock waves, stars: neutron, stars: rotation, supernovae: general

1 Introduction

Hydrodynamic instabilities play an important role in the neutrino-driven mechanism which may explain the explosion of massive stars. By generating non-radial motions of matter below the shock wave during the first second of the collapse of the massive star, instabilities are able to trigger an asymmetric explosion. The Standing Accretion Shock Instability (SASI, Blondin et al. 2003) causes global shock oscillations and induces large scale asymmetries ($l \sim 1$,2). 3D simulations showed that SASI spiral modes can dominate the dynamics of the flow below the shock (Blondin & Mezzacappa 2007; Iwakami et al. 2008; Fernández 2010; Hanke et al. 2013; Abdikamalov et al. 2014). The spiral modes of SASI can redistribute angular momentum (Blondin & Mezzacappa 2007; Foglizzo et al. 2012). In the case where the progenitor is non-rotating, the SASI spiral modes have the potential to explain pulsar spin periods of a few hundreds of milliseconds (Guilet & Fernández 2014). This angular momentum redistribution by the SASI can occur only if the symmetry between SASI spiral modes rotating in opposite directions breaks in the non-linear regime. In this proceeding, our aim is to characterize the timescale for symmetry breaking between SASI spiral modes and to determine whether it is short enough to take place before an explosion sets in. In Sect. 2 we introduce our 2D numerical simulations in cylindrical geometry, and obtain constraints on the symmetry breaking mechanism in Sect. 3.

2 Method

The physical system consists of a standing accretion shock in a steady-state flow. As in Yamasaki & Foglizzo (2008) we restrict our simulation domain to the equatorial plane of the progenitor for the sake of simplicity. We use a cylindrical geometry, which has the advantage of allowing the study of non-axisymmetric modes in 2D simulations. The shock wave initially stands at a radius $r_{\rm sh}$ from the center. The accreting matter is described by a perfect gas with an adiabatic index $\gamma = 4/3$. Above the shock, the gas flows inwards radially. The gas decelerates through the stationary shock and accretes on the hard surface of the neutron star at the radius r_*. The gravity is Newtonian and self-gravity is neglected. We neglect heating to avoid convective motions

[1] Laboratoire AIM, CEA/DSM-CNRS-Université Paris Diderot, IRFU/Service dAstrophysique, CEA-Saclay F-91191, France
[2] Max-Planck-Institut fur Astrophysik, Karl-Schwarzschild-Str. 1, D-85748 Garching, Germany

and include cooling to mimic neutrino emission by electron capture with the approximation $\mathcal{L}_0 \propto p^{3/2}\,\rho$, as in Blondin & Mezzacappa (2007) where p and ρ denote the pressure and the density. The cooling is dominant only in a narrow region close to the accretor. The flow is supersonic above the shock with an incident Mach number $\mathcal{M}_1 = 5$ at $r = r_{\rm sh}$ and subsonic below the shock. The two solutions are connected by the Rankine-Hugoniot jump conditions for an ideal gas, neglecting the dissociation of iron.

Our computational domain does not include the proto neutron star. Its surface corresponds to the inner boundary of the domain. We use cylindrical coordinates $(r,\,\phi)$ with $r \in [r_*,\,3\,r_{\rm sh}]$ and $\phi \in [0,\,2\,\pi]$. We impose reflexive conditions at the inner boundary. The flow at the outer boundary is given by the upstream steady state solution. The initial condition corresponds to the stationary flow obtained by solving the time-independent continuity, Euler and energy equations. To perform time-dependent hydrodynamic calculations, we employ a version of the Godunov code RAMSES (Teyssier 2002; Fromang et al. 2006) with a constant grid and no AMR. The numerical resolution is 600 to 1000 cells in the radial direction and 1000 to 1600 cells in the azimuthal direction. High resolution is required to resolve properly the dynamics of the flow in the vicinity of the proto neutron star with steep gradients. We define the radii ratio $R = r_{\rm sh}/r_*$. The initial value of R is chosen by adjusting the cooling normalization constant. As in Fernández & Thompson (2009) we use a cutoff in entropy in the cooling function to turn off the cooling in the first few cells outside r_* to avoid the divergence of the numerical solution. The cooling function is such that:

$$\mathcal{L} = \mathcal{L}_0\,\exp\left[-\left(\frac{s}{k\,s_{\rm min}}\right)^2\right] \tag{2.1}$$

$s = (\gamma-1)^{-1}\ln\left(p/\rho^\gamma\right)$ is an entropy function, $s_{\rm min}$ its value at $r = r_*$ and k a real number chosen to introduce only minimal modification to the postshock steady state flow. To test the robustness of our code, we computed the growth rates and the frequencies of the unstable modes of the SASI in the linear regime and obtained a very satisfactory agreement with the values of Yamasaki & Foglizzo (2008) computed with a perturbative analysis: the discrepancies are less than 2% for the frequencies and less than 8% for the growth rates.

We let the steady state flow relax on the numerical grid for a hundred dynamical timesteps and then introduce two entropy perturbations at pressure equilibrium in the supersonic flow to trigger SASI spiral modes $m = 1$ and $m = -1$. The linear phase of SASI lasts approximately 2 SASI oscillation periods and the simulation finishes at $t = 1s$. Without any perturbations, our code is perfectly spherically symmetric, the SASI does not develop and the shock remains circular. Moreover, if the two perturbations have exactly the same amplitude, the symmetry does not break and we obtain a stationary sloshing mode in the non linear regime which can be seen as a sum of the two counter-rotating spiral modes. In order to study the symmetry breaking we vary the relative perturbation amplitudes of the two spiral modes and define the initial asymmetry by $\epsilon = (A_{\rm r}^2 - A_{\rm l}^2)/(A_{\rm r}^2 + A_{\rm l}^2)$ where $A_{\rm r}$ and $A_{\rm l}$ respectively stand for the amplitudes of the shock displacement associated to the modes $m = 1$ and $m = -1$. We also vary the radii ratio R. This ratio selects the unstable modes of SASI and affects their growth rates (Foglizzo et al. 2007). We neglect the initial rotation of the progenitor in our setup which would favour the prograde SASI mode (Yamasaki & Foglizzo 2008). Finally we have set two different methods to estimate the timescale for symmetry breaking. The first one is based on the time evolution of the angular momentum flux at the inner boundary. This flux is very close to zero before the symmetry breaking and start to deviate from zero when one of the spiral modes dominates the dynamics. The second method uses the triple point that forms in the shock wave (Blondin & Mezzacappa 2007). We track the triple point in our simulations and compute the time evolution of its rotation rate. This rotation rate evolves rather randomly before the symmetry breaking and becomes almost constant afterwards. The two methods are consistent within a SASI oscillation period which is sufficient for our study.

3 Characterization of the symmetry breaking

We perform a total of 80 simulations varying R and ϵ such that $R = \{1.67,\,2,\,2.22,\,2.5,\,3,\,4\}$ and $10^{-3} \le |\epsilon| \le 1$. For large values of $|\epsilon|$, a strong spiral mode is triggered in the linear phase of SASI and saturates in the non-linear regime. For lower values ($|\epsilon| \le 0.2 - 0.3$) the initial asymmetry is too small to lead to a symmetry breaking in the linear phase during which spiral modes and sloshing mode of a given index m grow at the same rate. By varying R, our simulations show that symmetry breaking is not a systematic behaviour of the SASI. Indeed, we do not obtain any symmetry breaking when $R \le 2$. For these values of R, we show that sloshing modes dominate the dynamics of SASI in the non-linear regime. Even if we consider an extreme case: $\epsilon = 1$ meaning that only one of the two spiral modes is triggered and dominates the linear regime, a sloshing mode dominates the non-linear regime as in the left panel of Fig. 1. Our simplified setup shows that if $R \leq 2$ and if we assume that initial asymmetries in the progenitor are weak, then there is no sign of symmetry breaking and SASI is unable to redistribute angular momentum.

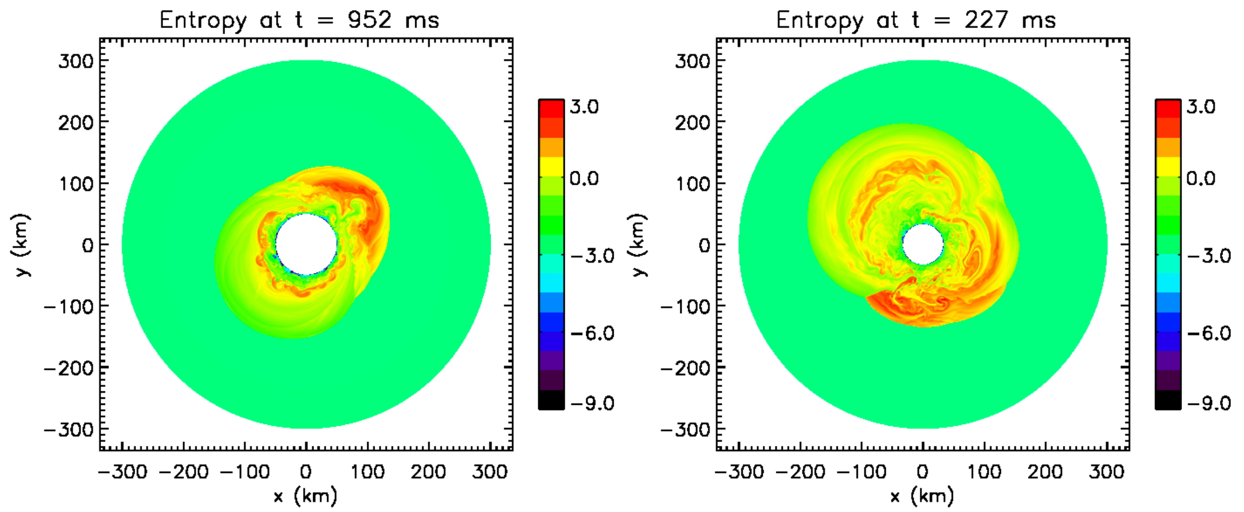

Fig. 1. Left: Snapshot of the entropy at $t = 952$ ms for $R = 2$ and $\epsilon = 1$. A sloshing motion dominates the non-linear regime despite a strong initial asymmetry. **Right:** Snapshot of the entropy at $t = 227$ ms for $R = 3$ and $\epsilon = 0.1$. The symmetry breaking has already occured.

We now focus on the case $R > 2$ for which we obtain systematically a symmetry breaking. For $R = 2.22$ and weak initial asymmetry, the timescale for symmetry breaking is comparable to the critical time of 1 s after bounce (around 30 SASI oscillation periods) whereas for $R = \{2.5, 3, 4\}$ the symmetry breaking occurs within 3 to 10 SASI oscillations in the non-linear phase as in the right panel of Fig. 1. However, for low values of the initial asymmetry $|\epsilon| \leq 0.2$, there is no clear trend between the level of initial asymmetry and the timescale for symmetry breaking. More precisely, a decrease in ϵ does not increase this timescale which is rather chaotic. For some cases where $|\epsilon| \leq 0.1$, the sign of ϵ does not determine the direction of rotation of the shock wave. We have extensively tested the code to check that this non-deterministic phenomenon is not due to a numerical artefact. We propose a physical interpretation to this feature of the SASI. We suggest that parasitic instabilities that grow on an unstable mode, and which can explain the SASI saturation amplitude (Guilet et al. 2010) might modify in a stochastic way the level of asymmetry between the spiral modes. This might be enough, if initially $|\epsilon| \leq 0.1$, to change the dominating spiral mode before a symmetry breaking occurs. A statistical approach is therefore required to address the issue of a timescale for symmetry breaking between spiral modes in order to get a general picture in this parameter space. Fig. 2 shows the number of SASI oscillations to reach the symmetry breaking for an initial asymmetry $|\epsilon|$ and for $R = \{2.22, 2.5, 3, 4\}$. We do not mention cases for $R = \{1.67, 2\}$ here because they do not lead to a symmetry breaking. The size of the error bars is 2 SASI oscillations and corresponds to the precision of our methods to evaluate the timescale. For $R = \{2.22, 2.5\}$ and $|\epsilon| < 0.2$ the variations of the number of SASI oscillations to reach symmetry breaking are greater than the error bars. This illustrates the stochasticity of symmetry breaking for weak initial asymmetries.

Finally, we propose a physical mechanism for the symmetry breaking, which is based on the effect of the rotation induced by the spiral modes on their growth rate. Guilet & Fernández (2014) showed that the rotation induced by spiral modes scales as $A_{\rm r}^2 - A_{\rm l}^2$, the rotation below the shock being in the same direction as the spiral mode of largest amplitude. Moreover, Yamasaki & Foglizzo (2008) showed that the growth rates of unstable modes vary linearly with the angular momentum, prograde modes begin favored and retrograde modes being damped. If the rotation induced by the spiral modes has a similar effect on the growth rate, then the growth of the spiral mode of largest amplitude would be favored thus potentially leading to a symmetry breaking. This model needs to be further developed to be compared to the results of the numerical simulations.

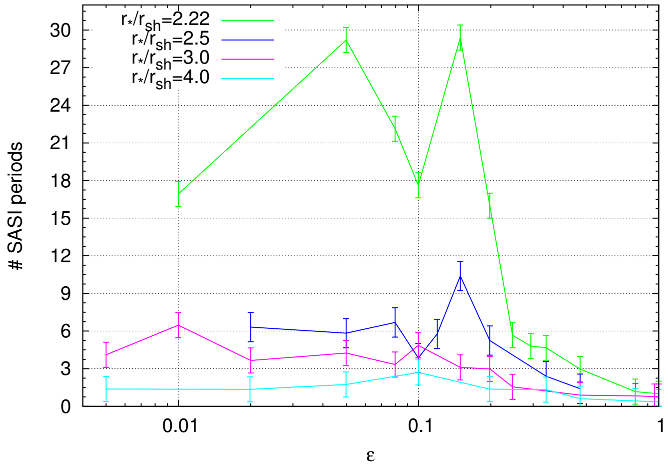

Fig. 2. Number of SASI oscillations before reaching the symmetry breaking with respect to the initial asymmetry ϵ. From top to bottom are shown ratios $R = 0.45, 0.4, 0.33, 0.25$. The size of the error bars is 2 SASI oscillations.

4 Conclusion

We have used a simplified model (Blondin & Mezzacappa 2007; Foglizzo et al. 2007; Yamasaki & Foglizzo 2008; Fernández & Thompson 2009) to study the SASI in the non-linear regime with 2D numerical simulations on a cylindrical domain. We varied the radii ratio R and the initial asymmetry ϵ of the perturbations to study the timescale for symmetry breaking. Our simulations show that the symmetry breaking between SASI spiral modes occurs only for some values of R. Moreover, when it occurs, the symmetry breaking is affected by a non-deterministic phenomenon which requires a statistical approach for small initial asymmetries.

Characterizing the symmetry breaking is essential to understand the conditions under which a strong spiral mode dominates the non-linear regime and redistributes angular momentum. Our study proposes a path towards an analytical description of the symmetry breaking.

The spin of the neutron star at birth can be either dominated by the conservation of the initial angular momentum of the pulsar or by the redistribution of angular momentum due the SASI spiral modes. The question of the threshold between these two regimes will be addressed in future work in which initial rotation will be included in our setup.

Numerical simulations were performed using HPC resources from GENCI-TGCC (Grant t2014047094) made by GENCI. This work is part of ANR funded project SN2NS ANR-10-BLAN-0503. JG acknowledges support from the Max-Planck–Princeton Center for Plasma Physics.

References

Abdikamalov, E., Ott, C. D., Radice, D., et al. 2014, ArXiv e-prints
Blondin, J. M. & Mezzacappa, A. 2007, Nature, 445, 58
Blondin, J. M., Mezzacappa, A., & DeMarino, C. 2003, ApJ, 584, 971
Fernández, R. 2010, ApJ, 725, 1563
Fernández, R. & Thompson, C. 2009, ApJ, 697, 1827
Foglizzo, T., Galletti, P., Scheck, L., & Janka, H.-T. 2007, ApJ, 654, 1006
Foglizzo, T., Masset, F., Guilet, J., & Durand, G. 2012, Physical Review Letters, 108, 051103
Fromang, S., Hennebelle, P., & Teyssier, R. 2006, A&A, 457, 371
Guilet, J. & Fernández, R. 2014, MNRAS, 441, 2782
Guilet, J., Sato, J., & Foglizzo, T. 2010, ApJ, 713, 1350
Hanke, F., Müller, B., Wongwathanarat, A., Marek, A., & Janka, H.-T. 2013, ApJ, 770, 66
Iwakami, W., Kotake, K., Ohnishi, N., Yamada, S., & Sawada, K. 2008, ApJ, 678, 1207
Teyssier, R. 2002, A&A, 385, 337
Yamasaki, T. & Foglizzo, T. 2008, ApJ, 679, 607

SF2A 2014
J. Ballet, F. Bournaud, F. Martins, R. Monier and C. Reylé (eds)

SIMULATION OF THE MICROWAVE EMISSION FROM EXTENSIVE AIR SHOWERS

Sandra Le Coz[1]

Abstract. Ultra-high energy cosmic rays are detected through the extensive air showers they create when entering the atmosphere. The electromagnetic content of air showers is at the origin of different types of electromagnetic wave emissions, in different wavelength ranges. Air shower fluorescence light is detected routinely in ground-base detectors such as the Pierre Auger Observatory or Telescope Array. Decametric emissions (MHz) have been observed by different cosmic ray experiments equipped with antennas. Novel detection techniques based on the postulated GHz emission from molecular bremsstrahlung in air showers are also currently being studied. They are motivated by the observation of a microwave emission due to the low energy shower electrons generated by a high-energy electron beam passing through targets, in accelerator experiments. A fast simulation of this microwave emission from extensive air showers is reported here.

Keywords: cosmic rays, astroparticles, composition, radio, molecular bremsstrahlung

1 Introduction

1.1 Ultra-high energy cosmic rays

Cosmic rays are particles in relativistic motion through the interstellar and intergalactic media. They were discovered a century ago, through the particle showers they generate when entering the atmosphere. The detection of these shower particles was at the origin of the discovery of numerous subatomic particles, before the accelerator era. The increasing number of experiments dedicated to the detection of cosmic rays, at the ground, with balloons or in orbit, has allowed the measurement of the energy spectrum at Earth. Regardless of the energy, cosmic rays are mainly composed of protons and helium nuclei, including a fraction of heavier nuclei and electrons. At the highest energies, the flux is very low, reaching 1 particle per km^2 per year above 10^{19} eV. The question of the origin, the acceleration mechanisms and the mass composition of these ultra-high energy cosmic rays remains. Giant ground-based detectors are dedicated to their study. These detectors sample the particles of the air shower that reach the ground with a duty cycle of nearly 100% and/or detect the fluorescence light emitted along the air shower development, only on clear and moonless nights, that is about 10% of the time.

1.2 Fluorescence detection of extensive air showers

The fluorescence detectors of air shower experiments such as the Pierre Auger Observatory (The Pierre Auger collab. 2004, 2010) or Telescope Array (Tokuno & the Telescope Array collab. 2012) observe the shower's longitudinal development, collecting the fluorescence light emitted in the UV range by air-nitrogen, excited by the electrons of the shower. As the amount of collected light is related to the total deposited energy of the shower, fluorescence detectors allow the absolute energy calibration of surface detectors. Hence, the energy of cosmic rays may be inferred 100% of the time, on a model-free basis. As a proton interacts less with the atmosphere and generates a shower deeper than heavy nuclei (for the same total energy), the atmospheric depth X_{max} where the longitudinal development of the shower reaches the maximum number of particles is used to infer the mass. Because of shower to shower fluctuations and because of the overlap of proton and iron X_{max} distributions (the two extreme masses), the inference of mass is only possible stastistically and not event by event. Comparing the mean value and standard deviation of X_{max} with the values predicted by extrapolated

[1] Laboratoire de Physique Subatomique et de Cosmologie, Université Grenoble-Alpes, CNRS/IN2P3, Grenoble, France

hadronic models for proton and iron, the mass composition studied with Auger data is found to be compatible with protons up to 2×10^{19} eV and grows heavier as energy increases beyond this (The Pierre Auger collab. 2013). For Telescope Array, the mass composition is reported to be compatible with protons even at the highest energies (Tameda et al. 2013), but inference methods are a bit different. Due to the low flux and the low duty cycle of fluorescence detectors, the mass inference at the highest energies is statistically somewhat limited. A complementary detection technique may help to improve the situation : the radiodetection of air showers.

1.3 Radiodetection of extensive air showers

The electrons of air showers are not only related to fluorescence light, but are also at the origin of different types of electromagnetic wave emissions, in different wavelength ranges. Air shower decametric emissions (MHz) had been observed with aerials by different cosmic ray experiments (also using surface detector arrays) in the 50-60's, but the technique had sunk into oblivion in the 70's because of fluorescence detector developments. Triggered by the limitations of the latter, and by signal processing enhancements, a renewed interest has arisen in the 2000's. If fully realized, the radio detection (MHz or GHz) would offer a lot of advantages such as a low atmosphere attenuation and a near 100% duty cycle, to be compared to the 10% of fluorescence detectors. Recent experiments such as CODALEMA (in Nançay radio observatory; Ardouin 2005) and LOPES (using interferometry at Karlsrhue Institute of Technology; Falcke 2005) proved that the radio signal produced by an air shower allows to reconstruct its energy and direction. There is a consensus on the mechanisms at the origin of the emission: a geomagnetic deviation effect was identified in the 60's and a negative charge excess variation effect was confirmed around 2010 by the afore-mentioned experiments and by AERA (at the Pierre Auger Observatory; Schröder & the Pierre Auger collab. 2013; The Pierre Auger collab. 2014). All these MHz radiations are emitted anisotropically, along the shower axis.

Novel detection techniques based on the GHz emission from air showers are also being studied nowadays. They are mainly motivated by the observation by Gorham (2008) of a microwave emission thought to be due to low-energy electrons generated by a high-energy electron beam passing through targets, in an accelerator experiment at SLAC (Stanford). According to this purported mechanism of production, the GHz radiation may present the advantage of being emitted isotropically, and therefore to be detectable far away from the shower axis. Consequently, the Pierre Auger collaboration has been developing microwave (GHz) detection prototypes (Bérat & the Pierre Auger collab. 2013), such as AMBER (Gorham 2008), MIDAS (Alvarez-Muniz 2013), or EASIER (Gaior & the Pierre Auger collab. 2013), aiming to obtain valuable observables related to air showers.

2 Simulation of the GHz emission

2.1 Derivation of a molecular bremsstrahlung yield

The Gorham (2008) SLAC experiment consists of a beam of electrons passing through alumina targets, in order to create an electromagnetic shower that reaches a maximum of development when entering an anechoic chamber. In the chamber, antennas detect the radiation emitted at microwave frequencies by the shower. The recorded signal allows us to derive a yield for the microwave emission. We define this yield as the ratio between the energy deposited through microwave radiation per unit frequency, $E_{MW}/\Delta\nu$, and the total energy deposited, E_{dep}. Considering the features of the beam (and making an assumption on the number of electrons at the maximum of development), the features of the detection system, and the recorded signal, we get

$$Y_{MW} = \frac{E_{MW}/\Delta\nu}{E_{dep}} \sim 2 \times 10^{-18}\text{Hz}^{-1}. \tag{2.1}$$

The radiation detected at SLAC has been understood as molecular bremsstrahlung radiation. Indeed, air shower electrons lose the main part of their energy by exciting or ionizing the air components : the oxygen and nitrogen. Nitrogen excitation is at the origin of the fluorescence light while air ionization is at the origin of secondary low-energy electrons. These secondary electrons interact in turn with the air, mainly with neutral components, more numerous than the ionized ones. This interaction between a low-energy electron and the electromagnetic field of neutral air molecules is quasi-elastic, and a bremsstrahlung radiation is emitted. As the secondary electrons are emitted without any favored direction, the bremsstrahlung radiation would be statistically isotropically emitted, and unpolarized. We derive now a phenomenological yield for the molecular bremsstrahlung emission.

The number of photons emitted per unit frequency per secondary electron depends on its velocity v, on the number of targets per unit volume n_m and on the interaction cross section Q,

$$\phi = n_m v Q. \tag{2.2}$$

According to Yamabe et al. (1983), the differential molecular bremsstrahlung (free-free interaction) cross section, per unit frequency ν of the emitted photon is given by

$$\frac{dQ}{d\nu}(e,\nu) = \frac{Q_{ff}}{\nu}(e,\nu), \tag{2.3}$$

where e is the kinetic energy of the electron and

$$Q_{ff}(e,\nu) = \frac{4}{3\pi}\frac{\alpha^3}{Ry}e\left(1-\frac{h\nu}{2e}\right)\sqrt{1-\frac{h\nu}{e}}Q_m(e), \tag{2.4}$$

with $\alpha = 7.3\times10^{-3}$ the fine-structure constant, $Ry = 13.6$ eV the Rydberg energy, $h = 6.63\times10^{-34}$ J.s the Planck constant, and $Q_m(e)$ the cross section for momentum transfer collisions of the electrons with the air targets. $Q_m(e)$ values are given for O_2 and N_2 in tables by Itikawa (2006, 2009). Considering only low frequency photons, we have $h\nu << e$. Equation 2.4 may therefore be rewritten as $Q_{ff}(e,\nu) = (4\alpha^3/3\pi Ry)eQ_m(e)$.

According to Opal (1971), the kinetic distribution of secondary electrons is expected to follow

$$f(e) = \frac{k}{1+\left(\frac{e}{e_0}\right)^{2.1}}, \tag{2.5}$$

with $k \sim 1/20.9$ eV^{-1} the normalizing constant, $e_0(N_2) = 13$ eV and $e_0(O_2) = 17.4$ eV. This distribution is derived from experiments where primary electrons from 100 to 2000 eV scatter on oxygen and nitrogen.

The molecular bremsstrahlung radiation is limited by the attachment of electron to neutral dinitrogen, mainly occuring in 3 body reactions with 2 dinitrogen or with 1 dioxygen and 1 dinitrogen. According to Nijdam (2011), the lifetime of secondary electrons is expected to be

$$\tau = \frac{1}{n_m^2(k_{att,1}[O_2]^2 + k_{att,2}[O_2][N_2])}, \tag{2.6}$$

depending on attachment constants $k_{att,1} = 2\times10^{-30}$ cm^6 s^{-1}, $k_{att,2} = 8\times10^{-32}$ cm^6 s^{-1}, on atmospheric components fractions $[O_2] = 0.2095$, $[N_2] = 0.7808$, and on the number of air molecules per unit volume, which has a value at sea level of $n_m = 2.58\times10^{19}$ cm^{-3}.

Knowing that the emitted power is equivalent to the number of photons emitted per unit time multiplied by the energy of photons $h\nu$, and taking into account the bremsstrahlung cross section, the energy distribution and the lifetime of secondary electrons, we get the total power emitted per unit frequency as a function of time by a set of $n_{e,0}$ secondary electrons,

$$\frac{P}{\Delta\nu} = n_{e,0}\exp\left(-\frac{t}{\tau}\right)\frac{4}{3\pi}\frac{\alpha^3}{Ry}n_m h\int_0^\infty vf(e)eQ_m(e)de. \tag{2.7}$$

To estimate the fraction of the energy deposited by the electrons of the shower through molecular bremsstrahlung, we define a yield

$$Y_{MBR} = \frac{E_{MBR}/\Delta\nu}{E_{dep}}, \tag{2.8}$$

with E_{MBR} the energy deposited by the electrons of the shower through molecular bremsstrahlung and E_{dep} the total energy deposited. Considering that E_{MBR} is the integral over time of the power derived above, and that to create the $n_{e,0}$ secondary electrons we need an energy $E_{dep} = n_{e,0}w_i$, with $w_i = 34$ eV the mean energy required to create an electron-ion pair in air (given by the ICRU Report 1993), we finally get

$$Y_{MBR}(z) = \frac{\tau}{w_i}\frac{4}{3\pi}\frac{\alpha^3}{Ry}n_m h\int_0^\infty vf(e)eQ_m(e)de \sim 6\times10^{-18}\frac{\rho_0}{\rho(z)}\text{Hz}^{-1}, \tag{2.9}$$

with $\rho(z)$ the density of the air regarding the altitude z and ρ_0 the density of the air at sea level. This phenomenological yield is of the same order of magnitude as the yield we derived from the results of the Gorham (2008) SLAC experiment at sea level.

2.2 Algorithm

To estimate the received signal at one antenna, we have to generate the air shower development, the molecular bremsstrahlung radiation, and to consider its propagation and the antenna response. In the simulation, the longitudinal development (number of electrons as a function of the atmospheric depth) of the air shower is given by the Gaisser & Hillas (1977) function, while the lateral extension of the shower is described by the NKG formula (Nishimura & Kamata 1958; Greisen 1960). Given the energy, the arrival direction and the mass of the cosmic ray, the shower is then generated. At each shower step, the energy emitted through bremsstrahlung is derived from the total deposited energy using

$$E_{MBR} = E_{dep} Y_{MBR} \Delta\nu, \tag{2.10}$$

with $\Delta\nu$ the antenna bandwidth. This energy is then split into pieces to take into account the secondary electrons lifetime. All the pieces of energy are then propagated to the antenna, taking into account the air index for radio waves, the distance between the emission step and the antenna, and the effective area of the antenna at the angle between its axis and the axis of propagation of the radiation to the antenna. The pieces of energy are then put into bins of time, according to their arrival time and to the digitization frequency of the antenna system. For each bin of time, the total energy is then divided by the duration of the bin and we finally get a signal in terms of power as a function of time, such as the signal depicted in Fig. 1.

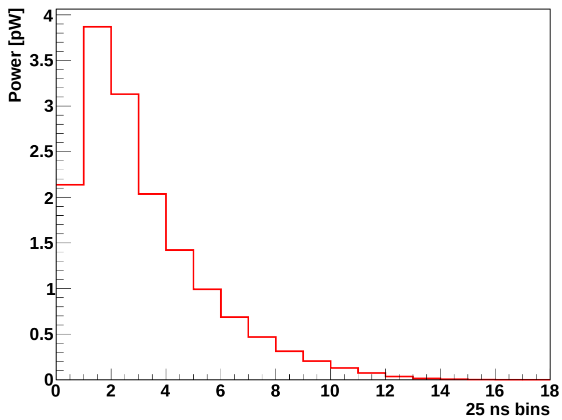

Fig. 1. Output of the simulation. Example of a simulated signal digitized at a frequency of 40 MHz.

2.3 Results

The simulation is carried out for a 10^{19} eV air shower. A proton is at the origin of the shower, with a zenith angle of 30°. The emitted radiation is detected at an altitude of 1400 m with a C-band LNBf (3.4-4.3 GHz), usually used for TV receiving, looking at the zenith. The signal is digitized at a frequency of 40 MHz. We consider two features of the signal, the maximum of the power and the number of 25 ns bins for which the power is above 10% of the maximum power. These features are depicted in Fig.2 as a function of the antenna position (X, Y coordinates) in the shower core frame. In this frame, the shower core is therefore in ($X = 0, Y = 0$), and the shower axis is along the positive part of the X-axis. After all, at 200 m from the shower core, we expect a maximum power of 6×10^{-12} W and 20 bins above 10% of the maximum power. At 1500 m, the maximum of the signal falls by 2 orders of magnitude and its duration is ten times longer.

3 Conclusions

The radiodetection of air showers would be attractive, in order to understand better the matter of the mass composition of ultra-high energy cosmic rays. We derived a bremsstrahlung yield, which has a value at sea level of $Y_{MBR}(z) \sim 6 \times 10^{18}$ Hz^{-1}, that is the same order of magnitude as the yield we derived from the Gorham (2008) SLAC experiment results. For a 10^{19} eV air shower, we simulated the signal detected by a C-band

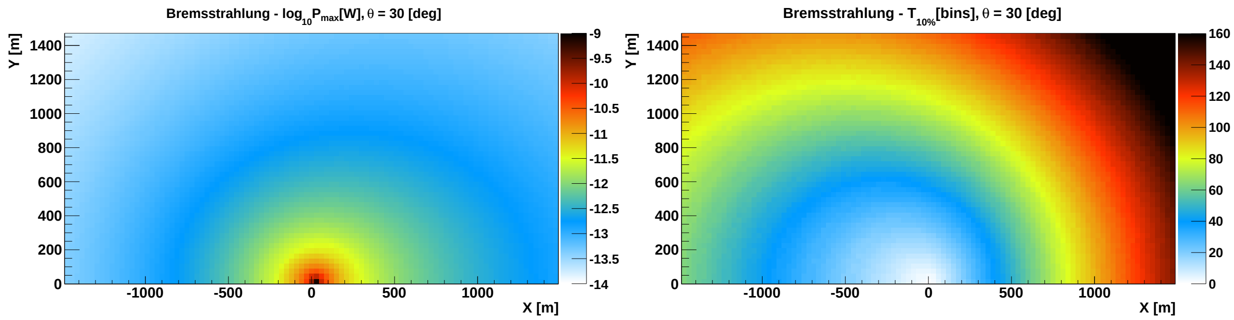

Fig. 2. Features of the simulated signal as a function of the antenna position in the shower-core frame (see text). **Left:** Logarithm of the maximum of the power in pW. **Right:** Number of 25 ns bins for which the power is above 10% of the maximum power.

TV-antenna. At a few hundred meters from the shower core, we estimated the signal to be of an order of magnitude of 1 pW, and to last a few tens of 25 ns bins.

I acknowledge the support of the Joseph Fourier University and of the French Agence Nationale de la Recherche 321 (ANR) under reference ANR-12-BS05-0005-01. I also thank the Pierre Auger collaboration and the SF2A local organization committee.

References

Alvarez-Muniz, J. *et al.*. 2013, Nucl. Inst. Meth. Phys. Res., 719, 70
Ardouin, D. *et al.*. 2005, Nucl. Instrum. Meth. A, 555, 148
Bérat, C. & the Pierre Auger collab. 2013, Nucl. Instr. and Meth. A, 718, 471
Falcke, H. *et al.*. 2005, Nature, 435, 313
Gaior, R. & the Pierre Auger collab. 2013, ICRC (Rio de Janeiro)
Gaisser, T. K. & Hillas, A. M. 1977, 15th ICRC, 8, 353
Gorham, P. W. *et al.*. 2008, Phys. Rev. D, 78, 032007
Greisen, K. 1960, Ann. Rev. Nucl. Part. Sci., 10, 63
ICRU Report. 1993, 31
Itikawa, Y. 2006, J. Phys. Chem, 35, 31
Itikawa, Y. 2009, J. Phys. Chem, 38, 1
Nijdam, A. 2011, ApJ, 44, 455201
Nishimura, J. & Kamata, K. 1958, Progr. Theor. Phys., 6, 93
Opal, C. B. 1971, J. Chem. Phys., 55, 4100
Schröder, F. G. & the Pierre Auger collab. 2013, ICRC (Rio de Janeiro)
Tameda, Y., the Telescope Array, & Hires collab. 2013, EPJ Web Conf., 53, 04005
The Pierre Auger collab. 2004, Nucl. Instrum. Meth. A, 523, 50
The Pierre Auger collab. 2010, Nucl. Instr. and Meth. A, 620, 227
The Pierre Auger collab. 2013, JCAP, 026, 02
The Pierre Auger collab. 2014, Phys. Rev. D, 89, 052002
Tokuno, H. & the Telescope Array collab. 2012, Nucl. Instr. and Meth. A, 676, 54
Yamabe, C., Buckman, S. J., & Phelps, A. V. 1983, Phys. Rev. A, 27, 3

SF2A 2014
J. Ballet, F. Bournaud, F. Martins, R. Monier and C. Reylé (eds)

2004 – 2014: TEN YEARS OF RADIATIVE TRANSFER WITH STOKES

F. Marin[1] and R. W. Goosmann[2]

Abstract. Since it became publicly available in 2004, the radiative transfer code STOKES has been used to model the spectroscopic, polarimetric, timing and imaging signatures for different astrophysical scenarios. Ten years later, at the release of a new version of the Monte Carlo code, we make a census of the different scientific cases explored with STOKES and review the main results obtained so far.

Keywords: Polarization, Radiative transfer, Scattering

1 Introduction

STOKES is a Monte Carlo radiative transfer code initially developed by René W. Goosmann for his master thesis that was supervised by C. M. Gaskell. Since 2010, Frédéric Marin contributes significantly to the development of the code and it further benefits from feedback and small extensions implemented by a growing number of users. Originally created to reproduce ultraviolet (UV) and optical polarization measurements in radio-quiet active galactic nuclei (AGN), the code has evolved toward more versatile versions. The latest public version of the code, STOKES 1.2, can be downloaded from the project web page http://www.stokes-program.info/.

STOKES is written in C/C^{++} and simulates the radiative transfer with polarization for multiple scattering, absorption and/or reemission processes in up to 10^4 reprocessing media. The geometry of the emitting source and of the scattering structures can be selected from a list of morphologies (toroidal, spherical, hourglass-shaped, spherical or more complex, segmented structures) and each region can be characterized by its density, temperature and a three-dimensional velocity field. For line emission, Lorentzian flux profiles with user-defined full width at half maximum and intensity are assumed. Thomson, Compton and Mie scattering algorithms, using Mueller matrices and a Stokes vectorial representation, govern the polarization state of the photon from its emission until its eventual escape from the model region. The resulting continuum and line spectra can be evaluated at different inclinations and azimuthal viewing angles since the code is fully three-dimensional. The reader is referred to the user manual of STOKES for further details of the code. Several examples of model calculations can also be found on the web page.

In this conference note, we give a concise overview of major results achieved with STOKES for different astrophysical cases over the last ten years. Note that some of the following results, especially those related to the X-ray domain, are based on more advanced versions than STOKES 1.2 that are not yet public.

2 Applications and results

2.1 Isolated structures

The first public version 1.0 of STOKES was described in Goosmann & Gaskell (2007) and applied to model the effects of different AGN reprocessing morphologies on the UV/optical polarized flux. Dusty tori, polar cones and electron disks were studied for a range of geometrical shapes, opening angles and optical depths. Goosmann & Gaskell (2007) found that the shape of the torus funnel significantly influences the scattering and polarization efficiency, with compact tori (with a steep inner surface) scattering more light along equatorial inclinations than

[1] Astronomical Institute of the Academy of Sciences, Bočni II 1401, 14131 Prague, Czech Republic
[2] Observatoire Astronomique de Strasbourg, Université de Strasbourg, CNRS, UMR 7550, 11 rue de l'Université, 67000 Strasbourg, France

extended tori of the same opening angle. Confined to produce optical* polarization degrees P lower than 20%, circumnuclear structures are less efficient polarizers than polar outflows seen at edge-on (type-2) orientations. While electron-scattering produces wavelength-independent polarization, dusty outflows, representative of the so-called narrow line regions (NLR) in AGN, show reddened spectra for polar inclinations (type-1) and bluer spectra at type-2 viewing angles.

The case of the NLR has been explored in more detail by Goosmann et al. (2007a,b). The authors modeled the polarization induced by Mie reprocessing inside a polar, hourglass-shaped structure filled with two different types of dust. The dust composition and grain size distribution was based on (1) extinction curves observed in our Galaxy (Mathis et al. 1977) and (2) a dust mixture inferred from extinction properties of AGN (Gaskell et al. 2004). When the NLR is filled with dust of the AGN type, weaker polarization spectra and a net decrease of polarization around 4000 Å occur at shorter wavelengths. This is due to a flatter grain size distribution causing a lower scattering efficiency. As a result, AGN dust scatters less flux towards type-2 viewing angles.

2.2 AGN modeling and the polarization dichotomy

2.2.1 The unified model

Once the polarimetric signatures of individual scattering regions explored, the effects of radiative coupling between the inner and outer parts of AGN were included. To do so, three to four reprocessing regions were placed around a central, point source: (1) an equatorial, radiation-supported, fully ionized disk producing most of the polarized flux with a polarization position angle parallel to the symmetry axis of the AGN, (2) an equatorial, obscuring, dusty torus preventing radiation to escape along the midplane, (3) collimated outflows, either filled with electrons (ionized winds) or dust (NLR). Goosmann (2007), Marin & Goosmann (2011), Marin et al. (2012c) and Marin & Goosmann (2012) explored the resulting polarization and stated which constrains can be derived from the observed continuum polarization.

It was found that a flat, equatorial reprocessing region with an optical depth of $1-3$ is required to generate the observed parallel polarization in type-1 AGN, suggesting optically thick accretion flows at the outer edge of type-1 AGN accretion disks. Additionally, a wide torus half-opening angle ($\sim 60°$) enhances the production of parallel polarization, whereas narrow tori and/or a higher optical depth in the polar outflows produce perpendicular polarization when seen at a type-1 viewing angle. At type-2 inclinations, all cases modeled produce strong ($\gg 20\%$) perpendicular polarization. This is not in agreement with previous spectropolarimetric observations of Seyfert-2 galaxies, which report lower ($< 10\%$) polarization percentages. A wide torus/wind half-opening angle helps to mitigate the discrepancy with respect to the observations but the resulting type-2 polarization fraction remains high. Adding the NLR to the three-component model lowers the production of parallel polarization at type-1 viewing angles and helps to decrease the amount of polarization at type-2 viewing angles. A more recent, very careful comparison between the models and the observed polarization has been done in Marin (2014, see also Sect. 2.2.3).

2.2.2 Application to a peculiar case: NGC 1068

The simplest approach of the unified model described in Antonucci (1993) assumes that the accretion disk, the dusty torus and the polar outflows are symmetric with respect to the rotational axis of the disk. In this picture, the alignment of the ejection winds with the circumnuclear, equatorial matter is due to a collimation effect, while a symmetric mass transfer between the inner parts of the torus funnel and the outer edges of the accretion disk would stabilize the two regions along the midplane. However, this picture has been questioned by the mid-infrared interferometric measurements of Raban et al. (2009), who suggest that the polar winds of NGC 1068 (represented as a bi-conical structure) are inclined by 18° with respect to the obscuring torus axis.

To investigate the impact of the non-alignment of the ionized winds on the resulting polarization signature of NGC 1068 and, by extension, on the unified model of AGN, a multi-wavelength study was carried out with STOKES. In the X-ray domain, Goosmann & Matt (2011b,a) explored a variety of AGN inclinations and different hydrogen column densities of the reprocessing material. Under specific conditions, the misalignment of the polar winds with respect to the torus axis can be determined from a rotation of the polarization position angle between the soft and the hard X-ray band. In addition to this, soft X-ray polarimetry can probe the true orientation of the ionization cones. A similar study in the UV/optical waveband by Marin et al. (2012a)

*Goosmann (2009) presents the X-ray counterpart of the optical model and illustrates the performance of an X-ray polarimeter.

successfully reproduces the observed type-1/type-2 polarization dichotomy (i.e. parallel polarization for type-1 AGN and perpendicular polarization at type-2 viewing angles) and shows that the polarization is dominated by scattering in the polar outflows and therefore traces the wind's tilting angle with respect to the torus axis.

2.2.3 Observations versus modeling

Our modeling of NGC 1068 highlights the impact of the system's orientation on the net polarization, in particular for an asymmetric geometry. For a given model, changing the orientation of the observer can lead to significantly different results, especially when the line of sight is close to the horizon of the circumnuclear torus. It is therefore important to examine a given model at all inclinations and to compare the spectropolarimetric results with the observed data. However, this approach was hampered by the lack of a data base combining inclination and polarization information until the recent AGN compendium was gathered by Marin (2014).

The compendium agrees with past empirical results, i.e. type-1 AGN show low polarization degrees ($P < 1\%$) predominantly associated with a parallel polarization position angle while type-2 objects show stronger polarization percentages ($P > 7\%$)[†] with perpendicular polarization angles. The transition between type-1 and type-2 inclination occurs between 45° and 60°, a range likely including AGN classified as borderline objects, where the observer's line of sight crosses the horizon of the equatorial dusty medium. Thanks to this new catalog, the relevance of new AGN models can be investigated more properly.

2.3 The polarization of broad emission lines and off-axis irradiation

The profile and polarization of broad emission lines can put tight constraints on the geometry of the broad line region. The relative offset in blueshift between high and low ionization emission lines could be explained by multiple scattering of the line photons in the accretion flow (Gaskell & Goosmann 2013). The technique of *polarization reverberation mapping* was introduced by Gaskell et al. (2012) as a new way to explore the inner structure of AGN. The cross-correlation between the two light curves of the spectral flux and the polarized flux was established and modeled with STOKES to constrain the distance between the continuum source and the reprocessing mirrors. For this purpose, the code was enabled to take into account timing properties (Goosmann et al. 2008).

Lately, we started to explore the consequences of a new paradigm for the accretion disk emission. Assuming that a significant fraction of the disk's optical/UV luminosity is emitted by temporary off-axis sources (for instance, hot clumps), the characteristic polarization profiles across broad emission lines can be explained in a straightforward manner and do not require any contribution from the equatorial scattering disk nor from rotating winds (Goosmann et al. 2013). Observed polarization variability on time-scales of the BLR light crossing time would strongly support this new interpretation.

2.4 Constraining the morphology of disk-born outflows

Despite a wide panel of observational emission and absorption line features to investigate, the morphology of the inner AGN regions remains debated. Theories interpreting the reprocessing regions of AGN as dynamical structures propose an alternative solution to mostly static media simulated so far (Elvis 2000). In this picture, radiation-driven outflows, potentially responsible for a large fraction of AGN feedback, are launched from the accretion disk over a small range of radii and then bent outward and driven into a radial direction by radiation pressure. Along the equatorial plane, shielded from the full continuum by the highly ionized matter, dust may survive long enough to create a failed dusty wind.

This scenario is alternative to the torus-based unified model and was tested for its polarization properties by Marin & Goosmann (2013b,c,a). A model solely composed of ionized winds is unable to reproduce the expected polarization dichotomy and underestimates the observed optical polarization percentage of both type-1 and type-2 AGN. A dust-filled outflow produces very low, wavelength-dependent polarization degrees, associated with a photon polarization angle perpendicular to the projected symmetry axis of the model; the polarization percentages are ten times lower than what can be produced by a toroidal model, with a maximum polarization degree found at intermediate viewing angles (i.e. when the observers line-of-sight crosses the wind). To

[†]Note that most, if not all, type-2 AGN polarization measurements from the literature are dominated by relatively large, unpolarized starlight fluxes that are insufficiently corrected for (see discussion in Sect. 2.3 of Marin (2014). The revisited polarization of type-2 AGN included in the compendium often have lower limits.

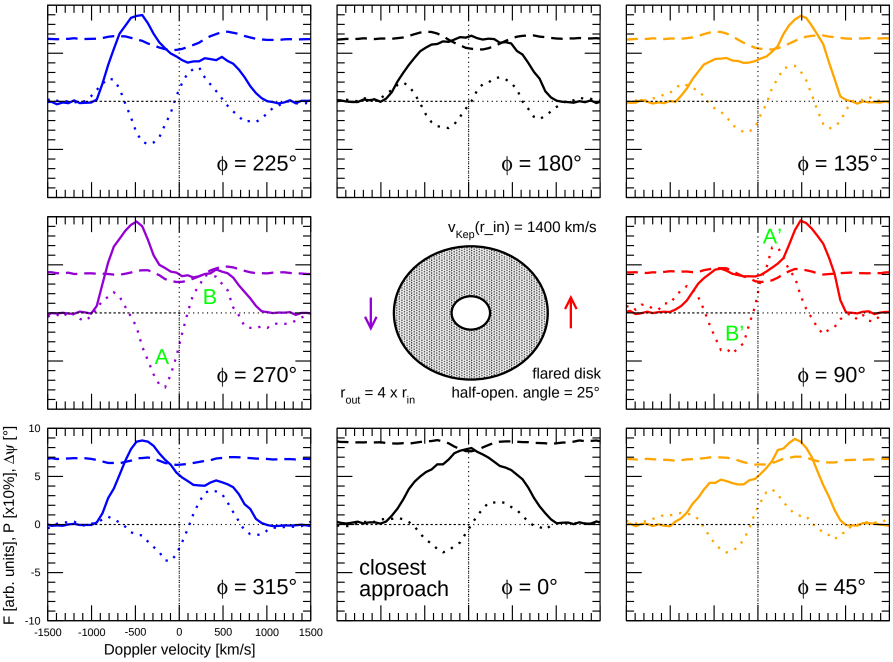

Fig. 1. Modeling the spectropolarimetric appearance of a broad emission line as a function of the azimuthal phase ϕ with an off-axis continuum source. The eight panels show the profile of the line flux, F (solid line), the polarization percentage (dashes), and the variation of the polarization position angle (dots) in Doppler velocity space. Figure taken from Goosmann et al. (2013).

agree with the observations, a two-phase outflow is necessary. It can generate both the observed polarization dichotomy and acceptable levels of polarization degree if the wind has a bending angle of 45° (thus lower than what was predicted by the initial, phenomenological model). The conical shells need to have a half-opening angle comprised between 3° − 10° and the absorbing dust column at the wind base should correspond to an optical depth (integrated over 2000 − 8000 Å) of 1 − 4.

2.5 Probing the physical origin of the asymmetric 6.4 keV iron line

More recent versions of STOKES include radiative processes in the X-ray range. We extended our polarization studies to the 1 – 100 keV band and showed that there is important work to be done for X-ray polarimetry. This new window would be an independent and complementary tool to spectral and timing analyses. We focused on a strongly debated topic of X-ray astrophysics, i.e. the relativistic reflection versus complex absorption scenarios that are proposed to explain the iron line broadening in a number of Seyfert 1 AGN. We managed to derive strong observational predictions for a future spectropolarimetric X-ray mission (Soffitta et al. 2013).

In Marin et al. (2012b), we modeled the polarization signature of MCG-6-30-15 resulting from a partial covering scenario where a clumpy gas distribution is thought to obscure the equatorial plane. We compared the results to a reflection model based on the lamppost geometry and found that the shape of the polarization degree and position angle as a function of photon energy are distinctly different between the reflection and the absorption cases: disk scattering and general relativistic effects produce significantly stronger polarization in the soft energy band than absorption. The spectrum of the polarization angle adds additional constraints: its has a constant value in the absorption case while smooth rotations of the polarization angle with photon energy are detected in the relativistic reflection scenario. We modeled the polarization signature of NGC 1365, a "changing look" AGN where variations of cold absorbers on the line of sight cause extreme and short emission variability. We showed in Marin et al. (2013) that a large, soft X-ray observatory or a medium-sized mission equipped with a hard (6 − 35 keV) polarimeter could break the degeneracy between the two scenarios. We summarized and extended our results in Marin & Tamborra (2013).

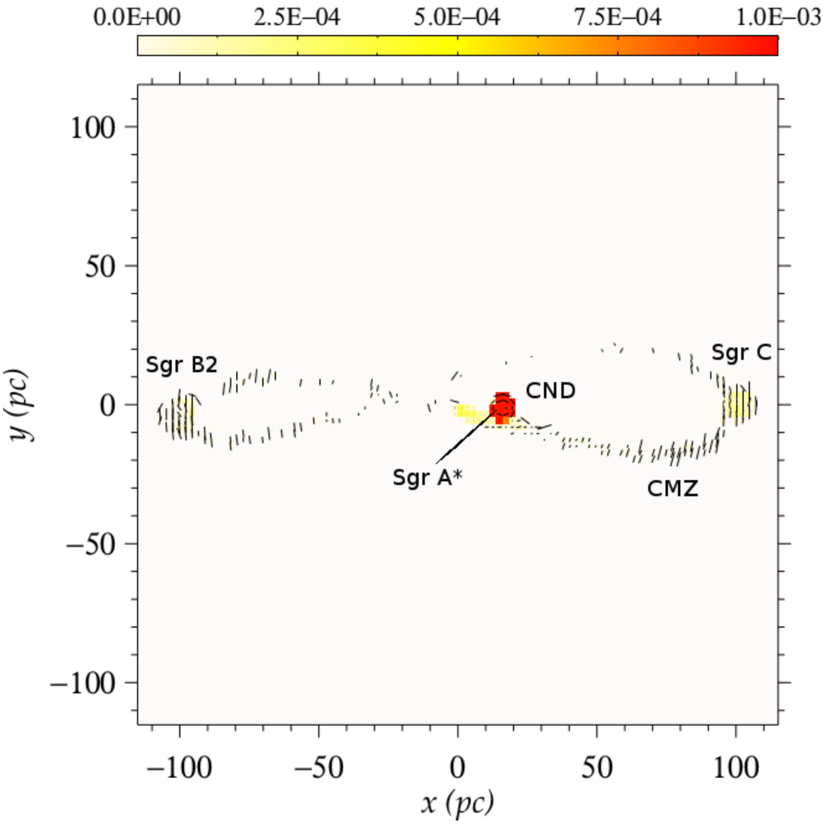

Fig. 2. Integrated 8 – 35 keV model image of the polarized flux, PF/F_*, for the 2° × 2° region around the Galactic Center. PF/F_* is color-coded, with the color scale shown on top of the image (in arbitrary units). The polarization degree and position angle are represented by black bars drawn in the center of each spatial bin. A vertical bar indicates a polarization angle of $\psi = 90°$ and a horizontal bar stands for an angle of $\psi = 0°$. The length of the bar is proportional to P. Figure taken from Marin et al. (2014a)

2.6 X-ray mapping of the Galactic Center

While dedicated to the modeling of AGN, STOKES can be adapted to a variety of other sources, such as the Galactic Center, hosting the closest-to-Earth supermassive black hole. Around the potential well of Sgr A* is a concentration of active star formation sites and gigantic, reprocessing molecular clouds that make the center of the Milky Way an excellent site for X-ray polarization studies. The reprocessing scenario is strongly supported by past X-ray observations of the Eastern massive molecular cloud Sgr B2 that revealed a very steep spectrum with a strong emission line at 6.4 keV related to iron fluorescence. This suggests that part of the diffuse emission of Sgr B2 is due to reprocessing.

The line-of-sight towards Sgr A* being opaque to UV/optical emission, STOKES was applied in the X-ray range to test if a significant X-ray polarization signal could be detected from the Galactic Center. Marin et al. (2014a,b) found that a model where Sgr A* is radiatively coupled to a fragmented circumnuclear disc (CND), an elliptical twisted ring representative of the central molecular zone (CMZ), and the two main, bright molecular clouds Sgr B2 and Sgr C, produces a variety of polarization signatures. Polarization mapping integrated over 8 – 35 keV reveals that Sgr B2 and Sgr C, situated at the two horizontal extensions of the CMZ, present the highest polarization degrees, both associated with a polarization position angle normal to the scattering plane. The CND shows a lower, barely detectable polarization degree and the CMZ polarization is spatially variable. Independently of their spatial location, the two reflection nebulae are found to always produce high polarization degrees ($\gg$ 10%). Finally, it has been shown that a 500 ks observation with a broadband imaging polarimeter on-board of a mid-sized mission could constrain the location and the morphology of the scattering material with respect to the emitting source.

3 Concluding remarks

STOKES is a versatile Monte Carlo code for modeling polarization produced by absorption, reemission and scattering in many astrophysical situations. Its capability to produce UV/optical polarization signatures allows direct comparison with contemporary measurements, but is also a prime tool to evaluate the putative X-ray polarization from different environments. Follow-up investigations in the infrared band are currently under examination. If you have questions about STOKES, contact us by email at admin@stokes-program.info.

The authors thank C. M. Gaskell and F. Tamborra for their involvement in the STOKES code; the former for being behind the firsts lines of the code, the latter for his implication and help in the infrared and X-ray domain. We further acknowledge our colleagues, who keep using STOKES and thank them for their feedback and exciting applications.

References

Antonucci, R. 1993, ARA&A, 31, 473

Elvis, M. 2000, ApJ, 545, 63

Gaskell, C. M. & Goosmann, R. W. 2013, ApJ, 769, 30

Gaskell, C. M., Goosmann, R. W., Antonucci, R. R. J., & Whysong, D. H. 2004, ApJ, 616, 147

Gaskell, C. M., Goosmann, R. W., Merkulova, N. I., Shakhovskoy, N. M., & Shoji, M. 2012, ApJ, 749, 148

Goosmann, R. W. 2007, in Proceedings of RAGtime 8/9: Workshops on Black Holes and Neutron Stars, ed. S. Hledík & Z. Stuchlík, 61–69

Goosmann, R. W. 2009, in SF2A-2009: Proceedings of the Annual meeting of the French Society of Astronomy and Astrophysics, ed. M. Heydari-Malayeri, C. Reyl'E, & R. Samadi, 151

Goosmann, R. W. & Gaskell, C. M. 2007, A&A, 465, 129

Goosmann, R. W., Gaskell, C. M., & Marin, F. 2013, ArXiv e-prints

Goosmann, R. W., Gaskell, C. M., & Shoji, M. 2007a, in IAU Symposium, Vol. 238, IAU Symposium, ed. V. Karas & G. Matt, 375–376

Goosmann, R. W., Gaskell, C. M., & Shoji, M. 2007b, in Astronomical Society of the Pacific Conference Series, Vol. 373, The Central Engine of Active Galactic Nuclei, ed. L. C. Ho & J.-W. Wang, 485

Goosmann, R. W., Gaskell, C. M., & Shoji, M. 2008, in SF2A-2008, ed. C. Charbonnel, F. Combes, & R. Samadi, 231

Goosmann, R. W. & Matt, G. 2011a, in SF2A-2011: Proceedings of the Annual meeting of the French Society of Astronomy and Astrophysics, ed. G. Alecian, K. Belkacem, R. Samadi, & D. Valls-Gabaud, 583–586

Goosmann, R. W. & Matt, G. 2011b, MNRAS, 415, 3119

Marin, F. 2014, MNRAS, 441, 551

Marin, F., Goosmann, R., & Dovčiak, M. 2012a, Journal of Physics Conference Series, 372, 012065

Marin, F. & Goosmann, R. W. 2011, in SF2A-2011: Proceedings of the Annual meeting of the French Society of Astronomy and Astrophysics, ed. G. Alecian, K. Belkacem, R. Samadi, & D. Valls-Gabaud, 597–600

Marin, F. & Goosmann, R. W. 2012, in SF2A-2012: Proceedings of the Annual meeting of the French Society of Astronomy and Astrophysics, ed. S. Boissier, P. de Laverny, N. Nardetto, R. Samadi, D. Valls-Gabaud, & H. Wozniak, 587–590

Marin, F. & Goosmann, R. W. 2013a, MNRAS, 436, 2522

Marin, F. & Goosmann, R. W. 2013b, in SF2A-2013: Proceedings of the Annual meeting of the French Society of Astronomy and Astrophysics, ed. L. Cambresy, F. Martins, E. Nuss, & A. Palacios, 475–478

Marin, F. & Goosmann, R. W. 2013c, in SF2A-2013: Proceedings of the Annual meeting of the French Society of Astronomy and Astrophysics, ed. L. Cambresy, F. Martins, E. Nuss, & A. Palacios, 479–482

Marin, F., Goosmann, R. W., Dovčiak, M., et al. 2012b, MNRAS, 426, L101

Marin, F., Goosmann, R. W., Gaskell, C. M., Porquet, D., & Dovčiak, M. 2012c, A&A, 548, A121

Marin, F., Karas, V., Kunneriath, D., & Muleri, F. 2014a, MNRAS, 441, 3170

Marin, F., Karas, V., Kunneriath, D., Muleri, F., & Soffitta, P. 2014b, ArXiv e-prints

Marin, F., Porquet, D., Goosmann, R. W., et al. 2013, MNRAS, 436, 1615

Marin, F. & Tamborra, F. 2013, ArXiv e-prints

Mathis, J. S., Rumpl, W., & Nordsieck, K. H. 1977, ApJ, 217, 425

Raban, D., Jaffe, W., Röttgering, H., Meisenheimer, K., & Tristram, K. R. W. 2009, MNRAS, 394, 1325

Soffitta, P., Barcons, X., Bellazzini, R., et al. 2013, Experimental Astronomy, 36, 523

PROBING THE GALACTIC CENTER WITH X-RAY POLARIMETRY

F. Marin[1], V. Karas[1], D. Kunneriath[1], F. Muleri[2] and P. Soffitta[2]

Abstract. The Galactic center (GC) holds the closest-to-Earth supermassive black hole (SMBH), which makes it the best laboratory to study the close environment of extremely massive compact objects. Polarimetry is sensitive to geometry of the source, which makes it a particularly suitable technique to probe the medium surrounding the GC SMBH. The detection of hard X-ray spectra and prominent iron Kα fluorescence features coincident with localized gas clouds (e.g. Sgr B2, Sgr C) is known for nearly twenty years now and is commonly associated with a past outburst of the SMBH whose radiation is reprocessing onto the so-called "reflection nebulae". Since scattering leads to polarization, the re-emitted signal from the giant molecular clouds in the first 100 pc of the GC is expected to be polarized. X-ray polarization measurement is thus particularly adapted to probe the origin of the diffuse X-ray emission from the GC reflection nebulae and reveal the past activity of the central SMBH. In this research note, we summarize the results from past and current polarimetric simulations in order to show how a future X-ray polarimeter equipped with imaging detectors could improve our understanding of high-energy astrophysics.

Keywords: Galaxy: center, Galaxy: nucleus, Polarization, Radiative transfer, Scattering

1 Introduction

Using the ART-P telescope on-board of *Granat*, Sunyaev et al. (1993) were the first to image the Galactic center (GC) from the soft (2.5 keV) to the hard (22 keV) X-ray band. The discovery of a source characterized by a spherical morphology in the soft band, and by an extended (i.e. elongated along the Galactic plane) shape in the hard X-ray range, lead Sunyaev et al. (1993) to suggest that part of the hard X-ray emission could be due to Compton-scattered photons originating from a nearby compact source and reprocessed by dense molecular clouds. Later, X-ray images and spectra of the GC obtained by Koyama et al. (1996), using the Advanced Satellite for Cosmology and Astrophysics (*ASCA*), revealed fluorescent Kα emission lines from cold iron atoms in Sgr B2. Associated with a hard X-ray spectral slope, Koyama et al. (1996) estimated that the diffuse thermal emission could be due to a past intense irradiation from Sgr A*, the central supermassive black hole (SMBH) that lies in the GC. Such an argument is in agreement with the predictions of Sunyaev et al. (1993) and further detections from other extended gas cloudlets tend to corroborate this idea. In particular, Murakami et al. (2001) presented the first *ASCA* evidence of diffuse hard X-ray emission associated with strong 6.4 keV fluorescence line and large absorption from the Sgr C complex. Hard X-ray continuum and Fe Kα emission have also been found in several other GC molecular clouds: Sgr B1 (Koyama et al. 2007), M0.74-0.09 (Koyama et al. 2007), G0.11-0.11 (Ponti et al. 2010), M0.74-0.09 (Nobukawa et al. 2011), M1 and M2 (Ponti et al. 2010), the Arches cluster (Yusef-Zadeh et al. 2002) and the molecular complex called the Bridge (Bamba et al. 2002).

To uncover the nature of the hot diffuse X-ray emission and test the hypothesis of the flaring theory, Churazov et al. (2002) postulated that an X-ray mission equipped with a state-of-the-art polarimeter would be necessary. Indeed, if past radiation from Sgr A* is reprocessed by extended, distant reflection nebulae, the resulting X-ray emission should be polarized. In order to lay the groundwork for a future polarimetric explorer, several studies have been done (Churazov et al. 2002; Matt 2010; Marin et al. 2014), estimating the polarization degree and the orientation of the polarization position angle that a potential mission could detect. Hence, in this research note, we summarize the work accomplished so far to evaluate the net X-ray polarization emerging from the largest and brightest (i.e. easier to detect) GC molecular clouds.

[1] Astronomical Institute of the Academy of Sciences, Boční II 1401, CZ-14100 Prague, Czech Republic
[2] INAF/IAPS, Via del Fosso del Cavaliere 100, I-00133 Roma, Italy

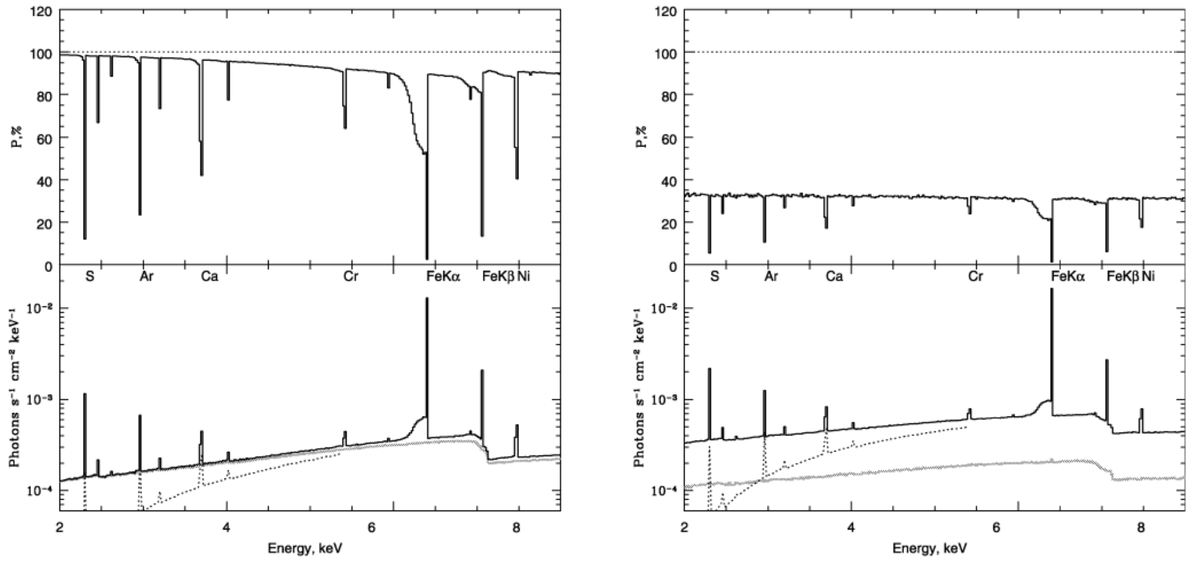

Fig. 1. Reflected energy spectrum and polarization degree of a spherical gas cloud illuminated by a distant continuum source. *Top*: Polarization degree P, *bottom*: intensity spectra. The left column is representative of a gas clump situated at the same distance from the observer as the source, while the right column presents results for a cloud situated 100 pc away. Spectra are taken from Churazov et al. (2002).

2 Evaluating the polarization emerging from the GC

So far, there have been two main publications exploring the resulting X-ray polarization emerging from the GC. The first one, from Churazov et al. (2002), focused on the reprocessing molecular cloud Sgr B2 and estimated the net soft X-ray polarization signature of this cloud. The second paper, by Marin et al. (2014), modeled the $2^\circ \times 2^\circ$ ($\sim 288 \times 288$ pc; at 8.5 kpc $1'' \approx 0.04$ pc) central region of the Milky Way at energies higher than 8 keV and included polarization maps. We now review the main results from the two complementary publications.

2.1 Sgr B2 in the soft X-ray band

Churazov et al. (2002) investigated the polarization emerging from a single cloud of radius 10 pc representative of the reflection nebulae Sgr B2. In their simulation, the spherical gaseous medium was filled with neutral, solar abundance matter and had a Thomson optical depth of 0.5. It was irradiated by a steady beam of unpolarized photons with energy ranging from 2 to 8 keV. Photoelectric absorption, fluorescent emission and Compton scattering by bound electrons were included and the molecular cloud was located at 100 pc from the continuum source, which is representative of the known projected distance from Sgr A* (Murakami et al. 2001). However, since the three-dimensional parametrization of the GC is unknown, the reflecting nebula can be shifted from the Galactic plane but still conserve the same radial projections. To investigate this effect, Churazov et al. (2002) located their cloud model at two different positions: at the same distance and 100 pc away from the observer than the emitting region.

Their work is summarized in Fig. 1 and the general result is that the reflected radiation should be highly polarized ($> 30\%$) with a direction of polarization normal to the scattering plane. The amount of P is a function of the three-dimensional position of the cloud, decreasing when Sgr B2 departs from the Galactic plane. Local dilution of the polarization degree by fluorescent photons (being unpolarized) is symptomatic of the composition of the cloud, and the slow but steady decrease of P with energy is due to multiple scatterings.

Thus, using a simple model, Churazov et al. (2002) proved that any detection of polarized X-ray emission from the reflection nebulae around Sgr A* would give constraints on the morphology, composition and position of the scattering clouds.

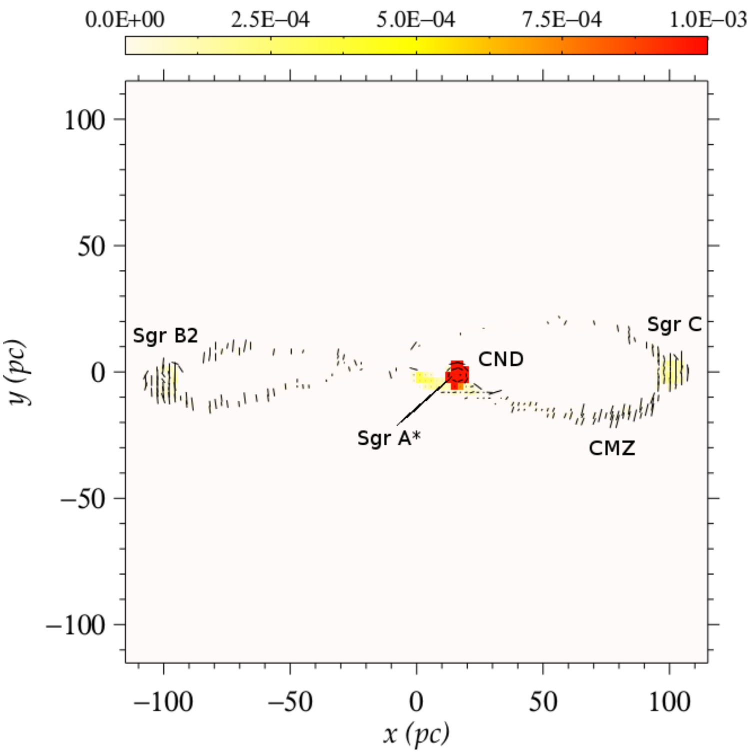

Fig. 2. Integrated 8 – 35 keV model image of the polarized flux, PF/F_*, for the 2° × 2° region around the GC. PF/F_* is color-coded, with the color scale shown on top of the image (in arbitrary units). P and ψ are represented by black bars drawn in the center of each spatial bin. A vertical bar indicates a polarization angle of $\psi = 90°$ and a horizontal bar stands for an angle of $\psi = 0°$. The length of the bar is proportional to P. The polarization map is taken from Marin et al. (2014).

2.2 Broadband GC polarization imaging

The results obtained by Churazov et al. (2002) are valid in the 2 – 8 keV band for small hydrogen column densities ($n_H < 10^{22}$ cm^{-2}). At larger n_H, the emission below 5 keV is expected to be highly suppressed. In addition to that, past X-ray observations (Koyama et al. 1986, 1989) revealed the presence of a diffuse plasma emission toward the GC that may additionally dilute the polarization signal below 7 keV. Hence, to avoid most of the dilution by the GC plasma emission and extend the soft X-ray simulations achieved by Churazov et al. (2002), 8 – 35 keV modeling has been undertaken by Marin et al. (2014).

In our recent work, Marin et al. (2014) took into account the dense and warm environment around the central few parsecs around Sgr A* (known as the circumnuclear disc, CND); a cold dusty structure in the shape of a continuous chain of irregular clumps representative of the central molecular zone (CMZ, Molinari et al. 2011); the two bright, complex reflection nebulae Sgr B2 and Sgr C (located at the two extrema of the CMZ); and a continuum source displaced by $\sim$ 22 pc in projection from the center of the model toward the Western galactic longitude (to be consistent with the shifted gas distribution within the CMZ (Molinari et al. 2011).

The polarization map presented in Fig. 2 is extracted from Marin et al. (2014). It is found that the polarized flux, PF/F_*, traces the overall shape of the GC, emphasizing the ∞-shaped CMZ. PF/F_* reaches a maximum at the location of the non-axisymmetric CND surrounding Sgr A*, but the local, integrated P is low ($\sim$ 1.0%). Sgr B2 and Sgr C show the secondary, brightest polarized flux knots of the map, associated with P = 66.5% for Sgr B2 and P = 47.8% for Sgr C. The difference in P is due to the asymmetrical spatial location of the cloud with respect to Sgr A*. Both the clouds present a polarization position angle ψ perpendicular to the vertical axis of the model (normal to the scattering plane). P is found to vary for each CMZ cloud and reaches a maximum for the Eastern and Western sections of the elliptical twisted ring but it is most likely that a large fraction of the ∞-shaped ring will be diluted by background, unpolarized emission from both plasma emission and Sgr A*. Finally, when integrating the whole 2° × 2° GC polarized emission, the model produces a net polarization degree of 0.9% associated with ψ = -22.8°. The combined emission from Sgr A* and the CND thus dominates the whole polarization picture.

Marin et al. (2014) extended the modeling of Churazov et al. (2002) by radiatively coupling the primary source to a large panel of reprocessing targets. They also extend their cloud parametrization to explore the influence of the location of the scattering nebulae on polarization (not shown in this research note), finding that the two reflection nebulae always produce high polarization degrees ($\gg 10\%$).

3 The need for a dedicated X-ray polarimetry mission

It has been shown by Churazov et al. (2002) and Marin et al. (2014) that the GC is expected to provide a variety of polarization signals where maximum P is expected to arise from reflection nebulae. Marin et al. (2014) also computed the minimum detectable polarization (MDP) that the *NHXM* (New Hard X-ray Mission, Tagliaferri & NHXM Consortium 2012; Tagliaferri et al. 2012) could have reached and found that such polarization levels are detectable using a 500 ks observation. Errors on ψ being marginal, the detection of ψ normal to the scattering plane would be unambiguous.

Was the GC active a few hundreds years ago? X-ray polarimetry can definitively prove or reject this hypothesis since the main molecular clouds should be highly polarized ($\gg 10\%$) with the electric vector perpendicular to the line connecting Sgr A* to the reprocessing nebula. To spatially constrain the three-dimensional location of each GC component with respect to the central SMBH, it will be necessary to observe at least two molecular clouds. An X-ray mission equipped with a polarization imaging detector, such as the Gas Pixel Detector (GPD) based on the photoelectric effect (Costa et al. 2001), is ideally suited since polarization mapping would reveal the complex morphology of the GC, spatially resolving the largest reflection nebulae, differentiating them from neighborhood sources and potentially enabling the investigation of stratified light echoes from the past activity of Sgr A*.

A dedicated space mission for imaging X-ray polarimetry such as the non-selected projects *NHXM* or *IXPE* (the Imaging X-ray Polarimeter Explorer, Weisskopf et al. 2008) would have been sufficiently sensitive to measure the polarization emerging from the $2^\circ \times 2^\circ$ GC, even below 8 keV where plasma emission is acting like an unpolarized background and can be further substracted from past spectral data. Finally, X-ray polarization measurement would ultimately test the alternative scenario for the origin of X-ray emission from Sgr B2 and Sgr C in which X-ray features are produced by low-energy cosmic-ray electrons rather than by Compton scattering.

The authors would like to acknowledge the financial support from the COST Action MP1104 and COST-CZ LD12010 .

References

Bamba, A., Murakami, H., Senda, A., et al. 2002, ArXiv Astrophysics e-prints

Churazov, E., Sunyaev, R., & Sazonov, S. 2002, MNRAS, 330, 817

Costa, E., Soffitta, P., Bellazzini, R., et al. 2001, Nature, 411, 662

Koyama, K., Awaki, H., Kunieda, H., Takano, S., & Tawara, Y. 1989, Nature, 339, 603

Koyama, K., Inui, T., Hyodo, Y., et al. 2007, PASJ, 59, 221

Koyama, K., Maeda, Y., Sonobe, T., et al. 1996, PASJ, 48, 249

Koyama, K., Makishima, K., Tanaka, Y., & Tsunemi, H. 1986, PASJ, 38, 121

Marin, F., Karas, V., Kunneriath, D., & Muleri, F. 2014, MNRAS, 441, 3170

Matt, G. 2010, X-ray polarimetry and radio-quiet AGN, ed. R. Bellazzini, E. Costa, G. Matt, & G. Tagliaferri, 122

Molinari, S., Bally, J., Noriega-Crespo, A., et al. 2011, ApJ, 735, L33

Murakami, H., Koyama, K., Tsujimoto, M., Maeda, Y., & Sakano, M. 2001, ApJ, 550, 297

Nobukawa, M., Ryu, S. G., Tsuru, T. G., & Koyama, K. 2011, ApJ, 739, L52

Ponti, G., Terrier, R., Goldwurm, A., Belanger, G., & Trap, G. 2010, ApJ, 714, 732

Sunyaev, R. A., Markevitch, M., & Pavlinsky, M. 1993, ApJ, 407, 606

Tagliaferri, G., Hornstrup, A., Huovelin, J., et al. 2012, Experimental Astronomy, 34, 463

Tagliaferri, G. & NHXM Consortium. 2012, Mem. Soc. Astron. Italiana, 83, 360

Weisskopf, M. C., Bellazzini, R., Costa, E., et al. 2008, in Society of Photo-Optical Instrumentation Engineers (SPIE) Conference Series, Vol. 7011

Yusef-Zadeh, F., Law, C., Wardle, M., et al. 2002, ApJ, 570, 665

SF2A 2014
J. Ballet, F. Bournaud, F. Martins, R. Monier and C. Reylé (eds)

THE MASS COMPOSITION OF ULTRA-HIGH ENERGY COSMIC RAYS WITH THE PIERRE AUGER OBSERVATORY

D. Martraire[1] and the Pierre Auger Collaboration[2]

Abstract. Ultra-high energy cosmic rays are the most energetic particles known in nature. The Pierre Auger Observatory was built to study these amazing particles to determine their origin. The study of their mass composition can help to constrain the models concerning their origins and their production mechanisms in the astrophysical sources. To this aim, several methods have been developed to infer the composition using the Auger surface detector array data. The main difficulty is to isolate the muonic component in the signal measured by the surface detector. We present the results of the composition parameters derived from the ground level component and compare them to the predictions for different nuclear masses of the primary particles and hadronic interaction models.

Keywords: Pierre Auger Observatory, ultra-high energy cosmic rays, composition, muons, hadronic interaction models

1 Introduction

The composition of the UHECRs (Ultra High Energy Cosmic Rays) is one of the challenging questions. Improving our knowledge about the composition of cosmic rays allows us to constrain the models concerning their origins and their production mechanisms in the astrophysical sources.

When a cosmic-ray particle reaches Earth, it collides with a nucleus high in the atmosphere, producing many secondary particles, which share the energy of the original primary particle. The secondary particles subsequently collide with other nuclei in the atmosphere, creating a new generation of energetic particles that continue the process. The resulting particle cascade, called an extensive air shower, arrives at ground level with billions of hadrons and electromagnetic (EM) particles extending over tens of km^2.

The Pierre Auger Observatory, located on the Pampa Amarilla at 1400 m a.s.l., is the largest cosmic-ray observatory ever built. Its hybrid design allows us to collect the shower particles with a surface detector array (SD) and to observe the longitudinal development of EM profiles by collecting the UV light with the fluorescence detector (FD). The SD consists of 1660 water Cherenkov detectors in a 1.5 km triangular grid over 3000 km^2, whereas the FD is composed of 24 telescopes distributed over four sites overlooking the array. More details on the observatory can be found in Abraham et al. (2004); Allekotte et al. (2008); Abraham et al. (2010).

One way to determine the mass is to study the longitudinal development of the electromagnetic component of a shower. The depth of the shower maximum, $X_{\max}$, is sensitive to the primary particle (Baltrusaitis et al. 1998). However $X_{\max}$ measurements suffer from low statistics due to the duty cycle of only 13% of the fluorescence detector and the cuts imposed to avoid a biased datasets (de Souza 2013).

The Pierre Auger Collaboration has proposed different methods to assess the muon content of the extensive air shower taking advantage of the large statistical sample provided by the almost 100% duty cycle of the surface detector array. Estimating the muon content in atmospheric showers was recognized a long time ago as an essential tool for primary identification, and the Auger surface detector array was designed to have an enhanced sensitivity to muons compared to photons and electrons. However the signals due to the muonic and electromagnetic components overlap, and it is not straightforward to measure them separately.

[1] Institut de Physique Nucléaire d'Orsay, CNRS/IN2P3, Orsay, France
[2] Pierre Auger Observatory, Av. San Martín Norte 304, 5613 Malargüe, Argentina
(Full author list: `http://www.auger.org/archive/authors_2014_06.html`)

When a charged particle of sufficient energy passes through the water in a SD station, it produces Cherenkov photons. After a few reflections on the liner enclosing the water, their distribution is isotropized. Their distribution is sampled by the FADCs from three photomultiplier tubes at the top of the detector. The observed signal is proportional to the geometric path of the particle in water, and therefore there is not a difference between signals produced by muons compared to those produced by electrons or positrons. The main difference between incident EM particles and muons is their energy spectrum. Usually, the muons have enough energy to go through the detector and give a signal of the order of 1 Vertical Equivalent Muon (VEM) or more if they are inclined. On the contrary, most of electromagnetic particles have an energy below a few tens of MeV, and generally they deposit their whole energy within the water, giving a signal well below 1 VEM. However, the muons are much less abundant, so that their contribution is overlapped by the tail of the EM component.

The techniques developed by the Auger Collaboration are based on the time profile and spectral characteristics of the Cherenkov light signal generated by shower particles in the water of the detectors. The main difficulty is to identify the muonic component overlaped by the EM one. We present two types of methods: the analysis of the muon fraction with the temporal structure of the SD signals in vertical showers and the analysis of the muon content in inclined showers.

2 Muon fraction from the temporal structure of the SD signals

The number of muons can be used as an observable to study the composition of the primary particle. Two different methods are used to assess the fraction of the signal attributed to muons with respect to the total signal, $f_\mu = S_\mu/S$: a multivariate method and a smoothing method.

The basic idea of the multivariate method relies on using the characteristics of the muon signal in the FADC signal to reconstruct the muon fraction f_μ :

$$f_\mu = a + b\theta + cf_{0.5}^2 + d\theta P_0 + er$$

where θ is the reconstructed zenith angle of the shower and r is the distance of the detector from the reconstructed shower axis. $f_{0.5}$ is the proportion of the signal in FADC bins larger than 0.5 VEM, and P_0 is the normalized zero-frequency component of the power spectrum (Kégl 2013).

Both $f_{0.5}$ and P_0 are sensitive to large relative fluctuations and short signal, which are the signatures of high muon content. The parameters of the fit (a, b, c, d, e) are estimated using simulations described in Kégl (2013).

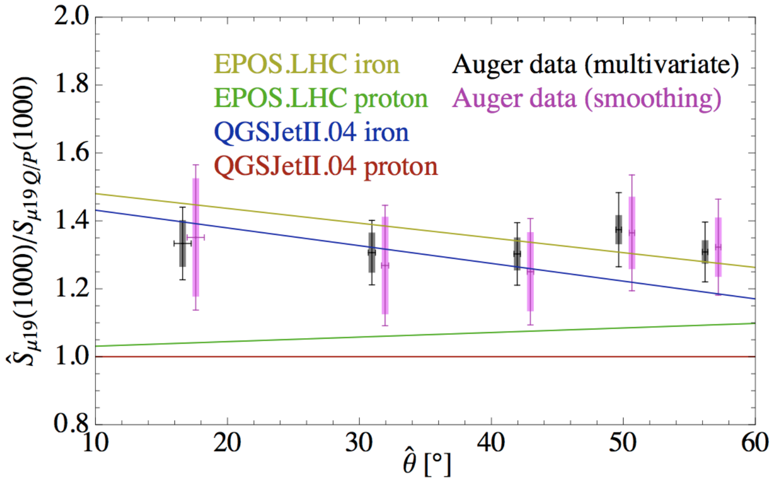

Fig. 1. The measured muon signal rescaling to $E = 10^{19}$ eV and at 1000 m from the shower axis vs. zenith angle, with respect to QSGJetII-04 proton simulations as a baseline. The rectangles represent the systematic uncertainties, and the error bars represent the statistical uncertainties added to the systematic uncertainties. See Kégl (2013) for details.

The smoothing method consists in running a low-pass filter a few times on the signal to gradually separate the low-frequency EM component from the high-frequency one which is assigned to muons. For the first run, the signal is smoothed by a moving average of size L over the FADC. The window size L is tuned using simulations to follow the low frequencies corresponding to the EM signal. At large angles (above 50°) a wider window is needed whereas to extract the EM component in vertical showers a narrower window is more suitable, since the EM component is more similar to the muonic signal. So, the window size L increases with the zenith angle as $L = 7.83 + 0.09\,\theta/\mathrm{deg}$. The procedure is repeated four times, re-smoothing each time the smoothed signal obtained at the previous iteration. The final muon signal is the sum of the non-smoothed positive differences.

The muon fraction is estimated only for the detectors at 1000 m from the shower core and for an energy $E = 10^{19}$ eV. The muon signal can be retrieved by multiplying the muon fraction by the total signal. The results with respect to QSGJetII.04 with proton primaries as baseline are shown in figure 1. The results of the two methods are in very good agreement with a value between 1.3 and 1.4 as a function of the zenithal angle. While the measured angular dependence of the muonic signal is found to be similar to the prediction obtained for proton showers and QSGJetII.04, the magnitude of the muonic signal is comparable to the predictions for iron showers.

It is interesting to note that depending on the hadronic interaction models, especially at larger angle (above 50°), the composition favours particles heavier than iron. This observation shows the limit of these methods. Moreover, the distribution of the depth of shower maximum at 10^{19} eV observed by the fluorescence detector is not compatible with a composition dominated by iron or heavier elements. So, we conclude that the muonic signal is not well reproduced by the shower simulations. More details on this analysis can be found in Kégl (2013).

3 Muon Production Depth (MPD)

The arrival times of the muons reaching the water-Cherenkov detectors can be used to obtain the distribution of the muon production distances along the shower axis. As a first approximation, we assume that the muons travel in straight lines at the speed of the light, c, with trajectories not parallel to the shower axis. The muon time of flight relative to the arrival time of the shower-front plane for each position at ground (r,ζ) is given by: $ct_g = \sqrt{r^2 + (z - \Delta)^2} - (z - \Delta)$, where Δ is the distance from the point at ground to the shower plane.

The muon production point along the shower axis z, taking into account the muon delay as the kinematic time t_ϵ (due to the finite energy of the muons), is approximated as

$$z \simeq \frac{1}{2}\,\frac{r^2}{ct - < ct_\epsilon >} + \Delta$$

From the muon production distance, the MPD X^μ is reconstructed as an integration of the atmospheric density, ρ, over the range of production distance:

$$X^\mu = \int_z^\infty \rho(z')dz'$$

The shape of the MPD distribution is fitted by a Gaisser-Hillas function and the maximum of the muon profile, X^μ_{max}, varies as a function of the mass of the primary particle. So, this parameter is an efficient observable for composition studies.

Like the previous methods, we are only concerned about the muonic component to build the MPD. The EM component is a contamination that must be eliminated. The approach chosen is to use only the inclined events with a zenithal angle range from 55° to 65°. In order to have a good time resolution of the single muons only stations at a distance of $r > 1700$ m are selected. For these data, most of the EM particles are absorbed by the atmosphere. The behaviour of the $\langle X^\mu_{\mathrm{max}}\rangle$ as a function of $\log_{10}(E)$ is shown in figure 2. The uncertainties represent the standard error on the mean and the parentheses represent the systematic uncertainty which is 17 g cm^{-2}.

The data are compared to air shower simulations using different hadronic interaction models for proton and iron primaries. Both models have the same muonic elongation rate but with considerable differences in the absolute value of $\langle X^\mu_{\mathrm{max}}\rangle$ which can completely change the interpretation of the composition. Indeed, the QSGJetII.04 model suggests a change in composition, from proton to iron, as the energy increases, whereas the EPOS-LHC model shows a composition heavier than iron. This provides evidence of the limitations of the current hadronic interaction models in inferences about the mass composition of UHECRs. However, the MPD suffers of low statistics due to the different cuts applied for the selection of the data to eliminate the EM component. So, with the actual method we cannot really conclude about mass composition. Several studies are trying to extend the MPD to lower zenithal angles.

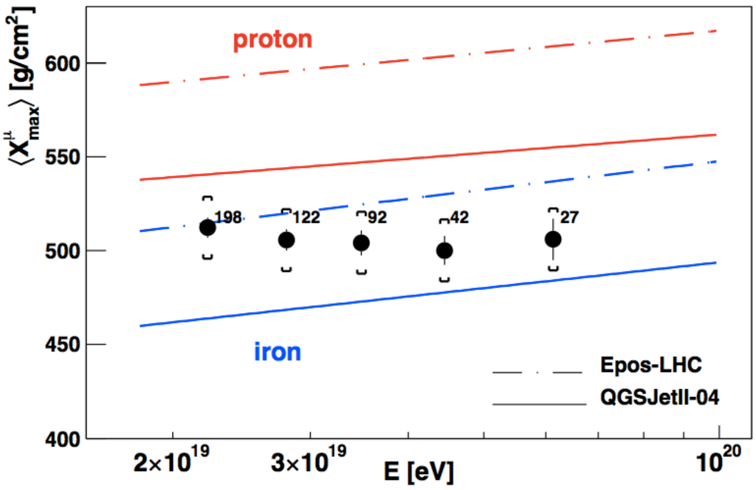

Fig. 2. $\langle X^{\mu}_{\rm max} \rangle$ as a function of energy. The straight lines represent the predictions of two hadronic interaction models for proton and iron primaries. The number of events in each energy bin is indicated and the parentheses represent the systematic uncertainties. See Garcia-Gamez (2013) for details.

4 Conclusion

The Pierre Auger Observatory offers the possibility to study the mass composition of UHECRs with the surface detector array. Different methods are used to identify the muonic component through the characteristics of the muon signal or using inclined events. Although the muon content at ground is sensitive to the masses of the primary particles, the interpretation is obtained comparing the data to the predictions of high-energy interaction models. The MPD is a promising method but more statistics is needed to understand the mass composition at ultra-high energies.

The results of the different methods show the necessity to achieve a clean separation of the electromagnetic and muonic components of the shower. With the present design, the Auger Observatory measures the muonic component with poor precision through indirect methods. A precise measurement of the number of muons is the key to estimate the primary mass on a shower-by-shower basis to study fundamental interactions at the highest energy. There are several ideas for the upgrade of the Auger Observatory to measure muons with the required precision (Bueno 2014).

References

Abraham, J. et al. [Pierre Auger Collaboration], Nucl. Instrum. Meth. A 523, 50 (2004)

Abraham, J. et al. [Pierre Auger Collaboration], Nucl. Instrum. Meth. A 620, 227 (2010) [arXiv:0907.4282[astro-ph.IM]]

Allekotte, I. et al. [Pierre Auger Collaboration], Nucl. Instrum. Meth. A 586, 409 (2008) [arXiv:0712.2832[astro-ph]]

Baltrusaitis, R. M. et al. [Fly's Eye Collaboration], Proceedings of the 19th International Cosmic Ray Conference, La Joya, USA, 30 (1998) 166

Bueno, A. [Pierre Auger Collaboration], Proceedings of the 26th Rencontres de Blois (2014)

Garcia-Gamez, D. [Pierre Auger Collaboration], Proceedings of the 33rd International Cosmic Ray Conference, Rio de Janeiro, Brazil (2013) [arXiv:1307.5059 [astro-ph.HE]]

Kégl, B. [Pierre Auger Collaboration], Proceedings of the 33rd International Cosmic Ray Conference, Rio de Janeiro, Brazil (2013) [arXiv:1307.5059 [astro-ph.HE]]

de Souza, V. [Pierre Auger Collaboration], Proceedings of the 33rd International Cosmic Ray Conference, Rio de Janeiro, Brazil (2013) [arXiv:1307.5059 [astro-ph.HE]]

SF2A 2014
J. Ballet, F. Bournaud, F. Martins, R. Monier and C. Reylé (eds)

THE PROMPT EMISSION OF GAMMA-RAY BURSTS

R. Mochkovitch[1]

Abstract. Gamma-ray bursts are the brightest objects in the Universe. Their prompt emission, mostly in soft gamma-rays (from a few keV to a few MeV) is followed by an afterglow that can be detected for weeks and months and where the emitted radiation becomes progressively softer from X-rays to visible and finally radio wavelengths. The physics of both the prompt and afterglow phases is uncertain and especially the origin of the prompt emission remains highly debated. This review presents a short summary of the situation.

Keywords: Gamma-ray bursts, Relativistic hydrodynamics, Shocks, Radiation processes

1 Introduction

In spite of the temporal and spectral data that have now been accumulated for several thousands of bursts, there are still several distinct possibilities to explain the prompt phase. The origin of the energy and the acceleration mechanisms that power a relativistic outflow from the central engine, the dissipation (comptonization below the photosphere, internal shocks, magnetic reconnection) and radiation processes responsible for the observed emission are not fully understood.

2 Observational summary

2.1 Temporal properties

Gamma-ray bursts are characterized by a great diversity in duration and temporal behaviors. They are short events, but nevertheless the prompt phase covers an interval of six orders of magnitude in duration from a few milliseconds to several thousands of seconds. The distribution of duration is bimodal with two peaks at respectively 0.3 and 30 s (Kouveliotou et al. 1993). The short events are supposed to be associated to the merging of compact objects (two neutron stars or a neutron star and a black hole) while long ones come from the collapse of massive stars (at least one burst, GRB 030329 has been clearly found in coincidence with a type Ic supernova, i.e. the explosion of a Wolf-Rayet star; Stanek et al. 2003).

The light curves in the keV-MeV spectral range, where most of the energy is released, can generally be represented by a succession of elementary "pulses", with a fast rise and a slower decay. Some light curves are simple with just one or a few pulses, while others are extremely complicated with many overlapping pulses.

Only a few events have been captured in the optical during the prompt phase either by fast response cameras following an alert or simply by chance. Again, the behavior in the optical range can very much differ from one burst to another. In GRB 990123 the visible light curve exhibits a power law decline (Gisler et al. 1999) while in GRB 041219A and GRB 080319B it seems to (approximately) follow the variations seen at high energy (Vestrand et al. 2005; Beskin et al. 2010). But in GRB 041219A the optical flux fits well with an extrapolation of the spectrum at low energy while in GRB 080319B (the so-called "naked-eye burst") it is hundreds times brighter.

[1] UPMC-CNRS, UMR7095, Institut d'Astrophysique de Paris, 75014 Paris, France

2.2 Spectral properties

GRB spectra can be represented in first approximation by the phenomenological Band function, which is simply two smoothly connected power-laws of respective indices α and β at low and high energy. The distribution of α is approximately normal, centered at $\alpha = -1$, while values of β extend from -2 to -4, with an average at -2.5 (Preece et al. 2000). The break energy, which is also the peak of the spectrum in $E^2N(E)$ (where $N(E)$ is the number of photons per unit energy) corresponds to the typical energy of photons that carry the bulk of the burst power. The distribution of the peak energy is approximately log-normal with a maximum at about 200 keV (Preece et al. 2000).

Recent results obtained with the GBM instrument onboard *Fermi*, which has an excellent spectral coverage, allow to go beyond the Band function and have identified in a few events a possible underlying thermal contribution below the broken power-law main component (Guiriec et al. 2011). In some cases an additional power-law, apparently extending from low energy (10 keV) to very high energy (100 MeV) is also detected (Ackermann et al. 2010).

3 Models

3.1 Basic requirements

When, following the discovery of the afterglows by the Beppo-SAX satellite in 1997 the first redshifts were measured (Metzger et al. 1997), it appeared that GRBs were located at cosmological distances (the largest confirmed redshift now exceeds $z = 8$!) which implied that the sources were able to release in a few seconds from 10^{51} to 10^{54} erg (assuming isotropic emission). Since the observed light curves sometimes vary on time scales as short as a few milliseconds, it also implied that the sources had to be compact. The resulting photon density is therefore huge and because GRB spectra often extend beyond 511 keV, extensive pair creation could be expected, leading to a very large Thomson opacity. The spectra show no evidence of that and the classical solution of this so-called "opacity problem" (first discussed in the context of radio sources by M. Rees in 1966) is to suppose that the radiation is emitted by material moving at relativistic velocities towards the observer. Then, the energy of the observed photons is reduced by the Lorentz factor Γ of the flow in the frame of the emitting material, while in the observer frame the photons are affected by relativistic beaming and move on quasi-parallel trajectories, which strongly raises the photon annihilation threshold. The constraints on the Lorentz factor depend on the burst spectrum and emitted power but typically a minimum $\Gamma_{\rm min} \sim 100$ appears necessary, with $\Gamma_{\rm min}$ possibly reaching 1000 in the most extreme cases (for example for events detected by Fermi/LAT and producing GeV photons; Lithwick & Sari 2001; Hascoët et al. 2012b).

3.2 Acceleration of the flow

The central source must therefore be able to accelerate the flow to ultra-relativistic velocities, which is not an easy task, especially in long GRBs where the progenitor is supposed to be a massive Wolf-Rayet star whose core is collapsing to a black hole, so that the outflow has to drill its way out of the stellar envelope. Two possible mechanisms have been considered to accelerate the flow:

- Thermal acceleration: energy is injected at the base of the flow in thermal form; this would be the case if the source of energy is $\nu\bar{\nu}$ annihilation of neutrinos emitted by the hot accretion torus surrounding the black hole (Zalamea & Beloborodov 2011). The hot plasma then adiabatically expands. The Lorentz factor first increases proportionally with radius until it reaches a final value $\Gamma_{\rm f} = E_{\rm th}/Mc^2$, where $E_{\rm th}$ is the injected thermal energy and M the amount of mass entrained in the flow (Piran 1999).

- Magnetic acceleration: in this case the flow is initially magnetically dominated and the acceleration occurs via a direct transfer of magnetic into kinetic energy. The acceleration is slower than in the previous case going as $R^{1/3}$ (at least in the simplest models; Drenkhahn & Spruit 2002). An important question concerns the amount of residual magnetization at infinity $\sigma_\infty = e_{\rm mag}/e_{\rm K}$ where $e_{\rm mag}$ and $e_{\rm K}$ are respectively the magnetic and kinetic energy densities (see 3.3.2 below).

3.3 *Dissipative processes*

3.3.1 Below the photosphere

GRBs are observed because part of the thermal, kinetic or magnetic energy of the outflow is converted into radiation. In photospheric models, the observed luminosity is supposed to come directly from the photosphere when the trapped thermal energy is eventually released where the optical depth of the expanding flow goes below unity. An obvious difficulty is that the resulting spectrum should be close to a blackbody. A solution to this problem is to consider that dissipative processes occur below the photosphere at optical depths of a few (Rees & Mészáros 2005; Beloborodov 2010). Several possible processes have been considered: (i) neutron-proton collision if neutrons decoupled from the flow before it has been fully accelerated so that protons and neutrons have different terminal Lorentz factors (ii) shocks or (iii) reconnection if the flow is magnetized. All these processes ultimately produce energetic electrons that can undergo inverse Compton collisions with the thermal photons. This can transform the spectrum, replacing the exponential cut-off of the Planck function by a power-law tail.

3.3.2 Above the photosphere

Dissipative processes can also occur above the photosphere. The most extensively studied possibility is the restitution of a fraction of the flow kinetic energy through internal shocks between shells moving at different Lorentz factors. An alternative consists to again invoke reconnection if the ejecta is magnetized, as it can happen either below or above the photosphere.

- Internal shocks: the general idea of internal shocks is vey simple. It supposes that the distribution of Lorentz factor in the flow is not uniform so that shells with high Lorentz factors are able to catch up and collide with slower ones (Kobayashi et al. 1997; Daigne & Mochkovitch 1998). For example, the relative velocity of two shells moving respectively at $\Gamma_1 = 100$ and $\Gamma_2 = 300$ is $v_{\rm rel} = c\,(\Gamma_2^2 - \Gamma_1^2)/(\Gamma_2^2 + \Gamma_1^2) = 0.8\,c$. When they collide, the dissipated energy is used to accelerate electrons and amplify the magnetic field. The electrons then lose energy by emitting synchrotron (and inverse Compton) radiation, which is responsible for the observed flux. Internal shocks can however form only if the residual magnetization of the flow is small ($\sigma_\infty < 0.1$) which, in the case of magnetic aceleration, supposes that magnetic energy has been almost completely converted into kinetic energy.

- Reconnection: in reconnection models, which are well suited to the case where $\sigma_\infty > 0.1$, the energy released by reconnection accelerates electrons that again emit synchrotron radiation. These models are still in their infancy due to the complications of the physics of reconnection. The most elaborated one is the ICMART (Internal-Collision-induced MAgnetic Reconnection and Turbulence) model, that in some way couples internal shocks and reconnection (Zhang & Yan 2011). Light curves can be calculated from ICMART but not yet spectra that could be compared to observed ones (Zhang & Zhang 2014).

3.4 *Evaluating and testing the models*

3.4.1 Pros and cons

Among the three models proposed to explain the prompt emission, internal shocks is the one which is the most easily calculable and therefore the one that makes the largest number of predictions. Many of them are in reasonable agreement with the data such as the various relations linking temporal and spectral properties (hardness-duration and hardness-intensity relations, evolution of pulse widths as a function of energy, etc, see Bošnjak & Daigne 2014, for details). But the internal shock model also faces several problems: (i) to get a peak of the synchrotron emission at a few hundreds keV, it appears necessary to transfer a large fraction of the shock dissipated energy to only a very small fraction of the electron population ($\sim 1\%$). Internal shocks are mildly relativistic, with the relative Lorentz factor of the colliding shells being typically between 1 and 2. Contrary to the ultra-relativistic case, this regime has not been explored by simulations, but transferring most of the shock dissipated energy to just a few electrons appears quite challenging; (ii) even if electrons can be properly accelerated, radiative efficiency requires that synchrotron emission should take place in the "fast cooling regime" (where the radiative time scale is short compared to the hydrodynamic time scale) but then the spectral index of the spectrum at low energy should be -1.5 while the average observed value is -1 (Ghisellini et al. 2000). Some possible solutions to this problem have been proposed but none appears fully satisfactory.

Photospheric and reconnection models make much less predictions than internal shocks. Especially in the case of reconnection, light curves (but not spectra) have been produced by only one group (Zhang & Zhang 2014), so that comparison to observation is very limited. Reconnection simply appears natural if the outflow keeps a large magnetization far from the source. The radiation process, as for internal shocks, is synchrotron with the same potential problems regarding the shape of the spectrum.

Photospheric models are favored if the acceleration of the flow has a thermal origin because of the large amount of energy that can be released at transparency. To transform the Planck spectrum into a broken power-law a sub-photospheric dissipation process is however necessary and a potential difficulty is that it has to work in a variety of regimes since, as a function of time during the prompt phase, the peak energy of the spectrum can vary by a factor of one hundred (and even more in some cases) with the photospheric radius also experiencing large changes.

3.4.2 Temporal tests

The X-ray light curve of the early afterglow of most GRBs obtained by the XRT instrument onboard *Swift* starts with a steep decay where the X-ray flux $F_X \propto t^{-3}$. A nice geometrical interpretation has been proposed for this behavior (Kumar & Panaitescu 2000). It may correspond to the signal from the last shell of the ejecta that has been illuminated at the end of the prompt phase. Due to the curvature of the shell, the radiation emitted by a surface element away from the line of sight reaches the observer with a delay. The calculation shows that the resulting behavior fits well with the observed decay, but only if the radius of the shell is large, as it is in models where dissipation takes place beyond the photosphere, the best agreement being obtained in the case of internal shocks (Hascoët et al. 2012a). In photospheric models the early steep decay cannot be explained by this geometrical effect and should therefore correspond to an effective behavior of the central engine.

3.4.3 Spectral tests

The observation of an underlying thermal component in the spectrum a few GRBs by the GBM instrument onboard *Fermi* is very important if it is confirmed in the future. Indeed, the presence of such a component is a natural prediction of the internal shock and reconnection models while it is not expected in photospheric models (Hascoët et al. 2013). In the two former cases, the main spectrum is formed above the photosphere and the photospheric emission (with approximately a Planck shape) is produced independently and simply adds its contribution to the total. In the latter case, what we see <u>is</u> the thermal contribution that has been modified by dissipative processes below the photosphere. One therefore does not expect that it will show up as an additional component in the observed spectrum.

Another possible test comes from the prompt optical emission when its appears correlated to the gamma-rays. This may suggest that both are produced at comparable radii. If this is the case, photospheric models might be in trouble, due to the risk of self-absorption that would cut-off the spectrum at low energy.

3.4.4 Polarization tests

Data from the IBIS instrument onboard INTEGRAL indicate a high degree of polarization in the prompt emission of some GRBs (Götz et al. 2009, 2013). These observations favor models with synchrotron emission (i.e. internal shocks or reconnection) under the additional condition that the magnetic field is ordered in the emission zone. In photospheric models the polarization averages to zero except if the jet is viewed on the edge or if there is a synchrotron contribution together with the photospheric one.

4 Conclusions

This short review has shown that many uncertainties remain about the origin of the prompt emission in gamma-ray bursts. All proposed models have virtues and drawbacks. We have presented some possible tests that can be used to discriminate among them. Spectral tests are promising as more and more spectra covering a broad range (from a few keV to 100 GeV) are being obtained by the two instruments (GBM and LAT) onboard the *Fermi* satellite. The development of polarimeters working in the hard X-ray domain will be also very useful to confirm and extend the results obtained by the IBIS instrument.

I thank Frédéric Daigne for many helpful discussions and advices.

References

Ackermann, M., Asano, K., Atwood, W. B., et al. 2010, ApJ, 716, 1178

Beloborodov, A. M. 2010, MNRAS, 407, 1033

Beskin, G., Karpov, S., Bondar, S., et al. 2010, ApJ, 719, L10

Bošnjak, Ž. & Daigne, F. 2014, A&A, 568, A45

Daigne, F. & Mochkovitch, R. 1998, MNRAS, 296, 275

Drenkhahn, G. & Spruit, H. C. 2002, A&A, 391, 1141

Ghisellini, G., Celotti, A., & Lazzati, D. 2000, MNRAS, 313, L1

Gisler, G., Akerlof, C. W., Balsano, R. J., et al. 1999, in American Institute of Physics Conference Series, Vol. 499, American Institute of Physics Conference Series, ed. S. P. Brumby, 82–89

Götz, D., Covino, S., Fernández-Soto, A., Laurent, P., & Bošnjak, Ž. 2013, MNRAS, 431, 3550

Götz, D., Laurent, P., Lebrun, F., Daigne, F., & Bošnjak, Ž. 2009, ApJ, 695, L208

Guiriec, S., Connaughton, V., Briggs, M. S., et al. 2011, ApJ, 727, L33

Hascoët, R., Daigne, F., & Mochkovitch, R. 2012a, A&A, 542, L29

Hascoët, R., Daigne, F., & Mochkovitch, R. 2013, A&A, 551, A124

Hascoët, R., Daigne, F., Mochkovitch, R., & Vennin, V. 2012b, MNRAS, 421, 525

Kobayashi, S., Piran, T., & Sari, R. 1997, ApJ, 490, 92

Kouveliotou, C., Meegan, C. A., Fishman, G. J., et al. 1993, ApJ, 413, L101

Kumar, P. & Panaitescu, A. 2000, ApJ, 541, L51

Lithwick, Y. & Sari, R. 2001, ApJ, 555, 540

Metzger, M. R., Djorgovski, S. G., Kulkarni, S. R., et al. 1997, Nature, 387, 878

Piran, T. 1999, Phys. Rep., 314, 575

Preece, R. D., Briggs, M. S., Mallozzi, R. S., et al. 2000, ApJS, 126, 19

Rees, M. J. & Mészáros, P. 2005, ApJ, 628, 847

Stanek, K. Z., Matheson, T., Garnavich, P. M., et al. 2003, ApJ, 591, L17

Vestrand, W. T., Wozniak, P. R., Wren, J. A., et al. 2005, Nature, 435, 178

Zalamea, I. & Beloborodov, A. M. 2011, MNRAS, 410, 2302

Zhang, B. & Yan, H. 2011, ApJ, 726, 90

Zhang, B. & Zhang, B. 2014, ApJ, 782, 92

SF2A 2014
J. Ballet, F. Bournaud, F. Martins, R. Monier and C. Reylé (eds)

ACCRETION DISK FLUX MODULATION: NEWTONIAN VERSUS GR EFFECTS.

P. Varniere[1] and F. Vincent[2]

Abstract. Compact objects are prone to the most extreme gravity fields and it is generally accepted that the motion of plasma in their close neighborhood is only properly described in the framework of general relativistic magnetohydrodynamics (GR-MHD). Nevertheless, a lot of the models trying to explain the origin of the fast flux modulation observed in X-rays do not take into account the full GR. Using a simple analytical model for non-axisymmetric structure in a thin disk we compute the observed flux and compare the results obtained in the Newtonian case with a full GR account of a Schwarschild black hole. This allows us to see that, while the purely newtonian approach does give a modulation and was enough of a proof of principle, we are missing several aspects.

Keywords: black hole, GR

1 Introduction

Accreting black holes exhibit variabilities on a wide range of timescales spanning from years down to milliseconds. While the change in the accretion rate probably causes the variability on timescales longer than days (Lasota 2001), the cause for behavior happening from the tens of seconds to milliseconds is likely rooted in some instabilities in the inner part of the accretion disk itself (Remillard *et al.* 2002). The disk in those systems is not resolved, therefore its structure cannot be directly imaged. A long standing question is how any unresolved structure in those disks can give rise to a detectable modulation of the observed flux. An early attempt (Varniere & Blackman 2005) showed a proof of principle in the newtonian case. But those objects are subject to strong gravity and ultimately we ask the question of the impact of full general relativity (GR) and, more importantly for observation, in which cases is it required to use full GR to study this modulation. Indeed, some of the lower frequencies would be associated with structures orbiting far enough in the disk for GR effects to be negligible. We will map out different cases to see when that is actually the case and what could be the observational signature of the change from non-GR to GR.

1.1 Parametrizing non-axisymmetric structures in accretion disk

Rather than taking full MHD simulations of spiral-inducing instabilities in the different conditions we wish to explore, we decided to create a simple, analytical, model for the non-axisymmetric structure in order to test more cleanly the different parameters. Indeed, in a full simulation changing one parameter in the initial condition can have repercussions on several parameters and therefore it is harder to study the different effects separately.

Here we are trying to minimize the number of parameters to characterize non-axisymmetric structures in the disk. In that respect, we add to the disk axisymmetric thickness $h_o(r)$ a component that depends on the azimuthal angle and position $h_1(r,\vartheta) = d(r).s(r-r_s,\vartheta)$. We choose to decompose this additional component as a height function d that depends only on r and a shape function s which is finite only near the disc structure causing the non-axisymmetry. For simplicity we take the shape function to be gaussian and the thickness function to be a power-law of r-only and related to the equilibrium thickness $h_o(r)$. This provides a simple but useful framework to model non-axisymmetric structures.

[1] APC, Université Paris 7
[2] Nicolaus Copernicus Astronomical Center, ul. Bartycka 18, PL-00-716 Warszawa, Poland

We modeled the non-axisymmetric structure by a spiral localized at $r_s = r_c e^{\alpha\vartheta}$ with r_c the position where the structure begins and α its opening angle.

$$h(r,\vartheta) = h_o(r) \cdot \left(1 + \gamma\left(\frac{r_c}{r}\right)^{\beta} \cdot e^{-0.5\left(\frac{r-r_s}{\delta}\right)^2}\right) \tag{1.1}$$

β measures how fast the thickness decreases from the maximum, δ parametrizes the radial extent of the structure, while γ relates to the unperturbed thickness of the disk. From that we simply compute the temperature assuming hydrostatic equilibrium.

In the cases presented here most of the above parameters are fixed in order to focus on the difference between newtonian and GR cases in function of a few key parameters. We take a thin disk with an unperturbed aspect-ratio of 10^{-2}, the spiral is taken to have a corotation radius $r_c = 2r_{in}$ where r_{in} is the position of the inner edge of the disk and an opening of $\alpha = 0.15$. This was taken so that we can easily distinguish the spiral from the unperturbed disk. For the same reason we have $\gamma = 2$, $\delta = 0.05$ and $\beta = 1$ which gives a rather large spiral on the disk. Using these rather extreme parameters we are not trying to reproduce *realistic* observations but rather have a strong signal on which we can see the GR effect clearly.

It was shown in Varniere & Blackman (2005) that spirals could be at the origin of the flux modulation even when they are unresolved. To go beyond that we look at the exact origin of the modulation. It appears that the key component to the modulation is due to the velocity in the disk, indeed special relativity cannot be neglected in the inner region of those accretion disks, which causes a sufficient time delay between the impact time of the geodesics that reach the observer.

1.2 the GYOTO code

In order to simulate the observed light-curve, we use the open-source general relativistic ray-tracing code GYOTO (Vincent *et al.* 2011). We assume the spiral to be at rest in a reference frame corotating with the disk at the Keplerian velocity at radius r_c. Null geodesics are integrated backward in time from a distant observer to the disk. When the disk is hit, the outgoing flux is assumed to follow the blackbody law at the local temperature. Two kinds of ray-tracing have been performed. The first kind (*Schwarzschild* or *full-GR* case in the following) takes into account the Schwarzschild metric, thus all special and general relativistic effects for a non-rotating black hole. The second kind (*Newtonian* in the following) assumes straight geodesics, without any special or general relativistic effects. Unless otherwise stated, the inclination angle is taken to be 45° which is a very intermediate value. Our goal is to determine in what cases the Newtonian integration gives a similar result with the full-GR case and what are the main differences.

2 Case of a non-axisymmetrical structure at $10r_{LSO}$

To start we take a disk relatively far from the last stable orbit with an inner radius at $r_{in} = 5r_{LSO}$ while the non-axisymmetrical structure starts at $r_c = 10r_{LSO}$.

Fig. 1. shows the light curve for both the Newtonian (in black) and Schwarschild (in red) cases. The flux normalization is the same for all the plots and is associated to the case where the disk is at the last stable orbit, namely the maximum emission. Indeed, as the disk gets further away from the last stable orbit its temperature and therefore its total emission decreases. As the structure gets further away from the last stable orbit, it is expected that GR will become negligible and a newtonian calculation will be enough to get an accurate measurement. What we see here is, that for a spiral corotation located at $10r_{LSO}$, GR effects are not negligible when looking at the total flux modulation. The base effect is a special relativity effect but, not only the GR add to the time delay, we also have the beaming effect becoming important.

3 Case of a non-axisymmetrical structure at $2r_{LSO}$

In Fig. 2 we now look at a "strong gravity" case, where the inner edge of the disk is located at the last stable orbit and the non-axisymmetrical structure starts at twice that distance, we obtain, as before, a stronger modulation in the GR case but we also see that the light curves are not in phase anymore.

It will be interesting to see if such shift in the phase could be detected as the inner edge of the disk moves closer to the last stable orbit. It could lead to a new explanation for some of the unusual time-lag in

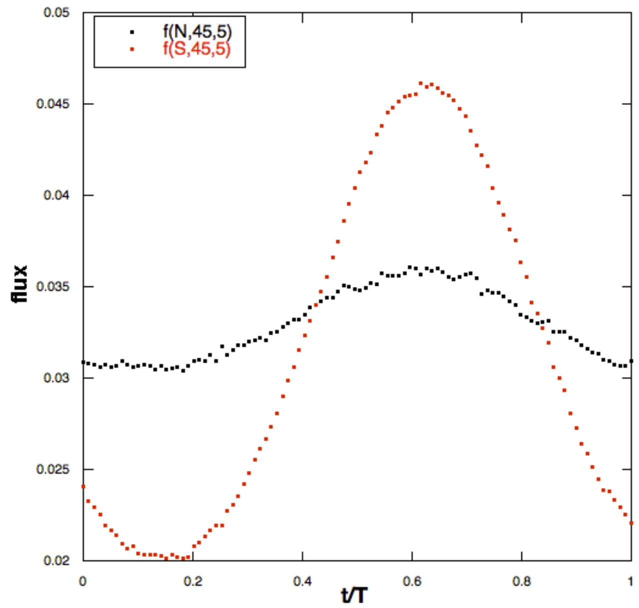

Fig. 1. Comparison of the light curve obtained when looking at 45° and the inner edge of the disk is at $5r_{LSO}$. N stands for Newtonian and S for Schwarschild.

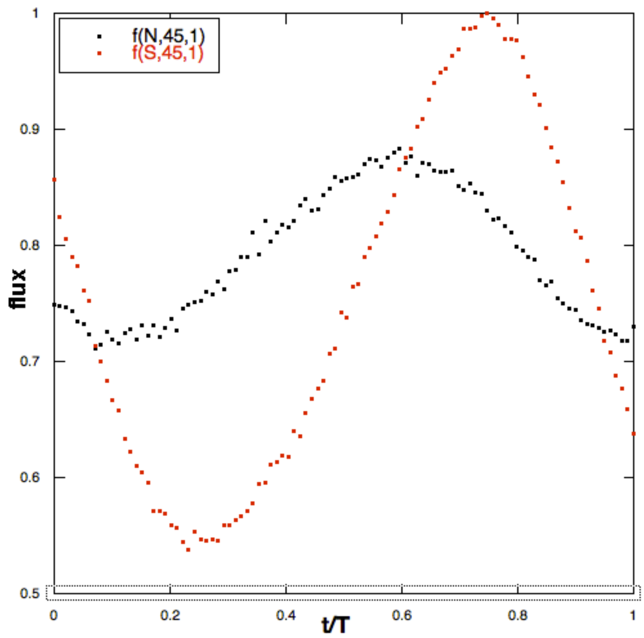

Fig. 2. Comparison of the light curve obtained when the inner edge of the disk is at r_{LSO}.

microquasars, especially as this effect will probably be amplified when taking into account the spin of the black hole.

4 Preliminary report on what impacts the rms amplitude

From the purely observational point of view we are interested by what could impact the rms amplitude of the modulation. Using our simple model we already see two parameters, that we have access to through observations, have important consequences on the rms amplitude of the same disk structure.

4.1 Impact of the inner edge of the disk

If we now compare the normalized flux we get in the case of a Schwarschild black-hole depending on where the inner edge of the disk is, we see in Fig. 3 that, while the total flux is higher the closer we get to the last stable orbit, the relative importance of the spiral increases with distance. This gives the modulation a stronger rms amplitude when the disk is further away. It will be interesting to compare the evolution of the maximum rms amplitude as function of the inner edge of the disk with observations.

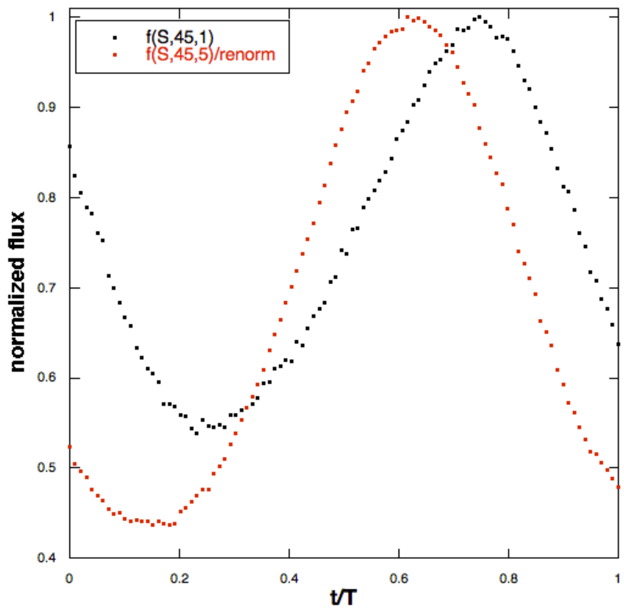

Fig. 3. Comparison of the light curve obtained when the inner edge of the disk is at r_{LSO} and at five times that distance. We renormalized the light curve in the case where the inner edge is at $5r_{LSO}$ to have the same max value at in the r_{LSO} case for easier comparison.

While it will be interesting to compare the evolution of the maximum rms amplitude as function of the inner edge of the disk with observations, this is beyond the scope of these preliminary results. Indeed, we need first to gather enough observational data and then compare how different spirals behave to see if the trends are similar. Adding a non-zero spin will also be needed and will add another degree of freedom which might prevent any firm conclusion.

4.2 Impact of the inclination angle

It was long hypothesized that higher inclination angles (more "edge-on") would lead to stronger modulation. This is what we observed when comparing the same disk at 45° and 85° as can be seen on Fig. 4.

But, in the high-inclination case, we also observed a distortion of the light-curve that could lead to the PDS of such signal having a complex harmonic structure while the "real" signal is a simple $m = 1$ mode. It will be interesting to explore this in more detail and look at how much stronger the effect is for high spins. It might be an alternative explanation for the complex harmonic structure observed in microquasars.

5 Conclusions

Here we are presenting preliminary results on the impact of a full GR ray-tracing calculation when computing the flux from a disk harboring non-axisymmetric structures. We used a very simplified disk structure model and mainly showed the necessity, even for structures away from the last stable orbit, to take full GR into account.

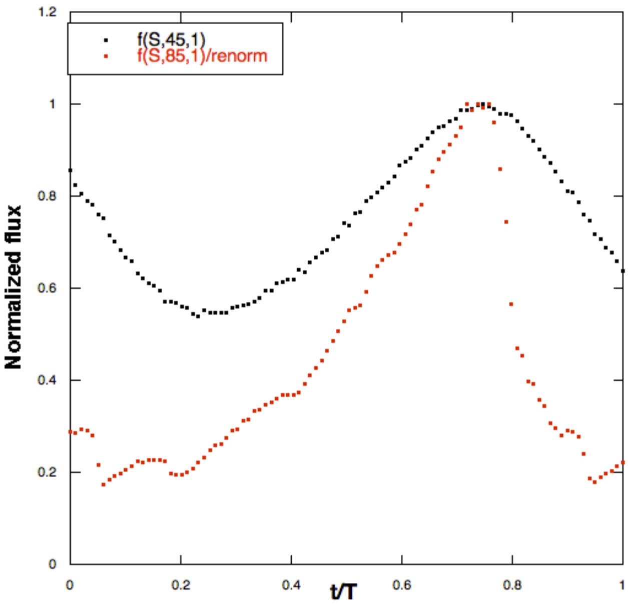

Fig. 4. Comparison of the light curve obtained at different inclination angle

PV and FHV acknowledge financial support from the French Programme National des Hautes Energies (PNHE). PV acknowledge financial support from the UnivEarthS Labex program at Sorbonne Paris Cite (ANR-10-LABX- 0023 and ANR-11-IDEX-0005-02). FHV acknowledge financial support support by the Polish NCN grant 2013/09/B/ST9/00060. Computing was partly done using the Division Informatique de l'Observatoire (DIO) HPC facilities from Observatoire de Paris (http: //dio.obspm.fr/Calcul/)and at the FACe (Francois Arago Centre) in Paris.

References

Lasota, J.-P. 2001, New Astronomy Reviews, 45, 449

Remillard, R. A., Muno, M. P., McClintock, J. E., Orosz, J. A. 2002, ApJ, 580, 1030

Varniere, P. & Blackman, E.G., 2005, New Astronomy, Volume 11, Issue 1, p. 43.

Vincent, F. H., Paumard, T., Gourgoulhon, E., & Perrin, G. 2011, Classical and Quantum Gravity, 28, 225011.

SF2A 2014
J. Ballet, F. Bournaud, F. Martins, R. Monier and C. Reylé (eds)

INFLUENCE OF AN AGN COMPLEX PHOTON FIELD ON THE JET BULK LORENTZ FACTOR THROUGH COMPTON ROCKET EFFECT

T. Vuillaume[1], G. Henri [1] and P-O. Petrucci [1]

Abstract. Radio-loud active galactic nuclei are among the most powerful objects in the universe. In these objects, most of the emission comes from a relativistic jet getting its power from the accretion of matter on a supermassive black-hole. However, despite many studies, the jets acceleration to relativistic speeds is still misunderstood. The bulk Lorentz factor characterizing the speed of these flows cannot be precisely measured and only limits have been established.

It is widely admitted that jets are composed of relativistic particles emitting light through several physical processes, one of them being the comptonization of photons coming from external sources to the jet. It has been shown that this emission can drive a group of highly relativistic leptons placed in an external photon field to relativistic bulk motions through the Compton rocket effect. In this work, we investigate this process and compute the resulting bulk Lorentz factor in the complex photon field of an AGN composed of several external photon sources.

To do so, we model the sources present in the inner parts of an AGN (the accretion disk, the dusty torus and the broad line region), taking precisely into account their geometry and anisotropy to numerically compute the bulk Lorentz factor of the jet at every altitude.

The study shows interesting and unexpected behaviors of the bulk Lorentz factor with acceleration and deceleration zones in the jet. We investigate the patterns of the bulk Lorentz and Doppler factors along the jet for one geometry example and discuss the implications of these patterns on the AGN emission.

Keywords: AGN jets – bulk Lorentz factor – Compton Rocket – variability

1 Introduction

It is now widely admitted that AGN's jets hold relativistic flows. First evidences go back to the 70's with the observation of superluminal motions (Cohen et al. 1971) which are only possible for actual speeds of $0.7c$ at least. However, a lot of questions on the speed of these flows remain. Mainly, we still do not know the mechanism driving them to relativistic speeds or neither do we know the spatial distribution of these speeds. They are characterized by their bulk Lorentz factor $\Gamma_b = \left(1-\beta_b^2\right)^{-1/2}$ rather than their speed V_b with $\beta_b = V_b/c$. Up to now, it appears that the most complex studied variations of longitudinal bulk Lorentz factor have followed power laws with an accelerating and/or a decelerating phase (Marscher 1980, Ghisellini et al. 1985, Boutelier et al. 2008).

Our work takes place in the two-flow paradigm (Sol et al. 1989) where the jet is composed of a mildly relativistic sheath, filled with e^-/p^+ and an ultra-relativistic spine composed of e^-/e^+ pairs responsible for most of the emission. The outer jet acts as an energy reservoir for the particles of the spine, which will be continuously thermalized along the jet via the second order Fermi process. This is in agreement with diffuse X-ray emission observed in FRI which favors a distributed particle acceleration rather than localized shocks (Hardcastle et al. 2007). In this paradigm, the plasma is subject to the Compton rocket effect which will naturally drive the flow to relativistic speeds.

[1] Institut de Planétologie et d'Astrophysique de Grenoble

2 Γ_b & equilibrium

O'dell (1981) showed that "a plasma of relativistic particles exposed to an anisotropic radiation field acts as a rocket - a Compton rocket" because of the reaction force imposed by the inverse Compton radiation from the particles. In the Thomson regime, this force is proportional to the flux in the rest frame $H^* = \frac{1}{4\pi}\int I^*_{\nu_s}(\Omega^*_s, \Gamma)\cos\theta^*_s \mathrm{d}\Omega^*_s \mathrm{d}\nu^*_s$. Thus, the bulk of particles reaches an equilibrium velocity, which can be represented by the equilibrium bulk Lorentz factor Γ_{eq}, when $H^* = 0$. In the vicinity of a supermassive black-hole, core of an AGN, lie several sources of soft photons. These sources will induce an anisotropic radiation field in the jet and thus allow the Compton rocket effect to take place. Hence, to compute the equilibrium bulk Lorentz factor along the jet, we need to compute precisely the external photon field at every altitude. Here, we model the AGN including three main sources of soft photons: a standard accretion disk, a dusty torus in thermal equilibrium and a broad line region (BLR) modeled as a spherical shell of clouds (see figure 1)

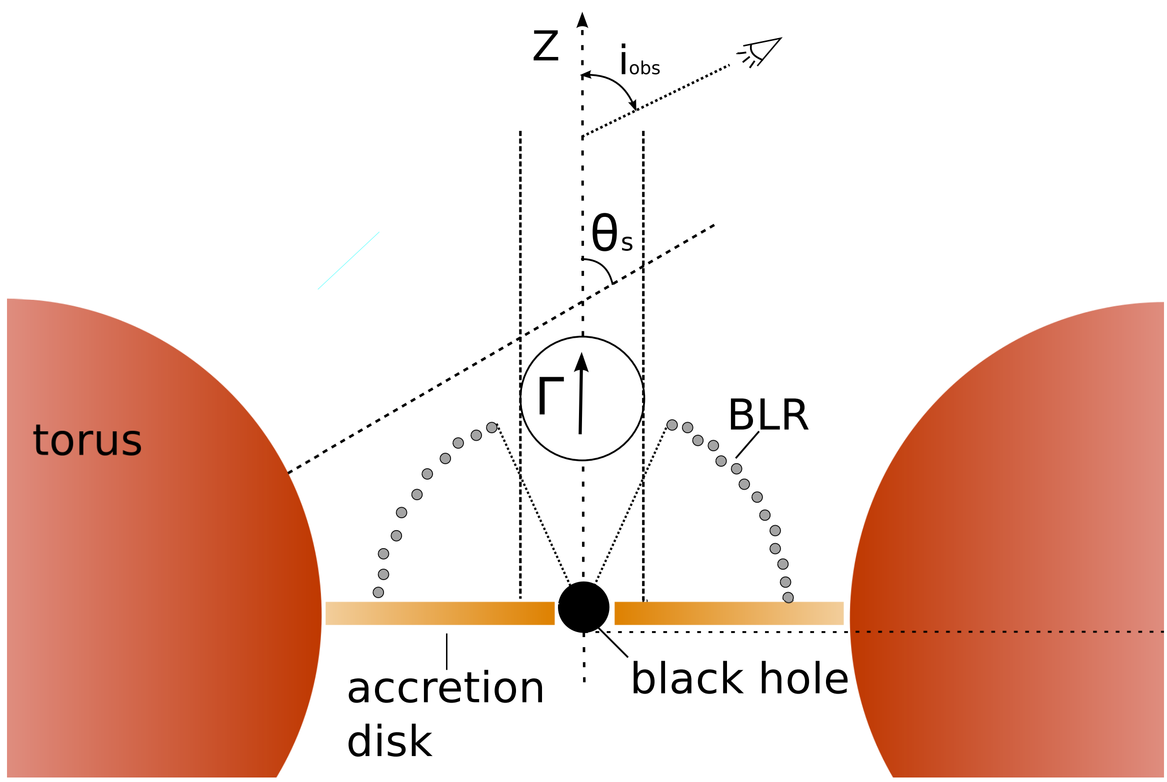

Fig. 1. The big picture: sketch edge on of the global model geometry (not to scale) with the accretion disk, the dusty torus and the BLR.

3 Evolution of Γ_{eq} along the jet

Figure 2 represents Γ_{eq} for different configurations of external sources.

Let's start with the simplest feature, an infinite accretion disk. Photons from the accretion disk are moving upward parallel to the axis which corresponds to a positive flux in the bulk rest frame $H^* > 0$. This leads to an inverse Compton emission backward and thus a reaction force forward, which at the end is accelerating the flow (Γ_{eq} increases).

However, because of aberration effects, the situation is more complex for the dusty torus and the BLR. Until a certain altitude, photons from the dusty torus or from the BLR generate a negative rest frame flux, $H^* < 0$ which provoke a backward force, or Compton drag, decelerating the flow. It is only up to a point, depending on the sources size, that the flow is able to accelerate again.

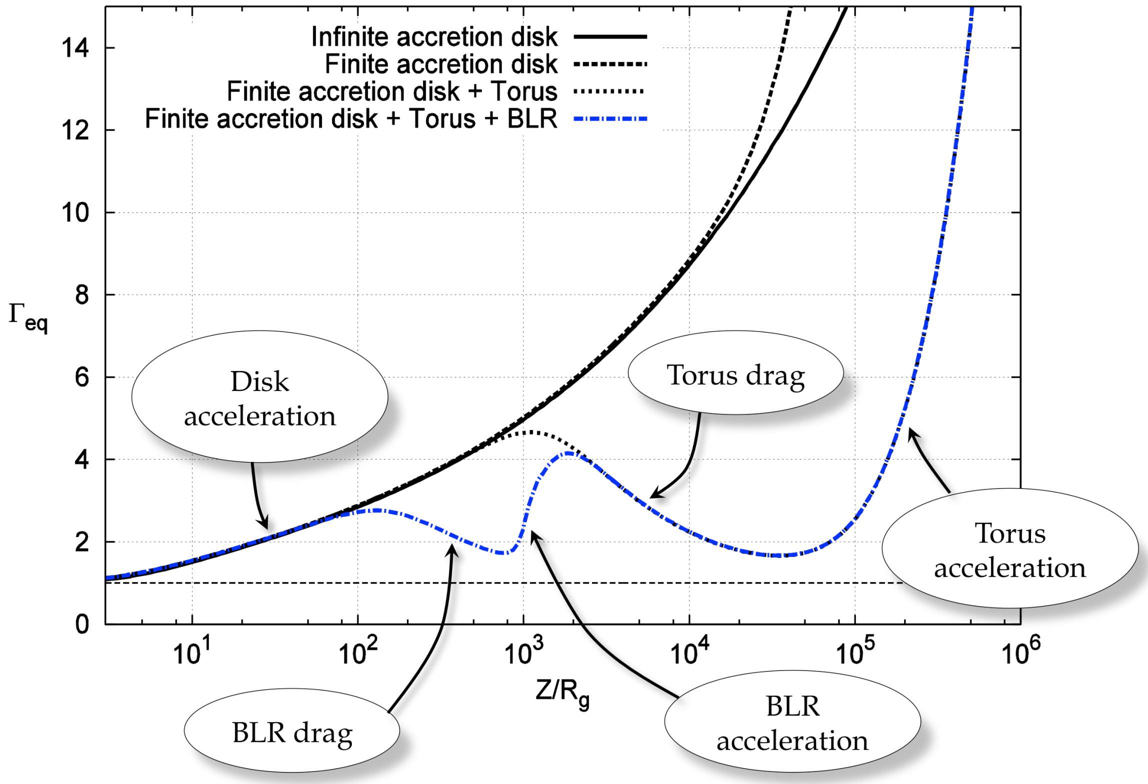

Fig. 2. Γ_{eq} resulting of the Compton rocket effect for different external photon sources. The geometry is described in figure 1 with the following parameters: finite and infinite accretion disk have an inner radius $R_{in} = 3R_g$. The finite disk has an outer radius $R_{out} = 5 \times 10^4 R_g$. $D_{torus} = 10^5 R_g$, $R_{torus} = 5 \times 10^4 R_g$, $R_{BLR} = 10^3 R_g$

4 Evolution of δ_{eq} along the jet

The relativistic bulk Doppler factor is defined as:

$$\delta_b = \frac{1}{\Gamma_b\,(1 - \beta_b\,\mu_{obs})} \tag{4.1}$$

with $\mu_{obs} = \cos i_{obs}$ (see figure 1 for a definition of i_{obs}).

Figure 3 represents the evolution of the Doppler factor δ_{eq} along the jet for different observational angles but for the same bulk Lorentz factor Γ_{eq} corresponding to the one computed in figure 2.

The luminosity seen by an observer goes as $L_{obs} = \delta^4 L^*$. This is why an observer will mainly (or preferentially) see emission zones of maximum δ_{eq}. Because of the variations of Γ_{eq} along the jet, an observer will see preferentially certain zones of the jet, and thus brighter spots. But, high δ_{eq} correspond to different zones depending on the observational angle. For face-on objects, high δ_{eq} correspond to high Γ_{eq} whereas for edge-on objects, high δ_{eq} correspond to low Γ_{eq} and thus an observer will not see the same parts of the same jet depending on how he looks at it.

It is also interesting noticing that objects seen at more extremes angles ($\mu \approx 1$ or $\mu \approx 0$) will show more ample variations of δ_{eq} and thus highest differences of luminosity between parts of the jet whereas jets seen at moderate angles ($\mu = 0.6 \approx \beta$ here) will seem more homogeneous.

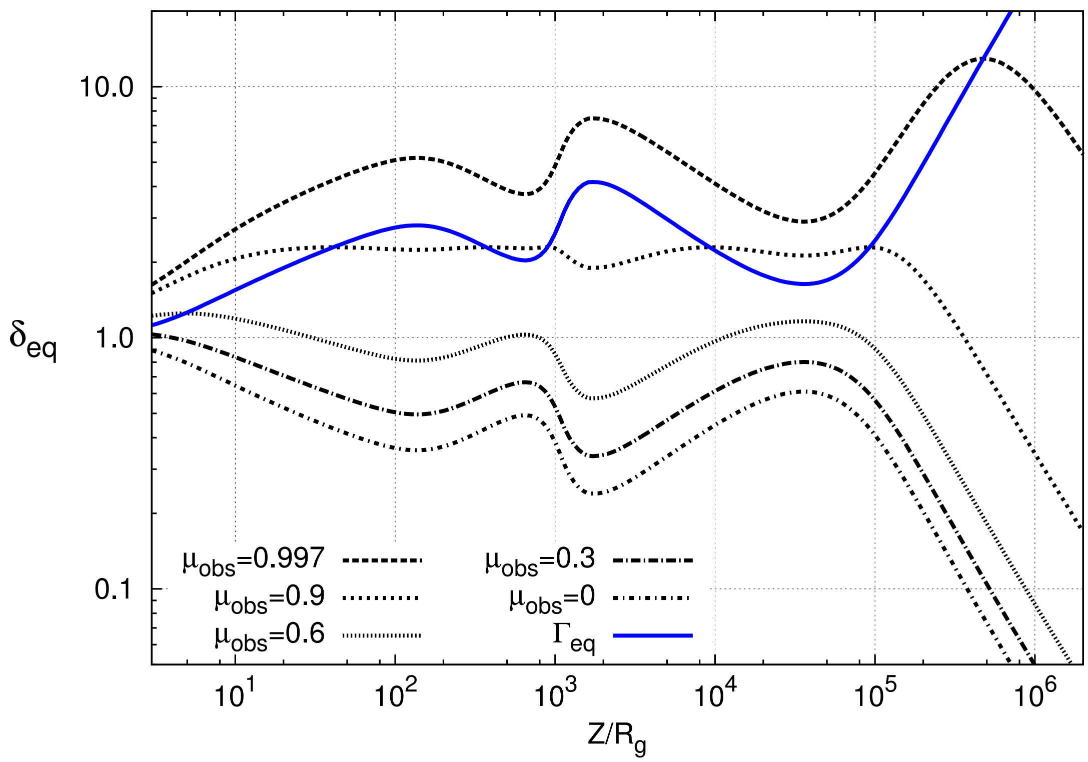

Fig. 3. Equilibrium bulk Doppler factor in function of the altitude for several observational angles i_{obs} ($\mu_{obs} = \cos i_{obs}$). The geometry is described figure1. The Doppler factors are computed for the same Lorentz factor computed figure 2 (blue line).

5 Conclusions

The question of the acceleration of AGNs jets is still a matter of discussion as we do not know the underlying processes nor the precise speeds of the flows. The solution implied by the Compton rocket effect is elegant as it can naturally lead to relativistic speeds and is viable in the two-flow paradigm. In this work, we embrace this framework and study the influence of several external photon sources (the accretion disk, the dusty torus and the broad line region) on the Compton rocket effect and on the induced bulk Lorentz factor. To do so, we carefully computed the resulting equilibrium bulk Lorentz factor, Γ_{eq}, of a flow driven by the Compton rocket effect taking into account the anisotropy of the emission. With several external sources, Γ_{eq} will show important changes along the jet, leading to acceleration and deceleration phases. We also discussed the implications of this variations on the Doppler factor and on observations of jets.

We would like to thanks the CNES for its financial support.

References

Boutelier, T., Henri, G., & Petrucci, P.-O. 2008, Monthly Notices of the Royal Astronomical Society: Letters, 390, L73

Cohen, M. H., Cannon, W., Purcell, G. H., et al. 1971, Astrophysical Journal, 170, 207

Ghisellini, G., Maraschi, L., & Treves, A. 1985, Astronomy and Astrophysics, 146, 204

Hardcastle, M. J., Kraft, R. P., Sivakoff, G. R., et al. 2007, The Astrophysical Journal Letters, 670, L81

Marscher, A. P. 1980, The Astrophysical Journal, 235, 386

O'dell, S. L. 1981, Astrophysical Journal, 243, L147

Sol, H., Pelletier, G., & Asseo, E. 1989, Monthly Notices of the Royal Astronomical Society (ISSN 0035-8711), 237, 411

Session 05

Atelier de préparation à l'exploitation scientifique de l'instrument GRAVITY

SF2A 2014
J. Ballet, F. Bournaud, F. Martins, R. Monier and C. Reylé (eds)

PLANET FORMATION IN MULTIPLE STELLAR SYSTEMS: GG TAU A

E. Di Folco[1,2], A. Dutrey[1,2], S. Guilloteau[1,2], J.-B. Le Bouquin[3], S. Lacour[4], J.-P. Berger[5], R. Köhler[6] and V. Piétu[7]

Abstract. GG Tau is a hierarchical quadruple system of young, low-mass stars. Because of its well-studied bright circumbinary ring of dust and gas surrounding the main binary GG Tau A, it is a unique laboratory to study planet formation in the disturbed environment of binary/multiple stellar systems. We have started a large observing program of GG Tau A that combines several high-resolution instruments in a multi-wavelength approach. We have recently reported the detection of a new low-mass companion in GG Tau A that turns out to itself be a triple system. This discovery was possible thanks to the very high angular resolution of the near-IR instrument PIONIER on the VLT interferometer, and was confirmed with sub-aperture masking techniques on VLT/NaCo. The detected close binary GG Tau Ab ($\rho = 0.032''$, or about 5 AU) provides a natural explanation for two enigmas: the discrepancy between the dynamical mass and the spectral type estimates in GG Tau A, and the absence of dust thermal emission in the vicinity of the Ab component. GRAVITY will provide the adequate angular resolution to complete the astrometric characterization of the close binary in the next 10 years. With now 5 coeval low-mass stars, GG Tau is an ideal laboratory to calibrate stellar evolution tracks at young ages (few Myr). Beyond this peculiar system, GRAVITY also has a strong potential to study the impact of multiplicity on the existence of disks, and *in fine* on planet formation mechanisms in multiple systems.

Keywords: Stars: binaries:close ; Planetary systems: proto-planetary disks ; Techniques: high angular resolution, interfeometry

1 Planet formation in binary systems

Planet formation is a common process that can occur in different environments. Exoplanet discoveries have revealed that giant planets can form and remain in stable orbits in multiple stellar systems (e.g., the Kepler systems 16, 34, 35, Doyle et al. 2011; Welsh et al. 2012), and are found both in S-type and P-type orbits (circumstellar and circumbinary case, respectively). Since about 50 % of Sun-like stars are found in binary or multiple systems in our Galaxy (for a recent review, see Duchêne & Kraus 2013), a sizable fraction of planets may have formed in such systems. The impact of stellar host multiplicity on planet formation scenarios therefore deserves serious investigation. This has only recently been made possible with the advent of very high angular resolution instruments at both infrared (IR) and sub-millimeter wavelengths (e.g., Kraus et al. 2012; Akeson & Jensen 2014; Tang et al. 2014).

Young stars in a binary system are expected to be surrounded by two circumstellar (CS) disks, located inside their Roche lobes and an outer circumbinary ring or disk outside the outer Lindblad resonances (e.g., Artymowicz & Lubow 1994). Theory of gravitational tides predicts that the outer radius of the CS disks and the inner radius of the outer ring are set by tidal truncation induced by the central binary. Hydrodynamical simulations predict

[1] Univ. Bordeaux, Laboratoire d'Astrophysique de Bordeaux, UMR 5804, F-33270, Floirac, France
[2] CNRS, LAB, UMR 5804, F-33270 Floirac, France
[3] UJF-Grenoble 1/CNRS-INSU, Institut de Planétologie et d'Astrophysique de Grenoble UMR 5274, F-38041, Grenoble, France
[4] LESIA, CNRS/UMR-8109, Observatoire de Paris, UPMC, Université Paris Diderot, 5 place J. Janssen, F-92195, Meudon, France
[5] European Southern Observatory, D-85748, Garching by München, Germany
[6] Max-Planck-Institut für Astronomie, Königstuhl 17, D-69117 Heidelberg, Germany
[7] IRAM, 300 rue de la piscine, F-38406 Saint-Martin d'Hères, France

that the inner CS disks are not completely cutoff from the outer circumbinary disk, and that material flowing in the form of *streamers* through the central cavity may replenish the CS disks. Without external feeding, the CS disks would quickly vanish as the gas and dust accrete onto the stars, which can severely affect their potential to form planets. Recent IR studies of pre-main sequence (PMS) binaries in the Taurus molecular cloud have revealed that the disk frequency dramatically drops for stellar separations smaller than about 40 au, i.e., $\rho < 0.3''$ at the distance of the closest star forming region, 140 pc (Kraus et al. 2012). Investigating the survival of CS disks (through a direct characterization of the disk properties and of gas kinematics) in close binary systems is therefore a crucial step to quantitatively evaluate the impact of stellar multiplicity on planet formation mechanisms. This requires sub-arcsec imaging capabilities, that only long-basline interferometers (or sub-aperture masking techniques on 10 m class telescopes) can offer.

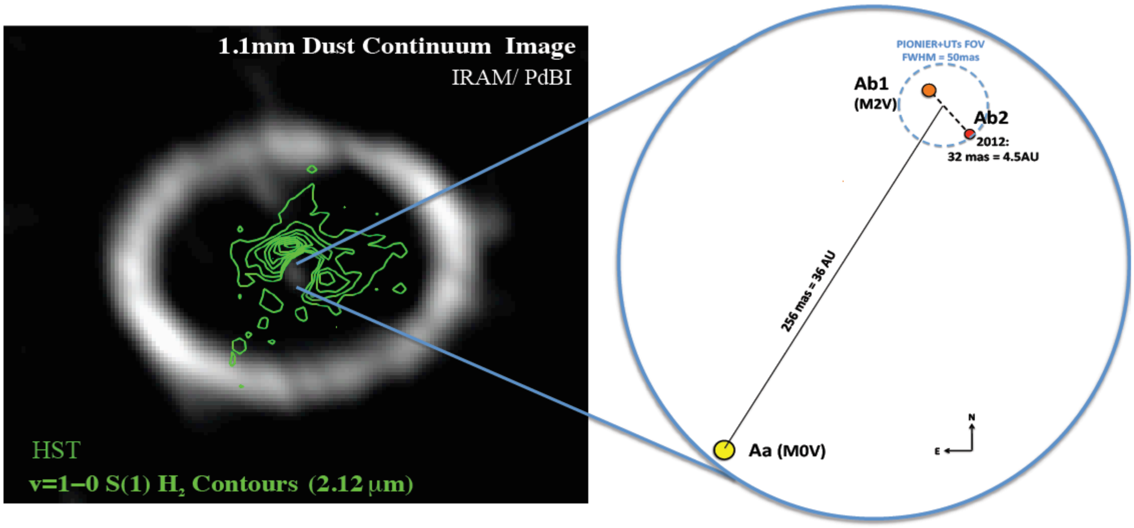

Fig. 1. Global picture of the GG Tau A triple system: **Left:** thermal emission of the outer disk/ring observed with the IRAM Plateau de Bure interferometer at 1.1 mm, from Piétu et al. (2011). The central dust emission is centered on the Aa component. **Right:** zoom on the newly identified triple system showing the derived Ab close-binary characteristics in october 2012 (adapted from Di Folco et al. 2014).

2 The emblematic multiple system GG Tau A: recent discoveries

We have recently undertaken a high-angular resolution observing program from UV to mm wavelengths of a prototypical young, low-mass, multiple stellar system: GG Tau A. Our project combines the HST, VLT/VLTI and ALMA instruments to probe the accretion and tidal mechanisms in this complex proto-planetary system. GG Tau A is one of the best-studied nearby T Tauri binaries, with a 0.26" separation (36 au on the sky plane). It stands out among young binaries because of its massive ($0.15\,M_\odot$) and bright outer ring of dust and gas which was initially discovered at mm wavelengths by Dutrey et al. (1994) and then imaged in scattered light by Roddier et al. (1996). The circumbinary disk has been resolved in thermal dust emission, and the CO gas proved to rotate at Keplerian speed (Dutrey et al. 1994; Guilloteau et al. 1999). The outer disk extends from 180 AU out to about 800 AU. One remarkable characteristics of this system is that most ($\sim 80\,\%$) of the mass is confined in an 90 au broad ring (190-280 au) which is expected to be the reservoir of material to replenish the CS disk(s). Indirect evidence for gas flow from the ring through the central cavity has been found from ^{12}CO J=2-1 gas image (Guilloteau & Dutrey 2001) and from near-IR H_2 transitions (Beck et al. 2012, tracing possible accretion shocks,). The existence of two inner CS disks is independently attested by mm emission centered on GG Tau Aa (Piétu et al. 2011), strong H_α accretion, [OI] line detection (White et al. 1999; Hartigan & Kenyon 2003), and 10μm silicate feature from hot grains in both Aa and Ab surroundings (Skemer et al. 2011).

We have recently reported the detection of a new stellar component in the GG Tau A binary system using VLTI/PIONIER instrument (Le Bouquin et al. 2011) and sub-aperture masking (SAM) techniques on the VLT/NaCo imager (Lacour et al. 2011). Thanks to the tiny 50 mas (FWHM) field of view (FOV) of VLTI+UTs in *H* band, we were able to separately target GG Tau Aa (M0V) and Ab (M2V) with PIONIER in *H* band. We

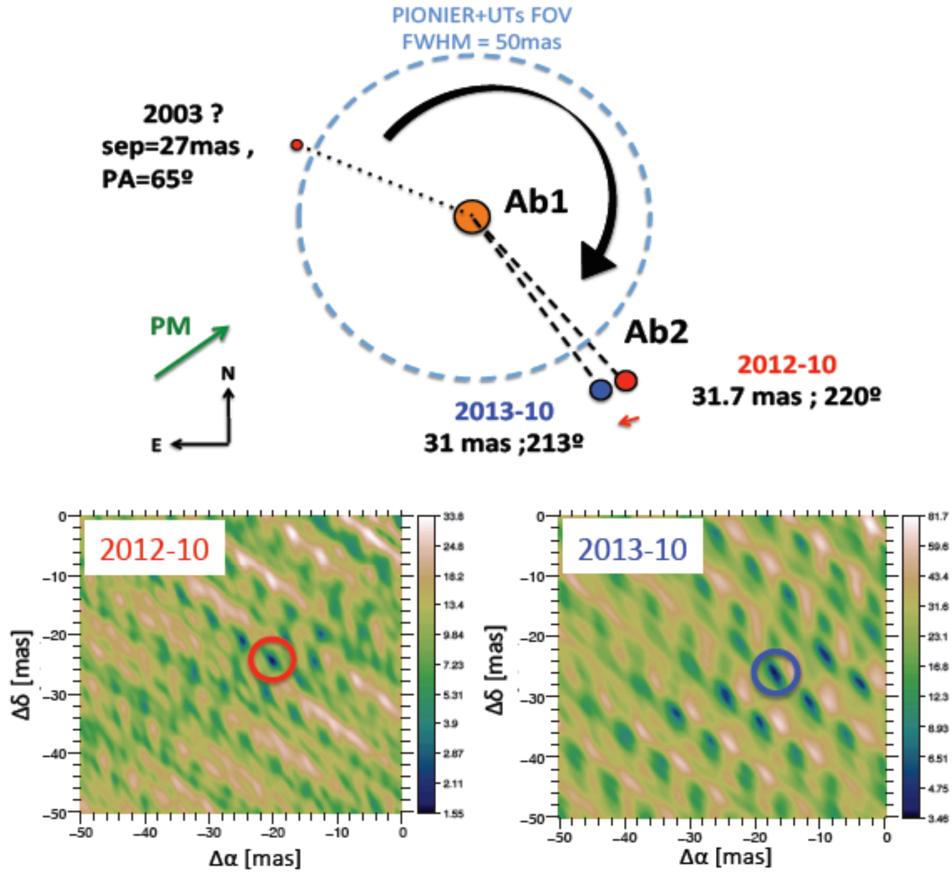

Fig. 2. Summary of GG Tau Ab close-binary astrometric measurements with VLTI/PIONIER and VLT/NaCo (2012-2013), and the tentative a posteriori identification in NaCo archival data (2003). Lower panels display the VLTI χ^2 maps that illustrate the degeneracies of the model-fitting and the impact of SNR on the close-binary identification for such faint targets ($H \sim 9$, weather conditions were much better during the 2012 observing campaign).

discovered a closure phase signal as large as 30 deg, which can be unambiguously interpreted as the signature of a companion around Ab (Di Folco et al. 2014) (see Fig. 1 for a global picture of the triple system). Its separation (32 mas) and PA (220 deg) were confirmed with NACO-SAM observations in H/Ks bands in 2012. A second epoch measurement in 2013 with PIONIER (Fig. 2) confirmed that Ab2 is a bound object that rotates in the same direction as the main binary and the outer ring (as determined by the velocity field derived from the spectro-imaging of CO gas, e.g., Guilloteau et al. 1999). From the approximate measurement of the Ab1/Ab2 flux ratio (in H, Ks and L' bands), we estimated a probable spectral type M3 for Ab2.

This new component adds $\sim 0.3\,M_\odot$ in the system, with two major consequences. First, it yields a better agreement between the stellar mass (Aa+Ab) and the dynamical mass: Hartigan & Kenyon (2003) had revised the Aa and Ab spectral types to M0 and M2 (resp.), based on an improved spectral analysis, however, it resulted in a discrepancy of $\sim 0.3\,M_\odot$ with the dynamical mass inferred from the Keplerian rotation of CO gas in the CB ring ($1.28 \pm 0.07\,M_\odot$, Guilloteau et al. 1999). Secondly, it provides a logical explanation for the lack of sub-mm/mm continuum emission around Ab attested by PdBI (Piétu et al. 2011) and ALMA observations (Dutrey et al. 2014). The new components Ab1–Ab2 are indeed surrounded by Roche lobes of radius ~ 2 AU. Tidal effects natural prevent the existence of dust disk(s) large and massive enough to be strong mm emitters (but they remain warm enough to produce the detected 10μm silicate feature).

The new stellar component was tentatively recovered from archival NaCo data, acquired in burst mode in 2003, which provides a possible third epoch observation (Fig. 2). All together, these astrometric measurements enable a preliminary fit of the orbital parameters, suggesting a (deprojected) semi-major axis $a \sim 5.6$ au, an 100 deg inclined orbit of 16 yr period, and a moderate eccentricity $e = 0.38$.

3 Potential for binary system characterization with VLTI/GRAVITY

A robust characterization of the orbital parameters definitely requires more astrometric measurements. The angular separation of the close-binary Ab1-Ab2 ($10-30\,$mas), and the suggested orbital period make it an ideal target for the GRAVITY instrument. Few measurements during the next decade should be enough to determine the orbital parameters of the close-binary. In combination with a 0.1"-resolution mapping of the CO gas distribution in the cavity with ALMA, it should also be possible to directly probe the imprint of the binary on the accretion streamers that supply the inner circumstellar disks with fresh material from the outer ring. Although the spatial resolution of VLTI in the H and K bands remains too limited to provide an accurate determination of the CS disks characteristics around CTTS at the distance of Taurus (the disk surrounding Aa was only marginally resolved in our UTs observations, see Di Folco et al. 2014, for more details), it will be possible to take advantage of the high sensitivity of GRAVITY to observe a large set of PMS close-binary stars. Since the close-binary systems (with $\rho \lesssim 40\,$AU or 0.3" at $140\,$pc) are key targets to investigate the impact of multiplicity on disks survival and planet formation, GRAVITY is expected to provide new constraints for a large set of PMS binary systems (through orbital characterization and IR flux ratio determination). It will in particular complement sub-aperture masking techniques that proved to be efficient in the $30-300\,$mas range in order to study the closest systems, where the impact of multiplicity is naturally expected to be the strongest. In addition, determination of PMS binary parameters will also be essential to compare and validate the stellar evolution models especially in the $1-5\,$Myr age range and low-mass regime ($M_\star \lesssim 0.5 M_\odot$).

4 Conclusions

This result illustrates the potential for VLTI instruments to probe the dynamics of PMS close-binary stars and the strong synergy with the sub-millimeter array ALMA to investigate the favorable physical conditions for planets to form in young, multiple stellar systems. The direct characterization of close-binary orbits with GRAVITY along the next decade can play an important role in constraining the evolution of angular momentum in complex multiple systems, and to investigate the impact of multiplicity on planet formation mechanisms.

E. Di Folco and S. Guilloteau acknowledge the support of PNPS and PNP for this project.

References

Akeson, R. L. & Jensen, E. L. N. 2014, ApJ, 784, 62

Artymowicz, P. & Lubow, S. H. 1994, ApJ, 421, 651

Beck, T. L., Bary, J. S., Dutrey, A., et al. 2012, ApJ, 754, 72

Di Folco, E., Dutrey, A., Le Bouquin, J.-B., et al. 2014, A&A, 565, L2

Doyle, L. R., Carter, J. A., Fabrycky, D. C., et al. 2011, Science, 333, 1602

Duchêne, G. & Kraus, A. 2013, ARA&A, 51, 269

Dutrey, A., Di Folco, E., Guilloteau, S., et al. 2014, Nature, in press

Dutrey, A., Guilloteau, S., & Simon, M. 1994, A&A, 286, 149

Guilloteau, S. & Dutrey, A. 2001, in IAU Symposium, Vol. 200, The Formation of Binary Stars, ed. H. Zinnecker & R. Mathieu, 229

Guilloteau, S., Dutrey, A., & Simon, M. 1999, A&A, 348, 570

Hartigan, P. & Kenyon, S. J. 2003, ApJ, 583, 334

Kraus, A. L., Ireland, M. J., Hillenbrand, L. A., & Martinache, F. 2012, ApJ, 745, 19

Lacour, S., Tuthill, P., Amico, P., et al. 2011, A&A, 532, A72

Le Bouquin, J.-B., Berger, J.-P., Lazareff, B., et al. 2011, A&A, 535, A67

Piétu, V., Gueth, F., Hily-Blant, P., Schuster, K.-F., & Pety, J. 2011, A&A, 528, A81

Roddier, C., Roddier, F., Northcott, M. J., Graves, J. E., & Jim, K. 1996, ApJ, 463, 326

Skemer, A. J., Close, L. M., Greene, T. P., et al. 2011, ApJ, 740, 43

Tang, Y.-W., Dutrey, A., Guilloteau, S., et al. 2014, ApJ, 793, 10

Welsh, W. F., Orosz, J. A., Carter, J. A., et al. 2012, Nature, 481, 475

White, R. J., Ghez, A. M., Reid, I. N., & Schultz, G. 1999, ApJ, 520, 811

SF2A 2014
J. Ballet, F. Bournaud, F. Martins, R. Monier and C. Reylé (eds)

OBSERVATION OF ASTEROIDS WITH GRAVITY - PHYSICAL CHARACTERIZATION OF BINARY SYSTEMS

A. Matter[1 2], M. Delbo[3], B. Carry[4] and P. Tanga[3]

Abstract. Density and internal structures are among the most important characteristics of asteroids, yet these properties are also some of the least known. For distant asteroids (in the Main Belt and beyond) these properties were up to now accessible only for the largest (>100 km in size) asteroids. Going to smaller and fainter asteroids can revolutionize our understanding because we will be sampling a new regime in physical properties. Here we discuss how ground-based optical interferometry with the GRAVITY instrument can be used to observe the motion of asteroid satellites to determine the mass of small binary systems. Following the expected sensitivity performances in K-band of GRAVITY, we present a sample of binary targets potentially observable in single-field mode. The feasibility of such observations will strongly be dependent on the ability of the control software of GRAVITY to track objects moving at high rate on the sky (differential motion ~ 10 mas.s^{-1}). Although the dual-field mode could allow to increase the sample of small binary asteroids observable, it seems to be currently unfeasible given the high differential motion of asteroids.

Keywords: interferometry, asteroids, internal structure, density

1 Introduction

Density and internal structure are probably the most fundamental and at the same time the least constrained characteristics of asteroids. They indeed reflect the accretional and collisional environment of the early solar system. Moreover, because some asteroids are analogs to the building blocks that formed the terrestrial planets 4.56 Gy ago, the density and internal structures of minor bodies inform us about the formation conditions and evolution processes of planets and the solar system as a whole. Any deviation of the asteroids bulk density from its potential meteorite analogs grain density provides an estimate of the bulk porosity of the asteroid. Such a bulk porosity is directly linked to the past collisional evolution of the asteroid belt and the solar system. For instance, current collisional models (Benz & Asphaug 1999; Jutzi et al. 2010) predict that most asteroids larger than a few 100 m are fractured aggregates held together by gravity only ('rubble-pile'). Their gravitational reaccumulation follows the catastrophic disruption of a larger parent body (Michel et al. 2001). Models of formation of binary systems also predict particular configuration and bulk porosities. For instance, close and small similar-sized components are expected to have formed by a rotational breakup of a parent porous body, due to spin-up effects, thus leading to a rubble-pile structure (Walsh et al. 2012).

Testing these models is highly needed because our knowledge of the collisional process is still poor and needs to be confronted to a large variety of validation tests (e.g. impact experiments at small scale, asteroid family formation at large scale, and comparison with bulk porosity measurements).

Mass and volume are required to determine the bulk density of an asteroid and infer its bulk porosity. Volume determination is often affected by large uncertainties when the object shape is approximated with a sphere, or when a radiometric diameter (obtain from thermal modeling of the infrared flux) is taken at face value. This can lead to a relative error on the bulk density of at least 60% (see e.g., Carry 2012). Masses of asteroids are also poorly determined and biased towards the very large asteroids. The most used method, which consists in

[1] Univ. Grenoble Alpes, IPAG, F-38000 Grenoble, France.
[2] CNRS, IPAG, F-38000 Grenoble, France.
[3] UNS-CNRS-Observatoire de la Côte d'Azur, Laboratoire Lagrange, BP 4229 06304 Nice cedex 04, France.
[4] IMCCE, Observatoire de Paris, UPMC, CNRS, 77 Av. Denfert Rochereau, 75014 Paris, France.

tracking the motions of asteroids that gravitationally interact with one another, requires modeling the orbits of multiple asteroids over long periods of time and high accuracy astrometry. The best data are for the largest asteroids (1) Ceres, (2) Pallas, and (4) Vesta (Carry 2012). It is expected that Gaia will enable us to derive the masses of the largest 100 asteroids (Mouret et al. 2007). An approach that is not biased towards large objects is the observation of asteroid satellites. This is the most productive method of asteroid mass determination. It can provide accurate masses of asteroids since, by Kepler's third law ($P^2/a^3 = 4\pi^2/(GM)$), the orbital period P and semimajor axis a of the satellite uniquely determine the mass of the system. The best observations yield typical errors of $\sim 10\%$ (Carry 2012). The challenge is to determine the semimajor axis of the system, and in general this requires spatially resolving the secondary from the primary. In particular, interferometry offer unprecedented high angular resolution to measure (1) the size of an asteroid projected along the interferometer baseline and (2) the semimajor axis of the orbits of asteroid satellites. The orbital elements (period, anomaly, ...) of the binary asteroid targets are in general well known and constrained from photometric lightcurve observations. We can note that a good lightcurve coverage during mutual eclipsing events can also offer the possibility of constraining the shape of the binaries and the relative size of the components. In principle, their absolute size and density can also be derived (Scheirich et al., 2009) but only under strong assumptions on the shape, that one should avoid if a low uncertainty on density is needed. Also, this method is shown to work best for asteroids visible at high phase angles - such as near-Earth asteroids. Main Belt photometric binaries remain essentially out of reach of a purely photometric approach.
Using the VLTI/MIDI instrument (Leinert et al. 2003), we have already demonstrated the potential of long-baseline interferometry for the determination of physical properties of asteroids, including size, basic shape, and surface properties (Delbo et al. 2009; Matter et al. 2011, 2013). We also demonstrated recently the capabilities of the MIDI instrument to observe small photometric binary asteroids and derive, in combination with optical lightcurves, their physical properties (Carry et al., submitted to Icarus). In the following, we discuss how ground-based optical interferometry can be used to observe the motion of asteroid satellites to determine the mass of small binary systems. We then focus on the case of the GRAVITY instrument and present a sample of binary targets potentially observable according to the expected sensitivity performances in K-band of GRAVITY. Finally, the feasability of both the single-field and dual-field modes is discussed.

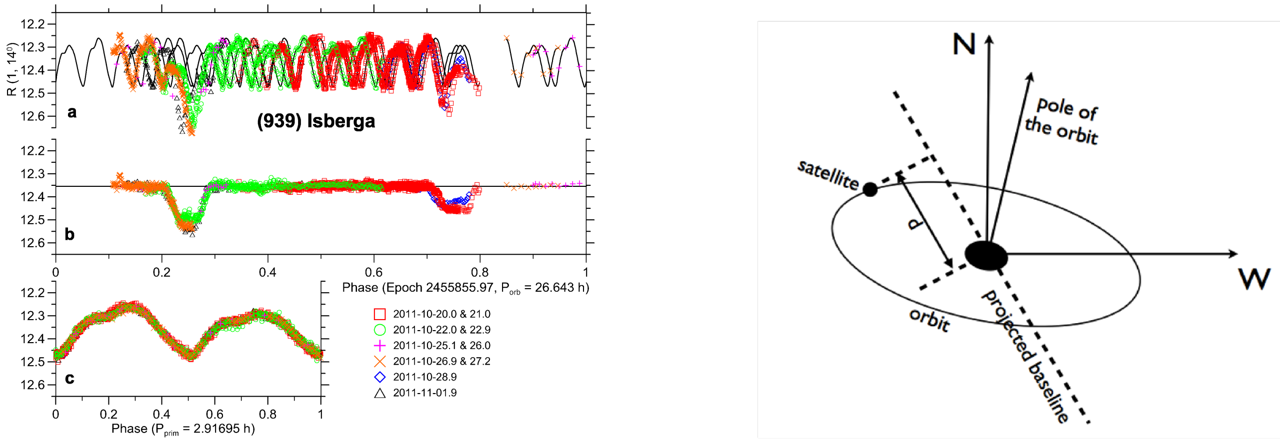

Fig. 1. Left: Example of lightcurves of the small main-belt binary asteroid (939) Isberga, taken from Carry et al. (submitted), showing the mutual eclipses and photometric variability induced by the primary rotation. a) All the lightcurves acquired between 20 October 2011 and 11 November 2011 folded over the synodic orbital period of 26.643 h; b) the same as above, with the orbital component of the lightcurve only; c) the rotation component of the lightcurve only, folded over the rotation period of 2.91695 h. **Right:** Geometry of the orbit of a binary asteroid on the plane of the sky at the time of an interferometric measurement.

2 The method

Studying the density and internal structure of asteroids requires the determination of mass and volume. One one hand, measurements of asteroid interferometric signals along different baselines and at different epoch - exploiting the rotation of the body about its axis and change in obliquity - allow to refine asteroids size measurements and calculate more accurate volumes then those based on a spherical approximation. On the other hand, the observation of asteroid satellites can provide very accurate masses since, by Kepler's third law, the orbital period and semi-major axis of the system uniquely determine the mass of the bodies. When combined with lightcurve observations, a single interferometric measurement can, in principle, be sufficient to determine the semi-major axis of the binary orbit (see right panel of Fig.1). Indeed, the lightcurve of a binary system at the epoch of its discovery already provides its orbital period and basic information about the orientation of the orbit in space (orbit pole) and the orbital anomaly (simply by the detection of the eclipse and occultation events). Then, the amount of available lightcurve data usually increase in the years following the binary system discovery because of the follow up of the asteroid by photometric observations (see left panel of Fig.1). The increasing amount of data allows orbital and physical parameters of the system to be refined. However, several interferometric observations of the systems are preferred in order to measure more accurately the motion of the components, the evolution of their apparent separation, and ultimately the semi-major axis. The separation and the sizes of the components along different directions (the system orbital period is of the order of the day, so during one night the components will significantly rotate under the baseline) can be obtained by fitting a binary model to the interferometric data (see Delbo et al. 2009). Given the orbital period, the orbit, and the semi-major axis, masses can be determined. From the masses and the shapes we can infer bulk densities, which will be compared to its potential meteorite analogs grain density to provides an estimate of the bulk porosity.

3 The targets

With more than 200 binary systems including about 100 main belt objects, and more discoveries announced almost monthly, the study of mutual orbits can provide numerous mass determinations. Figure 3 shows a sample

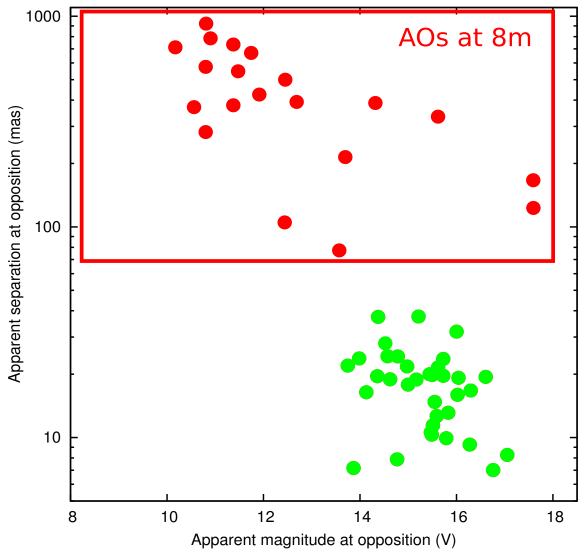

Fig. 2. Sample of binary asteroids in the Main Belt; red spots indicate binary systems discovered and spatially resolved by adaptive optics direct imaging with 8m-class telescopes, while green spots indicate binary systems detected by photometry only (transits/eclipses). This plot shows the separation of the two components vs the system magnitude under best observing conditions (the object apparent separation is computed at its average opposition distance). For photometric binaries, the separation is guessed from a fit of the photometry itself combined to reasonable assumptions on the density or on the albedo.

of asteroids with satellites known today in the Main Belt. Only asteroids in the upper left corner (in red), bright and with primary-secondary separation in excess of 100 mas, can be resolved today using direct imaging with adaptive optics (AOs) at 8m-class telescopes. Ideal targets for interferometric observations are those asteroids, with separation $<<$ 100 mas, that can not be easily resolved by AOs. These asteroids are known to have a satellite from photometric lightcurve studies (green spots in Fig.3). With nominal spatial resolution down to ~ 2 mas in K-band, the new VLTI instrument GRAVITY can be used to characterize binary asteroids that are too compact to be imaged with other techniques. The measurement of the separation of a binary astronomical source is a classical application of interferometry, and Delbo et al. (2009) and Carry et al. (submitted) describe

Name	Apparition	V range
(317) Roxane	2015,2016,2017,2018,2019	11.8-13.9
(809) Lundia	2015	11.8-13.9
(854) Frostia	2015	13.9-14.0
(1052) Belgica	2015	13.8-13.9
(1089) Tama	2016,2019	13.1-13.9
(1139) Atami	2016,2017	13.0-13.9
(1453) Fennia	2019	13.7-13.9
(1717) Arlan	2019	13.9-14.0
(1727) Mette	2018	13.9-14.0
(1866) Sisyphus	2019	12.8-14.0
(2121) Sevastopol	2016	13.9-14.0
(2044) Wirt	2016	13.7-13.9
1999 kw4	2018,2019	12.7-13.4
2003 yt1	2016	11.8-13.3

Table 1. Sample of photometric binary asteroids observable with GRAVITY in single-field mode (V $\leq$ 14) in the next 3-4 years.

the application of this technique in the case of asteroids observed with MIDI at the VLTI. In particular, a binary source produces a visibility that depends on the square root of cos $\left(2\pi\frac{B}{\lambda}\rho\right)$, where B is the projected length of the interferometer baseline, λ the observing wavelength, and ρ the angular separation of the binary components in the plane of the sky projected along B. Given the long baseline length allowed by the VLTI (up to 200m), one can in principle measure the separation of very compact systems ($<< 50-100$ mas). However, one of the major limitations of the first generation of ground based interferometers was the target magnitude. For instance the limiting magnitude with the near-infrared VLTI instrument AMBER is V$\sim$10 when used the 8m UTs, which prevents the observation of all of the more interesting binaries, with V>10. Bright binary asteroids have usually large separations such that they can be resolved by means of adaptive optics at 10m class telescopes. We think that the real challenge for interferometric observation of solar system minor bodies is the spatial resolution of compact and faint binary asteroids. These objects are routinely discovered by lightcurve observations performed with CCD photometric campaigns at smaller (1-2m) telescopes.

4 Observation of binary asteroids with GRAVITY

GRAVITY is the near-infrared focal instrument of the VLTI (Eisenhauer et al. 2011). It will operate in K-band (i.e. from 2.0 to 2.4 μm) combining the light from four Unit Telescopes (UTs) or Auxiliary Telescopes (ATs); (light is injected into optical fibers before recombination), and measuring fringes from six baselines simultaneously. Aside from classical visibility and closure phase measurements, this instrument will provide high precision narrow-angle astrometry and phase-referenced interferometric imaging. In single-field mode, where fringe tracking is performed 'on-axis' namely on the science target, the expected GRAVITY limiting magnitude is K=11 (correlated flux). Up to this limiting magnitude, GRAVITY should provide high signal-to-noise ratio ($\sim$ 10) visibilities and 2° accuracy on closure phases for a few minutes of integration (Eisenhauer et al. 2011). As asteroids are usually rather dark and red objects, their typical color V-K is $\sim$ 2.5. Therefore, considering a limiting magnitude of V=14, we calculated the observability from Paranal, namely the different periods of apparition, of all the photometric binaries brigther than V=14 in the next 3-4 years. This is shown in Table 1. About 15 objects would be potential binary targets for GRAVITY in single-field mode. We mention that the assumed limiting magnitude is expected to lead to high signal-to-noise ratio visibilities and accurate closure phases. To increase the sample of potential binary targets for GRAVITY in single-field mode, we could think of relaxing such a constraint on the V magnitude once the instrument will be optimized; this should lead to lower but still decent signal-to-noise ratios ($\sim$ 3).

Another way to increase the number of potential targets would be to consider the dual-field mode of GRAVITY. In this mode, fringe tracking and reference phase measurement are performed 'off-axis' on a reference star with K=10-11 located within 2" from the science target. In this case, the expected GRAVITY limiting magnitude would be K=16 (correlated flux), which translates to V$\simeq$ 19. As asteroids are moving targets, close encounter events with reference stars are possible at different epochs and can be calculated from softwares available from the Internet (e.g., WinOCCULT).

However, a critical aspect that could affect the feasibility of both the single-field and dual-field modes is the differential motion rate of asteroids. Indeed, for typical main-belt asteroids orbiting the Sun between ~ 2 and 3 AU, the orbital keplerian velocity ranges from 30 to 21 km.s^{-1}. As seen from the Earth, this translates to an apparent differential motion of 20 to 10 mas.s^{-1}, respectively. With such a differential motion, the asteroid would cross the interferometric field-of-view of 70 mas of GRAVITY, which corresponds to the injection cone of the optical fibers, in a few seconds. The global field-of-view of 2", which includes the reference star, would be crossed in about 3 minutes. This appears to be too fast to allow dual-field mode with a sufficient integration time (at least 1 min) on the science target. In single-field mode, the tracking on the science target at such apparent rate ($\sim$ 10 mas.s^{-1}) seems problematic with the first version of the control software of GRAVITY. Nevertheless, it should be possible to include, in a future version of the control software, a functionality of high speed tracking on sources with high differential motion. It should allow to follow directly the asteroids with the 'science fiber' and acquire fringes during a sufficient integration time.

5 Conclusions

Binary and multiple systems have been discovered in all populations of asteroids and other solar system small bodies. Furthermore, it is expected that about 15% of asteroids smaller than 10 km in diameter have a satellite. This latter population of binary asteroids is especially important because the observations of the motion of the components allows one to derive the dynamical mass of the system from Keplers third law. Combined to information on their size, and thus volume, bulk density and then porosity can be derived. Such an information on the asteroids internal structure is fundamental to constrain the models of collisional evolution including the formation of multiple systems. Here we discussed how ground based optical interferometry can provide the required sensitivity and spatial resolution to measure the size and separation of the components of faint and distant small binary asteroids; a population that is not spatially resolvable by direct imaging with current 8m-class telescopes. Finally, we show that the GRAVITY instrument be used for the observations of a significant sample ($\sim$ 15) of small binary asteroids in the next 3-4 years. However, the feasibility of such an observation in single-field mode will be dependent on the ability of GRAVITY to track moving objects with high differential motion. Indeed, with a typical differential motion of 10 mas.s^{-1} for the Main-Belt asteroids, the control software of GRAVITY will have to include an additional functionality of high speed tracking to follow directly the asteroids with the 'science fiber' and acquire fringes during a sufficient integration time. As to the dual-field mode, it currently seems unfeasible given the high differential motion of Main-Belt asteroids, which will not allow sufficient integration time on the target while passing close to the reference star.

We thank the GRAVITY team and especially T. Paumard for interesting and fruitful discussions.

References

Benz, W. & Asphaug, E. 1999, Icarus, 142, 5

Carry, B. 2012, Planet. Space Sci., 73, 98

Delbo, M., Ligori, S., Matter, A., Cellino, A., & Berthier, J. 2009, Astrophysical Journal, 694, 1228

Eisenhauer, F., Perrin, G., Brandner, W., et al. 2011, The Messenger, 143, 16

Jutzi, M., Michel, P., Benz, W., & Richardson, D. C. 2010, Icarus, 207, 54

Leinert, C., Graser, U., Przygodda, F., et al. 2003, Ap&SS, 286, 73

Matter, A., Delbo, M., Carry, B., & Ligori, S. 2013, Icarus, 226, 419

Matter, A., Delbo, M., Ligori, S., Crouzet, N., & Tanga, P. 2011, Icarus, 215, 47

Michel, P., Benz, W., Tanga, P., & Richardson, D. C. 2001, Science, 294, 1696

Mouret, S., Hestroffer, D., & Mignard, F. 2007, A&A, 472, 1017

Walsh, K. J., Richardson, D. C., & Michel, P. 2012, Icarus, 220, 514

SF2A 2014
J. Ballet, F. Bournaud, F. Martins, R. Monier and C. Reylé (eds)

IMAGE RECONSTRUCTION IN POLYCHROMATIC INTERFEROMETRY

F. Soulez[1]

Abstract. As the first VLTI 4 telescopes beam combiner, PIONIER made routine interferometric imaging possible at the VLTI. With its higher spectral resolution, GRAVITY will be able to produce hyperspectral images with the resolution of the millisecond of arc. However only few algorithms have been proposed for the reconstruction of such hyperspectral images. Among the various approaches for polychromatic reconstruction we present the MiRA-3D algorithm developed in Lyon and its results on simulations and data on PIONIER.

Keywords: Image reconstruction ; Optical interferometry ; VLTI

1 Introduction

The objective of stellar interferometric imaging is to recover an approximation of the specific brightness distribution $I(\lambda, \boldsymbol{\theta})$ of the observed astronomical object given measurements which are sparse samples of the spatial Fourier transform $\hat{I}(\lambda, \boldsymbol{\nu})$ of $I(\lambda, \boldsymbol{\theta})$. In its simplest form, it consists on a coherent recombination of the light from a pair of telescopes pointing the same target. By varying the optical path delay between the two arms of the interferometer, one observes fringes. Without atmospheric turbulence, the contrast and the phase of those fringes are the amplitude ρ and the phase ϕ respectively of the complex value $\hat{I}(\lambda, \boldsymbol{\nu}) = \rho(\lambda, \boldsymbol{\nu}) \exp(\phi(\lambda, \boldsymbol{\nu}))$ at the spatial frequency $\nu = B/\lambda$ with B the projected baseline between both telescopes.

Unfortunately all ground based interferometers are subject to atmospheric turbulence. This have mainly two consequences:

- the boiling of speckle patterns in the telescope focal plane causes random variation of the transmission $A_i(\nu, t)$ of each telescope i and thus the observed contrast of the fringes,
- it introduces a random delay in the optical path causing random variations of the observed phase.

The first problem is overcome by normalizing the observed contrast by the flux in the photometric channel of each telescope. As consequence, the estimated amplitudes are only relative to the integrated flux (*i.e.*the amplitude at $\nu = 0$).

Two solutions are usually proposed to have an estimate of phases. The first is to measure the atmospheric random delay using a reference source. This phase reference is implemented in the GRAVITY beam combiner. The second solution is to measure quantities unaffected by such random delay, namely:

- powerspectrum: $P(\lambda, \boldsymbol{\nu}) = \left|\hat{I}(\lambda, \boldsymbol{\nu})\right|^2$,
- bispectrum: $B(\lambda, \boldsymbol{\nu}, \boldsymbol{\nu}') = \hat{I}(\lambda, \boldsymbol{\nu})\, \hat{I}(\lambda, \boldsymbol{\nu}')\, \hat{I}^*(\lambda, \boldsymbol{\nu} + \boldsymbol{\nu}')$,
- phase closure: $\Psi(\lambda, \nu, \nu') = \arg B(\lambda, \boldsymbol{\nu}, \boldsymbol{\nu}') = \Phi(\lambda, \boldsymbol{\nu}) + \Phi(\lambda, \boldsymbol{\nu}) - \Phi(\lambda, \boldsymbol{\nu} + \boldsymbol{\nu})$,
- differential phase: $\Delta\Phi(\lambda, \boldsymbol{\nu}_m) = \Phi_(\lambda, \boldsymbol{\nu}_m) - \Phi(\lambda_{\mathsf{ref}}, \boldsymbol{\nu}_m)$

Due to its technical complexity, very few beam combiners provide a phase reference and rely on these non linear measurements. These non linearities introduce some important difficulties in the image reconstruction task as it worsens the noise statistics and makes the problem non convex (*i.e.* the solution may not be unique and depends on the initialization of the algorithm).

[1] Centre de Recherche Astrophysique de Lyon

2 Image reconstruction

The reconstruction of a monochromatic image from optical interferometry data is a challenging task which has been the subject of fruitful research and resulted in various algorithms. Most of these algorithms can be placed in a *maximum a posteriori* framework: the maximum entropy method BSMEM (Buscher 1994; Baron & Young 2008), WISARD (Meimon et al. 2005), MiRA (Thiébaut 2008), IRBis (Hofmann et al. 2014), PAINTER (Schutz et al. 2014) and MiRA3D which is currently in development at CRAL. As without phase reference the problem is non convex, all these methods that rely on continuous optimization methods may end in some local optima. To provide a better estimate of the global optimum, some authors proposed stochastic methods: MACIM (Ireland et al. 2008) and SQUEEZE (Baron et al. 2010).

Although most beam combiners are now polychromatic only few of these methods (namely: PAINTER, MiRA3D and SQUEEZE) were specifically designed for such hyperspectral data. When dealing with multi-spectral data, a first possibility is to process each wavelength independently and reconstruct a monochromatic image for each subset of measurements from a given spectral channel. For instance, this is what have been done by le Bouquin et al. (2009) for the multi-spectral images of the Mira star T Lep. Another possibility is to exploit some assumed spectral continuity of $I(\lambda, \theta)$ and process the multi-spectral data globally to reconstruct an approximation of the 3-D distribution $I(\lambda, \theta)$. Although demonstrated in a different context of integral field spectral spectroscopy, this latter approach has proven to be more powerful (Soulez et al. 2011; Bongard et al. 2011).

In the continuation of our previous works (Thiébaut & Soulez 2012; Soulez & Thiébaut 2013), this paper briefly describes the MiRA-3D algorithm that exploits the advantages of a global multi-spectral processing of optical interferometric data.

3 The MiRA3D algorithm

In the *maximum a prosteriori* framework, the reconstructed image $\boldsymbol{x}$ is the solution the most probable according to some priors that fit the measurements $\boldsymbol{m}$. In other words, it is the best compromise between some priors on the observed object and the fidelity to the data. In MiRA3D, it is achieved by minimizing the sum of a regularization function f_{prior} and a likelihood function (*e.g.* the χ^2 for Gaussian errors). A "so-called" hyperparameter μ is necessary to adjust the compromise between the priors and the agreements to the measurements:

$$\boldsymbol{x}^+ = \operatorname*{arg\,min}_{\boldsymbol{x} \in \mathbb{X}} \mu \underbrace{f_{\mathsf{prior}}(\boldsymbol{x})}_{\text{regularization}} + \underbrace{f_{\mathsf{data}}(\boldsymbol{x}|\boldsymbol{m})}_{\text{likelihood}} \tag{3.1}$$

where $\mathbb{X}$ is the feasible set described by some strict physicaly based constraints: positivity and normalization:

$$\mathbb{X} = \{\boldsymbol{x} \in \mathbb{R}^n : \boldsymbol{x} \geq 0 \ ; \ \forall \lambda, \sum_k x_{k,\lambda} = 1.\} . \tag{3.2}$$

Unfortunately, in interferometry the non-linearity of the likelihood function and the constraints on the image make the direct minimization of Eq. (3.1) numerically cumbersome for classical optimization algorithm. To damper this problem, in MiRA 3D, we introduce two auxiliary variables $\boldsymbol{y}$ and $\boldsymbol{z}$ and solve:

$$\boldsymbol{x}^+ = \operatorname*{arg\,min}_{\boldsymbol{x}} \mu \, f_{\mathsf{prior}}(\boldsymbol{z}) + f_{\mathsf{data}}(\boldsymbol{y}|\boldsymbol{m}) \quad \text{s.t.} \begin{cases} \boldsymbol{y} & = \mathbf{H} \cdot \boldsymbol{x} \, , \\ \mathbf{A} \cdot \boldsymbol{x} & = \boldsymbol{z} \, , \\ \boldsymbol{z} & \geq 0 \, , \\ \sum_\lambda \boldsymbol{x} & = 1 \, . \end{cases} \tag{3.3}$$

where $\boldsymbol{y}$ is the vector of complex amplitudes involved in each measurement. It is linked to the image $\boldsymbol{x}$ by the non uniform Fourier operator $\mathbf{H}$. Depending on the priors $\boldsymbol{z}$ lies in the image domain (*i.e.*$\mathbf{A} = \mathbf{Id}$) or any other space linearly mapped by $\mathbf{A}$. For example, in the case of a classical quadratic smoothing priors acting on spatial gradient, $\mathbf{A}$ is a spatial derivative operator and $f_{\mathsf{prior}}(\boldsymbol{z}) = \|\boldsymbol{z}\|^2$. Written this way, the image reconstruction problem is split in 3 much simple problems that are alternatively solved using an Alternating Directing Method of Multiplier (ADMM) (Boyd et al. 2010).

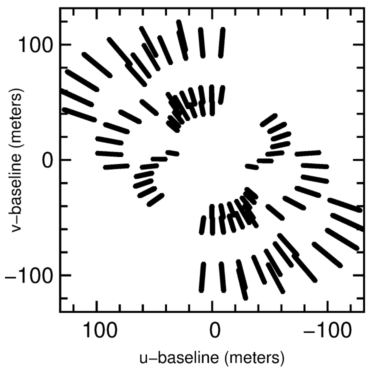

Fig. 1. (u, v) coverage

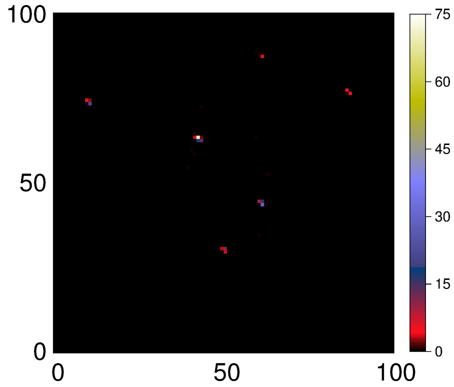

Fig. 2. Reconstructed image (spectraly integrated)

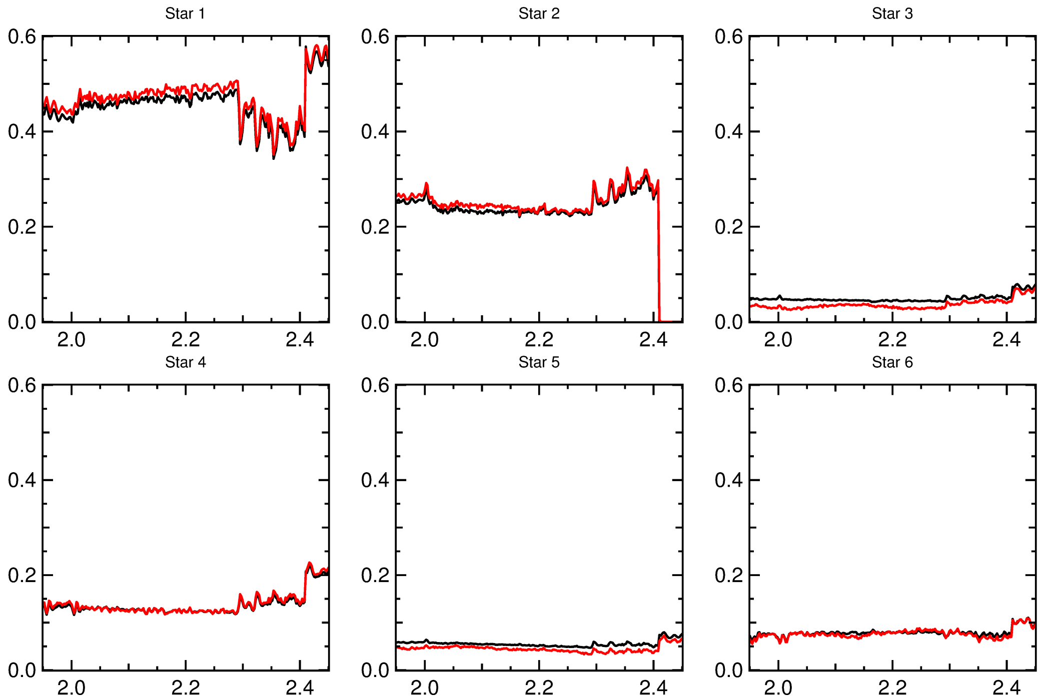

Fig. 3. Estimated (in black) and theoretical (in red) spectra for each 6 stars.

4 Results

4.1 The phase referenced case: GRAVITY

We have tested our method on a simulation of the VLTI GRAVITY instrument. In its phase referenced mode, it produces multispectral complex visibilities. These complex visibilities depend linearly of the intensity distribution, the reconstruction problem is then convex. The simulated data consists on six unresolved stars with different spectra observed by the 4 UTs with 240 spectral channels from 1.95 µm to 2.45 µm and 42 baselines (about 10080 complex visibilities). (u, v) coverage is presented Fig. 1.

We reconstruct an hyperspectral image with 240 spectral channels and 100×100 pixels of size 1×1 mas. The prior used is the joint (Fornasier & Rauhut 2008) sparsity that assumes that there are few sources and those sources are located at the same position. The reconstructed image spectraly integrated in the K band is shown Fig. 2. The six stars are recovered and there is not any false detection. The shape of each reconstructed star is due to the beam and its centroid indicated its position with an error lower than 0.15 mas. The 6 reconstructed spectra presented in Fig. 3 are very close to the theoretical spectra.

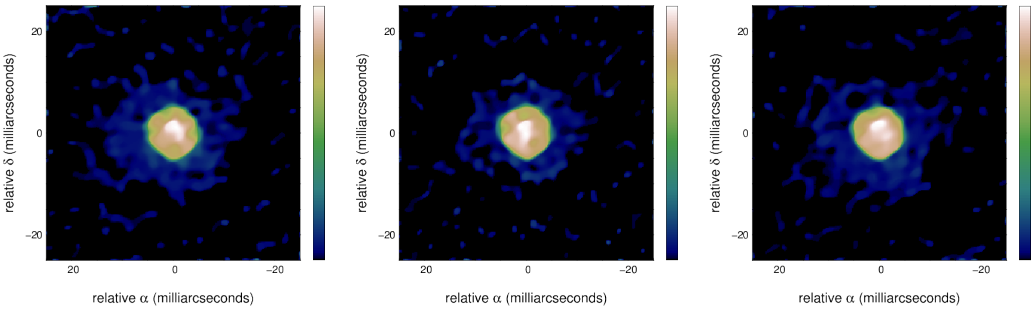

1.61 µm 1.67 µm 1.73 µm

Fig. 4. Reconstruction of the Mira star R Car for the three wavelengths of PIONIER

4.2 Without phase reference: PIONIER

In the context of the "2014 interferometric imaging beauty contest" (Monnier et al. 2014), we have reconstructed image of the oxygen rich Mira R Car. This data was acquired using PIONIER in the context of a technical run aiming at demonstrating VLTI imaging capability. PIONIER is the first four beams combiner of the VLTI. It provides powerspectra and closure phase in 3 spectral channels in H band. Contrary to the GRAVITY phase referenced case, the reconstruction problem is non convex. It is regularized using the multi-spectral total variation (Sapiro & Ringach 1996). This prior favors smooth objects while preserving sharp edges and favors colocalization of those edges along spectral dimension.

In the reconstructed image presented Fig. 4, the R Car object is composed of a disk of about 10 mas in diameter. This disk is not uniform and especially there is marginally resolved brighter spot (14 % brighter) of about 3 mas in width located 1 mas north of the center of the disk. This disk is surrounded by an approximately circular shell of about 22 mas in diameter. The optical thickness of this shell differs from one spectral channel to another, especially it seems to be more optically thin in the 1.67 µm than in the 1.61 µm.

The author thanks T. Paumard who provides the GRAVITY simulated data and J.P. Berger who provides the R Car data.

Our algorithm has been implemented and tested with YORICK (`http://yorick.sourceforge.net/`) which is freely available.

This work is supported by the POLCA project (*Percées astrophysiques grâce au traitement de données interférométriques polychromatiques* funded by the French ANR: ANR-10-BLAN-0511).

References

Baron, F., Monnier, J. D., & Kloppenborg, B. 2010, in SPIE Astronomical Telescopes+ Instrumentation, International Society for Optics and Photonics, 77342I–77342I

Baron, F. & Young, J. S. 2008, in SPIE Conference, Vol. 7013, 144

Bongard, S., Soulez, F., Thibaut, ., & Pcontal, E. 2011, Monthly Notices of the Royal Astronomical Society, 418, 258

Boyd, S., Parikh, N., Chu, E., Peleato, B., & Eckstein, J. 2010, Foundations and Trends in Machine Learning, 3, 1

Buscher, D. F. 1994, in IAU Symp. 158, ed. J. G. Robertson & W. J. Tango, 91–+

Fornasier, M. & Rauhut, H. 2008, SIAM Journal on Numerical Analysis, 46, 577

Hofmann, K., Weigelt, G., & Schertl, D. 2014, Astronomy & Astrophysics, 565, A48

Ireland, M. J., Monnier, J. D., & Thureau, N. 2008, in Proc. SPIE, Vol. 6268, 62681T

le Bouquin, J.-B., Lacour, S., Renard, S., Thibaut, ., & Merand, A. 2009, Astron. Astrophys., 496, L1

Meimon, S., Mugnier, L. M., & le Besnerais, G. 2005, Optics Letters, 30, 1809

Monnier, J. D., Berger, J.-P., Le Bouquin, J.-B., et al. 2014, in SPIE Astronomical Telescopes+ Instrumentation, 91461Q–91461Q

Sapiro, G. & Ringach, D. L. 1996, IEEE Trans. Image Process., 5, 1582

Schutz, A., Ferrari, A., Mary, D., et al. 2014, JOSA A, 31, 2334

Soulez, F. & Thiébaut, E. 2013, in Improving the performances of current optical interferometers, International Colloquium at haute provence observatory, St Michel l'observatoire, France, .

Soulez, F., Thibaut, ., Bongard, S., & Bacon, R. 2011, in 3rd IEEE WHISPERS, Lisbon, Portugal

Thiébaut, E. 2008, in Proc. SPIE, Vol. 7013, 70131I

Thiébaut, É. & Soulez, F. 2012, in SPIE Astronomical Telescopes+ Instrumentation, 84451C–84451C

Session 06

Réunion des utilisateurs des télescopes français de 2 mètres (TBL et OHP/193)

SF2A 2014
J. Ballet, F. Bournaud, F. Martins, R. Monier and C. Reylé (eds)

TELESCOPE BERNARD LYOT BEYOND NARVAL: NEO-NARVAL AND SPIP

R. Cabanac[1], TBL Team[1], Neo-Narval Team[1,2] and SPIP Team[2]

Abstract. The present communication describes two instruments proposed for Telescope Bernard Lyot...

Keywords: instrumentation, spectropolarimeter, Infrared, exoplanet formation, stellar magnetism

1 Introduction

The Pic du midi 2-m Telescope Bernard Lyot (TBL; 15 technical, 5 science staff) is a National Facility run by Observatoire Midi-Pyrnes (Univ. Toulouse, CNRS). Major upgrades of TBL large equipments (driving motors, dome, cooling plants, hydraulic systems) have been done in the past 5 years securing operations of the telescope until 2030. Since 2009, TBL offers 240 nights/year is full service mode to French and European (via OPTICON) communities. TBL has been housing the spectropolarimeter Narval since 2007 on a science case focussing on stellar magnetism accross the H-R diagram. The dedication of TBL to Narval has produced a highly efffective science return, and numerous pionneering studies on stellar magnetism (cf contributions in these proceedings, Users meeting session). Narval has now been used for 8 years under high pressure (> 2) with no sign of stalling for the coming years. In order to stimulate thinking on future instrumentation, TBL Science Council made a call for ideas in 2012. Two projects were proposed on complementary science cases. Neo-Narval (PI T. Boehm, IRAP) for the study of evolved stars and planets, SPIP (PI J.F. Donati, IRAP, co-PI G. HEBRARD, IAP) for the study of young planetary systems and the discovery of exo-earths. The 2014 INSU AA prospective fully supports the development of Neo-Narval and supports SPIP with recommendations of carefully phasing that development with other IR spectropolarimetric projects. The 2 instruments are briefly presented in sections 2 and 3.

2 Study of evolved systems: Neo-Narval

2.1 Neo-Narval Science Case

Neo-Narval science case* is around three main topics. The first topic is the study of evolved stars and planetary systems. In particular, more and more hot Jupiters are known to spiral in towards their host stars. Direct measurements of planet engulment will be at graps of Neo-Narval. Physics of evolved sub-giant to giant phases, and the fate and impact of magnetic fields at those phases will be probed. The second topics is a continuation of Narval science case on stellar magnetism studies accross the HR diagram where much needs to be done still to understand evolution on magnetic activity over years. And finally, Neo-Narval will be a unique instrument to study magnetic jitter in stars, and its impact on exoplanet detections.

2.2 Neo-Narval Overview

In order to achieve the proposed science goals, the science requirements are to reach a velocimetry stability of $<$3m/s, to perform polarimetry analyses in Stokes QUV over the visible spectrum 0.370-1μm at a resolution > 50000.

[1] OMP, 57, Ave. d'Azereix, 65000, TARBES
[2] OMP, 14, avenue Edouard Belin, 31400, TOULOUSE
*full science case at `http://www.tbl.obs-mip.fr/INSTRUMENTATION2/neonarval`.

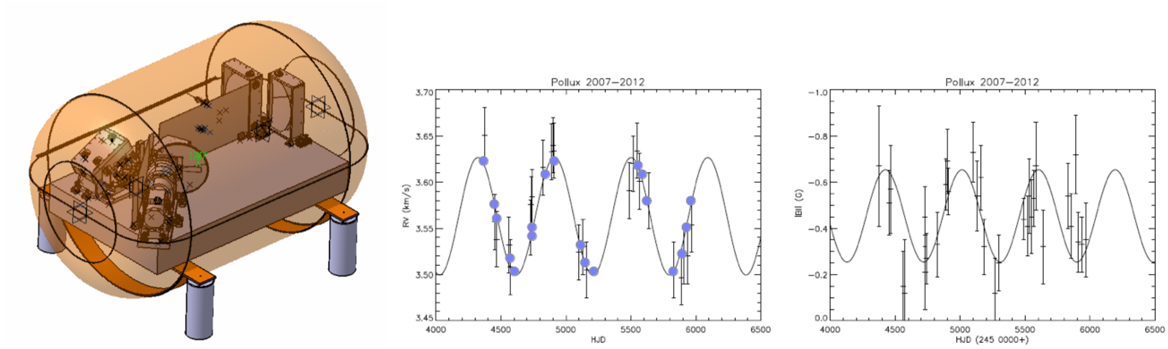

Fig. 1. Left: One design for Neo-Narval **Right:** Expected velocimetry improvement (filled circle) compared to existing Narval sensitivity, and magnetic jitter analysis on Pollux (cf science case).

Reaching the science requirements is possible using Narval with careful technical upgrades on the existing instrument. Those improvments are routinely implemented in SOPHIE, HARPS and other stabilized spectrographs around the world by teams who accepted to share their expertise with Neo-Narval technical team. Specifically one needs to stabilize the refraction index to 10^{-6} within the diffractive (grating) and refractive (crossdispersing prisms) optics of the spectrograph. One can show that stabilizing spectrograph temperature to 0.01K and volume V to $\rho_{gas}\Delta V/V < 10^{-6}$ will do, where ρ_{gas} is the enclosure gas density in bar. In turn, that can be achieved using isobaric and isothermal enclosures for the spectrograph, octogonal fiber injection for pupil stabilisation, and a realtime wavelength calibration (and velocimetry-optimized reduction pipeline). Additional upgrades will be necessary on Narval science camera (faster electronics, lower noise, Deeply depleted E2V chips) and on the polarimeter rhomboedra coders to improvment the instrument operation robustness and efficiency.

2.3 Neo-Narval implementation plan

The total budget (without human ressources) of the project is 500,000 euros. The technical team composed by IRAP, OMP, and TBL, with the expertise support of SOPHIE and HARPS teams. Neo-Narval is expected to have its first light in 2017. Funding is now secured from local sources (CPER 2015-2020). The current calendar proposes to finalize the enclosure designs in 2015, upgrade the camera, injection and polarimeter in 2015, start building an enclosure prototype in 2016-2017, for a final integration at the end 2017. A major constraint for Neo-Narval implementation is that Narval will observe continuously over 2015-2017, hence any upgrade to Neo-Narval shall have a minimal impact on TBL/Narval operations. TBL team, responsible of the integration, has a known expertise in phasing upgrades with minimal impact on observations.

3 Planet formation and young exo-Earth finder: SPIP

3.1 SPIP Science Case

SPIP science case[†] is challenging and clearly supports the future of Pic du midi beyond 2020. Being a copy of SPIRou (CFHT), SPIP covers the same topics over the brightest end of SPIRou targets. Namely, SPIP is build to explore new planetary systems close to the sun, and in particular exo-Earths orbiting the habitable zone around M dwarfs. A second hot topic probed by SPIP will be the formation of stars and their planetary systems. Models show that magnetic fields are paramount in young protoplanetary disks. Depending on their strength, magnetic field can seed or suppress planetoid formation. SPIP/SPIRou will be the first instruments able to gather observations of magnetic field in young protoplanetary systems. Finally, SPIP will perform detailled studies of evolved fully convective systems.

[†]full science case at `http://www.tbl.obs-mip.fr/INSTRUMENTATION2/spip`.

3.2 SPIP Overview

Science requirements of SPIP can be summarized as follows. A complete and simultaneous wavelength coverage of 0.98-2.35 μm (Y to K bands). A spectral resolution of 75000, a radial velocity precision of 1m/s. SPIP must perform a polarimetry analysis in all Stokes parameters QUV over the full spectral range (achromatic). It is expected to reach a sensitivity of S/N$\sim$100 per pixel of 2.3 km/s @ H=9.5.

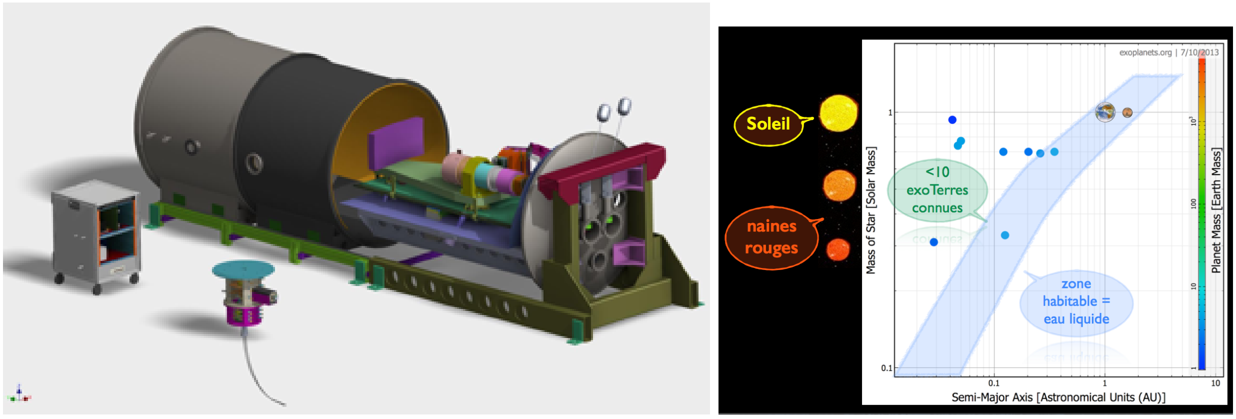

Fig. 2. Left: SPIP mechanical design **Right:** SPIP is expected to probe young planetary systems around young M stars

Contrary to Neo-Narval, reaching such requirements for SPIP required the development of a completely new instrumental concept now finalized for SPIRou, including a redesigned polarimeter and Cassegrain module using a high efficiency IR guiding camera, fluoride optical fibers connecting polarimeter and spectrograph, a new design for the image slicer, a spectrograph fully enclosed in a cryocooled vessel (operating Temperature 80 K, stabilized to mK) based on HARPS / Sophie. SPIP is expected to be an exact copy of SPIRou excepting for the entrance collimator adapted to TBL focal ratio and seeing.

3.3 SPIP implementation plan

SPIP budget is 4.5 million euros (hardware only). The budget for SPIP is not yet secured, and will probably shift from the current CPER to the next one (2021-2026), which makes full sense in terms of phasing Narval $\rightarrow$ Neo-Narval $\rightarrow$ SPIP. This shift also harmoniously fits the current technical schedule and commitments of OMP/IRAP technical teams. Duplication of an existing instrument is at grasp of TBL team, the previous experience with Narval has been fully successful. The success of SPIP integration will depend heavily on the support of SPIRou team. The human ressources will come from TBL, OMP and IRAP SPIRou team. Current first light for SPIP is now expected in 2022.

4 Conclusions

Thanks to the commitment of CNRS/INSU and Université de Toulouse to support funding and staff to TBL at Pic du midi, French astronomers still have access to a state-of-the-art facility. The proposed new instrumentation, a funded Neo-Narval and to-be-funded SPIP warrant a bright future for TBL over the coming decade. In addition to their own science cases, both instruments will play a strong role in support to space-based missions (GAIAI, TESS, CHEOPS, PLATO) and ground-based large facilities (ALMA, NOEMA, LOFAR, SKA). In addition to science, TBL offers a unique opportunity for training young astronomers in astronomical observations and service observing on a top-level observing facility.

References

Neo-Narval Science case, Boehm, T. et al., 2014, `http://www.tbl.obs-mip.fr/INSTRUMENTATION2/neonarval`

SPIP Science case, Donati, J.F. and Hebrard G., 2012, `http://www.tbl.obs-mip.fr/INSTRUMENTATION2/spip`

SF2A 2014
J. Ballet, F. Bournaud, F. Martins, R. Monier and C. Reylé (eds)

MUTUALIZED SERVICE FOR THE MANAGEMENT OF THE ASTRONOMICAL OBSERVATIONS AT THE TBL AND THE OHP

E. Cottalorda[1]

Abstract. This article proposes the creation of a mutualized service for the management of the astronomical observations at the TBL and the OHP, which objective would be to optimize the scientific management of the observations, by mutualizing manpower and financial means for the two national telescopes in France.

Keywords: astronomical observations / management of observation / french national telescopes

1 Introduction

The purpose of this service would be to optimize the management of astronomical observation for the Telescope Bernard Lyot (TBL) and the observatoire de Haute-Provence (OHP), by mutualizing manpower and financial means.

The main objctives guiding the mutualization would be:

- Optimize observation according to scientific goals, possibilities of telescopes and scientific instruments
- Maintain and develop scientific management of the observations for the french observatories at an international level.
- Extend the service to the french radio observatories.
- Work in narrow link with international observatories, in order to define and set up standards for scientific management of the observations.

2 Optimization of the use of telescopes

Many telescopes, potentially useful for international research, are currently under used in France. Actually, we notice a lack of human and financial means, to maintain intrumentations and telescopes , due to the french commitment in large international projects (ALMA,VLT, . . .). Moreover, there is a little demand for certain instruments, due to a misunderstanding of their possibilities, and to an offer of bigger and better placed telescopes.

Faced with that, the mutualized service would use students and PhD students to perform the service observations, to decrease the manpower cost; and it could promote the under used instruments towards the community, to look for practicable scientific projects on these instruments.

[1] TBL from 03/2008 to 12/2009

3 Optimization of the management of the astronomical observations

An administrative fragmentation has lead to a local vision to the detriment of a more global vision of the research. We can also observe that the non mutualized management of astronomical observations leads to difficulties, such as a non optimal planning of the observations in the framework of visitor mode, and to a lack of service observers and night technicians.

The mutualized service could solve some of this problems, by promoting a global vision of the observations and their scientific management. Indeed it could provide service observers, by confederating the forces in presence (service observers, PhD students, astronomers cnap . . .). So, the service observer could optimize the scientific planning of the night, according to the conditions of observation, rank of mission, and scientific goals.

4 Interest of the service

For the OSUs/universities, the interests of the mutualized service are to lean on specialized people for the scientific management of observations, and to fill the lack of staff in service observers and/or night technicians.

For the community, the interests of the mutualized service are to optimize the observations , and to save time of research for the researchers. The mutualized service could permit a better using of non used telescopes for scientific programs.

5 Conclusion

Faced to with the previous problems, we propose the creation of a mutualized service for the management of the astronomical observations, first of all just for the TBL and the OHP.

The service should have the following missions:

- Management of proposal requests .
- Management of proposals.
- Study of the technical and observationnelle feasibility for the proposals.
- Compute the statistic of observations and proposals.
- Organization of the committees of scientific selection, as well as the calendars of the various telescopes.

Thank you, particulary for Dr rémi Cabanac (director of TBL)!

Service mutualisé de gestion scientifique des observations au TBL et à l'OHP

Eric Cottalorda
cottalorda.eric@voila.fr — 06 50 01 40 62

Présentation du concept

Il s'agit de proposer la création d'un service mutualisé de gestion scientifique des observations, dont l'objectif serait d'optimiser la gestion scientifique des observations, en mutualisant les moyens humains et fianciers, dans le cadre des restrictions budgétaires.

Objectifs

Les objectifs imédiats d'un tel service seraient:

- Optimiser les observations: Selon les objectifs scientifiques, les possibilités des instruments et des télescopes, et les conditions d'observation.
- Maintenir et développer la gestion scientifique des observations des observatoires français à un niveau international.

Les objectifs à long terme d'un tel service seraient:

- Etendre le service aux observatoires radio.
- Travailler en lien étroit avec les grands observatoires internationaux, pour définir et mettre en place des normes pour la gestion des observations.

Présentation d'une séquence d'observation en mode service

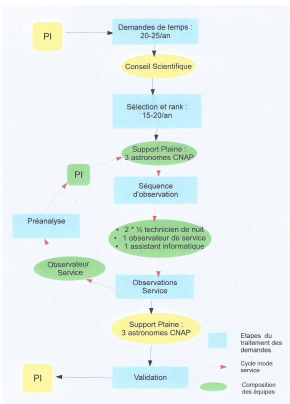

Figure 1: Séquence d'observation au TBL

Optimisation de l'utilisation des télescopes

Sous utilisation de télescopes

Un grand nombre de télescopes potentiellement utilisables pour une recherche de niveau international sous utilisés. Les causes principales en sont:

- Le manque de moyens (financiers et humains) nécessaires à leur entretien et à leur fonctionnement, principalement dû à l'engagement de la France dans de grands projets internationaux (VLT, ELT, etc...).
- Le peu de demandes de certains de ces instruments du à l'offre d'instruments, plus grands et mieux situés, et à une méconnaissance des possibilités des télescopes du réseau (le TBL du pic du midi et le T193 de l'observatoire de Haute-Provence n'arrivant pas à couvrir la demande).

Solutions contre la sous-utilisation

- Le service utiliserait des étudiants et thésards pour réaliser les observations de service, permettant ainsi une diminution du coût de la main d'oeuvre.
- Le service pourrait faire la promotion des instruments sous-utilisés vers la communauté, et rechercher des projets scientifiques réalisables sur ces intruments.

Optimisation de la gestion scientifique des observations

Difficultés de gestion scientifique des observations

La gestion scientifique non mutualisée pose un certain nombre de difficultés:

- Planification non optimale des observations, en terme de conditions d'observation et de possibilités des instruments, dans le cadre des observations en mode visiteur.
- Manque d'observateurs de service et/ou opérateurs.
- Fragmentation administrative, ayant pour conséquence une vision locale, au détriment d'une vision plus globale de la recherche.

Solutions pour optimiser la gestion scientifique des observations

- L'observateur de service peut optimiser la planification des observations de la nuit, en fonction des conditions d'observation, du rank de la mission, et des objectifs scientifiques.
- Le service pourrait assurer une présence en observateurs de service, en confédérant les forces en présence (Observateurs de service, thésards, stagiaires, astronomes CNAP).
- Le service permettrait de promouvoir une vision globale de la gestion scientifique des observations.

Missions du service

- Gestion des appels d'offres des télescopes.
- Gestion des demandes de temps des télescopes.
- Etude de la faisabilité technique et observationnelle des proposals sur la période demandée.
- Etablissement des statistiques sur les observations et les demandes de temps.
- ▷1. Organisation des comités de sélection scientifique, ainsi que des calendriers des différents télescopes.

Intérêts du service pour les OSUs/Universités

- S'appuyer sur des personnes spécialisées pour la gestion scientifique.
- Permettre de combler le manque d'effectifs en observateurs de service et/ou techniciens de nuits.

Intérêts du service pour la communauté

- optimiser les observations.
- Gain de temps de recherche pour les chercheurs.
- Permettre une meilleure utilisation des télescopes non utilisés pour des programmes scientifiques.

Présentation d'un organigramme du service mutualisé

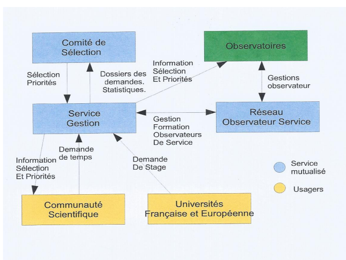

Figure 2: Exemple d'un organigramme du service mutualisé

Fig. 1. Poster

SF2A 2014
J. Ballet, F. Bournaud, F. Martins, R. Monier and C. Reylé (eds)

DERIVATION OF THE MASS RATIOS OF 20 NEW DOUBLE-LINED SPECTROSCOPIC BINARIES*

J.-L. Halbwachs[1], F. Arenou[2], D. Pourbaix[3], B. Famaey[1], P. Guillout[1], Y. Lebreton[2,4], J.-B. Salomon[1], L. Tal-Or[5], R. Ibata[1] and T. Mazeh[4]

Abstract. The secondary component was detected in the spectra of 20 systems which were previously single-lined spectroscopic binaries (SB1s) with known orbital elements. The mass ratio of each new double-lined spectroscopic binary (SB2) was derived through two methods: (1) computation of an SB2 orbit using the old measurements of the radial velocity in addition to the new ones, and, (2) direct computation of the mass ratio from the variations of the radial velocities of the components. Some results are presented here.

Keywords: binaries: spectroscopic

1 Introduction

The double-lined spectroscopic binaries (SB2s) are at the root of the less model–dependent methods used to derive the stellar masses. Their orbital elements are used to derive the products $\mathcal{M}_* \sin^3 i$, where $\mathcal{M}_*$ is the mass of a component and i is the inclination of the orbital plane. The astrometric measurements obtained with the Gaia satellite will make possible the derivation of i for a lot of astrometric binaries. In order to obtain accurate masses with Gaia, an observational program is on going since 2010 at the OHP observatory with the T193/Sophie instrument, in order to improve the orbital elements of a selection of known SBs (Halbwachs & Arenou 2009; Halbwachs et al 2014a,b). The selection included 152 SB1s, but an additional component was found for 25 of them, including 5 multiple systems. A preliminary list of SB2s newly discovered, including a rough estimation of the mass ratios, $q = \mathcal{M}_2/\mathcal{M}_1$, was presented in Halbwachs et al. (2011). Three years later, it is now possible to derive accurately q for all of the new SB2s. This is done hereafter, using two different methods: (a) the derivation of the spectroscopic orbital parameters, combining the newly obtained radial velocities (RVs) with old measurements of the primary components, and (b) derivation of q from the variations of the new RVs of the components.

2 Derivation of the spectroscopic orbital parameters

The number of radial velocity measurements obtained with Sophie is usually not sufficient to derive accurately the semi-amplitudes of the RV variations for both components. However, when the old measurements of the primary component are taken from the on–line SB9 catalogue (`http://sb9.astro.ulb.ac.be//`, Pourbaix et al. 2004), only three additional observations of the secondary component, taken at different phases, are required. The semi-amplitude of the RV of the secondary component was thus derived for 19 new SB2s. The calculation was not possible for one SB2, since the old measurements were never published. For the others, the mass ratio was derived from $q = K_1/K_2$.

---

* BASED ON OBSERVATIONS PERFORMED AT THE HAUTE-PROVENCE OBSERVATORY

[1] Observatoire Astronomique de Strasbourg, Université de Strasbourg, CNRS, UMR 7550, 11, rue de l'université, F-67000 Strasbourg, France

[2] GEPI, Observatoire de Paris, F-92195 Meudon, France

[3] FNRS, Institut d'Astronomie et d'Astrophysique, Université libre de Bruxelles, boulevard du Triomphe, 1050 Bruxelles, Belgium

[4] Institut de Physique de Rennes, Université de Rennes 1, CNRS UMR 6251, F-35042 Rennes, France

[5] School of Physics and Astronomy, Tel Aviv University, Tel Aviv 69978, Israel

3 Derivation of q from the RV variations of both components

Wilson (1941) has pointed out that the mass ratio may be directly obtained from a few measurements of the RVs of both components. It is given by the equation:

$$q = \Delta V_1 / \Delta V_2 \tag{3.1}$$

where ΔV is a variation of the RV of a component, in absolute value. Again, three RV measurements of both components are sufficient to derive q and its uncertainty, but the old measurements are not used. The results are presented in Halbwachs et al (2014a).

4 Comparison between the two methods

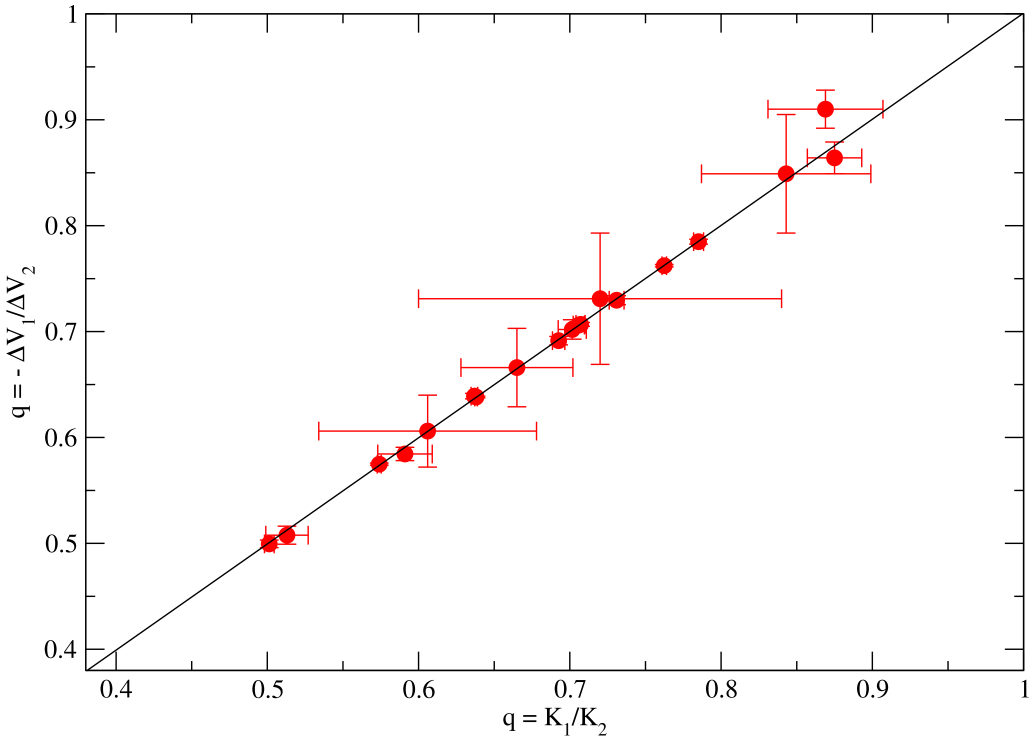

Fig. 1. The mass ratios derived from the variations of RV vs those coming from the semi-amplitudes K_1 and K_2.

The mass ratios obtained in Sect. 2 and 3 are compared in Fig. 1. As expected, they are quite similar, but the error bars of the latter method are a bit smaller than those of the former. The values of the mass ratios are between around 0.5 and around 0.9.

5 Properties of the new secondary components

In this section, we discuss why the secondary components of the 20 new SB2s were not detected before, when the old SB1 orbit were obtained with a spectrograph or with a spectrovelocimeter less efficient than Sophie. An examination of the cross-correlation function (CCF) of the spectra shows that the new SB2s may be classified in two categories:

- Systems with a small secondary dip (Fig. 2, left panel). The depth of the secondary dip is around 10 % of that of the primary, indicating that the secondary component is significantly fainter than the primary star. The mass ratio is then small (i.e. around 0.7 or less) when both components are on the main sequence, but it is large when the primary star is evolved.

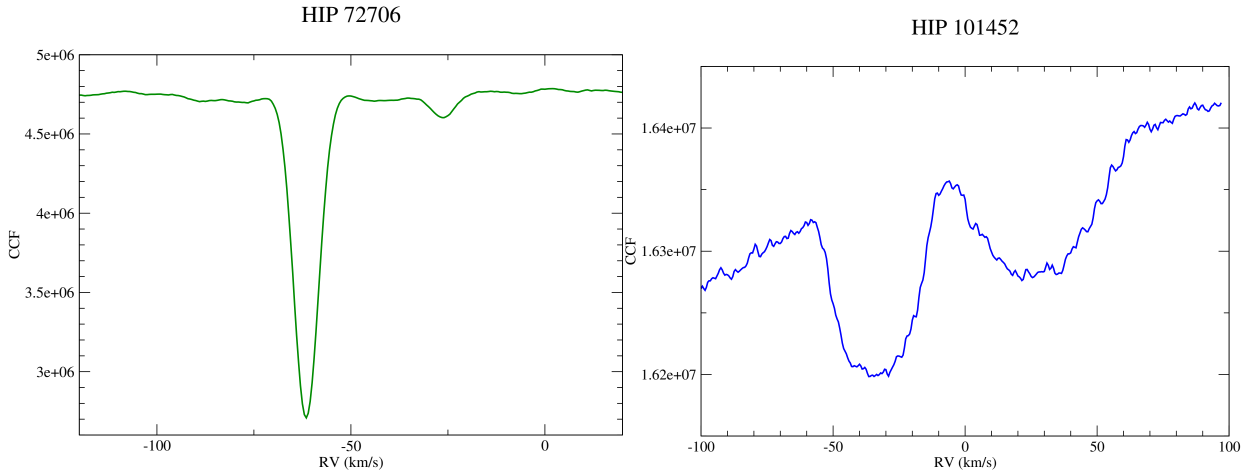

Fig. 2. Left: CCF of a newly discovered SB2 with a small secondary dip. **Right:** CCF of a new SB2 with very wide dips.

- Systems with very wide secondary dip (Fig. 2, right panel). The dips of both components of these systems are enlarged by a fast rotation. The lines of the secondary spectrum were too wide to be detected with an old spectrograph, or the secondary dip was too wide to be visible with a spectrovelocimeter like Coravel.

6 Conclusions

These 20 new SB2s illustrate the excellent capacity to find faint secondary components with the Sophie spectrograph. The methods used to derive the mass ratios and the results obtained for each star are fully developed in Halbwachs et al (2014a).

It is a pleasure to thank Dr X. Delfosse for helpful suggestions, and Prof. L. Lucy for providing a relevant reference. This project is supported by the french INSU-CNRS “Programme National de Physique Stellaire” and “Action Spécifique Gaia”. We are grateful to the staff of the Haute–Provence Observatory, and especially to Dr F. Bouchy, Dr H. Le Coroller, Dr M. Véron, and the night assistants, for their kind assistance. We used two facilities operated at CDS, Strasbourg, France: the Simbad object database and the VizieR catalogue database.

References

Halbwachs, J.-L., & Arenou, F. 2009, Proceedings SF2A 2009, M. Heydary–Malayeri, C. Reylé et R. Samadi édr., p. 53

Halbwachs, J.-L., Arenou, F., Famaey, B., Guillout, P., Lebreton, Y., & Pourbaix, D. 2011, Proceedings SF2A 2011 – G. Alecian, K. Belkacem, S. Collin, R. Samadi & D. Valls-Gabaud edr., 303

Halbwachs, J.-L., Arenou, F., Pourbaix, D., Famaey, B., Guillout, P., Lebreton, Y., Salomon, J.-B., Tal-Or, L., Ibata, R. & Mazeh, T. 2014a, MNRAS (accepted), arXiv:1409.1384

Halbwachs, J.-L., Arenou, F., Famaey, B., Guillout, P., Lebreton, Y., Ibata, R., Mazeh, T., Pourbaix, D., Salomon, J.-B. & Tal-Or, L. 2014b, this volume

Pourbaix, D., Tokovinin, A.A., Batten, A.H., Fekel, F. C., Hartkopf, W. I., Levato, H., Morell, N. I., Torres, G., & Udry, S. 2004, A&A 424, 727

Wilson, O.C. 1941, ApJ 93, 29

SF2A 2014
J. Ballet, F. Bournaud, F. Martins, R. Monier and C. Reylé (eds)

A SEARCH FOR VEGA-LIKE FIELDS IN OB STARS

C. Neiner[1], C. P. Folsom[2,3] and A. Blazere[1,2]

Abstract. Very weak magnetic fields (with a longitudinal component below 1 Gauss) have recently been discovered in the A star Vega as well as in a few Am stars. According to fossil field scenarios, such weak fields should also exist in more massive stars. In the framework of the ANR project Imagine, we have started to investigate the existence of this new class of very weakly magnetic stars among O and B stars thanks to ultra-deep spectropolarimetric observations. The first results and future plans are presented.

Keywords: stars: magnetic fields, stars: individual: γ Peg, stars: individual: ι Her

1 Introduction

The magnetic fields present in OBA stars are of fossil origin, i.e. they result from the seed field present in the molecular cloud from which the star was formed, rather than being produced by a currently active dynamo like in the Sun. This original field may have also been enhanced during the early phases of the life of the star, when it was fully convective, however such a dynamo early in the star's life is no longer active.

This fossil magnetic field relaxes onto a stable oblique mainly dipolar field detectable at the stellar surface (Duez et al. 2010). According to observations, this happens in ~10% of the OBA stars (e.g. Wade et al. 2014b). Fossil field scenarios predict that the remaining ~90% of OBA stars should host very weak fields, either because of a bifurcation between stable and unstable large-scale magnetic configurations in differentially rotating stars (Lignières et al. 2014) or because those 90% of stars did not reach a stable configuration yet (Braithwaite & Cantiello 2013). Such very weak fields were recently discovered in some A stars: Vega (Lignières et al. 2009), Sirius (Petit et al. 2011), and a few Am stars (see Blazere et al., these proceedings). They are called "Vega-like" fields.

In the frame of the ANR Imagine project, we aim to test the existence of such very weak fields in more massive (OB) stars.

2 First results

We have accumulated high resolution, high signal-to-noise spectropolarimetric Narval observations of the bright slowly rotating B2 star γ Peg. We analysed these observations using the Least-Squares Deconvolution (LSD) technique (Donati et al. 1997) to derive magnetic Zeeman signatures in spectral lines and the longitudinal magnetic field. With a Monte Carlo simulation we derived the maximum strength of the field possibly hosted by γ Peg. We found that no magnetic signatures are visible in the very high quality spectropolarimetric data. The average longitudinal field measured in the Narval data is $B_l = -0.1 \pm 0.4$ G (see Fig. 1; Neiner et al. 2014). The precision we reached is thus similar to the one used for the field detection in A stars. We derive a very strict upper limit on the strength of any dipolar field possibly hidden in the noise of our data of $B_{\rm pol} \sim 40$ G.

A similar study on the B3 star ι Her was performed with high resolution, high signal-to-noise spectropolarimetric ESPaDOnS data (Wade et al. 2014a). The same analysis technique was used. No Zeeman signatures were detected in the Stokes V profiles. The longitudinal magnetic field in the average profile was measured to

[1] LESIA, Observatoire de Paris, CNRS UMR 8109, UPMC, Université Paris Diderot, 5 place Jules Janssen, 92190 Meudon, France
[2] IRAP, CNRS/Université de Toulouse, 14 avenue E. Belin, 31400 Toulouse, France
[3] IPAG, UJF-Grenoble 1/CNRS-INSU, UMR 5274, 38041 Grenoble, France

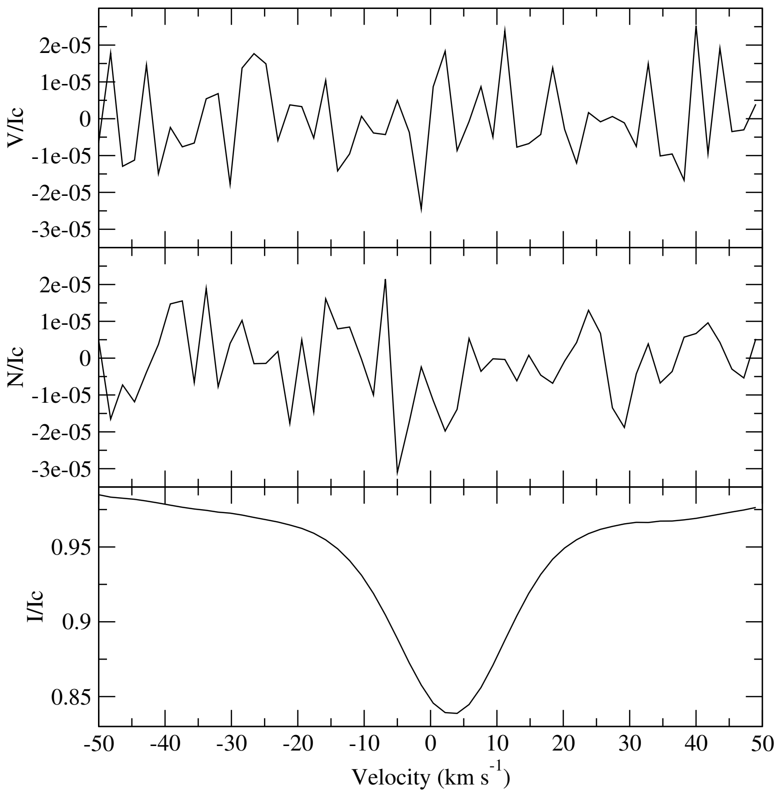

Fig. 1. LSD Stokes V (top), Null polarisation (middle) and I profiles (bottom) of γ Peg. Stokes V shows no magnetic signature. Taken from Neiner et al. (2014).

be $B_l = -0.2 \pm 0.3$ G. Again, the precision is similar to the one used for the field detection in A stars. An upper limit of the dipolar field strength of $B_{pol} \sim 8$ G is derived by Wade et al. (2014a). However, note that their method for extracting dipolar field upper limits is less conservative than the one we used for γ Peg.

From these two studies we conclude that no magnetic field is detected in either of the two B stars, despite having reached a precision of the longitudinal magnetic field measurement similar to the one used to detect very weak fields in A stars.

3 Detectability of Vega-like fields in OB stars

To check the detectability of Vega-like fields in OB stars, we can compare the observations of γ Peg and ι Her with synthetic Stokes V profiles corresponding to the surface magnetic field strength and geometry of Vega, but computed for the spectral characteristics of γ Peg and ι Her. For this we used the magnetic maps of Vega from Petit et al. (2010), with model line parameters and $v \sin i$ corresponding to our observations of γ Peg and ι Her. Since the inclination of the rotation axis is not known for either star, two test values were used.

The results for ι Her were presented in Wade et al. (2014a). They conclude that is is unlikely a magnetic field identical to Vega's field would have been detected, unless the observations were made from a particularly favorable angle. However, they also conclude that a magnetic field with the same geometry but $\sim$4 times stronger would almost certainly have been detected.

Here we present the maps of the magnetic field (Fig. 2) and Stokes V line profiles (Fig. 3) we would have observed if γ Peg hosted the same field as Vega, either with the same inclination angle as Vega ($i = 7°$), or with $i = 45°$. Since the rotation period of γ Peg is unknown, and our observations (distributed over one month) likely cover several rotational cycles, we consider a rotationally averaged model line profile. For γ Peg we find similar results to ι Her: a magnetic field identical to Vega's field is unlikely to have been detected, but one $\sim$4 times stronger would have likely been detected.

We conclude that, to detect a field like the one of Vega but on an early B star, we would need to measure longitudinal fields with a precision of 0.1 G (rather than 0.3-0.4 G reached for ι Her and γ Peg and sufficient

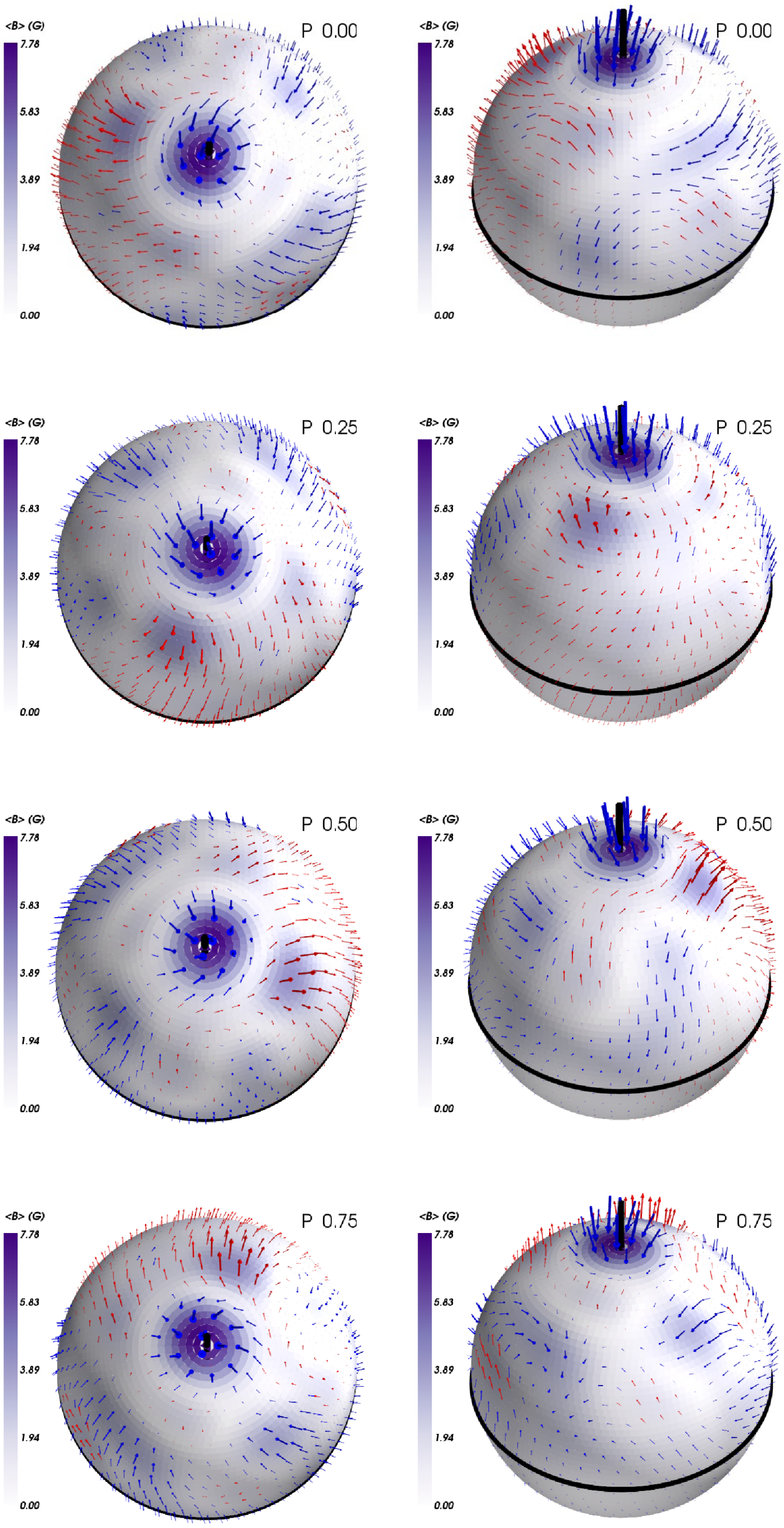

Fig. 2. Maps of the field of Vega applied to γ Peg as seen at various phases (top to bottom) and under two different inclination angles. **Left:** i=7° as for Vega. **Right:** i=45°.

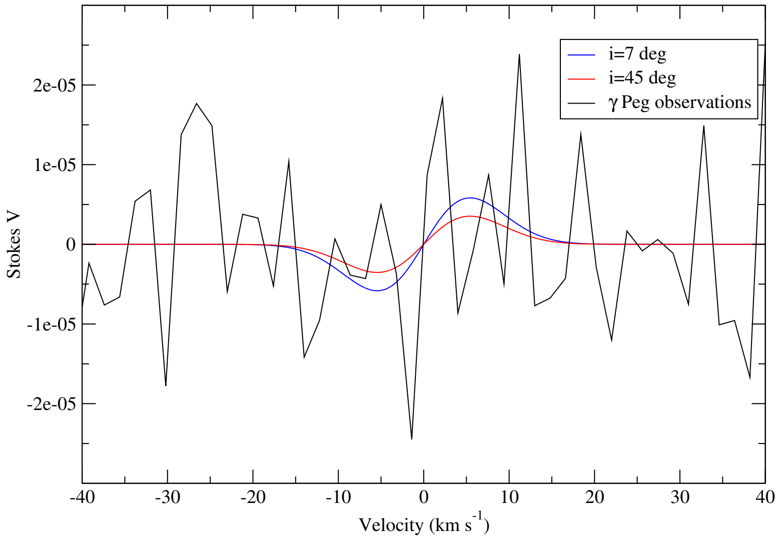

Fig. 3. Expected (rotationally averaged) Stokes V profile if γ Peg hosted a magnetic field identical to that of Vega, for two different inclination angles, compared to the mean observed profile.

for A stars). While it is unlikely we would have detected a magnetic field identical to Vega's field on γ Peg or ι Her, we would have likely detected a field with a peak strength approximately four times as strong as that of Vega. The precision required for O stars is probably even higher.

4 Future work and conclusions

To investigate the presence of Vega-like fields in OB stars, it will be necessary to reach a precision on the longitudinal field measurements of at least 0.1 G. This will require the co-addition of many Narval, ESPaDOnS or HarpsPol observations to reach a huge signal-to-noise, i.e. it will require a large amount of telescope time for each target. We will thus very carefully select the best O and B targets and propose observations of only a few optimal stars.

In this way we will test the existence of a new class of very weakly magnetic stars, currently only observed among A stars, and characterise it. The existence of this new class of objects among all OBA stars would lead to a revolution similar to the one we underwent 15 years ago with the discovery of intermediate fields in OB stars.

This work is supported by the ANR Imagine project. This research has made use of the SIMBAD database operated at CDS, Strasbourg (France), and of NASA's Astrophysics Data System (ADS).

References

Braithwaite, J. & Cantiello, M. 2013, MNRAS, 428, 2789

Donati, J.-F., Semel, M., Carter, B. D., Rees, D. E., & Collier Cameron, A. 1997, MNRAS, 291, 658

Duez, V., Braithwaite, J., & Mathis, S. 2010, ApJ, 724, L34

Lignières, F., Petit, P., Aurière, M., Wade, G. A., & Böhm, T. 2014, in IAU Symposium, Vol. 302, IAU Symposium, 338

Lignières, F., Petit, P., Böhm, T., & Aurière, M. 2009, A&A, 500, L41

Neiner, C., Monin, D., Leroy, B., Mathis, S., & Bohlender, D. 2014, A&A, 562, A59

Petit, P., Lignières, F., Aurière, M., et al. 2011, A&A, 532, L13

Petit, P., Lignières, F., Wade, G. A., et al. 2010, A&A, 523, A41

Wade, G. A., Folsom, C. P., Petit, P., et al. 2014a, MNRAS, 444, 1993

Wade, G. A., Grunhut, J., Alecian, E., et al. 2014b, in IAU Symposium, Vol. 302, IAU Symposium, 265

Session 07

Herschel: le bilan en planétologie (système solaire et disques de débris)

SF2A 2014
J. Ballet, F. Bournaud, F. Martins, R. Monier and C. Reylé (eds)

RESOLVING THE INCONSISTENCY BETWEEN THE ICE GIANTS AND COMETARY D/H RATIOS

Mohamad Ali-Dib[1], Olivier Mousis[1], Jean-Marc Petit[1] and Jonathan I. Lunine[2]

Abstract. The properties and chemical compositions of giant planets strongly depend on their formation locations. The formation mechanisms of the ice giants Uranus and Neptune, and their elemental and isotopic compositions, have long been debated. The density of solids in the outer protosolar nebula is too low to explain their formation within a timescale consistent with the presence of the gaseous protoplanetary disk, and spectroscopic observations show that both planets are highly enriched in carbon, very poor in nitrogen, and the ices from which they originally formed might had deuterium-to-hydrogen ratios lower than the predicted cometary value, unexplained properties observed in no other planets. Here we show that all these properties can be explained naturally if Uranus and Neptune both formed at the carbon monoxide iceline location, namely the region where this gas condensates in the protosolar nebula. This outer region of the protosolar nebula intrinsically has enough surface density to form both planets from carbon-rich solids but nitrogen-depleted gas, in abundances consistent with their observed values. Water rich interiors originating mostly from transformed CO ices reconcile the D/H value observed in Uranus and Neptune with the cometary value.

Keywords: Planets formation, Uranus, Neptune, volatiles enrichment

1 Introduction

Uranus and Neptune are the outermost planets of the solar system. Dynamical evolution simulations show that they should have formed in the cold outer protosolar nebula (hereafter PSN), in contrast with Jupiter and Saturn that formed in the inner relatively warm regions (Gomes et al. 2005; Morbidelli et al. 2005; Tsiganis et al. 2005). This poses the problem of how did large density of solids exist that far out in the disk, since it is thought to decrease with the inverse heliocentric distance (Pollack et al. 1996). A large solids surface density is needed to form the planetary cores quickly enough to accrete gas in the currently accepted models of cores formation (Helled & Bodenheimer 2014).

With atmospheric C/H ratios measured to be enhanced by factors of $\sim$30 to 60 times the solar value (Fegley et al. 1991), both planets appear highly enriched in carbon. In comparison, the C/H ratios in Jupiter and Saturn have been measured to be about 4 and 7 times the solar value respectively (Wong et al. 2004; Fletcher et al. 2009), and are thought to be consistent with some core-accretion formation models.

The nitrogen abundance is also surprising, since both planets have very low N/H ratios ($\sim$ 1% of the solar value) (de Pater & Richmond 1989; de Pater et al. 1989; Gautier & Owen 1989). Jupiter and Saturn on the other hand are enriched in nitrogen by a factor $\sim$ 4 compared to the solar value (Wong et al. 2004; Fletcher et al. 2009). This large difference motivated several studies that tried to explain the N depletion in Uranus and Neptune, with little success (Fegley et al. 1991; Atreya et al. 1995). This differential enrichment found in Uranus and Neptune, in contrast with the uniformly enriched Jupiter and Saturn, hints to different formation mechanisms.

[1] Université de Franche-Comté, Institut UTINAM, CNRS/INSU, UMR 6213, Besançon Cedex, France
[2] Center for Radiophysics and Space Research, Space Sciences Building, Cornell University, Ithaca, NY 14853, USA

The Deuterium to Hydrogen (D/H) ratio, strongly temperature dependent and considered an indicator of ices formation location, is also problematic for Uranus and Neptune. This ratio was measured in both atmospheres. These measurements were coupled to planets interiors models (Helled et al. 2011) to obtain the D/H ratios for the original water proto-ices that contributed in forming the planets (hereafter proto-ices). By making the assumption that the water in their interiors originated entirely from nebular H_2O ice, its D/H value was found $\sim$ 6 times lower than the cometary values (Feuchtgruber et al. 2013). This is surprising because Uranus and Neptune are supposed to have formed in the region of the comets and thus their proto-ices should have cometary D/H. This led to speculations on the origin of their proto-ices and the interiors of Uranus and Neptune (Feuchtgruber et al. 2013).

2 Qualitative solution

We explain all these unique properties at once with our scenario where Uranus and Neptune form at the CO iceline. An iceline is a region in protoplanetary disks where the temperature becomes sufficiently low for a specific species to condense into ices. The CO condenses at $\sim$ 25 K (Fray & Schmitt 2009), placing its iceline in the outer disk at $\sim$ 30 AU (Qi et al. 2013). The surface densities of the solids are known to increase substantially on icelines due to the outward diffusion and the subsequent condensation of the inner disk vapor at the narrow iceline location (Stevenson & Lunine 1988). Since CO is the major C-bearing volatile in the PSN (Prinn 1993), its iceline should be very rich in solids. This implies that planets forming in this region should be very rich in carbon.

On the other hand the iceline for N_2 (the major N bearing species in PSNs (Prinn 1993)) is located slightly outward of the CO iceline (Fray & Schmitt 2009). The proximity of the two icelines leads to a natural depletion in N_2 vapor at the CO iceline since the vapor diffusion depletes the area immediately inward of an iceline more quickly than that further away (Stevenson & Lunine 1988). Therefore planets forming at the CO iceline should also be significantly depleted in nitrogen, compared to the solar N/H abundance.

Finally, coupling the D/H observations in Uranus and Neptune with our model where only a small fraction of the water present in the planets interiors is of nebular origin, and the rest originating from the conversion of CO into H_2O, leads to a higher D/H ratio for the proto-ices that formed the planets. The value found is compatible with internal structure models and the formation location of the planets in the same region as comets.

3 Quantitative discussion

To quantify this scenario, we used a dynamical volatiles transport and distribution model tracking the evolution of CO and N_2 solids and vapor in a standard model of the PSN (Hueso & Guillot 2005). This model (Ali-Dib et al. 2014) takes into account the major dynamical and thermodynamical effects relevant to volatiles: turbulent gas drag (Stepinski & Valageas 1996; Hughes & Armitage 2010) and sublimation (Supulver & Lin 2000) for solids, in addition to gas diffusion (Stevenson & Lunine 1988) and condensation (Ros & Johansen 2013) for vapors. A simulation (Ali-Dib et al. 2014) starts with matter distributed homogeneously throughout the PSN with CO and N_2 abundances set to the C and N solar abundances, respectively. Solids are assumed to be decimetric pebbles (Ros & Johansen 2013) at their respective iceline. Inside the icelines there is only vapor. Since the sublimation temperatures for CO and N_2 are respectively 25 and 24 K (Fray & Schmitt 2009), their icelines are located in our model at 28 and 32 AU. The exact sublimation temperature of these ices does not affect our scenario, it is only the difference between the two temperatures that is key to our results. The model then tracks the subsequent evolution of the system as a function of time and location.

The distribution of volatiles is controlled by the balance of two important effects: the outward diffusion of the gas and the ices inward migration followed by sublimation. The diffusion is induced by the concentration gradient due to the existence of the iceline, and the inward drift is caused by the solid particles losing energy due to gas friction. In our model the diffusion of vapor is shown to be much faster than its replenishment inside the icelines by sublimating ices. This leads to depletion in vapors inside the icelines and concentration of solids at the iceline positions. Figure 1 represents the evolution of CO and N_2 vapors inside their respective icelines. In 1.6×10^5 years, there is very little vapor left inside the icelines. All the missing vapor has been condensed into

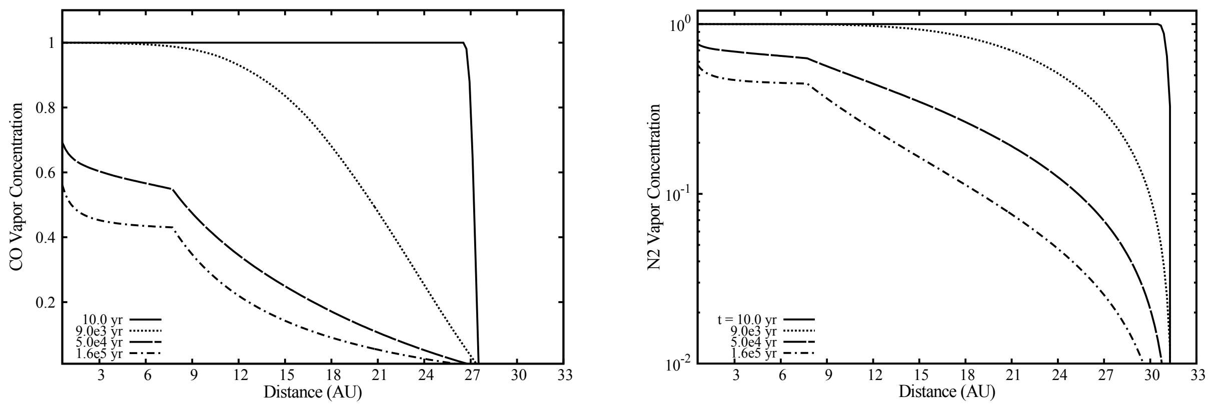

Fig. 1. Vapors concentrations of CO (left panel) and N_2 (right panel). The concentrations are normalized with respect to solar value. Vapors evolution is tracked inside their respective icelines as a function of time and distance to the star. In both cases there is a gradual location dependent depletion in the concentration due to gas diffusion being faster than replenishment through solid particles drift. N_2 is depleted by up to two orders of magnitude on the CO iceline.

solids at the icelines. Figure 2 shows the evolution of solid CO normalized density as a function of time in the region near the iceline where all the CO ices concentrated. This solids density increases along with the decrease in the CO vapor concentration. In 1.6×10^5 years the surface density at the CO iceline increases to a minimum of $\sim$ 12 g cm^{-2}, a value consistent with the estimations of the density of solids needed to form the cores of Uranus and Neptune (Dodson-Robinson & Bodenheimer 2010). After core formation and the subsequent gas envelope accretion (Pollack et al. 1996), the accreted CO will dissolve and transform into gaseous H_2O and CH_4, resulting in the observed highly enriched atmospheric gaseous CH_4. Hence, the C/H and O/H ratios increases to $\sim 52\times$ solar value. The predicted C/H value matches the measured values (Fegley et al. 1991; Baines et al. 1995) and the O/H ratio is consistent with observations, provided that the CO observed in the upper stratosphere of both planets comes primarily from an external source, a scenario consistent with recent observations (Luszcz-Cook & de Pater 2013; Cavalié et al. 2014; Irwin et al. 2014). Figure 1b shows that at CO iceline location, N_2 vapor is depleted by a factor up to 100 with respect to solar value. This implies that any planet forming in this region should be impoverished in nitrogen by factors similar to these inferred in Uranus and Neptune.

To calculate the proto-ices D/H ratio in a manner consistent with Uranus and Neptune internal structures, previous works supposed that primordial water ice (and thus with cometary D/H value) represents up to $\sim$ 90% of the planets mass (Helled et al. 2011). This required the value of the to proto-ices D/H to be $\sim 5\times10^{-5}$ (Feuchtgruber et al. 2013), a value a factor 5 (and can get up to an order of magnitude in some models) lower than the average cometary D/H value of $\sim 2-4\times10^{-4}$ (Feuchtgruber et al. 2013). There is no obvious reason why this should have been so. Using the observed planetary D/H for Uranus and Neptune, we perform the same calculations but assuming that most of the H_2O in the interior has CO as origin and is thus irrelevant to D/H calculations. By restricting the contributing proto-ices to solar H_2O abundance, we obtained D/H(proto-ices) $\sim$ 3.7 and 4.1×10^{-4} respectively for Uranus and Neptune, very close to the average cometary D/H ratio. Our scenario is found consistent with the dynamical models of the solar system evolution.

Finally, our scenario follows on from previous models (Stevenson & Lunine 1988), where Jupiter is formed on the H_2O iceline, a hypothesis to be firmly tested by *Juno*. It expands this hypothesis to other planets and shows how this mechanism can solve certain long standing problems.

References

Ali-Dib, M., Mousis, O., Petit, J.-M., & Lunine, J. I. 2014, ApJ, 785, 125

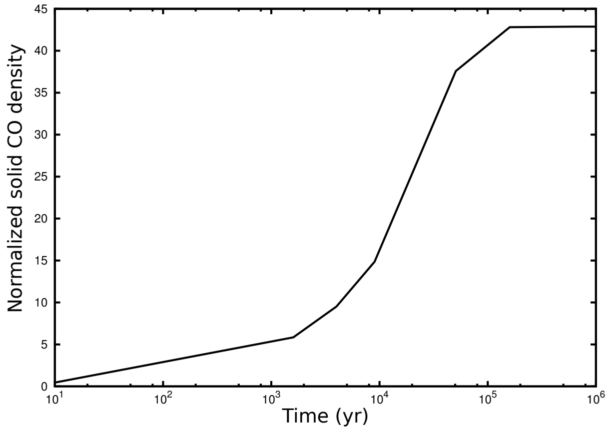

Fig. 2. The density of solid CO at its iceline. The density is normalized with respect to solar value. Solid CO density increase as a function of time due to vapor diffusion from the inner nebula. In 2×10^5 years, The density and chemical composition of this region becomes compatible with Uranus and Neptune.

Atreya, S. K., Edgington, S. G., Gautier, D., & Owen, T. C. 1995, Earth Moon and Planets, 67, 71

Baines, K. H., Mickelson, M. E., Larson, L. E., & Ferguson, D. W. 1995, Icarus, 114, 328

Cavalié, T., Moreno, R., Lellouch, E., et al. 2014, A&A, 562, A33

de Pater, I., & Richmond, M. 1989, Icarus, 80, 1

de Pater, I., Romani, P. N., & Atreya, S. K. 1989, Icarus, 82, 288

Dodson-Robinson, S. E., & Bodenheimer, P. 2010 Icarus, 207, 491

Fegley, B., Jr., Gautier, D., Owen, T., & Prinn, R. G. 1991, Uranus, 147

Feuchtgruber, H., Lellouch, E., Orton, G., et al. 2013, A&A, 551, A126

Fray, N., & Schmitt, B. 2009, Planet. Space Sci., 57, 2053

Fletcher, L. N., Orton, G. S., Teanby, N. A., Irwin, P. G. J., & Bjoraker, G. L. 2009, Icarus, 199, 351

Gautier, D., & Owen, T. 1989, Origin and Evolution of Planetary and Satellite Atmospheres, 487

Gomes, R., Levison, H. F., Tsiganis, K., & Morbidelli, A. 2005, Nature, 435, 466

Helled, R., Anderson, J. D., Podolak, M., & Schubert, G. 2011, ApJ, 726, 15

Helled, R., & Bodenheimer, P. 2014, arXiv:1404.5018

Hueso, R., & Guillot, T. 2005, A&A, 442, 703

Hughes, A. L. H., & Armitage, P. J. 2010, ApJ, 719, 1633

Irwin, P. G. J., Lellouch, E., de Bergh, C., et al. 2014, Icarus, 227, 37

Luszcz-Cook, S. H., & de Pater, I. 2013, Icarus, 222, 379

Morbidelli, A., Levison, H. F., Tsiganis, K., & Gomes, R. 2005, Nature, 435, 462

Pollack, J. B., Hubickyj, O., Bodenheimer, P., et al. 1996, Icarus, 124, 62

Prinn, R. G. 1993, Protostars and Planets III, 1005

Qi, C., Öberg, K. I., Wilner, D. J., et al. 2013, Science, 341, 630

Ros, K., & Johansen, A. 2013, A&A, 552, A137

Stepinski, T. F., & Valageas, P. 1996, A&A, 309, 301

Stevenson, D. J., & Lunine, J. I. 1988, Icarus, 75, 146

Supulver, K. D., & Lin, D. N. C. 2000, Icarus, 146, 525

Tsiganis, K., Gomes, R., Morbidelli, A., & Levison, H. F. 2005, Nature, 435, 459

Wong, M. H., Mahaffy, P. R., Atreya, S. K., Niemann, H. B., & Owen, T. C. 2004, Icarus, 171, 153

SF2A 2014
J. Ballet, F. Bournaud, F. Martins, R. Monier and C. Reylé (eds)

THE ORIGIN OF EXTERNAL OXYGEN IN JUPITER AND SATURN'S ENVIRONMENTS

T. Cavalié[1], E. Lellouch[2], P. Hartogh[1], R. Moreno[2], F. Billebaud[3, 4], D. Bockelée-Morvan[2], N. Biver[2], T. Cassidy[5], R. Courtin[2], J. Crovisier[2], M. Dobrijevic[3,4], H. Feuchtgruber[6], A. González[7], T. Greathouse[8], C. Jarchow[1], M. Kidger[9], L. M. Lara[7], M. Rengel[1], G. Orton[10], H. Sagawa[11] and M. de Val-Borro[12]

Abstract. This paper reviews the recent findings of the Herschel Solar System Observations Key Program (Hartogh et al. 2009b), as well as ground-based supporting observations, regarding the origin of external oxygen in the environments of Jupiter and Saturn. Herschel-HIFI and PACS observations have been used to shown that the Shoemaker-Levy 9 comet is the source of Jupiter's stratospheric water, and that Enceladus (and its geysers) are most probably the source of water for Saturn and Titan.

Keywords: Jupiter, Saturn, Titan – Atmospheres – Herschel

1 Introduction

The detection of H_2O and CO_2 in the stratospheres of the Giant Planets and Titan with the Infrared Space Observatory in the late 1990s (Feuchtgruber et al. 1997; Coustenis et al. 1998) raised the question of the origin of oxygen compounds in their upper atmospheres. Oxygen-rich deep interiors of the Giant Planets cannot explain this discovery because these species are trapped by condensation below their tropopauses (except CO_2 in Jupiter and Saturn). So, these species must come from external sources, which can be: (i) a permanent flux from interplanetary dust particles (IDP) produced from asteroid collisions and comet activity (Prather et al. 1978), (ii) local sources from planetary environments (icy rings and satellites) (Strobel & Yung 1979; Connerney 1986; Prangé et al. 2006), and/or (iii) cometary Shoemaker-Levy 9 type impacts (Lellouch et al. 1995). Disentangling the various sources at Jupiter and Saturn was a key objective of the Herschel key program HssO (Herschel Solar System Observations) (Hartogh et al. 2009b). In this paper, we will review the recent results obtained with Herschel-HIFI and -PACS (Pilbratt et al. 2010; de Graauw et al. 2010; Poglitsch et al. 2010) on the origin of external oxygen in Jupiter and Saturn's environments. These results are presented in more details in Cavalié et al. (2013), Hartogh et al. (2011), and Moreno et al. (2012).

[1] Max-Planck-Institut für Sonnensystemforschung, 37077, Göttingen, Germany
[2] LESIA, Obs. Paris, Meudon, France
[3] Univ. Bordeaux, LAB, UMR 5804, 33270 Floirac, France
[4] CNRS, LAB, UMR 5804, 33270 Floirac, France
[5] Laboratory for Atmospheric and Space Physics, University of Colorado, Boulder, USA
[6] Max-Planck-Institut für extraterrestrische Physik, Garching, Germany
[7] Instituto de Astrofísica de Andalucía (CSIC), Granada, Spain
[8] Southwest Research Institute, San Antonio, USA
[9] Herschel Science Centre, European Space Astronomy Centre, Madrid, Spain
[10] Jet Propulsion Laboratory, Pasadena, USA
[11] Kyoto Sangyo University, Kyoto, Japan
[12] Department of Astrophysical Sciences, Princeton University, Princeton, USA

2 Jupiter

Observations carried out in the late 1990s have shown that CO* and CO_2 have been delivered by the Shoemaker-Levy 9 (SL9) comet impacts in Jupiter's southern hemisphere in July 1994 (Bézard et al. 2002; Lellouch et al. 2002). Despite a number of converging indications that H_2O in Jupiter also originates from the SL9 event, the direct proof, i.e., the evidence for spatial variations of H_2O in Jupiter, was missing prior to Herschel (Bjoraker et al. 1996; Bergin et al. 2000; Lellouch et al. 2002; Cavalié et al. 2008, 2012).

Water has been mapped in Jupiter with the Wide Band Spectrometer (WBS) of HIFI on July 7, 2010, at 1669.9 GHz (179.5 μm).In addition, a water map at 66.44 μm (= 4512 GHz) has been obtained with the 5×5 receiver array of PACS on December 15, 2010. A full description of the HIFI and PACS data reduction is given in Cavalié et al. (2013). The observed lines depend on both the stratospheric temperature and H_2O abundance. This is why temperature was monitored with the NASA Infrared Telescope Facility (IRTF) in parallel.

The HIFI and PACS observations show consistently that the emission was stronger in the southern hemisphere of the planet. All lines have been modeled with a 1D radiative transfer code detailed in Cavalié et al. (2008, 2014). Both temperature and abundance variability has been investigated. Stratospheric temperature maps have been compared to the IRTF observations and they are in disagreement. Therefore, temperature is not the cause of the hemispherical asymmetry seen in the water emission. It is then due to an asymmetry in the water latitudinal distribution. The HIFI and PACS maps show consistently that there is 2-3 times more water in Jupiter's southern hemisphere than in its northern hemisphere (see Fig. 1). This is thus interpreted as a an aftermath of the SL9 impacts of 1994 that occurred at 44°S. An IDP source should have produced a more uniform distribution. Moreover, the spectrally resolved HIFI lines enable to constrain the vertical distribution of the bulk of stratospheric water. It is found that water resided at pressures p <2 mbar, also in agreement with expectations from a comet impact in 1994 (Moreno et al. 2003) and in disagreement with an IDP source (Cavalié et al. 2012).

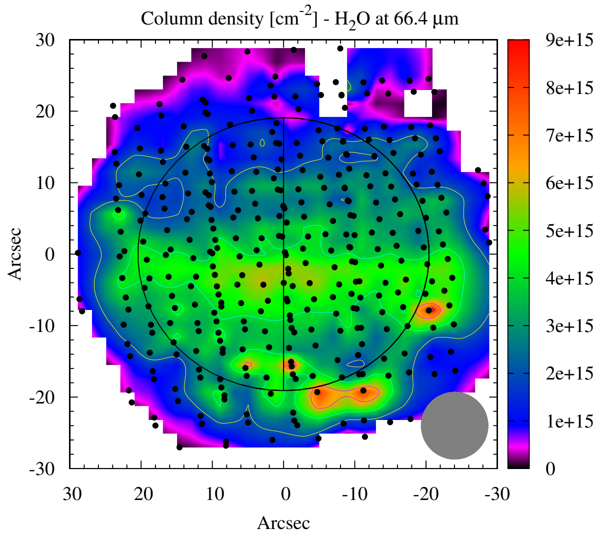

Fig. 1. Column density of water (in cm^{-2}) in Jupiter's stratosphere derived from the PACS map at 66.4 μm. Black ellipse: Jupiter; black vertical line: Jupiter's rotation axis; gray filled circle: PACS beam; black dots: observation pointings. *(Fig. 15 from Cavalié et al. 2013)*

3 Saturn

A decade after the ISO detection of external water in the giant planet stratospheres, the Cassini probe discovered geysers at the south pole of Saturn's moon Enceladus (Hansen et al. 2006; Porco et al. 2006). These geysers

*Bézard et al. (2002) additionally found that the jovian CO also originated from ancient SL9-type impacts and from an internal source.

are mainly composed of water (Waite et al. 2006). In 2009-2010, Herschel-HIFI observed Saturn to determine the vertical profile of water and hence its origin. However, the observations at 557 GHz did not lead to the expected emission line previously observed by Bergin et al. (2000), but to an intriguing spectral feature with wings in emission and a strong absorption at the core. Hartogh et al. (2011) have demonstrated by developing appropriate excitation and torus models that the absorption is due to a cold torus of gaseous water located at the orbital distance of Enceladus, which was shadowing Saturn from Herschel (see Fig. 2 left). In 2009, the ring plane was indeed crossing the observer plane.

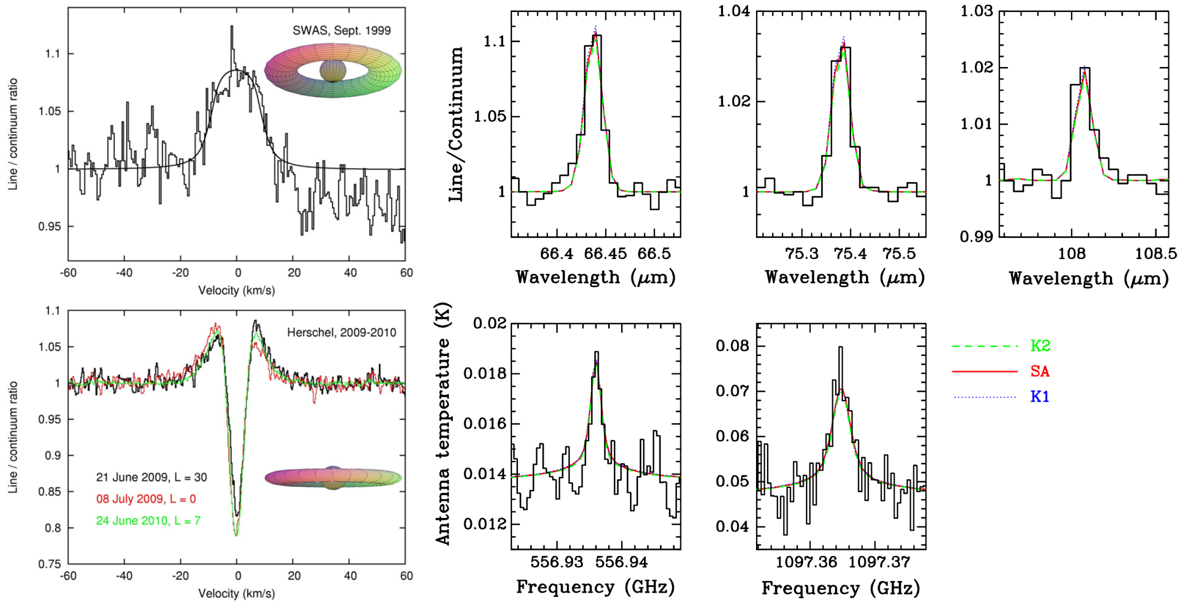

Fig. 2. *Left:* H_2O line at 557 GHz, as observed by SWAS in 1999 (Bergin et al. 2000) and by Herschel in 2009-2010 (Hartogh et al. 2011) with sub-observer latitudes of $-21°$ and $\sim 0°$, respectively. The absorption core seen in 2009-2010 is caused by a torus of gaseous water located at the orbital distance of Enceladus. *Right:* Observations of water in Titan with HIFI and PACS in 2010-2011. *(Figs. 1 and 3 from Hartogh et al. (2011) and Moreno et al. (2012), respectively)*

The temporal evolution of the Enceladus torus, whose source is undoubtedly the Enceladus geysers, has been predicted by Cassidy & Johnson (2010) with a diffusion model in which water molecules scatter around the equatorial plane of Saturn due to molecular collisions. This model predicts a small fraction of the torus water eventually rains onto Saturn's stratosphere. The next step of this work is to take the water influx predictions of Cassidy & Johnson (2010) into account in a latitude-altitude photochemical model to derive the spatial distribution of water in Saturn's stratosphere and to compare it to PACS disk-resolved observations of water (Cavalié et al., in prep.). Interestingly, ground-based observations have shown that CO in Saturn's stratosphere probably originates from a large comet impact, rather than from another source (e.g. Enceladus).

4 Titan

Moreno et al. (2012) have observed water lines in Titan's atmosphere with Herschel-HIFI† and -PACS in 2010-2011. The analysis of the lines (see Fig. 2 right), combined with the development of a new photochemical model, led to new constraints on the water vertical profile. The water influx is 10 times less than required to match the observed CO_2 mole fraction. However, water has a shorter atmospheric lifetime than CO_2 (9 years vs 450 years) so that the oxygen influx into Titan could be much smaller currently than its average value over the past centuries.

Moreno et al. (2012) have shown that both an interplanetary particle source or Enceladus can provide enough water to Titan, but Enceladus was tentatively favored as this source is more prone to temporal variability. A

†Interestingly, the HIFI observations led to the fortuitous detection of HNC (Moreno et al. 2011).

recent paper by Lara et al. (2014) has shown with photochemical computations that Enceladus is indeed a more favorable source than any other. A decrease of the Enceladus source by a factor of 5 to 20 is required over the last few centuries to reconcile the water and CO_2 observations.

5 Conclusions

Jupiter The SL9 source is now confirmed for Jupiter's stratospheric water (Cavalié et al. 2013). The monitoring of SL9-derived species will continue in the next years to constrain Jupiter's dynamics and to prepare for future JUICE/SWI observations (Hartogh et al. 2009a).

Saturn and Titan There are strong and consistent indications that Enceladus is the ultimate source of water in Saturn's environment (Hartogh et al. 2011; Moreno et al. 2012; Lara et al. 2014). The PACS observations of Saturn (Cavalié et al., in prep.) may provide additional proof by validating the model of Cassidy & Johnson (2010). Regarding Titan, complementary clues are needed to firmly validate the Enceladus source, like the detection of other molecules from coming from this moon in Titan's atmosphere (Dobrijevic et al. 2014; Hickson et al. 2014).

T. Cavalié ackowledges the Centre National d'Études Spatiales (CNES) for funding. E. Lellouch, R. Moreno, and F. Billebaud wish to thank the Programme National de Planétologie (PNP) for funding. L.M. Lara's work has been supported by the Ministry of Innovation and Science through the project AyA 2009-08011. The MPS contribution has been supported by the grant of the German Research Foundation DFG HA 3261/7-1.

References

Bergin, E. A., Lellouch, E., Harwit, M., et al. 2000, ApJ, 539, L147
Bézard, B., Lellouch, E., Strobel, D., Maillard, J.-P., & Drossart, P. 2002, Icarus, 159, 95
Bjoraker, G. L., Stolovy, S. R., Herter, T. L., Gull, G. E., & Pirger, B. E. 1996, Icarus, 121, 411
Cassidy, T. A. & Johnson, R. E. 2010, Icarus, 209, 696
Cavalié, T., Billebaud, F., Biver, N., et al. 2008, Planet. Space Sci., 56, 1573
Cavalié, T., Biver, N., Hartogh, P., et al. 2012, Planet. Space Sci., 61, 3
Cavalié, T., Feuchtgruber, H., Lellouch, E., et al. 2013, A&A, 553, A21
Cavalié, T., Moreno, R., Lellouch, E., et al. 2014, A&A, 562, A33
Connerney, J. E. P. 1986, Geophysical Research Letters, 13, 773
Coustenis, A., Salama, A., Lellouch, E., et al. 1998, A&A, 336, L85
de Graauw, T., Helmich, F. P., Phillips, T. G., et al. 2010, A&A, 518, L6
Dobrijevic, M., Hébrard, E., Loison, J. C., & Hickson, K. M. 2014, Icarus, 228, 324
Feuchtgruber, H., Lellouch, E., de Graauw, T., et al. 1997, Nature, 389, 159
Hansen, C. J., Esposito, L., Stewart, A. I. F., et al. 2006, Science, 311, 1422
Hartogh, P., Barabash, S., Bolton, S., et al. 2009a, EPSC Abstracts, 4, EPSC2009
Hartogh, P., Lellouch, E., Crovisier, J., et al. 2009b, Planet. Space Sci., 57, 1596
Hartogh, P., Lellouch, E., Moreno, R., et al. 2011, A&A, 532, L2
Hickson, K. M., Loison, J. C., Cavalié, T., Hébrard, E., & Dobrijevic, M. 2014, A&A, in press
Lara, L. M., Lellouch, E., González, M., Moreno, R., & Rengel, M. 2014, A&A, 566, A143
Lellouch, E., Bézard, B., Moses, J. I., et al. 2002, Icarus, 159, 112
Lellouch, E., Paubert, G., Moreno, R., et al. 1995, Nature, 373, 592
Moreno, R., Lellouch, E., Lara, L. M., et al. 2011, A&A, 536, L12
Moreno, R., Lellouch, E., Lara, L. M., et al. 2012, Icarus, 221, 753
Moreno, R., Marten, A., Matthews, H. E., & Biraud, Y. 2003, Planet. Space Sci., 51, 591
Pilbratt, G. L., Riedinger, J. R., Passvogel, T., et al. 2010, A&A, 518, L1
Poglitsch, A., Waelkens, C., Geis, N., et al. 2010, A&A, 518, L2
Porco, C. C., Helfenstein, P., Thomas, P. C., et al. 2006, Science, 311, 1393
Prangé, R., Fouchet, T., Courtin, R., Connerney, J. E. P., & McConnell, J. C. 2006, Icarus, 180, 379
Prather, M. J., Logan, J. A., & McElroy, M. B. 1978, ApJ, 223, 1072
Strobel, D. F. & Yung, Y. L. 1979, Icarus, 37, 256
Waite, J. H., Combi, M. R., Ip, W.-H., et al. 2006, Science, 311, 1419

SF2A 2014
J. Ballet, F. Bournaud, F. Martins, R. Monier and C. Reylé (eds)

TAU CETI: OUR NEAREST COUSIN

E. Di Folco[1, 2], J. Péricaud[1,2], J.-C. Augereau[3] and J. Marshall[4]

Abstract. The 10 Gyr old G8V star τ Ceti is the closest Solar analogue. It harbors the less massive exo-Kuiper belt detected so far among debris disks stars. With a total disk mass only ten times larger than that of our Kuiper belt, it represents a case study of evolved debris disks. Whether its disk has been continuously eroded by steady-state collisions of planetesimals or recently regenerated by a dynamical instability remains a puzzling question. The detection of the dust points to the existence of (undetected) planetary bodies, which are expected to sculpt the belt and may scatter material inwards to the terrestrial planet region, where hot dust is also observed. Unfortunately, the disk morphology remains unknown. We report a recent Herschel PACS (70 μm and 160 μm)detection of a 15 au ring-like structure which is in conflict with the earlier SCUBA discovery. The disk is partly resolved by Herschel and we derive its morphology and the dust properties from the images and SED analysis with the GraTer modeling code. τ Ceti is a unique laboratory to highlight the long-term dynamical evolution of planetary systems and may represent an alternative outcome to the evolution of our Solar system.

Keywords: subject, verb, noun, apostrophe

1 Scientific background: the closest Kuiper belt analogue

Planetary systems around main-sequence stars can be indirectly revealed by the presence of massive belts of dust grains produced by collisions of planetesimals (see Wyatt 2008; Krivov 2010; Matthews et al. 2014, for recent reviews on debris disks). In our Solar system, the Edgeworth-Kuiper Belt (EKB) bears witness to the past dynamical history of our planetary system. The bulk of its mass ($\sim 0.12\,M_\oplus$) is located between 35 and 50 AU (Vitense et al. 2010, 2012, for detailed modeling). According to current models, it is believed to have been formed by the gravitational interaction of primordial planetesimals with the giant planets during a phase of outward migration (e.g., Morbidelli 2010, for an overview of the Nice model). Whilst up to recently all detected debris disks were much more massive than the EKB, Herschel sensitivity allows to investigate fainter systems that are more sibling to our Solar system.

τ Ceti, at a distance of 3.65 pc, is the nearest single solar-type star to the Sun. It is therefore a prime candidate for detailed imaging of mature planetary systems. Combining interferometric measurement of the stellar radius (Di Folco et al. 2004, 2007) with the asteroseismic estimate of the density, Teixeira et al. (2009) inferred a stellar mass $M_\star = 0.78 \pm 0.01\,\mathrm{M}_\odot$. Di Folco et al. (2004) also derived an age of 10.0 ± 0.5 Gyr for this G8V dwarf which thus appears to be older than the Sun, and as such to host the oldest resolved debris disk around a main-sequence star. Whether its massive belt is a remnant of the primordial debris disk or has been recently regenerated remains a puzzling enigma.

First detected with IRAS (Backman et al. 1986), and ISO (Habing et al. 2001) at 60 and 170 μm, its cold dust belt ($T \sim 60$ K) was first imaged at 850 μm by Greaves et al. (2004). The disk emission was marginally resolved by SCUBA on JCMT, suggesting a very inclined structure at a position angle $PA = 6°$ with an outer edge of 55 AU. The total flux density (5.8 ± 0.6 mJy, of which 1.1 mJy comes from the star) corresponds to a sub-mm grain mass of $5.10^{-4}\,\mathrm{M}_\oplus$, which is extrapolated to $M_{\mathrm{disk}} = 1.2\,\mathrm{M}_\oplus$ by assuming a collisional cascade with parent bodies as large as 50 km and an age of 10 Gyr. This mass is an order of magnitude larger than that

[1] Univ. Bordeaux, Laboratoire d'Astrophysique de Bordeaux, UMR 5804, F-33270, Floirac, France
[2] CNRS, LAB, UMR 5804, F-33270 Floirac, France
[3] UJF-Grenoble 1/CNRS-INSU, Institut de Planétologie et d'Astrophysique de Grenoble UMR 5274, F-38041, Grenoble, France
[4] Depto. de Fisica Teorica, universidad Autonoma de Madrid, Cantoblanco, 28049, Spain

of today's Kuiper Belt ($\sim 0.12\,M_{\oplus}$, e.g., Vitense et al. 2010), whereas it is the less massive belt imaged so far among debris disks. The decline of disks fractional excess, and hence of mass, with age could be explained by steady-state processing (Löhne et al. 2008), although a possible delayed stirring (Wyatt 2008) cannot be ruled out .

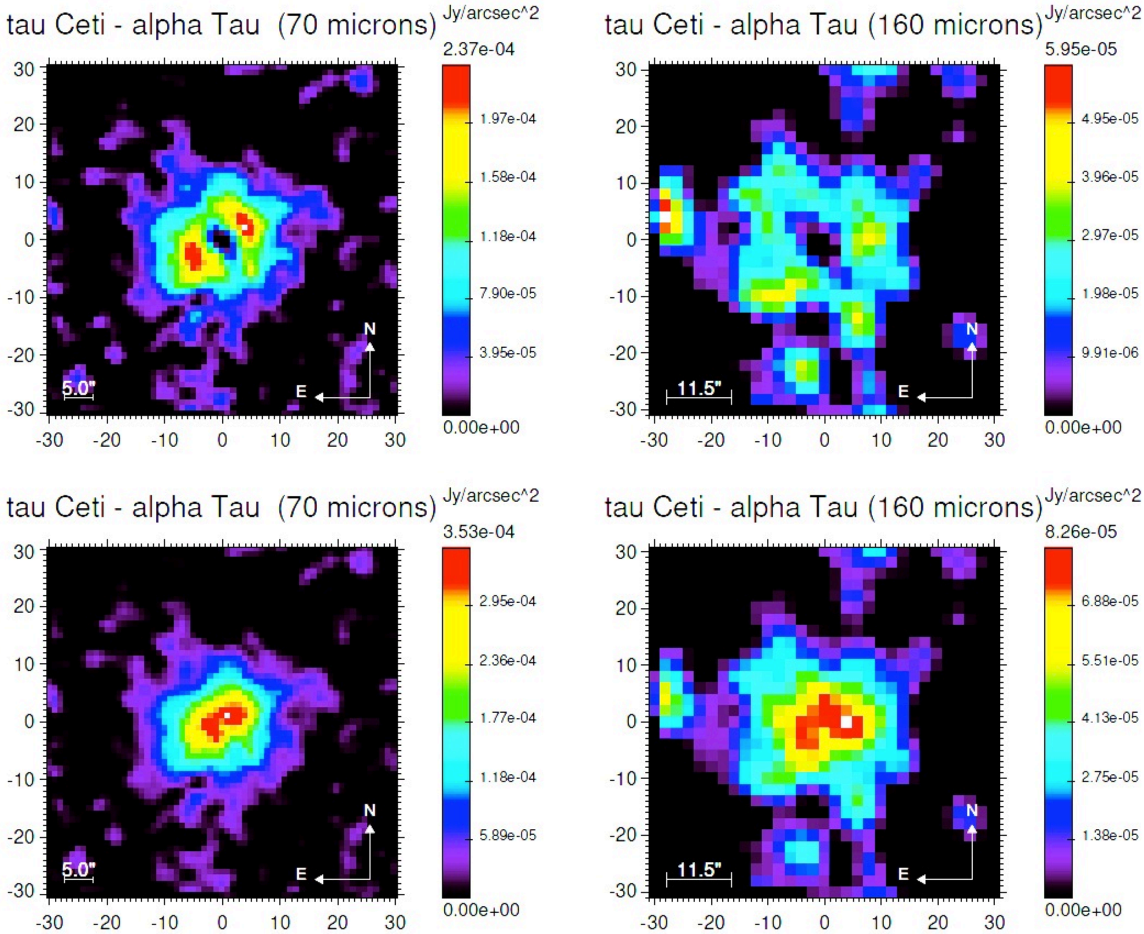

Fig. 1. Herschel-PACS images of the debris disk around τ Ceti at 70 μm (left) and 160 μm (right). **Top panels:** the PSF observed on a reference (point-like) star has been subtracted to the reduced image of τ Ceti after normalizing the PSF at the maximum of the image surface brightness: it highlights the resolved disk emission. **Bottom:** same image subtraction process but the reference image is normalized at the expected photospheric flux of τ Ceti: it highlights the contribution of the disk alone to the total emission.

2 Herschel-PACS detection

We collected archival Herschel data from the PACS and SPIRE instruments. Aperture photometry is calculated in a 20" radius circle and confirms a significant IR excess longward of $\lambda = 70\,\mu$m. The disk flux excess is detected up to 350 μm, it can be fitted with a modified black-body at a temperature of about 85 K, which corresponds to grains at a typical distance of about 10 au around this G8V star. We also analyzed the PACS images at 70 and 160 μm. We used the reference star α Tau to estimate the point spread function (PSF), this star was observed with the same scanning mode of the PACS instrument. In Fig.1, we display the PSF-subtracted images in order to enhance the resolved emission beyond the contribution of the unresolved photosphere of τ Ceti. This is done as follows: we subtract the image of the reference star after normalizing the latter at the maximum value of the surface brightness in the τ Ceti image, this leaves a null value at the center of the image with two wings that reveal the extended emission that is due to the debris disk emission. in this process, part of the disk emission is also subtracted. We thus propose a second set of PSF-subtracted images, where we normalize the PSF surface brightness at the expected photospheric level of τ Ceti (modeling the stellar SED with a Nextgen model that fits the short wavelength flux density). In this way, only the photospheric emission is subtracted and the image is supposed to trace the disk emission. The PSF width is estimated to about 6" at 70 μm and 12" at 160 μm. The resolved emission is prominent at 70 μm, and less significant at 160 μm. It is detected out to about 50 au in the 70 μm image, the disk emission appears to be inclined with a position angle $PA = 135 \pm 10$ deg. We also estimate a disk inclination of 40 ± 3 deg by fitting the image isophots with elliptical lines. We note that the image is significantly different from the detection reported with the SCUBA instrument by Greaves et al. (2004). The Herschel detection shows a moderately inclined system oriented in a direction that is orthogonal to the resolved emission claimed by the latter authors. We also report no major azimutal brightness asymmetry in the far-IR images.

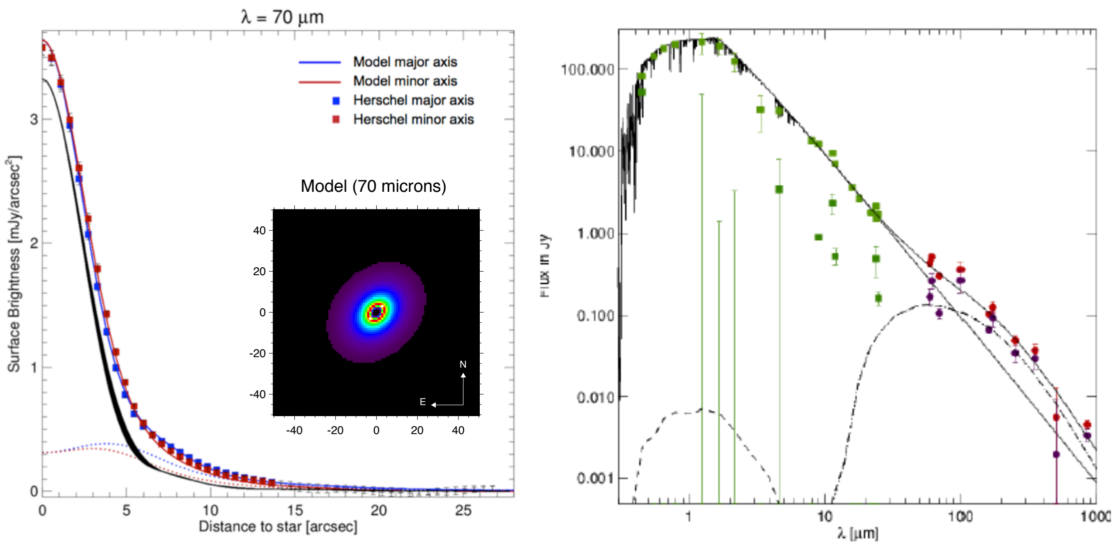

Fig. 2. Left: PACS Image profiles at 70 μm along the minor and major axis (dots) compared to the best-fit model estimates (colored solid lines). The best model emission is illustrated in the inset. **Right:** Spectral energy distribution for the star and the disk (solid line is the best Nextgen model, red dots are the photometric values taken into account n the fit), and for the disk alone (purple markers for the Herschel + SCUBA measurements, dashed and dash-dotted lines for the best-fit model).

3 Disk modeling with GraTer

We used the GraTer code (e.g., Lebreton et al. 2012) to constrain the physical parameters of the debris disk using the simultaneous constraints of the disk SED and the resolved images. only the 70 μm image was taken into account as it provides the most significant detection. The SED and the image profiles are fitted simultaneously. We assume for the dust grains distribution a ring-like structure, peaking at radius R_0, with adjustable inner and outer slopes. The grains size distribution index (κ), the minimum grain size ($s_{\rm min}$) and the total mass ($M_{\rm d}$) are free parameters. We fixe the outer radius of the disk at 100 au, and consider only pure silicate grains. About 10^6 models have been computed, a Bayesian analysis yields the probability density functions for the fitted parameters, which allows us to estimate robust uncertainties. We find that the ring of grains partly resolved in the Herschel images peaks at 15 ± 1 au, with an outer slope of $\alpha = -1.3 \pm 0.2$. The size distribution index is consistent with what is expected from a typical collisional cascade $\kappa = -3.42 \pm 0.02$, and the minimum grain size is found to be very small ($\sim 10^{-2}\,\mu$m). The result of the fitting procedure can be found in Fig.2, where our model of dust emission at 70 μm is also illustrated. These result are consistent with the preliminary analysis recently proposed by Lawler et al. (2014). The the stirring mechanism that ensures the production of dust in such an old system is not yet understood. The disk luminosity is clearly too large to be the result of a long-term steady-state collisional cascade lasting for 7–10 Gyr, following Wyatt (2008). The total dust mass is one order of magnitude larger than in our present-day EKB. A delayed stirring must be invoked, with multiple possible physical causes (recent collision, planet or planet migration-induced mechanism, late-heavy bombardment-like event...).

4 Conclusions

We have analyzed the far-IR images of the old debris-disc surrounding the nearby solar-type star τ Ceti. The partially resolved emission allow us to constrain, through a detailed modeling of the thermal dust grain emission, the main characteristics of the dust ring. Our results suggest that the grains are arranged in a ring-like structure with a radial extension comparable to that of the Edgeworth-Kuiper belt in our solar system. τ Ceti is a remarkable system because its disk of cold debris is about one order of magnitude more massive than our EKB, while the system appears to be much older than ours. Our modeling yields for the cold dust belt typical characteristics of collision dominated structures. The origin of the dynamical stirring for a 10 Gyr old system remains to be found. Detailed imaging at higher spatial resolution with ALMA should help characterizing the parent bodies of the observed grains in the far-IR domain. It should also solve the surprising discrepancy between the far-IR and the sub-mm emission morphology.

E. Di Folco acknowledge the support of PNP for this study.

References

Backman, D. E., Gillett, F. C., & Low, F. J. 1986, Advances in Space Research, 6, 43
Di Folco, E., Absil, O., Augereau, J.-C., et al. 2007, A&A, 475, 243
Di Folco, E., Thévenin, F., Kervella, P., et al. 2004, A&A, 426, 601
Greaves, J. S., Wyatt, M. C., Holland, W. S., & Dent, W. R. F. 2004, MNRAS, 351, L54
Habing, H. J., Dominik, C., Jourdain de Muizon, M., et al. 2001, A&A, 365, 545
Krivov, A. V. 2010, Research in Astronomy and Astrophysics, 10, 383
Lawler, S. M., Di Francesco, J., Kennedy, G. M., et al. 2014, MNRAS, 444, 2665
Lebreton, J., Augereau, J.-C., Thi, W.-F., et al. 2012, A&A, 539, A17
Löhne, T., Krivov, A. V., & Rodmann, J. 2008, ApJ, 673, 1123
Matthews, B. C., Krivov, A. V., Wyatt, M. C., Bryden, G., & Eiroa, C. 2014, ArXiv e-prints
Morbidelli, A. 2010, Comptes Rendus Physique, 11, 651
Teixeira, T. C., Kjeldsen, H., Bedding, T. R., et al. 2009, A&A, 494, 237
Vitense, C., Krivov, A. V., Kobayashi, H., & Löhne, T. 2012, A&A, 540, A30
Vitense, C., Krivov, A. V., & Löhne, T. 2010, A&A, 520, A32
Wyatt, M. C. 2008, ARA&A, 46, 339

SF2A 2014
J. Ballet, F. Bournaud, F. Martins, R. Monier and C. Reylé (eds)

INSIGHTS ON COMPLEX EXOPLANETARY SYSTEMS AND THEIR DYNAMICAL HISTORY WITH HERSCHEL

V. Faramaz[1], H. Beust[1], J.-C. Augereau[1], P. Kalas[2], J.R. Graham[2] and The Herschel-DUNES team

Abstract. Resolved images of debris disks often reveal spatial asymmetries which can be interpreted as the dynamical signatures of hidden massive perturbers, potentially planets. The capabilities of *Herschel*[*] have lead for instance to the resolution of an eccentric debris disk around ζ^2 Reticuli, and confirmed the existence of an eccentric dust belt around Fomalhaut. These indicate the presence of massive and eccentric belt-shaping perturbers.

We present here how dynamical modeling using N-body numerical simulations allows us to explain the structure of the debris disk of ζ^2 Reticuli and set constraints on a potential planetary perturber. We also show how such numerical simulations allows us to get insights the dynamical history of the Fomalhaut planetary system. Indeed, the orbit of the planet Fom b, which was thought to shape the belt, and detected near its inner edge, is highly eccentric and incompatible with the present dynamical status of the belt. This gives clues for the presence of another more massive perturber in the system, that is, the belt-shaping planet of the Fomalhaut system is yet undetected. Investigation of the dynamics of this two-planets system has revealed a robust three-step process by which an eccentric massive perturber such as the belt-shaping unseen Fom c sets less massive bodies on orbits similar to that of Fom b. This process provides a plausible dynamical scenario for the Fomalhaut system history. In addition, it may be at the origin of inner belts in the Fomalhaut system, and provide a solution to the presence of unusual high levels of dust in the vicinity of a significant number of stars with age > 100 Myr.

Keywords: Circumstellar matter – Planetary systems – Methods: N-body Simulations – Celestial mechanics – Stars: Fomalhaut – ζ^2 Reticuli.

1 Introduction

At least $\sim 20\%$ of the planetary systems are known to harbor debris disks (Marshall et al. 2014). Spatially resolved structures in debris disks can provide clues to the invisible planetary component of those systems. Such planets may be responsible for sculpting these disks and may leave their signature through various asymmetries such as wing asymmetries, resonant clumpy structures, warps, spirals, gaps, or eccentric ring structures (see, e.g., Wyatt 1999).

The diversity of these asymmetries is to be compared with the variety of exoplanetary systems discovered around main sequence stars since 1995 (51 Peg b, Mayor & Queloz 1995). In particular, the common discovery of significantly eccentric planets is in complete contrast with the circular planetary orbits of our solar system (median eccentricity of 0.29 for planets with orbital period greater than 6 days Udry & Santos 2007). This has revealed that our own Solar System is far from being a reference, and that our current planetary systems formation and evolution models, which were naturally built from its study, require refinements. Therefore, the study of systems containing eccentric perturbers and their dynamical history is crucial to achieve these refinements.

We focus here on two systems which eccentric debris disks were observed with *Hershel*, surrounding ζ^2 Reticuli and Fomalhaut. Results of dynamical modeling and investigation of the dynamical history of the ζ^2 Reticuli and Fomalhaut systems thanks to N-body simulations are presented in Sect. 2 and Sect. 3, respectively.

[1] Univ. Grenoble Alpes, IPAG, F-38000 Grenoble, France – CNRS, IPAG, F-38000 Grenoble, France
[2] Department of Astronomy, 601 Campbell Hall, University of California at Berkeley, Berkeley, CA 94720, USA
[*] *Herschel* Space Observatory is an ESA space observatory with science instruments provided by European-led Principal Investigator consortia and with important participation from NASA.

2 The ζ^2 Ret system: Can eccentric debris disks be long-lived?

Recent *Herschel*/PACS observations of the debris disk surrounding the 2-3 Gyr old star ζ^2 Reticuli, obtained as part of the DUNES key program (Eiroa et al. 2013), reveal an asymmetric double-lobed circumstellar feature (Fig. 1, left panel), interpreted as a ring like structure seen almost edge-on with an elliptical shape and minimum eccentricity of 0.3, at $\sim$ 100 AU (Eiroa et al. 2010). This provides evidence for the presence of a massive eccentric perturber in this system. The case of ζ^2 Ret is particularly interesting since the system is Gyr-old and thus gives a picture of what mature systems containing an eccentric perturber can look like. These systems are rarely accessible to observations and represent less than 5% of the total resolved circumstellar emissions. It is indeed because debris disks tend to lose luminosity on long-term periods: the dust grains emitting at infrared wavelengths are continuously blown away by radiation pressure (see e.g. Thébault & Augereau 2007) while replenished via collisional processes among the km-sized parent bodies (Backman & Paresce 1993). Since the parent bodies population is not replenished, the amounts of dust, and thus the disk luminosity in mid-far IR decreases adiabatically (Krivov 2010), until instrument sensitivity does not allow us to detect them anymore. In the ζ^2 Ret system, one might question whether the disk asymmetry can be sustained on Gyr timescales, or whether the dynamical history of this system would rather involve a recent setting of the belt-shaping massive perturber on its eccentric orbit.

A detailed modeling of the structure of this debris disk consists in performing N-body simulations with trial eccentric perturbers, exploring their dynamical influence on massless planetesimals on Gyr timescales, and determine which of these perturbers can create a 0.3 eccentric parent debris ring. The dust production resulting from the collisional activity of these parent planetesimals, along with their emission can then be computed to produce synthetic images fully comparable to *Herschel*/PACS observations (see Fig. 1, right panel).

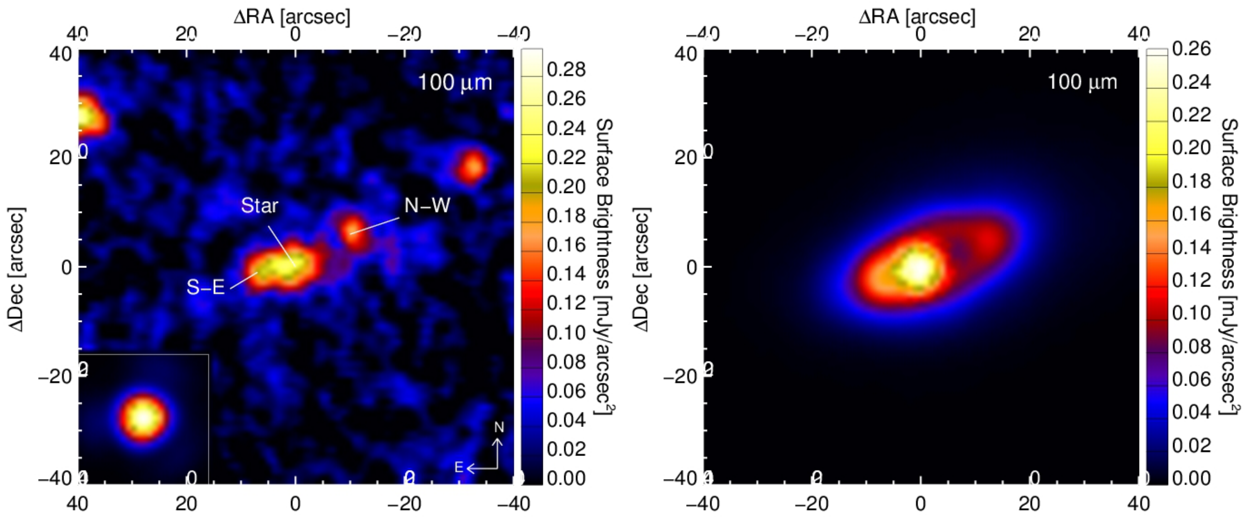

Fig. 1. Left: Herschel/PACS image at 100 microns. **Right:** Synthetic image of a resulting disk in one of our simulations with $e > 0.3$ as seen with Herchel/PACS at 100 microns.

This leads to constraints on the mass and orbital characteristics of the putative perturber: ζ^2 Ret hosts a planetary companion with minimum orbital eccentricity 0.3 at several tens of AU from the host star (Faramaz et al. 2014). In addition, Faramaz et al. (2014) showed that eccentric debris disks can be sustained on Gyr timescales, which involves that the dynamical history of this system does ot necessarily involves a recent access of the massive shepherding planet to its current eccentric orbit.

3 The Fomalhaut system: a dynamical history involving an unseen Fom c?

Fomalhaut (α Psa) is a 440 Myr old (Mamajek 2012) A3V star, located at 7.7 pc (van Leeuwen 2007; Mamajek 2012). Fomalhaut is surrounded by an eccentric dust ring (e = 0.11 ± 0.01) (Kalas et al. 2005). This eccentric shape hinted at the presence of a massive body orbiting inside the belt on an eccentric orbit, dynamically shaping the belt (Quillen 2006; Deller & Maddison 2005). This hypothesis was apparently confirmed by the direct detection of a companion near the inner edge of the belt, Fomalhaut b (hereafter Fom b) (Kalas et al. 2008). However, orbital fitting for this perturber has revealed a highly eccentric and crossing-belt orbit, near with apsidal alignement with the belt, which cannot be responsible for the disk shaping (Graham et al. 2013; Beust et al. 2014). The most straightforward solution to this apparent paradox is to suppose the presence of a second more massive and yet undetected body in the system (hereafter named Fom c), which is responsible for the disk shaping because of a predominant dynamical influence. This implies that Fom b is rather a low-mass body compared to the putative Fom c, as confirmed by recent dynamical or photometric studies which suggest that it is no more than Earth- or Super-Earth sized (Beust et al. 2014; Janson et al. 2012; Galicher et al. 2013).

However, in this configuration, which is illustrated in the bottom panel of Fig. 2, the orbit of the belt-shaping putative planet Fom c would be crossed by that of Fom b, which would make this two-planet system highly unstable and require Fom b to have been set recently on its current orbit. It could have been put there by a more or less recent scattering event, potentially with Fom c (Beust et al. 2014).

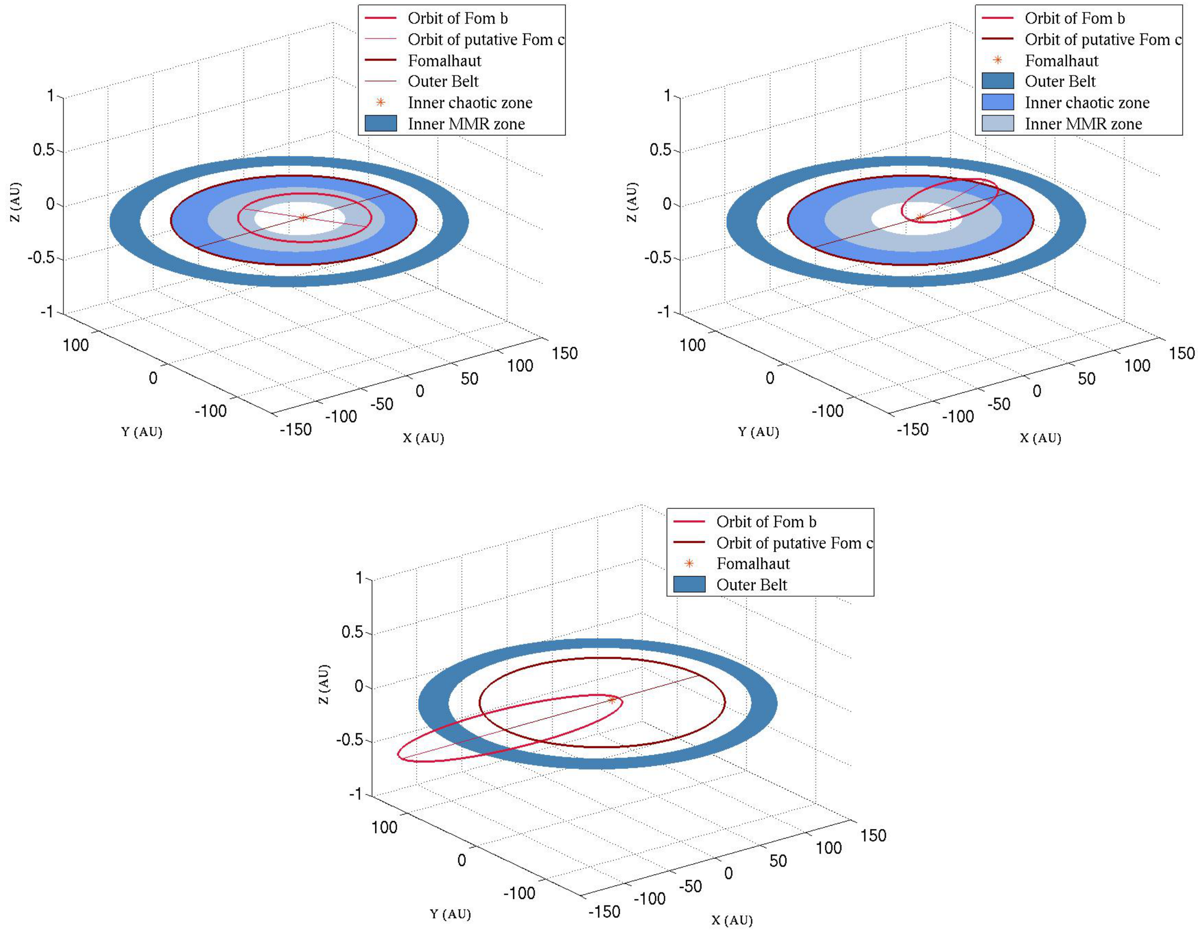

Fig. 2. Top-left: Probable initial configuration of the Fomalhaut system. Fom b is in MMR with the belt shaping eccentric Fom c. **Top-right:** Probable intermediary configuration of the Fomalhaut system. MMRs with an eccentric perturber generate very eccentric orbits, which leads Fom b to cross the chaotic zone of Fom c and be scattered by it on its current orbit. **Bottom:** Probable current configuration of the Fomalhaut system.

Investigation of the dynamics of this two-planet system in Faramaz et al., in prep., where Fom c is a massive belt-shaping body and Fom b a much less massive body originating from the inner parts of the system, has revealed a three-step dynamical scenario involving interactions with the putative eccentric Fom c, which can both explain why Fomalhaut b is on such an eccentric orbit and why it was set on it recently:

1. *Mean-Motion Resonances between Fom b and the suspected Fom c :* Fom b is likely to have formerly resided in an inner mean-motion resonance (MMR) with the additional planet, as illustrated in the top-

right panel of Fig. 2. MMRs with an eccentric perturber such as the belt-shaping putiative Fom c induce a gradual eccentricity increase, which can lead Fom b to cross the chaotic zone of Fom c, where it can then be scattered by Fom c on its current orbit (top-left panel of Fig. 2). The dynamical timescale involved in this process, that is, the typical time necessary for Fom b to reach a sufficient orbital eccentricity from its MMR position and be scattered on its current orbit, strongly depends on the mass of the putative Fom c. In particular, the scattering event can be delayed on timescales comparable to the age of the system with a Neptune or Saturn-sized Fom c, which would explain why Fom b was recently set on its orbit.

2. *Close encounter with the suspected Fom c:* inspection of the close-encounters between Fom b and the putative Fom c reveals that these can set Fom b on an orbit with semi-major axis compatible with this of Fom b, but that they also preferentially produce orbits which are not eccentric enough to be compatible with that of the observed one ($a = 81 - 415\,\mathrm{AU}$ and $e = 0.69 - 0.98$, in the 95% level of confidence Beust et al. 2014).

3. *Secular evolution with the suspected Fom c:* an additional eccentricity increase can be provided by the mean of secular evolution of Fom b under the influence of the putative eccentric Fom c, which is indeed mainly expected at semi-major axes with $a = 81 - 415\,\mathrm{AU}$. However, this eccentricity increase is accompanied by an apsidal alignement with the belt-shaping Fom c, and thus with the belt, which may explain the tendency for the observed orbit to be apsidally aligned with the belt.

The whole process is summarized and illustrated in Fig. 3.

In addition, in the case an eccentric planet such as the putative Fom c coexists with km-sized solid planetesimals, interactions that generates orbits such as that of Fom b can be expected to apply in a very general manner (Faramaz et al., in prep.). Therefore, one should probably expect the Fomalhaut system to contain a broad population of solid bodies on highly eccentric orbits, which can lead them to approach their host star extremely closely when being at periastron. Then, if these solids endure any collisional activity, they may feed the inner parts of the system with dust, which results in hot or warm inner belts. This is extremely interesting in the context of the Fomalhaut system, since both a warm and a hot inner belts were detected (Lebreton et al. 2013). A straightforward question to address then is whether the dynamical scenario constrained in Faramaz et al. (in prep) also explains the presence of these inner belts.

4 Conclusions

Searching for gravitational signatures in debris disks is a particularly helpful indirect detection technique when orbital separations prevent us from detecting these planets via classical detection techniques such as radial-velocities or transits, which are biased to catch short-period objects. This is indeed the case for the Gyr-old system of ζ^2 Ret, which eccentric debris disk was unraveled by *Herschel*. A subsequent dynamical study has revealed that this type of pattern could be sustained over Gyr timescales, and allowed to set first contraints on the belt-shaping perturber at work in this system. However, Faramaz et al. (2014) suggest the eccentric structure of the debris disk of this system could be produced either by an inner or an outer companion. Since the ring limiting radii and its global eccentricity are not well constrained, the parameter space explored is large, that is, there is solution degeneracy. The large orbital separation of this planetary companion, along with its age, makes it very challenging to observe. The only possible way to detect it is to characterize it through its gravitational print on the disk, and thus, to obtain better and more detailed constraints on the geometry of this debris disk, which are hoped to be obtained with facilities such as ALMA.

The study of the Fomalhaut system has revealed a robust process by which orbits such as this of Fom b naturally result from interactions between low-mass solid bodies and an eccentric massive perturber such as this which shapes the outer belt of this system. In addition, this process involves a delay in the production of Fom b-like orbits, which can be greater than 100 Myr if the eccentric massive perturber is Saturn-Neptune sized. This can provide an explanation both for the shape of the outer belt and the current dynamical status of Fom b, and may also explain the presence of inner belts in this system. This also indicates that warm and hot inner belts potentially resulting from this process may start to be produced very late in the history of a system. This may indeed give a solution to the yet unexplained detection of numerous hot belts in systems older than 100 Myr, and which contain levels of dust too large to be sustained over a system's age (Absil et al. 2013; Ertel et al. 2014; Bonsor et al. 2012, 2014). Indeed, such a process involves that one should not necessarily assume that hot belts in systems older than 100 Myr have been sustained over the system's age (Faramaz et al., in prep).

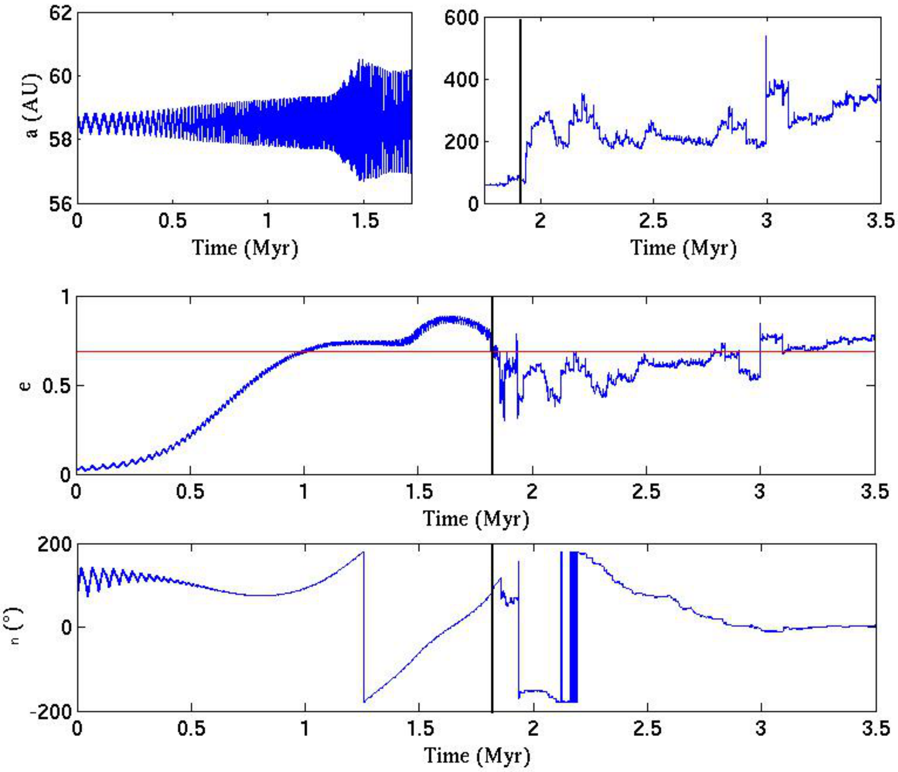

Fig. 3. Example of the three-step process that may have led Fom b on its current orbit. We display the evolutions in time of the semi-major axis a, eccentricity e, and longitude of periastron ν of a massless test-particle initially in 5:2 MMR with a $3M_{\rm Jup}$ Fom c, with semi-major axis 108.6 AU and orbital eccentricity 0.1. Note that this process can be generated via several other MMRs. The test-particle endures a three-step dynamical evolution, starting with a resonant evolution, where its semi-major axis suffers small oscillations around the exact resonant location, and its eccentricity largely increases, while co-evolving with the longitude of periastron. The vertical black line at $\sim 2Myr$ indicates the second step of the process, that is, a close encounter with Fom c when the highly eccentric orbit of the test-particle leads its orbit to cross the chaotic zone of Fom c. Note that this delay of several Myr with a Jupiter sized Fom c increases up to several 100 Myr with a Saturn-Neptune sized Fom c. The semi-major axis of the test-particle is compatible with this of Fom b after the close encounter, but its eccentricity remains smaller than 0.69 *(horizontal red line)*, and thus is incompatible with that of Fom b. The third step consists mainly in a secular evolution of the test-particle with the eccentric Fom c, although its orbit endures small chaotic variations. This secular evolution allows the eccentricity to increase and become greater than 0.69, which occurs when there is an apsidal alignement between the perturber and the test-particle, that is, when the longitude of periastron of the test-particle is close to zero.

The authors acknowledge the support of the ANR-2010 BLAN-0505-01 (EXOZODI) and of the CNRS's PNP program. P.K. and J.R.G. thank support from NASA NNX11AD21G, GO-11818, GO-12576, and NSF AST-0909188. Computations presented in this paper were performed at the Service Commun de Calcul Intensif de l'Observatoire de Grenoble (SCCI) on the super-computer funded by the Agence Nationale pour la Recherche under contracts ANR-07-BLAN-0221, ANR-2010-JCJC-0504-01 and ANR-2010-JCJC-0501-01.

References

Absil, O., Defrère, D., Coudé du Foresto, V., et al. 2013, A&A, 555, A104

Backman, D. E. & Paresce, F. 1993, in Protostars and Planets III, ed. E. H. Levy & J. I. Lunine, 1253–1304

Beust, H., Augereau, J.-C., Bonsor, A., et al. 2014, A&A, 561, A43

Bonsor, A., Augereau, J.-C., & Thébault, P. 2012, A&A, 548, A104

Bonsor, A., Raymond, S. N., Augereau, J.-C., & Ormel, C. W. 2014, ArXiv e-prints

Deller, A. T. & Maddison, S. T. 2005, ApJ, 625, 398

Eiroa, C., Fedele, D., Maldonado, J., et al. 2010, A&A, 518, L131

Eiroa, C., Marshall, J. P., Mora, A., et al. 2013, A&A, 555, A11

Ertel, S., Augereau, J.-C., Thébault, P., et al. 2014, in IAU Symposium, Vol. 299, IAU Symposium, ed. M. Booth, B. C. Matthews, & J. R. Graham, 338–339

Faramaz, V., Beust, H., Thébault, P., et al. 2014, A&A, 563, A72

Galicher, R., Marois, C., Zuckerman, B., & Macintosh, B. 2013, ApJ, 769, 42

Graham, J. R., Fitzgerald, M. P., Kalas, P., & Clampin, M. 2013, in American Astronomical Society Meeting Abstracts, Vol. 221, American Astronomical Society Meeting Abstracts, 324.03

Janson, M., Carson, J. C., Lafrenière, D., et al. 2012, ApJ, 747, 116

Kalas, P., Graham, J. R., Chiang, E., et al. 2008, Science, 322, 1345

Kalas, P., Graham, J. R., & Clampin, M. 2005, Nature, 435, 1067

Krivov, A. V. 2010, Research in Astronomy and Astrophysics, 10, 383

Lebreton, J., van Lieshout, R., Augereau, J.-C., et al. 2013, A&A, 555, A146

Mamajek, E. E. 2012, ApJ, 754, L20

Marshall, J. P., Moro-Martín, A., Eiroa, C., et al. 2014, A&A, 565, A15

Mayor, M. & Queloz, D. 1995, Nature, 378, 355

Quillen, A. C. 2006, MNRAS, 372, L14

Thébault, P. & Augereau, J.-C. 2007, A&A, 472, 169

Udry, S. & Santos, N. C. 2007, ARA&A, 45, 397

van Leeuwen, F., ed. 2007, Astrophysics and Space Science Library, Vol. 350, Hipparcos, the New Reduction of the Raw Data

Wyatt, M. C. 1999, PhD thesis, Royal Observatory, Blackford Hill, Edinburgh EH9 3HJ, UK

LIDT-DD: A NEW HYBRID MODEL TO UNDERSTAND DEBRIS DISCS OBSERVATIONS - THE CASE OF MASSIVE COLLISIONS.

Q. Kral[1], P. Thébault[1], J.-C. Augereau[2], A. Boccaletti[1] and S. Charnoz[3]

Abstract. LIDT-DD is a new hybrid model coupling the collisional and dynamical evolution in debris discs in a self-consistent way. It has been developed in a way that allows to treat a large number of different astrophysical cases where collisions and dynamics have an important role. This interplay was often totally neglected in previous studies whereas, even for the simplest configurations, the real physics of debris discs imposes strong constraints and interactions between dynamics and collisions.

After presenting the LIDT-DD model, we will describe the evolution of violent stochastic collisional events with this model. These massive impacts have been invoked as a possible explanation for some debris discs displaying pronounced azimuthal asymmetries or having a luminosity excess exceeding that expected for systems at collisional steady-state. So far, no thorough modelling of the consequences of such stochastic events has been carried out, mainly because of the extreme numerical challenge of coupling the dynamical and collisional evolution of the released dust.

We follow the collisional and dynamical evolution of dust released after the breakup of a Ceres-sized body at 6 AU from its central star. We investigate the duration, magnitude and spatial structure of the signature left by such a violent event, as well as its observational detectability. We use the GRaTer package to estimate the system's luminosity at different wavelengths and derive synthetic images for the SPHERE/VLT and MIRI/JWST instruments.

Keywords: planetary system – debris discs – massive collisions – circumstellar matter

1 Introduction

The collisional breakup of large planetesimals has been invoked as a possible cause for some pronounced structures observed in resolved debris discs. It has also been considered as an explanation for some "anomalously" bright discs that are too old for their luminosity to be explained by a steady-state erosive collisional cascade (Wyatt 2008; Gáspár et al. 2013).

Although this important issue has been explored in some past numerical studies, these numerical models were limited by the absence of (or a very simplified) coupling between the collisional and dynamical evolutions of the post-breakup fragment cloud (Kenyon & Bromley 2004; Jackson & Wyatt 2012; Jackson et al. 2014).

We propose here to address this problem using the new generation LIDT-DD code, specifically developed for the coupled study of collisions and dynamics in debris discs (Kral et al. 2014). Our main objective is to estimate the observability and the longevity of the dust disc formed in the aftermath of such a violent and transient event. We focus especially on how the concurring effects of collisions and radiation pressure affect the asymmetric post-breakup structures.

2 The LIDT-DD model

For a full description of our code, we refer the reader to Kral et al. (2013). Let us here briefly summarize its main characteristics as well as the main important features that have been implemented so far.

[1] LESIA-Observatoire de Paris, UPMC Univ. Paris 06, Univ. Paris-Diderot, France
[2] Univ. Grenoble Alpes and CNRS, IPAG, F-38000 Grenoble, France
[3] Laboratoire AIM, Université Paris Diderot / CEA / CNRS, Institut Universitaire de France

The basic principle of the LIDT-DD model is to couple a Lagrangian approach for the dynamics to a particle-in-a-box statistical Eulerian one for the collisional evolution (Charnoz & Taillifet 2012). At a given location in the system, all particles of a given size *and* sharing similar dynamical characteristics are gathered into larger super-particles (called "tracers"), whose dynamical evolution is followed with an N-body scheme, while their collisional evolution is investigated with a statistical approach, considering all mutual tracer-tracer impacts at any given location in the system.

The procedure to evolve both the tracers' dynamics and collisions can be sketched as follows. Each particle in the code is a super-particle representing a vast population of same-sized physical particles. The positions and velocities of the tracers are integrated with a Bulirsh-Stöer scheme (N-body approach) that is able to include different type of forces (Poynting-Robertson drag, radiation pressure, gravitational interactions, gas drag if needed). Once the dynamics has been integrated over one time step, the system is divided into spatial cells. The collisional evolution is then estimated cell by cell, by taking into account all potential tracer-tracer encounters within each cell. Although LIDT-DD is intrinsically 3-D and tracers dynamics is integrated in the vertical direction, we use a 2-D grid (r,θ) for these "collisional cells", each individual cell having a finite vertical extension equal to the tracers' inclination times the radial distance. All tracer-tracer collisions are then treated with a statistical procedure, taking into account the mutual velocities between tracers and the number density of real physical particles they represent. The size-distribution of the fragments produced by each of these impacts is estimated with the collisional outcome prescription used in the statistical code of Thebault & Augereau (2007). Its main parameter is the critical specific energy Q^* required for dispersing at least 50% of the target. Both fragmenting ($Q > Q^*$, where Q is the collision kinetic energy per target unit mass), and cratering (or "erosive", $Q < Q^*$) impacts are taken into account. The collisional debris are then redistributed, according to their sizes and dynamical characteristics, into newly-created tracers. The feedback of collisions onto the old and new tracers (momentum redistribution and energy loss) is taken into account. After each time step, tracers of a given spatial cell are sorted into dynamical "families", in order not to lose important information about the dynamical complexity of the system (for instance, at a given location, grains having similar sizes can have different origins and thus different dynamical evolutions). Eventually, to avoid an unmanageable increase of the number of tracers, the code is looking, at the end of each time step, for redundant tracers which are then merged into the nearest tracers representing the same size and dynamical family.

3 Massive collisions

For a full description of our results, we refer the reader to Kral et al. (2014). Here we recall the setup and give the most important results found by our study.

3.1 Setup

We follow the evolution of a massive amount of small fragments, of mass $M_{\rm frag} = 10^{21}$ kg, released by a violent phenomenon, in the inner regions (at $r_{\rm init} = 6\,$AU) of a planetary system around an A7V star. If we assume that $M_{\rm frag}$ corresponds to the mass of the object that has been shattered, then this object's radius is $\sim 500\,$km, approximately the size of Ceres.

Given that the breakup of such a large object requires an impact with a massive projectile, and that the probability for such two-body encounters is likely to decrease with object sizes, we consider here that $v_{\rm frag}$, the velocities of the escaping post-impact fragments, are randomly distributed between 0 and $v_{\rm esc}$, where $v_{\rm esc}$ is the escape velocity of the initial target. The initial velocity has then two components: 1) the Keplerian velocity of the progenitor parent body, and 2) a kick velocity, which has no reasons not to be isotropic (Jackson & Wyatt 2012), where kick angles are isotropically distributed onto a sphere. The initial eccentricity and inclination distributions of the ejecta are then automatically obtained from this constraint on $v_{\rm frag}$. For our nominal set-up, we obtain $< e > = 2 < i > \sim 0.037$.

For the grain composition, crucial for the calculation of collision outcomes and for estimating their response to radiation pressure (value of β), but also for the production of synthetic images and SEDs with GRaTer, we consider generic astrosilicates (Draine 2003). For estimating observed luminosities, we consider that the star+disc system is at a distance of 30 pc.

The differential size distribution of the initial fragments follows a steep power law in $dN/ds \propto s^{-3.8}$, corresponding to the crushing law expected for the outcome of violent collisions (Takasawa et al. 2011; Leinhardt & Stewart 2012). The minimum size is taken to be around the blow-out size $s_{\rm cut}$ induced by radiation pressure,

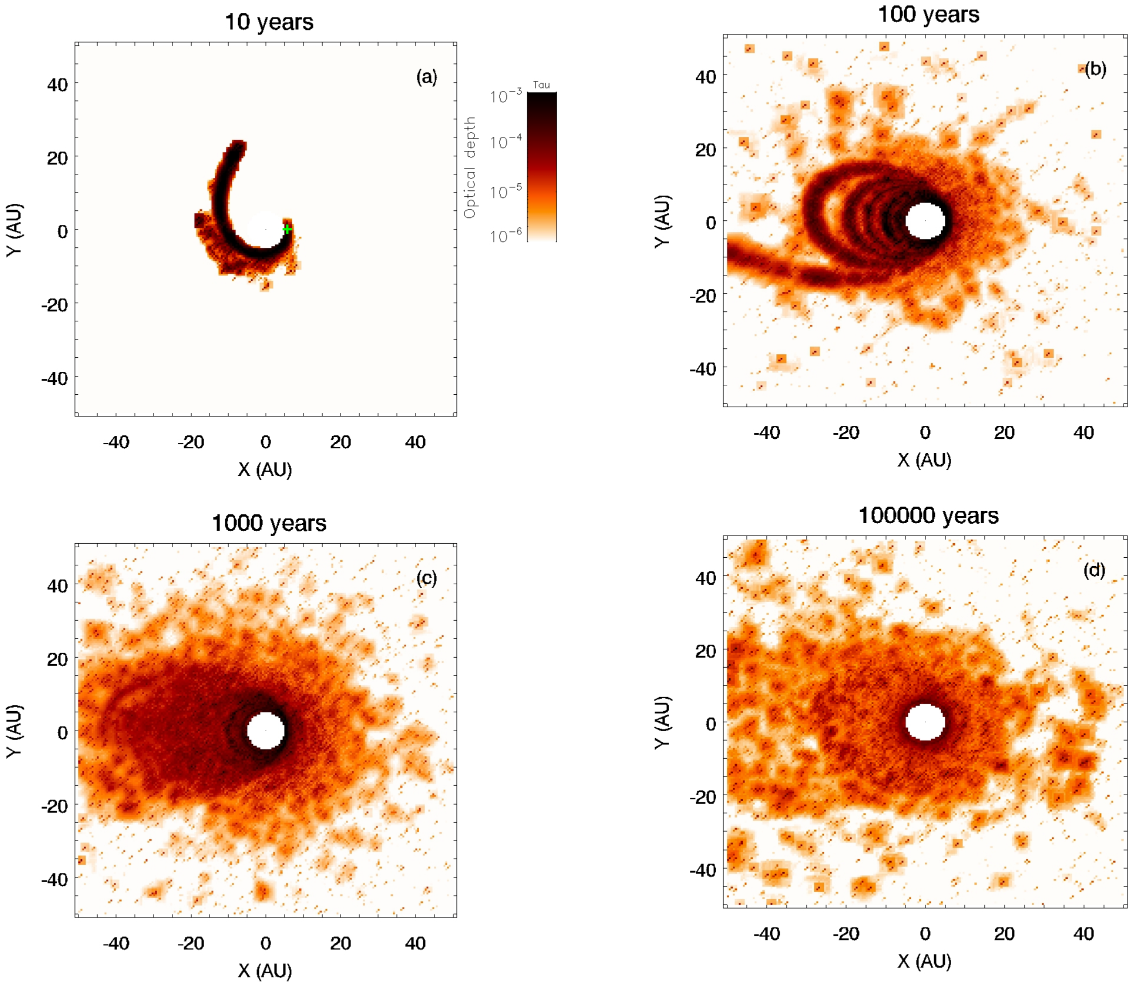

Fig. 1. Evolution of the system after the release of 10^{21}kg of material at 6 AU from the central A7V star. 2-D map of the optical depth at different epochs after the initial breakup. The green cross on plot (a) is the location of the initial breakup.

i.e., $\simeq 1.8\mu$m for compact astrosilicates around an A7V star. The maximum size of the initial fragments is set at 1m.

3.2 Results

3.2.1 Spatial Signature

In the immediate aftermath of the initial breakup, a one-armed spiral forms and propagates outwards (Fig. 1a). This spiral corresponds to the peak luminosity of the system's post-breakup evolution (see Fig. 2). Its outer parts consist mostly of small grains close to the blowout size, which are placed on highly-eccentric orbits by radiation pressure. The spiral fades out quickly and morphs into elongated concentric "ripples", which become more and more tightly wound with time (Fig. 1b). These features arise because all released fragments' orbits have to pass through the initial release position at X=6 AU, Y=0. As time goes by, however, these ripple features fade away and become undetectable after ~ 1000 years.

Next, the system enters a more long-lived phase where it assumes the shape of an asymmetric eccentric disc (Fig. 1c). This elongated shape is due to the fact that, during this period, most grains still have their orbits passing by a point close to the initial release location, and that the disc's geometrical cross section is dominated by small grains, close to the blowout limit, which have high-e orbits. Note, however, that the bulk of the system's *mass*, which is contained in the biggest particles, is located in a nearly-circular ring passing by the release point at 6 AU. This ring forms due to Keplerian shear over a few dynamical periods. Its width is set by the initial velocity dispersion of the post-release fragments. This ring logically also corresponds to the region where most of the collisional activity takes place. Hence, another brightness asymmetry created by the clustering of orbits close to the release point is clearly seen during the early evolution phase (Fig. 1c).

As time goes by, however, the asymmetric elongated disc structure progressively fades out. Figs 1c,d clearly show that the initially tenuous outer regions of the right-hand side progressively fill up with matter. This matter consists mostly of small grains, placed on high-e orbits by radiation pressure, which have been produced by second (or more) generation collisions in regions that are no longer that of the initial breakup. One of the main production sources is the aforementioned inner ring made of all the biggest initially released fragments.

3.2.2 Detectability

In order to estimate the detectability of this flux excess, we plot on Fig. 2 (left) the evolution of the disc-integrated flux at 24μm, as observed at a 30pc distance. As a typical criterion for detectability, we take as a reference the performance of the Spitzer/MIPS instrument at 24 microns. We consider that the disc-to-star flux ratio should exceed 10% for a 3 sigma, or larger, detection of an excess above the stellar photosphere.

As can be seen, for our nominal case, the disc signature remains detectable, at 24μm, for the whole duration of the simulation (10^5 years). Since $F_{\rm dust}/F_{\rm star}$ follows an approximate $t^{-0.3}$ decrease, it is easy to extrapolate the Fig. 2 (left) curve to later times. The extrapolated time at which the system reaches the critical $F_{\rm dust}/F_{\rm star} \sim 0.1$ value is then $\sim 10^6$ years, which gives the approximate duration of the detectability phase.

Another important result is that, in the inner disc regions ($\sim$ 6 AU) considered here, the flux excess due to one massive impact greatly exceeds that of a debris disc at steady-state, i.e., a disc whose luminosity is due to a "standard" collisional cascade. We verify this by plotting in Fig. 2 (left) the maximum possible luminosity (in black), at 2 different ages (1 and 10 Myrs after the equilibrium collisional cascade phase is reached), expected for such a steady-state disc. As can be clearly seen, our post massive-breakup disc is, for the whole duration of the simulation, at least one order of magnitude brighter than even a very young steady-state disc only 1 Myrs after its collisional cascade phase has begun.

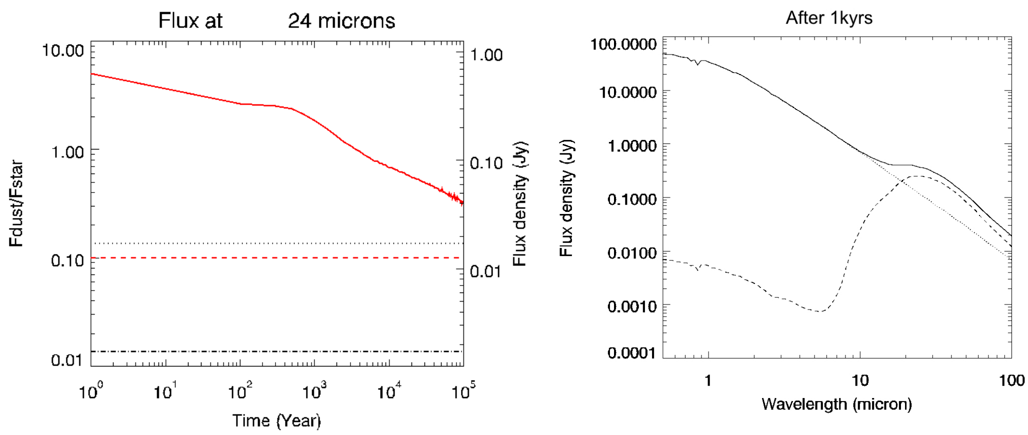

Fig. 2. Left : Evolution of the disc-integrated flux at 24 μm (red solid line). The red dashed line marks a dust-to-star flux ratio equal to 0.1, taken as our detectability criteria. The dotted and dash-dotted black lines give the maximum possible luminosity, at 1Myrs and 10Myrs, for a hypothetical collisional cascade at steady-state. The X-axis indicates the time after the breakup in years. The right-hand side Y-axis indicates the absolute flux in Jy, while the left-hand side axis displays the ratio of the disc flux to that of the stellar photosphere. **Right** : SED of the integrated system at 1 kyrs after the breakup. The full line represents the total (stellar photosphere + disc) luminosity, while the dashed line represents the sole contribution of the dust disc and the dotted one is that of the stellar photosphere.

Fig. 2 (right) shows the star+disc integrated SED, at 1kyrs after breakup, as computed with the GRaTer package. The excess due to the post-breakup dust appears clearly in the mid-IR domain, peaking around 25μm. This is confirmed by the synthetic images obtained with the GRaTer package at different wavelengths, showing that the dust disc is at its brightest in this $\lambda \sim 25\mu$m domain (see Fig. 3).

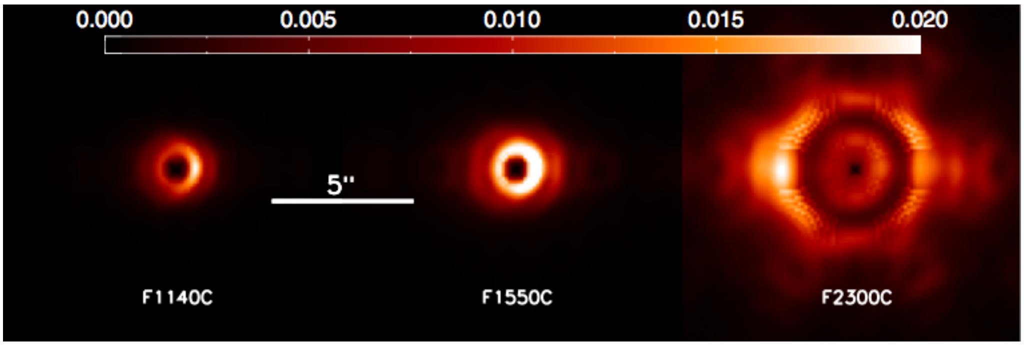

Fig. 3. Synthetic images, for the system in its "asymmetric disc" phase (at 10^4 years), at 10 pc, with the MIRI/JWST instrument with different filters at 11.4, 15.5 and 23μm (from left to right) obtained with the reference star subtraction method. The color scale gives the flux ratio with respect to the brightest pixel in the PSF (Point Spread Function).

We decided to go one step further and test the observability of the collision-induced discs with the expected performance of two instruments: SPHERE, at the VLT (Beuzit et al. 2008), and MIRI, the mid-IR instrument of JWST (Wright et al. 2010). We here compare the intensity level of the synthetic disc images to the residual starlight after processing the data, determined from simulations. Details about the procedure to create the synthetic images for each instrument are given in Kral et al. (2014).

The synthetic image with SPHERE (not shown here) at 1.6μm shows the potential to detect a left/right asymmetry in the inner region after a massive breakup happening at 10 pc, but the outer regions of the disc are undetectable.

Fig. 3 shows what would be seen by MIRI in thermal emission in the aftermath of such a collision. The 11.4μm image at 10 pc is relatively similar to the one obtained with the SPHERE simulation. It mainly shows the inner ring at the release distance (6 AU) and clearly reveals the increased luminosity of the right-hand side (the collision point) as compared to the left one. The situation is basically the same at 15.5μm, except that the image is brighter, which is logical because we are here closer to the wavelength at which the disc luminosity peaks. The disc brightness is such that even a system 500 times fainter would still be above the detectability limit. The peak luminosity is reached on the 23μm image, but the $2''$ Lyot coronagraph does here occult a large part of the disc. The central shadowed region reduces to 20 AU, so that the external regions of the post-breakup disc become visible. Interestingly, the brightest side of the disc is now the left region. This is a logical result, because this left outer region is mostly populated by small grains collisionally produced in the dense right-hand-side ansae of the ring and placed on eccentric orbits by radiation pressure.

We conclude that multi-wavelength observations with SPHERE, and above all MIRI, have the potential to resolve the signature of massive collisional events in the inner regions of nearby debris discs.

4 Conclusions

We presented the principle of the new LIDT-DD model and we have shown its potential on a first astrophysical case, that of massive collisions in an otherwise dust-empty region. This configuration had already been investigated in some previous studies, but so far only with simplified collisional and/or dynamical prescriptions (Lisse et al. 2009; Jackson & Wyatt 2012; Johnson et al. 2012; Jackson et al. 2014). LIDT-DD allows us to relax most of these restrictive assumptions by self-consistently following the collisional and dynamical fate of the breakup fragments.

Our simulations have shown (Kral et al. 2014) that the breakup of a Ceres-sized body at 6 AU from an A star leads to a luminosity excess that greatly exceeds that of a standard disc at collisional steady-state. The breakup's aftermath can be decomposed into three distinct phases. Firstly, a bright spiral, composed of close-to $\beta = 0.5$ grains, quickly forms and evolves into ripple-like structures over a few dynamical timescales. In parallel, a narrow ring, made of the largest breakup fragments, forms by Keplerian shear at the radial location of the release. The second phase, which is more long-lived, corresponds to an asymmetric disc, brighter and more compact on the side of the initial breakup and more extended and diffuse on the opposite side. The luminosity of this disc decreases with time, while its asymmetries are progressively resorbed by collisional activity. The third and final phase corresponds to the symmetrization of the system, which occurs on a timescale of a few 10^5 years. An important point is that asymmetries are here resorbed by collisional activity *alone*, in the absence of planets or any other perturbing bodies or processes. More specifically, they are resorbed by the gradual dispersion of material due to the coupled effect of successive collisions and Keplerian motion, and the reprocessing of new fragments in regions initially devoid of material.

Using the GRaTer package, we find that the flux excess created by the initial breakup should be clearly detectable, at $24\,\mu$m, for the reference case of a Ceres mass body at 6 AU from an A7V star. This luminosity excess should be observable in photometry, at 30 pc, for at least $\sim 10^6$ years with Spitzer/MIPS.

To assess the observability of the asymmetries, we compute synthetic images for the SPHERE/VLT and MIRI/JWST instruments. With SPHERE at 1.6μm, the left/right asymmetry at the collision point (6 AU) should be detectable from a 10 pc distance, but just above the detection limit. The situation is more favourable with MIRI, as the same asymmetry should be clearly seen, at 10 pc, well above the detection limit at 11.4 and 15.5μm. At 23μm, because of the large Lyot coronagraph, only the external regions of the disc can be mapped out, but the left/right asymmetry is here also detected, albeit with the anti-breakup side now being the brightest. This is an expected result and could be used as an indicator of the signature of massive collisional events.

The present study has shown the potential of the LIDT-DD code for future investigations of massive collisions, in particular when coupled to the GRaTer package to produce accurate SEDs and synthetic images.

Q.K. acknowledges financial support from the French National Research Agency (ANR) through contract ANR-2010 BLAN-0505-01 (EXOZODI). SC acknowledges the financial support of the UnivEarthS Labex program at Sorbonne Paris Cit (ANR-10-LABX-0023 and ANR-11-IDEX-0005-02).

References

Beuzit, J.-L., Feldt, M., Dohlen, K., et al. 2008, Proc. SPIE, 7014,

Charnoz, S., Taillifet, E., 2012, ApJ, 753, 119

Draine, B. T. 2003, ARA&A, 41, 241

Gáspár, A., Rieke, G. H., & Balog, Z. 2013, ApJ, 768, 25

Jackson, A. P., & Wyatt, M. C. 2012, MNRAS, 425, 657

Jackson, A. P., Wyatt, M. C., Bonsor, A., & Veras, D. 2014, MNRAS, 440, 3757

Johnson, B. C., Lisse, C. M., Chen, C. H., et al. 2012, ApJ, 761, 45

Kenyon, S. J., & Bromley, B. C. 2004, AJ, 127, 513

Kral, Q.; Thebault, P.; Charnoz, S., 2013, A&A, 558, A121

Kral, Q., Thebault, P., Augereau, J.-C., Boccaletti, A., & Charnoz, S. 2014, arXiv:1409.7609

Leinhardt, Z. M., & Stewart, S. T. 2012, ApJ, 745, 79

Lisse, C. M., Chen, C. H., Wyatt, M. C., et al. 2009, ApJ, 701, 2019

Takasawa, S., Nakamura, A. M., Kadono, T., et al. 2011, ApJL, 733, L39

Thebault, P., Augereau, J. C., 2007, A&A, 472, 169

Wright, G. S., Rieke, G., Boeker, T., et al. 2010, Proc. SPIE, 7731,

Wyatt, M. C. 2008, ARA&A, 46, 339

SF2A 2014
J. Ballet, F. Bournaud, F. Martins, R. Monier and C. Reylé (eds)

DETAILED MODELS OF A SAMPLE OF DEBRIS DISKS: FROM HERSCHEL, KIN AND SPITZER TO THE JWST

J. Lebreton[1], C. Beichman[1,2] and J.C. Augereau[3]

Abstract. Dusty debris disks surrounding main sequence stars are extrasolar equivalents to the Solar System populations of asteroids, icy bodies and dust grains. Many were observed in thermal emission by Herschel with unprecedented wavelength coverage and spatial resolution, complementing available scattered light images, mid-infrared spectra and interferometric measurements. We present detailed models of the HD 181327 and HD 32297 disks obtained with the GRaTer radiative transfer code and made possible thanks to Herschel. We then focus on the intriguing case of the nearby F2V star η Corvi that shows strong infrared excess despite an estimated age of 1.4 Gyr. We establish a detailed model of its disk from the sub-AU scale to its outermost regions based on observations from the Keck Interferometer Nuller, Herschel and Spitzer. These bright and extended disks will be of prime interest for future observations with the JWST. We finally discuss new debris disks science that will be addressed with the NIRCam and MIRI instruments.

Keywords: Debris disks, radiative transfer, Herschel, JWST, HD 181327, HD 32297, η Crv

1 Introduction

Debris disks are the dusty component of planetary systems. The grains are the by-product of collisions occurring between large planetesimals (comets, asteroids, Kuiper Belt objects). They are distinct from protoplanetary disks because they have no (or little) gas and they are optically thin: their evolution is driven by photo-gravitational forces and collisions. In favorable cases in which the disks can be imaged, structures such as belts, clumps or, asymmetries, and measurements of the dust density profile are precious clues of the dynamical activity of the global planetary system. Famous examples of structured debris disks include β Pictoris (Golimowski et al. 1993), Fomalhaut (Kalas et al. 2005) and AU microscopii (Augereau & Beust 2006).

There are only few cases of disks that harbor unambiguous spectral features (*e.g.* Beichman et al. 2005). Yet details on the properties of debris disks can be retrieved using radiative transfer models such as the one implemented in the GRaTer code (Augereau et al. 1999; Lebreton et al. 2012, 2013). In cases where both high-resolution images (e.g. Herschel, HST) and detailed Spectral Energy Distributions (SED) are available, it becomes possible to infer the properties of the dust and to constrain the collisional and dynamical activity of a planetary systems.

2 HD 181327: A very young, 90 AU-wide debris disk

In Lebreton et al. (2012), we performed a detailed study of the HD181327 debris disk based on observations from Herschel. The star is an F5/6V member of the β Pictoris moving group located at 51.8 pc. It has thus a well determined age ($\sim$ 20Myr) that corresponds to the earliest stages of a debris disk life. Its disk is very bright and it is extended enough to be resolved by Herschel/PACS at 70μm (Figure 1). Higher-resolution images were obtained with the HST, the latest of which were shown by (Schneider et al. 2014, with STIS). We inverted the HST/NICMOS surface brightness images in order to construct radial density profiles. The

[1] Infrared Processing and Analysis Center / NASA Exoplanet Science Institute, California Institute of Technology, Pasadena, CA 91125, USA.
[2] Jet Propulsion Laboratory, California Institute of Technology, 4800 Oak Grove Dr., Pasadena, CA 91107, USA
[3] UJF-Grenoble 1 / CNRS-INSU, Institut de Planétologie et d'Astrophysique de Grenoble (IPAG) UMR 5274, Grenoble, F-38041, France

dust is distributed in a narrow belt at 89.5 AU, slightly inclined with respect to the plane of the sky. SED measurements are available for a wide-range of wavelengths from the mid-infrared to the millimeter domain, including extensive coverage from Herschel/PACS and SPIRE and Spitzer/MIPS, MIPS-SED and IRS. Having a well-defined radial density profile is a prerequisite to study the dust properties in details. We used it has an input in the GRaTer code, we parameterized the size distribution and composition, solved the radiative transfer and computed optical efficiencies to generate synthetic SEDs. We found that simple icy grain models (silicate or carbonaceous material) fail at reproducing the overall SED and we rather proposed a self-consistent model (Figure 2) consisting of porous grains ($63 \pm 21\%$ "empty"), made of carbon and silicate, mixed with water ice ($67 \pm 7\%$ in volume fraction). The size distribution consistent with a collisional equilibrium and the radiation pressure blowout of small grains. The disk has a total mass of $0.05 \pm 0.02\, M_\oplus$ in grains smaller than 1 mm and we can extrapolate that there are as much as $50\, M_\oplus$ of planetesimals smaller than 1 AU in the belt. Our conclusion on the composition of the grains is strongly attested by the statistical Bayesian inference method we developped. We also note that there is no need for a secondary belt located closer to the star and that if one was detected, in would not impact our conclusions on the dust properties.

3 HD 32297: Icy dust in a bright edge-on disk

In a second paper (Donaldson et al. 2013), we applied the same methodology to another young debris disk. HD 32297 is a 30 Myr star and unlike HD 181327, it is edge-on. This makes it a favorable case for high-resolution coronagraphic imaging from the ground. In this case, the disk surface density profile is based on images obtained with the VLT/NaCo instrument (Boccaletti et al. 2012). We find that the disk is composed of a dust belt at 110 AU and that it requires an additional dust component around near the habitable zone to explain the mid-infrared SED. Based on a this two-component model of the SED from Herschel, Spitzer and ancillary measurements, we find that the HD 32297 dust is very similar to the one of HD 181327. It includes 50% of ice and is is 90% porous. Overall, we conclude that these dust models including silicates, carbonaceous material, water ice and porosity and reminiscent of comet-like compositions should be used to properly interpret the properties of debris disks. We proved that the presence of ice can be inferred depsite the absence of strong solid-state features.

Recently, we obtain new images of the disk with the Palomar/P1640 coronagraph that suggest one side of the disk is brighter and/or more extended than the other side. Future scattered light studies could allow us to measure the dependence of the size distribution to distance, bringing more constraints on the dynamics and collisions.

4 η Corvi: A cold and a warm debris rings around a Gyr old star

η Crv is a nearby (18.2 pc) F2V star surrounded by a massive debris disk despite an estimated age of 1.4 Gyr. The peculiarity of this object is its strong and structured mid-infrared excess that provides information on the properties of its warm dust component. We revised the Spitzer/IRS spectra of the disk (Chen et al. 2006) and carefully proceeded to the photosphere subtraction. The relative excesses below 18μm are small and are very sensitive to assumptions on the stellar spectrum. The disk has two spatially separated components as it clearly appears in the Herschel/PACS images at 70, 100 and 160μm (Figure 1). The outer one reaches the maximum of its surface brightness at 6 to 7.5" along the major axis. There is marginal evidence for side-to-side asymmetry or offset but at smaller scale that the PACS resolution. The inner component (exozodi) is unresolved by Herschel. We used interferometric nulls from the Keck Interferometer Nuller to spatially constrain the exozodi location and correct it with respect to what is inferred from simple SED fitting. We modeled in details the two-component debris disk from the sub-AU scale to its outermost regions by fitting simultaneously the interferometric nulls, the Herschel images and the spectro-photometric data against a large parameter space. We found that the cold material resides at an orbital distance of 133 AU and is consistent with a collisional cascade occurring in a parent reservoir of ice-free planetesimals. The warm component is located between 0.2 and 1 AU and its surface density decreases slowly. The exozodiacal dust has a very high albedo produced by forsterite-rich grains with an overabundance of small grains. Our analysis provides accurate estimates of the fundamental parameters of the disk: its surface density profile, grain size distribution composition and mass. The overall architecture of the system is very similar to that of the Fomalhaut debris disk. Given its age we support previous claims that the system is likely encountering a violent Late Heavy Bombardment (Lisse et al. 2012). Our study is presented in Lebreton J. et al. (2015) (submitted).

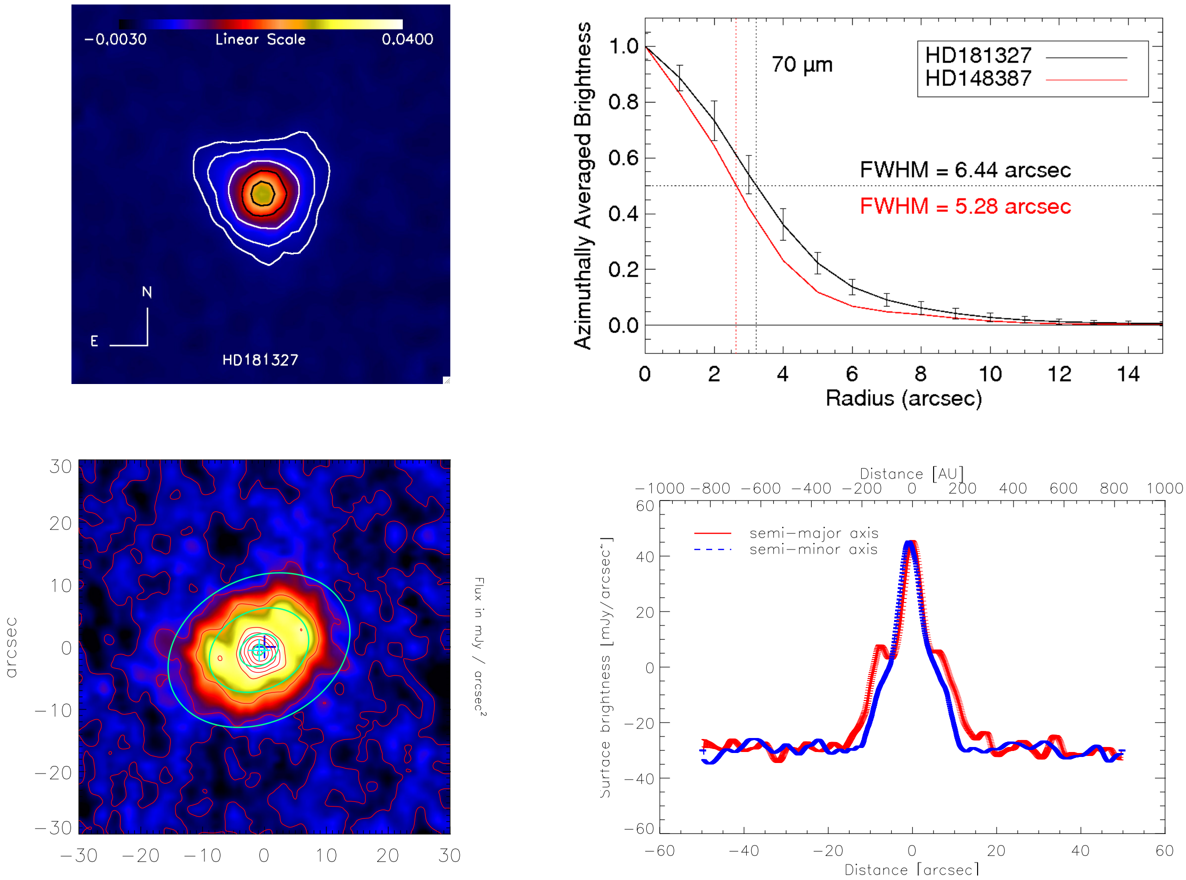

Fig. 1. Herschel/PACS 70μm images (**Left**) and radial brightness profiles (**Right**) of **Top:** HD 181327 and **Bottom:** η Crv. The HD 181327 profile is compared with the PSF reference HD 148387 to show that the disk is resolved. The η Crv profile is resolved along both axis of the inclined disk; along the major axis, the outer belt is clearly distinguishable. The HD 32297 data are not shown because the disk is spatially unresolved.

5 JWST perspectives

The James Webb Space Telescope is scheduled for launch in 2018. Two instruments will be particularly interesting for debris disk studies. NIRCam is a near-infrared imager operating in the 1 to 5 μm range. MIRI has a camera and a spectrograph, it operates between and 5 and 23 μm. Both instruments are equipped with coronagraphs and will offer an inner working angle and resolution comparable to the HST, but in a whole new wavelength range.

Debris disks are faint in scattered light and they rarely have strong spectral features. Yet icy debris disks detected by Herschel have a detectable ice features at 3 microns. Imaging the disks within several NIRCam filters will make it possible to detect dips in the spectrum providing the first unambiguous detections of debris disk ices. The ice-line is of prime importance in the formation and evolution of planetary systems and we may also be able to locate ices other than H_2O, such as CO_2, CO or NH_3, either by looking for features in the 4 to 5 μm range or by measuring color gradients within the medium-band filters. The colors and spectra of minor bodies in the Solar System provide a lot of constraints on its formation history and JWST will make it possible to conduct these studies for extrasolar planetary systems.

MIRI will permit to observe the mid-infrared silicate absorption bands. A more complete coverage of the SED at the transition between scattered- and thermal light-dominated regimes will further constrain the grain optical properties and help understand discrepancies between scattered light images and far-infrared models. Finally in terms of imaging, NIRCam and MIRI will teach us a lot about debris disk structures such as asymmetries, clumps, gaps or spiral structures providing further constraints on the systems dynamics. In Lebreton et al.

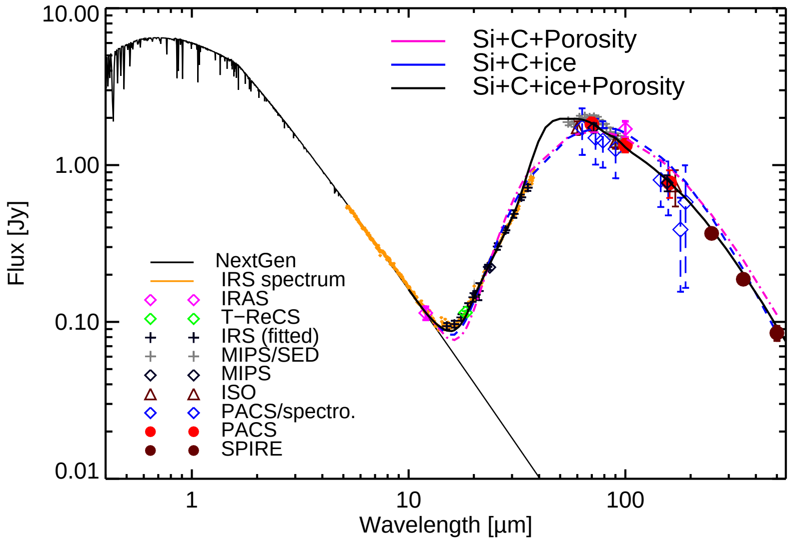

Fig. 2. Spectral Energy Distribution and models of the HD 181327 debris disk. The figure is an update since Lebreton et al. (2012) incorporating new data from Herschel/SPIRE. Three of the best models are shown with reduced $\chi^2 =$ 6.1, 4.5, 1.6 respectively (44 or 43 degrees of freedom).

2015b (in preparation) we will present simulations of the performances of NIRCam and develop concepts for debris disks studies.

6 Acknowledgment

We acknowledge the numerous authors who participated to this work and refer to the cited journal articles for the complete list of contributors. JL thanks the SF2A for its support.

References

Augereau, J. & Beust, H. 2006, Astronomy & Astrophysics, 455, 987

Augereau, J. C., Lagrange, A. M., Mouillet, D., Papaloizou, J. C. B., & Grorod, P. A. 1999, Astronomy & Astrophysics, 348, 557

Beichman, C. A., Bryden, G., Gautier, T. N., et al. 2005, The Astrophysical Journal, 626, 1061

Boccaletti, A., Augereau, J.-C., Lagrange, A.-M., et al. 2012, A&A, 544, A85

Chen, C. H., Sargent, B. A., Bohac, C., et al. 2006, The Astrophysical Journals, 166, 351

Donaldson, J. K., Lebreton, J., Roberge, A., Augereau, J.-C., & Krivov, A. V. 2013, The Astrophysical Journal, 772, 17

Golimowski, D. A., Durrance, S. T., & Clampin, M. 1993, ApJ, 411, L41

Kalas, P., Graham, J. R., & Clampin, M. 2005, Nature, 435, 1067

Lebreton, J., Augereau, J.-C., Thi, W.-F., et al. 2012, Astronomy & Astrophysics, 539, A17

Lebreton, J., van Lieshout, R., Augereau, J.-C., et al. 2013, Astronomy & Astrophysics, 555, A146

Lebreton J., Beichman, C., Bryden, G., et al. 2015, Submitted to The Astrophysical Journal

Lisse, C. M., Wyatt, M. C., Chen, C. H., et al. 2012, the Astrophysical Journal, 747, 93

Schneider, G., Grady, C. A., Hines, D. C., et al. 2014, AJ, 148, 59

Session 08

Interaction étoiles planètes

SF2A 2014
J. Ballet, F. Bournaud, F. Martins, R. Monier and C. Reylé (eds)

HYDRODYNAMICAL SCALING LAWS TO STUDY TIDAL DYNAMICS IN PLANETARY SYSTEMS

P. Auclair-Desrotour[1,2], C. Le Poncin-Lafitte[3] and S. Mathis[2,4]

Abstract. Tidal dissipation in stars and planets intrinsically depends on the nature of their tidal response, which is directly linked to their internal structure and rheology. Indeed, solids and fluids do not behave in the same way, the response of the second being highly resonant. This study, focused on viscous friction acting on tidal waves, uses a local model to provide scaling laws allowing to better understand the physics of dissipation in the fluid regions of celestial bodies. It shows how the nature and properties of low-frequency tidal gravito-inertial waves change with fluid parameters such as viscosity, thermal diffusivity, rotation and stratification. Besides, the scaling laws derived from the local model are applied to the tidal dynamics of a two-body system that highlights the impact of the characteristics of dissipation.

Keywords: hydrodynamics, waves, turbulence, planet-star interactions

1 Introduction

Since the theoretical calculations carried out by Lord Kelvin (Kelvin 1863), who was the first to consider a tidally deformed celestial body, tides have occupied a central place in the study of planetary systems. In this context, gravitational tides have been studied mainly thanks to the developments made by Love and the corresponding Love numbers (Love 1911). Then, Goldreich brought a major contribution in the 1960's with the introduction of the tidal quality factor Q, which is a general way to take into account tidal dissipation in celestial mechanics (Goldreich & Soter 1966). This is of great importance since tides drive the secular orbital/spin evolution of stars, planets and satellites by converting their mechanical kinetic energy into internal heating (Laskar et al. 2012; Bolmont et al. 2014).

However, the mechanisms driving tidal dissipation are not the same in solids and fluids. They depend on the nature of the materials that compose a body and on the structure of this later. Studies dealing with the effects of gravitational perturbations in rocky cores and planets (see for example Efroimsky & Lainey 2007; Efroimsky 2012; Remus et al. 2012b) show that the Q factor of these solid bodies varies regularly with the forcing frequency, which obviously does not match with the case of fluid bodies. Indeed, numerous works published during the last decades (Zahn 1966, 1975; Ogilvie & Lin 2004, 2007; Remus et al. 2012a, for stars and the envelopes of giant planets) attest of the resonant response of fluid bodies to tidal perturbations, this behavior being synonym of a strong dependence of the Q factor on the tidal frequency and of an erratic evolution of the orbital dynamics (Auclair-Desrotour et al. 2014).

Such a behavior is explained by dissipation mechanisms, like the viscous friction, thermal diffusion and Ohmic diffusion (in the presence of a magnetic field), acting on fluid tidal waves. This work focuses on viscous friction within a low-frequency range and does not take into account magnetic aspects. So, high-frequency acoustic waves are left aside, like Alfvén waves which propagate in magnetized fluid regions, and gravito-inertial waves only remain. These laters predominate the tidal response of stars, the external envelope of giant planets and the fluid layers of rocky planets and satellites like the Earth or Europa.

[1] IMCCE, Observatoire de Paris, UMR 8028 du CNRS, UPMC, 77 Av. Denfert-Rochereau, 75014 Paris, France
[2] Laboratoire AIM Paris-Saclay, CEA/DSM - CNRS - Université Paris Diderot, IRFU/SAp Centre de Saclay, F-91191 Gif-sur-Yvette Cedex, France
[3] SYRTE, Observatoire de Paris, UMR 8630 du CNRS, UPMC, 77 Av. Denfert-Rochereau, 75014 Paris, France
[4] LESIA, Observatoire de Paris, CNRS UMR 8109, UPMC, Univ. Paris-Diderot, 5 place Jules Janssen, 92195 Meudon, France

Inertial waves are driven by rotation, gravity waves by stratification, and their restoring forces are the Coriolis acceleration and the buoyancy respectively. Their characteristic frequencies are the so-called inertial frequency 2Ω, Ω being the spin frequency of the body, and the Brunt-Väisälä frequency N corresponding to the radial variations of the specific entropy. Gravito-inertial waves result from their coupling in stably stratified rotating fluid regions. Thus, to study their complex dissipation by using a reduced local model appears as an interesting way to explore its behavior over large domains of parameters (see also Ogilvie 2005; Jouve & Ogilvie 2014). Such studies are complementary of those carried out with complex global models.

The aim of the present work is to propose a method to investigate the dependence of tidal dissipation on the fluid parameters. Using a fluid box in which rotation, stratification, viscosity and thermal diffusivity are taken into account, scaling laws describing viscous friction on tidal waves are obtained (Auclair-Desrotour, Mathis, Le Poncin-Lafitte in preparation for the complete derivation). Next, these scaling laws are used to illustrate, through the concrete example of a planet-satellite system, how the quality factor Q and the evolution of orbital dynamics are linked to the fluid parameters (see Auclair-Desrotour et al. 2014).

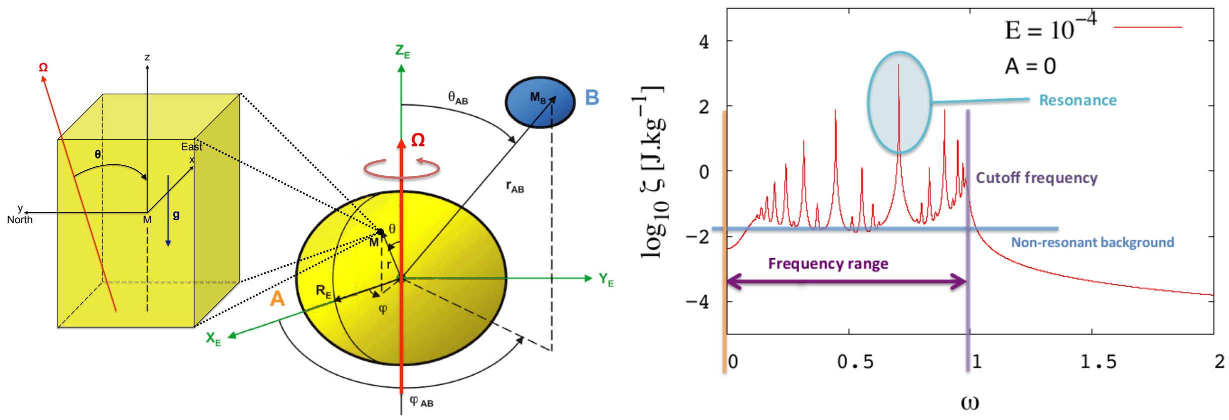

Fig. 1. Left: The local analytical model: a Cartesian fluid section of a rotating fluid body A tidally excited by a perturber B. The control parameters are the viscosity ν, thermal diffusivity κ and frequencies 2Ω and N of the fluid. **Right:** A typical dissipation spectrum computed from the local model. ζ is the energy dissipated by viscous friction per mass unit over a rotation period in the box; $\omega = \chi/2\Omega$ is the tidal frequency of the perturbation normalized by the inertial frequency 2Ω; $E = 2\pi^2\nu/\left(\Omega L^2\right)$ is the Ekman number and $K = 2\pi^2\kappa/\left(\Omega L^2\right)$ the normalized thermal diffusivity. Here $K = 0$ and $A = 0$, which means that the waves are purely inertial and viscously damped (top left blue zone in Fig. 2).

2 Hydrodynamical scaling laws

The model used here generalizes the first local model presented in Ogilvie & Lin (2004). Consider a local section of a fluid region in a rotating star, planet or satellite tidally excited by a perturber. It is a rotating Cartesian box of side length L inclined with respect to the spin axis of the body $\boldsymbol{\Omega}$ by a colatidude θ (Fig. 1). The coordinate z corresponds to the radial direction, x and y to the azimutal and latitudinal ones. In the box, the fluid is supposed homogeneous of density ρ, kinetic viscosity ν and thermal diffusivity κ. Three dimensionless control parameters are identified: $A = (N/2\Omega)^2$ giving the nature of the waves ($A \ll 1$ for inertial waves, $A \gg 1$ for gravity ones), the so-called Ekman number $E = 2\pi^2\nu/\left(\Omega L^2\right)$ weighting the terms of viscous diffusion with respect to the Coriolis terms, and $K = 2\pi^2\kappa/\left(\Omega L^2\right)$ which is a equivalent of E for thermal diffusion. The Prandlt number $Pr = E/K$ compares the viscous and thermal diffusions (see Fig. 2).

Decomposing variables into Fourier series allows to compute an analytical expression for the energy ζ per mass unit dissipated by viscous friction over a rotation period ($T = 2\pi/\Omega$). This gives access to the properties of the dissipation spectrum (Fig. 1), which has the shape of a batch of resonances located between ω_- and ω_+ (see Gerkema & Shrira 2005, for their expression). Four different asymptotical behaviors are identified. They are represented in Fig. 2 and illustrated by the corresponding spectra. Scaling laws for the viscous friction are derived analytically in each regime for the positions ω_{mn}, widths at mid-height l_{mn} and heights H_{mn} of resonances ($m, n \in \mathbb{Z}$), the number of peaks $N_{\rm kc}$, the height of the non-resonant background $H_{\rm bg}$ (that

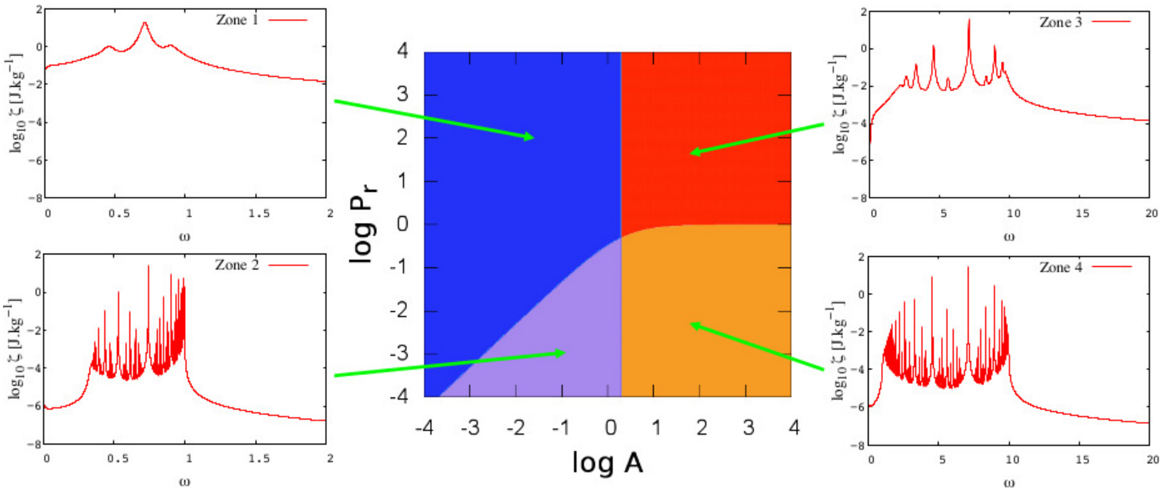

Fig. 2. Asymptotical behaviors of the tidal waves. Zones colored in blue and purple correspond to inertial waves, the two other to gravity waves ; zones colored in blue and red correspond to the case where viscous diffusion predominates over thermal diffusion, the two zones below corresponding to the opposite case.

corresponds to the so-called equilibrium tide) and the sharpness ratio $\Xi = H_{11}/H_{\rm bg}$ of the spectrum. Ξ gives the relative contrast between the resonances and the background (Table 1).

Table 1. Scaling laws for the properties of the energy viscously dissipated for the different regimes (we define $A_{11} \equiv 2\cos^2\theta$ and $Pr_{11} \equiv A/(A + A_{11})$). **Top left:** Inertial waves dominated by viscosity. **Top right:** Gravity waves dominated by viscosity. **Bottom left:** Inertial waves dominated by heat diffusion. **Bottom right:** Gravity waves dominated by heat diffusion. F is the amplitude of the forcing.

Domain	$A \ll A_{11}$		$A \gg A_{11}$	
$Pr \gg Pr_{11}$	$\frac{\chi_{mn}}{2\Omega} \propto \frac{n}{\sqrt{m^2+n^2}}\cos\theta$	$N_{\rm kc} \propto E^{-1/2}$	$\frac{\chi_{mn}}{2\Omega} \propto \frac{m}{\sqrt{m^2+n^2}}\sqrt{A}$	$N_{\rm kc} \propto A^{1/4}E^{-1/2}$
	$l_{mn} \propto E$	$H_{mn} \propto F^2E^{-1}$	$l_{mn} \propto E$	$H_{mn} \propto F^2E^{-1}$
	$H_{\rm bg} \propto F^2E$	$\Xi \propto E^{-2}$	$H_{\rm bg} \propto F^2EA^{-1}$	$\Xi \propto AE^{-2}$
$Pr \ll Pr_{11}$	$\frac{\chi_{mn}}{2\Omega} \propto \frac{n}{\sqrt{m^2+n^2}}\cos\theta$	$N_{\rm kc} \propto A^{-1/2}K^{-1/2}$	$\frac{\chi_{mn}}{2\Omega} \propto \frac{m}{\sqrt{m^2+n^2}}\sqrt{A}$	$N_{\rm kc} \propto A^{1/4}K^{-1/2}$
	$l_{mn} \propto AK$	$H_{mn} \propto F^2A^{-2}EK^{-2}$	$l_{mn} \propto K$	$H_{mn} \propto F^2EK^{-2}$
	$H_{\rm bg} \propto F^2E$	$\Xi \propto A^{-2}K^{-2}$	$H_{\rm bg} \propto F^2EA^{-1}$	$\Xi \propto AK^{-2}$

3 Impact on tidal dynamics

As described above, the properties of the dissipation directly impact the long-term evolution of planetary systems. This point is easily illustrated through the case of a two-bodies coplanar system, for example a satellite orbiting circularly around a planet (e.g. the Mars-Phobos case studied by Efroimsky & Lainey 2007). If we introduce in the dynamical equations a frequency-dependent tidal quality factor (e.g. Mathis & Le Poncin-Lafitte 2009), which is proportional to the inverse of ζ in our local model, the semi-major axis a of the system evolves erratically (Fig. 3). Instead of falling on the planet regularly with an increasing velocity as in the case corresponding to Kaula's constant Q model (Kaula 1964), the satellite only comes nearer to it, jumping from a position to an other each times it meets a peak of resonance. Under some assumptions detailed in Auclair-Desrotour et al. (2014), the amplitude of a jump Δa can be written as a function of the frequency ω_p, width at mid-height l_p and sharpness ratio $\Xi_p = H_p/H_{\rm bg}$ of a peak,

$$\frac{\Delta a}{a} \approx \frac{2l_{\rm p}}{3\sqrt{\sqrt{2}-1}\,(1+\omega_{\rm p})}\left[\sqrt{\Xi_p}-1\right]^{\frac{1}{2}}. \tag{3.1}$$

Each of these characteristics are now given explicitly as functions of the internal parameters of the fluid, A, E and K thanks to scaling laws obtained in Table 1. For example, the variations of the width l_{11} and sharpness Ξ of the main dissipation resonance with the Ekman number E are represented in Fig. 3.

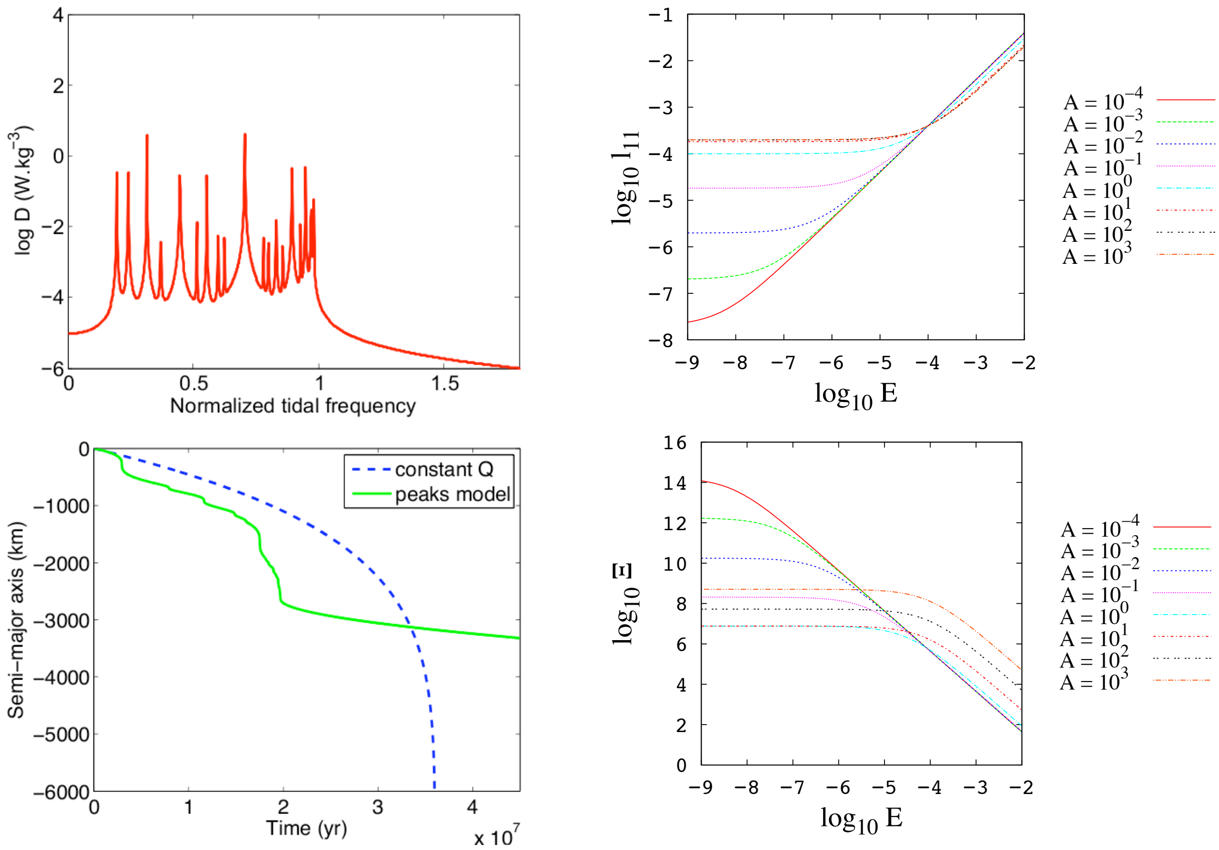

Fig. 3. Top left: A synthetical dissipation spectrum generated using the local model of the fluid box. D is proportional to ζ. **Bottom left:** The corresponding evolution of the semi-major axis a of the fluid planet-satellite system (for details, see Auclair-Desrotour et al. 2014). **Top right:** Width at mid-height of the main resonance of ζ as a function of the Ekman number $E = 2\pi^2\nu/\left(\Omega L^2\right)$ for different values of $A = (N/2\Omega)^2$. **Bottom right:** Sharpness of the main resonance of ζ as a function of the Ekman number E for different values of A.

4 Conclusions

The properties of fluid tidal dissipation have a direct impact on the secular dynamics of planetary systems. Indeed, dissipation resonances cause local rapid changes of orbital parameters, that are tightly related to the widths and heights of the peaks. In this context, our local model provides scaling laws that describe the evolution of the complex and resonant tidal dissipation as a function of fluid parameters. Moreover, It seems to be an interesting qualitative tool to unravel the complex physics of dissipation. In a near future, our method could be extended to magnetized fluid regions. It would allow to study Alfvén waves in addition to gravito-inertial waves and to refine the map of the asymptotical behaviors (Fig. 2) with new regimes. This will contribute to improve tidal dissipation modeling in studies of the dynamical evolution of planetary systems.

References

Auclair-Desrotour, P., Le Poncin-Lafitte, C., & Mathis, S. 2014, A&A, 561, L7
Bolmont, E., Raymond, S. N., von Paris, P., et al. 2014, ApJ, 793, 3
Efroimsky, M. 2012, ApJ, 746, 150
Efroimsky, M. & Lainey, V. 2007, Journal of Geophysical Research (Planets), 112, 12003
Gerkema, T. & Shrira, V. I. 2005, Journal of Fluid Mechanics, 529, 195
Goldreich, P. & Soter, S. 1966, Icarus, 5, 375
Jouve, L. & Ogilvie, G. I. 2014, Journal of Fluid Mechanics, 745, 223
Kaula, W. M. 1964, Reviews of Geophysics and Space Physics, 2, 661
Kelvin, L. 1863, Phil. Trans. Roy. Soc. London, Treatise on Natural Philosophy, 2, 837
Laskar, J., Boué, G., & Correia, A. C. M. 2012, A&A, 538, A105
Love, A. E. H. 1911, Some Problems of Geodynamics (Cambridge University Press)
Mathis, S. & Le Poncin-Lafitte, C. 2009, A&A, 497, 889
Ogilvie, G. I. 2005, Journal of Fluid Mechanics, 543, 19
Ogilvie, G. I. & Lin, D. N. C. 2004, ApJ, 610, 477
Ogilvie, G. I. & Lin, D. N. C. 2007, ApJ, 661, 1180
Remus, F., Mathis, S., & Zahn, J.-P. 2012a, A&A, 544, A132
Remus, F., Mathis, S., Zahn, J.-P., & Lainey, V. 2012b, A&A, 541, A165
Zahn, J. P. 1966, Annales d'Astrophysique, 29, 489
Zahn, J.-P. 1975, A&A, 41, 329

SF2A 2014
J. Ballet, F. Bournaud, F. Martins, R. Monier and C. Reylé (eds)

TIME EVOLUTION OF A VISCOUS PROTOPLANETARY DISK WITH A FREE GEOMETRY AND REALISTIC OPACITIES.

K. Baillié[1] and S. Charnoz[1]

Abstract. Aiming to model the favorable conditions for planetary formation, we have designed a hydrodynamical numerical model for the spreading of protoplanetary disks based on a self-consistent coupling between the disk thermodynamics, photosphere geometry and dynamics (Baillié & Charnoz., 2014, ApJ 786, 35). We retrieved the recurrent observational properties of protoplanetary disks around young Classical T Tauri type stars. One of the novelty of our approach lies in the proper treatment of the disk geometry, leading to the presence of non-irradiated zones. In addition, we show the importance of the physical composition of the disk: using a full-opacity model, our disk temperature takes into account the various changes of phases experienced by the different components of our gas-dust disk. This is crucial for estimating the resonant torques that a potential planet would experience in an evolved disk: these corotation and Lindblad torques are very sensitive to the discontinuities in surface-mass density and temperature gradients. From these torques, we show that there are some preferential zones for planetary embryos to accumulate and some regions could be totally depleted in planetary cores.

Keywords: Protoplanetary disks, Planets and satellites: formation, Planet-disk interactions, Accretion disks, Planets and satellites: dynamical evolution and stability, Hydrodynamics

1 Introduction

Recent observations of young star environments were able to provide physical constraints on protoplanetary disks from different regions. For example, Isella et al. (2009) analyzed the Taurus region while Andrews et al. (2009, 2010) focused on the Orion and Ophiuchus regions. While they noticed some common characteristics in regions that are not genetically related (in particular in the asymptotic behaviours of the surface mass density or pressure scale height profiles), numerical simulations from Baillié & Charnoz (2014) were able to retrieve these properties. Their viscous spreading hydrodynamical code involves coupling the photosphere geometry, the disk thermodynamics and its dynamics. In the present work, we improve this code by considering the disk composition and its evolution with the midplane temperature. We then use the evolved disks generated by this code to build migration torque maps for a putative planetary core within the disk. These torques are composed of a Lindblad contribution and a corotation contribution. Some places in the disk midplane seem to be able to accumulate planetary embryos while some others seem to be totally depleted in planets.

2 Model

2.1 Dynamical and thermodynamical evolution

The present numerical model is based on the hydrodynamical code described in Baillié & Charnoz (2014), following the viscous evolution of a viscous α disk (Shakura & Sunyaev 1973). Most of the usual asumptions are removed: we follow the disk evolution from an already formed Minimum Mass Solar Nebula and not just its final steady state. We jointly calculate the photosphere geometry: the angle at which the photosphere sees the star is governing the amount of energy that the photosphere is receiving from the star. Therefore, the disk is not only heated by viscous heating but also by stellar irradiation. The iterative process calculating the temperature also calculates a consistent photosphere height, therefore coupling the disk geometry with the disk

[1] Laboratoire AIM, Université Paris 7 Denis Diderot, CEA, CNRS, 91191 Gif-sur-Yvette, France

Elements	Condensation/Sublimation Temperature
Water ice	160 K
Volatile Organics	275 K
Refractory Organics	425 K
Troilite (FeS)	680 K
Olivine, pyroxene ([Fe,Mg] silicates)	1500 K

Table 1. Phase changes temperatures affecting the disk gas opacity.

thermodynamics, which is also linked to the dynamical evolution through the viscosity, as detailed in Equation 2.1 (Lynden-Bell & Pringle 1974) obtained from the mass and angular momentum conservation.

$$\frac{\partial \Sigma(r,t)}{\partial t} = \frac{3}{r}\frac{\partial}{\partial r}\left(\sqrt{r}\,\frac{\partial}{\partial r}\left(\nu(r,t)\,\Sigma(r,t)\,\sqrt{r}\right)\right) \tag{2.1}$$

2.2 *Opacity model*

The main elements of the disk dust are listed in Table 1 with their sublimation temperatures. As the midplane temperature varies accross the protoplanetary disk, the physical phases of the various elements change as well. This affects the disk opacity which in turn affects the temperature. Therefore, we tabulate the dust opacity as a function of the temperature and we use this updated local opacity in our iterative process for the determination of the temperature and geometry. We use the tabulated values from Semenov et al. (2003) summarized in Figure 1.

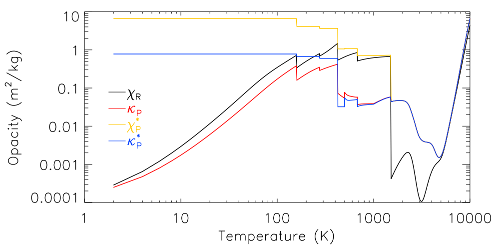

Fig. 1. Opacity variations with local temperature. Black: Rosseland mean opacity in extinction. Red: Planck mean opacity in absorption. Yellow: Planck mean opacity in extinction at stellar irradiation temperature. Blue: Planck mean opacity in absorption at stellar irradiation temperature.

The various opacities show very abrupt drops around the sulbimation temperatures of the dust elements.

3 Viscous evolution

Figure 2 shows the evolution of the surface mass density and temperature radial profiles as the disk viscously spreads. Previous conclusions form Baillié & Charnoz (2014) are retrieved: the disk reaches a steady state in a few million years, characterized by a uniform mass flux and a shallower surface mass density profile than initially. The asymptotic trends also recall the observations as we tend to $\Sigma \propto r^{-1}$.

3.1 *Detailed temperature profile*

The temperature remains mainly decreasing with the increasing radial distance. The disk appears to cool down as it ages. The thermal profiles reveal temperature plateaux coinciding with the sublimation temperatures reported in Table 1. The usual snow and sublimation lines are therefore enlarged and we may define a snow region in place of a snow line.

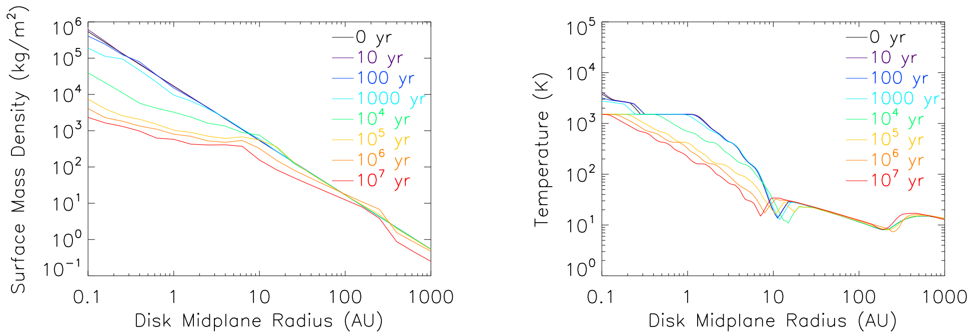

Fig. 2. Left: Surface mass density radial profile evolution for an initial minimum mass solar nebula in the case of a self-consistently calculated geometry with a full continuous model of opacities. **Right:** Corresponding mid-plane temperature radial profile evolution.

4 Migration torques

An already formed planetary embryo exchanges angular momentum with the disk (Goldreich & Tremaine 1979; Ward 1988; Artymowicz 1993; Jang-Condell & Sasselov 2005) due to the resonances excited by the planet in the disk. The planet exerts a torque on the disk and therefore the disk exerts an opposite torque on the planet. We assume that the disk structure is not modified by the presence of the planet.

4.1 Lindblad torques

We identify the Linblad resonances with a planet located at r_P by their wavenumber $m(r) = \sqrt{\frac{\kappa^2(r)}{(\Omega(r)-\Omega(r_P))^2 - \frac{c_s^2(r)}{r^2}}}$ where $c_s(r)$ is the local sound speed as defined in BC14 and $\kappa(r)$ is the epicyclic frequency. We use here the approach of Ward (1997) and Hasegawa & Pudritz (2011) who considered m as a continuous variable, function of the radius r and defined a midplane torque density exerted by the disk on the planet:

$$\frac{\mathrm{d}^2\Gamma}{\mathrm{d}z\mathrm{d}r}(r) = \epsilon\, 2\, q^2\, G\, M_* \left(\frac{r}{r_P}\right)^2 \frac{m^4}{(1+4\xi^2)} \frac{\Sigma(r)\,\psi^2}{h_{pres}(r)} \tag{4.1}$$

where $\epsilon = +1$ for $r > r_P$ and $\epsilon = -1$ for $r < r_P$, $q = \frac{M_P}{M_*}$, $\xi(r) = \frac{m(r)\,c_s(r)}{r\,\kappa(r)}$ and ψ is defined by $\psi = \left(1 + \frac{r_P}{r}\right)\frac{K_1(\Lambda)}{2} + \left(\frac{\epsilon}{2m} + 2\sqrt{1+\xi^2}\right)\frac{K_0(\Lambda)}{\sqrt{r/r_P}}$, where K_i is the modified Bessel function of the second kind of order i and $\Lambda = m\,\frac{\left|\frac{r}{r_P}-1\right|}{\sqrt{\frac{r}{r_P}}}$. Thus, it is possible to integrate the Lindblad resonant torque density over r.

4.2 Corotation torques

Using the formulas of Paardekooper et al. (2010) and Bitsch et al. (2014), we can estimate the entropic and barotropic corotation torque contributions:

$$\Gamma_{\mathrm{hs,entro}} = -\frac{\Gamma_0(r_P)}{\gamma^2}\, 7.9 \left(-\frac{\partial \ln T}{\partial \ln r}(r_P) + (\gamma-1)\frac{\partial \ln \Sigma}{\partial \ln r}(r_P)\right) \tag{4.2}$$

$$\Gamma_{\mathrm{hs,baro}} = -\frac{\Gamma_0(r_P)}{\gamma}\, 1.1 \left(\frac{\partial \ln \Sigma}{\partial \ln r}(r_P) + \frac{3}{2}\right) \tag{4.3}$$

with $\gamma = 1.4$, the adiabatic index, $\Gamma_0(r_P) = \left(\frac{q}{h}\right)^2 \Sigma(r_P)\, r_P^4\, (\Omega(r_P))^2$, $h = \frac{h_{pres}(r_P)}{r_P}$, and $\Omega(r_P)$ the keplerian angular velocity at the planet position in the disk.

4.3 Planetary traps and deserts

The total torque exerted by the disk on the planet is then given by $\Gamma_{\rm tot} = \Gamma_{\rm Lindblad} + \Gamma_{\rm hs,entro} + \Gamma_{\rm hs,baro}$. This total torque strongly depends on the temperature and surface mass density gradients. A negative total torque reflects an inward planetary migration whereas a positive sign shows an outward migration. Figure 3 shows the total torque exerted by the disk on a planet located at a given radial distance r from the star after 1 million years of evolution of the protoplanetary disk. While the total torque is negative everywhere in the case of a constant opacity model, structures appear when the opacity takes into account the dust composition: 0-torque lines appear and define a diverging radius around 10 AU where the region is depleted in planets (planetary desert), and a converging radius around 16 AU where planets can accumulate (planetary trap).

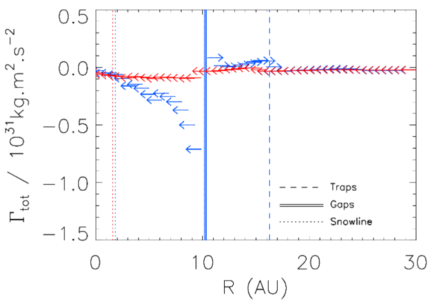

Fig. 3. Total torque exerted by the disk on a $10M_{\rm Earth}$-planet (red: constant opacity model; blue: full opacity model).

5 Conclusions and perspectives

The proper consideration of the disk composition and the physical phase of each element generates temperature irregularities (temperature plateaux, peaks and troughs) that could significantly affect the migration torques exerted by the disk on a putative planet. With these refinements, it appears possible to actually trap planets at a specific radius, or to clear a specific position of all planetesimals. After 1 Myr, we identify a planetary trap around 16 AU and a planetary desert around 10 AU. Other sources of irregularities beyond the scope of the present paper could also generate potential torque inversion and therefore planet trapping: radial variations of the viscous turbulence α, presence of deadzones, multiple-planet systems ...

This work was supported by IDEX Sorbonne Paris Cité. We acknowledge the financial support from the UnivEarthS Labex program of Sorbonne Paris Cité (ANR-10-LABX-0023 and ANR-11-IDEX-0005-02).

References

Andrews, S. M., Wilner, D. J., Hughes, A. M., Qi, C., & Dullemond, C. P. 2009, ApJ, 700, 1502
Andrews, S. M., Wilner, D. J., Hughes, A. M., Qi, C., & Dullemond, C. P. 2010, ApJ, 723, 1241
Artymowicz, P. 1993, ApJ, 419, 155
Baillié, K. & Charnoz, S. 2014, ApJ, 786, 35
Bitsch, B., Morbidelli, A., Lega, E., & Crida, A. 2014, A&A, 564, A135
Goldreich, P. & Tremaine, S. 1979, ApJ, 233, 857
Hasegawa, Y. & Pudritz, R. E. 2011, MNRAS, 417, 1236
Isella, A., Carpenter, J. M., & Sargent, A. I. 2009, ApJ, 701, 260
Jang-Condell, H. & Sasselov, D. D. 2005, ApJ, 619, 1123
Lynden-Bell, D. & Pringle, J. E. 1974, MNRAS, 168, 603
Paardekooper, S.-J., Baruteau, C., Crida, A., & Kley, W. 2010, MNRAS, 401, 1950
Semenov, D., Henning, T., Helling, C., Ilgner, M., & Sedlmayr, E. 2003, A&A, 410, 611
Shakura, N. I. & Sunyaev, R. A. 1973, A&A, 24, 337
Ward, W. R. 1988, Icarus, 73, 330
Ward, W. R. 1997, Icarus, 126, 261

SF2A 2014
J. Ballet, F. Bournaud, F. Martins, R. Monier and C. Reylé (eds)

THE PHOTOSPHERE-CORONA INTERFACE: ENRICHEMENT OF THE CORONA IN LOW FIP ELEMENTS AND HELIUM SHELLS

C. Bazin[1], S. Koutchmy[1], P. Lamy[2] and I. Veselovski[3]

Abstract. Slitless consecutive spectra were obtained during the contacts of the last total solar eclipses (2008, 2009, 2010, 2012, et 2013). They allowed to show that the overabundance of low First Ionisation Potential (FIP) elements (Fe II, Ti II, Ba II) in the corona comes from the low layers of the solar atmosphere, just near and above the temperature minimum region of the high photosphere. All spectra are recorded with a fast CCD/CMOS camera, with an equivalent radial resolution of 60 milliarcseconds, or 45 km in the solar atmosphere, above a solar edge not affected by the parasitic light like it is outside of total eclipse conditions. Many emission lines of low FIP elements appear in regions situated between 200 to 600 km above the solar limb defined by the true continuum measured between the lines. This continuum appears at these altitudes where the beta of the plasma is near 1. The He I 4713 Å and He II 4686 Å (Paschen alpha line) shells appear at the height of 800 km above the solar edge and higher. The light curve $I = f(h)$ of each ion is located at a particuliar altitude in the solar atmosphere. The scale height corresponds to a density variation, which allows to evaluate the temperature thanks to the hydrostatic equilibrium assumption. Moreover, with ionised Titanium lines taken as markers, we show a similarity between the photosphere-corona interface and the prominence-corona interface. We discuss the role of the magnetic field and the ambipolar diffusion for supplying the corona in mass, without taking into account the role of spicules. The photo-ionisation of the helium lines by the EUV coronal lines is illustrated thanks to an extract of SDO/AIA coronal stacked image simultaneously obtained.

Keywords: solar photosphere-corona interface, first ionisation potential, FIP, temperature minimum, loop prominence, chromosphere-corona transition region, interspicule region

1 Introduction

We report on the analysis of slitless flash spectra obtained at the 22 July 2009 solar total eclipse using a fast CCD camera taking frames at a rate of 15 images/second and a 12 bit dynamic range. The flash spectra are seen as many thin crescents, corresponding to the myriad of emission lines originating from the photosphere/chromosphere-corona interface. The edge of the Moon is used like a natural occulter of the solar limb, allowing to explore the regions situated from the low photosphere (extreme-limb) to the chromosphere without parasitic light coming from the solar disk. The radial resolution is 45 km after having stacked 6 spectra every 3 spectra and the spatial resolution is 1150 km/pixel in azimuthal direction where some structuration from macrospicules and inhomogeneities begin to be resolved in the image of the He I 4471 Å high FIP line.

2 Analysis and emission line identification

We performed intensity measurements in the monochromatic emission line images. Figure 1 illustrates two extracts of flash spectra, where a myriad of emission lines like the line of Titanium, Ti II 4468 Å, which is used as a marker for the interfaces analysis. At left we indicate the correspondance between the lunar profile with mountains and valleys and the shape of the emission lines (profile of the Moon prepared by P. Rocher from IMCCE). We selected this Ti II 4468 Å ion for localizing a low FIP element at low altitudes, close to the

[1] Institut d'Astrophysique de Paris, UMR 7095, 98 bis Bd Arago, 75014 Paris, France
[2] Laboratoire d'Astrophysique de Marseille LAM, UMR 7326, France
[3] Moscow State University Lomonossov, Nuclear Phys. Institute, Moscow, Russia

temperature minimum, going to higher altitudes at the extremity of the monochromatic crescent image. Figure 1 shows a monochromatic image of a loop prominence in the same Ti II 4468 Å low FIP line as the one seen at lower altitudes in the photosphere-chromosphere interface. This suggests that some low FIP elements could supply mass in the chromosphere-corona transition region, where the prominence are seen. We used also results coming from the last 3 November 2013 hybrid total eclipse for analyzing more precisely the correspondence between the Baily's Bead in spectra, the low FIP lines emissions, and the lunar profile, see Figure 2.

The light curves in Figure 3 allow to separate the continuum from the low FIP Fe II ion emission.

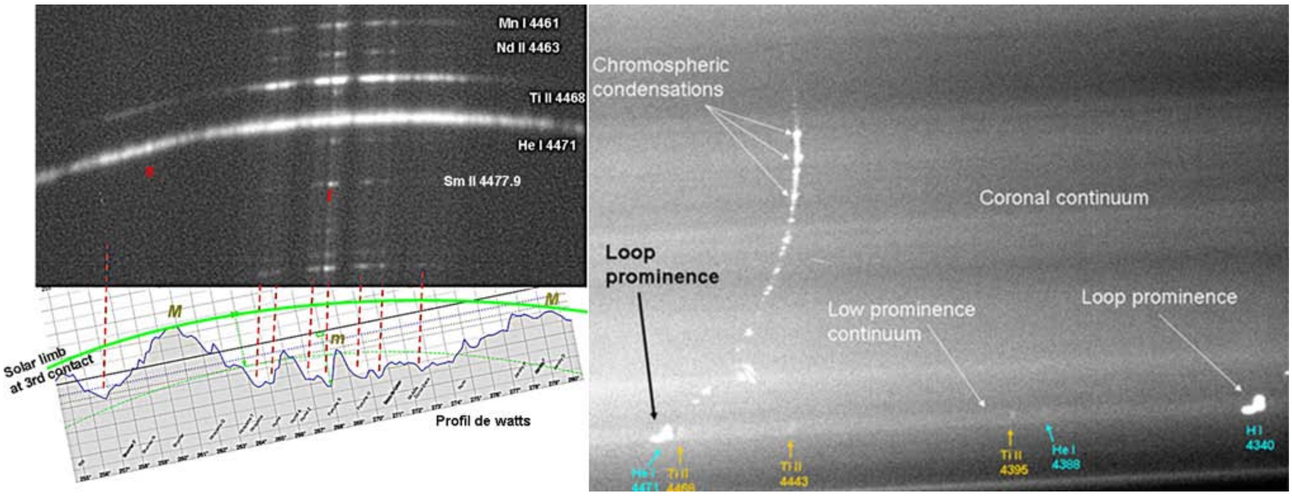

Fig. 1. Extract of flash spectra at the third contact (end of the totality) of the 22 July 2009 total solar eclipse. At left, low FIP emission lines and the helium shell He I 4471 Å seen as crescents. 18 stacked and aligned spectra corresponding to altitudes ranging from 1550 to 1780 km in the radial direction. At right, 50 stacked and aligned spectra before the third contact performed to increase the signal to noise ratio, at the averaged altitude corresponding to 7000 km above the solar limb. The coronal continuum corresponds to the narrow bright bands. At the extremity of the He I 4471 Å shell, some chromospheric condensations appear (some other are small prominences) but no correlation with the coronal continuum bands is evident. Note the Ti II 4468 Å, Ti II 4443 Å and Ti II 4395 Å monochromatic images of the loop prominence which are seen at the end of the crescent producing a band in the continuum.

3 Helium shells and low FIP lines in the low interface region

The analysis of the flash spectra shows the helium shells (He I 4713 and He II 4686) and low FIP lines like the line of the Fe II 4629 Å appearing at lower altitudes, below 800 km, close to the temperature minimum region, see Figure 3. By using the AIA/SDO images taken at the same time as the eclipse totality, we compared the same east solar edge in the 193 Fe XII line with the one of the flash spectra at the same scale, see Figure 4. This allows to compare the shells extension, by comparing the optically thin rather cool lines in the visible (see Hirayama & Irie 1984), and the low corona EUV lines of Fe XII at 2 MK at the solar edge. The dark thin features are spicules seen in absorption, corresponding to cool plasma. They appear close to the EUV limb, at height below 5 Mm, corresponding to the He shell extension.

4 Discussion and Conclusions

The identification of the low FIP element Ti II simultaneously seen in the photosphere-chromosphere/corona interface and in the prominence-corona interface suggests that this element could have been guided or transported by the presence of the magnetic field. The magnetic field is responsible of the inhomogeneities, seen in the macrospicular region. The structuration of the low altitude layers where each ion is created and of the continuum at 4500 Å at separated layers, suggest some effects of ambipolar diffusion occuring in the interspicular medium. The separation between the continuum and the low FIP lines in the region of the temperature minimum could be due to the temperature bifurcation, where the elements begin to be ionised.

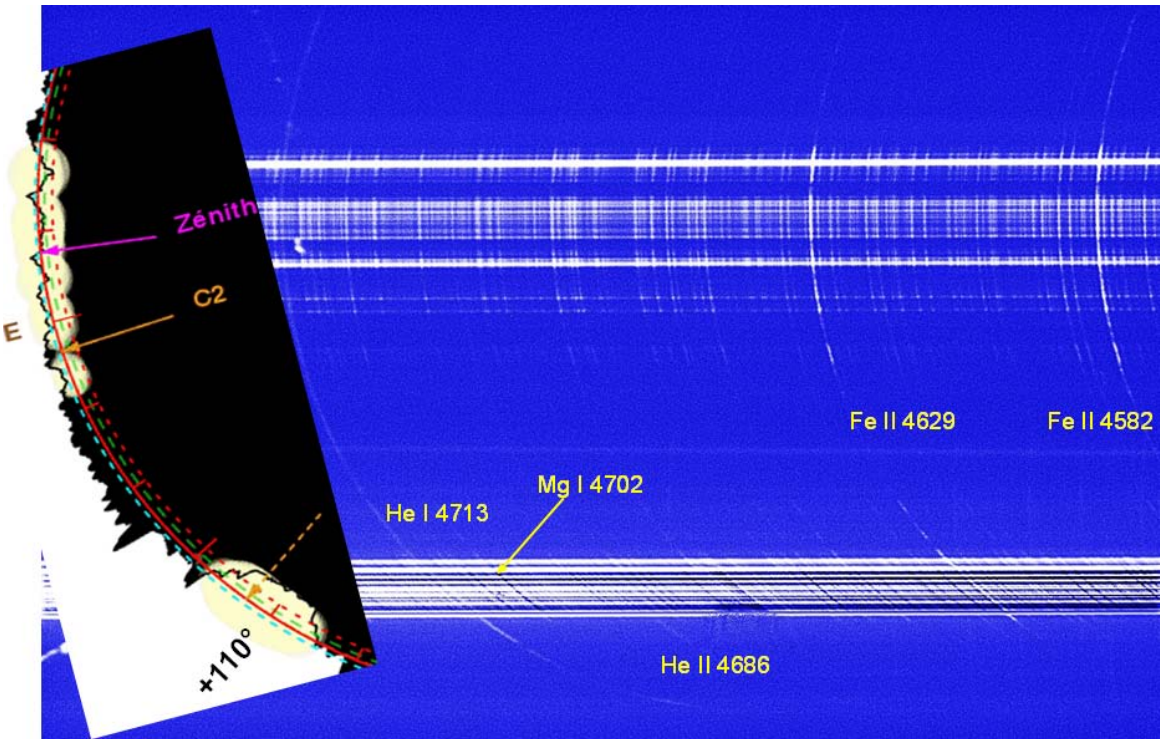

Fig. 2. Baily's Bead continuum in spectrum and emission lines limited by the Lunar profile (cartoon at left from Xavier Jubier) on the flash spectra from the last total hybrid eclipse of 3 November 2013 (Uganda): Helium shells of He I 4713 Å and of He II 4686 Å observed in extension towards the polar regions, and appearing in lower layers (h = 800 km); brightenings from the low FIP elements lines.

References

Bazin, C. 2013, PhD thesis `http://tel.archives-ouvertes.fr/tel-00921889`

Bazin, C., Koutchmy, S. 2013, Journal of Advanced Research, 4(3), 307-313

Bazin, C., Koutchmy, S. and Tavabi, E. 2011, in *Proceedings of the second international symposium*, Hady A. and Dame L. (eds), Cairo University Press, 19

Bazin, C., Koutchmy, S. and Tavabi, E. 2013, Topical Issue of Solar physics, 286, 255-270

Hirayama, T., Irie, M. 1984, Sol. Phys., 90, 291

Kaguya database: `http://l2db.selene.darts.isas.jaxa.jp`

Lebecq, C., Koutchmy, S., Stellmacher, G. 1985, A&A, 152, 175

Vernazza J. E., Avrett E. H., Loeser, R. 1981, ApJ Suppl. Series, 45, 635-725

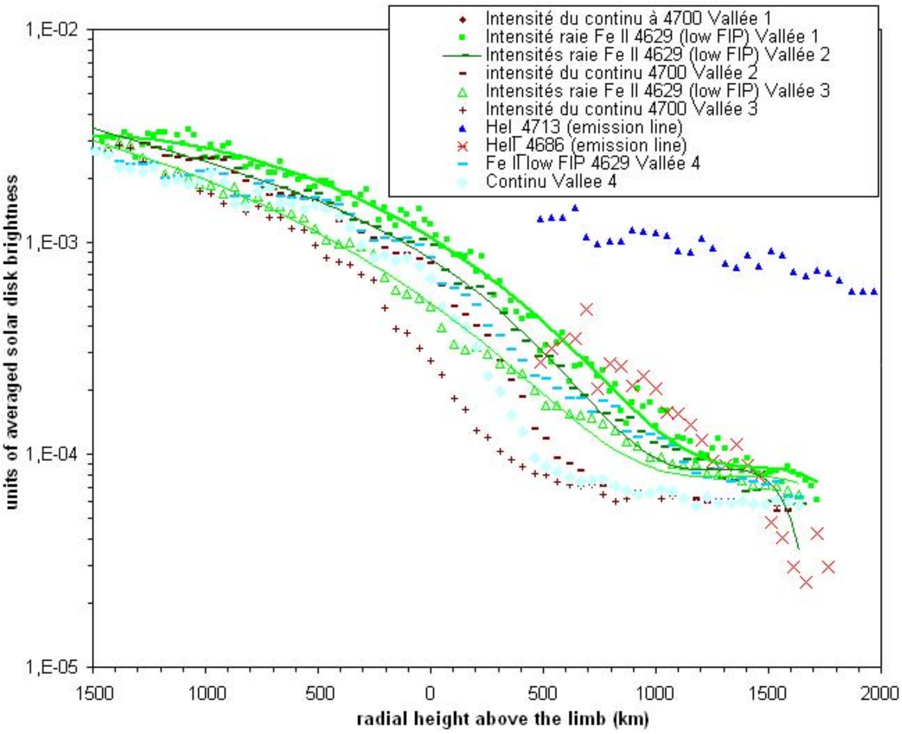

Fig. 3. Light curves using successive spectra where the true continuum (without parasitic light) is isolated from the many low FIP emission lines shown with different colours. The light curves come from the sequence after removing the neutral density filters used to reduce the light before Baily beads appear.

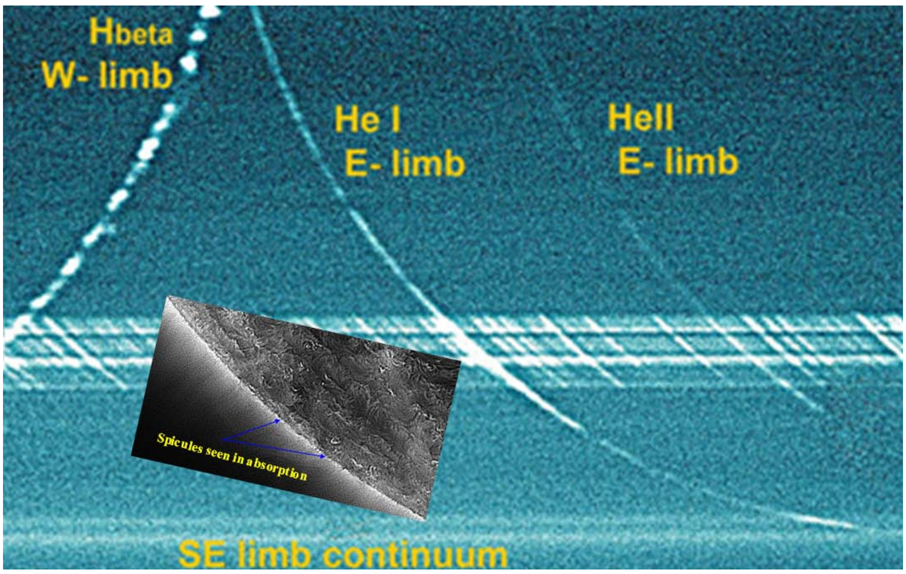

Fig. 4. New flash spectra from the total hybrid eclipse of 3 November 2013 (Uganda): Helium shells (He I 4713 Å and He II 4686 Å) observed in a larger extension towards the polar regions, and appearing in lower layers ($h < 800$ km): brightening of the low First Ionisation Potential elements. Inserted is an AIA image at 193 Å in the same field of view as the flash spectra during the 3 November 2013 total eclipse (14h13 to 14h25 TU), 13 images in the same region as flash spectra have been stacked and processed (unsharp masking). The spicules are seen in absorption (dark). At higher altitudes, the jets and loops appear in emission. Note that they are not the prolongation of spicules at higher altitude, but they could be new magnetic structures heated at 2 MK.

SF2A 2014
J. Ballet, F. Bournaud, F. Martins, R. Monier and C. Reylé (eds)

PLANET FREQUENCY FROM MICROLENSING OBSERVATIONS

A. Cassan[1] and C. Ranc[1]

Abstract. Galactic gravitational microlensing is a very efficient technique to detect brown dwarfs and extrasolar planets at large orbital distances from their stars, and down to Earth-mass planets. More than 50 planets have been discovered so far, with 31 already published. Recent statistical results on the frequency of exoplanets based on several years of microlensing observations find that planets should be the rule rather than the exception, and confirm that super-Earth are much more frequent that giant planets in the Galaxy.

Keywords: Gravitational microlensing - Extrasolar planets - Planets and satellites: detection.

1 Detections

Galactic gravitational microlensing was proposed twenty years ago as a very promising method to detect extrasolar planets (Mao & Paczynski 1991) located at great distances from Earth ($1 - 10$ kpc). In 2003, after a decade of monitoring marked by great technical improvements, the MOA and OGLE collaborations discovered the first microlensing exoplanets (Bond et al. 2004). Since then, microlensing has contributed major exoplanet discoveries, such as the first cool super-Earth OGLE-BLG-2005-390Lb (Beaulieu et al. 2006; Kubas et al. 2008), a frozen super-Earth orbiting a star at the bottom of the main sequence (Kubas et al. 2012) or free-floating planets (Sumi et al. 2011). So far 31 planets have been published (Fig. 1), 20 more are now confirmed, and ongoing 2014 season has already revealed several new candidates.

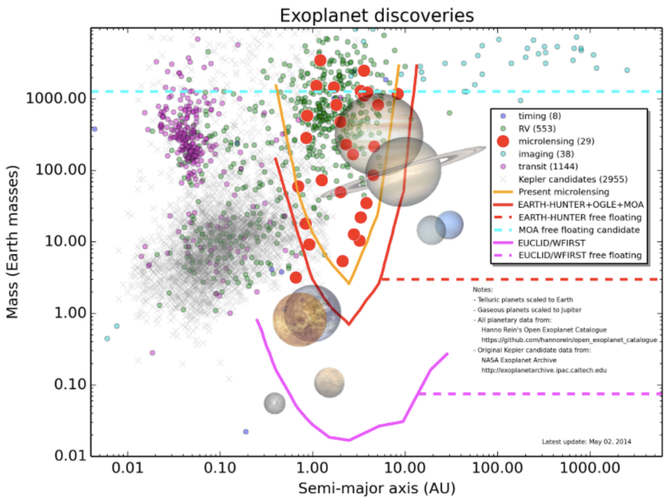

Fig. 1. Exoplanet discoveries, as a function of planetary mass and semi-major axis. Red dots mark microlensing planets, while solid lines encompass the core microlensing sensitivity using ground-based telescopes (red and orange) or a spacecraft (pink). The dashed lines indicate the typical minimum masses of free-floating planets detectable with microlensing (figure: courtesy J.-B. Marquette).

[1] Sorbonne Universités, UPMC Univ Paris 06, CNRS, UMR 7095, Institut d'Astrophysique de Paris, F-75014, Paris, France

Amongst the different methods to search for exoplanets, gravitational microlensing is up to now the only method able to detect low-mass planets (Neptunes, super-Earths) at large orbits (several astronomical units). The search for extrasolar planets using microlensing is right now in great expansion in terms of observing facilities, thanks to the development of networks of robotic telescopes.

2 Statistics, PLANET data 2002-07

We have conducted a statistical analysis (Cassan et al. 2012) that involves six years of microlensing observations gathered between 2002-07 by the PLANET and OGLE collaborations (Fig. 2). From these data combined with results from previous independent microlensing studies, we estimated the frequency of cool extrasolar planets with masses ranging from 5 Earths to 10 Jupiters and orbits between $0.5 - 10$ AU. We found an average of 1.6 planet per star, which suggests that planets around Milky Way stars are the rule, rather than the exception.

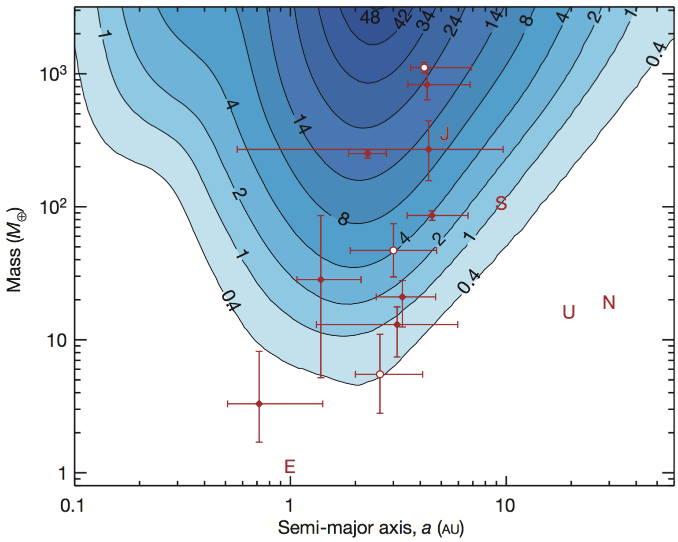

Fig. 2. Detection sensitivity diagram of PLANET 2002-07 data, as a function of planet mass and semi-major axis. Blue contours show the expected number of detections from the survey if all lens stars have exactly one planet with orbit size a and mass M. Red points with error bars mark all microlensing planet detections between 2002-07, while white dots further signal data consistent with PLANET detection efficiency (figure from Cassan et al. 2012).

3 Planet frequency

Microlensing surveys confirm that low-mass planets, such as super-Earth, are more frequently found around stars than giant planets. The mass function derived from microlensing data (Cassan et al. 2012) predicts slightly more planets than other techniques, as seen in Fig. 3. These methods, however, probe a different range in host star masses and orbital separations, in particular, most microlensing planets are located beyond the snow line.

4 The Future : networks of robotic telescopes and space-based observatories

During the last decade, microlensing has slowly evolved from a strategy of manual follow-up of selected microlensing targets to a more automated survey, mainly due to the development of robotic telescopes with wide-field cameras. With 700 alerts per year in 2009 to about 2500 in 2011, the OGLE collaboration has already quadrupled its number of alerted microlensing events, leading to a leap forward in the number of targets. The RoboNet collaboration (Tsapras et al. 2009) has been operating first generation robotic telescopes for more than ten years. A highly valuable experience has been gathered to prepare the upcoming new generation microlensing surveys. Today, the network has reached the required degree of efficiency to open a new window for microlensing searches. In parallel, many progresses have been made in terms of modeling algorithms, in particular for automated online modeling (Cassan et al. 2010; Cassan 2008; Kains et al. 2012). Future satellite

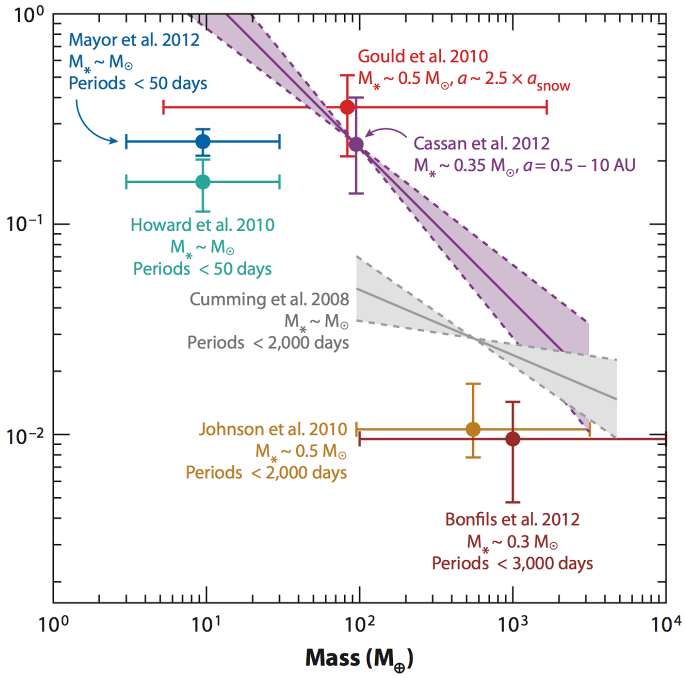

Fig. 3. Comparison of different planetary mass functions versus planetary mass, as derived from microlensing (violet, red) and Doppler (other colours) surveys. For each measurement, typical host star masses and orbit size ranges are indicated (figure from Gaudi 2012).

missions (possibly onboard Euclid or WFIRST) should also detect a large number of planets and free-floating planets (Penny et al. 2013), and constrain the planetary mass functions down the mass of Mars.

References

Beaulieu, J.-P., Bennett, D. P., Fouqué, P., et al. 2006, Nature, 439, 437

Bond, I. A., Udalski, A., Jaroszyński, M., et al. 2004, ApJ, 606, L155

Cassan, A. 2008, A&A, 491, 587

Cassan, A., Horne, K., Kains, N., Tsapras, Y., & Browne, P. 2010, A&A, 515, A52

Cassan, A., Kubas, D., Beaulieu, J.-P., et al. 2012, Nature, 481, 167

Gaudi, B. S. 2012, ARA&A, 50, 411

Kains, N., Browne, P., Horne, K., Hundertmark, M., & Cassan, A. 2012, MNRAS, 426, 2228

Kubas, D., Beaulieu, J. P., Bennett, D. P., et al. 2012, A&A, 540, A78

Kubas, D., Cassan, A., Dominik, M., et al. 2008, A&A, 483, 317

Mao, S. & Paczynski, B. 1991, ApJ, 374, L37

Penny, M. T., Kerins, E., Rattenbury, N., et al. 2013, MNRAS, 434, 2

Sumi, T., Kamiya, K., Bennett, D. P., et al. 2011, Nature, 473, 349

Tsapras, Y., Street, R., Horne, K., et al. 2009, Astron. Nach., 330, 4

SPIN-ORBIT ANGLE DISTRIBUTION AND THE ORIGIN OF (MIS)ALIGNED HOT JUPITERS

A. Crida[1] and K. Batygin[2]

Abstract. The angle between the orbital plane and the stellar equator (called the spin-orbit angle) has been measured for about 60 hot Jupiters, half of them showing significant misalignment. This challenges scenarios of the formation of hot Jupiters. Recently, it has been proposed that misalignment could be a consequence of the torquing of the proto-planetary disk by a transcient binary companion of the host star.

Here, we analyse the geometry of the problem, and compare the probability density function (PDF) of the projected spin-orbit angle expected in various mechanisms, with the observed one. Scattering models and the Kozai cycle with tidal friction models can not be solely responsible for the production of all hot Jupiters. Conversely, the presently observed distribution of the spin-orbit angles is compatible with most hot Jupiters having been transported by smooth migration inside a proto-planetary disk, itself possibly torqued by a companion.

Keywords: Planets and satellites: formation, Planets and satellites: dynamical evolution and stability, Planet-disk interactions, Methods: statistical

1 Introduction

As stars spin, part of their surface moves towards us, while on the other side, the surface moves away from the observer. As a consequence, half of a star is slightly blue-shifted and the other half red-shifted, which results in a broadening of the spectral lines. When an exoplanet transits in front of its star, it blocks successively the light coming from regions with a different redshift. This results in a signal in the radial velocity measurement of the star, called the Rossiter - Mac Laughlin effect (Mac Laughlin 1924). Using this, one can infer the angle between the stellar spin axis and the trajectory of the planet, projected on the plane of the sky (e.g., Winn et al. 2007; Triaud et al. 2010). This angle is called the "spin-orbit angle", generally noted β or λ.

The 61 measurments known to date are binned in the histogram shown on Figure 1. They all concern hot Jupiters, giant planets with short periods, for which the measure is easier. While 34 are measured to be smaller than $20°$, that is compatible with perfect alignement of the orbital plane and the equatorial plane of the star, half of them show misalignement, and even retrograde orbits ($\beta > 90°$). This questions the origin of these planets. While most researchers consider that in situ formation of hot giant planets is very unlikely, two kinds of mechanisms have been invoked to move a giant planet close to its parent star : (i) early, smooth migration in the plane of the gaseous proto-planetary disk (Lin & Papaloizou 1986; Crida & Morbidelli 2007), (ii) late, more violent orbital change due to planet-planet scattering, Kozai resonance with a companion, or tidal interaction with the central star and combinations of these processes (e.g. Rasio & Ford 1996; Ford & Rasio 2008; Fabrycky & Tremaine 2007; Naoz et al. 2011). In case (ii), a change of the orbital plane is likely, causing spin-orbit mislignment. In case (i), the orbital plane stays in the proto-planetary disk plane, supposedly equal to the stellar equatorial plane ; however, (Batygin 2012) has shown that the proto-planetary disk could precess around the axis of a transcient stellar companion, so that smooth migration is not incompatible with spin-orbit misalignment. In Crida & Batygin (2014), we analyse the distribution of the spin-axis angle, with a careful analysis of projection effects, and compare it with the distribution expected for various mechanisms. These results are briefly presented here, where section 2 explains how to link the real spin-orbit angle to the projected one on the plane of the sky, and section 3 compares observations with a few mechanisms available in the litterature.

[1] Laboratoire Lagrange, UMR 7293 ; Université Nice Sophia-antipolis / CNRS / Observatoire de la Côte d'Azur ; Boulevard de l'Observatoire, CS 34229, 06300 Nice, France. crida@oca.eu

[2] Institute for Theory and Computation, Harvard-Smithsonian Center for Astrophysics, 60 Garden St., Cambridge, MA 02138, USA.

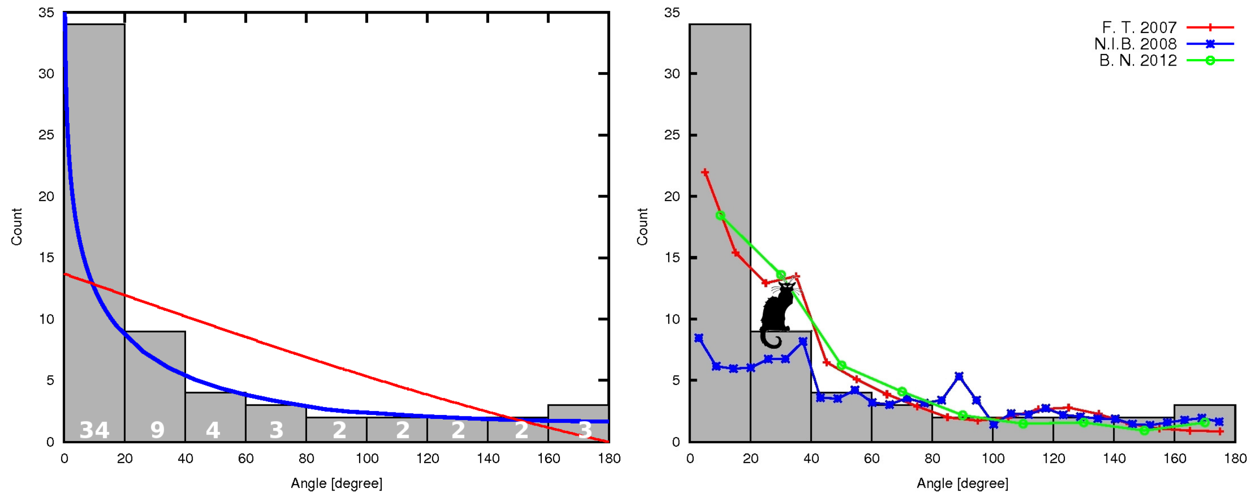

Fig. 1. Grey-shaded histogram: observed projected spin-orbit angle β (taken as $|\beta|$ or $|\lambda|$ in the data from `exoplanets.org`). **Left:** red thin line: distribution of Ψ, given by Eq. (3.1); blue thick line: corresponding PDF of β. **Right:** red line with + symbols labelled `F.T. 2007`: distribution of β expected in the Fabrycky & Tremaine (2007) mechanism of Kozai cycles with tidal friction (their Fig. 10b providing Ψ in bins of 10°); blue line with stars labelled `N.I.B.2008`: distribution found by Nagasawa et al. (2008) in their model of planet-planet scattering, tidal circularisation, and Kozai mechanism (their fig. 11c); green line with circles labelled `B.N.2012`: example of distribution found by Beaugé & Nesvorný (2012) in their model of multi-planet scattering (their fig. 16). All the distributions of β have been normalised to have 18 cases with $\beta > 40^\circ$, for an easier comparison.

2 The 3D geometry of the spin-orbit angle and projection effects

The true misalignment angle is actually the angle between two vectors in 3D space: $\vec{L}_p$, the orbital angular momentum of the planet, and $\vec{L}_s$, the angular momentum of the spin of the star. As such, it can only lie between 0 and 180 degrees (there are no negative angles in 3D). This real, 3D angle is denoted below as Ψ. For a fixed Ψ, which β will be observed ? What is the probability density function (PDF) of β ?

On Figure 2, the yellow sphere is the unit sphere, centred on the star O, and the vertical axis is $\vec{L}_p$. The stellar spin axis $\vec{L}_s$ points towards S, whose colatitude is Ψ by definition, and longitude (azimuth) ϕ_S, unkonwn. The top left panel is the circle gathering all the points of colatitude Ψ, so that $A'A = A'S = A'R = \sin\Psi$ and $A'S' = \sin\Psi\,|\sin\phi_s|$.

In the projected plane (shown in bottom left of Fig. 2), the angle between the north pole of the orbit and the spin of the star appears to be $\beta = \widehat{A'OS'}$. One can see that $\tan\beta = A'S'/OA'$, where $OA' = \cos\Psi$ is negative when $\Psi > \pi/2$. Finally,

$$\beta = \arctan\left(|\sin\phi_s|\,\tan\Psi\right) \equiv G(\phi_s) \tag{2.1}$$

As the distribution of ϕ_s is uniform in the interval $[0;2\pi[$, and $|\sin(x)| = |\sin(\pi - x)| = |\sin(\pi + x)| = |\sin(2\pi - x)|$, it is sufficient to consider a uniform distribution for $0 \leqslant \phi_s < \pi/2$, with probability density $2/\pi$. In this case, β is a monotonic function of ϕ_s. It is well known that if X is a random variable of probability density function f_X, and $Y = G(X)$ with G a monotonic function, then the PDF of Y is $f_Y(y) = f_X\left(G^{-1}(y)\right) \times \left|\left(G^{-1}\right)'\right|(y)$. Thus, using Eq. (2.1) for fixed Ψ, the PDF of β is:

$$f(\beta|\Psi) = \begin{cases} \dfrac{2}{\pi}\dfrac{1+\tan^2\beta}{(\tan^2\Psi - \tan^2\beta)^{1/2}} & \text{if } \beta \in \mathcal{T} = \{0 \le \beta < \Psi < \frac{\pi}{2}\} \cup \{\frac{\pi}{2} < \Psi < \beta \le \pi\}\ , \\ 0 & \text{otherwise} \end{cases} \tag{2.2}$$

One can check analytically that $\int_0^\pi f(\beta|\Psi)\,\mathrm{d}\beta = 1$ for all Ψ. If now Ψ has its own PDF $w(\Psi)$ (such that $\int_0^\pi w(\Psi)\,\mathrm{d}\Psi = 1$), the corresponding PDF of β will be:

$$f(\beta) = \int_{\Psi=0}^{\Psi=\pi} f(\beta|\Psi)\,w(\Psi)\ \mathrm{d}\Psi\ . \tag{2.3}$$

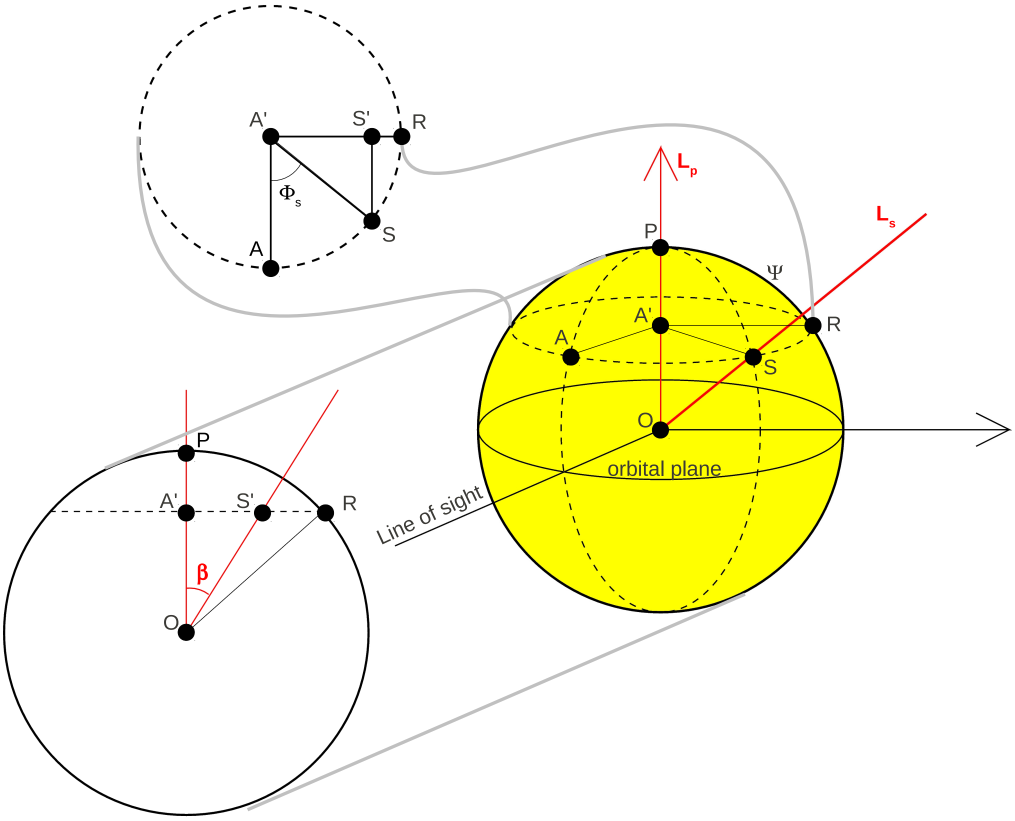

Fig. 2. Right : 3D representation of the problem. The yellow sphere is the unit sphere centred on the star. P marks the direction of the orbital angular momentum vector $\vec{L}_p$ and S that of the stellar spin $\vec{L}_s$. The dashed circle passing through points A and S gathers all the points making an angle Ψ with P. It is represented in the top left.
Top left : The circle of the unit sphere gathering all the points at colatitude Ψ with respect to the orbital angular momentum vector of the planet. A is the point facing the observer ; S is the point corresponding to the direction of the stellar spin. A and S are projected on the diameter of this circle perpendicular to the line of sight onto A' and S' ; ϕ_s is then $\widehat{AA'S}$.
Bottom left : The projected plane, as seen by the observer. The previous dashed circle is now a dashed horizontal line, on which A' and S' are the projections of A and S along the direction of the line of sight. The arc PR defines an angle Ψ, while the projected spin orbit angle β is $\widehat{A'OS'}$, marked in red.

3 Application to proposed mechanisms

3.1 *Disk torquing*

A simple description of the disk torquing model by Batygin (2012) is the following : the angle between the stellar equatorial plane and the orbital plane of the companion star is i', randomly distributed in 3D, that is between 0 and $\pi/2$ with a PDF $\sin(i')$. Then, the disk precesses around this axis, while the star is unperturbed. As a consquence, Ψ oscillates periodically between 0 and $2i'$. When the companion star leaves, Ψ is fixed, at any value in this interval. This gives to the spin-orbit angle the PDF :

$$w(\Psi) = \frac{1}{2}\left[\mathrm{Si}(\pi/2) - \mathrm{Si}(\Psi/2)\right] \ , \quad \text{where } \mathrm{Si}(x) = \int_0^x \frac{\sin t}{t}\,\mathrm{d}t \ . \tag{3.1}$$

This function is represented as the thin, almost straight, red line in the left panel of Figure 1. The blue, thick, curved line represents the corresponding PDF of β, as given by Eqs (2.3) and (3.1). The difference between the two curves enlightens the necessity of taking into account the projection effects. The blue curve is in good qualitative agreement with the observed distribution. In fact, the only difference with the observations lies in an underestimation of the proportion of aligned cases. But this shouldn't be a problem : not all stars have a transcient companion during their formation, that perturbs their proto-planetary disk. The excess of aligned cases may simply reflect the fact that in a few systems, the proto-planetary disk have never left the equatorial plane of the star.

To check this, we have performed Monte-Carlo simulations of disk torquing, taking into account the magnetic coupling between the star and the disk (Batygin & Adams 2013), and with random orbital parameters for the binary. We find that the distribution beyond $\beta > 40°$ is extremely robust. On the other hand, the fraction of aligned systems strongly depends on the distribution of the maximum semi-major axis of the binaries, namely it increases when wider binaries are considered.

3.2 Other mechanisms

The left panel of Figure 1 shows the distribution of β that would be given by a few mechanisms found in the litterature (see caption). In all three cases, we have taken the PDF of Ψ provided in the paper, and transformed it into a distribution of β using our Eq. (2.3), in order to compare with the observations (histogram in the background). The distributions have been normalized to have 18 cases with $\beta > 40°$, like in the observations.

We see that all of them reproduce satisfactorily the almost flat distribution of β beyond 60°, but all fail at reproducing the observed distribution at $\beta < 40°$. In particular, one sees a significant lack of aligned systems. Hence, none of these mechanisms can be responsible for the production of most hot Jupiters.

4 Summary

1. The *real* spin-orbit angle Ψ, is a 3D angle and so lies between 0 and 180°. The *projected* spin-orbit angle β is in the plane of the sky, but its direction (clockwise or counterclockwise) only depends on whether we see the ascending or descending node, and cannot be determined by observations. Reporting negative angles doesn't make sense.

2. We provide an easy way to connect the distributions of the real and projected spin-orbit angles distributions (Eqs (2.2) and (2.3)). Any model pretending to explain the spin-orbit misalignments should be tested against the observed distribution, using this link.

3. About half of the hot Jupiters are well aligned ; this can not be explained by the Kozaï Cycles with Tidal Friction or scattering models. Thus, at least a third of the hot Jupiters must have been formed by standard type II migration in an aligned disk.

4. Type II migration in a torqued disk also leads to the production of misaligned hot Jupiters, and our analytical model and monte-carlo simulations show that the expected distribution of β in this case is in very good agreement with the observations.

In the end, based solely on the distribution of the observed projected spin-orbit angle, it seems that type II migration could be the dominant mechanism of formation of hot Jupiters, misaligned or not.

References

Batygin, K. 2012, Nature, 491, 418
Batygin, K. & Adams, F. C. 2013, ApJ, 778, 169
Beaugé, C. & Nesvorný, D. 2012, ApJ, 751, 119
Crida, A. & Batygin, K. 2014, A&A, 567, A42
Crida, A. & Morbidelli, A. 2007, MNRAS, 377, 1324
Fabrycky, D. & Tremaine, S. 2007, ApJ, 669, 1298
Ford, E. B. & Rasio, F. A. 2008, ApJ, 686, 621
Lin, D. N. C. & Papaloizou, J. 1986, ApJ, 309, 846
Mac Laughlin, D. B. 1924, ApJ, 60, 22
Nagasawa, M., Ida, S., & Bessho, T. 2008, ApJ, 678, 498
Naoz, S., Farr, W. M., Lithwick, Y., Rasio, F. A., & Teyssandier, J. 2011, Nature, 473, 187
Rasio, F. A. & Ford, E. B. 1996, Science, 274, 954
Triaud, A. H. M. J., Collier Cameron, A., Queloz, D., et al. 2010, A&A, 524, A25
Winn, J. N., Johnson, J. A., Peek, K. M. G., et al. 2007, ApJ, 665, L167

SF2A 2014
J. Ballet, F. Bournaud, F. Martins, R. Monier and C. Reylé (eds)

PHOTOPHORESIS IN PROTOPLANETARY DISKS: A NUMERICAL APPROACH

N. Cuello[1], F. C. Pignatale[1] and J.-F. Gonzalez[1]

Abstract. It is widely accepted that rocky planets form in the inner regions of protoplanetary disks (PPD) about 1 - 10 AU from the star. However, theoretical calculations show that when particles reach the size for which the radial migration is the fastest they tend to be accreted very efficiently by the star. This is known as the radial-drift barrier. We explore the photophoresis in the inner regions of PPD as a possible mechanism for preventing the accretion of solid bodies onto the star. Photophoresis is the thermal creep induced by the momentum exchange of an illuminated solid particle with the surrounding gas. Recent laboratory experiments predict that photophoresis would be able to stop the inward drift of macroscopic bodies (from 1 mm to 1 m in size). This extra force has been included in our two-fluid (gas+dust) SPH code in order to study its efficiency. We show that the conditions of pressure and temperature encountered in the inner regions of PPD result in strong dynamical effects on the dust particles due to photophoresis. Our simulations show that there is a radial and a vertical sorting of the dust grains according to their sizes and their intrinsic densities. Thus, our calculations support the fact that photophoresis is a mechanism which can have a strong effect on the morphology of the inner regions of PPD, ultimately affecting the fate of planetesimals.

Keywords: protoplanetary disk, photophoresis, hydrodynamics, planet formation

1 Introduction

Thousands of extra-solar planets have been detected in the past 20 years (Batalha et al. 2013), which undoubtedly shows that planets are common byproducts of stars. It is currently accepted that planets form in protoplanetary dusty disks around young stellar objects. This means that, throughout the evolution of the protoplanetary disk, dust grains have to grow from μm sizes to kilometric sizes to form planetesimals. However, the study of the motion of solids inside the disk leads to the so-called radial-drift barrier. This issue was first pointed out by Weidenschilling (1977) by solving the equation of motion for dust particles embedded in the gas disk of a PPD. A solid body orbiting a star in a keplerian fashion loses angular momentum through the interaction with the gas which orbits at a subkeplerian velocity. This is because the gas phase, which is assumed to be in hydrostatic equilibrium, is pressure supported while the dust phase is not. The difference between the orbital velocities of each phase can be interpreted as a headwind in the rest frame of the particle, which causes the particle to spiral down into the star.

Several mechanisms have been proposed to break the radial-drift barrier such as radial mixing (Keller & Gail 2004, and references therein), magnetic braking and dead zones (Armitage 2011), particle traps (Fouchet et al. 2010; Pinilla et al. 2012), meridional circulation (Fromang et al. 2011) and radiation pressure force (Vinković 2014). However, it remains unclear if a single mechanism or a combination of them could actually prevent accretion. The aim of this work is to consider an extra mechanism called photophoresis, which has been first introduced by Rohatschek (1995) through the study of illuminated particles in aerosols. Duermann et al. (2013) measured the strength of the photophoresis force on illuminated plates under similar temperature and pressure conditions that those found in PPD. Then, via an interpolation of their results, they computed the acceleration felt by solids of different sizes and porosities orbiting a 1 solar mass star. Plugging this extra force into the equations of motion for dust particles in a 1D model, they predicted that photophoresis might be able to

[1] Université de Lyon, Lyon, F-69003, France; Université Lyon 1, Observatoire de Lyon, 9 avenue Charles André, Saint-Genis Laval, F-69230, France; CNRS, UMR 5574, Centre de Recherche Astrophysique de Lyon; Ecole Normale Supérieure de Lyon, F-69007, France. e-mail: `nicolas.cuello@univ-lyon1.fr`

stop the inward drift for large bodies ranging from a millimeter to a meter. Since the force is size dependent (Duermann et al. 2013), the photophoresis effects would ultimately lead to a radial sorting among different grain populations. However, to date, no studies have explored the complex dynamics obtained when considering this extra mechanism. This work is the first attempt to understand how photophoresis shapes the inner regions of PPD between 0.1 and 5 AU through numerical simulations.

In section 2, we give a brief overview of the photophoresis force; in section 3, we explain how we model the PPD by means of SPH simulations; in section 4, we present our results, and our conclusions are reported in section 5.

2 Photophoresis force

Rohatschek (1995) derived the first semi-empirical model for the photophoretic force which connects low and high pressure regimes based on experiments and theoretical calculations. Indeed, there are three regimes for the photophoretic force, $F_{\rm ph}$, according to the pressure, p, of the gaseous environment around an illuminated particle: the low pressure regime for which $F_{\rm ph} \propto p$, the high pressure regime for which $F_{\rm ph} \propto 1/p$, and, in between, the transition regime when $F_{\rm ph}$ reaches its maximum. These regimes are determined by the value of a quantity called the Knudsen number defined as $\mathrm{Kn} = \lambda/\mathrm{a}$, where λ is the mean free path of the gas molecules and a is the radius of the solid particle. Thus, $\mathrm{Kn} \gg 1$ for the low-pressure regime, whereas $\mathrm{Kn} \ll 1$ for the high-pressure regime. The semi-empirical expression for the photophoretic force reads as follows:

$$F_{\rm ph} = \frac{2F_{\rm max}}{\frac{p}{p_{\rm max}} + \frac{p_{\rm max}}{p}} \,, \tag{2.1}$$

with

$$F_{\rm max} = \frac{a^2}{2} D \sqrt{\frac{\alpha}{2}} \frac{I}{k} \,, \tag{2.2}$$

$$p_{\rm max} = \frac{3T}{\pi a} D \sqrt{\frac{2}{\alpha}} \,, \tag{2.3}$$

$$D = \frac{\pi \bar{c} \eta}{2T} \sqrt{\frac{\pi \kappa}{3}} \,, \tag{2.4}$$

$$\bar{c} = \sqrt{\frac{8RT}{\pi \mu}} \,, \tag{2.5}$$

where I is the irradiance of the incident beam of light, α is the thermal accommodation coefficient (dimensionless and often taken equal to 1), k is the thermal conductivity of the solid particle, T is the gas temperature, η is the viscosity of the gas, κ is the thermal creep coefficient, which is equal to 1.14 (Rohatschek 1995), R is the universal gas constant and μ is the molar mass of the gas particle.

The photophoretic force can also be split into two components: the ΔT-force mainly driven by the gradient of temperature between the illuminated and shadowed sides of the solid particle, and the $\Delta\alpha$-force which depends on the differences in composition of the particle. In this work, we consider homogeneous particles for which we vary the chemical composition and the size. Thus, we only need to compute the $\Delta\alpha$-force. Due to the lack of thermal conductivity data for large bodies, it is difficult to fix a value for k which would depend on the temperature and the size. However, Opeil et al. (2012) and Loesche & Wurm (2012) showed, through measurements in chondrules and heat transfer calculations respectively, that a low porosity in dust aggregates suffices to lower thermal conductivities. For instance, the thermal conductivity for bulk silicates is of the order of magnitude of 1 $\mathrm{W\,m^{-1}\,K^{-1}}$ (Opeil et al. 2012), while if we consider the same silicates with a few percent of void, k drops by at least one order of magnitude. This motivates our choice of a constant thermal conductivity $k = 0.1$ $\mathrm{W\,m^{-1}\,K^{-1}}$ as in Duermann et al. (2013). All the other quantities on which equations (2.2) to (2.5) depend are functions of the disk local conditions and can be easily computed in our code as showed in the next section.

3 Simulations

In order to be able to compare our results to Duermann et al. (2013) we chose to study the same disk model, namely the Minimum Mass Solar Nebula (MMSN) of Hayashi (1981). We consider a protoplanetary disk of

0.013 $M_\odot$ mass with 1% of dust by mass around a 1 $M_\odot$ star and a radial extension from 0.1 to 36 AU. The disk is vertically isothermal and $T(r) \propto r^{-q}$ with $q = 1/2$. We focus on the inner regions from 0.1 to 5 AU since it is the range for which the photophoretic force is the more efficient (Duermann et al. 2013).

We adapt the code of Barrière-Fouchet et al. (2005) to our study by including an extra term in the equation of motion for the dust particles. Gas and dust are considered as two separated fluids, which interact through aerodynamical drag. The code solves the equations of motion for each phase through the SPH formalism. Price (2012) reviews the method and presents the recent developments. The equation of motion for the gas SPH particles reads:

$$\frac{\mathrm{d}\boldsymbol{v_a}}{\mathrm{dt}} = \boldsymbol{P_{ab}} + \boldsymbol{M_{aj}} + \boldsymbol{D_{aj}} + \boldsymbol{G_a}, \tag{3.1}$$

which is the sum of the pressure term P_{ab}, the mixed pressure term M_{aj}, the drag term D_{aj} and the gravity of the central star G_a. The subscripts a and b refer to gas particles and i and j for dust particles. For the dust particles the equation of motion is the following:

$$\frac{\mathrm{d}\boldsymbol{v_i}}{\mathrm{dt}} = \boldsymbol{M_{ib}} + \boldsymbol{D_{ib}} + \boldsymbol{G_i} + \boldsymbol{F_i^{\mathrm{photo}}}, \tag{3.2}$$

where, in addition to the mixed pressure M_{ib}, the drag D_{ib} and the gravity G_i terms, we add the photophoresis force given by Equation (2.1). It is important to note that the gas feels the pressure force whereas the dust does not, and that only the dust phase feels the photophoresis force. The photophoretic force depends upon the local properties of the gas at the position $\boldsymbol{r}$ of the dust particle: the temperature, the pressure, the viscosity and the amount of energy received from the star. In our simulations we consider that the medium is optically thin so that the radiant flux density at a given position $\boldsymbol{r}$ is simply computed as the luminosity over the surface of the sphere of radius r. This constitutes the main limitation of our calculations since photophoresis has no effect in optically thick regions. We are currently developing a more detailed model to include this effect.

In the simulations, we let a gaseous disk evolve from an initial surface density distribution given by $\Sigma \propto r^{-3/2}$. The initial velocity is keplerian, given by $v_k = \sqrt{GM_\odot/r}$. The reference values at 1 AU for the pressure and the temperature power laws are given by the MMSN model of Hayashi (1981). Once the gas disk reaches equilibrium, we inject the dust particles on top of the gas particles with the same velocity. This state constitutes our initial state (Fig. 1-a). Then, we let the system evolve for an evolutionary time of 30 years approximately, *i.e.* 30 orbits at 1 AU. We run a series of simulations to study the dependence of the photophoresis on the chemical composition (iron and silicates) and on the size of the solid bodies (1 cm, 10 cm and 1 m).

4 Results

We show the initial state of the dust phase at $t = 0$ (Fig. 1-a), the final state of the dust phase for 10 cm silicate grains with photophoresis (Fig. 1-b), for 10 cm silicate grains without photophoresis (Fig. 1-c) and for 10 cm iron grains with photophoresis (Fig. 1-d). We observe that there is a strong dust sedimentation as already observed in the simulations by Barrière-Fouchet et al. (2005). Radial migration is dramatically affected by the inclusion of photophoresis in the equations of motion. In fact, whithout photophoresis, the dust particles start to spiral down to the star and there is no outward motion. On the contrary, when we take photophoresis into account, the particles which are very close to the star between 0.1 and 1.8 AU tend to move outwards until they reach a stable orbit at around 1.8 AU for 10 cm grains. The location of the inner rim, *i.e.* the radial migration, depends on the grain size: its position is at 0.5, 1.9, 1.5 AU for 1 cm, 10 cm and 1 m particles respectively. We see the strongest effect for 10 cm while the grains of 1 cm and 1 m are less affected by photophoresis. This result matches with the analytical calculation by Duermann et al. (2013).

Fig. 1-b and Fig. 1-d show the different behavior for two different chemical compositions for a grain size of 10 cm: we notice that the vertical sedimentation is more efficient for iron grains than for silicates. This phenomenon is also observed in simulations without photophoresis since it solely depends on the intrinsic density ($\rho^{\mathrm{sil}} = 3.2$ $\mathrm{g\,cm^{-3}}$ and $\rho^{\mathrm{iron}} = 7.8$ $\mathrm{g\,cm^{-3}}$). Nevertheless, if we consider a more realistic disk made of a mixture of different species with a given distribution of sizes, then the sedimentation coupled with the different inner rim location patterns will have an effect on the mixing of solids in the inner regions of PPD. This will be the subject of a future work.

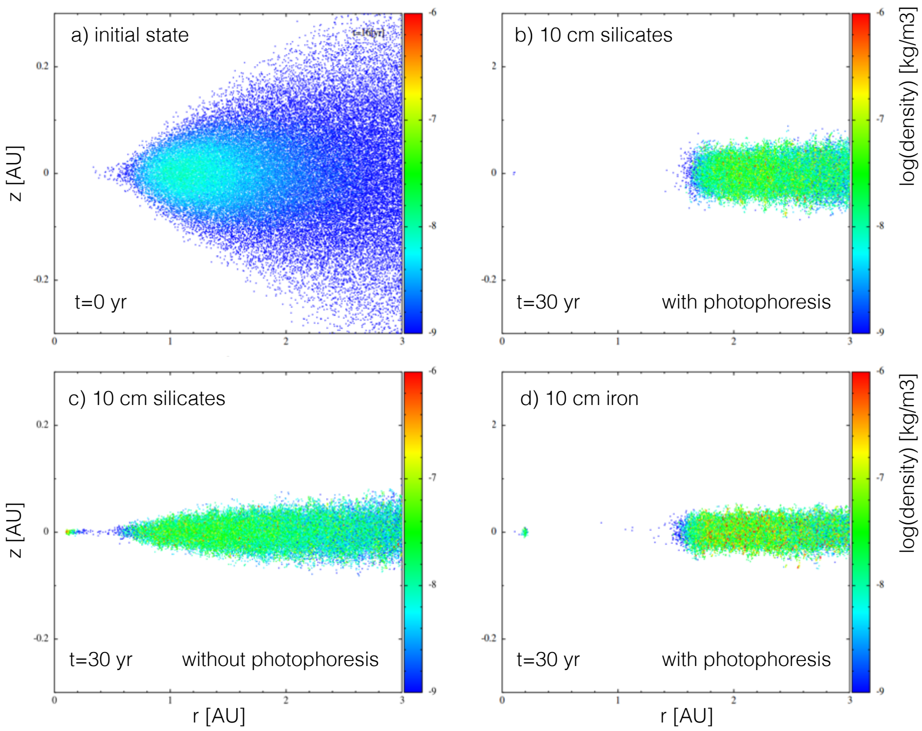

Fig. 1. Meridian plane cut of the dust distribution for the initial state of the dust phase (a) and the final state after 30 years of evolution for 10 cm silicate grains with photophoresis (b), without photophoresis (c) and with photophoresis for iron grains (d).

5 Conclusions and future work

We have included photophoresis in our simulations in order to understand its effects on the inner regions of PPD. Even though our calculations present some limitations, our results show that photophoresis affects the structure of the inner rim of the dusty disk whereas the gaseous disk remains unchanged. Moreover, these preliminary results are in accordance with the predictions made by Duermann et al. (2013) concerning the different accumulation zones for different grain populations. Future work will explore the effect of this accumulation on the growth of large solids in the inner regions of PPD where we expect terrestrial planets to form. In fact, even if photophoresis is mainly effective for centimeter and meter sized bodies, it might lead to an efficient pile-up of particles close to the star. Chatterjee & Tan (2014) recently proposed an inside-out planet formation scenario based on magneto-rotational instabilities (MRI). In this case, pebbles collect at the pressure maximum associated with the transition from a dead zone to an inner MRI-active zone. Alternatively, taking into account photophoresis effects, solid bodies could accumulate and grow at the stable point defined by the transition between the optically thin and optically thick regions. In the optically thin part, particles move outwards since they mainly feel photophoresis, whereas in the optically thick one they move inwards due to the radial drift. If the dust-to-gas ratio is high enough in the accumulation zone, a planet could form at this location. Both mechanisms lead to systems with tightly-packed inner planets. It worths noticing that this planetary architecture seems to be one of the principal outcomes of planet formation since it has been detected in a large fraction of targets (more than 10% of the stars) by the *Kepler* mission (Batalha et al. 2013).

This research was supported by the Programme National de Physique Stellaire, the Programme National de Planétologie of CNRS/INSU. The authors are grateful to the LABEX Lyon Institute of Origins (ANR-10-LABX-0066) of the Université de Lyon for its financial support within the program "Investissements d'Avenir" (ANR-11-IDEX-0007) of the French government operated by the National Research Agency (ANR). All the computations were performed at the Service Commun de Calcul Intensif de l'Observatoire de Grenoble (SCCI). Figure 1 was made with SPLASH (Price 2007).

References

Armitage, P. J. 2011, ARA&A, 49, 195
Barrière-Fouchet, L., Gonzalez, J.-F., Murray, J. R., Humble, R. J., & Maddison, S. T. 2005, A&A, 443, 185
Batalha, N. M., Rowe, J. F., Bryson, S. T., et al. 2013, ApJS, 204, 24
Chatterjee, S. & Tan, J. C. 2014, The Astrophysical Journal, 780, 53
Duermann, C., Wurm, G., & Kuepper, M. 2013, A&A, 558, A70
Fouchet, L., Gonzalez, J.-F., & Maddison, S. T. 2010, A&A, 518, A16
Fromang, S., Lyra, W., & Masset, F. 2011, A&A, 534, A107
Hayashi, C. 1981, Progress of Theoretical Physics Supplement, 70, 35
Keller, C. & Gail, H.-P. 2004, A&A, 415, 1177
Loesche, C. & Wurm, G. 2012, A&A, 545, A36
Opeil, C. P., Consolmagno, G. J., Safarik, D. J., & Britt, D. T. 2012, Meteoritics and Planetary Science, 47, 319
Pinilla, P., Birnstiel, T., Ricci, L., et al. 2012, A&A, 538, A114
Price, D. J. 2007, PASA, 24, 159
Price, D. J. 2012, Journal of Computational Physics, 231, 759
Rohatschek, H. 1995, Journal of Aerosol Science, 26, 717
Vinković, D. 2014, A&A, 566, A117
Weidenschilling, S. J. 1977, MNRAS, 180, 57

SF2A 2014
J. Ballet, F. Bournaud, F. Martins, R. Monier and C. Reylé (eds)

WHAT CAN STELLAR MAGNETIC FIELDS TELL US ABOUT STAR-PLANET INTERACTIONS?

R. Fares[1], C. Moutou[2] and J.-F. Donati[3]

Abstract. Interactions between hot-Jupiters and their host stars are expected to occur in close-in planetary systems. These interactions influence the planet (via tidal heating, evaporation of the atmosphere, orbital evolution, etc.), but can also influence the star. Magnetospheric interactions can enhance stellar chromospheric activity. On the other hand, tidal interactions influence the stellar magnetic field. Thus, studying this magnetic field can give us insights into the interactions occurring in these systems.

I will present the results of the first spectropolarimetric survey of hot-Jupiter hosting stars. The stellar magnetic properties will be presented and compared with those of cool stars without hot-Jupiter companions. From this survey, we observed the first large-scale magnetic cycle for a star other than our Sun, which shows a flip in polarity occurring on yearly timescales. I will discuss the possible role of star-planet interactions on short cycles such as this.

In addition to this observational aspect, I will discuss the effect the stellar magnetic field on the planet, planetary environment and planetary radio emission.

Keywords: Techniques: polarimetric, Stars: magnetic field, Stars: solar-type

1 Introduction

The discovery of the first exoplanet around a solar-like star in 1995 (Mayor & Queloz 1995) opened the door to a new era in planetary science. In two decades, thousands of exoplanets have been detected. The characteristics of these exoplanets and their orbits are diverse. An non-negligeable fraction of the first detections consisted of hot-Jupiters. A hot-Jupiter is a Jupiter-mass planet orbiting very close to its parent star, usually within 0.1 au. Those systems challenged our understanding of planet formation and migration. Interactions between the planet and the star are expected to occur, because of the proximity and the masses of the two bodies. These interactions will affect the planet, but they are also thought to affect the star.

Tidal interactions were invoked to try to explain the inflated radius of some exoplanets, the orbital obliquities, and the excess rotation of some stellar hosts (see, e.g. Ibgui et al. 2010; Winn et al. 2010; Pont 2009; Brown et al. 2011). It was recently suggested that elliptical (or tidal) instabilities, generated by interactions between tidal waves, can induce magnetic field in stars (Cébron & Hollerbach 2014).

On the other hand, magnetospheric interactions affect the two bodies in different ways. They can induce planetary radio emission (see Zarka 2007, for a review). Different emission scenarios and predictions were discussed in the literature (Grießmeier et al. 2007; Jardine & Collier Cameron 2008; Nichols 2012; Vidotto et al. 2012), but so far detections of exoplanetary radio emission have not been confirmed, only non-detection (and thus upper limits) and hints of detections are reported (Smith et al. 2009; Lecavelier des Etangs et al. 2013; Sirothia et al. 2014). Stellar activity can be enhanced by magnetospheric interactions (Cuntz et al. 2000), an enhancement modulated by the planetary orbital period. This was observed for some systems, but the same systems don't show such enhancement at different observing epochs (Shkolnik et al. 2003, 2005, 2008). The change in the configuration of the large-scale magnetic field from one epoch to the other might be responsible for that, given that these interactions depend primarily on the magnetic field (see, McIvor et al. 2006; Lanza

[1] School of Physics and Astronomy, University of St Andrews, KY16 9SS, St Andrews, UK
[2] CFHT Corporation, 65-1238 Mamalahoa Hwy, Kamuela, Hawaii 96743, USA
[3] Université de Toulouse / CNRS-INSU, IRAP / UMR 5277, F-31400 Toulouse, France

2009). Enhancement in stellar X-ray activity was reported in Kashyap et al. (2008), a conclusion contradicted by Poppenhaeger et al. (2010).

Those different studies, although contradictory sometimes, show that the knowledge of the large-scale magnetic field of the star is necessary to model the interactions, interpret observations and make realistic predictions for induced emission. Comparing the magnetic properties of a sample of hot-Jupiter hosts to those of stars without known hot-Jupiter is important to study if the tidal and magnetospheric interactions influence the characteristics of the magnetic fields. We remind the reader here that for these cool stars, the magnetic field is produced by dynamo mechanism operating in the outer convective envelope of the star.

2 Stellar sample and study of magnetic field

In order to study if tidal and magnetospheric interactions affect the magnetic field of planet hosting stars, we have chosen a small sample of 10 hot-Jupiter hosts. The sample consists of F, G and K dwarfs, with a rotation period between 2 and 40 days. The hot Jupiter around these stars has a mass between 0.2 and 20 Jupiter mass. We were able to detect the field for 7 stars (τ Boo, HD189733, HD179949, HD73256, HD102195, HD46375, HD130322). Three of those stars have multi-epoch observations, allowing the study of the evolution of the field. We were unable to detect the field of Corot-7, HAT-P-2, XO-3.

Studying the large-scale field of stars can be done using spectropolarimetry and indirect imaging techniques such as Zeeman-Doppler Imaging (ZDI) (Donati et al. 1997, 2006). Spectropolarimetry consists of studying the polarisation inside the spectral lines. When the spectral lines are formed, if there is a magnetic field, it would induce Zeeman splitting, and the spectral lines will be polarised. In order to infer the magnetic field, one can study the polarisation signatures induced by this field, and, by mean of tomographic imaging, reconstruct the large-scale field. High resolution spectra can be collected using spectropolarimeters such as ESPaDOnS at CFHT and NARVAL at TBL. It is important to note here that the polarisation in spectral lines of cool stars induced by their magnetic field is extremely small, usually within the error bars. In order to be able to detect the signal, we use a multi-line technique, called Least-Square Deconvolution (LSD, Donati et al. 1997). LSD combines the information from many spectral lines and produces a mean profile with a higher S/N ratio than for single lines. Zeeman-Doppler Imaging is a tomographic imaging technique. It allows the reconstruction of the large-scale magnetic field map of a star, using the polarimetric information in spectra collected over one or more stellar rotation. Actually, different field orientation (e.g. radial, azimuthal) produces different polarisation signatures. When the star rotates, the signatures of a particular magnetic region will be shifted due to the Doppler effect. The signature in the profile will also depend of the position of the feature on the stellar surface. Collecting spectra over a stellar rotation allows, using ZDI (and maximum-entropy regularisation), to produce the simplest magnetic map that would produce the polarisation signatures in the collected spectra (Vogt et al. 1987; Semel 1989). The magnetic field orientation, the location and the strength of the features can thus be determined using ZDI.

As already mentioned, one needs a high S/N time-series of spectra to be able to perform ZDI. Depending on the spectral type, magnitude and characteristics of the star, a single map reconstruction can require up to three observing nights.

3 Field topologies and evolution

3.1 Field characteristics

We reconstructed the magnetic maps of the seven stars for which we have detected a magnetic field. Each map is a description of the field in a spherical coordinate system, with the radial, azimuthal and meridional components reconstructed. Using ZDI, we can calculate all the field characteristics, i.e. field strength, the energy in the poloidal and toroidal components, the degree of axisymmetry. Our analysis (Fares et al. 2009, 2010, 2012, 2013) shows that the general characteristics of the field of planet hosts of our sample is not different from those not harbouring a hot-Jupiter. Tidal and magnetospheric interactions, although present in these systems, don't seem to influence the global field characteristics. For cool stars more massive than about 0.8 solar mass, there seems to be a trend in the field characteristics: stars with a Rossby number greater than one have weak fields, with a dominant axisymmetric poloidal component. Stars with a Rossby number less than one have stronger fields, dominated by the toroidal component, with a non-axisymmetric poloidal component. Stars hosting a hot-Jupiter show similar characteristics, see Fig 1.

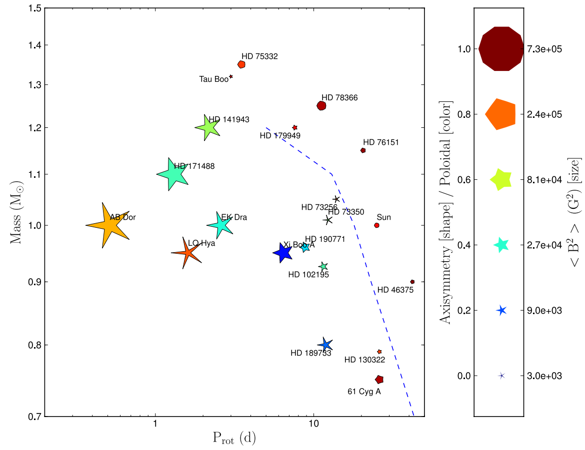

Fig. 1. Mass-rotation diagram of 18 reconstructed stellar magnetic fields. Planet host stars have their names indicated in red, while other stars without detected hot Jupiters have their names indicated in black. The dashed line represent Rossby number = 1.0. The size of the symbol represents the field strength, its colour the contribution of the poloidal component to the field, and its shape how axisymmetric the poloidal component is. Fig. from Fares et al. (2013)

3.2 Field evolution

τ Boo was observed over many observing epochs, covering 5 years. This system is particular because the star is an F star, with a shallow convective envelope, orbited by a massive planet of about 6 Jupiter mass. The planet and the star are synchronised, i.e. the star has the same rotational period as the planetary orbital period, both of 3.3 days. We observed, for the first time for a star other than the Sun, a flip in the polarity of the large-scale magnetic field. This flip happens every year, indicating a cycle of 2 years (or less). Such a cycle is a fast cycle when compared to the solar 22 year cycle. The origin of such a short cycle is not yet understood, it might be due to the shallow convective envelope, or to the synchronisation of the outer envelope with the planet, possibly by tidal interactions. More observations of F stars are needed, as well as observations of planet hosts in order to conclude on the effect of tidal interactions on short cycles.

4 Stellar corona and beyond

Using the reconstructed magnetic maps, we can extrapolate the magnetic field to the stellar corona. The theoretical modelling of the stellar corona can be done using a potential field source surface model (e.g. McIvor et al. 2006), a force free model (e.g. **?**) or a stellar wind model (e.g. Vidotto et al. 2012). In all cases, when the map is reconstructed, it can be used as a boundary condition for the field extrapolation, making the modelling of the corona more realistic. Fig 2 shows an example of such extrapolation, for HD189733, using a potential field source surface model.

From this extrapolation, one can study the environment around the planet and on the planetary orbit. We calculate the stellar magnetic energy at the position of the planet. Since the stellar magnetic field is not a simple axisymmetric field, this energy is variable on the orbit. This implies that the environment surrounding around the planet on its orbit is variable, see fig 2.

From the study the magnetic energy around the planet, we can predict the planetary radio emission from interactions, using, for example, the magnetic energy model of Zarka (2007); Grießmeier et al. (2007). We find that the radio emission is variable on the orbit, and is modulated by the beat period between the rotation of the star and the orbital period of the planet. This variability reflects the variability in the planetary environment.

5 Conclusions

Star-Planet interactions in close-in planetary systems affect both the planet and the star. The stellar large-scale magnetic field influence these interactions and can be influenced by them. We studied the magnetic field of a sample of hot-Jupiter hosting stars. We found that the magnetic field characteristics are not different from

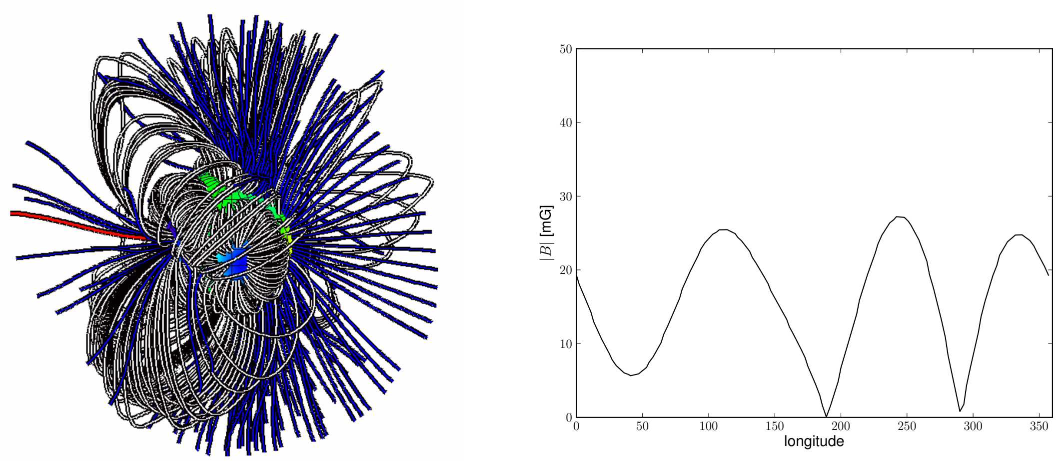

Fig. 2. Left: The extrapolated magnetic field of HD 189733 for June 2007. White lines corresponds to the closed magnetic lines, blue ones to the open field lines, and the red line corresponds to the field line joining the planet to the star at a given (arbitrarily selected) orbital and rotation phase. **Right:** The magnetic field at the distance of the planet as a function of stellar longitude for June 2007, adapted from Fares et al. (2010)

those of stars without a hot-Jupiter. However, the magnetic field of τ Boo varies over a cycle of 2 years, a fast cycle compared to the solar one. The shallow convective envelope, high differential rotation, but also the synchronisation with the planet, and thus tidal interactions might be responsible for such a short cycle. Our studies show that in order to understand the environment around the planet, one must study the stellar field. This is also the case for predicting realistically the planetary emission due to star-planet interactions. Finally, multi-wavelength campaigns allow characterising the system from the stellar surface till the planetary orbit. In case of positive detection (bow shock, radio emission), the magnetic field of the planet can be inferred.

References

Brown, D. J. A., Collier Cameron, A., Hall, C., Hebb, L., & Smalley, B. 2011, MNRAS, 415, 605
Cébron, D. & Hollerbach, R. 2014, ApJ, 789, L25
Cuntz, M., Saar, S. H., & Musielak, Z. E. 2000, ApJ, 533, L151
Donati, J.-F., Howarth, I. D., Jardine, M. M., et al. 2006, MNRAS, 370, 629
Donati, J.-F., Semel, M., Carter, B. D., Rees, D. E., & Collier Cameron, A. 1997, MNRAS, 291, 658
Fares, R., Donati, J.-F., Moutou, C., et al. 2009, MNRAS, 398, 1383
Fares, R., Donati, J.-F., Moutou, C., et al. 2012, MNRAS, 423, 1006
Fares, R., Donati, J.-F., Moutou, C., et al. 2010, MNRAS, 406, 409
Fares, R., Moutou, C., Donati, J.-F., et al. 2013, MNRAS, 435, 1451
Grießmeier, J.-M., Zarka, P., & Spreeuw, H. 2007, A&A, 475, 359
Ibgui, L., Burrows, A., & Spiegel, D. S. 2010, ApJ, 713, 751
Jardine, M. & Collier Cameron, A. 2008, A&A, 490, 843
Kashyap, V. L., Drake, J. J., & Saar, S. H. 2008, ApJ, 687, 1339
Lanza, A. F. 2009, A&A, 505, 339
Lecavelier des Etangs, A., Sirothia, S. K., Gopal-Krishna, & Zarka, P. 2013, A&A, 552, A65
Mayor, M. & Queloz, D. 1995, Nature, 378, 355
McIvor, T., Jardine, M., & Holzwarth, V. 2006, MNRAS, 367, L1
Nichols, J. D. 2012, MNRAS, 427, L75

Pont, F. 2009, MNRAS, 396, 1789

Poppenhaeger, K., Robrade, J., & Schmitt, J. H. M. M. 2010, A&A, 515, A98

Semel, M. 1989, A&A, 225, 456

Shkolnik, E., Bohlender, D. A., Walker, G. A. H., & Collier Cameron, A. 2008, ApJ, 676, 628

Shkolnik, E., Walker, G., & Bohlender, D. 2003, ApJ, 597, 1092

Shkolnik, E., Walker, G., Bohlender, D., Gu, P., & Kürster, M. 2005, ApJ, 622, 1075

Sirothia, S. K., Lecavelier des Etangs, A., Gopal-Krishna, Kantharia, N. G., & Ishwar-Chandra, C. H. 2014, A&A, 562, A108

Smith, A. M. S., Collier Cameron, A., Greaves, J., et al. 2009, MNRAS, 395, 335

Vidotto, A. A., Fares, R., Jardine, M., et al. 2012, MNRAS, 423, 3285

Vogt, S. S., Penrod, G. D., & Hatzes, A. P. 1987, ApJ, 321, 496

Winn, J. N., Fabrycky, D., Albrecht, S., & Johnson, J. A. 2010, ApJ, 718, L145

Zarka, P. 2007, Planet. Space Sci., 55, 598

SF2A 2014
J. Ballet, F. Bournaud, F. Martins, R. Monier and C. Reylé (eds)

INERTIAL WAVES IN DIFFERENTIALLY ROTATING LOW-MASS STARS AND TIDES

M. Guenel[1], C. Baruteau[2], S. Mathis[1] and M. Rieutord[2]

Abstract.
Star-planet tidal interactions may result in the excitation of inertial waves in the convective region of stars. Their dissipation plays a prominent role in the long-term orbital evolution of short-period planets. If the star is assumed to be rotating as a solid-body, the waves' Doppler-shifted frequency is restricted to $[-2\Omega, 2\Omega]$ (Ω being the angular velocity of the star) and they can propagate in the entire convective region. However, turbulent convection can sustain differential rotation with an equatorial acceleration (as in the Sun) or deceleration that may modify waves propagation. We thus explore the properties of inertial modes of oscillation in a conically differentially rotating background flow whose angular velocity depends on the latitudinal coordinate only, close to what is expected in the external convective envelope of low-mass stars. We find that their frequency range is broadened by differential rotation, and that they may propagate only in a restricted part of the envelope. In some cases, inertial waves form shear layers around short-period attractor cycles. In others, they exhibit a remarkable behavior when a turning surface or a corotation layer exists in the star. We discuss how all these cases can impact tidal dissipation in stars.

Keywords: hydrodynamics - waves - planet-star interactions

1 Introduction

The tidal force exerted by a planet or a stellar companion on its host star may excite inertial waves in the external convective envelope of low-mass stars (see Ogilvie & Lin 2007), which are low-frequency waves whose restoring force is the Coriolis acceleration. The dissipation of the energy and angular momentum carried away by these waves may play an important role on the orbital architecture of planetary systems and on the rotation of their components (see Albrecht et al. 2012; Ogilvie 2014), yet it has only recently started being investigated. It has been shown by Baruteau & Rieutord (2013) that differential rotation may strongly affect the propagation and dissipation of linear inertial modes of oscillations. Their study was restricted to shellular and cylindrical rotation profiles, but turbulent convection can also establish conical — solar/antisolar-type — differential rotation profiles (see Matt et al. 2011; Gastine et al. 2014), as is observed in the Sun. In this work, we explore the propagation and dissipation of linear inertial modes of oscillation in stellar convective envelopes (for low-mass stars only) with conical differential rotation that depends mainly/only on the colatitude.

2 Tidal inertial waves in a differentially rotating shell

2.1 The set-up

We model the convective envelope of a low-mass star as a rotating homogeneous incompressible viscous fluid inside a spherical shell of aspect ratio η and external radius R. The fluid is assumed to have a conical differential rotation profile *i.e.* depending only on the colatitudinal coordinate θ :

$$\Omega(\theta) = \Omega_{\rm ref}\left(1 + \varepsilon \sin^2\theta\right) = \Omega_{\rm ref}\left(1 + \varepsilon \frac{s^2}{s^2 + z^2}\right), \quad \text{with} - R \leqslant s, z \leqslant R. \tag{2.1}$$

We use standard cylindrical coordinates (s, ϕ, z), with the z-axis aligned with the rotation axis. $\Omega_{\rm ref}$ denotes the angular velocity at the rotation axis while ε gives the behavior of the differential rotation, *i.e.*:

[1] Laboratoire AIM Paris-Saclay, CEA/DSM/IRFU/SAp - Université Paris Diderot - CNRS, 91191 Gif-sur-Yvette, France
[2] IRAP, Observatoire Midi-Pyrénées, 14 avenue Edouard Belin, 31400 Toulouse, France

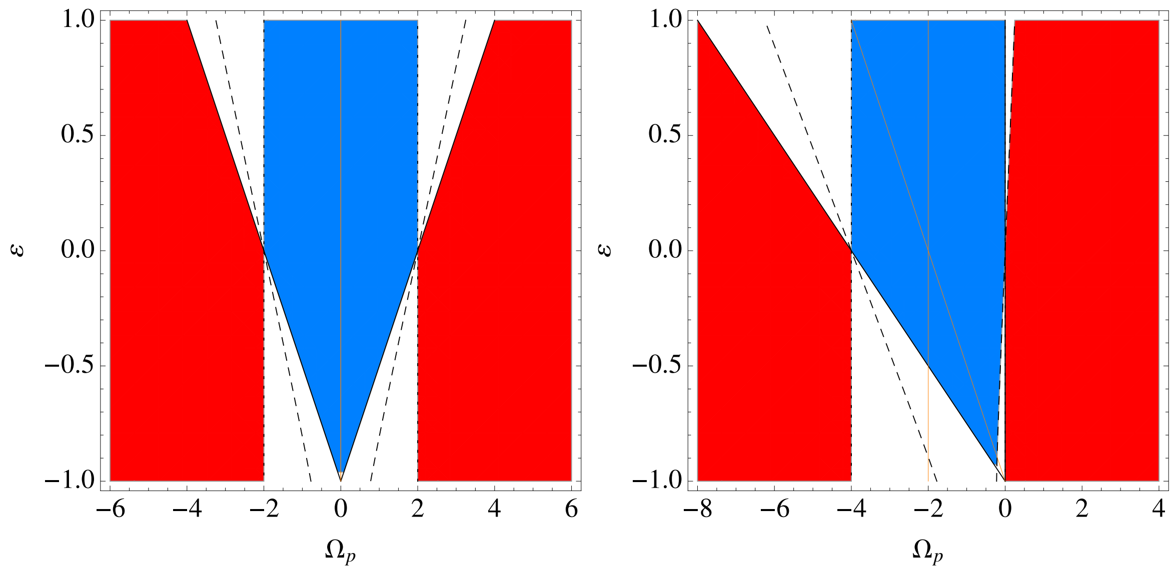

Fig. 1. Illustration of the two kinds of inertial modes propagating in a fluid with conical rotation profile $\Omega(\theta)/\Omega_{\rm ref} = 1 + \varepsilon \sin^2 \theta$. **Left :** $m = 0$. **Right :** $m = 2$. **Blue :** D modes that propagate in the whole shell ($\xi > 0$ everywhere). **White :** DT modes that exhibit at least one turning surface inside the shell (the sign of ξ changes in the shell). **Red :** No inertial modes may propagate ($\xi < 0$ everywhere). **Orange :** The modes in the region between the two orange lines feature a corotation layer inside the shell.

- $\varepsilon > 0$ that corresponds to the case of solar differential rotation (equatorial acceleration),
- $\varepsilon < 0$ for anti-solar differential rotation (polar acceleration).

For the sake of simplicity, we ignore the non-linear interactions between the different waves, as well as the interaction between waves and convection. In an inertial frame, we look for velocity ($\mathbf{u}$) and reduced pressure (p) perturbations proportional to $\exp(i\Omega_p t + im\phi)$ that satisfy the linear system :

$$\begin{cases} i\tilde{\Omega}_p \mathbf{u} + 2\Omega \mathbf{e_z} \times \mathbf{u} + s\,(\mathbf{u}\cdot\nabla\Omega)\,\mathbf{e_\phi} = -\nabla p + \nu\nabla^2\mathbf{u} \\ \nabla\cdot\mathbf{u} = 0 \end{cases}, \tag{2.2}$$

where $\tilde{\Omega}_p(\theta) = \Omega_p + m\Omega(\theta)$ is the Doppler-shifted frequency of the mode, ν is the viscosity and (s, z, ϕ) are the cylindrical coordinates defined above. We may use both rigid and/or stress-free boundary conditions at the inner and outer boundaries of the shell.

2.2 Modification of inertial waves by conical differential rotation

Combining the linearized hydrodynamical equations and using the short-wavelength approximation, we get the following Poincaré equation for the pressure perturbation p only:

$$\frac{\partial^2 p}{\partial s^2} + \frac{A_z}{\tilde{\Omega}_p^2}\frac{\partial^2 p}{\partial s \partial z} + \left(1 - \frac{A_s}{\tilde{\Omega}_p^2}\right)\frac{\partial^2 p}{\partial z^2} = 0, \tag{2.3}$$

where

$$A_s(\theta) = \frac{2\Omega}{s}\frac{\partial}{\partial s}(s^2\Omega) \quad \text{and} \quad A_z(\theta) = \frac{2\Omega}{s}\frac{\partial}{\partial z}(s^2\Omega). \tag{2.4}$$

Rayleigh's stability criterion requires $A_s > 0$ everywhere in the shell, which yields $\varepsilon \geqslant -1$. Note also that in the case of solid-body rotation, we obtain $A_s = 4\Omega^2$ and $A_z = 0$. This equation is hyperbolic and waves propagate when the discriminant $\xi(\theta) = A_z^2 + 4\tilde{\Omega}_p^2\left(A_s - \tilde{\Omega}_p^2\right)$ is positive. In that case the equation governing the path of characteristics in a meridional plane, along which energy propagates, reads :

$$\frac{dz}{ds} = \frac{1}{2\tilde{\Omega}_p^2}\left(A_z \pm \xi^{1/2}\right). \tag{2.5}$$

If ξ vanishes somewhere in the shell, the paths of characteristics bounce off "turning surfaces" where $\xi = 0$ (see the lower plots of fig. 2). Moreover, corotation resonances occur when $\tilde{\Omega}_p = 0$.

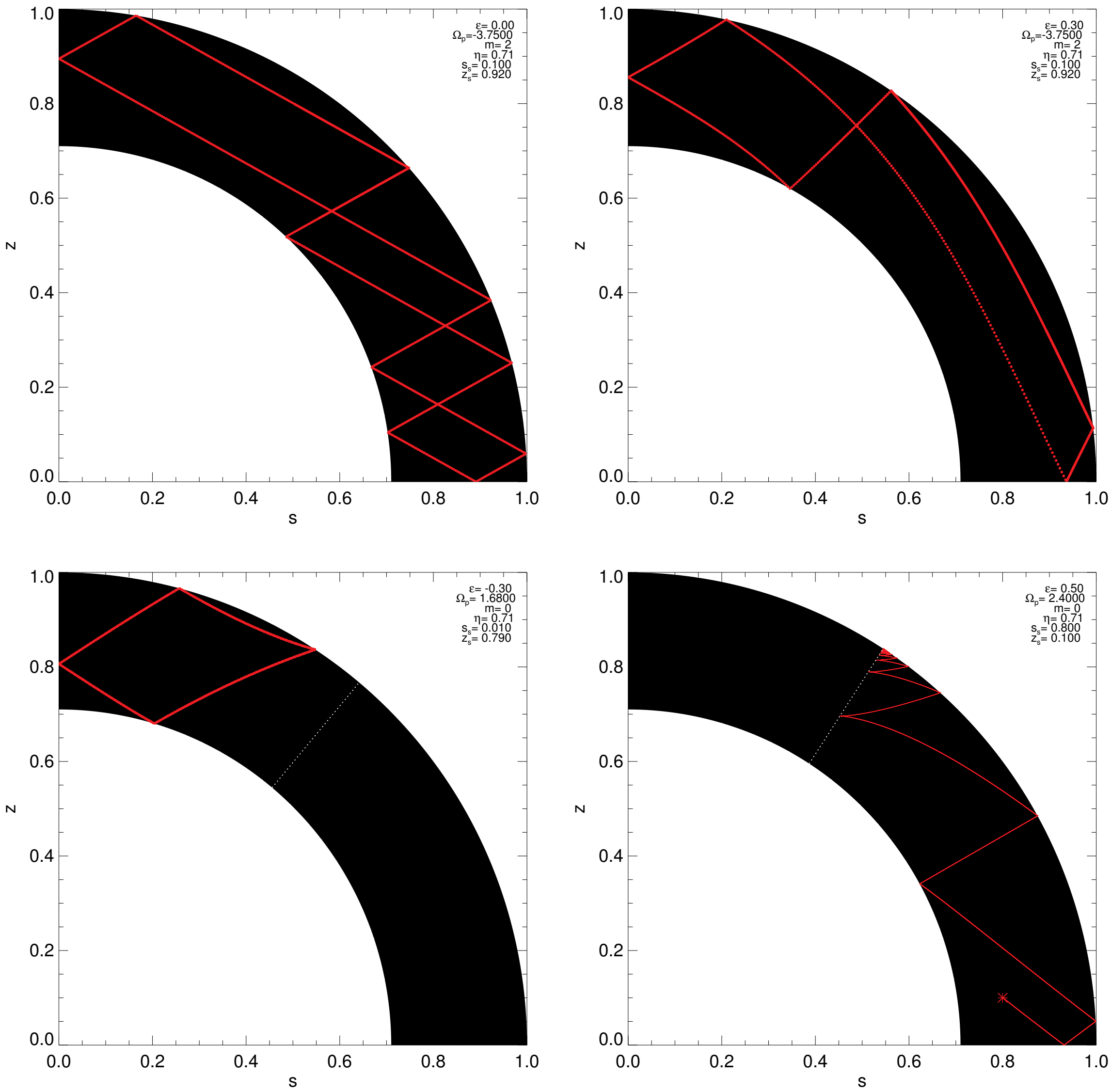

Fig. 2. Upper left : Example of an attractor cycle of the path of characteristics for a D mode with $m = 2$, $\Omega_p/\Omega_{\rm ref} = -3.75$, solid-body rotation ($\varepsilon = 0$) and the solar aspect ratio $\eta = 0.71$. **Upper right :** Same for a D mode in a solar-like convective envelope ($\varepsilon = 0.3$). **Lower left :** Same for a DT mode with $m = 0$, frequency $\Omega_p/\Omega_{\rm ref} = 1.68$ and anti-solar conical rotation ($\varepsilon = -0.3$), the dotted line representing the turning surface. **Lower right :** Illustration of the focusing of the paths of characteristics at the intersection of the turning surface (dotted line) and the outer boundary of the shell ($m = 0$, $\Omega_p/\Omega_{\rm ref} = 2.4$ and $\varepsilon = 0.5$).

The study of the Poincaré equation 2.3 allows to identify waves modification by the conical differential rotation. First, the usual frequency-range $\tilde{\Omega}_p \in [-2\Omega_{\rm ref}, 2\Omega_{\rm ref}]$ can be broadened by differential rotation as shown in fig. 1. When $\varepsilon \neq 0$ we find that the slope of characteristics now depends on (s, z), which means their paths are not straight lines anymore but curved lines (see the upper plots of fig. 2),. Additionally, some modes can be trapped (latitude-wise) because of the existence of a turning surface at which ξ vanishes (see lower left-hand plot of fig. 2). Following the same terminology as in Baruteau & Rieutord (2013), we call them DT modes (D for differential rotation, and T for turning surface) in opposition to the D modes which propagate in the entire shell. When $m \neq 0$, corotation layers may exist in the shell where $\tilde{\Omega}_p = 0$, with locally vertical paths of characteristics. Paths of characteristics may still converge towards short-period cycles or "attractors", as in the case of solid-body rotation, but we find that they may also focus at the intersection of a turning surface with the boundaries of the shell as illustrated by the lower right-hand plot of fig. 2.

2.3 First numerical solutions

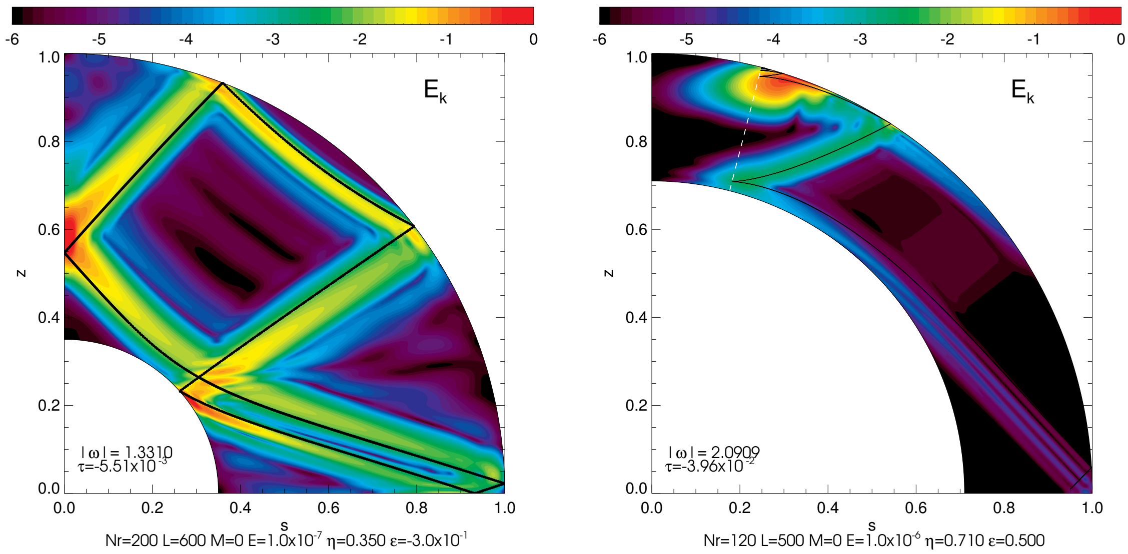

Fig. 3. Left : Kinetic energy of a D mode with anti-solar differential rotation ($m = 0$, $\Omega_p/\Omega_{\rm ref} = 1.33$, $\eta = 0.35$, $\varepsilon = -0.3$ and $E = 10^{-7}$) . Note that in the Sun, $\varepsilon \approx 0.3$. **Right :** Kinetic energy of a DT mode in a solar-like convective envelope ($m = 0$, $\Omega_p/\Omega_{\rm ref} = 2.09$, $\eta = 0.71$, $\varepsilon = 0.5$ and $E = 10^{-6}$). The focusing of the path of characteristics around $(s, z) = (0.25, 0.95)$ creates an accumulation of kinetic energy around this region.

We solve Eqs. (2.2) along with stress-free boundary conditions using a spectral code (see details in Rieutord 1987). We show in fig. 3 two examples of linear modes of oscillations in the case of conical differential rotation for $m = 0$ for different Ekman numbers, defined by $E = \nu/(\Omega_{\rm ref} R^2)$ in our framework. Notice that the agreement between the structure of the kinetic energy of the mode (in colors) and the paths of characteristics (overplotted in black) is good, which confirms the validity of our results. In a near future, we will carry out the same type of calculations for tidally-forced inertial modes, which will allow us to evaluate the tidal dissipation which is due to inertial waves in the convective envelope of differentially rotating low-mass stars.

3 Conclusions

This work is a first step towards the understanding of the physics of tidally excited inertial waves under conditions that are close to those of differentially rotating external convective envelopes of low-mass stars. The next step will be to introduce a forcing term in the equation of momentum in order to simulate the action of a companion.

References

Albrecht, S., Winn, J. N., Johnson, J. A., et al. 2012, ApJ, 757, 18

Baruteau, C. & Rieutord, M. 2013, Journal of Fluid Mechanics, 719, 47

Gastine, T., Yadav, R. K., Morin, J., Reiners, A., & Wicht, J. 2014, MNRAS, 438, L76

Matt, S. P., Do Cao, O., Brown, B. P., & Brun, A. S. 2011, Astronomische Nachrichten, 332, 897

Ogilvie, G. I. 2014, ARA&A, 52, 171

Ogilvie, G. I. & Lin, D. N. C. 2007, ApJ, 661, 1180

Rieutord, M. 1987, Geophysical and Astrophysical Fluid Dynamics, 39, 163

SF2A 2014
J. Ballet, F. Bournaud, F. Martins, R. Monier and C. Reylé (eds)

UNDERSTANDING TIDAL DISSIPATION IN GASEOUS GIANT PLANETS : THE RESPECTIVE CONTRIBUTIONS OF THEIR CORE AND ENVELOPE

M. Guenel[1], S. Mathis[1] and F. Remus[2]

Abstract. Tidal dissipation in planetary interiors is one of the key physical mechanisms that drive the evolution of star-planet and planet-moon systems. New constraints are now obtained both in the Solar and exoplanetary systems. Tidal dissipation in planets is intrinsically related to their internal structure. In particular, fluid and solid layers behave differently under tidal forcing. Therefore, their respective dissipation reservoirs have to be compared. In this work, we compute separately the contributions of the potential dense rocky/icy core and of the convective fluid envelope of gaseous giant planets, as a function of core size and mass. We then compare the associated dissipation reservoirs, by evaluating the frequency-average of the imaginary part of the Love numbers k_2^2 in each region. We demonstrate that in general both mechanisms must be taken into account.

Keywords: hydrodynamics - waves - planet-star interactions - planets and satellites: dynamical evolution and stability

1 Introduction

The orbital and rotational evolution of a close-in planet around its host star or of a moon around a planet is strongly dependent on the tidal dissipation inside each body (Goldreich & Soter 1966). However, the response of fluid and solid planetary layers to tidal excitation is not well-understood yet, as well as the associated dissipative processes which are very different in each type of region (e.g. Mathis & Remus 2013; Auclair-Desrotour et al. 2014). For these reasons, there is a strong need for reliable calculations of the dissipation rate of the energy of tidal displacements in each kind of planetary layer.

Recent progress on observational constraints was obtained using high-precision astrometry measurements in the solar system (Lainey et al. 2009, 2012) especially for Jupiter and Saturn, and space-based high-resolution photometry for exoplanetary systems (Albrecht et al. 2012). These results showed that there may be a strong tidal dissipation in gaseous giant planets, and its smooth dependence on the tidal frequency in the case of Saturn indicates that the inelastic dissipation in their central dense core may be strong (e.g. Remus et al. 2012, 2014; Storch & Lai 2014). However, on one hand, the mass, the size, and the rheology of these cores are still unknown. On the other hand, inertial waves, whose restoring force is the Coriolis acceleration, may be excited by tides in the surrounding fluid convective envelope. Moreover, it seems that turbulent friction acting on these waves can be strong too (e.g. Ogilvie & Lin 2004; Ogilvie 2013). As a consequence, it is necessary to develop new models that take into account the appropriate dissipative mechanisms, so that we can predict how much energy each type of layer can dissipate. This should be achieved not only for gaseous giant planets but for all multi-layer planets, that may consist of differentiated solid and fluid layers.

In this work, we used a simplified two-layer model that accounts for the internal structure of gaseous giant planets. We used the frequency-dependent Love number to evaluate the reservoirs of dissipation in both regions, in a way introduced by Ogilvie (2013). It allows us to give the first direct comparison of the respective strengths of different dissipative mechanisms occurring in a given planet. In sec. 2, we describe the main characteristics of our simplified planetary model. Next, we recall the method we used to compute the reservoirs of dissipation that is a result of viscoelastic dissipation in the core (Remus et al. 2012, 2014) and of turbulent dissipation in the fluid envelope (Ogilvie 2013). In sec. 3, we explore their respective strength for possible values for the parameters of our two-layer model. Finally, we discuss our results and the potential applications of this method.

[1] Laboratoire AIM Paris-Saclay, CEA/DSM/IRFU/SAp - Université Paris Diderot - CNRS, 91191 Gif-sur-Yvette, France
[2] IMCCE, Observatoire de Paris, CNRS UMR 8028, UPMC, USTL, 77 Avenue Denfert-Rochereau, 75014 Paris, France

2 Modelling tidal dissipation in gaseous giant planets

2.1 The two-layer model

This model features a central planet A of mass M_p and mean radius R_p assumed to be in moderate solid-body rotation Ω with $\epsilon^2 \equiv \Omega^2/\sqrt{\mathcal{G}M_p/R_p^3} \ll 1$ (see fig. 1). In this regime, the Coriolis acceleration, which scales as Ω, is taken into account while the centrifugal acceleration, which scales as Ω^2 is neglected. The planet A has a rocky (or icy) solid core of radius R_c, density ρ_c and rigidity G that is surrounded by a convective fluid envelope of density ρ_o. Both regions are assumed to be homogeneous for the sake of simplicity. Finally, a point-mass tidal perturber B of mass M_B is orbiting around A with a mean motion n.

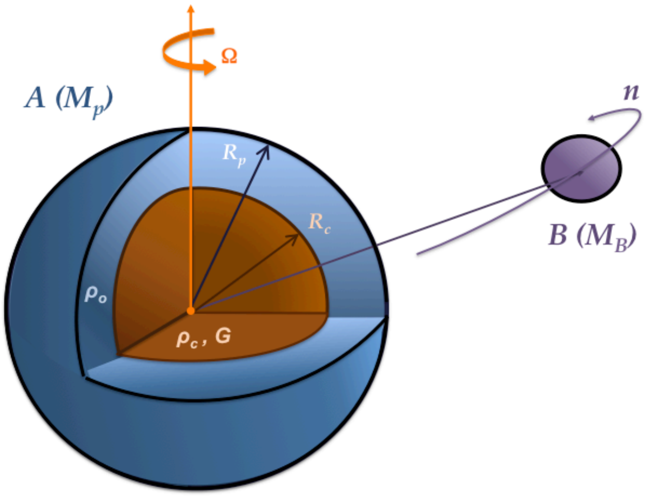

Fig. 1. The two-layer model.

2.2 Mechanisms of dissipation

The time-dependent tidal potential exerted by the companion leads to two different dissipation mechanisms. In the following, we detail how they operate and the hypotheses we used to evaluate their respective strength.

- First, we consider the viscoelastic dissipation in the solid core, for which we assume that the rheology follows the linear rheological model of Maxwell with a rigidity G and a viscosity η ; we also assume that the surrounding envelope is inviscid and only applies hydrostatic pressure and gravitational attraction on the core.

- Then, the turbulent viscosity in the fluid convective envelope dissipates the kinetic energy of tidal inertial waves propagating in that region. The restoring force of inertial waves is the Coriolis acceleration and their frequency is smaller than the Coriolis frequency : $\omega \in [-2\Omega, 2\Omega]$. Moreover, their kinetic energy may concentrate and form shear layers around attractor cycles, which leads to enhanced damping by turbulent viscosity. In order to compute it, the core is assumed to be perfectly rigid.

2.3 Evaluation of the tidal dissipation reservoirs

We compute for each of these mechanisms the "reservoir of dissipation", a weighted frequency-average of the imaginary part of the Love number $k_2^2(\omega) = \Phi_2^{2\prime}/U_2^2$ (which is the ratio between the Y_2^2-components of the Eulerian perturbation Φ' of the self-potential of body A, and of the tidal potential U) defined as :

$$\int_{-\infty}^{+\infty} \mathrm{Im}\left[k_2^2(\omega)\right] \frac{\mathrm{d}\omega}{\omega} = \int_{-\infty}^{+\infty} \frac{\left|k_2^2(\omega)\right|}{Q_2^2(\omega)} \frac{\mathrm{d}\omega}{\omega}, \tag{2.1}$$

where $Q_2^2(\omega)$ is the corresponding tidal quality factor.

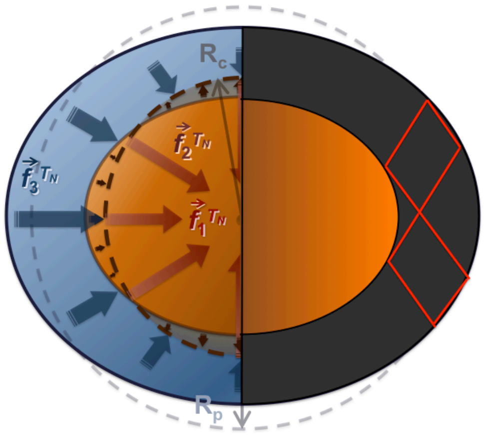

Fig. 2. Left : Gravitational forces ($\vec{f}_1$), internal constraints ($\vec{f}_2$) and hydrostatic pressure ($\vec{f}_3$) acting on the solid core, which is deformed by the tidal force exerted by the companion. **Right :** Attractor formed by a path of characteristics of inertial waves.

- We find for the viscoelastic dissipation mechanism (see Remus et al. 2012, 2014; Guenel et al. 2014):

$$\int_{-\infty}^{+\infty} \mathrm{Im}\left[k_2^2(\omega)\right] \frac{\mathrm{d}\omega}{\omega} = \frac{\pi\, G\,(3+2\,\alpha)^2\,\beta\,\gamma}{\delta\,(6\,\delta+4\,\alpha\,\beta\,\gamma\,G)}, \tag{2.2}$$

  where α, β and δ are positive functions of the aspect and density ratios $(R_c/R_p, \rho_o/\rho_c)$, whereas γ only depends on R_c and ρ_c. This result is remarkably independent of the viscosity η while $\mathrm{Im}\left[k_2^2(\omega)\right]$ is not.

- Meanwhile, Ogilvie (2013) provides us for inertial waves :

$$\int_{-\infty}^{+\infty} \mathrm{Im}\left[k_2^2(\omega)\right] \frac{\mathrm{d}\omega}{\omega} = \frac{100\pi}{63}\epsilon^2 \frac{(R_c/R_p)^5}{1-(R_c/R_p)^5} \times \left[1+\frac{1-\rho_o/\rho_c}{\rho_o/\rho_c}\,(R_c/R_p)^3\right]\left[1+\frac{5}{2}\frac{1-\rho_o/\rho_c}{\rho_o/\rho_c}\,(R_c/R_p)^3\right]^{-2}. \tag{2.3}$$

3 Comparison of the two dissipation mechanisms

- Our goal is to compare quantitatively the respective strength of the two dissipative mechanisms in order to determine if one of them can be neglected in gaseous giant planets similar to Jupiter and Saturn. Their respective mass and radius are $M_p = \{317.83, 95.16\}\, M_\oplus$ and $R_p = \{10.97, 9.14\}\, R_\oplus$ ($M_\oplus = 5.97\,10^{24}$ kg and $R_\oplus = 6.37\,10^3$ km being the Earth's mass and radius). Their rotation rate is $\Omega_{\{\mathrm{J,S}\}} = \left\{1.76\,10^{-4}, 1.63\,10^{-4}\right\}\mathrm{rad}\cdot\mathrm{s}^{-1}$. Internal structure models for these bodies are still not well constrained (Guillot 1999; Hubbard et al. 2009). This is why we choose to explore wide ranges of core radii (left) and core masses (right) in fig. 3.
- We choose to use as a reference $G^{\mathrm{R}}_{\{\mathrm{J,S}\}} = \left\{4.46\,10^{10}, 1.49\,10^{11}\right\}$ Pa that allows the viscoelastic dissipation model to match the dissipation measured by Lainey et al. (2009, 2012) in Jupiter at the tidal frequency of Io and in Saturn at the frequency of Enceladus (with $\eta_{\{\mathrm{J,S}\}} = \left\{1.45\,10^{14}, 5.57\,10^{14}\right\}$ Pa $\cdot$ s).
- Figure 3 shows that for both dissipation models and both planets, the tidal dissipation reservoirs generally increase with the core radius (left) while they slightly decrease with increasing core mass — or decreasing ρ_o/ρ_c (right). These plots show that in Jupiter- and Saturn-like gaseous giant planets, the two distinct mechanisms exposed earlier can both contribute to tidal dissipation, and that therefore none of them can be neglected in general (see Guenel et al. 2014).

4 Conclusions

In the case of Jupiter and Saturn-like planets, we show that the viscoelastic dissipation in the core could dominate the turbulent friction acting on tidal inertial waves in the envelope. However, the fluid dissipation

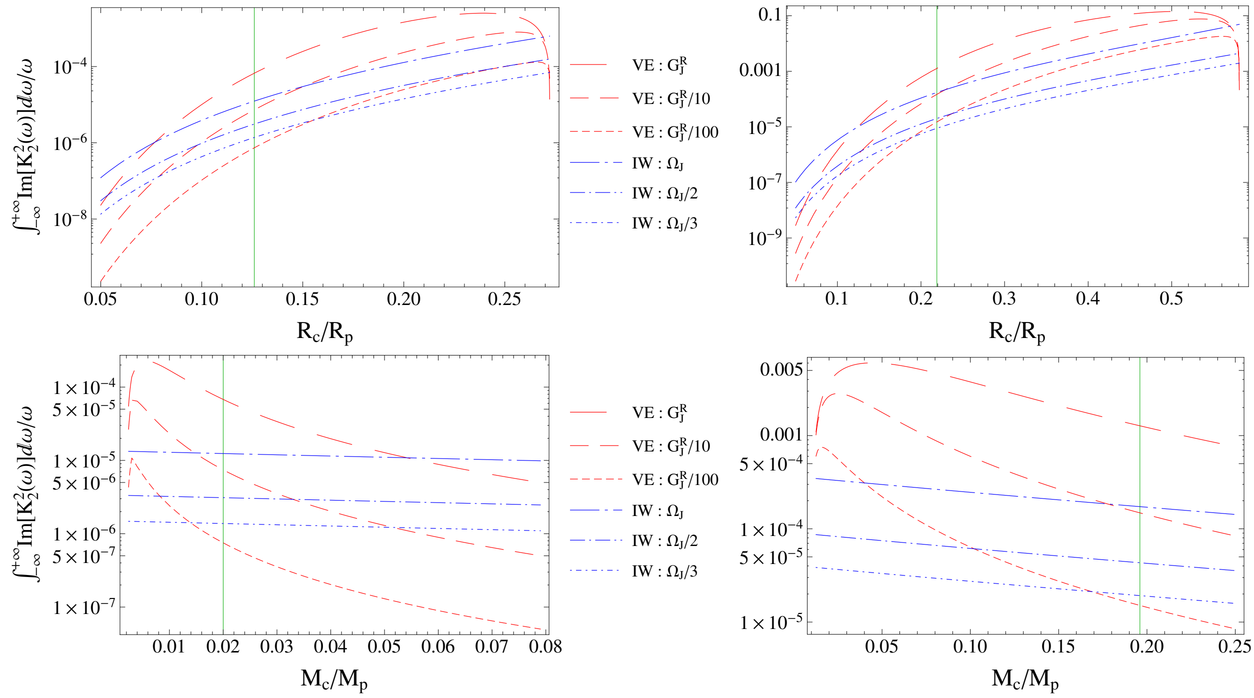

Fig. 3. Left : Dissipation reservoirs for the viscoelastic (VE) dissipation in the core (red curve) and the turbulent friction acting on inertial waves (IW) in the fluid envelope (blue curves) in Jupiter- (above) and Saturn-like planets (below) as a function of R_c/R_p, Ω, and G, with fixed R_p and M_p. We use the values $M_c/M_p = \{0.02, 0.196\}$ for Jupiter and Saturn respectively. The vertical green line corresponds to $R_c/R_p = \{0.126, 0.219\}$. **Right :** Similar to the left-side but now as a function of M_c/M_p with fixed M_p and R_p. We adopt $R_c/R_p = \{0.126, 0.219\}$ for Jupiter and Saturn respectively. The wide M_c-ranges [1,3 - 25] $M_\oplus$ for Jupiter and [2 - 24] $M_\oplus$ for Saturn cover the values considered possible by various internal structure models (Guillot 1999; Hubbard et al. 2009). The vertical green line corresponds to $M_c/M_p = \{0.02, 0.196\}$.

would not be negligible. This demonstrates that it is necessary to build complete models of tidal dissipation in planetary interiors from their deep interior to their surface without any arbitrary a-priori.

References

Albrecht, S., Winn, J. N., Johnson, J. A., et al. 2012, ApJ, 757, 18

Auclair-Desrotour, P., Le Poncin-Lafitte, C., & Mathis, S. 2014, A&A, 561, L7

Goldreich, P. & Soter, S. 1966, Icarus, 5, 375

Guenel, M., Mathis, S., & Remus, F. 2014, A&A, 566, L9

Guillot, T. 1999, Planet. Space Sci., 47, 1183

Hubbard, W. B., Dougherty, M. K., Gautier, D., & Jacobson, R. 2009, The Interior of Saturn, ed. M. K. Dougherty, L. W. Esposito, & S. M. Krimigis, 75

Lainey, V., Arlot, J.-E., Karatekin, Ö., & van Hoolst, T. 2009, Nature, 459, 957

Lainey, V., Karatekin, Ö., Desmars, J., et al. 2012, ApJ, 752, 14

Mathis, S. & Remus, F. 2013, in Lecture Notes in Physics, Berlin Springer Verlag, Vol. 857, Lecture Notes in Physics, Berlin Springer Verlag, ed. J.-P. Rozelot & C. . Neiner, 111–147

Ogilvie, G. I. 2013, MNRAS, 429, 613

Ogilvie, G. I. & Lin, D. N. C. 2004, ApJ, 610, 477

Remus, F., Mathis, S., Zahn, J.-P., & Lainey, V. 2012, A&A, 541, A165

Remus, F., Mathis, S., Zahn, J.-P., & Lainey, V. 2014, ArXiv e-prints

Storch, N. I. & Lai, D. 2014, MNRAS, 438, 1526

SF2A 2014
J. Ballet, F. Bournaud, F. Martins, R. Monier and C. Reylé (eds)

IMPACT OF MAGNETIC FIELD ON RADIAL VELOCITY MEASUREMENTS.

É.M. Hébrard[1], J.-F. Donati[1], X. Delfosse[2], J. Morin[3], I. Boisse[4], C. Moutou[5] and G. Hébrard[6]

Abstract. Very low-mass stars are very promising targets for planet-search programs, in particular to discover super-Earths / Earths located in their habitable zone. Their detection is in principle accessible to the existing velocimeters of highest radial-velocity (RV) precision, but challenging due to activity (i.e., dark spots and magnetic regions at their surfaces) which generate a noise level in RV curves (RV jitter). It can severely limit our practical ability at detecting Earth-like planets. To overcome this intrinsic limitation, a promising option consists in modeling directly the stellar activity behind the activity jitter, and in particular the magnetic field that gives rise to it. To do this, simultaneous observations in velocimetry (for activity jitter) and in spectropolarimetry (for the Zeeman signatures in spectral lines tracing the presence of a large-scale field) are needed. We present here our first results both on the simulations on the impact of magnetic fields on line profiles (bisectors & RV data), and on the simultaneous observations done thanks to HARPSPol@LaSilla and NARVAL@TBL/SOPHIE@OHP on a small sample.

Keywords: magnetic fields, starspots, radial velocity, spectropolarimetry

1 Introduction

The first exoplanets were found nearly two decades ago. Since then, the attention has switched from simply looking for exoplanets to characterizing super-Earths / Earths within the habitable zones (HZs) of their host stars, i.e. in the orbital range where liquid water can be stable at the planetary surfaces. Despite the high precision of existing velocimeters, a major issue remains to detect them with radial velocity technique. We remain confronted with the interference of stellar noise. Stellar activity (e.g., spots, granulation, magnetic fields) can impact the shape of stellar spectral lines and thus induce apparent RV variations mimicking those induced by an orbiting planet (e.g., Queloz et al. 2001), called RV jitter. To improve the detection threshold with RV techniques, we need to efficiently diagnose the activity jitter to be able to filter out ultimately RV curves from stellar RV signals.

To diagnose the RV jitter and avoid misinterpreting RV data, it is crucial to accurately characterize the impact of stellar activity on usual proxies such as line bisectors. RV jitter results from the presence of inhomogeneities at the surface of the star, carried across the visible disk by rotation and impacting the position and shape of line profiles. By analyzing in detail the shape of spectral lines, one can distinguish planetary signals from activity jitters. Existing studies on RV jitters (such as Queloz et al. 2001; Desort et al. 2007; Boisse et al. 2011), mainly focus on the impact of cool/dark spots. They show that spots can impact in various ways RVs and line bisectors depending on the characteristics of the spot and the star. In particular, they find that in case of surface brightness inhomogeneities, there is an anti-correlation between the RV signal and the bisector slope. As most part of activity features is believed to be caused by magnetic areas, an investigation of the impact of the magnetic field on the spectral appearance is needed. The magnetic field may introduce significant distortions through the Zeeman effect. A recent study focuses on the impact of magnetic fields on RV measurements (Reiners et al. 2013). They conclude that magnetic regions can significantly distort near infra-red (nIR) stellar

[1] CNRS-INSU; IRAP-UMR 5277, 14 Av. E. Belin, F–31400 Toulouse, France. e-mail: elodie.hebrard@irap.omp.eu
[2] UJF-Grenoble 1 / CNRS-INSU, IPAG UMR 5274, Grenoble, F-38041, France
[3] LUPM, Université Montpellier II, CNRS, UMR 5299, Place E. Bataillon, 34095 Montpellier, France
[4] Aix-Marseille Université, CNRS, LAM, UMR 7326, 13388 Marseille, France
[5] CNRS, Canada-France-Hawaii Telescope Corporation, 65-1238 Mamalahoa Hwy, Kamuela, HI 96743, USA
[6] Université Pierre et Marie Curie, UMR 7095 CNRS, 98 bis bd. Arago, 75014 Paris, France

line profiles through Zeeman broadening and therefore affect RV measurements at the $\sim$1 m s^{-1} level, even in visible domain. In the first section, we extend this study to describe how Zeeman broadening distorts line positions and shapes.

To better characterize the activity jitter, a powerful option is to use simultaneous observations to combine different aspects of the activity impact. So far, the most common contemporaneous survey is RV & photometric survey to follow the brightness evolution due to spots and plages carried across the visible disk by rotation. Another possible survey consists in a simultaneous follow-up in spectropolarimetry to track in particular the large-scale magnetic field. The idea is thus to carry out a simultaneous monitoring of the activity jitter and of the magnetic topology in order to look for potential correlations between the two. Then, from this empirical relation and the underlying link between spot distributions and large-scale magnetic topologies, we will work out a way of filtering the activity jitter from RV data. In the second section, we present the preliminary result of this promising option.

2 Model of the impact of magnetic fields on line bisectors.

We investigate how magnetic regions affect the radial velocity $V_{\rm r}$ and the line shape depending on a number of key parameters (e.g., the projected rotation velocity $v \sin i$, the inhomogeneity latitude θ, the magnetic field strength B, the central wavelength of the study λ_0). To assess the line shape evolution, we calculate the velocity span (as introduced, e.g., by Gray 1982; Queloz et al. 2001) $V_{\rm s}$, given by $V_{\rm t} - V_{\rm b}$, where $V_{\rm t}$ and $V_{\rm b}$ are respectively the average velocity at the top and bottom part of the bisector*. The distortion induced by a cool spot being mostly local, we find that $V_{\rm b}$ and $V_{\rm t}$ are correlated, for all stellar configurations and spot parameters.

If we look more precisely at the case of a magnetic field region at photospheric temperature, we find that magnetic regions have an effect on line profiles, especially at nIR wavelengths, showing both similarities and differences with the case of dark spots. In particular, although we always observe an anti-correlation between $V_{\rm r}$ and $V_{\rm s}$, $V_{\rm b}$ and $V_{\rm t}$ can either be anti-correlated or correlated, depending on whether the Zeeman splitting is respectively smaller or larger than $v \sin i$. This anti-correlation is what differs most from the case of cool spots, and reflects that the Zeeman distortion affects simultaneously, but in opposite directions, $V_{\rm b}$ and $V_{\rm t}$ when the magnetic region crosses the center of the visible hemisphere (see Fig. 1). Looking at the correlation between $V_{\rm b}$ and $V_{\rm t}$ can bring further information, allowing to distinguish dark spots from magnetic regions in some specific cases especially in the nIR. To better emphasize this difference between line profile distortions caused by a magnetic region and a cool spot respectively, we show dynamic spectra of profile residuals for both cases (see Fig. 2) - residuals being computed as the difference between the distorted line profiles and the undistorted ones (corresponding to a quiet photosphere). Looking at dynamic spectra is an interesting option to diagnose the nature of the magnetic activity affecting RV curves. We clearly observe that a magnetic feature impacts the whole line profile, including wings and far wings. In the case of a cool magnetic spot, the impact of a magnetic field on the bisector is only visible at low photosphere-to-spot brightness contrasts, i.e., mostly for M dwarfs in the nIR. More details on the simulations and the results can be found in Hébrard et al. (2014).

3 Observations in spectropolarimetry.

As magnetic fields play an important role in the formation of the surface features inducing RV jitter, we performed a spectropolarimetric survey with HARPSPol@LaSilla and investigated how the collected data set can help to highlight the link between large scale magnetic field and RV jitter. With spectropolarimetry, we collect a set of circularly polarized spectra (or Stokes V signatures) at different observational phases. We can use them to infer the rotational period of the star. Moreover we can compute the longitudinal magnetic filed defined as the line of sight projected component of the magnetic field vector, which can help us to characterize stellar activity through the rotational modulations it usually exhibits. Finally, thanks to a tomographic technique like Zeeman-Doppler Imaging (ZDI), we can invert the sets of Stokes V signatures to reconstruct the parent large-scale magnetic field map (orientation & intensity).

We present here only the results obtained for Gl358, a moderately active M-dwarf. We gathered 23 measurements from january to march 2014 for this M3 star ($M_\star$= 0.41 M$_\odot$). The Stokes V signatures allow us to infer a rotational period of 25.4 $\pm$ 0.3 days, in good agreement with what we expect from the periodogram of velocities of Bonfils et al. (2012). Using ZDI technique, we recover the large scale magnetic field orientation and

*The top and bottom parts include all points within 10-40% and 60-90% of the full line depth, respectively.

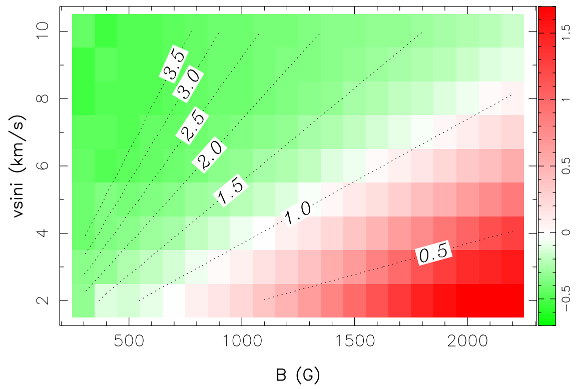

Fig. 1. Effect of $v \sin i$ and B on the average slope of V_t as a function of V_b. Red corresponds to a correlation, whereas green corresponds to an anti-correlation. Dotted lines trace contours of constant $\frac{v \sin i}{\Delta v_B}$. Results are shown for a star with $i = 90°$ and $v \sin i = 5$ km s^{-1} and an equatorial magnetic area at photospheric temperature ($b = 0$) covering 1% of the stellar surface.

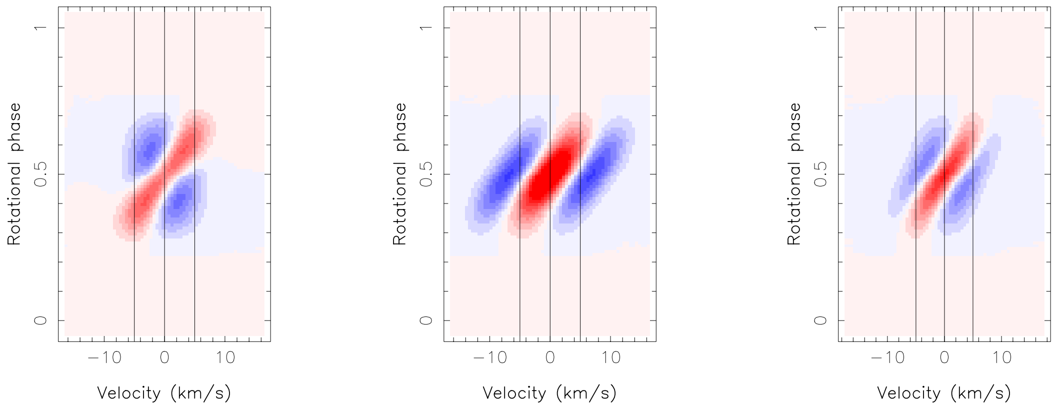

Fig. 2. Dynamic spectra of the line profile residuals in the case of a cool spot (contrast of 100% with the quiet photosphere & $B = 0$ kG left panel), of a magnetic region at photospheric temperature ($B = 1.8$ kG middle panel), and of a cool magnetic spot (contrast of 40% and $B = 1$ kG left panel). From left to right, the vertical lines correspond to velocity of -$v \sin i$, 0 and +$v \sin i$. Each horizontal strip corresponds to a color-coded difference spectrum at a given rotation phase, with blue and red respectively standing for differences of -10 and +10%. Results are shown for a star with $i = 90°$, $v \sin i = 5$ km s^{-1} and an equatorial surface feature covering 1% of the surface.

intensity (see top panel of Fig. 3). This star exhibits a rather simple large-scale magnetic structure. The field is a mostly axisymmetric poloidal field enclosing ~95 % of the reconstructed magnetic energy. This poloidal component can be approximated with a dominant dipole with a polar intensity of -110 G at 45° to the line of sight (towards phase ~ 0.2). Given the stellar inclination of $i \sim 60°$, the magnetic equator is clearly visible at phase ~ 0.75. Moreover, the preliminary analysis (see bottom panel of Fig. 3) shows that RVs and the full width at half maximum (FWHM) both exhibit rotational modulation with the same period as the longitudinal magnetic field B_l, with RV and B_l varying in quadrature. These two results suggest there is a cool spots cluster at phase ~ 0.75 (at mid-phase between RV maximum and minimum), i.e., close to the magnetic equator of the star ($B_l \sim 0$ G). This is observed on other stars (Hébrard et al. in prep.).

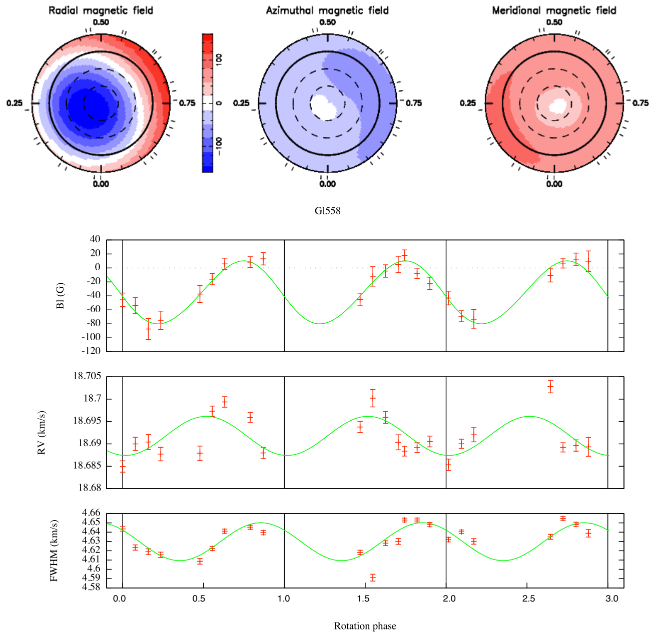

Fig. 3. Top: Large-scale magnetic field map of Gl358. The star is viewed in flattened polar projection. The pole is in the center, the bold circle depicts the stellar equator and the outer line represents the -30° latitude. We represent the three spherical components of the field. The radial ticks indicate the observational phases. **Bottom:** B_l (in G), RV (in km s^{-1}) and FWHM (in km s^{-1}) as a function of the rotation phase, collected with HARPSPol (red crosses with typical errors of resp. 6 G, 1.3 m s^{-1}& 2 m s^{-1}). The green curves represent an adjustment of a periodic wave (i.e sine+cosine at the stellar rotation period).

4 Conclusions

Impacting both RV and line profile shape, the magnetic field has to be taken into account to better understand, diagnose and filter the stellar activity jitter. Its impact is amplified in the nIR, so that new instruments like SPIRou@CFHT dedicated to simultaneous nIR high precision velocimetry / spectropolarimetry, will bring precious further information to characterize the RV jitter. Moreover, a spectropolarimetric survey provide key information to constrain the spots distribution on the stellar surface. Further studies are needed to get a brightness map and confirm our results (for instance inverting the Stokes I profile residuals). Ultimately we will obtain a valid filtering technique with which we can remove RV jitter from RV curves. It is done with success for young stars (such as T-Tauri stars, see Donati et al. (2014)). We are adapting and testing this method to slower and much less active stars.

We gratefully acknowledge financial support from the ‘Programme National de Physique Stellaire’ (PNPS) and the ‘Programme National de Planétologie’ (PNP) of CNRS/INSU, France, which allowed the coauthors to regularly meet during the course of this work.

References

Boisse, I., Bouchy, F., Hébrard, G., et al. 2011, A&A, 528

Bonfils, X., Delfosse, X., Udry, S., & Forveille. 2012, A&A, 549

Desort, M., Lagrange, A., Galland, F., Udry, S., & Mayor, M. 2007, A&A, 473, 983

Donati, J.-F., Hébrard, É., Hussain, G., & Moutou, C. 2014, MNRAS, 443, 25992611

Gray, D. F. 1982, ApJ, 255, 200

Hébrard, É., Donati, J.-F., Delfosse, X., et al. 2014, MNRAS, 443, 25992611

Queloz, D., Henry, G., Sivan, J., et al. 2001, A&A, 379

Reiners, A., Shulyak, D., Anglada-Escudé, G., et al. 2013, A&A, 552

SF2A 2014
J. Ballet, F. Bournaud, F. Martins, R. Monier and C. Reylé (eds)

IMPACT OF STELLAR ACTIVITY ON THE DETERMINATION OF STELLAR PARAMETERS WITH INTERFEROMETRY

R. Ligi[1], D. Mourard[1], A.-M. Lagrange[2], K. Perraut[2] and A. Chiavassa[1]

Abstract.
With the new space missions dedicated to exoplanet detection and characterization, like PLATO, CHEOPS, TESS, the determination of stellar parameters with high accuracy becomes more and more essential. However, direct or indirect estimations of stellar parameters are affected by stellar activity (magnetic spots, bright plages, granulation) that introduces bias that lower those parameters accuracy. Improving the sensitivity and resolution of future interferometers will allow enlarging the number of common targets of space and ground instruments, and accessing the accuracy needed to distinguish between planetary signals and stellar activity signals. After presenting how visible interferometry contributes to the direct and accurate determination of stellar parameters and thus planetary ones, the impact of stellar activity on interferometric observables and stellar parameters will be presented. Finally, solutions to distinguish between exoplanet and spot signals will be discussed.

Keywords: Stellar physics, exoplanets, stellar activity, interferometry

1 Introduction

Our knowledge of stars hosting exoplanets constitutes the basics of our comprehension of extra-solar systems. Particularly, the accurate determination of stellar radius allows a direct determination of planetary ones when exoplanets transit their star, which gives access to many other planetary parameters, like their density or composition provided radial velocity measurements or orbital parameters are also available. Figure 1 (Fressin et al. 2012, Fig. 3) shows the expected composition of transiting exoplanets, which cannot be precisely determined because of the large error bar on their radius and mass. It is even more true for planets different from that found in our solar system, whose composition is not determined (e.g., the super-Earth HD97658 b (Howard et al. 2011) and the sub-Neptune GJ1214 b (Valencia et al. 2013)). However, for most exoplanets, the host star radius is determined through totally model-dependent methods, and their values can differ according to the models used.

Radial velocity (RV) and transit measurements are the most prolific methods in exoplanet discovery. They respectively provide the ratio of the minimum mass of exoplanet to the stellar mass ($M_{\rm p}\sin(i)/M_\star$) and the ratio of the exoplanet and stellar radii ($R_{\rm p}/R_\star$). Those ratios are generally known to better than 1% precision. Therefore, to obtain the planetary radius and mass with such an accuracy, we need to reach this accuracy on the stellar radius and mass. Beyond the difficulty to reach such precision and exactitude with stellar models, stellar activity (magnetic spots, bright plages, granulation) adds noise on RV and transit measurements, but also on direct measurements of stellar parameters, that can in turn add a bias in derived stellar and planetary parameters. With the development of the sensitivity of interferometers, it will become possible to detect weaker signals from the stars including signals of stellar activity. Then, it will be necessary to relate each signal to its physical origin to distinguish between activity and exoplanet signals, which will enable the characterization of both phenomena. In particular, we will have to tackle signals containing the signature of stellar activity and will have to extract them in order to make exact and accurate estimation of stellar and planetary parameters.

In Section 2 we describe how space mission and ground-based instruments together can lead to a better characterization of stars and exoplanets and in Section 3 we show how this characterization can be impacted by stellar activity.

[1] Laboratoire Lagrange, UMR 7293 UNS-CNRS-OCA, Boulevard de l'Observatoire, CS 34229, 06304 NICE Cedex 4, France.
[2] UJF-Grenoble1/CNRS-INSU, Institut de Planétologie et d'Astrophysique de Grenoble, UMR 5274, Grenoble, F-38041, France

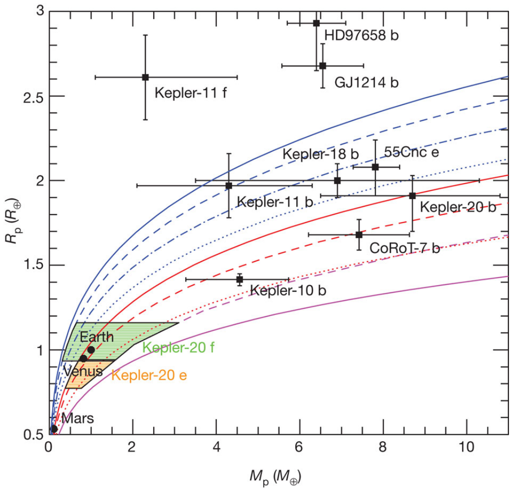

Fig. 1. Mass versus radius relation for small planets (Fig. 3, Fressin et al. 2012). The curves represent theoretical constant-temperature mass-radius relation : water ice (solid blue), MgSiO3 perovskite (solid red), iron (solid magenta). The non-solid lines are mass radius relations for differentiated planets (see Fressin et al. 2012, for details).

2 Determining accurate stellar parameters with combined methods

The next decade will be marked by the development of space missions whose goal is both the characterization of stars and exoplanets. For instance, PLATO mission (Rauer & Catala 2012) has been selected by ESA and should be launched in 2024. The goal of this mission is to detect and characterize exoplanets in the solar neighbourhood thanks to the transit method and to measure stellar seismic activity to precisely determine their age together. The goal of CHEOPS mission (Broeg et al. 2013) is to characterize Earth-sized to Neptune-sized planets with very high precision photometry, whereas TESS mission (Ricker et al. 2010) will discover planetary transits.

However, the scientific exploitation of these missions will be greatly reinforced with independent measurements achieved from the ground. Indeed :

- the transit method allows obtaining the planetary radius if the stellar radius is known. Currently, the ratio between the planetary and stellar radii provided by photometry is more precise than the measurement of stellar radii by a factor 10 ;

- moreover, seismic data together with a direct measurement of the stellar radius bring a better accuracy on ages ($< 10\%$, see e.g. Lebreton & Goupil 2014) and stellar masses ($< 3\%$, see e.g. Creevey et al. 2007). Indeed, the determination of global stellar parameters can be derived from asteroseismology but uncertainties and the difficulties in identifying the modes of oscillation, particularly in classical pulsators, remain. The interferometric radius decreases these uncertainties and help constraining the models used in asteroseismic studies (Cunha et al. 2007).

The stellar radius takes part in the determination of many other parameters through stellar modelisation. All of this highlights the necessity of its very precise and direct determination. This actually applies to every stellar parameters together. Indeed, we need an accurate knowledge of host stars, in particular their age, to get a clear vision of the story of star-planet systems. Contrary to previous missions CoRoT and *Kepler*, which discovered exoplanets around very faint stars, and whose parameters are thus very difficult to constrain with ground instruments, the targets of these missions will be bright stars, which means accessible with interferometry. It will therefore be possible to accurately determine their radius and thus planetary radii and masses. Indeed, interferometry allows the direct determination of angular diameters with a precision better than 2% (and sometimes 1%) (see e.g. Ligi et al. 2012). Combined with the distance, we obtain a direct estimation of the radius, which means as independent of models as possible, and exact. Currently, the accuracy on the distance significantly limits the accuracy on stellar radii but Gaia will soon provide (mid 2016) distances with an accuracy better than 2%, that will allow reaching an accuracy better than 2% on stellar radii.

3 Tackling stellar activity

At the same time, the study of stellar activity (dark spots, bright plages, granulation) is becoming increasingly important in this context. Beyond the fact that it helps understanding stellar structure and evolution, it is of primordial importance in the quest for exoplanets, for three main reasons: (i) it can allow the improvement of the signal/noise ratio and the detection of smaller, terrestrial-like planets for both RV and transit techniques, (ii) it permits the achievement of a better knowledge of the fundamental parameters of the star (radius, age etc.), which has a significant impact on the characterization of the detected planets, (iii) it has an impact on habitability studies because stellar activity is a crucial parameter for the evolution of a planet atmosphere and climate. Stellar activity is known to add a jitter in RV measurements (Lagrange et al. 2010; Meunier et al. 2010; Oshagh et al. 2013) that can mimic exoplanetary signatures and also impacts interferometric observables (Chiavassa et al. 2012, 2014). Some attempts have been made to detect this signature on infrared interferometry (Matter et al. 2010; Zhao et al. 2008, 2011), but never in visible wavelengths.

The code `COMETS` (*COde for Modeling ExoplaneTs and Spots*, Ligi et al. 2014) aims at studying the impact of exoplanets and magnetic spots on interferometric observables (squared visibilities, phases) and allows comparing the results with current available facilities like VEGA/CHARA (Mourard et al. 2009; Ligi et al. 2013) considering realistic achievable precisions.

In this paper, Ligi et al. (2014) present a pionier work exploring the influence of the parameter space (exoplanet position, exoplanet diameter, spot temperature and star diameter) on the minimum baseline length (MBL) required to detect the transiting exoplanet signal on the squared visibility and the phase. The variation of the MBL as a function of the parameters is similar in the presence of an exoplanet or of a spot. However, the spot's temperature causes a contrast with the photosphere which is different from the contrast caused by a transiting exoplanet, which enables to distinguish between the two. The MBL as a function of the parameters can be fitted by an analytical law from which a general formula is derived.

Figure 2 shows the phases corresponding to different configurations : a single star, a star with a transiting exoplanet of various diameters and/or a spot. The star with a spot and/or an exoplanet has a different signal from that of a single star. When the spot and the exoplanet have the same size (left panel), the exoplanet signal (in red) is generally higher than the spot one (in orange) from the 3^{rd} lobe of visibility, but it is mixed up with the spot signal until the 2^{nd} lobe. When the exoplanet is smaller (right panel), its signal is lower than the signal of the spot, even if its contrast with the stellar photosphere is higher. This shows the difficulty to disentangle between spot and exoplanet. In this latter case, the signal induced by both spot and exoplanet in the 2^{nd} lobe is hardly higher than the signal induced by the spot alone. The exoplanet signal is thus hard to extract, unless measurements from the 4^{th} lobe are possible. On the contrary, when $\theta_s = \theta_p$, the signal provoked by both spot and exoplanet is higher by a few degrees than the signal of the spot alone, and reaches a few degrees from the 2^{nd} lobe that should be detectable with existing baselines. For both cases, not taking into account the spot leads here to a bad interpretation of the signal, like a bigger transiting planet, and highlights the necessity of observing the star out of the transit to characterize the stellar activity, that could be substracted from the signal recorded during the transit time to allow the characterization of the exoplanet.

According to these simulations, existing baseline lengths are sufficient to detect the signal of a transiting Jupiter or a small spot, but instruments need to reach accuracies better than 0.5% on squared visibilities and 1° on phases to achieve this goal, which is beyond current instrument accuracies. Measurements in the second lobe of visibility is essential because exoplanet signals can only be seen at these spatial frequencies. Then, phase measurements would allow the characterization of exoplanets more easily, provided that the signal to noise ratio is sufficient to measure this second order observable. Exoplanets and spots do not have the same interferometric signatures, but their signals are mixed up during the transit (see Fig 2). Combining photometric or velocimetric measurements with interferometric ones could be a solution to distinguish between both signals. We have shown that this is possible if the planet crosses the star in few hours/days, provided that the transit time is sufficient to get a detectable signal on interferometric observables. Conversely, observing out of the transit directly provides information about stellar activity.

Other effects should not be forgotten, like the granulation, as shown by Chiavassa et al. (2014) who use realistic three-dimensional radiative hydrodynamical simulations obtained with the Stagger-Grid (Magic et al. 2013) to study its impact on interferometric observables. The granulation perturbs closure phase measurements in particular from the second lobe of visibility, depending on the spectral type, the interferometric instrument used and the wavelength probed. Its signal can also be mixed with a transiting exoplanet signal but they could be differenciated at specific wavelengths (optical or infrared).

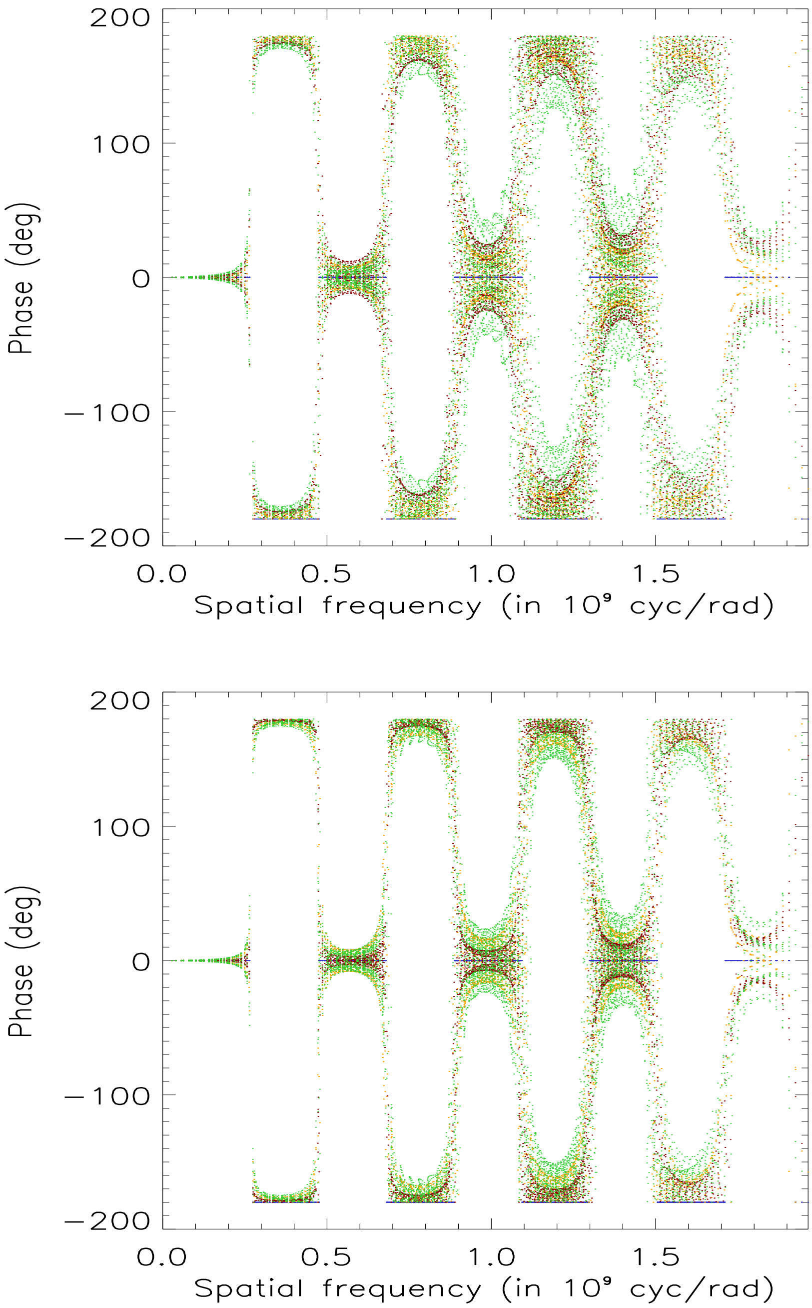

Fig. 2. Phases of a single star (blue), a star with a spot (orange) at (0.2, 0.2) mas, a star with a transiting exoplanet (red) at (0.2, 0.0) mas on the stellar disk and a star with both (green). The spots diameter is $\theta_s = 0.10$ mas and the stars diameter is 1 mas. The exoplanets diameter is either $\theta_p = 0.10$ mas (upper panel) or $\theta_p = 0.05$ mas (bottom panel).

4 Conclusion

The synergy between star and planet studies will be greatly developed in the next years which should lead to a better knowledge of exoplanets but also of stellar systems in general. The combination of measurements from space and ground based instruments will provide a better characterization of stellar radii, masses and ages, and thus allow the determination of exoplanet composition and age with unprecendented precision. Interferometry is essential to determine stellar parameters, but it will also be able to tackle stellar activity if instrument sensitivities are developed enough. This is essential to extract exoplanet signals and eliminate false positives. Then, the questions of habitability of exoplanets can be addressed with a better knowledge and efficiency.

RL acknowledges the Ph.D. financial support from the Observatoire de la Côte d'Azur and the PACA region and support from OCA after her Ph.D. R.L. also thanks Orlagh Creevey for her help in the study of stellar parameters accuracies.

References

Broeg, C., Fortier, A., Ehrenreich, D., et al. 2013, in European Physical Journal Web of Conferences, Vol. 47, European Physical Journal Web of Conferences, 3005

Chiavassa, A., Bigot, L., Kervella, P., et al. 2012, A&A, 540, A5

Chiavassa, A., Ligi, R., Magic, Z., et al. 2014, A&A, 567, A115

Creevey, O. L., Monteiro, M. J. P. F. G., Metcalfe, T. S., et al. 2007, ApJ, 659, 616

Cunha, M. S., Aerts, C., Christensen-Dalsgaard, J., et al. 2007, A&A Rev., 14, 217

Fressin, F., Torres, G., Rowe, J. F., et al. 2012, Nature, 482, 195

Howard, A. W., Johnson, J. A., Marcy, G. W., et al. 2011, ApJ, 730, 10

Lagrange, A.-M., Desort, M., & Meunier, N. 2010, A&A, 512, A38

Lebreton, Y. & Goupil, M. J. 2014, A&A, 569, A21

Ligi, R., Mourard, D., Lagrange, A. M., et al. 2012, A&A, 545, A5

Ligi, R., Mourard, D., Lagrange, A.-M., Perraut, K., & Chiavassa, A. 2014, A&A, accepted, arXiv:1410.5333

Ligi, R., Mourard, D., Nardetto, N., & Clausse, J.-M. 2013, Journal of Astronomical Instrumentation, 02, 1340003

Magic, Z., Collet, R., Asplund, M., et al. 2013, A&A, 557, A26

Matter, A., Vannier, M., Morel, S., et al. 2010, A&A, 515, A69

Meunier, N., Desort, M., & Lagrange, A.-M. 2010, A&A, 512, A39

Mourard, D., Clausse, J. M., Marcotto, A., et al. 2009, A&A, 508, 1073

Oshagh, M., Boisse, I., Boué, G., et al. 2013, A&A, 549, A35

Rauer, H. & Catala, C. 2012, in EGU General Assembly Conference Abstracts, Vol. 14, EGU General Assembly Conference Abstracts, ed. A. Abbasi & N. Giesen, 7033

Ricker, G. R., Latham, D. W., Vanderspek, R. K., et al. 2010, in Bulletin of the American Astronomical Society, Vol. 42, American Astronomical Society Meeting Abstracts #215, 450.06

Valencia, D., Guillot, T., Parmentier, V., & Freedman, R. S. 2013, ApJ, 775, 10

Zhao, M., Monnier, J. D., Che, X., et al. 2011, PASP, 123, 964

Zhao, M., Monnier, J. D., ten Brummelaar, T., Pedretti, E., & Thureau, N. 2008, in IAU Symposium, Vol. 249, IAU Symposium, ed. Y.-S. Sun, S. Ferraz-Mello, & J.-L. Zhou, 71–77

SF2A 2014
J. Ballet, F. Bournaud, F. Martins, R. Monier and C. Reylé (eds)

TIDAL FRICTION IN ROTATING TURBULENT CONVECTIVE STELLAR AND PLANETARY REGIONS

S. Mathis[1,2], P. Auclair-Desrotour[1,3], M. Guenel[1] and C. Le Poncin-Lafitte[4]

Abstract. Turbulent friction in stellar and planetary convection zones is one of the key physical mechanisms that drive the dissipation of the kinetic energy of tidal flows in stars and planets hosting companions. This friction acting both on the equilibrium tide and on tidal inertial waves thus deeply impacts the dynamics of the spin of the host star/planet and the orbital architecture of the surrounding system. It is thus very important to obtain robust prescription for this friction. In the current state-of-the-art, it is modeled by a turbulent viscosity coefficient using mixing-length theory. However, none of the existing prescriptions take into account the action of the possibly rapid rotation that strongly affects convective flows. In this work, we propose such a new prescription that takes into account rotation and discuss the possible implication for tidal dissipation in rotating stars and planets.

Keywords: hydrodynamics, waves, turbulence, planet-star interactions

1 Introduction and context

Tidal friction is one of the mechanisms that drive the evolution of planetary systems (e.g. Hut 1981; Laskar et al. 2012; Mathis & Remus 2013; Ogilvie 2014). In this context, tidal friction in the turbulent convective envelopes of low-mass stars and giant planets and the cores of telluric planets must be carefully evaluated. In the present state-of-the-art, the turbulent friction acting on tidal flows in these regions (e.g. Ogilvie & Lin 2004, 2007; Remus et al. 2012) is modeled thanks to an effective turbulent viscosity coefficient (Zahn 1966). This corresponds to the assumptions that it can be described through a viscous force while we have a scale-separation between tidal and turbulent convective flows. The properties of the turbulent viscosity thus described the effective efficiency of the couplings between turbulence and tidal flows. Therefore, it depends on the frequency of the forcing as well as on the dynamical parameters that impact stellar and planetary convection (Zahn 1966; Goldreich & Keeley 1977; Goodman & Oh 1997; Penev et al. 2007; Ogilvie & Lesur 2012).

Among them, rotation is one of the parameters that must be taken into account. Indeed, the Coriolis acceleration strongly affects the dynamics of turbulent convective flows (e.g. Brown et al. 2008; Julien et al. 2012; Barker et al. 2014). Therefore, it is absolutely necessary to get a robust prescription for the turbulent friction applied on tidal waves by rotating convection in stars and planets as a function of their angular velocity that evolves during their evolution. To reach this objective, properties of rotating turbulent flows such as their characteristic velocities and length scales must be known if we wish to model this friction using the mixing-length framework (Zahn 1966). In this context, the work by Stevenson (1979) is particularly interesting since they are derived in the asymptotic regimes of slow and rapid rotation. Moreover, these asymptotic scaling laws have been now confirmed by Barker et al. (2014) using high-resolution non-linear 3-D Cartesian simulations of turbulent convection. In this work, we thus propose a new prescription for tidal friction in rotating turbulent convective regions that takes rotation into account using the results obtained by Stevenson (1979) and Barker et al. (2014).

[1] Laboratoire AIM Paris-Saclay, CEA/DSM - CNRS - Université Paris Diderot, IRFU/SAp Centre de Saclay, F-91191 Gif-sur-Yvette Cedex, France
[2] LESIA, Observatoire de Paris, CNRS UMR 8109, UPMC, Univ. Paris-Diderot, 5 place Jules Janssen, 92195 Meudon, France
[3] IMCCE, Observatoire de Paris, UMR 8028 du CNRS, UPMC, 77 Av. Denfert-Rochereau, 75014 Paris, France
[4] SYRTE, Observatoire de Paris, UMR 8630 du CNRS, UPMC, 77 Av. Denfert-Rochereau, 75014 Paris, France

2 Prescription for the friction in rotating turbulent convective layers

2.1 State of the art

The first study of the friction applied by turbulent convection on tidal flows was achieved by Zahn (1966) in the case of stars (see also Zahn 1989). In his work, he examined the coupling between turbulence and the large-scale equilibrium tide induced by the hydrostatic adjustment of the star due to the tidal perturber (e.g. Remus et al. 2012). His approach was based on three main assumptions. First, he assumed that the friction applied by turbulence can be described thanks to a viscous force involving an eddy-viscosity $\nu_{\rm T}$. Second, he assumed a scale-separation between tidal and turbulent convective flows. Finally, the characteristic velocity and length scale of turbulent convection, respectively $V_{\rm c}$ and $L_{\rm c}$, were described using the mixing-length theory. In this framework, he proposed the following prescription for the eddy-viscosity:

$$\nu_{\rm T;NR} = \frac{1}{3} V_{\rm c} L_{\rm c}\, f\left(\frac{P_{\rm tide}}{T_{\rm c}}\right). \tag{2.1}$$

In this expression, NR stands for *Non-Rotating convection* and f is a function that describes the loss of efficiency of tidal friction in the case of rapid tide when $P_{\rm tide} \ll T_{\rm c}$, $P_{\rm tide}$ and $T_{\rm c}$ being respectively the tidal period and the characteristic convective turn-over time (see Zahn 1966; Goldreich & Keeley 1977; Goodman & Oh 1997; Penev et al. 2007; Ogilvie & Lesur 2012, for detailed discussions of f).

However, as pointed above (rapid) rotation strongly affects turbulent convective flows (e.g. Chandrasekhar 1953; Brown et al. 2008; Julien et al. 2012; Barker et al. 2014). Therefore, $V_{\rm c}$, $L_{\rm c}$, and as a consequence $\nu_{\rm T}$, vary with rotation. In the present state-of-the-art, we are thus in a situation where the action of the Coriolis acceleration is taken into account in the physical description of tidal flows (e.g. Ogilvie & Lin 2004, 2007; Remus et al. 2012) while it is ignored in the one of the turbulent friction while the angular velocity of celestial bodies varies along their evolution (e.g. Gallet & Bouvier 2013, for solar-type stars).

2.2 Modelling and assumptions

To study the modification of the turbulent friction applied on tidal flows in rotating stellar and planetary convective regions, we use theoretical results first derived by Stevenson (1979) and confirmed by high-resolution numerical simulations computed by Barker et al. (2014) in Cartesian geometry. We thus choose to consider a local Cartesian set-up with a box centered around a point M in a rotating convective zone (see fig. 1); (M, x, y, z) is the associated reference frame. We introduce the angular velocity Ω of the studied body. The box has a characteristic length L and is assumed to have an homogeneous density ρ. Its vertical axis is inclined with an angle θ with respect to the rotation axis.

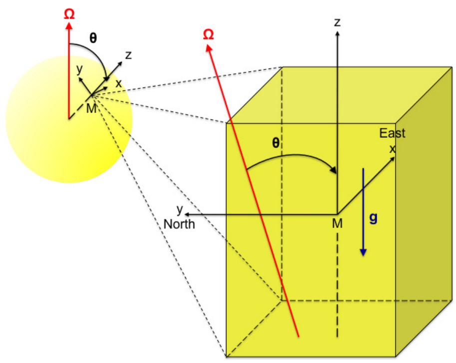

Fig. 1. The local Cartesian model. The spin $\vec{\Omega}$ is represented by the red arrow and the gravity $\vec{g}$ by the blue one.

Next, we introduce the control parameters of the system:

- the convective Rossby number defined as in Stevenson (1979)

$$R_{\rm o}^{\rm c} = \left(\frac{V_{\rm c}\,(\Omega=0)}{L_{\rm c}\,(\Omega=0)\, 2\Omega|\cos\theta|}\right) = \frac{T_\Omega}{T_{\rm c}\,(\Omega=0)}, \tag{2.2}$$

where we introduce the characteristic convective turn-over time $T_{\rm c} = \dfrac{L_{\rm c}}{V_{\rm c}}$ and the dynamical one $T_\Omega = \dfrac{1}{2\Omega}$; $R_{\rm o}^{\rm c} \ll 1$ and $R_{\rm o}^{\rm c} \gg 1$ correspond to rapid and slow rotation regimes respectively;

- the Ekman number
$$E = \frac{2\pi^2 \nu_{\rm T}}{\Omega L^2}, \tag{2.3}$$
which compares the respective strength of the viscous force and of the Coriolis acceleration.

2.3 The new eddy-viscosity prescription

As in previous works, which do not take into account the action of rotation on convection (see sec. 2.1), we assume i) that the turbulent friction on tidal velocities can be modeled through a viscous force involving an eddy-viscosity coefficient and ii) a scale-separation between turbulent convective and tidal flows.

To derive this coefficient as a function of rotation, we have to know the variation of $V_{\rm c}$ and $l_{\rm c}$ as a function of Ω and to verify that the mixing-length approach, which is generally used in stellar and planetary models, can be assumed in our context. In this framework, this is the great interest of the work by Barker et al. (2014). They demonstrated that scaling laws obtained by Stevenson (1979) for $V_{\rm c}$ and $L_{\rm c}$ as a function of $R_{\rm o}^{\rm c}$ using such a mixing-length formalism is robust and verified when computing high-resolution Cartesian numerical simulations of rotating turbulent convective flows in a set-up corresponding to the one studied here for $\theta \approx 0$.

We can thus generalize the prescription proposed in eq. (2.1) to the rotating case by writing*

$$\nu_{\rm T;RC} = \frac{1}{3} V_{\rm c}\left(R_{\rm o}^{\rm c}\right) L_{\rm c}\left(R_{\rm o}^{\rm c}\right) f\left(\frac{P_{\rm tide}}{T_{\rm c}}\right), \tag{2.4}$$

where RC stands for *Rotating Convection.* To get $V_{\rm c}\left(R_{\rm o}^{\rm c}\right)/V_{\rm c}\left(\Omega=0\right)$ and $L_{\rm c}\left(R_{\rm o}^{\rm c}\right)/L_{\rm c}\left(\Omega=0\right)^\dagger$, we use the scaling laws that have been derived by Stevenson (1979) and verified by Barker et al. (2014):

- in the *slow rotation* regime ($R_{\rm o}^{\rm c} \gg 1$), we have
$$\frac{V_{\rm c}\left(R_{\rm o}^{\rm c}\right)}{V_{\rm c}\left(\Omega=0\right)} \approx \left(1 - \frac{1}{242\left(R_{\rm o}^{\rm c}\right)^2}\right) \quad \text{and} \quad \frac{L_{\rm c}\left(R_{\rm o}^{\rm c}\right)}{L_{\rm c}\left(\Omega=0\right)} \approx \left(1 + \frac{1}{82\left(R_{\rm o}^{\rm c}\right)^2}\right)^{-1}; \tag{2.5}$$
- in the *rapid rotation* regime ($R_{\rm o}^{\rm c} \ll 1$), we have
$$\frac{V_{\rm c}\left(R_{\rm o}^{\rm c}\right)}{V_{\rm c}\left(\Omega=0\right)} \approx 1.5 (R_{\rm o}^{\rm c})^{1/5} \quad \text{and} \quad \frac{L_{\rm c}\left(R_{\rm o}^{\rm c}\right)}{L_{\rm c}\left(\Omega=0\right)} \approx 2 (R_{\rm o}^{\rm c})^{3/5}. \tag{2.6}$$

We also define a first Ekman number computed with the turbulent viscosity prescription where the modification of turbulent friction by rotation is ignored ($E_{\rm NR}$) or taken into account ($E_{\rm RC}$), i.e.

$$E_{\rm NR} = \frac{2\pi^2 \nu_{\rm T;NR}}{\Omega L^2} \quad \text{and} \quad E_{\rm RC} = \frac{2\pi^2 \nu_{\rm T;RC}}{\Omega L^2}. \tag{2.7}$$

In fig. 2, we plot $\nu_{\rm T;RC}/\nu_{\rm T;NR}$ and the corresponding ratio for the Ekman number $E_{\rm RC}/E_{\rm NR}$ as a function of $R_{\rm o}^{\rm c}$.

The small-dashed green and continuous blue lines correspond to the slow- and rapid-rotation asymptotic regimes respectively (the red long-dashed line corresponding to the non-rotating case). In the regime of rapidly rotating convective flows ($R_{\rm o}^{\rm c} \ll 1$), the turbulent friction decreases by several orders of magnitude with a scaling $\nu_{\rm T;RC}/\nu_{\rm T;NR} \propto \left(R_{\rm o}^{\rm c}\right)^{4/5} \propto \Omega^{-4/5}$. It can be understood coming back on the action of (rapid) rotation on the convective instability and turbulence. The Coriolis acceleration tends to stabilize the flow and thus the degree of turbulence decreases with increasing rotation as well as the corresponding eddy-viscosity.

---

*It must be pointed that the *isotropic* eddy-viscosity must be considered as a qualitative quantity because rapid rotation leads to strongly anisotropic turbulent flows (e.g. Julien et al. 2012).

†As Stevenson (1979), we define $L_{\rm c}$ as the smallest length-scale characterizing the dominant convective mode with a wave vector k_c.

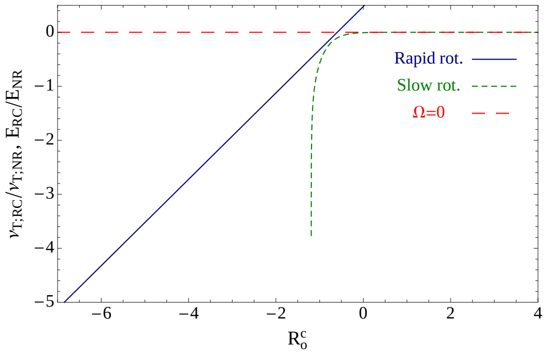

Fig. 2. The ratio $\nu_{\mathrm{T;RC}}/\nu_{\mathrm{T;NR}}$ (and $E_{\mathrm{RC}}/E_{\mathrm{NR}}$) as a function of R_o^c. The small-dashed green and continuous blue lines correspond to the slow- and rapid-rotation asymptotic regimes respectively. The red long-dashed line corresponds to the non-rotating case.

3 Consequences for the linear tidal dissipation

The linear response of planetary and stellar convection zones to tidal perturbations is constituted by the superposition of a non-wave like displacement, the equilibrium tide, and of tidally excited inertial waves, the dynamical tide. The restoring force of inertial waves is the Coriolis acceleration. Because of their dispersion relation $\chi = 2\Omega\, k_z/|\vec{k}|$, where χ is their frequency and $\vec{k}$ their wave number, they propagate only if $\chi \in [-2\Omega, 2\Omega]$. To understand the impact of rapid rotation on the turbulent friction derived in the previous section on both the equilibrium and dynamical tides, we now consider the linear response of the Cartesian set-up studied here (cf. fig. 1) to a periodic forcing. We follow the local analytical approach, which has been introduced by Ogilvie & Lin (2004) and Auclair-Desrotour et al. (2014b) to understand tidal dissipation in convective regions, with taking into account here the inclination angle θ between the spin ($\vec{\Omega}$) and the gravity ($\vec{g}$) at M (see fig. 1).

Because of the form of the forced velocity field, the tidal dissipation spectrum and the corresponding energy dissipated per rotation period (ζ) is a complex resonant function of the normalized tidal frequency ($\omega \equiv \chi/2\Omega$). It corresponds to resonances of the inertial waves that propagate in planetary and stellar convection zones. An example of such resonant spectra is represented in fig. 3 (left panel) for $E = 10^{-4}$ and $\theta = 0$. Following Auclair-Desrotour et al. (2014b), we characterize ζ by the following characteristics:

- the non-resonant background of the dissipation spectra H_{bg}; it scales as $H_{\mathrm{bg}} \propto E$;
- the number of resonant peaks N_{kc}; it scales as $N_{\mathrm{kc}} \propto E^{-1/2}$;
- their width at half-height l_{mn}; it scales as $l_{mn} \propto E$;
- their height H_{mn}; it scales as $H_{mn} \propto E^{-1}$;
- the sharpness of the spectrum defined as $\Xi = H_{11}/H_{\mathrm{bg}}$; it scales as $\Xi \propto E^{-2}$.

From now on, X_{RC} is a quantity evaluated with E_{RC} (i.e. with $\nu_{\mathrm{T;RC}}$) while X_{NR} is computed using E_{NR} (i.e. with $\nu_{\mathrm{T;NR}}$).

We can thus deduce interesting conclusions from obtained results both on the equilibrium and dynamical tides.

- The *equilibrium tide*: in our local Cartesian set-up, it is represented by the non-resonant background H_{bg}. Using Eq. (2.7), we thus deduce that its efficiency scales as $\Omega^{-9/5}$ in the regime of rapid rotation. This loss of efficiency of the equilibrium tide in rapidly rotating convective regions is illustrated in fig. 3 where we plotted the ratio $H_{\mathrm{bg;RC}}/H_{\mathrm{bg;NR}}$ as a function of R_o^c.
- The *dynamical tide:* we use scaling laws obtained for the resonances of tidal inertial waves. We deduce that as soon as studied convective regions are in the regime of rapid rotation, their number and height respectively increase as $N_{\mathrm{kc}} \propto \Omega^{9/10}$ and $H_{mn} \propto \Omega^{9/5}$ while their width decreases as $l_{mn} \propto \Omega^{-9/5}$. The

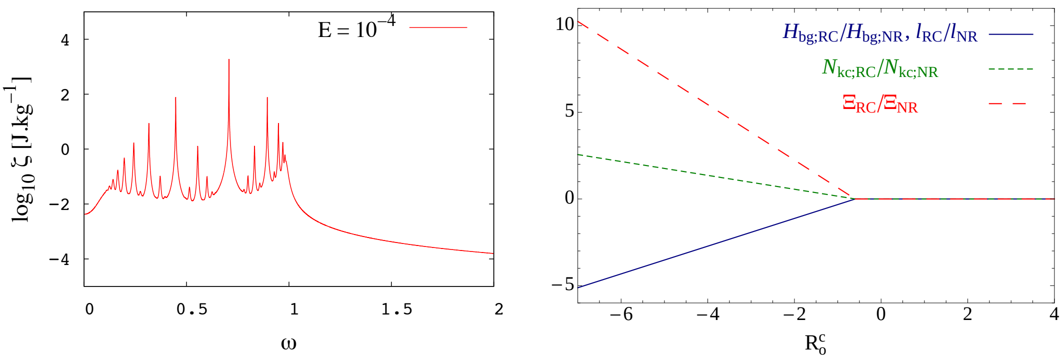

Fig. 3. Left: the complex variation of tidal dissipation in convective layers as a function of the normalized tidal frequency $\omega \equiv \chi/2\Omega$ for $E = 10^{-4}$ and $\theta = 0$. **Right:** variation of $H_{\mathrm{bg;RC}}/H_{\mathrm{bg;NR}}$, $l_{\mathrm{RC}}/l_{\mathrm{NR}}$, $N_{\mathrm{kc;RC}}/N_{\mathrm{kc;NR}}$, and $\Xi_{\mathrm{RC}}/\Xi_{\mathrm{NR}}$ as a function of $R_{\mathrm{o}}^{\mathrm{c}}$ in logarithmic scales.

sharpness of ζ is increased as $\Xi \propto \Omega^{18/5}$. This variation of the properties of the resonant tidal dissipation spectra is illustrated in fig. 3 (right panel) where we plot the ratios $N_{\mathrm{kc;RC}}/N_{\mathrm{kc;NR}}$, $l_{\mathrm{RC}}/l_{\mathrm{NR}}$, and $\Xi_{\mathrm{RC}}/\Xi_{\mathrm{NR}}$ as a function of $R_{\mathrm{o}}^{\mathrm{c}}$. As demonstrated by Auclair-Desrotour et al. (2014a), this has important consequences for the evolution of the spin of the body and of the orbits of the companions. For example, the relative migration induced by a resonance scales as $\Delta a/a \equiv l_{mn}\,\Xi^{1/4} \propto \Omega^{-9/10}$.

4 Conclusions

Thanks to the results obtained by Barker et al. (2014) on the scalings of velocities and length scales in rotating turbulent convection zones, we proposed a new prescription for the eddy-viscosity coefficient that allows to describe the linear tidal friction in such regions as a function of the convective Rossby number ($R_{\mathrm{o}}^{\mathrm{c}}$). In their work, Barker et al. (2014) indeed confirmed scalings as a function of rotation that have been first derived by Stevenson (1979) using mixing-length theory. Using these results, we straightforwardly derived our new prescription for the turbulent friction that depends on rotation and that generalizes previous studies where its action was ignored. We then demonstrated that the eddy-viscosity is decreased by several orders of magnitude in the rapidly rotating regime that leads to a deep modification of the tidal dissipation spectrum. As demonstrated by Auclair-Desrotour et al. (2014a), it must be taken into account in the simulation of the dynamical evolution of planetary systems. Indeed, the angular velocity of their components vary along their evolution because of applied tidal (and electromagnetic) torques that are themselves function of the rotation rate. In a forthcoming work, we will apply our new prescription to the evolution of star-planet and planet-moon systems and of multiple stars. Direct non-linear interactions and couplings between tidal waves and turbulent convection will also be examined.

References

Auclair-Desrotour, P., Le Poncin-Lafitte, C., & Mathis, S. 2014a, A&A, 561, L7

Auclair-Desrotour, P., Mathis, S., & Le Poncin-Lafitte, C. 2014b, ArXiv e-prints

Barker, A. J., Dempsey, A. M., & Lithwick, Y. 2014, ArXiv e-prints

Brown, B. P., Browning, M. K., Brun, A. S., Miesch, M. S., & Toomre, J. 2008, ApJ, 689, 1354

Chandrasekhar, S. 1953, Royal Society of London Proceedings Series A, 217, 306

Gallet, F. & Bouvier, J. 2013, A&A, 556, A36

Goldreich, P. & Keeley, D. A. 1977, ApJ, 211, 934

Goodman, J. & Oh, S. P. 1997, ApJ, 486, 403

Hut, P. 1981, A&A, 99, 126

Julien, K., Knobloch, E., Rubio, A. M., & Vasil, G. M. 2012, Physical Review Letters, 109, 254503

Laskar, J., Boué, G., & Correia, A. C. M. 2012, A&A, 538, A105

Mathis, S. & Remus, F. 2013, in Lecture Notes in Physics, Berlin Springer Verlag, Vol. 857, Lecture Notes in Physics, Berlin Springer Verlag, ed. J.-P. Rozelot & C. . Neiner, 111–147

Ogilvie, G. I. 2014, ARA&A, 52, 171

Ogilvie, G. I. & Lesur, G. 2012, MNRAS, 422, 1975

Ogilvie, G. I. & Lin, D. N. C. 2004, ApJ, 610, 477

Ogilvie, G. I. & Lin, D. N. C. 2007, ApJ, 661, 1180

Penev, K., Sasselov, D., Robinson, F., & Demarque, P. 2007, ApJ, 655, 1166

Remus, F., Mathis, S., & Zahn, J.-P. 2012, A&A, 544, A132

Stevenson, D. J. 1979, Geophysical and Astrophysical Fluid Dynamics, 12, 139

Zahn, J. P. 1966, Annales d'Astrophysique, 29, 489

Zahn, J.-P. 1989, A&A, 220, 112

SF2A 2014
J. Ballet, F. Bournaud, F. Martins, R. Monier and C. Reylé (eds)

CONSTRAINING STELLAR MAGNETIC ACTIVITY WITH ASTEROSEISMOLOGY

S. Mathur[1]

Abstract. Stellar magnetic activity results from the interaction between rotation, convection, and magnetic field. Unfortunately the detailed mechanism of this process is not completely understood. While there is a long history of spectroscopic surveys to tackle this problem, they only provide observables of the stellar surfaces. The fact that different manifestations of magnetic variability can be observed (either a regular cycle, a non-regular variability or no temporal variation) is linked to the internal properties of the stars and raises the following question: Which conditions and properties of the stars govern these different behaviors? To better understand the detailed mechanism driving solar and stellar magnetic activity and better constrain the 3D dynamo models, it is important to know the characteristics of their magnetic field, the property of the convection, and the rotation profile (internal and at the surface) of the stars. This is where asteroseismology has a key role. Indeed, with missions such as CoRoT and *Kepler*, we have access to high-precision photometric observations where asteroseismology puts strong constraints on the internal structure and dynamics of the stars. Here, I discuss what seismology brings to the big picture of stellar magnetic activity by presenting the recent results obtained with space missions such as CoRoT and *Kepler* with a focus on solar-like stars.

Keywords: Asteroseismology, stellar activity, rotation

1 Introduction

In the past, stellar magnetic activity studies were mostly based on spectroscopic observations. The Mount Wilson survey (Wilson 1978) was one of the first surveys that followed a few hundreds of stars for more than a decade allowing the detection of long magnetic activity cycles. In particular, this survey showed that stars can behave quite differently in terms of magnetic activity. Some stars have regular cycles like the Sun, others present a more chaotic variability while the last groups of stars have very flat magnetic activity (e.g. Baliunas et al. 1995). More surveys were led later with the Solar Stellar Spectrograph at the Lowell Observatory (Hall et al. 2007) or the Small and Moderate Aperture Research Telescope System at the Cerro Tololo Interamerican Observatory for instance(Metcalfe et al. 2010). While these surveys are based on the measurement of the CaHK line more recently the first big spectropolarimetric survey was led by the Bcool teams who studied 170 stars at the Telescope Bernard Lyot and the Canada-France-Hawaii Telescope (Marsden et al. 2013). These two methods are complementary as spectroscopic observations allow us to determine indirect magnetic proxies that measure the chromospheric emission, while spectropolarimetry provides measurement of the magnetic field and its mapping on the stellar surface. Moreover these surveys emphasized the existence of relationships between the surface rotation period and the magnetic cycle period. Indeed, fast rotators seem to have shorter cycle periods (Saar & Brandenburg 2002; Böhm-Vitense 2007).

For stars like the Sun, we know that magnetic activity results from the interaction of rotation, convection, and magnetic fields. The most common model is the $\alpha\Omega$ dynamo where the Ω effect is related to the distortion of the poloidal field lines due to the latitudinal differential rotation while the α effect is still under controversies. These dynamo models require information on the structure and dynamics of the stars: the depth of the convection zone, the rotation profile from the interior to the surface, and the strength of the magnetic field, which are illustrated in Figure 1.

However the detailed mechanisms of magnetic activity cycles, including the solar one, are not completely understood. For instance, we need to improve solar activity prediction (length, strength of cycles). We also need to understand what is the relation between rotation period, cycle period and properties of the stars (mass,

[1] Space Science Institute, 4750 Walnut street Suite 205, Boulder, CO, 80301, USA

structure...). Another question that needs to be addressed is: why do some stars show (regular) cycles and others don't? Magnetic activity is tightly related to deep layers of the Sun and the stars. To be able to go further into our theoretical understanding of stellar activity, we need to have a deeper knowledge of the internal structure and dynamics of the stars. This can be achieved thanks to asteroseismology that has been revolutionizing stellar physics for the past decade.

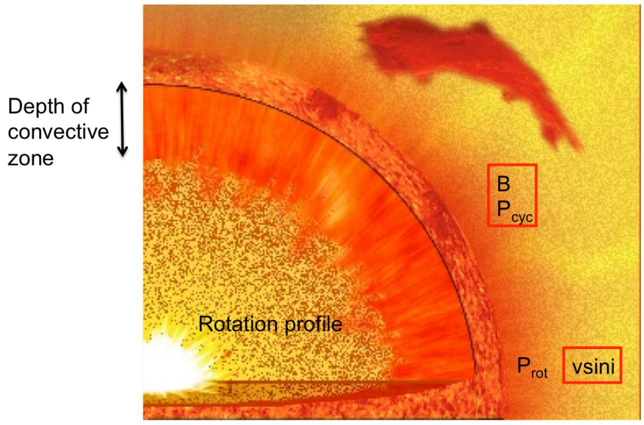

Fig. 1. Cut of a star like the Sun with the different ingredients needed in dynamo models: the depth of the convective zone, the internal rotation profile, the magnetic field, the surface rotation period, and the cycle period. The quantities in a red box are the ones spectroscopy has access to, though photometric data can also provide the latter. The other ones can be obtained with photometric data through asteroseismic studies. (Adapted from a photo courtesy of SoHO Consortium)

2 Constraints provided by seismology

Thanks to the exquisite photometric data collected by missions such as CoRoT (Baglin et al. 2006) and *Kepler* (Borucki et al. 2010), not only the panorama on the exoplanet side has changed by increasing the statistics and discovering smaller planet and new types of systems (e.g. Batalha et al. 2011; Lissauer et al. 2011; Barclay et al. 2013), but our knowledge of the stellar structure, dynamics and evolution has also tremendously improved (e.g. Bedding et al. 2011; Mosser et al. 2012b). We will see here what seismology can offer to better understanding stellar magnetic activity.

We briefly remind here the basis of asteroseismology but we refer to Aerts et al. (2010) for a deeper description. By measuring the brightness changes of the stars, we can study the different types of waves propagating in the stars. For a star like the Sun, acoustic waves (or p modes) are excited by the turbulent motions in the outer layers of the convection zone. Figure 2 (left panel) shows a power spectrum for a solar-like star. It shows a repeated pattern and the frequency of this repetition is called the mean large frequency separation (noted $\Delta\nu$), which is the frequency difference between two consecutive orders of the same degree modes. Another typical parameter that is easily measured in the power spectrum is the frequency of maximum power (ν_{max}) (e.g. Mathur et al. 2010).

By combining $\Delta\nu$ and ν_{max} with the star effective temperature, we obtain a first determination of the mass and radius of the stars through scaling relations based on the Sun (e.g. Kjeldsen & Bedding 1995). We can even go further if we can detect individual acoustic modes frequencies and make use of stellar evolution models to fit both spectroscopic constraints and seismic observables. Different methods can be used to find the best-fit models: grid-based models (Chaplin et al. 2014), applying a genetic algorithm like the Asteroseismic Modeling Portal (AMP, Metcalfe et al. 2009), implementing Bayesian methods (Gruberbauer et al. 2013), Modules for Experiments in Stellar Astrophysics code (MESA, Paxton et al. 2013). Even though, we are aware that they are based on given physics implemented in the stellar evolution codes, they allow us to infer the internal structure of the stars and in particular have a first estimation of the depth of the convective zone, which is an important ingredient in dynamo models, that can be complemented by the measurement of the convective characteristic time scales (Mathur et al. 2011b). A large number of solar-like stars have already been modeled now using

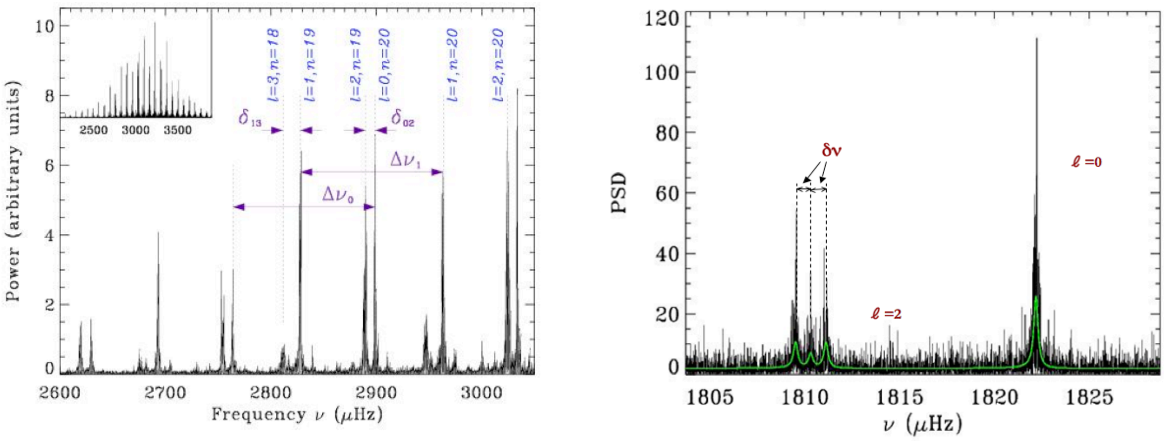

Fig. 2. Left panel: Power density spectrum of the light curve of the Sun obtained with SoHO, revealing a rich spectrum of nearly equidistant peaks. The frequencies and their spacings provide direct access to the mass, radius and age of the stars. Right panel: lifting of the degeneracy of the m components with rotation. Three components (m=-2,0,2) are visible for the ℓ=2 mode.

either grid-based models (Chaplin et al. 2014) or AMP (Mathur et al. 2012; Metcalfe et al. 2014), whenever individual modes can be characterized (Appourchaux et al. 2012).

Furthermore, the rotation affects the modes by lifting the degeneracy of modes of degree ℓ larger than 1. As shown in Figure 2 (right panel), the mode ℓ=1 is split and the distance between the two components is proportional to the rotation rate of the star in the layers probed by the mode and to the inclination angle of the star (Ballot et al. 2006). For the Sun, the measurement of several thousands of modes splittings allowed us to determine quite precisely the rotation profile of the Sun down to 0.2$R_\odot$ (García et al. 2008b). In order to go further down, we need to detect the splittings of gravity modes (Mathur et al. 2008) that live most of their time in the radiative zone and are evanescent in the convection zone, making them very difficult to detect (García et al. 2007, 2008a). However, for more evolved stars, because of the coupling between the g-mode cavity and the p-mode cavity it is possible to detect the mixed modes (Beck et al. 2011; Mosser et al. 2011). Their detection in sub giants and red giants along with their splittings led to very interesting results regarding the core rotation of these evolved stars (Beck et al. 2012; Deheuvels et al. 2012; Mosser et al. 2012a; Deheuvels et al. 2014), which rotates more than 5 times faster than the rest of the radiative zone.

Finally, magnetic activity has also an impact on the modes. Indeed we know for the Sun that there is a relationship between the magnetic activity and the p-mode parameters. When magnetic activity increases the amplitude of the modes decreases and the frequencies shift towards higher frequencies. This behavior has also been observed in the CoRoT target solar-like stars, HD49933 (García et al. 2010; Salabert et al. 2011). Chaplin et al. (2011) also confirmed using a larger *Kepler* sample that the p-mode amplitudes are lower for more active stars, suggesting that magnetic activity suppresses the modes.

3 Photometric data

The photometric data provide some additional information on the surface variability. The presence of spots creates a modulation in the light curves that is related to the surface rotation of the star (e.g. García et al. 2009; Mathur et al. 2011a) that can be measured using spot modeling techniques (Mosser et al. 2009; Fröhlich et al. 2012; Lanza et al. 2014). Hence, we can study the low-frequency part of the power spectrum to estimate the surface rotation rate. Different techniques can be used: periodogram (Nielsen et al. 2013), auto-correlation function(McQuillan et al. 2014), or time-frequency analysis (Ceillier et al. 2014). With the periodogram technique we have to be very careful as the harmonic could be detected instead of the fundamental one. The other two methods are more robust against this issue. These methods have been applied to a large sample of *Kepler* targets now allowing to study the transport of angular momentum along the evolution stage but also as a function of the mass. Another application is the study of age-rotation relationships in particular for main-sequence stars (do Nascimento et al. 2014). For instance, Garcia et al. (2014) who studied a sample of solar-like stars with detected solar-like oscillations and thus with asteroseismic ages showed that relationships derived in the past by Skumanich (1972) or Barnes (2003) still hold for field stars observed by *Kepler*.

Since the light curves contain the information of the presence of star spots, we can compute photometric indexes of magnetic activity by taking the standard deviation of the time series. Because of the link between rotation and magnetic activity, we can use our knowledge of the surface rotation of the stars to compute a new magnetic index based on subseries of length proportional to $P_{\rm rot}$. This ensures that we measure a variability related to the magnetic activity. This has been measured for around 300 solar-like stars by Garcia et al. (2014). They showed in particular that the Sun is not a particular star in terms of magnetic index. But we have to keep in mind that these indexes represent the average magnetic activity during the four years of the *Kepler* observations so if the cycle length is much longer, this index could be biased.

We can also use the time-frequency analysis based on the wavelets to study the magnetic activity of the stars. Figure 3 (top panel) shows the light curve of an F star observed by *Kepler*. The Wavelet power spectrum (middle panel) provides a rotation period around 9 days for this star. By projecting this wavelet power spectrum on the x-axis we obtain a magnetic proxy similar to the sunspots number. We detect some variability for this star but no cycle is firmly detected. This analysis was done for 22 F stars (Mathur et al. 2014b) and M dwarfs (Mathur et al. 2014c) and a few candidates for magnetic activity cycles detected have been outlined.

4 Conclusions

To conclude, seismology provides a large number of constraints for understanding the stellar magnetic activity processes: internal structure of the stars, internal rotation profile and changes due to magnetic activity. Photometric data also provides crucial information on the surface rotation and the surface magnetic activity. It is still important to complement these measurements with spectroscopy and spectropolarimetry to have a full view of the magnetism processes (Mathur et al. 2013). The next step is to test the current dynamo models on these observations, which we are starting to do now (Mathur et al. 2014a).

These studies are also important to characterize the magnetic activity of planet host stars as it impacts the definition of their habitability zones. With the large amount of data already collected by the *Kepler* mission, we are now starting to study the surface rotation and the magnetic activity of red giants (Ceillier et al. in prep.). Kepler gave us a unique opportunity with 4 year long continuous observations. The PLATO mission(PLAnetary Transits and Oscillations of stars Rauer et al. 2014) selected by ESA is the next mission that will provide similar long time series for a large portion of the sky enabling us to study magnetic variability.

This work was supported by NASA grant NNX12AE17G. SM acknowledges travel support from SF2A, PNPS, and AIM.

References

Aerts, C., Christensen-Dalsgaard, J., & Kurtz, D. W. 2010, Asteroseismology, ed. Aerts, C., Christensen-Dalsgaard, J., & Kurtz, D. W.

Appourchaux, T., Chaplin, W. J., García, R. A., et al. 2012, A&A, 543, A54

Baglin, A., Auvergne, M., Boisnard, L., et al. 2006, in COSPAR, Plenary Meeting, Vol. 36, 36th COSPAR Scientific Assembly, 3749

Baliunas, S. L., Donahue, R. A., Soon, W. H., et al. 1995, ApJ, 438, 269

Ballot, J., García, R. A., & Lambert, P. 2006, MNRAS, 369, 1281

Barclay, T., Rowe, J. F., Lissauer, J. J., et al. 2013, Nature, 494, 452

Barnes, S. A. 2003, ApJ, 586, 464

Batalha, N. M., Borucki, W. J., Bryson, S. T., et al. 2011, ApJ, 729, 27

Beck, P. G., Bedding, T. R., Mosser, B., et al. 2011, Science, 332, 205

Beck, P. G., Montalban, J., Kallinger, T., et al. 2012, Nature, 481, 55

Bedding, T. R., Mosser, B., Huber, D., et al. 2011, Nature, 471, 608

Böhm-Vitense, E. 2007, ApJ, 657, 486

Borucki, W. J., Koch, D., Basri, G., et al. 2010, Science, 327, 977

Ceillier, T., Garcıa, R. A., Salabert, D., & Mathur, S. 2014, This volume

Chaplin, W. J., Basu, S., Huber, D., et al. 2014, ApJS, 210, 1

Chaplin, W. J., Bedding, T. R., Bonanno, A., et al. 2011, ApJ, 732, L5

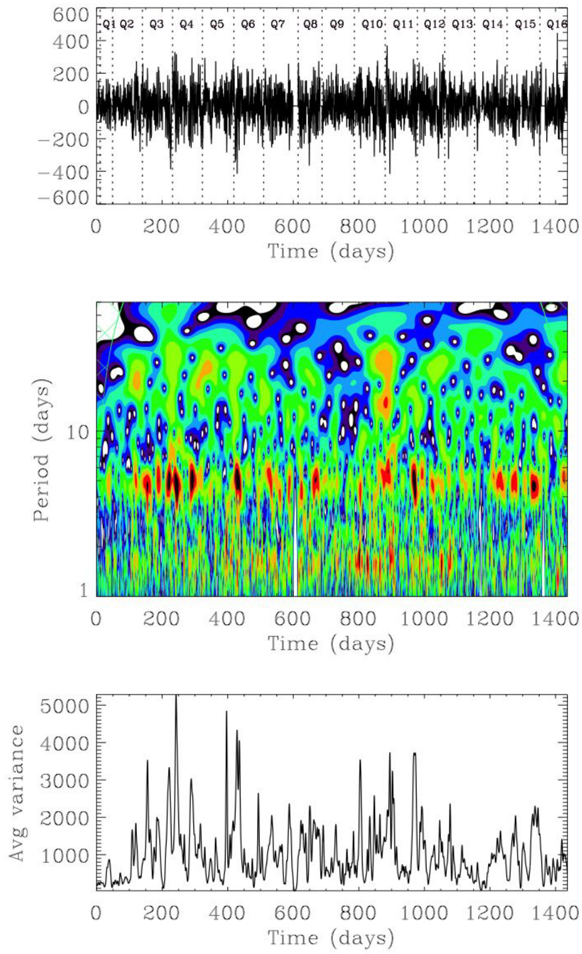

Fig. 3. Wavelet analysis of KIC 10016239. Top panel: temporal variation of the flux after the corrections applied as in (García et al. 2011) and rebinned to 2 h. Middle panel: wavelet power spectrum as a function of time and period. The green grid represents the cone of influence that provided reliable region in the WPS. Red and dark colours correspond to strong power while blue corresponds to weak power. Bottom upper panel: projection of the WPS on the time axis between periods of 6 and 8 days. Extracted from Mathur et al. (2014b).

Deheuvels, S., Doğan, G., Goupil, M. J., et al. 2014, A&A, 564, A27

Deheuvels, S., García, R. A., Chaplin, W. J., et al. 2012, ApJ, 756, 19

do Nascimento, Jr., J.-D., García, R. A., Mathur, S., et al. 2014, ApJ, 790, L23

Fröhlich, H.-E., Frasca, A., Catanzaro, G., et al. 2012, A&A, 543, A146

Garcia, R. A., Ceillier, T., Salabert, D., et al. 2014, ArXiv e-prints 1403.7155

García, R. A., Hekker, S., Stello, D., et al. 2011, MNRAS, 414, L6

García, R. A., Jiménez, A., Mathur, S., et al. 2008a, Astronomische Nachrichten, 329, 476

García, R. A., Mathur, S., Ballot, J., et al. 2008b, Sol. Phys., 251, 119

García, R. A., Mathur, S., Salabert, D., et al. 2010, Science, 329, 1032

García, R. A., Régulo, C., Samadi, R., et al. 2009, A&A, 506, 41

García, R. A., Turck-Chièze, S., Jiménez-Reyes, S. J., et al. 2007, Science, 316, 1591

Gruberbauer, M., Guenther, D. B., MacLeod, K., & Kallinger, T. 2013, MNRAS, 435, 242

Hall, J. C., Lockwood, G. W., & Skiff, B. A. 2007, AJ, 133, 862

Kjeldsen, H. & Bedding, T. R. 1995, A&A, 293, 87
Lanza, A. F., Das Chagas, M. L., & De Medeiros, J. R. 2014, A&A, 564, A50
Lissauer, J. J., Fabrycky, D. C., Ford, E. B., et al. 2011, Nature, 470, 53
Marsden, S. C., Petit, P., Jeffers, S. V., et al. 2013, ArXiv e-prints 1311.3374
Mathur, S., Augustson, K. C., Brun, A. S., Garcia, R. A., & Metcalfe, T. S. 2014a, ArXiv e-prints 1408.5926
Mathur, S., Eff-Darwich, A., García, R. A., & Turck-Chièze, S. 2008, A&A, 484, 517
Mathur, S., García, R. A., Ballot, J., et al. 2014b, A&A, 562, A124
Mathur, S., García, R. A., Morgenthaler, A., et al. 2013, A&A, 550, A32
Mathur, S., García, R. A., Régulo, C., et al. 2010, A&A, 511, A46
Mathur, S., Handberg, R., Campante, T. L., et al. 2011a, ApJ, 733, 95
Mathur, S., Hekker, S., Trampedach, R., et al. 2011b, ApJ, 741, 119
Mathur, S., Metcalfe, T. S., Woitaszek, M., et al. 2012, ApJ, 749, 152
Mathur, S., Salabert, D., García, R. A., & Ceillier, T. 2014c, Journal of Space Weather and Space Climate, 4, A15
McQuillan, A., Mazeh, T., & Aigrain, S. 2014, ApJS, 211, 24
Metcalfe, T. S., Basu, S., Henry, T. J., et al. 2010, ApJ, 723, L213
Metcalfe, T. S., Creevey, O. L., & Christensen-Dalsgaard, J. 2009, ApJ, 699, 373
Metcalfe, T. S., Creevey, O. L., Doğan, G., et al. 2014, ApJS, 214, 27
Mosser, B., Barban, C., Montalbán, J., et al. 2011, A&A, 532, A86
Mosser, B., Baudin, F., Lanza, A. F., et al. 2009, A&A, 506, 245
Mosser, B., Goupil, M. J., Belkacem, K., et al. 2012a, A&A, 548, A10
Mosser, B., Goupil, M. J., Belkacem, K., et al. 2012b, A&A, 540, A143
Nielsen, M. B., Gizon, L., Schunker, H., & Karoff, C. 2013, A&A, 557, L10
Paxton, B., Cantiello, M., Arras, P., et al. 2013, ApJS, 208, 4
Rauer, H., Catala, C., Aerts, C., et al. 2014, Experimental Astronomy
Saar, S. H. & Brandenburg, A. 2002, Astronomische Nachrichten, 323, 357
Salabert, D., Régulo, C., Ballot, J., García, R. A., & Mathur, S. 2011, A&A, 530, A127
Skumanich, A. 1972, ApJ, 171, 565
Wilson, O. C. 1978, ApJ, 226, 379

SF2A 2014
J. Ballet, F. Bournaud, F. Martins, R. Monier and C. Reylé (eds)

A 2D DUST CHEMISTRY OF THE INNER SOLAR NEBULA

F.C. Pignatale[1,2], K. Liffman[3], S.T. Maddison[2] and G. Brooks[2]

Abstract. The chemical composition of the dust in the inner layers of protoplanetary discs is unknown since infrared observation only probe the chemistry of the thin surface layer of discs. Given that planets formation occurs in the midplane, direct important information from the bulk chemistry of the disc is missing, and modelling is required. We compute for the first time the 2D chemical distribution of condensates in the inner Solar Nebula using a thermodynamic equilibrium model, and derive timescales for vertical settling and radial migration of the dust to predict the chemical evolution of the dust. We find two enstatite-rich zones within 1 AU from the protosun: a band ∼0.1 AU thick in the upper layer of the disc interior to 0.8 AU, and in the disc midplane out to ∼0.4 AU.

Our results are consistent with infrared observation of protoplanetary disc which show emission of enstatite-rich dust arising from the inner warmer surface of the disc. The inner midplane of the disc is a chemically diverse zone in which enstatite-rich dust coexists with sulfides and unprocessed material. Our finding of two enstatite-rich zones in the disc supports recent evidence that Mercury and enstatite chondrites shared a bulk material with similar composition.

The derived timescales for vertical settling suggest that dust can be chemically sorted in the hotter, inner surface of the disc leading to fractionated Mg-Fe-poor gas which can produce enstatite-rich dust. We suggest that the migration of enstatite-rich grains toward the midplane and-or condensation after gas fractionation may account for the formation of the bulk material which then formed the EL (low-Fe) chondrites.

Keywords: Protoplanetary discs, Solar Nebula, chemistry, planets, meteorites

1 Introduction

Infrared observations only probe the chemistry of the surface of protoplanetary discs (Henning & Meeus 2011), and thus direct information of the dust chemistry in the midplane, where planets formation occurs, is missing. 1D radial condensation sequences modelled to resemble the midplane of discs provided a general agreement with the derived bulk chemical composition of the Solar System planets, with refractory material and silicates in the inner region (Yoneda & Grossman 1995; Gail 1998), but cannot account for the global chemistry of a multilayered disc, where temperature and pressure are a function of both radius and height above the midplane. Furthermore, 1D condensation sequences fail to reproduce the complex chemistry of meteorites. Moreover, dynamical processes, such as dust vertical settling and radial migration (Barrière-Fouchet et al. 2005) and the dead zone (Gammie 1996), play an important role in mixing the dust and determining its distribution within the discs, and thus they need to be taken in account.

In order to address these limitations, we compute for the first time the two dimensional chemical distribution of condensates in the inner Solar Nebula using a thermodynamic equilibrium model, and derive timescales for vertical settling and radial migration of the dust to predict the chemical evolution of the condensates. With mapping the 2D dust chemistry in the disc, we also aim to provide the necessary chemical background for future complex studies on dust and gas interaction and dynamics.

[1] Université de Lyon, Lyon, F-69003, France; Université Lyon 1, Observatoire de Lyon, 9 avenue Charles André, Saint-Genis Laval, F-69230, France; CNRS, UMR 5574, Centre de Recherche Astrophysique de Lyon; Ecole Normale Supérieure de Lyon, F-69007, France. e-mail: `francesco.pignatale@univ-lyon1.fr`

[2] Swinburne University of Technology, Melbourne, Australia

[3] CSIRO, Melbourne, Australia

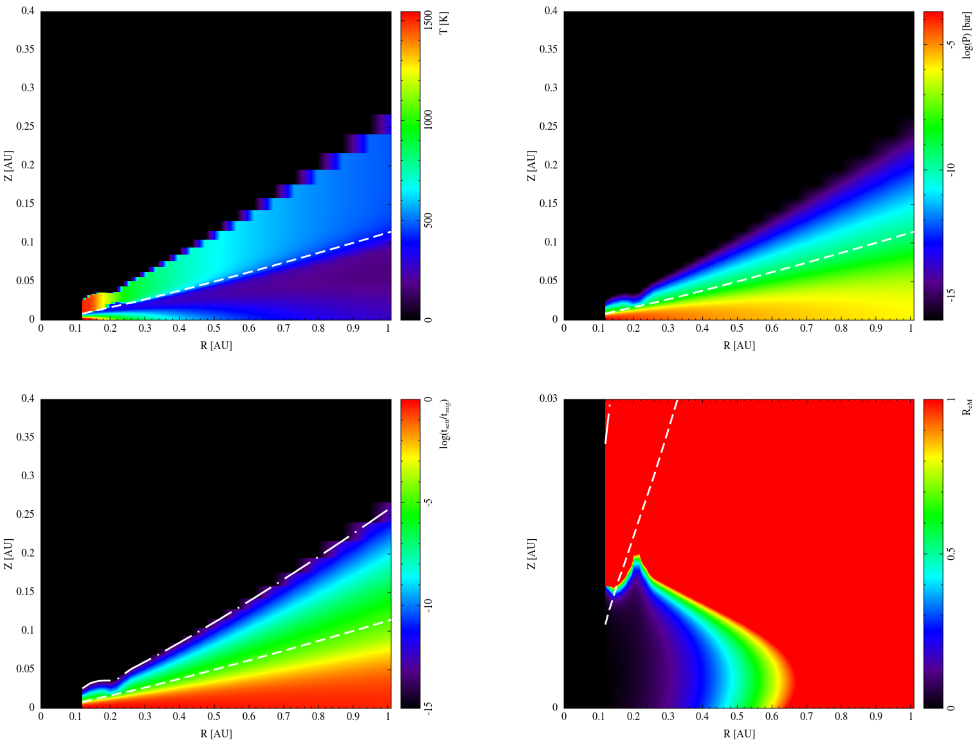

Fig. 1. Top row: temperature distribution (left), and pressure distribution (right) of the disc (D'Alessio et al. 1998). The dashed line represents the disc optically thin limit, the dot-dash line defines the disc contour. Bottom row: τ_{set}/τ_{mig} (left), and calculated $Re_{\rm M}$ (right) (note the change of scale in the z-axis).

2 Model

The temperature and pressure distribution within the disc, $T(R,Z)$ and $P(R,Z)$ are determined using the 2D disc model of D'Alessio et al. (1998, 1999) (Fig. 1). We chose a star-disc system with $M_* = 1\,{\rm M}_\odot$, $\dot{M} = 10^{-8}\,{\rm M}_\odot{\rm yr}^{-1}$, and $\alpha = 0.01$, assuming a 1 Myr old star.

We derive the 2D distribution of condensates by determining the thermodynamic equilibrium of an initial gas mixture, given a set of temperatures and pressures, using the Gibbs free energy minimization technique (DeHoff 1993). We utilize the FactSage software package (Bale et al. 2002, 2009), which uses the minimization method described by Eriksson & Hack (1990) and Eriksson & Konigsberger (1995). The initial gas mixture is composed of the 15 most abundant elements of the solar photosphere from Asplund et al. (2009), with their abundances normalized to 100 kmol. We assume that the gas is initially homogeneous throughout the disc and we perform equilibrium calculations using (T,P) at each location (R,Z) in the disc. The list of possible compounds that can condense comprise 170 gases and 317 solids. We use the ideal solution for modelling the phase behaviour in this region of the disc.

In the midplane, the stellar radiation is strong enough to heat the disc over 1000 K. Thus, for this disc, equilibrium is a reasonable assumption for the surface out to 0.8 AU and in the midplane within 0.4 AU. The optically thick zone of the disc beyond 0.4 AU, where the temperature decreases dramatically, will not be considered in our discussions.

We follow the approach of Liffman & Brown (1996) and Liffman & Toscano (2000) to derive the timescale of dust vertical settling (τ_{set}) within our disc model. τ_{set} is proportional to $1/a_p\rho_p$ where a_p is the dust grain radius, ρ_p is the dust grain density. The dust radial migration timescale (τ_{mig}) for a particle at distance R from the star is obtained by Hartmann (2000), and it is function of the average kinematic viscosity, and the inner boundary of the disc. For these calculations the value of the dust density, ρ_p, is chosen to represent the average density of silicates, 3 g cm^{-1}, and $a_p = 0.1\mu$m, which is the average size of forsterite grains as modelled by infrared observation (Bouwman et al. 2008). R_{in} is set to 0.1 AU.

To solve for the extent of the dead zone we calculate the magnetic Reynolds number, $Re_{\rm M}$, at each location

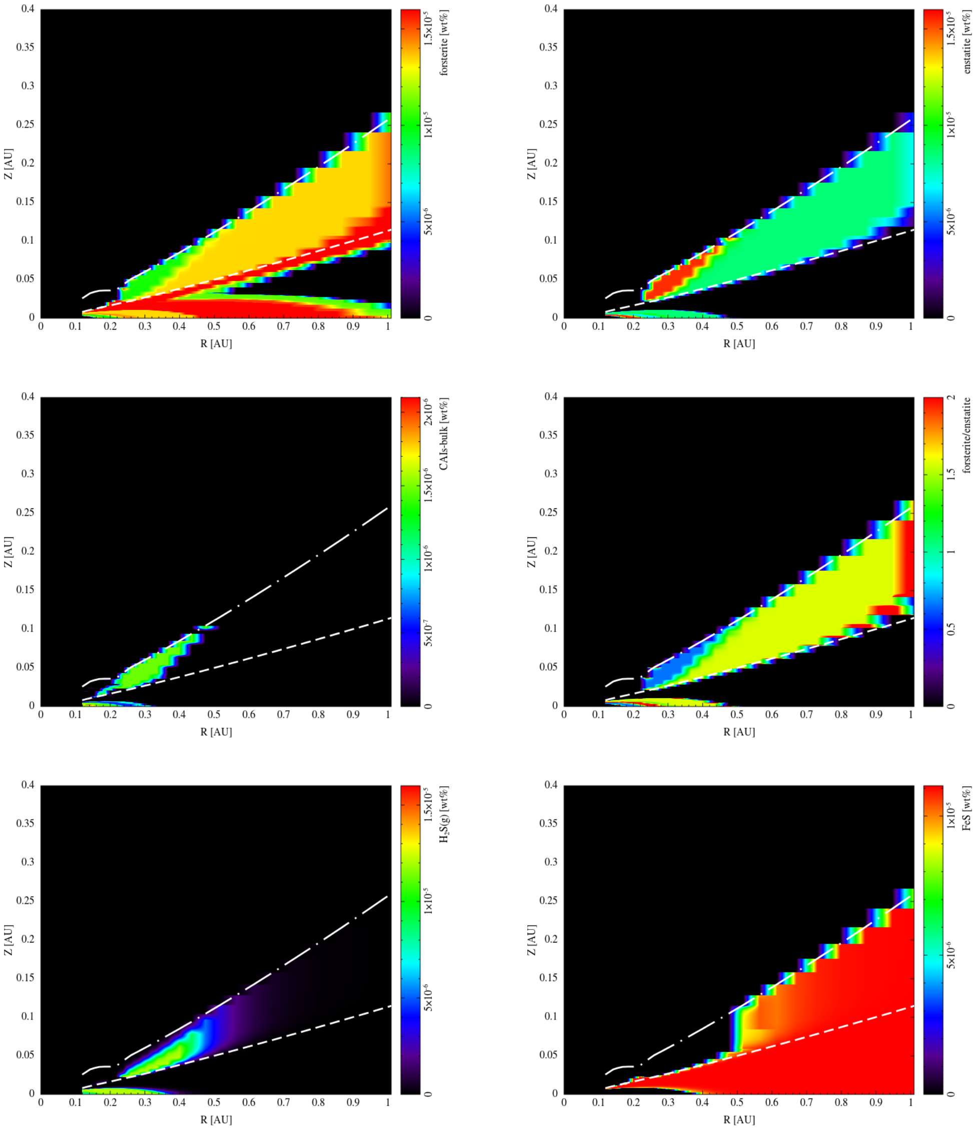

Fig. 2. Top row: forsterite (left) and enstatite (right) distribution. Mid row: CAIs-bulk components (left) and forsterite-to-enstatite (fo/en) ratio (right). Bottom row: H_2S(g) (left) and FeS (right) distribution. Note the change of scales in the color bar. Dashed line, limit under which the disc becomes optically thick. Dashed-dot line, disc contour.

in the disc following Gammie (1996). The magneto-rotational instability, which drives accretion in the disc, will be suppressed if $Re_{\rm M} \leq 1$ (Gammie 1996). In Fig.1 we report the τ_{set}/τ_{mig} ratio (bottom-left) and $Re_{\rm M}$ (bottom-right) in all the region of our disc.

3 Results and discussion

Figure 2 (top row), shows the 2D distribution of forsterite (Mg_2SiO_4) and enstatite ($MgSiO_3$), and (middle row) the location in which the calcium-aluminium bulk components* (CAI-bulk) condense and the forsterite-to-enstatite (fo/en) ratio. In the bottom row we report the H_2S(g) and FeS distribution.

We find that stable enstatite is limited to two well-defined zones within the disc: a band ∼0.1 AU thick

*These include hibonite ($CaAl_{12}O_{19}$), gehlenite ($Ca_2Al_2SiO_7$), akermanite ($Ca_2MgSi_2O_7$), Mg-spinel ($MgAl_2O_4$), grossite ($CaAl_4O_7$) and anorthite ($CaAl_2Si_2O_8$).

in the upper layer of the disc interior to 1 AU, and in the disc midplane out to ∼0.4 AU. Forsterite is more abundant in a wider zone in the outer upper layer of the disc and the stability zone in the midplane reaches 1 AU. However, as previously stated, the zone beyond 0.4 AU falls in the non-equilibrium zone.

There are also two stability zones in the inner 1 AU of the disc where CAI-bulk components are present: one in the upper layer of the disc between $0.2 \leq$ R(AU) ≤ 0.5 and another 0.01 AU thick zone in the midplane between the inner boundary of the disc and 0.3 AU. A "cloud" of H_2S(g) is stable between 0.25 and 0.5 AU below the surface of the disc, and a thick zone of stability out to 0.4 AU is present in the midplane.

Regions in which $fo/en \leq 1$ are present in both the surface and midplane of the disc. The average grain composition where $fo/en \leq 1$ is forsterite (Mg_2SiO_4) 20.2 wt%, enstatite ($MgSiO_3$) 29.6 wt%, metals ($Fe-Ni$) 47.2 wt%, diopside ($CaMgSi_2O_6$) 1.3 wt%, others 1.7 wt%. No sulfides condensed in this region.

Disc surface. On the surface of the disc, the main silicates are all distributed in the optically thin region (Fig.2). Infrared observations of the upper layers of protoplanetary discs show a spatial variation of the forsterite and enstatite distribution, with more enstatite in the warm inner regions than in the cooler outer regions where forsterite dominates (Kessler-Silacci et al. 2006; Bouwman et al. 2008; Meeus et al. 2009). The reason for this distribution remains uncertain. To account for the forsterite observed in the outer regions of discs several theories have been proposed: thermal annealing of enstatite from heating shocks (Fabian et al. 2000; Harker & Desch 2002) or an efficient radial grain transport mechanism which distributes the forsterite formed via condensation in the inner zones of the disc toward the cooler regions (van Boekel et al. 2004; Juhász et al. 2012).

Our 2D distribution of enstatite-rich dust is in good agreement with observations. Furthermore, the enstatite-rich dust can constitute the bulk material from which forsterite can form due to secondary processes. We see forsterite-rich dust naturally distributed in the outer surface of the disc. However, equilibrium calculations in this low temperature region might fail to predict the real dust composition because of kinetics barriers.

Disc midplane. Looking at our 2D distribution, the limitations of 1D condensation sequences clearly emerges. The midplane region of the disc within 0.4 AU is not chemically radially sorted as 1D calculations predict. It is a zone in which high-temperature material, enstatite-rich dust, sulfides and unprocessed dust can coexist. The presence of the dead zone in the midplane might prevent this mixture from migrating inwards. Since grain growth in this zone of the disc is very efficient, with grains reaching cm-size in a few thousand years (Laibe et al. 2008), enstatite-rich planetesimals may form in short timescales. Our results are compatible with recent observations and analysis from the Messenger X-Ray Spectrometer which suggest that the surface of the Mercury comprises Mg-rich minerals like enstatite and it is enriched in sulfur (Weider et al. 2012).

Dust dynamics. The derived vertical settling timescales of the dust on the surface of our disc suggests that condensed dust can quickly migrate towards the midplane and accumulate at the boundary of the dead zone. Thus, enstatite-rich grains can traverse the sulfides-rich regions and can experience secondary alterations during transient events such as outburst and shocks (Lehmann et al. 1995).

Furthermore, since vertical settling is function of the composition and the size of the grains, vertical chemical sorting of dust can also occur in the surface of our disc. Iron-rich and silicate-rich grains, which condense in the inner hotter surface of the disc, can leave their location of formation, not reacting with the surrounding gas and thus producing fractionated gas with Mg/Si and Fe/Si ratios lower than the initial solar with values close to the low-Fe enstatite chondrites (EL), rare objects with pure enstatite as the main pyroxene compound (Weisberg & Kimura 2012). A further condensation of gas with low Mg/Si leads to enstatite-rich dust (Ferrarotti & Gail 2001).

We suggest that the migration of enstatite-rich grains toward the midplane and-or condensation after gas-fractionation may account for the formation of the bulk material which constitute the EL chondrites.

4 Conclusions

In this work we derived for the first time the 2D condensates distribution in the inner Solar Nebula. We found two enstatite-rich zones: in the inner upper layer and in the inner midplane of the disc. The inner midplane is a chemically diverse zone in which high temperature crystalline material, enstatite-rich dust and unprocesses material can coexist and be trapped in the dead zone. Our results are compatible with infrared observation and recent discovery on the Mercury's enstatite-rich composition.

We presented a simplified model whereby dust efficiently settles toward the midplane, experiencing secondary alteration and fractionating the gas. These processes can account for the bulk material which formed rare objects like enstatite chondrites. Our finding of two enstatite-rich zone in the disc supports recent evidence that Mercury and enstatite chondrites shared a bulk material with similar composition.

This work was supported by the Swinburne University Postgraduate Research Awards (FCP) and CSIRO Astrophysics and Space Science (KL). FCP is grateful to the LABEX Lyon Institute of Origins (ANR-10-LABX-0066) of the Université de Lyon for its financial support within the program "Investissements d'Avenir" (ANR-11-IDEX-0007) of the French government operated by the National Research Agency (ANR). The authors wish to thank Paola D'Alessio for providing the detailed structure of the disc model and Jean-François Gonzalez for helping with the visualization of the data.

References

Asplund, M., Grevesse, N., Sauval, A. J., & Scott, P. 2009, ARA&A, 47, 481

Bale, C., Belisle, E., Chartrand, P., et al. 2009, CALPHAD, 33, 295

Bale, C., Chartrand, P., Decterov, S., Eriksson, C., & et. al. 2002, CALPHAD, 2, 189

Barrière-Fouchet, L., Gonzalez, J.-F., Murray, J. R., Humble, R. J., & Maddison, S. T. 2005, A&A, 443, 185

Bouwman, J., Henning, T., Hillenbrand, L. A., & et al. 2008, ApJ, 683, 479

D'Alessio, P., Calvet, N., Hartmann, L., Lizano, S., & Cantó, J. 1999, ApJ, 527, 893

D'Alessio, P., Cantö, J., Calvet, N., & Lizano, S. 1998, ApJ, 500, 411

DeHoff, R. 1993, Thermodynamics in Materials Science (McGraw-Hill International Editions)

Eriksson, C. & Hack, K. 1990, Metall. Trans., 21

Eriksson, C. & Konigsberger, E. 1995, CALPHAD, 19, 207

Fabian, D., Jager, C., Henning, T., Dorschne, J., & Mutschke, H. 2000, in ESA Special Publication, Vol. 456, ISO Beyond the Peaks: The 2nd ISO Workshop on Analytical Spectroscopy, ed. A. Salama, M. F. Kessler, K. Leech, & B. Schulz, 347

Ferrarotti, A. S. & Gail, H. 2001, A&A, 371, 133

Gail, H.-P. 1998, A&A, 332, 1099

Gammie, C. F. 1996, ApJ, 457, 355

Harker, D. E. & Desch, S. J. 2002, Apjl, 565, L109

Hartmann, L. 2000, Accretion processes in star formation, Vol. 32 (Cambridge University Press)

Henning, T. & Meeus, G. 2011, Dust Processing and Mineralogy in Protoplanetary Accretion Disks, ed. P. J. V. Garcia, 114–148

Juhász, A., Dullemond, C. P., van Boekel, R., et al. 2012, ApJ, 744, 118

Kessler-Silacci, J., Augereau, J.-C., Dullemond, C. P., & et al. 2006, ApJ, 639, 275

Laibe, G., Gonzalez, J.-F., Fouchet, L., & Maddison, S. T. 2008, A&A, 487, 265

Lehmann, T., Reipurth, B., & Brandner, W. 1995, A&A, 300, L9

Liffman, K. & Brown, M. J. I. 1996, in Chondrules and the Protoplanetary Disk, 285–302

Liffman, K. & Toscano, M. 2000, Icarus, 143, 106

Meeus, G., Juhász, A., Henning, T., & et al. 2009, A&A, 497, 379

van Boekel, R., Min, M., Leinert, C., et al. 2004, Nature, 432, 479

Weider, S. Z., Nittler, L. R., Starr, R. D., et al. 2012, Journal of Geophysical Research (Planets), 117, 0

Weisberg, M. K. & Kimura, M. 2012, Chemie der Erde, 72, 101

Yoneda, S. & Grossman, L. 1995, Geochim. Cosmochim. Acta, 59, 3413

SF2A 2014
J. Ballet, F. Bournaud, F. Martins, R. Monier and C. Reylé (eds)

BROWN DWARFS DETECTIONS THROUGH MICROLENSING

C. Ranc[1], A. Cassan[1], PLANET, MOA, μFUN and RoboNet

Abstract. Gravitational microlensing is known to be a powerful method to hunt for extrasolar planets and brown dwarfs. Recently, several brown dwarfs companions to stars have been detected through microlensing, as well as brown dwarfs binaries. We present the discovery of a new $\sim 40\,M_{\rm J}$ brown dwarf orbiting a K-dwarf at ~ 4 AU, located at ~ 4 kpc from the Earth. Besides using the standard photometric light curves gathered from different round-the-world observatories, its characterization involved high-resolution adaptative optics measurements from NaCo at VLT which allowed to break the degeneracies between the physical parameters and provide the exact mass and projected separation of the system.

Keywords: Gravitational lensing: micro - Brown dwarfs - Planets and satellites: detection.

1 Introduction

Gravitational microlensing is a powerful technique to detect extrasolar planets (Mao & Paczynski 1991), and holds great promises in detecting populations of brown dwarfs companions to stars. Compared to other detection techniques, microlensing provides unique information on the population of exoplanets, because it allows the detection of very low-mass planets (down to the mass of the Earth) at large orbital distances from their star (0.5 to 10 AU). It is also the only technique that allows the discovery of planets at distances from Earth greater than a few kiloparsecs, up to the bulge of the Galaxy.

Milestone discoveries include detections such as the detection of the first cool super-Earth OGLE-BLG-2005-390Lb (Beaulieu et al. 2006), a frozen super-Earth orbiting a star at the bottom of the main sequence (Kubas et al. 2012) or the detection of a population of free-floating planets located at Galactic distances (Sumi et al. 2011). So far 31 planets have been published, but several more are currently being analyzed. Detections and non-detections inform us on the abundance of planets as a function of planetary mass. Recent microlensing studies imply that low-mass planets, in particular super-Earths, are far more abundant than giant planets, and reveal that there are, on average, one or more bound planets per Milky Way star (Cassan et al. 2012).

Brown dwarfs, on the other hand, have found to be intrinsically rare. While a number of brown dwarfs companions to stars have been detected by other methods, there are still few detections by microlensing, mainly because until now, observing priority has been given to low-mass objets. New advances in using networks of robotic telescopes are today changing the situation, many more detections are to be expected in a near future. With these detections, microlensing should provide a unique view of brown dwarfs around low-mass stars (M dwarfs), which will complement the currently available sample which contains mainly solar-type stars. These expected detections will help to understand the current lack of brown dwarf around 40-50 Jupiter masses at short orbital distances (the "brown dwarf desert" in Marcy & Butler 2000), and explore more precisely the population of objects in the mass range 10-80 $M_{\rm J}$ at orbital distances of 0.5-10 AU.

2 Brown dwarfs detections by microlensing

Gould et al. (2009) announced the first detection of a $0.056 \pm 0.004\ M_{\odot}$ field brown dwarf located in the thick-disk of the Milky Way using a terrestrial parallax signature in the light curve of OGLE-2007-BLG-224. After an advanced analysis of the event OGLE-2008-BLG-510/MOA-2008-BLG-369 including the effects of systematics on the lens properties, Bozza et al. (2012) showed that both binary-lens and binary-source models

[1] Sorbonne Universités, UPMC Univ Paris 06, UMR 7095, Institut d'Astrophysique de Paris, F-75014, Paris, France

are compatible with the data, including a lens consisting of an M-dwarf orbited by a strong brown dwarf, solution also proposed by Shin et al. (2012a). After a full analysis of microlensing events characterized by a low mass ratio, Shin et al. (2012b) identified two brown dwarfs among seven good candidates: OGLE-2011-BLG-0172/MOA 2011-BLG-104 is due to a $0.02 \pm 0.01\,M_{\odot}$ brown dwarf orbiting a low-mass M-dwarf, while MOA 2011-BLG-149 is due to a lens composed of a $0.019 \pm 0.002\,M_{\odot}$ brown dwarf orbiting a low-mass M-dwarf as well. Another detection of a $0.05\,M_{\odot}$ brown dwarf orbiting an M-star was reported by Bachelet et al. (2012) who derived the physical properties of the lens using Galactic models. In the analysis of the anomalous microlensing event MOA-2010-BLG-073 involving a source star previously known to be photometrically variable and irregular, Street et al. (2013) found the lens to be composed of a $11.0 \pm 2.0\,M_{\rm J}$ substellar companion at the planet/brown dwarf boundary orbiting a $0.16 \pm 0.03\,M_{\odot}$ M-star. Finally, Jung et al. (2014) reported the discovery of a $0.013 \pm 0.002\,M_{\rm J}$ brown dwarf orbiting a very low mass star, both objects being close to the boundary between planet/brown dwarf on the one hand and brown dwarf/star on the other hand.

Moreover, a new population of low mass brown dwarfs hosting planets in a very tight orbit was proposed by Choi et al. (2013) from the analysis of the events OGLE-209-BLG151/MOA-2009-BLG232 and OGLE-2011-BLG-0420. These two systems consist in two super-Jupiter of $0.0075 \pm 0.0003\ M_{\odot}$ and $0.0094 \pm 0.0005\ M_{\odot}$ orbiting a $0.018 \pm 0.001\ M_{\odot}$ and a $0.025 \pm 0.001\ M_{\odot}$ brown dwarf respectively, with a projected separation lower than 0.4 AU in both cases. Similarly, Han et al. (2013) reported another $0.022 \pm 0.002\ M_{\odot}$ field brown dwarf hosting a $1.9 \pm 0.2\ M_{\rm J}$ planet in a tight system.

If gravitational microlensing is usually promoted cause its unique sensitivity to low mass planets, these recent discoveries confirmed the ability of microlensing to detect brown dwarfs in very different contexts, from solitary objects to brown dwarfs orbiting low mass stars, including brown dwarfs hosting planets. This method is also well suited to explore the transition between super-Jupiters and brown dwarfs, without little bias in brightness and in distance in the Milky Way when using direct imaging (Close et al. 2003). The brown dwarfs detected so far by microlensing constitute approximately a third of the planets detected and published using this method. Five companion brown dwarfs have been clearly identified and published among 2009 to 2013 observing seasons. We report the temporary first results revealing a sixth brown dwarf detected in 2007.

3 The event MOA 2007-BLG-197

During a gravitational microlensing event, the light from a distant star (called the source) in the Galactic bulge is deflected due to a space-time curvature in the vicinity of a planetary system called the lens, resulting in multiple images of the source. These images can't be resolved by a single telescope, but an amplification of the flux from the source may be detected, and its time dependance strongly depends on the mass distribution on the lens plane. This is why this method is that sensitive to the low mass ratio binary systems.

The event MOA 2007-BLG-197 was first detected by MOA collaboration in May 2007, and was fully followed by PLANET/RoboNet and μFUN collaborations (six telescopes) as soon as a single-lens model, *i.e.* a single lens star, obviously failed to describe the observations. The light curve of this event presented in Fig. 1, exhibits features specific to binary systems. The caustic exit is particularly noteworthy and was densely followed, but the analysis of the light curve suffers from the missing caustic entry that could give crucial constraints. Additional NaCo high-resolution images were obtained at the Very Large Telescope and balanced this lack of information.

Since the light curve exhibits caustic-crossing features, we take into account finite-source effects on the models. The measurements are fitted by eleven parameters. The different parameters are added successively starting with a static model, so that the most subtle effects are sought step by step, and the degeneracies explored thanks to a Markov Chain Monte Carlo algorithm. As there is no shared calibration between all the telescopes, two additional parameters per observatory are required: the flux from the source, and the blending.

As expected for long timescale events (several months), annual parallax features have been detected in the light curve, as well as the orbital motion of the lens, breaking model degeneracies, and thus providing a measurement of the lens mass, distance, and transverse velocity. However, the dynamic of the caustic seems very slow, and parallax remains partly degenerated with orbital motion cause lack of constraints during the caustic entry.

The best-fitting light curve points out that blending dominates, suggesting that NaCo images and CMD constrain the lens spectral type rather the source. The high-resolution adaptative optics (AO) images provide measurements of near J, H and K_s colors of the event. The combination of the high-resolution images, the CMD and the best-fitting set of parameters in a Bayesian framework led to balanced the not well constrained parallax and orbital motion. The preliminary resulting model gives a lens composed by a $36\,M_{\rm J}$ brown dwarf

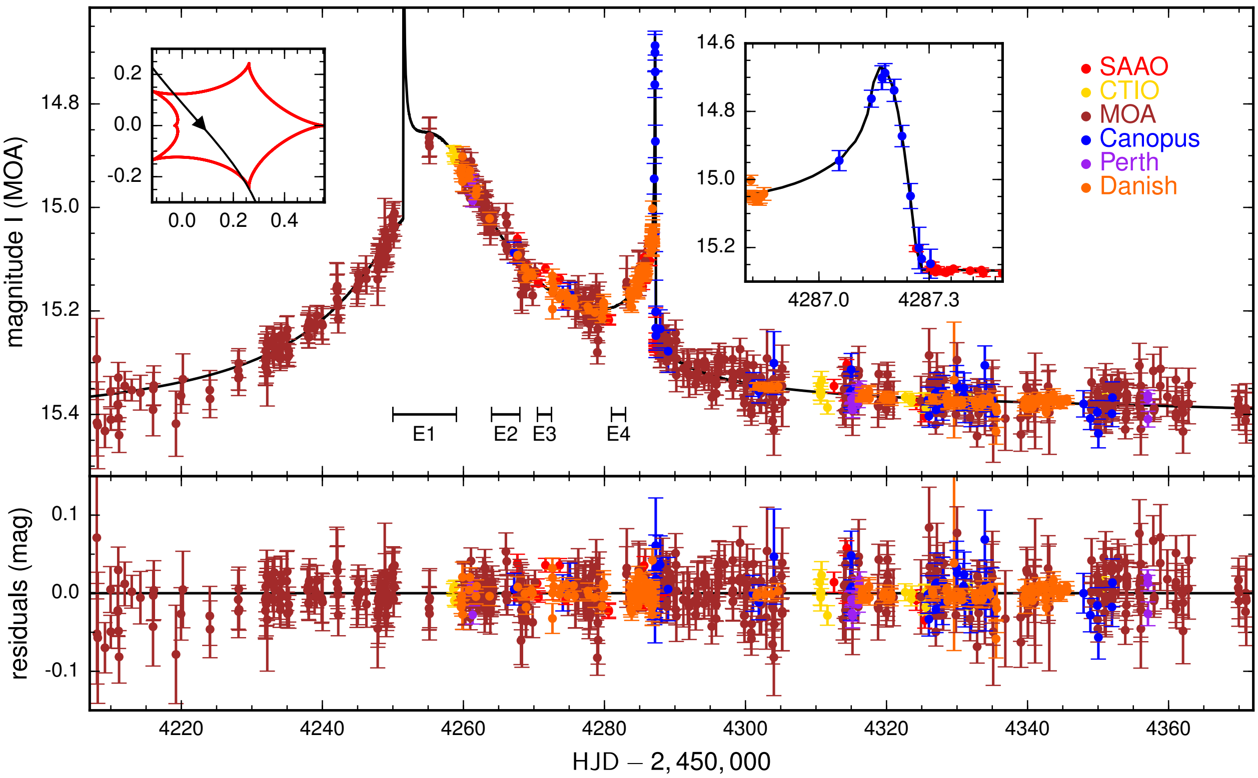

Fig. 1. In the upper panel, the light curve of MOA 2007-BLG-197 and the best-fitting model (solide line) are plotted. On the left-hand side, the caustic structure at the time of closest approach is drawn in red, and the trajectory of the source relative to the caustic is shown in black (Einstein units). In the lower panel, the residuals are reported. In both panels, the color refers to the observatory which performed the measurements. Adapted from Ranc *et al.*, in prep.

orbiting a Main Sequence star at 4 AU, this system being located at 3.7 kpc from the Earth (Ranc *et al.*, in prep.).

References

Bachelet, E., Fouqué, P., Han, C., et al. 2012, A&A, 547, A55

Beaulieu, J.-P., Bennett, D. P., Fouqué, P., et al. 2006, Nature, 439, 437

Bozza, V., Dominik, M., Rattenbury, N. J., et al. 2012, MNRAS, 424, 902

Cassan, A., Kubas, D., Beaulieu, J.-P., et al. 2012, Nature, 481, 167

Choi, J.-Y., Han, C., Udalski, A., et al. 2013, ApJ, 768, 129

Close, L. M., Biller, B., Hoffmann, W. F., et al. 2003, ApJ, 598, L35

Gould, A., Udalski, A., Monard, B., et al. 2009, ApJ, 698, L147

Han, C., Jung, Y. K., Udalski, A., et al. 2013, ApJ, 778, 38

Jung, Y. K., Udalski, A., Sumi, T., et al. 2014, ArXiv e-prints

Kubas, D., Beaulieu, J. P., Bennett, D. P., et al. 2012, A&A, 540, A78

Mao, S. & Paczynski, B. 1991, ApJ, 374, L37

Marcy, G. W. & Butler, R. P. 2000, PASP, 112, 137

Shin, I.-G., Han, C., Choi, J.-Y., et al. 2012a, ApJ, 755, 91

Shin, I.-G., Han, C., Gould, A., et al. 2012b, ApJ, 760, 116

Street, R. A., Choi, J.-Y., Tsapras, Y., et al. 2013, ApJ, 763, 67

Sumi, T., Kamiya, K., Bennett, D. P., et al. 2011, Nature, 473, 349

SF2A 2014
J. Ballet, F. Bournaud, F. Martins, R. Monier and C. Reylé (eds)

INFLUENCE OF THE MASS DISTRIBUTION ON THE MAGNETIC FIELD TOPOLOGY IN SPHERICAL, ANELASTIC DYNAMO SIMULATIONS

R. Raynaud[1], L. Petitdemange[1] and E. Dormy[2]

Abstract. Numerical modelling of convection driven dynamos in the Boussinesq approximation revealed fundamental characteristics of the dynamo-generated magnetic fields. However, Boussinesq models are not adequate for describing convection in stratified systems, and thus the validity of these previous results remains to be assessed for gas giants and stars. To that end, we carried out a systematic parameter study of spherical dynamo models in the so-called anelastic approximation, which allows for a reference density profile while filtering out sound waves for faster numerical integration. We show that the dichotomy of dipolar and multipolar dynamos identified in Boussinesq simulations is still present in anelastic models, and dipolar dynamos require that the typical length scale of convection is an order of magnitude larger than the Rossby radius. However, the established distinction between dipolar and multipolar dynamos tends to be less clear than it was in Boussinesq studies, since we found a large number of models with a considerable equatorial dipole contribution together with an intermediate overall dipole field strength. This tendency can be found in very weakly stratified models, but it was not reported for previous Boussinesq models assuming a homogeneous mass distribution. In contrast, anelastic models usually assume a central mass distribution, which leads to a gravity profile proportional to $1/r^2$. Actually, we show that this choice can result in changes in the magnetic field topology that are mainly due to the concentration of convective cells close to the inner sphere.

Keywords: dynamo, magnetohydrodynamics, magnetic fields, stars: magnetic field

1 Introduction

Dynamo action, i.e. the self-amplification of a magnetic field by the flow of an electrically conducting fluid, is considered to be the main mechanism for generating of magnetic fields in the universe for a variety of systems, including planets, stars, and galaxies. Because of the difficulty simulating turbulent fluid motions, one must resort to some approximations to model the fluid flow, whose convective motions are assumed to be driven by the temperature difference between a hot inner core and a cooler outer surface. A strong simplification can be achieved when applying the Boussinesq approximation, which performs well in so far as variations in pressure scarcely affect the density of the fluid. However, this approximation will not be adequate for describing convection in highly stratified systems, such as stars or gas giants. A common approach to overcoming this difficulty is then to use the anelastic approximation, which allows for a reference density profile while filtering out sound waves for faster numerical integration. This approximation was first developed to study atmospheric convection (Ogura & Phillips 1962; Gough 1969). It has then been used to model convection in the Earth core or in stars and is found in the literature under slightly different formulations (Gilman & Glatzmaier 1981; Braginsky & Roberts 1995; Lantz & Fan 1999; Anufriev et al. 2005; Berkoff et al. 2010; Jones et al. 2011; Alboussière & Ricard 2013). Nevertheless, the starting point in the anelastic approximation is always to consider convection as a perturbation of a stratified reference state that is assumed to be close to adiabatic.

Observations of low mass stars have revealed very different magnetic field topologies from small scale fields to large scale dipolar fields (Donati & Landstreet 2009; Morin et al. 2010), and highlight possible correlations between differential rotation and magnetic field topologies (Reinhold et al. 2013). Boussinesq models partly reproduce this diversity (Busse & Simitev 2006; Sasaki et al. 2011; Schrinner et al. 2012). For anelastic models, not only previously proposed scaling laws (Christensen & Aubert 2006), but also the dichotomy between dipolar and "non-dipolar" (or multipolar) dynamos seems to hold (Gastine et al. 2012; Yadav et al. 2013; Schrinner et al. 2014). These are characterized by different magnetic field

[1] LERMA, Observatoire de Paris, PSL Research University, CNRS, UMR 8112, F-75014, Paris, France
[2] IPGP, CNRS UMR 7154, 75005 Paris, France

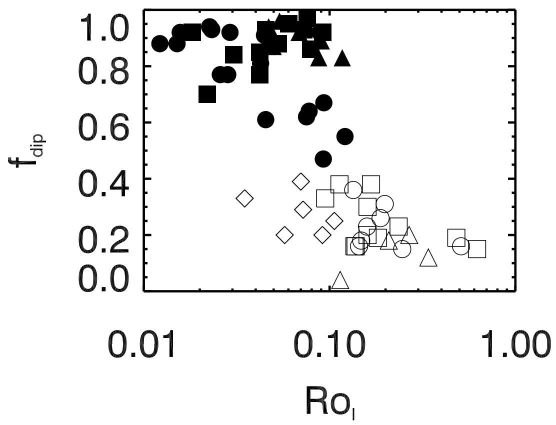

(a) Boussinesq models (Schrinner et al. 2012).

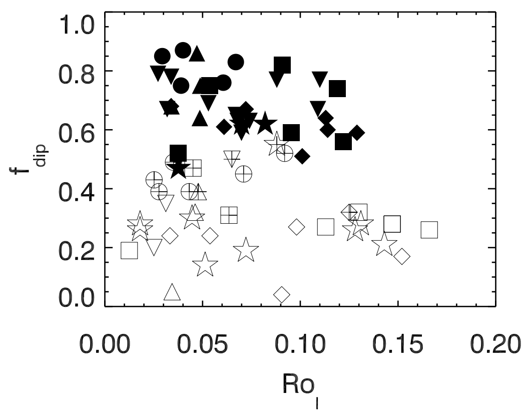

(b) Anelastic models (Schrinner et al. 2014).

Fig. 1. $f_{\rm dip}$ versus Ro_ℓ. Filled symbols stand for dipolar, open symbols for multipolar dynamos. A cross inscribed in some open symbols means that the field of these models exhibits a strong equatorial dipole component. In figure (a), the symbol shape indicates different types of mechanical boundary conditions: circles mean no-slip conditions at both boundaries, triangles are models with a rigid inner and a stress-free outer boundary, and squares stand for models with stress-free conditions at both boundaries. In figure (b), the symbol shape indicates the number of density scale heights: $N_\varrho = 0.5$: circle; $N_\varrho = 1$: upward triangle; $N_\varrho = 1.5$: downward triangle; $N_\varrho = 2$: diamond; $N_\varrho = 2.5$: square; $N_\varrho = 3, 3.5, 4$: star.

configurations: dipolar dynamos are dominated by a strong axial dipole component, whereas multipolar dynamos usually present a more complex geometry with higher spatial and temporal variability. However, as we can see in Fig. 1, this distinction is somewhat less clear for anelastic models, due to the presence of multipolar models with a high equatorial dipole contribution which induces an intermediate dipole field strength.

Raynaud et al. (2014) aim to clarify the reasons likely for the emergence of an equatorial dipole contribution when measuring the dipole field strength at the surface of numerical models. Since our approach closely follows previous methodology for studying the link with Boussinesq results, we decided to focus in more detail on one important change that comes with the anelastic approximation, assuming that all mass is concentrated inside the inner sphere to determine the gravity profile. In contrast, as proposed by the Boussinesq dynamo benchmark Christensen et al. (2001), it was common for geodynamo studies to assume that the density is homogeneously distributed. This leads to different gravity profiles, the first being proportional to $1/r^2$, whereas the second is proportional to r. We show that the choice of the gravity profile may have strong consequences on the dynamo-generated field topology.

2 Set up

We rely on the LBR-formulation of the anelastic approximation, named after Lantz & Fan (1999) and Braginsky & Roberts (1995), as it is used in the dynamo benchmarks proposed by Jones et al. (2011). A detailed presentation of the equations can be found in Schrinner et al. (2014). We consider a spherical shell of width d and aspect ratio $\chi = r_{\rm i}/r_{\rm o}$, rotating about the z axis at angular velocity $\mathbf{\Omega}$ and filled with a perfect, electrically conducting gas with kinematic viscosity ν, thermal diffusivity κ, specific heat c_p, and magnetic diffusivity η (all assumed to be constant). In contrast to the usual Boussinesq framework, convection is driven by an imposed entropy difference Δs between the inner and the outer boundaries, and the gravity is given by $\mathbf{g} = -GM\hat{\mathbf{r}}/r^2$ where G is the gravitational constant and M the central mass, assuming that the bulk of the mass is concentrated inside the inner sphere. We impose stress free boundary conditions for the velocity field at both the inner and the outer sphere, the magnetic field matches a potential field inside and outside the fluid shell, and the entropy is fixed at the inner and outer boundaries.

The system is control by seven parameters, namely the Rayleigh number $Ra = GMd\Delta s/(\nu\kappa c_p)$, the Ekman number $E = \nu/(\Omega d^2)$, the Prandtl number $Pr = \nu/\kappa$, and the magnetic Prandtl number $Pm = \nu/\eta$, together with the aspect ratio χ, the polytropic index n, and the number of density scale heights $N_\varrho = \ln(\varrho_{\rm i}/\varrho_{\rm o})$ that define the reference state. Raynaud et al. (2014) restrict the investigation of the parameter space keeping E= 10^{-4}, $Pr = 1$, $\chi = 0.35$, and $n = 2$ for all simulations. Furthermore, to differentiate the effects related to the change in gravity profile from those related to the

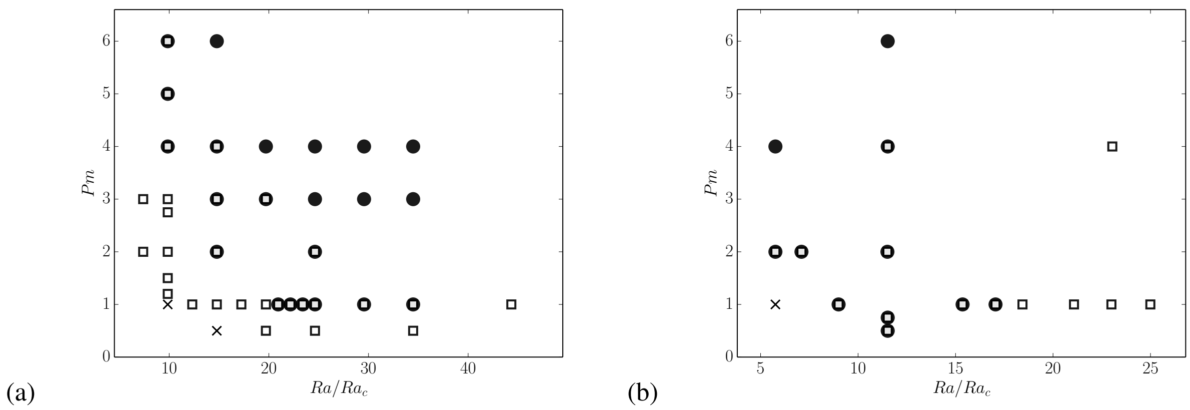

Fig. 2. Dipolar (black circles) and multipolar (white squares) dynamos as a function of Ra/Ra_c and Pm, for a central mass (a) and a uniform mass distribution (b). Crosses indicate the absence of a self-sustained dynamo.

anelastic approximation, we decided to perform low N_ϱ simulations so that we can assume that stratification no longer influences the dynamo process. In practice, we choose $N_\varrho = 0.1$, and the simulations are thus very close to the Boussinesq limit.

A measure of the velocity field amplitude is given by the Rossby number $Ro = \sqrt{2E_k}E/Pm$, where E_k is the kinetic energy density. To distinguish between dipolar and multipolar dynamo regimes, we know from Boussinesq results that it is useful to measure the balance between inertia and Coriolis force, which can be approximated in terms of a local Rossby number $Ro_\ell = Ro_c\,\ell_c/\pi$, which depends on the characteristic length scale of the flow rather than on the shell thickness (Christensen & Aubert 2006; Olson & Christensen 2006; Schrinner et al. 2012). The dipolarity of the magnetic field is characterized by the relative dipole field strength, $f_{\rm dip}$, originally defined as the time-average ratio on the outer shell boundary S_o of the dipole field strength to the total field strength. We also define a relative *axial* dipole field strength $f_{\rm dip_{ax}}$ by filtering out non-axisymmetric contributions.

3 Results

Figure 2(a) shows the regime diagram we obtained, as a function of the Rayleigh and magnetic Prandtl numbers. For $Pm = 1$, the transition from the dipolar to the multipolar branch can be triggered by an increase in Ra. In that case, the transition is due to the increasing role of inertia (corresponding to $Ro_\ell \sim 0.1$ in Fig. 3). Alternatively, the transition from multipolar to dipolar dynamo can be triggered by increasing Pm. Then, the multipolar branch is lost when the saturated amplitude of the mean zonal flow becomes too small to prevent the growth of the dipolar solution (see Schrinner et al. 2012). It is worth noting that the two branches overlap for a restricted parameter range for which dipolar and multipolar dynamos may coexist. In that case, the observed solution strongly depends on the initial magnetic field, so we tested both weak and strong field initial conditions for all our models to delimit the extent of the bi-stable zone with greater accuracy. Actually, multipolar dynamos are favoured by the stronger zonal wind that may develop with stress-free boundary conditions, allowing for this hysteretic transition. Finally, we see that the dynamo threshold is lower for multipolar models, which allows the multipolar branch to extend below the dipolar branch at low Rayleigh and magnetic Prandtl numbers. We see in Fig. 2(b) that this is different from Boussinesq models with a uniform mass distribution (after Schrinner et al. 2012).

Figure 3(a) shows that the tendency highlighted in Fig. 1(b) already exits at low N_ϱ, and thus cannot be accounted for only in terms of anelastic effects. When the equatorial dipole component is removed to compute $f_{\rm dip_{ax}}$, we recover a more abrupt transition, as we can see in Fig. 3(b): dipolar dynamos are left unchanged, whereas multipolar dynamos of intermediate dipolarity are no longer observed, which confirms that the increase in $f_{\rm dip}$ is due to a significant equatorial dipole component. Moreover, we show in Raynaud et al. (2014) that these equatorial dipoles are preferably localized close to the dynamo threshold of the multipolar branch, at low Rayleigh and magnetic Prandtl numbers.

Then, the only significant parameter that is changed between Fig. 1(a) and Fig. 3(a) is the choice of the gravity profile, and this is sufficient to explain the emergence of the equatorial mode. Indeed, with a central mass distribution, convection cells now form and stay closer to the inner sphere, as we can see in Fig. 4(a,b) that shows equatorial cuts of the radial component of the velocity and magnetic fields, for both gravity profiles. This strong difference in the flow reflects on the

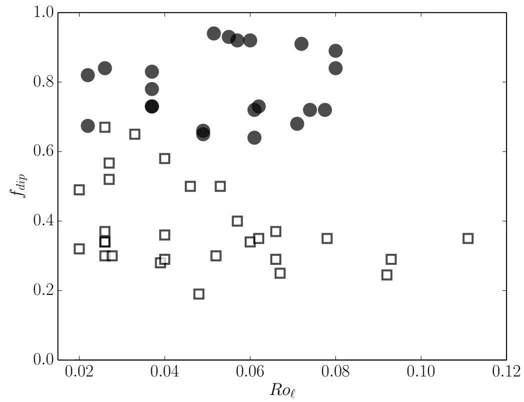

(a)

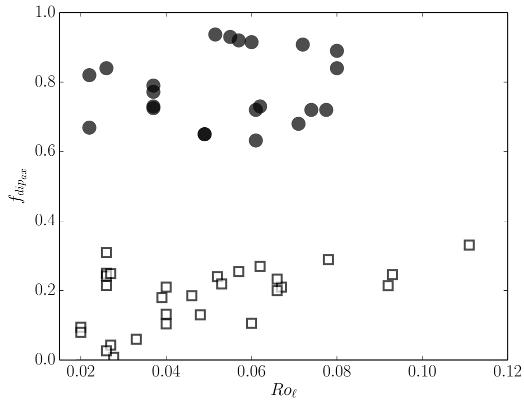

(b)

Fig. 3. (a): $f_{\rm dip}$ versus Ro_ℓ. (b): $f_{\rm dip_{ax}}$ versus Ro_ℓ. The meaning of the symbol shapes is defined in the caption of Fig. 2.

localization of the active dynamo regions (see Fig. 4 (c,d)). With a gravity profile proportional to $1/r^2$, the magnetic field is mainly generated close to the inner sphere, where the convection cells form. Consequently, our measure of the dipole field strength $f_{\rm dip}$ at the surface of the outer sphere appears to be biased, since it will essentially be sensitive to the less diffusive large scale modes. This filter effect is likely to be responsible for the increase in $f_{\rm dip}$ reported in some anelastic dynamo models.

4 Conclusion

Raynaud et al. (2014) focussed on very weakly stratified anelastic dynamo models with a central mass distribution and investigated the bifurcations between the dipolar and multipolar dynamo branches. We recovered in parts the behaviour that has been observed for Boussinesq models with a uniform mass distribution. We show that the dipolar branch can now lose its stability and switch to the multipolar branch at low Rayleigh and magnetic Prandtl numbers. The multipolar dynamos that are observed in this restricted parameter regime usually present a stronger equatorial dipole component at the surface of the outer sphere. These results shed interesting light on the systematic parameter study of spherical anelastic dynamo models started by Schrinner et al. (2014). We showed that magnetic field configurations with a significant equatorial dipole contribution can already be observed in the Boussinesq limit, and revealed that the choice of gravity profile has a strong influence on the fluid flow and thus on the dynamo generated magnetic field, depending whether one considers a uniform or a central mass distribution. In the parameter space, we showed that multipolar dynamos with a significant equatorial dipole contribution are preferably observed close to the dynamo threshold.

Observational results from photometry (Hackman et al. 2013) and spectropolarimetry (Kochukhov et al. 2013) of rapidly rotating cool active stars reveal that the surface magnetic field of these objects can be highly non-axisymmetric. Further investigation of direct numerical simulations is therefore required to better understand the influence of the Prandtl number and the density stratification on the magnetic field topology.

References

Alboussière, T. & Ricard, Y. 2013, Journal of Fluid Mechanics, 725, 1

Anufriev, A. P., Jones, C. A., & Soward, A. M. 2005, Physics of the Earth and Planetary Interiors, 152, 163

Berkoff, N. A., Kersale, E., & Tobias, S. M. 2010, Geophysical and Astrophysical Fluid Dynamics, 104, 545

Braginsky, S. I. & Roberts, P. H. 1995, Geophysical and Astrophysical Fluid Dynamics, 79, 1

Busse, F. H. & Simitev, R. D. 2006, Geophys. Astrophys. Fluid Dyn., 100, 341

Christensen, U. R. & Aubert, J. 2006, Geophy. J. Int., 166, 97

Christensen, U. R., Aubert, J., Cardin, P., et al. 2001, Phys. Earth Planet. Inter., 128, 25

Donati, J.-F. & Landstreet, J. D. 2009, ARA&A, 47, 333

Gastine, T., Duarte, L., & Wicht, J. 2012, A&A, 546, A19

Gilman, P. A. & Glatzmaier, G. A. 1981, ApJS, 45, 335

Gough, D. O. 1969, Journal of Atmospheric Sciences, 26, 448

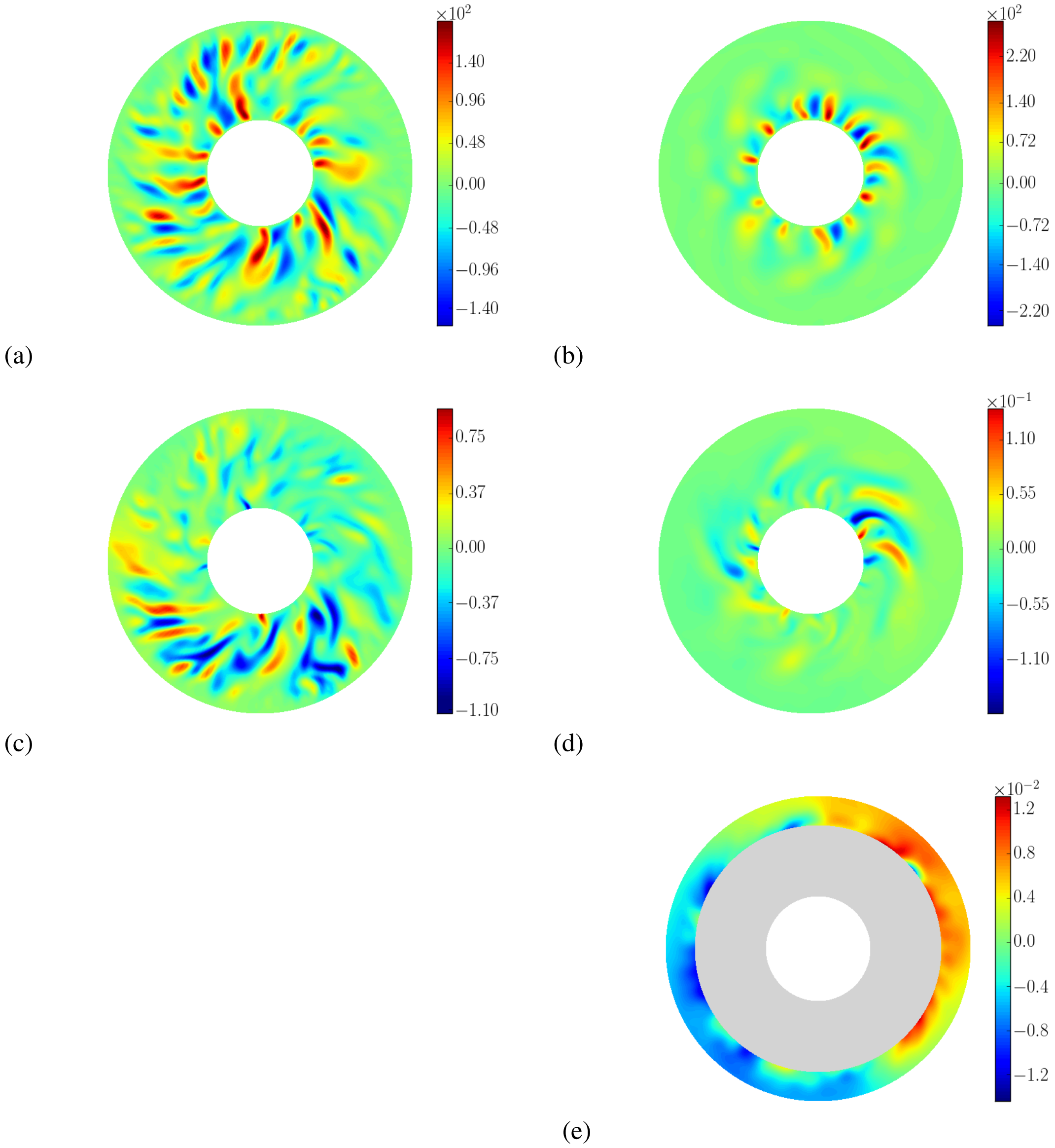

Fig. 4. Equatorial cross sections of v_r (a)-(b) and B_r (c)-(d), for a uniform (left) and a central (right) mass distribution. In both cases, $Ra/Ra_c \sim 10$ and $Pm \sim 1$. Colour in Fig. (d) is rescaled in Fig. (e) to highlight the emergence of a $m = 1$ mode at the outer sphere.

Hackman, T., Pelt, J., Mantere, M. J., et al. 2013, A&A, 553, A40

Jones, C. A., Boronski, P., Brun, A. S., et al. 2011, Icarus, 216, 120

Kochukhov, O., Mantere, M. J., Hackman, T., & Ilyin, I. 2013, A&A, 550, A84

Lantz, S. R. & Fan, Y. 1999, ApJS, 121, 247

Morin, J., Donati, J.-F., Petit, P., et al. 2010, MNRAS, 407, 2269

Ogura, Y. & Phillips, N. A. 1962, Journal of Atmospheric Sciences, 19, 173

Olson, P. & Christensen, U. R. 2006, Earth and Planetary Science Letters, 250, 561

Raynaud, R., Petitdemange, L., & Dormy, E. 2014, A&A, 567, A107

Reinhold, T., Reiners, A., & Basri, G. 2013, A&A, 560, A4

Sasaki, Y., Takehiro, S.-i., Kuramoto, K., & Hayashi, Y.-Y. 2011, Physics of the Earth and Planetary Interiors, 188, 203

Schrinner, M., Petitdemange, L., & Dormy, E. 2012, ApJ, 752, 121

Schrinner, M., Petitdemange, L., Raynaud, R., & Dormy, E. 2014, A&A, 564, A78

Yadav, R. K., Gastine, T., Christensen, U. R., & Duarte, L. D. V. 2013, ArXiv e-prints

SF2A 2014
J. Ballet, F. Bournaud, F. Martins, R. Monier and C. Reylé (eds)

MODELLING THE CORONA OF HD 189733 IN 3D

A. Strugarek[1], A. S. Brun[2], S. P. Matt[3], V. Reville[2], J. F. Donati[4], C. Moutou[5] and R. Fares[6]

Abstract. The braking of main sequence stars originates mainly from their stellar wind. The efficiency of this angular momentum extraction depends on the rotation rate of the star, the acceleration profile of the wind and the coronal magnetic field. The derivation of scaling laws parametrizing the stellar wind torque is important for our understanding of gyro-chronology and the evolution of the rotation rates of stars. In order to understand the impact of complex magnetic topologies on the stellar wind torque, we present three-dimensional, dynamical simulations of the corona of HD 189733. Using the observed complex topology of the magnetic field, we estimate how the torque associated with the wind scales with model parameters and compare those trends to previously published scaling laws.

Keywords: stars, magnetism, stellar winds

1 Introduction

Magnetized stellar winds have long been recognized as the major source of angular momentum extraction in main sequence stars (Parker 1958; Weber & Davis 1967; Mestel 1968). In order to reliably assess the stellar wind torque, the acceleration profile and the magnetic field geometry of the wind are required. It was recently demonstrated that, in particular, complex magnetic topologies of cool stars have a major impact on the torque (see, *e.g.* Cohen & Drake 2014; Réville et al. 2014) compared to more simple topologies. Three dimensional numerical simulations provide a reliable way to compute, in a dynamically self-consistent way, the torque arising from stellar wind with complex magnetic fields. However, no parametrization of fully three-dimensional, non-axisymmetric stellar wind torques has yet been proposed in the literature.

We report here an ongoing effort in developing magnetohydrodynamics (MHD) simulations of the stellar winds of cool stars in three dimensions using complex magnetic field topologies. We consider one-fluid and ideal models of stellar winds which are simple compared to the most recent solar wind models (see, *e.g.*, Oran et al. 2013; Sokolov et al. 2013). However, they inherit important conservation properties from their 2.5D counterparts (see Strugarek et al. 2012, 2014b) which makes them reliable to derive general scaling laws for the stellar wind breaking.

We focus, in this proceeding, on the extension of our three-dimensional stellar wind model (see Strugarek et al. 2014b) to take into account arbitrarily complex magnetic topology. As a test-bench we use the case of HD 189733 (see Section 2), which has already been modelled in 3D by Llama et al. (2013). We vary one of the free parameters of the model, the Alfvén speed at the base of the corona (Section 3), and compare our results with previously published results. Furthermore, the various cases presented here allow us to compare the results of fully three-dimensional simulations with scaling laws that were derived in a magnetic topology-independent manner in axisymmetric geometry (Réville et al. 2014). We find a good general agreement with this law, though the predicted torque is found to be generally larger than the one we found with our 3D models. Given that the scaling law was derived in axisymmetric geometry (in 2D), we find the general agreement satisfactory and are encouraging for further exploration of this scaling law, using fully three-dimensional numerical simulations.

[1] Département de physique, Université de Montréal, C.P. 6128 Succ. Centre-Ville, Montréal, QC H3C-3J7, Canada
[2] Laboratoire AIM Paris-Saclay, CEA/Irfu Université Paris-Diderot CNRS/INSU, F-91191 Gif-sur-Yvette.
[3] Astrophysics group, School of Physics, University of Exeter, Stocker Road, Exeter EX4 4QL, UK
[4] Laboratoire d'Astrophysique, Observatoire Midi-Pyrénées, 14 Av. E. Belin, F-31400 Toulouse, France
[5] Aix-Marseille Université, CNRS, LAM (Laboratoire dAstrophysique de Marseille) UMR 7326, 13388 Marseille, France
[6] SUPA, School of Physics and Astronomy, University of St Andrews, North Haugh, St Andrews KY16 9SS, UK

2 Characteristics of HD 189733

The properties of the planet-hosting HD 189733 star have been reported in Bouchy et al. (2005). It is a K2V star with a mass $M_\star = 0.82 \pm 0.03 M_\odot$ and a radius $R_\star = 0.76 \pm 0.01 R_\odot$ (Winn et al. 2007). The rotation period of HD 189733 has been characterized by several teams using photometry (Hébrard & Lecavelier des Etangs 2006; Winn et al. 2007), and is reported between 11.8 and 13.4 days. Here we adopt a rotation period of 12 days.

We use the spectro-polarimetric magnetic maps of HD 189733 obtained by Fares et al. (2010) that where observed in July 2008 with NARVAL. We show in figure 1 the reconstructed components of the magnetic field in spherical coordinates (top to bottom) in orthographic projection viewed from the north pole (left), the equator (middle) and the south pole (right). The magnetic field is highly non-axisymmetric and derives from 20 spherical harmonics modes ($l_{max} = 5$).

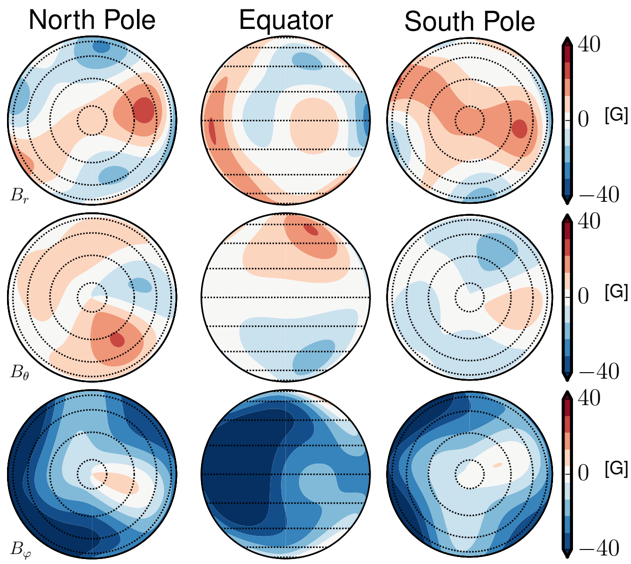

Fig. 1. Spectro-polarimetric reconstruction of the coronal magnetic field of HD 189733 in July 2008 (see Fares et al. 2010). The amplitude of the field is given in Gauss.

3 Modelling the wind of HD 198733

3.1 Numercial Model and Parameters

Following the work in 2.5D axisymmetric geometry described by Strugarek et al. (2014c) and in 3D by Strugarek et al. (2014b), we adapted our stellar wind model to account for the magnetic topology of observed stars. We use the PLUTO code (Mignone et al. 2007) which solves the following set of ideal MHD equations:

$$\partial_t \rho + \boldsymbol{\nabla} \cdot (\rho \mathbf{v}) = 0 \tag{3.1}$$

$$\partial_t \mathbf{v} + \mathbf{v} \cdot \boldsymbol{\nabla} \mathbf{v} + \frac{1}{\rho} \boldsymbol{\nabla} P + \frac{1}{\rho} \mathbf{B} \times \boldsymbol{\nabla} \times \mathbf{B} = \mathbf{a}\,, \tag{3.2}$$

$$\partial_t P + \mathbf{v} \cdot \boldsymbol{\nabla} P + \rho c_s^2 \boldsymbol{\nabla} \cdot \mathbf{v} = 0\,, \tag{3.3}$$

$$\partial_t \mathbf{B} - \boldsymbol{\nabla} \times (\mathbf{v} \times \mathbf{B}) = 0\,, \tag{3.4}$$

where ρ is the plasma density, $\mathbf{v}$ its velocity, P the gas pressure, $\mathbf{B}$ the magnetic field, and $\mathbf{a}$ is composed of the gravitational acceleration (which is time-independent) and of the Coriolis and centrifugal forces. The equations are solved in a frame rotating at the stellar rotation rate $\Omega_\star$. The sound speed is given by $c_s = \sqrt{\gamma P/\rho}$, with γ the ratio of specific heats. We use an ideal gas equation of state

$$\rho \varepsilon = P / (\gamma - 1)\ , \tag{3.5}$$

where ε is the specific internal energy per mass. We use an *hll* solver combined with a *minmod* limiter. A second-order Runge-Kutta is used for the time evolution, resulting in an overall second-order accurate numerical method. The solenoidality of the magnetic field is ensured with a constrained transport method (see Mignone et al. 2012). We refer the interested reader to (Mignone et al. 2007) for an extensive description of the various numerical methods that PLUTO offers. For this first study, we use a low-resolution grid of 224^3 points for a domain size of $[-20, 20]^3$. 96^3 uniform grids points are use to discretize the $[-1.5, 1.5]^3$ domain and stretched grids are used elsewhere.

The first control parameter of the modelled stellar wind is the ratio of specific heats γ. In order to ensure that the MHD modelling the wind produces velocities compatible with solar inferences (of the order of 400-500 km s^{-1} at 1 AU in the case the Sun), we choose a close-to-isothermal value of $\gamma = 1.05$. The structure of the stellar wind is then controlled by a set of parameters that can be written as velocity ratios at the surface of the star (see, *e.g.*, Matt et al. 2012).

In this work we model the corona of HD 189733. The escape velocity at the surface of HD 189733 is $v_{\rm esc} = 6.41 \times 10^7$ cm/s. We choose a standard coronal temperature of 2×10^6 K (equivalent to Llama et al. 2013) that sets the normalized sound speed at the surface of the star to $c_s/v_{\rm esc} = 0.29$. The rotation period of the star is 12 days, which results in a normalized rotation velocity $v_{\rm rot}/v_{\rm esc} = 5.0 \times 10^{-3}$. Based on these parameters, the stellar wind is then driven by our boundary conditions representing the base of the corona (see Strugarek et al. 2014a,c, for complete discussions on those boundary conditions).

The last parameter controlling the stellar wind is the magnetic field. We use the radial component of the observed magnetic field (Figure 1) and perform a potential extrapolation to define the 3D magnetic field in the whole domain at initialization (see the Appendix C in Schrijver & DeRosa 2003, for a full description of the potential extrapolation technique). The magnetic field in the boundary condition –which is effectively impacting the wind driving– depends only marginally on the exact location of the source surface used for the potential extrapolation. The initial magnetic field in the whole domain is directly related to the location of the source surface, but this initial condition is rapidly modified by the wind that establishes a steady-state configuration with both open and closed field regions that is independent of the initial potential field. As a result, the choice of the source surface has no impact on our simulation results as long as it is sufficiently distant from the stellar surface.

The amplitude of the magnetic field is constrained by the observations (Figure 1), but the density at the base of the corona is not. Hence, the Aflv́en speed at the base of our model is not well constrained. It can generally be related to the mass loss rate induced by the stellar wind (see Matt et al. 2012; Réville et al. 2014), which in some cases can be deduced from observations of astrospheric Lyα absorption (Wood 2004). However, we lack such observations for HD 189733 and are thus compelled to test a range of Alfvén speeds. We hereafter define the maximum Alfvén speed at the base of the corona by $v_a = \max(B)/\sqrt{4\pi\rho_\star}$, where B is the total magnetic field amplitude and $\rho_\star$ the density at the base of the corona. B is constrained by the observations, hence we choose three different base density values $\rho_\star \in \left\{1.51 \times 10^{-14},\, 2.13 \times 10^{-15},\, 8.3 \times 10^{-16}\right\}$ g cm^{-3} that lead to the averaged velocity ratios $v_a/v_{\rm esc} \in \{2.58,\, 6.79,\, 11.0\}$. The highest density we chose corresponds to the base density value chosen by Llama et al. (2013) which was tuned to reproduce the observed X-ray luminosity of HD 189733.

3.2 Results

In Figure 2 we show three dimensional renderings of the dynamical corona of HD 189733 for the three Alfvén velocities we considered. The blue (negative) and orange (positive) map shows the radial magnetic field at the base of the corona, where the stellar wind is driven in our model. The coronal magnetic field lines are shown in light blue, and the Alfvén surface is labelled by the transparent grey surface. We observe that for increasing base Alvén velocity, the Alfvén surface is further away from the star, retaining a similar global shape. This is a simple consequence of the decrease of the base density in the corona: the magnetic tension strengthens compared to the intertial and pressure forces of the wind, and the magnetic field retains more closed field lines, where the coronal plasma is imprisoned and the stellar wind hindered.

We can estimate *a posteriori* the mass loss rate $\dot{M}_w$ and angular momentum loss rate $\dot{J}_w$ of the stellar winds. In the third case ($v_a/v_{\rm esc} = 11$), we find a mass loss rate of $4.35 \times 10^{-13}\, M_\odot$ yr^{-1}, which is very close to the mass loss rate of $4.5 \times 10^{-13}\, M_\odot$ yr^{-1} found by Llama et al. (2013). The two other cases have higher mass loss rates, respectively 8.66×10^{-12} and 1.16×10^{-12} $M_\odot$ yr^{-1}. Following Matt et al. (2012); Réville et al. (2014),

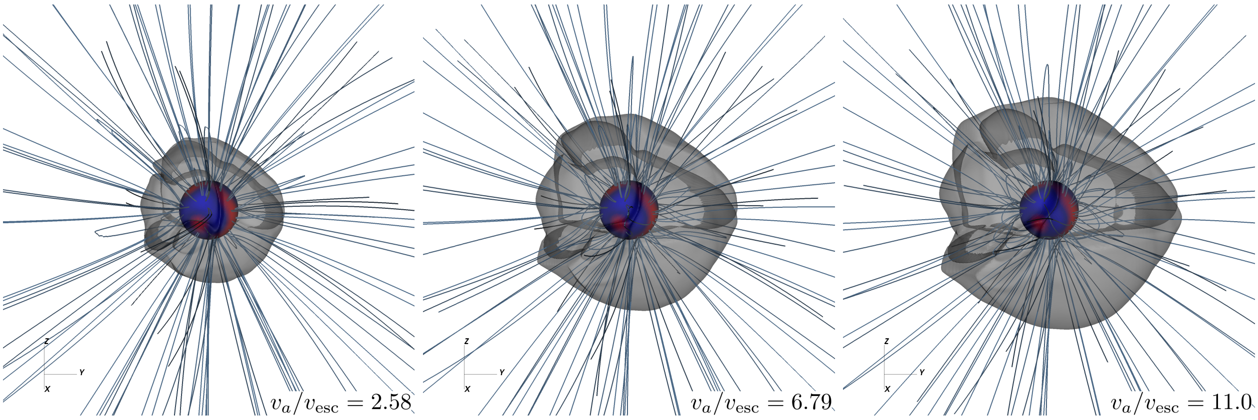

Fig. 2. 3D renderings of the coronal magnetic field (blue lines) of HD 189733. The color sphere shows the radial component of the magnetic field at the surface of the star. The transparent blue surface labels the Alfvén surface of the wind. From left to right, $v_a/v_{\rm esc}$ is 2.58, 6.79, and 11.0.

we define a torque-derived, effective Alfvén radius by relating the two loss rates through

$$\frac{R_a}{R_\star} \equiv \sqrt{\frac{-\dot{J}_w}{\dot{M}_w \Omega_\star}} \, ,$$

where $\Omega_\star$ is the rotation rate of the star. It was recently shown by Réville et al. (2014) that this effective Alfvén radius –at least in 2.5D axisymmetric models– can be related to the wind magnetization parameter

$$\Upsilon_o \equiv \frac{\Phi_o^2}{R_\star^2 \dot{M}_w v_{\rm esc}} \, ,$$

where the open magnetic flux is given by

$$\Phi_o = \int_S |\mathbf{B} \cdot \mathrm{d}\mathbf{S}| \, ,$$

where $\int_s .\mathrm{d}\mathbf{S}$ stand for the integral over a closed surface at a sufficiently large distance from the central star for the magnetic field lines to be all open. The average Alfvén radius and the magnetic confinement parameter are related through

$$\frac{R_a}{R_\star} = K_3 \left[\frac{\Upsilon_o}{\sqrt{1+(f/K_4)^2}} \right]^m \tag{3.6}$$

where the coefficients K_3, K_4 and m were determined empirically by Réville et al. (2014) to be $K_3 = 1.4 \pm 0.1$, $K_4 = 0.06 \pm 0.01$ and $m = 0.31 \pm 0.02$.

We compute R_a and Υ_o in our three models and display them in Figure 3. The scaling law predicted by Réville et al. (2014) is shown by the black line. The grey area labels the error bars of this scaling law. Our cases seem to follow roughly the scaling-law trend, but appear to be shifted downwards. This is in reality awaited since our reference scaling law was derived with a fixed sound speed ratio of $c_s/v_{esc} = 0.222$ (see Réville et al. 2014). In our case, we consider a much larger sound speed $c_s/v_{esc} = 0.2913$. By simply multiplying the K_3 coefficient (see equation (3.6)) by 0.65 (close to the ratio of the sound speed considered by Réville et al. (2014) and the one considered here), our results are nicely reconciled with the predicted scaling-law (red dashed line and red area). The power-law trend that was derived from axisymmetric models with only three different topologies (Réville et al. 2014) seems to apply, at least at first order, to non-axisymmetric topologies involving numerous spherical harmonics modes.

4 Conclusions

We have presented a set of simulations to model the coronal structure around distant stars based on observed magnetic maps. We applied this method to the case of HD 189733. Due to the lack of constrains on the

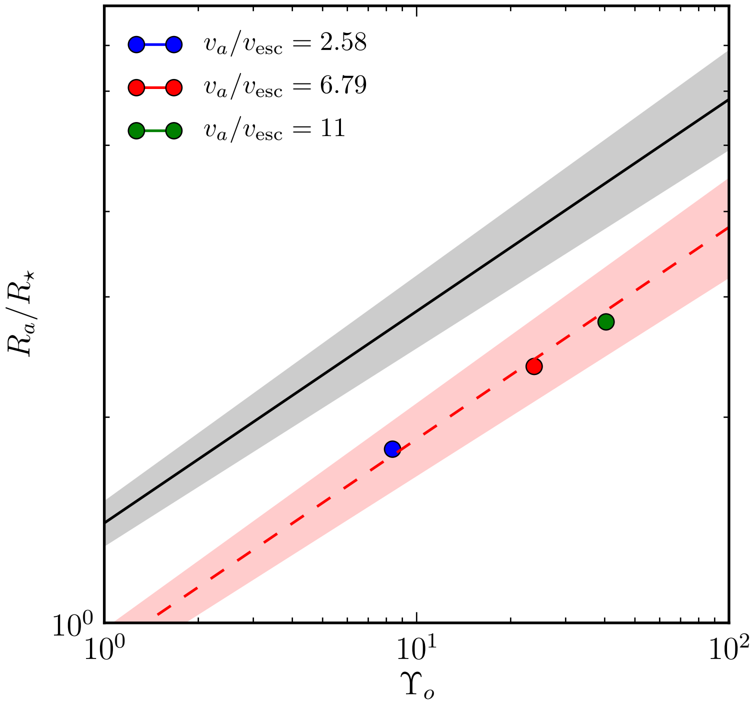

Fig. 3. Generalized Alfvén radius as a function of the wind magnetization parameter Υ_o (see text). The black line and grey area show the scaling law prediction from Réville et al. (2014). The dashed red line and red area represent the same scaling law, modified to account a different sound speed at the base of the corona.

mass loss rate of the star, models of the stellar wind of HD 189733 have free parameters, which we varied to explore their impact on the coronal structure, and on the mass and angular momentum loss rates of the star. In spite of the low resolution we used, and the complexity of the magnetic field topology, we find a good general agreement with the torque scaling law that was derived in 2.5D geometry by Réville et al. (2014) and our results compare very well with previous models of the corona of HD 189733 (Llama et al. 2013). Nevertheless, the slight discrepancies compared to the predicted torque scaling law warrant higher-resolution runs. Furthermore, HD 189733 is a slow-rotator; we intend to confirm the torque scaling law with three-dimensional simulations in the rapid-rotator regime as well in a near future.

HD 189733 is known to harbor a close-in Jupiter-like planet, HD 189733b, which orbits at 0.031 AU around its host ($R_p = 1.15\,R_J$ and $M_p = 1.13\,M_j$, see Boisse et al. 2009). It was recently suggested that due to its proximity, HD 189733b could possess a variable-size bow-shock along its phase, which could in principle be detected in near-UV transit lights (Llama et al. 2013). Such observations would then be extremely useful to better constrain stellar wind models. The wind model we presented here is a first step toward the global modelling of the star-planet system in the spirit of Cohen et al. (2014); Strugarek et al. (2014c).

AS thank A. Vidotto for discussions about the modelling of the corona of HD 189733. This work was supported by the ANR 2011 Blanc Toupies and the ERC project STARS2 (207430). The authors acknowledge CNRS INSU/PNST and CNES/Solar Orbiter fundings. AS acknowledges support from the Canada's Natural Sciences and Engineering Research Council and from the Canadian Institute of Theoretical Astrophysics (National fellow). We acknowledge access to supercomputers through GENCI (project 1623), Prace, and ComputeCanada infrastructures.

References

Boisse, I., Moutou, C., Vidal-Madjar, A., et al. 2009, A&A, 495, 959

Bouchy, F., Udry, S., Mayor, M., et al. 2005, A&A, 444, L15

Cohen, O. & Drake, J. J. 2014, ApJ, 783, 55

Cohen, O., Drake, J. J., Glocer, A., et al. 2014, ApJ, 790, 57
Fares, R., Donati, J.-F., Moutou, C., et al. 2010, MNRAS, 406, 409
Hébrard, G. & Lecavelier des Etangs, A. 2006, A&A, 445, 341
Llama, J., Vidotto, A. A., Jardine, M., et al. 2013, MNRAS, 2442
Matt, S. P., MacGregor, K. B., Pinsonneault, M. H., & Greene, T. P. 2012, ApJ, 754, L26
Mestel, L. 1968, MNRAS, 138, 359
Mignone, A., Bodo, G., Massaglia, S., et al. 2007, ApJS, 170, 228
Mignone, A., Zanni, C., Tzeferacos, P., et al. 2012, The Astrophysical Journal Supplement, 198, 7
Oran, R., van der Holst, B., Landi, E., et al. 2013, ApJ, 778, 176
Parker, E. N. 1958, ApJ, 128, 664
Réville, V., Brun, A. S., Matt, S. P., & Strugarek, A. 2014, submitted to ApJ
Schrijver, C. & DeRosa, M. 2003, Sol. Phys., 212, 165
Sokolov, I. V., van der Holst, B., Oran, R., et al. 2013, ApJ, 764, 23
Strugarek, A., Brun, A. S., & Matt, S. 2012, in SF2A-2012: Proceedings of the Annual meeting of the French Society of Astronomy and Astrophysics. Eds.: S. Boissier, 419–423
Strugarek, A., Brun, A. S., Matt, S. P., & Réville, V. 2014a, Nature of Prominences and their role in Space Weather, 300, 330
Strugarek, A., Brun, A. S., Matt, S. P., & Réville, V. 2014b, th Cambridge Workshop on Cool Stars, Stellar Systems, and the Sun, Proccedings of Lowell Observatory, 1
Strugarek, A., Brun, A. S., Matt, S. P., & Réville, V. 2014c, ApJ, 795, 86
Weber, E. J. & Davis, L. J. 1967, ApJS, 148, 217
Winn, J. N., Holman, M. J., Henry, G. W., et al. 2007, The Astronomical Journal, 133, 1828
Wood, B. E. 2004, *Liv. Rev. Sol. Phys.*, 1, 2

SF2A 2014
J. Ballet, F. Bournaud, F. Martins, R. Monier and C. Reylé (eds)

CONSEQUENCES OF THE ACCRETION OF PLANETARY MATTER ON THE CHEMICAL COMPOSITION OF THE STARS.

S. Vauclair[1] and G. Vauclair[1]

Abstract. The question of the possible modification of the abundances observed at the surface of stars in case of accretion of planetary matter has been debated for several years. Here we present some recent studies on this subject. At the beginning of the stars' life on the main sequence, contrary to what was assumed in the past, heavy matter accretion cannot lead to any overabundance of heavy elements because of the double-diffusive instability induced by the inversion of the mean molecular weight. This instability leads to partial extra-mixing which, in some cases, may induce lithium destruction. On the other hand, helium settling leads to stabilizing μ-gradients inside the stars during stellar evolution, so that heavy matter accretion can modify the observed chemical composition as long as the global μ-gradient does not become unstable.

Keywords: stars, accretion, chemical composition, hydrodynamics, mixing processes, lithium

1 Introduction

The question of the possible modifications of the metallic abundances in stellar outer layers as a result of the accretion of heavy planetary matter has been a subject of debate for many years. The observed exoplanet-host stars are, on average, metal-rich compared to stars without observed planets (Santos et al. (2001), Ghezzi et al. (2010a)). This average metal excess was a subject of discussion during at least one decade. Two options could arise at first sight. The high metallicity could be pristine, which means that a high metallicity in the original nebula helps planet formation, or it could be due to the accretion of planetary matter onto the star. Nowadays, this second possibility is completely excluded, for several reasons, one of them being that the metal-rich accreted matter cannot remain inside the outer convective zone. It rapidly falls down inside the star due to double-diffusive (thermohaline) convection (Vauclair (2004)), in such a way that no overabundance can remain (Garaud (2011)). On the other hand, this leads to extra mixing which may have some importance for the lithium destruction problem (Théado & Vauclair (2012)). We also have evidences of accretion of planetary matter onto white dwarf stars, due to observed heavy elements in their atmospheres, in relation to the presence of debris disks (Farihi et al. (2012)). Here again, double-diffusive (thermohaline) convection occurs below the outer convection zones and must be taken into account in the computations. In this paper, we give a short review of the hydrodynamical process referred to as thermohaline convection. Then we discuss its consequences in the case of accretion of heavy matter onto the stars, first for exoplanet-host stars, second for the special case of very old stars which accrete matter from a companion, and finally for white dwarfs.

2 The double-diffusive instability

In oceanography, the double-diffusive convection is a well-known physical process. In this context it is refereed to as thermohaline convection. The instability is induced by warm salted water lying on top of colder fresh water. The instability produces the so-called salt-fingers (see for instance Stern (1960), Veronis (1965), Kato (1966), Turner (1973), Shen & Veronis (1997), Turner & Veronis (2000), Yoshida & Nagashima (2003), Ruddick & Gargett (2003)).

[1] IRAP/OMP Université Paul Sabatier/CNRS, 14 avenue Edouard Belin, 31400-Toulouse

A density anomaly ratio is defined as: $R_\rho = \alpha\nabla T/\beta\nabla S$, with $\alpha = (1/\rho)(\partial\rho/\partial T)_{S,P}$ and $\beta = (1/\rho)(\partial\rho/\partial S)_{T,P}$, where ρ, T and S are the density, the temperature and the salinity respectively. The thermohaline instability develops when $1 \leq R_\rho \leq \tau^{-1}$, where the inverse Lewis number τ is the ratio of the salt to the temperature diffusivity: $\tau = \kappa_S/\kappa_T$.

Similar situations occur in stars. The role of the salt is played by the mean molecular weight, μ. Two kinds of double-diffusive instabilities may occur inside stars. The first one is the semi-convection which may develop when a stable μ gradient occurs in a region of unstable temperature gradient. The second one is the equivalent of the thermohaline convection, also called ' ' fingering convection" in this case, which may happen when an unstable μ gradient develops in a region of stable temperature gradient. These instabilities occur when the medium is stable against dynamical convection.

In stars, the equivalent of R_ρ is R_0 defined as: $R_0 = \delta(\nabla_{ad} - \nabla_{rad})/\phi\nabla\mu$, where $\delta = (\partial\ln\rho/\partial\ln T)$, $\phi = (\partial\ln\rho/\partial\ln\mu)$, and $\nabla\mu = d\ln\mu/\mu$. In this case the inverse Lewis number τ is the ratio of the particles to the temperature diffusivities: $\tau = \kappa_\mu/\kappa_T$. The fingering instability develops when $1 \leq R_0 \leq \tau^{-1}$. It has recently been explored through 3D numerical simulations for a range of characteristic physical parameters (Traxler et al. (2011), Brown et al. (2013), Zemskova et al. (2014)).

The fingering instability may develop under various conditions. It may occur when the stars accrete heavy material. This happens in the case of the exoplanet host stars accreting planetary matter, in the case of stars accreting enriched matter from an evolved companion as in the carbon enriched metal poor (CEMP) stars and in the case of the white dwarfs accreting heavy material from a debris disk.

It may also develop due to the accumulation of heavy elements in specific layers. This happens when the radiative acceleration on such elements exceeds gravity and decreases upwards (Richard et al. (2001), Vauclair & Théado (2012)). 3D numerical simulations have been done to refine the detailed hydrodynamics and give prescriptions to be used in 1D stellar models(see Zemskova et al. (2014)).

Fingering convection has also been invoked to explain abundance anomalies in red giant branch stars but it has been proved to have too small an effect to account for the observations (Wachlin et al. (2014) and references therein).

3 The case of the Exoplanet-Host Stars

As pointed out by (Santos et al. (2001), the overmetallicity of exoplanet-host stars does not depend on their effective temperatures, which means that they are independent of the depth of the convective zones. Vauclair (2004) showed how the accreted matter builds an inverse μ-gradient which leads to thermohaline (fingering) convection, so that the heavy elements are rapidly mixed inside the star. When this effect is taken into account, the accreted heavy elements are expected to be mixed down to similar depths, much below the convective zone, for all stars. At the end, a very small μ-gradient may remain, which is now proved much too small to account for the observed overmetallicity (Garaud (2011)).

This result is consistent with the detailed observations of Ghezzi et al. (2010c) who found that the overmetallicity of the subgiant exoplanet host stars was very similar to that of the main sequence ones, which would not be the case if it was due to accreted matter remaining inside the convective zone. It is also consistent with the observations by Teske et al. (2013) of the two stars of a binary system, one holding a planet contrary to the second (see also Schuler et al. (2011) for a similar case, as discussed below). The two stars are found quite similar for all astrophysical parameters, including detailed chemical composition. On the other hand, Ghezzi et al. (2010b) found that the overmetallicity is different for stars holding jovian planets and stars holding neptunian planets, which would be an indication that the type of planets which may form depend of the initial metallicity. All these considerations converge on the fact that the overmetallicity observed in exoplanet-host stars is pristine. This does not mean that accretion did not take place, but that the accreted material did not stay in the stellar outer layers.

An important consequence of the mixing process induced by the accretion of heavy elements is that it can modify the internal stellar structure, and also destroy some lithium at the beginning of the star's life on the main sequence. This was already suggested by Théado, Bohuon & Vauclair (2010) and confirmed by Garaud (2011) and Théado & Vauclair (2012). Lithium depletion in solar-type stars remains a challenge for stellar models. Extra mixing below the outer convective zone is needed to explain the observed abundances in the Sun, the solar analogs and the solar twins (e.g., Do Nascimento et al. (2009)). Several processes have been invoked in the past to account for this lithium depletion, like rotational induced mixing, but they fail to account for all the observed features and observed abundance dispersion.

The lithium abundance differences between exoplanet-host stars and stars without detected planets is still a subject of debate. Ghezzi et al. (2010a) gave a recent review on that subject and showed that an overall comparison between the two samples gives no obvious differences except in the range 5700 K $< T_{eff} <$ 5850 K where the lithium abundance is $\approx$ 0.26 dex lower in stars with planets than in stars without planets. This is the typical effective temperature range where the bottom of the convective zone becomes close enough to the lithium destruction region, so that the final lithium abundances are very sensitive to the mixing processes occuring there.

A spectacular result in that respect was obtained by Schuler et al. (2011) who determined the detailed astrophysical parameters and chemical compositions of the two components of the binary system 16 Cygni. The main particularity of that system is that 16 Cyg B hosts a giant planet whereas 16 Cyg A has no detected planet. The two stars are very similar, with effective temperatures of 5796$\pm$34 K for 16 Cyg A and 5753$\pm$30K for 16 Cyg B. They also have similar gravities, log g = 4.38$\pm$0.12 for 16 Cyg A and 4.40$\pm$0.12 for 16 Cyg B. The abundances of 15 elements were derived with high signal to noise ratio echelle spectra. They were found indistinguisable between the two stars... except for lithium, which is depleted by a factor at least 4.5 in 16 Cyg B compared to 16 Cyg A. According to the Théado & Vauclair (2012)'s results, this could be an indication of the accretion of planetary matter onto 16 Cyg B followed by thermohaline convection.

4 The case of the Carbon-Enhanced Metal Poor stars

Carbon-enhanced metal poor stars (CEMPs) show abundance anomalies which could be accounted for in case of accretion from an AGB companion. Stancliffe et al. (2007) pointed out that in case of accretion of metal-rich matter, this material would subsequently fall down inside the star due to thermohaline convection. In a more recent paper (Thompson et al. (2008)), we suggested that, between the stellar birth and the time when the AGB sends its processed material onto it, the main sequence star had time to suffer helium and heavy element diffusion below its convective zone, thereby creating a stabilizing μ-gradient. In the presence of this diffusion-induced μ-gradient, outside matter may accumulate in the convection zone until the overall μ-gradient becomes flat (see also Stancliffe & Glebbeek (2008), Stancliffe et al. (2009), Stancliffe (2010)). In this case, the thermohaline mixing is strongly limited by the pre-existing stable μ-gradient, induced by helium settling. This is not expected to occur in the case of exoplanets-host stars which accrete matter at the very beginning of their lives, when atomic diffusion has not yet had time to build important helium gradients.

5 The case of the white dwarfs

A large fraction of DA and DB white dwarfs, maybe as large as $\approx$50%, shows absorption lines of heavy elements in their spectra (Desharnais et al. (2008), Zuckerman et al. (2010), Zuckerman et al. (2011), Gänsicke et al. (2012), Koester et al. (2014)). Many of these stars also show evidence of infrared-excess in their spectral energy distribution. This proves the existence of debris disks orbiting the white dwarfs. It also proves that an ongoing accretion of material originating from the disk is polluting the chemical composition of the white dwarf outer layers. These polluted DA and DB white dwarfs are then classified as DAZ and DBZ. When different heavy elements are present, their relative abundance ratios are similar to those measured for the rocky planetesimals, asteroid-type, in the solar system (Melis et al. (2011), Dufour et al. (2012), Gänsicke et al. (2012), Xu et al. (2014)). It strongly suggests that these debris disks are the remnants of the primordial planetary system.

From the derived abundances of the heavy elements it is possible to estimate the accretion rates. To derive such rates, it was previously assumed that the accreted heavy elements are mixed in the outer convection zone, or in the radiative atmosphere when there is no convection zone, and then diffuse downwards due to the efficient gravitational settling. Accretion rates were then estimated by assuming a steady state between accretion and gravitational settling (see for instance Farihi et al. (2012)).

However, the importance of the thermohaline (fingering) convection induced by the increase of heavy elements abundances in the outer stellar layers has been overlooked in these estimates. Due to this process, the accreted material is mixed much deeper in the outer layers of the white dwarf. As a consequence larger accretion rates are required in order to reproduce the observed heavy elements abundances. A preliminary study of the consequences of the fingering convection on the derived accretion rates shows that the effect may be important for the accretion rates on DAZ white dwarfs but not in the case of the DBZ (Deal et al. (2013)). According to this study, the fingering convection starts in the DAZ as soon as the relative increase of the mean molecular weight in the polluted layers, $\Delta\mu/\mu$, exceeds $\approx 10^{-6}$.

As an example, in a typical DA white dwarf of $0.59M_{\odot}$, with an effective temperature of 10600 K, the accretion rate needed to reproduce an observed Ca abundance [Ca/H]= -7.2, is four times larger when thermohaline convection is taken into account, than when it is estimated with gravitational settling only. This discrepancy rises to a factor 200 for a DA model with 12800 K. On the contrary, for the DB white dwarfs, the simulations show no or only marginal fingering instability. The main reason is that in DB white dwarfs the depth of the convection zone is much deeper than in DA white dwarfs. As a consequence of the physical conditions which prevail below the convection zone, the parameter R_0 exceeds the inverse Lewis number so that fingering convection is not triggered. This effect is a very simple and straightforward explanation of the apparent paradox raised by the DAZ and DBZ observations.

6 Conclusions

The important conclusions of these studies are :

- The abundances observed at the stellar surfaces are not always representative of the original abundances. This is important in the framework of the chemical evolution of galaxies.
- When computing the abundances evolution at the surface of stars, it is not enough to take into account microscopic diffusion processes and accretion of external matter. The induced thermohaline (fingering) process and its consequences have also to be investigated.
- Thermohaline convection induced by accretion of heavy matter and/or internal accumulation of heavy elements in specific layers leads to extra-mixing which may help understanding the observed lithium abundances, and may also modify the internal stellar structure.
- At the epoch of precise determination of the internal structure of stars with the help of asteroseismology, this microscopic-macroscopic connexion cannot be ignored.

References

Brown, J.M., Garaud, P. and Stellmach, S. 2013, ApJ, 768, 34
Deal, M., Deheuvels, S., Vauclair, G., Vauclair, S. and Wachlin, F.C. 2013, A&A, 557, 12
Desharnais, S., Wesemael, F., Chayer, P. et al. 2008, ApJ, 672, 540
Do Nascimento, J.D.Jr., Castro, M., Meléndez, J. et al. 2009, A&A, 501, 687
Dufour, P., Kilic, M., Fontaine, G. et al. 2012, ApJ, 749, 6
Farihi, J., Gänsicke, B., Wyatt, M.C. et al. 2012, MNRAS, 424, 464
Gänsicke, B., Koester, D., Farihi, J. et al. 2012, MNRAS, 424, 333
Garaud, P. 2011, ApJ, 728, 30
Ghezzi, L., Cunha, K., Smith, V.V. & de la Reza, R. 2010b, ApJ, 724, 154
Ghezzi, L., Cunha, K., Smith, V.V. et al. 2010a, ApJ, 720, 1290
Ghezzi, L., Cunha, K., Schuler, S.C. & Smith, V.V. et al. 2010c, ApJ, 725, 721
Kato, S. 1966, PASJ, 18, 374
Koester, D., Gänsicke, B. and Farihi, J. 2014, A&A, 566, 34
Melis, C., Farihi, J., Dufour, P. et al. 2011, ApJ, 732, 90
Richard, O., Michaud, G. and Richer, J. 2001, ApJ, 558, 377
Ruddick, B. & Gargett, A.E. 2003, PrOce, 56, 381
Santos, N.C., Israelian, G. & Mayor, M. 2001, A&A, 373, 1019
Schuler, S.C., Cunha, K., Smith, V.V. et al. 2011, ApJL, 737, L32
Shen, C.Y. & Veronis, G. 1997, JGR, 10223131
Stancliffe, R.J., Glebbeek, E., Izzard, R.G and Pols, O.R. 2007, A&A, 464, 57
Stancliffe, R.J. & Glebbeek, E. 2008, MNRAS, 389, 1828
Stancliffe, R.J., Churck, R.P., Angelou, G.C. and Lattanzio, J.C. 2009, MNRAS, 396, 2313
Stancliffe, R.J. 2010, MNRAS, 403, 505
Stern, M.E. 1960, Tellus, 12, 172
Teske, J.K., Cunha, K., Schuler, S.C. et al. 2013, ApJ, 778, 132

Théado, S., Bohuon, E. & Vauclair, S. 2010, Light Elements in the Universe, Proceedings of the International Astronomical Union, IAU Symposium, Volume 268, p. 427-428

Théado, S. & Vauclair, S. 2012, ApJ, 744, 123

Thompson, I.B., Ivans, I.I., Bisterzo, S. et al. 2008, ApJ, 677, 556

Traxler, A., Garaud, P. and Stellmach, S. 2011, ApJ, 728, L29

Turner, J.S. 1973, E&PSL, 17,369

Turner, J.S.& Veronis, G. 2000, JFM, 405, 269

Vauclair, S. 2004, ApJ, 605, 874

Vauclair, S. & Théado, S. 2012, ApJ, 753, 49

Veronis, G. 1965, Tellus, 17, 77

Wachlin, F.C., Vauclair, S. and Althaus, L.G. 2014, arXiv 1409.4216

Xu, S., Jura, M., Koester, D. et al. 2014, ApJ, 783, 79

Yoshida, J. & Nagashima, H. 2003, PrOce, 56, 435

Zemskova, V., Garaud, P., Deal, M. and Vauclair, S. 2014, arXiv 1407.1437

Zuckerman, B., Melis, C., Klein, B. et al. 2010, ApJ, 722, 725

Zuckerman, B., Koester, D., Dufour, P. et al. 2011, ApJ, 739, 101

Session 09

Comment fabrique-t-on une galaxie ? L'évolution des baryons dans les halos de matière noire

SF2A 2014
J. Ballet, F. Bournaud, F. Martins, R. Monier and C. Reylé (eds)

GALAXY CLUSTERS IN THE COSMIC WEB

A. Acebrón[2,1], F. Durret[2], N. Martinet[2], C. Adami[3], L. Guennou[4] and the DAFT/FADA team

Abstract. Simulations of large scale structure formation in the universe predict that matter is essentially distributed along filaments at the intersection of which lie galaxy clusters. We have analysed 9 clusters in the redshift range $0.4 < z < 0.9$ from the DAFT/FADA survey, which combines deep large field multi-band imaging and spectroscopic data, in order to detect filaments and/or structures around these clusters. Based on colour-magnitude diagrams, we have selected the galaxies likely to be in the cluster redshift range and studied their spatial distribution. We detect a number of structures and filaments around several clusters, proving that colour-magnitude diagrams are a reliable method to detect filaments around galaxy clusters. Since this method excludes blue (spiral) galaxies at the cluster redshift, we also apply the LePhare software to compute photometric redshifts from BVRIZ images to select galaxy cluster members and study their spatial distribution. We then find that, if only galaxies classified as early-type by LePhare are considered, we obtain the same distribution than with a red sequence selection, while taking into account late-type galaxies just pollutes the background level and deteriorates our detections. The photometric redshift based method therefore does not provide any additional information.

Keywords: Cosmology, Cosmic Web, Filaments, Galaxy Clusters

1 Introduction

Formation and evolution of structures in the Universe is still one of the major issues in modern astronomy.
N-body simulations of the dark matter distribution on very large scales (Bond et al. 1996) predict that structures of galaxies consist of rich and poor clusters, connected by filaments and sheets, with regions largely devoid of galaxies (voids) in between. Due to the recent availability of new, better quality, wide and deep field surveys, intensive observations followed (large galaxy redshift surveys, York et al. 2010 for instance) showing that matter is not randomly distributed but is rather concentrated along filaments at the intersection of which lie galaxy clusters forming the cosmic web. However, fewer investigations have focussed on the detection of filaments around galaxy clusters in order to comprehend their formation and evolution processes.
In hierarchical structure formation modelling, galaxy clusters grow through repeated mergers with other galaxy clusters, groups, etc., but also accreting matter from their environment (Zeldovich et al. 1982) which occurs in a highly non-isotropic manner: galaxy filaments feed clusters along preferred directions (Pimbblet, 2005).
Although ubiquitous in large-scale galaxy surveys, filaments have proven difficult to characterise physically, owing to their low density or because elongated structures of galaxies in some cases turn out to be the result of recent cluster mergers. Colour-magnitude diagrams and photometric redshift computations are the most efficient methods to analyse wide fields.
Previous works have shown that the detection of filaments around galaxy clusters is possible though (see for example: Dietrich et al. 2005 and 2012; Tanaka et al. 2007; Jauzac et al. 2012). The DAFT/FADA (Dark energy American French Team, PIs: C. Adami, M. Ulmer, and D. Clowe) program, which is a combined France/USA effort, aims to produce a large survey of rich clusters with photometric redshifts for all the galaxies, by combining HST archives with ground-based photometry on 4m class telescopes, of 90 high redshift ($0.4 <$ z < 0.9) massive

[1] Observatoire de Paris-Meudon, UFE, 92195 Meudon Cedex, France
[2] UPMC Université Paris 06, UMR 7095, Institut d'Astrophysique de Paris, 98bis Bd Arago, F-75014, Paris, France
[3] LAM, OAMP, Université Aix-Marseille & CNRS, Pôle de l'Etoile, Site de Château Gombert, 38 rue Frédéric Joliot-Curie, 13388 Marseille 13 Cedex, France
[4] IAS, CNRS & Université Paris Sud, Bâtiment 121, 91405 Orsay, France

(M > 2 × 10^{14} $M_\odot$) clusters of galaxies. DAFT/FADA is therefore a promising database to detect filaments around galaxy clusters.
We have focused on the analysis of coulour-magnitude diagrams and photometric redshift computations from BVRIz bands with the aim of detecting large scale structures around several clusters.
We present hereafter in section 2 the data and methods used in this study, followed in section 3, by the results and discussion. Throughout the report, we use the standard cosmological model with $\Omega_M = 0.3$, $\Omega_\Lambda = 0.7$ and $H_0 = 70$ km s^{-1} Mpc^{-1}.

2 Data and methods

2.1 The optical and spectroscopic data

In order to detect filaments and/or groups of galaxies around galaxy clusters we use deep wide-field multi-band imaging (see details on the reduction process in Guennou et al. 2010) and spectroscopic data.
From all the clusters of the DAFT/FADA database we only consider clusters having good-quality deep wide field images (since we aim to detect large-scale structures) and spectroscopic redshift catalogues, retrieved from the NED archive, in a 30 arcmin radius around each cluster. The coordinates of the cluster centers are taken from NASA/IPAC Extragalactic Database (NED, `http://ned.ipac.caltech.edu/`).
Our data come in majority from 4m to 8m class telescopes like the Canada France Hawaii Telescope (CFHT, 3.6m), Subaru (8.2m), SOAR (4.1m). The images were obtained using the dithering technique.
For each cluster we work with 5 different bands (B or u, V or g, R, I, z). We use only V or g and I for the colour-magnitude diagrams and all the bands to compute photometric redshits with LePhare package in section 3. We have analyzed 9 clusters in the redshift range 0.4<z<0.9.

2.2 Coulour-magnitude diagrams

In this section we present all the steps to obtain colour-magnitude diagrams in order to select early-type galaxies at redshifts close to that of the cluster. We plot V-I as a function of I in order to encompass the Balmer break (400 nm) in this redshift range.
SExtractor (Bertin & Arnouts 1996) is used to extract the magnitudes (in the AB system) of all the sources in our images in the V and I bands separately. SExtractor extracts not only galaxies and stars but also defects in the image.
Since we are only interested in analyzing galaxy magnitudes, we separate stars and defects from galaxies in our I band catalogue. To do so, we plot the maximum surface brightness $\mu_{max}(I)$ in the I band as a function of I. Stars and defects are located in precise regions in this plot and can easily be removed from our catalogues. We only consider galaxies with a magnitude brighter than I=23, which is the completeness level for the clusters we have studied. Thus, we obtain a catalogue containing only galaxies brighter than I=23, for which we also measured magnitudes in the V band and added spectroscopic redshifts when available.
Magnitudes are corrected for Galactic dust extinction using the Galactic dust full-sky maps of Schlegel et al. (1998).

The (V-I) vs. I colour-magnitude diagram is shown in Fig. 1 for the cluster MACS 0717.5+3745. Since we are working on large field images, we detect many sources that, at first sight, pollute the red sequence. We then plot the galaxies located in a radius of 1 Mpc from the cluster centre in order to better detect the cluster red sequence. Also, the galaxies having spectroscopic data, allow us to clearly identify the red sequence since they are located on it. We compute the best fit to the (V-I) vs. I relations for magnitudes I$\leq$23 by applying a linear regression to the galaxies located in a radius of 1 Mpc around the central coordinates (taken from NED). We then eliminate the galaxies located more than $\pm$0.6 away from this relation and recompute the (V-I) vs. I relation, keeping the galaxies located $\pm$0.3 mag away from the sequence as shown in Fig. 1. These galaxies thus have a high probability of being at the same redshift as the cluster.
With this method we select galaxies with a high probability to belong to the cluster but, in the process, we lose some spiral (blue) galaxies which can be at the cluster redshift but fall below the red sequence.

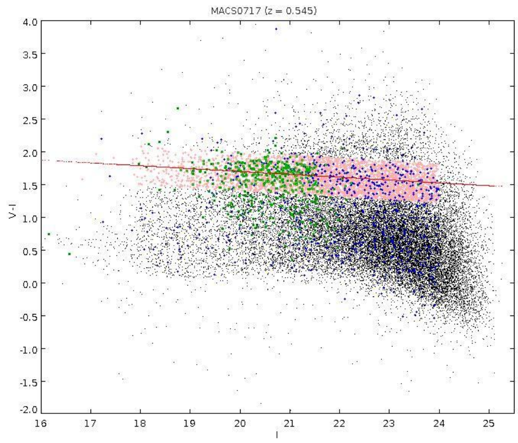

Fig. 1. (V - I) vs I colour-magnitude diagram for MACS 0717.5+3745. The black points show all the galaxies in the images. The blue points correspond to the galaxies located in a radius of 1 Mpc from the cluster centre. The green points are the galaxies with spectroscopic redshifts in the cluster. The pink points are the galaxies located ±0.3 mag away from the cluster red sequence, and are considered to be at the cluster redshift (see text).

2.3 *Photometric redshift computation*

We now present a second method to detect filaments around the clusters in our sample. The first DAFT/FADA paper (Guennou et al. 2010) established the reference basis for the photometric redshift computation.
Having a large sample of spectroscopic redshifts is obviously a better and a more precise way to detect filaments than using photometric redshifts. However, obtaining a large sample of spectroscopic redshifts requires a great amount of telescope time, while photometric redshifts can be computed for very large samples of galaxies, but of course with a lower precision than spectroscopic redshifts. We compute our photometric redshifts (hereafter photo-zs) with the LePhare package (see Arnouts et al. 1999; Ilbert et al. 2006 for details) and present here the main points of the technique.
We provide LePhare with a catalogue including, for each object, the coordinates of the object, the magnitudes (extinction corrected) in all 5 optical bands and their errors, and spectroscopic redshifts when available. LePhare compares the observed magnitudes with those of template galaxies with the aim of estimating the redshift and/or other parameters, such as the photometric type (numbers 1-7 correspond to early type galaxies, numbers 8-12 to early spirals galaxies, numbers 20-31 to very blue galaxies).
The program performs a χ^2 fitting analysis between the observed and template fluxes to estimate the redshift. Since we did not observe all the clusters with the same telescope and filters (and even for some clusters, the data in the 5 bands came from various telescopes), we had to convert our magnitudes into a single magnitude system (the VLT/FORS2 BVRIz system) with LePhare. This was done in particuler to compare our photo-zs based on 5 optical bands with those of Martinet et al. (2014), who used one more band (infrared), and therefore obtained photo-zs expected to be more precise, but in smaller fields (the infrared images are smaller than the optical ones).
We also included spectroscopic redshifts as inputs (when available) since LePhare can estimate possible shifts in photometric zero-points by comparing the photometric and spectroscopic redshifts.
The comparison of the 5 band and 6 band photo-zs shows they are in quite good agreement in the redshift range $0.45 < z < 0.9$, so we will be able to search for large scale structures based on the photo-zs we obtained in the large fields covered by the 5 optical bands.

3 Results

We show in Fig. 2 the distribution maps of the galaxies selected by colour-magnitude relations for three clusters: MACS 1621.4+3810, MACS 1423.8+2404 and MACS 0717.5+3745. The galaxy distributions around these clusters show clear elongations of several Mpc in length.
The six other clusters that we analysed do not show clear elongations.

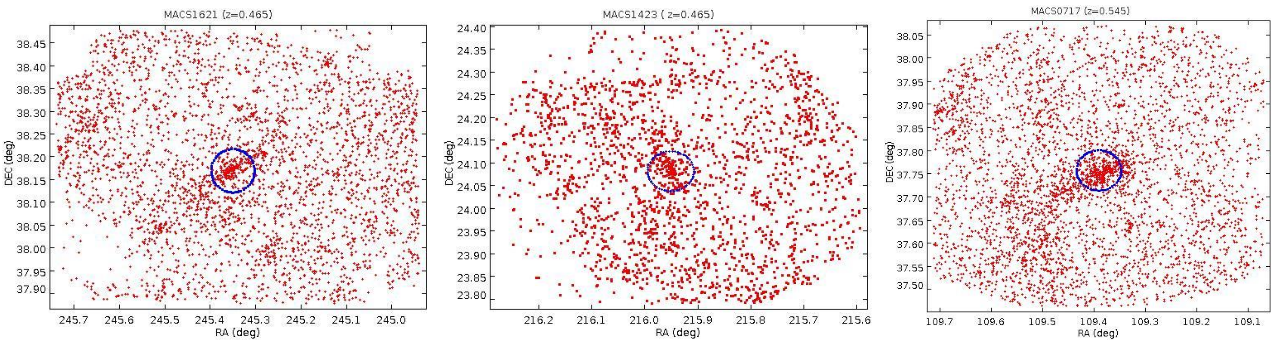

Fig. 2. Distribution maps of the galaxies selected to be at redshifts similar to those of the clusters, based on the (V-I) vs. I colour-magnitude diagrams, for MACS 1621.4+3810 (left), MACS 1423.8+2404 (center) and MACS 0717.5+3745 (right). The blue circles show the positions of the cluster centers according to the NED/IPAC coordinates and have a radius of 1 Mpc.

4 Discussion and conclusions

The DAFT/FADA project possesses a promising database to analyse large scale structures such as filaments and/or groups around galaxy clusters. We have searched for filaments around 9 galaxy clusters with two different methods based on optical imaging and spectroscopic data.
The colour-magnitude diagram method has proven to be reliable for this cosmic quest: we have detected elongations of several Mpc around several clusters.
We have also tested computing photo-zs using 5 optical bands and compared our results with 6-band photo-zs. The selection based on photometric redshifts hasn't given any additional information relatively to that based on the colour-magnitude relation, since only elliptical galaxies are well constrained by LePhare.
Although the methods we have used have some limitations (only ellipticals are considered with colour-magnitude diagrams and late-type galaxies are badly constrained with LePhare), they nonetheless do allow to reliably detect elongations. For example, the elongation found in MACS 0717.5+3745 is confirmed by weak lensing and spectroscopy (Jauzac et al. 2012, Martinet et al. 2015, in preparation).
Another limitation of our work is that galaxy filaments do not have yet a specific definition (Pimbblet, 2005): do they have to have a minumum length, are they above a threshold in the galaxy density relative to the average background level, etc? This lack of precise definition will certainly require further analysis.
As a continuation of the work presented here, we intend to apply the colour-magnitude diagram method to the 18 remaining DAFT/FADA clusters for which we have deep wide field imaging), and also to other surveys like the CFHTLS which has more than 4000 candidate clusters up to z=1.4 detected by our team (Durret et al. 2011).

Once a great number of filaments has been detected around clusters, the properties of galaxies in the filaments could also be analyzed, such as the morphological properties of the galaxies in the filaments (early-type, late-type) and also the position angles of their spins relative to the filament.

Continuing this cosmic quest and detecting filaments around galaxy clusters would thus help us to understand better the formation and evolution of galaxy clusters.

Acknowledgements
A. Acebrón thanks CNRS for financial support during this internship. We also acknowledge long term financial support from CNES.

References

Arnouts S., Cristiani S., Moscardini L. et al. 1999, MNRAS 310, 540
Bertin E. & Arnouts S. 1996, A&A 117, 393
Bond J.R., Kofman L., Pogosyan D. 1996, Nature 380, 3320
Dietrich, J. P.; Schneider, P. ; Clowe, D. et al., 2005, A&A 440, 453

Dietrich, J. P.; Werner, N.; Clowe, D. et al., 2012, Nature 487, 202
Durret F., Adami C., Cappi A. et al. 2011, A&A 535, 65
Guennou L., Adami C., Ulmer M.P. et al. 2010, A&A 523, 21
Ilbert O., Arnouts S., McCracken H.J. et al. 2006, A&A 457, 841
Jauzac M., Jullo E., Kneib J.P. 2012, MNRAS 426, 3369
Martinet N., Durret F., Adami C. et al. 2014, A&A in revision
Pimbblet K.A. 2005, PASA 22, 136
Schlegel D.J., Finkbeiner D.P., Davis M. 1998, ApJ 500, 525
Tanaka, M.; Hoshi, T,; Kodama, T. & Kashikawa, N., 2007, MNRAS 379, 1546
York D.G., Adelman J., Anderson Jr J.E. et al. 2000, AJ 120, 1579
Zeldovich Ia. B., Einasto J., Shandarin S. F. 1982, Nature 300, 407

SF2A 2014
J. Ballet, F. Bournaud, F. Martins, R. Monier and C. Reylé (eds)

SIMULATING MOCK CATALOGUES TO PROVIDE ACCURATE CLUSTER SELECTION FUNCTIONS.

B. Ascaso[1], S. Mei[1] and N. Benitez[2]

Abstract. Galaxy clusters are one of the main probes to constrain dark energy parameters in the present theories of formation and evolution of the Universe. Many present and future surveys are expected to provide large number of clusters ranging both a wide range of mass and redshift. In this summary, we introduce recent results on present galaxy cluster and groups samples extracted from datasets with different properties. In particular, we demonstrate that datasets with similar depth are able to detect clusters and groups with high reliably down to lower masses if the photometric redshift resolution is higher. We also present preliminary work performed on predicting the cluster selection function for clusters in next generation surveys. We first describe the main mock catalogue, transformed to make the photometry more realistic for each different survey and we finally report some results regarding the photometric redshift accuracy obtained for the next-generation surveys considered and their corresponding cluster selection functions obtained.

Keywords: Galaxies: clusters: general, Galaxies: groups: general, Cosmology, Cosmology: cosmological parameters, Cosmology: observations, Cosmology: dark matter, Cosmology: dark energy, Cosmology: large-scale structure of Universe, Galaxies: evolution

1 Introduction

Galaxy cluster surveys are very powerful tools to constrain cosmological scenarios and study evolutionary trends on galaxy evolution in dense environments. At present, a wide range of surveys exists in the literature, many of which have been detecting galaxy clusters with a variety of optical/IR methods (see Ascaso 2013 and references herein), as well as other non-optical techniques such as X-rays, SZ techniques, Weak Lensing, etc (e.g. Allen et al. 2011). With the advent of the next-generation surveys, a large percentage of the observable sky will be completed and we need to estimate the selection function of the future cluster samples with high accuracy to exploit at maximum their potential at setting constraints on cosmology and galaxy evolution scenarios.

In this summary, we start in section §2 by reviewing some results on present cluster samples detected with the Bayesian Cluster Finder (sect §2). Then, in section §3, we introduce a representative sample of next-generation surveys and the numerical simulation used in this work to reproduce realistically the properties of these surveys. Finally, in section §4, we mention briefly some results on the photometric redshift performance and selection function of these next generation surveys.

2 Galaxy cluster samples in present surveys

2.1 The Bayesian Cluster Finder

The Bayesian Cluster Finder (BCF, Ascaso et al. 2012, 2014) is a technique developed to detect galaxy clusters based on the matched filter algorithm (Postman et al. 1996) from a Bayesian point of view. The method is able to determine the position, redshift and richness of the cluster through the maximization of a filter depending on galaxy luminosity, density and photometric redshift combined with a galaxy cluster prior that accounts for color-magnitude relations and brightest cluster galaxy-redshift relation. One of the main advantages of this method is that galaxy clusters and groups without a well-formed red sequence can still be detected.

[1] Observatoire de Paris, 77 Denfert Rochereau, 75014, Paris, France
[2] Instituto de Astrofísica de Andalucía, Glorieta de la Astronomía s/n, 18008, Granada, Spain

2.2 Considered present surveys

Currently, we have applied the BCF to three present surveys: the CFHTLS-Archive Research survey (CARS, Erben et al. 2009), the Deep Lens Survey (DLS, Wittman et al. 2002) and the Advanced Large, Homogeneous Area Medium Band Redshift Astronomical (ALHAMBRA) Survey (Moles et al. 2008). Each of these surveys was designed with different purposes and therefore, they have very different features.

The CARS is a wide-area (37 deg^2) relatively deep (I$\leq$25.5 mag/arcsec^2), five-band optical survey, providing a expected photometric resolution, $\Delta z/(1+z)$, of $\sim$ 0.06 (Erben et al. 2009). The DLS is a 20 deg^2 very deep (R$\leq$27.5 mag/arcsec^2), four ($BVRz^{'}$) optical survey, with an expected photometric resolution of $\sim$ 0.08 (Schmidt & Thorman 2013). Finally, the ALHAMBRA survey is a smaller area (4 degrees square survey divided in 8 different regions), imaged with 20 narrow-band filter and three infrared JHK bands, providing a photometric resolution of $\sim$ 0.01 (Molino et al. 2014) and an estimated depth of $F_{814W} \leq 24.5 mag/arcsec^2$.

We have applied the BCF to these different surveys to detect galaxy clusters and groups (see Ascaso et al. (2012), Ascaso et al. (2014) and Ascaso et al. in prep for the CARS, DLS and ALHAMBRA survey respectively). The resulting cluster and group samples are spread within different redshift and masses ranges and we have demonstrated that all the detections agree well (>80%) with overlapping optical, spectroscopy, weak lensing and X-ray samples confirming the reliability of the methodology.

One remarkable result extracted from the comparison of these surveys is the fact that, for a similar depth survey, the photometric resolution of the survey is directly related to the minimum mass threshold that we expect to detect galaxy clusters with high completeness and purity. For instance, based on simulations, we obtain that for the ALHAMBRA survey, we can reliably detect groups down to $10^{13.7} M_{\odot}$ whereas for the CARS survey, the mass threshold we obtained was $10^{14.2} M_{\odot}$. This discovery has motivated us for investing effort in investigating the performance of the photometric redshift of next-generation surveys and developing techniques to improve their performance, if possible (see next section).

3 Galaxy cluster samples in next generation surveys

While present optical cluster samples do not allow to significantly set constrains on dark energy models such as the dark energy equation of state; this is not the case for samples extracted from next generation surveys where unexplored ranges of redshift and mass are going to be explored. We then present here a project consisting of studying consistently the photometric redshift performance of different next-generation surveys to measure their cluster selection function. We will eventually set cosmological constraints on dark energy parameters with a variety of models.

3.1 Next generation surveys considered

We have selected three of the most relevant next-generation stage IV surveys (Albrecht et al. 2006). Following a chronological order of starting date, we have first considered the Javalambre-Physics of the Accelerated Universe Astrophysical Survey* (J-PAS, Benitez et al. 2014). This survey, starting in 2015, is a 54-narrow band, very wide field cosmological survey covering 8600 square degrees of the northern sky imaged from the Javalambre Observatory in Teruel (Spain). The depth of the survey is expected to be ∼23.5 AB in all bands and the overall photometric redshift performance of 0.003(1+z) down to 22.5 AB according to simulations (Benitez et al. 2014, Ascaso et al. 2014 in prep, Zandivarez et al. (2014)).

Secondly, we have considered the Large Synoptic Survey Telescope† (LSST, Ivezic et al. 2008), starting in 2018. The LSST will become a large, wide-field ground-based survey, imaging the whole visible southern sky from an 8.4m telescope Cerro Pachon (Chile) with six broad-band optical bands *ugrizy* down to r=27.5 AB after coadding 10 years of operations.

Finally, in 2020 the Euclid survey‡(Laureijs et al. 2011) will be started. The Euclid Wide Field will cover 15,000 square degrees of the sky in the near IR (YJH), down to ∼24 mag in H band providing also near-IR spectroscopy and the survey will also include two Deep Fields, about 2 magnitude deeper than the wide survey which will cover around 20 square degrees each. The Euclid space observations will be combined with other space and ground-based observations to obtain the source photometric redshifts and physical properties.

*http://j-pas.org/
†http://www.lsst.org/lsst/
‡http://www.euclid-ec.org/

Among the optical surveys that will be available from the ground, one is already available, the Sloan Digital Sky Survey (SDSS), and two are planned: the LSST and the Dark Energy Survey (DES, The Dark Energy Survey Collaboration 2005). Hence, we will consider two cases for this survey: the case where the optical counterpart will come from the DES + LSST and the case where the optical counterpart will only come from the DES survey.

3.2 Creating realistic mock catalogues

We have developed a method that, given an input mock catalogue, is able to recalibrate the photometry by using a fully representative empirical set of realistic templates and simulate the expected conditions for a particular survey (Ascaso et al. in prep). This methodology was already applied in Arnalte-Mur et al. (2014), where we showed that obtaining photometric redshifts directly from mock photometry mimicking the ALHAMBRA survey provided a mean photometric redshift dispersion three times higher than the expected for the real data (Molino et al. 2014).

As a basis to create our mock catalogues, we have used a mock catalogue based on the publicly available light cone mock catalogues by Merson et al. (2013). These catalogs are extracted from an N-body simulation from the Millennium simulation, (Springel 2005) and semi-analytic model of galaxy formation from GALFORM (Cole et al. 2000; Bower et al. 2006). The chosen mock catalogue covers 500 deg^2 down to very deep magnitudes (K$\sim$24). It is well known that semi-analytic galaxy formation models are not fully representing the observational universe. Some of the inconsistencies between those models and the observations are related to the inconsistency with the stellar mass function (see Mitchell et al. (2013) and references herein), luminosity function (e.g. Gonzalez-Perez et al. 2014), chemical abundances (e.g. De Lucia & Borgani 2012) and colors (e.g. Henriques et al. 2012), consequently producing a wrong tilt of the color-magnitude relation, 'plume' effects of redder galaxies belonging to the cluster spread within 1-2 bright magnitudes, absence of a smooth-transitory green valley and other related effects. These effects generally lead to an underestimation of the photometric redshift uncertainties.

We have applied the methodology described above to the Merson et al. catalogues. After re-creating the new photometry using the mentioned technique, we obtained that the photometric redshift accuracy exactly matched that obtained from real data (Ascaso et al., in preparation).

4 Results

We have studied the performance of the photometric redshift for each of the surveys considered as a function of magnitude and redshift. Also, we have considered making different quality cuts with the purpose of selecting a best quality subsample that can result into a best measurement for different scientific purposes.

We have disentangled some of the advantages of using each of these different datasets in terms of photometric redshift resolution. First, the advantage of using multi band narrow-band surveys is directly related to the level of photometric redshift accuracy and photometric redshift bias expected for the survey down to moderate magnitudes ($m < 23$) and redshift ranges ($z < 0.8$) . On the other hand, deep broad-band optical surveys allow to explore the luminosity function in the optical range even if with worse photometric redshift resolution. They are also an excellent complement for deep infrared surveys, particularly to dramatically decrease the rate of outliers and improve the photometric redshift accuracy. Finally, the deep infrared surveys provide an excellent photometric redshift accuracy in a wide range of redshift ($z < 3$) with a moderate rate of catastrophic outliers.

We have been detecting galaxy clusters in the mock catalogues and we have computed the completeness and purity of the results as a function of redshift and richness as shown in Fig.1 for the case of J-PAS. Based on these results, we expect to detect galaxy clusters and groups with completeness rates $> 80\%$ and purity rates $> 70\%$ for clusters and groups down to $M > 3 \times 10^{13} M_\odot$ up to redshift 0.8. At higher redshifts, the completeness rates decays. Let's note that the extremely good quality of the photometric redshifts in the J-PAS survey make these results comparable to what we would expect for a low-resolution spectroscopic survey, in agreement to our results found with present cluster samples (section 2.2).

We have finally created a cosmological pipeline that, based on the selection function provided by different survey, computes the Fisher Matrix of the cluster counts and provides different constraints for different cosmological parameters.

A way more extended and detailed version of these results will come up soon in a series of papers (Ascaso et al. in prep).

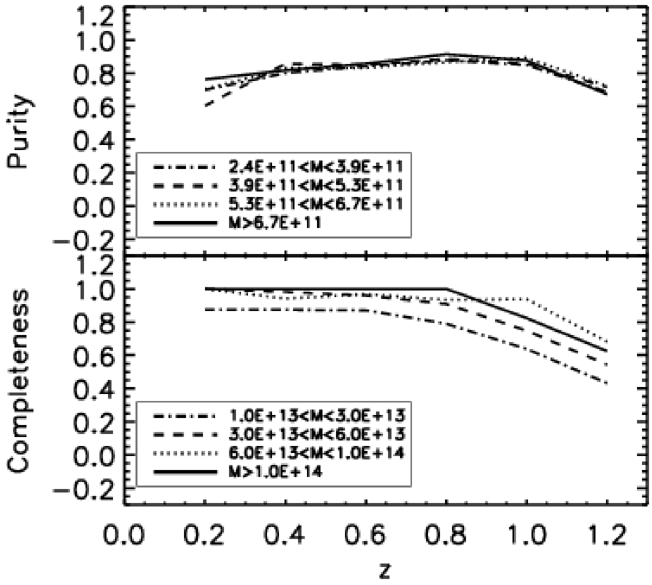

Fig. 1. Purity (top plot) and completeness (bottom plot) rates as a function of redshift for different dark matter halo and total stellar mass bins. While purity remains almost constant (~ 0.7) as a function of redshift, being lower for lower masses, we find a decreasing in the completeness rate with both redshift and mass.

References

Albrecht, A., Bernstein, G., Cahn, R., et al. 2006, ArXiv Astrophysics e-prints

Allen, S. W., Evrard, A. E., & Mantz, A. B. 2011, ARA&A, 49, 409

Arnalte-Mur, P., Martínez, V. J., Norberg, P., et al. 2014, MNRAS, 441, 1783

Ascaso, B. 2013, in Highlights of Spanish Astrophysics VII, ed. J. C. Guirado, L. M. Lara, V. Quilis, & J. Gorgas, 115–125

Ascaso, B., Wittman, D., & Benítez, N. 2012, MNRAS, 420, 1167

Ascaso, B., Wittman, D., & Dawson, W. 2014, MNRAS, 439, 1980

Benitez, N., Dupke, R., Moles, M., et al. 2014, ArXiv e-prints

Bower, R. G., Benson, A. J., Malbon, R., et al. 2006, MNRAS, 370, 645

Cole, S., Lacey, C. G., Baugh, C. M., & Frenk, C. S. 2000, MNRAS, 319, 168

De Lucia, G. & Borgani, S. 2012, MNRAS, 426, L61

Erben, T., Hildebrandt, H., Lerchster, M., et al. 2009, A&A, 493, 1197

Gonzalez-Perez, V., Lacey, C. G., Baugh, C. M., et al. 2014, MNRAS, 439, 264

Henriques, B. M. B., White, S. D. M., Lemson, G., et al. 2012, MNRAS, 421, 2904

Ivezic, Z., Tyson, J. A., Abel, B., et al. 2008, ArXiv e-prints

Laureijs, R., Amiaux, J., Arduini, S., et al. 2011, ArXiv e-prints

Merson, A. I., Baugh, C. M., Helly, J. C., et al. 2013, MNRAS, 429, 556

Mitchell, P. D., Lacey, C. G., Baugh, C. M., & Cole, S. 2013, MNRAS, 435, 87

Moles, M., Benítez, N., Aguerri, J. A. L., et al. 2008, AJ, 136, 1325

Molino, A., Benítez, N., Moles, M., et al. 2014, MNRAS, 441, 2891

Postman, M., Lubin, L. M., Gunn, J. E., et al. 1996, AJ, 111, 615

Schmidt, S. J. & Thorman, P. 2013, MNRAS, 431, 2766

Springel, V. 2005, MNRAS, 364, 1105

The Dark Energy Survey Collaboration. 2005, ArXiv Astrophysics e-prints

Wittman, D. M., Tyson, J. A., Dell'Antonio, I. P., et al. 2002, in Society of Photo-Optical Instrumentation Engineers (SPIE) Conference Series, Vol. 4836, Survey and Other Telescope Technologies and Discoveries, ed. J. A. Tyson & S. Wolff, 73–82

Zandivarez, A., Díaz-Giménez, E., Mendes de Oliveira, C., et al. 2014, A&A, 561, A71

SF2A 2014
J. Ballet, F. Bournaud, F. Martins, R. Monier and C. Reylé (eds)

THE VIOLENT YOUTH OF BRIGHT AND MASSIVE CLUSTER GALAXIES AND THEIR MATURATION OVER 7 BILLION YEARS

B. Ascaso[1], B. Lemaux[2], L. M. Lubin[3], R.R. Gal[4], D.D. Kocevski[5], N. Rumbaugh[3] and G. Squires[6]

Abstract. In this talk, I will present recent research on the formation and evolution mechanisms of the brightest cluster galaxies (BCGs) over cosmic time. At high redshift (z∼0.9) we selected BCGs and most massive cluster galaxies (MMCGs) from the Cl1604 supercluster and compared to low-redshift (z∼0.1) counterparts drawn from the MCXC meta-catalog and supplemented by SDSS imaging and spectroscopy. We observed striking differences in the morphological, color, spectral, and stellar mass properties of the BCGs/MMCGs in the two samples. High-redshift BCGs/MMCGs were, in many cases, star-forming, late-type galaxies, with blue broadband colors, properties largely absent amongst the low-redshift BCGs/MMCGs. The stellar mass of BCGs was found to increase by an average factor of 2.51±0.71 from z∼0.9 to z∼0.1. Through this and other comparisons we conclude that a combination of major merging (mainly wet or mixed) and in situ star formation are the main mechanisms which build stellar mass in BCGs/MMCGs. The stellar mass growth of the BCGs/MMCGs also appears to grow in lockstep with both the stellar baryonic and total mass of the cluster. Additionally, BCGs/MMCGs were found to grow in size, on average, a factor of ∼3 while their average Sérsic index increased by ∼0.45 from z∼0.9 to z∼0.1, also supporting a scenario involving major merging, though some adiabatic expansion is required. These observational results are compared to both models and simulations to further explore the implications on processes which shape and evolve BCGs/MMCGs over the past ∼7 Gyr.

Keywords: techniques: photometric, techniques: spectroscopic, galaxies: clusters: general, galaxies: elliptical and lenticular, cD, galaxies: evolution, galaxies: formation

1 Data

In this work, we consider the Brightest Cluster Galaxy (BCG) and Most Massive Cluster Galaxy (MMCG) of the $z \sim 0.9$ Cl1604 supercluster, which contains clusters and groups that span a wide range in halo mass, and a comparison sample of comparable clusters at low-redshift ($z \sim 0.1$) observed as part of the Sloan Digital Sky Survey (SDSS).

1.1 *The Cl1604 supercluster at* $z \sim 0.9$

The Cl1604 supercluster, located at $z \sim 0.9$, is one of the most well-characterized superclusters in the high-redshift universe and it has exhaustively observed as part of the Observations of Redshift Evolution in Large Scale Environment survey (ORELSE; Lubin et al. 2009). The supercluster consists of three galaxy clusters and five groups (Gal et al. 2008).

There exists a vast number of observations for this supercluster (see Lemaux et al. (2012); Ascaso et al. (2014) and references herein). In this work, we have using the fact that the systems have been spectroscopically sampled to a completeness limit of $M_g = -20.35$ and, additionally, they have associated deep F606W/F814W HST ACS imaging down to 27.2 and 26.8 mags for point sources in the shallowest regions.

[1] Observatoire de Paris, 77 Denfert Rochereau, 75014, Paris, France
[2] Laboratoire dAstrophysique de Marseille, 38 rue F. Joliot-Curie, 13388, Marseille, France
[3] University of California Davis, One Shields Avenue, 95616, Davis, CA, USA
[4] Institute for Astronomy, University of Hawaii, 2680 Woodlawn Drive, Honolulu, HI 96822, USA
[5] University of Kentucky, 505 Rose Street, Lexington, KY 40506, USA
[6] Spitzer Science Center, California Institute of Technology, M/S 220-6, 1200 E. California Blvd, Pasadena, CA 91125, USA

For each cluster or group, we select the BCG as the member galaxy with the brightest $F814W$ magnitude within $r_{\rm proj} < 1h_{70}^{-1}$ Mpc of the luminosity-weighted cluster/group center. We also selected the MMCG in a nearly identical manner as the BCGs, with the exception that the stellar mass derived through SED-fitting process or through the K-band imaging was used in place of the $F814W$ magnitude. In all cases galaxies with stellar masses within 1σ of that of the galaxy with the highest measured mass were also selected and our analysis was repeated for each potential MMCG (setting a maximum of three MMCG "candidates" for each cluster/group). The final sample of 17 galaxies consisted of eight BCGs and nine MMCGs.

1.2 MCXC clusters at $z \sim 0.1$

We drew a sample of low-redshift clusters from the Meta-Catalog of the compiled properties of X-ray detected galaxy Clusters (MCXC; Piffaretti et al. 2011). This catalog contains a large number of galaxy clusters with well-defined and homogeneously measured X-Ray luminosities. Moreover, it overlaps with the SDSS, allowing us to access to an enormous dataset of well-calibrated and internally consistent multiwavelength imaging and spectroscopy.

We selected a sample of galaxy clusters from the MCXC catalog by cross correlating it with the SDSS DR8 public database. For those clusters which fell within the SDSS footprint we required that any potential comparison cluster have *i*) imaging in the g' band to sufficient depth to make valid morphological comparisons ($\sim$ 23.5 mag/arcsec^2), *ii*) sufficient photometry to estimate stellar masses (i.e., measured magnitudes in all SDSS bands), *iii*) spectroscopy of at least 80% of potential member galaxies brighter than $M_{g'} = -20.35$ that lie within a projected distance of $1h_{70}^{-1}$ Mpc from the cluster center, and *iv*) spectroscopy of the 10 brightest objects in the g' band within a projected distance of $1h_{70}^{-1}$ Mpc from the cluster center as defined by the MCXC X-Ray centroid. Imposing these criteria resulted in a sample of 100 low-redshift clusters out of the 1743 clusters contained within the MCXC catalog. Finally, we excluded those clusters with questionable color-magnitude diagram or velocity dispersion measurement obtaining a final sample of 81 clusters with a median redshift of $\langle z \rangle = 0.08$ and a redshift range of $z = 0.02 - 0.21$.

The BCG and MMCG for each cluster was selected in a manner identical to that of the Cl1604 BCGs, with the selection being performed in the g' band (see Ascaso et al. 2014 for further details). Only 13 had a BCG that differed from the MMCG.

2 Results

We investigated the evolution of color, morphological, stellar mass, and spectral properties of BCGs/MMCGs over the past $\sim$ 7 Gyr. Our results are as follows.

- *Color and luminosity evolution:* A large fraction ($\sim$ 35%) of the combined Cl1604 BCG/MMCG sample were observed with colors blueward of the red sequence for its parent cluster or group. In contrast, only a small fraction ($\sim$ 2%) of the BCGs/MMCGs at low redshift were observed to be similarly offset of the red sequence. The gap in magnitude between the BCG and the next brightest cluster/group galaxy in the average Cl1604 cluster/group was found to be less than half that of the average MCXC cluster.

- *Morphology evolution:* Exactly half of the Cl1604 BCG sample were galaxies classified with late-type morphologies and a large fraction ($\sim$ 40%) of had signs of interaction. In contrast, only 2.5% the BCGs at low redshift were classified as late-type and the fraction of those undergoing interactions was less than half of that of the Cl1604 sample. In addition, the Cl1604 BCGs were observed in some stage of a merging event greater than five times more frequently than the low-z BCGs. These numbers did not change appreciably when the MMCGs of the two samples were considered.

- *Spectral evolution:* A majority ($\sim$53%) of the combined Cl1604 BCG/MMCG sample show significant ongoing star formation. In contrast, only a small fraction $\sim$ 4% of the MCXC BCGs/MMCGs were observed with ongoing star formation. From a stacked spectrum of galaxies, the average star formation rate of the Cl1604 BCGs/MMCGs was found to be $\langle SFR \rangle = 10.5 \pm 0.5\ \mathcal{M}_{\odot}\ {\rm yr}^{-1}$. This value is in stark contrast with the average SFR of the MCXC-SDSS BCG/MMCG, which was consistent with zero. In addition, strong Balmer absorption features and weak features associated with older stellar populations were observed in the Cl1604 BCG/MMCG stacked spectrum, which indicated a considerably younger mean luminosity-weighted stellar age as compared to the MCXC/SDSS sample. Even those

Cl1604 BCGs/MMCGs considered passive (SSFR $< 10^{11} yr^{-1}$) showed signs of a moderately young stellar population.

- *Stellar mass evolution:* The average $z \sim 0.9$ Cl1604 BCG was observed to be deficient in stellar mass by a factor of 2.51±0.71 relative to a (cluster total mass) matched sample of $z \sim 0.1$ MCXC BCGs. The average MMCG in Cl1604 was found to be deficient in stellar mass by a factor of 1.78±0.45 relative to the MMCGs same matched low-redshift sample. Surprisingly, this growth factor is consistent with both the increase in total mass and increase of total stellar baryonic mass of the clusters over the same redshift interval. This result strongly suggested that the growth of the stellar mass of a BCG/MMCG is intimately linked with both the total stellar (contained in galaxies) and dark matter growth of the clusters.

- *Radial distribution of stellar mass:* A comparison was made between the stellar mass surrounding the BCGs/MMCGs at low and high redshift in the form of companion galaxies. A marked increase of stellar mass at low (projected) radii $R_{\rm proj} < 0.3R_{vir}$ was observed surrounding the Cl1604 BCGs/MMCGs relative to the MCXC BCGs/MMCGs (see Fig. 1). Merging timescales were calculated for all companion galaxies to the Cl1604 BCGs/MMCGs that had the possibility of merging within ≤7 Gyr. Of the 15 merger candidates surrounding the Cl1604 BCGs/MMCGs with small enough merging timescales, 14 would result in a major merging event (≤4:1 mass ratio). These potential merging events are primarily comprised of the mixed or wet variety. From these merging events alone, the average Cl1604 BCG will increase in stellar mass by a factor of 2.23±0.73 and the average Cl1604 MMCG by a factor of 1.35±0.31 under the assumption of 100% retention of stellar matter.

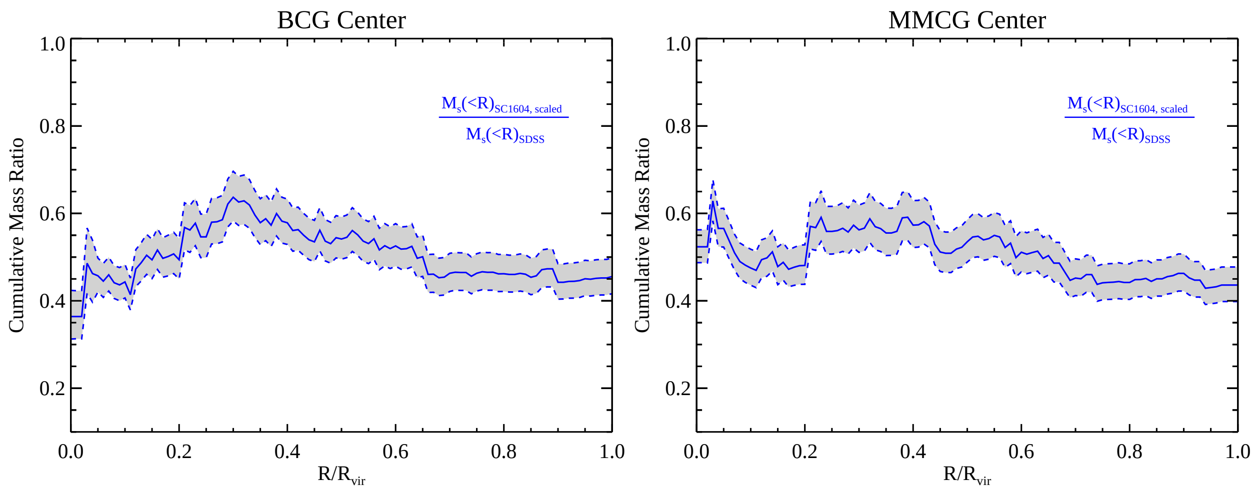

Fig. 1. The ratio of the Cl1604 to the MCXC radial stellar mass cumulative distribution using the BCG (left panel) and the MMCG (right panel) as centers. The blue line shows the average ratio between the the cumulative stellar mass distribution in the average Cl1604 cluster/group and that of the average MCXC cluster in the comparison sample. The gray shaded region denotes the sample variance at each radius. The projected radial distance of members of all clusters and groups are normalized by the virial radii of their parent structures. An increase in the ratio in either panel indicates an excess in stellar mass surrounding the average BCG/MMCG in the high-redshift clusters and groups relative to that surrounding the average low-redshift BCG/MMCG. The average BCG at high redshift shows a decided excess of stellar mass at a relatively low (normalized) radius increasing steadily out to $R \sim 0.3R_{vir}$. The average MMCG at high redshift also shows a sharp excess of stellar mass in its immediate surroundings relative to the average low-redshift MMCG, but only at very small (normalized) radius ($R < 0.05R_{vir}$). This excess indicates the presence of extremely massive companions of the high-redshift MMCGs that are not present at low redshift.

- *Structural parameter evolution*: By fitting the surface brightness profiles of all BCGs/MMCGs in both the high- and low-redshift samples to a single Sérsic profile, we found an increase of a factor of ~ 3 of the size (r_e) of BCGs/MMCGs over the past ~ 7 Gyr. The factor of this size increase was invariant with respect to which low-redshift sample we chose to compare the Cl1604 BCGs/MMCGs to. An increase in the average Sérsic index was also measured over the same redshift range, though its evolution was milder, with an observed increase of $n(z=0) - n(z) \sim 0.5$.

3 Conclusions

From our observational data alone, we strongly favored a scenario in which BCGs/MMCGs grow through a combination of *in situ* star formation and major merging events, the latter likely causing subsequent increases in star formation activity. Though we could not completely rule out the involvement of minor mergers in building up at least a small fraction of the stellar mass of the BCGs/MMCGs over the past $\sim$ 7 Gyr, the aforementioned scenario is wholly consistent with all of the results in this study. These observational results were then compared to a variety of hydrodynamical simulations (Hopkins et al. 2010) and semi-analytic models (De Lucia & Blaizot 2007). Through these comparisons we found that the observed prevalence of (potentially) impending major merging events amongst the Cl1604 BCGs/MMCGs was sufficient to explain the evolution in the size of BCGs/MMCGs from $z \sim 0.9$ to $z \sim 0.1$. However, the observed evolution in the average Sérsic index was not as dramatic as that predicted from a large number of major merging events. In order to explain this mild evolution, we appealed to adiabatic expansion, a process which will serve to soften the evolution of Sérsic indices of galaxies and a process which naturally follows from the ignition of an AGN as a result of a wet or mixed merging event.

This study represents one of the most comprehensive studies of the evolution of BCGs/MMCGs over cosmic time to date in terms of the sheer amount of spectroscopic and imaging data utilized for the galaxy populations of clusters at both high and low redshift. From this study we were able to draw a definitive picture of the evolution of BCGs/MMCGs in the Cl1604 supercluster. However, the sample of BCGs/MMCGs used here, especially at high redshift, remains somewhat small, and given the large amount of intrinsic variance amongst galaxy cluster populations observed at all redshifts, it is not entirely clear how applicable this picture is to the evolution of an "average" BCG over the past $\sim$ 7 Gyr. It is encouraging that our results, or at least those which can be directly compared, show broad agreement with similar samples of BCGs taken from other surveys. However, future work remains to utilize data from the $\sim$ 50 high-redshift clusters and groups of the full ORELSE sample, as well as datasets available from other high-redshift cluster surveys (e.g., EDisCS, GCLASS), to determine if the mode of evolution observed here amongst the Cl1604 BCGs/MMCGs is fully representative of that of typical BCGs observed across the universe.

All the results and techniques developed in this work can be found in Ascaso et al. (2014).

References

Ascaso, B., Lemaux, B. C., Lubin, L. M., et al. 2014, MNRAS, 442, 589

De Lucia, G. & Blaizot, J. 2007, MNRAS, 375, 2

Gal, R. R., Lemaux, B. C., Lubin, L. M., Kocevski, D., & Squires, G. K. 2008, ApJ, 684, 933

Hopkins, P. F., Bundy, K., Hernquist, L., Wuyts, S., & Cox, T. J. 2010, MNRAS, 401, 1099

Lemaux, B. C., Gal, R. R., Lubin, L. M., et al. 2012, ApJ, 745, 106

Lubin, L. M., Gal, R. R., Lemaux, B. C., Kocevski, D. D., & Squires, G. K. 2009, AJ, 137, 4867

Piffaretti, R., Arnaud, M., Pratt, G. W., Pointecouteau, E., & Melin, J.-B. 2011, A&A, 534, A109

SF2A 2014
J. Ballet, F. Bournaud, F. Martins, R. Monier and C. Reylé (eds)

GALAXY STELLAR MASS ASSEMBLY: SUPERNOVA FEEDBACK, PHOTO-IONIZATION AND NO-STAR-FORMING GAS RESERVOIR.

M. Cousin[1]

Abstract. Semi-analytical models are currently the best way to understand the formation of galaxies within the cosmic dark-matter structures. While they fairly well reproduce the local stellar mass functions, they fail to match observations at high redshift. The inconsistency indicates that the gas accretion in galaxies and the transformation of gas into stars, are not well followed. With a new SAM: eGalICS, we explore the impacts of classical mechanisms (supernova feedback, photo-ionization) onto the stellar mass assembly. Even with a strong efficiency, these two processes cannot explain the observed stellar mass function and star formation rate distribution. We introduce an ad-hoc modification of the standard paradigm, based on the presence of a no-star-forming gas component in galaxy discs. We introduce this reservoir to generate a delay between the accretion of the gas and the star formation process. The new stellar mass function and SFR distributions are in good agreement with observations.

Keywords: Galaxies: formation - Galaxies: evolution - Cosmology: dark-matter haloes

1 Introduction

Cosmological models based on the Λ-CDM paradigm have proved remarkably successful at explaining the origin and evolution of structures in the Universe. The description of smaller scales (galaxies) is more problematic. Twenty years ago, Kauffmann et al. (1993) pointed out the so-called substructure problem. Indeed the large amount of power on small scales in the $\Lambda - CDM$ paradigm generates an over-estimate of the number of small objects (with properties close to dwarf galaxies). The over-density of substructures is clearly seen in N-body simulations at low redshift ($z \simeq 0$). Dark matter haloes with mass comparable to that of our Galaxy ($M_h \simeq 10^{12} M_\odot$) contain more than one hundred substructures. On the contrary, the observations of the Local Group count at most fifty satellite galaxies. This effect is even more problematic at high redshift ($z > 1$). Indeed, coupled with the poor understanding of the star formation process in these small haloes, the standard scenario produces a large excess of stellar mass in low-mass structures (Guo et al. 2011).

To limit the number of dwarf galaxies, galaxy formation models such as semi-analytical model (SAM) or cosmological hydrodynamic simulations, invoke gas photoionization and strong supernova feedback (Efstathiou 1992; Shapiro et al. 1994; Babul & Rees 1992; Quinn et al. 1996; Thoul & Weinberg 1996; Bullock et al. 2000; Gnedin 2000; Benson et al. 2002; Somerville 2002; Croton et al. 2006; Hoeft et al. 2006; Okamoto et al. 2008; Somerville et al. 2008, 2012).

We use a revised version of the GalICS semi-analytical model (SAM) (Cousin et al 2014-b). This new version include a description of the baryonic physic based on the most recent prescriptions extracted from analytical works and/or hydrodynamic simulations. With this SAM we explore the impacts of classical photoionization and supernova (SN)-feedback recipes on fundamental the stellar mass function (SMF).

We show that the basic models fail to reproduce these kinds of measurements, and propose the existence of a *no-star-forming* gas reservoir in galaxy discs to reconcile the models with the observations.

This conclusion is based on the analysis of a set of four different prescriptions of star-formation regulation processes. These four different models are listed in the table 1. In the first model, m_0, the star formation

[1] Institut d'Astrophysique Spatiale, Université Paris-Sud 11, bat 121, 91405 ORSAY

Model	Definitions / Comments	Colour plots
m_0	Okamoto et al. (2008), without (sn/agn)-feedback	red
m_1	Okamoto et al. (2008) photoionization and our sn-feedback processes (*reference*)	orange
m_2	Gnedin (2000) photoionization and our sn-feedback processes	green
m_3	*reference* + *no-star-forming* gas disc component	purple

Table 1. List of SAMs compared

activity is not regulated. Indeed this first model does not use any feedback or photo-ionization prescription. The model m_1 uses a SN feedback recipe and a photo-ionization model based on the Okamoto et al. (2008) prescription. The model m_2 is based on the same SN model, than model m_1, but it uses the Gnedin (2000) photoionization prescription. Finally, the last model, m_3, applies a new model of gas cycle. It assumes the existence of a *no-star-forming* gas reservoir in galaxy discs.

2 Supernovae feedback

In a given stellar population, massive stars evolve quickly and end their life as supernovae. This violent death injects gas and energy in the interstellar medium. The gas is heated and a fraction can be ejected from the galaxy plane and feed the surrounding host-halo phase.

Supernova feedback is therefore a crucial ingredient. In the majority of SAM (e.g. Kauffmann et al. 1993; Cole et al. 1994, 2000; Silk 2003; Hatton et al. 2003; Somerville et al. 2008), and according to some observational studies (e.g. Martin 1999; Heckman et al. 2000; Veilleux et al. 2005), the *SN-reheating* or *SN-ejecta* rate is linked to the star formation rate. As proposed by Dekel & Silk (1986), we computed the ejected mass rate due to supernovae by using kinetic energy conservation. The ejected mass rate $\dot{M}_{ej,SN}$ due to SN is linked to the star formation rate $\dot{M}_\star$ by using the individual supernova kinetic energy $E_{sn,k}$ as follows:

$$\dot{M}_{ej,SN} V_{wind}^2 = 2\varepsilon_{ej}\eta_{sn} E_{sn,k} \dot{M}_\star \tag{2.1}$$

To break the degeneracy between the ejected mass and the velocity of the wind, we must add a constraint on the wind velocity. We rely on Bertone et al. (2005) in which the wind velocity is linked to the star formation rate (Martin 1999). It seems to be independent of the galaxy morphology (Heckman et al. 2000; Frye et al. 2002). We therefore use Eq. 9 in Bertone et al. (2005) to model the wind velocity.

On average, wind velocities obtained with this prescription are larger than in other studies (e.g. Somerville et al. 2008; Dutton & van den Bosch 2009). Indeed it is common to use galaxy escape velocity to describe the wind, which is, for the ejection process, the minimal required value. Therefore, the ejected mass is maximal (see Dutton & van den Bosch (2009), their discussion in Sect.7.3). Consequently, our loading factor ($\dot{M}_{ej,SN}/\dot{M}_\star$) is smaller than in other models and therefore our mean ejected mass is also lower.

The influence of the efficiency value has been tested in the range $\varepsilon_{ej} \in [0.05, 10]$. Obviously a strong increase of the SN-efficiency increases the amount of ejected gas. The star formation activity is therefore reduced but this effect affects only the amplitude and not the shape of the stellar mass function. Moreover, looking at the amplitude, its decrease is not enough to be in agreement with the observations.

Despite the different parameterizations and energy injection scales for supernovae, currently the classical semi-analytical models do not seem to be able to explain the high redshift behaviour of the mass function in the low-mass range (see also Fig. 23 in Guo et al. (2011), and Fig. 11 in Ilbert et al. (2013)). Even if some SAMs, as Somerville et al. (2008), Guo et al. (2011) or Henriques et al. (2013), use a dedicated parametrization, to reproduce the galaxy properties at $z = 0$, it seems that, at high redshift, the low-mass range problem of the stellar-mass function is not only linked to a SN-feedback efficiency calibration. Indeed, Guo et al. (2011) (their Figs. 8 and 23) show that the number of low-mass star-forming galaxies are still larger than that observed.

Note also that a strong increase of the SN-wind efficiency, in low-mass structures, leads to very high mass-loading factors ($\dot{M}_{ej}/\dot{M}_\star > 10$, Henriques et al. (2013) their Fig. 3). Such factors are much larger that those derived from spectroscopic observations (e.g. Sturm et al. 2011; Rubin et al. 2011; Bouché et al. 2012) even if the measurement of this parameter is difficult and is currently performed on massive systems.

3 Photoionization

Originally proposed by Doroshkevich et al. (1967), photoionization has been developed in the CDM paradigm by Couchman & Rees (1986), Ikeuchi (1986), and Rees (1986). The idea is quite simple: the ultraviolet (UV) background generated by the quasars and first generations of stars heats the gas. In the small structures, the temperature reached by the gas is then too high, preventing it to collapse into dark matter haloes. The accretion of the gas on the galaxies, and thus the star formation, is thus reduced.

In our hybrid SAMs, the baryonic mass is added progressively following the dark-matter smooth accretion:

$$\dot{M}_b = f_b^{ph-ion}(M_h, z)\dot{M}_{dm} \tag{3.1}$$

where

$$f_b^{ph-ion}(M_h, z) = \langle f_b \rangle \left[1 + (2^{\alpha/3} - 1)\left(\frac{M_h}{M_c(z)}\right)^{-\alpha}\right]^{-3/\alpha} \tag{3.2}$$

In this definition, $\langle f_b \rangle = 0.18$ is the universal baryonic fraction, M_h the dark matter halo mass, and $M_c(z)$ the filtering mass corresponding to the mass where the halo lost half of its baryons. Finally, α is a free parameter that mainly controls the slope of the transition. In our case, we use the Okamoto et al. (2008) prescription ($\alpha = 2$ and $M_c(z) = 8.22 \times 10^9 \exp(-0.7\mathrm{z})$ $[\mathrm{M}_\odot]$).

We consider that the photoionization effect is important when $f_b^{ph-ion} < 0.5 \langle f_b \rangle$. In this context, the significant decrease of $f_b^{ph-ion}/\langle f_b \rangle$ appears for the mass resolution ($M_h^{min} = 1.707 \times 10^9\ M_\odot$) only for redshift $z < 1$. In this case, the gas heating due to the UV background cannot affect, at high redshift, the baryonic assembly of small structures. Some other SAM (e.g. , (e.g. Benson et al. 2002; Somerville 2002; Croton et al. 2006; Hoeft et al. 2006; Okamoto et al. 2008; Somerville et al. 2008, 2012) use a different parametrization based on Gnedin (2000) ($\alpha = 1$ and with a different filtering mass). This other he Gnedin (2000) prescription reduces more the stellar mass formed in the small dark matter mass regime than the Okamoto et al. (2008) prescription. Indeed, with this model, photoionization starts to play a role at $z \simeq 8$.

4 An ad-hoc recipe to reconcile models and observations

At high redshift ($z > 1$), as shown in Fig. 1, the amplitude of the faint-end of the stellar mass function is dramatically overestimated by the models (m_0, m_1 and m_2). This result is consistent with the overestimate of stellar mass in low-mass dark matter haloes: small structures form too many stars. In general, this problem is addressed by a strong SN-feedback and/or photoionization. As shown previously, photoionization and SN-feedback cannot be sufficient to reduce significantly the star formation in low-mass objects. Strong feedback models give some good integrated (at $z \simeq 0$) results (Guo et al. 2011; De Lucia & Blaizot 2007) but fail at higher redshift (see Ilbert et al. 2013, their Fig. 11).

We propose in this section a strong modification of the implementation of the star-formation mechanism in our semi-analytical model to try to reconcile models and observations.

When accreted on the galaxy disc, the surface density of fresh gas (considered as homogeneously distributed) is low. Progressively the gas, controlled by the turbulence and gravity energy balance, is more and more structured (Kritsuk & Norman 2011). The energy injected by the accretion process must be dissipated before star-formation process can start. As the dissipation scale is much smaller than the energy injection scale, we assume that the energy cascade introduces a delay between the accretion time and the star formation time.

To model this process, we introduce in our model m_3 a new gas component in galaxy discs: the *no-star-forming* gas. The delay between the accretion time of fresh gas and the time when this gas is converted into stars is modelled by a transfer rate between the *no-star-forming* gas and the *star-forming* gas reservoir($g^\star$) that follows:

$$\dot{M}_{g^\star,in} = \dot{M}_{g,out} = \varepsilon_\star min\left[1, \left(\frac{M_h}{10^{12}\ M_\odot}\right)^3\right]\frac{M_g}{t_{dyn}} \tag{4.1}$$

where M_g is the mass of *no-star-forming* gas, t_{dyn} is the disc dynamical time and $\varepsilon_\star = 0.02$ an efficiency parameter, identical to the star formation efficiency used in standard SAM. This conversion rate has not been defined to follow explicitly ISM physic but is calibrated to reproduce the stellar-to-halo mass-relation (SHMR) (e.g. Leauthaud et al. 2012; Moster et al. 2010; Behroozi et al. 2010; Béthermin et al. 2012). This formulation has no other purpose than to highlight the order of magnitude of the regulation process that has to be introduced.

5 The stellar/gas-mass function

5.1 The stellar-mass function

We show in Figs 1 and 2 the stellar-mass functions predicted by our models. In Fig 1 are shown *standard* models, m_0(red), without regulation process, m_1(orange) with a SN feedback model and the Okamoto et al. (2008) photo-ionization prescription and m_2(green) with the same SN feedback model but with the Gnedin (2000) photo-ionization prescription. Model outputs are compared with observational data from Ilbert et al. (2010), Ilbert et al. (2013), Yang et al. (2009) and Caputi et al. (2011).

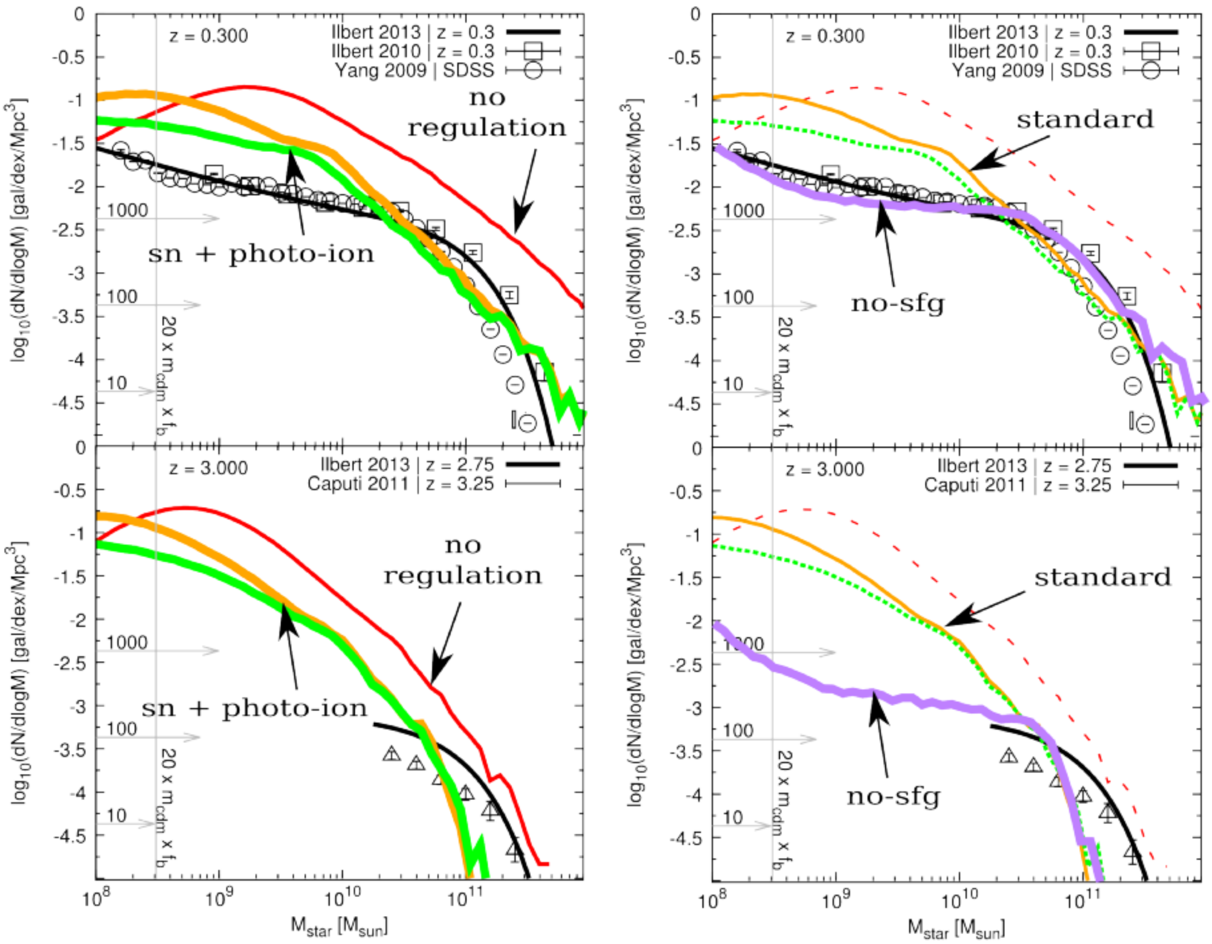

Fig. 1. Left: Stellar mass functions for two different redshift bins, $z = 0.3$ (top panel) and $z = 3.0$ (bottom panel) and for our standard models, m_0 (red), m_1 (orange) and m_2 (green). **Right:** Stellar mass functions extracted from our *ad-hoc* model (purple) for two different redshift bins, $z = 0.3$ (top panel) and $z = 3.0$ (bottom panel). Other model m_0 (red), m_1 (orange) and m_2 (green) are recalled. **Both:** We compare our results with Ilbert et al. (2010, 2013) (squares), Yang et al. (2009) (circles) and Caputi et al. (2011) (triangles) observations. The horizontal arrows show the link between the density and the number of haloes in our simulation volume.

It is clear that models m_0, m_1 and m_2 fail to reproduce the low-mass end of the stellar mass function. The disagreement is both on the amplitude (one order of magnitude higher at low mass) and on the shape of the mass function. Note that the discrepancy increase with the redshift.

With the *ad-hoc* model(purple), in the low mass range, the levels of the stellar mass functions are in good agreement with observations for a wide range of stellar masses. This indicates that only a strong modification (a decrease in our case) of the mass of gas instantaneously available to form stars, allows to modulate the star formation activity in low mass structures and to reconcile SAM with the observations.

Concerning the high-mass end of the stellar-mass function, all models under-predict the number of massive galaxies. For $z = 4$ and $z = 3$ the comparison with Ilbert et al. (2010) and Ilbert et al. (2013) observational mass functions indicate that the massive galaxies in our models are two time less massive than the observed distribution. This is also observed in other recent SAMs (see e.g., Henriques et al. 2013, their Figs. 4-5-6, and Guo et al. 2011, their Fig. 23). The only way to reconcile models and observation in this high-mass regime is to consider a model without any regulation mechanism (model m_0).

5.2 The gas-mass function

In our *ad-hoc* model, we have chosen to modify the standard star formation paradigm, through the introduction of a delay between gas accretion and star formation. The step during which the *no-star-forming* gas is converted into *star-forming* gas strongly reduces the star formation activity, and therefore the stellar mass building-up.

In Fig. 2, we show the predicted gas-mass functions, together with the local HI mass function computed by Zwaan et al. (2005), and the molecular gas mass function coming from Berta et al. (2013). The gas-mass functions extracted from our models are computed using all galaxies contained in our simulated volume, and taking into account the total gas mass in galaxy discs.

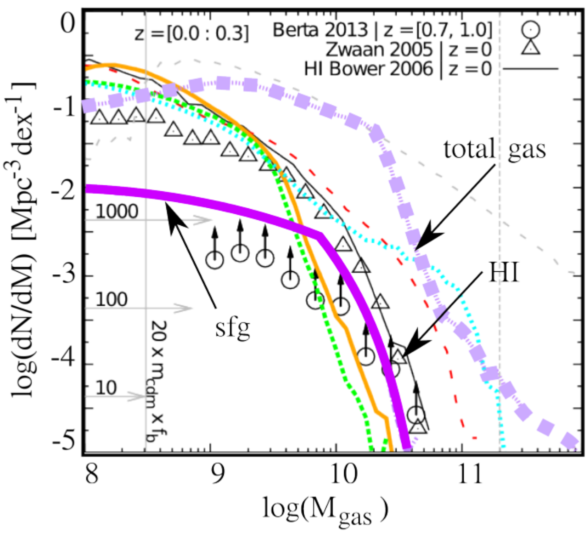

Fig. 2. Gas mass functions predicted by our SAMs. The colour code is detailed in Table 1. In the case of m_4, we plot the total (*star-forming* + *no-star-forming*) and the *star-forming* gas mass function. We compare our results with the molecular gas mass function computed by Berta et al. (2013) (lower limits, circles) and with the local HI mass function computed by Zwaan et al. (2005) (triangles). The black solid line shows the HI mass function predicted by Lagos et al. (2011), using Bower et al. (2006) SAM. The horizontal arrows show the link between the density and the number of haloes in our simulation volume.

The gas-mass functions predicted by our reference model m_1 and its variation (m_2) are very close. Indeed, the two models use the same prescription for gas ejection. In the case of the new model m_3, we plot together in Fig. 2 the total and the *star-forming* gas-mass function. As expected, the amount of total gas in $m4$ is larger than in the reference model m_1 or its variations (m_2).

We also show in Fig. 2 the HI-mass fonction derived by Lagos et al. (2011) using the SAM of Bower et al. (2006). At first order, it is comparable to the mass-function evolution from our reference model m_1, which is reassuring and expected.

At $z \simeq 0$, the amount of total gas predicted by m_4 is larger than the measurement of the HI gas and the lower values of the molecular gas. Independently of each other, the HI and the molecular gas represent only a fraction of the total gas mass contained in a galaxy. However, we can note that for the high-mass range, the *star-forming* gas mass function predicted by m_3 is in good agreement with the HI mass function measured by Zwaan et al. (2005). Even if the total gas mass predicted by m_3 seems large, without any measurement of this total mass, it is difficult to conclude. The total gas mass function appears today as one of the key observables which will allow us to determine the optimal efficiency of gas ejection process and star formation.

6 Discussion, conclusion

We have presented different processes which act on galaxy formation, and more precisely on the star formation activity. We have tested two photoionization models and we have applied a supernovae feedback models. We showed that classical models fail to reproduce the faint-end of the stellar-mass function. They over-predict the stellar mass in the low mass dark matter haloes ($M_h < 10^{10}\ M_\odot$). Even when a strong photoionization and SN-feedback are used, the models form too many stars in the low-mass range. Moreover, recent observations indicate that the loading factors ($\dot{M}_{ej}/\dot{M}_\star$) are much smaller that those predicted by such models. A strong SN-feedback generates a strong decrease of the amount of gas, that has to be compensated at low z, for example by some gas reincorporation (Henriques et al. (2013)). Such a problem in the low-mass structures is invariably present, even in the most recent SAMs (Guo et al. 2011; Bower et al. 2012; Weinmann et al. 2012), and as explained by Henriques et al. (2013) can thus be viewed as a generic problem.

In addition to these standard models, we have proposed an other model in which we have strongly limited the star formation efficiency in low-mass haloes. This model is based on a 2-phase gaseous disc with, on the one hand the *star-forming* gas, and on the other hand, the *no-star-forming* gas. This *ad-hoc* modification leads to very good results mainly for the stellar-mass functions. The gas-mass function predicted by the *ad-hoc* model may indicate that galaxies have a gas content that is too large, even if the comparison with observations is difficult as the total gas mass function is not known. In the future, the measurement of the gas mass function will be a key observable that will constrain the balance between the ejection process and gas regulation in galaxies.

We acknowledge financial support from "Programme National de Cosmologie and Galaxies" (PNCG) of CNRS/INSU, France.

References

Babul, A. & Rees, M. J. 1992, MNRAS, 255, 346
Behroozi, P. S., Conroy, C., & Wechsler, R. H. 2010, ApJ, 717, 379
Benson, A. J., Lacey, C. G., Baugh, C. M., Cole, S., & Frenk, C. S. 2002, MNRAS, 333, 156
Berta, S., Lutz, D., Nordon, R., et al. 2013, A&A, 555, L8
Bertone, S., Stoehr, F., & White, S. D. M. 2005, MNRAS, 359, 1201
Béthermin, M., Doré, O., & Lagache, G. 2012, A&A, 537, L5
Bouché, N., Hohensee, W., Vargas, R., et al. 2012, MNRAS, 426, 801
Bower, R. G., Benson, A. J., & Crain, R. A. 2012, MNRAS, 422, 2816
Bower, R. G., Benson, A. J., Malbon, R., et al. 2006, MNRAS, 370, 645
Bullock, J. S., Kravtsov, A. V., & Weinberg, D. H. 2000, ApJ, 539, 517
Caputi, K. I., Cirasuolo, M., Dunlop, J. S., et al. 2011, MNRAS, 413, 162
Cole, S., Aragon-Salamanca, A., Frenk, C. S., Navarro, J. F., & Zepf, S. E. 1994, MNRAS, 271, 781
Cole, S., Lacey, C. G., Baugh, C. M., & Frenk, C. S. 2000, MNRAS, 319, 168
Couchman, H. M. P. & Rees, M. J. 1986, MNRAS, 221, 53
Croton, D. J., Springel, V., White, S. D. M., et al. 2006, MNRAS, 365, 11
De Lucia, G. & Blaizot, J. 2007, MNRAS, 375, 2
Dekel, A. & Silk, J. 1986, ApJ, 303, 39
Doroshkevich, A. G., Zel'dovich, Y. B., & Novikov, I. D. 1967, Soviet Ast., 11, 233
Dutton, A. A. & van den Bosch, F. C. 2009, MNRAS, 396, 141
Efstathiou, G. 1992, MNRAS, 256, 43P
Frye, B., Broadhurst, T., & Benítez, N. 2002, ApJ, 568, 558
Gnedin, N. Y. 2000, ApJ, 542, 535
Guo, Q., White, S., Boylan-Kolchin, M., et al. 2011, MNRAS, 413, 101
Hatton, S., Devriendt, J. E. G., Ninin, S., et al. 2003, MNRAS, 343, 75
Heckman, T. M., Lehnert, M. D., Strickland, D. K., & Armus, L. 2000, ApJS, 129, 493
Henriques, B. M. B., White, S. D. M., Thomas, P. A., et al. 2013, MNRAS, 431, 3373
Hoeft, M., Yepes, G., Gottlöber, S., & Springel, V. 2006, MNRAS, 371, 401
Ikeuchi, S. 1986, Ap&SS, 118, 509

Ilbert, O., McCracken, H. J., Le Fevre, O., et al. 2013, ArXiv e-prints
Ilbert, O., Salvato, M., Le Floc'h, E., et al. 2010, ApJ, 709, 644
Kauffmann, G., White, S. D. M., & Guiderdoni, B. 1993, MNRAS, 264, 201
Kritsuk, A. G. & Norman, M. L. 2011, ArXiv e-prints
Lagos, C. D. P., Baugh, C. M., Lacey, C. G., et al. 2011, MNRAS, 418, 1649
Leauthaud, A., Tinker, J., Bundy, K., et al. 2012, ApJ, 744, 159
Martin, C. L. 1999, ApJ, 513, 156
Moster, B. P., Somerville, R. S., Maulbetsch, C., et al. 2010, ApJ, 710, 903
Okamoto, T., Gao, L., & Theuns, T. 2008, MNRAS, 390, 920
Quinn, T., Katz, N., & Efstathiou, G. 1996, MNRAS, 278, L49
Rees, M. J. 1986, MNRAS, 218, 25P
Rubin, K. H. R., Prochaska, J. X., Ménard, B., et al. 2011, ApJ, 728, 55
Shapiro, P. R., Giroux, M. L., & Babul, A. 1994, ApJ, 427, 25
Silk, J. 2003, MNRAS, 343, 249
Somerville, R. S. 2002, ApJ, 572, L23
Somerville, R. S., Gilmore, R. C., Primack, J. R., & Domínguez, A. 2012, MNRAS, 423, 1992
Somerville, R. S., Hopkins, P. F., Cox, T. J., Robertson, B. E., & Hernquist, L. 2008, MNRAS, 391, 481
Sturm, E., González-Alfonso, E., Veilleux, S., et al. 2011, ApJ, 733, L16
Thoul, A. A. & Weinberg, D. H. 1996, ApJ, 465, 608
Veilleux, S., Cecil, G., & Bland-Hawthorn, J. 2005, ARA&A, 43, 769
Weinmann, S. M., Pasquali, A., Oppenheimer, B. D., et al. 2012, MNRAS, 426, 2797
Yang, X., Mo, H. J., & van den Bosch, F. C. 2009, ApJ, 695, 900
Zwaan, M. A., Meyer, M. J., Staveley-Smith, L., & Webster, R. L. 2005, MNRAS, 359, L30

SF2A 2014
J. Ballet, F. Bournaud, F. Martins, R. Monier and C. Reylé (eds)

GALAXY CLUSTERS IN THE SDSS STRIPE 82

F. Durret[1], C. Adami[2], E. Bertin[1], J. Hao[3], I. Márquez[4], N. Martinet[1], S. Maurogordato[5], T. Sauvaget[6], N. Scepi[7] and M.P. Ulmer[8]

Abstract.

We have searched for galaxy clusters in the Stripe 82 region of the Sloan Digital Sky Survey with AMACFI (Adami & MAzure Cluster FInder, Adami & Mazure 1999), and applied the same method to the Millennium simulation to estimate our detection efficiency and the approximate masses of the detected clusters. We detected 956 clusters at a 3σ level and above, in the redshift range $0.1 \leq z \leq 0.75$, with estimated mean masses between $\sim 10^{13}$ and a few 10^{14} $M_{\odot}$. Considering all the cluster galaxies (i.e. within a 2 Mpc radius of the cluster to which they belong and with a photo$-z$ differing by less than ± 0.1 from that of the cluster), we stacked clusters in various redshift bins to derive colour–magnitude diagrams and are in the process of deriving galaxy luminosity functions (GLFs).

For each galaxy brighter than $M_r < -19.5$, we computed the disk and spheroid components by applying a new version of SExtractor, and by stacking clusters we determined how the disk to spheroid flux ratio varies with cluster redshift and mass. The percentage of early to late type galaxies in clusters ranges roughly between 40% and 50%, and the fraction of late type to early type galaxies shows a slight increase ($\leq 10\%$) with redshift and a decrease ($\sim 10\%$) with cluster detection level, i.e. cluster mass.

From the properties of their galaxies, the *candidate clusters* detected here seem in majority to be "real" clusters, with typical cluster properties.

Keywords: Clusters of galaxies, SDSS Stripe 82

1 Introduction

The discovery of new galaxy clusters is important for two main reasons. First, clusters are important *per se*, since their detailed analysis allows to understand how galaxies form and evolve in various environments. And second, they play an important part in cosmology, since their number as a function of redshift allows to set constraints on cosmological parameters.

A number of methods is available to detect clusters in imaging surveys, among which AMACFI (Adami & MAzure Cluster FInder, Adami & Mazure 1999). We have applied this method to the CFHTLS Deep and Wide fields (Mazure et al. 2007, Adami et al. 2010, Durret et al. 2011) and recently applied this method to the SDSS Stripe 82 field (Durret et al. 2014, A&A to be submitted).

[1] UPMC Université Paris 06, UMR 7095, Institut d'Astrophysique de Paris, 98bis Bd Arago, F-75014, Paris, France
[2] LAM, OAMP, Université Aix-Marseille & CNRS, Pôle de l'Etoile, Site de Château Gombert, 38 rue Frédéric Joliot-Curie, 13388 Marseille 13 Cedex, France
[3] ETS Corporate Headquarters, 660 Rosedale Road, Princeton, NJ 08541, USA
[4] Instituto de Astrofísica de Andalucía, CSIC, Glorieta de la Astronomía s/n, 18008, Granada, Spain
[5] OCA, Cassiopée, Boulevard de l'Observatoire, B.P. 4229, F-06304 NICE Cedex 4, France
[6] Observatoire de Paris-Meudon, GEPI, 92195 Meudon Cedex, France
[7] ENS-Cachan, 61 avenue du Président Wilson, 94235 Cachan, France
[8] Department of Physics & Astronomy, CIREA, Northwestern University, Evanston, IL 60208-2900, USA

2 The data and method

The SDSS has obtained many scans in the so-called Stripe 82 (hereafter S82) field, defined by right ascension approximately in the range $310° - 59°$ and declination $|\delta| < 1.25°$ (J2000). Five photometric bands are available: u, g, r, i, and z.

We started with a catalogue of 13,621,718 objects, with positions, magnitudes and photometric redshifts (hereafter photo$-z$s), made by Reis et al. (2012). This catalogue is limited in magnitude to $i < 23$. To avoid incompleteness, we cut this catalogue at $z_{phot} \leq 0.75$ and were then left with a catalogue of 6,110,921 objects, used to detect cluster candidates.

We also retrieved the magnitude catalogue of 8,485,885 objects (Annis et al. 2011) which we later cross-correlated with the photo$-z$ catalogue to obtain a complete catalogue of 4,999,968 galaxies that was fed into the Le Phare software (Arnouts et al. 1999, Ilbert et al. 2006) to compute the absolute magnitudes that we will exploit to compute Galaxy luminosity functions (GLFs).

We applied the AMACFI to our photo$-z$ catalogue. As in Adami et al. (2010), we also applied it to the Millennium simulation (Springel et al. 2005), to assess the quality of the detections and to obtain a rough estimate of the relation between the cluster masses and the significance level at which clusters were detected.

We first divided the photo$-z$ catalogue in slices of 1 deg in right ascension, to make the data manageable (in ram-active CPU memory). Each subcatalogue was then divided in slices of 0.1 in redshift. We built galaxy density maps for each redshift slice, based on an adaptative kernel technique described in Mazure et al. (2007), with 100 bootstrap resamplings of the maps to estimate correctly the background level. The pixel size was 1.002 arcmin. We then detected structures in these density maps with the SExtractor software (Bertin & Arnouts 1996) in the different redshift bins at various significance levels: 3σ, 4σ, 5σ, 6σ, and 9σ (as defined by SExtractor).

The structures were then assembled in larger structures (called *detections* in the following) using a friends-of-friends algorithm (see Adami & Mazure 1999). Two *detections* with centers distant by less than 2 arcmin (twice the pixel size defined above) were merged into a single one which was assigned the redshift of the *detection* having the highest S/N. We did not merge *detections* within 2 arcmin into a single one if their photometric redshifts differed by more than 0.09, to avoid losing clusters that could be more or less aligned along the line of sight but located at very different redshifts. The typical uncertainty on cluster positions is therefore about 2 arcmin.

In this way, we obtained a final catalogue of 956 candidate clusters detected at a significance level between 3σ and 9σ. This catalogue will be available at the VizieR interface of the Simbad database `http://vizier.u-strasbg.fr/viz-bin/VizieR`.

We extracted the objects in the S82 with a spectroscopic redshift (z_{spec}) measurement and correlated this spectroscopic catalogue with our photo-z catalogue. We found a correct agreement between z_{spec} and photo-z, with a dispersion around the 1:1 relation between 0.05 and 0.1, confirming that photo$-z$s have errors between 0.05 and 0.1.

3 The cluster characteristics

In the catalogue of 956 cluster candidates, the numbers of clusters detected at or above the various significance levels of 3σ, 4σ, 5σ, 6σ, and 9σ are: 956, 416, 219, 130, and 30.

The photometric redshift distribution of the cluster surface density (i.e. the number of clusters divided by the surface covered by our catalogue, taken to be 270 deg^2) is shown in Fig. 1 for the 956 clusters detected in S82. The median redshift of our clusters is 0.35, in good agreement with the median redshift $< z >= 0.32$ found by Geach et al. (2011) for their sample of 4098 clusters (see below). The density of detected clusters falls quite rapidly for $z > 0.4$.

As expected, there are fewer high redshift clusters detected at high ($\geq 5\sigma$) than at low (3σ and 4σ) significance level.

By applying the same detection method to the Millennium simulation, we have shown (see Adami et al. 2010, hereafter A10, Table 2) that there is a rough correspondence between the cluster detection level and its mass. We have redone the same exercise here, selecting data from the Millennium simulation and adapting them to the conditions of the S82 data analysed here, i.e. with errors on photometric redshifts between ± 0.05 and ± 0.1, a limiting redshift $z \leq 0.75$ and a magnitude limit $i \leq 21$. We find that even for the most massive haloes the percentage of detection is small: at most 25%. So all we can give is an order of magnitude: clusters detected at 3σ and 4σ have masses in the range $[10^{13} - 9 \times 10^{13}\ M_{\odot}]$ while clusters detected at 6σ have masses

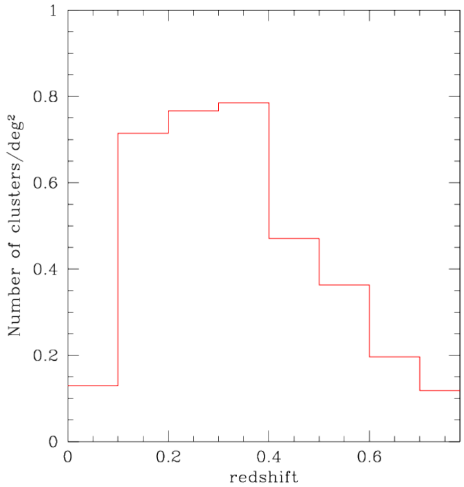

Fig. 1. Histogram of the surface density of the clusters detected in S82 in photometric redshift bins of 0.1.

in the range $[4 \times 10^{13} - 3 \times 10^{14}$ M$_\odot$]. As in A10, due to the fact that the Millennium simulation only covers an area corresponding to 1 deg^2, it includes no cluster corresponding to a 9σ detection in our study, so we cannot estimate the typical mass of the clusters detected at a 9σ level. All we can say is that these clusters must have masses larger than 10^{14} M$_\odot$.

Geach et al. (2011) detected 4098 clusters in the S82 region, but with a different definition, since they consider that a cluster begins with 5 galaxies. With this definition, it is not surprising that they detect many more clusters than us. The cross-correlation of our cluster catalogue with that of GMB, allowing a maximum identification distance of 3 arcmin, leads to 572 clusters in common. This matching radius was chosen to maximize the number of matches, taking into account the fact that the uncertainty on the cluster centers is about 2 arcmin. Out of these 572 clusters, 359 are at a redshift $z \leq 0.4$. If we consider only the 416 clusters that we detect at a significance level of 4σ or higher, 300 are at $z \leq 0.4$, and out of these 300, 225 are in common with GMB. So we can conclude that 75% of the clusters that we detect at a significance level of at least 4σ and at a redhift $z \leq 0.4$ are in common with GMB. If we now consider the clusters that we detect at a higher significance level, we find that 93% of the clusters detected at 5σ and above have a GMB counterpart, and *all* the candidate clusters that we detect at 6σ and above can be identified with a GMB cluster.

These results are satisfactory, since in spite of the differences in the methods applied to detect clusters and in the definition of what we and GMB consider as clusters, a very high percentage of the clusters that we detect at 5σ and above are also in the GMB catalogue. This means that both methods are powerful to detect the most massive clusters.

4 Properties of stacked clusters

Colour magnitude diagrams of clusters stacked in redshift bins show a red sequence, which is particularly well defined in the (r-i) versus i plot. This allows us to select cluster galaxies along the red sequence and derive GLFs. We are in the process of computing GLFs in bins of redshift but have not completed this work at the time of submission of the present contribution. All our future results will be described in a forthcoming paper (Durret et al. 2014, A&A to be submitted).

5 Morphological properties of cluster galaxies

Based on the catalogue of clusters that we have detected we have analysed statistically the morphological properties of the galaxies having a large probability of being in these clusters, i.e. for a given cluster, all the galaxies within 2 Mpc of the cluster center and with a photo$-z$ within ± 0.1 of the cluster photo-z.

To estimate the morphological properties of the galaxies, we extracted images of 4850×4850 pixels^2, with a pixel scale of 0.396 arcsec/pixel, in the g, r and i bands, around each cluster. We applied a new tool developed in SExtractor that calculates for each galaxy the respective fluxes in the bulge (spheroid) and disk. This new experimental SExtractor feature fits to each galaxy a two-dimensional model including a de Vaucouleurs spheroid (the bulge) and an exponential disk. The PSF model used in the fit was derived with the PSFEx software (Bertin 2011) from a selection of point source images. The model fitting was carried out in the g, r, and i bands.

We applied this tool to look for differences in galaxy morphologies as a function of redshift and of significance level of the cluster detection (which is related to cluster mass) by computing for each galaxy the flux in the disk f_{disk} and that in the spheroid $f_{spheroid}$. We classified a galaxy as early type if $f_{spheroid} > f_{disk}$ and as late type if $f_{disk} \geq f_{spheroid}$. SExtractor also computes the errors on these fluxes and on the $f_{spheroid}/f_{disk}$ flux ratio.

Before stacking clusters, and searching for variations of galaxy morphologies with redshift, we made a cut in absolute magnitude in order to have comparable samples in all the redshift bins. This cut was made at $M_r \geq -19.5$, where the error on the flux ratio remains smaller than 20% for a majority of galaxies.

We limited our sample to the 416 clusters detected at a 4σ level and above, to have a sample of clusters as reliable as possible. Since no significant difference is observed between the bulge to disk decompositions in the g, r and i bands, we will only present results in the r band.

We stacked clusters in six redshift bins: $z \leq 0.15$, $0.15 < z \leq 0.25$, $0.25 < z \leq 0.35$, $0.35 < z \leq 0.45$, $0.45 < z \leq 0.55$ and $z > 0.55$ and computed the percentages of late type galaxies. If we assume that there is no observational bias due to the loss of spatial resolution for galaxies when redshift increases, we find that the percentage of late type galaxies tends to decrease with redshift, opposite to what is expected. We also stacked clusters in four bins of detection level: 4σ, 5σ, 6σ and 9σ, which roughly correspond to cluster mass bins. We find that the percentage of late type galaxies tends to increase with significance level, oppositely to what is expected (more massive clusters are expected to host more early type galaxies).

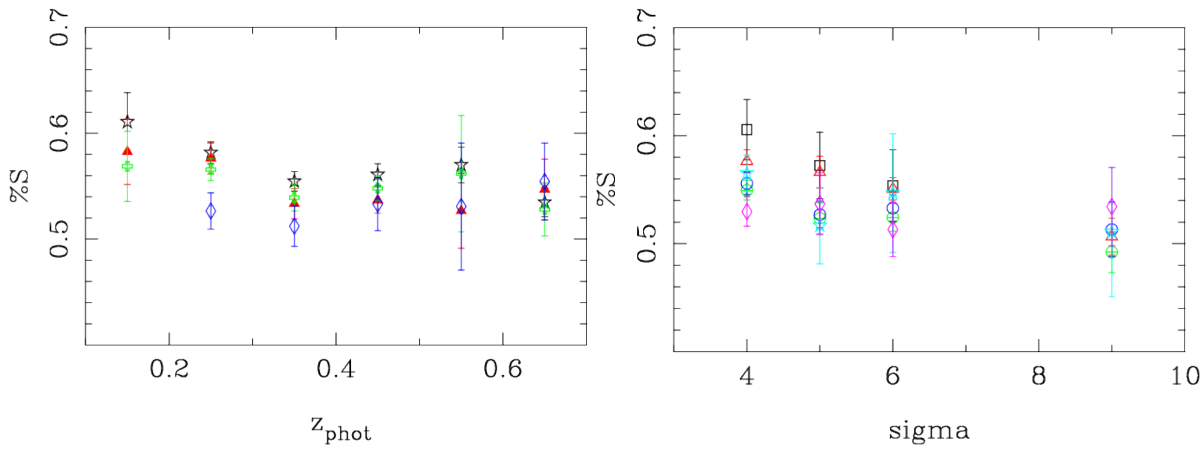

Fig. 2. Left: percentage of late type galaxies as a function of redshift, based on the bulge to disk decomposition in the r band. The data points are colour–coded as a function of detection level: black stars for 4σ, red triangles for 5σ, green squares for 6σ and blue diamonds for 9σ. **Right**: percentage of late type galaxies as a function of detection level, based on the bulge to disk decomposition in the r band. The data points are colour–coded in bins of redshift: black squares for $z \leq 0.15$, red triangles for $0.15 < z \leq 0.25$, green circles for $0.25 < z \leq 0.35$, blue circles for $0.35 < z \leq 0.45$, cyan stars for $0.45 < z \leq 0.55$, and magenta diamonds for $z > 0.55$. In both figures, the correction factors mentioned in the text have been applied.

We performed simulations to test the hypothesis that these unexpected results could be due to an observational bias. We found that, as a bias due to redshift, the percentage of late type galaxies tends to decrease with redshift and that of early types to increase. Therefore, when estimating the early type to late type ratio, a correcting factor must be applied to correct for this bias.

If we apply this correction factor (that varies with redshift), we obtain the results displayed in Fig. 2. In these two figures, error bars were taken to be Poissonian: $\sqrt{N}/N$, where N is the number of late type galaxies corresponding to each point.

We can see in these figures that the percentages of late type galaxies range between 50% and 60%. These percentages remain quite constant for $z > 0.3$, while at lower redshift they tend to decrease a little with redshift, at least in the first bin or two of significance level, except for the most massive clusters (those detected at 9σ). Comparably, the percentages of late type galaxies are found to decrease with detection level (i.e. with mass) in the two or three bins of lowest redshift, while variations become smaller for $z \geq 0.35$.

6 Summary and conclusions

Based on the photometric redshift (hereafter photo$-z$) catalogue of Reis et al. (2012), we have searched for galaxy clusters in the Stripe 82 region of the Sloan Digital Sky Survey by applying the AMACFI cluster finder (Mazure et al. 2007). We detected 956 clusters at a 3σ level and above, in the redshift range $0.1 \leq z \leq 0.75$, with estimated mean masses between $\sim 10^{13}$ and a few 10^{14} $M_{\odot}$. A large fraction of these candidate clusters are in common with Geach et al. (2011).

The morphological analysis of the *cluster galaxies* shows that the fraction of late type to early type galaxies shows a slight increase ($\leq 10\%$) with redshift and a decrease ($\sim 10\%$) with significance level, i.e. cluster mass. This result is obtained after correcting for a bias due to the effect of increasing redshift that we quatified through simulations.

From the properties of their galaxies, the 956 candidate clusters detected here with AMACFI seem in majority to be "real" clusters, with typical cluster properties. Spectroscopic confirmation is of course necessary. It would require too much telescope time to observe all these clusters, but spectroscopic data are already available in the SDSS for some of them, and we intend to use this information in a near future. As yet another confirmation to the reality of the clusters detected in S82, we intend to identify our candidate clusters with diffuse X-ray sources detected by XMM-Newton (Takey et al. 2014).

Besides, by stacking the *cluster galaxies* in various redshift bins, we find a clear red sequence in the $(r - i)$ versus i colour-magnitude diagram, and the preliminary galaxy luminosity functions of *cluster galaxies* that we have obtained are typical of cluster GLFs. These properties make us confident that we have detected in majority *bona fide* clusters.

A comparison between our technique applied to the same data set as GMB indicates that if the candidates based on our method are 6σ detections, the sample should be well over 93% complete. In this case, the technique used to make the cluster catalog should not dominate the derivation of cosmological parameters. So AMACFI appears well adapted to search for clusters to do cosmology, though of course it should be coupled with other cluster finders to improve the robustness of detections.

We acknowledge long term financial support from CNES.

References

Adami C. & Mazure A. 1999, A&AS 134, 393
Adami C., Durret F., Benoist C. et al. 2010, A&A 509, 81
Annis J., Soares-Santos M., Lupton R.H. et al. 2011, arXiv:1111.6619
Arnouts S., Cristiani S., Moscardini L. et al. 1999, MNRAS 310, 540
Bertin E. & Arnouts S. 1996, A&A 117, 393
Bertin E. 2011, ASPC 442, 435
Geach J.E., Murphy D.N.A., Bower R.G. 2011, MNRAS 413, 3059
Ilbert O., Arnouts S., McCracken H.J. et al. 2006, A&A 457, 841
Mazure A., Adami C., Pierre M. et al. 2007, A&A 467, 49
Reis R.R.R., Soares-Santos M., Annis J. et al. 2012, ApJ 747, 59
Springel V., White S.D.M., Jenkins A. et al. 2005, Nature 435, 629
Takey A., Schwope A., Lamer G. 2014, A&A 564, 54

SF2A 2014
J. Ballet, F. Bournaud, F. Martins, R. Monier and C. Reylé (eds)

MAGNETOGENESIS AT COSMIC DAWN

J.-B. Durrive[1,2] and M. Langer[1,2]

Abstract. We present a mechanism for generating cosmological magnetic fields during the Epoch of Reionization, based on the photoionization of intergalactic hydrogen. A general formula is presented, together with an example numerical application which yields magnetic field strengths between 10^{-23} to 10^{-19} G on intersource scales. This mechanism, which operates all along Reionization around any ionizing source, participates to the premagnetization of the whole intergalactic medium. Also, the spatial configuration of these fields may help discriminate them from those produced by other mechanisms in future observations.

Keywords: Cosmology:theory, magnetic fields, large-scale structure of universe

1 Introduction

The Universe is magnetized at all scales: magnetic fields are observed in stars, galaxies and galaxy clusters, at essentially every stage of their evolution. The origin of such fields is however still an open question, especially on cosmological scales (e.g. Ryu et al. (2012)). The current paradigm is based on the idea that they where first generated very early in the history of the Universe with very weak strengths. Only then were they amplified during the formation of large scale structures, essentially through turbulent motions, and thus reached the values we observe today. However the evolution of structures has been strongly non-linear, i.e. far too complex for us to recover, from present day measurements, any information on the strength and configuration of the fields at the time they were generated. But recent high energy gamma ray observations suggest that a substantial fraction, if not the whole, of the intergalactic space is magnetized too. This is extremely interesting since unlike within structures, the non-linearity in the intergalactic medium has been only mild at most. Therefore, intergalactic magnetic fields may have conserved signatures of their initial properties. Understanding present-day intergalactic magnetic fields could thus be the key to understanding the origin of cosmic magnetism. Numerous mechanisms to account for the existence of such fields have already been proposed. But none of them is entirely satisfactory. The difficulty is to generate large enough strengths at large enough scales. Usually proposed mechanisms fail to comply with both requirements at the same time, or they need to invoke exotic physics in order to do so.

2 The mechanism

Revisiting Langer et al. (2005), we present an analytical model of cosmological magnetogenesis based on plasma-radiation interactions which occur during the Epoch of Reionization. As the first luminous objects formed, they emitted ionizing radiation which photoionized the neutral intergalactic medium (IGM), thus generating currents and inducing magnetic fields. The reionization of the Universe was accomplished by Population III stars, first galaxies and first quasars. Each source formed a fully ionized area (Strömgren sphere) around itself but long mean free path photons (UV and X) escaped into the IGM. Those photons knocked out free a fraction of bound electrons and transferred to them their momentum, generating radial currents and induced magnetic fields. But magnetic fields generated by adjacent currents compensate each other, unless these currents have different intensities. This condition is actually satisfied thanks to inhomogeneities in the IGM. Therefore magnetic fields

[1] Institut d'Astrophysique Spatiale, Bâtiment 121, Univ. Paris-Sud, UMR8617, Orsay, F-91405
[2] CNRS, Orsay, F-91405.

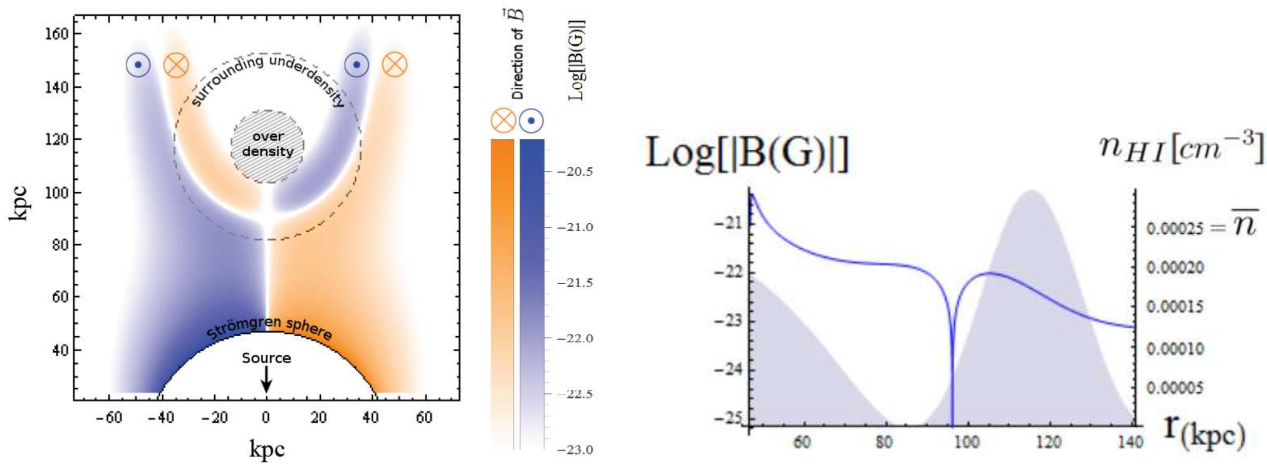

Fig. 1. Left: Spatial distribution around an IGM inhomogeneity of the B-field (in Gauss) with a $z = 10$ galaxy source. The symbols $\odot$ and $\otimes$ indicate that the field points towards and away from the reader, respectively. **Right:** Strength of the B-field along a path through the inhomogeneity (sketched in grey).

are generated *where the IGM is inhomogeneous.* More precisely, we show in detail in Durrive & Langer (2014) that sources generate outside their Strömgren spheres the following magnetic field:

$$\vec{B}(t,\vec{r}) = \frac{1}{ex_e}\left(N_1\frac{\vec{\nabla}x_e}{x_e} + N_2\vec{\nabla}\int_{r_s}^{r} n_{HI}dr\right) \times \frac{\hat{r}}{4\pi r^2}\ t$$

where, for $i = 1, 2$, $N_i(t,\vec{r}) = \int_{\nu_0}^{\infty} f_{\rm mt}\sigma_\nu^i L_\nu e^{-\tau_\nu}d\nu$. In this expression, the first term is local while the second is global. They correspond to the necessity that two adjacent currents have different intensities. This is satisfied either when the matter configuration differs in two adjacent volume elements, or when the intensity of the ionizing radiation incident on two adjacent volume elements differs. This is reflected in the equation above, where the local term corresponds to local inhomogeneities in the electron fraction, and the global term corresponds to the transverse variation of photon absorption along adjacent lines-of-sight. In addition, we recover naturally the geometric dilution of photons, the strength being proportional to r^{-2}. Note also that the strength is linearly growing with time, essentially because we assumed a constant luminosity, and the mechanism operates until the source dies. N_1 and N_2 characterize the impact that the source has at distance $\vec{r}$ at time t. Indeed, they contain the fraction of momentum transferred from photons to electrons $f_{\rm mt}$, the photoionization cross section σ_ν, the spectrum of the source L_ν and the optical depth τ_ν.

This analytical formula is valid for any ionizing source during Reionization. As an illustrative numerical application, we considered the case of Population III clusters and first galaxies with spectra computed with the Yggdrasil model (Zackrisson et al. (2003)), as well as quasars with spectra fitted from observations (Shang et al. (2011)), with a mildly non-linear inhomogeneity outside the Strömgren sphere of the source. The results are that, depending on their spectrum, luminosity, lifetime and epoch, different sources generate different magnetic fields (cf. figures 1 and 2). Namely, Pop III clusters generate stronger fields on short scales, while quasars

Redshift	*Source*	*Log*[B(*G*)]	*scale* (*kpc*)	$\frac{1}{2}d_{intersource}$ (*kpc*)
30	*Pop III*	$-19/-21$	0.3/1	10
20		$-19/-21$	0.5/1	
20	*First galaxy*	$-20/-22$	10/15	25
10		$-21/-22$	30/100	
10	*Quasar*	$-21/-22$	300/1000	1000
6		$-22/-23$	500/1500	

Fig. 2. Typical values of the resulting fields and scales.

magnetize less but over huge distances. First galaxies combine high amplitudes and large scales (intersource scales). Also, the geometrical configuration of the fields relfects the axisymmetry of the matter distribution with respect to the ionizing source, and fields generated in overdensities have opposite orientation to those generated in underdensities (cf. figure 1).

3 Conclusion

The mechanism presented here operates with any ionizing source, at any time during the Epoch of Reionization. The resulting magnetic strengths are comparable to those generated by other astrophysical mechanisms, but they appear on entire intersource distances. Therefore it contributes to the premagnetization of the whole Universe. Also, the specific spatial configuration of the generated fields might help discriminate from other cosmological magnetogenesis mechanisms with future observations (e.g. SKA) of the evolved magnetic fields.

In future work we shall consider more realistic (aspherical) Strömgren spheres. It will increase the anisotropy, thus should increase the strength of the fields as they rely on gradients. Also, it will be interesting to look at the statistical properties at large scales by considering a distribution of inhomogeneities. Finally, the processing of the fields by large scale turbulence from structure formation will be considered.

This work has been funded by the P2IO LabEx (ANR-10-LABX-0038) in the framework 'Investissements d'Avenir' (ANR-11-IDEX-0003-01) managed by the French National Research Agency (ANR).

References

Durrive, J.-B. & Langer, M. 2014, to be submitted

Langer, M., Aghanim, N., & Puget, J.-L. 2005, A&A, 443, 367

Ryu, D., Schleicher, D., Treumann, R., Tsagas, C., & Widrow, L. 2012, Space Sci Rev, 166, 1

Shang, Z., Brotherton, M., & Beverley, J., e. a. 2011, ApJS, 196, 2

Zackrisson, E., Rydberg, C.-E., Schaerer, D., Östlin, G., & Tuli, M. 2003, ApJ, 740, 13

SF2A 2014
J. Ballet, F. Bournaud, F. Martins, R. Monier and C. Reylé (eds)

ON THE STABILITY OF SELF-GRAVITATING FILAMENTS

J. Freundlich[1], C. J. Jog[2], F. Combes[1] and S. Anathpindika[2]

Abstract. Filamentary structures are very common in astrophysical environments and are observed at various scales. On a cosmological scale, matter is usually distributed along filaments, and filaments are also typical features of the interstellar medium. Within a cosmic filament, matter can possibly contract and form galaxies, whereas an interstellar gas filament can clump into a series of bead-like structures which can then turn into stars. To investigate the growth of such instabilities and the properties of the resulting substructures, we consider idealized self-gravitating filaments and derive the dispersion relation for perturbations within them. We assume no specific density distribution, treat matter as a fluid, and use hydrodynamics to derive the linearized equations that govern the growth of perturbations. Assuming small local perturbations leads to a dispersion relation analogous to the spherical Jeans case: perturbations of size higher than the Jeans length collapse and asymmetries regarding their growth rates arise only because of rotation. For perturbations of arbitrary size, the dispersion relation retains its complex terms: all modes are potentially unstable, but elongated perturbations near the axis of the cylinder grow faster. Prolate substructures and global collapse are favored, which is corroborated by most observations of interstellar filaments.

Keywords: gravitation, hydrodynamics, instabilities, large-scale structure of the Universe, ISM: structure

1 Introduction

Although filaments have been observed since decades within molecular clouds (e.g., Schneider & Elmegreen 1979), cosmological simulations and high-resolution observations of the interstellar medium only recently showed the key role played by filamentary structures at various scales in astrophysics. Filamentary structures are indeed ubiquitous and involved in processes as varied as gas accretion onto galaxies and the formation of stars in the interstellar medium.

On cosmological scales, matter is usually distributed along filaments, forming a cosmic web that connects galaxies to one another (e.g., Bond et al. 1996) and provides a gas reservoir from which galaxies grow and accrete (e.g., Kereš et al. 2005; Dekel et al. 2009). The inner core of many of these filaments may be predominantly made of gas, as notably shown by simulations by Harford et al. (2008), motivating models which treat them as self-gravitating, isothermal or barotropic cylinders in hydrostatic equilibrium.

In the interstellar medium, observations show filamentary structures on much smaller scales (e.g., André et al. 2010; Arzoumanian et al. 2011). Motivated by Herschel observations of star-forming environments, André et al. (2010) suggest a scenario in which the formation of turbulence-driven filaments in the interstellar medium represents the first step towards core and star formation. The densest filaments would then fragment into pre-stellar cores owing to gravitational instability. Simulations reveal filamentary features arising either from turbulence (e.g., Padoan et al. 2001) or from intermediate stages of gravitational collapse (e.g., Gomez & Vazquez-Semadeni 2014).

2 Studying the growth of instabilities through linearized equations

The standard Jeans instability describes the collapse of a spherical gas cloud when the inner pressure is not strong enough to support the self-gravitating gas. The cylindrical case is more complicated and has not been fully investigated yet. Our goal is to obtain a dispersion relation for small perturbations arising in an idealized

[1] LERMA, Observatoire de Paris, CNRS, 61 av. de l'Observatoire, 75014 Paris, France
[2] Department of Physics, Indian Institute of Science, Bangalore 560012, India

filament in order to better understand the behavior of such perturbations, and to compare their properties with available observations and simulations. In order to do so, we derive the linearized dynamical equations that govern the perturbations and obtain the resulting dispersion relation, first for local perturbations within a rotating filament (section 3), and then for perturbations of any extent within a non-rotating filament (section 4).

Our idealized picture consists of an infinite self-gravitating cylinder with pressure and density related by a barotropic equation of state. We neglect the role of magnetic fields for simplicity, treat matter as an inviscid fluid and use hydrodynamics to obtain the linearized equations that govern the perturbations. Cylindrical symmetry involves no dependance on the axial and azimuthal coordinates z and ϕ for the unperturbed system, and we only consider axisymmetric perturbations. The unperturbed system is assumed to be at equilibrium, and we further assume that all fluid particles share the same initial axial velocity, $\vec{v_0}(R,\phi) = R\Omega_0(R)\ \vec{e_\phi}$, where $\Omega_0(R)$ is the undisturbed angular velocity, $\vec{e_\phi}$ the azimuthal unit vector and R the radial distance. The calculations are valid for any density profile $\rho_0(R)$, and the unperturbed gravitational field $\Phi_0(R)$ is set by the Poisson equation.

Assuming axisymmetric perturbations of the generic form $e^{-i\omega t}e^{ik_R R}e^{ik_z z}$ and introducing Oort constant $B(R) = -\frac{1}{2}\left[\Omega_0(R) + \frac{\partial}{\partial R}\left(R\Omega_0(R)\right)\right]$, the dynamics of the perturbed system is determined by the following set of linearized first-order equations, where the infinitesimal disturbances are denoted by an index 1 while an index 0 corresponds to the unperturbed system (e.g., Mikhailovskii & Fridman 1973):

$$\omega v_{1R} - 2i\Omega_0 v_{1\phi} = -i\frac{\partial h_1}{\partial R} + k_R\Phi_1 \tag{2.1}$$

$$\omega v_{1\phi} - 2iBv_{1R} = 0 \tag{2.2}$$

$$\omega v_{1z} = k_z c_0^2\frac{\rho_1}{\rho_0} + k_z\Phi_1 \tag{2.3}$$

$$\omega\rho_1 + i\frac{1}{R}\frac{\partial}{\partial R}\left(R\rho_0 v_{1R}\right) - k_z\rho_0 v_{1z} = 0 \tag{2.4}$$

$$\frac{1}{R}\frac{\partial}{\partial R}\left(R\frac{\partial\Phi_1}{\partial R}\right) - k_z^2\Phi_1 = 4\pi G\rho_1. \tag{2.5}$$

These equations correspond respectively to the three projections of the equation of motion, the continuity equation, and the Poisson equation. The linearized barotropic equation of state yields for its part an enthalpy perturbation

$$h_1 = c_0^2\ \frac{\rho_1}{\rho_0} \tag{2.6}$$

where $c_0(R)$ is the effective sound speed, defined by $c_0^2 = \partial p_0/\partial\rho_0$ and potentially varying with radius. The pressure support could be thermal as well as turbulent.

3 Local perturbations in a rotating filament

We first assume local perturbations: the typical scale of the perturbation is small compared to that of the unperturbed quantities, i.e., $k_R R_0 >> 1$, where R_0 is the typical radius for the unperturbed distribution. This assumption is analogous to the Wentzel-Kramers-Brillouin approximation (WKB) used in quantum physics and leads to the following local dispersion relation (Freundlich et al. 2014):

$$\omega^4 + \omega^2\left(4\pi G\rho_0 - c_0^2k^2 - \kappa^2\right) + \kappa^2k_z^2\left(c_0^2 - \frac{4\pi G\rho_0}{k^2}\right) = 0 \tag{3.1}$$

where $k = \sqrt{{k_R}^2 + {k_z}^2}$ corresponds to the total wavenumber and $\kappa(R)$ is the epicyclic frequency, defined by $\kappa^2 = -4\Omega_0 B$. $\rho_0(R)$ and $c_0(R)$ are respectively the initial density distribution and the effective sound speed.

This polynomial equation can be treated as a second order polynomial expression in ω^2 and it can be shown that its two roots ω_-^2 and ω_+^2 are real, with $\omega_-^2 < \omega_+^2$ and $\omega_+^2 \geq 0$. The system is thus globally stable to axisymmetric perturbations when $\omega_-^2 \geqslant 0$ and unstable when $\omega_-^2 < 0$, as growing modes require a non-zero imaginary part. Rotation generates asymmetries in the distribution of ω_-^2 in the phase plane (k_R, k_z) but the induced boundary between the stable and unstable regimes is symmetrical: the system is stable when $k^2 \geqslant k_{\rm crit}$ with $k_{\rm crit} = 4\pi G\rho_0/c_0^2$, and unstable below, which corresponds to the standard Jeans criterion. When there is no rotation, the dispersion relation further reduces to the standard dispersion relation for collapsing spherical systems. Figure 1 shows an illustrative example of the distribution of ω_-^2 for a rotating filament, where the asymmetries generated by rotation and the symmetrical boundary between stable and unstable regimes in the phase plane (k_R, k_z) are visible.

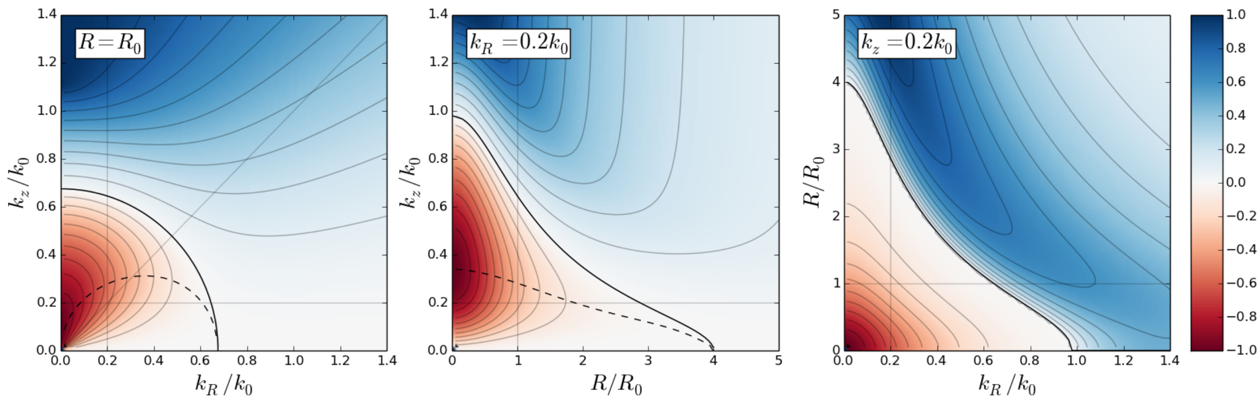

Fig. 1. As an illustrative example, we model a filament from the Taurus molecular cloud, TMC-1, with a Plummer-like density profile (Malinen et al. 2012) and plot the resulting distribution of ω_-^2 in the planes $R = R_0$, $k_R = 0.2k_0$, and $k_z = 0.2k_0$, where $k_0 = \sqrt{4\pi G\rho_c}/c_0$ is a characteristic wavenumber depending on the central density ρ_c. Negative values of ω_-^2 correspond to an unstable filament, and the solid black curve separates the stable and unstable regimes ($k = k_{\rm crit}$). The dashed line corresponds to the minimum value of the frequency, i.e., to the most unstable mode.

4 Global perturbations in a non-rotating filament

The local WKB assumption prevents the perturbations feeling the large-scale geometry of the system and thus leads to the standard spherical Jeans case when there is no rotation. Releasing the WKB assumption should enable to better understand the specific effects of cylindrical geometry. Without this assumption and for non-rotating cylinders, the dispersion relation retains its complex terms and all modes are thus potentially unstable:

$$\omega^2 = -4\pi G\rho_0 \frac{k^2}{k^2 - i\frac{k_R}{R}}\left[1 - i\frac{k_R}{k^2}\left(\frac{1}{R} + \frac{1}{\rho_0}\frac{\partial\rho_0}{\partial R}\right)\right] + c_0^2k^2 - ik_R\left[\frac{c_0^2}{R} + \frac{\partial c_0^2}{\partial R}\right] - \left[\frac{1}{R} + \frac{1}{\rho_0}\frac{\partial\rho_0}{\partial R}\right]\left[\frac{\partial c_0^2}{\partial R} - c_0^2\frac{1}{\rho_0}\frac{\partial\rho_0}{\partial R}\right]. \tag{4.1}$$

Our previous calculations (Freundlich et al. 2014) included rotation. But although signs of rotation such as transverse velocity gradients are observed for interstellar filaments, and notably for TMC-1 in the Taurus molecular cloud (Olano et al. 1988), there generally does not seem to be a global coherent rotation of such filaments (e.g., Falgarone et al. 2001). This is why we restricted our calculations to non-rotating filaments here, as a first approximation.

As shown in Figure 2, this dispersion relation 4.1 shows that elongated perturbations near the axis of the filament grow faster, thus favoring elongated substructures. This is corroborated by observations, as most observations in the Taurus molecular cloud or in other molecular clouds favor prolate structures within interstellar filaments and tend to show that cores are stretched along the direction of the filaments (e.g., Curry 2002; Hartmann 2002).

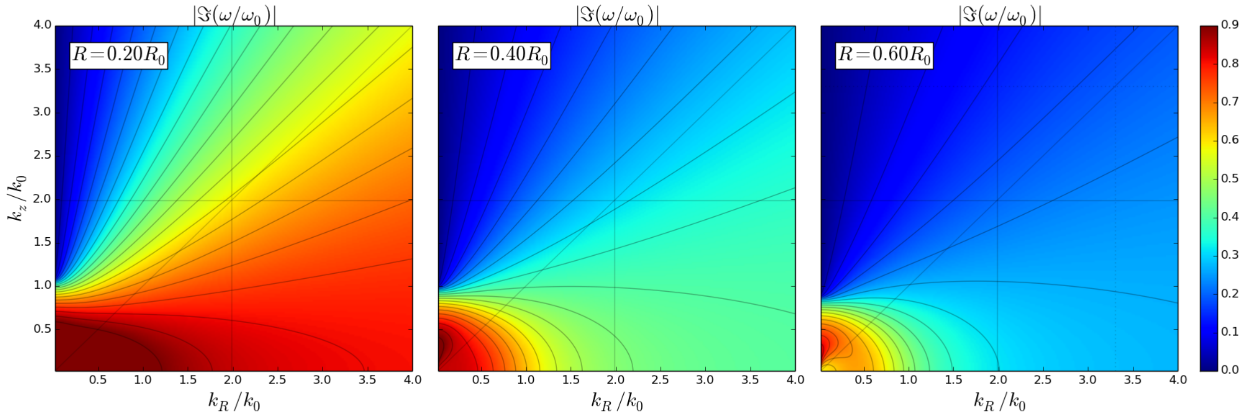

Fig. 2. Imaginary part of the angular frequency for an idealized filament inspired by TMC-1 in the phase plane (k_R, k_z) for three different radii, as derived from equation 4.1. The plotted quantity is a measure of the growth rate of the perturbations, thus prolate structures with $k_z < k_R$ are likely to be favored and we expect them to be more elongated nearest to the center of the filament, as shown by the change with radius of the isocontour lines.

5 Conclusion

We derived a dispersion relation for axisymmetric perturbations in infinite, self-gravitating, gaseous filaments in two different cases: (i) for perturbations of small extent when the filament is rotating (section 3), and (ii) for perturbations of any extent when the filament is not rotating (section 4). The gas is assumed to be barotropic, and the relations are valid for any type of density profile. In the first case, perturbations of size higher than the Jeans length collapse and asymmetries only arise because of rotation, whereas in the second case, all modes are potentially unstable but elongated perturbations near the axis of the cylinder grow faster, which is corroborated by most observations of interstellar filaments.

Our model assumes an infinite and isolated filament, but we could generalize our calculations to a cylinder of finite size and take into account the effects of the environment and of more complex velocity distributions. This work should be complemented by more detailed comparisons with observations and by numerical studies of the formation and subsequent collapse of idealized filaments, which we plan to do in future studies.

This work benefited from the European Research Council Advanced Grant Program number 267399 - Momentum, and J. F. acknowledges support from the Indo French Center for the Promotion of Advanced Research (IFCPAR/CEFIPRA) through a Raman-Charpak fellowship.

References

André, P., Menshchikov, A., Bontemps, S., et al. 2010, A&A, 518, 102
Arzoumanian, D., André, P., Didelon, P., et al. 2011, A&A, 529, 6
Bond, J. R., Kofman, L., & Pogosyan, D. 1996, Nature, 380, 603
Curry, C. L. 2002, ApJ, 576, 849
Dekel, A., Birnboim, Y., Engel, G., et al. 2009, Nature, 457, 451
Falgarone, E., Pety, J., & Phillips, T. G. 2001, ApJ, 555, 178
Freundlich, J., Jog, C. J., & Combes, F. 2014, A&A, 564, 7
Gomez, G. C. & Vazquez-Semadeni, E. 2014, submitted to ApJ [arXiv:1308.6298]
Harford, A. G., Andrew, J. S., & Gnedin, N. Y. 2008, MNRAS, 389, 880
Hartmann, L. 2002, ApJ, 578, 914
Kereš, D., Katz, N., Weinberg, D. H., & Davé, R. 2005, MNRAS, 363, 2
Malinen, J., Juvela, M., Rawlings, M. G., et al. 2012, A&A, 544, 50
Mikhailovskii, A. B. & Fridman, A. M. 1973, Soviet Physics - JETP, 17, 57
Olano, C. A., Walmsley, C. M., & Wilson, T. L. 1988, A&A, 196, 194
Padoan, P., Juvela, M., Goodman, A. A., & Nordlund, Å. 2001, ApJ, 553, 227
Schneider, S. & Elmegreen, B. G. 1979, ApJS, 41, 87

SF2A 2014
J. Ballet, F. Bournaud, F. Martins, R. Monier and C. Reylé (eds)

DISC GALAXIES: MOLECULAR HYDROGEN, STAR FORMATION AND RADIAL MIGRATION

A. Halle[1], F. Combes[2], P. Di Matteo[3] and M. Haywood[3]

Abstract. We show the importance of molecular hydrogen to simulate the evolution of disc galaxies with improved realistic interstellar medium and stellar formation. The inclusion of H_2 cooling is especially important in the low-metallicity regions such as the outer parts of discs, in which it allows for some slow star formation.

We study the evolution of the obtained stellar components of these galaxies and focus on the radial migration that occurs due to the resonances of the bar and transient spiral arms in the disc.

Keywords: Galaxies: evolution — Galaxies: ISM — Galaxies: spiral — Galaxies: star formation — Galaxies: structure

1 Introduction

The interstellar medium of disc galaxies is highly multiphase with the coldest and densest hydrogen phase consisting mainly of molecular hydrogen. This molecular phase is thus strongly correlated with star formation, as shown by Bigiel et al. (2008) in resolved observations of local disc galaxies. H_2 can play an especially important role for star formation in the low metallicity outer parts of disc galaxies. Ultraviolet observations by GALEX have shown that star formation can be active at large radii, much farther than the optical radius R_{25}, in regions where H_α observations are not able to reveal moderate-age populations of stars (Thilker et al. 2005; Gil de Paz et al. 2005, 2007). The presence of molecular hydrogen and star formation in outermost discs of spirals is also of prime importance to study cold gas accretion, which is considered one key factor in galaxy evolution (e.g. Kereš et al. 2005; Dekel et al. 2009).

We have performed simulations of isolated disc galaxies that include some detailed low-temperature cooling, especially H_2 cooling. We study the star formation and the evolution of the stellar component of the disc. Stars in galactic discs do not remain at their birth radius. In addition to epicyclic motion, the oscillations around a guiding radius, they undergo some radial migration due to angular momentum transfer (Sellwood & Binney 2002, e.g.). This radial migration impacts the stellar age and metallicity profiles. It could reconcile inside-out formation scenarios with some 'U-shaped' stellar age profiles inferred from observations (Bakos et al. 2008; Barker et al. 2007; Williams et al. 2009, e.g.) but its importance is still debated, for example in the Milky Way (Haywood et al. 2013).

2 Molecular hydrogen effect on star formation

In Halle & Combes (2013) we present simulations of Sb type disc galaxies performed with the N-body SPH Gadget-2 code (Springel 2005) to which we added some baryonic physics including some stochastic star formation reproducing a Schmidt law, kinetic core-collapse supernovae feedback, and detailed cooling including low-temperature cooling due to metals and H_2. The metallicity of the gas is assumed to decrease with radius. We computed a local mass fraction of H_2 using an adaptation of the semi-analytic recipe developed by

[1] Institut d'Astrophysique de Paris, 98 bis boulevard Arago, 75013 Paris, France
GEPI, Observatoire de Paris, 5 place Jules Janssen 92190 Meudon, France
[2] LERMA, Observatoire de Paris, 61 avenue de l'Observatoire 75014 Paris, France
[3] GEPI, Observatoire de Paris, 5 place Jules Janssen 92190 Meudon, France

(Krumholz et al. 2008, 2009; McKee & Krumholz 2010), using the UV flux from young stars formed in the disc. More details on the parameters of the simulations and on the baryonic physics recipes can be found in Halle & Combes (2013).

The total neutral H gas, HI and H_2 components of a simulated gas disc are shown on Fig. 1. It can be seen that the disc is much thinner in H_2 than in HI. H_2 is distributed in thin or clumpy regions (bar, spiral arms, various clumps), while the distribution of HI is more diffuse. Density peaks due to these features of the gas occur at larger radii when molecular hydrogen allows the gas to cool down in the low metallicity outer discs. Molecular hydrogen thus allows for these outer parts of discs to exhibit some slow star formation. The comparison to simulations without H_2 can be seen on Fig. 2 where the left panel shows the difference of extension of discs of formed stars and the right panel shows the SFR as a function of galactocentric radius. There is an increase in SFR at large radii for all SNII feedback efficiencies that were tested. We also show the surface SFR is more correlated with the H_2 gas than with the HI gas, as obtained in observations (Bigiel et al. 2008, e.g.) (see Fig. 25 of Halle & Combes (2013)).

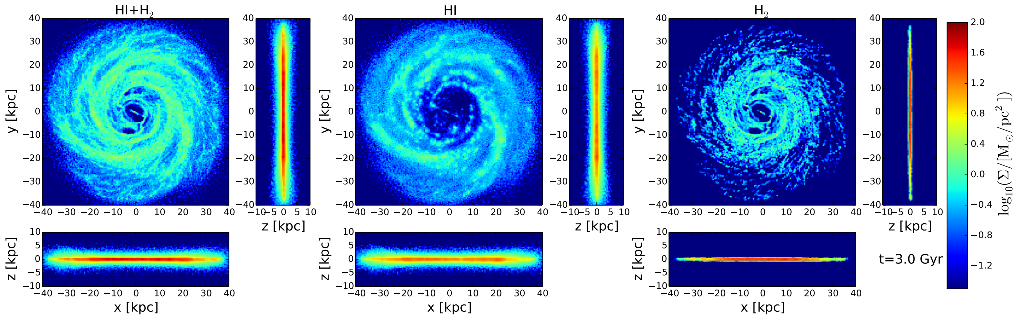

Fig. 1. Left: Surface density map of HI + H_2. **Middle:** Surface density map of HI. **Right:** Surface density map of H_2. The colour bar is the same for all plots and is shown on the right.

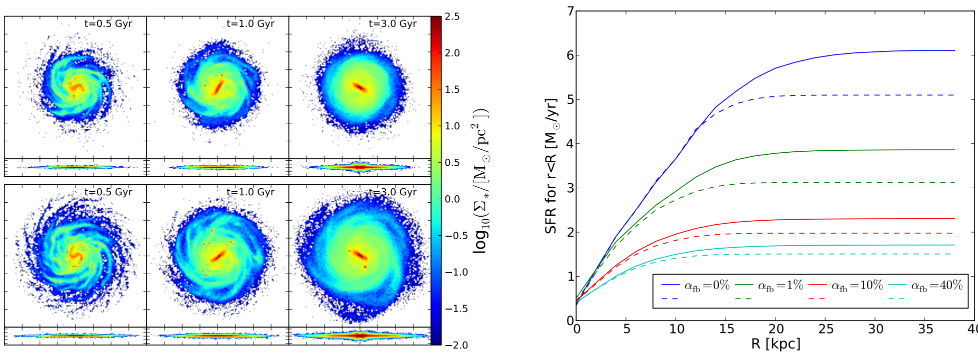

Fig. 2. Left: Surface density of stars formed during simulations after 0.5 Gyr, 1 Gyr and 3 Gyr of evolution with the same parameters except for the presence or absence of H_2. Top row: no H_2 cooling. Bottom row: H_2 cooling. **Right:** Cumulative SFR as a function of galactocentric radius, averaged on the first Gyr, for runs with varying feedback efficiencies. Solid lines: run with H_2. Dashed lines: run without H_2.

3 Radial migration

Radial stellar migration in galactic discs has been attracting an increasing attention, including some theoretical or numerical work (Sellwood & Binney 2002; Minchev et al. 2012; Roškar et al. 2012, e.g.), and studies based on observations of the stars in the Milky Way (Haywood 2008; Haywood et al. 2013, e.g.). In galactic discs where density waves such as bars or spiral arms occur, stars can gain or lose angular momentum, leading to outward, respectively inward migration. The result of this mechanism is that stars can be found at a galactocentric radius differing significantly from their birth radius. Another reason for apparent radial migration is simply the nature of orbits in axisymmetric or nearly axisymmetric potentials : Stars oscillate radially around a guiding radius.

The importance of the redistribution of stars in galactic discs having a strong bar is shown in Di Matteo et al. (2014). Stars initially at large radii are found to be parts of the central bar. This redistribution can be seen on Fig.3 where stars that are initially in 5 kpc wide annuli in one of our simulations are represented at different times. Stars migrate both inwards and outwards, and stars as far as 15 kpc from the centre can contribute (marginally) to the central bar of final size $\sim$ 8kpc.

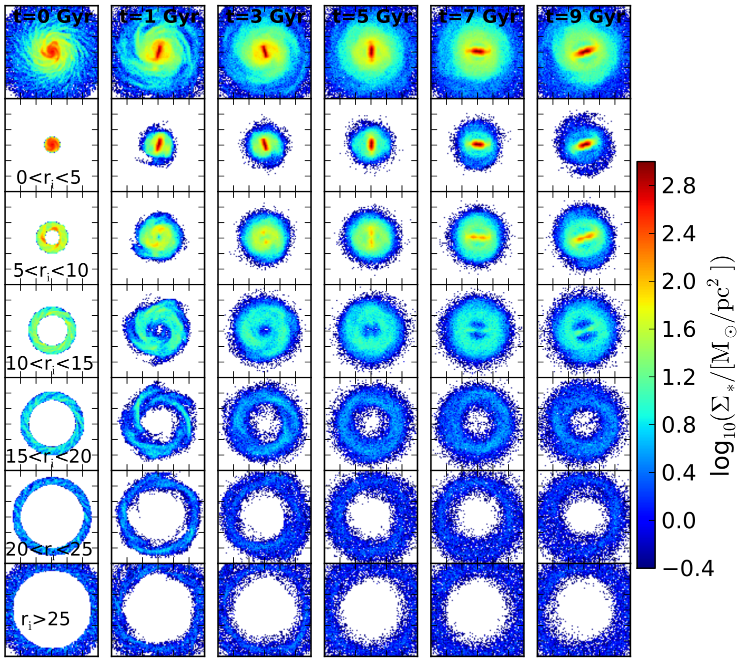

Fig. 3. From top to bottom: Face-on density distribution of stars with different birth radii. Different columns correspond to different times, as indicated. The total stellar density distribution is given in the top row. From Di Matteo et al. (2014).

We are interested in distinguishing the effects of 'blurring', that is the apparent radial migration due to epicyclic motion, from the effects of 'churning', that is the change of guiding radius (according to the terminology of Schönrich & Binney (2009)). The changes in galactocentric radius and guiding radius between two simulation times are visible in Fig. 4. The amplitude of the variations in guiding radius is significantly lower than the amplitude of variations in galactocentric radius. The vertical lines and surrounding shaded regions show the locations of the inner Lindblad resonance (ILR), corotation, and outer Lindblad resonance (OLR) of the bar. These radii shift with time because the bar slows down as it transfers angular momentum to the outer disc and to the bulge and dark matter halo. It can be seen on Fig. 4 that most of the radial migration occurs near the corotation of the bar. Transient spiral arms are also present in our simulations, and are responsible from some features visible on Fig. 4 at large radii, but the bar remains the strongest potential perturbation, and the main cause of radial migration. In the upcoming paper Halle et al. (2014), we detail the study of radial migration based on these simulations, with a quantification of the phenomenon including the fraction of migrators of several amplitudes in radial variation obtained at different galactocentric radii.

4 Conclusions

Molecular hydrogen is essential to take into account to study star formation in the outer parts of galactic discs. In the simulations of Halle & Combes (2013) we show the inclusion of H_2 cooling in simulations of isolated Sb-type galaxies with a low gas metallicity in the outer parts allows for slow star formation to occur at large galactocentric radii.

The evolution of the stellar discs (age profile and metallicity) is impacted by local star formation but also

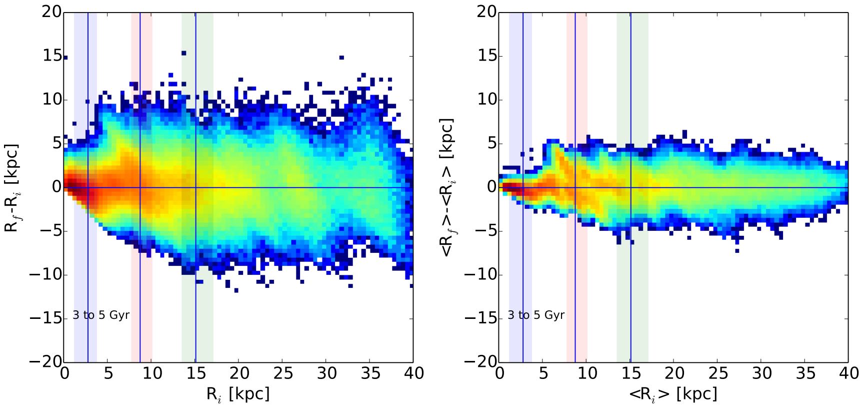

Fig. 4. Left: Distribution of the variation in galactocentric radius of the stars between 3 Gyr and 5 Gyr of evolution. **Right:** Distribution of the variation in guiding radius of the stars between 3 Gyr and 5 Gyr of evolution. The 2D histograms are mass-weighted and the colour code is logarithmic. The vertical lines show the locations of resonances of the bar as explained in the text.

by radial migration seeded by resonances in the disc. In our simulations, the bar is the main seed for stellar migration. We study this process by distinguishing the 'blurring' due to epicyclic motion around a guiding radius from the 'churning' that is a change of the guiding radius. The whole study of radial migration in our simulations will be detailed in the upcoming Halle et al. (2014).

References

Bakos, J., Trujillo, I., & Pohlen, M. 2008, ApJ, 683, L103

Barker, M. K., Sarajedini, A., Geisler, D., Harding, P., & Schommer, R. 2007, AJ, 133, 1125

Bigiel, F., Leroy, A., Walter, F., et al. 2008, AJ, 136, 2846

Dekel, A., Birnboim, Y., Engel, G., et al. 2009, Nature, 457, 451

Di Matteo, P., Haywood, M., Gómez, A., et al. 2014, A&A, 567, A122

Gil de Paz, A., Boissier, S., Madore, B. F., et al. 2007, ApJS, 173, 185

Gil de Paz, A., Madore, B. F., Boissier, S., et al. 2005, in Bulletin of the American Astronomical Society, Vol. 37, American Astronomical Society Meeting Abstracts, 178.02

Halle, A. & Combes, F. 2013, A&A, 559, A55

Halle, A., Di Matteo, P., & Haywood, M. Combes, F. 2014, A&A, in prep.

Haywood, M. 2008, MNRAS, 388, 1175

Haywood, M., Di Matteo, P., Lehnert, M. D., Katz, D., & Gómez, A. 2013, A&A, 560, A109

Kereš, D., Katz, N., Weinberg, D. H., & Davé, R. 2005, MNRAS, 363, 2

Krumholz, M. R., McKee, C. F., & Tumlinson, J. 2008, ApJ, 689, 865

Krumholz, M. R., McKee, C. F., & Tumlinson, J. 2009, ApJ, 693, 216

McKee, C. F. & Krumholz, M. R. 2010, ApJ, 709, 308

Minchev, I., Famaey, B., Quillen, A. C., et al. 2012, A&A, 548, A126

Roškar, R., Debattista, V. P., Quinn, T. R., & Wadsley, J. 2012, MNRAS, 426, 2089

Schönrich, R. & Binney, J. 2009, MNRAS, 396, 203

Sellwood, J. A. & Binney, J. J. 2002, MNRAS, 336, 785

Springel, V. 2005, MNRAS, 364, 1105

Thilker, D. A., Bianchi, L., Meurer, G., et al. 2005, in Bulletin of the American Astronomical Society, Vol. 37, American Astronomical Society Meeting Abstracts, 202.02

Williams, B. F., Dalcanton, J. J., Dolphin, A. E., Holtzman, J., & Sarajedini, A. 2009, ApJ, 695, L15

SF2A 2014
J. Ballet, F. Bournaud, F. Martins, R. Monier and C. Reylé (eds)

THE FIRST HST FRONTIER FIELDS CLUSTER : SEARCH FOR Z >7.5 GALAXIES

N. Laporte[1], F. E. Bauer[1, 2], S.Kim[1], R. Pelló[3], I. Pérez-Fournon[6, 4], D. Schaerer[5] and A. Streblyanska[4, 6]

Abstract. At the end of 2013, HST has started its most recent flagship program : the "Frontier Fields", aiming to observe 6 galaxies clusters. These images will reach a depth comparable to the HUDF but in a cluster field. The first release of Abell 2744, the first Frontier Fields target, has been made public on December 17 2013. We have used this dataset combined with Spitzer images to search for Lyman Break galaxy (LBG) at z >6.5 in the 4.9 arcmin^2 field of view, bright enough to be observed by current spectrographs. The brightest high-z object is found at z∼8 with a modest amplification factor (μ∼1.5). Its SED shows an optical break between ACS and WFC3 data and another one between the two first channels of IRAC/Spitzer. This "break" at 4.5 microns can be explained by strong [OIII] and Hβ lines at z ∼8. Its properties deduced by SED-fitting are the following : SFR of 8-60 $M_\odot$/yr, stellar mass of (2.5-10)$\times 10^9 M_\odot$ and a size of r =0.35±0.15 kpc. Its brightness makes it one of the brightest z∼8 objects to date, and it could be observed by current NIR-spectrographs installed on 8-10m class telescopes in a reasonable amount of time.

Keywords: Galaxies: distances and redshifts, Galaxies: evolution, Galaxies: formation, Galaxies: high-redshift, Galaxies: photometry, Galaxies: star formation

1 Introduction

Observations probing the edges of the Universe is one of the most intriguing challenges of the coming decade, particularly with respect to detecting the first population III stars (e.g. O'Shea & Norman 2007) and the first galaxies at z>12 (Bromm & Yoshida 2011). Several telescopes and instruments are under development and have put these topics in their key objectives. Ten years ago, only a dozen objects at z> 6 had been discovered (Kneib et al. 2004), with none above z>7.5. Nowadays, the number of z∼6, z∼7, and $z\geq$8 galaxies selected in deep surveys count in the 1000s (e.g. Le Fevre et al. 2014), several 100s (e.g. Bouwens et al. 2011) and ∼300 (e.g. Labbé et al. 2013), respectively. Thanks to these huge numbers of objects, the evolution and properties of galaxies is relatively well-constrained up to z∼6, with many secure spectroscopic confirmations (Jiang et al. 2013). Beyond z ∼6, however, spectroscopic follow-up remains extremely challenging due to the decreasing mean brightness of these objects (Finkelstein et al. 2013) and the fact that several $z\geq$8 candidates have been finally identified as mid-z interlopers (e.g. Hayes et al. 2012). Several theoretical studies have demonstrated the interest of combining lensing fields and large deep blank fields to search for high-z galaxies over a large range of luminosities (Maizy et al. 2010). This has been confirmed by most of the current surveys, such as the *Hubble Ultra Deep Field* (Beckwith et al. 2006) and *CLASH* (Postman et al. 2012) carried out with HST.

[1] Instituto de Astrofísica, Facultad de Física, Pontificia Universidad Catlica de Chile, 306, Santiago 22, Chile
[2] Space Science Institute, 4750 Walnut Street, Suite 205, Boulder, Colorado 80301
[3] IRAP, CNRS - 14 Avenue Edouard Belin - F-31400 Toulouse, France
[4] Departemento de Astrofisica, Universidad de La Laguna (ULL), E-38205 La Laguna, Tenerife, Spain
[5] Observatoire de Genéve - 51 Chemin des Maillettes - CH-1290 Sauverny - Switzerland
[6] Instituto de Astrofísica de Canarias (IAC), E-38200 La Laguna, Tenerife, Spain

Cluster Name	RA [J2000]	DEC [J2000]	z	Observations
Abell 2744	00:14:21.2	-30:23:50.1	0.308	Oct. 2013 - Jul. 2014
MACS0416.1-2403	04:16:08.9	-24:04:28.7	0.396	Jan. 2014 - Sep. 2014
MACS0717.5+3745	07:17:34.0	+37:44:49.0	0.545	Aug. 2014 - Apr. 2015
MACS1149.5+3745	11:49:36.3	+22:23:58.1	0.543	Nov. 2014 - Jun. 2015
Abell S1063	22:48:44.4	-41:31:48.5	0.348	2016 *(to be approved)*
Abell 370	02:39:52.9	-01:34:36.5	0.375	2016*(to be approved)*

Table 1. *HST* Frontier Fields observation schedule

2 The HST Frontier Fields

The new flagship program of HST, the Frontier Fields (hereafter, HFFs) started at the end of 2013, leveraging deep ACS and WFC3 observations combined with gravitational lensing to observe six massive galaxy clusters along with six deep blank fields (see Table 1). Thanks to the huge depth of *HST* images, ultra faint galaxies at very high-z (m_{F160W} ~31-32 AB) will be detected in HFF data (Richard et al. 2014). Several studies have already demonstrated that the number of $z \geq 8$ objects expected in the full Frontier Fields survey is $\geq$130 (Coe et al. 2014). Six teams have provided lensing models for each cluster (Bradač et al. 2009, Richard et al. 2014, Merten et al. 2011, Zitrin et al. 2013, Johnson et al. 2014 and Mohammed et al. 2014), and derived amplification maps at several redshift.

We combined the first full HFF dataset behind Abell 2744 (140 orbits in total - ID : 13386, 13495 - PI : S. Rodney, J. Lotz) with *Spitzer* Frontier Fields observations (50h on source - PI : T. Soifer and P. Capak) and HAWKI/VLT K_s image (27h - ID : 092.A-0472 - PI : G. Brammer) to search for bright $z \geq 7.5$ objects. The properties of data we used in this study are presented on table 2.

3 Lyman Break Galaxies behind Abell 2744

We applied the Lyman Break Galaxy technique (Steidel et al. 1999) combining non-detections in F435W, F606W, F814W and detections in F125W, F140W, as well as color criteria on Abell 2744 images. After visual inspection, 2 sources, well detected in F125W, F140W and F160W, appear as excellent z ~8 candidates with $m_{H_{160}}$=26.2±0.1 AB. Moreover these two galaxies are located in a clean region of the data making the photometry free of contamination by neighboring objects. These objects have been selected independently and confirmed in several recent studies (Atek et al. 2014, Coe et al. 2014 and Zheng et al. 2014). In the following we will focus on Abell2744_Y1, which is not detected at 3.6μm, but is clearly detected at 4.5μm (Figure 1), suggesting contribution of strong [OIII]+Hβ at $z \geq 7.5$ (Labbé et al. 2013, Smit et al. 2014, Finkelstein et al. 2013).

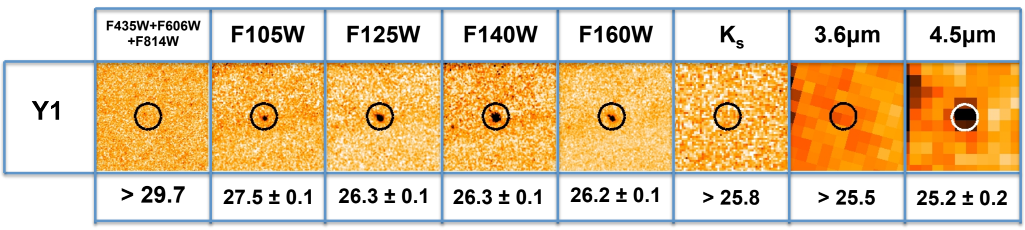

Fig. 1. Thumbnail images of the brightest z~8 candidate selected behind Abell 2744. The size of each stamp is 4"×4" and the position of Abell2744_Y1 is displayed by a black 0.4" radius circle (white circle at 4.5μm for clarity purpose)

4 Properties of the brightest z~8 candidate

We computed the photometric redshift of Abell2744_Y1 using an adapted version of *Hyperz* (Bolzonella et al. 2000) and templates including nebular emissions. The best SED-fit is found at $z \approx 8$, with the 1σ confidence

Filter	$\lambda_{central}$ [μm]	$\Delta\lambda$ [μm]	t_{exp} [ks]	m(5σ) [AB]	Instrument
F435W	0.431	0.073	16.16	28.5	ACS
F606W	0.589	0.156	13.25	28.7	ACS
F814W	0.811	0.166	13.25	28.7	ACS
F105W	1.050	0.300	46.52	29.1	WFC3
F125W	1.250	0.300	16.32	28.7	WFC3
F140W	1.400	0.400	22.43	28.8	WFC3
F160W	1.545	0.290	46.57	28.8	WFC3
K_s	2.146	0.324	97.4	25.5	HAWKI
3.6	3.550	0.750	90.9	25.5	IRAC
4.5	4.493	1.015	90.9	25.0	IRAC

Table 2. Properties of *HST*, *VLT* and *Spitzer* data on Abell 2744. - ACS limiting magnitudes are deeper than those published in Laporte et al. (2014) because in that proceeding we use the full dataset.

interval spanning z∼7.5 - 8.5, and no low-z solution in the redshift probability distribution. The best solution is always found at high-z no matter which library templates we used or what the Spitzer non-detection limits we assumed at 3.6μm (2 or 3σ). If we force a low-z solution by limiting the redshift range to 0-3, a value of z∼2 is found (although with poor χ^2). For instance, the Spitzer detections are incompatible with this solution (Laporte et al. 2014). We estimated an amplification factor of $\mu\approx1.5$ using the public lensing model provided by the CATS group (Richard et al. 2014). This factor is consistent with those found using other public lensing models produced by Merten (μ=1.50), Sharon (μ=1.91), Williams (μ=1.16) and Zitrin (μ=1.33-2.11), suggesting a moderate amplification regime.

The Star Formation Rate (SFR) estimated from the best SED-fit ranges from 8 to 60 $M_\odot$/yr depending on the adopted metallicity and minimum age imposed, its stellar mass $M_\star\sim(2.5\text{-}10)\times10^9$ $M_\odot$ and the specific SFR deduced is sSFR∼1Gyr^{-1}. We derived its size following two methods: SExtractor half light radius (Bertin & Arnouts 1996) corrected for PSF broadening and GALFIT modeling (Peng et al. 2002) assuming a Sersic profile. The results are similar suggesting $r\sim0.3\pm0.1$ kpc after correction for magnification, that is consistent with values published in recent studies (e.g. Ono et al. 2013)

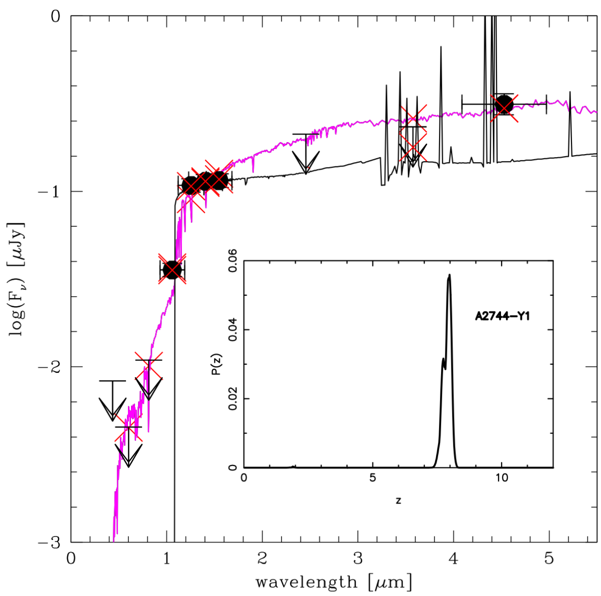

Fig. 2. Best SED-fit of the brightest z∼8 candidate selected in the first HFF dataset. The black line displays the best fit without any constraints on the redshift, the magenta line shows the best fit assuming a low-z solution ($z\leq3$). Upper limits are plotted at 1σ, 5σ and 3σ for ACS, HAWKI and IRAC data respectively. The P(z) is over-plotted.

5 Discussion and Conclusions

The SED of Abell2744_Y1 is comparable to the recent $z \sim 7.5$ LBG confirmed by spectroscopy (Finkelstein et al. 2013) regarding its spectral break between optical and NIR data (F125W-F606W > 2mag) and the detection at 4.5μm in conjunction with a non-detection at 3.6μm with similar depth. Furthermore the H_{160}-[3.6] <0.5 and J_{125} - H_{160} are in good agreement with the trend observed by (Labbé et al. 2013) (cf. figure 2 of that paper) for $z \sim 8$ objects. The colors of these 2 objects fulfill the color criteria defined by Oesch et al. (2012) and Lorenzoni et al. (2011) and their *intrinsic* SEDs are similar to the $z \sim 8$ candidates selected in the CANDELS survey (Grogin et al. 2011).

The brightness of this $z \sim 8$ object makes it observable by most of the current spectrographs installed on 8-10m class telescopes. Spectroscopic follow-up with MMIRS/Magellan (McLeod et al. 2012) is on-going and should reveal the nature and properties of this object at short term.

We acknowledge support from CONICYT-Chile grants Basal-CATA PFB-06/2007 (NL, FEB, SK), Gemini-CONICYT #32120003 (NL), "EMBIGGEN" Anillo ACT1101 (FEB), FONDECYT 1141218 (FEB), and Project IC120009 “Millennium Institute of Astrophysics (MAS)” of the Iniciativa Científica Milenio del Ministerio de Economía, Fomento y Turismo (FEB), the Spanish Ministry of Economy and Competitiveness (MINECO) under the 2011 Severo Ochoa Program MINECO SEV-2011-0187 (AS), the French Agence Nationale de la Recherche bearing the reference ANR-09-BLAN-0234 (RP).

References

Atek, H., Richard, J., Kneib, J.-P., et al. 2014, ApJ, 786, 60
Beckwith, S. V. W., Stiavelli, M., Koekemoer, A. M., et al. 2006, AJ, 132, 1729
Bertin, E. & Arnouts, S. 1996, A&AS, 117, 393
Bolzonella, M., Miralles, J.-M., & Pelló, R. 2000, A&A, 363, 476
Bouwens, R. J., Illingworth, G. D., Oesch, P. A., et al. 2011, ApJ, 737, 90
Bradač, M., Treu, T., Applegate, D., et al. 2009, ApJ, 706, 1201
Bromm, V. & Yoshida, N. 2011, ARA&A, 49, 373
Coe, D., Bradley, L., & Zitrin, A. 2014, ArXiv e-prints
Finkelstein, S. L., Papovich, C., Dickinson, M., et al. 2013, Nature, 502, 524
Grogin, N. A., Kocevski, D. D., Faber, S. M., et al. 2011, ApJS, 197, 35
Hayes, M., Laporte, N., Pelló, R., Schaerer, D., & Le Borgne, J.-F. 2012, MNRAS, 425, L19
Jiang, L., Egami, E., Mechtley, M., et al. 2013, ApJ, 772, 99
Johnson, T. L., Sharon, K., Bayliss, M. B., et al. 2014, ArXiv e-prints
Kneib, J.-P., Ellis, R. S., Santos, M. R., & Richard, J. 2004, ApJ, 607, 697
Labbé, I., Oesch, P. A., Bouwens, R. J., et al. 2013, ApJ, 777, L19
Laporte, N., Streblyanska, A., Clement, B., et al. 2014, A&A, 562, L8
Le Fevre, O., Tasca, L. A. M., Cassata, P., et al. 2014, ArXiv e-prints
Lorenzoni, S., Bunker, A. J., Wilkins, S. M., et al. 2011, MNRAS, 414, 1455
Maizy, A., Richard, J., de Leo, M. A., Pelló, R., & Kneib, J. P. 2010, A&A, 509, A105
McLeod, B., Fabricant, D., Nystrom, G., et al. 2012, PASP, 124, 1318
Merten, J., Coe, D., Dupke, R., et al. 2011, MNRAS, 417, 333
Mohammed, I., Liesenborgs, J., Saha, P., & Williams, L. L. R. 2014, MNRAS, 439, 2651
Oesch, P. A., Bouwens, R. J., Illingworth, G. D., et al. 2012, ApJ, 759, 135
Ono, Y., Ouchi, M., Curtis-Lake, E., et al. 2013, ApJ, 777, 155
O'Shea, B. W. & Norman, M. L. 2007, ApJ, 654, 66
Peng, C. Y., Ho, L. C., Impey, C. D., & Rix, H.-W. 2002, AJ, 124, 266
Postman, M., Coe, D., Benítez, N., et al. 2012, ApJS, 199, 25
Richard, J., Jauzac, M., Limousin, M., et al. 2014, MNRAS, 444, 268
Smit, R., Bouwens, R. J., Labbé, I., et al. 2014, ApJ, 784, 58
Steidel, C. C., Adelberger, K. L., Giavalisco, M., Dickinson, M., & Pettini, M. 1999, ApJ, 519, 1
Zheng, W., Shu, X., Moustakas, J., et al. 2014, ArXiv e-prints
Zitrin, A., Meneghetti, M., Umetsu, K., et al. 2013, ApJ, 762, L30

HIGH RESOLUTION SPECTROSCOPY OF RED GIANT BRANCH STARS AND THE CHEMICAL EVOLUTION OF THE FORNAX DWARF SPHEROIDAL GALAXY

B. Lemasle[1], T.J.L. de Boer[2], V. Hill[3], E. Tolstoy[4], M. J. Irwin[2], P. Jablonka[5, 6], K. Venn[7], G. Battaglia[8, 9], E. Starkenburg[7, 10], M. Shetrone[11], B. Letarte[12], P. Francois[6, 13], A. Helmi[4], F. Primas[14], A. Kaufer[15] and T. Szeifert[15]

Abstract. From VLT-FLAMES high-resolution spectra, we determine the abundances of several α, iron-peak and neutron-capture elements in 47 Red Giant Branch stars in the Fornax dwarf spheroidal galaxy. We confirm that SNe Ia started to contribute to the chemical enrichment of Fornax at [Fe/H] between –2.0 and –1.8 dex. Combining these abundances with accurate age estimates, we date the onset of SNe Ia to ≈ 12–10 Gyrs ago. Our results are compatible with an initial mass function that lacks the most massive stars and with a star formation going on throughout the whole history of Fornax.

Keywords: stars: abundances, galaxies: individual: Fornax dwarf spheroidal, galaxies: evolution

1 Introduction

The wide variety of Star Formation Histories (SFH) observed in Local Group dwarf spheroidal galaxies (dSphs) makes them an ideal laboratory for studying the physical processes driving the evolution of galaxies. In addition, they provide valuable clues on the formation and evolution of our own Milky Way. Fornax is one of the most luminous and most massive dSphs (Mateo 1998). If star formation was going on over almost its entire history (e.g., de Boer et al. 2012b), Fornax is nevertheless dominated by its intermediated age population, in particular a 4 Gyr old population at [Fe/H] ≈ −1.0 dex. We have studied the chemical evolution of Fornax by determining the abundances of several α, iron peak and n-capture elements in 47 Red Giant Branch (RGB) stars ≈0.4 degrees offset from the centre of the galaxy and covering the whole metallicity range. We also derived accurate ages from the age probability distribution from the colour-magnitude diagram of Fornax.

[1] Anton Pannekoek Institute, University of Amsterdam, Science Park 904, PO Box 94249, 1090 GE, Amsterdam, The Netherlands
[2] Institute of Astronomy, University of Cambridge, Madingley Road, Cambridge, CB3 0HA, UK
[3] Observatoire de la Côte d'Azur, CNRS UMR 7293, BP4229, 06304, Nice Cedex 4, France
[4] Kapteyn Astronomical Institute, University of Groningen, Postbus 800, 9700 AV, Groningen, The Netherlands
[5] Laboratoire d'astrophysique, École Polytechnique Fédérale de Lausanne (EPFL), Observatoire de Sauverny, 1290 Versoix, Switzerland
[6] GEPI, Observatoire de Paris, CNRS, Université Paris Diderot, Place Jules Janssen, 92190 Meudon, France
[7] Department of Physics and Astronomy, University of Victoria, 3800 Finnerty Road, Victoria, BC, V8P 1A1, Canada
[8] Istituto de Astrofisica de Canarias, calle via Lactea s/n, 38205 San Cristobal de La Laguna (Tenerife), Spain
[9] Universidad de La Laguna, Dpto. Astrofsica, E-38206 La Laguna, Tenerife, Spain
[10] CIFAR Global Scholar
[11] McDonald Observatory, The University of Texas at Austin, 1 University Station, C1400, Austin, TX 78712-0259, USA
[12] Dept of Physics, North-West University, Mafikeng Campus, Private Bag X2046, Mmabatho 2745, South Africa
[13] UPJV, Université de Picardie Jules Verne, 33 rue St. Leu, 80080 Amiens, France
[14] European Southern Observatory, Karl Schwarzschild Str. 2, 85748, Garching b. München, Germany
[15] European Southern Observatory, Alonso de Cordova 3107, Santiago, Chile

2 Data and analysis

We obtained FLAMES/GIRAFFE high resolution (HR) spectra using the HR10, HR13 and HR14 gratings for 47 RGB stars. Most of them were selected for membership from low resolution spectra in the calcium triplet (CaT) region (Battaglia et al. 2006) while the remaining stars were selected from their position on the (I, V-I) CMD (Battaglia et al. 2006, ESO/WFI).

We determined both the radial velocities (V_r) and the equivalent widths of the absorption lines with the DAOSPEC software (Stetson & Pancino 2008). From a Gaussian fit to the data, we derived a systematic radial velocity peak of 49.65±1.46 km s^{-1}, σ=14.6±1.51 km s^{-1}. This value falls below previous determinations over the whole galaxy from CaT (Battaglia et al. 2006, V_r=54.1±0.5 km s^{-1}, σ=11.4±0.4 km s^{-1}) or magnesium triplet (Walker et al. 2009, V_r=55.2±0.1 km s^{-1}, σ=11.7±0.9 km s^{-1}); or in the centre of Fornax from high resolution spectra (Letarte et al. 2010, V_r=55.9 km s^{-1}, σ=14.2 km s^{-1}) If we select the Fornax members that overlap our HR sample in the CaT data of Battaglia et al. (2006), we find a similar mean radial velocity (50.99±0.94 km s^{-1}, σ=12.70±0.96 km s^{-1}). This indicates that slightly lower V_r are typical from this region of Fornax and suggests that the kinematics of Fornax depends on position.

We used a grid of OSMARCS atmosphere models in spherical symmetry (Gustafsson et al. 2008) with [α/Fe] increasing when [Fe/H] decreases and computed abundances with *calrai*, a LTE spectrum synthesis code originally developed by Spite (1967) and regularly updated since then. Both temperature and surface gravities are computed from photometric data. $T_{\rm eff}$ is the average of the temperatures derived from the five different colours (B-V), (V-I), (V-J), (V-H) and (V-K), and the calibration for giants from Ramìrez & Meléndez (2005). Surface gravities *log g* are derived using our temperature estimates, a distance modulus of μ_v=20.84±0.04 mag (Pietrzyński et al. 2009) and the bolometric correction from Alonso et al. (1999), Different stellar masses ranging from 0.9 to 1.3 $M_\odot$ are assigned to the stars depending on their metallicity. We checked the photometric $T_{\rm eff}$ by ensuring that [FeI/H] does not depend on the excitation potential χ_{ex} and obtained the value of the microturbulent velocity v_t by requiring that [FeI/H] does not depend on EW.

To determine the ages of an individual RGB star, a global synthetic CMD of Fornax is first built from the SFH (de Boer et al. 2012a). All the stars with the same magnitude and the same metallicity (within the observational uncertainties) are then extracted from the synthetic CMD and the mean age and the standard deviation of this subsample are adopted respectively as the age of the individual RGB star and its associated uncertainty. To take into account population gradients within Fornax, the SFH is computed in 5 different annuli at different distances from the centre of Fornax.

3 Results and discussion

3.1 *The classical time-delay scenario*

The left panel of Fig. 1 shows that the old, metal-poor stars of Fornax are typically Mg-rich while the young metal-rich stars are Mg-poor. The same outcome applies to the other α-elements, in particular Si and Ca (not shown here). Such a feature is also observed in other dSphs. In a now traditional interpretation (e.g. Tinsley 1979; Matteucci 2003), the low [α/Fe] in the dSphs are believed to originate in the time delay between type II and type Ia Supernovae (respectively SNe II and SNe Ia): SNe II are the main contributor to the enrichment of the interstellar medium (ISM) in α-elements and because of their short timescale, the ISM is enriched by the massive stars very rapidly after the beginning of star formation. In contrast, SNe Ia contribute only later to the chemical enrichment and their onset leads to low [α/Fe] values.

In this scenario, the evolution of [Mg/Fe] with [Fe/H] (Fig. 1, left panel) indicates that the Mg "knee" where [Mg/Fe] turns down after the onset of SNe Ia took place at [Fe/H] between –2.0 and –1.8 dex. This result perfectly matches the value of –1.9 dex recently found by Hendricks et al. (2014). From the evolution of [Mg/Fe] with age (Fig. 1, right panel) we find that the [Mg/Fe] knee occurred approximately between 12–10 Gyrs ago.

These values are similar to those recently found for the Sculptor dSph where the Mg knee takes place at 10.9±1.0 Gyr and at a metallicity of ≈–1.8 dex (Tolstoy et al. 2009; de Boer et al. 2012a). Because SF efficiency scales with galaxy mass, it was expected that Fornax (∼10 times more massive than Sculptor) produces more metals and keeps a larger fraction of them. Indeed several observational evidences argue against strong galactic winds, for instance the continuous SFH, the steady decline in [Mg/Fe] or the high values of the [Ba/Fe] and [La/Fe], the latter two indicating that the Asymptotic Giant Branch (AGB) yields have not been lost.

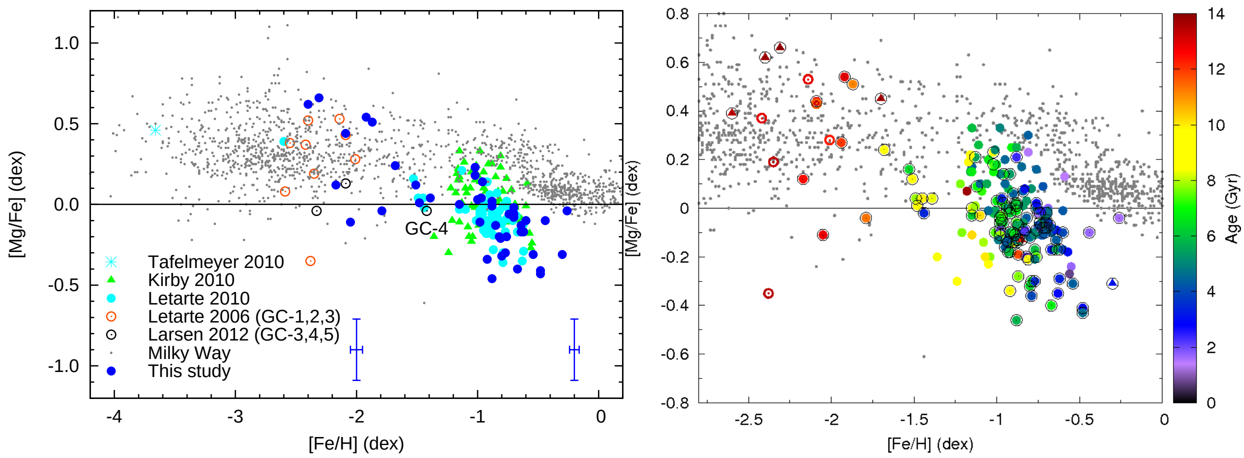

Fig. 1. Left: The distribution of [Mg/Fe] for our sample of RGB stars in the Fornax dSph as blue filled circles. The cyan filled circles are the data of Letarte et al. (2010) and the cyan triangle the metal-poor star of Tafelmeyer et al. (2010). The orange open circles are the stars in Fornax globular clusters from Letarte et al. (2006). We also show the stars from the medium resolution sample of Kirby et al. (2010) that have uncertainties in [Fe/H] and [Mg/H] lower than 0.2 dex and that are not included in the HR samples. Milky Way halo stars from Venn et al. (2004) and Frebel (2010) and references therein are in small grey dots. Representative error bars are given for the metal-poor ([Fe/H]<–1.4 dex) and metal-rich ([Fe/H]>–1.4 dex) regimes. **Right:** [Mg/Fe] vs [Fe/H] from MR/HR spectroscopic measurements of Fornax RGB stars (coloured filled circles/triangles). The colours represent the age in Gyr, derived from the SFH. Stars in the Milky Way are shown for comparison (small grey points). Field stars for which the probability distribution for age could be determined are shown as filled circles, while filled triangles show stars for which no statistical age estimate could be derived. For those stars, only an age estimate is given, based on the closest distance from synthetic CMD satisfying the magnitude and metallicity constraints. Globular cluster stars are shown as open circles. Stars belonging to the high resolution samples (this study, Letarte et al. 2010) are surrounded by black open circles.

A merger scenario is then very attractive: with a low original mass, Fornax could experience an early enrichment similar to Sculptor and reach its current higher mass via a merger event. Such a scenario has already been proposed by several authors: based on kinematics, Amorisco & Evans (2012c) suggested that Fornax is the outcome of the late merger of a bound pair. In a successfull attempt to recover the shell-like substructures that can be found in Fornax (e.g., de Boer et al. 2013, and references therein), Yozin & Bekki (2012) proposed a merger event with a low-mass companion (5% of the Fornax mass) that occured between 3.5 and 2.1 Gyr ago. On the other hand, recent collision between Milky Way satellites are much less probable than it was at the early times of the Local Group (e.g., De Rijcke et al. 2004)

3.2 A top-light IMF ?

A steep (or "top-light") initial mass function has often been proposed for dwarf galaxies (e.g., Tolstoy et al. 2003; Kroupa et al. 2013). As far as Fornax is concerned, the case was advocated by Tsujimoto (2011) with a detailed model of the galaxy and by Li et al. (2013a) when comparing the nucleosynthesis in the Milky Way and in Fornax. Analysing RGB stars in Sagittarius (a dSph with a mass similar to Fornax), McWilliam et al. (2013) conclude that the low [α/Fe] observed are not the result of the time-delay scenario but rather the outcome of a top-light IMF where the most massive stars (>30 $M_\odot$) are missing. Indeed, the production of O and Mg is dominated by the most massive SNe II (Woosley & Weaver 1995). McWilliam et al. (2013) also proposed that the r-process elements are mostly originating from low mass SNe II, providing a very straightforward explanation for the supersolar [Eu/Mg] we find in Fornax in the case of a top-light IMF. Other results like low values of [Ni/Fe], high values of [Ba/Fe] underline the strong influence of SNe Ia and AGB stars in driving the abundance pattern of Fornax and are therefore compatible with a steep IMF.

However it is important to note that most of these studies considered only the metal-rich regime of Fornax or Sagittarius. Moreover, the presence of globular clusters in both these galaxies indicates that in the early times, gas was present in large enough quantities to form the largest molecular clouds and in turn the most massive stars (Oey 2011). This seems to contradict the steep IMF hypothesis, which is the natural outcome of systems where gas is not present in sufficient quantities.

4 Conclusions

We confirm that in Fornax, SNe Ia started to contribute to the chemical enrichment of the ISM at [Fe/H] between –2.0 and −1.8 dex. We find that the onset of SNe Ia took place ≈12–10 Gyrs ago. These value are similar to those reported for the Sculptor dSph despite the fact that Fornax is much more massive than Sculptor. Low [Mg/Fe], supersolar [Eu/Mg] suggest a top-light IMF in Fornax. Low [Ni/Fe], high [Ba/Fe] in the metal-rich regime reflect the strong influence of SNe Ia and AGB stars in the abundance pattern of Fornax. The time-delay and the top-light IMF scenarios are not mutually exclusive and are probably going on simultaneously in Fornax.

It is a pleasure to thank both the Local and Science Organisation Committees for a stimulating "Semaine de l'Astrophysique Française".

References

Alonso, A., Arribas, S., Martínez-Roger, C. 1999, A&AS 140, 261
Amorisco, N. C., Evans, N. W., 2012, ApJ 756, 2
Battaglia, G., Tolstoy, E., Helmi, A., Irwin, M. J., Letarte, B., Jablonka, P., Hill, V., Venn, K. A., Shetrone, M. D., Arimoto, N., Primas, F., Kaufer, A., François, P., Szeifert, T., Abel, T., Sadakane, K., 2006, A&A 459, 423
de Boer, T. J. L., Tolstoy, E., Hill, V., Saha, A., Olsen, K., Starkenburg, E., Lemasle, B., Irwin, M. J., Battaglia, G., 2012, A&A 539, A103
de Boer, T. J. L., Tolstoy, E., Hill, V., Saha, A., Olszewski, E. W., Mateo, M., Starkenburg, E., Battaglia, G., Walker, M. G., 2012, A&A 544, A73
de Boer, T. J. L., Tolstoy, E., Saha, A., Olszewski, E. W., 2013, A&A 551, A103
De Rijcke, S., Dejonghe, H., Zeilinger, W. W., Hau, G. K. T., 2004, A&A, 426, 53
Frebel, A., 2010, AN 331, 474
Gustafsson, B., Edvardsson, B., Eriksson, K., Jørgensen, U. G., Nordlund, Å., Plez, B., 2008, A&A 486, 951
Hendricks, B., Koch, A., Lanfranchi, G. A., Boeche, C.,Walker, M., Johnson, C. I., Penarrubia, J., Gilmore, G., 2014, ApJ 785, 102
Kirby, E. N., Guhathakurta, P., Simon, J. D., Geha, M. C., Rockosi, C. M., Sneden, C., Cohen, J. G., Sohn, S. T., Majewski, S. R., Siegel, M., 2010, ApJ SS 191, 352
Kroupa, P., Weidner, C., Pflamm-Altenburg, J., Thies, I., Dabringhausen, J., Marks, M., Maschberger, T., 2013
Letarte, B., Hill, V., Jablonka, P., Tolstoy, E., François, P., Meylan, G., 2006, A&A 453, 547
Letarte, B., Hill, V., Tolstoy, E., Jablonka, P., Shetrone, M., Venn, K. A., Spite, M., Irwin, M. J., Battaglia, G., Helmi, A., Primas, F., François, P., Kaufer, A., Szeifert, T., Arimoto, N., Sadakane, K., 2010, A&A 523, A17
Li, H., Cui, W., Zhang, B., 2013a, ApJ 775, 12
Mateo, M., 1998, ARA&A 36, 435
Matteucci, F., 2003, Ap&SS 284, 539
McWilliam, A., Wallerstein, G., Mottini, M., 2013, ApJ 778, 149
Oey, M. S., 2011, ApJL 739, 46
Pietrzyński, G., Górski, M., Gieren, W., Ivanov, V. D., Bresolin, F., Kudritzki, R-P., 2009, AJ 138, 459
Ramìrez, I., Meléndez, J., 2005, ApJ 626, 465
Spite, M., 1967, AnAp 30, 211
Stetson, P. B., Pancino, E., 2008, PASP 120, 1332
Tafelmeyer, M., Jablonka, P., Hill, V., Shetrone, M., Tolstoy, E., Irwin, M. J., Battaglia, G., Helmi, A., Starkenburg, E., Venn, K. A., Abel, T., François, P., Kaufer, A., North, P., Primas, F., Szeifert, T., 2010, A&A 524, A58
Tinsley, B. M., 1979, ApJ 229,1046
Tolstoy, E., Venn, K. A., Shetrone, M., Primas, F., Hill, V., Kaufer, A., Szeifert, T., 2003, AJ 125, 707
Tolstoy, E., Hill, V., Tosi, M., 2009, ARA&A 47, 371
Tsujimoto, T., 2011, ApJ 778, 149
Venn, K. A., Irwin, M., Shetrone, M. D., Tout, C. A., Hill, V., Tolstoy, E., 2004, AJ 128, 1177
Walker, M. G., Mateo, M., Olszewski, E. W., Sen, B., Woodroofe, M., 2009, AJ 137, 3109
Woosley, S. E., Weaver, T. A., 1995, ApJS 101, 181
Yozin, C., Bekki, K., 2012, ApJ 756, 18

SF2A 2014
J. Ballet, F. Bournaud, F. Martins, R. Monier and C. Reylé (eds)

GALAXY CLUSTER DETECTION IN THE NEXT GENERATION VIRGO CLUSTER SURVEY (NGVS)

R. Licitra[1,2], S. Mei[1,2], A. Raichoor[1], T. Erben[3], H. Hildebrandt[3], O. Ilbert[4], M. Huertas–Company[1,2], L. Van Waerbeke[5], P. Côté[6], J.-C. Cuillandre[7], P.A. Duc[8], L. Ferrarese[6], S.D. J. Gwyn[6], A. Lancon[9], R. Munoz[9,10] and T. Puzia[10]

Abstract. We describe our cluster detection algorithm *Red–GOLD*, based on the search of red–sequence galaxy overdensities. In this work, the algorithm is optimized to search for clusters up to $z \sim 1$ using optical data. We applied this algorithm to semi–analytic simulations and we found that for haloes more massive than $M \geq 10^{14}\ M_{\odot}$ the completeness is 80% and the purity is $\sim 81\%$, up to redshift $z = 1$.

Keywords: galaxies, clusters, large survey

1 Introduction

Being galaxy clusters the most massive bound structures in the Universe, they represent a powerful tool to probe the large-scale structure predicted by the standard cosmological model, and to understand how environmental effects affect galaxy evolution. To conduct these studies and obtain reliable results, it is important to build complete and pure cluster catalogs.

2 Observations and data description

We applied our detection algorithm to optical data coming from the Next Generation Virgo Cluster Survey (NGVS), a *large program* on the *Canada France Hawaii Telescope* (CFHT), centred on the M87 galaxy and images the Virgo cluster from the inner regions up to its virial radius in 5 optical bands u^*, g, r, y, z, with a surface brightness depth of $\mu_g \sim 29/mag/arcsec^2$, never attained before in this region (Ferrarese et al. 2012).

The NGVS observations were carried out with MegaCam, the optical imager mounted on MegaPrime, the prime focus of the CFHT. For our analysis, we used the same reduction and photometric catalog as Raichoor et al. (2014). We refer to this last work for details. Briefly, the NGVS images were processed with the $ELIXIR^*$ pipeline at the Canadian Astronomical Data Centre (CADC[†]). The astrometric and photometric calibration, and the image co-addition and mask creation are described in Raichoor et al. (2014) and follow the reduction

[1] GEPI, Paris Observatory, 77 av. Denfert-Rochereau, 75014 Paris, France
[2] Université Paris Denis Diderot, 75205 Paris Cedex 13, France
[3] Argelander-Institut fur Astronomie, University of Bonn, Auf dem Hugel 71, D-53121 Bonn, Germany
[4] Aix Marseille Université, CNRS, Laboratoire d'Astrophysique de Marseille, UMR 7326, F-13388 Marseille, France
[5] Department of Physics and Astronomy, University of British Columbia, 6224 Agricultural Road, Vancouver, B.C., V6T 1Z1, Canada
[6] Herzberg Institute of Astrophysics, National Research Council of Canada, Victoria, BC, V9E 2E7, Canada
[7] CanadaFranceHawai Telescope Corporation, Kamuela, HI 96743, USA
[8] Laboratoire AIM Paris-Saclay, CEA/IRFU/SAp, CNRS/INSU, Université Paris Diderot, F-91191 Gif-sur- Yvette Cedex, France
[9] Observatoire astronomique de Strasbourg, Université de Strasbourg, CNRS, UMR 7550, 11 rue de l'Université, F-67000 Strasbourg, France
[10] Institute of Astrophysics, Pontificia Universidad Católica de Chile, Av. Vicuna Mackenna 4860, 7820436 Macul, Santiago,Chile
[*] http://www.cfht.hawaii.edu/Instruments/Elixir/
[†] http://www4.cadc-ccda.hia-iha.nrc-cnrc.gc.ca/cadc/

procedures from Erben et al. (2013). The photometric catalogs were obtained with the method described in Hildebrandt et al. (2012) with the global point–spread–function (PSF) homogenisation. Multi–wavelength catalogs were derived using SExtractor (Bertin & Arnouts 1996) in dual-image mode on each single pointing on the convolved images. The un–convolved y- band observations having the better average seeing ($0.52'' \pm 0.04''$), were chosen as detection images. Photometric errors were measured in the un–convolved images as described in Raichoor et al. (2014), from the noise estimation in 2,000 random apertures in each bandpass, in each pointing. In the un–convolved images, this corresponds to ~ 1.5 the photometric errors given by SExtractor. A zero point uncertainty, estimated comparing our photometry field–to–field and to the SDSS, was added in quadrature (see also Gwyn 2012).

The original NGVS observing strategy was to cover the entire field with the 5 bands (see Ferrarese et al. (2012)). However, due to the exceptionally bad weather, the observations in the r–band are available only on 34 out to 117 fields, which roughly correspond to 30 deg^2, and are shallower than originally planned.

3 Detection technique

Our algorithm, named Red-sequence Galaxy Overdensity cLuster Detector (*Red–GOLD*; Licitra et al., in preparation), is based on the detection of red-sequence galaxy overdensities: it relies on the observational evidence that red-sequence galaxies are tightly distributed in the colour-magnitude diagram, following an almost flat relation, at least up to redshift $z \sim 1.5$ (Blakeslee et al. 2006, Postman et al. 2005, Desai et al. 2007 Kodama et al. 1998 Muzzin et al. 2013 Mei et al. 2009). The use of high quality photometric redshifts described in Raichoor et al. (2014) allowed us to minimise projection effects.

The method consists in the detection of spatial overdensities of red early-type galaxies and the confirmation of a tight red-sequence in the colour-magnitude relation. To reduce the contamination due to projection effects when estimating the red–sequence galaxy overdensities, we selected passive galaxies using two pairs of filters simultaneously, roughly corresponding to the U-B and B-V rest-frame colours. We used Bruzual & Charlot (2003) (BC03) stellar population models to compute predicted colours through the theoretical Spectral Energy Distributions (SEDs): we assumed a passive evolution, a galaxy formation redshift $z_{form} = 3$ and a solar metallicity, $Z = 0.02$. In addition to our colour selection, we required that red galaxies are also defined as ETGs according to the spectral classification given by *LePhare* (Arnouts et al. (1999), Arnouts et al. (2002), Ilbert et al. (2006)), i.e. objects which show spectral characteristics typical of early-type galaxies.

We defined our cluster detections identifying structures with a high density contrast with respect to the mean value of the background. We centered our detections on a bright red ETG, considering the galaxy with the highest number of red companions, weighted on luminosity. This approach is compatible with previous analysis, showing that centroids do not well approximate the cluster centres, while the brightest cluster member lying near the X-ray centroid seems to trace very well the cluster centre (George et al. 2011, George et al. 2012). Finally, we confirmed our cluster candidates and refined our photometric redshift estimation, fitting the red–sequence and imposing upper limits for the red–sequence parameters, based on previous works (e.g., Mei et al. 2009). To remove multiple detections we iteratively filtered our catalogue, checking for detections characterised by at least half of members in common. Then, we simply retained only the detection with the highest signal–to–noise ratio, weighted on luminosity.

4 The NGVS cluster catalog

We applied this detection technique to the 104 deg^2 of NGVS to look for galaxy structures up to $z \sim 1$. We built two different cluster catalogues for fields with and without r–band observations, because we used a slightly different configuration, choosing different bands to isolate red–sequence galaxies.

4.1 Cluster catalogue with the r–band observations

We detected 287 structures in the ~ 30 deg^2 covered by the r–band, i.e. ~ 9 detections per square degree. The 62% of the cluster candidates have at least one spectroscopic member in less than $2'$ with $|z_{spec} - z_{cluster}| < 0.1$.

We compared our low-redshift detections with the red–Mapper catalog (Rykoff et al. 2014): red–Mapper has been applied to the SDSS data and we can use this catalog to empirically test the detections up to $z \sim 0.55$. We calculated how many red–Mapper detections are found with our algorithm. Of the 82 red–Mapper detections in the ~ 30 deg^2 covered by r–band observations, we recovered 80 clusters, i.e. the $\sim 98\%$ of the red–Mapper cluster candidates. We checked for the two unmatched red–Mapper cluster candidates and from visual inspection we found that one is a poor system and the second lies on the edge of the NGVS field.

4.2 Cluster catalogue without the r–band observations

In the fields not covered by the r–band observations, we applied our algorithm considering different colour pairs as a function of redshifts, basically replacing the r–band with the y–band. With only four bands the photometric redshift estimates are more noisy (see Raichoor et al. 2014) but they remain accurate for our purposes. Therefore, we still used the photometric redshifts and the spectral classification to isolate red-sequence galaxies.

We found 864 cluster detections up to $z = 1$, i.e. ~ 10 clusters per square degree. 61% of the cluster candidates have at least one spectroscopic member in less than $2'$ with $|z_{spec} - z_{cluster}| < 0.1$.

When comparing our detections to the red–Mapper catalog, this comparison confirms that we are able to efficiently detect galaxy clusters also when using only four optical bands, recovering a similar fraction of the red–Mapper detections. Also in this case, when checking for the unmatched red–Mapper detections, we found that they are poor systems. With only four optical bands, though, we find it more uncertain to assign cluster membership, due to the higher photometric redshift uncertainties.

5 Completeness and purity of our algorithm from Millennium Simulation

We applied our detection algorithm to the Millennium Simulation (Springel et al. 2005). Among the different realisations of mock galaxy catalogues based on semi-analytical models, we used lightcones from Henriques et al. (2012), which consist in 24 independent catalogs, built on the models by Guo et al. (2011). Although, many improvements have been made with respect to previous simulations (e.g. the stellar mass function), the Guo models still show some discrepancies with the observations: in particular, galaxy colours are difficult to reproduce in an accurate way since they depends on different parameters, as metallicity, star-formation history and dust. Guo et al. (2011) showed that already at z=0, there is a discrepancy between the colours predicted in their models and the SDSS observations, overpredicting the fraction of red dwarf galaxies ($M < 10^{9.5}\ M_\odot$), with colours redder than observed. Instead, at $M > 10^{10.5} M_\odot$, the colours are bluer with respect to the observations. Moreover, assuming that ETGs are bulge-dominated, i.e. characterised by $B/T \geq 0.7$, we found that the early-type galaxy abundance in galaxy clusters is not well reproduced, systematically underestimating the fraction of early-type objects.

This deeply affects the comparison with results obtained with our algorithm, as it relies on the search of red-sequence galaxies and we have to take into account this effect. For that reason, we corrected mock catalogs in order to obtain a realistic galaxy distribution in simulated clusters and accurate colours.

In the upper panel of Figure 1, we show two examples of the colour-magnitude relation for two clusters at redshift $z = 0.23$ and $z = 0.93$: blue dots are cluster members, yellow triangles represent ETGs, i.e. members with $B/T \geq 0.7$, and red points are ETGs with colours in agreement with predicted ones, based on BC03 models. Both problems are clearly visible: the total number of ETGs is too small and only a small fraction of ETGs matches predicted colours.

Since we should consider colour cuts shifted with respect to the original BC03 predictions for both early and late type galaxies in all environments, we did not change the colours in the mock catalogues. Instead, we modified the colours predicted by BC03 stellar population models to match the Millennium galaxy colours to avoid to introduce biases in the galaxy large-scale properties. To do that, we identified early-type galaxies as objects with $B/T \geq 0.7$ and we defined a preliminary cluster catalogue in each lightcone as structures composed by at least 5 members, identified as objects characterised by the same FOF ID. We considered all bulge-dominated galaxies brighter than $0.2\ L^*$ in narrow redshift slices of 0.05 and we built the histogram of galaxy colours for each redshift bin. We fit this distribution with a Gaussian and we considered the mean $\bar{c}$ and the standard deviation σ_c of this distribution as a function of redshift. To apply appropriate color constraints, we imposed colour cuts in order to match the mean colour obtained from Henriques lightcones.

Moreover, for each cluster in the preliminary catalogue, we added a given fraction of early-type galaxies ($B/T \geq 0.7$): this fraction is a value randomly extracted from a Gaussian with a mean value $\bar{x} = 70$ and with $\sigma = 10$. For groups, we used the same prescriptions as for clusters, but we extracted values from a Gaussian with a mean value of 50 instead of 70 as for clusters. Finally, for field galaxies, we randomly modified a fraction of red galaxies to reach $\sim 30\%$ of ETGs at each redshift. We also added uncertainties to magnitudes, and redshifts, to reflect realistic photometry and photometric redshifts for the NGVS.

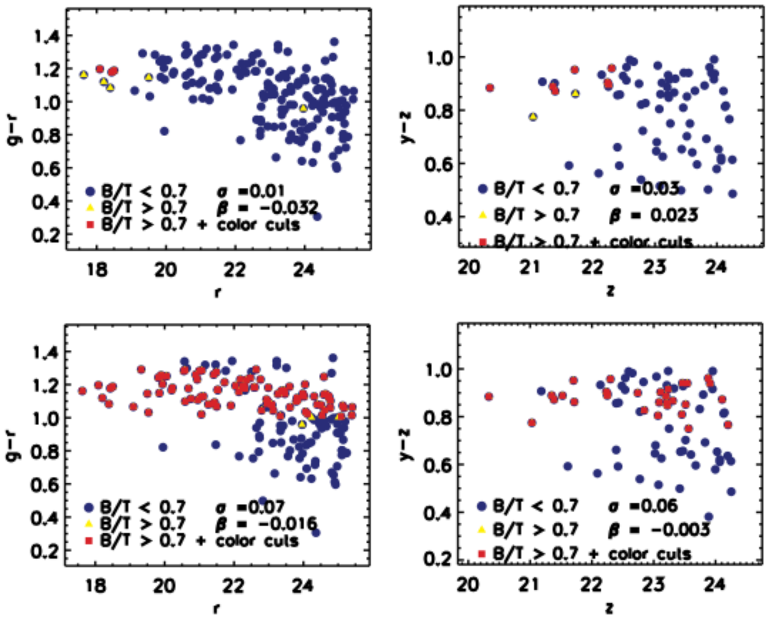

Fig. 1. Upper panel: colour-magnitude relation of two clusters in Henriques et al. (2012) lightcones at $z = 0.23$ and $z = 0.93$. Blue dots are cluster members, yellow triangles represent members with $B/T \geq 0.7$ and red points are ETGs characterised by colours in agreement with predicted ones from BC03 models. Lower panel: colour-magnitude relation for the same clusters, when predicted colours have been shifted and ETGs added.

When applying our detection method, we considered a colour cut around the mean colour $\bar{c} \pm 3\sigma_c$ corresponding at that redshift. In the lower panel of Figure 1, we show the corrected colour-magnitude-relation for the two clusters. Then, we run our detection code on mock catalogues to estimate completeness and purity, assuming the same requirements used with the NGVS sample: we found a completeness of $94\%, 80\%, 72\%, 35\%$ respectively at $M \geq 2 \times 10^{14}\ M_{\odot}, M \geq 10^{14}\ M_{\odot}, M \geq 5 \cdot 10^{13}\ M_{\odot}$ and $M \geq 1 \cdot 10^{13}\ M_{\odot}$ for $0.1 \leq z \leq 1.0$ while for $0.1 \leq z \leq 1.2$ we reach respectively $94\%, 75\%, 64\%, 33\%$ in completeness. In both cases, the overall purity is of $\sim 81\%$.

6 Conclusions

We presented the cluster detection algorithm *Red–GOLD* based on searching red–sequence galaxy overdensities, using colours and photometric redshifts and its application to the NGVS optical data. We found ~ 10 clusters per square degree up to $z \sim 1$. We tested our detection algorithm using semi-analytic simulations by Henriques et al. (2012): after correcting these lightcones to well reproduce the cluster red–sequence, we found a completeness of $94\%, 80\%$ up to $z = 1$, for clusters more massive than $M \geq 2 \times 10^{14}\ M_{\odot}, M \geq 10^{14}\ M_{\odot}$, respectively. Our estimated purity is $\sim 81\%$, at both mass limits.

References

Arnouts, S., Cristiani, S., Moscardini, L., et al. 1999, MNRAS, 310, 540
Arnouts, S., Moscardini, L., Vanzella, E., et al. 2002, MNRAS, 329, 355
Bertin, E. & Arnouts, S. 1996, A&AS, 117, 393
Blakeslee, J. P., Holden, B. P., Franx, M., et al. 2006, ApJ, 644, 30
Bruzual, G. & Charlot, S. 2003, MNRAS, 344, 1000
Desai, V., Dalcanton, J. J., Aragón-Salamanca, A., et al. 2007, ApJ, 660, 1151
Erben, T., Hildebrandt, H., Miller, L., et al. 2013, MNRAS, 433, 2545
Ferrarese, L., Côté, P., Cuillandre, J.-C., et al. 2012, ApJS, 200, 4
George, M. R., Leauthaud, A., Bundy, K., et al. 2012, ApJ, 757, 2

George, M. R., Leauthaud, A., Bundy, K., et al. 2011, ApJ, 742, 125
Guo, Q., White, S., Boylan-Kolchin, M., et al. 2011, MNRAS, 413, 101
Gwyn, S. D. J. 2012, AJ, 143, 38
Henriques, B. M. B., White, S. D. M., Lemson, G., et al. 2012, MNRAS, 421, 2904
Hildebrandt, H., Erben, T., Kuijken, K., et al. 2012, MNRAS, 421, 2355
Ilbert, O., Arnouts, S., McCracken, H. J., et al. 2006, A&A, 457, 841
Kodama, T., Arimoto, N., Barger, A. J., & Arag'on-Salamanca, A. 1998, A&A, 334, 99
Mei, S., Holden, B. P., Blakeslee, J. P., et al. 2009, ApJ, 690, 42
Muzzin, A., Wilson, G., Demarco, R., et al. 2013, ApJ, 767, 39
Postman, M., Franx, M., Cross, N. J. G., et al. 2005, ApJ, 623, 721
Raichoor, A., Mei, S., Erben, T., et al. 2014, ArXiv e-prints
Rykoff, E. S., Rozo, E., Busha, M. T., et al. 2014, ApJ, 785, 104
Springel, V., White, S. D. M., Jenkins, A., et al. 2005, Nature, 435, 629

SF2A 2014
J. Ballet, F. Bournaud, F. Martins, R. Monier and C. Reylé (eds)

GALAXY LUMINOSITY FUNCTION: EVOLUTION AT HIGH REDSHIFT

Nicolas Martinet[1], Florence Durret[1], Loïc Guennou[2], Christophe Adami[3] and the DAFT/FADA team[4]

Abstract. There are some disagreements about the abundance of faint galaxies in high redshift clusters. DAFT/FADA (Dark energy American French Team) is a medium redshift ($0.4 < z < 0.9$) survey of massive galaxy clusters ideal to tackle these problems. We present cluster galaxy luminosity functions (GLFs) based on photometric redshifts for 30 clusters in B, V, R and I restframe bands. We show that completeness is a key parameter to understand the different observed behaviors when fitting the GLFs. We also investigate the evolution of GLFs with redshift for red and blue galaxy populations separately. We find a drop of the faint end of red GLFs which is more important at higher redshift while the blue GLF faint end remains flat in our redshift range. These results can be interpreted in terms of galaxy quenching. Faint blue galaxies transform into red ones which enrich the red sequence from high to low redshifts in clusters while some blue galaxies are still accreted from the environment, compensating for this evolution so that the global GLF does not seem to evolve.

Keywords: galaxies: cluster: general - galaxies: evolution - galaxies: formation - galaxies: luminosity function, mass function

1 Introduction

The evolution of galaxy population in clusters is still an ongoing problem. In particular, the behaviour of the faint end of the galaxy luminosity function (GLF) of clusters gives us some clues about cluster formation and evolution. The disagrement found in the litterature arises from the use of small data sets, differences in observations and in techniques. Most authors find that the GLF faint end is decreasing at high redshift (e.g. Rudnick et al. 2009) but some authors still see a flat faint end at the same redshift (e.g. De Propris et al. 2013). The first observation would require a galaxy type evolution inside clusters while the second would result in fixed galaxy populations from redshift around $z = 0.9$ until now.

We want to address this problem with the largest galaxy cluster sample dedicated to this kind of studies to conclude on the different observed scenarii. We show here some preliminary results for a small number of clusters. A complete description of this work, taking into account about 30 clusters can be found in Martinet et al. (in revision).

DAFT/FADA is a survey of about 90 massive clusters at medium high redshift ($0.4 < z < 0.9$) based on HST data and on a ground based follow up on 4m class telescopes. The work presented here concerns a subsample of 6 clusters for which we have gathered ground based images in the u or B, V, R, I, Z optical bands and also in the J or Ks near infrared bands. The various telescopes used are CFHT, Subaru, VLT, WIYN, SOAR and CTIO.

[1] UPMC Université Paris 06, UMR 7095, Institut d'Astrophysique de Paris, 98bis Bd Arago, 75014, Paris, France
[2] Institut d'Astrophysique Spatiale (IAS), Université Paris Sud, Bâtiment 121, 91405 Orsay, France
[3] LAM, OAMP, Université Aix-Marseille & CNRS, Pôle de l'Etoile, Site de Château Gombert, 38 rue Frédéric Joliot-Curie, 13388 Marseille 13 Cedex, France
[4] send offprint comments to Nicolas Martinet: martinet@iap.fr

2 Measuring Galaxy Luminosity Functions (GLF)

Magnitudes are extracted using Sextractor (Bertin & Arnouts 1996) and are corrected from the extinction calculated from dust maps of Schlegel et al. (1998).

In order to properly estimate the cluster membership of galaxies, we compute photometric redshifts (photo-zs) for each galaxy with the LePhare software (Ilbert et al. 2006). The use of the combined optical and near infrared images plus a spectroscopic calibration allows us to achieve a precision of $\sigma_{photoz} = 0.06$ for every type of galaxy. Once photometric redshifts are calculated, we transpose our magnitudes measured on images from various telescopes into the VLT filters to homogenize our sample.

We also accurately measure the completeness of our data in each image. To do this we simulate stars of various magnitudes using the extracted PSF of the image and then insert and redetect these fake stars in the initial images. In average, our data are 90% complete until a magnitude of i=23.2. The k-correction is taken into account both for galaxies and when converting the completeness limit from apparent to absolute magnitudes.

GLFs are obtained by summing galaxies in bins of absolute magnitude in a 1 Mpc radius around the cluster optical center. Galaxies are said to belong to the cluster if their photo-zs lie in an interval of ± 0.2 around the cluster spectroscopic redshift. This large interval is chosen to be about 3σ of the standard deviation on our photo-zs. Background galaxies are then subtracted using field GLFs from Ilbert et al. (2005) calculated in the same redshift bins. Finally GLFs from different clusters are stacked together by averaging their galaxy numbers in the same absolute magnitude bins. Only clusters with the same 90% completeness limit can be stacked in this way, leading to stacks including different numbers of clusters.

We have also separated the early type and late type populations. This separation is done in a (V-I) versus I color magnitude diagram for galaxies already selected to belong to the cluster based on their photo-z. The red sequence is determined by a fixed slope (Durret et al. 2011) and a width of ± 0.3 in colour. The ordinate varies with redshift and is thus fitted on diagrams for each cluster. Galaxies within the red sequence correspond to early type galaxies, also refered to as red galaxies, and galaxies below the red sequence correspond to late type galaxies or blue galaxies. The other steps of the reduction are done in the same way as for all galaxy GLFs.

3 Evolution with type and redshift

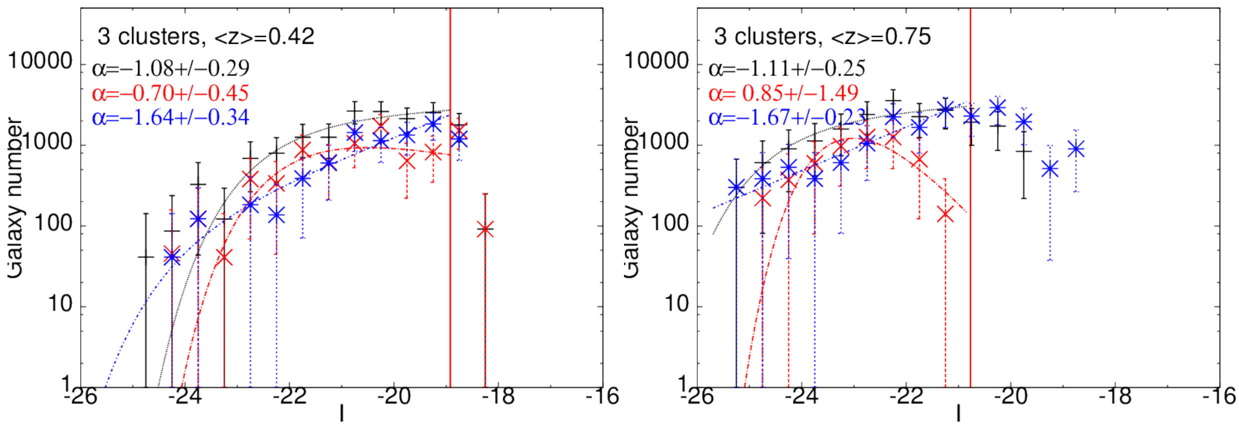

Fig. 1. Evolution of total, early type and late type I restframe band GLFs with redshift. **Left**: GLFs for three clusters at intermediate redshifts ($0.40 < z < 0.65$) stacked together. **Right**: GLFs for three clusters at higher redshift ($0.65 < z < 0.90$) stacked together. Total, early type and late type GLFs are respectively shown in black, red and blue. The α parameter is also displayed for each population. The vertical red line corresponds to the 90% completeness limit and only bins brighter than this limit are taken into account when performing the fit.

GLFs are usually fitted with Schechter functions (eq. 3.1, Schechter 1976).

$$N(M) = 0.4\log(10)\phi^*[10^{0.4(M^*-M)}]^{\alpha+1}\exp(-10^{0.4(M^*-M)}) \tag{3.1}$$

We investigated the variation of these Schechter parameters with various cluster observables (optical band, mass, redshift, completeness, environment, ...) and those results can be found in Martinet et al. (in revision). Here we only discuss the variation of the faint end slope with redshift in the I restframe band and for different galaxy populations. The faint end is characterized by the α parameter, with $\alpha = -1$ corresponding to a flat faint end, $\alpha < -1$ to a steep faint end and $\alpha > -1$ to a decreasing faint end.

Fig. 1 shows total, early type and late type I restframe band GLFs along with their best Schechter fits for stacks of three intermediate redshift clusters ($0.40 < z < 0.65$) and three higher redshift clusters ($0.65 < z < 0.90$).

When looking at all galaxy types together and at blue galaxies, we see no significant variation from one redshift range to another. All type GLFs remain flat with α very close to -1 and blue GLFs remain steep. However, when looking at red GLFs, we see a small drop of the faint end at intermediate redshift that becomes more important at high redshift. This drop means faint early type galaxies are not found in clusters at high redshift. This result goes in favor of an evolutionary scenario in which blue late type galaxies are quenched into red early types to populate the faint part of the red sequence from high redshift until today. In the mean time the abence of variation of the blue faint end means clusters are enriched in faint blue galaxies at any redshift since $z = 0.9$.

4 Conclusions

With this subsample of our data, we see a drop at the faint end of the red sequence GLF which is redshift dependent. On the other hand the blue and total GLFs remain respectively steep and flat with redshift at their faint end.

We conclude that galaxies in clusters still have to evolve from $z = 0.9$ to appear as they are at redshift zero. Blue galaxies transform into red ellipticals and progressively populate the red sequence until today while some blue faint galaxies keep being accreted.

We acknowledge long term financial support from CNES.

References

Bertin, E. & Arnouts, S. 1996, A&AS, 117, 393

De Propris, R., Phillipps, S., & Bremer, M. N. 2013, MNRAS, 434, 3469

Durret, F., Laganá, T. F., & Haider, M. 2011, A&A, 529, A38

Ilbert, O., Arnouts, S., McCracken, H. J., et al. 2006, A&A, 457, 841

Ilbert, O., Tresse, L., Zucca, E., et al. 2005, A&A, 439, 863

Martinet, N., Durret, F., Guennou, L., et al. in revision, A&A

Rudnick, G., von der Linden, A., Pelló, R., et al. 2009, ApJ, 700, 1559

Schechter, P. 1976, ApJ, 203, 297

Schlegel, D. J., Finkbeiner, D. P., & Davis, M. 1998, ApJ, 500, 525

UNDERSTANDING THE STATE OF THE GAS SURROUNDING ANDROMEDA'S BLACK HOLE.

A.-L. Melchior[1, 2] and F. Combes[1, 3]

Abstract. A millimeter CO survey has been performed at IRAM of the gas surrounding Andromeda's black hole. Several velocity components are detected supporting the presence of a relic 0.7-kpc ring, signing a possible frontal collision with M32. A multiwavelength analysis of this central field of M31 has been carried out in order to get clues on the location and state of this gas. Viaene et al. (2014) estimate in this central zone a star formation rate of order 3×10^{-4} $M_\odot\,yr^{-1}$, based on infrared data. Beside a 200 Myr A-star cluster detected close to the black hole, no trace of recent star formation is observed in UV. In parallel, Halpha gas is present but due to shocks as the [NII]/Halpha ratio is larger than 3. The issue is thus to understand why the cold molecular gas is quenched and not forming stars.

Keywords: Galaxies: kinematics and dynamics, Galaxies: ISM, Galaxies: interactions, Radio lines: galaxies

1 Introduction

M31 is usually described as a quiescent galaxy with little star formation $0.25^{+0.06}_{-0.04}\,M_\odot\,yr^{-1}$ (e.g. Barmby et al. 2006; Tabatabaei & Berkhuijsen 2010; Azimlu et al. 2011; Ford et al. 2013) and with an ultra-weak nuclear activity (del Burgo et al. 2000). While the centre of M31 hosts a massive black hole with a mass of $0.7 - 1.4 \times 10^8 M_\odot$ (Bacon et al. 2001; Bender et al. 2005), it is one of the most underluminous supermassive black hole (Garcia et al. 2010), although since 2008, it started to murmur (Li et al. 2011). The gas content of this region is small compared to the Central Molecular Zone in the Milky Way. Kruijssen et al. (2014) discuss that in the CMZ the star formation rate is 10 times weaker than in the Galactic disc. We discuss that even though our neighbouring galaxy M31 has exhausted most of its gas in the central region, the gas present there does not behave like in the main disc and does not exhibit obvious signs of star formation either.

2 CO mapping and kinematics

We map at IRAM-30m the main parts of M31's inner ring in ^{12}CO(2-1). We also observed the inner parts as described in Melchior & Combes (2013). More recently some ^{12}CO(1-0) observations with Pic-de-Bure interferometer have been performed. The kinematics thus achieved is displayed in Fig. 1. As first discussed in Melchior & Combes (2011), we observe components on both sides of the systemic velocity (-300 km s^{-1}) along the minor axis. These components are decoupled from the main disc (whose expected velocity is close to systemic at these positions). Also the inner ring velocities do not rotate around the optical centre where is located the central black hole. Last, in the North-West side a weak component is detected at the systemic velocity. Due to the high inclination (77 deg) of the main large-scale disc, it could be the projection of the disc, even though it could also be a more face-on inner disc (a third component).

In Fig. 1, we also display the contours (4, 7.5 and 10 mJy/pixel) of the Herschel/PACS 100 μm map (Viaene et al. 2014). The CO is not detected in all the positions of the inner ring. The detections are weak (at the mK level) and it is probable that more gas exists below the detection threshold.

[1] LERMA, UMR8112, Observatoire de Paris, 61, avenue de l'Observatoire, Paris, F-75014, France
[2] Sorbonne Universités, UPMC Univ Paris 06, UMR8112, LERMA, F75005, Paris, France
[3] Collège de France, avenue Marcelin Berthelot, Paris, F-75005, France

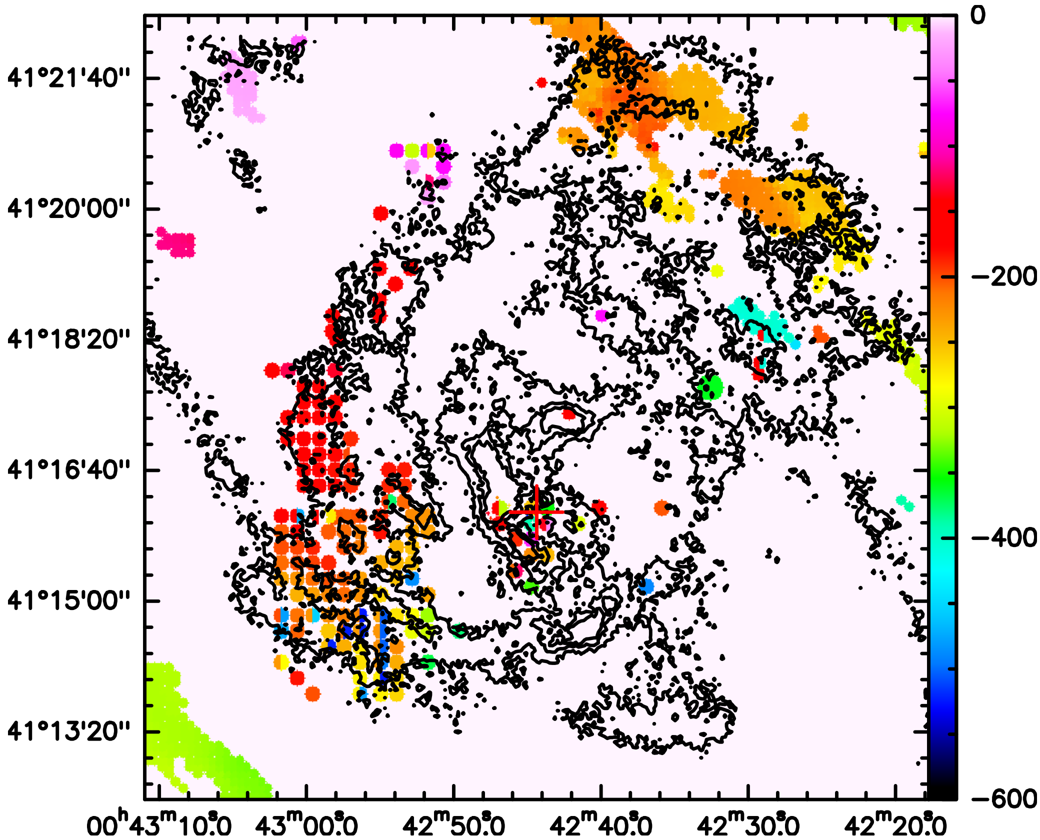

Fig. 1. CO velocities gathered from new IRAM (30m radiotelescope and Pic-de-Bure interferometer) observations and from Nieten et al. (2006) (courtesy M. Guélin). The contours (4, 7.5 and 10 mJy/pixel) correspond to the 100 μm map produced by Viaene et al. (2014). CO gas is detected along the inner ring. The velocity field exhibits several components with different position angles from the main disc rotation. Several counter-rotations are observed especially along the minor axis. The location of the optical peak (and position of the black hole) indicated with a cross is clearly off-centred.

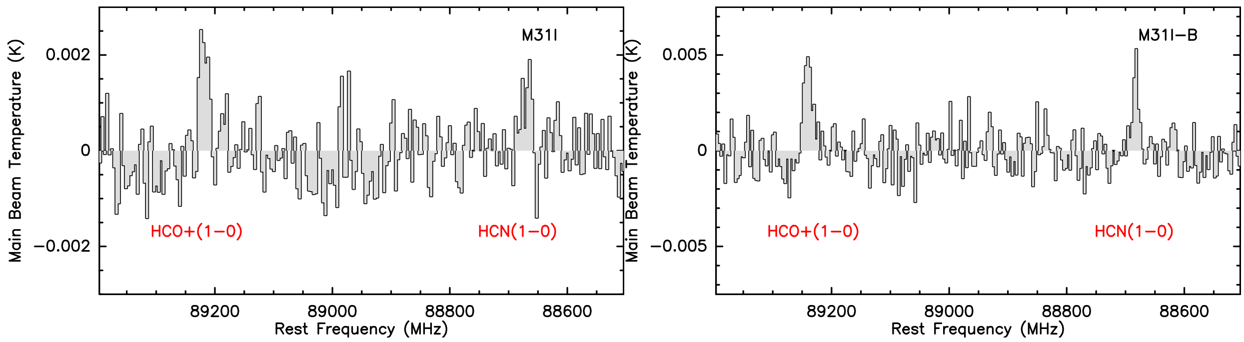

Fig. 2. Observations of dense gas in the North-West side in the inner ring. **Left:** HCO+(1-0) and HCN(1-0) lines observed at $00^h42^m29.1^s$, $+41°18'3.6$" (J2000.0) in the rest-frame of the Andromeda galaxy. **Right:** HCO+(1-0) and HCN(1-0) lines observed at $00^h42^m26.4^s$, $+41°17'58.0$" (J2000.0) in the rest-frame of the Andromeda galaxy.

3 Dense molecular gas

We observed at IRAM-30m with the EMIR receiver dense gas molecular lines in two bands: 87.4-91.4 GHz and 218.65-222.65 GHz. In two positions (as displayed in Fig. 2), we have detected HCO+(1-0) and HCN(1-0) corresponding to the receding component. ^{13}CO emission has been detected in 10 positions on both sides of the inner axis, with velocities corresponding to ^{12}CO. We have a detection of C^{18}O at the systemic velocity, which

Table 1. Summary of the main detections of dense gas. For each line, we provide the central velocity V_0, the FWHM velocity dispersion Δv, the main-beam temperature T_{peak} and the integrated line I_{CO}. We provide the N_{H_2} column densities computed using a standard $X_{CO} = 2 \times 10^{20}\,\mathrm{cm}^{-2}\,(\mathrm{K\,km\,s^{-1}})^{-1}$ following Dame et al. (2001) and assuming CO(2-1)/(1-0) ratio of 0.8 as computed in Melchior & Combes (2011) for a detection within 10" of our position M31I. The velocities V_0 and dispersions Δv flagged with a "*" have been fixed to the ^{12}CO values for the fit performed to compute I_{CO} and T_{peak}.

Parameters	M31I(2)	M31I(3)	M31I-B(1)				
	^{12}CO(2-1)				^{13}CO(2-1)		
V_0 (km/s)	-402±3	-291±9	-463±1	V_0 (km/s)	-402*	-291*	-463*
Δv (km/s)	62±12	69±18	36±2	Δv (km/s)	62*	69*	36*
T_{peak} (mK)	146	77	138	T_{peak} (mK)	4.6	4.9	4.5
I_{CO} ($\mathrm{K\,km\,s^{-1}}$)	9.6±0.5	6±1	5.3±0.2	I_{CO} ($\mathrm{K\,km\,s^{-1}}$)	0.30±0.06	0.36±0.06	0.48±0.04
N_{H_2} ($10^{20}\,\mathrm{cm}^{-2}$)	19±1	12±2	10.6±0.4				
	C^{18}O(2-1)				^{12}CO(1-0)		
V_0 (km/s)		-291*		V_0 (km/s)	-412±1	-279±3	
Δv (km/s)		69*		Δv (km/s)	34±3	46±5	
T_{peak} (mK)		4.5		T_{peak} (mK)	127	51	
I_{CO}	<0.21	0.29±0.07	<0.17	I_{CO}	4.6±0.8	2.5±0.3	
	HCO+(1-0)				HCN(1-0)		
V_0 (km/s)	-400±5		-473±4	V_0 (km/s)	-409±4		-471±2
Δv (km/s)	60±10		65±10	Δv (km/s)	25±7		32±8
T_{peak} (mK)	3.6		5.3	T_{peak} (mK)	3.0		6.1
I_{HCO+}	0.23±0.04		0.36±0.04	I_{HCN}	0.08±0.02		0.21±0.04

Table 2. Indicative abundances. For each transition, we provide the measured abundances assuming LTE and optically thin conditions. We consider the average of the measurements available for each transition. We provide in the third column the relative abundance of ^{12}CO with respect to the transition In the fourth column, we provide expected for the Galactic interstellar medium (at 4 kpc derived from Bergin et al. (1995) and Wilson & Rood (1994)). The last column provides the ratios of the transition intensities of each CO transition wih respect to ^{12}CO(2-1) and the other molecules with respect to ^{12}CO(1-0). Each set of lines has been observed with similar beams.

	Measured values (LTE)		Galactic values	
Transition	$X^{Observed}$	^{13}CO/Mol	X^{GISM}	^{12}CO/Mol
^{12}CO(2-1)	9.5×10^{-6}	1	2.8×10^{-5}	1
^{13}CO(2-1)	3.2×10^{-7}	29.7	5.28×10^{-7}	53
C^{18}O(2-1)	2.9×10^{-7}	32.3	8.56×10^{-8}	327
Transition	$X^{Observed}$	^{12}CO(1-0)/Mol	X^{GISM}	^{12}CO(1-0)/Mol
^{12}CO(1-0)	1.65×10^{-5}	1	2.8×10^{-5}	1
HCN(1-0)	1.29×10^{-10}	1.29×10^{5}	1.9×10^{-9}	1.57×10^{5}
HCO+(1-0)	2.10×10^{-10}	0.79×10^{5}	4.7×10^{-10}	1.35×10^{5}

does not correspond to the HCN and HCO+ detection. The characteristics of the components with more that 3 lines are presented in Tab. 1. Beside the ^{12}CO(2-1) and (1-0) measurements, all the detections are weak with main-beam temperatures at the mK level. We measure $I_{HCN}/I_{CO} = 1/58$. This is quite different from values observed for starbursts in the range 1/3-1/10. It is quite typical of Galactic values. If one assumes that the gas is in Local Thermal Equilibrium and optically thin, one can compute the abundances of the gas in each detected component and transition. Viaene et al. (2014) has computed a dust temperature of 20 K at the corresponding positions. We thus assume a kinetic temperature of 20 K. The results are provided in Tab. 2, together with abundances measured in the Milky Way. The measured ^{12}CO /C^{18}O ratio is a factor 10 times weaker than expected. As C^{18}O is optically thin, this ratio is due to the fact that ^{12}CO is optically thick. However, the C^{18}O intensity is comparable with the measured ^{13}CO intensity. Rather than a relative excess of C^{18}O, one could rather argue for a deficit of ^{13}CO, since such a ^{13}CO deficit was first observed by Casoli et al. (1991) in mergers. The ^{13}CO is under-abundant with respect to C^{18}O. Davis (2014) also find an anticorrelation of ^{13}CO and the star formation and gas surface densities in local galaxies. This could be the signature of a 200 Myr old starburst triggered by the collision with M32 proposed by Block et al. (2006).

4 Conclusions

We have mapped in CO the inner ring of M31. The kinematics display a complex configuration along the minor axis with multiple components along the line of sight (identified by different velocities). In the North-West side of the inner ring, several dense gas lines have been detected. A simple analysis assuming that the gas is in Local Thermal Equilibrium and optically thin (except for ^{12}CO) shows that the abundances do not correspond to the Galactic values. We argue that the observed deficit of ^{13}CO with respect to C^{18}O and excess of HCN(1-0) with respect to HCO+(1-0) could be due to a 200 Myr old starburst which could have been triggered by a frontal collision with M32.

Optical ionised gas offers the perspective especially with the SITELLE instrument to be installed at CFHT (Brousseau et al. 2014). It should enable to map the whole area in several lines with an unprecented sensibility. It will be possible to get the kinematics of the whole area for several optical lines. In order to check the feasibility of this type of work not done since Boulesteix et al. (1987) and get the velocity field, we observed in September-October 2014 with a Fabry-Perot device on T1.6m telescope at Observatoire du Mont-Megantic (Canada) H_α and [NII]. Rubin & Ford (1971) got the only existing data showing that the [NII]/H_α ratio is of order 2-3 in this area. The gas could be dominated by shocks which could explain the absence of star-formation. A similar phenomenon could apply to the CMZ in the Milky Way (Kruijssen et al. 2014).

We thank the IRAM teams for their support for the observations and the data reduction. We thank M. Guélin from making available to us the IRAM-30m M31 large CO survey. We are grateful to Sébastien Viaeney for preparing Herschel data cutouts for us.

References

Azimlu, M., Marciniak, R., & Barmby, P. 2011, AJ, 142, 139

Bacon, R., Emsellem, E., Combes, F., et al. 2001, A&A, 371, 409

Barmby, P., Ashby, M. L. N., Bianchi, L., et al. 2006, ApJ, 650, L45

Bender, R., Kormendy, J., Bower, G., et al. 2005, ApJ, 631, 280

Bergin, E. A., Langer, W. D., & Goldsmith, P. F. 1995, ApJ, 441, 222

Block, D. L., Bournaud, F., Combes, F., et al. 2006, Nature, 443, 832

Boulesteix, J., Georgelin, Y. P., Lecoarer, E., Marcelin, M., & Monnet, G. 1987, A&A, 178, 91

Brousseau, D., Thibault, S., Fortin-Boivin, S., et al. 2014, Proc. SPIE, 9147

Casoli, F., Dupraz, C., Combes, F., & Kazes, I. 1991, A&A, 251, 1

Dame, T. M., Hartmann, D., & Thaddeus, P. 2001, ApJ, 547, 792

Davis, T. A. MNRAS, accepted

del Burgo, C., Mediavilla, E., & Arribas, S. 2000, ApJ, 540, 741

Ford, G. P., Gear, W. K., Smith, M. W. L., et al. 2013, ApJ, 769, 55

Garcia, M. R., Hextall, R., Baganoff, F. K., et al. 2010, ApJ, 710, 755

Kruijssen, J. M. D., Longmore, S. N., Elmegreen, B. G., et al. 2014, MNRAS, 440, 3370

Li, Z., Garcia, M. R., Forman, W. R., et al. 2011, ApJ, 728, L10

Melchior, A.-L., Viallefond, F., Guélin, M., & Neininger, N. 2000, MNRAS, 312, L29

Melchior, A.-L., & Combes, F. 2011, A&A, 536, A52

Melchior, A.-L., & Combes, F. 2013, A&A, 549, A27

Nieten, C., Neininger, N., Guélin, M., et al. 2006, A&A, 453, 459

Rubin, V. C., & Ford, W. K., Jr. 1971, ApJ, 170, 25

Tabatabaei, F. S., & Berkhuijsen, E. M. 2010, A&A, 517, A77

Viaene, S., Fritz, J., Baes, M., et al. 2014, A&A, 567, A71

Wilson, T. L., & Rood, R. 1994, ARA&A, 32, 191

SF2A 2014
J. Ballet, F. Bournaud, F. Martins, R. Monier and C. Reylé (eds)

PROBING GAS FLOWS AROUND GALAXIES WITH SINFONI

C. Peroux[1]

Abstract. The circumgalactic medium (CGM) of typical galaxies is crucial to our understanding of the cycling of gas into, through and out of galaxies. One way to probe the CGM is to study gas around galaxies detected via the absorption lines they produce in the spectra of background quasars. We present high-resolution SINFONI 3D observations of galaxies responsible for high-N HI quasar absorbers. These data allow to determine in details the kinematics of the objects. In addition, we use several indicators to determine the direction of the gas flows in and out of these galaxies. We also compare the gas-phase and stellar metallicities to constrain the star formation history of these galaxies based on VLT/X-Shooter observations. This allows us to compare the neutral and ionised phase metallicities in the same objects and relates these measures to possible signature of low-metallicity gas accretion or outflows of gas enriched by star formation.

Keywords: quasars: absorption lines, Galaxies: kinematics and dynamics, intergalactic medium

1 Introduction

Tremendous progress has been made over the last decade in establishing a broad cosmological framework in which galaxies and large-scale structure develop hierarchically over time, as a result of gravitational instability of material dominated by dark matter (e.g. Springel & Hernquist 2003). A picture arises where galaxy formation is fed by inflows of gas from the inter-galactic medium - IGM (e.g. Keres et al. 2005), counteracted by strong galactic winds (e.g. Oppenheimer et al. 2010), which in concert establish the growth rate of gas and stars within galaxies at all cosmic epochs. These processes can be collectively described as a 'baryon cycle'.

The next challenge is this field is to establish a direct comparison between observations and theoretical predictions. Outflows are ubiquitous in galaxies at various redshifts (e.g. Steidel et al. 2010). However, given the unknown in the ionisation state and number of phases in the gas, it is at present very difficult to measure the mass in these outflows (e.g. Genzel et al. 2010). Moreover, galaxies with the IGM by pervading it with ionising photons, by polluting it with heavy elements formed in stars and supernovae through these supersonic galactic winds. Observations of galaxies in absorption in the spectrum of a background quasar, the so-called quasar absorbers, indicate the presence of metals down to low over-densities at all redshifts (Tumlinson et al. 2011) which, in various models, is interpreted as a signature of strong galactic outflows (Oppenheimer & Davé 2006).

The observational evidence for inflows are even more challenging and just a handful of claims have been reported so far (Bouché, et al. 2013). However, accretion is required to explain some of the basic observed properties of galaxies including the gas-phase metallicity (e.g. Erb et al. 2006) and the cosmological evolution of neutral gas mass (Zafar et al. 2013b). The circum-galactic medium (CGM), broadly defined as the interface between galaxies and the IGM (Shull 2014), is at the heart of these physical processes. The baryon cycle of gas travelling into, through, and out of galaxies is taken place in this CGM.

2 The SINFONI Integral Field Spectroscopy Sample for Galaxy Counterpart to Damped Lyman-α Systems

A way to study the detailed processes at play in the CGM is to bring together, in a unified picture, data on cold gas (<100,000 K), metals and stellar content of the same galaxies. Indeed, the gas from the diffuse medium

[1] Aix Marseille Universit, CNRS, LAM (Laboratoire d'Astrophysique de Marseille) UMR 7326, 13388, Marseille, France

surrounding galaxies, is detected via the absorption lines it produces in the spectra of background quasars, and provides a powerful tool to study the CGM of galaxies (Stewart et al. 2011; Stinson et al. 2012). Samples of the strongest of these quasar absorbers, the so-called Damped Lyman-α systems (DLAs), now amount to several hundreds (Prochaska et al. 2005; Noterdaeme et al. 2009; Noterdaeme et al. 2012; York et al. in prep) and the number of known sub-Damped Lyman-α systems (sub-DLAs; Péroux et al. 2003) is also growing (Zafar et al. 2013a). These HI-selected sight-lines offer the prospect to study the direct surroundings of intermediate-redshift galaxies in the few cases where the absorbing-galaxy has been identified.

With the aim of studying the flows of gas in and out of galaxies, we have taken advantage of the 3D spectroscopy at near-IR wavelengths made possible by SINFONI on VLT to successfully detect the galaxies responsible for quasar absorbers (see Fig. 1 for an example). We have been able to detect five high-N(HI) absorbing-galaxies out of 16 searched for at $z \simeq 1$–2. In these studies, using SINFONI data at a resolution of 0.8-arcsec ($\sim$6 kpc at z$\sim$1), we identified galaxy counterparts for the absorbers and estimated star formation rates and emission metallicities from emission line detections. We also acquired X-Shooter emission-line spectra covering the observed wavelength 300 nm to 2.5 μm for these absorbing-galaxies (see Fig. 2). The slit was oriented to obtain a spectrum of both the background quasar and the galaxy responsible for the high-N(HI) quasar absorber. These data thus allow for a robust estimate of HII abundance in these and allow for a comparison of the metallicities in the neutral and ionised phase of the same objects.

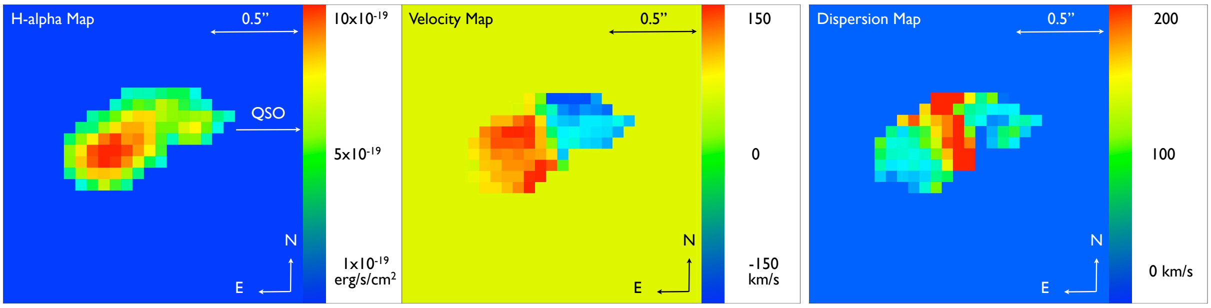

Fig. 1. H-α flux map, H-α velocity field and H-α velocity dispersion maps of the sub-DLA-galaxy towards Q2352-0028, zabs=1.0318. The velocity map indicates a strong gradient as expected from a rotating disc (Péroux et al. 2013).

3 Results

The SINFONI data are used to measure the dynamical masses of the systems which are found to range from $10^{9.8}$ to $10^{10.9}$ M$_\odot$. The mass of gas, however, is found to be between $10^{8.8}$ to $10^{9.7}$ M$_\odot$. We note that whenever the halo masses have been derived, these are significantly larger than the gas masses. Moreover, for the rotating galaxies, we are able to estimate the mass of the halo in which the absorbers reside assuming the systems are virialised. We find large values ranging from $10^{11.8}$ to $10^{12.8}$ M$_\odot$. These halo masses are an order of magnitude larger than the one derived by Pontzen et al. (2008) based on dedicated Smoothed-Particle Hydrodynamics (SPH) simulations. In fact, these authors predict that the major contributors to the population of DLAs are haloes of masses 10^9<M$_{\rm halo}$<10^{11} $M_\odot$, with a peak at M$_{\rm halo}$=10^{10} $M_\odot$. It is possible that the 5 high-N(HI) absorbers we have detected amongst 16 searched for are thus the high mass end of the DLA distribution.

In addition, our measurements of the absorbing-galaxy cross-section and M$_{\rm halo}$ imply that the systems have halo masses 4 to 5 orders of magnitude larger or cross-sections 3 orders of magnitude smaller than required to lie on the relation predicted by Pontzen et al. (2008). In fact, these authors note that their estimate of the cross-sections are larger than in previous simulations (Gardner et al. 1997; Nagamine et al. 2004) and suggest that this might be due to their particular feedback implementation. While the systems observed here are relatively metal-rich and hence expected to have (or have had) large SFR, the detection rate of our sample indicates that theses are representative of more than just a few percent of the DLA population. In two of the cases, additional HST imaging allows to determine the stellar mass of the absorbing-galaxies. These are derived to be $10^{9.5}$ to $10^{9.3}$ M$_\odot$, respectively (see Krogager et al. 2013; Christensen et al. 2014). These measurements allow for a direct test of the mass-metallicity relation in quasar absorbers claimed by several authors (Ledoux et al. 2006; Möller et al. 2013; Christensen et al. 2014).

Our results based on X-Shooter data suggest that the abundances derived in absorption along the line-of-sight to background quasars are a reliable measures of the overall galaxy metallicities (Péroux et al. 2014). The 2D metallicity maps based on SINFONI observations show small negative metallicity gradients. The flat slopes are in line with the differences observed between the two phases of the gas. These results suggest that a comparison of the HI and HII metallicities is a robust indicator of the internal gradients. In addition, we use several indicators to measure the quantity of dust in the ionised and neutral phases of these systems. The presence of dust in the HI phase can be estimated from the observed depletion of refractory elements. We find measures from the Balmer decrement of the galaxies to be in line with values derived from element ratios in the HI gas.

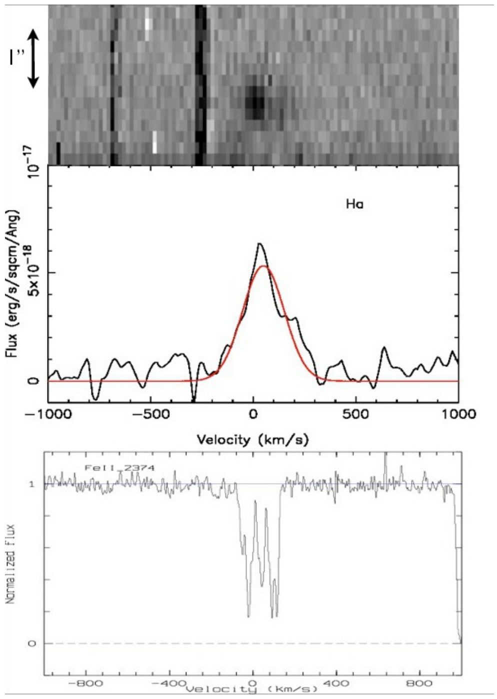

Fig. 2. Emission and absorption lines in the sub-DLA towards Q2352-0028. The black streaks in the 2D image are sky lines. The range of velocities spread by both the emission and the absorption profiles are comparable (Péroux et al. 2014).

4 Conclusions

We further use several indicators to study the flow of gas around these absorbing-galaxies. Indeed, the observations presented here allow to combine various tests which, together, can put constrains on the directions of the flows around z$\sim$1 or 2 galaxies. Based on arguments on the star formation per unit area, we argue that all systems might produce winds. In all five cases, we measure EW(MgII λ 2796) $>$ 1Å at the position of these absorbers and find that the saturated profiles extend both sides of the galaxies systemic redshifts, which are believed to be signatures of winds. Using a comparison of the emission and absorption kinematics, as well as inclination and orientation arguments, we find that two of the systems show signature of an outflow in the velocity profile. For the remaining three systems, it is difficult to reach definitive conclusions. In particular, there are two cases where the presence of two separate objects detected in HST and SINFONI imaging complicate the interpretation. Finally, 2D abundance maps and measure of the metallicity gradients in three of the five systems do not indicate signatures expected from infall of fresh gas onto the galaxies. Overall, our data are therefore consistent with the gas seen in absorption being due to material co-rotating with the halo of their discs although some lines of evidence might support the presence of outflows traced in absorption. In two cases, we have the strongest evidence for the presence of outflows. This is also supported by a large value of star formation rate per unit area, $\Sigma_{\rm SFR}$.

This work has benefited from support of the 'Agence Nationale de la Recherche' with reference ANR-08-BLAN-0316-01.

References

Bouché, N., Murphy, M. T., Kacprzak, G. G., Péroux, C., Contini, T., Martin, C. & Dessauges-Zavadsky, M., 2013, Nature, 341, 40

Christensen, L.; Moller, P.; Fynbo, J. P. U. & Zafar, T., 2014, MNRAS, 445, 225

Erb, D. K., Shapley, A. E., Pettini, M., Steidel, C. C., Reddy, N. A. & Adelberger, K. L., 2006, ApJ, 644, 813

Gardner, J. P., Katz, N., Weinberg, D. H. & Hernquist, L., 1997, ApJ, 486, 42

Genzel, R., et al., 2010, MNRAS, 407, 2091

Keres, D., Katz, N., Weinberg, D. H. & Davé, R., 2005, MNRAS, 363, 2

Krogager, J-H, Fynbo, J., Ledoux, C., Christensen, L., Gallazzi, A., Laursen, P., Möller, P., Noterdaeme, P., Péroux, C., Pettini, M., Vestergaard, M., 2013, MNRAS, 433, 309

Ledoux, C., Petitjean, P., Fynbo, J. P. U., Möller, P. & Srianand, R., 2006, A&A, 457, 71

Möller, P., Fynbo, J. P. U., Ledoux, C. & Nilsson, K. K., 2013, MNRAS, 430, 2680

Nagamine, K., Springel, V. & Hernquist, L., 2004, MNRAS, 348, 421

Noterdaeme, P., Petitjean, P., Ledoux, C. & Srianand, R., 2009, A&A, 505, 1087

Noterdaeme, P., et al., 2012, A&A, 547L, 1

Oppenheimer, B. D. & Davé, R., 2006, MNRAS, 373, 1265

Oppenheimer, B. D.; Davé, R., Keres, D., Fardal, M., Katz, N., Kollmeier, J. A. & Weinberg, D. H., 2010, MNRAS, 406, 2325

Péroux, C., Dessauges-Zavadsky, M., D'Odorico, S., Kim,T. S., & McMahon, R., 2003, MNRAS, 345, 480.

Péroux, C., Bouché, N., Kulkarni, V. P. & York, D. G., 2013, MNRAS, 436, 2650

Péroux, C., Kulkarni, V. P. & York, D. G., 2014, MNRAS, 437, 3144

Pontzen, A., Governato, F., Pettini, M., Booth, C. M., Stinson, G., Wadsley, J., Brooks, A., Quinn, T. & Haehnelt, M., 2008, MNRAS, 390, 1349

Prochaska, J. X., Herbert-Fort, S. & Wolfe, A. M., 2005, ApJ, 635, 123

Shull, J. M., 2014, ApJ, 784, 142

Springel, V. & Hernquist, L., 2003, MNRAS, 339, 289

Steidel, C. C., et al., 2010, ApJ, 717, 289

Stewart, K. R., Kaufmann, T., Bullock, J. S., Barton, E. J., Maller, A. H., Diemand, J. & Wadsley, J., 2011, ApJ, 738, 39

Stinson, G., S., et al., 2012, MNRAS, 425, 1270

Tumlinson, J. et al., 2011, Science, 334, 948

Zafar, T., Péroux, C., Popping, A., Deharveng, J.-M., Milliard, B. & Frank, S., 2013b, A&A, 556, 141

Zafar, T., Popping, A. & Péroux, C., 2013a, A&A, 556, 140

SF2A 2014
J. Ballet, F. Bournaud, F. Martins, R. Monier and C. Reylé (eds)

PHOTOMETRIC REDSHIFTS FOR THE NGVS

A. Raichoor[1], S. Mei[1,2], T. Erben[3], H. Hildebrandt[3], M. Huertas-Company[1,2], O. Ilbert[4], R. Licitra[1,2], N.M. Ball[5], S. Boissier[4], A. Boselli[4], Y.-T. Chen[6], P. Côté[5], J.-C. Cuillandre[7], P.A. Duc[8], P.R. Durrell[9], L. Ferrarese[5], P. Guhathakurta[10], S.D.J. Gwyn[5], J.J. Kavelaars[5], A. Lancon[11], C. Liu[12], L.A. MacArthur[5], M. Muller[10], R.P. Muñoz[13], E.W. Peng[14], T.H. Puzia[13], M. Sawicki[15], E. Toloba[10,16], L. Van Waerbeke[17], D. Woods[17] and H. Zhang[14,18]

Abstract. We present the photometric redshift catalog for the Next Generation Virgo Cluster Survey (NGVS), a 104 deg^2 optical imaging survey centered on the Virgo cluster in the u^*, g, r ,i, z bandpasses at point source depth of 25-26 ABmag. It already is the new optical reference survey for the study of the Virgo cluster, and will be also used for multiple ancillary programs. To obtain photometric redshifts, we perform accurate photometry, through the PSF-homogenization of our data. We then estimate the photometric redshifts using *Le Phare* and BPZ codes, adding a new prior extended down to $i_{AB} = 12.5$ mag. We assess the accuracy of our photometric redshifts as a function of magnitude and redshift using ∼80,000 spectroscopic redshifts from public surveys. For $i_{AB} < 23$ mag or $z_{\rm phot} < 1$ galaxies, we obtain photometric redshifts with $|bias| < 0.02$, a scatter increasing with magnitude (from 0.02 to 0.05), and less than 5% outliers.

Keywords: Galaxies: distances and redshifts – Galaxies: high-redshift – Galaxies: photometry techniques: photometric.

1 Introduction

Current large surveys (e.g., the Sloan Digital Sky Survey; SDSS; York et al. 2000) and future missions (e.g., such as EUCLID; Laureijs et al. 2011) open a new era for many field of astronomy, such as galaxy evolution and

[1] GEPI, Observatoire de Paris, CNRS, Université Paris Diderot, 61, Avenue de l'Observatoire 75014, Paris France
[2] Université Paris Denis Diderot, F-75205, Paris Cedex 13, France
[3] Argelander-Institut für Astronomie, University of Bonn, Auf dem Hügel 71, D-53121 Bonn, Germany
[4] Aix Marseille Université, CNRS, Laboratoire d'Astrophysique de Marseille, UMR 7326, F-13388 Marseille, France
[5] Herzberg Institute of Astrophysics, National Research Council of Canada, Victoria, BC, V9E 2E7, Canada
[6] Insitute of Astronomy and Astrophysics, Academia Sinica, P.O. Box 23-141, Taipei 106, Taiwan
[7] Canada–France–Hawaïi Telescope Corporation, Kamuela, HI 96743, USA
[8] Laboratoire AIM Paris-Saclay, CEA/IRFU/SAp, CNRS/INSU, Université Paris Diderot, F-91191 Gif-sur-Yvette Cedex, France
[9] Department of Physics and Astronomy, Youngstown State University, Youngstown, OH, USA
[10] UCO/Lick Observatory, Department of Astronomy and Astrophysics, University of California Santa Cruz, 1156 High Street, Santa Cruz, California 95064, USA
[11] Observatoire astronomique de Strasbourg, Université de Strasbourg, CNRS, UMR 7550, 11 rue de l'Université, F-67000 Strasbourg, France
[12] Center for Astronomy and Astrophysics, Department of Physics and Astronomy, Shanghai Jiao Tong University, 800 Dongchuan Road, Shanghai 200240, China
[13] Institute of Astrophysics, Pontificia Universidad Católica de Chile, Av. Vicuña Mackenna 4860, 7820436 Macul, Santiago, Chile
[14] Department of Astronomy, Peking University, Beijing 100871, China
[15] Department of Astronomy and Physics, St. Mary's University, Halifax, NS B3H 3C3, Canada
[16] Observatories of the Carnegie Institution for Science, 813 Santa Barbara Street, Pasadena, CA 91101, USA
[17] Department of Physics and Astronomy, University of British Columbia, 6224 Agricultural Road, Vancouver, B.C., V6T 1Z1, Canada
[18] Chinese Academy of Sciences South America Center for Astronomy, Camino El Observatorio #1515, Las Condes, Santiago, Chile

Table 1. Average characteristics of the NGVSLenS co-added data used in this study.

Filter	expos. time [ks]	$m_{\rm lim}^{\dagger}$ [AB mag]	seeing ["]
$u^*(u.MP9301)$	6.3	25.60 ± 0.16	0.83 ± 0.07
$g(g.MP9401)$	3.5	25.73 ± 0.13	0.77 ± 0.08
$r(r.MP9601)$	2.6	$24.68 \pm 0.50^{\star}$	0.74 ± 0.14
$i(i.MP9702)$	2.3	24.41 ± 0.13	0.52 ± 0.04
$z(z.MP9801)$	4.6	23.62 ± 0.16	0.70 ± 0.08

†: $m_{\rm lim}$ is the 5σ detection limit in a 2" aperture.
*: for the r-band, the minimum and maximum values for $m_{\rm lim}$ are 23.56 and 25.52, respectively.

cosmology, with access to homogeneous measurements of a multitude of fundamental galaxy properties. In this context, a crucial quantity is the galaxy redshift: spectroscopic redshifts (spec-z's) being observationally too costly for 10^6-10^8 objects, photometric redshifts (photo-z's) allow consistent measurement of redshifts for large numbers of galaxies, including relatively faint ones. The main limitations to estimate accurate photo-z's are the wavelength coverage of key spectral features (e.g., the Lyman-break and the 4,000 Å/Balmer break), and the quality and homogeneity of the photometry.

We present here the estimation of photo-z's for the Next Generation Virgo Cluster Survey (NGVS; Ferrarese et al. 2012). The NGVS is a comprehensive optical imaging survey of the Virgo cluster, from its core to its virial radius – covering a total area of 104 deg^2 – in the Canada-France-Hawaii Telescope (CFHT) u^*griz bandpasses. Currently, ∼70% of the NGVSLenS has not been imaged yet with the r-band. The NGVS will serve as the optical reference survey over the Virgo cluster, and will leverage the numerous other surveys targeting Virgo at shorter and longer wavelengths.

The results presented here are detailed in Raichoor et al. (2014).

2 NGVSLenS data and photometric catalogs

For this analysis, we use a NGVS dataset whose reduction is optimized for *background-science* (e.g., detection of high-redshift galaxy cluster candidates, Licitra et al., *in preparation*; strong and weak lensing studies, Gavazzi et al., *in preparation*): we label this dataset NGVSLenS.

To process the NGVS data for *background-science* applications, we use the algorithms and processing pipelines (THELI) developed within the Canada-France-Hawaii-Telescope Lensing Survey (CFHTLenS; see Heymans et al. 2012; Hildebrandt et al. 2012; Erben et al. 2013, and `http://cfhtlens.org`), a survey originated from the Wide component of the Canada-France-Hawaii-Telescope Legacy Survey (CFHTLS; Gwyn 2012) which was also obtained with MegaCam. In addition, the survey characteristics and the observing strategies of CFHTLS and NGVS are very similar. This allowed for a direct transfer of our CFHTLS expertise to the NGVS. The NGVSLenS dataset average characteristics are summarized in Table 1.

As studied in detailed in Hildebrandt et al. (2012), a requirement to estimate precise photo-z's is accurate photometry, in particular high precision color measurements. To do so, we implement the following procedure (*global* mode of Hildebrandt et al. 2012): the i-band, which has the best seeing (0.52" ± 0.04"), is used to detect objects and estimate their total magnitude; then, for each field, all images are first homogenized to the same PSF and then used to estimate accurate colors. In addition, we pay special attention to the photometric error estimation, to overcome a possible underestimation due to noise correlation introduced by image resampling.

3 Photometric redshift estimation

With the photometric catalogs described in the previous section in hand, we are able to estimate the photo-z's. We use two template-based codes to estimate photo-z's: *Le Phare* (Arnouts et al. 2002; Ilbert et al. 2006) and BPZ (Benítez 2000). For both codes, we use the recalibrated template set of Capak et al. (2004), which is built from the four Coleman et al. (1980) observed galaxy spectra (El, Sbc, Scd, Im), with two additional observed starburst templates from Kinney et al. (1996).

Le Phare and BPZ run in a similar way using a Bayesian approach. Both codes were designed for high redshift studies: they use similar priors for $i > 20$ mag galaxies, built with observed data. We use the SDSS Galaxy Main Sample spectroscopic survey (Strauss et al. 2002) to establish the prior for $12.5 < i \leq 17$ mag galaxies, and extrapolate the prior for $17 < i < 20$ mag galaxies.

4 Photometric redshift accuracy

To measure the accuracy of our photo-z's, we use a large sample of galaxy spec-z's (83.3×10^3 galaxies).

Our NGVSLenS spectroscopic sample (26.1×10^3 galaxies) is a compilation of several spectroscopic surveys having different target selections (SDSS: Eisenstein et al. 2001; Strauss et al. 2002; Dawson et al. 2013; spectroscopic programs targeting candidate globular clusters or UCDs: Peng et al., *in preparation*, Zhang et al., *submitted*; Zhang et al., *in preparation*, and spec-z's from the VDGC survey: Guhathakurta et al., *in preparation*). It is rather shallow ($z \leq 0.8$) and highly biased at $z \geq 0.3$ towards luminous red galaxies (LRGs), from the SDSS.

In order to assess the quality of our photometric redshifts up to $z < 1.5$, we use the CFHTLenS data, which are covered by deep and intensive spectroscopic surveys (DEEP2/EGS: Davis et al. 2003; Newman et al. 2013; VIPERS: Guzzo et al. 2013; F02 and F22 fields of the VVDS: Le Fèvre et al. 2013). Our CFHTLenS spectroscopic sample includes 57.2×10^3 spec-z's and spreads over ∼42 deg^2. Starting from the CFHTLenS THELI coadded-images, we re-estimate for the CFHTLenS the photometry and photo-z's, with the THELI pipeline including our introduced modifications.

By comparing with the NGVSLenS photometric objects, our combined spectroscopic sample spans with high coverage the color-color space for $i < 23$ mag objects, and satisfactorily covers the $23 < i < 24$ mag objects (the regions within the 68% contours are well populated by our spectroscopic sample).

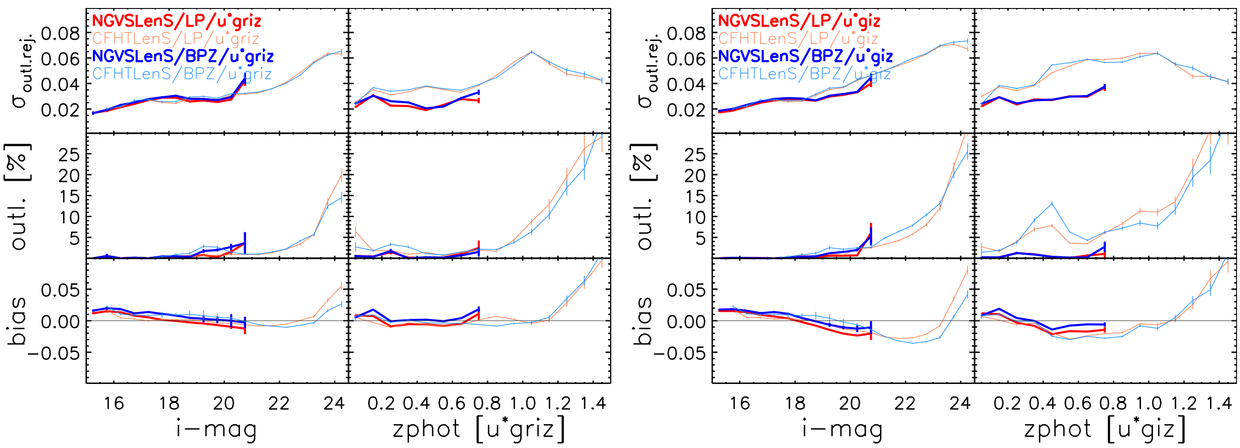

Fig. 1. Left: Statistics for photo-z's estimated with u^*griz bands as a function of magnitude (*left panel*) and redshift (*right panel*). Photo-z's estimated with *Le Phare* are in red and those estimated with BPZ are in blue. Dark thick lines represent the NGVSLenS spectroscopic sample (low redshift); light thin lines represent the CFHTLenS spectroscopic sample (high redshift). We report quantities only for the bins where we have more than 50 galaxies. Error bars are calculated assuming a Poissonian distribution. **Right**: same, but for photo-z's estimated with u^*giz bands.

In Figure 1, we quantify, as a function of magnitude and redshift, the accuracy of our photo-z's when they are estimated with the u^*griz-bands (left figure) or with the u^*giz-bands (right figure). For each object in our spectroscopic sample, we calculate $\Delta z = \frac{z_{\rm phot}-z_{\rm spec}}{1+z_{\rm spec}}$ and classify it as an outlier if $|\Delta z| > 0.15$. For each considered sample, we report *bias*: the median value of Δz; *outl.*: the percentage of outliers; and $\sigma_{\rm outl.rej.}$: the standard deviation of Δz when outliers have been excluded.

When the photo-z's are estimated with the u^*griz-bands (*left* figure), we observe that the two codes and the two datasets (NGVSLenS and CFHTLenS) provide consistent behavior over our tested ranges in magnitude or photo-z. The only difference between the two datasets is in the $0.3 < z_{\rm phot} < 0.6$ range for the $\sigma_{\rm outl.rej.}$: the smaller $\sigma_{\rm outl.rej.}$ for the NGVSLenS sample is a direct consequence being of our NGVSLenS spectroscopic sample in this redshift range is highly biased towards LRGs. Overall, the quality of our photo-z's decreases with increasing magnitude or redshift: the *bias* becomes significant (> 0.02) for faint ($i > 23$ mag) or high-z ($z > 1.2$) objects, and the $\sigma_{\rm outl.rej.}$ goes from $\sim$0.02 for bright/low-z objects to $\sim$0.06 for faint/high-z objects. For $z_{\rm phot} > 1.2$, our optical data do not bracket the 4,000 Å break, and the photo-z's are less reliable.

When the photo-z's are estimated with the u^*giz-bands (*right* figure), our photo-z's are less accurate in the $0.3 < z_{\rm phot} < 0.8$ range, where the r-band filter is essential to constrain the 4,000 Å break. In this redshift interval, we have a $-0.05 < bias < -0.02$, a $\sigma_{outl.rej} \sim 0.06$ and an outlier rate that peaks at 10-15%. This effect is less pronounced for our NGVSLenS spectroscopic sample because it is highly biased towards LRGs: the prior – more peaked and at lower redshift than for average galaxies at similar redshift – helps to obtain fewer false values for the posterior.

In addition, we also make an analysis of the angular correlation function $w(\theta)$, to internally assess the quality of our photo-z's using the whole NGVSLenS sample with $i \leq 23$ mag and $0.1 \leq z_{\rm phot} \leq 1.2$.

5 Conclusion

We estimated the photo-z's for the 104 deg^2 of the NGVS. Using a robust spec-z sample (83.3×10^3 galaxies), we estimated our photo-z's properties for $i_{AB} < 24.5$ or $z_{\rm phot} < 1.4$, as a function of magnitude and redshift. The NGVSLenS catalogs will be public on June, 1st 2015 on the NGVS website*. Before that date, please contact us if you would like to use them †.

The French authors acknowledge the support of the French Agence Nationale de la Recherche (ANR) under the reference ANR10-BLANC-0506-01-Projet VIRAGE. SM acknowledges financial support from the Institut Universitaire de France (IUF). H.H. is supported by the DFG Emmy Noether grant Hi 1495/2-1. C.L. acknowledges support from the National Natural Science Foundation of China (Grant No. 11203017, 11125313 and 10973028). R.P.M. acknowledges support from FONDECYT Postdoctoral Fellowship Project No. 3130750. E.W.P. acknowledges support from the National Natural Science Foundation of China under Grant No. 11173003, and from the Strategic Priority Research Program, "The Emergence of Cosmological Structures", of the Chinese Academy of Sciences, Grant No. XDB09000105. T.H.P. acknowledges support from FONDECYT Regular Grant (No. 1121005) and BASAL Center for Astrophysics and Associated Technologies (PFB-06). H.Z. acknowledges support from the China–CONICYT Post-doctoral Fellowship, administered by the Chinese Academy of Sciences South America Center for Astronomy (CASSACA).

References

Arnouts, S., Moscardini, L., Vanzella, E., et al. 2002, MNRAS, 329, 355
Benítez, N. 2000, ApJ, 536, 571
Capak, P., Cowie, L. L., Hu, E. M., et al. 2004, AJ, 127, 180
Coleman, G. D., Wu, C.-C., & Weedman, D. W. 1980, ApJS, 43, 393
Davis, M., Faber, S. M., Newman, J. A., et al. 2003, Proc.SPIE Int.Soc.Opt.Eng., 4834, 161
Dawson, K. S., Schlegel, D. J., Ahn, C. P., et al. 2013, AJ, 145, 10
Eisenstein, D. J., Annis, J., Gunn, J. E., et al. 2001, AJ, 122, 2267
Erben, T., Hildebrandt, H., Miller, L., et al. 2013, MNRAS
Ferrarese, L., Côté, P., Cuillandre, J.-C., et al. 2012, ApJS, 200, 4
Guzzo, L., Scodeggio, M., Garilli, B., et al. 2013
Gwyn, S. D. J. 2012, AJ, 143, 38
Heymans, C., Van Waerbeke, L., Miller, L., et al. 2012, MNRAS, 427, 146
Hildebrandt, H., Erben, T., Kuijken, K., et al. 2012, MNRAS, 421, 2355
Ilbert, O., Arnouts, S., McCracken, H. J., et al. 2006, A&A, 457, 841
Kinney, A. L., Calzetti, D., Bohlin, R. C., et al. 1996, ApJ, 467, 38
Laureijs, R., Amiaux, J., Arduini, S., et al. 2011, ArXiv e-prints
Le Fèvre, O., Cassata, P., Cucciati, O., et al. 2013, A&A, 559, A14
Newman, J. A., Cooper, M. C., Davis, M., et al. 2013, ApJS, 208, 5
Raichoor, A., Mei, S., Erben, T., et al. 2014, ApJ, in press (arxiv: 1410.2276)
Strauss, M. A., Weinberg, D. H., Lupton, R. H., et al. 2002, AJ, 124, 1810
York, D. G., Adelman, J., Anderson, Jr., J. E., et al. 2000, AJ, 120, 1579

*https://www.astrosci.ca/NGVS/The_Next_Generation_Virgo_Cluster_Survey/Home.html
†simona.mei@obspm.fr

SF2A 2014
J. Ballet, F. Bournaud, F. Martins, R. Monier and C. Reylé (eds)

THERMAL AND RADIATIVE AGN FEEDBACK : WEAK IMPACT ON STAR FORMATION IN HIGH-REDSHIFT DISK GALAXY SIMULATIONS

O. Roos[1], S. Juneau[1], F. Bournaud[1] and J. M. Gabor[1]

Abstract. Active Galactic Nuclei (AGNs) release huge amounts of energy in their host galaxies, which, if the coupling is sufficient, can affect the interstellar medium (ISM). We use a high-resolution simulation (~ 6 pc) of a z ~ 2 star-forming galaxy hosting an AGN, to study this not yet well-understood coupling. In addition to the often considered small-scale thermal energy deposition by the AGN, which is implemented in the simulation, we model long-range photo-ionizing AGN radiation in post-processing, and quantify the impact of AGN feedback on the ability of the gas to form stars. Surprisingly, even though the AGN generates powerful outflows, the impact of AGN heating and photo-ionization on instantaneous star formation is weak : the star formation rate decreases by a few percent at most, even in a quasar regime ($L_{bol} = 10^{46.5}$ erg s^{-1}). Furthermore, the reservoirs of atomic gas that are expected to form stars on a 100 - 200 Myrs time scale are also marginally affected. Therefore, while the AGN-driven outflows can remove substantial amounts of gas in the long term, the impact of AGN feedback on the star formation efficiency in the ISM of high-redshift galaxies is marginal, even when long-range radiative effects are taken into account.

Keywords: Active Galactic Nuclei, AGN feedback, high-redshift, star formation, Giant Molecular Clouds, numerical methods, radiative transfer

1 Introduction

Both observations and simulations give contradicting clues about the role of Active Galactic Nuclei (AGNs) in galaxy evolution, and especially about their impact on star formation (SF). As resolution improved, simulations started to show that AGNs can both quench galaxies by expelling all their gas through outflows and preventing it from falling back (e.g. Di Matteo et al. 2005), *and* trigger SF through jet-induced shock waves (Gaibler et al. 2012; Dugan et al. 2014), and jet- or wind-induced ram pressure (Silk 2013). Observationnally, evidence favoring both mechanisms can be found (e.g. Feain et al. (2007); Elbaz et al. (2009) for jet-induced SF ; Schawinski et al. (2007) for negative AGN feedback). Lately, studies also began to show that AGN outflows could have no impact on the global star formation rate (SFR) of their host (Gabor & Bournaud 2014), and that, averaged over an extended period of time, all star-forming galaxies (SFGs) host transient active episodes (Hickox et al. 2014), suggesting that the impact of AGN on SF could strongly depend on the time scale considered.

AGN feedback can be seen as twofold in SFGs* : a thermal part, heating and pushing the gas away from the galactic center, creating outflows ; and a radiative part, ionizing gas and creating radiative pressure in the ISM. Until now, it is computationally difficult to run a simulation with both high resolution and a complete treatment of the radiative transfer (RT). However, many authors have shown that accounting for AGN photo-ionization could significantly change the properties of the ISM (Maloney 1999; Proga et al. 2014) and therefore the SFR of the galaxy. Different approaches can be used to bypass this problem: several teams implemented simplified RT or ionization computation, directly in their simulations, with a lower resolution ISM (e.g. Rosdahl et al. 2013; Vogelsberger et al. 2014). We treat RT in post-processing, in order to keep a high resolution allowing us to probe the *instantaneous* effects of AGN radiation on a multi-phase ISM, with well-resolved giant molecular clouds (GMCs) and report the results presented in Roos et al. (2014).

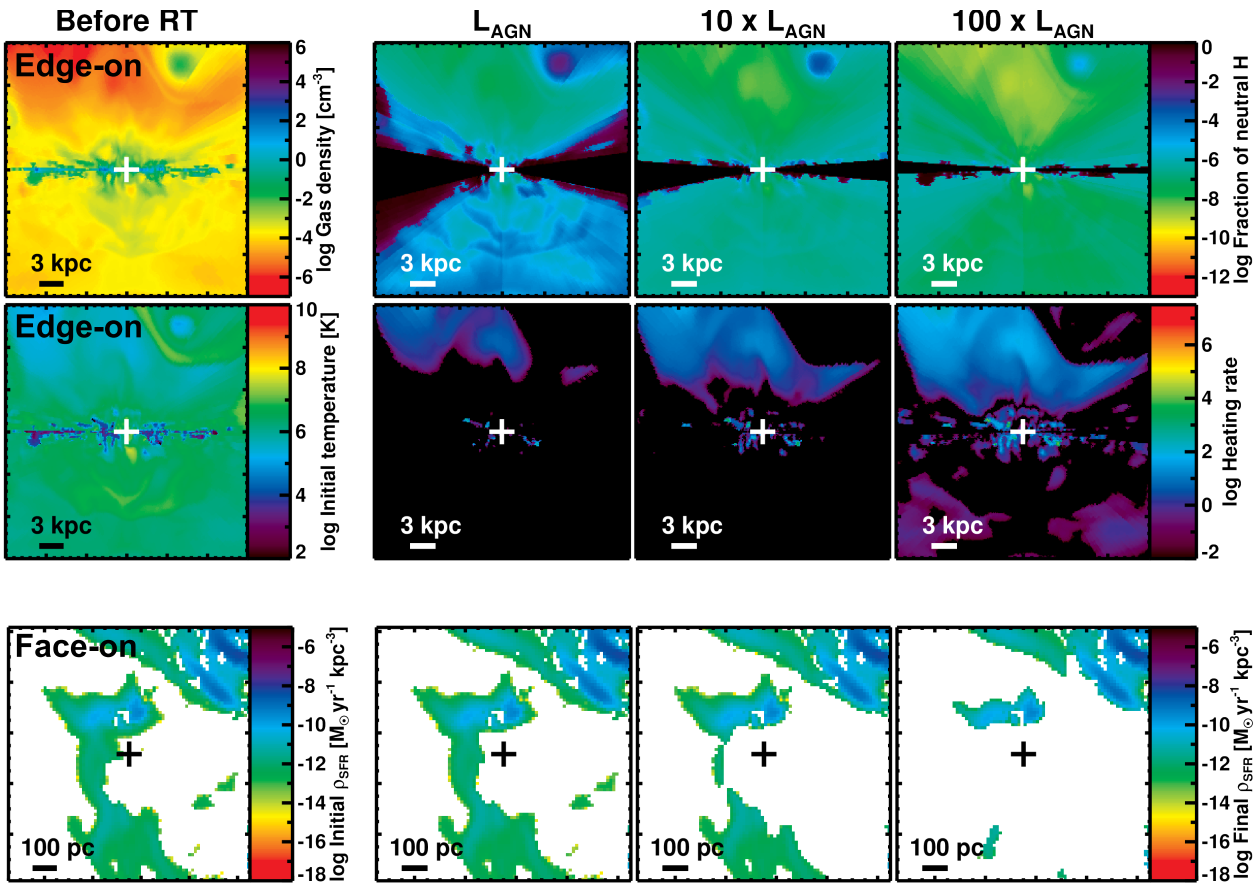

Fig. 1. Maps of a thin slice of the RT-processed galaxy for one representative snapshot. The two upper rows show the galactic disk edge-on at large scale. The bottom row displays a zoom on the AGN ('+' symbol), with a face-on view of the galactic disk. Left column shows the gas density, temperature and density of SFR before RT. The right columns show the effect of AGN ionization for the three AGN regimes, with the ionization fraction of hydrogen (top), the heating rate (middle) and the density of SFR (bottom). Even if most of the halo is ionized/heated by the AGN in all regimes, only the diffuse star-forming regions at the center of the galaxy (< 1 kpc) are prevented from forming stars due to AGN photo-ionization, and the bulk of the star-forming gas remains unaffected.

2 Distribution of ionized gas and instantaneous SFR reduction

We use 6 snapshots of a high-resolution (~ 6 pc) simulation representing an isolated clumpy SFG at redshift 2 (Gabor & Bournaud 2013), including standard thermal AGN feedback (Booth & Schaye 2009). We post-process them with the RT code Cloudy (last described by Ferland et al. 2013), as introduced by Roos et al. (2014). This allows us to compute the combined effect of AGN photo-ionization and thermal feedback on the ionization state and temperature of the gas, and therefore on the SFR of the galaxy. However, the RT study is instantaneous and we cannot directly probe coupling to long-term gas dynamics or AGN variability. In the RT-process, the AGN is considered as the only ionizing source, and gas is considered initially neutral (see Roos et al. 2014, arXiv:1405.7971 for further details). Three AGN luminosity regimes were studied:

- a typical AGN, with $L_{bol} = 10^{44.5}$ erg s^{-1}, present in ~ 30 % of typical SFGs with masses between 10^{10} and 10^{11} M$_\odot$ (Mullaney et al. 2012; Juneau et al. 2013),
- a strong AGN, with $L_{bol} = 10^{45.5}$ erg s^{-1}, present in ~ 3 % of typical SFGs in the same mass range,

[1] CEA-Saclay, 91190 Gif-sur-Yvette, France

*We do not consider radio mode feedback (jets), which mainly affects early-type galaxies by maintaining their halo hot.

- a typical QSO, with $L_{bol} = 10^{46.5}$ erg s^{-1}, which is rare in typical SFGs in the same mass range.

Figure 1 displays maps of a thin slice of the simulated galaxy centered on the AGN, before and after the RT process. The effect of AGN photo-ionization and heating is clearly visible at large scale in the halo (top and middle rows), and the amount of heated/ionized gas increases with AGN luminosity. The propagation of AGN radiation through the ISM highly depends on the distribution of gas into clumps. Indeed, the presence of holes between the dense star-forming clumps of the ISM allows QSO radiation to reach a radius of up to ~ 8 kpc in the galactic disk, while dense clumps are able to screen it at very small scale length. However, the impact of AGN feedback on the SFR of the galaxy remains small at all AGN luminosities, since only diffuse star-forming regions in the center of the galaxy (up to 1 kpc radius in the QSO regime) are prevented from forming stars.

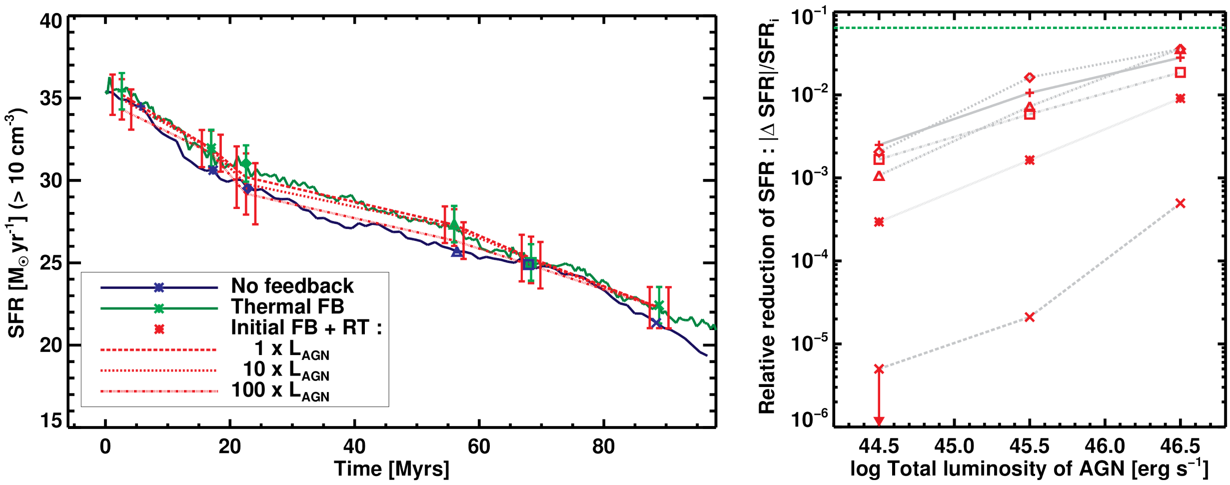

Fig. 2. Left: SFR of the galaxy as a function of time. *Green:* SFR with thermal AGN feedback, before RT. *Red:* SFR with thermal AGN feedback, after RT, with AGN luminosity as labelled ($L_{AGN} = 10^{44.5}$ erg s^{-1}). *Blue:* SFR without AGN feedback. The difference between the green and the blue curves shows the SFR fluctuations between two runs of a simulation*. Each symbol corresponds to one snapshot. For clarity, the error bars of the typical AGN (QSO) were shifted 1.5 Myrs to the left (right). Green error bars show the expected variability of the SFR. Red error bars account for the latter, plus resampling errors induced by the RT-process (see Roos et al. (2014) for further details). **Right:** Relative reduction of SFR as a function of AGN luminosity. The green line shows the expected SFR variability between two runs of the same simulation. Clearly, the impact of AGN feedback (thermal+radiative) is not significant.

Figure 2 (left) shows the temporal evolution of the SFR of the galaxy and confirms the idea that the bulk of the star-forming gas is left unaffected, since the SFR of the simulation with AGN feedback is only slightly reduced after the RT-process, for all snapshots studied, whatever the luminosity. Furthermore, this decrease is smaller than the typical variability of the SFR expected from such a simulation, as shown with the SFR of the run without AGN feedback.[†] Figure 2 (right), showing the relative reduction of SFR $|\Delta SFR_{pre-post}| / SFR_{pre-RT}$ as a function of AGN luminosity, further illustrates this behaviour. Indeed, it is clear that, even though there is an increasing trend with AGN luminosity, the reduction of the SFR due to both AGN photo-ionization and AGN heating is smaller than the expected variability of the SFR, and is therefore not significant.

3 Impact of AGN feedback on 100 - 200 Myrs time scale star formation

Despite the instantaneous character of our study, we can give clues about the SFR evolution on a time scale of a few 100 Myrs, by focusing on the impact of AGN radiation on the future sites of SF: reservoirs of atomic gas in the ISM, and in the envelopes of GMCs ($n = 0.3 - 10$ cm^{-3}; Dobbs & Bonnell (2008)). Such regions are likely to collapse on a few 100 Myr-scale and create new stars, only if there is no source of external heating,

[†]Here, the SFR of the run with AGN feedback being higher than that without AGN feedback is unlikely due to SF-triggering and is likely caused by a random realisation of the cloud distribution. Such variations can be of a few percent of the total SFR.

such as an AGN. The instantaneous impact of AGN radiation on atomic gas reservoirs is displayed in Table 1. With a typical 1/3 AGN duty cycle, according to which the AGN is "on" with a typical AGN or strong AGN luminosity 1/3 of the time – rare QSO episodes may also occur, it is very unlikely that the AGN will be able to quench SF on a time-scale of a few 100 Myrs. Nonetheless, if a long-lasting QSO episode occured ($\sim$ 100 Myrs, because of, e.g., a merger), the effects on future 100-Myr scale SF could be of greater importance.

Table 1. Effect of AGN on future (100 - 200 Myrs) star formation. Rates are given for atomic gas ($0.3 - 10$ cm^{-3}).

Regime	Heated mass rate	Ionized mass rate
Typical AGN	$0 - 4$ %	$0 - 2$ %
Strong AGN	$0.2 - 9$ %	$0.01 - 3$ %
Typical QSO	$2 - 30$ %	$0.1 - 8$ %

The impact on longer-term SF (up to 1 Gyr) depends on the ability of the AGN to keep the halo hot over an extended period of time, which can prevent gas supplies. As the halo of our simulated disk is not designed to be realistic, and the galaxy is not in its cosmological context, we cannot draw any conclusion about this topic.

4 Conclusions

We performed a complete treatment of the RT on 6 snapshots of a simulated SFG at high-redshift in post-processing. The high resolution ($\sim$ 6 pc) of the simulation allows us to probe the different phases of the ISM, from the diffuse halo, to the reservoirs of atomic gas and the GMCs. Our main findings are as follows:

- The clumpy distribution of gas in the ISM plays a major role in the propagation of AGN radiation: while dense star-forming clumps can block AGN radiation at a very small scale length, diffuse interclump regions allow it to go further in the disk (up to 8 kpc in the QSO regime).
- Most of the gas affected by the AGN (in the form of winds, heating, or photo-ionization) is diffuse, and located in the halo or the interclump medium. GMCs are marginally heated, and thus the SFR reduction induced by both AGN heating and photo-ionization is of a few percent at most in the QSO regime.
- Moreover, even though the AGN generates powerful winds, no SF quenching is expected on a time scale of a few 100 Myrs under the assumption of a typical AGN duty cycle, since the AGN has a weak impact on the sites of future star formation (atomic gas).

References

Booth, C. M. & Schaye, J. 2009, Mon. Not. R. Astron. Soc., 398, 53
Di Matteo, T., Springel, V., & Hernquist, L. 2005, Nature, 1
Dobbs, C. L. & Bonnell, I. a. 2008, Mon. Not. R. Astron. Soc., 385, 1893
Dugan, Z., Bryan, S., Gaibler, V., Silk, J., & Haas, M. 2014, Submitted to ApJ
Elbaz, D., Jahnke, K., Pantin, E., Le Borgne, D., & Letawe, G. 2009, Astron. Astrophys., 1374, 1359
Feain, I. J., Papadopoulos, P. P., Ekers, R. D., & Middelberg, E. 2007, Astrophys. J., 872
Ferland, G. J., Porter, R. L., van Hoof, P. A. M., et al. 2013, Rev. Mex. Astron. y Astrofísica, 49, 137
Gabor, J. M. & Bournaud, F. 2013, Mon. Not. R. Astron. Soc., 16, 1
Gabor, J. M. & Bournaud, F. 2014, Mon. Not. R. Astron. Soc., 13, 1
Gaibler, V., Khochfar, S., Krause, M., & Silk, J. 2012, Mon. Not. R. Astron. Soc., 425, 438
Hickox, R. C., Mullaney, J. R., Alexander, D. M., et al. 2014, Astrophys. J., 782, 11
Juneau, S., Dickinson, M., Bournaud, F., et al. 2013, Astrophys. J., 764, 176
Maloney, P. R. 1999, Astrophys. Space Sci., 266, 207
Mullaney, J. R., Daddi, E., Béthermin, M., et al. 2012, Astrophys. J., 753, L30
Proga, D., Jiang, Y.-F., Davis, S. W., Stone, J. M., & Smith, D. 2014, Astrophys. J., 780, 51
Roos, O., Juneau, S., Bournaud, F., & Gabor, J. M. 2014, Submitted to ApJ, arXiv:1405.7971
Rosdahl, J., Blaizot, J., Aubert, D., Stranex, T., & Teyssier, R. 2013, Mon. Not. R. Astron. Soc., 436, 2188
Schawinski, K., Thomas, D., Sarzi, M., et al. 2007, Mon. Not. R. Astron. Soc., 18, 1
Silk, J. 2013, Astrophys. J., 772, 112
Vogelsberger, M., Genel, S., Springel, V., et al. 2014, Mon. Not. R. Astron. Soc., 444, 1518

SF2A 2014
J. Ballet, F. Bournaud, F. Martins, R. Monier and C. Reylé (eds)

GALAXY FORMATION HISTORY THROUGH HOD MODEL FROM EUCLID MOCK CATALOGS

Z. Sakr[1,2,3] and C. Benoist[3]

Abstract. Halo Occupation Distribution (HOD) is a model giving the average number of galaxies in a dark matter halo, function of its mass and other intrinsic properties, like distance from halo center, luminosity and redshift of its constituting galaxies. It is believed that these parameters could also be related to the galaxy history of formation. We want to investigate more this relation in order to test and better refine this model. To do that, we extract HOD indicators from EUCLID mock catalogs for different luminosity cuts and for redshifts ranges going from $0.1 < z < 3.0$. We study and interpret the trends of indicators function of these variations and tried to retrace galaxy formation history following the idea that galaxy evolution is the combination rather than the conflict of the two main proposed ideas nowadays: the older hierarchical mass merger driven paradigm and the recent downsizing star formation driven approach.

Keywords: Halo Occupation Distribution, EUCLID, Mock catalogs, Galaxy Formation

1 Introduction

Long time passed before advances in the theory of dark matter halo formation (DMH) by hierarchical mass merger driven process and its relation to galaxy formation (from the fact that inflow of gas into DMH potential well to a high cold gas density (White & Rees 1978) could trigger star formation) could be tested through N body simulations combined with semi analytic approach (Lacey & Cole 1993). Many advances in trying to model galaxy halo's number or the Halo Occupation Distribution (HOD) will follow after but it was mainly Kauffmann et al. (1999) and Benson et al. (2000) who stated first that the average number of galaxies in a given DMH, which is directly related to the HOD, depends as a power law on its mass. This law has been later refined to explain why it breaks on small and very large scale by taking into account the role of other parameters, like distance of galaxies from halo center, thus dividing them into big massive luminous centrals and smaller satellites (Berlind & Weinberg 2002; Kravtsov et al. 2004), or luminosity of halo's constituting galaxies (Zheng et al. 2005). Attempts also where made to include evolution of halo's number of progenitors through redshift (Zheng et al. 2007).

Several groups (Zehavi et al. 2005; Zheng et al. 2007; Abbas et al. 2010; Coupon et al. 2012) have tried to investigate galaxy formation by studying HOD obtained from a fit to a correlation function extracted from different surveys. We aim at doing the same with the difference that we compute HOD directly from mock catalogs constructed by Merson et al. (2013) from simulations of future observations by EUCLID space mission. This will be a test of the upcoming EUCLID mission and an attempt to extent works cited before as none of them have used a sample of galaxies as large and deep at the same time as EUCLID, with redshift reaching $z \sim 3.0$ and potential galaxy number observed, in the order of 50×10^6 (Euclid Definition Study Report 2011).

Many concordant evidences and observations (see Silk & Mamon 2012, and references therein), have helped establish a hierarchical theory of galaxy formation as a continuation to the DMH bottom up scenario of large scale structures evolution. This theory (from White & Rees (1978); White & Frenk (1991)to Hopkins et al. (2006, 2008)) has been challenged by other observational data of galaxy mass downsizing from $z \sim 1-2$ zone down to low redshifts (Cowie et al. 1996). This led Heavens et al. (2004) and De Lucia et al. (2006) to suggest

[1] NDU, Louaizeh Zouk Mosbeh, Lebanon
[2] USJ, Mar Roukoz Dekwaneh, Lebanon
[3] Laboratoire Lagrange, OCA, CNRS, UNS, boulevard de l'Observatoire 06304 Nice Cedex, France

that it is due to the fact that most early type massive galaxies stop forming stars first due to different quenching processes, while late type lower mass ones remains active and become quiescent later (Kauffmann et al. 2003).

In this study, we extract HOD's mean galaxy number for different luminosity cuts and redshifts ranges. We then calculate for each extraction its specific indicators like M_{min} (resp. M_{amp}) mass of halo hosting one central (resp. satellite) galaxies, the index α of the power law, the average halo mass $\bar{M}_{halo}$ weighted by galaxy number and galaxy satellites fraction f_{sat}. After that, we try to interpret the change in their trend, function of redshift and luminosity, in the light of the previously advanced ideas of galaxy formation.

2 Data selection

EUCLID is a space telescope developed by ESA to be launched in 2019. It will perform visible and near-infrared imaging up to 24.5 mag apparent magnitude and NIR spectroscopy in AB system for wavelength range going from 460 nm to 2000 nm. This will allow him to scan $\sim 50 \times 10^6$ galaxies in a large region of 15,000 deg^2 with depth reaching $z \sim 3$ (see Euclid Definition Study Report 2011). To test the benefit of such an unprecedented deep and large survey on galaxy history of formation through cosmic time, we used mock catalogs constructed by Merson et al. (2013). These mock catalogs were constructed by grafting a semi-analytic model of galaxy formation, GALFORM from Lagos et al. (2011) onto the N-body dark matter halo merger trees of the Millennium Simulation by Springel et al. (2005). From the different outputs of these constructions we use the EUCLID 100 Hband DEEP lightcone implemented using the Lagos12 GALFORM model. The lightcone covers the redshift range $z \sim 0.0$ to $z \sim 3.0$ and has a sky coverage of 100.21 deg^2, with an apparent magnitude cut $m < 27$ mag and a cosmology of $\Omega_m = 0.25$; $\Omega_\Lambda = 0.75$; $h = 0.73$; $n_s = 1$; $\sigma_8 = 0.9$. We want to extract the HOD from our mock catalog to study how this distribution vary according to halo mass of course, but also redshift range and luminosity cut. We take redshift bin to be $\Delta z \sim 0.1$. This range will allow us first to spot changes in trends related to galaxy formation and evolution from local universe to redshift $z \sim 1$ as well as when passing to $z \sim 1-2$ zone and higher. We move next to the luminosity criteria and begin with an absolute H band magnitude range between $-20 > M_H > -21$ for all redshift limited samples. We stay on a stable number of galaxies within this magnitude variation which is also above the threshold brightness that insure completeness for all the samples in our redshift ranges. Taking these considerations into account, we varied this luminosity range by $\Delta M \sim 0.1$ to get more samples and compare their plots of variation. We come at the end to the choice of the mass bin. The whole mass range up to $\sim 10^{15} M_\odot$ will be divided to 500 bins. This is small enough to detect the HOD indicators mentioned before, which are in the order of $M_{min} \sim 10^{11} M_\odot$ and $M_{amp} \sim 10^{13} M_\odot$ and large enough to insure the robustness of the bin as a sample of number of halos. We also limit ourselves to $10^{14} M_\odot$ as upper limit as the number of halos above that value drops below 10 (Left Panel of Fig. 1) and the systematic statistical error becomes higher than 10%

3 Method and results

To model HOD, we use Berlind & Weinberg (2002) and Kravtsov et al. (2004) parametrization $\langle N(M) \rangle = 1$ for $M > M_{min}$, the minimum halo mass for hosting one central galaxy and $\langle N(M) \rangle = 1 + (M/M_{amp})^\alpha$ for $M > M_{crit}$, M_{amp} being the mass above which the halo could host a satellite. After calculating mean galaxy number per halo mass for samples chosen according to the previous section (see Left of Fig. 1 as example for one redshift range), we calculate Mmin, Mamp and α, then extract three more indicators : weighted average halo mass $\bar{M}_{halo}$, galaxy average number per halo $\bar{n}$ and galaxy satellite fraction f_{sat} and represent their variation in function of z (Left Panel of Fig. 2) or in function of luminosity (Right Panel of Fig 2).

To summarize, we say that M_{min} and M_{amp} decrease from high z to touch a bottom at $z \sim 1.5 - 2$ before rising a little again after, with a linear correlation between M_{min} and $M_{amp} \sim 15 - 18$ in accordance with Zheng et al. (2005) simulations studies and Coupon et al. (2012) observations studies for lower values of redshift. These trends are consistent with those found in both the local (Zehavi et al. 2005, 2011) and distant Universe studies (Zheng et al. 2007; Abbas et al. 2010). Also they concord in the general trends with results on observations between $z \sim 0.2$ and $z \sim 1.2$ done by Coupon et al. (2012).

As a first general interpretation (more thorough analyzes in upcoming Sakr & Benoist paper) of these trends we say that combining the hierarchical and the downsizing theory could account for most of their behavior. We divide the redshift range in three parts, $2.0 < z < 3.0$, in which galaxy increase formation rate and increase mass

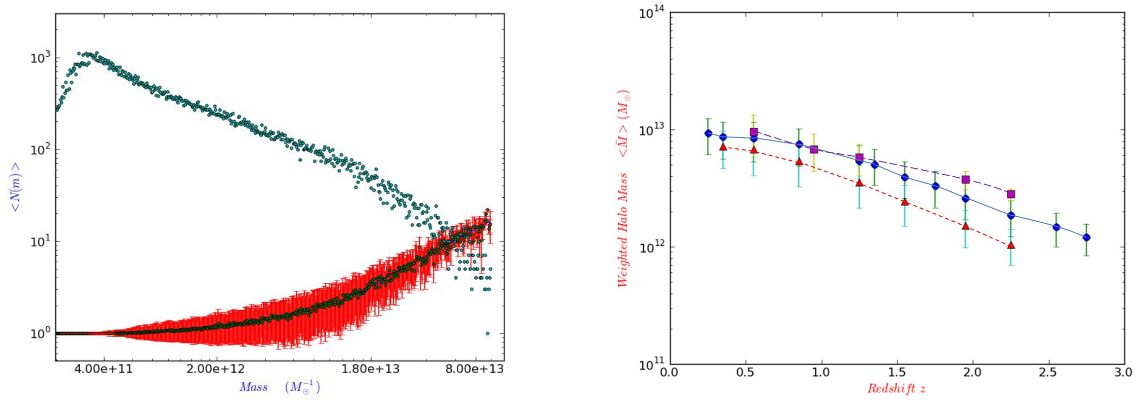

Fig. 1. Left: mean galaxy number per halo mass plot (Red Dots) with halo count (Blue Dots) for $0.8 < z < 0.9$ having $-20 > M_H > -21$. **Right:** weighted halo mass function of redhsift with $-18.5 > M_H > -19$ (Dotted Line) $-20 > M_H > -21$ (Solid Line) $-21.5 > M_H > -22$ (Dashed Line)

is fueled by high merger rate of early structure formed in high density peaks along with active star formation of the still young galaxies, $2.0 < z < 1.0$, where this process culminate and stabilize with downsizing effect beginning to show and finally $1.0 < z < 0.0$ where big merger rate and new born galaxies drops and early galaxies type quench star formation while late type small are still active resulting in a downturn of the previous trend (not the absence of this behavior for high luminosity cuts leaving only massive early type galaxies that follow the hierarchical theory). This conciliates discrepancies mentioned previously and concords with the same trend observed for the three zone for star formation rate (Cucciati et al. 2012) or galaxy pair merger rate established by Conselice et al. (2008) with a pivot at $z \sim 1$. It accounts also for the decrease of the rate of big mergers noticed by de Ravel et al. (2009) along with an increase of minor mergers from López-Sanjuan et al. (2010). It is also consistent with the halo mass distribution function of redshift (Kravtsov et al. 2004) suggesting an increase with low z in the number of small size DMH 'incubation' containers resulting in low mass galaxies forming in a rate higher than for the massive ones.

4 Conclusions

The results obtained, showed that we can extend HOD model from only a manifestation of the hierarchical theory of galaxy formation to include other suggested ideas like, as we tried to do, the newly supported by many observational evidences, downsizing approach. However this couldn't be done without calculating the variation of HOD's related indicators over a large range of redshift and luminosity. This show the need of conducting large deep spectroscopic surveys like the future Euclid space mission where no restrictions coming from the need to maintain a specific criteria can filter the large population observed to insignificant statistical samples. Also these results could serve as a test for an eventual scientifically meaningful model that will parametrize HOD according to redshift, as such an operation could give more precise physical meaning to the trends we obtained and help clarify many issues related to galaxy formation.

References

Abbas, U., de la Torre, S., Le Fèvre, O., et al. 2010, MNRAS, 406, 1306

Benson, A. J., Cole, S., Frenk, C. S., Baugh, C. M., & Lacey, C. G. 2000, MNRAS, 311, 793

Berlind, A. A. & Weinberg, D. H. 2002, ApJ, 575, 587

Conselice, C. J., Rajgor, S., & Myers, R. 2008, MNRAS, 386, 909

Coupon, J., Kilbinger, M., McCracken, H. J., et al. 2012, A&A, 542, A5

Cowie, L. L., Songaila, A., Hu, E. M., & Cohen, J. G. 1996, AJ, 112, 839

Cucciati, O., Tresse, L., Ilbert, O., et al. 2012, A&A, 539, A31

De Lucia, G., Springel, V., White, S. D. M., Croton, D., & Kauffmann, G. 2006, MNRAS, 366, 499

de Ravel, L., Le Fèvre, O., Tresse, L., et al. 2009, A&A, 498, 379

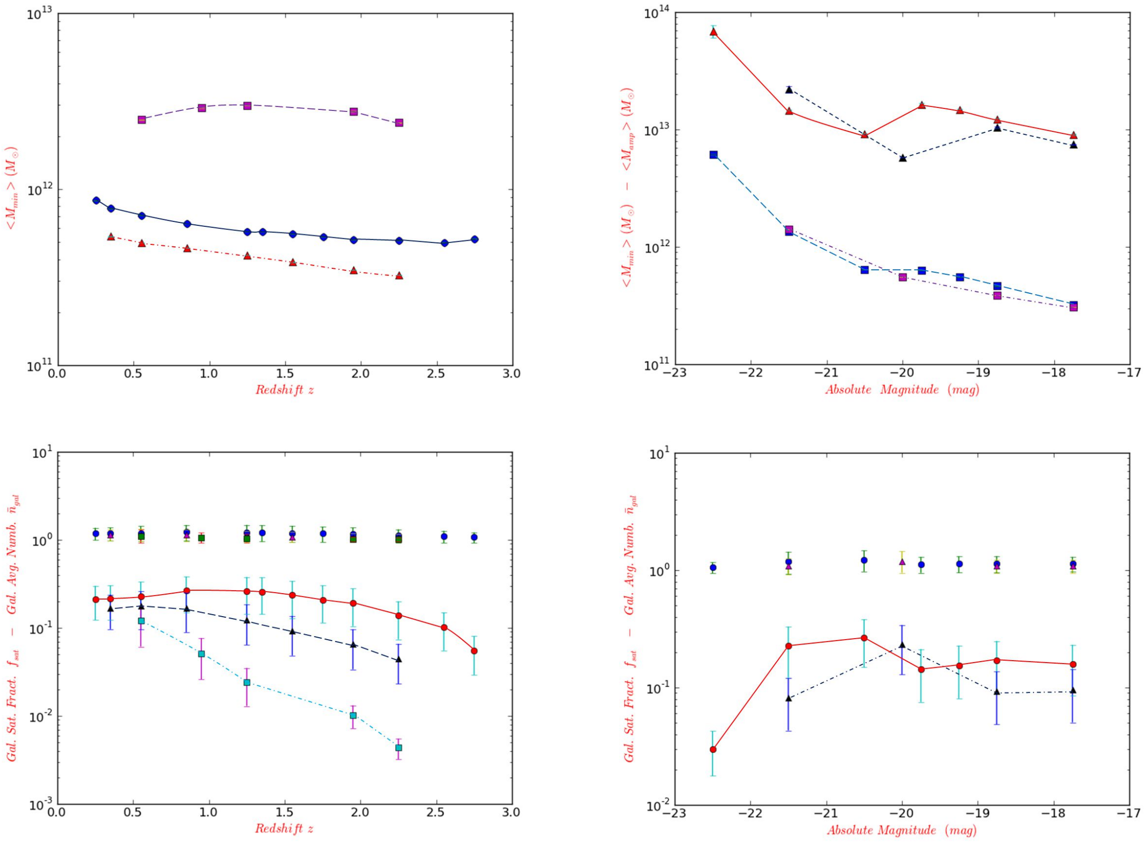

Fig. 2. Top Left: M_{min} function of z for different luminosity cuts. $-18.5 > M_H > -19$ (Dotted Line) $-20 > M_H > -21$ (Solid Line) $-21.5 > M_H > -22$ (Dashed Line). **Top Right:** M_{min} and M_{amp} function of luminosity for different z. $0.8 > z > 0.9$ (Solid Line for M_{amp} dashed for M_{min}) $1.5 < z < 1.6$ (Dotted Line for M_{amp} dash-dotted for M_{min}).**Down Left:** galaxy fraction and satellite fraction function of z for different luminosity cuts: $-18.5 > M_H > -19$ (Dotted Line) $-20 > M_H > -21$ (Solid Line) $-21.5 > M_H > -22$ (Dashed Line). **Down Right:**galaxy fraction and satellite fraction function of luminosity for different z: $0.8 < z < 0.9$ (Solid Line) $1.5 < z < 1.6$ (Dashed Line)

Heavens, A., Panter, B., Jimenez, R., & Dunlop, J. 2004, Nature, 428, 625
Hopkins, P. F., Hernquist, L., Cox, T. J., & Kereš, D. 2008, ApJS, 175, 356
Hopkins, P. F., Somerville, R. S., Hernquist, L., et al. 2006, ApJ, 652, 864
Kauffmann, G., Colberg, J. M., Diaferio, A., & White, S. D. M. 1999, MNRAS, 303, 188
Kauffmann, G., Heckman, T. M., White, S. D. M., et al. 2003, MNRAS, 341, 33
Kravtsov, A. V., Berlind, A. A., Wechsler, R. H., et al. 2004, ApJ, 609, 35
Lacey, C. & Cole, S. 1993, MNRAS, 262, 627
Lagos, C. D. P., Baugh, C. M., Lacey, C. G., et al. 2011, MNRAS, 418, 1649
Laureijs, R., Amiaux, J., Arduini, S., et al. 2011, ArXiv e-prints
López-Sanjuan, C., Balcells, M., Pérez-González, P. G., et al. 2010, ApJ, 710, 1170
Merson, A. I., Baugh, C. M., Helly, J. C., et al. 2013, MNRAS, 429, 556
Silk, J. & Mamon, G. A. 2012, Research in Astronomy and Astrophysics, 12, 917
Springel, V., White, S. D. M., Jenkins, A., et al. 2005, Nature, 435, 629
White, S. D. M. & Frenk, C. S. 1991, ApJ, 379, 52
White, S. D. M. & Rees, M. J. 1978, MNRAS, 183, 341
Zehavi, I., Zheng, Z., Weinberg, D. H., et al. 2011, ApJ, 736, 59
Zehavi, I., Zheng, Z., Weinberg, D. H., et al. 2005, ApJ, 630, 1
Zheng, Z., Berlind, A. A., Weinberg, D. H., et al. 2005, ApJ, 633, 791
Zheng, Z., Coil, A. L., & Zehavi, I. 2007, ApJ, 667, 760

SF2A 2014
J. Ballet, F. Bournaud, F. Martins, R. Monier and C. Reylé (eds)

3C 285: A NEARBY GALAXY WITH JET-INDUCED STAR FORMATION

Q. Salomé[1], P. Salomé[1] and F. Combes[1]

Abstract. We present IRAM-30m CO observations of 3C 285, which is an example of jet-induced star formation. We observed the central galaxy and along the radio jet. The central galaxy presents a double-horn profile, which we interpret with a simple analytical model as the result of a narrow ring of disk.

In the star-forming spot (so-called 09.6), at a distance of ∼ 70kpc from the galaxy, we determined an CO interesting upper limit. Plotted in a diagram of Σ_{SFR} vs Σ_{gas}, 09.6 appears to form stars at least as efficiently as typical spiral galaxies. This result supports the AGN positive feedback scenario.

Keywords: Methods:data analysis, Galaxies:evolution, interactions, star formation, Radio lines:galaxies

1 Introduction

Jet-induced star formation has been debated for decades (eg. van Breugel et al. 2004). Evidence has been found only for 4 objects: (1) Centaurus A, where the jet is encountering gas in the shells along its way (Schiminovich et al. 1994; Charmandaris et al. 2000); (2) Minkowski Object (van Breugel et al. 1985); (3) 3C 285 (van Breugel & Dey 1993); (4) at z = 3.8, the radio source 4C 41.17 (Bicknell et al. 2000; De Breuck et al. 2005; Papadopoulos et al. 2005).

3C 285 is a double-lobed powerful FR-II radio galaxy where both lobes have a complex filamentary structure. In the eastern radio lobe, there is a radio jet with unresolved radio knots. A slightly resolved object is located near the eastern radio jet (3C 285/09.6), at a projected distance of ∼ 70kpc from the galaxy centre. 3C 285/09.6 is a small, kiloparsec-sized object where star formation seems to be triggered by the jet from the radio source 3C 285 (van Breugel & Dey 1993).

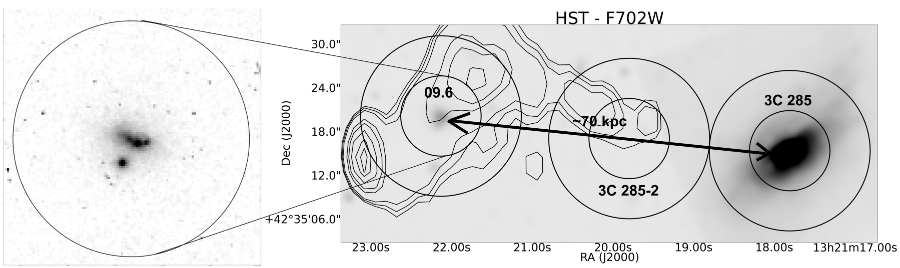

Fig. 1: Contour map of the eastern lobe of 3C 285 observed at 21 cm (van Breugel & Dey 1993) with 5″ resolution, as extracted from the VLA archive (NED, Leahy & Williams 1984), overlaid on a slightly smoothed Hα image from HST in the F702W filter (data from the HST archive, PI: Crane). The observed positions are shown by the CO(1-0) 24″ and CO(2-1) 12″ IRAM-30m beams (circles). Details of the 09.6 spot are shown in the circle on the left, and show that the spot is resolved in two or maybe three sub-structures.

To better understand the impact of the AGN interaction with the intergalactic medium on star formation, CO(1-0) and CO(2-1) have been observed along the jet axis of 3C 285 (see also Salomé et al. 2014). The observations were made with the IRAM 30m telescope on March 2014, using the EMIR receiver with the WILMA backend (bandwidth of 3.7 GHz; resolution of 2 MHz). At redshift z=0.0794, those lines are observable at frequencies of 106.780 GHz and 213.580 GHz, which leads to beams of 24″ and 12″. Three regions were observed: the central galaxy 3C285, the 09.6 spot and an intermediate position (3C 285-2) along the jet (cf. figure 1).
Our main goal was to determine whether star formation is more efficient in the shocked region along the jet. Throughout this work, we assume the cold dark matter concordance Universe, with $H_0 = 70\text{km.s}^{-1}.\text{Mpc}^{-1}$, $\Omega_m = 0.30$ and $\Omega_\Lambda = 0.70$.

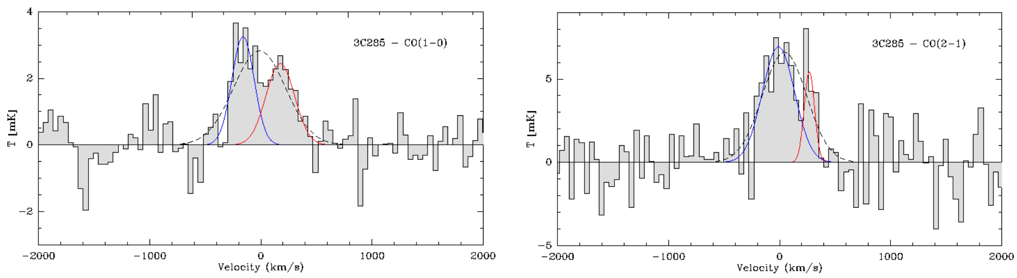

Fig. 2: *Left:* CO(1-0) spectrum for 3C 285. *Right:* CO(2-1) spectrum for 3C 285. Both spectra, are smoothed to a spectral resolution of ∼ 45km/s. The dash line fits all the emission, whereas the red and blue lines fit the double-horn profile.

2 Results

CO luminosities The central galaxy 3C 285 was detected in both CO(1-0) and CO(2-1), whereas there is no detection for the other positions. Each line was fitted by a gaussian in order to get its characteristics (table 1). The CO luminosity L'_{CO} was calculated with the formula from Solomon et al. (1997). Then, the molecular gas mass was estimated from the line luminosity L'_{CO}, using a standard Milky Way conversion factor of 4.6 $M_{\odot}$.(K.km.s^{-1}.pc^2)$^{-1}$ (Solomon et al. 1997).

Source	line	Δv (km.s^{-1})	I_{CO} (K.km.s^{-1})	L'_{CO} (10^8 K.km.s^{-1}.pc^2)	M_{H_2} (10^9 $M_{\odot}$)
3C 285	CO(1-0)	553 ± 51	1.66 ± 0.15	22 ± 2	10.3 ± 0.9
	CO(2-1)	472 ± 55	3.31 ± 0.36	-	-
09.6 spot	CO(1-0)	-	< 0.100	< 1.4	< 0.62
	CO(2-1)	-	< 0.216	-	-
3C 285-2	CO(1-0)	-	< 0.159	< 2.1	< 0.99
	CO(2-1)	-	< 0.322	-	-

Table 1: Results of the observations at IRAM 30m. For non-detections, an upper limits is computed at 3σ, with a line width of Δv = 64 km.s^{-1} for 09.6 and 3C 295-2 (van Breugel & Dey 1993). More informations are given in Salomé et al. (2014).

Line width and morphology 3C 285 presents a broad line profile covering negative and positive velocities. This could result from the rotation of the galaxy around its main axis, as suggested by the apparent double-horn profile (figure 2). The double-horn profile of CO(1-0) emission is well defined, whereas it is less obvious in CO(2-1). In addition, the spectra show no kinematic effect of a molecular outflow, at the level of the 30m sensitivity.

Star formation rate and depletion time The Hα and IR emission is often used as tracers of star formation. We derived a star formation rate from the Hα (Baum & Heckman 1989; van Breugel & Dey 1993) and IR emission (computed with Herschel-SPIRE data from the archive), following the methods of Kennicutt & Evans (2012) and Calzetti et al. (2007). The total SFR is the sum of the SFR derived from the Hα and the IR emission. Table 2 summarises the SFR of the different sources (see Salomé et al. 2014 for more details). The depletion time is the time to consume all the gas with the present star formation rate: $t_{depl} \sim M_{gas}/SFR$.

Source	$SFR_{H\alpha}$	SFR_{TIR}	$SFR_{24\,\mu m}$	SFR_{total}
3C 285	1.34	19.7	12.0	21.04
09.6 spot	0.15	< 0.79	0.61	0.76

Table 2: SFR in $M_{\odot}$.yr^{-1} for 3C 285 and the 09.6 spot. The Hα, TIR and 24 μm SFR were calculated with Kennicutt & Evans (2012) and Calzetti et al. (2007). The total SFR is a combination of those SFR.

3 Discussion

A compact molecular ring in 3C 285 In order to interpret the kinematics of our CO data, we use a simple analytical model which computes the velocity spectrum of the galaxy (Wiklind et al. 1997). This allows to determine the gas concentration in 3C 285. For 3C 285, the half-light radius is ∼ 8.3 kpc (Roche & Eales 2000), with a stellar mass of $\sim 2 \times 10^{11}$ $M_{\odot}$. The density profile derived by the model indicates that **the gas is distributed in a narrow ring** that

[1] LERMA, Observatoire de Paris, CNRS UMR 8112, 61 avenue de l'Observatoire, 75014 Paris, France

extends at distances up to ∼ 3.5 kpc with an average radius ∼ 1.5 kpc (for more details, refer to Salomé et al. 2014), but this need to be confirmed by interferometric data. The gas ring may be interpreted as the result of a past merger event; the gas being now in equilibrium in the ring. This phenomenon is also observed in other gas rich early-type galaxies, like in the most famous example Centaurus A.

A Kennicutt-Schmidt law? We have calculated the gas and SFR surface densities (Σ_{gas}, Σ_{SFR}; the values can be found in Salomé et al. 2014). For 3C 285, both quantities are smoothed over the CO(1-0) IRAM-30m beam, whereas for the 09.6 spot, the surface densities are estimated on the area of the Hα emission (in a radius of $\sim 1.65''$). Plotting this in the Σ_{SFR} vs Σ_{gas} diagram (see figure 3, Bigiel et al. 2008; Daddi et al. 2010), both positions follow a Schmidt-Kennicutt law $\Sigma_{SFR} \propto \Sigma_{H_2}^{N}$ (Kennicutt 1998).

Source	M_{gas} ($M_\odot$)	M_* ($M_\odot$)	f_{gas}	SFR ($M_\odot$.yr^{-1})	t_{dep} (Gyr)	sSFR (Gyr^{-1})
3C 285	1.03×10^{10}	4.20×10^{11}	0.025	21.04	0.49	5.0×10^{-2}
09.6 spot	$< 6.2 \times 10^{8}$	1.9×10^{9}	< 0.326	0.76	< 0.82	4.0×10^{-1}

Table 3: Molecular gas, stellar masses and gas fraction for 3C 285 and 09.6. The stellar mass of 3C 285 is given in Tadhunter et al. (2011), whereas that of 09.6 is calculated with the mass-to-light ratio (Bell & de Jong 2001). The depletion time is computed from the CO-derived gas masses and the SFR.

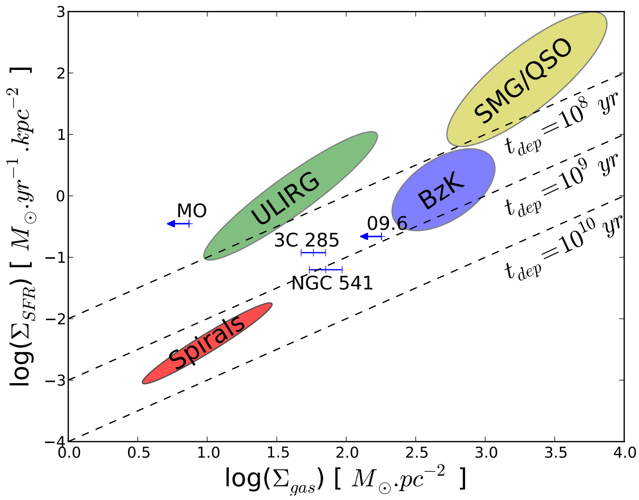

Fig. 3: Σ_{SFR} vs. Σ_{gas} diagram for the sources studied in Salomé et al. (2014). The diagonal dashed lines show lines of constant SF efficiency, indicating the level of Σ_{SFR} needed to consume 1%, 10%, and 100% of the gas reservoir in 10^8 years. Thus, the lines also correspond to constant gas depletion times of, from top to bottom, 10^8, 10^9, and 10^{10} yr The coloured regions come from Daddi et al. (2010).

As a conclusion, figure 3 shows that **09.6 form stars at least as efficiently as typical spiral galaxies**. This **support the AGN positive feedback scenario** that predicts an enhanced star formation activity along the shocked region inside the radio-jets. To accurately determine the SFE in the 09.6 spot, high-resolution interferometric data are required. In order to do so, we have proposed a follow-up with the Plateau de Bure interferometer.

References

Baum, S. A. & Heckman, T. 1989, ApJ, 336, 681
Bell, E. F. & de Jong, R. S. 2001, ApJ, 550, 212
Bicknell, G. V., Sutherland, R. S., van Breugel, W. J. M., et al. 2000, ApJ, 540, 678
Bigiel, F., Leroy, A., Walter, F., et al. 2008, AJ, 136, 2846
Calzetti, D., Kennicutt, R. C., Engelbracht, C. W., et al. 2007, ApJ, 666, 870
Charmandaris, V., Combes, F., & van der Hulst, J. M. 2000, A&A, 356, L1
Daddi, E., Elbaz, D., Walter, F., et al. 2010, ApJ, 714, L118
De Breuck, C., Downes, D., Neri, R., et al. 2005, A&A, 430, L1
Kennicutt, R. C. & Evans, N. J. 2012, ARA&A, 50, 531
Kennicutt, Jr., R. C. 1998, ApJ, 498, 541
Leahy, J. P. & Williams, A. G. 1984, MNRAS, 210, 929
Papadopoulos, P. P., Greve, T. R., Ivison, R. J., & De Breuck, C. 2005, A&A, 444, 813
Roche, N. & Eales, S. A. 2000, MNRAS, 317, 120

Salomé, Q., Salomé, P., & Combes, F. 2014, A&A, submitted
Schiminovich, D., van Gorkom, J. H., van der Hulst, J. M., & Kasow, S. 1994, ApJ, 423, L101
Solomon, P. M., Downes, D., Radford, S. J. E., & Barrett, J. W. 1997, ApJ, 478, 144
Tadhunter, C., Holt, J., Delgado, R. G., et al. 2011, MNRAS, 412, 960
van Breugel, W., Filippenko, A. V., Heckman, T., & Miley, G. 1985, ApJ, 293, 83
van Breugel, W., Fragile, C., Anninos, P., & Murray, S. 2004, IAUS, 217, 472
van Breugel, W. J. M. & Dey, A. 1993, ApJ, 414, 563
Wiklind, T., Combes, F., Henkel, C., & Wyrowski, F. 1997, A&A, 323, 727

SF2A 2014
J. Ballet, F. Bournaud, F. Martins, R. Monier and C. Reylé (eds)

LYMAN-α BLOBS: POLARIZATION ARISING FROM COLD ACCRETION

M. Trebitsch[1], A. Verhamme[1,2], J. Blaizot[1] and J. Rosdahl[1,3]

Abstract. Over the past twenty years, diffuse, extended Lyman-α nebulae have been observed around all kind of extragalactic sources. Whether they are referred to as Lyman-α "nebulae", "halos" or "blobs", their true nature remains unknown. Various mechanisms have been invoked to explain the origin of their luminosity: photoionisation of the gas by a nearby quasar, scattering of radiation produced in star-forming galaxies, or radiation cooling of the gas heated while falling into the dark matter halo along accretion streams.

Recent observations showed that those Lyα sources are polarized. We post-processed a simulation of a blob with a Monte-Carlo transfer code, and we found that the "accretion streams" scenario is compatible with polarimetric observations.

Keywords: scattering, polarization, diffuse radiation, intergalactic medium, galaxies: high-redshift, methods: numerical

1 Introduction

Lyman-α blobs (LABs) are a class extended high-z Lyα nebulae (HzLANs) seen at $z \simeq 2-6$ and usually associated with various types of objects (Lyman-break galaxies, sub-mm or infrared sources, quasars), but not always. They are very similar in size, shape and spectral properties to the Lyα nebulae that are observed around high-z radio galaxies.

The origin of the Lyα emission is still debated, with several plausible scenarios: Lyα scattering in galactic outflows, fluorescence of infalling gas illuminated by a nearby quasar, radiation cooling in galactic winds, cooling of accretion streams. Our work follows the study of Rosdahl & Blaizot (2012), who investigated this "accretion streams" scenario. They showed that gravitational heating of accretion streams in massive halos can by itself explain the Lyα emission of LABs observed at $z = 3$. Their predicted sizes and luminosities are also compatible with observations.

Hayes et al. (2011) found that the Lyα emission of a LAB at $z = 3.1$ was linearly polarized, with the polarization structured in rings around the Lyα peak. Using theoretical models of Dijkstra & Loeb (2008), this has been interpreted as an evidence supporting the idea that the Lyα emission is centrally produced. Using a Monte Carlo method, we predict the polarization signal that could be observed in the "accretion streams" scenario.

2 Methodology

2.1 LAB Simulation

We use the H2 blob simulations from Rosdahl & Blaizot (2012). They used the AMR code `RamsesRT` (Teyssier 2002; Rosdahl et al. 2013), coupling radiative transfer of ultraviolet photons to the hydrodynamics. The simulation makes use of a zoom technique allowing a spatial resolution of 434 pc. The simulation describes a large blob with $M_{\rm halo} \simeq 10^{12}\ M_\odot$ at $z = 3$. The radiation-hydrodynamics (RHD) solver allows to resolve the competition between heating of the infalling gas and radiative Lyα cooling, and thus to compute accurately the gas temperature, ionisation state and Lyα emissivity.

[1] Université de Lyon, Lyon, F-69003, France;
Université Lyon 1, Observatoire de Lyon, 9 avenue Charles André, Saint-Genis Laval, F-69230, France;
CNRS, UMR 5574, Centre de Recherche Astrophysique de Lyon;
École Normale Supérieure de Lyon, Lyon, F-69007, France
[2] Observatoire de Genève, Université de Genève, 51 Ch. des Maillettes, CH-1290 Sauverny, Switzerland
[3] Leiden Observatory, Leiden University, P.O. Box 9513, 2300 RA Leiden, the Netherlands

2.2 Lyman-α radiative transfer

We followed the transfer of the photons through the blob with a modified version of the Monte Carlo radiative transfer code `MCLya`, described first in Verhamme et al. (2006). Our new version of the code includes nebular emission from the ionised gas and polarized transfer (Trebitsch et al. 2014, in prep.). We keep track of the polarization by assuming each Monte Carlo photon is 100% linearly polarized following the prescription of Rybicki & Loeb (1999).

We take into account both the nebular emission of the ionised gas inside the halo and the emission from galactic sources (i.e. HII regions around young, massive stars). To model the Lyα transfer in the (unresolved) interstellar medium, we assume a Lyα escape fraction of 5% for the galactic sources (Garel et al. 2012). The emission from the gas accounts for $L_{\rm gas} = 2.04 \times 10^{43}$ erg.s^{-1}, and the galactic emission accounts for 9×10^{42} erg.s^{-1}.

3 Results

With the output of `MCLya`, we can construct mock maps of the blob for surface brightness and polarization degree. We produce such maps for multiple directions, and for each map, we compute the surface brightness (SB) and polarization radial profiles. We then average the profiles over 100 lines of sight.

3.1 Surface Brightness

On Fig. 1, we compare the median SB profile (solid, red line) to various observations of LABs and Lyman-α emitters. Our profile is compatible with most observations. The top (bottom) dashed, black line show the SB profile including only nebular (galactic) emission. Outside the inner region of the blob, the contribution of the gas is dominant.

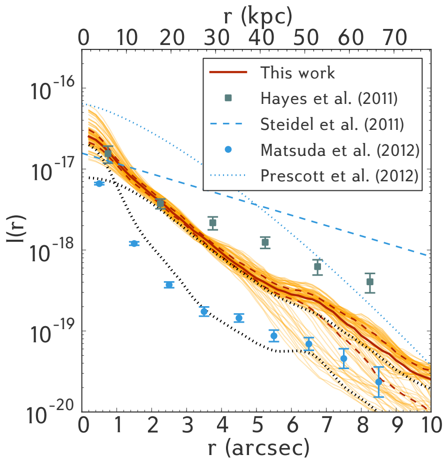

Fig. 1. Comparison of SB profiles. The red, solid line is the SB profile expected from the sum of both gas and galactic contributions. The thin, orange lines represents the profile for each line of sight, and the red, dashed lines show the interquartile range. The black, dotted lines show the splitting between the galactic (lower) and extragalactic (upper) contributions. Two observational data taken from the literature (Steidel et al. 2011; Prescott et al. 2012) are shown in blue, data points are Hayes et al. (2011) observations (teal) and Matsuda et al. (2012) stacked profile (blue).

3.2 Polarization

We compare our results to the polarimetric observations of Hayes et al. (2011). Figure 2 shows side by side the polarization profiles computed taking into account only in-situ gas emission (left panel), only the galactic contribution to the Lyα emission (middle panel) and the combination of the two (right panel). On the right panel, the polarization signal rises up to 15%, completely consistent with the observation of Hayes et al. (2011). We also rule out the scenario in which the Lyα emission of LABs purely originates from a central galaxy.

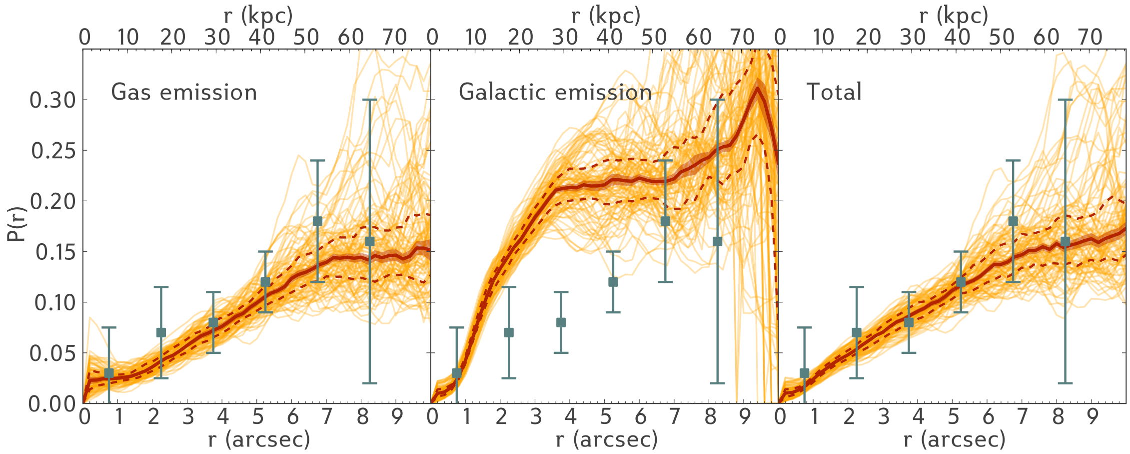

Fig. 2. Polarization radial profiles. **Left:** extragalactic emission, **Center:** galactic emission, and **Right:** the overall Lyα emission. The thin, orange lines show the profile corresonding to each line of sight; the solid, red line is the median profile; the dispersion along different line of sight is represented by the two dashed, red lines (first and third quartiles). The red area show the 3σ confidence limits. The data points are taken from Hayes et al. (2011).

4 Discussion

Our main results are the following:

- Lyman-α cooling radiation emitted inside the infalling gas and scattered through the blob gives a surface brightness profile consistent with observations.
- While previous idealised studies suggest that this extended contribution will prevent polarization to arise, we show that a complex but more realistic distribution of gas produces a polarized signal. On the contrary the polarization radial profiles computed by only taking the extragalactic contribution into account is compatible with observational data.
- A Lyα escape fraction of the galactic contribution of 5% is enough to find a good agreement with Hayes et al. (2011) results. This means that a non-negligible extragalactic contribution to the luminosity is compatible with current polarimetric observations.

We would like to thank Matthew Hayes and Claudia Scarlata for stimulating discussions, as well as Léo Michel-Dansac, Stéphanie Courty and Gérard Massacrier.

References

Dijkstra, M. & Loeb, A. 2008, MNRAS, 386, 492
Garel, T., Blaizot, J., Guiderdoni, B., et al. 2012, MNRAS, 422, 310
Hayes, M., Scarlata, C., & Siana, B. 2011, Nature, 476, 304
Matsuda, Y., Yamada, T., Hayashino, T., et al. 2012, MNRAS, 425, 878
Prescott, M. K. M., Dey, A., Brodwin, M., et al. 2012, ApJ, 752, 86
Rosdahl, J. & Blaizot, J. 2012, MNRAS, 423, 344
Rosdahl, J., Blaizot, J., Aubert, D., Stranex, T., & Teyssier, R. 2013, MNRAS
Rybicki, G. B. & Loeb, A. 1999, ApJ, 520, L79
Steidel, C. C., Bogosavljević, M., Shapley, A. E., et al. 2011, ApJ, 736, 160
Teyssier, R. 2002, A&A, 385, 337
Trebitsch, M., Verhamme, A., Blaizot, J., & Rosdahl, J. 2014, in prep.
Verhamme, A., Schaerer, D., & Maselli, A. 2006, A&A, 460, 397

Session 10

NOEMA

SF2A 2014
J. Ballet, F. Bournaud, F. Martins, R. Monier and C. Reylé (eds)

PDBI HIGH-RESOLUTION HIGH-SENSITIVITY IMAGING OF A STRONGLY LENSED SUBMILLIMETER SOURCE AT Z=5.24

F. Boone[1], F. Combes[2], M. Krips[3], J. Richard[4], T. Rawle[5], E. Egami[6], J.-P. Kneib[7], D. Schaerer[1,8], M. Dessauges-Zavadsky[8], R. Pello[1], B. Clément[4] and HLS team

Abstract. We have obtained Plateau de Bure Interferometer observations of HLSJ091828.6+514223 (z=5.24) at six different frequencies to cover the CO(6-5), CO(7-6), CI, H_20_p(2,0,2-1,1,1), [NII] and [CII] lines. The high resolution and high sensitivity of these multi-configuration observations allow us to detect the various line velocity components as well as the continuum and to resolve spatially their emission. This wealth of information is used to tackle the problem of lens and source modeling. A methodology is implemented to produce image plane maps, optimize the lens model, and finally inverse the PdBI data in the source plane. The image plane and source plane maps are constructed by fitting directly the pixels to the PdBI visibilities with the non-negative least square method. The preliminary results thus obtained are presented.

Keywords: high-redshift, gravitational lensing, submillimeter galaxies, molecular gas, dust emission

1 Introduction

HLSJ091828.6+514223 was discovered in the *Herschel* Lensing Survey (HLS, Egami et al. 2010) with an exceptionally bright flux of $\sim$200 mJy at 500μm. It is located behind the lensing galaxy cluster Abell 773 (z=0.22) and is further magnified by a z=0.63 galaxy. IRAM-30m with the EMIR backend allowed us to determine the redshift of the source at z=5.243 and to detect the CO(7-6), CO(6-5), CO(5-4), C I($^3P_2-^3P_1$) H_2O_p(2,0,2-1,1,1) and [NII]205μm lines (Combes et al. 2012). The CO(2-1) line was also detected at the EVLA.

We then simultaneously observed this bright northern submillimeter source at SMA and Plateau de Bure Interferometer (PdBI) to resolve the emission and detect the [CII] line. A deep analysis of the SMA data with a discussion of the various velocity components and PDR modeling is reported by Rawle et al. (2014).

Here we report on the high-resolution and high-sensitivity PdBI observations. We describe the method implemented to obtain a reliable lens model and to invert (or delens) the data.

2 Observations

From 2012 to 2014 we have obtained a total of 12 tracks with the 6 antennas of the Plateau de Bure Interferometer (PdBI) connected to the WIDEX correlator providing 3.6 GHz bandwidth. We observed at six different frequencies to cover the CO(6-5), CO(7-6), CI, H_20_p(2,0,2-1,1,1), [NII] and [CII] lines. The observations are summarized in the Table 1. The angular resolutions obtained are all below 1″ and reach 0.3″ at 304 GHz.

3 Imaging with the non negative least squares method

Because the emission detected with PdBI at all frequencies is compact (<5″ in diameter) and the signal-to-noise ratio is high, it is possible to solve the imaging problem with a least squares method. The flux of each pixel of

[1] IRAP, CNRS OMP-UPS, 14, avenue Edouard Belin 31400 Toulouse
[2] LERMA, Observatoire de Paris, 61 avenue de l'Observatoire, 75014 Paris, France
[3] IRAM, 300 rue de la Piscine, Domaine Universitaire, 38406 Saint Martin d'Hres, France
[4] Centre de Recherche Astrophysique de Lyon, Université Lyon 1, 9 Avenue Charles André, F-69561 Saint Genis Laval, France
[5] European Space Astronomy Centre (ESAC)/ESA, Villanueva de la Cañada, E-28691 Madrid, Spain
[6] Steward Observatory, University of Arizona, 933 North Cherry Avenue, Tucson, AZ 85721, USA
[7] Laboratoire d'astrophysique, Ecole Polytechnique Fédérale de Lausanne, Observatoire de Sauverny, 1290 Versoix, Switzerland
[8] Observatoire de Genève, Université de Genève, 50 Ch. des Maillettes, 1290 Versoix, Switzerland

Table 1. PdBI Observations of HLSJ091828.6+514223.

Freq [GHz]	line	config	beam [″]	noise [mJy] in 20 MHz channels
111	CO(6-5)	A	0.8×0.7	0.57
129	CO(7-6)+CI	ABD	0.9×0.7	0.49
158	H_2O_p(2,0,2-1,1,1)	AC	0.7×0.6	0.61
218	–	A	0.48×0.31	1.46
234	[NII]	ABCD	0.46×0.46	0.72
304	[CII]	A	0.31×0.27	2.68

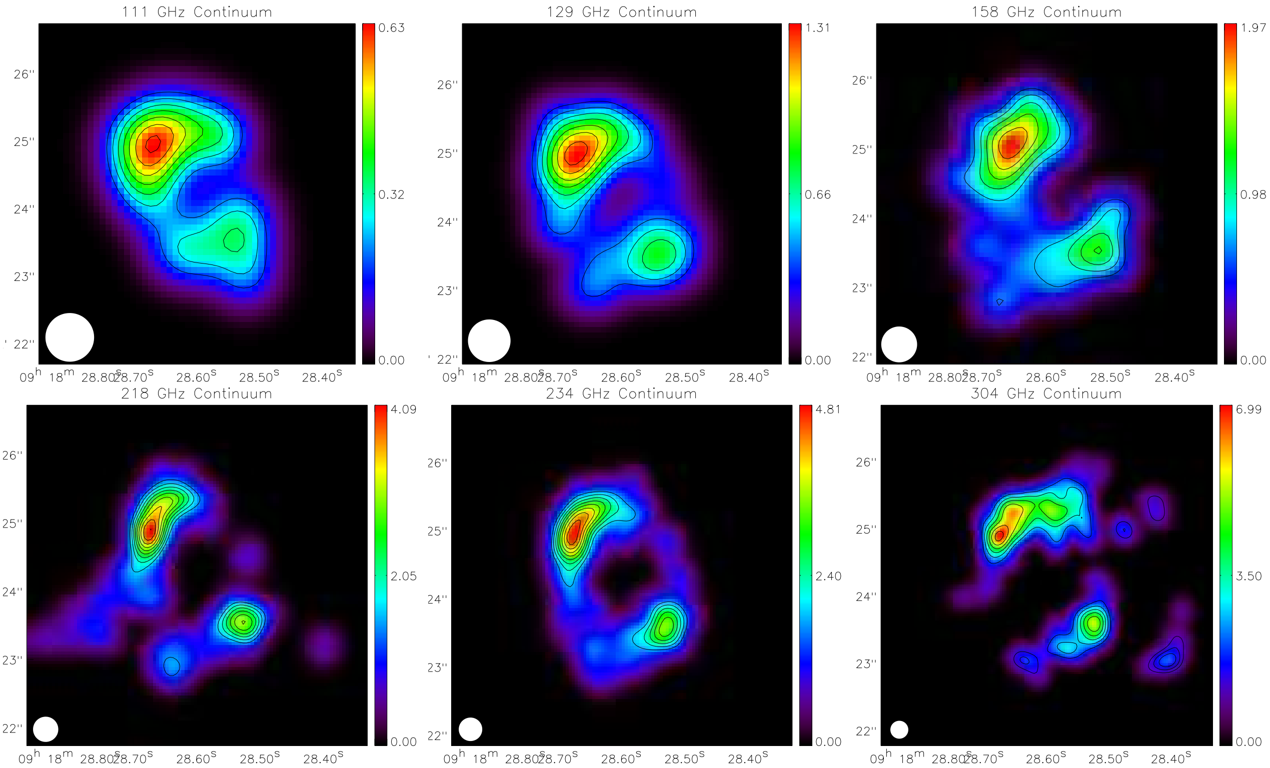

Fig. 1. PdBI continuum maps (2.5″ in size) obtained with the NNLS method. From left to right and from top to bottom the frequencies are 111, 129, 158, 218, 234 and 304 GHz. In each frame the white circle represents the resolution.

the region of interest in the image (sky) plane is considered as a free parameter, $s_i > 0$. The pixel values are the solution to the matrix equation:

$$V_i = \sum_j^{N_{\rm pix}} {\rm s}_j \times F_{ij}, \tag{3.1}$$

where, V_i are the complex visibilities measured at the coordinates (u_i, v_i) in the Fourier plane, $N_{\rm pix}$ is the number of pixels in the image plane and $F_{ij} = \mathcal{F}_j(u_i, v_i)$, where $\mathcal{F}_j(u, v)$ is the Fourier transform ($\mathscr{F}\{\}$) of a map in which $s_k = 0\ \forall k \neq j$ and $s_j = 1$, i.e.,

$$\mathcal{F}_j(u,v) = \mathscr{F}\{\delta(x - x_j, y - y_j)\} = \cos(2\pi(u\frac{x_j}{\lambda} + v\frac{y_j}{\lambda})) + i\sin(2\pi(u\frac{x_j}{\lambda} + v\frac{y_j}{\lambda})), \tag{3.2}$$

where (x_j, y_j) are the coordinates of the $j^{\rm th}$ pixel. We solve Eq. 3.1 with the non-negative least square method (Lawson & Hanson 1974) using pixels of size $dx = 0.5 \times$ BFWHM (beam full width at half maximum) in a circular region of radius $R = 2.5''$. The six maps thus obtained for the continuum are shown in Fig. 1, and the maps obtained for the four velocity components of the [CII] lines are shown in Fig. 2. By construction these maps have no negative values as opposed to those obtained with the CLEAN method (due to negative residuals).

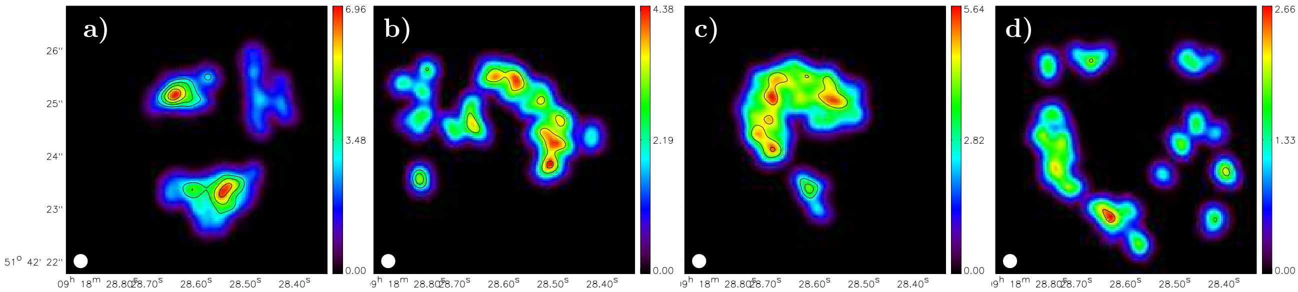

Fig. 2. PdBI maps of the four [CII] line velocity components obtained with the NNLS method. From left to right the integrated velocity intervals in km/s are [-30,420] (a), [-320, -30] (b), [-600,-320] (c) and [-1000, -600] (d).

4 Lens modeling

Modeling this lens is not straightforward because the source seems to be extended in the continuum at all wavelengths at which it is detected as well as in all the line velocity components. It is not possible to fit the lens parameters to accurate optical observations of a background point source as usually done for lensed quasars (e.g., Anh et al. 2013). This leads to degeneracies between source and lens parameters. The most compact images obtained in continuum at 304 GHz resemble a double system (Fig. 1) and can therefore be used to constrain the lens along one direction only. In addition, the various velocity components suggest that we are dealing with a complex source possibly composed of interacting galaxies and/or outflows/inflows (Rawle et al. 2014).

However, the lensing cluster A773 at $z = 0.22$ was already modeled by Richard et al. (2010) based on many multiple arc systems and the main lensing galaxy at $z = 0.63$ was detected with Subaru with no obvious companions (Combes et al. 2012) . We can therefore fix the cluster model to the one found by Richard et al. (2010) and add a single halo component for the additional lensing galaxy. We have therefore 5 free parameters: the galaxy center coordinates, its mass, ellipticity and position angle.

To optimize the lensing galaxy parameters we select intensity peaks in the NNLS maps of the continuum and the line components with high S/N. We use the LENSTOOL software (Kneib et al. 1996; Jullo et al. 2007) to take all these constraints into account assuming the peaks of a given velocity component are the multiple images of a single source. Although this assumption may not be valid for all the peaks (because the source is extended), by minimizing the number of sources the software is able to find the optimal solution.

5 Delensing PdBI data

Once a reliable lens model is obtained it is possible to delens the interferometric data and thus obtain directly source plane maps by using the same method as for image plane maps (Section 3). Indeed, Eq. 3.1 still applies with the definition of $\mathcal{F}_j(u,v)$ (Eq. 3.2) replaced by:

$$\mathcal{F}_j(u,v) = \mathscr{F}\{\mathscr{L}\{\mathcal{G}(x-x_j, y-y_j)\}\}, \tag{5.1}$$

where $\mathscr{L}$ represents the lensing operator, and where the δ functions representing the pixels have been replaced by Gaussian functions $\mathcal{G}$ to prevent discontinuities close to the caustic lines. To fully sample the source plane the Gaussian functions are taken circular with a FWHM equal to twice their separation.

We performed this lens inversion by applying the NNLS method to the PdBI data and we thus obtained a total of 30 source maps (6 continuum and 4 components for each of the 6 lines). For illustration we show the source maps obtained for the 304 GHz continuum and for one of the [CII] components together with the corresponding image maps in Fig.3. In Fig.4 we show the 4 velocity components of the [CII] line overlaid on the 304 GHz continuum. The continuum peak could be a galaxy nucleus surrounded by a rotating disk (red and blue contours). A complete interpretation of the various components will be discussed in a forthcoming paper.

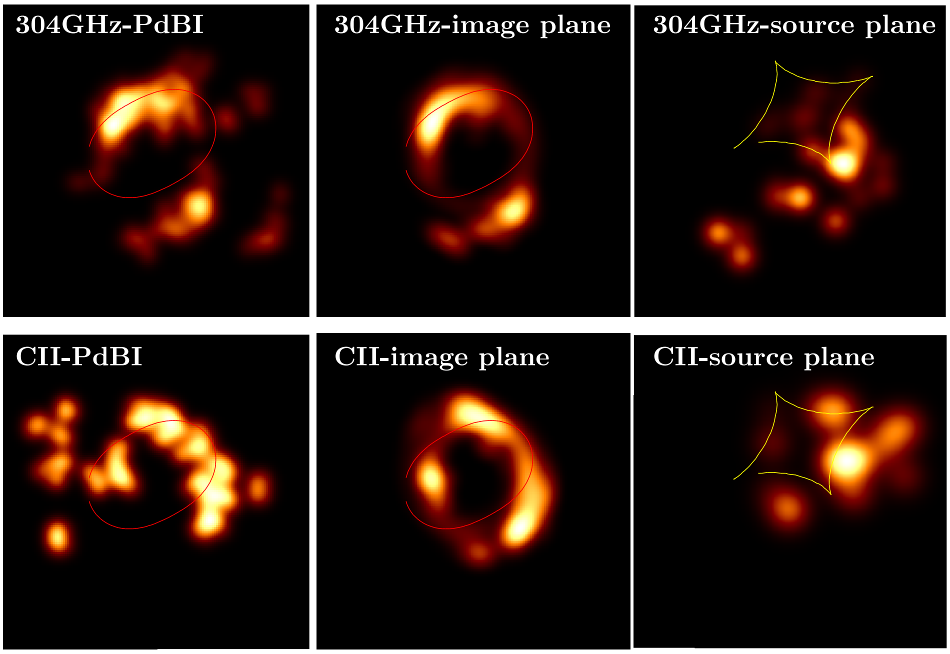

Fig. 3. The delensed source maps obtained for the 304 GHz and the [CII] line in the [-320, -30] km/s velocity interval are shown in the right-hand side frames. The corresponding image plane maps are shown in the middle frames and can be compared to the image plane maps obtained directly from the PdBI data shown on the left-hand side (same as in Figs. 1 and 2).

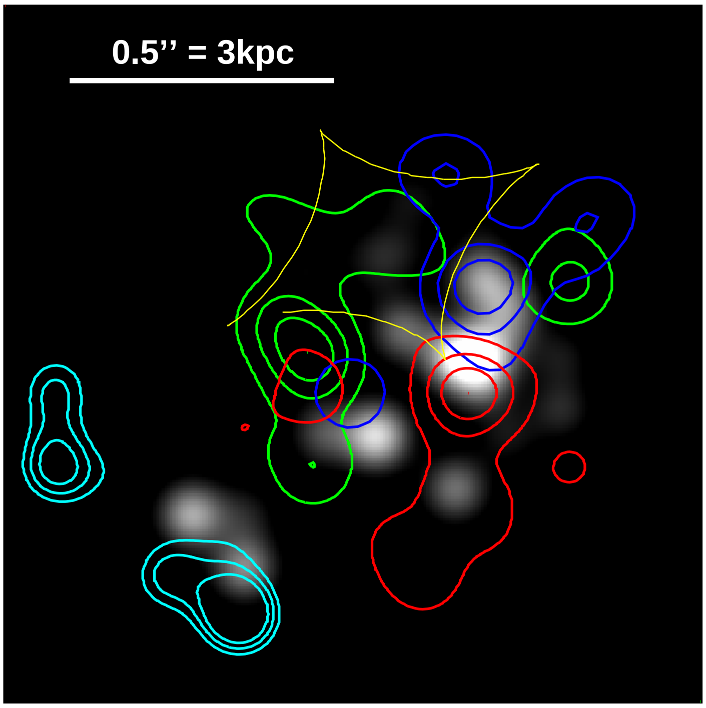

Fig. 4. Source plane delensed maps. The grey scale intensity map shows the 304 GHz continuum emission, the red, blue, green and cyan contours represent the [CII] line emission in the velocity intervals [-30,420], [-320, -30], [-600,-320] and [-1000, -600] km/s, respectively (see Fig. 2). The yellow line shows the caustic curve from the best lens model.

6 Conclusions

We have obtained a unique set of observations of HLSJ091828.6+514223 with PdBI. We developed methods and tools to allow their interpretation in the source plane. This will be the subject of a forthcoming paper.

We are very grateful to the IRAM staff for their kind help with the observations. We thank the Action Specifique ALMA of the CNRS for its support.

References

Anh, P. T., Boone, F., Hoai, D. T., et al. 2013, A&A, 552, L12

Combes, F., Rex, M., Rawle, T. D., et al. 2012, A&A, 538, L4

Egami, E., Rex, M., Rawle, T. D., et al. 2010, A&A, 518, L12

Jullo, E., Kneib, J.-P., Limousin, M., et al. 2007, New Journal of Physics, 9, 447

Kneib, J.-P., Ellis, R. S., Smail, I., Couch, W. J., & Sharples, R. M. 1996, ApJ, 471, 643

Lawson, C. L. & Hanson, R. J. 1974, Solving least squares problems

Rawle, T. D., Egami, E., Bussmann, R. S., et al. 2014, ApJ, 783, 59

Richard, J., Smith, G. P., Kneib, J.-P., et al. 2010, MNRAS, 404, 325

SF2A 2014
J. Ballet, F. Bournaud, F. Martins, R. Monier and C. Reylé (eds)

HIGH-REDSHIFT STAR FORMATION EFFICIENCY AS UNCOVERED BY THE IRAM PHIBSS PROGRAMS

J. Freundlich[1], P. Salomé[1], F. Combes[1], L. Tacconi[2], R. Neri[3], S. Garcia-Burillo[4], R. Genzel[2,5,6], T. Contini[7,8], S. Lilly[9] and the PHIBSS Consortium

Abstract. The evolution of the cosmic star formation rate (SFR) is characterized by a peak around redshift z=2-3 and a subsequent drop by an order of magnitude. High levels of star formation are sustained by a continuous supply of fresh gas and high molecular gas fractions. But once galaxies exceed a certain mass or enter a harsh environment, star formation is quenched, and different phenomena could explain the resulting evolution of the cosmic SFR. Is it mostly driven by the available molecular gas, or because star formation processes are more efficient at high redshift? Here we present the results and the perspectives of the PHIBSS programs, which aim at understanding early galaxy evolution and the winding-down of star formation from the perspective of the galaxies' molecular gas reservoirs. These programs use statistically meaningful samples of galaxies belonging to the massive end of the star formation main-sequence at different redshifts. The previous IRAM PHIBSS program has already uncovered large molecular gas reservoirs at redshifts z$\sim$1-2, with gas fractions 4 to 10 times higher than in the local Universe, and the ongoing IRAM and ALMA programs extend the sample to a wider range of redshifts and to a more complete sampling of the stellar mass-SFR plane. The IRAM PHIBSS2 legacy program is designed to make full use of the upcoming NOEMA capabilities.

Keywords: galaxies: evolution, galaxies: high-redshift, galaxies: structure, stars: formation, galaxies: ISM

1 Introduction

Our Galaxy only forms a few stars per year, as most nearby spiral galaxies. But ten billion years ago, between redshifts 2 and 3, observed galaxies formed their stars at rates up to 20 times higher (Noeske et al. 2007; Daddi et al. 2007). What are the causes of the decrease of the star formation activity after this peak?

Stars are formed from cold molecular gas clouds which collapse due to their gravitational pull. A high star formation rate (SFR) thus means a significant gas content, either brought by major mergers or by continuous processes such as smoother gas accretion along streams of the cosmic web (Kereš et al. 2005; Dekel et al. 2009a). Observations show that high-redshift galaxies near the star formation peak are indeed much more gas-rich and clumpy than their low-redshift counterparts (Daddi et al. 2010; Tacconi et al. 2010; Förster Schreiber et al. 2011), but many other parameters may intervene, from environmental effects, morphological quenching, and feedback mechanisms from stars and AGN, to the star formation efficiency itself (SFE=SFR/M_{gas}). This latter quantity has notably been shown to decrease significantly after z = 1 (Combes et al. 2011, 2013) and could thus contribute substantially to the evolution of the cosmic SFR. Is the evolution of the cosmic SFR after

[1] LERMA, Observatoire de Paris, CNRS, 61 av. de l'Observatoire, 75014 Paris, France
[2] Max-Planck-Institut für Extraterrestrische Physik (MPE), Giessenbachstrasse 1, 85748 Garching, Germany
[3] IRAM, 33 rue de la Piscine, 38406 St. Martin d'Hères, Grenoble, France
[4] Observatorio Astrononómico Nacional (OAN), Apartado 1143, 28800 Alcalá de Henares, Madrid, Spain
[5] Dept. of Physics, Le Conte Hall, University of California, CA 94721 Berkeley, USA
[6] Dept. of Astronomy, Campbell Hall, University of California, CA 94721 Berkeley, USA
[7] Institut de Recherche en Astrophysique et Planétologie (IRAP), CNRS, 14 av. Édouard Belin, 31400 Toulouse, France
[8] IRAP, Université de Toulouse, UPS-OMP, Toulouse, France
[9] Institute for Astronomy, Department of Physics, ETH Zurich, CH-8093 Zurich, Switzerland

the star formation peak mostly driven by the declining cold gas reservoir, or are the star formation processes qualitatively different at the corresponding redshifts?

If the averaged evolution of the cosmic SFR displays a peak around z=2-3 and a subsequent drop by an order of magnitude, the galaxy distribution is far from homogeneous. There is indeed a bimodality between blue star-forming disks on one side and red passive galaxies on the other. The blue star-forming galaxies lie on a tight relationship in the stellar mass-SFR plane, the main sequence of star formation (MS; Noeske et al. 2007; Elbaz et al. 2007; Daddi et al. 2007; Wuyts et al. 2011). At a given stellar mass $M_\star$, the SFR on the MS drops by a factor ~ 20 from z$\sim$ 2 to the present time. Typical star-forming galaxies are expected to follow the MS until their star formation activity is quenched, and then to rapidly transit down to the red sequence (e.g., Bouché et al. 2010). This transition is still poorly understood.

The PHIBSS programs study the molecular gas properties of star-forming galaxies on and around the MS and aim at better understanding the winding-down of star formation and the quenching processes with a statistical sample of galaxies at high redshift. Cold molecular gas is traced through the CO rotational lines, and the programs also include high-resolution observations to study the star formation efficiency at sub-galactic scales. The main goals of the PHIBSS programs are to study the evolution with redshift of the molecular gas fraction (f_{gas}) and the SFE in normal MS star-forming galaxies, to characterize the dependance of these quantities on stellar mass and morphology in order to compare with feedback and quenching models, to examine the inner gas dynamics, and to probe the physical gas properties through multiple CO transitions. The first IRAM PHIBSS Large Program (L. Tacconi, F. Combes, et al.) focussed on the massive tail ($M_\star > 3.10^{10}$ $M_\odot$) of the MS at z=1.2 and 2.2 and comprised 52 CO detections and 8 high-resolution imaging observations, while the ongoing PHIBSS2 programs triple the number of observed galaxies and better sample the $M_\star$-SFR plane. Here we focus on the results of the first IRAM PHIBSS program concerning the star formation efficiency, first from the galaxy-averaged observations, and then from the resolved observations.

2 Galaxy-averaged star formation relations

The IRAM PHIBSS Large Program first enables to characterize the galaxy-averaged properties of the molecular gas in high-redshift MS galaxies, and to study their evolution with redshift. It notably shows that most of these galaxies are clumpy disks, as the two galaxies displayed in the left panel of Fig. 1 (Tacconi et al. 2010, 2013). The PHIBSS program also confirms the presence of large molecular gas fractions in high-redshift MS galaxies, with mean values reaching 33% at z$\sim$1.2 and 47% at z$\sim$2.2 (Tacconi et al. 2013). This is to be compared with the 8% that are observed at z=0 (Leroy et al. 2008; Saintonge et al. 2011). Gas-rich disks are more likely to be gravitationally unstable, and thus to display clumpy features and to form stars.

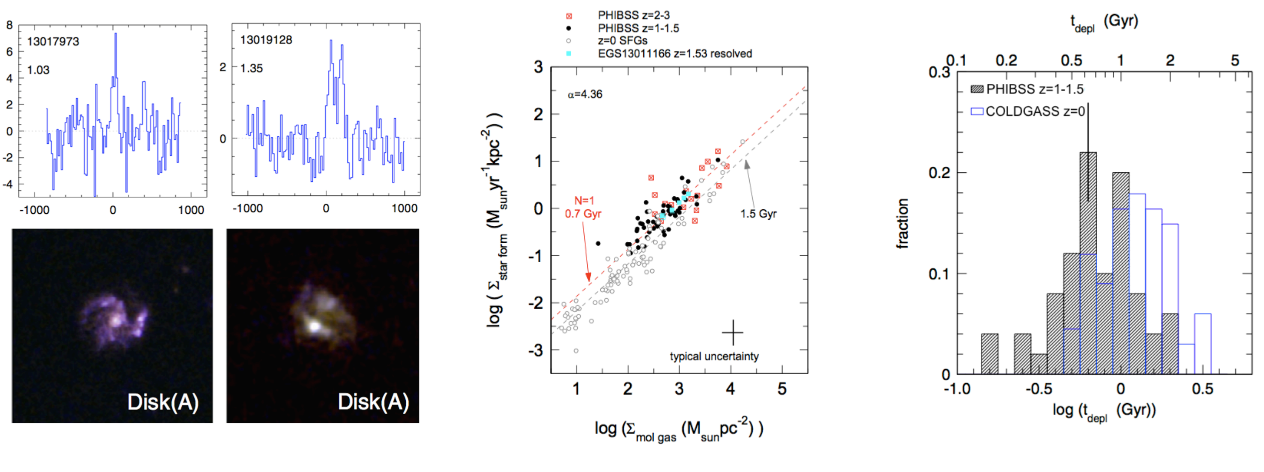

Fig. 1. HST images and galaxy-integrated CO velocity spectra for two galaxies from the PHIBSS program, displaying disk-like features (left); the near-linear KS scaling relation between the molecular gas and SFR surface densities (middle); and the distribution of depletion times (right). In the last two plots, the PHIBSS high-redshift data points are compared to z=0 samples. Whereas the galaxy-averaged KS relation is comparable at low and high redshifts, the slight decrease of the depletion time with redshift might indicate a more efficient star formation at high redshift (Tacconi et al. 2013).

The Kennicutt-Schmidt (KS) relation between the gas and SFR densities characterizes the star formation efficiency, and is shown to be near linear at low redshift (Kennicutt 1998; Kennicutt & Evans 2012). As shown in the middle panel of Fig. 1, the same trend is observed at z=1-3 for the galaxies of the PHIBSS sample (Genzel et al. 2010; Tacconi et al. 2013). Nevertheless, the mean depletion time ($t_{depl} = M_{gas}/SFR$) of 0.7 Gyr is slightly lower than at present time: as this timescale represents the time needed for a galaxy to consume all its gas in order to form stars, it implies a faster star formation duty cycle and a need for gas replenishment at the peak of the star formation activity. The right panel of Fig. 1 compares the distribution of depletion times in the PHIBSS high-redshift sample with the COLDGASS sample at z=0. The depletion time is the inverse of the SFE, which could thus be slightly higher at high-redshift.

The PHIBSS program also shows that the specific star formation rate (sSFR = SFR/M_{star}) correlates strongly with the gas fraction: the variation of the sSFR between z=3 and z=0, as well as the vertical offset of a galaxy from the MS in the $M_\star$-SFR plane, are mainly controled by the molecular gas fraction (Tacconi et al. 2013).

3 Resolved kinematics and star formation relations at sub-galactic scales

The IRAM PHIBSS program also includes high-resolution observations of the molecular gas for a subsample of 8 galaxies, carried at the IRAM Plateau de Bure interferometer. The angular resolution attained by these observations reaches 0.3″-1″, which enables to fathom star formation processes at sub-galactic scales, as 1″ notably corresponds to ∼8 kpc at z=1.2.

Sub-arcsecond galaxy kinematics give access to good quality rotation curves and to the velocity dispersion. The left panel of Fig. 2 shows the superposition of two HST broad-band images with the CO high-resolution observations for one galaxy from the PHIBSS sample, as well as its velocity and velocity dispersion maps, and its rotation curve (Tacconi et al. 2010). A rotating disk is clearly visible. The high-redshift disks are more turbulent by a factor ∼5 than their low-redshift counterparts (Tacconi et al. 2013), which is compatible with models where clumpy cosmic streams feed the disk and trigger violent gravitational instabilities (e.g., Dekel et al. 2009b).

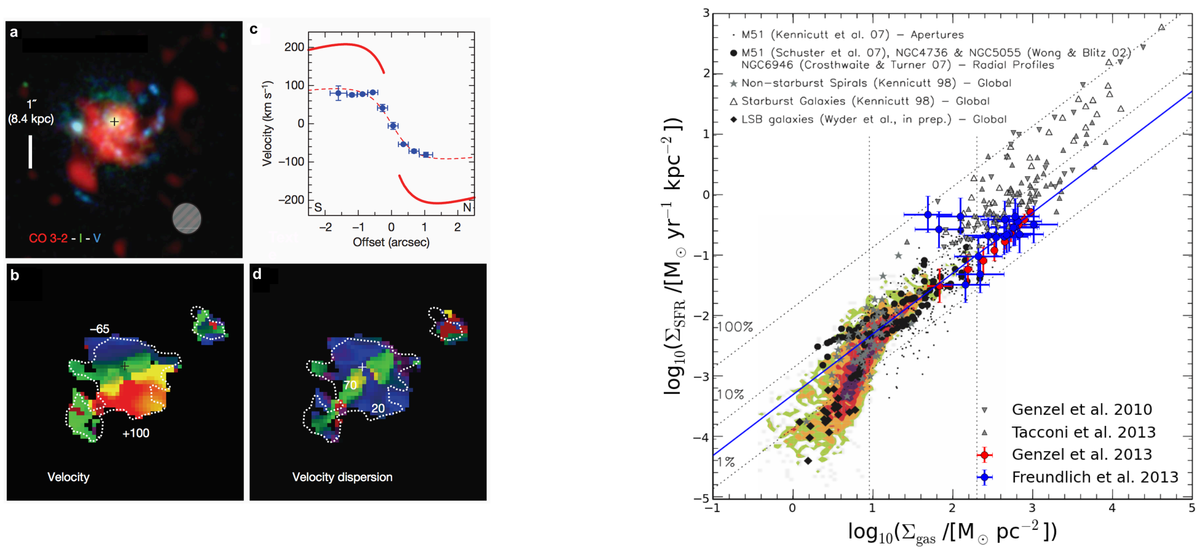

Fig. 2. Left: (a) CO line emission with HST I and V bands images of the z=1.2 source EGS13035123; (b) its velocity map; (c) the corresponding rotation curve, with the best fitting exponential disk model indicated as a dashed line; and (d) the velocity dispersion map deduced by substracting the modeled rotation to the observed velocity (Tacconi et al. 2010). Right: Spatially resolved molecular KS relation for ensembles of clumps of four galaxies from the PHIBSS sample (Freundlich et al. 2013) and for binned groups of pixels in EGS13011166 (Genzel et al. 2013), superimposed on the sub-galactic KS diagram obtained at low redshift by Bigiel et al. (2008). The solid blue line corresponds to a constant depletion time $t_{depl} = 1.9$ Gyr, and the grey data points to galaxy-averaged measurements.

Resolved kinematics also enables to separate smoothed ensembles of clumps due to their different velocities, and to obtain a resolved KS relation averaged at a scale of about $1''$ (8 kpc) for four galaxies of the PHIBSS sample (Freundlich et al. 2013). The CO line luminosity from the IRAM observations traces the cold molecular gas, while the [OII] line from Keck DEEP2 spectra is empirically calibrated to trace the SFR. The results are compatible with a linear relation and a constant depletion time of 1.9 Gyr, and fit well with the corresponding low-redshift observations, as shown in the right panel of Fig. 2. These results seem to point towards similar star formation processes at high and low redshifts, but a bigger statistical sample would be necessary to obtain more meaningful mean depletion times for the substructures of high-redshift galaxies.

Genzel et al. (2013) further obtain a pixel by pixel KS relation for one typical z=1.53 massive star-forming galaxy from the PHIBSS sample, EGS13011166, and take into account extinction and Hα observations to show that the shape and the slope of the KS relation depend strongly on the extinction correction that is applied. Using resolved extinction maps instead of a single value for the whole galaxy significantly changes the depletion times that are obtained from sub-galactic observations.

4 Conclusion and perspectives

The IRAM PHIBSS survey shows that the evolution of the cosmic SFR is mostly driven by the available gas reservoir, but the slightly shorter depletion times that are observed might also indicate that star formation is somewhat more efficient at high redshift. On sub-galactic scales, it was possible to draw a KS relation for ensembles of clumps of four massive galaxies at z=1.2 and on a pixel basis for one galaxy at z=1.53.

The ongoing IRAM PHIBSS2 Legacy Program (F. Combes, S. Garcia-Burillo, R. Neri, L. Tacconi, et al.) will more than triple the number of high-redshift normal star-forming galaxies with CO measurements, extend their redshift range, and include galaxies below the MS. This four year program is phased to optimize and exploit the NOEMA capabilities as they come online: the smaller integration times and the increased sensitivity will permit a statistical gain and a better sampling of the $M_\star$-SFR plane. Complementary ALMA programs will further contribute to extend the sample owing to an even higher sensitivity (R. Genzel et al.), probe higher CO transitions to study the gas excitation and the physical conditions of the gas in early star-forming systems (A. Weiss et al.), and possibly obtain high-resolution images and kinematics of the molecular gas in galaxies at intermediate redshifts (Freundlich et al.).

References

Bigiel, F., Leroy, A., Walter, F., et al. 2008, AJ, 136, 2846

Bouché, N., Dekel, A., Genzel, R., et al. 2010, ApJ, 718, 1001

Combes, F., García-Burillo, S., Braine, J., et al. 2011, A&A, 528, A124

Combes, F., García-Burillo, S., Braine, J., et al. 2013, A&A, 550, A41

Daddi, E., Bournaud, F., Walter, F., et al. 2010, ApJ, 713, 686

Daddi, E., Dickinson, M., Morrison, G., et al. 2007, ApJ, 670, 156

Dekel, A., Birnboim, Y., Engel, G., et al. 2009a, Nature, 457, 451

Dekel, A., Sari, R., & Ceverino, D. 2009b, ApJ, 703, 785

Elbaz, D., Daddi, E., Le Borgne, D., et al. 2007, A&A, 468, 33

Förster Schreiber, N. M., Shapley, A. E., Genzel, R., et al. 2011, ApJ, 739, 45

Freundlich, J., Combes, F., Tacconi, L. J., et al. 2013, A&A, 553, A130

Genzel, R., Tacconi, L. J., Gracia-Carpio, J., et al. 2010, MNRAS, 407, 2091

Genzel, R., Tacconi, L. J., Kurk, J., et al. 2013, ApJ, 773, 68

Kennicutt, R. C. & Evans, N. J. 2012, ARA&A, 50, 531

Kennicutt, Jr., R. C. 1998, ApJ, 498, 541

Kereš, D., Katz, N., Weinberg, D. H., & Davé, R. 2005, MNRAS, 363, 2

Leroy, A. K., Walter, F., Brinks, E., et al. 2008, AJ, 136, 2782

Noeske, K. G., Weiner, B. J., Faber, S. M., et al. 2007, ApJ, 660, L43

Saintonge, A., Kauffmann, G., Kramer, C., et al. 2011, MNRAS, 415, 32

Tacconi, L. J., Genzel, R., Neri, R., et al. 2010, Nature, 463, 781

Tacconi, L. J., Neri, R., Genzel, R., et al. 2013, ApJ, 768, 74

Wuyts, S., Förster Schreiber, N. M., van der Wel, A., et al. 2011, ApJ, 742, 96

SF2A 2014
J. Ballet, F. Bournaud, F. Martins, R. Monier and C. Reylé (eds)

"PARTICLE TRAPS" AT PLANET GAP EDGES IN DISKS: EFFECTS OF GRAIN GROWTH AND FRAGMENTATION

J.-F. Gonzalez[1], G. Laibe[2], S. T. Maddison[3], C. Pinte[4,5] and F. Ménard[4,5]

Abstract. We model the dust evolution in protoplanetary disks (PPD) with 3D, Smoothed Particle Hydrodynamics (SPH), two-phase (gas+dust) hydrodynamical simulations. The gas+dust dynamics, where aerodynamic drag leads to the vertical settling and radial migration of grains, is consistently treated. In a previous work, we characterized the spatial distribution of non-growing dust grains of different sizes in a disk containing a gap-opening planet and investigated the gap's detectability with ALMA. Here we take into account the effects of grain growth and fragmentation and study their impact on the distribution of solids in the disk. We show that rapid grain growth in the "particle traps" at the edges of planet gaps are strongly affected by fragmentation. We discuss the consequences for ALMA and NOEMA observations.

Keywords: protoplanetary disks, planet-disk interactions, hydrodynamics, methods: numerical, submillimeter: planetary systems

1 Introduction

Planets are thought to form from the aggregation of sub-μm dust grains in PPD around young stars. While small dust grains easily stick during collisions to form aggregates up to cm or dm sizes, the subsequent growth to planetesimal size is probably the biggest problem in the theory of planet formation. Three "barriers" to planet formation, preventing this step, have been identified. The radial-drift barrier (Weidenschilling 1977; Laibe et al. 2012; Laibe 2014) occurs when grains are migrating inwards due to gas drag so rapidly that they fall onto the star in a fraction of both the disk lifetime and the planet formation timescale. This is the case for cm- to m-sized grains, whereas small grains are strongly coupled to the gas and follow its motion, and large grains are largely insensitive to gas drag and stay on their Keplerian orbits. However, Laibe et al. (2008) showed that growing grains can overcome the fast-migration regime and decouple from the gas before being lost from the disk. The fragmentation barrier (Dullemond & Dominik 2005; Blum & Wurm 2008) happens when dust grains collide at relative velocities too high for them to stick, they instead shatter upon impact. Finally, the bouncing barrier (Zsom et al. 2010; Windmark et al. 2012) occurs at velocities lower than the fragmentation threshold, when grains bounce off each other. Accounting for stochastic motion, Garaud et al. (2013) showed that the low-velocity tail of the distribution allowed collisional growth to larger sizes, thus overcoming both the bouncing and fragmentation barriers.

"Particle traps" are other solutions to the barriers of planet formation, they are locations of pressure maximum, towards which gas drags the dust grains. The concentration of grains lowers their relative velocities and eases their growth. Several types of particle traps have been proposed: anticyclonic vortices (Barge & Sommeria 1995; Méheut et al. 2012), the snow line or the dead zone (Kretke & Lin 2007; Dzyurkevich et al. 2010), planet gap edges (Fouchet et al. 2007, 2010; Gonzalez et al. 2012), or any kind of "pressure bump" in the gas surface density (Pinilla et al. 2012). In this study, we focus on particle traps at planet gap edges.

[1] Université de Lyon, Lyon, F-69003, France; Université Lyon 1, Observatoire de Lyon, 9 avenue Charles André, Saint-Genis Laval, F-69230, France; CNRS, UMR 5574, Centre de Recherche Astrophysique de Lyon; École Normale Supérieure de Lyon, Lyon, F-69007, France
[2] School of Physics and Astronomy, University of Saint Andrews, North Haugh, St Andrews, Fife KY16 9SS, UK
[3] Centre for Astrophysics and Supercomputing, Swinburne Institute of Technology, PO Box 218, Hawthorn, VIC 3122, Australia
[4] UMI-FCA, CNRS/INSU France (UMI 3386), and Departamento de Astronomía, Universidad de Chile, Casilla 36-D Santiago, Chile
[5] UJF-Grenoble 1 / CNRS-INSU, Institut de Planétologie et d'Astrophysique de Grenoble, UMR 5274, Grenoble, F-38041, France

2 Hydrodynamical simulations

In a previous work (Fouchet et al. 2010), we ran simulations of the dynamics of grains of constant size in a PPD containing a planet using our 3D, two-fluid (gas+dust), SPH code (Barrière-Fouchet et al. 2005). We modeled a disk of mass $M_{\rm disk} = 0.02\ M_\odot$ orbiting a 1 $M_\odot$ star and containing 1 % of dust by mass. We studied the evolution of the dust phase for grains of 100 μm, 1 mm and 1 cm and for planets of 0.1, 0.5, 1 and 5 $M_{\rm J}$, on a circular orbit of radius 40 AU. We found that in all cases, the gap created in the dust phase was deeper and wider than in the gas, as a result of the dust motion towards the gas pressure maxima at the gap edges. We computed synthetic ALMA images of our simulated disks with a 1 and a 5 $M_{\rm J}$ planet (Gonzalez et al. 2012). We found that gap detection is robust and that ALMA should discover a large number of them.

We now study the effect of grain growth and fragmentation on the dust dynamics in the same disk containing a 5 $M_{\rm J}$ planet on the same orbit. Grain growth is implemented in our code as detailed in Laibe et al. (2008). We introduce fragmentation by defining a velocity threshold $V_{\rm frag}$, to which we compare the relative velocity $V_{\rm rel}$ of dust grains. When $V_{\rm rel} < V_{\rm frag}$, grains grow and when $V_{\rm rel} > V_{\rm frag}$, they shatter, leading to a decrease of the size of the representative SPH particles. $V_{\rm frag}$ is a free parameter of our simulations and we assume it to be constant. We ran simulations for pure growth (equivalent to $V_{\rm frag} = +\infty$) and with fragmentation for $V_{\rm frag} = 10$, 15, 20 and 25 m s^{-1}. We start from an initially uniform grain size $s_0 = 10\ \mu$m. Both gas and dust phases contain 200,000 SPH particles and all simulations were evolved for 100 000 yr.

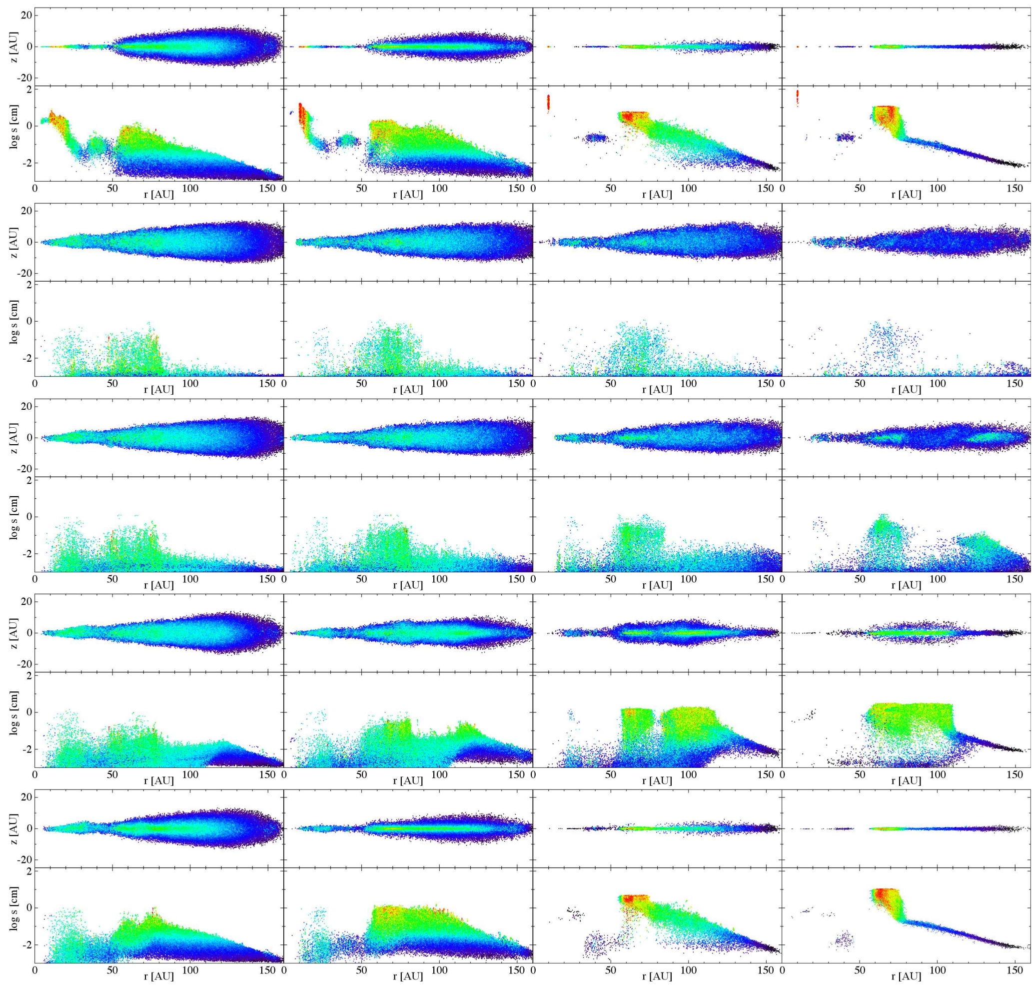

Fig. 1. Time evolution of the dust phase in the simulation with pure growth and with fragmentation for $V_{\rm frag} = 10$, 15, 20 and 25 m s^{-1}, from top to bottom. For each simulation, the top panel show a meridian plane cut of the dust distribution and the bottom panel shows the radial grain size distribution. *From left to right:* Snapshots at $t = 6\,000$, 12 000, 25 000 and 50 000 yr. The color represents the volume density, from 10^{-15} (black) to 5×10^{-11} kg m^{-3} (red).

Figure 1 shows the dust distribution in the meridian plane together with the radial distribution of grain sizes at $t = 6\,000$, $12\,000$, $25\,000$ and $50\,000$ yr for the five simulations. In the pure growth case, as was found by Laibe et al. (2008) in a disk without planets, particles typically grow as they settle to the midplane, then enter the fast migration regime while experiencing little growth. Grains initially close to the disk inner edge are thus lost to the star, as is the case for the moderately dense clump of centimetric particles seen interior to 10 AU in the 6 000 yr snapshot. Further out, grains migrate towards and accumulate at both gap edges, where their density is higher and their growth more efficient. At 12 000 yr, the detached group of particles at the disk inner edge contains the last grains to be lost to the star. Just outside of 10 AU, particles have outgrown the fast migration regime (for ~ 1 cm here), are now decoupled from the gas and grow without migrating. At 25 000 yr, all grains in the inner disk are concentrated in a narrow, dense ring where they grow further. The outer gap edge has also become very dense. Finally, at 50 000 yr, the gap only contains particles that are trapped in corotation with the planet. Large grains are present at both gap edges, showing the efficiency of these particle traps in helping to form solids larger than the cm sizes. Gap edges therefore appear as potential sites for the formation of additional planets.

When fragmentation is included, for $V_{\rm frag} = 10$ and $15\ {\rm m\,s^{-1}}$ grains are not able to grow large enough in the inner disk to overcome the radial-drift barrier. The inner disk is progressively lost to the star. For $V_{\rm frag} = 10\ {\rm m\,s^{-1}}$, fragmentation even prevents the majority of the grains from decoupling from the gas, they therefore follow the gas through the gap and migrate into the inner disk where their inward drift continues. The dust disk slowly drains and its density after 50 000 yr is very low. For $V_{\rm frag} = 15\ {\rm m\,s^{-1}}$, the planet gap is shallow, but the density difference is large enough to trap grains at the outer gap edge, where they start to overcome the fast migrating regime after 25 000 yr and grow slowly to reach cm sizes at 50 000 yr. In the very outer disk regions, the relative velocities between grains are low enough to remain below the fragmentation threshold and allow them to grow very slowly. Higher threshold values of $V_{\rm frag} = 20$ and $25\ {\rm m\,s^{-1}}$ help to retain more grains in the inner disk and a fraction of them overcomes the radial-drift barrier. A small population of grains survive in the inner disk after 25 000 yr, but do not grow much larger than cm sizes due to a limited reservoir. For $V_{\rm frag} = 20\ {\rm m\,s^{-1}}$, growth is more efficient at the outer gap edge as well as in the disk outer regions, so that an extended ring of cm grains forms at 50 000 yr. For $V_{\rm frag} = 25\ {\rm m\,s^{-1}}$, the outer disk is almost unaffected by fragmentation: it is very similar to the case with pure growth, with very efficient growth past cm sizes in a dense ring at the outer gap edge.

The fragmentation barrier appears as a major problem here. Low values of $V_{\rm frag} \sim 1 - 10\ {\rm m\,s^{-1}}$, are usually favored and are considered in most studies (e.g. Birnstiel et al. 2010; Pinilla et al. 2012)), they do not lead to any significant growth past the radial-drift barrier. Planets do exist however, and grains must be able to grow in PPD. Is this possible for $V_{\rm rel} \geq 20\ {\rm m\,s^{-1}}$? The answer seems to be yes. When taking into account grain porosity, numerical simulations have obtained values of $V_{\rm frag}$ of several tens of ${\rm m\,s^{-1}}$ (Wada et al. 2009; Meru et al. 2013). Both laboratory experiments (Teiser & Wurm 2009) and N-body simulations (Wada et al. 2013) have shown that mass transfer in high mass ratio collisions can lead to even higher values. Even if such cases represent only a fraction of all grain collisions in PPD, they may be enough to allow part of the dust population to grow to eventually form planetesimals.

3 Synthetic images

In order to determine the impact of growth and fragmentation on the planet gap detectability with ALMA and to assess whether the fragmentation threshold can be constrained by observations, we computed synthetic images from the resulting disk structure of each of our simulations. We first used the 3D Monte Carlo continuum radiative transfer code MCFOST (Pinte et al. 2006, 2009) to produce raw intensity maps from the dust distributions. These maps were then passed to the CASA* simulator for ALMA, to obtain synthetic images for a given observing configuration (wavelength, angular resolution, integration time). The procedure is described in detail in Gonzalez et al. (2012). To better compare with the images produced in the case of non-growing grains, we chose the standard disk parameters of Gonzalez et al. (2012): nearly face-on orientation, a distance $d = 140$ pc, a declination $\delta = -23^\circ$ and their optimal observing parameters for gap detection: integration time $t = 1$ h and angular resolution $\theta = 0.1''$ for 4 different wavelengths: 350 μm, 850 μm, 1.3 mm and 2.7 mm. The resulting images can also be used to estimate NOEMA's ability to detect gaps since it will reach a similar angular resolution to a factor of 2 at most. The smaller number of antennas will be partly compensated by

*http://casa.nrao.edu

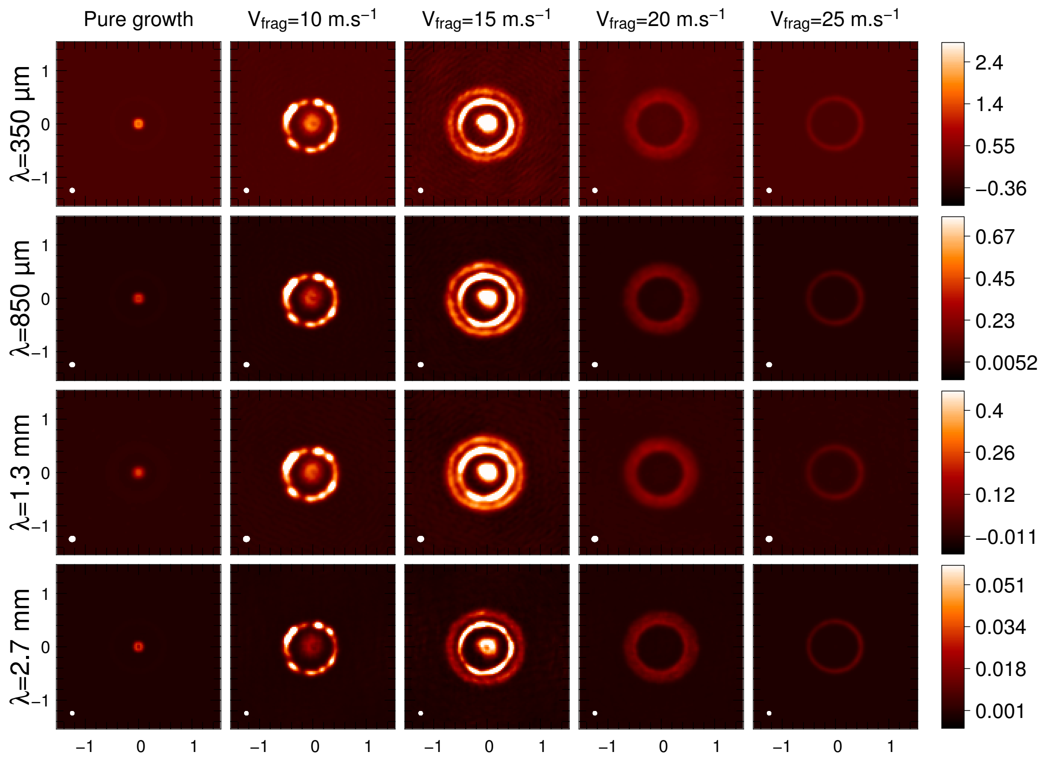

Fig. 2. Simulated ALMA observations of a disk viewed face-on at $d = 140$ pc and $\delta = -23°$ for an integration time of 1 h and angular resolution of $0.1''$. *From left to right:* Simulations with pure growth and with fragmentation for $V_{\mathrm{frag}} = 10$, 15, 20 and 25 $\mathrm{m\,s^{-1}}$. *From top to bottom:* $\lambda = 350$ μm, 850 μm, 1.3 mm and 2.7 mm. The scale on each image is in arcseconds, with the beam size represented at its bottom left corner, and the colorbar gives the flux in mJy/beam. (Note that the flux scale changes in each row, due to the different beam size.)

better sensitivy and by the longer exposure times needed for *uv*-plane coverage, thus allowing to reach similar fluxes. The images for pure growth and the four different fragmentation thresholds are shown in Fig. 2.

The images do not show the gap for all simulations. Indeed, the disk appearance at a given wavelength results from a combination of the dust density and the grain size. For non-growing grains (Gonzalez et al. 2012), computations chose grain sizes that contribute the most to the ALMA wavelengths and the planet gap was prominent in all cases. For growing and fragmenting grains, their sizes evolve and may end up outside the optimal range ($s \sim 20$ μm $-$ 1 mm for $\lambda = 350$ μm to 2.7 mm) for most of the dust population. This is the case when grains can efficiently reach large sizes: in the pure growth case or when $V_{\mathrm{frag}} \geq 20$ $\mathrm{m\,s^{-1}}$. Only a small fraction of grains have the appropriate sizes in a thin annulus in the outer disk, producing a faint ring in the images. For the pure growth case, the high density at the inner gap edge makes it detectable, even though the grain sizes are outside the optimal range. A prominent gap is seen only for the lower values $V_{\mathrm{frag}} = 10$ and 15 $\mathrm{m\,s^{-1}}$, for which there is a large enough population of grains of the right size at both gap edges. Unfortunately, the differences between each case are not large enough to unambiguously discriminate one from the other: the problem is too degenerate to constrain the fragmentation threshold.

4 Conclusion

We have run 3D hydrodynamical simulations of the evolution of dust grains in a PPD containing a planet in order to study the effect of growth and fragmentation on the formation of large solids at "particle traps" located at planet gap edges. Such traps are a possible solution to the barriers of planet formation, allowing the formation of planetesimals. We found that fragmentation strongly limits the growth of dust grains even in the presence of dust traps and, in combination with radial drift, contributes to the loss of the inner disk. However, large values of the fragmentation threshold ($V_{\mathrm{frag}} \geq 20$ $\mathrm{m\,s^{-1}}$), recently found to be realistc under certain conditions, allow grains to grow above centimetric sizes, and possibly to planetesimal sizes.

We produced synthetic images from our simulated disks and found that gap detection by ALMA or NOEMA is made more difficult by large values of the fragmentation threshold. However, discriminating between different values of $V_{\rm frag}$ from submillimeter images seems impractical without additional constraints.

This research was partially supported by the Programme National de Physique Stellaire and the Programme National de Planétologie of CNRS/INSU, France, and the Agence Nationale de la Recherche (ANR) of France through contract ANR-07-BLAN-0221. J.-F. Gonzalez's research was conducted within the Lyon Institute of Origins under grant ANR-10-LABX-66. G. Laibe is grateful for funding from the European Research Council for the FP7 ERC advanced grant project ECOGAL. C. Pinte acknowledges funding from the European Commission's FP7 (contract PERG06-GA-2009-256513) and ANR (contract ANR-2010-JCJC-0504-01). Computations were performed at the Service Commun de Calcul Intensif de l'Observatoire de Grenoble (SCCI). Figure 1 was made with SPLASH (Price 2007).

References

Barge, P. & Sommeria, J. 1995, A&A, 295, L1

Barrière-Fouchet, L., Gonzalez, J.-F., Murray, J. R., Humble, R. J., & Maddison, S. T. 2005, A&A, 443, 185

Birnstiel, T., Dullemond, C. P., & Brauer, F. 2010, A&A, 513, A79

Blum, J. & Wurm, G. 2008, ARA&A, 46, 21

Dullemond, C. P. & Dominik, C. 2005, A&A, 434, 971

Dzyurkevich, N., Flock, M., Turner, N. J., Klahr, H., & Henning, T. 2010, A&A, 515, A70

Fouchet, L., Gonzalez, J.-F., & Maddison, S. T. 2010, A&A, 518, A16

Fouchet, L., Maddison, S. T., Gonzalez, J.-F., & Murray, J. R. 2007, A&A, 474, 1037

Garaud, P., Meru, F., Galvagni, M., & Olczak, C. 2013, ApJ, 764, 146

Gonzalez, J.-F., Pinte, C., Maddison, S. T., Ménard, F., & Fouchet, L. 2012, A&A, 547, A58

Kretke, K. A. & Lin, D. N. C. 2007, ApJ, 664, L55

Laibe, G. 2014, MNRAS, 437, 3037

Laibe, G., Gonzalez, J.-F., Fouchet, L., & Maddison, S. T. 2008, A&A, 487, 265

Laibe, G., Gonzalez, J.-F., & Maddison, S. T. 2012, A&A, 537, A61

Méheut, H., Meliani, Z., Varnière, P., & Benz, W. 2012, A&A, 545, A134

Meru, F., Geretshauser, R. J., Schäfer, C., Speith, R., & Kley, W. 2013, MNRAS, 435, 2371

Pinilla, P., Birnstiel, T., Ricci, L., et al. 2012, A&A, 538, A114

Pinte, C., Harries, T. J., Min, M., et al. 2009, A&A, 498, 967

Pinte, C., Ménard, F., Duchêne, G., & Bastien, P. 2006, A&A, 459, 797

Price, D. J. 2007, PASA, 24, 159

Teiser, J. & Wurm, G. 2009, MNRAS, 393, 1584

Wada, K., Tanaka, H., Okuzumi, S., et al. 2013, A&A, 559, A62

Wada, K., Tanaka, H., Suyama, T., Kimura, H., & Yamamoto, T. 2009, ApJ, 702, 1490

Weidenschilling, S. J. 1977, MNRAS, 180, 57

Windmark, F., Birnstiel, T., Güttler, C., et al. 2012, A&A, 540, A73

Zsom, A., Ormel, C. W., Güttler, C., Blum, J., & Dullemond, C. P. 2010, A&A, 513, A57

SF2A 2014
J. Ballet, F. Bournaud, F. Martins, R. Monier and C. Reylé (eds)

DARK CLOUD CHEMISTRY OF NITROGEN HYDRIDES WITH THE HERSCHEL SPACE OBSERVATORY

R. Le Gal[1], P. Hily-Blant[1,2] and A. Faure[1]

Abstract. Stars form in dark clouds. A complete knowledge of dark cloud chemical composition can be helpful to understand star- and planet-formation processes. Nitrogen is the sixth most abundant interstellar element, and also a basic component of prebiotic molecules. Yet, the reservoir of gaseous nitrogen in dark clouds is not precisely known. It is expected to be mainly N and/or N_2, but both are unobservable in dark gas. Their abundances therefore derive indirectly from those of other N-bearing species through chemical modelling. In this context, our work focuses on a revision of the nitrogen-hydride chemistry in dark clouds using fundamental rotational transitions of NH, NH_2, and NH_3 observed with *Herschel*/HIFI towards a sample of low-mass protostellar objects. To this purpose, we update and upgrade a chemical network containing the chemistry of the *ortho* and *para* forms of nitrogen-hydride molecules, allowing to reproduce the NH : NH_2 : NH_3 ratios observed with *Herschel*/HIFI towards IRAS 16293-2422, putting constraints on the budget of gas-phase carbon, oxygen and sulphur. Furthermore, our results explain the non-thermodynamical *ortho*-to-*para* ratio of ammonia observed in cold diffuse gas.

Keywords: gas-phase astrochemistry, interstellar molecule abundances, dark cloud conditions.

1 Introduction

Nowadays, a comprehensive view of the chemical content of the densest parts of the interstellar medium (ISM), where stars form, is still lacking. One such issue regards the nitrogen chemistry in dark clouds. Our strategy has been to compare recent *Herschel* observations with chemical models in order to constrain, and so try to understand, the nitrogen chemistry.

1.1 Nitrogen riddle

Nitrogen (^{14}N) is, in abundance, the sixth element in our local Universe (after the hydrogen, helium, carbon, oxygen and neon elements, see *e.g.* Nieva & Przybilla 2012) with a nuclear spin $I = 1$ playing a crucial role in nitrogeneous molecule spectroscopy by inducing an hyperfine structure. As of today, almost 70 N-bearing species have been detected through their rotational transitions in the gas-phase ISM from diatomic molecules, *e.g.* CN (McKellar 1940; Adams 1941) and NH (Meyer & Roth 1991), to complex organic molecules (COMs) with up to 13 atomes, with $HC_{11}N$ (Bell et al. 1997), in a wide range of astrophysical objects in our Galaxy and in more distant galaxies, from diffuse gas (Liszt & Lucas 2001) to prestellar cores (Bergin & Tafalla 2007) and protoplanetary disk (Dutrey et al. 2007). N-bearing molecules can thus serve as tools to probe the physico-chemistry of the ISM. For instance, CN is a probe of magnetic fields in dense regions (thanks to the Zeeman effect, see *e.g.* Crutcher 2012), N_2H^+ and its isotopologue N_2D^+ are tracers of the high density regions ($n \sim 10^5\,\mathrm{cm}^{-3}$, Pagani et al. 2007; Crapsi et al. 2007), the inversion transitions of ammonia can probe the gas temperature in molecular clouds (Walmsley & Ungerechts 1983; Maret et al. 2009). Nitrogen is also an essential component of Earth-like life-related molecules, explaining why there is a great interest in its initial form during planet formation (Geiss & Bochsler 1982; Mumma & Charnley 2011).

So, a natural question arising is : What is the nitrogen reservoir in the ISM? Is it in the form of NH_3, hidden in ices, or in gaseous form as N or N_2, or in something else? The problem is that, in dark clouds, neither of these two latter forms are observable. But, other N-bearing molecules can serve as indirect probes, for instance nitriles (HCN, HNC, CN *etc.*) and nitrogen hydrides (NH, NH_2, NH_3).

[1] Université Grenoble Alpes/CNRS, Institut de Planétologie et d'Astrophysique de Grenoble (IPAG) UMR 5274, France
[2] Institut Universitaire de France

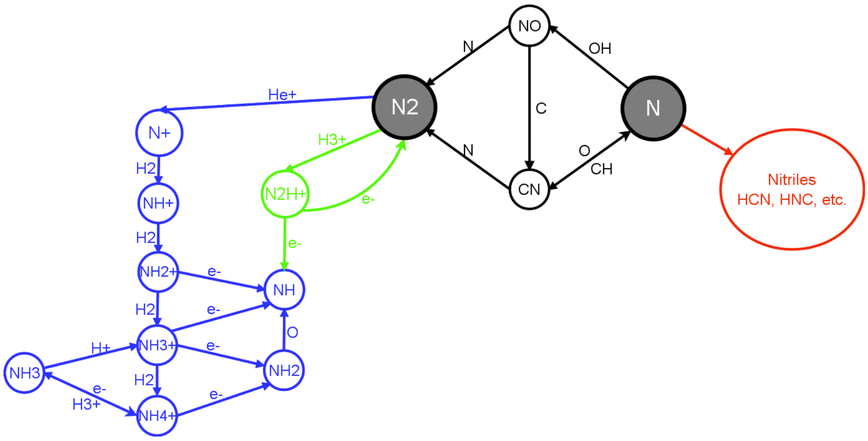

Fig. 1. The principal gas-phase reactions involved in the first stages of nitrogen-hydride interstellar chemistry in dark clouds. The main formation route of NH is highlighted (green). Adapted from Hily-Blant et al. (2013).

1.2 Interstellar nitrogen chemistry

The reduced network presented on Figure 1, representing the first stages of nitrogen-hydride chemistry in dark gas, shows that nitriles result from atomic nitrogen and N-hydrides from molecular nitrogen. The latter point is specific to nitrogen chemistry in cold gas. As for carbon or oxygen chemistry, the ionic form of the atomic element is needed to form hydrides, but, in the case of nitrogen chemistry, the ionisation potential of nitrogen is higher (14.53 eV) than that of hydrogen. Moreover, the reaction between N and ${H_3}^+$ is endoenergetic contrary to its analogues in carbon and oxygen chemistry. N^+ is in fact mainly formed from the dissociative ionisation reaction between N_2 and He^+, (the direct cosmic-ray ionisation being less efficient) and can then initiate the nitrogen-hydride formation. As a consequence, the N/N_2 ratio could, for instance, be constrained *via* a combination of nitrile and N-hydride observations.

Our study of the interstellar nitrogen chemistry has focussed on the three nitrogen hydrides NH, NH_2, and NH_3 in cold gas, thanks to hitherto unprecedented observations performed with the HIFI instrument (Roelfsema et al. 2012) onboard the *Herschel* Space Observatory (HSO) (Pilbratt et al. 2010). Ratios of these N-hydrides have been derived in diffuse cold gas with $NH : NH_2 : NH_3 \approx 1 : 1 : 1$ (Persson et al. 2010), and, in the cold envelope of the low-mass protostar IRAS 16293-2422, with $NH : NH_2 : NH_3 \approx 3 : 1 : 20$ (Hily-Blant et al. 2010; Le Gal et al. 2014).

The reduced chemical network, Figure 1, also shows that one of the first stages of the interstellar chemistry of nitrogen hydrides is the N to N_2 conversion. This process has profound consequences on the kinetics of interstellar nitrogen chemistry because neutral-neutral reaction rates are typically ten to a hundred times lower than Langevin rates, characteristic of ion-neutral reactions. Therefore, the synthesis of nitrogen hydrides, under cold conditions, is considered to be a slow process compared to carbon- or oxygen-hydride formation proceeding directly through ion-neutral reactions.

1.3 Influence of the H_2 o/p

On the reduced network presented in Figure 1, the main pathway of the NH formation is highlighted in green. We see that it differs from the synthesis of NH_2 and NH_3. NH predominantly results from the dissociative recombination (DR) of N_2H^+, itself deriving from the proton-exchange reaction $N_2 + H_3^+$, while NH_2 and NH_3 proceed from the DR of NH_4^+, which itself results from a series of H_2 hydrogenations from N^+ (product of the reaction $N_2 + He^+$, as previously discussed). Therefore, H_2 plays an important role in the formation of NH_2 and NH_3 but not in that of NH.

H_2 forms on grain surfaces in its two nuclear configurations, *ortho* (H_2(o)) and *para* (H_2(p)), in an H_2 o/p ratio supposed to be equal to its nuclear spin statistical value of 3 : 1. Once formed, H_2 undergoes proton-exchange reactions with the major protonated ions of the medium (H^+, H_3^+, and HCO^+) which tend to decrease the H_2 o/p towards the thermal value. Below 100 K, the two H_2 spin modifications are essentially in their fundamental states, separated by an energy of 170.5 K, H_2(o) lying above the H_2(p). The key reaction $N^+ + H_2$, initiating N-hydride formation, has a small endoenergeticity close to this energy difference ($\sim$ 200 K, according to Gerlich 2008). Dislaire et al. (2012) have revised the rate of this reaction using all available experimental data, showing that, when the temperature decreases, the impact of the H_2 o/p value on the reaction rate increases. So the formation of NH_2 and NH_3 depends on the H_2 o/p, in contrast to the NH formation. In that way, Dislaire et al. (2012) have shown that the NH : NH_2 ratio measurement can constrain the H_2 o/p in dark clouds : H_2 o/p $\approx 10^{-3}$. This value is consistent with the Flower et al. (2006b) prediction, who pointed out that at low temperature the H_2 o/p thermal value is not reached due to the competition between the H_2 recycling on grains and the proton-exchange reactions. Typically at 10 K, this value is by four orders of magnitude higher than the Boltzmann equilibrium value ($\approx 3 \times 10^{-7}$ at 10 K). Pagani et al. (2009) obtained a similar conclusion using the deuterium fractionation of molecules (H_2 o/p $\lesssim 10^{-1}$).

2 Modelling

2.1 A new *ortho-para* nitrogen chemical network

Our work has consisted in revising the *ortho-para* chemical network of nitrogen hydrides in order to understand their abundances, derived from *Herschel*/HIFI observations towards low-mass protostars, in cold gas. As mentioned above, Dislaire et al. (2012) have stressed the critical influence of the H_2 o/p on the N-hydride chemistry. In the continuity of this work, we undertook the update of N-chemistry with self-consistent computation of the H_2 o/p. To this purpose, we employed the chemical network initially developed by Flower et al. (2006a) including the *ortho* and *para* forms of H_2 and N-hydrides. Another advantage of this network is that it only contains a small number of reactions (1755) and species (146) compared to those commonly used (such as the OSU and UMIST networks, containing each $\sim$ 6000 reactions and $\sim$ 600 species without including *ortho* and *para* forms).

We first updated the ion-molecule hydrogen chemistry of this network using the recent data of Honvault et al. (2011, 2012), Dos Santos et al. (2007), McCall et al. (2004), and Hugo et al. (2009) for the reaction $H^+ + H_2$, $H_3^+ + H_2$ and $H_3^+ + e^-$. Then, we updated the N-hydride *ortho-para* synthesis, including nuclear spin branching ratios, as detailed in Rist et al. (2013). We also updated the N to N_2 conversion reactions, thanks to new theoretical calculations and experimental measurements (Jorfi & Honvault 2009; Daranlot et al. 2011, 2013), showing that the kinetic rates are lower than previously thought, implying a slowing down of the chemistry. This confirms that nitrogen-hydride synthesis is a late process. We also updated the branching ratios (BR) for the DR of nitrogen-hydride ions (see Hily-Blant et al. 2010, and reference therein), and especially the rate and BR of the N_2H^+ DR, with a 7% BR into NH (see Vigren et al. 2012). Some oxygen reactions such as the H_3O^+ DR (Jensen et al. 2000) and the H_3^+ + O reaction (KIDA recommandation, Wakelam et al. 2012) were also updated.

2.2 Building our model

Gas-grain reactions are not considered in this work, except for the H_2 formation and charge-exchange reactions. Our new gas-phase chemical network contains 103 species and 907 reactions and is valid up to a temperature of $\simeq$ 50 K. The rate equations were solved with the chemical code of Flower et al. (2006a) to obtain the gas-phase abundance as function of time, until a steady-state is reached, for a temperature of 10 K, a density $n_H = 10^4\,cm^{-3}$, and an ionisation rate $\zeta = 1.3 \times 10^{-17}\,s^{-1}$. The freeze-out of gas-phase species onto grains was included through depleted initial abundances (Le Gal et al. 2014). Concerning these initial abundances, we note that the elemental oxygen abundance is uncertain by up to one order of magnitude and the elemental sulphur abundance by three orders of magnitude. As a result, we chose to vary these two parameters in our model, resulting in particular in an elemental gas-phase C/O ratio varying between 0.3 and 1.5 (*via* the oxygen abundance).

2.3 Results

Our new chemical model emphasizes the influence of several parameters in the nitrogen-hydride chemistry, as the gas-phase elemental C/O ratio or the elemental gas-phase amount of sulphur (Le Gal et al. 2014). The impact of the gas-phase elemental C/O ratio on N-hydride abundances results from the fact that N_2 involves carbon and oxygen for its formation *via* the N + CH or N + OH reactions. We identified two distinct regimes : a low C/O regime with C/O < 0.8 and a high C/O regime where C/O > 1. For these regimes N_2:N > 1 and the fractional abundance (with respect to hydrogen nucleus) of NH_3 is a few 10^{-8}, but in the high C/O regime

NH and NH_2 abundances are significantly lower because atomic carbon becomes one of their main destroyer. Concerning the total gas-phase amount of sulphur $[S]_{tot}$, we showed that its enhancement drastically diminishes the efficiency of the N to N_2 conversion. Sulphur is indeed mostly in its ionic form S^+, due to its low ionisation potential (10.36 eV), making it the main carrier of positive charge when its abundance increases. It is also the main destroyer of CH and OH, essential to the N to N_2 conversion. Thus, a high elemental gas-phase sulphur abundance (8.0×10^{-6}) diminishes by up to two orders of magnitude the abundances of several nitrogen species.

Finally, we obtain a *best model* for an elemental gas-phase C/O ratio of 0.8 and a total gas-phase sulphur abundance of $[S]_{tot} = 8.0 \times 10^{-8}$, reproducing the observations of NH, NH_2, and NH_3 performed by *Herschel*/HIFI in typical dark gas physical conditions, towards the Sun-like protostar IRAS 16293-2422 (Hily-Blant et al. 2010). At that time, this was not possible with any existing chemical models.

On the left panel of Figure 2 we see that our chemical model predicts $NH{:}NH_2 > 1$, as observed in the cold envelope of IRAS 16293-2422, confirming the main pathway to form NH suggested by Dislaire et al. (2012) and experimentally confirmed by Vigren et al. (2012): the N_2H^+ DR. Our *best model* thus leads to $NH : NH_2 : NH_3 \sim 3 : 1 : 3$, compatible with the observed ratio of $3 : 1 : 20$, within the error bar of observations. Higher values of $[S]_{tot}$ are also possible, but abundances as high as 8.0×10^{-6} are clearly excluded by our steady state models, as well as a C/O ratio outside the range $0.7 - 0.8$. For early times ($\sim 2 - 5$ Myrs), the observations can be reproduced with similar total abundance of sulphur, (*i.e.* $[S]_{tot} < 8.0 \times 10^{-6}$) and a slightly higher C/O, in the $0.9 - 1.1$ range. We also observe (see left panel of Figure 2) that the H_2 o/p is $\sim 10^{-3}$, as in Dislaire et al. (2012), and it does weakly depend on C/O.

Besides, thanks to our new chemical network, we published in Faure et al. (2013) an explanation to the non-thermodynamical NH_3 o/p ratio (< 1) observed by Persson et al. (2012). The right panel of Figure 2 represents our chemical model predictions for the NH_2 and NH_3 *ortho*-to-*para* ratios which are in good agreement with the observed ratios of 2.3 (C. Persson priv. comm.) and ~ 0.7 (Persson et al. 2012), derived in a 30 K gas. Those ratios are thus compatible with a pure gas-phase chemistry obeying nuclear spin selection rules in an H_2(p) enriched gas (*i.e.* o/p $H_2 < 10$ %).

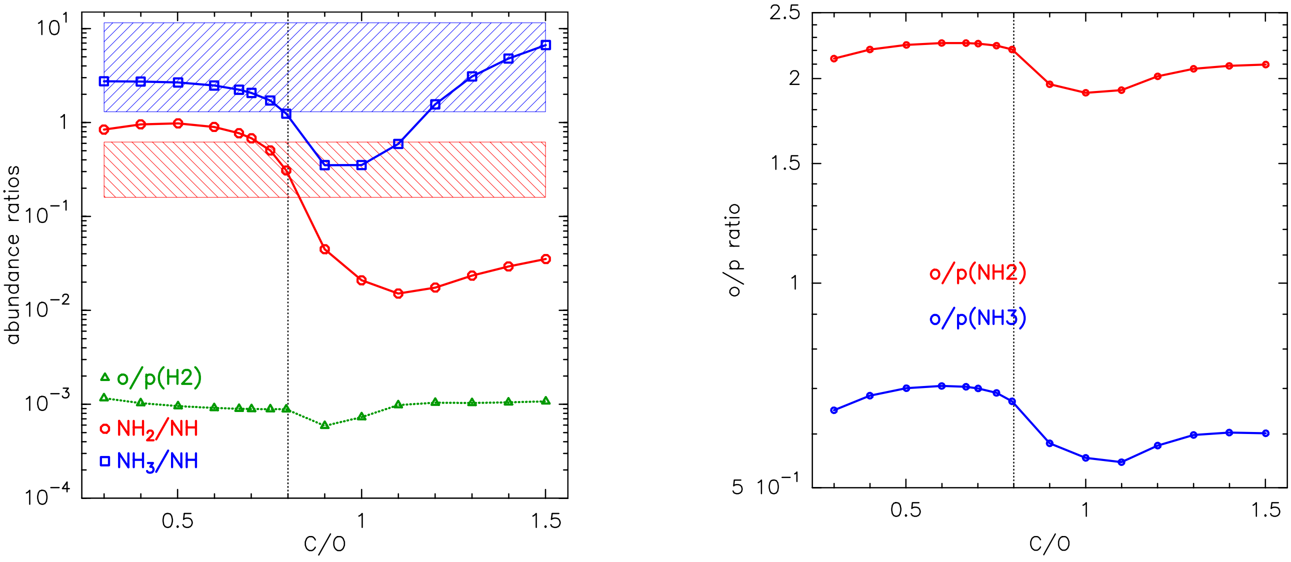

Fig. 2. Left: Nitrogen-hydride ratios (blue and red) derived from observations towards IRAS 16293-2422 (hatched boxes) *vs* our steady-state model predictions (solid lines) with the evolution of the H_2 o/p at steady-state (green), as a function of the elemental gas-phase C/O. **Right:** Evolution of our NH_2 and NH_3 o/p steady-state model predictions with C/O.

3 Conclusions and future works

The aim of our work was to understand in details the gas-phase processes of nitrogen chemistry in dark gas conditions, relying on cold envelope observations in foreground of different low-mass protostars, representatives of dark gas conditions. In Le Gal et al. (2014), the comparison being restricted to only one astrophysical object

(IRAS 16293-2422), one is led to question the validity and, where appropriate, to question the generalisation of these results in other cold protostellar envelopes. This is why we are now working on *Herschel*/OT1 (PI: Hily-Blant) data obtained in the cold envelope of a sample of other low-mass protostars. These data have provided detections in absorption, in the foreground of *continuum* emitted by deeply embedded protostars, of several rotational lines of ammonia and hyperfine structures of fundamental rotational transitions of amidogen (NH_2) and imidogen (NH), allowing a robust determination of their column densities. Overall, $NH:NH_2 \sim 2:1$ towards three other protostellar envelopes, confirming the $NH > NH_2$ result found in the cold envelope of IRAS 16293-2422 (Hily-Blant et al. 2010). Analysis of these data is still in progress.

References

Adams, W. S. 1941, ApJ, 93, 11

Bell, M. B., Feldman, P. A., Travers, M. J., et al. 1997, ApJ, 483, L61

Bergin, E. A. & Tafalla, M. 2007, ARA&A, 45, 339

Crapsi, A., Caselli, P., Walmsley, M. C., & Tafalla, M. 2007, A&A, 470, 221

Crutcher, R. M. 2012, ARA&A, 50, 29

Daranlot, J., Hu, X., Xie, C., et al. 2013, Physical Chemistry Chemical Physics (Incorporating Faraday Transactions), 15, 13888

Daranlot, J., Jorfi, M., Xie, C., et al. 2011, Science, 334, 1538

Dislaire, V., Hily-Blant, P., Faure, A., et al. 2012, A&A, 537, A20

Dos Santos, S. F., Kokoouline, V., & Greene, C. H. 2007, J. Chem. Phys., 127, 124309

Dutrey, A., Henning, T., Guilloteau, S., et al. 2007, A&A, 464, 615

Faure, A., Hily-Blant, P., Le Gal, R., Rist, C., & Pineau des Forêts, G. 2013, ApJ, 770, L2

Flower, D. R., Pineau des Forêts, G., & Walmsley, C. M. 2006a, A&A, 456, 215

Flower, D. R., Pineau des Forêts, G., & Walmsley, C. M. 2006b, A&A, 449, 621

Geiss, J. & Bochsler, P. 1982, Geochim. Cosmochim. Acta, 46, 529

Gerlich, D. 2008, *Low temperatures and cold molecules*, i. Smith edn. (Imperial College Press), 121–174

Hily-Blant, P., Bonal, L., Faure, A., & Quirico, E. 2013, Icarus, 223, 582

Hily-Blant, P., Maret, S., Bacmann, A., et al. 2010, A&A, 521, L52

Honvault, P., Jorfi, M., González-Lezana, T., Faure, A., & Pagani, L. 2011, Physical Chemistry Chemical Physics (Incorporating Faraday Transactions), 13, 19089

Honvault, P., Jorfi, M., González-Lezana, T., Faure, A., & Pagani, L. 2012, Physical Review Letters, 108, 109903

Hugo, E., Asvany, O., & Schlemmer, S. 2009, J. Chem. Phys., 130, 164302

Jensen, M. J., Bilodeau, R. C., Safvan, C. P., et al. 2000, ApJ, 543, 764

Jorfi, M. & Honvault, P. 2009, Journal of Physical Chemistry A, 113, 10648

Le Gal, R., Hily-Blant, P., Faure, A., et al. 2014, A&A, 562, A83

Liszt, H. & Lucas, R. 2001, A&A, 370, 576

Maret, S., Faure, A., Scifoni, E., & Wiesenfeld, L. 2009, MNRAS, 399, 425

McCall, B. J., Huneycutt, A. J., Saykally, R. J., et al. 2004, Phys. Rev. A, 70, 052716

McKellar, A. 1940, PASP, 52, 187

Meyer, D. M. & Roth, K. C. 1991, ApJ, 376, L49

Mumma, M. J. & Charnley, S. B. 2011, ARA&A, 49, 471

Nieva, M.-F. & Przybilla, N. 2012, A&A, 539, A143

Pagani, L., Bacmann, A., Cabrit, S., & Vastel, C. 2007, A&A, 467, 179

Pagani, L., Vastel, C., Hugo, E., et al. 2009, A&A, 494, 623

Persson, C. M., Black, J. H., Cernicharo, J., et al. 2010, A&A, 521, L45+

Persson, C. M., De Luca, M., Mookerjea, B., et al. 2012, A&A, 543, A145

Pilbratt, G. L., Riedinger, J. R., Passvogel, T., et al. 2010, A&A, 518, L1

Rist, C., Faure, A., Hily-Blant, P., & Le Gal, R. 2013, Journal of Physical Chemistry A, 117, 9800

Roelfsema, P. R., Helmich, F. P., Teyssier, D., et al. 2012, A&A, 537, A17

Vigren, E., Zhaunerchyk, V., Hamberg, M., et al. 2012, ApJ, 757, 34

Wakelam, V., Herbst, E., Loison, J.-C., et al. 2012, ApJS, 199, 21

Walmsley, C. M. & Ungerechts, H. 1983, A&A, 122, 164

Session 11

Atelier AS Gaia

SF2A 2014
J. Ballet, F. Bournaud, F. Martins, R. Monier and C. Reylé (eds)

PREPARING THE MODELLING OF GAIA PRODUCTS FOR GALACTIC STRUCTURE AND DYNAMICS WITH MOCK DATASETS

Laurent Chemin[1, 2]

Abstract. A series of workshops – the 'Gaia Challenge' – has been initiated in 2013 to prepare the scientific exploitation of Gaia data. The first position and velocity observables from Gaia will be released early in 2017. Within this context, I present results from numerical tools developed to constrain Galactic structural and dynamical properties from pseudo Gaia observables (mock data).

Keywords: Galaxy, Milky Way, Structure, Dynamics, Gaia, stars, pattern speed, mass model

1 The Gaia Challenge: preparing the exploitation of Gaia

The European Space Agency Gaia mission* is currently scanning the whole sky. It has been designed to constrain the 2×3D position and velocity space of the Milky Way from an astrometric and photometric survey of about $\sim 10^9$ stars, complemented with a spectroscopic survey of $\sim 10^8$ stars. The Gaia Challenge† collaboration has been recently initiated to prepare the scientific exploitation of Gaia data. Its aim is to develop, improve and apply various techniques to mock Gaia data in order to recover important physical quantities of the Galaxy, like its gravitational potential and the phase-space structure of stars. It is organized around five working groups: 'Streams & Halo Stars', 'Collisional Systems', 'Discs', 'Spherical & Triaxial', and 'Astrophysical Parameters' of stars. The mock Gaia observables come from N-body simulations.

I present here two preliminary results from the numerical tools I have developed for Galactic structure and dynamics, within the framework of the Discs working group. The pseudo-observational Gaia dataset necessary to develop these tools have been obtained from N-body simulations of Hunt & Kawata (2013) and Hunt et al. (2013).

2 Pattern speeds of the Galactic bar and spiral density waves

The pattern speeds (Ω_p) of bars and spirals are fundamental parameters in galactic dynamics. They are needed to determine the orbital structure of dynamical tracers (stars, gas clouds) in discs, and the location of resonances with the disc itself, which in return are essential to understand the structure of discs. One of the many issues for the analysis of Gaia data will be to derive Ω_p of the Galactic bar and other density waves.

Several methods have been proposed by Gaia challengers. For instance, Monari et al. (2013) analyze the U, V velocity space at different Galactic radii and in the Solar neighbourhood to infer the location of the Outer Lindblad Resonance of the bar. Then, the corotation radius and Ω_p can be deduced once a Galactic rotation curve is known. For this challenge, I propose to apply the Tremaine-Weinberg method (Tremaine & Weinberg 1984, hereafter TW). Only Debattista et al. (2002) investigated the possibility to use the radio emission from OH/IR stars to constrain Milky Way pattern speeds by the TW method. However the method has been applied almost exclusively to other galaxies. In particular, it has allowed to show how stellar bars preferentially rotate

e-mail: astro.chemin@gmail.com
[1] Univ. Bordeaux, LAB, UMR 5804, F-33270, Floirac, France
[2] CNRS, LAB, UMR 5804, F-33270, Floirac, France
*http://www.cosmos.esa.int/web/gaia
†http://astrowiki.ph.surrey.ac.uk/dokuwiki/doku.php?id=start

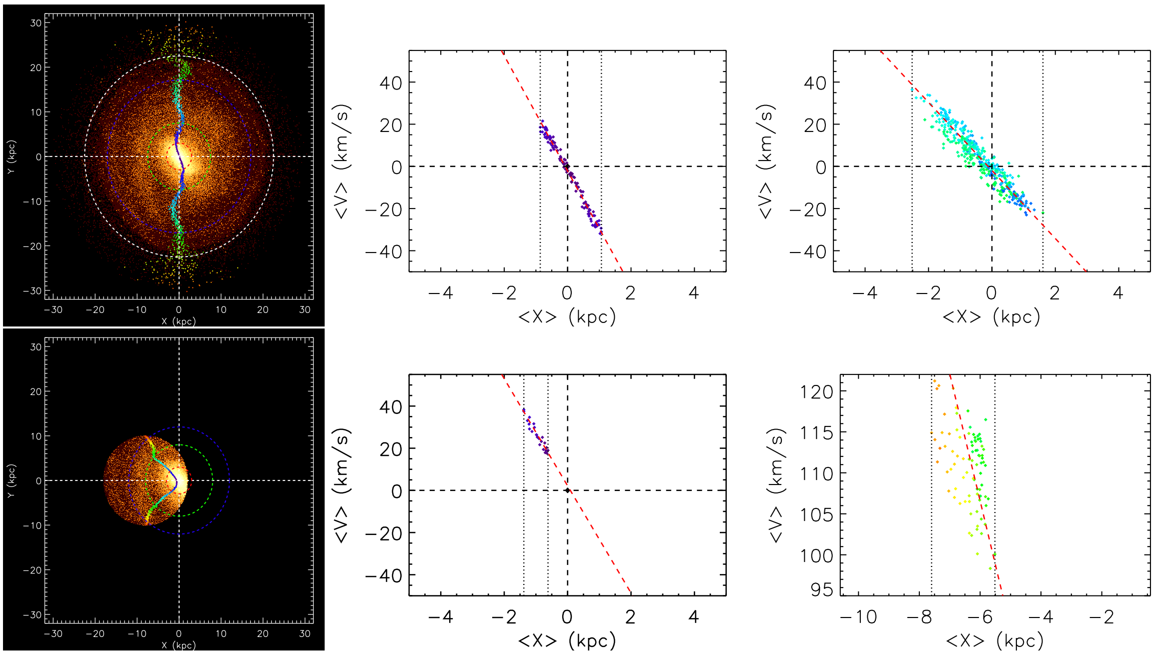

Fig. 1. Derivation of Galactic pattern speeds from mock Gaia data, with the Tremaine-Weinberg method. The top panels are results for the reference full simulation, the bottom panel for the limited volume 'Gaia' dataset. The reconstructed stellar surface density map is shown in the left-hand column, Eq. 2.1 for the bar pattern speed in the middle column, and for the inner spiral pattern speed in the right-hand column. Linear fits to the relationships are the dashed lines, and the colour code simply marks the $y-$coordinate of each point. Dashed circles mark the radii that identify the regions needed for linear fits of the bar and spiral arms pattern speeds.

fastly in early-type discs, while more dark matter dominated discs tend to have slower bars (Corsini 2011, and references therein).

Assuming that the observed kinematical tracer satisfies the continuity equation, and that the target density wave has a well defined pattern angular speed, the method stipulates that integrals of velocities with respect to position are linked with Ω_p and integrals of position with respect to position. From a Galactic viewpoint, the TW method writes in Cartesian coordinates:

$$\int_{-\infty}^{\infty} \Sigma(x,y,t)\ v_y(x,y,t)\ dx = \Omega_p \int_{-\infty}^{\infty} \Sigma(x,y,t)\ x\ dx \tag{2.1}$$

where Σ is the mass surface density of the tracer, and v_y the $y-$component of its velocity vector which is related to the U, V Galactic velocity components and the azimuthal angle θ by $v_y = V\cos(\theta) + U\sin(\theta)$. Since the $x-$ and v_y-integrals vary as y varies due to variation in surface density and velocities, the pattern speed is the slope of Eq. 2.1 in the $< x >, < v_y >$ parameter space.

I have used the barred+spiral disc simulations by Hunt et al. (2013) as provisional mock data. The Navarro-Frenk-White dark matter halo contribution has a virial mass of $\mathrm{M}_{200} = 2\ 10^{12}\ \mathrm{M}_{\odot}$, and a halo concentration of $c = 9$ in the initial simulations. The mock Gaia data consist in equatorial positions, parallaxes, proper motions, radial velocities and Gaia magnitudes, which have been converted to the Galactic rest frame using $x, y, z = -8, 0, 0$ kpc and $U, V, W = 0, 228, 0$ km s^{-1} as Sun parameters. Each particle can be considered as a group of a few thousand red clump stars. Surface density maps and velocity fields have first been built. I have considered all 'stars' within $|z| = 1$ kpc from the equatorial plane. To demonstrate the feasibility of the method with the most accurate distances, all stars distant by more than 10 kpc from the Sun position have been discarded from the mock data. This limited Gaia-observable volume is indeed the expected one where Gaia distance accuracy will be $\leq$10% for bright stars. For sake of comparison, the TW method is also applied to the whole mock disc data, again with the only $|z| \leq 1$ kpc constraint (top panels of Fig. 1). Then, integrals of Eq. 2.1 have been calculated for about 1300 $y-$ wedges parallel to the $y = 0$ axis, separated by Δy =50 pc. The derived $x-$integrals of the right-member in Eq. 2.1 are shown as coloured dots in Fig. 1. The colour code

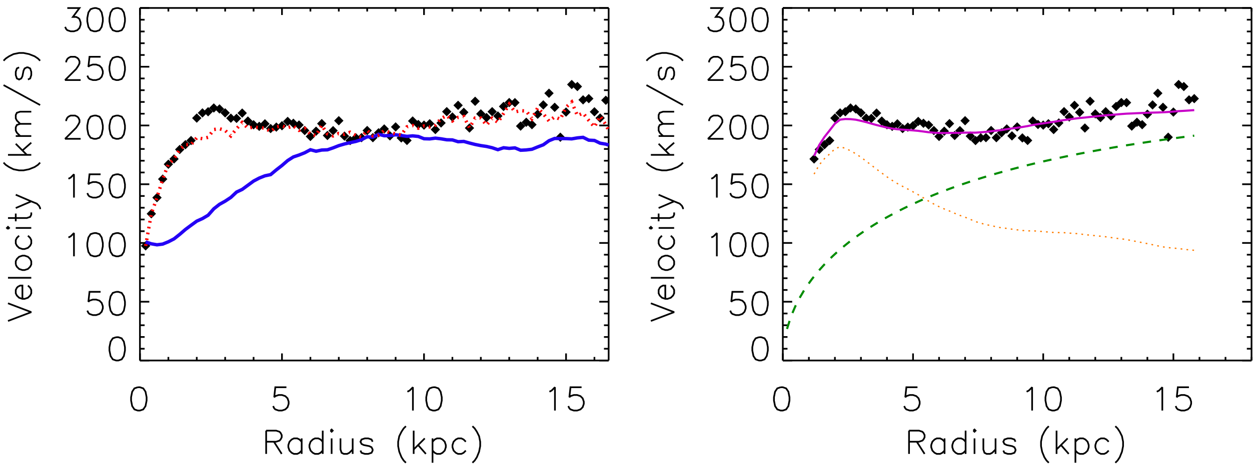

Fig. 2. Left: Derived rotation curve with and without asymmetric drift correction (filled diamonds and blue solid line, respectively) from the mock Gaia data. The mock data are based on N-body simulations of Hunt et al. (2013). The red dotted line is the rotation curve from the reference full volume mock dataset. **Right:** Mass distribution model of the rotation curve. A solid line represents the total mass model, a dotted line the stellar disc contribution, a dashed line the dark matter halo contribution (Navarro-Frenk-White model).

from blue to red colours is for increasing values of $|y|$. Then, the regions where the $x-$locations significantly deviate from $x = 0$ and where the v_y-integral converge have been isolated to identify the regions of the stellar bar and spiral arms, and linear fits to the $< x >, < v_y >$ relationship yield the slope of Eq. 2.1 for each of these regions.

With the reference full simulated volume, it is found a bar pattern speed $\Omega_p = 27$ km s^{-1} kpc^{-1}, and two inner and outer spiral patterns of angular speed of 16 and 9 km s^{-1} kpc^{-1}, respectively. The isolated data corresponding to the bar and inner spiral patterns are shown in middle and right panels of Fig. 1.

The shape of the integrals are different for the limited Gaia-like volume. Here, the opposite disc half to the Sun with respect to the Galactic Centre cannot be observed. As a consequence, the bar region at $y < 0$ is not seen in the density map, and all the positive $x-$integrals seen in the upper panels have naturally disappeared. The $x-$integrals quickly converge towards the location of the spiral structure, as this latter rapidly dominates the stellar mass density for $x, y < 0$. Then, once bar and spiral points have been isolated, it is found $\Omega_p = 25$ km s^{-1} kpc^{-1} for the bar, and $\Omega_p = 16$ km s^{-1} kpc^{-1} for the inner spiral arm. No outer arm is seen in the limited volume. Both values remain in agreement with the whole mock data, though the bar pattern speed is slightly smaller. This latter result is expected because integrals are performed within $[-\infty, \infty]$, and the $x-$integrals in the bar region have become contaminated by the slower spiral structure. The 'loss' of bar surface density is made at the benefits of the 'gain' of spiral surface density. I expect that a radially dependent TW method would avoid that minor artefact. This will constitute future improvements for this work. Another improvement will be for instance to develop a derivation tool based on a two-dimensional reference grid. This should significantly improve the estimate of the bar pattern speed.

3 Mass distribution modelling

More important objectives of the Gaia mission will be to determine the structure and the mass distribution of the Milky Way Disc from the 2×3D position and velocity space. Promising methods for dynamical modelling are e.g. action-based distribution functions (e.g. Bovy & Rix 2013) or made-to-measure models (e.g. Hunt & Kawata 2013). I am developing tools that build stellar density map(s), the Galactic U, V, W velocity fields, derive Galactic structural parameters (e.g. disc scalelength and scaleheight), velocity dispersion profiles and rotation curve, the asymmetric drift correction, and fit mass distribution models using a library of dark matter halo models.

Figures 2 and 3 present some of the provisional results obtained using a mock Gaia dataset based on simulations of Hunt et al. (2013). Results are for the same volume limited mock dataset as in §2 and Fig. 1.

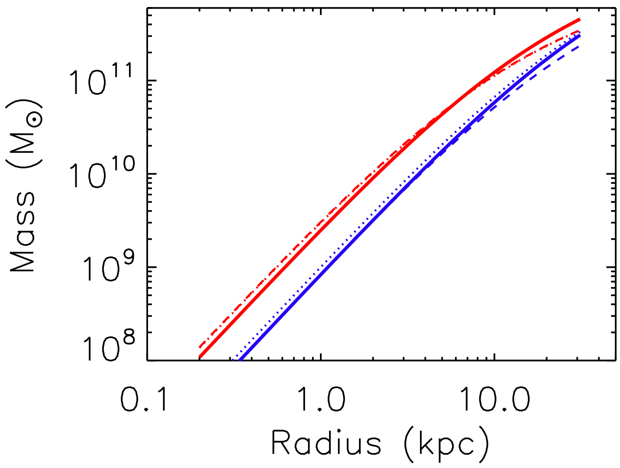

Fig. 3. Input and fitted mass profiles of the dark matter halo. Blue lines are for bar+spiral mock Gaia data (red lines for another type of mock data not discussed in the text). A solid line corresponds to the input Navarro-Frenk-White dark matter contribution in the simulations of Hunt et al. (2013), a dashed line to the fitted mass profile to the full mock volume, and a dotted line to fitted mass profile fitted to the volume-limited mock data.

The average radial force and azimuthal velocity curve profiles are derived (solid line in Fig. 2), to which is quadratically subtracted the asymmetric drift to yield the rotation curve (filled symbols). The rotation curve expected from the full reference mock volume is the dotted line. It is interesting to note that the shape of the rotation curve from the limited mock volume differs by ~ 20 km s^{-1} from the one in the whole mock volume, for $R = 1.5 - 3$ kpc. This is caused by the asymmetric stellar density and velocity distributions within the bar region. Within the whole mock volume, density and kinematical asymmetries are more efficiently averaged (all azimuthal angles are used), while the volume-limited mock data automatically enhance stellar asymmetries (azimuth is only partially covered by selection effects).

Mass models have then been fitted to the rotation curve using the surface density profile of the stellar disc and a Navarro-Frank-White dark matter halo model. The inferred mass profile is shown in Fig. 3 (blue dotted line). The difference with the input NFW mass model of Hunt et al. (2013) (solid line) is negligible, even with the volume-limited mock dataset. The estimated dark matter parameters are $M_{200} = 1.95\ 10^{12}\ M_\odot$ and $c = 10.4$, whose parameters are indeed in excellent agreement with the input halo contribution in Hunt et al. (2013).

4 Conclusions

The development of numerical tools to prepare the scientific exploitation of Gaia products is ongoing. Provisional results show that the derivation of fundamental dynamical parameters is still possible using a limited volume of mock Gaia astrometric and kinematical data from numerical simulations.

It is however important to note that the credibility of these modelling tools is tightly linked to the ability of simulations to mimic realistic pseudo-Gaia products for tens of millions of particles. For now, I have only worked with ideal cases from the initial simulations by Gaia Challenge' numericians. The selection function is quite arbitrary to mimic a limited volume, since particles represent a single stellar population, and neither interstellar extinction laws as function of location in the disc nor the Gaia data error model have been used. In a near future, thanks to the improvement of the numerical simulations, it is envisaged to study the impact of such selection and systematic effects.

The Gaia Challenge is supported by the Gaia Research for European Astronomy Training ESF programme. It is a pleasure to thank the Gaia Challenge organizers, Gaia challengers and the Gaia team at Laboratoire d'Astrophysique de Bordeaux for fruitful discussions and help in this work. I gratefully acknowledge financial support from Centre National d'Études Spatiales and from ASGaia.

References

Bovy, J. & Rix, H.-W. 2013, ApJ, 779, 115
Corsini, E. M. 2011, Memorie della Societa Astronomica Italiana Supplementi, 18, 23
Debattista, V. P., Gerhard, O., & Sevenster, M. N. 2002, MNRAS, 334, 355
Hunt, J. A. S. & Kawata, D. 2013, MNRAS, 430, 1928
Hunt, J. A. S., Kawata, D., & Martel, H. 2013, MNRAS, 432, 3062
Monari, G., Antoja, T., & Helmi, A. 2013, ArXiv e-prints
Tremaine, S. & Weinberg, M. D. 1984, ApJ, 282, L5

SF2A 2014
J. Ballet, F. Bournaud, F. Martins, R. Monier and C. Reylé (eds)

METAL-POOR BENCHMARK STARS AND GAIA

O. Creevey[1], J. Thévenin[2], U. Heiter[3], D. Mourard[2], P. Berio[2], T. Boyajian[4], P. Kervella[5], N. Nardetto[2] and L. Bigot[2]

Abstract. Gaia will deliver stellar properties for up to 1 billion stars. Effective temperatures, surface gravity, and ages are some of the *products* of the coordination unit 8. To properly calibrate Gaia data and the methods that are used, extensive ground-based data has been obtained on sets of *calibration stars*. There are a list of about 40 of the brightest benchmark stars, and here we report on our recent work relating to some nearby metal-poor benchmarks observed using interferometric instruments. We determined their angular diameters and along with distances and bolometric fluxes we obtain their effective temperatures ($T_{\rm eff}$), radii and surface gravity ($\log g$) with very little model-dependence. The $T_{\rm eff}$ can differ a lot from those determined using spectroscopic measurements, and with both $T_{\rm eff}$ and log g pre-determined these stars provide a testbed for stellar atmospheres. Using evolutionary models we then determined their masses and ages. We find that to match the observations we are required to significantly lower the mixing-length parameter α from the usual solar-calibrated value $\alpha_{\odot}$, which brings into question the exploitation of predefined stellar model grids constructed using an $\alpha_{\odot}$. We emphasize the important role of characterising the brightest stars where many independent observations allow us to pinpoint shortcomings in models and methods.

Keywords: metal-poor stars, stellar parameters, interferometry, spectroscopy, Gaia

1 Introduction

Bright metal-poor ([M/H] < 1.0) stars have a valuable role to play for advancing our understanding of different aspects of astrophysics. For one, the atmospheres of metal-poor stars require extra care where non-LTE effects and certain atomic collisions can not be ignored. These affect the determination of absolute chemical abundances (Idiart & Thévenin 2000), and thus have consequences for our understanding of the evolution of the galaxy. Secondly, being some of the oldest stars in our Galaxy, they are tracers of the initial conditions in the Milky Way, and determining their ages constrains the age of the Galaxy independent of cosmological observations. Thirdly, they may be considered *problem stars* where classical stellar evolutionary tracks fail to match their observed positions in the HR diagram (Creevey et al. 2012). As nearby stars they can be measured in many different ways and this allows us to look at the details in the models and thus bring to light the shortcomings. For large-scale ground-based and space-based surveys, bright nearby stars play an important role in calibration, and such is the case for the recently launched Gaia spacecraft.

Gaia (Perryman 2005) is an ESA mission designed to measure distances and kinematics of a sample of 1 billion stars from the Milky Way. It provides a full-sky coverage down to a magnitude of ~ 20. It has astrometric, photometric, spectrophotometric, and spectroscopic[*] capabilities. One of its main deliverables which will serve many different astrophysical communities is a catalogue of precise parallactic and kinematical information for each of the 1 billion stars. These data are processed and will be delivered by coordination units dedicated to these tasks. Within the Gaia consortium the coordination unit 8 (CU8), entitled astrophysical parameters, is

[1] Institut d'Astrophysique Spatiale, Université Paris XI, UMR 8617, CNRS, Batiment 121, 91405 Orsay Cedex, France
[2] Laboratoire Lagrange, Université de Nice Sophia-Antipolis, UMR 7293, CNRS, Observatoire de la Côte d'Azur, Nice, France
[3] Institutionen fr fysik och astronomi, Uppsala universitet, Box 516, 751 20 Uppsala, Sweden
[4] Department of Astronomy, Yale University, New Haven, CT 06511, USA
[5] LESIA, Observatoire de Paris, CNRS UMR 8109, UPMC, Université Paris Diderot, 5 place Jules Janssen, 92195 Meudon, France

[*] Radial velocities will be available to magnitude ~ 17.

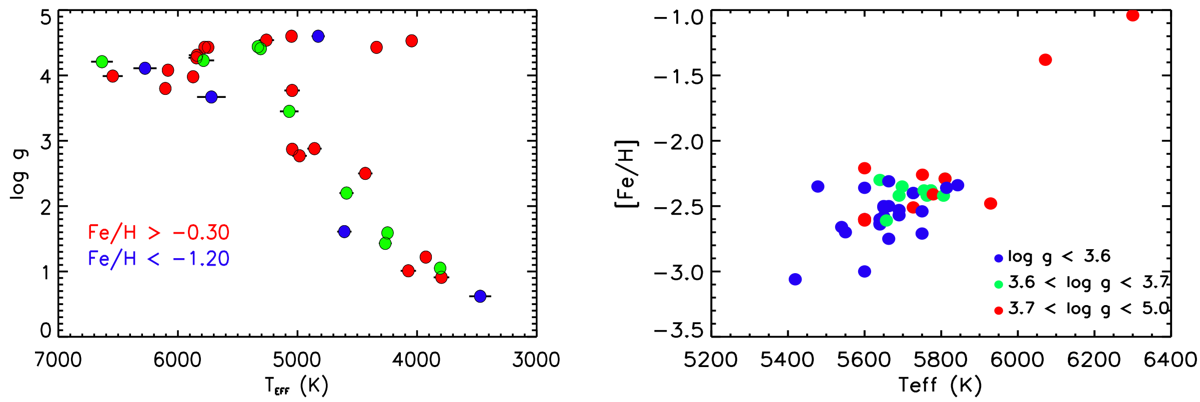

Fig. 1. Left: Gaia benchmark stars. **Right:** Published iron abundances of the metal-poor star HD 140283.

dedicated to extracting fundamental parameters such as $T_{\rm eff}$, $\log g$, metallicities and ages for one billion stars. These parameters are derived primarily by three main packages: GSP_Phot, GSP_Spec, and FLAME. The first two derive atmospheric parameters from the photometry and spectroscopy, respectively, and the latter derives masses and ages. In order to deliver these properties as accurately and as precisely as possible, the analysis tools need to be calibrated with bright nearby stars, ones which, for example, can be measured with interferometry. A list of benchmark stars have been defined by the Stellar Atmospheres Models Group† (Heiter et al. in prep., Blanco-Cuaresma et al. 2014; Jofre et al. 2013) and huge efforts and collaborations are underway for obtaining and interpreting data for these stars from ground-based instruments. These stars are shown in Fig. 1 (left), along with various determinations of $T_{\rm eff}$ and [Fe/H] from the literature of HD 140283 (right, Soubiran et al. 2010), illustrating the importance of determining $T_{\rm eff}$ independently of stellar atmospheres. Here we report on our interferometric observations of some bright nearby metal-poor stars.

2 Observations

2.1 Interferometric observations

We are conducting an observational interferometric program using the CHARA array. We have obtained observations using the infra-red Classic and visible VEGA interferometers. We extracted visibilities for a total of six metal-poor stars and here we describe our results for a giant HD 122563, a sub-giant HD 140283 and a dwarf HD 103095 (Gmb 1830) (Creevey et al. 2012, 2014). The observations were obtained between the years 2007 and 2014 in two- or three-telescope mode with Classic and VEGA on CHARA. For HD 122563 we also took data from the PTI archive (1999-2002). To determine the angular diameters θ for the stars we fitted visibility functions to the interferometric visibility data. The visibility measurement is a function of the distance between the telescopes (the baseline), the wavelength of observation λ, and the angular diameter of the star (θ). Two examples of the data and fits to a 3D/1D limb-darkened disk function are shown in Fig. 2. These data were obtained with the Classic instrument on CHARA and the Palomar Testbed Interferometer (PTI) (left) and the VEGA instrument on CHARA (right). In Table 1 we give the uniform-disk (UD), 1-D limb-darkened (1D) and 3-D limb-darkened (3D) angular diameters. The 1D diameters were fitted using limb-darkening coefficients from Claret (2000) and Claret et al. (2012). The 3D diameters were obtained using convection simulations (see e.g. Bigot et al. 2011; Chiavassa et al. 2012).

To convert the angular diameter to the fundamental properties, the radius R, effective temperature $T_{\rm eff}$, and surface gravity g, we use the following equations

$$R = \frac{\theta}{\pi}, \qquad T_{\rm eff} = \left(\frac{1}{\sigma_{\rm SB}}\frac{F_{\rm BOL}}{\theta^2}\right)^{0.25}, \qquad g = \frac{GM}{R^2}, \tag{2.1}$$

†`http://www.astro.uu.se/~ulrike/GaiaSAM/`

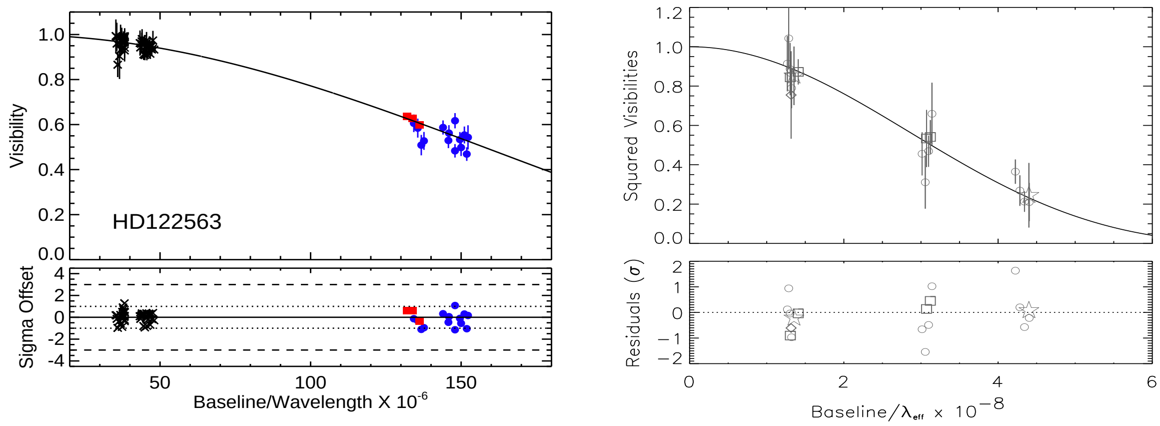

Fig. 2. Fit of visibility data for HD122563 and HD140283 (left/right) to 1D limb-darkened disk function.

Table 1. Angular diameters of three metal-poor stars. Units in milliarcseconds (mas).

	$\theta_{\rm UD}$	$\theta_{\rm 1D}$	$\theta_{\rm 3D}$
HD 122563	0.924 ± 0.011	0.948 ± 0.012	0.940 ± 0.011
HD 140283	0.340 ± 0.012	0.353 ± 0.013	0.353 ± 0.013
HD 103095	0.664 ± 0.015	0.679 ± 0.015	....

where π is the parallax, $F_{\rm BOL}$ is the bolometric flux received at the top of the Earth's atmosphere, $\sigma_{\rm SB}$ is the Stefan-Boltzmann constant, G is the gravitational constant, and M is the stellar mass. These parameters are given in Table 2. M can be estimated from stellar evolution tracks and/or spectral typing and even assuming a conservative precision of 20%, $\log g$ can be derived to 0.1 dex. $F_{\rm bol}$ can be determined using different methods (see below).

2.2 Photometric and astrometric observations

To determine the bolometric flux of the star we need to measure its spectral energy distribution (SED). The SED that we observe, however, is a set of points corresponding to different wavelength regions, e.g. BVRI photometry. Additionally the observed SED can also contain a reddened component from interstellar extinction. The amount of absorption is given by A_V. For our stars we used the classical formula using the observed V magnitude, bolometric corrections along with an assumed A_V, and SED fitting using a compilation of photometry-converted-to-flux measurements. The parallaxes are taken from the Hipparcos catalogue (van Leeuwen 2007) and Bond et al. (2013) for HD 140283.

3 Analysis

3.1 Comparison of Spectroscopic and Interferometric $T_{\rm eff}$

The determination of a spectroscopic $T_{\rm eff}$ is difficult for metal-poor stars due to, for example, deviations from local thermodynamic equilibrium. In Figs. 3 we show a comparison between our interferometrically derived $T_{\rm eff}\pm1\sigma$ (shaded region) along with spectroscopic determinations of $T_{\rm eff}$ and [Fe/H] taken from the PASTEL catalogue (Soubiran et al. 2010). There is excellent agreement between interferometric and spectroscopic values for HD 122563 and HD 140283 for the most recent spectroscopic determinations. The dashed lines for HD 140283 represent the zero-reddened solution. However, for HD 103095 there is quite a large offset. This could be explained by a systematic error affecting the interferometric observations, or difficulties with model atmospheres for deriving $T_{\rm eff}$ at high $\log g$. Further investigation is needed.

Table 2. Complementary observations and derived parameters for three metal-poor stars.

	HD 122563	HD 140283*	HD 103095
[Fe/H]/Class	–2.5/III	–2.5/IV	–1.4/V
V (mag)	6.19 ± 0.02	7.2 ± 0.01	6.45 ± 0.02
π (mas)	4.22 ± 0.035	17.15 ± 0.14	109.99 ± 0.41
A_V (mag)	0.01 ± 0.01	0.0/0.1 ± 0.04	0.00 ± 0.01
[Z/X$_s$]	–2.3 ± 0.1	–2.1 ± 0.2	–1.3 ± 0.1
θ (mas)	0.940 ± 0.011	0.353 ± 0.013	0.679 ± 0.015
$F_{\rm bol}$†	13.16 ± 0.36	3.89/4.22 ± 0.066/0.067	8.27 ± 0.08
R (R$_\odot$)	23.9 ± 1.9	2.21± 0.08	0.664± 0.015
$T_{\rm eff}$ (K)	4585 ± 43	5534/5647 ± 103/105	4818 ± 54
L (L$_\odot$)	232 ± 6	4.12/4.47 ± 0.10	0.213 ± 0.002
$\log g$	1.57 ± 0.06	3.65 ± 0.06	4.57 ± 0.07
M (M$_\odot$)	0.855 ± 0.025	0.780/0.805 ± 0.010	0.635 ± 0.025
t (Gyr)	$12.6^{+1.1}_{-1.6}$	13.7/12.2 ± 0.7/0.6	$12.1^{2.0}_{-2.2}$
$\log g_{\rm model}$	1.60 ± 0.04	3.64/3.65 ± 0.03/0.02	4.60 ± 0.02
α	1.31 ± 0.10	1.0 ± 0.3	0.68 ± 0.10
Y_i	0.245 ± 0.015	0.245	0.235 ± 0.025

*Two solutions are given based on different interstellar absorption values A_V. †Units of $F_{\rm bol}$ are 1e-8 × erg s^{-1} cm^{-2}.

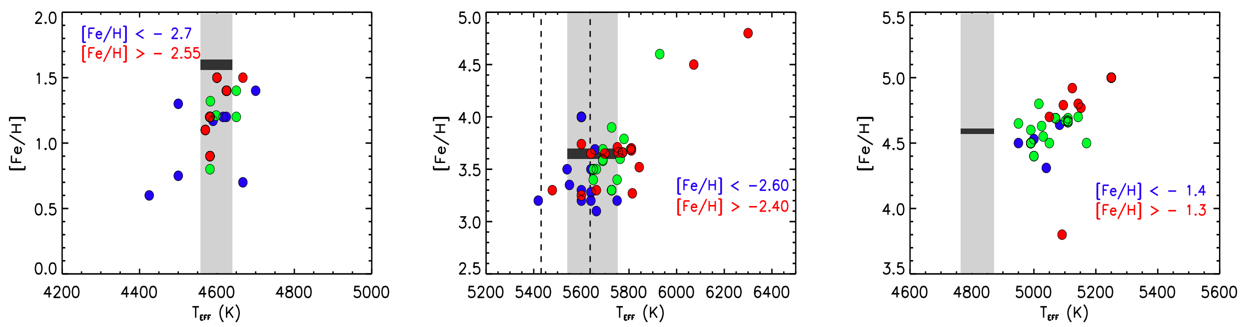

Fig. 3. Comparison of $T_{\rm eff}$ from the literature and interferometry (shaded) for HD 122563, HD 140283, HD 103095 (L–R).

3.2 *Interpretation of observations with models*

We used the CESAM2K stellar evolution code (Morel 1997; Morel & Lebreton 2008) to derive the mass M and the age t of the three stars. This was done by fitting L, $T_{\rm eff}$ and the metallicity [M/H] to fine-tuned stellar evolution tracks. For the dwarf and sub-giant star we included elemental diffusion in the models to help explain the observed surface metallicity and to better estimate the stellar age. In order to match the observations it was necessary to significantly reduce the value of the mixing-length parameter α from that of the Sun. With an assumption on either the mixing-length parameter or the initial helium abundance of the star, the other can be determined along with the mass and the star's age. These stellar parameters are given in the lower part of Table 2.

4 Conclusions

Interferometry allows the direct measure of stellar observables, and when combined with the distance and $F_{\rm bol}$, R, $T_{\rm eff}$, L and $\log g$ can be determined with none or very little model-dependence. For metal-poor stars, the determination of $T_{\rm eff}$ independent of stellar atmospheres provides critical tests of the models. Gaia will deliver atmospheric properties along with masses and ages of up to 1 billion stars. Independent determinations of these properties for several benchmark stars serve as important calibration measures of the Gaia pipelines GSP_Phot, GSP_Spec (atmospheric properties) and FLAME (luminosities, masses, ages).

References

Bigot, L., Mourard, D., Berio, P., et al. 2011, A&A, 534, L3

Blanco-Cuaresma, S., Soubiran, C., Jofré, P., & Heiter, U. 2014, ArXiv e-prints

Bond, H. E., Nelan, E. P., VandenBerg, D. A., Schaefer, G., & Harmer, D. 2013, in American Astronomical Society Meeting Abstracts, Vol. 221, American Astronomical Society Meeting Abstracts, 443.08

Chiavassa, A., Bigot, L., Kervella, P., et al. 2012, A&A, 540, A5

Claret, A. 2000, A&A, 363, 1081

Claret, A., Hauschildt, P. H., & Witte, S. 2012, A&A, 546, A14

Creevey, O., Thévenin, F., Berio, P., et al. 2014, ArXiv e-prints

Creevey, O. L., Thévenin, F., Boyajian, T. S., et al. 2012, A&A, 545, A17

Idiart, T. & Thévenin, F. 2000, ApJ, 541, 207

Jofre, P., Heiter, U., Soubiran, C., et al. 2013, ArXiv e-prints

Morel, P. 1997, A&AS, 124, 597

Morel, P. & Lebreton, Y. 2008, Ap&SS, 316, 61

Perryman, M. A. C. 2005, in Astronomical Society of the Pacific Conference Series, Vol. 338, Astrometry in the Age of the Next Generation of Large Telescopes, ed. P. K. Seidelmann & A. K. B. Monet, 3

Soubiran, C., Le Campion, J.-F., Cayrel de Strobel, G., & Caillo, A. 2010, A&A, 515, A111

van Leeuwen, F. 2007, A&A, 474, 653

SF2A 2014
J. Ballet, F. Bournaud, F. Martins, R. Monier and C. Reylé (eds)

ADDITIONAL AUXILIARY DATA FOR THE GAIA-RVS

F. Crifo[1], L. Chemin[2], G. Jasniewicz[3], D. Katz[1], O. Marchal[1], P. Sartoretti[1], C. Soubiran[2], F. Thévenin[4] and T. Zwitter[5]

Abstract. The Gaia-RVS will measure some 10^8 stellar radial velocities using the correlation method with well-adapted template spectra for each individual case. Ground-based RV standards will be used to fix the zero-point.

Gaia instruments are "self-calibrating" and no calibration device is available on board. But for the beginning of the mission, until the needed calibration parameters become available, the calibrations have to come from external sources, i.e. existing ground-based observations of already very well-known objects. Therefore beside the basic list of 1400 very stable and well-measured primary standards, several secondary RV lists have been built recently. The basic list itself will be extended with around 500 new "primary standard".

The libraries of existing spectra have been carefully investigated: a lot of high-quality material is available for the start of the reductions and for the validation of the pipeline results.

In addition, as the data expected from the photometric instrument are not available at the beginning, very large lists with atmospheric parameters (T_{eff} , $\log g$, metallicity) have been produced from the literature.

Grids of 3D atmospheric models have been calculated, in order to select the best template for the correlation; they will be used in the future and will automatically take into account the stellar convective shift across the HR diagram.

Keywords: Stars: fundamental parameters; Techniques: radial velocities; Surveys: Gaia.

1 Need for additional ground-based data

Gaia was successfully launched December 19th, 2013. After arrival at the L2 point in January 2014, the commissioning period was somewhat extended due to some initial unexpected difficulties. The routine scanning of the sky started on July 25. Spectra are now regularly produced and reduced on the ground. However the reduction process is supposed to use data concerning the targets, that should be derived from the BP/RP observations. Such data is of course not yet available. Therefore several lists of preliminary data have been built:

- the Initial Gaia Source List (IGSL), built by R. Smart (see Smart 2013);
- the list of radial velocity standards (Soubiran et al. 2013; Crifo et al. 2010) for which in addition atmospheric parameters (T_{eff} , $\log g$, $[Fe/H]$) have been searched in the literature.

However, for this beginning period, it is also desirable to have MORE standards available, on the order of 1 per hour: this is a total of about 2000 stars if they are regularly distributed over the whole sky. Despite our efforts, it is not the case with the present list of 1400 standards, with which the largest interval between two consecutive transits may be as large as 8 hours, while the rotation period of Gaia is 6 hours. Therefore it was decided to build additional lists of standards, with of course less accuracy and reliability than the main list, as new observations cannot be conducted on time. A total of 10000 stars are expected.

Also, lists of atmospheric parameters have been compiled for large sets: Hipparcos stars, Tycho stars, part of 2MASS stars. The ESA/Gaia Technical Note (TN) by Katz et al. (2012) describes the list of additional ground-based data needed. The TN by Marchal et al. (2014) describes the practical realization of these lists and their inclusion in the reduction pipeline.

[1] GEPI (UMR 811 du CNRS; Université Paris 7, FRANCE), Observatoire de Paris, 92190 MEUDON, FRANCE
[2] LAB, UMR 5804, Université de Bordeaux, CNRS, 2 rue de l'Observatoire, F-33270 FLOIRAC, FRANCE
[3] GRAAL, UMR 524, CNRS, Université Montpellier 2, FRANCE
[4] OCA/Cassiopée, UMR CNRS 6062, Observatory of the Côte d'Azur, Le Mont Gros, BP 4229, 06304 Nice Cedex 4, FRANCE
[5] University of Ljubljana, SLOVENIA

2 Secondary RV standards

A total of about 10000 stars should be provided. Radial velocities for secondary standards have to come from existing catalogue compilations, with the following conditions: FGK types, V≤ 11; not known as double or variable, stable in RV, and with a "clean environment" to avoid overlap of neighbouring spectra.

The sources we used are:

1. Good Hipparcos (HIP) stars already examined during the search of primary list (the so-called "masterlist" with no disturbing neighbours, described in Crifo et al. 2010) but with RVs from literature. The XHIP Catalogue (Anderson & Francis 2012), which compiles a very large set of data of all types for the HIP stars, was adopted as RV source. 7730 stars are found, with an RV accuracy better than 1 km/s. This list is described in the TN by Crifo et al. (2014).

2. A subset of 3800 stars selected in the RAVE survey, with: at least 2 observations; error $\leq$ 1 km/s; 4500 K $\leq T_{eff} \leq$ 7000 K; V $\leq$11; and provided in the TN by Zwitter et al. (2014).

3. 2259 stars selected in the archives of the ELODIE and SOPHIE spectrographs at OHP, 25% of which have enough observations to prove their long-term stability and become additional primary standards (see the TN by Soubiran et al. 2014a). A selection is still going on within the ESO archive and the libraries of spectra from ESPADONS and NARVAL, the HR spectrographs at CFHT and TBL (Pic du Midi). This spectral library is detailed in the TN by Chemin & Soubiran (2014).

4. Other data available for RV validation, particularly for faint stars.

Figure 1 (left) shows the present map of standards: black = primaries ; red = HIP/XHIP secondaries (list 1); green = RAVE selection (list 2) . With the secondary standards the stellar density is enhanced with respect to the primary ones only; however we notice that the area along the Galactic Plane is still underpopulated, particularly in the South.

Figure 1 (right) shows the first comparison of a RVS spectrum; and the same star as in the NARVAL spectra library: it is possible here to see the quality of the RVS spectra.

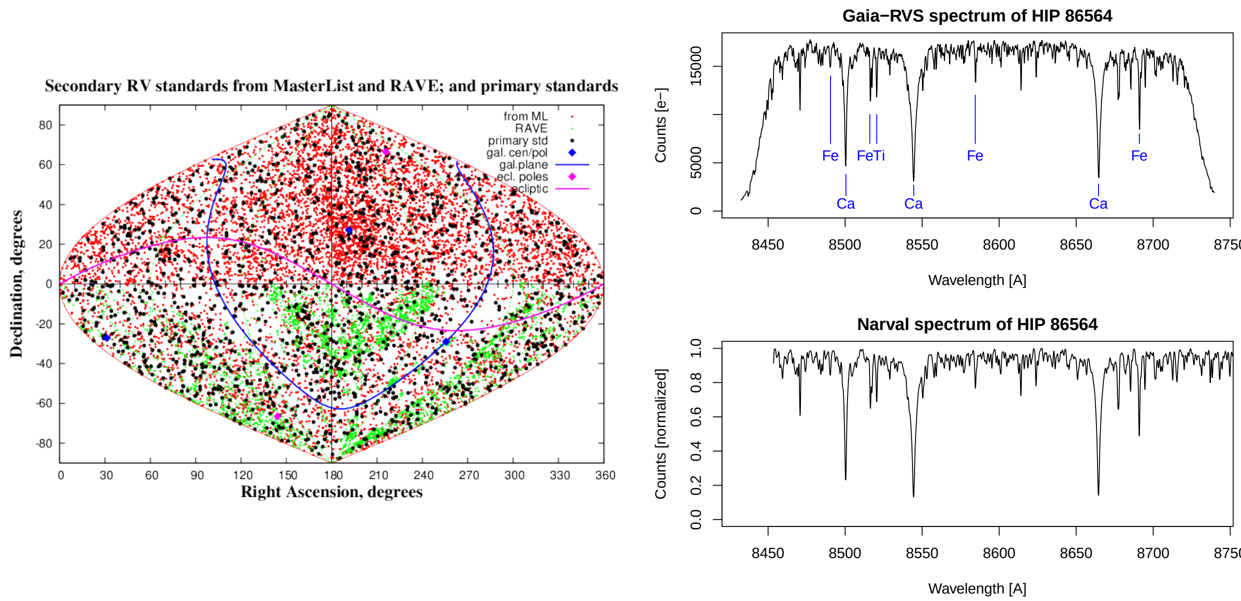

Fig. 1. Left: Map of standards. **Right:** RVS spectrum of HIP 86564 compared with a ground-based spectrum obtained with NARVAL. The NARVAL spectrum has been convolved with the RVS nominal resolution.

3 Atmospheric Parameters (AP)

In the reduction procedure, the RV is calculated by several methods. All of them use the correlation with a synthetic template spectrum adapted to the star. Synthetic spectra are currently computed with 1D or 2D atmospheric models. In a near future they will be computed from 3D models (T_{eff} , $\log g$, $[Fe/H]$), see sect. 4. For each star, approximate values of the three parameters must be known in advance and tabulated in auxiliary lists.

Large-scale analyses have been performed and libraries of APs have been made, from existing lists and catalogues. In particular the TN by Soubiran et al. (2014b) includes parameters from Casagrande et al. (2011) and Ammons et al. (2010), and the TN by Zwitter et al. (2013) derives effective temperatures from 2MASS photometry. The most important parameter is T_{eff} , which remains poorly known for spectral types earlier than F8 and for stars fainter than V=13. Comparisons have been made between various sources to check the validity of the parameters. For instance, Figure 2 shows the comparison between temperatures in the TN of Soubiran et al. (2014b) and Zwitter et al. (2013) with temperatures from Casagrande et al. (2011) for cool stars.

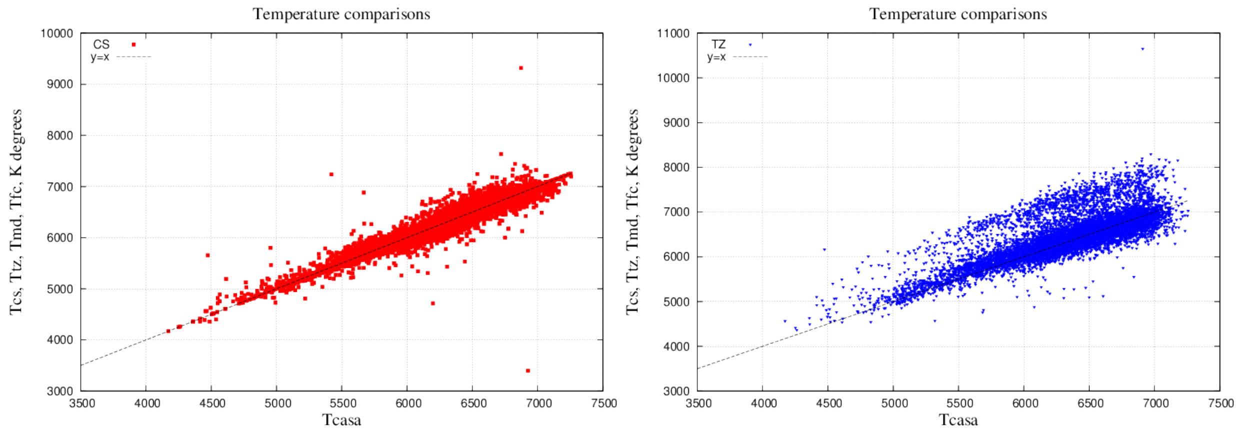

Fig. 2. T_{eff} **comparisons. Left:** Soubiran et al. (2014b) vs Casagrande et al. (2011). **Right:** Zwitter et al. (2013) vs Casagrande et al. (2011).

4 Grids of synthetic spectra

Calculating a 3D synthetic spectrum adapted to each RVS source cannot be envisaged, for reasons of disk space and computational time. Therefore high-resolution synthetic spectra will be calculated only for a limited number of points on a 3D-grid in (T_{eff} , $\log g$, $[Fe/H]$) space. For a given star of known AP, the spectrum is interpolated between the closest points of the grid.

Figure 3 (left) shows the grid with the calculated points, for cool stars. The point not exactly aligned in the grid marks the location of the Sun. Figure 3 (right) shows the difference between spectra computed with different parameters.

5 Conclusion

All kinds of auxiliary data for stars, and in particular ground-based RVs and synthetic spectra are of central importance for the calibration and the zero-point determination of the RVS. They are currently playing a crucial role at the beginning of the mission. At this time (launch + 6 months), there is a large effort within DU640 to gather these required auxiliary data.

Many thanks go to all the CU6 staff not listed in the authors; and to the Centre de Données de Strasbourg, where an incredible amount of recent and old data can be retrieved quite easily.

Short remark: In the bibliographic list here below, the papers referenced as “Gaia Data processing...”, that describe the most accurately the developments made within the Gaia DPAC Consortium, are NOT accessible to non-members of the Consortium. Sorry for that.

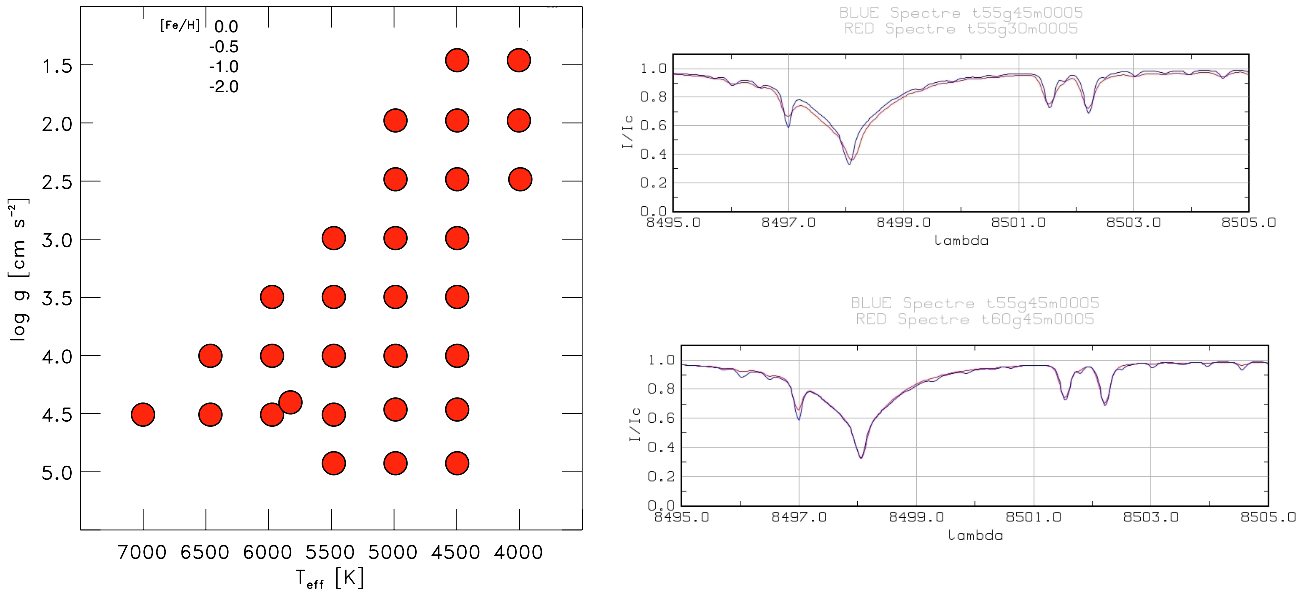

Fig. 3. Left: Grid of calculated synthetic spectra, with the nodes. **Right:** Calculated synthetic spectra, effects of gravity (upper panel) and T_{eff} (lower panel). From Chiavassa et al. 2014 (private communication).

References

Ammons, S. M., Robinson, S. E., Strader, J., et al. 2010, VizieR Online Data Catalog, 5136, 0

Anderson, E. & Francis, C. 2012, Astronomy Letters, 38, 331

Casagrande, L., Schönrich, R., Asplund, M., et al. 2011, A&A, 530, A138

Chemin, L. & Soubiran, C. 2014, Gaia Data Processing & Analysis Consortium Internal Publications, GAIA-CU6-TN-LAB-LCH-002-1

Crifo, F., Jasniewicz, G., Soubiran, C., et al. 2010, A&A, 524, A10

Crifo, F., Sartoretti, P., & Katz, D. 2014, Gaia Data Processing & Analysis Consortium Internal Publications, GAIA-C6-TN-OPM-FCO-002-1

Katz, D., Soubiran, C., Chemin, L., et al. 2012, Gaia Data Processing & Analysis Consortium Internal Publications, GAIA-C6-TN-OPM-DK-015-01

Marchal, O., Sartoretti, P., Crifo, F., & Katz, D. 2014, Gaia Data Processing & Analysis Consortium Internal Publications, GAIA-C6-TN-OPM-OML-002-1

Smart, R. 2013, Gaia Data Processing & Analysis Consortium Internal Publications, GAIA-C3-TN-OATO-RLS-004-02

Soubiran, C., Chemin, L., & Lecampion, J.-F. 2014a, Gaia Data Processing & Analysis Consortium Internal Publications, GAIA-C6-TN-LAB-CS-013-1

Soubiran, C., Jasniewicz, G., Chemin, L., et al. 2013, A&A, 552, A64

Soubiran, C., Lecampion, J.-F., & Chemin, L. 2014b, Gaia Data Processing & Analysis Consortium Internal Publications, GAIA-C6-TN-LAB-CS-011-2

Zwitter, T., Kos, J., & Zerjal, M. 2013, Gaia Data Processing & Analysis Consortium Internal Publications, GAIA-C6-TN-LU-TZ-1-2

Zwitter, T., Kos, J., & Zerjal, M. 2014, Gaia Data Processing & Analysis Consortium Internal Publications, GAIA-C6-TN-LU-TZ-2-D

SF2A 2014
J. Ballet, F. Bournaud, F. Martins, R. Monier and C. Reylé (eds)

GAIA AND THE EXTRAGALACTIC

C. Ducourant[1], A. Krone-Martins[2], L. Galluccio[3] and R. Teixeira[4]

Abstract. Gaia's main goal is to study the Milky Way and its stellar content and to provide us with their highly accurate astrometric and photometric parameters. However the satellite will also survey many other objects. Gaia will especially observe a few millions of tiny galaxies of the local Universe and will give us a unique chance to access to a whole sky survey of these objects that no ground-based survey such as Sloan Digital Sky Survey has ever recorded, thanks to its high resolution. We present here the "Extended Object" DPAC DU470 work to retrieve the morphology of such objects and a theoretical study concerning the expected detections by Gaia. We show that most of the detected galaxies by Gaia will be bulge-type and elliptical.

Keywords: Gaia, quasars, galaxies, gravitational lens

1 Introduction

In the Gaia Data Processing and Analysis Consortium (DPAC), the division unit Extended Objects (DU470) is a group which has dedicated its efforts to retrieve from Gaia observations the objects presenting a spatial extension (essentially galaxies) (Krone-Martins et al. 2013). Its aim is to extract the morphology of a category of tiny galaxies, very rarely observed from the ground, and to characterize their morphology by measuring their bulges and disks characteristics. The DU470 group is also interested in the QSOs which are the objects that will allow Gaia to perform its global solution and from which a sub sample will allow the link between the Gaia sphere (defined in optical) and the ICRF sphere (defined in radio).

2 The detection of galaxies

Gaia observes in Time Delay Integration mode which is to say that it is going to measure any object brighter than magnitude G=20. The stars from the Milky Way will therefore be observed together with a large sample of galaxies. For the detection, the Video Processing Unit (VPU) analyses the light profile of the candidate and if it is sufficiently similar to a star profile, the object will be detected. After the detection process by the VPU, a window is centered onto the detected object and the data from this window is transmitted to earth. So a galaxy with a flat profile (such as a disk galaxy) will probably not pass the VPU test and so will not be detected while a galaxy with a bright bulge will probably be detected. Moreover the size of the windows transmitted to earth will never exceed $4.72''$ which is another constraint on the detection of extragalactic objects.

A recent theoretical study developed within DU470 (de Souza et al. 2014) has shown that the satellite will rarely succeed in observing the pure disk galaxies. On the contrary the spheroidal component of elliptical galaxies and bulges having higher central surface brightness and steeper brightness profile should be more easily detected.

To validate this theoretical estimation of the detectability of the extragalactic objects we have performed numerical simulations of 10 000 galaxies (De Bruijne et al. 2014) with disks half intensity radius ranging from 0.2 to $2''$ by $0.1''$ steps and integrated magnitudes from G=14 to 20 by 0.2 mag steps. We used the *skymaker*

[1] Observatoire de Bordeaux, BP 89, 33271 Floirac Cedex.
[2] SIM, Universitè de Lisbonne, Portugal.
[3] Observatoire de la Côte d'Azur, Nice, France.
[4] IAG, Université de SAppl. Opt.Paulo, Brésil.

and the GIBIS Gaia simulators for the simulation and the detection of objects in the conditions of the mission. In Fig. 1 we present the detection rate of these galaxies as function of their morphologic and photometric characteristics. It is obvious from this figure that most of spiral galaxies (pure disks situation) will not be detected by the satellite and therefore that the data corresponding to them will not be transferred to earth. On the contrary the pure bulges galaxies appear well detected by the satellite. The faintest of these will be detected only if their half light radius is small enough.

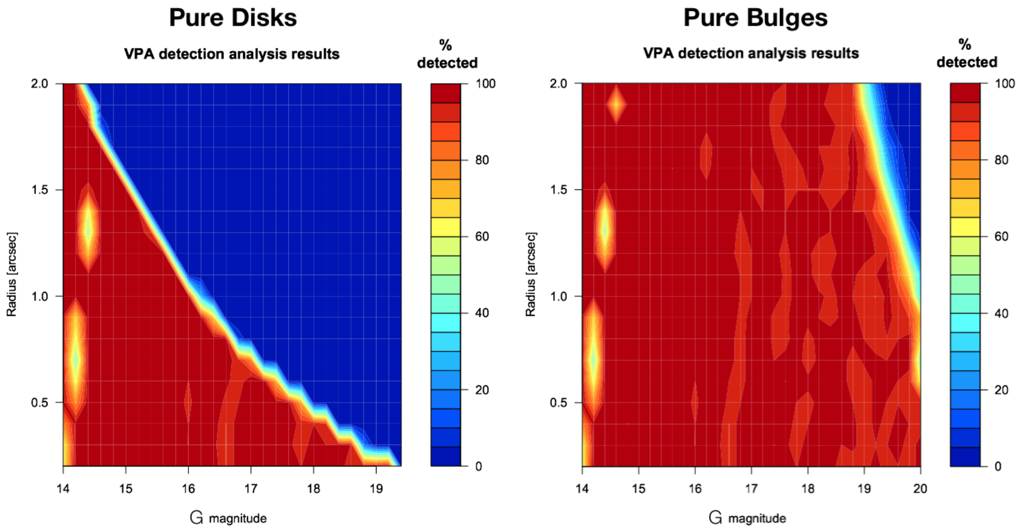

Fig. 1. Detection efficiency functions of pure disks and pure bulges galaxies.

3 The coverage fraction at the end of the mission

Once the observations (i.e. the pixels values) of a galaxy are sent to ground base segment, is it possible to retrieve its morphology? The Gaia observations are very specific; windows of variable sizes (depending on the magnitude of the object) are extracted onboard around the detections. Most extragalactic objects will fall in the magnitude range G=18-20. For these objects the Sky Mapper data will be two dimensional (SM window size = $4.72''$x$2.12''$) and the Astro Field Data will mostly be one dimensional (AF window size = $0.71''$x $2.12''$). These observational windows are formed by samples (binned pixels) of rectangular shape ($0.236''$x $0.79''$) for SM and ($0.059''$x $2.12''$) for AF. Various attempts of two dimensional image reconstruction have been performed (Dollet et al. 2004). The quality of the morphology that one will be able to recover for extended objects with Gaia will obviously strongly rely on the variety of transit angles under which the satellite will observe the object as illustrated in Fig. 2.

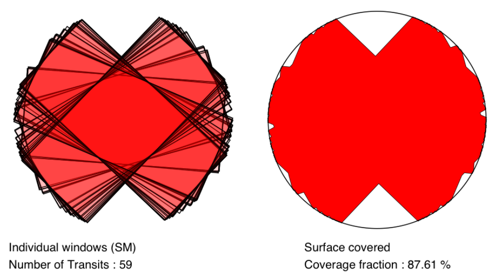

Fig. 2. Surface covered by various observations of a single extended objects.

We present the coverage fraction at the end of the mission as function of the galactic latitude in Fig. 3.

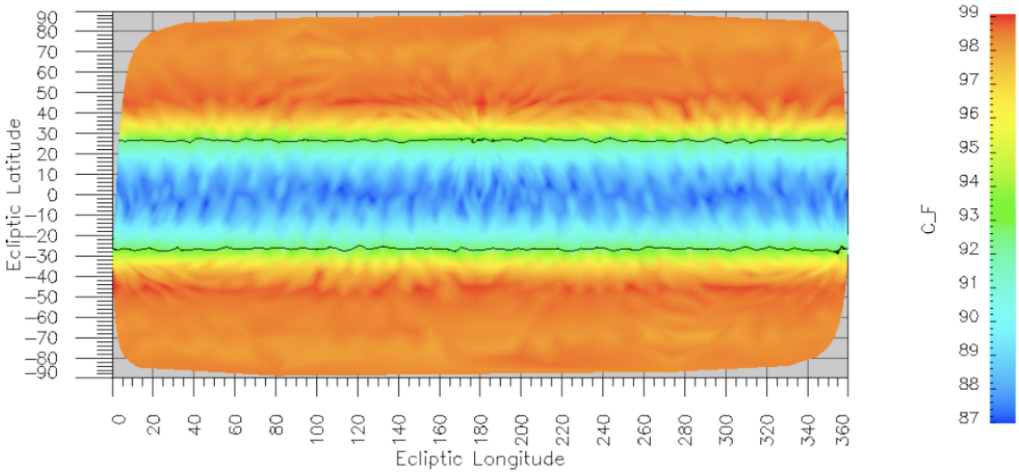

Fig. 3. Dependence of coverage fraction (CF) as function of ecliptic position at the end of the mission.

4 The recovery of the morphological parameters of the galaxies

To recover the morphological information of the extended objects we perform a global analysis (based on Genetic Algorithms and Radon transforms) of the individual Astro Field and Sky Mapper observations to fit the appropriate bulb and disk profiles. Our forward model aims at measuring the characteristic parameters such as size and boxyness of bulb and disk, axis ratio, position angle and relative surface brightness of each component by fitting simultaneously an exponential disk and a Sersic bulge. A total of 11 parameters are searched for. Using the nominal scanning law of Gaia, AF and SM synthetic observations of the objects are produced for the entire time of the mission. The signal of these images are then combined into the Radon space to produce the synthetic Radon image of the object. This image is then compared to the observed Radon image of the object, the L^2 norm is minimized and the process is iterated until convergence. To test the efficiency of our model, we have performed simulations of 10 000 galaxies with radius at half intensity variying from 0 to 4″. We present in Fig. 4 the efficiency of the recovery of the bulge and disk radius.

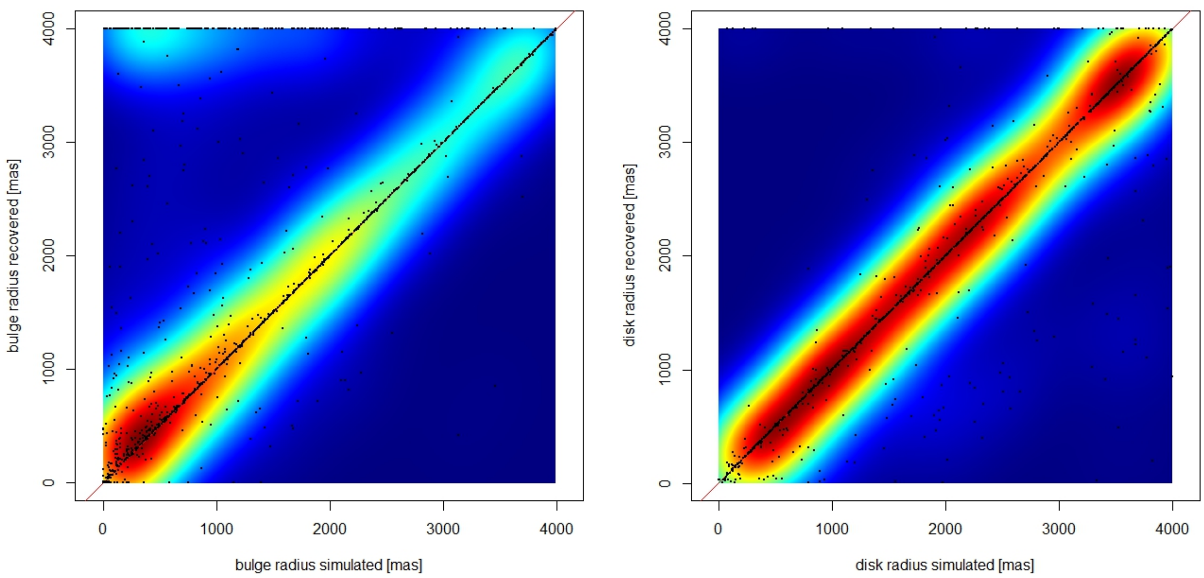

Fig. 4. Left: Recovery of Bulge radius (red=100%). **Right:** Recovery of Disk radius.

In this last figure one can observe an excellent recovery of the simulated Disk radius while the large simulated bulges are poorly recovered. This is easily explained by the fact that the high resolution information of Gaia is provided by the AF observations along scan (AL) in very small windows (0.71″x 2.12″).

5 The QSOs of Gaia

The QSOs are a special type of objects which have a great importance for the Gaia mission. Indeed, the global astrometry of Gaia will be based on a subsample of the 500 000 QSOs that Gaia should detect. Popović et al. (2012) has showed that a perturbation in the disk of the host galaxy can cause a significant offset to the photocenter in the Gaia observations. It is therefore important to be able to diagnose an eventual perturbation of the quasar astrometry due to his host galaxy (originated for example by a star burst in the disk). That is why we have adapted our forward model to this specific case in order to measure the offset between the disk center and the QSO center together with the morphologic parameters of the host galaxy. We show in Fig. 6 the recovery of this offset by our adapted model in 10 000 simulations (the offset varies from 0 to ±1″).

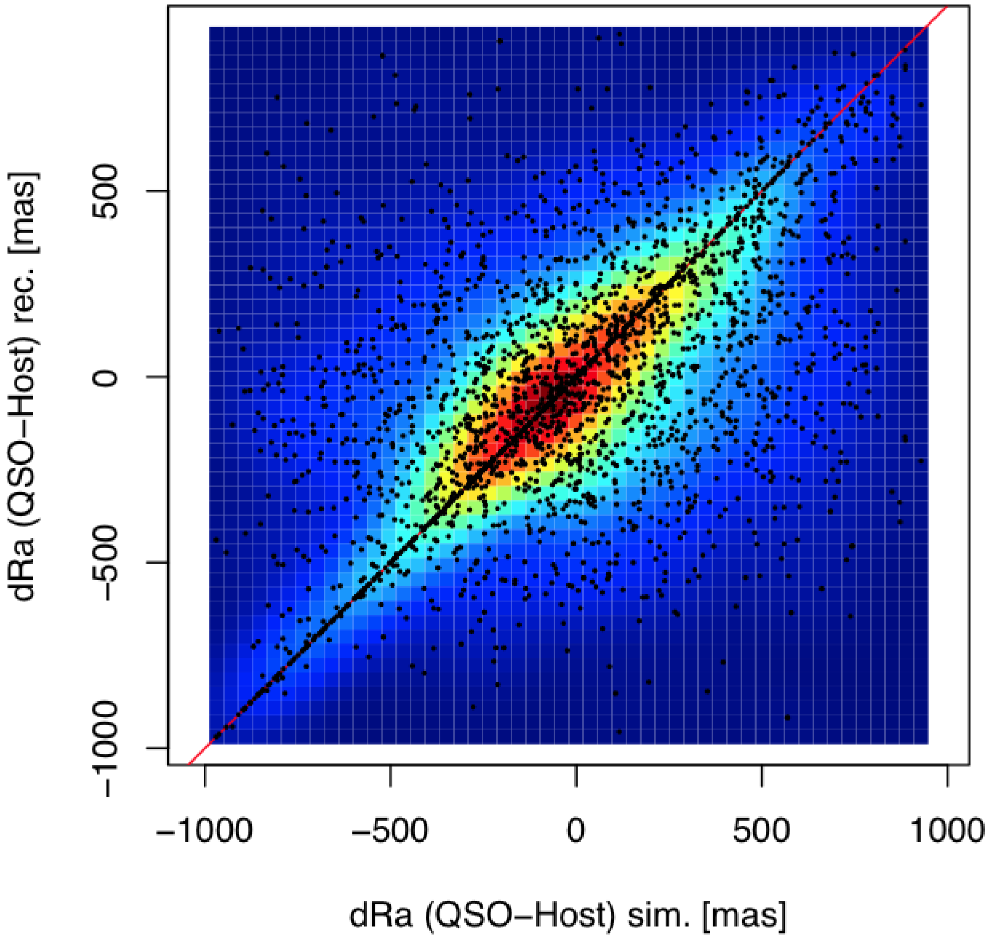

Fig. 5. Recovered offset in right ascension between QSO and host galaxy.

In this last figure we see that it is possible to diagnose problematic QSOs and even to measure the amplitude of the astrometric perturbation. When all classified QSOs will have been so analyzed, it will be possible to select a clean sample of QSOs without structure in optics to perform the global solution of Gaia. Then from these objects, we will select the QSOs called Defining source in the ICRF that will be used to perform the link between the radio and the Gaia system.

6 Conclusion

In this work we have shown that it is possible to enlarge the Gaia horizons by recovering the morphology of the extragalactic objects that the satellite is observing and so, provide important information about the local Universe. The systematic analysis of the QSOs host galaxies will allow a selection of a pure sample of point-like QSOs that could safely be used to perform the most accurate global solution and also to perform the link of the Gaia sphere with the ICRF reference system.

References

De Bruijne, J., Allen, M., Prodhomme, T., Krone-Martins, A., & Azaz., S. 2014, A&Asubmitted

de Souza, R. E., Krone-Martins, A., dos Anjos, S., Ducourant, C., & Teixeira, R. 2014, A&A, 568, A124

Dollet, C., Bijaoui, A., & Mignard, F. 2004, A&A, 426, 729

Krone-Martins, A., Ducourant, C., Teixeira, R., et al. 2013, A&A, 556, A102

Popović, L. Č., Jovanović, P., Stalevski, M., et al. 2012, A&A, 538, A107

SF2A 2014
J. Ballet, F. Bournaud, F. Martins, R. Monier and C. Reylé (eds)

THE PROGRAMME "ACCURATE MASSES FOR SB2 COMPONENTS"*

J.-L. Halbwachs[1], F. Arenou[2], B. Famaey[1], P. Guillout[1], R. Ibata[1], Y. Lebreton[2,3], T. Mazeh[4], A. Nebot[1], D. Pourbaix[5], J.-B. Salomon[1] and L. Tal-Or[4]

Abstract. A selection of spectroscopic binaries (SBs) are observed since 4 years with the T193/Sophie spectrograph, in order to improve their orbital elements. Our aim is to derive accurate stellar masses when the astrometric measurements of Gaia will be available. The last progresses of the programme are presented.

Keywords: binaries: spectroscopic

1 Introduction

An observation program is on going since 2010 at the OHP observatory with the T193/Sophie, in order to improve the orbital elements of a selection of 200 known spectroscopic binaries (SBs) (Halbwachs & Arenou 2009; Halbwachs et al 2014). Our long-term goal is the derivation of accurate stellar masses from the orbital elements of the double-lined spectroscopic binaries (SB2s), taking into account the astrometric measurement of the Gaia satellite. We present the status of this programme after 4 years of observations during which 727 spectra were obtained.

2 Selection of the double-lined binaries

After rejection of a few stars known as multiple systems, the initial selection contained 200 stars: 49 SB2s and 151 single-lined spectroscopic binaries (SB1s). Thanks to the Sophie spectrograph, it was possible to detect an additional component for 25 SB1s. Among these stars, 20 were confirmed as SB2s, and 5 appeared to be multiple systems in reality (Halbwachs et al 2014). Therefore, the present list of targets consists in 69 SB2s, plus 7 stars with uncertain status. The number of observations made for each category of stars is presented in Fig.1. A few discarded stars received a number of spectra much larger than the others; these stars are usually multiple systems which were erroneously considered as new SB2s when an additional component was discovered. The "SB1s still to observe" are SB1s with a cross-correlation function (CCF) exhibiting a dip too wide to allow the detection of the secondary component when they were observed. These stars must be observed again at the phase corresponding to the maximum difference between the radial velocities (RVs) of the components. However, they are low-priority targets, since it will probably not be possible to obtain enough measurements of the secondary RV to derive accurately the masses of the components.

* BASED ON OBSERVATIONS PERFORMED AT THE HAUTE-PROVENCE OBSERVATORY

[1] Observatoire Astronomique de Strasbourg, Université de Strasbourg, CNRS, UMR 7550, 11, rue de l'université, F-67000 Strasbourg, France
[2] GEPI, Observatoire de Paris, F-92195 Meudon, France
[3] Institut de Physique de Rennes, Université de Rennes 1, CNRS UMR 6251, F-35042 Rennes, France
[4] School of Physics and Astronomy, Tel Aviv University, Tel Aviv 69978, Israel
[5] FNRS, Institut d'Astronomie et d'Astrophysique, Université libre de Bruxelles, boulevard du Triomphe, 1050 Bruxelles, Belgium

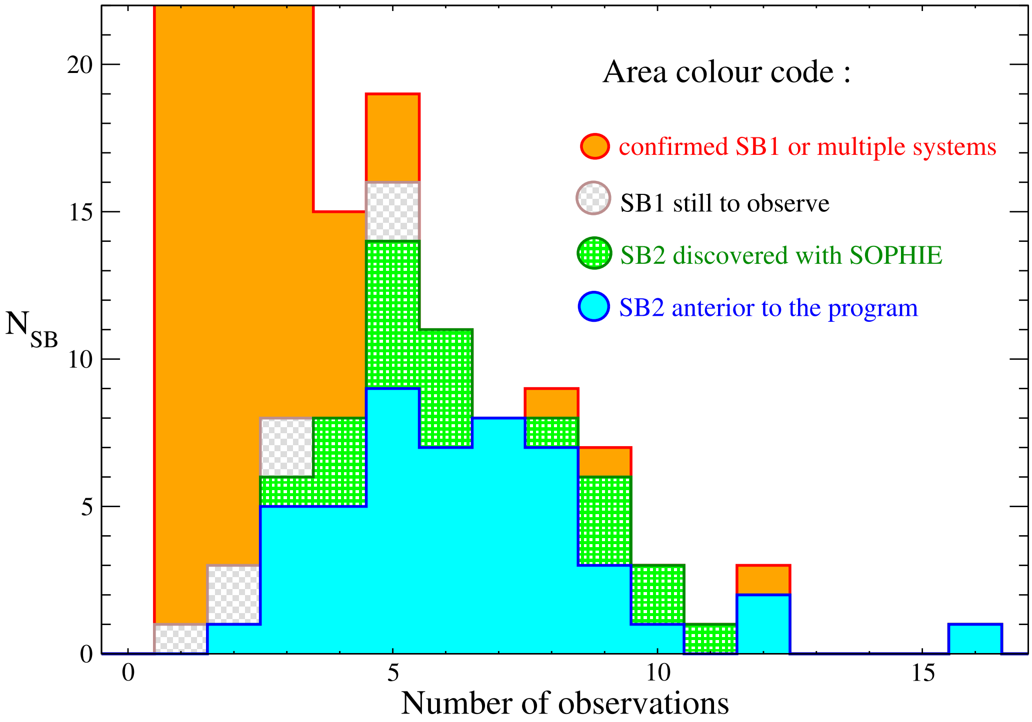

Fig. 1. Histogram of the programme stars according to the numbers of spectra they received, after semester 2013B.

3 Computability of accurate SB orbits

The elements of the spectroscopic orbits were already derived from our Sophie observations for a few SB2s (Halbwachs et al 2012, 2013), but they are not considered as definitive. An SB1 orbital solution consists in 6 parameters: the RV of the barycentre, V_0, the period, P, the eccentricity, e, the periastron epoch, T_0, the periastron longitude, ω, and the semi-amplitude of RV, K_1. Therefore, 7 measurements are a minimum to derive the elements of a SB1 orbit and their uncertainties. For a SB2, the semi-amplitude of the secondary RVs, K_2, is still added to the parameters, and a systematic shift between the RVs of both components must also be added; at the same time, an observation may provide 2 RV measurements, one for each component. With the reasonable assumption that the RV of the primary component may always be measured, it is then sufficient to have 6 observations with 3 measurements of the secondary RV to derive an SB2 orbit with uncertainties: the 6 measurements of the primary RV provide the six elements of the primary orbit, and the 3 measurements of the secondary count for the mass ratio, i.e. for K_2, for the shift between the RV, and for the uncertainties.

However, the minimum of 6 spectra is realistic only when the RV measurements are obtained with reliable estimations of the uncertainties. Otherwise, it is necessary to verify the uncertainties for each component, i.e. to derive separately the SB1 orbital elements of each component. A minimum of 7 spectra, with the secondary RV estimated for each of them, is then required, in order to derive the χ^2 and the F_2 estimator of the goodness-of-fit of the SB1 orbital solution of each component (Stuart & Ord 1994):

$$F_2 = \sqrt{\frac{9\nu}{2}} \left(\sqrt[3]{\frac{\chi^2}{\nu}} + \frac{2}{9\nu} - 1 \right) \tag{3.1}$$

where ν is the number of degrees of freedom. When the uncertainties used in the derivation of χ^2 are realistic, F_2 obeys the normal distribution $\mathcal{N}(0,1)$; therefore, it is usually between -2 and 2. If F_2 is abnormally large, the uncertainties of the RVs must be increased.

With only 7 spectra, the correction of the uncertainties is a bit hazardous, since we have only one degree of freedom. It comes from Eq. 3.1 that, for a target value of F_2, χ^2 is given by the equation:

$$\chi^2(F_2) = \nu \left(1 + \frac{F_2}{\sqrt{4.5\nu}} - \frac{1}{4.5\nu} \right)^3 \tag{3.2}$$

Therefore, when $\nu = 1$, $F_2 = 0$ if $\chi^2 = 0.47$, and $F_2 = 1$ if $\chi^2 = 1.95$. Since the correction to apply to the uncertainties is $\sqrt{\frac{\chi^2(F)}{\chi^2(0)}} = 2.04$, the relative uncertainty of the corrected errors is a bit more than 100 %. This is quite large, and it is necessary to increase the number of measurements to have a reliable correction. With 5 degrees of freedom, i.e. with 11 RV measurements, the accuracy of the uncertainties is 35 %, which is much more acceptable. So we consider that an orbit is reliable if it is derived from a minimum of 11 RV measurements of the secondary component.

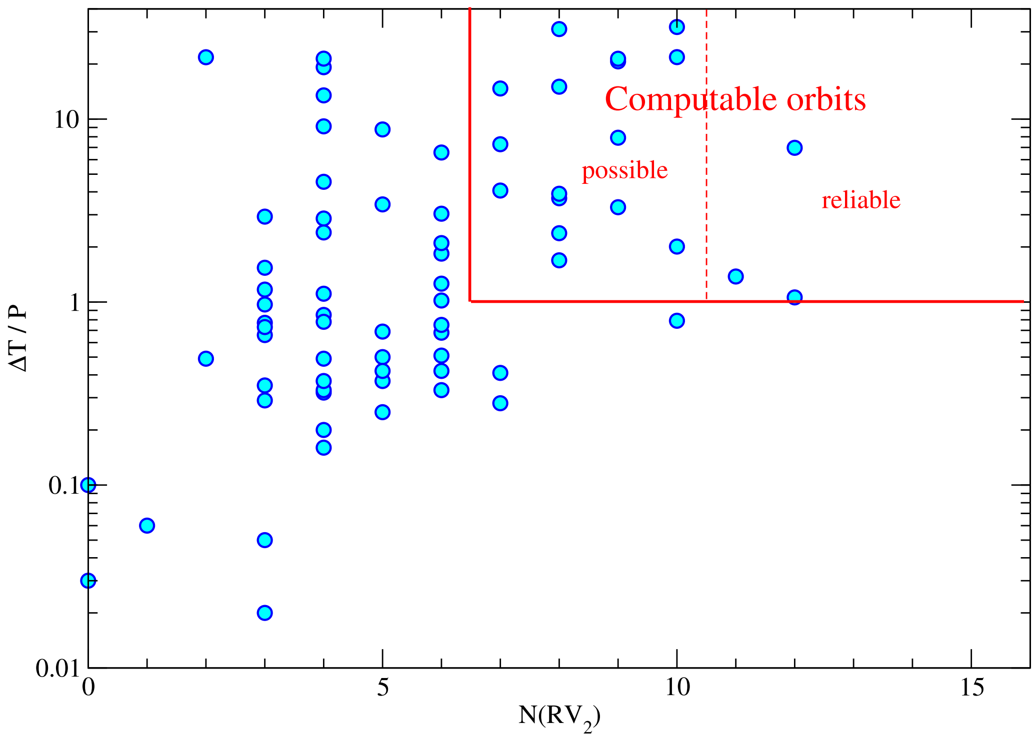

Fig. 2. The number of covered periods vs the number of detections of the secondary dip of the SB2, after semester 2013B.

In addition to the number of measurements, another condition is that the observations must cover a complete orbital period. In Fig. 2, all the SB2s are plotted in a “period coverage vs number of secondary measurements” diagram. It appears that only 3 stars seem to satisfy the conditions to have a reliable orbit, but, in reality, 2 of them received several observations during the same night. Therefore, only one SB2 may be considered as satisfactorily observed. More observations are requested for all the others. It is worth noticing that the calculation used to select the SBs for which accurate masses should be obtained was based on simulations assuming observations distributed over 7 years. The low number of SBs with a derivable orbit after 4 years is not abnormal.

4 Future prospects

4.1 Addition of SBs brighter than 6 mag

At the end of 2013, it appeared that the stars brighter than 6 mag would also receive astrometric measurements from Gaia, when $V > 2$ mag. Ninety-one bright stars, including 16 SB2s, were then added. Except for one star observed with the VLTI (Sect.4.2, hereafter), these stars will be observed with a low priority, during spare time or when the weather conditions are too bad for the faint stars. However, due to bad weather conditions during the two last missions, five candidate new SB2s were already found among these stars.

4.2 Derivation of masses from VLTI measurements

Observing time has been obtained at the VLTI in order to observe 3 SB2s of our programme, including one star from the bright supplement. It will then be possible to derive masses before the end of the Gaia mission, and to validate the masses that we will obtain from Gaia.

5 Conclusions

Our programme is nicely going on. The number of SB2s with a derivable orbit is still small, but it should grow fast during the next years. Accurate masses for a total of around 180 components should be obtained at the end of the Gaia mission if the observations with the T193/Sophie are continued at the same rate.

This project is supported by the french INSU-CNRS “Programme National de Physique Stellaire” and “Action Spécifique Gaia”. We are grateful to the staff of the Haute–Provence Observatory, and especially to Dr F. Bouchy, Dr H. Le Coroller, Dr M. Véron, and the night assistants, for their kind assistance.

References

Halbwachs, J.-L., & Arenou, F. 2009, Proceedings SF2A 2009, M. Heydary–Malayeri, C. Reylé et R. Samadi édr., p. 53

Halbwachs, J.-L., Arenou, F., Famaey, B., Guillout, P., Lebreton, Y., & Pourbaix, D. 2012, Proceedings SF2A 2012, S. Boissier, P. de Laverny, N. Nardetto, R. Samadi, D. Valls-Gabaud & H. Wozniak édr., p. 87

Halbwachs, J.-L., Arenou, F., Guillout, P., Pourbaix, D., Tal-Or, L., Famaey, B., Lebreton, Y., & Mazeh, T. 2013, Proceedings SF2A 2013, L. Cambrésy, F. Martins, E. Nuss, A. Palacio édr., p. 127

Halbwachs, J.-L., Arenou, F., Pourbaix, D., Famaey, B., Guillout, P., Lebreton, Y., Salomon, J.-B., Tal-Or, L., Ibata, R. & Mazeh, T. 2014, MNRAS (accepted), arXiv:1409.1384

Stuart, A., & Ord, K. 1994, Kendall's Advanced Theory of Statistics, vol. 1 (Edward Arnold, London)

SF2A 2014
J. Ballet, F. Bournaud, F. Martins, R. Monier and C. Reylé (eds)

RAVE: RESULTS AND UPDATES FROM DATA RELEASE 4

G. Kordopatis[1,2] and RAVE collaboration

Abstract. The *RAdial Velocity Experiment* (RAVE) published in November 2013 its fourth data release with the stellar atmospheric parameters, abundances, distances, radial velocities, proper motions and spectral morphological flags of more than 4×10^5 targets. With that, a plethora of papers ranging from the mass of the Milky Way to the mapping of the Diffuse Interstellar Band, and from the chemo-dynamical history and properties of the disc to the Galaxy's bar pattern speed have also been published. Being one of the largest spectroscopic surveys in the magnitude range of Gaia, RAVE has helped to pave the way for the exploitation of the Gaia catalogs. Here, we review some of these results and present some perspectives about future RAVE data releases.

Keywords: Surveys, Stars: kinematics and dynamics, Galaxy: stellar content, Galaxy: structure

1 Introduction

The *Radial Velocity Experiment* (Steinmetz et al. 2006) is to date one of the largest spectroscopic surveys of Milky Way stars available to the community. The project finished its observations in April 2013, after obtaining more than half a million spectra of 480,000 stars in the magnitude range $8 < I < 12$ mag. RAVE used the 6dF instrument mounted on the 1.2 m Schmidt telescope of the Anglo-Australian Observatory in Siding Spring, Australia. The targeted spectral region (8410–8794 Å) contains the infrared Calcium triplet and is similar to the wavelength range chosen for Gaia's *Radial Velocity Spectrometer* (RVS, Cropper & Katz 2011). The effective resolution of $R = \lambda/\Delta\lambda \sim 7,000$ enables us to measure line-of-sight velocities with a median precision better than $1.5\,\mathrm{km\,s^{-1}}$. The distribution on the sky of the observed RAVE targets, as of the end of the project (April 2013), is shown in Fig. 1 and covers a large fraction of the sky accessible from the southern hemisphere. One of the major improvements of the RAVE fourth data release (noted DR4 hereafter, Kordopatis et al. 2013a), compared to the previous data releases (Zwitter et al. 2008; Siebert et al. 2011), is its more thorough metallicity calibration based on the RAVE observations of cluster stars and the availability of high-resolution spectra of already observed RAVE targets. In this proceeding we therefore focus in summarising the results of RAVE obtained with DR4. We refer to Siebert (2012) for an overview of the results of the project up to DR3. Section 2 presents the new algorithms used to obtain the stellar parameters, abundances and distances. Sections 3 and 4 outline the main results obtained on the Milky Way structure, dynamics and evolution. Finally, Sect. 5 presents future prospects of the RAVE project.

2 New pipelines used in the fourth data release

2.1 Atmospheric parameters, chemical abundances and detection of chromospheric activity

A new pipeline for spectral automatic parameterisation has been applied on the totality of the RAVE spectra, based on the one presented in Kordopatis et al. (2011a). Compared to previous data releases, the spectral degeneracies are better taken into account, since the employed grid of synthetic spectra has a reduced dimensionality of the parameter space, excludes the core of the Calcium triplet lines and takes into account photometric constraints from the *Two Micron All Sky Survey* (2MASS, Skrutskie et al. 2006). The effective temperatures,

[1] Leibniz-Institut für Astrophysik Potsdam (AIP), An der Sternwarte 16, 14482 Potsdam, Germany
[2] Institute of Astronomy, University of Cambridge, Madingley Road, Cambridge CB3 0HA, United Kingdom

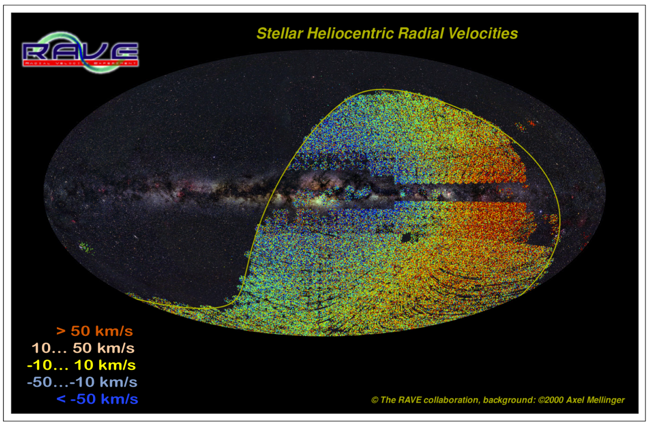

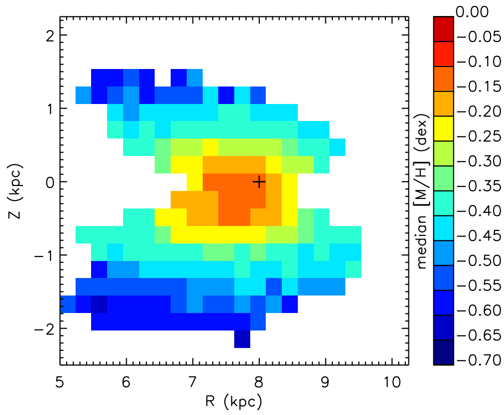

Fig. 1. Left: RAVE footprint on the sky as in April 2013, in Galactic coordinates. The points are colour-coded according to their measured heliocentric radial velocity. **Right:** Median metallicities of the stars as a function of the Galactocentric position (taken from Kordopatis et al. 2013b). Assumed Sun's position is indicated by a "+" sign, at $(R, Z) = (8, 0)$ kpc.

surface gravities and overall metallicities are hence computed in that frame. In addition, the chemical abundance pipeline presented in Boeche et al. (2011) has been improved, in order to obtain the abundances of six elements, namely magnesium, aluminium, silicon, titanium, iron, and nickel. In the same way as for the previous data releases, the methods presented in Matijevič et al. (2011, 2012) and Žerjal et al. (2013) identify and flag, based on spectral morphology, the spectroscopic binaries and peculiar stars, as for example the ones with chromospheric activity. The above pipelines allow us to obtain all the possible parameters relative to the stellar atmospheres that will be used as input for the computation of the stellar distances and from there for the measurement of the global Galactic chemo-dynamical properties.

2.2 *Computation of the line-of-sight distances*

RAVE DR4 publishes two sets of distances, computed from different algorithms. The first one is based on the Zwitter et al. (2010) method that projects the atmospheric parameters on theoretical isochrones introducing only a mild prior on the evolutionary stage at which the star is expected to belong to. The other method, based on the Bayesian approach of Burnett et al. (2011), includes a prior on position, extinction, stellar age and metallicity taken from a realistic Galaxy model, and infers the distance to the star, which is expressed as the expected distance modulus, parallax or line-of-sight distance of the targets, with corresponding uncertainty (Binney et al. 2014a). These distances have been tested on *Hipparcos* targets and cluster members (Binney et al. 2014a, Anguiano et al. submitted), showing relatively small deviations from true values for the types of stars most commonly observed by RAVE. The probed Galactocentric distances ($5 \lesssim R \lesssim 9.5$ kpc), colour-coded according to the mean metallicity of the stars are illustrated in Fig. 1 (taken from Kordopatis et al. 2013b).

3 Milky Way structure and dynamics

Galactic archaeology, achieved through the development of population synthesis codes (e.g.: Galaxia, Sharma et al. 2011) or through models allowing us to disentangle the mechanisms responsible for the evolution of the Galaxy, rely on our knowledge of the Milky Way's structure and kinematics of its stars.

Sharma et al. (2014) took advantage of the large size of RAVE to measure and constrain the age-velocity dispersion relation for the three kinematic components, the radial dependence of the velocity dispersions, the Solar peculiar motion ($\mathrm{U}_\odot = 10.96^{+0.14}_{-0.13}, \mathrm{V}_\odot = 7.53^{+0.16}_{-0.16}, \mathrm{W}_\odot = 7.539^{+0.095}_{-0.09}\,\mathrm{km\,s^{-1}}$), the circular speed at the Sun ($\Theta_0 = 232.8^{+1.7}_{-1.6}\,\mathrm{km\,s^{-1}}$), and the fall of mean azimuthal motion with height above the mid-plane. They found that the Shu distribution function (Sharma & Bland-Hawthorn 2013) describes best the kinematic distributions of the stars and that the radial scale length of the velocity dispersion profile of the thick disc is smaller than that of the thin disc. Binney et al. (2014b) also highlight the non-Gaussianity of the velocity distribution functions and give formulae from which the shape and orientation of the velocity ellipsoid can be determined at any location.

On the other hand, Williams et al. (2013) studied in detail the stellar kinematics in the Solar suburb, concentrating on north-south differences. They found a complex three-dimensional structure in velocity space, with among others a clear vertical rarefaction-compression pattern up to 2 kpc above the plane, suggestive of wave-like behaviour produced by either internal evolution of the Galaxy (e.g.: Faure et al. 2014) or external factors such as accretions (e.g.: Widrow et al. 2014) .

Using a stellar sample ten times larger than RAVE DR1 employed by Smith et al. (2007), the Galactic escape speed has been re-evaluated by Piffl et al. (2014b) to $533^{+54}_{-41}\,\mathrm{km\,s^{-1}}$, confirming previous results and constraining even more the 90% confidence interval. From the escape speed the authors further derived estimates of the mass of the Galaxy using a simple mass model and found that the dark matter and baryon mass interior to three virial radii is $1.3^{+0.4}_{-0.3} \times 10^{12}\mathrm{M_\odot}$, in good agreement with recently published mass estimates based on the kinematics of more distant halo stars and the satellite galaxy Leo I.

Bienaymé et al. (2014) used a subsample of $\sim 4,500$ red clump stars and determined the vertical force at two distances from the plane, the local dark matter density ($\rho_{\mathrm{DM}_{z=0}} = 0.0143 \pm 0.0011\,\mathrm{M_\odot\,pc^{-3}}$) and the baryonic surface mass density ($\Sigma_{\mathrm{baryons}} = 44.4 \pm 4.1\,\mathrm{M_\odot\,pc^{-2}}$). They found evidence for an unexpectedly large amount of dark matter at distances greater than 2 kpc from the plane. On the same topic, Piffl et al. (2014a) modelled the kinematics of giant stars that lie within ~ 1.5 kpc from the Sun and found that the dark mass contained within the isodensity surface of the dark halo that passes through the Sun ($6 \pm 0.9 \times 10^{10}\,\mathrm{M_\odot}$), and the surface density within 0.9 kpc of the plane ($69 \pm 10\,\mathrm{M_\odot\,pc^{-2}}$) are almost independent of the halo's axis ratio q. They estimated that the baryonic mass is at most 4.3 per cent of the total Galaxy mass.

Finally, Antoja et al. (2014) utilised the moving groups available in the database and found that the azimuthal velocity of the Hercules structure decreases as a function of Galactocentric radius. The authors then modelled this behaviour to impose constraints on the bar's pattern speed. The combined likelihood function of the bar's pattern speed and angle has its maximum for a pattern speed of $\Omega_b = (1.89 \pm 0.08) \times \Omega_0$, where Ω_0 is the local circular frequency. Assuming a Solar radius of 8.05 kpc and a local circular velocity of $238\,\mathrm{km\,s^{-1}}$, this corresponds to $\Omega_b = 56 \pm 2\,\mathrm{km\,s^{-1}\,kpc^{-1}}$.

4 Milky Way internal evolution and accretion history

The spatial variations of the chemical properties of the stars and the inter-stellar medium, together with the correlation between the stellar kinematics and their abundances hold important information on the formation and evolution of the Galactic structures. Their measurement requires large statistical samples spanning volumes of several kiloparsecs wide in order to detect large-scale trends and identify rare stellar populations.

An estimation of the amount of interstellar matter along the line-of-sight towards the observed stars can be obtained by analysing the absorption lines in the RAVE spectra, originated from the Diffuse Interstellar Bands (DIBs). Kos et al. (2013, 2014) measured the equivalent width of the DIBs present in the spectra, and produced the first pseudo three-dimensional map of the strength of the DIB at 8620 Å, covering the nearest 3 kpc from the Sun. The authors found that the DIB follows the interstellar dust spatial distribution of extinction, however with a significantly larger vertical scale height. On the other hand, the youngest stellar populations present in RAVE have been investigated by Conrad et al. (2014). In their paper, the authors extract from the RAVE database members of 110 open clusters, and update present cluster catalogues with measures of radial velocities and overall metallicities.

Using the fact that DR4 has large statistical sample of stars at different Galactic regions, Boeche et al. (2013, 2014) measured the radial and vertical gradients in metallicity and individual $\alpha-$elements in the Galaxy. They found a radial gradient $\partial[\mathrm{Fe/H}]/\partial R \sim -0.054\,\mathrm{dex\,kpc^{-1}}$ close to the Galactic plane ($|Z| < 0.4$ kpc) that becomes flatter for larger distances above the plane. Other elements are found to follow the same trend although with some variations from element to element, showing that the thick disc experienced a different chemical enrichment history than the thin disc.

Kordopatis et al. (2013b) selected stars located between 1 and 2 kpc from the Galactic plane in order to investigate the properties of the metal-weak tail of the thick disc. The authors found a kinematic signature of thick disc stars down to metallicities of -2 dex, having the suggested correlation between metallicity and azimuthal velocity of the canonical thick disc stars, of $\partial V_\phi/\partial[\mathrm{M/H}] \approx -50\,\mathrm{km\,s^{-1}\,dex^{-1}}$ (e.g. Kordopatis et al. 2011b, 2013c; Lee et al. 2011). The authors interpreted this result as evidence that radial migration could not have been the main mechanism at the origin of the formation of the thick disc.

Minchev et al. (2014) focused on stars in the Solar vicinity, and analysed the velocity dispersion of the giant disc stars as a function of metallicity and $\alpha-$abundances. The authors found that the metal-poor stars first show an increase in their velocity dispersion, then a decline for the most $\alpha-$enhanced stars ([Mg/Fe] > 0.4 dex). By comparing with their chemo-dynamical evolution models of the Milky Way, the authors suggested that this behaviour is evidence of the merger history of the Galaxy and that the stars responsible for the velocity dispersion decrease are stars that reached the Solar neighbourhood through radial migration from the inner Galaxy. Evidence of radial migration towards the metal-rich end distribution in the disc has also been found in Kordopatis et al. (2014), based on the orbits of the super-Solar metallicity stars.

Finally, Kunder et al. (2014) investigated the chemo-dynamical properties of the stars in the RAVE database around the globular clusters M 22, NGC 1851 and NGC 3201, to assess whether the brightest clusters in the Galaxy might actually be the remnant nuclei of accreted dwarf spheroidal galaxies. The authors report some stars belonging to these clusters being at projected distances of ~ 10 degrees away from their respective cores. In addition, in both of the radial velocity histograms of the regions surrounding NGC 1851 and NGC 3201, a peak of stars at $230\,\mathrm{km\,s^{-1}}$ is seen, consistent with extended tidal debris from ω Centauri.

5 Perspectives and relation with Gaia

Future RAVE data releases are planned to improve, among others, the calibration of the metal-rich end of the metallicity distribution. This will be achieved thanks to the constant addition of metallicity measurements coming from benchmark stars (e.g.: Jofré et al. 2014) and high-resolution spectra of super-solar metallicity stars (see Kordopatis et al. 2014, submitted). In addition, high-precision APASS photometry will also be included in the pipeline to put more weight on the photometric priors (Munari et al. 2014), and hence reducing even more the spectral degeneracies intrinsic to the Calcium triplet wavelength region, responsible to a large extent for the uncertainties in the stellar parameters. Finally, the spectroscopic distances in the catalogue will also be updated for the most metal-poor stars ([M/H] < 1 dex), by including lower-metallicity isochrones.

The Gaia satellite will obtain proper motions of exquisite quality and distances derived by parallax, overtaking RAVE's precisions by orders of magnitude (Prusti 2012). However, atmospheric parameters and radial velocities for the Gaia stars obtained by the onboard instruments "Blue" and "Red spectro-photometers" and the RVS will not be published before the end of 2016 (Brown 2012). Until then, RAVE will represent one of the most significant samples in Gaia's magnitude range, from which Galactic archaeology is possible.

G.K. would like to thank the AS-Gaia and the SF2A for financial support. Funding for RAVE has been provided by: the Australian Astronomical Observatory; the Leibniz-Institut für Astrophysik Potsdam (AIP); the Australian National University; the Australian Research Council; the French National Research Agency; the German Research Foundation (SPP 1177 and SFB 881); the European Research Council (ERC-StG 240271 Galactica); the Instituto Nazionale di Astrofisica at Padova; The Johns Hopkins University; the National Science Foundation of the USA (AST-0908326); the W. M. Keck foundation; the Macquarie University; the Netherlands Research School for Astronomy; the Natural Sciences and Engineering Research Council of Canada; the Slovenian Research Agency; the Swiss National Science Foundation; the Science & Technology Facilities Council of the UK; Opticon; Strasbourg Observatory; and the Universities of Groningen, Heidelberg and Sydney. The research leading to these results has received funding from the European Research Council under the European Union's Seventh Framework Programme (FP7/2007-2013)/ERC grant agreement no. 321067. The RAVE web site is at `http://www.rave-survey.org`.

References

Antoja, T., Helmi, A., Dehnen, W., et al. 2014, A&A, 563, A60

Bienaymé, O., Famaey, B., Siebert, A., et al. 2014, ArXiv e-prints

Binney, J., Burnett, B., Kordopatis, G., et al. 2014a, MNRAS, 437, 351

Binney, J., Burnett, B., Kordopatis, G., et al. 2014b, MNRAS, 439, 1231

Boeche, C., Siebert, A., Piffl, T., et al. 2014, A&A, 568, A71

Boeche, C., Siebert, A., Piffl, T., et al. 2013, A&A, 559, A59

Boeche, C., Siebert, A., Williams, M., et al. 2011, AJ, 142, 193

Brown, A. 2012, in Dynamics Meets Kinematic Tracers

Burnett, B., Binney, J., Sharma, S., et al. 2011, A&A, 532, A113

Conrad, C., Scholz, R.-D., Kharchenko, N. V., et al. 2014, A&A, 562, A54

Cropper, M. & Katz, D. 2011, in EAS Publications Series, Vol. 45, EAS Publications Series, 181–188

Faure, C., Siebert, A., & Famaey, B. 2014, MNRAS, 440, 2564

Jofré, P., Heiter, U., Soubiran, C., et al. 2014, A&A, 564, A133

Kordopatis, G., Gilmore, G., Steinmetz, M., et al. 2013a, AJ, 146, 134

Kordopatis, G., Gilmore, G., Wyse, R. F. G., et al. 2013b, MNRAS, 436, 3231
Kordopatis, G., Hill, V., Irwin, M., et al. 2013c, A&A, 555, A12
Kordopatis, G., Recio-Blanco, A., de Laverny, P., et al. 2011a, A&A, 535, A106
Kordopatis, G., Recio-Blanco, A., de Laverny, P., et al. 2011b, A&A, 535, A107
Kos, J., Zwitter, T., Grebel, E. K., et al. 2013, ApJ, 778, 86
Kos, J., Zwitter, T., Wyse, R., et al. 2014, ArXiv e-prints
Kunder, A., Bono, G., Piffl, T., et al. 2014, ArXiv e-prints
Lee, Y. S., Beers, T. C., An, D., et al. 2011, ApJ, 738, 187
Matijevič, G., Zwitter, T., Bienaymé, O., et al. 2012, ApJS, 200, 14
Matijevič, G., Zwitter, T., Bienaymé, O., et al. 2011, AJ, 141, 200
Minchev, I., Chiappini, C., Martig, M., et al. 2014, ApJ, 781, L20
Munari, U., Henden, A., Frigo, A., et al. 2014, AJ, 148, 81
Piffl, T., Binney, J., McMillan, P. J., et al. 2014a, ArXiv e-prints
Piffl, T., Scannapieco, C., Binney, J., et al. 2014b, A&A, 562, A91
Prusti, T. 2012, Astronomische Nachrichten, 333, 453
Sharma, S. & Bland-Hawthorn, J. 2013, ApJ, 773, 183
Sharma, S., Bland-Hawthorn, J., Binney, J., et al. 2014, ApJ, 793, 51
Sharma, S., Bland-Hawthorn, J., Johnston, K. V., & Binney, J. 2011, ApJ, 730, 3
Siebert, A. 2012, in SF2A-2012: Proceedings of the Annual meeting of the French Society of Astronomy and Astrophysics, ed. S. Boissier, P. de Laverny, N. Nardetto, R. Samadi, D. Valls-Gabaud, & H. Wozniak, 121–127
Siebert, A., Williams, M. E. K., Siviero, A., et al. 2011, AJ, 141, 187
Skrutskie, M. F., Cutri, R. M., Stiening, R., et al. 2006, AJ, 131, 1163
Smith, M. C., Ruchti, G. R., Helmi, A., et al. 2007, MNRAS, 379, 755
Steinmetz, M., Zwitter, T., Siebert, A., et al. 2006, AJ, 132, 1645
Žerjal, M., Zwitter, T., Matijevič, G., et al. 2013, ApJ, 776, 127
Widrow, L. M., Barber, J., Chequers, M. H., & Cheng, E. 2014, MNRAS, 440, 1971
Williams, M. E. K., Steinmetz, M., Binney, J., et al. 2013, MNRAS, 436, 101
Zwitter, T., Matijevič, G., Breddels, M. A., et al. 2010, A&A, 522, A54
Zwitter, T., Siebert, A., Munari, U., et al. 2008, AJ, 136, 421

RECONSTRUCTING THE SFH OF THE MILKY WAY

O. N. Snaith[1], M. Haywood[2], P. Di Matteo[3] and M. Lehnert[4]

Abstract. Recent galactic archaeology results suggest that the stellar mass budget of the Milky Way requires reassessment, particularly regarding the mass of the thick disc. Our results imply a massive thick disc and are in agreement with the results of redshift surveys of Milky Way-type galaxies. We report our previous work on recovering the SFH of the Milky Way from solar vicinity data and discuss how recent and future surveys will refine our understanding.

Keywords: Milky Way, star formation history, chemical evolution

1 Introduction

There are two main approaches to recovering the evolution of the Milky Way from observations. We can use Galactic Archaeology to reconstruct the behavior of the Galaxy, using the characteristics of different stellar populations, such as the chemical and dynamical properties of stars (a recent example being Bovy et al. 2012). The alternative is to study the properties of Milky Way-like galaxies at different redshifts, using large statistically significant samples of galaxies (e.g. van Dokkum et al. 2013). Here, we will discuss our method for recovering the star formation history (SFH) of the Milky Way (presented in detail in Snaith et al. 2014b), which mainly follows the Galactic Archaeology approach. We do, however, compare our results with the work of van Dokkum et al. (2013), who use the other method (see Snaith et al. 2014b, for further details.).

The Milky Way has, historically, been thought to consist of a dominant thin disc, with a less massive thick disc and much smaller stellar halo. However, recent results, (van Dokkum et al. 2013; Haywood et al. 2013; Snaith et al. 2014b) have called this into question, and suggest that the thick disc is substantially more massive than implied by the previous orthodoxy. A massive thick disc has been discussed before (e.g Fuhrmann et al. 2012; Gilmore & Wyse 1986) but has not, historically, been favoured.

Haywood et al. (2013) supported an alternative model of the Milky Way, based on solar vicinity data, which we explored in Snaith et al. (2014a,b) and Snaith et al. (2014b). In Snaith et al. (2014b) we reassessed the mass budget of the Milky Way by recovering the SFH that best replicates the chemical evolution of solar vicinity stars.

2 Data & Interpretation

We used a sample of 365 stars in the solar vicinity, with very precise abundances, kinematics and ages. These stars were selected by Haywood et al. (2013) from 1111 stars observed by Adibekyan et al. (2012). The ages were then calculated, taking into account the alpha abundances of the stars. Only stars with well defined ages were included in the Haywood et al. (2013) sample. Formal errors on the ages are 1-1.5 Gyr (increasing with age), due to uncertainties in stellar physics and atmospheric parameters.

The stars were divided into three subsamples. A first cut was made according to the metallicity-[α/Fe] distribution. At low metallicity ([Fe/H]<-0.2 dex) there are two parallel sequences. The lower alpha sequence was attributed in Haywood (2008) and Haywood et al. (2013) to stars from the outer thin disc which contaminate

[1] Department of Physics and Astronomy, University of Alabama, Box 870324, Tuscaloosa, AL 35487-0324, USA
[2] GEPI, Observatoire de Paris, CNRS, University Paris Diderot, 5 place Jules Janssen, 92190, Meudon, France
[3] 2
[4] Institut d'Astrophysique de Paris, UMR 7095, CNRS, Universie Pierre et Marie Curie, 98bis Bd Arago, 750514, Paris, France

the solar vicinity (green symbols on Fig. 1 panel a). The status of these objects has been confirmed on larger surveys (see Bovy et al. 2012, their figure 7).

Haywood et al. (2013) further labeled the stars not included in the outer disc as either thick disc or inner thin disc stars. This was done according to the distinct behavior of the alpha-age relation for stars older and younger than 8 Gyr, (blue and red points for Silicon in Fig. 1, panel b), reflecting the distinct SFR regimes at these two epochs.

We calculated the orbits of the stars in an axisymetric potential from Allen & Santillan (1991), using the velocity and position data observed by Adibekyan et al. (2012). The thick disk stars in the local vicinity have pericenters and apocenters which span from less than 2 kpc to about 10 kpc, and so cover the whole disc (Snaith et al. 2014a). With stars coming from across the disc, we assume that stars trace out the locus of the chemistry and age distribution representative of the entire disc.

3 The Model

We used a simple galactic chemical evolution (GCE) code, without any gas infall or outflows, to model the Milky Way (see Snaith et al. 2014a, Snaith et al. 2014b, Haywood 2014). The model assumes: (1) all gas which can form stars is present throughout the evolution, but makes no assumptions as to whether the gas is cold star forming gas, warm circumgalactic gas or hot halo gas. This assumption is equivalent to saying the accretion of gas is not significantly delayed and does not introduce any dependency of the SFR on the gas accretion (2) the gas is initially primordial. (3) The gas is homogeneous at all times. No a priori shape is given to the SFH, which is used as a free parameter to fit the data.

The ingredients into the model are: Nomoto et al. (2006), Iwamoto et al. (1999) and Karakas (2010) stellar yields, the Kroupa (2001) IMF, and the stellar lifetimes of Raiteri et al. (1996). The only input into the model is the SFH.

We then use a χ^2 fitting algorithm to match the chemical evolution of the model to the data by fitting the stellar age-[Si/Fe] distribution and recovering the best-fit star formation history. We fit the inner thick and thin discs with a single star formation history. The outer disk is the result of a different chemical evolution history, as suggested by Haywood et al. (2013), and shown in Snaith et al. (2014a). Here, we will only discuss the inner disc, see Snaith et al. (2014a) for a discussion of the outer disc.

4 Galactic Archaeology

Using the model outlined in the previous section, we identified the SFH which produced the age-[Si/Fe] distribution that best matches the data, (see Snaith et al. 2014a,b).

The chemical evolution track which results from the best fit SFH is shown in Fig. 1, and clearly fits the age-[Si/Fe] distribution (panel b), as well as the metallicity-[Si/Fe] distribution (panel a) of the inner discs. The track does, however, follow the upper limit of the age-metallicity distribution (panel c). The SFH itself (Fig. 2, panel a) shows four particular features: (1) the SFR during the thick disc phase is three times that of the thin disc, (2) the thick disc phase falls sharply at a lookback time 8 Gyrs, (3) the interface between the thick and thin discs shows a 1 Gyr dip in the star formation rate, (4) star formation in the thin disc is relatively constant.

Although the thick disc formation only lasts between 13-8 Gyr it is characterised by a considerably higher SFR than the thin disc. During the thick disc phase the Galaxy assembles $\sim$50% of its total stellar mass (Fig. 2, panel b). This makes a considerable change from models where the thick disc is small, or not explicitly included (e.g. Chiappini et al. 1997). Our SFH leaves us with a very massive thick disc, in tension with the canonical model of the Milky Way.

Using SEGUE data Bovy et al. (2012) found that the thick and thin stellar discs have different radial scale lengths. These are given as 1.8 kpc for the thick disc, and a mean of 3.6 kpc for the thin disc (the thin disc scale length is found to vary with metallicity in Bovy et al. 2012).

If we model the Milky Way as two exponential discs, using the radial scale length provided by Bovy et al. (2012), and take into account the standard surface density of thick and thin disc stars in the solar vicinity, then, a massive thick disc, comparable in mass to the thin disc, is implied. This lends considerable weight to the massive thick disc model of the Galaxy.

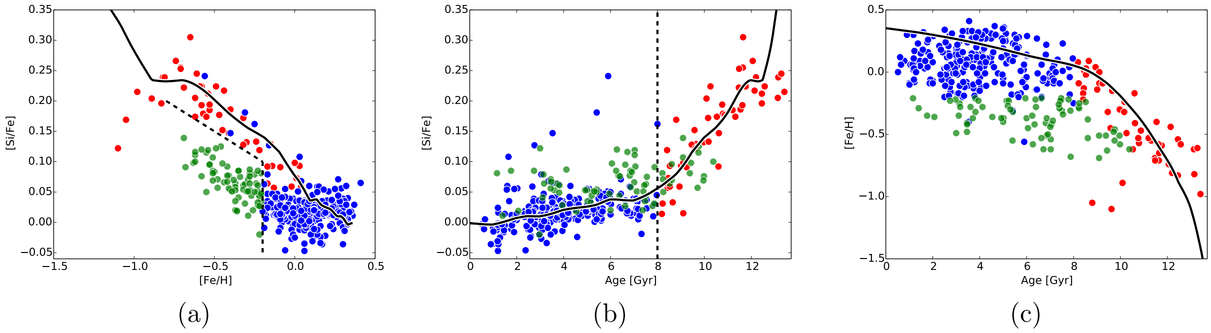

Fig. 1. The best fit chemical evolution tracks for the GCE model (black line) of Snaith et al. (2014a) and Snaith et al. (2014b). Panel (a) gives the metallicity-[Si/Fe] distribution, panel (b) gives the [Si/Fe] evolution with time and panel (c) gives the metallicity evolution with time. The red, blue and green points are stars assigned to the thick, inner thin and outer thin discs. The dashed line in panel (a) defines the outer thin disc while vertical dashed line in panel (b) is the split between the thick and thin discs . The data are taken from Haywood et al. (2013)

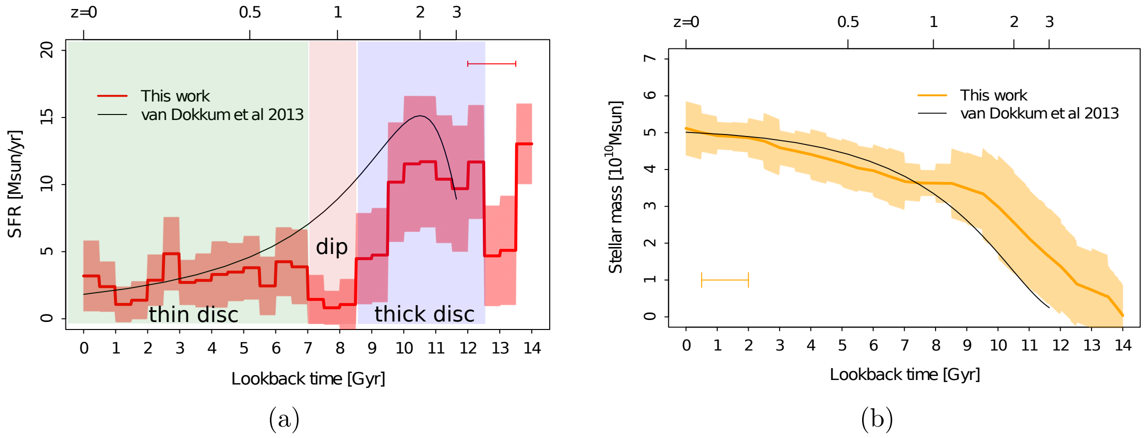

Fig. 2. Left: The SFH recovered for the inner disc of the Milky Way (from Snaith et al. 2014b) and the SFR evolution of Milky Way type galaxies (from van Dokkum et al. 2013). The coloured area shows the error due to bootstrapping the data. **Right:** The stellar mass assembly history (from Snaith et al. 2014b) of the Milky Way against that recovered by van Dokkum et al. (2013) for Milky Way type galaxies. This figure was taken from Snaith et al. (2014b).

5 Milky Way-type galaxy evolution

van Dokkum et al. (2013) explored the evolution of Milky Way-type galaxies out to z=2.5, and derived empirical expressions for their mass assembly and star formation rate.

It is clear from Fig. 2, taken from Snaith et al. (2014b), that much of the mass in Milky Way-type galaxies was assembled before a lookback time of 8 Gyrs (the black curves). With appropriate scaling this produces a mass assembly history similar to our recovered SFH (Snaith et al. 2014b).

It is clear that the van Dokkum et al. (2013) data implies a considerable fraction of the stellar mass in a Milky Way type galaxy forms before z=1, thus demonstrating that a massive thick disc for the Milky Way is unsurprising.

6 The Future

Gaia will produce a vast sample of Milky Way stars, covering a sizable fraction of stars in the disc and bulge. This mission will provide unparalleled data on the astrometric properties of stars. Spectroscopic surveys will be combined with distance measurements from Gaia, and will allow us to calculate much more accurate ages for stars. They will also provide alpha element abundances far beyond the solar vicinity.

We have illustrated in Snaith et al. (2014a) and Snaith et al. (2014b) that it is possible to reconstruct the star formation history of the Milky Way from solar vicinity data, if we assume that the solar vicinity contains stars representative of the entire disc. This is expected to be true (Snaith et al. 2014a) for old stars, but becomes less so for younger stars. The immense sample of stars, over a wide range of radii, expected in the future, will allow us to test that our results are valid beyond the solar vicinity.

Fuhrmann et al. (2012) and Gilmore & Wyse (1986) envisioned that the thick disc might have an important role in the history of the Milky Way. Our evidnce suggests that this is indeed the case. With this reappraisal it is important to discuss this in the context of idealized simulations (e.g. Di Matteo et al. 2014). A large thick disc has previously been neglected in many idealised models. It is essential to understand the features in a galaxy that are the result of a massive thick disc, so that such models can be tested by forthcoming observations.

7 Conclusions

Recently, highly precise observations have led to tension with the canonical model of a low mass thick disc. For example: (1) Haywood et al. (2013) interpret exquisite observations of the solar vicinity, and find that they imply a massive thick disc, (2) Snaith et al. (2014b) fit the Adibekyan et al. (2012) and Haywood et al. (2013) data using a GCE code and return a thick disc containing 50% of the Galaxy's stellar mass, (3) Bovy et al. (2012) utilize SDSS data to calculate local densities, and disc scale lengths. A massive thick disc arises from the geometry of the system. (4) van Dokkum et al. (2013) explore large scale surveys out to high redshifts, and find that a substantial fraction of the stellar mass of Milky Way type galaxies forms before z=1.

With the current and forthcoming Milky Way surveys providing ever larger and more precise data on Milky Way stars, it is important to improve our theoretical understanding of the Galaxy, including a massive thick disc, in order to interpret new data.

The authors acknowledge support from the French Agence Nationale de la Recherche (ANR) under contract ANR-10-BLAN-0508 (Galhis project). Support for ONS was partially provided by NASA through the Hubble Space Telescope Archival Research grant HST-AR-12837.01-A from the Space Telescope Science Institute, which is operated by the Association of Universities for Research in Astronomy, Incorporated, under NASA contract NAS5-26555. ONS thanks the support received from the European Science Foundation (ESF) within the framework of the ESF activity entitled 'Gaia Research for European Astronomy Training'

References

Adibekyan, V. Z., Sousa, S. G., Santos, N. C., et al. 2012, A&A, 545, A32

Allen, C. & Santillan, A. 1991, Rev. Mexicana Astron. Astrofis., 22, 255

Bovy, J., Rix, H.-W., Liu, C., et al. 2012, ApJ, 753, 148

Chiappini, C., Matteucci, F., & Gratton, R. 1997, ApJ, 477, 765

Di Matteo, P., Gómez, A., Haywood, M., et al. 2014, A&A, submitted

Fuhrmann, K., Chini, R., Hoffmeister, V. H., & Bernkopf, J. 2012, MNRAS, 420, 1423

Gilmore, G. & Wyse, R. F. G. 1986, Nature, 322, 806

Haywood, M. 2008, MNRAS, 388, 1175

Haywood, M. 2014, Mem. Soc. Astron. Italiana, 85, 253

Haywood, M., Di Matteo, P., Lehnert, M. D., Katz, D., & Gómez, A. 2013, A&A, 560, A109

Iwamoto, K., Brachwitz, F., Nomoto, K., et al. 1999, ApJS, 125, 439

Karakas, A. I. 2010, MNRAS, 403, 1413

Kroupa, P. 2001, MNRAS, 322, 231

Nomoto, K., Tominaga, N., Umeda, H., Kobayashi, C., & Maeda, K. 2006, Nuclear Physics A, 777, 424

Raiteri, C. M., Villata, M., & Navarro, J. F. 1996, A&A, 315, 105

Snaith, O., Haywood, M., Di Matteo, P., et al. 2014a, ArXiv e-prints:1410.3829

Snaith, O. N., Haywood, M., Di Matteo, P., et al. 2014b, ApJ, 781, L31

van Dokkum, P. G., Leja, J., Nelson, E. J., et al. 2013, ApJ, 771, L35

SF2A 2014
J. Ballet, F. Bournaud, F. Martins, R. Monier and C. Reylé (eds)

ON THE CHEMICAL COMPOSITION OF OPEN CLUSTERS

C. Soubiran[1], S. Blanco-Cuaresma[1] and U. Heiter[2]

Abstract. Open clusters are key objects to study the chemical evolution of the Galactic disk, but metallicities and detailed abundances are available for only a small fraction of them. We review here the current status of metallicity determinations. Open clusters are also perfect objects to test the chemical tagging method which intends to identify stars formed from the same molecular cloud. First results about this technique are presented, based on homogeneously derived chemical abundances for a large sample of stars in open clusters.

Keywords: Stars: abundances - Open clusters - Surveys

1 Introduction

Open clusters (OCs) represent an important tool for studying the chemical evolution of the galactic disk, thanks to their spatial distribution all over the disk, and their wide age range. Metallicities are also mandatory for the determination of OC ages by ischrone fitting. The measurement of detailed chemical abundances implies spectroscopic observations at high or medium resolution, which are available for only ∼10% of the currently known OCs (Heiter et al. 2014). The analysis of these observations are made by widely differing methods, so that the resulting chemical abundances are not homogeneous. The situation is changing rapidly thanks to the Gaia ESO survey (Gilmore et al. 2012), and other spectroscopic surveys, which are targetting large samples of OCs. The combination of the results from these different surveys needs however some calibration and homogenization. For faint OCs at large galactocentric distances, only metallicities based on photometric data can be determined. In a few years, Gaia will deliver the metallicities of the ∼2000 OCs known to date (Dias et al. 2002), and probably thousands of newly discovered ones. Here we present the current status of OC metallicities and abundances together with prospects in that field.

With precise elemental abundances for stars in OCs, it is possible to evaluate if stars born from the same molecular cloud have the same chemical signature, and if the chemical signatures are different from one OC to another. This would make it possible to use the chemical tagging method to reconstruct the star formation history in the galactic disk, as proposed by Freeman & Bland-Hawthorn (2002). Here we present an extensive test of the chemical tagging method.

2 The status of open cluster metallicities

Paunzen et al. (2010) have compiled a catalogue of OC metallicities based on photometric data. They searched the literature for [Fe/H] estimates on the basis of photometric calibrations in any available filter system. In total, they find 406 individual metallicity values for 188 OCs within 64 publications, which were averaged. They show that the metallicity distribution near the Sun is patchy and this influences the estimation of the Galactic metallicity gradient, even on a global scale. More distant OCs are needed to study the metallicity distribution beyond several kiloparsecs.

The situation of the metallicity of OCs from high and medium resolution spectroscopy has been evaluated by Heiter et al. (2014). They have considered the mean high-resolution spectroscopic metallicity per publication and they found significant differences, up to 0.6 dex, for the same OC. The largest differences are observed for

[1] LAB UMR 5804 - Univ. Bordeaux - CNRS, 2 rue de l'Observatoire, F-33270 Floirac
[2] Uppsala University, Box 516, 751 20 Uppsala, Sweden

the Hyades, Collinder 21 and NGC 6633. They also demonstrate that the dispersion within an OC can be significantly reduced by carefully selecting non binary star members, and by restricting their effective temperature and surface gravity ranges to 4400 – 6500 K and 2.0 – 4.5. With such criteria, they define a sample of 458 stars in 78 OCs from 86 publications which forms a set of high-quality cluster metallicities. Using this sample and the one by Paunzen et al. (2010), they show that photometric metallicities are systematically more metal-poor than spectroscopic ones by 0.11 dex. This carefully selected spectroscopic sample is the most accurate and homogeneous one to date for testing models predicting the radial metallicity gradient in the Galaxy. Heiter et al. (2014) show that none of the current models is able to reproduce the OC metallicities versus galactocentric distance. The metallicity dispersion in the solar neighbourhood is large, and OCs are on average more metal-rich than predicted by the models. There is a lack of OC at large galactocentric distances to safely constrain the metallicity gradient over the disk.

The situation will improve in the coming years thanks to several spectroscopic surveys focused on OCs and their chemical abundances. The Gaia ESO Survey (Gilmore et al. 2012) has a list of $\sim$100 OCs to be observed with FLAMES at the VLT. APOGEE will target OCs at large distances (Frinchaboy et al. 2013). The HERMES (Zucker et al. 2012) and WEAVE (Dalton et al. 2012) multi-object spectrographs also intend to investigate the OC chemical abundances. Metallicities will thus be available for a much larger number of OCs than today. However these surveys will use different instruments, resolutions, spectral ranges, line lists and methods to determine the stellar properties. If we want to avoid the current situation found in the literature where a large dispersion is seen in the OC metallicities, it is essential that these surveys coordinate their calibration procedures with common OCs. This will enable the stellar parameters and metallicities to be on the same scale, homogeneous, and thus the combination of the surveys will be possible for a better investigation of the chemical evolution of the galactic disk.

However, even if many more OCs will be soon observed at high spectral resolution, this will still represent a small fraction of all the known OCs : 2174 in the version 3.3 of the catalogues by Dias et al. (2002).

When considering only the metallicity, which is essential for the age determination of OCs, one should rely on photometric data. The new method developed by Netopil & Paunzen (2013) shows a better agreement of photometric and spectroscopic metallicities and will be applied to a large number of OCs. Thanks to this project, photometric and spectroscopic samples of OCs will be on a consistent metallicity scale which is essential for galactic studies. With photometric surveys, the sample of OCs can be extended to the outskirts of the Milky Way, where spectroscopic studies are almost impossible. In a few years, Gaia will provide the metallicity of all known OCs thanks to the APSIS pipeline based on spectrophotometric data for one billion stars (Bailer-Jones et al. 2013).

3 Chemical tagging in open clusters

The chemical tagging is a technique to identify stars formed from the same molecular cloud but subsequently separated. It is based on the principle that stars formed from the same molecular cloud share the same abundance pattern, assuming that the progenitor cloud was chemically homogeneous and well-mixed. Thus stars having the same abundance pattern are supposed to have formed in the same molecular cloud. It was suggested by Freeman & Bland-Hawthorn (2002) that this technique could enable to track individual stars back to their common formation sites and to reconstruct the history of star formation in the Galaxy. Before the chemical tagging technique can be applied to large scale studies, it is necessary to test it with stars known to have formed together, such as in OCs. The use of the chemical tagging technique with OCs should allow us to verify whether stars born together have a unique chemical signature, and whether the chemical signatures of OCs are distinguishable.

Before large spectroscopic surveys are available, some tests can be done using high-resolution spectra of OC stars available in public archives, complementing our own observations made in the frame of the Gaia preparation. A very homogeneous analysis of nearly 300 spectra of 189 stars in 32 OCs was performed using the iSpec code (Blanco-Cuaresma et al. 2014). Atmospheric parameters and elemental abundances were determined using 275 481 lines and 12 153 elemental abundances of 17 species. The sample was carefully cleaned of poor data and outliers in order to test the chemical tagging method in ideal conditions. First, a Principle Component Analysis (PCA) was performed to reduce the parameter dimension from 17 to 2. Then a clustering analysis was perfomed with the K-Means algorithm to group stars with similar chemical signatures.

The first result is that the dwarf and giant stars have different chemical signatures, and have to be considered separately when comparing OCs, as seen in Fig. 1. For instance in M67 (Fig. 2) the dispersion of chemical abundances is in general of the order of 0.10 dex when dwarfs and giants are mixed. When dwarfs and giants are considered separately, the dispersion in each group decreases below 0.05 dex for most of the elements. There are two main possible explanations for this finding, one astrophysical, one methodological : it could be due to different diffusion and mixing processes in the dwarf and giant phases, or it could also be due to the assumptions and simplifications (e.g. LTE and 1D model atmospheres) made in the spectral analysis.

A PCA and clustering analysis was performed with all the giants as shown in Fig. 3. A few OCs are well separated from the others, such as M67 and NGC6705, but for the vast majority, it is not possible to reliably distinguish the chemical properties of the stars of one cluster from those of another; although the clusters form clear groups, the overlap in derived abundances does not allow for clear discrimination.

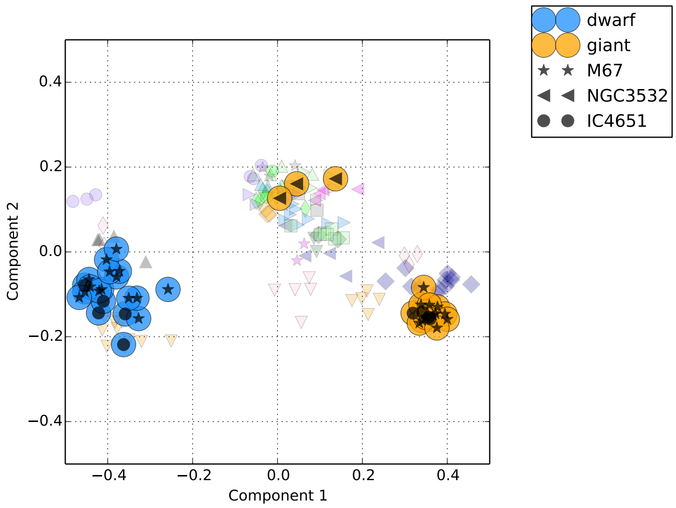

Fig. 1. Result of a PCA on OCs having both giants and dwarfs. The two groups well separated correspond to dwarfs and giants stars.

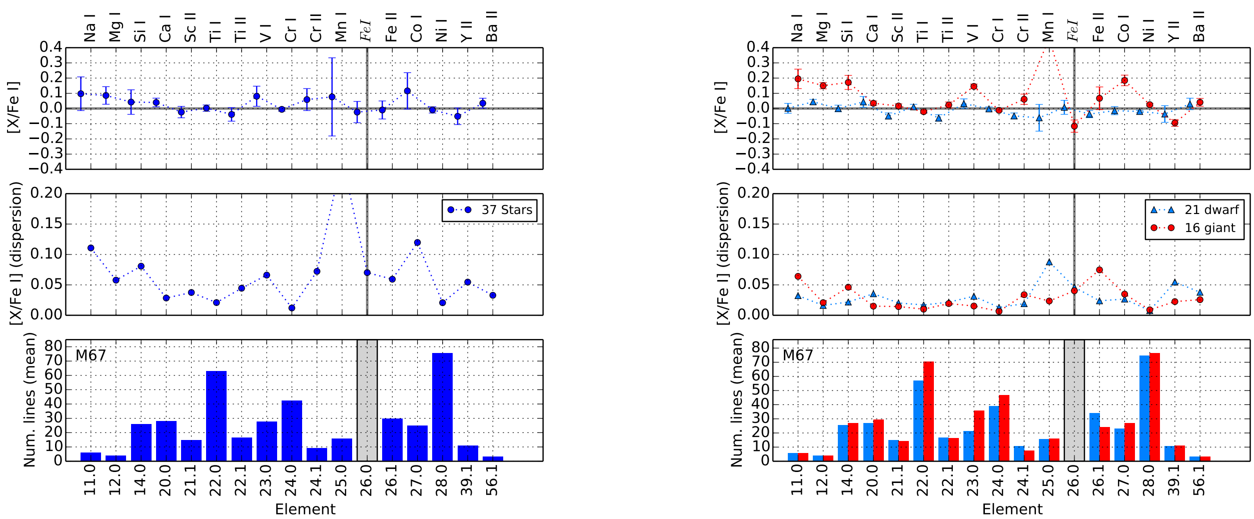

Fig. 2. Average chemical abundances (top), dispersion (middle) and mean number of lines (bottom) used for M67 stars (left) and divided into dwarfs and giants (right). All the abundance ratios are referenced to iron except iron itself, which is relative to hydrogen.

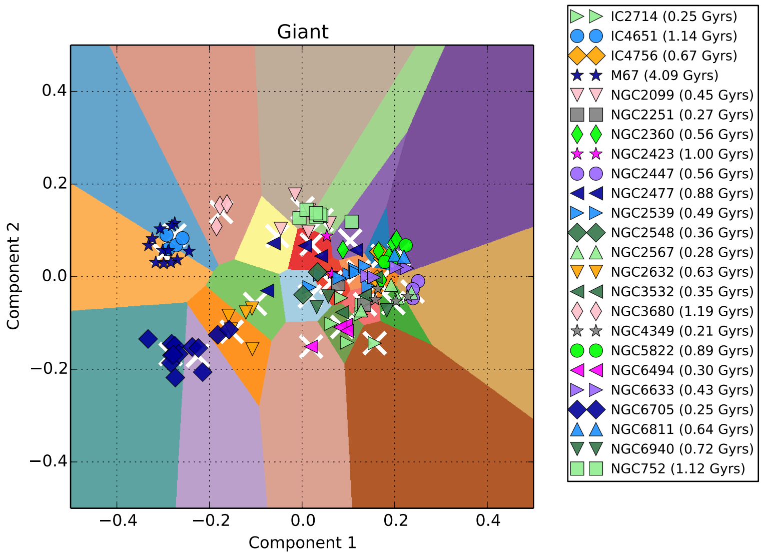

Fig. 3. Giants in OCs represented using the first two components of PCA. Background colors correspond to the clusters found by the K-Means algorithm.

4 Conclusions

To date less than 100 OCs have metallicities determined from high resolution spectroscopy. With photometric calibrations, and later with Gaia spectrophotometry, metallicities for all known OCs will be determined. Detailed abundances will be provided by high resolution spectroscopic surveys (Gaia ESO Survey, APOGEE, HERMES, WEAVE, etc), and other focused observing programmes, for a small fraction of OCs. Calibration and homogeneity is crucial when combining the results coming from these different sources.

From high quality spectra already available for a number of OCs, it was possible to test the chemical tagging method. It is shown that dwarfs and giants need to be considered separately when comparing elemental abundances from one OC to another. It is shown that only a few OCs have a distinct chemical signature from the bulk population. At the current level of precision, it seems difficult to apply the chemical tagging method to reconstruct the star formation history in the galactic disk.

Gaia will provide distances and proper motions, essential for membership, and ages for all known OCs, and will likely discover thousands of new ones. Highly valuable material will be available to probe the properties and evolution of the Milky Way thin disc with OCs, through their chemical abundance distribution and evolution with time.

References

Bailer-Jones, C. A. L., Andrae, R., Arcay, B., et al. 2013, A&A, 559, A74

Blanco-Cuaresma, S., Soubiran, C., Heiter, U., & Jofré, P. 2014, A&A, 569, A111

Dalton, G., Trager, S. C., Abrams, D. C., et al. 2012, in Society of Photo-Optical Instrumentation Engineers (SPIE) Conference Series, Vol. 8446, Society of Photo-Optical Instrumentation Engineers (SPIE) Conference Series

Dias, W. S., Alessi, B. S., Moitinho, A., & Lépine, J. R. D. 2002, A&A, 389, 871

Freeman, K. & Bland-Hawthorn, J. 2002, ARA&A, 40, 487

Frinchaboy, P. M., Thompson, B., Jackson, K. M., et al. 2013, ApJ, 777, L1

Gilmore, G., Randich, S., Asplund, M., et al. 2012, The Messenger, 147, 25

Heiter, U., Soubiran, C., Netopil, M., & Paunzen, E. 2014, A&A, 561, A93

Netopil, M. & Paunzen, E. 2013, A&A, 557, A10

Paunzen, E., Heiter, U., Netopil, M., & Soubiran, C. 2010, A&A, 517, A32

Zucker, D. B., de Silva, G., Freeman, K., Bland-Hawthorn, J., & Hermes Team. 2012, in Astronomical Society of the Pacific Conference Series, Vol. 458, Galactic Archaeology: Near-Field Cosmology and the Formation of the Milky Way, ed. W. Aoki, M. Ishigaki, T. Suda, T. Tsujimoto, & N. Arimoto, 421

SF2A 2014
J. Ballet, F. Bournaud, F. Martins, R. Monier and C. Reylé (eds)

GAIA-FUN-SSO: A NETWORK FOR GROUND-BASED FOLLOW-UP OBSERVATIONS OF SOLAR SYSTEM OBJECTS

W. Thuillot[1], B. Carry[1], J. Berthier[1], P. David[1], D. Hestroffer[1] and P. Rocher[1]

Abstract. Gaia-FUN-SSO (shortly described at https://www.imcce.fr/gaia-fun-sso/) is a ground-based network of observatories set up in the framework of the Gaia consortium (DPAC-CU4) for the follow-up of critical Solar System objects to be discovered from space by the Gaia satellite. Its goal is to retrieve from the ground a newly detected object and to complement the astrometry measurements carried out by Gaia to determine its heliocentric orbit. Data from both Gaia and the ground-based network will be sent to the Minor Planet Center, used to determine the orbit and thus to update the database of minor planet orbits, which is subsequently used by Gaia for the identification of moving objects. We are expecting the detection of many asteroids, mainly from the main belt, and also new near-Earth objects (NEO) at low solar elongation. Owing to the specific conditions of Gaia observations, we even expect the detection of objects whose orbit is fully contained within Earth's orbit (called inner-Earth or Atira asteroids). Several training campaigns have already been organized with the network and it is now able to enter in an operating mode when alerts will be triggered. We describe here the expected number of discoveries, the network, its activity, and the data processing of the central node of the network set in place for the operating mode.

Keywords: Gaia, Solar System Objects, asteroids, follow-up

1 Introduction

Launched in December 2013, the Gaia mission was commissioned in the first half of 2014 and entered in operations over the summer 2014. Owing to the observational mode, i.e. a survey based on a specific scanning law, transient events will be detected by Gaia but will not be monitored. Among these events, detection of supernovae, variable astrophysical objects, and so on are expected, but there will be detection of Solar System Objects (SSO) as well. All these detections require a rapid ground based follow-up. Otherwise the different phases of the photometric events (e.g., supernovae lightcurves) will not be observed and thus analysed. Furthermore the orbit of the moving objects may not be determined and these objects themselves may subsequently become intractable. To characterize these events, the Gaia Data Processing and Analysis Consortium (DPAC) has implemented the triggering of alerts to activate different follow-up networks which have been set up. Our team is particularly concerned with the SSO follow-up within the frame of the Coordination Unit 4 (CU4 - object processing) of the Gaia DPAC consortium. This article describes the deployed workchain for organizing such ground-based observations upon receiving an alert. This task is within the scope of the SSO short term data processing through a specific task (DU459 according to the Gaia designation) entitled "Ground-based follow-up observations". It combines two main objectives: ensuring quick astrometric observations on alert for validation of SSO discovery, and ensuring an astrometric follow-up for determination and improvement of the orbital parameters. For these goals two important actions have been performed: the set-up of a network of observing stations and the development of a data processing chain to feed the network with ephemerides of the critical objects.

2 Expected number of discoveries

Since the discovery of (1) Ceres in 1801, minor planets have been constantly discovered. The number of discoveries has strongly increased in the last 20 years, with new objects discovered daily. The current census

[1] IMCCE-Paris Observatory, 77 av. Denfert Rochereau 75014, Paris, France

of minor planets, from near-Earth asteroids to Kuiper Belt objects, is of 656,000 (October 2014). How many objects can we expect to be discovered by Gaia, with a limiting magnitude of 19.5? To answer this question we proceed as follows.

The evolution of the size-frequency distributions (based on their absolute magnitude H), for each population of small bodies – near-Earth asteroids (NEA), main-belt asteroids (MBA), Jupiter Trojans, Centaurs, and Kuiper Belt objects (KBO) –, are dominated by collisions, and follow power law (Dohnanyi 1969), as seen in Fig. 1. Therefore a fit to each of a power law can be used to extrapolate the number of objects observable within the limiting apparent magnitude of Gaia, at $V \approx 19.5$. The populations' 25%, 50%, and 75% quartiles semi-major axis and eccentricity, can be used to convert this limit into an absolute magnitude assuming an observing geometry at a solar elongation of 90°. The phase function is computed using Bowell H-G system. The resulting limiting magnitudes are plotted as vertical dashed lines in Fig. 1.

This simple computation, based on current census of asteroids, shows that the number of main-belt asteroids yet to be discovered within Gaia limiting apparent magnitude is of the order of 10^4, up to 3.10^4. The number of NEAs is much lower, only of the order of a few 10^2. Here, only the number of yet unknown asteroids is estimated and should be understood as an upper limit on the possible number of discoveries by Gaia.The following caveats need to be remembered. Slight changes in the power law, and/or different observing geometries (Gaia will observe from 45° to 135° solar elongation) yield slightly different estimates. Gaia may not observe all these objects, or other surveys may discover some of them before Gaia.

Therefore, under the assumption that 500 NEAs and 25,000 MBAs will be detected by Gaia, the expected number of alerts is of the order of a hundred per week, 2% of which will concern NEAs.

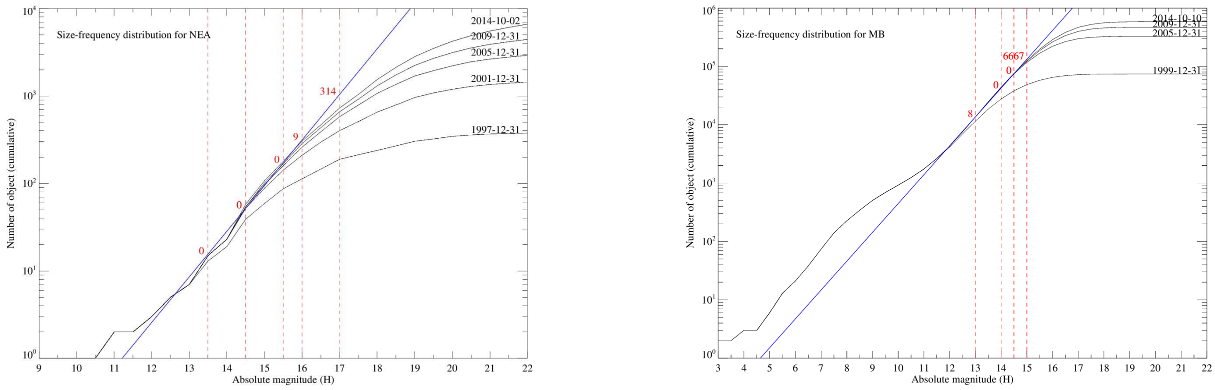

Fig. 1. Size-frequency distribution (in black) of Near-Earth Asteroids (NEA) and Main Belt Asteroids (MBA) , with fitted power law distribution (in blue).

3 The data processing and distribution chain

During the short term data processing, detected moving objects are considered to belong to the Solar system. Their measured positions are compared to the computed model ephemerides which use initial conditions provided by the ASTORB database (Muinonen & Bowell 1993) of orbital elements from the Lowell observatory, which is periodically updated to include all recent observations. This allows, at least in principle, the discrimination between known and unknown objects. Once a detection of a possibly new object is inferred, a series of tasks are performed, accurate astrometry measurement, the possible links with previously observed positions, and finally a simulation which provides all the orbits which are compatible with the observations using a MCMC (Monte Carlo Markov Chain) method (Muinonen et al. 2012), i.e. a list of all the possible orbital elements.

The IMCCE-Paris Observatory laboratory is the central node of a ground-based network, the Gaia-FUN-SSO network (Gaia Follow-Up Network for Solar System Objects). It will receive the lists of orbital elements, which are the essence of the alert for newly detected Solar System Objects, to be processed locally for dissemination to the observer community.

The role of this central node is to propagate (i.e., to compute the ephemeris of) the aforementioned preliminary orbits of the alert, and to identify regions of interest on the sky where observers are invited to search for the new object. For this, knowledge of topocentric parameters and instrumental characteristics (e.g., field of view, limiting magnitude) of each station allows to disseminate the alert in an efficient way: viz. only to observatories capable of performing the observation. A pipeline has been developed to carry out this task automatically.

As soon as an observer has recovered the object, he is invited to measure its astrometric position and to send the results to both the central node and the Minor Planet Center (MPC, Marsden et al. 1994) which centralizes all observations of minor planets. The MPC will take these observations and compare them with previous observations of poorly known asteroids and/or recent discoveries to test for possible links. The MPC will also compute the orbital elements of the objects and will integrate it into the following release (daily) of the public database. This will help subsequent identification of the object if observed by Gaia again because the update of the orbital database used in Gaia pipeline (ASTORB) closes the loop including the MPC and Lowell Observatory (see Fig. 2).

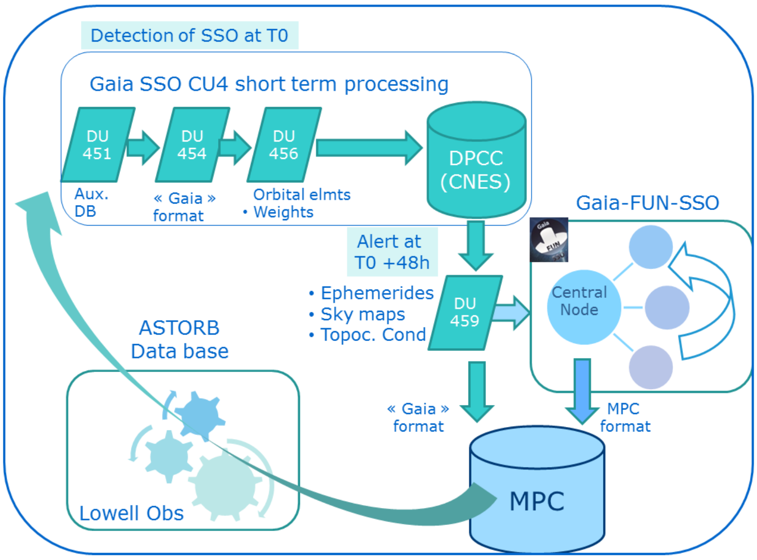

Fig. 2. Workchain of the ground-based network

4 The Gaia-FUN-SSO network

Since 2010, numerous observatories, both professional and amateur, have joined the Gaia-FUN-SSO network. A wiki has been set up at the address `https://www.imcce.fr/gaia-fun-sso/` to provide basic information and also to organize training observations. The network currently includes 54 observing stations, which represents 75 operating telescopes of different sizes. We took the opportunity of close approaches of near-Earth Objects with the Earth to organize nine training campaigns (2011 Nov-Dec. for 2005 YU55; 2012 Feb.-March for 1996 FG3; 2012 Feb.-March and 2012 Dec.-2013 Apr. for 99 942 Apophis; 2013 Feb.-March for 2012 DA14; 2013 Aug. for 2002 GT June; 2013 Oct.2014 Jan. for 2013 TV135; 2014 Apr. for 2007 HB15; 2014 June for 2014 HQ124) . These observations were similar (apparent magnitude, urge of observation, solar elongation) to those the network will have to conduct on alert.

In addition to the training campaigns, we also organized workshops in order to gather observers, to exchange information about the requirements and to be informed about the local instruments and activities. These workshops have been held in Paris Observatory in 2010 and 2012. A third one is organized on 24-26 November 2014 (see `http://www.imcce.fr/hosted_sites/gaiafun2014/`).

Fig. 3. Localization of the different stations of the Gaia-FUN-SSO network.

5 Conclusion

During its 5 year mission, Gaia will detect new Solar System Objects, up to a few hundred near-Earth asteroids and several thousands of asteroids in the main belt. Owing to the scanning mode of observation, there will be no possibility for Gaia to monitor these objects after detection, and their orbits are unlikely to be determined uniquely enough so as to not lose their track. To avoid this situation, a ground-based network, called the Gaia-FUN-SSO, has been set up. The Gaia mission will rely on the observatories of this network to observe, on alert and on a volonteering basis, the new objects and thus provide astrometric measurements to the Minor Planet Center. By this mean, the auxiliary database of orbital elements which allows Gaia to identify known objects, will be updated.

References

Dohnanyi, J. S. 1969, Journal of Geophysical Research, 74, 2531

Marsden, B. G., Green, D. W. E., & Williams, G. V. 1994, in IAU Symposium, Vol. 160, Asteroids, Comets, Meteors 1993, ed. A. Milani, M. di Martino, & A. Cellino, 489

Muinonen, K. & Bowell, E. 1993, Icarus, 104, 255

Muinonen, K., Granvik, M., Oszkiewicz, D., Pieniluoma, T., & Pentikäinen, H. 2012, Planet. Space Sci., 73, 15

Session 12

Atelier PNPS

SF2A 2014
J. Ballet, F. Bournaud, F. Martins, R. Monier and C. Reylé (eds)

AUTOMATED PROCEDURE TO DERIVE FUNDAMENTAL PARAMETERS OF B AND A STARS: APPLICATION TO THE YOUNG CLUSTER NGC 3293

E. Aydi[1], M. Gebran[1], R. Monier[2,3], F. Royer[4], A. Lobel[5] and R. Blomme[5]

Abstract. This work describes a procedure to derive several fundamental parameters such as the effective temperature, surface gravity, equatorial rotational velocity and microturbulent velocity. In this work, we have written a numerical procedure in Python which finds the best fit between a grid of synthetic spectra and the observed spectra by minimizing a standard chi-square. LTE model atmospheres were calculated using the ATLAS9 code and were used as inputs to the spectrum synthesis code SYNSPEC48 in order to compute a large grid of synthetic Balmer line profiles. This new procedure has been applied to a large number of new observations (GIRAFFE spectra) of B and A stars members of the young open cluster NGC3293. These observations are part of the GAIA ESO Survey. Takeda's procedure was also used to derive rotational velocities and microturbulent velocities. The results have been compared to previous determinations by other authors and are found to agree with them. As a first result, we concluded that using this procedure, an accuracy of ± 200 K could be achieved in effective temperature and ± 0.2 dex in surface gravities.

Keywords: Open Cluster, NGC 3293, Space Mission, Fundamental Parameters, Synthetic Spectra.

1 Introduction

Open clusters are of tremendous importance to astrophysics. Stars in clusters serve as "laboratories" for astronomers, as all are nearly at the same distance and have the same age and initial chemical composition. Hence open clusters are key objects in the study of stellar evolution (Edvardson 1993). The determination of the effective temperature and surface gravity of stars in open clusters are instrumental in assigning proper spectral types to each star and pre-requisites to the determination of other parameters as the projected rotational velocity, microturbulent velocity and chemical abundances (Evans et al. 2005). The quantity of available astronomical data has increased considerably with the implementation of extensive surveys such as SDSS and RAVE, and will continue to increase in the near future especially with the European Space Agency Gaia mission. Therefore, there is a need to analyze these data in an homogeneous and efficient way.

Gaia's Radial Velocity Spectrograph (RVS) will collect millions of stellar spectra at a resolution of R=11500. These spectra will allow us to derive fundamental parameters of these stars and the abundances of a few chemical elements.

The need of an automated procedure for classification of stars has been discussed recently using different codes and mathematical approaches. As an example, one can mention the MATISSE algorithm (Recio-Blanco et al. 2006) or Hekker et al. (2009) semi-automated procedures.

In this preliminary work, we present the first steps of an automated procedure aiming at determining several stellar parameters. The procedure is applied to a large sample of A and B stars members of the young open cluster NGC 3293 with an age ∼ 10 Myrs. The observations are part of the Gaia-ESO public survey. The effective temperatures ($T_{\rm eff}$) and surface gravities ($\log g$) of the selected stars were determined by adjusting a large grid of synthetic spectra to the observed ones, in particular to The Balmer line profiles. LTE model

[1] Department of Physics & Astronomy, Notre Dame Univeristy - Louaize, Zouk Mikael Lebanon
[2] LESIA/CNRS UMR 8109, Observatoire de Paris – Université Pierre et Marie Curie – Université Paris Denis Diderot, 5 place Jules Janssen, 92190 Meudon, France
[3] Laboratoire Lagrange, Université de Nice Sophia Antipolis, Parc Valrose, 06100 Nice, France
[4] GEPI/CNRS UMR 8111, Observatoire de Paris – Université Paris Denis Diderot, 5 place Jules Janssen, 92190 Meudon, France
[5] Royal Observatory of Belgium, Ringlaan 3, B–1180 Brussels, Belgium

atmospheres were calculated using the ATLAS9 code (Kurucz 1992) and were used in order to compute a large grid of synthetic Balmer line profiles using SYNSPEC48, Hubeny & Lanz (1992) spectrum synthesis code. Takeda's (1995) procedure was used in order to determine the projected rotational velocity $v_e \sin i$ and the microturbulent velocityξ_t.

2 Observation and data reduction

The selected stars are members of the young open cluster NGC 3293 which was observed in the frame of the Gaia-ESO survey. These spectroscopic data consist of three spectral ranges, two of which sample H_δ [4030 $\AA$ - 4200 $\AA$] and H_α [6300 $\AA$ - 6500 $\AA$], the third one samples several lines of the iron-peak elements from 4350 $\AA$ up to 4550 $\AA$. The targets were observed using the FLAMES-GIRAFFE spectrograph with a resolution of R $\sim$ 25000 mounted on the unit 2 telescope (UT2) of the European Southern Observatory (Paranal-Chile).
The selected spectra are calibrated using GIRAFFE ESO pipeline which involves mainly bias subtraction, scattered light removal, bad pixel masking, flat-fielding, extraction, and wavelength calibration.
After this reduction the flux is given in arbitrary units. The normalization of the spectrum is done using the IRAF (Image Reduction and Analysis Facility) software (Tody D. 1986). To ensure we correctly located regions free of lines (when available) in each order, we have computed synthetic spectra using the code SYNSPEC48 (Hubeny & Lanz 1992) assuming a solar metallicity for the various temperatures and surface gravities of our stars. The spectra were then rectified to the local continuum.

3 Model atmospheres and synthetic spectra calculations

The calculations of the LTE model atmospheres were carried out using Kurucz's ATLAS 9 code (Kurucz 1992). Model atmospheres were computed assuming a plane parallel geometry, hydrostatic equilibrium, radiative equilibrium and depth independent turbulent velocity fixed to 2 km.s^{-1} and solar abundances (Grevesse & Sauval 1998). We ran ATLAS 9 for effective temperatures ranging from 6000 K up to13000 K and for surface gravities from 3.0 dex up to 5.0 dex.

The model atmospheres computed with ATLAS 9 served as inputs to SYNSPEC48. Two important files are read as inputs before the computation of the theoretical flux: the ATLAS9 model atmosphere and the linelist for each of the three spectral regions aforementioned (compiled from Gebran et al. (2010)). Balmer lines were calculated using these set of model atmospheres for different $T_{\rm eff}$ and $\log g$ and concolved with i) a Gaussian profile having the instrumental FWHM and ii) a parabolic rotational profile for the appropriate $v_e \sin i$. All convolved spectra have a resolving power R $\sim$ 25000.
The grid obtained from SYNSPEC48 consists of $\sim$ 230000 synthetic spectra whose effective temperatures range from 6000 K to 13000 K calculated with a step $\Delta(T_{\rm eff}) = 50$ K, the surface gravities range from 3.0 dex to 5.0 dex calculated with a step $\Delta(\log g) = 0.05$ dex, and the projected rotaional velocities range from 0 to 200 km/s with a step $\Delta(v_e \sin i) = 5$ km/s.

4 The procedure

Our procedure, written in Python, looks for the best fit between a grid of synthetic spectra and the observed one. It performs the following sequence:
- Reading the data : the procedure reads both the synthetic and the observed spectra.
- Interpolation : An interpolation is performed so that the theoretical fluxes be evaluated at exactly the same wavelengths as the observed spectra.
- Radial velocity and scaling factors: radial velocity is derived during the procedure. A scaling factor was introduced so as to correct for any residual slope after continuum normalization.
- Chi-square calculation and minimization between observed and synthetic spectra from the grid.
- The results : $T_{\rm eff}$, $\log g$, $v_e \sin i$, and the radial velocity are derived automatically after running the procedure using our synthetic grid. All results were checked visually by over-plotting the best fit to the observation.

Tests were carried out over the whole range of $T_{\rm eff}$ and $\log g$ in order to check the efficiency of the procedure. As a test, we chose one of the synthetic spectrum and used it as a surrogate observed spectrum. After including all kinds of effects such as radial velocity shift, scaling factor, a decrease in the S/N, we always ended up having a consistent result.

In order to minimize the calculation time per observation, we attempted to decrease the number of computed spectra in our grid (originally $\sim 230{,}000$) leading to an increase of the fundamental parameters steps. For that reason, we have specifically studied the effect of each parameter alone on the final result over the entire range of effective temperatures, surface gravities and rotational velocities, our tests show that adopting a step of 100 K in $T_{\rm eff}$, 0.1 dex in $\log g$, and 50 km/s in $v_e \sin i$ leads to an accuracy of of $\pm$ 200 K in effective temperature and $\pm$ 0.2 dex in surface gravities. Using these steps will reduce the size of the grid to $\sim$ 7000 synthetic spectra which shortens the calculation time for each observation from 5 days to $\sim$ 4 hours.

5 Determination of $v_e \sin i$ and ξ_t

The second part of this work consisted in deriving accurate values for $v_e \sin i$ and ξ_t. These two parameters were derived iteratively using Takeda's (1995) procedure which minimizes the chi-square between the normalized synthetic spectrum and the observed one. The synthetic spectra were calculated using the previously determined $T_{\rm eff}$ and $\log g$.
Technically, rotational velocities ($v_e \sin i$) and microturbulent (ξ_t) velocities were derived using several weak and moderately strong FeII lines located between 4491.405 Å and 4508.288 Å and the MgII triplet at 4480 Å and assuming solar abundances.

6 Results

The procedure was applied to 80 stars. $T_{\rm eff}$, $\log g$, and preliminary values of $v_e \sin i$ was derived for all stars. More accurate values of $v_e \sin i$ and ξ_t were derived for 32 stars using Takeda's (1995) iterative procedure. Fig. 1 displays an example of the best fit between observed spectra (in black) and the synthetic ones (in red).

The left part of Fig. 2 displays the derived microturbulent velocities as a function of the effective temperatures derived from Takeda's procedure. These results show that ξ_t reaches its maximum around 8000 K (3$\pm$1 km/s) then decreases to 1 km/s around 6000 K and for high temperatures. This result agrees well with previous determinations : Gebran & Monier (2007), Gebran et al. (2013), Takeda et al. (2008) and with Smalley's (2004) prescriptions for convection for tepid stars.

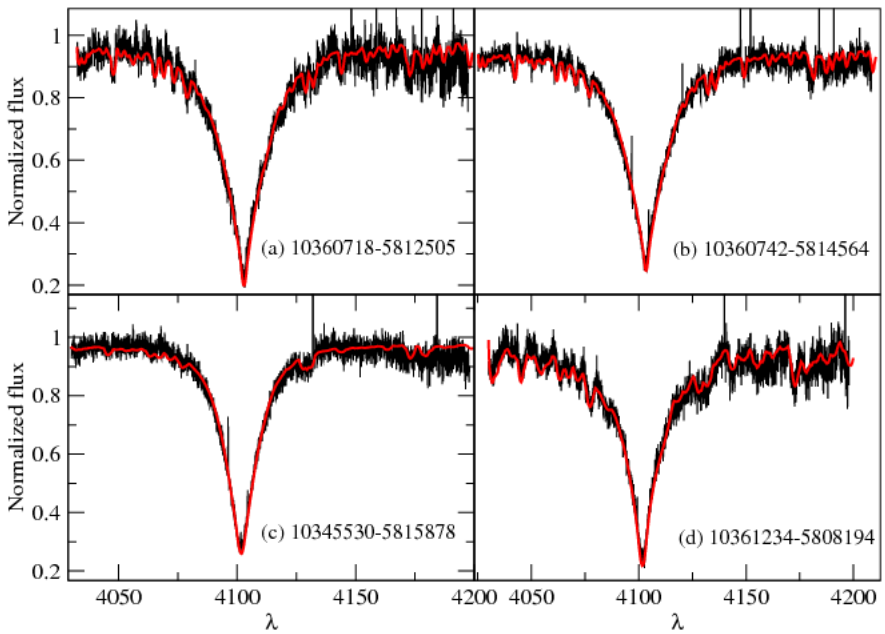

Fig. 1. Synthetic spectra (in red) superimposed to the observed ones (in black) for 4 stars member of NGC3293.

The right part of Fig. 2 displays the comparison between our derived effective temperature and the ones from the CASU GES archive (v2.1), as calculated by S. Koposov. We found very good agreement for most of the stars. Large discrepabcies exist for a few stars only which are assigned large temperatures in the GES archive. Our determinations differ by up to ~6000 K which is far larger than the expected error bar. The symbol depicted in red in the right part of Fig. 2 corresponds to the observed spectra displayed in Fig. 1(d). Our derived temperature for this star is about 4000 K lower than the one derived by the GES team whereas the surface gravities are very close.

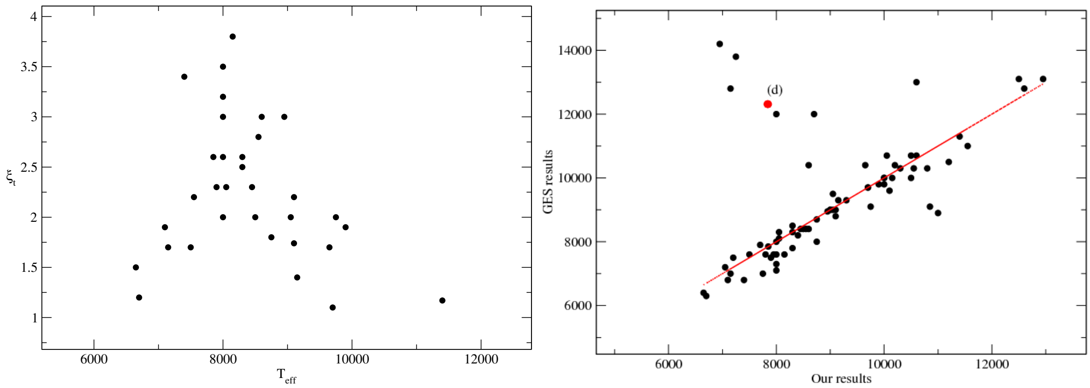

Fig. 2. Left: Microturbulent velocity in km/s as a function of effective temperature $T_{\rm eff}$ in K for the selected stars. **Right**: Comparison between the derived effective temperatures and the ones from the CASU GES archive (v2.1), as calculated by S. Koposov.

7 Conclusions and future works

The present procedure provides a fast automatic tool to provide estimates of the effective temperatures and surface gravities for a large number of stars. Hence, this procedure can be applied to large spectroscopic surveys (RAVE, Gaia, ...). The accuracy achieved using this procedure is about± 200 K in $T_{\rm eff}$ and ± 0.2 dex in $\log g$. The derived microturbulent velocities agree well with Gebran & Monier (2007), Gebran et al. (2013), Takeda et al. (2008) and with Smalley's (2004) prescriptions for B, A, and F stars.

This procedure is currently being improved so that it can derive the projected rotational velocity and microturbulent velocity without having to resort to Takeda's procedure. The results should be constrained using another Balmer line such as the H_α profile. More refinements such as adopting depth-dependent abundances and microturbulent velocities should ultimately be brought to the procedure. The derived parameters will ultimately be used to derive detailed elemental abundances for the studied stars and constrain physical processes at work in the radiative zones of tepid stars.

Acknowledgements: This work is based on observations collected with the FLAMES spectrograph at the VLT/UT2 telescope (Paranal Observatory, ESO, Chile), for the Gaia-ESO Large Public Survey, programme 188.B-3002.

References

Edvardsson, B., Andersen, J., Gustafsson, B., et al. 1993VizieR Online Data Catalog, 410, 20603

Evans, C. J., Smartt, S. J., Lee, J.-K., et al. 2005, A& A, 437, 467

Gebran, M., & Monier, R. 2007, IAU Symposium, 239, 160

Gebran, M., Vick, M., Monier, R., & Fossati, L. 2010, A&A, 523, A71

Gebran, M., Monier, R., Royer, F., Lobel, A., & Blomme, R. 2013, arXiv:1312.0442

Grevesse, N., & Sauval, A. J. 1998, Space Science Reviews, 85, 161

Hekker, S., Frémat, Y., Lampens, P., et al. 2009, MNRAS, 396, 1689

Hubeny, I., & Lanz, T. 1992, Bulletin of the American Astronomical Society, 24, 1152

Kurucz, R.L. 1992, Rev. Mexicana AyA 23, 45

Recio-Blanco, A., Bijaoui, A., & de Laverny, P. 2006, MNRAS, 370, 141

Sacco, G. G., Morbidelli, L., Franciosini, E., et al. 2014, A&A, 565, A113

Smalley B., Proceedings IAU Symposium n224, 2004
Takeda Y., 1995, PASJ 47, 287
Takeda, Y., Han, I., Kang, D.-I., Lee, B.-C., & Kim, K.-M. 2008, Journal of Korean Astronomical Society, 41, 83
Tody, D. 1986, PROCSPIE, 627, 733

SF2A 2014
J. Ballet, F. Bournaud, F. Martins, R. Monier and C. Reylé (eds)

IDENTIFICATION OF PROTOSTELLAR CLUSTERS IN THE INNER PART OF THE MILKY WAY : INTERACTION BETWEEN THE ISM AND STAR FORMING REGIONS.

M. Beuret[1], N. Billot[2], L. Cambrésy[1], D. Elia[3], S. Molinari[3], S. Pezzuto[3], M. Pestalozzi[3] and E. Schisano[3]

Abstract. Interactions between the interstellar medium (ISM) and young stellar objects (YSO) need to be investigated to better understand star formation. We used the Minimum Spanning Tree (MST) method to identify protostellar clusters in the inner part of galactic plane. Using heliocentric distance estimates, we obtained about 230 clusters over a 140×2 square degree region. Most of these clusters are correlated with Infrared Dark Cloud (IRDC) or HII regions. We conclude that clustering is more important for protostars than for prestellar clumps and that a strong correlation can be established between the distribution of HII regions, known star formation complexes and the YSOs identified in the Hi-GAL data.

Keywords: ISM : HII regions – Stars : formation – Stars : protostars

1 Introduction

The Herschel telescope provides us with a new perspective for characterizing Young Stellar Objects (YSOs) in the far-infrared and submillimeter wavelengths. We aim at studying clustering properties of nascent stars and the interaction between the interstellar medium and star forming regions. We use Herschel data from the Herschel Infrared Galactic Plane Survey (Hi-GAL, Molinari et al. 2010) together with information on the environmental conditions such as HII regions and infrared dark clouds (IRDC). The combination of heliocentric distance and Herschel resolutions at the different wavelengths (70, 160, 250, 350 and 500 μm) do not allow us to resolve individual objects as single sources but rather clumps with unresolved internal structure.

Here we consider the $-61° < l < +67°$ portion of the Hi-GAL compact source catalog (Elia et al. 2014, in preparation; for a preliminary example of source property estimation, see Elia et al. 2013), wich is the largest sample available of far-infrared sources, containing the physical properties of about 100000 objects. One of the important physical properties is the evolutionary stage. A general evolutionary classification is reported in this catalog, based on the availability of a detection at 70μm wich indicates the presence of one or more warm sources (protostellar sources, 25% of all objects), or not (starless sources, 75%). Therefore protostellar clumps present ongoing collapse, while starless are quiescent, and can be further classified in gravitationally bound (then prestellar, 60%), and unbound (15%).

Unbound clouds, prestellar and protostellar clumps have different spatial distributions (Fig. 1). In particular, the prestellar clumps are distributed over the major part of the probed sky while protostellar clumps are mainly concentrated on the galactic plane i.e. between -0.5 and 0.5 degrees. It is more difficult to characterize the unbound clump distribution as they may be misidentified with prestellar and protostellar clumps in the middle of the galactic plane. Indeed, we deal with clumps rather than individual objects so if a clump encompasses different classes of objects, the class of the clump will correspond to the warmest object.

[1] Observatoire astronomique de Strasbourg, Université de Strasbourg, CNRS, UMR 7550, 11 rue de l'Université, F-67000 Strasbourg, France
[2] Instituto de Radio Astronomía Milimétrica, Avenida Divina Pastora, 7, Local 20, 18012 Granada, Spain
[3] Instituto di Astrofisica e Planetologia Spaziali-INAF, Via Fosso del Cavaliere 100, I-00133 Roma, Italy

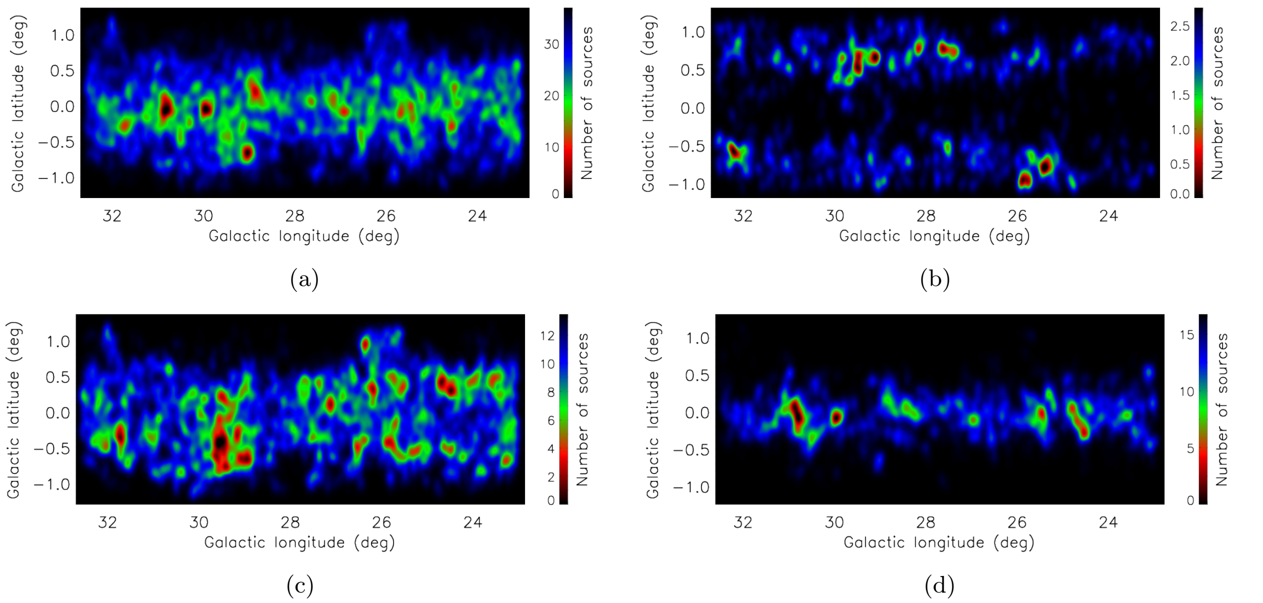

Fig. 1: Density map for the three classes of objects for the region from 20 to 32 degrees in galactic longitude. (a) - All objects. (b) - Unbound objects. (c) - prestellar cores. (d) - protostellar cores.

We focused our study on protostellar clumps because they exhibit a more clustered spatial distribution. Our study will be extended in Beuret et al. (2014, in preparation) to prestellar and unbound clumps.

In section 2 we introduce the MST method used to characterize the spatial distribution. Then we present our first results including all protostellar clumps. Section 4 deals with the role of the heliocentric distance estimates in our analysis. Finally, we conclude and discuss the results.

2 Minimum spanning tree method

We used the minimum spanning tree method (MST) to find clusters (e.g. Gutermuth et al. 2009 and Billot et al. 2011). This method aims at connecting all points with branches without creating closed loops while minimizing the total length of the branches. The solution of the MST analysis is unique. Then we compare the branch length distribution of the sources with a reference distribution (randomly distributed sources). It yields the estimation of a cut-off branch length by fitting segments on the cumulative distribution (Fig 2.b). Source overdensities are identified as a group of sources connected by branches shorter than the cut-off branch length. This procedure provides us with a cut-off criterion determined by the algorithm itself. Figure 2.c shows the result for these simulated clusters. The main clusters clearly appear in the result although they can break down into several smaller units.

3 Preliminary results

We applied the MST analysis to all protostellar clumps since those show the strongest clustering. Following Gutermuth et al. 2009, we define a cluster as a group with more than 10 sources. We found about 450 clusters. A good correlation can be established between the distribution of star forming clumps identified in Herschel data, HII regions from Paladini et al. (2003) in Figure 3, and IRDCs from Peretto et al. (2009) in Figure 4. About 75 % of clusters found with the MST method have one or more HII regions into an area of twice the cluster radius. In addition, we find that 78 % of MST clusters have one or more IRDCs in that area. Furthermore, some large clusters seem to have many sub-structures. That suggests these clusters would actually be a set of smaller structures.

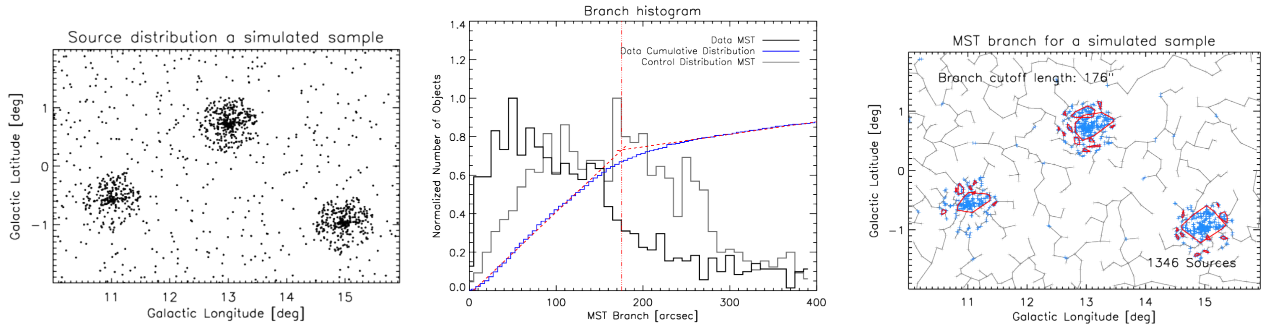

(a) (b) (c)

Fig. 2: (a) - Simulated sample with three simulated clusters. This simulated field was generated with randomly distributed sources for the background and a Gaussian distribution for clusters. (b) - Histogram of MST branch length. The blue line is the cumulative distribution. The two dashed red lines are the fitted segments. The dashed-dot line shows the cut-off branch length. (c) - Clusters found by MST method. The gray and blue color represent isolated and clustered sources, respectively. Red polygons are clusters with more than 10 sources.

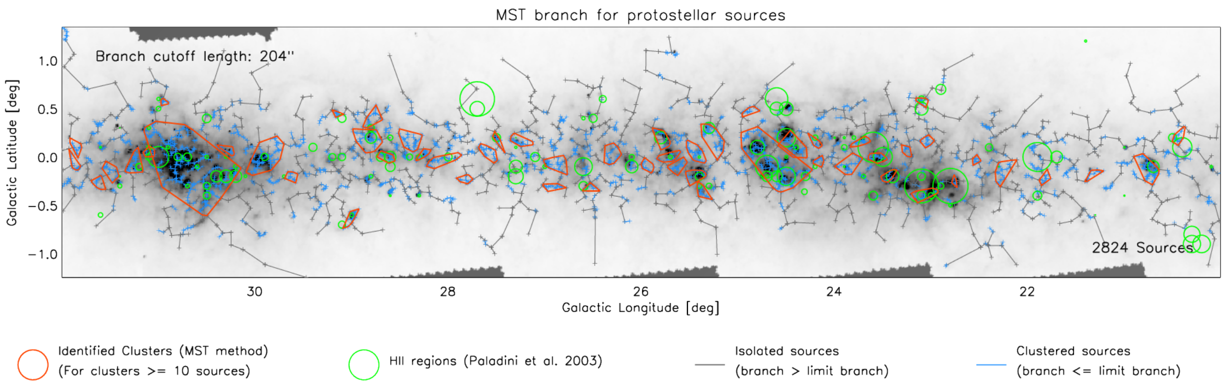

Fig. 3: Comparison between the distribution of clusters obtained from the MST analysis and HII regions from 20 to 32 degrees in galactic longitude. The background image shows the 70 μm surface brightness.

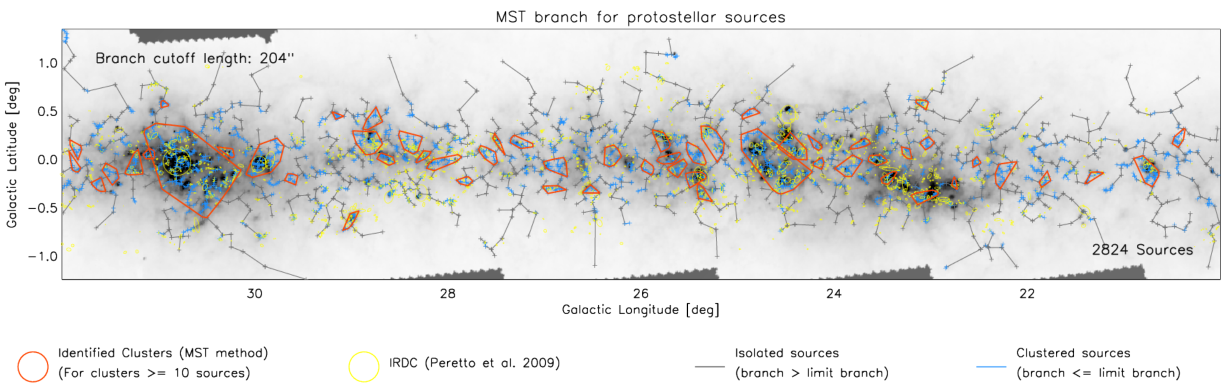

Fig. 4: Same as figure 3, but for IRDCS.

4 Heliocentric distances

The knowledge of distance helps at characterizing physical cluster properties. 63% of the protostellar sources, i.e about 16000 sources, have heliocentric distance estimates (For a preliminary example of heliocentric distance estimatations, see Russeil et al. 2011). As for the MST analysis without using heliocentric distances, we split the data into several 2D-boxes along the galactic longitude. All data have to be splitted again following the distance histogram distribution. An example is shown in the figure 5 which corresponds to the region between 20 and 32 degrees in galactic longitude. We smoothed the histogram to only accentuate the large overdensity of protostellar sources. Two or three regions in the histogram can be identified depending on the galactic longitudes probed because each box refers to different parts of the Milky Way especially for the spiral arms. This technique allows us to characterize cluster properties and to extract more physical clusters although it decreases their total number as it filters sources along the line of sight. Especially it allows us to only keep protostellar sources at the same distance within a cluster and so to compare physical cluster properties.

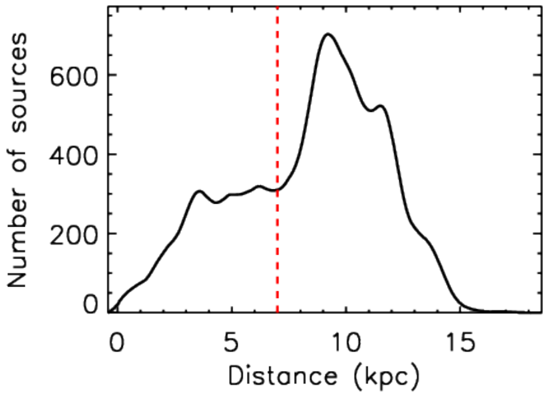

Fig. 5: Smoothed histogram of heliocentric distances for protostellar clumps into the range [20,32] (galactic longitude). Red dashed-dot lines is cut-off heliocentric distances.

Figure 6 presents the cluster distribution obtained with and without the heliocentric distance estimates. The average density is lower when the heliocentric distances are taken into account because we extract sources that really belong to the clusters. In fact the radius of each cluster is not significantly affected.

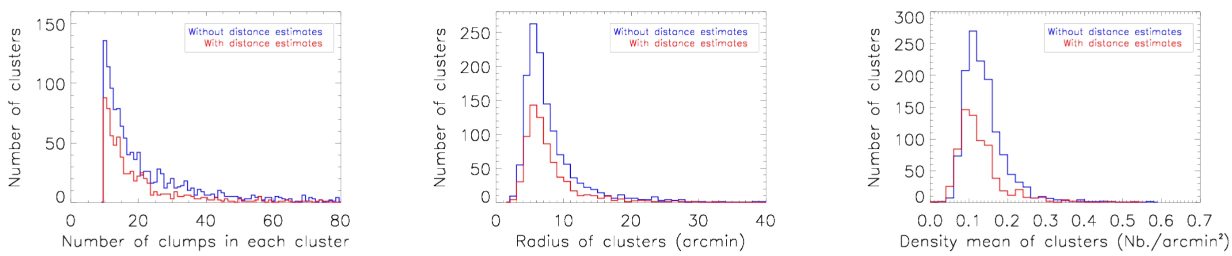

(a) (b) (c)

Fig. 6: Comparison between clusters found using heliocentric distance estimates (red) or not (blue). (a) - Histogram of the number of protostellar clumps in each cluster. (b) - Histogram of clusters radius in arcmin. (c) - Histogram of average source density per cluster in number of sources by arcmin^2.

Figure 7 compares the distribution of the MST clusters, the HII regions and the IRDCs. There are fewer clusters than on the distribution without distances as explained above. We find about 230 clusters with more than 10 sources. About 82 % of clusters found with the MST method have one or more HII regions located within twice the cluster radius. In addition, we found that 93 % of clusters have one or more IRDCs in that area. There is a stronger correlation between IRDCs, HII regions and clusters using heliocentric distance estimates than without these distances.

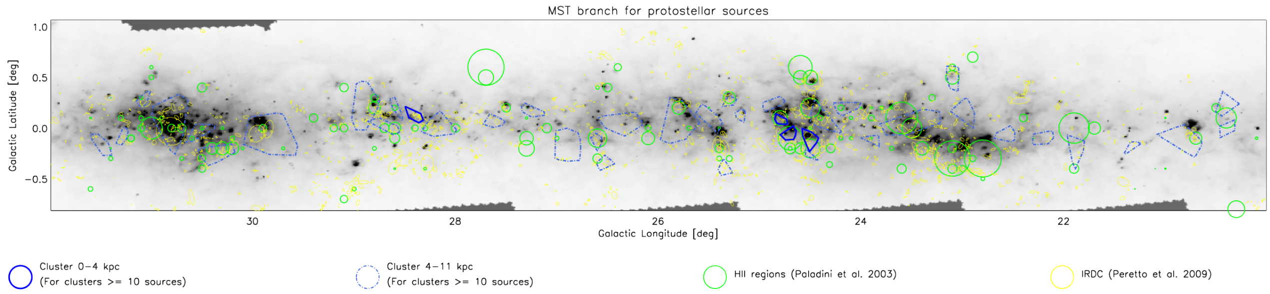

Fig. 7: Same as figures 3 and 4 but for clusters found with heliocentric distance estimates.

5 Conclusion

Heliocentric distance estimates are essential to characterize the physical cluster properties and to remove the sources that do not belong to the clusters. The correlation between the protostars, HII regions and IRDCs spatial distribution is better with these radial distances. HII regions are produced by massive stars so they can be related to high-mass star forming regions. These regions could actually explain the triggered stars formation. Furthermore, IRDCs are associated with star forming regions, especially for massive star formation. This correlation should help us identify the interaction between the interstellar medium and star forming regions, especially for massive star formation. The next step is to focus our study on clusters exhibiting interactions with the ISM. It will eventually allow us to improve our knowledge of triggered stellar formation.

We benefited from the progresses that have been made in this topic by the Hi-GAL team such as the large number of sources and the physical properties for each source. In the future, we should benefit from a larger sample of sources with heliocentric distance estimates leading to a better set of clusters.

The impact of the source spatial distribution on the efficiency of the MST method, the physical cluster properties and the role of prestellar clumps have not been discussed here. These points will be addressed in Beuret et al. (2014, in preparation).

References

Billot, N., Schisano, E., Pestalozzi, M. et al., 2011, ApJ, 735, 28
Elia, D., Molinari, S., Fukui, Y. et al., 2013, ApJ, 772, 45
Gutermuth, R. A., Megeath, S. T., Myers, P. C. et al., 2009, ApJS, 189, 352
Molinari, S., Swinyard, B., Bally, J. et al., 2010, PASP, 122, 314-325
Paladini R., Burigana, C., Davies, R. D. et al., 2003, A&A, 397, 213
Peretto R. & Fuller, G. A., 2009, A&A, 505, 405
Russeil D., Pestalozzi, M., Mottram, J. C. et al., 2011, A&A, 526, 151
Siebert A., Famaey, B., Binney, J. et al., 2012, MNRAS, 425, 2335

SF2A 2014
J. Ballet, F. Bournaud, F. Martins, R. Monier and C. Reylé (eds)

ULTRA-WEAK MAGNETIC FIELDS IN AM STARS: β UMA AND θ LEO

A. Blazère[1, 2], P. Petit[2], F. Lignières[2], M. Aurière[2], T. Böhm[2] and G. Wade[3]

Abstract. An extremely weak circularly-polarized signature was recently discovered in spectral lines of the chemically peculiar Am star Sirius A (Petit et al. 2011). This signal was interpreted as a Zeeman signature related to a sub-gauss longitudinal magnetic field, constituting the first detection of a surface magnetic field in an Am star. We present here ultra-deep spectropolarimetric observations of two other bright Am stars, β UMa and θ Leo, observed with the NARVAL spectropolarimeter. The line profiles of the two stars display circularly-polarized signatures similar in shape to the observations gathered for Sirius A. These new detections suggest that very weak magnetic fields may be present in the photospheres of a significant fraction of intermediate-mass stars, although the strongly asymmetric Zeeman signatures measured so far in Am stars (featuring a prominent positive lobe and no detected negative lobe) are not expected in the standard theory of the Zeeman effect.

Keywords: Stars: magnetic field, Stars: chemically peculiar

1 Introduction

Magnetic fields play an important role in the evolution of hot stars (O, B and A stars). However, the origin and even the basic properties of hot star magnetic fields are still poorly understood. About 7% of hot stars are found to be strongly magnetic with a longitudinal magnetic field in excess of 100 G (Wade et al. 2013). But recently, a sub-gauss longitudinal magnetic field has been discovered in the normal A star Vega (Lignières et al. 2009). This detection raises the question of the ubiquity of magnetic fields in objects belonging to this mass domain. In 2011, another polarimetric signal was detected in the bright Am star Sirius A (Petit et al. 2011). For this object, the polarized signature in circular polarization is not of null integral over the line profile as in other massive stars, since the Stokes V line profile exhibits a positive lobe dominating over the negative one (in amplitude and area). Here, we present the results of a magnetic field search carried out for two other bright Am stars: β UMa and θ Leo. The fundamental parameters of both targets are presented in Table 1. The Am stars are chemically peculiar stars exhibiting overabundances of iron-group elements such as zinc, strontium, zirconium and barium and deficiencies of others such as calcium and scandium. Most Am stars also feature low projected rotational velocities, as compared to normal A stars (Abt 2009).

2 Data analysis

Data were taken with the NARVAL spectropolarimeter. Narval is operated at the 2-meter Bernard Lyot Telescope (TBL), at the summit of Pic du Midi in the French Pyrénées. This fibre-fed spectropolarimeter was especially designed and optimized to detect stellar surface magnetic fields through the polarization they generate in photospheric lines and provides complete coverage of the optical spectrum from 3700 to 10500 Å on 40 echelle orders with a spectral resolution of 65000.

β UMa was observed in March/April 2010 and March/April 2011, while observations of θ Leo were collected in January/March/April 2012, March/April 2013 and May 2014 (see Table 2).

---

[1] LESIA, Observatoire de Paris, UMR 8109 du CNRS, UPMC, Université Paris-Diderot, 5 place Jules Janssen, 92195 Meudon, France
[2] Université de Toulouse & CNRS, Institut de Recherche en Astrophysique et Planétologie, Toulouse, France
[3] Department of Physics, Royal Military College of Canada, PO Box 17000 Station Forces, Kingston, ON K7K 0C6, Canada

Table 1. Fundamental parameters of β UMa and θ Leo

	β UMa	θ Leo
spectral type	A1V	A2V
T_{eff}	9600 K[a]	9350 K[b]
log g	3.83[c]	3.65[b]
Mass	2.7 $M_{\odot}^{d}$	2.5 $M_{\odot}^{d}$
Radius	3 $R_{\odot}^{a}$	4.3 $R_{\odot}^{a}$
vsini	23 km/s[e]	46 km/s[e]

[a] Boyajian et al. (2012) [c] Monier (2005)
[b] Smith & Dworetsky (1993) [d]Wyatt et al. (2007)
[e] Royer et al. (2002)

Table 2. Journal of observations

date	mid-HJD	star	T_{exp} (s)
17mar10	2455273.52016	β UMa	16 × 4 × 107
06apr10	2455293.41173	β UMa	17 × 4 × 107
10apr10	2455297.44406	β UMa	19 × 4 × 107
11apr10	2455298.39660	β UMa	19 × 4 × 107
25mar11	2455646.42619	β UMa	25 × 4 × 107
31mar11	2455652.50367	β UMa	25 × 4 × 107
02apr11	2455654.37913	β UMa	03 × 4 × 107
04apr11	2455656.46150	β UMa	24 × 4 × 107
22jan12	2455949.64440	θ Leo	05 × 4 × 180
23jan12	2455950.62844	θ Leo	05 × 4 × 180
24jan12	2455951.62417	θ Leo	05 × 4 × 180
25jan12	2455952.64032	θ Leo	05 × 4 × 180
14mar12	2456001.57862	θ Leo	05 × 4 × 180
15mar12	2456002.52449	θ Leo	10 × 4 × 180
24mar12	2456011.52572	θ Leo	05 × 4 × 180
25mar12	2456012.50225	θ Leo	05 × 4 × 180
27mar12	2456013.39956	θ Leo	10 × 4 × 180
21mar13	2456373.48791	θ Leo	09 × 4 × 180
23mar13	2456375.46496	θ Leo	09 × 4 × 180
16apr13	2456399.44433	θ Leo	09 × 4 × 180
17apr13	2456400.49237	θ Leo	09 × 4 × 180
22apr13	2456405.51179	θ Leo	09 × 4 × 180
23apr13	2456406.45400	θ Leo	09 × 4 × 180
24apr13	2456407.50188	θ Leo	09 × 4 × 180
14apr14	2456762.44478	θ Leo	05 × 4 × 180
07may14	2456785.40762	θ Leo	05 × 4 × 180
08may14	2456786.41135	θ Leo	05 × 4 × 180
09may14	2456787.41580	θ Leo	05 × 4 × 180
14may14	2456792.47117	θ Leo	05 × 4 × 180
15may14	2456793.41300	θ Leo	05 × 4 × 180

To test whether β UMa and θ Leo are magnetic, we applied the well-known and commonly used Least-Squares Deconvolution (LSD) technique (Donati et al. 1997) on each spectrum of both stars and computed LSD pseudo line profiles from all available photospheric lines. The line lists used are created from a list of lines extracted from the VALD data base (Piskunov et al. 1995; Kupka & Ryabchikova 1999) using the respective effective temperature and log g of both stars (Table 1). To further improve the signal-to-noise ratio, we then coadded all LSD profiles of each star, resulting in one single averaged LSD profile for each target. The result are shown in Figure 1.

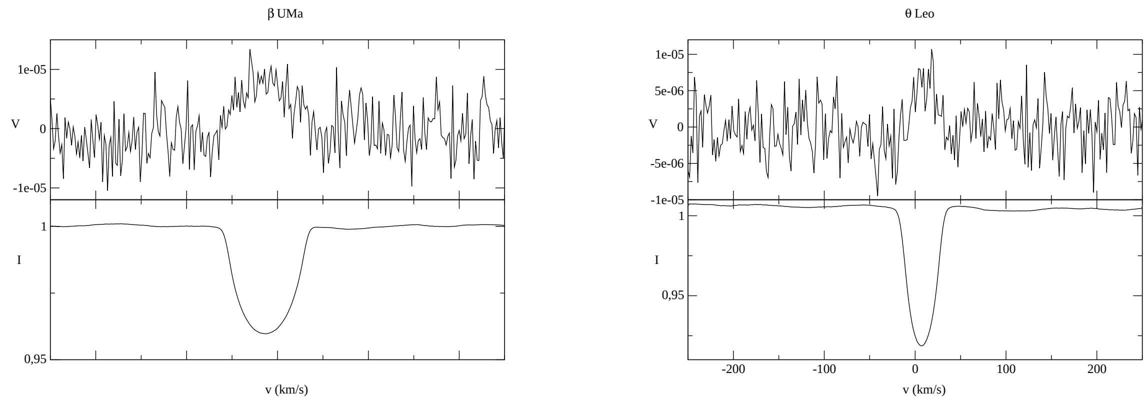

Fig. 1. Left: normalized Stokes I and V averaged LSD profiles for β UMa. Right: same figure for θ Leo.

3 Results

The line profiles of the two stars display circularly-polarized signatures similar in shape (see Figure 1) to the observations previously gathered for Sirius A. We have also separately coadded LSD profiles for each observing year (not shown here) to evaluate the temporal stability of this signal, concluding that the signatures are stable over the time-span of our observations.

4 Conclusions

These new detections may be interpreted to suggest that sub-gauss magnetic fields are present in the photosphere of a significant fraction of intermediate-mass stars, although the strongly asymmetric Zeeman signatures measured so far in Am stars (featuring a prominent positive lobe and essentially no negative lobe) are not expected in the standard theory of the Zeeman effect (see possible interpretations in Petit et al. 2011). New observations are currently being carried out to gain a better statistics of the prevalence of weak magnetic fields in intermediate-mass stars and evaluate the impact of various stellar parameters on the Vega-like magnetism.

We acknowledge support from the ANR (Agence Nationale de la Recherche) project Imagine. This research has made use of the SIMBAD database operated at CDS, Strasbourg (France), and of NASA's Astrophysics Data System (ADS).

References

Abt, H. A. 2009, AJ, 138, 28

Boyajian, T. S., McAlister, H. A., van Belle, G., et al. 2012, ApJ, 746, 101

Donati, J.-F., Semel, M., Carter, B. D., Rees, D. E., & Collier Cameron, A. 1997, MNRAS, 291, 658

Kupka, F. & Ryabchikova, T. A. 1999, Publications de l'Observatoire Astronomique de Beograd, 65, 223

Lignières, F., Petit, P., Böhm, T., & Aurière, M. 2009, A&A, 500, L41

Monier, R. 2005, A&A, 442, 563

Petit, P., Lignières, F., Aurière, M., et al. 2011, A&A, 532, L13

Piskunov, N. E., Kupka, F., Ryabchikova, T. A., Weiss, W. W., & Jeffery, C. S. 1995, A&AS, 112, 525

Royer, F., Gerbaldi, M., Faraggiana, R., & Gómez, A. E. 2002, A&A, 381, 105

Smith, K. C. & Dworetsky, M. M. 1993, A&A, 274, 335

Wade, G. A., Grunhut, J., Alecian, E., et al. 2013, IAUS 302, ArXiv e-prints 1310.3965

Wyatt, M. C., Smith, R., Su, K. Y. L., et al. 2007, ApJ, 663, 365

SF2A 2014
J. Ballet, F. Bournaud, F. Martins, R. Monier and C. Reylé (eds)

SURFACE ROTATION OF SOLAR-LIKE OSCILLATING STARS

T. Ceillier[1], R.A. García[1], D. Salabert[1] and S. Mathur[2]

Abstract. In this work, we use different methods to extract the surface rotation rate of *Kepler* targets showing solar-like oscillations.

Keywords: Asteroseismology, Stars: rotation, Stars: activity, Stars: solar-type, Stars: evolution, Stars: oscillations, *Kepler*

1 Introduction

Rotation is known to modify heavily the structure and evolution of a star, mainly through transport processes linked to meridional circulation. But as a star evolves, its rotation is modified by magnetic breaking and by its expansion during the subgiant and red giant phases. Moreover, it remains difficult to explain the internal rotation profiles derived thanks to asteroseimology (see for instance Ceillier et al. 2013).

That is why we study the surface rotation rates of *Kepler* solar-like oscillating stars - including Main-Sequence stars, subgiants and red giants - which are good asteroseimic targets. Using two different corrections of Kepler light curves - PDC-MAP (Thompson et al. 2013) and KADACS (García et al. 2011) - and two different analyses - wavelets decomposition (Mathur et al. 2010) and autocorrelation function (McQuillan et al. 2013), we derive a reliable surface rotation rate for a large number of these stars.

We also extract photometric levels of activity for these stars and, using the ages derived by Chaplin et al. (2014), we are able to better constrain the age-activity- rotation relations for the different categories of stars in our sample.

2 Methodology

In order to get a robust determination of rotation periods, we use two different ways of correcting the data as well as two different ways of getting an estimation of the rotation period. For each star, we use both data corrected using the PDC-MAP pipeline (Smith et al. 2012) and data corrected with the KADACS pipeline (García et al. 2011). For both sets of data, we get an estimation of the rotation period using both a wavelets analysis (see Mathur et al. 2013) and the autocorrelation function (following McQuillan et al. 2013). We then compare the four different results obtained. If they all concur, we select the period obtained as the rotation period with a high confidence. If it is not the case, we flag the rotation period as uncertain. As a last verification, we check visually all the stars for which a rotation period has been derived.

A good proxy of the activity of a star is the variance of the light curve. This measure is strongly linked to the surface rotation rate of the star. Taking this fact into account, we cut the lightcurve into $5 \times P_{rot}$-long parts and calculate the variance of each of these parts, $S_{ph,k=5}$. The average of these $S_{ph,k=5}$ defines the activity index $\langle S_{ph,k=5} \rangle$ of the star. The length of the parts $5 \times P_{rot}$ has been calibrated on the Sun and other well-known stars (Mathur et al. 2014). This activity index is thus more reliable than other variability indexes – such as the R_{var} defined by Basri et al. (2011) – because it is computed based on the rotation period of the star.

The results of this methodology applied on the sample of solar-like oscillating stars on the Main Sequence and the Subgiant phases have been reported in García et al. (2014).

[1] Laboratoire AIM, CEA/DSM/IRFU/SAp - CNRS - Univ. Paris Diderot, Centre de Saclay, 91191 Gif-sur-Yvette Cedex, France
[2] Space Science Institute, 4750 Walnut Street, Suite 205, Boulder, Colorado 80301 USA

3 Example for a red giant star

The same methodology has been also applied to a comprehensive sample of *Kepler* Red Giants and will be described in details in Ceillier et al. 2015 (in preparation). Due to their low activity levels, these stars are not supposed to show clear rotational modulations in their lightcurve. This is why only a small fraction of the global sample (around 2%) give conclusive results. These peculiar Red Giants could result from mergers, as discussed by Tayar et al. 2015 (in preparation).

An example of a Reg Giant star's light curve analysis can be seen in Fig. 1. The 70 days modulation is clearly visible.

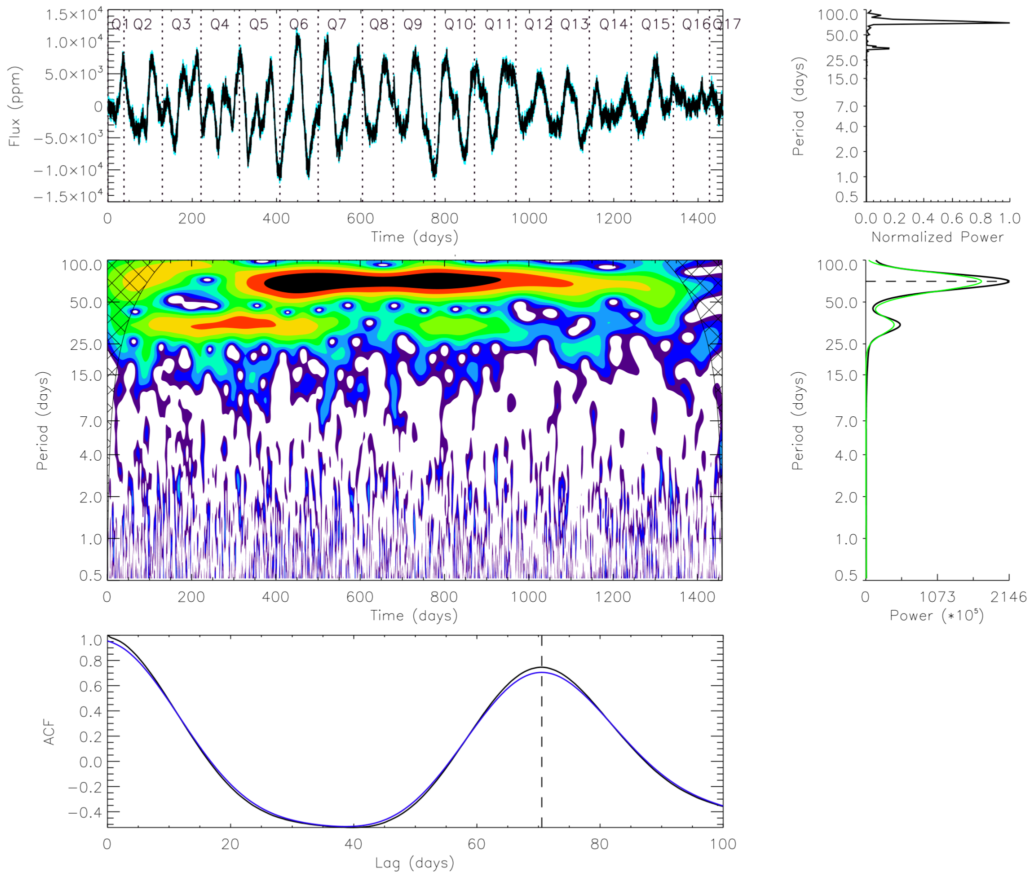

Fig. 1. Example of the analysis for KIC 2570214 (KADAC data). Top panel: Long-cadence *Kepler* light curve (cyan) and rebinned light curve (black), where vertical dotted lines indicate the transitions between the observing quarters. Top right panel: associated power density spectrum as a function of period between 0.5 and 100 days. Middle left panel: Wavelet Power Spectrum (WPS) computed using a Morlet wavelet between 0.5 and 100 days on a logarithmic scale. The black-crossed area is the cone of influence corresponding to the unreliable results. Middle right panel: Global Wavelet Power Spectrum (GWPS) as a function of the period of the wavelet and the associated fit composed from several gaussian functions (thin green line). The horizontal dashed line designates the position of the retrieved $P_{\rm rot}$. Bottom panel: AutoCorrelation Function (ACF) of the full light curve plotted between 0 and 100 days (black) and smoothed ACF (blue). The vertical dashed line indicates the returned $P_{\rm rot}$ for the ACF analysis.

4 Conclusions

We have now powerful and reliable methods to extract surface rotation rates from *Kepler* light curves. It is thus possible to derive surface rotation rates for a huge number of stars, spread over the whole HR diagram. While the results for dwarves (see García et al. 2014) confirm for field stars the age-rotation relation know as the Skumanish law (Skumanich 1972), the discovery of rapidly rotating, highly active red giant stars opens a new perspective for the evolution of these evolved stars.

SM acknowledges the support of the NASA grant NNX12AE17G. DS, RAG, SM, and TC received funding from the CNES GOLF and CoRoT grants at CEA. RAG also acknowledges the ANR (Agence Nationale de la Recherche, France) program IDEE (n ANR-12-BS05-0008) "Interaction Des Étoiles et des Exoplanètes".

References

Ceillier, T., Eggenberger, P., García, R. A., & Mathis, S. 2013, Astronomy and Astrophysics, 555, A54

Chaplin, W. J., Basu, S., Huber, D., et al. 2014, Astrophysical Journal, Supplement, 210, 1

García, R. A., Ceillier, T., Salabert, D., et al. 2014, ArXiv e-prints

García, R. A., Hekker, S., Stello, D., et al. 2011, Monthly Notices of the RAS, 414, L6

Mathur, S., Garcia, R. A., Metcalfe, T. S., Pinsonneault, M. H., & van Saders, J. 2013, in American Astronomical Society Meeting Abstracts, Vol. 221, American Astronomical Society Meeting Abstracts #221, #301.05

Mathur, S., García, R. A., Régulo, C., et al. 2010, Astronomy and Astrophysics, 511, A46

Mathur, S., Salabert, D., García, R. A., & Ceillier, T. 2014, Journal of Space Weather and Space Climate, 4, A15

McQuillan, A., Aigrain, S., & Mazeh, T. 2013, Monthly Notices of the RAS, 432, 1203

Skumanich, A. 1972, Astrophysical Journal, 171, 565

Smith, J. C., Stumpe, M. C., Van Cleve, J. E., et al. 2012, Publications of the ASP, 124, 1000

Thompson, S. E., Christiansen, J. L., Jenkins, J. M., et al. 2013, Kepler Data Release 21 Notes (KSCI-19061-001), Kepler mission

SF2A 2014
J. Ballet, F. Bournaud, F. Martins, R. Monier and C. Reylé (eds)

MEASUREMENTS OF EIGHT EARLY-TYPE STARS ANGULAR DIAMETERS USING VEGA/CHARA INTERFEROMETER

M. Challouf[1,2], N. Nardetto[1], D. Mourard[1], H. Aroui[2] and O. Delaa[1]

Abstract. The surface brightness color (SBC) relation is an important tool to derive the distance of extragalatic eclipsing binaries. We determined the uniform disc angular diameter of the eight following early-type stars using VEGA/CHARA interferometric observations: $\theta_{\rm UD}[\delta$ Cyg$] = 0.766 \pm 0.047$ mas, $\theta_{\rm UD}[\gamma$ Lyr$] = 0.742 \pm 0.010$ mas, $\theta_{\rm UD}[\gamma$ Ori$] = 0.701 \pm 0.005$ mas, $\theta_{\rm UD}[\zeta$ Peg$] = 0.539 \pm 0.009$ mas, $\theta_{\rm UD}[\lambda$ Aql$] = 0.529 \pm 0.003$ mas, $\theta_{\rm UD}[\zeta$ Per$] = 0.531 \pm 0.007$ mas, $\theta_{\rm UD}[\iota$ Her$] = 0.304 \pm 0.010$ mas and $\theta_{\rm UD}[8$ Cyg$] = 0.229 \pm 0.011$ mas (by extending V-K range from -0.76 to 0.02) with typical precision of about 1.5%. By combining these data with previous angular diameter determinations available in the literature, Challouf et al. (2014) provide for the very first time a SBC relation for early-type stars ($-1 \leq$V-K≤ 0) with a precision of about 0.16 magnitude or 7% in term of angular diameter (when using this SBC relation to derive the angular diameter of early-type stars).

Keywords: Stars: early-type, methods: data analysis, instrumentation: interferometers, techniques: medium spectral resolution

1 Introduction

The Optical Gravitational Lensing Experiment (OGLE) has been monitoring around 35 million stars in the LMC for more than 16 years. Using this unique data set, Pietrzyński et al. (2013) have detected a dozen of very long-period (60-772d) eclipsing binary systems composed of intermediate-mass, late-type giants located in a quiet evolutionary phase on the helium-burning loop. By observing spectroscopically eight of these systems intensively over the past 8 yr, the team could accurately measure the linear sizes of their components, while the angular sizes have been derived from the surface-brightness color relation (SBC relation). The LMC distance that was derived from these systems is accurate to 2.2% and provides a base for a 3% determination of the Hubble constant. The error budget on the LMC distance is as follows: photometry (15%), spectroscopy (5%), reddening (10%), uncertainty on the derived absolute radii (15%), and the remaining (about 55%) is due to the surface brightness color relation. Thus, the systematic uncertainty in the distance measurement comes mainly from the calibration of the SBC relation. The root mean squared scatter in the current SBC is 0.03 mag (Di Benedetto 2005), which translates to an accuracy of 2% in the respective angular diameters of the component stars. Conversely, early-type eclipsing binaries are very bright systems that are very easily detected in the LMC and even in M33. Even if these objects are promising for the distance scale calibration, the largest limitation when using these systems comes again from the surface brightness relation. In this context we have performed observations of a sample of 8 stars composed by 6 low rotators (λ Aql, γ Ori, γ Lyr, ζ Per, ι Her and 8 Cyg) and by 2 fast rotating stars (δ Cyg and ζ Peg). In our study we include two rotators in order to understanding the effect of rotation on the SBC relation. A theoretical study which aims at quantifying the impact of the fast rotation on the SBC relation for early-type stars is currently under progress and will appear in another paper. To observe this sample we used the resolving power of the Visible spEctroGraph and polArimeter (VEGA) beam combiner (Mourard et al. 2009, 2011) operating at the focus of the CHARA (The Center for High Angular Resolution Astronomy) Array (ten Brummelaar et al. 2005) located at Mount Wilson Observatory (California, USA). The CHARA array consists of six telescopes of 1 meter in diameter, configured in a Y shape, which offers 15 different baselines from 34 meters to 331 meters. These baselines can achieve a spatial resolution up to 0.3 mas in the visible which is necessary in order to resolve early-type stars.

[1] Laboratoire Lagrange, UMR7293, UNS/CNRS/OCA, 06300 Nice, France
[2] Laboratoire Dynamique Moléculaire et Matériaux Photoniques, UR11ES03, Université de Tunis/ESSTT, Tunisie

2 Deriving the angular diameters

The observations of our sample were performed during most 2 years. We started the first observation on July 23, 2011 and we ended our observation program on August 29, 2013. After calculate the raw visibilities of observations, the first step is to calibrate the visibility measurements of our targets using observations of reference stars. The need of transfer function analysis is useful to test the consistency of the reference stars, and to define a good strategy of calibration. The transfer function T calculated from the observations on the reference stars Cal using the following formula:

$$T^2 = \frac{\mu_{cal}^2}{V_{cal}^2} \tag{2.1}$$

where μ_{cal} is the measured squared visibility on a given calibrator, while V_{cal} is the expected squared visibility on the calibrator that we could calculate with the following relation:

$$V_{cal}^2 = 4\left(\frac{J_1(z)}{z} \right)^2 \tag{2.2}$$

with $J_1(z)$ is the first-order Bessel function and $z = \pi\theta_{\rm UD}B/\lambda$, where B is the projected basline, λ the wavelenght. $\theta_{\rm UD}$ is given for example by the SearchCal (`http://www.jmmc.fr/searchcal`) developed by the JMMC (Bonneau et al. 2006). We know that, under correct seeing conditions, the transfer function of VEGA/CHARA is stable at the level of 2% for more than one hour (Mourard et al. 2009). The estimate visibility on each bloc of observation is measured in a given spectral band using the estimator defined by Roddier & Lena (1984) (see also Mourard et al. 2009, 2011). The squared calibrated visibility (V_{target}^2) obtained from our VEGA observations are fitted with a model of uniform disc (see Fig. 1) using for instance LITpro (`http://www.jmmc.fr/litpro`) software developed by the JMMC (Tallon-Bosc et al. 2008). The fitting engine is based on a modified Levenberg-Marquardt algorithm combined with the trust regions method. The equivalent uniform disc angular diameter $\theta_{\rm UD}$ is then converted into a limb-darkened disc. The following formula of Hanbury Brown et al. (1974b):

$$\theta_{LD}(\lambda) = \theta_{UD}(\lambda)\left[\frac{(1 - U_\lambda/3)}{(1 - 7U_\lambda/15)}\right]^{1/2}, \tag{2.3}$$

provides an efficient way to perform the conversion using linear limb-darkening coefficients U_λ.

3 Results for the stars in our sample

Using the uniform disc model we can find the best fit of angular diameters ($\theta_{\rm UD}$) and by combination of these diameters with the limb-darkening coefficients (U_λ) we derived the limb-darkened angular diameters ($\theta_{\rm LD}$). All these parameters are listed in Table 1 for each star in our sample. We obtained $\theta_{\rm LD}$ ranges from 0.31 to 0.79 mas, with a relative precision from 0.5% to 3.5% (average of 1.5%). The reduced $\chi^2_{\rm red}$ is from 0.4 to 2.9 depending on the quality of the fit (Fig. 1).

Table 1. Angular diameters obtained with VEGA/CHARA and the corresponding surface brightness. The systematical uncertainties for the two fast rotating stars, ζ Peg and δ Cyg, are of 0.039 mas and 0.047 mas.

Star	$(V-K)_0$	$\theta_{\rm UD}[mas]$	χ^2	U_R	$\theta_{\rm LD}$ [mas]	$S_{\rm v}[mag]$
λ Aql	-0.265 ± 0.055	0.529 ± 0.003	1.0	0.301	0.544 ± 0.003	2.079 ± 0.030
γ Lyr	-0.102 ± 0.072	0.742 ± 0.010	2.9	0.402	0.766 ± 0.010	2.544 ± 0.059
γ Ori	-0.703 ± 0.097	0.701 ± 0.005	0.4	0.269	0.715 ± 0.005	0.909 ± 0.081
8 Cyg	-0.492 ± 0.147	0.229 ± 0.011	1.3	0.299	0.234 ± 0.011	1.456 ± 0.177
ι Her	-0.459 ± 0.076	0.304 ± 0.010	1.2	0.280	0.310 ± 0.010	1.225 ± 0.082
ζ Per	-0.592 ± 0.092	0.531 ± 0.007	1.2	0.343	0.542 ± 0.007	0.652 ± 0.081
ζ Peg	-0.204 ± 0.055	0.539 ± 0.009	1.7	0.442	0.555 ± 0.009	2.076 ± 0.152
δ Cyg	$+0.021 \pm 0.055$	0.766 ± 0.004	1.3	0.408	0.791 ± 0.004	2.318 ± 0.129

For the two rotators ζ Peg and δ Cyg in order to calculate the systematic error on the diameter determined by VEGA we derived the oblateness using the relation of van Belle et al. (2006), we found 1.07 and 1.06

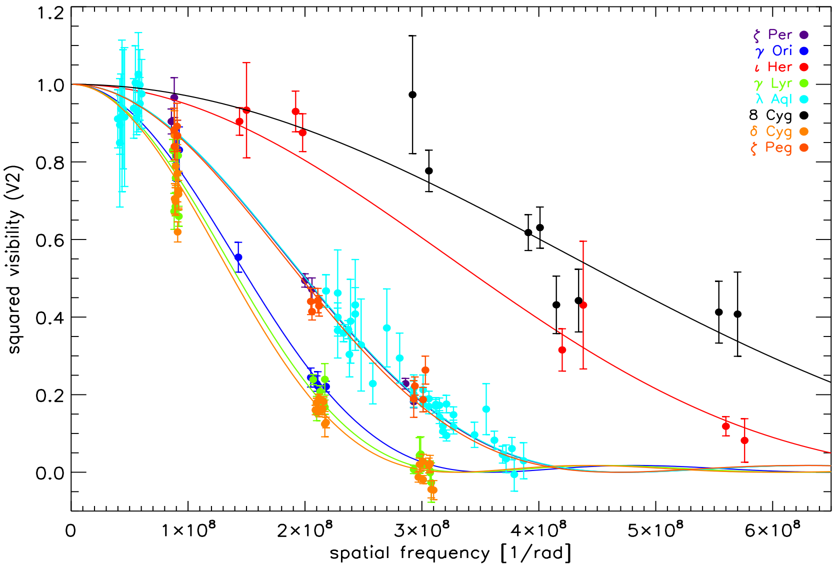

Fig. 1. Squared visibility for VEGA measurements of stars in our sample with their corresponding statistical uncertainties as function spatial frequency [1/rad]. The solid line is the model of the uniform disc angular diameter provided by the LITpro software.

respectively. Based on these two values we estimated the systematic error of about 0.039 mas for ζ Peg and 0.047 mas for δ Cyg.

The surface brightness S_V of a star is linked to its visual intrinsic dereddened magnitude m_{V_0} and its limb-darkened angular diameter θ_{LD}. In order to calibrate the SBC relation, we combine the eight limb-darkened angular diameters derived from the VEGA observations with different sets of diameters already available in the literature. We consider the angular diameter determination from Hanbury Brown et al. (1974a) (26 stars), Boyajian et al. (2012) (44 stars), Maestro et al. (2013) (9 stars) and Di Benedetto (2005) (45 stars). All the apparent magnitudes in V and K bands that we have collected from the literature are in the Johnson system (Johnson et al. 1966). For the dereddening of these magnitudes we need to calculate the extinction in the V band. We adopt the following strategy: For stars lying closer than 75 pc we using the simple relation $A_V = \frac{0.8}{\pi}$, where π is the parallax of the stars [in mas]. For distant stars we derive the absorption using the (B-V) extinction, $A_V = 3.1E(B-V)$ (Laney & Stobie 1993). We recalculate the intrinsic colors $(V-K)_0 = (V-K) - E(V-K)$ for all stars from the derived E(B-V) value using E(V-K)=2.7397E(B-V) (see Challouf et al. (2014)). Finally we find the relation:

$$S_{\rm v} = \sum_{n=0}^{n=5} C_n (V-K)_0^n \tag{3.1}$$

with, $C_0 = 2.624 \pm 0.009$, $C_1 = 1.798 \pm 0.020$, $C_2 = -0.776 \pm 0.034$, $C_3 = 0.517 \pm 0.036$, $C_4 = -0.150 \pm 0.015$, and $C_5 = 0.015 \pm 0.002$. This relation can be used consistently in the range $-0.9 \leq V-K \leq 3.7$ with $\sigma_{S_{\rm v}}$=0.10 mag.

4 Conclusions

In the present work, we determined the angular diameters of eight B- and A-type stars in the visible. We measured the visibilities calibrated for these stars with a good accuracy with typical precision of about 1.5% using the VEGA/CHARA instrument. These interferometric results are combined with other data and used by Challouf et al. (2014) to calibrate the surface brightness-color relation. They are found for the first time a relation with an accuracy of about 0.16 magnitude or 7% in term of angular diameter for -1≤V-K≤0 and a precision of 0.10 mag or 5% in term of angular diameter for V-K between -1 and 4. Further work is now in progress for quantifying the impact of rotation, in order to improve the accuracy of this relationship Sv, then applied to determine the distance of M31 and M33.

This research has made use of the SIMBAD and VIZIER (`http://cdsweb.u-strasbg.fr/`) databases at CDS, Strasbourg (France), and of the Jean-Marie Mariotti Center `Aspro` service (`http://www.jmmc.fr/aspro`) service and of electronic bibliography maintained by the NASA/ADS system. The research leading to these results has received funding from the European Community's Seventh Framework Programme under Grant Agreement 312430. The CHARA Array is funded by the National Science Foundation through NSF grants AST-0606958 and AST-0908253 and by Georgia State University through the College of Arts and Sciences, as well as the W. M. Keck Foundation. This research has largely benefited from the support, suggestions, advice of our colleague Olivier Chesneau, who passed away this spring. The whole team wish to pay homage to him.

References

Bonneau, D., Clausse, J.-M., Delfosse, X., et al. 2006, A&A, 456, 789

Boyajian, T. S., McAlister, H. A., van Belle, G., et al. 2012, ApJ, 746, 101

Challouf, M., Nardetto, N., Mourard, D., et al. 2014, ArXiv e-prints

Di Benedetto, G. P. 2005, MNRAS, 357, 174

Hanbury Brown, R., Davis, J., & Allen, L. R. 1974a, MNRAS, 167, 121

Hanbury Brown, R., Davis, J., Lake, R. J. W., & Thompson, R. J. 1974b, MNRAS, 167, 475

Johnson, H. L., Mitchell, R. I., Iriarte, B., & Wisniewski, W. Z. 1966, Communications of the Lunar and Planetary Laboratory, 4, 99

Laney, C. D. & Stobie, R. S. 1993, MNRAS, 263, 921

Maestro, V., Che, X., Huber, D., et al. 2013, MNRAS, 434, 1321

Mourard, D., Bério, P., Perraut, K., et al. 2011, A&A, 531, A110

Mourard, D., Clausse, J. M., Marcotto, A., et al. 2009, A&A, 508, 1073

Pietrzyński, G., Graczyk, D., Gieren, W., et al. 2013, Nature, 495, 76

Roddier, F. & Lena, P. 1984, Journal of Optics, 15, 171

Tallon-Bosc, I., Tallon, M., Thiébaut, E., et al. 2008, in SPIE, Vol. 7013

ten Brummelaar, T. A., McAlister, H. A., Ridgway, S. T., et al. 2005, ApJ, 628, 453

van Belle, G. T., Ciardi, D. R., ten Brummelaar, T., et al. 2006, ApJ, 637, 494

SF2A 2014
J. Ballet, F. Bournaud, F. Martins, R. Monier and C. Reylé (eds)

NON-LTE MODELING OF COLD STELLAR ATMOSPHERES

N. Feautrier[1], A. Spielfiedel[1], M. Guitou[2] and A. K. Belyaev[3]

Abstract. Non-LTE modelisation of stellar atmospheres requires an accurate knowledge of collisional rate coefficients (mainly with H atoms) that compete with radiative rates to populate the atomic levels. In the framework of the SAM-GAIA project we carry out an interdisciplinary work combining quantum chemistry and collision physics.

Present studies concern collisional excitation of MgI, CaI and OI by H-atoms. Considering the Mg-H case, the resulting cross sections and rate coefficients point out the sensitivity of the results with the quantum chemistry data. The calculations show that the usual approximate Drawin formula leads to errors by factors up to 10^5. As was already found in Li+H and Na+H collisions, excitation processes were found of the same order of magnitude as charge transfer processes. However, unlike Li and Na, Mg has different spin terms, singlet and triplet, leading both to doublet molecular MgH electronic states. Collisional rates between spin-allowed and optically spin-forbidden atomic states are found to be of the same order of magnitude although optically spin-forbidden states are only collisionally coupled. Thus, we may expect consequences on non-LTE calculations.

Keywords: atomic data, line formation, stars: abundances

1 Introduction

Non-LTE modeling implies a competition between radiative and collisional processes. The radiative data are well known thanks to the Opacity and the Iron projects. The influence of inelastic hydrogen atom collisions dominant in cold atmospheres on non-LTE spectral line formation has been, and remains to be, a significant source of uncertainty for stellar abundance analyses, due to the difficulty in obtaining accurate data for such low-energy collisions, either experimentally or theoretically. For lack of a better alternative, the classical so-called Drawin formula (Drawin 1969) is often used. The question is : does the Drawin formula provide reasonable estimates of this process ? After a brief presentation of the different steps used to obtain accurate quantum calculations for collisions with H atoms (Section 2), the comparison with the approximate formulae is made in Section 3. Finally, preliminary conclusions on stellar abundance determination are drawn.

2 Molecular data

In the standard adiabatic approach, the theoretical treatment of atomic collisions requires two steps: (i) calculations of fixed-nuclei potential energies and non adiabatic radial and rotational couplings, (ii) an appropriate treatment of the nuclear motion based on the previous calculated molecular data leading to the wave function for the nuclear motion. This leads in the Jacobi coordinates system to the usual close-coupled equations. But, most of the non-adiabatic couplings are nonzero when the internuclear distance goes to infinity. This corresponds to the fact that the Jacobi system is not appropriate for the description of the collisions partners long before and after the collision. To remove this difficulty, Belyaev et al. (2001) proposed a way to connect the R-matrix calculated at some R_0 internuclear distance from close coupled equations in the Jacobi coordinates system to the asymptotic S-matrix allowing the calculation of cross sections.

[1] LERMA (UMR8112 CNRS), Observatoire de Paris, 92195-Meudon, France
[2] MSME (UMR8208 CNRS), University Paris-Est, 77454 Marne la Vallée, France
[3] Dept. of Theoretical Physics, Herzen University, 191186 St Peterburg, Russia

The first step concerns quantum chemistry and the main challenge is to build large basis sets adapted to the study of highly excited states. All the electronic states arising from Mg+H for energies up to the Mg 3s3d ^{3}D, 3s4p ^{1}P and 3s4p ^{3}P states were considered using large active spaces and basis sets (Guitou et al. 2010; Belyaev et al. 2012). The energies and related couplings were calculated using the 2009.1 version of the MOLPRO code (*). The potential energy functions (PEFs) of the $^2\Sigma^+$ and $^2\Pi$ states are represented on Figure 1 as function of the internuclear distance. The more striking feature of these potentials is the presence in the $^2\Sigma^+$ of a series of avoided crossings due to a strong mixing with the Mg$^+$-H$^-$ ionic state. Those pseudo-crossings occur at larger and larger distances for the highest molecular states. This leads to ion-pair production and to the reverse reaction, mutual neutralization. This perturbation due to the Mg$^+$-H$^-$ ionic configuration leads to large non-adiabatic radial coupling terms among consecutive states. The cross sections for the excitation and ion-pair production processes show large variations in amplitude for different transitions (Belyaev et al. 2012). We point out that cross sections for transitions between spin-allowed and spin-forbidden atomic states are of the same order of magnitude owing to relevant molecular mechanisms. The role of $^2\Pi$ states was found smaller than that of $^2\Sigma^+$ states, except for transitions between some excited states (Rodionov et al. 2014).

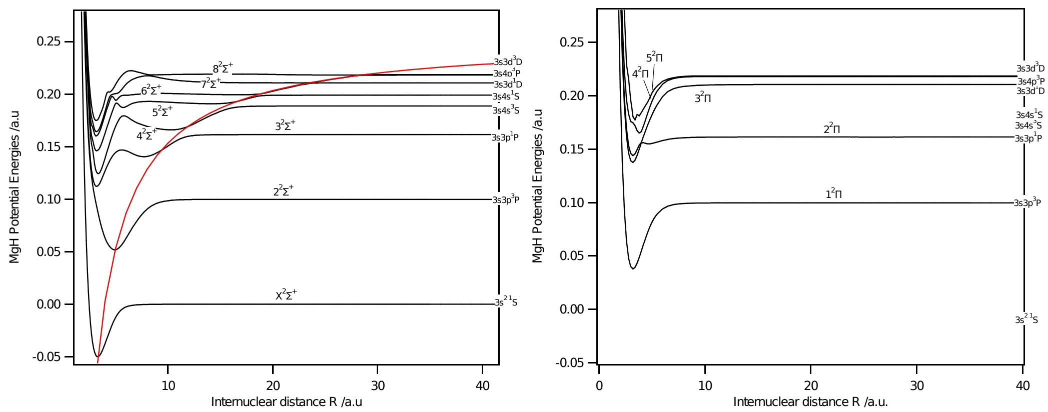

Fig. 1. Lowest interaction potentials **Left**: $^2\Sigma^+$ states (In red is the ionic interaction). **Right:** $^2\Pi$ states (Guitou et al. 2011).

3 Rate coefficients - Comparison with approximate formulae

From the cross sections, one can obtain the corresponding thermal rate coefficients at temperature T by an average over a Maxwellian velocity distribution. Rate coefficients at 4000 K for excitation and de-excitation processes :

$$\mathrm{Mg}(3\mathrm{s}\ nl\ ^{2S+1}L) + \mathrm{H(1s)} \rightleftharpoons \mathrm{Mg}(3\mathrm{s}\ n'l'\ ^{2S'+1}L') + \mathrm{H(1s)}$$

and for the charge transfer processes, ion-pair production and mutual neutralisation :

$$\mathrm{Mg}(3\mathrm{s}\ nl\ ^{2S+1}L) + \mathrm{H(1s)} \rightleftharpoons \mathrm{Mg}^+(3\mathrm{s}\ ^2S) + \mathrm{H}^-$$

were calculated among the $^2\Sigma^+$ states, including all the coupling tems. They are displayed in table 1. As expected, the rate coefficients follow the same trends as cross sections, i.e. large rate coefficients for ion-pair production/mutual neutralisation and large rates even for optically spin-forbidden transitions.

The ratio (Drawin/quantum) rate coefficients (expressed in terms of effective collision strengths†) are displayed in figure 2 vs the quantum results. The Drawin formula, which is an extension of the classical formula for ionisation of atoms by electron impact (Drawin 1969), cannot represent the physics of the quasi molecular interactions underlying the mechanisms of excitation by H atom collisions. This formula has only two parameters, ΔE and the f-value of the atomic transition. The most remarkable aspect of the Drawin formula results is that

* `http://www.molpro.net`

†For convenience, the collisional rate coefficients R_{ij} are expressed in terms of dimensionless collisional strengths $\gamma_{ij} = \gamma_{ji} = 4.96510^6 g_i \sqrt{T} R_{ji}$ where R_{ji} are the downward rate coefficients in unit of cm^{3}s^{-1}.

Table 1. Mg+H rate coefficients (in cm^3/s) at 4000 K.

Initial/Final states	3s ^{1}S	3p ^{3}P$_0$	3p ^{1}P$_0$	4s ^{3}S	4s ^{1}S	3d ^{1}D	ionic
3s ^{1}S	—	1.67 e-17	9.32 e-20	5.37 e-20	2.14 e-20	6.31 e-21	5.05 e-22
3p ^{3}P$_0$	4.87 e-15	—	2.76 e-13	7.95 e-14	2.07 e-14	4.35 e-15	1.47 e-16
3p ^{1}P$_0$	1.05 e-14	1.07 e-10	—	5.21 e-11	7.88 e-12	9.96 e-13	1.84 e-13
4s ^{3}S	5.26 e-14	2.67 e-10	4.52 e-10	—	1.38 e-10	1.18 e-11	9.14 e-12
4s ^{1}S	1.46 e-13	4.83 e-10	4.75 e-10	9.56 e-10	—	1.42 e-09	8.64 e-10
3d ^{1}D	2.23 e-14	5.28 e-11	3.12 e-11	4.28 e-11	7.41 e-10	—	1.73 e-10
ionic	2.42 e-13	2.42 e-10	7.84 e-10	4.48 e-09	6.10 e-08	2.35 e-09	—

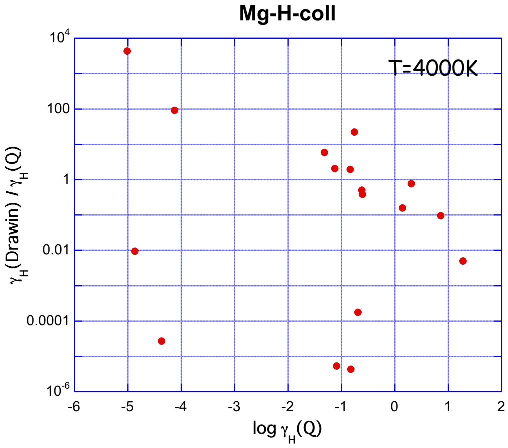

Fig. 2. Ratio γ_{Drawin}/γ_Q between the Drawin rates and the calculated quantum rates as function of the quantum rates.

among the 21 excitation transitions considered, only 5 transitions are optically allowed and could be calculated according to the Drawin formula. For the optically allowed transitions, the Drawin results are generally larger than the quantum results by a few orders of magnitude (Barklem et al. 2012). The same trend has been already found for Li and Na atoms (Barklem et al. 2011) in collision with H (Merle et al. 2013).

4 Conclusion and perspectives

As found previously in calculations for Li and Na, collisional excitation rate coefficients are smaller than rate coefficients for charge transfer. A comparison with the results found for Li and Na show that Mg-rate coefficients for excitation from the ground to the first excited states are roughly an order of magnitude larger (Barklem et al. 2012). Moreover, contrarily to Li and Na atoms, Mg has two spin symmetries and large collisional rates are found between singlet and triplet states which are only weakly radiatively coupled. This fact, together with the high rates lead one to expect that H-collisional processes could be important for non-LTE modeling.

However, the theoretical approaches used in the present work could not be easily generalized to more complex atoms, such as iron, or to very high electronic states. Our objective is then to develop approximate but realistic methods. Such work, in collaboration with Pr. A. K. Belyaev, is under progress (Belyaev 2013).

This work was partly supported by the French CNRS-PNPS (Programme National de Physique Stellaire), the GAIA program of Paris Observatory and by the Russian Fondation for Basic Research (grant N^o 13-03-00163-A). Part of the ab initio quantum chemistry calculations were performed using HPC resources from GENCI-[TGCC/CINES/IDRIS] (grant N^{o}2010040883) and on work stations at the Centre Informatique of Paris Observatory and at MSME laboratory (University of Paris-Est).

References

Barklem, P., Belyaev, A.-K., Guitou, M., et al. 2011, A&A, 530, A94

Barklem, P. S., Belyaev, A. K., Spielfiedel, A., Guitou, M., & Feautrier, N. 2012, A&A, 541, A80

Belyaev, A. K. 2013, A&A, 560, A60

Belyaev, A. K., Barklem, P. S., Spielfiedel, A., et al. 2012, Phys. Rev. A, 85, 032704

Belyaev, A. K., Egorova, D., Grosser, J., & Menzel, T. 2001, Phys. Rev. A, 64, 052701

Drawin, H. W. 1969, Z. Phys., 225, 483

Guitou, M., Belyaev, A. K., Barklem, P. S., Spielfiedel, A., & Feautrier, N. 2011, J. Phys. B: At. Mol. Opt. Phys., 44, 035202

Guitou, M., Spielfiedel, A., & Feautrier, N. 2010, Chemical Physics Letters, 488, 145

Merle, T., Thévenin, F., Belyaev, A. K., et al. 2013, in EAS Publications Series, Vol. 63, EAS Publications Series, 331–336

Rodionov, D., Belyaev, A. K., Guitou, M., et al. 2014, Izvestia of Herzen University, 165, 63

SF2A 2014
J. Ballet, F. Bournaud, F. Martins, R. Monier and C. Reylé (eds)

EVOLUTION OF THE CHEMICAL ELEMENT ABUNDANCES WITH AGE IN OPEN CLUSTERS: THE HYADES, PLEIADES, COMA BERENICES AND M6

T. Kılıçoğlu[1], R. Monier[2,3], M. Gebran[4] and L. Fossati[5]

Abstract. We compare the averaged photospheric abundances of A and F stars in open clusters of different ages: M6 ($\sim$ 80 Myr), Pleiades ($\sim$ 100 Myr), Coma Berenices ($\sim$ 450 Myr), and the Hyades ($\sim$ 800 Myr). The variation in the averaged abundances among F stars generally reflects the differences between the initial compositions of the clusters in their various birthplaces. The differences of the averaged chemical composition of A stars may also reveal the effects of radiative difussion for the stars of different ages. We also discuss the methods, resolutions and wavelength coverages of spectra and discrepancies in the derived microturbulent velocities among the various studies to check if these studies are comparable. We also present the pattern of mean abundances and metallicity for the M6 cluster determined by spectral analysis of GIRAFFE spectra acquired with the VLT, Paranal Observatory.

Keywords: Open clusters and associations: individual: Hyades, open clusters and associations: individual: Pleiades, open clusters and associations: individual: Coma Berenices, open clusters and associations: individual: M6

1 Introduction

The detailed chemical abundance analyses of open clusters, carried out over the last few decades, allow us to monitor the changes in abundances of the chemical elements during stellar evolution. Chemical abundance analyses, usually based on the analysis of spectra observed in the optical region, mostly reveal the chemical compositions of the photospheres of stars. For the A type main-sequence stars, these photospheric abundances are thought to be affected by radiative diffusion, and generally do not reflect the initial and bulk chemical composition of these stars. Conversely, the deep convective envelopes of the F type main-sequence stars mix the matter in their outer layers. The derived photospheric abundances should thus reflect their original values at time of stellar formation. In this study, we compare the mean abundances derived from A and F stars in several clusters of different ages.

2 Fundamental Parameters and Spectral Data of the Open Clusters

In order to compare the abundances of open clusters of different ages, we selected the papers of Gebran et al. (2008), Gebran & Monier (2008), Gebran et al. (2010), and Kılıçoğlu et al. (2014) who have analysed the Hyades, Pleiades, Coma Berenices, and M6 open clusters, respectively. The fundamental parameters of the clusters, which were retrieved from the SIMBAD and WEBDA databases, and spectral studies that were mentioned above (with references therein), are given in Table 1. The observational properties of the open clusters from selected studies are collected in Table 2.

[1] Ankara University, Faculty of Science, Department of Astronomy and Space Sciences, 06100, Ankara, Turkey
[2] LESIA, UMR 8109, Observatoire de Paris Meudon, Place J. Janssen, Meudon, France
[3] Laboratoire Lagrange UMR 7293, Université de Nice Sophia, Nice, France
[4] Notre Dame University, Faculty of Natural & Applied Sciences, Louaize, Lebanon
[5] Argelander-Institut für Astronomie der Universität Bonn, Auf dem Hügel 71, 53121, Bonn, Germany

Table 1. Fundamental Parameters of the M6, Hyades, Pleiades, and Coma Berenices Open Clusters

Cluster	l (°)	b (°)	Age (Myr)	Distance (PC)	Reddening	[Fe/H]
M6 (NGC 6405)	356.580	–0.777	80	400	0.144	0.07
Pleiades	166.571	–23.521	100	150	0.03	0.06
Coma Berenices	222.514	-83.4011	450	96	0.013	0.07
Hyades	180.060	-22.34	800	45	0.010	0.05

Table 2. Spectral Data of the M6, Hyades, Pleiades, and Coma Berenices Open Clusters

Cluster	Spectrograph	Wavelength interval (Å)	Res.	S/N	Code	Reference
M6 (NGC 6405)	FLAMES with GIRAFFE	4490–5080 5140–5350 5590–5840	7800 25900 24200	$\sim$ 200	ATLAS9[1] SYNSPEC48[2]	Kılıçoğlu et al. (2014)
Pleiades	ELODIE SOPHIE	3850–6811 3820–6930	42000 75000	$\sim$ 200	ATLAS9[1] SYNSPEC48[2]	Gebran & Monier (2008)
Coma Berenices	ELODIE	3850–6811	42000	$\sim$ 200	ATLAS9[1] SYNSPEC48[2] Takeda's code[3]	Gebran et al. (2008)
Hyades	SOPHIE AURELIE	3820–6930 5000–6200	75000 30000–60000	$\sim$ 200	ATLAS9[1] SYNSPEC48[2]	Gebran et al. (2010)

[1]Kurucz (1993), Sbordone et al. (2004), Sbordone (2005), [2]Hubeny & Lanz (1992), [3]Takeda (1995)

3 Microturbulent Velocities

The microturbulent velocities for the four clusters are compared in figure 1. There is no systematic difference between the microturbulent velocities of the clusters. For M6, we noticed that the microturbulence velocities of the stars having temperature between 7500-8500 K are not as large as for the other clusters. The main reason of this difference is that the M6 cluster has only one observed Am star. The relatively lower resolution of the spectra of M6 may also cause these slightly lower derived microturbulent velocities.

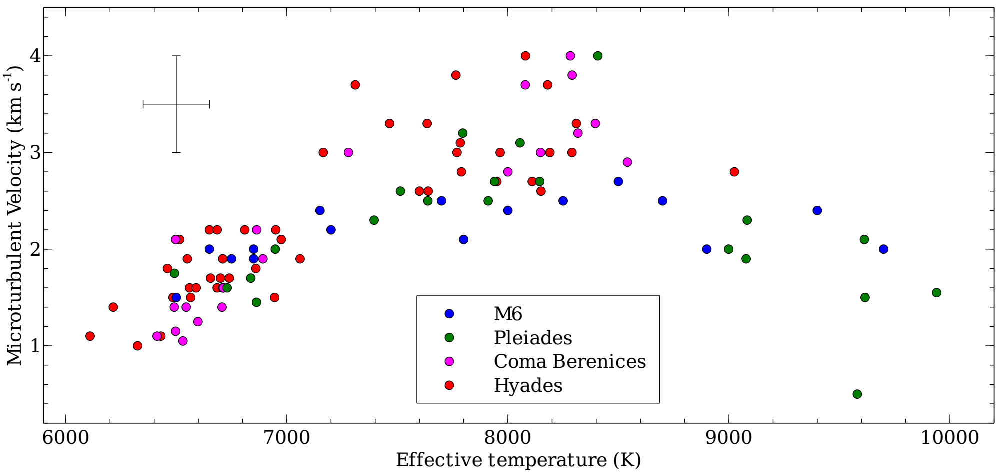

Fig. 1. Microturbulent velocity distribution with effective temperatures

4 Comparisions of the Mean Abundances of the M6, Pleiades, Coma Berenices and Hyades Open Clusters

We compared the mean abundances of A and F type stars in the four open clusters analyzed by Gebran et al. (2008), Gebran & Monier (2008), Gebran et al. (2010), and Kılıçoğlu et al. (2014). These studies use similar methods and spectral data to derive chemical abundances with few exceptions: The resolution of the spectra of the M6 cluster is slightly lower than the other clusters, and AURELIE spectra of the F stars in the Hyades have wavelength coverage of only about 1200 Å. We collected all derived elemental abundances of the chemically normal members, and computed the average of the abundances of the elements seperately for A and F stars, for each cluster.

We found that the M6 and Pleiades clusters, which have similar ages (∼ 100 Myr), also exhibit similar mean abundance patterns except for a few chemical elements. The mean abundance pattern of F stars in the M6 cluster shows that only Mg, Si and Ca elements are slightly less abundant than those of Pleiades. Thus, the initial chemical composition of these two clusters might be similar.

There seems to be large discrepancies between the abundances of A stars of the Pleiades and Coma Berenices (450 Myr) cluster. However, this should not be considered as a real difference, since the study of Gebran et al. (2010) covers mostly Am-type stars. The main abundances of A stars were derived form only three chemically normal A stars which are far from to reflect the overall cluster composition. In contrast, the mean abundance pattern of F stars in Coma Berenices is remarkably similar with those of Pleiades except Ca, Y, and Ba. The main differences between the mean abundances of A stars in the Pleiades and the relatively older Hyades cluster is that the Hyades are significantly enhanched in C, O and Sc.

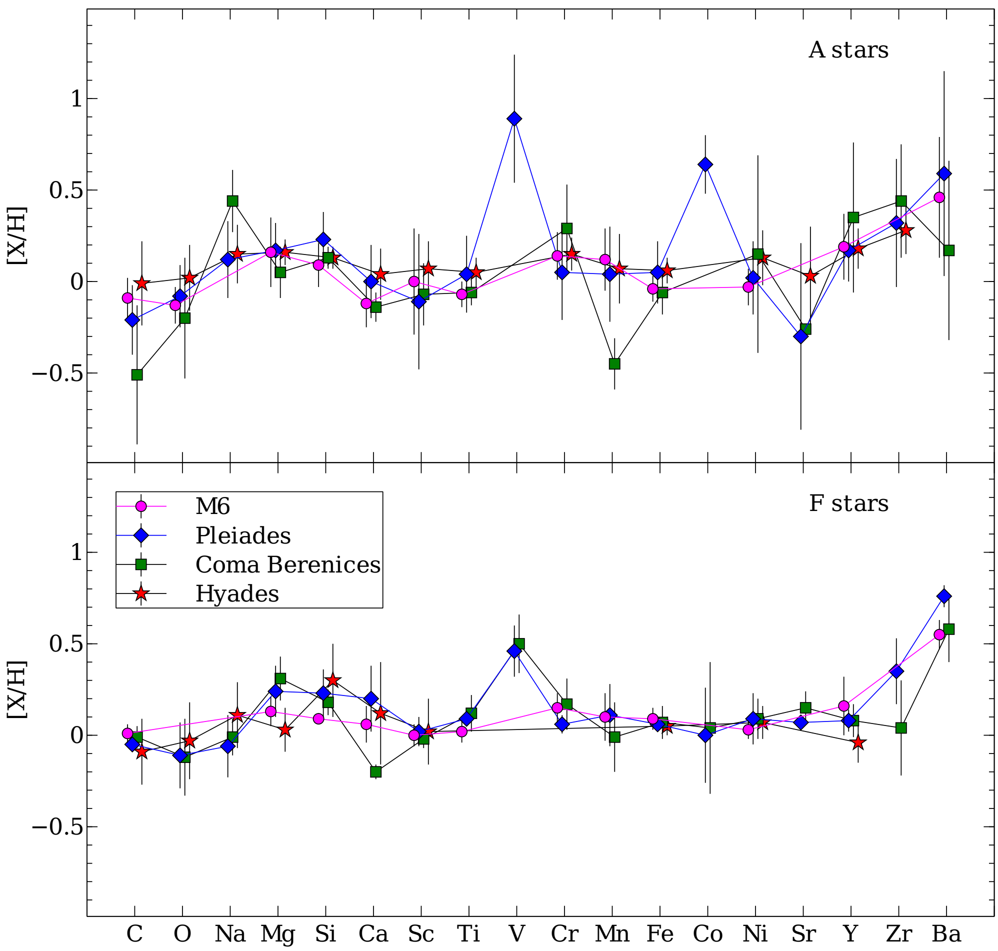

Fig. 2. The mean abundance patterns of the M6, Pleiades, Coma Berenices, and Hyades clusters, for chemically normal A type (upper panel) and F type (lower panel) stars (the bars represent star-to-star variations for corresponding element).

5 Summary and Discussions

If we exclude the mean abundance of Coma Berenices, which contains only three studied chemically normal A stars, the mean abundance pattern of chemically normal A stars in all clusters are found to be very similar. However, the Hyades, which is the oldest cluster in our samples, are slightly enhanced in light elements (C and O) to the other open clusters.

From Sc to Ni, we found that the mean abundance pattern of F stars in all clusters are quite similar. For the other chemical elements, the youngest and the oldest clusters (M6 and Hyades) exhibit a few discrepancies. Mg, Si and Ca are less abundant than other clusters for M6 cluster, while O, Na and Si are slightly enhanced in the Hyades.

In order to perform a better comparison, a study of high resolution spectra of F stars in Hyades, and chemically normal A star in Coma Berenices would be valuable. It is also necessary to ensure the homogeneity of data used to derive abundance pattern of these open clusters. The comparison presented in this paper already shows that the the mean abundance pattern of F type stars for M6, Pleiades, and Hyades clusters are surprisingly similar for many chemical elements.

References

Gebran, M. & Monier, R. 2008, A&A, 483, 567

Gebran, M., Monier, R., & Richard, O. 2008, A&A, 479, 189

Gebran, M., Vick, M., Monier, R., & Fossati, L. 2010, A&A, 523, A71+

Hubeny, I. & Lanz, T. 1992, A&A, 262, 501

Kılıçoğlu, T., Monier, R., & Fossati, L. 2014, ArXiv e-prints

Kurucz, R. 1993, ATLAS9 Stellar Atmosphere Programs and 2 km/s grid. Kurucz CD-ROM No. 13. Cambridge, Mass.: Smithsonian Astrophysical Observatory, 1993., 13

Sbordone, L. 2005, Memorie della Societa Astronomica Italiana Supplementi, 8, 61

Sbordone, L., Bonifacio, P., Castelli, F., & Kurucz, R. L. 2004, Memorie della Societa Astronomica Italiana Supplementi, 5, 93

Takeda, Y. 1995, PASJ, 47, 287

SF2A 2014
J. Ballet, F. Bournaud, F. Martins, R. Monier and C. Reylé (eds)

CONSTRAINING THE TRANSPORT PROCESSES IN STELLAR INTERIORS WITH RED GIANT STARS

Lagarde N.[1], Eggenberger P.[2], Miglio, A.[1,3] and Montalbàn, J.[4]

Abstract. Recent asteroseismic observations have led to the determination of the core rotation rate for a large number of red-giant stars by the study of rotational frequency splittings of l=1 mixed modes. We present how these observed core rotation rates can constrain the efficiency of an additional unknown physical transport process occurring in red-giant stars. We compare theoretical models including rotation-induced mixing and an additional viscosity in the transport of angular momentum, with asteroseismic observations during the red giant branch and the clump.

Keywords: Asterseismology, stars: structure, stars: evolution, stars: rotation, stars: interiors

1 Introduction

Red-giant stars are interesting targets to test and improve stellar evolution models. Numerous spectroscopic observations showed abundances anomalies in red giants brighter than the bump luminosity (e.g. Gratton et al. 2000; Smiljanic et al. 2009), which are not predicted by standard stellar models. Different transport processes have been proposed to understand the surface chemical properties of these stars. In particular, rotation-induced mixing, which changes the structure and chemical profiles during the main sequence but is not efficient enough to reproduce spectroscopic observations during the red giant branch (hereafter RGB Palacios et al. 2003, 2006). As shown by Charbonnel & Zahn (2007), thermohaline instability is a good candidate to explain abundance anomalies in low-mass red-giant stars. Charbonnel & Lagarde (2010) concluded that it is the dominating chemical transport process in low-mass red-giant stars ($M < 2.0\ M_\odot$), which governs their photospheric composition, while rotation-induced mixing with different initial velocities, explain surface abundances in more massive stars ($M > 2.0\ M_\odot$).

In recent years, a large number of asteroseismic data have been obtained for different kinds of stars, which allowed the detection and characterization of solar-like oscillations in a large number of red giants by space missions (e.g. De Ridder et al. 2009). Thousands of evolved stars (subgiant, giant and clump stars) have been already observed by CoRoT (Baglin et al. 2006) and *Kepler* (Borucki et al. 2010), allowing access to the properties of the stellar interiors of red giant stars.

2 Asteroseismology: new tool to improve stellar models

Determination of individual frequencies represents an excellent opportunity to deduce from asteroseismology stellar mass and radius (Beck et al. 2012), as well as distance and age (see Chaplin & Miglio 2013, and references therein). In addition, asteroseismology brings key information on the stellar structure with different acoustic radius (total, at the base of convective envelope or the base of the helium second ionization region), and with the period spacing of gravity modes for l=1. As proposed by Bedding et al. (2011) and Mosser et al. (2011),

[1] School of Physics and Astronomy, University of Birmingham, Edgbaston, Birmingham B15 2TT, UK
[2] Geneva Observatory, University of Geneva, Chemin des Maillettes 51, 1290 Versoix, Switzerland
[3] Stellar Astrophysics Centre (SAC), Department of Physics and Astronomy, Aarhus University, Ny Munkegade 120, 8000 Aarhus C, Denmark
[4] Institut dAstrophysique et de Géophysique, Université de Liège, Allée du 6 Août, Bât. B5c, 4000 Liège, Belgium

this quantity provides the evolutionary state of giant stars, distinguishing RGB and clump stars.

Moreover, thanks to asteroseismology, we can now determine the internal rotation of giant stars (Deheuvels et al. 2012, 2014; Beck et al. 2012; Mosser et al. 2012), and then test models of transport of angular momentum (Eggenberger et al. 2012; Ceillier et al. 2013; Marques et al. 2013). As underlined by Eggenberger et al. (2012) in the case of giant star KIC8366239, a discrepancy exists between the rotation profile deduced from asteroseismic observations and the profiles predicted from models including shellular rotation and related meridional flows and turbulence. They show that a most powerful mechanism is in action to extract angular momentum from the core of this star, and other red giant stars.

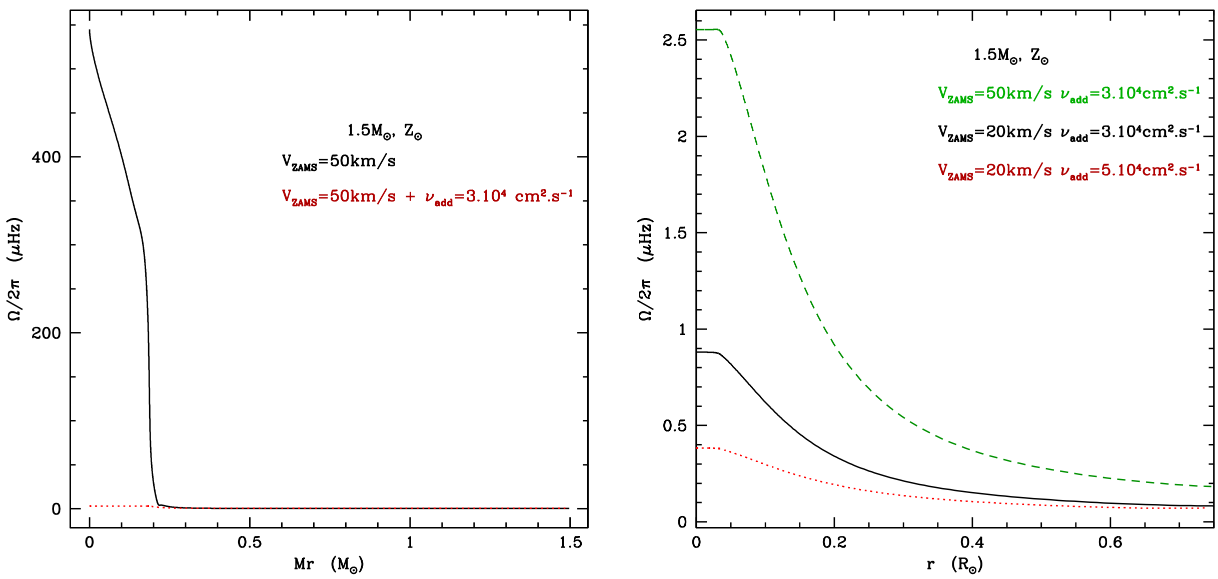

Fig. 1. Theoretical rotation profile in 1.5M$_\odot$ at solar metallicity at the beginning of the red giant branch (R$_\star$=4R$_\odot$): **Left:** in the case of standard rotating model with V$_{\rm ZAMS}$=50km.s^{-1} (black line) and including impact of an additional viscosity (V$_{ZAMS}$=50km.s^{-1}, $\nu_{\rm add}$=3.10^4 cm^2.s^{-1}, red dashed line) ; **Right panel** including an additional viscosity and two initial velocity at the ZAMS (V$_{\rm ZAMS}$=50km.s^{-1} $\nu_{\rm add}$=3.10^4 cm^2.s^{-1}, green dashed line) ; (V$_{\rm ZAMS}$=20km.s^{-1}, $\nu_{\rm add}$=3.10^4 cm^2.s^{-1}, black solid line), and (V$_{\rm ZAMS}$=20km.s^{-1}, $\nu_{\rm add}$=5.10^4 cm^2.s^{-1}, red dashed line)

As proposed by Eggenberger et al. (2012) to quantify the efficiency of this additional mechanism in the RGB stars, we include an additional viscosity in the equation of the transport of angular momentum, corresponding to an additional physical process for the transport of angular momentum in radiative zones (Eq 2.1):

$$\underbrace{\rho\frac{d(r^2\Omega)}{dt}}_{\substack{\text{stellar}\\ \text{contraction/expansion}}} = \underbrace{\frac{1}{5r^2}\frac{\partial}{\partial r}(\rho r^4 \Omega U_r)}_{\substack{\text{advection of}\\ \text{angular momentum}\\ \text{by meridional circulation}}} + \underbrace{\frac{1}{r^2}\frac{\partial}{\partial r}\left(r^4\rho(D+\nu_{add})\frac{\partial\Omega}{\partial r}\right)}_{\substack{\text{diffusion effect of}\\ \text{shear-induced turbulence}\\ \text{and additional viscosity}}}, \tag{2.1}$$

with r the stellar radius, ρ the density, ν_{add} the additional viscosity, Ω the angular velocity, and U$_r$ the vertical component of meridional circulation velocity.

This corresponds well to the two main mechanisms currently proposed to efficiently extract angular momentum from the central core of a solar-type star having a strong impact on the transport of angular momentum. We use the stellar evolutionary code *STAREVOL* (e.g. Palacios et al. 2006; Lagarde et al. 2012) to compute models presented here, including rotation-induced mixing all along the evolution.

Figure 1 displays effects of additional viscosity and different initial velocity on the theoretical rotation profiles for 1.5M$_\odot$ model at solar metallicity for a given stellar radius on the red giant branch. We underline on the left panel of Fig.1 the strong impact of ν_{add} on the core rotation rate which decreases by three orders of magnitude when we consider ν_{add} in the transport of angular momentum. In addition, at a given velocity an increase in ν_{add} results in a more efficient transport of angular momentum, hence in a flatter rotation profile in the radiative zone (right panel of Fig.1). ν_{add} allows us to determine the efficiency of an additional physical process needed on the RGB, which can be constrained thanks to asteroseismic measurements.

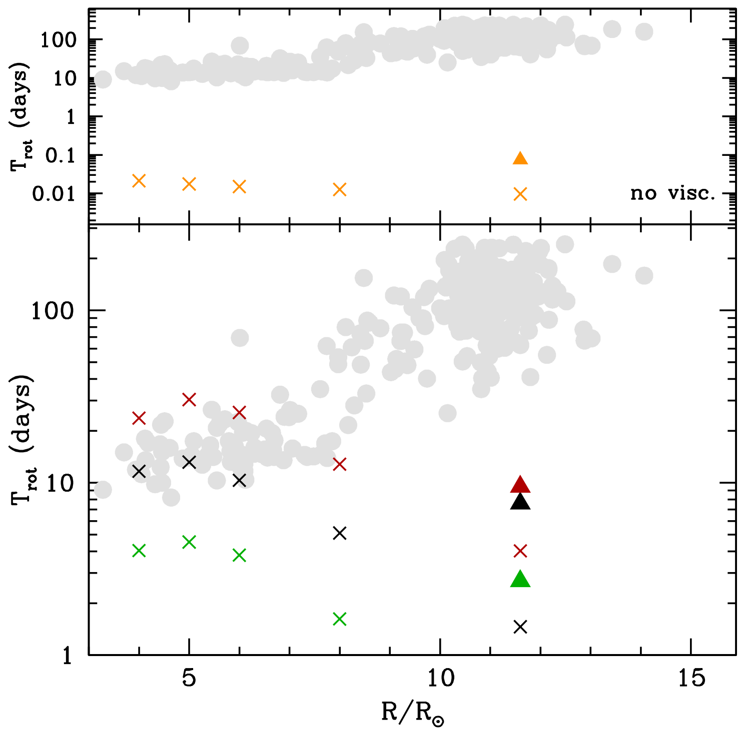

Fig. 2. Theoretical rotation periods of the core as a function of stellar radius of 1.5M$_\odot$ along the RGB (cross) and during the clump (triangle), compared to observations in field stars observed by Kepler from Mosser et al. (2012, , grey dots). Models follow standard rotating model (no viscosity, orange symbols), and including an additional viscosity at two initial velocities (V$_{ZAMS}$=50km.s^{-1} ν_{add}=3.10^4 cm^2.s^{-1}, red symbols) ; (V$_{ZAMS}$=20km.s^{-1}, ν_{add}=3.10^4 cm^2.s^{-1}, black symbols), and (V$_{ZAMS}$=20km.s^{-1}, ν_{add}=5.10^4 cm^2.s^{-1}, green symbols)

Figure 2 shows theoretical rotation period of the core for 1.5 M$_\odot$ along the RGB and during the clump, compared to observations in field stars observed by *Kepler* from Mosser et al. (2012). In the upper panel, orange symbols represent models with rotation (V$_{\rm ZAMS}$ = 50 km.s^{-1}), and without ν_{add}, and clearly shows that classical rotating models cannot represent observed core rotation rate in red giant stars, with predicted periods 2 to 3 orders of magnitude lower than observed. On the other hand, models at constant ν_{add} reproduce very well observations at the beginning of the RGB (Fig.2, lower panel). Observations show an increase of the core rotational period of giants as stars evolve, contrary to theoretical models (see also Fig. 2 and Cantiello et al. 2014). This implies an increase of the efficiency to transport the angular momentum along the red giant branch. However, we remark the same disagreement for clump stars (triangles on Fig.2), the observed and theoretical ratios between core rotational period of clump and RGB stars are slightly the same.

3 Conclusions

Thanks to asteroseismology, we can quantify the efficiency of an additional transport mechanism for the angular momentum along the red giant branch and during the He-burning. Observations by *Kepler* show an increase of this efficiency all along the red giant branch which is not reprouced by stellar models. Models used in this study including rotation-induced mixing all along the evolution of low-mass stars, will be useful to interpret observations from *Kepler* in field stars, and particularly in open clusters. A detailed study of theoretical models and individual frequencies for giant stars will be discussed in a forthcoming paper (Lagarde et al 2014 in prep.)

NL acknowledges financial support from Marie Curie Intra-european fellowship (FP7-PEOPLE-2012-IEF)

References

Baglin, A., Auvergne, M., Boisnard, L., et al. 2006, in 36th COSPAR Scientific Assembly, Vol. 36, 3749
Beck, P. G., Montalban, J., Kallinger, T., et al. 2012, Nature, 481, 55
Bedding, T. R., Mosser, B., Huber, D., et al. 2011, Nature, 471, 608
Borucki, W. J., Koch, D., Basri, G., et al. 2010, Science, 327, 977
Cantiello, M., Mankovich, C., Bildsten, L., Christensen-Dalsgaard, J., & Paxton, B. 2014, ApJ, 788, 93
Ceillier, T., Eggenberger, P., García, R. A., & Mathis, S. 2013, A&A, 555, A54
Chaplin, W. J. & Miglio, A. 2013, ARA&A, 51, 353
Charbonnel, C. & Lagarde, N. 2010, A&A, 522, A10+
Charbonnel, C. & Zahn, J. 2007, A&A, 476, L29
De Ridder, J., Barban, C., Baudin, F., et al. 2009, Nature, 459, 398
Deheuvels, S., Doğan, G., Goupil, M. J., et al. 2014, A&A, 564, A27
Deheuvels, S., García, R. A., Chaplin, W. J., et al. 2012, ApJ, 756, 19
Eggenberger, P., Montalbán, J., & Miglio, A. 2012, A&A, 544, L4
Gratton, R. G., Sneden, C., Carretta, E., & Bragaglia, A. 2000, A&A, 354, 169
Lagarde, N., Romano, D., Charbonnel, C., et al. 2012, A&A, 542, A62
Marques, J. P., Goupil, M. J., Lebreton, Y., et al. 2013, A&A, 549, A74
Mosser, B., Barban, C., Montalbán, J., et al. 2011, A&A, 532, A86
Mosser, B., Goupil, M. J., Belkacem, K., et al. 2012, A&A, 548, A10
Palacios, A., Charbonnel, C., Talon, S., & Siess, L. 2006, A&A, 453, 261
Palacios, A., Talon, S., Charbonnel, C., & Forestini, M. 2003, A&A, 399, 603
Smiljanic, R., Gauderon, R., North, P., et al. 2009, A&A, 502, 267

SF2A 2014
J. Ballet, F. Bournaud, F. Martins, R. Monier and C. Reylé (eds)

STELLAR OPACITY VALIDATIONS

M. Le Pennec[1], S. Turck-Chièze[1], X. Ribeyre[2] and J.E. Ducret[1,2]

Abstract.
This paper focuses on the radiative transfer in stars where opacities seem to raise problems : β-Cephei and solar-type stars. We first concentrate on the iron bump (log T = 5.25), responsible for β-Cephei pulsations through the κ-mechanism. To discriminate between the different opacity calculations used to predict their oscillations, new well-qualified calculations are used and compared to OP calculations. In parallel with this theoretical work, an experiment has been conducted at LULI 2000 in 2011 on iron and nickel. We show that this extended study pushes for the revision of the tables in the conditions corresponding to the iron bump region, at least for nickel. We will then deal with the Sun case for which we are preparing an opacity experiment on a high-energy laser, in some conditions of the radiative zone (T = [2 - 15 $\times 10^6$ K] and ρ = [0.2 - 150 g/cm^3]). To reach these high temperatures and densities at LTE and validate or not plasma effects and line widths, we are exploring an approach called the Double Ablation Front, driven by plasma radiative effects. The 1D simulations performed with the code CHIC show that with this technique, we could reach conditions equivalent to the conditions of half of the solar radiative zone.

Keywords: opacity, sun, massive stars, plasma physics

1 Introduction

Helioseismology and asteroseismology measurements provide very accurate diagnostics of the stellar structure by using the acoustic modes propagating into stellar interiors. If oscillation spectra are correctly interpreted, then a substantial amount of information can be extracted concerning the star. However, in some cases, the comparison between the seismic observations and the predictions coming from stellar models show discrepancies. We focus in this paper on two cases where these discrepancies are observed and could be attributed to the description of the microscopic physics: the envelopes of β-Cephei and the solar interior.

2 β-Cephei

β-Cephei are pulsating stars, progenitor of type II supernovae. They pulsate through the κ-mechanism, due in this case to M-shell transitions for the elements of the iron group (principally iron and nickel) which induce an opacity bump. This bump is very sensitive to the mass, the metallicity and the age of the considered star (Le Pennec & Turck-Chièze 2014), showing that a very precise determination of these three parameters as well as the proper knowledge of the opacities are needed to understand the structure and evolution of the star.
The first difficulty to interpret their oscillation spectrum comes from the fact that some modes are observed but not predicted by stellar models. Indeed, one observes modes which were calculated to be stable in theoretical predictions using OP or OPAL opacity tables (Pamyatnykh 1999; Zdravkov & Pamyatnykh 2009). Furthermore, depending on the mass of the star, some of the modes seem better predicted using OP (Seaton 2005) or OPAL (Rogers & Iglesias 1992; Iglesias & Rogers 1996) tables. This fact suggests that some of these opacities could be inaccurately determined for both tables (Salmon et al. 2012) or that some hydrodynamic process plays an important role not yet understood.

[1] Service d'Astrophysique, CEA/DSM/IRFU, CE Saclay, 91190 Gif-sur-Yvette, FRANCE
[2] Centre Lasers Intenses et Applications CELIA, UMR 5107 CNRS-CEA-Université de Bordeaux, UMR 5107, 351, cours de la Libération, F-33405 Talence, FRANCE

To understand the limitations of OP and OPAL, new codes have been developed, with different physical approaches. The comparison of these new calculations with the tables currently used in astrophysics shows large discrepancies for iron and nickel. If the quality of the calculations strongly depends on the quality of the atomic data, we see with this study that the number of levels taken into account in the opacity calculation is evidently crucial (Turck-Chièze et al. 2014). One could then be tempted to consider all the detailed radiative transitions with their configuration interaction to get a good determination of this quantity but this is presently limited by the computer capability. So, one has to find a compromise between detailed and statistical approaches and the execution time of such a process.

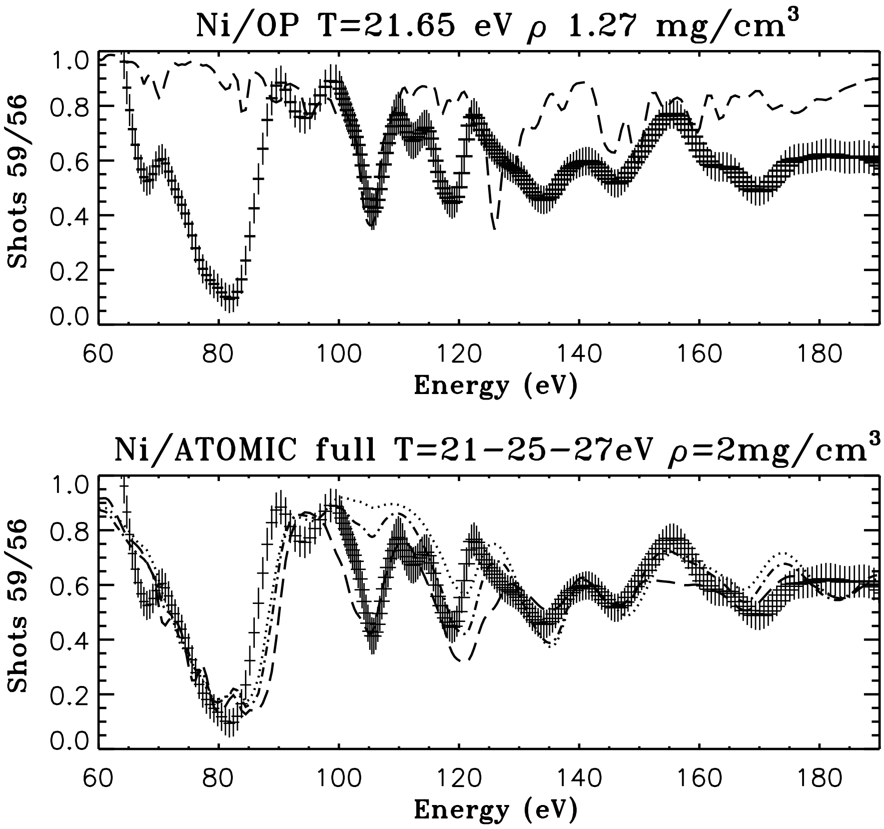

Fig. 1. Comparison of the nickel experimental spectrum (including an analysing error) with (up) the theoretical spectrum given by OP at the nearest node in the tables compared to the experimental conditions and with (bottom) ATOMIC calculations (Colgan et al. 2013) at 2 mg/cm^3 and several temperatures to show how calculations vary in the range where one can find gradient in the nickel foil. 1 eV = 11 604 K. From Turck-Chièze et al. (2014).

In parallel, an experiment has been performed on iron and nickel on LULI 2000 facility (Thais et al. 2014). As it is not possible to perform an experiment at the very low densities of these envelopes, equivalent conditions of plasma have been determined, where the degree of ionization is similar. In the case of nickel, the comparison of the experimental spectrum with previous calculations shows that both are not satisfactory. New calculations show better agreement with the experiment than OP calculations which were derived from iron calculations as shown on Figure 1. In the case of iron, new calculations are interesting to compare (Turck-Chièze et al. 2014). We will try to confirm these conclusions by analyzing two other elements contributing to the iron bump, which were measured during the same experimental campaign: copper and chromium.

New opacity tables for astrophysical use are in preparation in the range of density and temperature corresponding to the iron peak.

3 Solar radiative zone

The Sun is our closest star and thus used as a benchmark to study other stars. Its radius, luminosity and mass are known with great accuracy, that allows to make very precise models of the Sun. However, some doubts are raised on the accuracy of the used microscopic physics. Indeed, a discrepancy between helioseismic observations and predictions by SSM appeared in the solar sound speed profile. This discrepancy, of about 20 times the vertical error bar, put some questions on the solar radiative transfer (Turck-Chièze et al. 2011). Indeed, there exists several hypotheses to explain this difference. Among them:

- it could be due to macroscopic processes in the radiative zone not taken into account in the energetic balance of the Sun
- the radiative transfer calculations are not accurately estimated, either in the Rosseland mean value that could be underestimated or in the treatment of the radiative acceleration which limits the gravitational settling and could lead to incorrect internal abundances.

It could also be due to all these effects simultaneously. Determining where this discrepancy originates would be an important step toward our understanding of the Sun and solar-like stars.

The heavy elements significantly contribute to opacity even if they are present only at few percents in mass fraction in the solar mixture which is principally constituted of hydrogen and helium (Turck-Chièze et al. 2010). The most important contributors are:

- iron, which contributes to the total opacity (including H and He) at a level of 20% in most of the radiative zone because always partially ionized;
- oxygen, which becomes partially ionized at 0.6 $R_\odot$ and plays a major role at the basis of the convective zone. The increase of its opacity contribution triggers the convection;
- silicon, which plays a role at the level of 10% below 10 millions of degrees.

Hydrogen and helium are fully ionized in the radiative zone. The contributions to the opacity of iron, oxygen and silicon, when they are partially ionized, are more complex to calculate depending on the number of bound electrons. So, it could be useful to confirm the existing calculations by experiments, regarding the difficulty to compute the opacity of these elements.
Reproducing the solar interior conditions is a real challenge because one tries to reproduce the charge state distribution of the different elements together with the free-electron density (N_e) at the targeted conditions, that means density greater than solid and high temperature. Table 1 presents some values of the temperature and the free-electron density at different solar depths.

Solar radius ($r/R_\odot$)	T(eV)	N_e (cm^{-3})
0.5	340	8 x 10^{23}
0.6	270	2.5 x 10^{23}
0.7	200	1x 10^{23}

Table 1. Temperature and free-electron density at different depths of the Standard Solar Model computed with the MESA code for the Asplund et al. (2009) composition.

Bailey et al. (2007) have already measured on the Z-pinch facility the iron transmission at conditions lower than those at the basis of the convective zone at 156 eV. This first measurement agrees reasonably well with the compared theoretical calculations. Then, they have increased the temperature up to 196 eV and reached free-electron densities of several 10^{21} - 10^{22} cm^{-3} (Bailey et al. 2009; Nagayama et al. 2014). However, for this last measurement, an unexplained gap exists between the measurement and the theoretical calculations coming from different codes. It has already been shown that this difference is not attributed to the bound-bound transitions.

So we propose to use the Double Ablation Front (DAF) to reach conditions of Table 1 with high energy laser facilities and check the energy spectra of iron and other elements. This approach is based on the use of a moderated Z material (Si, SiO_2...) as target ablator, that increases the conversion of the laser energy in X rays compared to low Z ones. The energetic photons emitted by the corona* are absorbed in the more opaque region at the basis of the thermal wave, creating an additional ablation front (Sanz et al. 2009; Drean et al. 2010). The two ablation fronts (radiative and electronic) are separated by a density and temperature plateaux as shown on Figure 2 that are used to limit the gradient inside the sample (temperature and density). This multi-ablation structure was put in evidence experimentally on the GEKKO laser (Fujioka et al. 2004) and was produced recently at the OMEGA laser (Smalyuk et al. 2010).

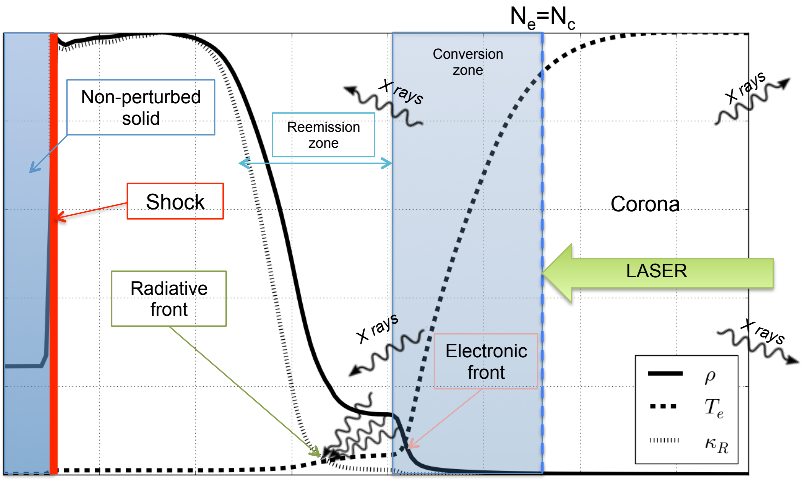

Fig. 2. Schematic structure of a Double Ablation Front: profiles of temperature, density and opacity at a give time in a layer of SiO_2 (Z=10). One can see two ablation fronts: one due to electrons (electronic front), the other due to photons (radiative front). Between the two fronts, there is a plateau region, that extends with time.

This approach could use planar targets composed by three layers of material. The sample of interest is tampered by two other layers, which depend on the chosen irradiation: one-side or symmetrical irradiation. We perform 1D simulations with these targets thanks to the CHIC code (Breil & Maire 2007) with various laser intensities and various widths of the target.
Some of our results are summarized in Table 2. We performed in this case simulations with iron as sample of interest and we used silicon as the ablator, to create the DAF structure. What is interesting to note is that with a moderate laser intensity, we seem to be able to reach thermodynamical conditions close to the conditions of half the solar radiative zone, near LTE conditions. Moreover, these conditions are reached with very low gradients in the target: around 8% in the simple irradiation case, lower than 6% in the symmetrical irradiation case (Le Pennec et al. submitted).

4 Conclusions

Discrepancies between seismic observations and models predictions require to check the opacity calculations. The study of the iron bump in the envelope of the β-Cephei shows the limitations of the astrophysical used tables. The development of new calculations and experiments have allowed to understand the limitations of the previous calculations and leads to the construction of new tables at the conditions of density and temperature of the iron peak. We are also presently adopting the same approach for the solar case by suggesting a new experimental scheme for opacity measurements. We hope to have the opportunity to validate experimentally this new concept with the LMJ-PETAL facility at Bordeaux.

*The corona is the heated plasma at keV temperature and free-electron density lower than the critical density defined by $N_c = \frac{1.1\times10^{21}}{(\lambda[\mu m])^2}$ [cm^{-3}].

Target	Irradiation type	I $_{laser}$ (10^{15} W/cm^2)	T$_{e\ mean}$ (eV)	ρ $_{mean}$ (g/cm^3)	N$_{e\ mean}$ (10^{23} cm^{-3})
Si / Fe / CH 8 μm / 0.1 μm / 7 μm	One-side	1.5	160 - 180	0.75 - 1	1.1 - 1.5
Si / Fe / Si 7 μm / 0.1 μm / 7 μm	Sym.	1.5	200 - 230	1.2 - 1.5	2.2 - 2.5
Si / Fe / Si 7 μm / 0.1 μm / 7 μm	Sym.	4.0	260 - 290	2.0 - 2.3	3.7 - 4.1

Table 2. Conditions obtained in the iron sample for the simulations of the proposed experimental scheme.

The authors thanks the SF2A organizing committee and the editors of the proceedings. Part of this work was supported by the ANR OPACITY. We would like to thank Y. Ralchenko for providing access to the FLYCHK code and CELIA for providing access to the CHIC code.

References

Bailey, J., Rochau, G., Iglesias, C., et al. 2007, Physical Review Letters, 99, 265002

Bailey, J., Rochau, G., Mancini, R., et al. 2009, Physics of Plasmas, 16, 058101

Breil, J. & Maire, P.-H. 2007, Journal of Computational Physics, 224, 785

Colgan, J., Kilcrease, D. P., Magee Jr, N. H., et al. 2013, High Energy Density Physics, 9, 369

Drean, V., Olazabal-Loumé, M., Sanz, J., & Tikhonchuk, V. 2010, Physics of Plasmas, 17, 122701

Fujioka, S., Sunahara, A., Ohnishi, N., & et al. 2004, Physics of Plasmas, 11, 2814

Iglesias, C. & Rogers, F. 1996, The Astrophysical Journal, 464, 943

Le Pennec, M., Ribeyre, X., Ducret, J.-E., & Turck-Chièze, S. submitted, High Energy Density Physics

Le Pennec, M. & Turck-Chièze, S. 2014, in IAU Symposium, ed. J. A. Guzik, W. J. Chaplin, G. Handler, & A. Pigulski

Nagayama, T., Bailey, J., Loisel, G., et al. 2014, Physics of Plasmas, 21, 056502

Pamyatnykh, A. 1999, Acta Astronomica, 49, 119

Rogers, F. & Iglesias, C. 1992, The Astrophysical Journal Supplement Series, 79, 507

Salmon, S., Montalbán, J., Morel, T., et al. 2012, Monthly Notices of the Royal Astronomical Society, 422, 3460

Sanz, J., Betti, R., Smalyuk, V. A., et al. 2009, Physics of Plasmas, 16, 082704

Seaton, M. 2005, Monthly Notices of the Royal Astronomical Society, 362, L1

Smalyuk, V. A., Betti, R., Delettrez, J. A., et al. 2010, Physical Review Letters, 104, 165002

Thais, F., Bastiani-Ceccotti, S., . . . , & ... 2014, to be submitted

Turck-Chièze, S., Le Pennec, M., Ducret, J.-E., et al. 2014, submitted

Turck-Chièze, S., Palacios, A., & Nghiem, P. 2010, The Astrophysical Journal, 715, 1539

Turck-Chièze, S., Piau, L., & Couvidat, S. 2011, The Astrophysical Journal Letters, 731, L29

Zdravkov, T. & Pamyatnykh, A. 2009, in American Institute of Physics Conference Series, ed. J. A. Guzik & P. Bradley, Vol. 1170

SF2A 2014
J. Ballet, F. Bournaud, F. Martins, R. Monier and C. Reylé (eds)

GRAVITO-INERTIAL MODES IN A DIFFERENTIALLY ROTATING SPHERICAL SHELL

G. M. Mirouh[1, 2], C. Baruteau[1,2], M. Rieutord[1,2] and J. Ballot[1,2]

Abstract. Oscillations have been detected in a variety of stars, including intermediate- and high-mass main sequence stars. While many of these stars are rapidly and differentially rotating, the effects of rotation on oscillation modes are poorly known. In this communication we present a first study on axisymmetric gravito-inertial modes in the radiative zone of a differentially rotating star. These modes probe the deep layers of the star around its convective core. We consider a simplified model where the radiative zone of a star is a linearly stratified rotating fluid within a spherical shell, with differential rotation due to baroclinic effects. We solve the eigenvalue problem with high-resolution spectral simulations and determine the propagation domain of the waves through the theory of characteristics. We explore the propagation properties of two kinds of modes: those that can propagate in the entire shell and those that are restricted to a subdomain. Some of the modes that we find concentrate kinetic energy around short-period shear layers known as attractors. We characterise these attractors by the dependence of their Lyapunov exponent with the Brunt-Väisälä frequency of the background and the oscillation frequency of the mode. Finally, we note that, as modes associated with short-period attractors form dissipative structures, they could play an important role for tidal interactions but should be dismissed in the interpretation of observed oscillation frequencies.

Keywords: asteroseismology, stars:rotation

1 Introduction

High-precision photometry provided by space missions, such as CoRoT and Kepler, have allowed measuring many oscillation frequencies in a variety of stars. In rotating stars, low-frequency modes correspond to modes restored by buoyancy and Coriolis forces, and are called gravito-inertial modes. Their excitation can be provided by internal mechanisms, such as the κ-mechanism. For planet-harbouring stars, tidal effects may excite such modes. Determining how tidally-excited waves deposit their energy and angular momentum helps predicting the orbital evolution of close-in planets.

We wish to have more insights into the modal properties of high- and intermediate-mass main sequence stars. High rotation rates have been detected in most of these stars (Royer 2009), while Espinosa Lara & Rieutord (2013) showed that the radial differential rotation increases throughout the evolution of these stars. The oscillation properties of rapidly and differentially rotating stars are less constrained than those of slow rotators. For instance, their spectra show no regular patterns as shown in delta Scuti stars (Mirouh et al. 2014). The fundamental parameters and the mode amplitudes are also modified by rotation, as shown for fast-rotating SPB stars detected outside of their expected instability domain (Mowlavi et al. 2013; Salmon et al. 2014).

Inertial modes in a differentially rotating convective layer have been studied by Baruteau & Rieutord (2013), but the influence of differential rotation on the properties of gravito-inertial modes in a radiative zone is still an uncharted territory. In those stars, gravito-inertial modes probe the internal layers of the radiative zone, around the convective core. A better characterisation of the oscillations could help constrain the physical model, in particular the core size.

[1] Université de Toulouse, UPS-OMP, IRAP, Toulouse, France
[2] CNRS, IRAP, 14 avenue Edouard Belin, 31400 Toulouse, France

2 Model

We model the outer radiative region of a star as a viscous fluid enclosed in a spherical shell. The convective core is not modeled. We impose a linear background temperature gradient through the radiative shell ($\boldsymbol{\nabla} T = -\beta \boldsymbol{r}/R$, where T is the background temperature, and β a positive constant). This gradient yields a linear stable stratification (Chandrasekhar 1961), where the Brunt-Väisälä frequency reads $n(r) = N \times r$ with N a constant.

Rieutord (2006) has shown that the baroclinic flow (i.e. the flow resulting from the combined effects of rotation and stratification) gives, for no-slip boundary conditions on both sides of the shell (Hypolite & Rieutord 2014), the following angular velocity profile $\Omega(r)$:

$$\frac{\Omega(r)}{\Omega(R)} = 1 + \int_r^R \frac{n^2(r')}{r'} dr' = 1 + \frac{N^2}{2}\left(1 - \frac{r^2}{R^2}\right).$$

This is the configuration that we have adopted, resulting in a shellular differential rotation. We also make use of the Boussinesq approximation.

We determine the properties of the linear oscillations in this model using two methods (see e.g. Rieutord & Valdettaro 1997; Dintrans et al. 1999; Baruteau & Rieutord 2013).

1. We solve the eigenvalue problem of the stellar oscillations with a spectral code. This is done by considering the linearised equations of motion, energy, and mass conservation, in which our quantities are decomposed as the sum of a background state and a perturbation in $\exp(i\omega t)$ (with ω the mode frequency in the inertial frame). The equations are then projected onto the spherical harmonics, as described in Rieutord (1987). We compute eigenvalues (and the associated eigenmodes) of the fully dissipative system.

2. We compute the paths of characteristics, in the non-dissipative limit. This approach consists in neglecting the viscous and thermal dissipations and allows us to reduce the set of linearised equations as a partial differential equation for the pressure perturbation, which is often referred to as the pressure operator. From this operator of hyperbolic or mixed type, we extract the equation of the characteristics (Friedlander & Siegmann 1982a).

In the present study the dissipative properties of the fluid are characterised by the Prandtl and the Ekman numbers, which are respectively defined as:

$$\mathrm{Pr} = \frac{\nu}{\kappa}, \qquad \mathrm{E} = \frac{\nu}{\Omega(R) R^2}, \tag{2.1}$$

where ν is the kinematic viscosity and κ the thermal diffusivity of the fluid.

In stars, $\mathrm{Pr} \sim 10^{-5}$ and $\mathrm{E} \sim 10^{-10} - 10^{-12}$. However, such small values require considerable spatial resolution, making the numerical problem ill-conditioned (Valdettaro et al. 2007). For a first numerical exploration, we set $\mathrm{Pr} = 10^{-2}$ and $\mathrm{E} = 10^{-8}$ and scan the (N^2, ω) plane.

3 Mode classification

The pressure operator defined in section 2 is of mixed type : depending on the parameters and the position in the star, the solutions may be evanescent or oscillatory. Therefore, for a given set of (N^2, ω), eigenmodes may occupy only a fraction of the spherical shell. This permits a classification of the modes in two categories, as in Baruteau & Rieutord (2013).

If waves can propagate in the whole shell, we call these modes D modes (for Differential rotation). Conversely, if the operator is elliptic in the whole shell, the oscillations are damped and we see no mode. If the type of the operator changes in the shell, the waves are confined to the hyperbolic domain in the shell. The boundaries of the propagation domain are called critical or turning surfaces, and we call DT modes the modes exhibiting this behaviour (for Differential rotation with a Turning surface).

Figure 1 shows the kinetic energy distribution of some axisymmetric ($m = 0$) modes for various values of η, N^2 and ω, in a meridional plane. The energy is focused along shear layers, which correspond to the trajectory of characteristics computed in the non-diffusive case. Varying parameters E and Pr changes the focusing of the modes towards the characteristics. At vanishing viscosities, the shear layers become singular. The mode on the left is an inertial mode with solid-body rotation ($N^2 = 0$, Ω constant), and is a D mode spanning the whole

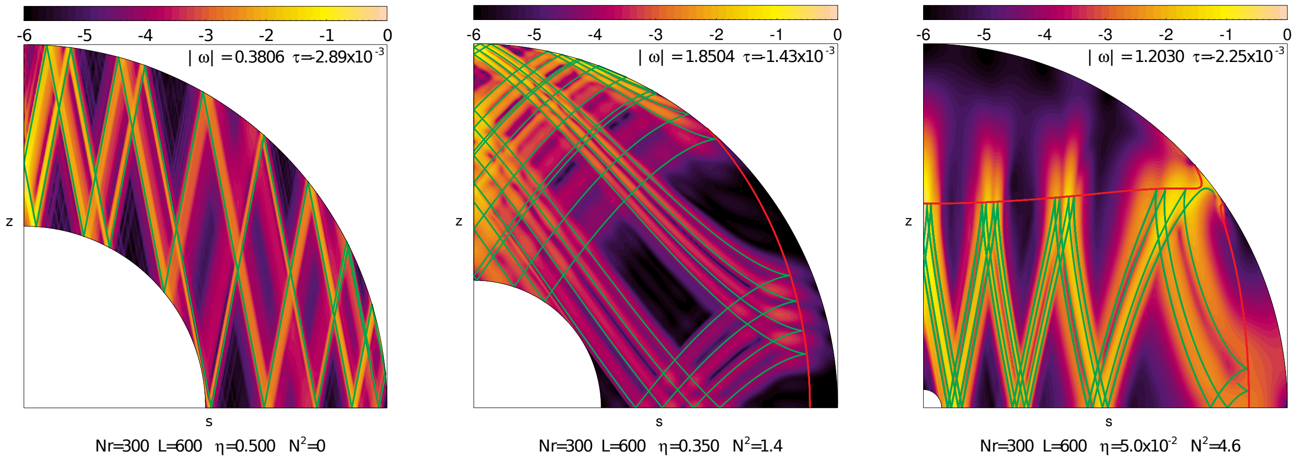

Fig. 1. Meridional slices of kinetic energy obtained by solving the dissipative linearised hydrodynamics equations, with attractors (green) and turning surfaces (red) overplotted. The energy is plotted on a logarithmic scale and normalised to its maximum value.

shell. The two other modes are gravito-inertial modes in a differentially rotating background. The oscillation is confined to a subdomain, bounded by one or several turning surfaces computed analytically.

We study the propagation properties of the oscillations for a range of N^2 and ω. Investigating the mathematical properties of the pressure operator yields the curves separating the D and DT modes geometries. Figure 2 summarises the various classes of modes in the parameter space (N^2, ω), each domain corresponding to a different geometry. The boundaries between the domains are calculated analytically, and confirmed by computing the type of the pressure operator numerically.

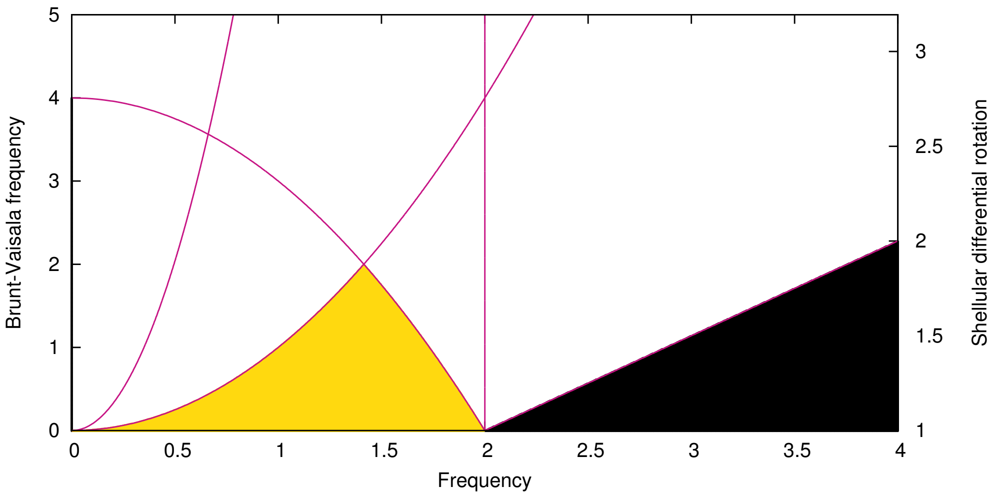

Fig. 2. Map of the axisymmetric D modes (yellow) and DT modes (white), for $\eta = 0.35$. The solid lines correspond to changes in the mode geometry shown in the miniatures. No modes exist in the black domain.

4 Attractors and dissipation

The modes shown in figure 1 feature only modes associated with short-period attractors.

Such modes are expected to be very damped, and thus should be excluded when trying to identify observed frequencies. However, as their dissipation rate is high, these modes are important for tidal interaction.

To determine whether characteristics tend or not towards a periodic structure, we compute the Lyapunov exponent of the characteristic trajectories (e.g. Rieutord et al. 2001). This exponent quantifies the convergence of the characteristics towards attractors. We have computed the Lyapunov exponent for all the D modes, as shown in figure 3. We see ridges where the Lyapunov exponent is very negative, corresponding to modes featuring short-period attractors, which slightly change their frequency and geometry when N^2 varies. However, most of the domain corresponds to longer-period attractors compatible with low dissipation, and therefore with excitable stellar pulsations.

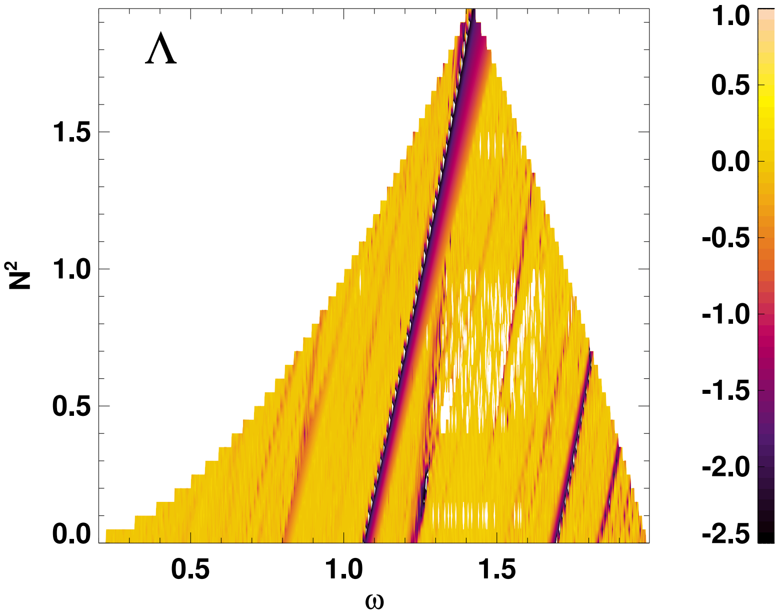

Fig. 3. Lyapunov exponent for D modes, as a function of stratification and wave frequency.

5 Conclusions and future prospects

For the first time, we compute the oscillations of a differentially rotating radiative region of star, where differential rotation is part of the baroclinic flow triggered by the combined effects of rotation and stable stratification.

We have given a first view of axisymmetric eigenmodes which may propagate in such a background flow. The next steps include investigating non-axisymmetric modes and using more realistic Brunt-Väisälä frequency profiles, before tackling the more realistic configuration of a two-dimensional compressible stellar model, as in the ESTER models (Espinosa Lara & Rieutord 2013).

References

Baruteau, C. & Rieutord, M. 2013, Journal of Fluid Mechanics, 719, 47

Chandrasekhar, S. 1961, Hydrodynamic and hydromagnetic stability (Clarendon Press, Oxford)

Dintrans, B., Rieutord, M., & Valdettaro, L. 1999, J. Fluid Mech., 398, 271

Espinosa Lara, F. & Rieutord, M. 2013, A&A, 552, A35

Friedlander, S. & Siegmann, W. 1982a, J. Fluid Mech., 114, 123

Hypolite, D. & Rieutord, M. 2014, to appear in A&A, 1, 1

Mirouh, G. M., Reese, D. R., Espinosa Lara, F., Ballot, J., & Rieutord, M. 2014, in IAU Symposium, Vol. 301, IAU Symposium, ed. J. A. Guzik, W. J. Chaplin, G. Handler, & A. Pigulski, 455–456

Mowlavi, N., Barblan, F., Saesen, S., & Eyer, L. 2013, A&A, 554, A108

Rieutord, M. 1987, Geophys. Astrophys. Fluid Dyn., 39, 163

Rieutord, M. 2006, A&A, 451, 1025

Rieutord, M., Georgeot, B., & Valdettaro, L. 2001, J. Fluid Mech., 435, 103

Rieutord, M. & Valdettaro, L. 1997, J. Fluid Mech., 341, 77

Royer, F. 2009, in Lecture Notes in Physics, Berlin Springer Verlag, Vol. 765, The Rotation of Sun and Stars, ed. J.-P. Rozelot & C. Neiner, 207–230

Salmon, S. J. A. J., Montalbán, J., Reese, D. R., Dupret, M.-A., & Eggenberger, P. 2014, A&A, 569, A18

Valdettaro, L., Rieutord, M., Braconnier, T., & Fraysse, V. 2007, J. Comput. and Applied Math., 205, 382

HD 30085: A NEW PT-HG RICH LATE B-TYPE STAR

R.Monier[1,2], M.Gebran[3], F.Royer[4] and E.Griffin[5]

Abstract. Using high dispersion high quality spectra of HD 30085 obtained with the echelle spectrograph SOPHIE at Observatoire de Haute Provence, we show that this star, hitherto classified as a A0IV superficially normal star, is actually a Chemically Peculiar star of the HgMn type. Spectrum synthesis reveals large overabundances of Mn, Sr, Y, Zr , Pt and Hg which are characteristic of HgMn stars. We therefore propose that this interesting object be reclassified as a B8 HgMn star.

Keywords: stars: individual, stars: Chemically Peculiar

1 Introduction

HD 30085, currently assigned an A0IV spectral type, is one of the slowly rotating A stars studied in Royer et al. (2014). The incentive of this recent work has been to reclassify the 47 early A stars in the northern hemisphere brighter than V=7.0 mag with low apparent projected velocities (less than 60 km s^{-1}). A first abundance analysis of high resolution well exposed spectra of these objects has sorted out the sample into 17 chemically normal stars (ie. whose abundances do not depart more than $\pm$ 0.20 dex from solar values), 12 spectroscopic binaries and 13 Chemically Peculiar stars (CP) among which 5 are new CP stars whose status still needs to be specified fully (Si rich Bp stars, HgMn stars or new Am star ?). HD 30085 is one of these new CP star. We present here new abundance determinations for HD 30085 which allow us to propose that this star is a new HgMn late B star.

2 Observations and reduction

HD 30085 has been observed twice at Observatoire de Haute Provence (OHP) using SOPHIE in its high resolution mode (R=75000) in February 2012 and December 2013. Three 15 minutes were obtained in February 2012 with a signal-to-noise ratio of about 220 and coadded into a mean spectrum. One single 20 minutes exposure was obtained in December 2013 with a signal-to-noise ratio of about 300.

3 Reassigning a proper spectral type to HD 30085

The following spectral regions have been used to readdress the spectral type of HD 30085. First, the red wing of H_ϵ from 3980 Å up to 4000 Å harbours the Hg II line at 3984 Å and several Zr II and Y II lines likely to be strengthened in a late B-type star of the HgMn type (figure 1). Second, the region from 4125 Å to 4145 Å contains the Si II Multiplet II doublet and the Mn II line at 4136.92 Å(figure 1). The seven lines used are collected in table 1 with their identifications and preliminary abundances (see next section). Their positions are marked by vertical lines in both figures (after a correction for a radial velocity of about 10 km s^{-1}).

[1] LESIA, UMR 8109, Observatoire de Paris Meudon, Place J.Janssen, Meudon, France
[2] LAGRANGE, UMR 7293, Universite de Nice Sophia, Nice, France
[3] Department of Physics and Astronomy, Notre Dame University Louaize, PO Box 72, Zouk Mikael, Lebanon
[4] GEPI, UMR 8111, Observatoire de Paris Meudon, Place J.Janssen, Meudon, France
[5] Dominion Astrophysical Observatory, 5071 West Saanich Road, Victoria, BC, V9E 2E7, Canada

Classification lines			
Wavelengths (Å)	Identification	Multiplet	Abundance
3982.44	Y II		200 ⊙
3983.87	Hg II	M 2	32000 ⊙
3990.96	Zr II		100 ⊙
3998.82	Zr II		100 ⊙
4128.07	Si II	M 2	2.5 ⊙
4130.88	Si II	M 2	2.5 ⊙
4136.92	Mn II		30 ⊙

Table 1. Preliminary abundances based on the seven lines used in this work.

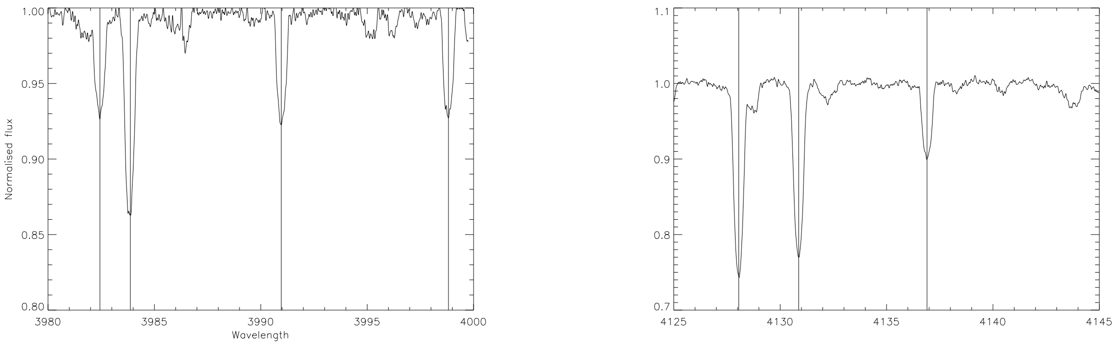

Fig. 1. Left: Hg II spectral line region (left). **R**ight: Si II Multiplet 2 spectral region.

4 Abundance determinations

4.1 Model atmospheres and spectrum synthesis

The effective temperature Teff and surface gravity log g of HD 30085 were first evaluated using Napiwotzky et al's (1993) UVBYBETA calibration of Stromgren's photometry in terms of effective temperature and surface gravity. A plane parallel model atmosphere assuming radiative equilibrium and hydrostatic equilibrium has been first computed using the ATLAS9 code (Kurucz, 1992), specifically the linux version using the new ODFs maintained by F. Castelli on her website. The linelist was built starting from Kurucz's (1992) gfhyperall.dat file * which includes hyperfine splitting levels. This first linelist was then upgraded using the NIST Atomic Spectra Database † and the VALD database operated at Uppsala University (Kupka et al., 2000) ‡.

A grid of synthetic spectra was computed with SYNSPEC48 (Hubeny & Lanz, 1992) to model the Si II, Mn II, Zr II and Hg II lines. The unknown abundance $[\frac{X}{H}]$ was varied until minimisation of the chi-square between the observed and synthetic spectrum.

4.2 Evidence for a Platinum excess

While modeling the Fe II lines in the 4500 Å- 4600Å region, we noticed a 2% feature at about 4514.15 Å which had no counterpart in our linelist. We have identified this feature as one of the strongest Pt II line expected at 4514.17 Å listed in VALD. No other line can reproduce the observed 2% line depth at this wavelength. Other lines of Pt II were also identified at shorter wavelengths to confirm the presence of platinum in HD 30085. In figure 2, the observed Pt II line profile at 4514.17 Å (solid line) is compared to three synthetic spectra (dashed lines) computed for 3 overabundances of platinum (2500, 3500 and 5000 ⊙). We also checked that a model

*http://kurucz.harvard.edu/linelists/
†http://physics.nist.gov/cgi-bin/AtData/linesform
‡http://vald.astro.uu.se/ vald/php/vald.php

computed for a solar platinum abundance yields no absorption at all at 4514.17 Å. From the 4514.17 Å line only, a provisional excess of platinum is derived to be about 3500 ± 1000.
The Hg overabundance is derived from the 3983.87 Å line of multiplet 2 including the hyperfine structure of various isotopes of Hg in a similar manner to Castelli & Hubrig (2004) modelling of HD 175640. The abundance that best fits the observed line profile is about 32000 ⊙. The abundance of Mn from the 4136.92 Å line is about 30 ⊙ and that of Zr derived from the 2 lines in Table 1 is about 100 ⊙. The Yttrium abundances from various Y II lines is about 200 ⊙.

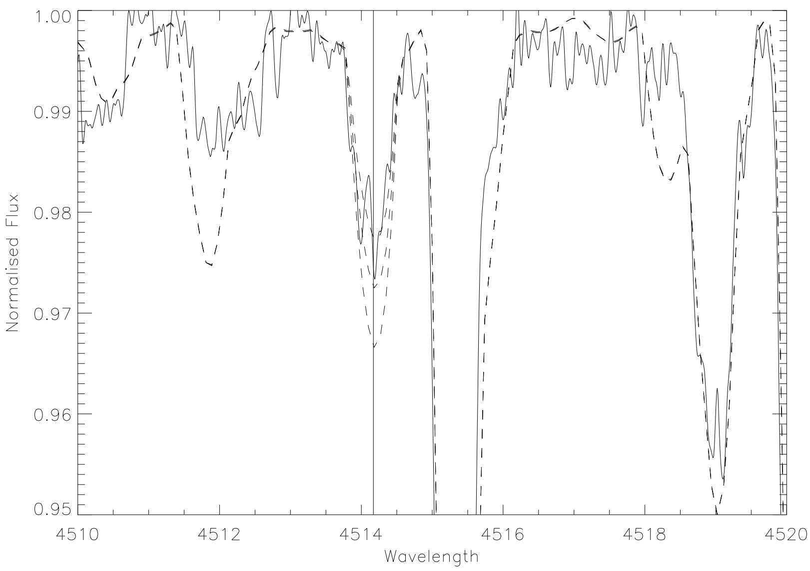

Fig. 2. Detection of the Pt II 4514.17 Å line (observed: thick line, models: dashed lines)

5 Conclusions

Whereas it was up to now classified as a normal early A star, our analysis of HD 30085 shows that it is actually a hotter star with peculiar abundances. Its effective temperature and surface gravity correspond to that of a B8V main sequence star. The overabundances in Mn, Sr, Y, Zr, Pt and Hg are characteristic of an HgMn star. It displays large overabundances of the Sr, Y and Zr triad which is however inverted compared to the solar system triad. The synthesis of the Hg II and Pt II lines reveals large overabundances of Pt and Hg (about 3500 and 32000 ⊙ respectively). We are currently performing a detailed abundance analysis of HD 30085 to complement the preliminary abundances presented here.

The authors acknowledge very efficient support from the night assistants at Observatoire de Haute Provence. They have used the NIST Atomic Spectra Database and the VALD database operated at Uppsala University (Kupka et al., 2000) to upgrade atomic data.

References

Castelli, F., Hubrig, S. 2004, A&A, 425, 265

Hubeny, I., Lanz, T. 1992, A&A, 262, 501

Kupka F., Ryabchikova T.A., Piskunov N.E., Stempels H.C., Weiss W.W., 2000, Baltic Astronomy, vol. 9, 590-594

Kurucz, R.L. 1992, Rev. Mexicana. Astron. Astrofis., 23, 45

Napiwotzki, R., Schoenberner, D., Wenske, V. 1993, A&A, 268, 653

Royer, F., Gebran, M., Monier, R., Adelman, S., Smalley, B., Pintado, O., Reiners, A., Hill, G., Gulliver, G. 2014 , A&A, 562A, 84R

SF2A 2014
J. Ballet, F. Bournaud, F. Martins, R. Monier and C. Reylé (eds)

REVIEW AND LATEST NEWS FROM THE VEGA/CHARA FACILITY

N. Nardetto[1], D. Mourard[1], K. Perraut[2], I. Tallon-Bosc[3], A. Meilland[1], P. Stee[1], R. Ligi[1], M. Challouf[1 4], J.-M. Clausse[1], P. Berio[1] and A. Spang[1]

Abstract.
The VEGA instrument located at the focus of the Center for High Angular Resolution Astronomy (CHARA) array in California is a collaborating project between the Lagrange laboratory in Nice, where it has been developed (Mourard et al. 2009, 2011), the IPAG (Grenoble) and CRAL (Lyon) laboratories, and the CHARA group at Mount Wilson Observatory*. The outcome from this international collaboration is to provide to the community a visible spectro-interferometer with an unprecedented angular resolution of 0.3 milli-second of arc (mas) together with a spectral resolution of 5000 or 30000. With such an instrument it becomes possible to determine simultaneously the size and the kinematic of the photosphere and/or of the circumstellar environment of the star as a function of the wavelength, which basically means for each spectral channel in the continuum and/or within spectral lines (in Hα for instance). The only limitation is to get enough signal to noise ratio in each spectral channel. We can currently reach a limiting magnitude of 8 in visible in medium spectral resolution (5000) and 4.5 in high resolution (30000). In this proceeding, we illustrate the two main subjects studied with the VEGA instrument, namely (1) how angular diameters are useful to accurately derive the fundamental parameters of stars, (2) how the spectral resolution can allow to study the kinematical structure of stars or even to derive chromatic images of stellar objects.

Keywords: instrumentation: high angular resolution instrumentation: interferometers

1 The VEGA instrument on CHARA interferometer

After the pioneering work at visible wavelengths on the GI2T interferometer (Mourard et al. 1994), a team led by D. Mourard decided, in 2005, to install the VEGA instrument on the Center for High Angular Resolution Astronomy (CHARA) array in California (ten Brummelaar et al. 2005) and the first light was obtained at fall 2007. CHARA consists of six one meter telescopes placed in pairs along the arms of a Y-shaped array. It yields 15 baselines ranging from 34m to 331m. Since summer 2009, the VEGA/CHARA instrument is routinely operating for almost 60 nights per year, with an increasing fraction done remotely from Nice observatory. The instrument is labeled as a French national observing service (SO2) since 2013 and is opened to the community through a collaboration with the VEGA team. We published in December 2009 (Mourard et al. 2009) the principle of this instrument as well as its measured performance and we also demonstrated the performance of the simultaneous combination of 3 and 4 telescopes (Mourard et al. 2011). More recently, we describe in Ligi et al. (2013) the different steps from the raw data to the final products, and how the Virtual Observatory principles have been implemented to allow an interoperability between several softwares developed by the Jean-Marie Mariotti Center (`http://www.jmmc.fr/`).

VEGA addresses today two main classes of scientific programs: fundamental stellar parameters thanks to the unique angular resolution given by the short wavelengths and the long baselines of CHARA (Sect. 1), and morphological and kinematical studies in circumstellar environments thanks to the unique spectral resolution we achieved (Sect. 2).

[1] Laboratoire Lagrange, UMR7293, Université de Nice Sophia-Antipolis, CNRS, Observatoire de la Côte d'Azur, Nice, France
[2] Université Grenoble Alpes, IPAG, F-38000 Grenoble, France CNRS, IPAG, F-38000 Grenoble, France
[3] Université de Lyon, 69003 Lyon, France; Université Lyon 1, Observatoire de Lyon, 9 avenue Charles André, 69230 Saint Genis Laval; CNRS, UMR 5574, Centre de Recherche Astrophysique de Lyon; Ecole Normale Supéerieure, 69007 Lyon, France
[4] Laboratoire Dynamique Moléculaire et Matériaux Photoniques, UR11ES03, Université de Tunis/ESSTT, Tunisie

*The instrument is opened to the community throughout a collaboration with the VEGA and CHARA teams, and all information about the instrument can be found here: `http://www-n.oca.eu/vega/en/publications/index.htm`.

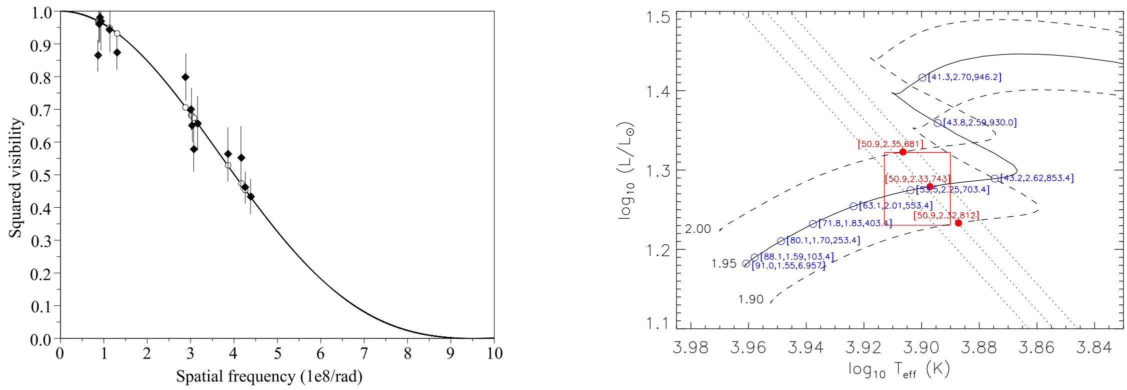

Fig. 1. Left. Squared visibility versus spatial frequency for 10 Aql obtained with the VEGA observations (diamonds). The solid line and the open circles represent the uniform-disk best model provided by LITpro model fitting tool (Tallon-Bosc et al. 2008). After a conversion, we obtain a very small and precise limb-darkened angular of $\theta_{\rm LD} = 0.275 \pm 0.009$ mas, which is at the limit of angular resolution of VEGA. Right. Evolutionary tracks with the observational 1-σ error box ($\log T_{\rm eff}$, $\log L$) in red and the diagonal dotted lines for R. The mass (in solar units) is indicated at the beginning of the evolutionary tracks. The best model is shown as full line, whereas the two extreme models are shown as dashed lines. For the best model, we show in brackets for several time steps (open circles) the evolution of the seismic mean large separation (μHz), the radius ($R_{\rm sun}$), and the age (My). The full circles represent the time at which the large separation equals the observed one, i.e. 50.95 μHz. This study from Perraut et al. (2013) is typical of what is currently done from optical interferometry.

2 The fundamental parameters

Any interferometer provides measurements of angular sizes of an object , like for instance an angular diameter. Such an observable, combined with the trigonometric parallax, provides the stellar radius in a geometric way that is as independent as possible of models. This becomes even more important in the context of Gaia launched last year. Such an approach has been successfully applied with VEGA/CHARA for several kinds of physical objects of interest.

First, the abnormal surface layers of rapidly oscillating Ap star may generate systematic errors in the determination of stellar luminosities and effective temperatures by spectrometric and/or photometric techniques (Matthews et al. 1999). Within this context, optical long-baseline interferometry allows a direct (and unbiased) measurement of the angular diameter of these apparent tiny stars which helps at determining their pulsation modes together with their temperature scale (Perraut et al. 2011, 2013). The way this is usually done is presented in Figure 1 in the case of 10 Aql. Another kind of approach is to use a direct interferometric determination of the angular diameter and advanced three-dimensional modeling, to derive the radius of seismic CoRoT targets in order to reduce the global stellar parameter space compatible with seismic data. This method has been applied to the HD49933 CoRoT target using VEGA/CHARA data (Bigot et al. 2011). This kind of analysis, is also extremely precious when studying metal poor stars, which indeed provides a wealth of chemical information about various stages of the chemical evolution of the Galaxy (Frebel 2010). The VEGA measurements of the benchmark Gaia star HD140283 are presented in Creevey et al. 2014 (in preparation). Third, the angular diameters as derived from stellar interferometry are of a tremendous importance for exoplanet host stars characterization. The precise radius of the star is indeed required to model the exoplanetary systems. This field of research is currently extremely active and one of the first contribution from the VEGA group can be found in Ligi et al. (2012) and in another paper in preparation. Another historical contribution from interferometric angular diameters is to study the surface brightness of stars, which are actually used in many fields of researches. One of the most recent application comes from the use of late-type eclipsing binaries to derive the distance of LMC (Pietrzyński et al. 2013). In order to extent the method and use bright early-type eclipsing binaries to derive the distance of distant galaxies in the local group like M31 and M33, one need a precise determination of the surface-brightness of hot stars. Such relation has been recently established by Challouf et al. (2014) as a function of the V-K color index with a precision of 0.16 magnitude.

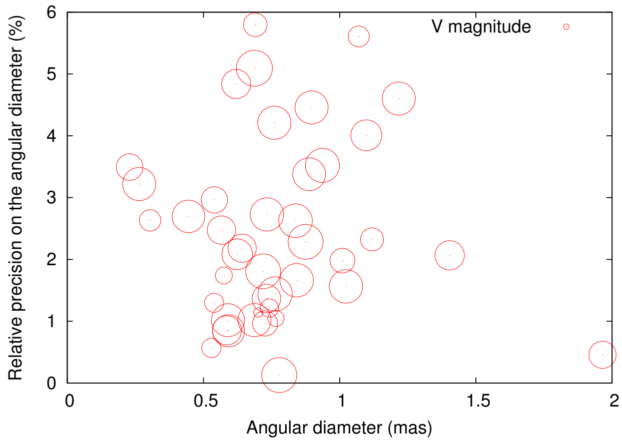

Fig. 2. Diagram showing all the angular diameter obtained with the VEGA/CHARA instrument up to now with their respective relative precision in %. The size of the dot provides the magnitude in V of the star, the larger the circle, the larger the magnitude.

To conclude this small review on fundamental parameters, we present in Fig. 2 most of the angular diameters that have been derived from VEGA instrument since 2009. The relative precision obtained is plotted as a function of the angular diameter while the size of the circles gives an indication about the m_V of the object. The fainter stars in this plot have a m_V magnitude of 6.5. The relative precision obtained is also related of course to the number of visibility measurements secured with the instrument. The average relative precision on our angular diameter is of about 2.5%, while for 15 stars we reach a precision of better than 1.5% (with magnitude from 1.5 to 6). A rough conclusion is that about 15 visibility measurements at least (or 5 observations with a CHARA triplet) are necessary to reach the 1.5% precision on a star of magnitude 6.

3 The kinematic of stars, their environment and imaging

By combining angular resolution to spectral resolution with VEGA/CHARA, it becomes possible to probe the kinematic of the close environment of a star. This is usually done by deriving the size of the material emitting within the Hα line. One can study for instance the mass transfer around young stellar objects (Perraut et al. 2010; Benisty et al. 2013), Be stars (Meilland et al. 2011) or, one of the most famous star in interferometry which is the interactive binary β Lyrae (Bonneau et al. 2011). But even for a star without environment, there is still the possibility to probe the differential rotation of the star within the photosphere, using for instance the Hα line in absorption. An attempt was made by Delaa et al. (2013) on the bright fast rotating star α Cep.

One interesting approach also with CHARA is to use the MIRC instrument (Monnier et al. 2008) as a imager in the K-band, and VEGA to probe the kinematical structure of the environment within the Hα line. This was done for the atypical star ϵ Aur. A disk is eclipsing the central star, the image of which has been restored by MIRC (Kloppenborg et al. 2010), while the structure of the Hα line emission was given by VEGA (Mourard et al. 2012). Similarly, several large campaigns have been organized recently by combining several interferometric instruments together with photometry and spectroscopy ones. This concerns mainly the prototype interactive binary β Lyrae, which is a very complex object (a second paper is in preparation) and the expanding Nova Delphini 2013 (Schaefer et al. 2014, in press Nature).

However, the main goal of spectro-interferometry is eventually to provide polychromatic images of an object. This would provide the image of the material with a given approaching or receding velocity (iso-velocity maps). Such an approach is currently applied to a fast rotating star ϕ Per (Mourard et al., in preparation).

4 Conclusion

The VEGA/CHARA instrument is currently providing geometrical and kinematical views for many objects in the solar neighbourhoods as well as robust constrains in term of stellar fundamental parameters. This is mainly due to this unique capability of combining high angular and high spectral resolution in the visible. These results require also the development of new models related to the structure, evolution and environment of stars (radiative transfer in gas and/or dust).

In order to push the sensitivity even further (and reach 10th magnitude), we are developing a prototype of new instrument in the visible using fibers and latest technologies of fast and sensitive analogic cameras (see Berio et al. 2014, SPIE, in press). This instrument would also take benefit from upcoming adaptive optics on the CHARA interferometer. Such specifications are opening new areas in term of stellar physics. The very high precision of such instrument would also create new synergies with Gaia and PLATO space missions.

References

Benisty, M., Perraut, K., Mourard, D., et al. 2013, A&A, 555, A113

Bigot, L., Mourard, D., Berio, P., et al. 2011, A&A, 534, L3

Bonneau, D., Chesneau, O., Mourard, D., et al. 2011, A&A, 532, A148

Challouf, M., Nardetto, N., Mourard, D., et al. 2014, ArXiv e-prints

Delaa, O., Zorec, J., Domiciano de Souza, A., et al. 2013, A&A, 555, A100

Frebel, A. 2010, Astronomische Nachrichten, 331, 474

Kloppenborg, B., Stencel, R., Monnier, J. D., et al. 2010, Nature, 464, 870

Ligi, R., Mourard, D., Lagrange, A. M., et al. 2012, A&A, 545, A5

Ligi, R., Mourard, D., Nardetto, N., & Clausse, J.-M. 2013, Journal of Astronomical Instrumentation, 2, 40003

Matthews, J. M., Kurtz, D. W., & Martinez, P. 1999, ApJ, 511, 422

Meilland, A., Delaa, O., Stee, P., et al. 2011, A&A, 532, A80

Monnier, J. D., Zhao, M., Pedretti, E., et al. 2008, in Society of Photo-Optical Instrumentation Engineers (SPIE) Conference Series, Vol. 7013, Society of Photo-Optical Instrumentation Engineers (SPIE) Conference Series

Mourard, D., Bério, P., Perraut, K., et al. 2011, A&A, 531, A110

Mourard, D., Clausse, J. M., Marcotto, A., et al. 2009, A&A, 508, 1073

Mourard, D., Harmanec, P., Stencel, R., et al. 2012, A&A, 544, A91

Mourard, D., Tallon-Bosc, I., Blazit, A., et al. 1994, A&A, 283, 705

Perraut, K., Benisty, M., Mourard, D., et al. 2010, ArXiv e-prints

Perraut, K., Borgniet, S., Cunha, M., et al. 2013, A&A, 559, A21

Perraut, K., Brandão, I., Mourard, D., et al. 2011, A&A, 526, A89

Pietrzyński, G., Graczyk, D., Gieren, W., et al. 2013, Nature, 495, 76

Tallon-Bosc, I., Tallon, M., Thiébaut, E., et al. 2008, in Society of Photo-Optical Instrumentation Engineers (SPIE) Conference Series, Vol. 7013, Society of Photo-Optical Instrumentation Engineers (SPIE) Conference Series

ten Brummelaar, T. A., McAlister, H. A., Ridgway, S. T., et al. 2005, ApJ, 628, 453

SF2A 2014
J. Ballet, F. Bournaud, F. Martins, R. Monier and C. Reylé (eds)

THE BRITE SPECTROPOLARIMETRIC SURVEY

C. Neiner[1] and A. Lèbre[2]

Abstract. The BRITE constellation of nanosatellites observes very bright stars to perform seismology. We have set up a spectropolarimetric survey of all BRITE targets, i.e. all ∼600 stars brighter than V=4, with Narval at TBL, ESPaDOnS at CFHT and HarpsPol at ESO. We plan to reach a magnetic detection threshold of $B_{pol} = 50$ G for stars hotter than F5 and $B_{pol} = 5$ G for cooler stars. This program will allow us to combine magnetic information with the BRITE seismic information and obtain a better interpretation and modelling of the internal structure of the stars. It will also lead to new discoveries of very bright magnetic stars, which are unique targets for follow-up and multi-technique studies.

Keywords: stars: magnetic fields, stars: individual: δ Oph, stars: individual: β Vir, stars: individual: ι Peg, stars: individual: λ And, stars: individual: ξ UMa

1 BRITE

The BRITE (BRIght Target Explorer) constellation of nano-satellites monitors photometrically, in 2 colours, the brightness and temperature variations of stars with V≤4, with high precision and cadence, in order to perform asteroseismology (Weiss et al. 2014). The mission consists of 3 pairs of nano-satellites, built by Austria, Canada and Poland, carrying 3-cm aperture telescopes. One instrument per pair is equipped with a blue filter; the other with a red filter. Each BRITE instrument has a wide field of view (∼24°), so up to 25 bright stars can be observed simultaneously, as well as additional fainter targets with reduced precision. Each field will be observed during several months. As of September 2014, 6 nano-satellites are already flying and 5 are observing. Each pair of nano-satellites can (but does not have to) observe the same field and thus increase the duty cycle of observations.

BRITE primarily measures pressure and gravity modes of pulsations to probe the interiors and evolution of stars through asteroseismology. Since the BRITE sample consists of the brightest stars, it is dominated by the most intrinsically luminous stars: massive stars at all evolutionary stages, and evolved cooler stars at the very end of their nuclear burning phases (cool giants and AGB stars). Analysis of OB star variability will help solve two outstanding problems: the sizes of convective (mixed) cores in massive stars and the influence of rapid rotation on their structure and evolution. In addition, measurements of the timescales involved in surface granulation and differential rotation in AGB stars, cool giants and cool supergiants will constrain turbulent convection models.

2 Combining asteroseismology and spectropolarimetry

The study of the magnetic properties of pulsating stars is particularly interesting since, when combined with the study of their pulsational properties, it provides (1) a unique way to probe the impact of magnetism on the physics of non-standard mixing processes inside these stars and (2) strong constraints on seismic models thanks to the impact of the field on mode splittings and amplitudes.

The combination of an asteroseismic study with a spectropolarimetric study has been accomplished for only a couple of massive stars so far, e.g. for the β Cep star V2052 Oph (Briquet et al. 2012). This star

[1] LESIA, Observatoire de Paris, CNRS UMR 8109, UPMC, Université Paris Diderot, 5 place Jules Janssen, 92190 Meudon, France
[2] LUPM - UMR 5299 - CNRS and Université Montpellier II - place E. Bataillon, 34090 Montpellier, France

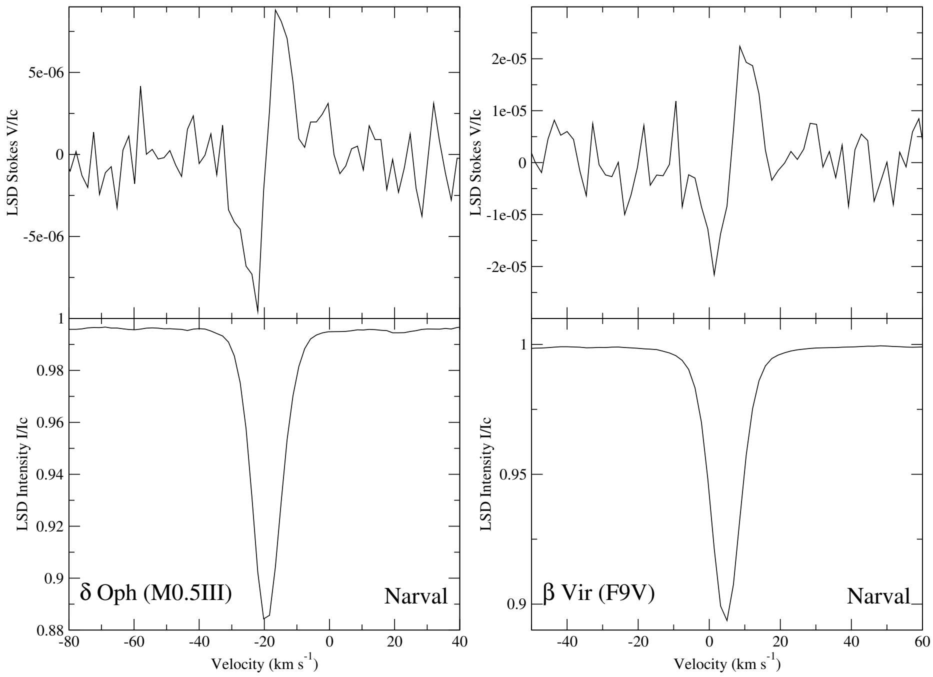

Fig. 1. Examples of magnetic field detections in the single cool stars δ Oph and β Vir. Shown are the LSD Stokes V magnetic signatures (top panels) and LSD intensity profiles (bottom panels).

presents a magnetic field with a strength at the poles of about 400 G that has been modelled thanks to Narval spectropolarimetry (Neiner et al. 2012). Moreover our asteroseismic investigations of this object showed that the stellar models explaining the observed pulsational behaviour do not have any convective core overshooting (Briquet et al. 2012). This outcome is opposite to other results of dedicated asteroseismic studies of non-magnetic β Cep stars (e.g. Briquet et al. 2007). Indeed, it is usually found that convective core overshooting needs to be included in the stellar models in order to account for the observations (Aerts et al. 2010). The most plausible explanation is that the magnetic field inhibits non-standard mixing processes inside V2052 Oph. Indeed the field strength observed in V2052 Oph is above the critical field limit needed to inhibit mixing determined from theory (e.g. Zahn 2011). These findings opened the way to a reliable exploration of the effects of magnetism on the physics of mixing inside stellar interiors of main-sequence B-type pulsators.

Conversely, the deformation of line profiles by pulsations is usually neglected when modelling the magnetic field present in pulsating stars. However, these deformations directly impact the shape of the Stokes V signatures and thus our ability to derive correct magnetic parameters. We recently developed a version of the Phoebe 2.0 code that allows us to model both the line and Stokes V profiles at the same time, taking pulsations into account, thus presenting for the first time coherent spectropolarimetric models including magnetism and pulsations (see Neiner et al. 2014). Thanks to this work, and the combination of seismic and spectropolarimetric data, much more reliable magnetic parameters can be derived for pulsators.

3 The BRITE spectropolarimetric survey

There are $\sim$600 stars brighter than V=4, which are the prime targets of BRITE. We started a systematic survey of all these BRITE targets with spectropolarimetry. Narval at TBL is used for all targets with declination above -20°, ESPaDOnS at CFHT for stars with declination between -45 and -20°, and HarpsPol at ESO for stars with declination below -45°.

From the results of the MiMeS project (Wade et al. 2014), we know that $\sim$10% of all O and B stars have detectable magnetic fields. A similar occurrence is found for A stars and down to F5. The magnetic fields observed in these stars are stable oblique dipoles of fossil origin, with surface strength at the poles from $B_{\rm pol} \simeq 100$ G to several kG. Therefore we aim at detecting all fields above 50 G. For stars cooler than F5, the magnetic fields have a dynamo origin and $\sim$50% of them are found to be magnetic on average (see Konstantinova-Antova et al. 2014). The cool giants and supergiants, however, have very weak fields with $B_{\rm pol}$

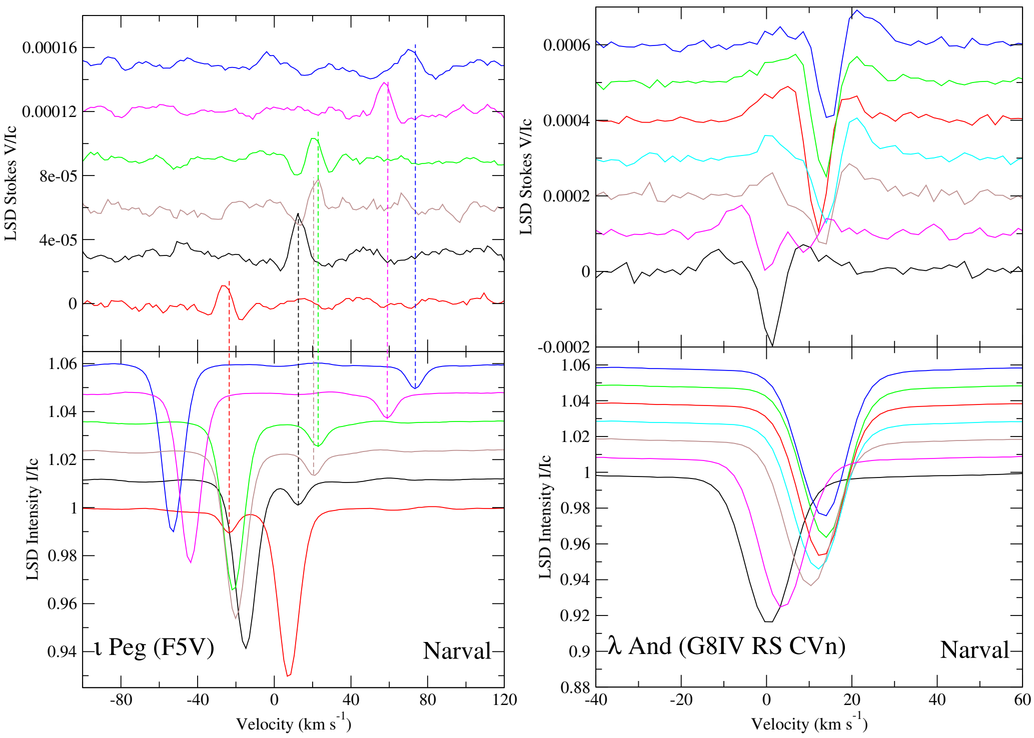

Fig. 2. Examples of magnetic field detections in the cool stars ι Peg and λ And, that have been followed-up with several observations. ι Peg is a binary star: the magnetic signature follows the radial velocity of the magnetic component. The panels are the same as in Figs. 1.

of the order of a few to 10 G. Therefore for these stars, we aim at detecting all fields above $B_{\rm pol} = 5$ G. For each star, we thus acquire one observation with a very high signal-to-noise, to reach the desired detection level.

Thanks to this very high signal-to-noise spectropolarimetric observation of each target, we will:

(1) discover new magnetic stars. This is particularly crucial for massive stars, since only ~65 magnetic OB stars are known as of today, including only a handful of pulsating massive stars (see Petit et al. 2013). Note that one measurement is enough to detect a field as magnetic signatures appear in Stokes V profiles even for cross-over phases (i.e. when the longitudinal field is null).

(2) help select the best high priority targets for BRITE, i.e. the magnetic massive ones and the most interesting cool ones. BRITE can observe all ~600 stars in 6 years if each field is observed 3 months on average, but it is useful to observe the most interesting targets first or longer. In particular the BRITE sample includes 11 O stars, 160 B stars (including 29 known β Cep stars, 20 known classical Be stars, and 22 chemically peculiar B stars), 106 A stars (including 6 known Ap stars), 12 eclipsing binaries, 7 known δ Scuti stars, 7 HgMn stars, 3 RR Lyrae stars, 1 known roAp, 22 cool sub-giant stars, several dozens red giants,... Magnetic stars among them will be prime targets for asteroseismology.

(3) determine the fundamental parameters of all targets for the BRITE seismic modelling: effective temperature, gravity, projected rotation velocity (vsini), as well as abundances in particular for magnetic and chemically peculiar stars (HgMn, Ap, Am...). See e.g. Fossati et al. (2014).

(4) provide a complete spectropolarimetric census of bright ($V \leq 4$) stars, by combining the Narval, ESPaDOnS and HarpsPol data, as well as archival data.

4 First results

The first Narval and ESPaDOnS observations already led to the discovery of 14 new magnetic stars. All of them are cool stars and several are binary objects. Examples of new detections obtained with Narval are shown in Figs. 1, 2 and 3.

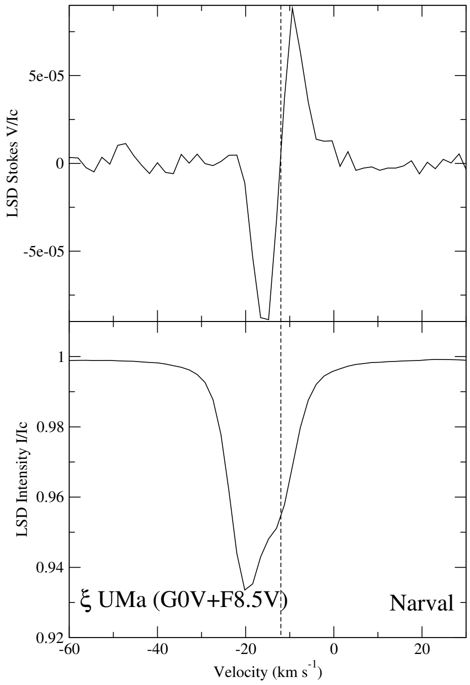

Fig. 3. Example of a magnetic field detection in the cool binary ξ UMa observed only one time. The field can still be attributed to the red-shifted component. The panels are the same as in Figs. 1.

5 Conclusions

By combining the data acquired with Narval, ESPaDOnS and HarpsPol, a complete spectropolarimetric census of bright (V$\leq$4) stars will be available. We will use this database to perform detailed unbiased statistics on the presence of detectable magnetic fields in stars. The data will also be made available to the community as a legacy, through the PolarBase database (Petit et al. 2014).

All the spectra (whether the star is magnetic or not) will also serve to determine the fundamental parameters of the BRITE stars, needed for seismic modelling. For magnetic stars, chemical peculiarities may appear in the spectra and will be studied as well. The best targets will be followed-up to characterise their magnetic fields in details and provide crucial inputs for seismic modelling.

This project is based on observations obtained at the Telescope Bernard Lyot (USR5026) operated by the Observatoire Midi-Pyrénées, Université de Toulouse (Paul Sabatier), Centre National de la Recherche Scientifique (CNRS) of France, at the Canada-France-Hawaii Telescope (CFHT) operated by the National Research Council of Canada, the Institut National des Sciences de l'Univers of the CNRS of France, and the University of Hawaii, and at the European Southern Observatory (ESO), Chile.

References

Aerts, C., Christensen-Dalsgaard, J., & Kurtz, D. W. 2010, Asteroseismology

Briquet, M., Morel, T., Thoul, A., et al. 2007, MNRAS, 381, 1482

Briquet, M., Neiner, C., Aerts, C., et al. 2012, MNRAS, 427, 483

Fossati, L., Zwintz, K., Castro, N., et al. 2014, A&A, 562, A143

Konstantinova-Antova, R., Aurière, M., Charbonnel, C., et al. 2014, in IAU Symposium, Vol. 302, IAU Symposium, 373

Neiner, C., Alecian, E., Briquet, M., et al. 2012, A&A, 537, A148

Neiner, C., Degroote, P., Coste, B., Briquet, M., & Mathis, S. 2014, in IAU Symposium, Vol. 302, IAU Symposium, 302

Petit, P., Louge, T., Théado, S., et al. 2014, PASP, 126, 469

Petit, V., Owocki, S. P., Wade, G. A., et al. 2013, MNRAS, 429, 398

Wade, G. A., Grunhut, J., Alecian, E., et al. 2014, in IAU Symposium, Vol. 302, IAU Symposium, 265

Weiss, W. W., Rucinski, S. M., Moffat, A. F. J., et al. 2014, PASP, 126, 573

Zahn, J.-P. 2011, in IAU Symposium, Vol. 272, IAU Symposium, ed. C. Neiner, G. Wade, G. Meynet, & G. Peters, 14

THE INFLUENCE OF THE MAGNETIC TOPOLOGY ON THE WIND BRAKING OF SUN-LIKE STARS.

V. Réville[1], A. S. Brun[1], S. P. Matt[2], A. Strugarek[1],[3] and R. Pinto[1],[4]

Abstract. Stellar winds are thought to be the main process responsible for the spin down of main-sequence stars. The extraction of angular momentum by a magnetized wind has been studied for decades, leading to several formulations for the resulting torque. However, previous studies generally consider simple dipole or split monopole stellar magnetic topologies. Here we consider in addition to a dipolar stellar magnetic field, both quadrupolar and octupolar configurations, while also varying the rotation rate and the magnetic field strength. 60 simulations made with a 2.5D, cylindrical and axisymmetric set-up and computed with the PLUTO code were used to find torque formulations for each topology. We further succeed to give a unique law that fits the data for every topology by formulating the torque in terms of the amount of open magnetic flux in the wind. We also show that our formulation can be applied to even more realistic magnetic topologies, with examples of the Sun in its minimum and maximum phase as observed at the Wilcox Solar Observatory, and of a young K-star (TYC-0486-4943-1) whose topology has been obtained by Zeeman-Doppler Imaging (ZDI).

Keywords: stars, magnetism, stellar winds, rotation

1 Introduction

To explain the observed pressure ratio of order 10^{14} between the base of the solar corona and the interstellar medium, Parker (1958) introduced the idea of a non-hydrostatic expanding solar atmosphere, the solar wind. This accelerated outflow has been observed since with typical speed between 400 km/s and 1000 km/s around the Earth. This process is thought to occur in all cool stars with an upper convective layer, *i.e.* from stellar type M to F, or $0.5M_\odot$ to $1.4M_\odot$. Schatzman (1962), Parker (1963), Weber & Davis (1967) and Mestel (1968) then introduced the effect of both magnetic field and rotation thus creating the magnetic rotator theory which is now the standard MHD theory for stellar winds and the main process responsible for the braking of solar-like stars observed all along the main sequence (Irwin & Bouvier 2009). It combines the driving of the wind due to the pressure gradient and the magneto-centrifugal effect. Weber & Davis (1967) used a simple one dimensional model (at the equator) to quantify the angular momentum carried by the plasma and demonstrated that the torque τ_w can be expressed:

$$\tau_w = \dot{M}_w \Omega_* R_A^2, \tag{1.1}$$

where $\dot{M}_w$ is the integrated mass loss rate, Ω_* the rotation rate of the star and R_A the Alfvén radius, *i.e.* the radius at which the velocity field reach the Alfvén speed $v_A = B_p/\sqrt{4\pi\rho}$ (B_p is the poloidal component of the magnetic field in this model).

In order to find a formulation for a realistic multi-dimensional outflow, we define an average value for the Alfvén radius (which is the cylindrical radius, the distance from the rotation axis) such that equation (1.1) is always true:

$$\langle R_A \rangle = \sqrt{\frac{\tau_w}{\dot{M}_w \Omega_*}} \tag{1.2}$$

[1] Laboratoire AIM, DSM/IRFU/SAp, CEA Saclay, 91191 Gif-sur-Yvette Cedex
[2] Department of Physics and Astronomy, University of Exeter, Stocker Road, Exeter EX4 4SB, UK
[3] Département de physique, Université de Montréal, C.P. 6128 Succ. Centre-Ville, Montréal, QC H3C-3J7, Canada
[4] LESIA, Observatoire de Paris-Meudon, 5 place Jules Janssen, 92195 MEUDON Cedex

2 Numerical setup

In our study we use the compressible MHD code PLUTO, to perform 2.5D simulations, similarly to Matt et al. (2012) and Matt & Pudritz (2008). We initialize the star thanks to a one dimensional Parker solution for the outflow and let the code evolve the equations of ideal MHD. The magnetic field is initially a pure dipole, quadrupole, octupole or the sum of the three components (see section 4). The outflow then non-linearly interacts with the magnetic field, opens part of the field lines and reach a steady-state. In Figure 1 we show the three different magnetic topologies in the initial and final states. For a precise description of the boundary conditions, see Strugarek et al. (2014) and Réville et al. (2014). We used 20 cases of Matt et al. (2012), that we ran with the three topologies.

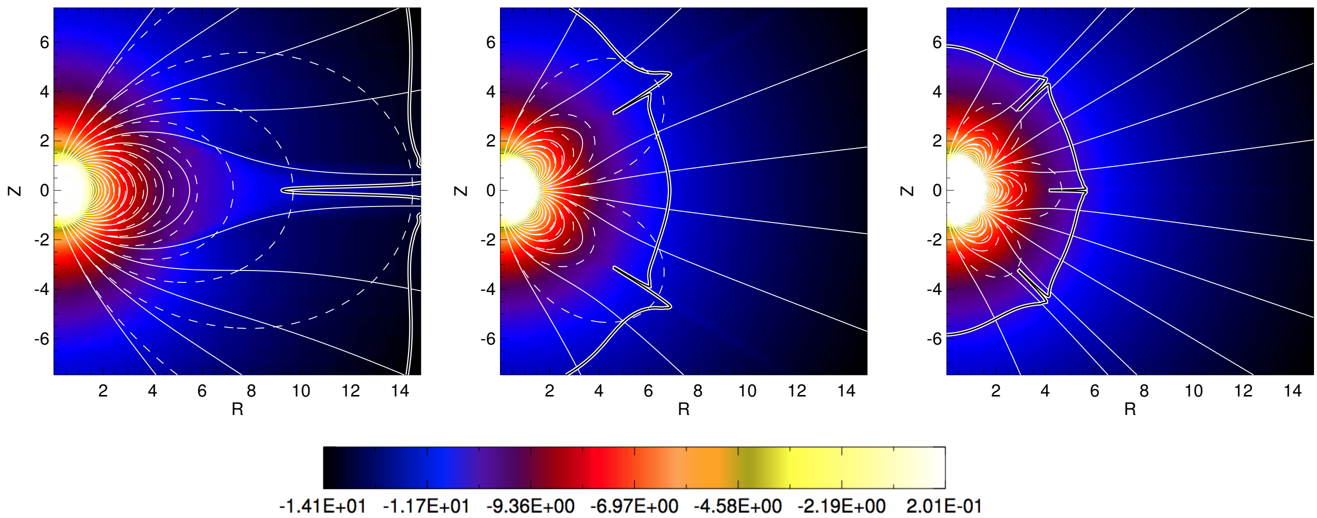

Fig. 1. Magnetic field lines of initial topologies (dashed lines) and final state (continuous lines) for a typical case (case 2 of Réville et al. (2014)) and the three topologies. The color background is the logarithm of density.

3 Braking Laws

We fit our set of simulations with the formulation of Matt et al. (2012):

$$\frac{\langle R_A \rangle}{R_*} = K_1 [\frac{\Upsilon}{(1+f^2/K_2^2)^{1/2}}]^m \quad \text{where} \quad \Upsilon \equiv \frac{B_*^2 R_*^2}{\dot{M}_w v_{esc}} \tag{3.1}$$

is the magnetization parameter introduced in Matt & Pudritz (2008). A similar parameter has been introduced before in ud-Doula & Owocki (2002)), where the terminal velocity v_∞ was used instead of the escape velocity $v_{esc} \equiv \sqrt{(2GM_*)/R_*}$. Both characterize the magnetization of the wind, which is the ratio of the magnetic field energy and the kinetic energy of the wind. B_* is the magnetic field strength taken at the surface and at the equator of the star, $\dot{M}_w$ is the integrated mass-loss rate and f is the fraction of break-up rate, *i.e.* the ratio between the rotation rate at the equator of the star (in our simulations the star has a solid body rotation) and the keplerian speed that is defined by:

$$f \equiv \Omega_* R_*^{3/2} (GM_*)^{-1/2}. \tag{3.2}$$

Table 1 shows the different parameters of the fit depending on the topology. The influence of topology can mainly be seen through the change in the power-law exponent m. It decreases with higher order multipole. This is due to the radial dependency of the magnetic field (see Kawaler 1988; Réville et al. 2014). Hence the braking is more efficient for lower order multipole for a given magnetic field strength. As shown in Matt & Pudritz (2008) and Matt et al. (2012), increasing the magnetic field strength increases the average Alfvén radius (and thus the torque) while increasing the rotation rate makes the average Alfvén radius smaller. Rotation adds acceleration through magneto-centrifugal forces (Ustyugova et al. 1999; Réville et al. 2014).

Topology	K_1	K_2	m
Dipole	2.0 ± 0.1	0.2 ± 0.1	0.235 ± 0.007
Quadrupole	1.7 ± 0.3	0.2 ± 0.1	0.15 ± 0.02
Octupole	1.7 ± 0.3	0.2 ± 0.1	0.11 ± 0.02
	K_3	K_4	m
Topology independent	1.4 ± 0.1	0.06 ± 0.01	0.31 ± 0.02

Table 1. Parameters of the fit to equation 3.1 made independently for each topology. The values K_1,K_2 and m corresponds to formulation 3.1 for the dipolar, quadrupolar and octupolar configurations. The parameter K_3 and K_4 for the topology independent formulation 3.4 are given as well.

In order to obtain a topology independent formulation for the magnetic torque we define a new magnetization parameter using the open flux:

$$\Upsilon_{open} \equiv \frac{\Phi_{open}^2}{R_*^2 \dot{M}_w v_{esc}}, \tag{3.3}$$

and consider a new formulation of $\langle R_A \rangle$ as a function of Υ_{open}:

$$\frac{\langle R_A \rangle}{R_*} = K_3 [\frac{\Upsilon_{open}}{(1+f^2/K_4^2)^{1/2}}]^m \tag{3.4}$$

Figure 2 shows on the left panel the unsigned magnetic flux integrated over concentric spheres for the three different topologies. Beyond a few stellar radii, all the field lines are open and the magnetic flux becomes constant. This constant value is the open flux Φ_{open} used in our new formulation. On the right panel of Figure 2, we show that a single braking law can be used to fit our 60 simulations. The parameter of the fit are given in Table 1.

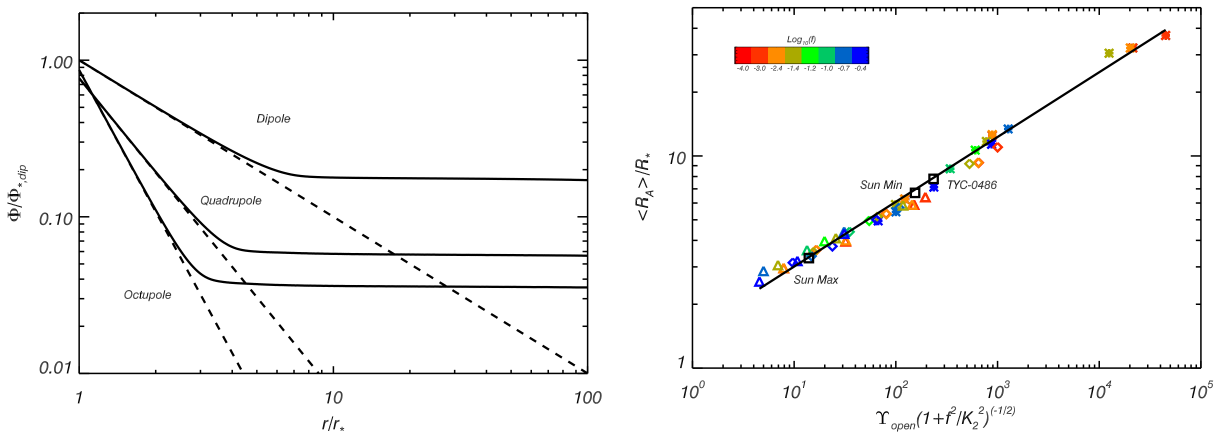

Fig. 2. The integrated unsigned magnetic fluxes for the three topologies are shown on the left panel. The one law fit for the three topologies is shown on the right panel. Colors represent the rotation rate, from red to blue as rotation increases. Symbols stand for the topology, stars for dipole, diamonds for quadrupole, triangles for octupole. The influence of the rotation is captured in x-axis variable. Black squares are complex topologies (Sun Min, Sun Max and TYC-0486-4943-1 introduced in section 4), which demonstrates that winds with combination of magnetic multipoles follow the same braking law as those with single-mode topologies.

4 Realistic Topologies

Our topology independent formulation is able to fit three different multipoles. However magnetic field topologies of stars are a combination of those three modes and higher order multipoles. We then tried to compare this formulation with the resulting torque of actual stars whose magnetic field is approximated as the sum of

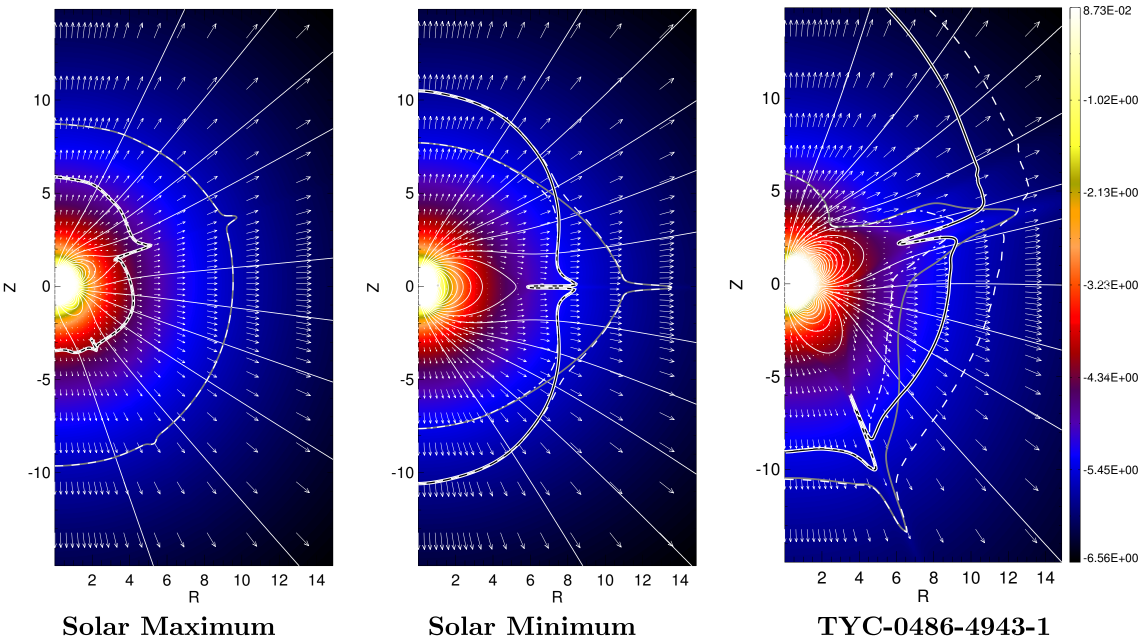

Fig. 3. Steady state solutions of three winds with a realistic magnetic topology extracted from Wilcox Solar Observatory data (DeRosa et al. 2012) for the solar cases and from a ZDI Map of TYC-0486-4943-1. Only the axisymmetric component till $l = 3$ are taken into account. The wind Alfvén surfaces are shown in the same format as Figure 1. The background is the logarithm of the density and we added velocity arrows in white.

a dipolar, quadrupolar and octupolar components. We took the axisymmetric components of these three modes of the Sun during the minimum and the maximum of activity of the cycle 22. The spherical harmonics decomposition have been obtained from magnetograms of the Wilcox Observatory (see DeRosa et al. 2012). The simulations gave us a torque that is predicted by our formulation as shown in Figure 2. We also used the spherical harmonics decomposition of the surface magnetic field of TYC-0486 obtained through Zeeman-Doppler-Imaging, and performed a simulation of the wind of this young K-Star (see Figure 3). The torque is again well predicted by our formulation even though we assume that the coronal temperature of this star is equal to the Sun's. Changing the temperature might change the braking law's coefficients K_3 and K_4 slightly but we expect m to be robust. A more systematic study is needed.

5 Open Flux Calculations and Perspectives

With our topology independent formulation, the stellar wind magnetic torque can be written:

$$\tau_w = \dot{M}_w^{1-2m} \Omega_* R_*^{2-4m} K_3^2 \left(\frac{\Phi_{open}^2}{v_{esc}(1 + f^2/K_4^2)^{1/2}}\right)^{2m}. \tag{5.1}$$

However the prediction of the open magnetic flux from the surface magnetic field is not a trivial task without running a MHD simulation. Some correlation with the surface flux have been proposed (Vidotto et al. 2014), but they rely on heavy 3D simulations that we eventually want to avoid to provide observers with efficient tools to compute the magnetic torque.

Considering a potential extrapolation of the surface magnetic field (Schrijver & De Rosa 2003), the location of the source surface is the only thing needed to compute the open flux. And such a reconstruction is by far easier to compute than a whole wind simulation. From our set of simulations we developed a method that minimizes the difference (through a gradient descent) between the potential extrapolation and the steady-state wind solution, and find an optimum value for the source surface. The comparison is shown in Figure 4, the white field lines are from our simulation while the cyan field lines are drawn from a potential that has been reconstructed using the optimum source surface we computed. Closed magnetic loops are well reproduced by this model. However the potential field extrapolation provides a magnetic field that is completely radial by definition beyond the source surface, whereas it is not exactly the case in our simulation, especially for highly

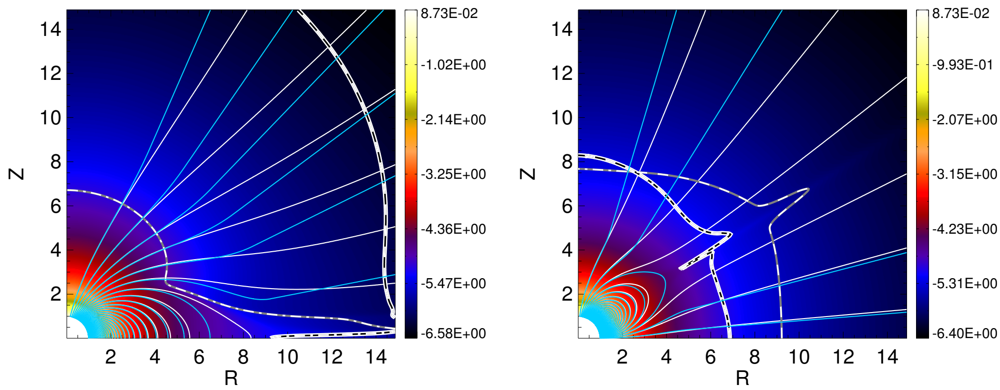

Fig. 4. Comparison of the field lines obtained with the wind simulation (in white) and a potential extrapolation at the optimum source surface (in cyan). In both cases (dipolar and quadrupolar), the magnetic loops are well reproduced.

rotating cases. But this has no influence on the value of the open flux, since the only thing that matters is how much magnetic flux is confined in the magnetic loops. We found that a good proxy for the location of the source surface radius is the average radius where the ram pressure plus the thermal pressure become higher than the magnetic pressure. The agreement for this average radius with the optimum source surface is within 10% for our slowly rotating dipolar cases. Taking into account rotation and topology might introduce some corrections, and more investigations are needed. They will be reported in a subsequent paper where we will provide tools to determine the source surface as a function of the stellar parameters.

Consequently, with our topology independent formulation and the open flux computed from ZDI Maps, we are able to give precise estimates of the torque exerted on the star, if the mass loss rate have been prescribed through analytical models (Cranmer & Saar 2011) or observations (Wood 2004). Interestingly, this formulation could also provide constraints on the mass loss rate of clusters whose braking time scales are known.

We would like to thank Colin Folsom, Pascal Petit for the magnetic field decomposition coefficients of TYC- 0486-4943-1, Jérome Bouvier and the ANR TOUPIES project which aim to understand the evolution of star?s spin rates, the ERC STARS2 (www.stars2.eu) and CNES support via our Solar Orbiter funding.

References

Cranmer, S. R. & Saar, S. H. 2011, ApJ, 741, 54

DeRosa, M. L., Brun, A. S., & Hoeksema, J. T. 2012, ApJ, 757, 96

Irwin, J. & Bouvier, J. 2009, in IAU Symposium, Vol. 258, IAU Symposium, ed. E. E. Mamajek, D. R. Soderblom, & R. F. G. Wyse, 363–374

Kawaler, S. D. 1988, The Astrophysical Journal, 333, 236

Matt, S. & Pudritz, R. E. 2008, ApJ, 678, 1109

Matt, S. P., Pinzón, G., Greene, T. P., & Pudritz, R. E. 2012, ApJ, 745, 101

Mestel, L. 1968, MNRAS, 138, 359

Parker, E. N. 1958, ApJ, 128, 664

Parker, E. N. 1963, Interplanetary dynamical processes.

Réville, V., Brun, A. S., Matt, S. P., Strugarek, A., & Pinto, R. P. 2014, submitted to ApJ

Schatzman, E. 1962, Annales d'Astrophysique, 25, 18

Schrijver, C. J. & De Rosa, M. L. 2003, Sol. Phys., 212, 165

Strugarek, A., Brun, A. S., Matt, S. P., & Reville, V. 2014, in IAU Symposium, Vol. 300, IAU Symposium, ed. B. Schmieder, J.-M. Malherbe, & S. T. Wu, 330–334

ud-Doula, A. & Owocki, S. P. 2002, ApJ, 576, 413

Ustyugova, G. V., Koldoba, A. V., Romanova, M. M., Chechetkin, V. M., & Lovelace, R. V. E. 1999, ApJ, 516, 221

Vidotto, A. A., Jardine, M., Morin, J., et al. 2014, MNRAS, 438, 1162

Weber, E. J. & Davis, Jr., L. 1967, ApJ, 148, 217

Wood, B. E. 2004, Living Reviews in Solar Physics, 1

SF2A 2014
J. Ballet, F. Bournaud, F. Martins, R. Monier and C. Reylé (eds)

THE STARK-B DATABASE VAMDC NODE FOR SPECTRAL LINE BROADENING BY COLLISIONS WITH CHARGED PARTICLES

S. Sahal-Bréchot[1], M.S. Dimitrijević[1, 2], N. Moreau[1] and N. Ben Nessib[3]

Abstract. "Stark broadening" theories and calculations have been extensively developed for about 50 years. Accurate spectroscopic diagnostics and modeling require the knowledge of numerous collisional line profiles. Nowadays, the access to such data via an on line database becomes essential. The aim of STARK-B is satisfy this need. It is a collaborative project between the Astronomical Observatory of Belgrade (AOB) and the LERMA at Observatory of Paris. It is a database of widths and shifts of isolated lines of atoms and ions due to electron and ion impacts that we have calculated and published in international refereed journals. It is devoted to spectroscopic diagnostics and modeling of stellar atmospheres and envelopes, laboratory plasmas, laser equipments and technological plasmas. Hence, the domain of temperatures and densities covered by the tables is wide and depends on the ionization degree of the considered ion. STARK-B has been fully opened to the international community since fall 2008 and is a node of VAMDC. VAMDC (Virtual Atomic and Molecular Data Centre) is an European Union funded collaboration between groups involved in the generation and use of atomic and molecular data. In the present paper, we will present STARK-B, its state of development, our current projects and future plans.

Keywords: Atomic data, Line: profiles, Astronomical databases: miscellaneous, Virtual observatory tools

1 Introduction

Broadening and shifting of spectral lines emitted or absorbed by neutral or ionized atoms or molecules in a gas or a plasma can be of various physical origin. The interaction of these atoms or molecules with the surrounding particles causes the so-called pressure broadening. The interpretation of pressure broadening is important for giving informations on the medium, such as temperature, densities of the perturbers, abundances of the emitting or absorbing atoms or molecules. If these perturbers are charged particles, electrons or ions, this broadening mechanism is called "Stark" broadening and concerns various plasmas. The range of densities of interest is large: 10^{10} to 10^{23} cm^{-3}. The range of temperatures of interest is also large: 2500K to about 610^6 K.

The theory has been extensively developed for about 50 years and is currently used for many spectroscopic diagnostics and modeling. At the same time, many laboratory experiments were developed and line broadening theory and experiments were compared and thus made together a lot of progress. Nowadays, the best agreement between theoretical and experimental results is of the order of 20%.

A number of its developments have been stimulated by the advances in astrophysics and especially stellar physics. Stark broadening is essential for interpreting the spectra of white dwarfs (e.g. Dufour et al. (2011)), since Stark broadening is the main broadening mechanism. Stark broadening is also important for interpreting and analyzing the spectra of A and B type stars and for including stratification in the modeling. Synthetic spectra achievement and modeling of stellar atmospheres and interiors require extensive sets of atomic data, including Stark broadening, and the use of databases is now indispensable. In addition, accurate spectroscopic diagnostics for laboratory plasmas, magnetic fusion plasmas (Tokamaks, e.g. ITER), inertial confinement fusion plasmas (e.g. laser LMJ) and technological plasmas (e.g. discharge lighting sources) are also needed for many lines of many ions, and Stark broadening can play an important role in the modeling. Many examples and references can be found in Dimitrijević & Sahal-Bréchot (2014).

[1] LERMA, Observatoire de Paris, ENS, UPMC, UCP, CNRS; 5 Place Jules Janssen, 92190 Meudon, France
[2] Astronomical Observatory, Volgina 7, 11060 Belgrade 38, Serbia
[3] Department of Physics and Astronomy, College of Science, King Saud University. Riyadh 11451, Saudi Arabia

Hence, calculations based on a simple but enough accurate and fast methods are necessary for obtaining numerous results. Furthermore, the development of powerful computers also stimulates the development of atomic data on a large scale. Hence, Dimitrijević, Sahal-Bréchot have and coworkers updated and operated at a large scale the numerical code created and based on the impact semiclassical-perturbation theory (SCP) developed for isolated lines by Sahal-Bréchot (1969a,b, 1974); Fleurier et al. (1977), after the pioneer work by Baranger (1958a,b,c). The theory was revisited by Sahal-Bréchot et al. (2014). More than 150 papers, which concern 123 neutral and ionized atoms broadened and shifted by collisions with electrons and ions are currently issued from the first update (Dimitrijević & Sahal-Bréchot 1984).

Then, the new need of creation of an on-line database appeared in the beginning of the 21th century, particularly in correlation with the birth and the growth of virtual Observatories and to the increasing need of exchange of interoperable data. Hence, our database was designed and STARK-B (Sahal-Bréchot et al. 2014) was created: it is a database of calculated widths and shifts of isolated lines of atoms and ions due to electron and ion collisions by Dimitrijević, Sahal-Bréchot and coworkers.

STARK-B is a collaborative project between AOB and LERMA. It is currently developed at Paris Observatory and has opened on line since the end of 2008 (Sahal-Bréchot et al. 2014). It is a part of the atomic and molecular databases of the Paris Observatory, and there is a link to the Serbian Virtual Observatory (SerVO 2014). It is in free access. A mirror site is planned at AOB. STARK-B has been a node of VAMDC (Virtual Atomic and Molecular Data Centre) since the end of 2009 (Dubernet et al. 2010; Rixon et al. 2011). This FP7 European project "Research Infrastructures was created in summer 2009 for 3.5 years. It is an interoperable e-Infrastructure for exchange of atomic and molecular data. This international consortium has built an e-science interoperable platform permitting an automated exchange of atomic and molecular data.

We begun by implementing the published data of all our papers calculated through the SCP theory and code. This first stage of development of STARK-B was ended in autumn 2012.

Then, we have begun to implement the data (about 70 publications concerning 90 neutral and ionized atoms) issued from the"MSE" method developed by Dimitrijević and coworkers (Dimitrijević & Konjević 1980; Dimitrijević & Kršljanin 1986; Dimitrijević & Popović 2001). This method, more approached than the SCP one, is used when the atomic structure data are not sufficiently complete to perform an adequate semiclassical calculation.

This will be presented below, as well as the state of advancement and our program of development of the database.

2 The theory and method of calculations leading to STARK-B data

2.1 Brief outline of the assumptions and approximations of the method

Stark broadening theory is based on the founding papers by Baranger (1958a,b,c).

The impact approximation is the first basic assumption: the duration of a collision must be much smaller than the mean interval between two collisions. So the collisions between the radiating atom (or ion) act independently and are additive. It is quite always valid for electron collisions and is generally valid for collisions with positive ions in the conditions of stellar atmospheres (Sahal-Bréchot 1969a,b). It can break down at high densities (laser fusion plasmas for instance).

The second basic assumption is the complete collision approximation: the radiating atom has no time to emit (or absorb) a photon during the collision process. In the line center, the impact approximation and the complete collision approximation are both valid, and the line broadening theory becomes an application of the theory of collisions between the radiating atom and the surrounding perturbers. In the line wings, the complete collision approximation can break down for ion collisions. However, the contribution of ion collisions is often smaller than 10% when compared to that of electrons.

The present method is limited to the case of isolated lines: the levels of the studied transition broadened by collisions do not overlap with the neighbouring perturbing levels. So, hydrogen and hydrogenic ionic lines, some specific helium lines and some lines arising from Rydberg levels are excluded from our calculations and consequently from STARK-B.

Therefore, the impact-complete collision-isolated lines approximation leads to a Lorentz line profile characterized by a width and a shift which depend on the physical conditions of the medium (temperature and density of the perturbers). The detailed formulae, which are not repeated here, can be found in Sahal-Bréchot et al. (2014) and earlier papers. In particular, the widths are given by a sum over atom-perturber cross-sections and an interference term multiplied by the relative velocity, followed by an average over the Maxwell distribution of relative velocities and multiplied by the density of perturbers.

Due to the impact approximation, widths and shifts are proportional to the density. However, at high densities, the Debye screening effect can be important and is taken into account in our calculations. This decreases the width and the shift which thus become not proportional to the density.

In addition, if LS coupling is valid, the different fine structure line of a same multiplet have the same width and shift, that of the multiplet (in frequency units). This is due to the fact that the electronic spin has no time to rotate during the collision and thus can be neglected for obtaining the cross-sections.

2.2 The semiclassical-perturbation (SCP) method

Most of our calculations have been performed with the semiclassical-perturbation method (SCP) developed by Sahal-Bréchot (1969a,b) and further papers: Sahal-Bréchot (1974) for complex atoms, Fleurier et al. (1977) for inclusion of Feshbach resonances in elastic cross-sections of radiating ions, and by Mahmoudi et al. (2008) for very complex atoms. The method was revisited in detail by Sahal-Bréchot et al. (2014). The numerical codes have been updated and operated by Dimitrijević and Sahal-Bréchot (Dimitrijević & Sahal-Bréchot (1984)) and further papers. When comparing to experimental results, the accuracy is about 20% for the widths but can be worse for the shifts.

For obtaining the cross-sections and the interference term which enter the calculations, we must calculate the S-matrix (the so-called collision matrix or scattering matrix). First, an atomic structure must be used and chosen for obtaining wave functions and energy levels. Second, a method of calculation of the S-matrix has to be chosen. Then, a coupling between the chosen atomic structure and the collisional part of the code is achieved for calculating Stark widths and shifts data.

2.2.1 The chosen atomic structure

In our earlier papers, the Coulomb approximation with quantum defect (Bates and Damgaard 1949), improved for high levels by Van Regemorter et al. (1979), were used, together with measured or calculated energy levels, e.g. Kramida et al. (2014) or other tables.

In the more recent papers modern *ab initio* methods are used. Modern atomic structure computer codes or their data obtained from a database can be downloaded on line. Thus the calculations of widths and shifts can be made from the beginning to the end without any additional external input or experimental adjustment. Then, the chosen atomic structure package enters our computer semi-classical code and that allows, when these methods are applicable, to obtain widths and shifts for several hundreds of lines in a same run. We have used:

- TOPbase, the Opacity Project atomic database, contains accurate calculated oscillator strengths and energy levels for abundant neutral and ionized atoms relevant for astrophysics. They have been obtained within the close-coupling scattering theory by means of the R-matrix method with innovative asymptotic techniques (Cunto et al. 1993). LS coupling is assumed. So, TOPbase data have been especially useful for light and low and moderately ionized atoms and ions: e.g. Larbi-Terzi et al. (2012) for C II lines.

- The Cowan code (Cowan 1981) is an online atomic structure package consisting of a set of computer programs for calculation of energy levels, radiative transition wavelengths and probabilities, etc. The Hartree-Fock-Slater multi-configuration expansion method with statistical exchange is the normal option since it is most computationally efficient. The relativistic corrections are treated by perturbations. So this method is especially suited to moderately heavy atoms which are little and moderately ionized: e.g. Hamdi et al. (2013) for Pb IV lines.

- SUPERSTRUCTURE (SST) (Eissner et al. 1974) is well suited for medium and highly charged ions. The wave functions are determined by diagonalization of the nonrelativistic Hamiltonian using orbitals calculated in a scaled Thomas-Fermi-Dirac-Amaldi potential. Relativistic corrections are introduced according to the Breit-Pauli approach. Atomic data are obtained in intermediate coupling: e.g. Ben Nessib et al. (2004) for Si V lines, and Hamdi et al. (2007) for Ne V lines.

Si V and Ne V line widths and shifts data have been calculated with both Bates & Damgaard and SST atomic data. The difference does not exceed 30%. C II widths and shifts data have been calculated with both TOPbase and Bates and Damgaard atomic data, and the difference does not exceed a few percent, except when configuration interaction plays an important role by allowing a forbidden transition. This remark is for giving an idea of the importance of the chosen atomic structure for obtaining Stark broadening data.

2.2.2 The semiclassical approximation for obtaining the S-matrix, the cross-sections and the interference term

The basic formalism has been revisited in detail by Sahal-Bréchot et al. (2014). The perturber is considered as a classical particle moving along a classical path unperturbed by the interaction with the radiating atom: straight paths for neutral radiators, hyperbolic paths for ion-electron and ion-ion collisions. Then the S-matrix has been obtained within the second order perturbation theory. The needed cross-sections are obtained through integration over the impact parameter of the transition probabilities. The needed cut-offs are determined in order to maintain the unitarity of the scattering S- matrix, and Debye screening is taken into account. This permitted to create a very fast computer code, which can now work on a personal laptop: one night of calculation is sufficient to obtain data for one or two hundred lines of a same neutral or ionized atom, and for a set of about 5 temperatures and 5 densities. For the purposes of STARK-B, this semiclassical-perturbation treatment is adapted and gives results with a sufficient accuracy (about 20%). This is especially the case if the perturbing levels are not too far from the levels of the studied line.

2.3 The MSE method

The“MSE” method developed by Dimitrijević and coworkers (Dimitrijević & Konjević 1980; Dimitrijević & Kršljanin 1986; Dimitrijević & Popović 2001) is more approached than the SCP one. It can be used when the atomic structure data are not sufficiently complete to perform an adequate semiclassical calculation. it uses a simplified atom quantum description, and the cross-sections are calculated by means of an effective Gaunt factor (Van Regemorter 1962; Griem 1968) revisited, and modified for ions with a charge $Z > 1$. The accuracy of the results is about 30-40%. Indeed, due to its simplicity, the MSE method is much faster than the SCP one.

3 The STARK-B database

3.1 Description of the database

The homepage proposes several menus, among which “Introduction”, “Data Description” and “Access to the Data”. “Introduction” recalls the approximations and methods of calculation. “Data Description” describes the data that are in the files. ”Access to the Data”provides a graphical interface: first, the user clicks on the wished element in the Mendeleev periodic table and then on the ionization degree of interest. Yellow cells contain data, while grey cells are empty. Next, with a few clicks, the user chooses the colliding perturber(s), the perturber density, the transition(s) defined by quantum numbers and the plasma temperature(s). The user can also make a query by domain of wavelengths instead by transitions. Then a table displaying the widths and shifts is generated. Bibliographic references are given and linked to the publications via the SAO/NASA ADS Physics Abstract Service (2014) and/or within DOI if available. The publications can be freely downloaded if the access is not restricted. The widths and shifts data can be downloaded in ASCII and in VOTable format (XML format), adapted to Virtual Observatories.

Since STARK-B is devoted to spectroscopic diagnostics and modeling of various plasmas in astrophysics, laboratory physics, technology and other topics, the range of temperatures and densities in the tables is wide and vary with the ionization degree of the considered ion. The temperatures vary from several thousands Kelvin for neutral atoms to several millions for highly charged ions. The perturber densities vary from 10^{12} cm^{-3} to several 10^{22}cm^{-3}. The data model (in particular the identification of the line transitions) follows the VAMDC standards, in order to allow interoperability with other atomic databases included in the Virtual Atomic and Molecular Data Center. The transitions are defined by configurations, terms, J-values, and wavelengths. The multiplet number is also often included and taken from the NIST database (Kramida et al. 2014). In addition, the widths and shifts data are provided in units of wavelengths (Å) and not in angular frequency units. It must be noticed that the wavelengths displayed in STARK-B are calculated from the energy levels that are used as input data in the SCP computer code. Consequently, the tabulated wavelengths are most often different from the measured ones, especially if the used energy levels are theoretically calculated: this is especially the case for the atomic structure data originating from TOPBase, SST or Cowan code. So, if widths and shifts data are needed for measured wavelengths ($\lambda_{measured}$), or for fine structure data whereas the data are only provided for multiplets, one has to multiply the STARK-B data by $(\lambda_{measured}/\lambda_{STARK-B})^2$.

In our tables, a positive shift is towards the red and a negative one towards the blue.

When the impact approximation approaches its limit of validity, a warning (an asterisk) is introduced at the left of the data. If the impact approximation is not valid, there is only an asterisk and no data in the corresponding cell. The isolated line approximation, which can approach its limit of validity at high densities is also checked in the tables. This is commented on the menu "Data description".

3.2 *Implementation of the published SCP data*

During the first stage of STARK-B development (from the end of 2008 to the end of 2012), we have implemented all the Stark broadening parameters calculated and published by means of the SCP computer code. Currently, the database contains SCP widths and shifts for spectral lines of the following elements and ionization degrees:

Ag I, Al I, Al III, Al XI, Ar I, Ar II, Ar III, Ar VIII, Au I, B II, B III, Ba I, Ba II, Be I, Be II, Be III, Br I, C II, C III, C IV, C V, Ca I, Ca II, Ca V, Ca IX, Ca X, Cd I, Cd II, Cl I, Cl VII, Cr I, Cr II, Cu I, F I, F II, F III ,F IV, F V, F VI, F VII, Fe II, Ga I, Ge I, Ge IV, He I, Hg II, I I, In II, In III, K I, K VIII, K IX, Kr I, Kr II, Kr VIII, Li I, Li II, Mg I, Mg II, Mg XI, Mn II, N I, N II, N III, N IV, N V, Na I, Na X, Ne I, Ne II, Ne II, Ne III, Ne IV, Ne V, Ne VIII, Ni II, O I, O II, O III , O IV, O V, O VI; O VII, P IV, P V, Pb IV, Pd I, Rb I, S III, S IV, S V, S VI, Sc III, Sc X, Sc XI, Se I, Si I, Si II, Si IV, Si IV, Si V, Si VI, Si XI, Si XII, Si XIII, Sr I, Te I, Ti IV, Ti XII, Ti XIII, Tl III, V V, V XIII, Y III, Zn I.

We will continue to implement the new results of calculations as soon as they are published. The description of newly added data with the date of importation appears under the menu "Updates". Also all updates with the date of the first importation and the importation of revised data are noted. Moreover, for further enquiries or user support, there is the menu "Contact" with the possibility to send an e-mail with questions to the corresponding persons.

3.3 *Fitting formulae as functions of temperature*

The beginning of stage 2 STARK-B development was devoted to implement fitting coefficients of the tabulated data with temperature. In fact, he theory of Stark broadening shows that the line widths decrease with temperature as $T^{-1/2}$ for ionized emitters at low temperature, and to $\log(T)/T^{1/2}$ for both neutral and ionized atoms at high temperatures. However, in astrophysics, especially for the modeling of stellar atmospheres, this is not sufficient. Fitting formulae and coefficients as functions of temperature for every line are needed, since such fitting coefficients are more efficient for the use in the computer codes for stellar atmosphere modeling than tabulated widths and shifts for a set of temperatures.

Consequently, in order to enable a more adequate use of STARK-B for stellar modeling, we derived (Sahal-Bréchot et al. 2011) a simple and accurate fitting formula based on a least-square method, which is logarithmic and represented by a second degree polynomial:

$$\begin{aligned} \log(w) &= a_0 + a_1 \log(T) + a_2 \left(\log(T)\right)^2 , \\ d/w &= b_0 + b_1 \log(T) + b_2 \left(\log(T)\right)^2 . \end{aligned} \tag{3.1}$$

It can be noted that Dimitrijević et al. (2007) proposed the fitting formula $w = C + AT^B$, but the present one is more accurate, due to the second degree term of the expansion. It should be also noted that none of them have a real physical sense.

Then, for each table of widths and shifts, a complementary table was added, with coefficients a_0, a_1, a_2 and b_0, b_1, b_2, obtained by using the above equations for the corresponding fitting with the temperature. These fitting coefficients can also be downloaded in ASCII and in VOTable format, and can be included in the computer codes for stellar atmospheres modeling.

We plan also to develop other fitting formulae as functions of perturber densities in order to make easier the use of data on high densities needed for white dwarf atmospheres and subphotospheric layers modeling.

3.4 *The current development of STARK-B: implementation of MSE data*

Since the end of 2013, we have begun to implement our Stark broadening data obtained with the Modified SemiEmpirical method. We recall that this approach is convenient for emitters where atomic data are not sufficiently complete to perform an adequate semiclassical perturbation calculation.

Up to now, Stark line widths and in some cases also shifts of the following emitters spectral lines:

Ag II, Al III, Al V, Ar II, *Ar III*, Ar IV, As II, As III, Au II, *B III*, B IV, Ba II, Be III, Bi II, Bi III, Br II, C III, C IV, *C V*, Ca II , Cd II, *Cd III*, Cl III, *Cl IV*, *Cl VI*, Co II, *Co III*, Cu III, Cu IV, Eu II, Eu III, F III, F V, F VI, Fe II, Ga II, *Ga III*, *Ge III*, *Ge IV*, I II, Kr II, Kr III, La II, La III, Mg II, Mg III, Mg IV, *Mn II*, *Mn III*, N II, N III, N IV, N VI, Na III, Na VI, Nd II, Ne III, Ne IV, Ne V, Ne VI, O II, O III, O IV, O V, P III, P IV, *P VI*, Pt II, *Ra II*, S II, S III, S IV, Sb II, Sc II, Se III, Si II, Si III, Si IV, Si V, Si VI, Sn III, Sr II, Sr III, Ti II, Ti III, V II, V III, V IV, Xe II, Y II, Zn II, Zn III, Zr II.

The data were inserted in the beginning of 2014 for the elements written in italics.

4 Future developments of STARK-B and conclusion

As soon as new data will be calculated and published, they will be added to the database. The implementation of our quantum data will be another future stage (e.g. Elabidi et al. (2008, 2009) and further papers). The further developments also concern insertion of little apps (fitting along principal quantum number for a given multiplet, charge of the ion collider along isoelectronic sequences, of the radiating ion, homologous ions...) by using fittings or systematic trends in order to obtain data that are missing on the database. In a more distant future, we would plan to put the SCP code on line.

The continuation of such developments and services of powerful and constantly updated online databases, like STARK-B, is crucial.

This work has been supported by the Paris Observatory, the CNRS and the PNPS (Programme National de Physique Stellaire, INSU-CNRS). The support of the Ministry of Education, Science and Technological Development of Republic of Serbia through projects 176002 and III44022 is also acknowledged. The cooperation agreements between Tunisia (DGRS) and France (CNRS) (project code 09/R 13.03, No.22637) are also acknowledged. This work has also been supported by the VAMDC (Virtual Atomic and Molecular Data Centre). VAMDC is funded under the Combination of Collaborative Projects and Coordination and Support Actions Funding Scheme of The Seventh Framework Program. Call topic: INFRA-2008-1.2.2 Scientific Data Infrastructure. Grant Agreement number: 239108. A part of his work has also been supported by the LABEX Plas@par project and received financial state aid managed by the Agence Nationale de la Recherche, as part of the programme "Investissements d'avenir" under the reference, ANR–11–IDEX–0004–02.

References

Baranger M., 1958a, Phys. Rev., 111, 481

Baranger M. 1958b, Phys. Rev., 111, 494

Baranger M. 1958c, Phys. Rev., 112, 885

Bates, D.R. & Damgaard, A. 1949, Trans. Roy. Soc. Lond., 242, 101

Ben Nessib, N., Dimitrijević, M.S. & Sahal-Bréchot, S. 2004, A&A, 423, 397

Cowan R.D. 1981, Robert, D. Cowan's Atomic Structure Code, in The Theory of Atomic Structure and Spectra, (University of California Press, Berkeley, CA, USA) `https://www.tcd.ie/Physics/people/Cormac.McGuinness/Cowan/`

Cunto, W., Mendoza, C., Ochsenbein, F. & Zeippen, C.J. 1993, A&A, 275, L5, `http://cdsweb.u-strasbg.fr/topbase/TheOP.html`, `http://cdsweb.u-strasbg.fr/topbase/topbase.html`

Eissner, W., Jones, M., & Nussbaumer, H. 1974, Comp. Phys. Com., 8, 270

Dimitrijević, M.S. & Konjević, N. 1980, JQSRT, 24, 451

Dimitrijević, M.S. & Kršljanin, V. 1986, A&A, 165, 24, 269

Dimitrijević, M. S., & Popović, L. Č. 2001, J. Appl. Spectr., 68, 893

Dimitrijević M.S., & Sahal-Bréchot S. 1984, JQSRT, 31, 301

Dimitrijević M.S., & Sahal-Bréchot S. 2014, Atoms, 2(3), 357, `http://www.mdpi.com/2218-2004/2/3/357`

Dimitrijević, M. S., Ryabchikova, T., Simić, Z., Popović,, L. Č., & Dačić, M. 2007, A&A, 469, 681-686

Dubernet, M.L., Boudon, V., et al. 2010, JQSRT, 111, 2151, `http://www.vamdc.eu/`

Dufour, P., Ben Nessib, N., Sahal-Bréchot, S., & Dimitrijević, M. S. 2011, Baltic Astronomy, 20, 511

Elabidi, E., Ben Nessib, N., Cornille, M., Dubau, J. & Sahal-Bréchot, S. 2008, J. Phys. B, 41, 025702:1

Elabidi, H., Sahal-Bréchot, S.& Ben Nessib, N. 2009, EPJD, 54, 51

Fleurier C., Sahal-Bréchot S. & Chapelle J. 1977, JQSRT, 17, 5954

Griem H. R. 1968, Phys. Rev., 165, 258

Hamdi, R.; Ben Nessib, N.; Dimitrijević, M.S.; Sahal-Bréchot, S. 2007, ApJS, 170, 243

Hamdi, R., Ben Nessib, N., Dimitrijević, M.S.& Sahal-Bréchot S. 2013, MNRAS, 431, 1039

Kramida, A. E., Ralchenko, Yu., Reader, J., and NIST ASD Team, NIST Atomic Spectra Database, (ver. 5.2), National Institute of Standards and Technology, Gaithersburg, MD, `http://physics.nist.gov/asd3`.

Larbi-Terzi, N., Sahal-Bréchot S., Ben Nessib, N. & Dimitrijević, M.S. 2012, MNRAS, 423, 766

Mahmoudi W., Ben Nessib N.& Sahal-Bréchot S. 2008, EPJD, 47, 7

Rixon, G., Dubernet, M.L., et al. 2011, 7th International Conference on Atomic and Molecular Data and their Applications -ICAMDATA-2010, AIP Conf. Proc., 1344, 107

Sahal-Bréchot S. 1969a, A&A, 1, 91

Sahal-Bréchot S. 1969b, A&A, 2, 322

Sahal-Bréchot S. 1974, A&A,35, 319

Sahal-Bréchot S. 1991, A&A, 245, 322

Sahal-Bréchot S., Dimitrijević M. S., & Ben Nessib N. 2011, Baltic Astronomy, 20, 523

Sahal-Bréchot, S., Dimitrijević, M. S., & Moreau, N. 2012, J. Phys.: Conf. Ser., 397, 012019

Sahal-Bréchot S., Dimitrijević M. S., & Ben Nessib N. 2014, Atoms, 2(2), 225, `http://www.mdpi.com/2218-2004/2/2/225`

Sahal-Bréchot, S., Dimitrijević, M. S., & Moreau, N. 2014, `http://stark-b.obspm.fr`

SAO/NASA ADS Physics Abstract Service, 2014, `http://www.adsabs.harvard.edu/`

Serbian Virtual Observatory, 2014, `http://servo.aob.rs`

Van Regemorter H. 1962, ApJ, 136, 906

Van Regemorter, H., Hoang Binh, Dy. & Prudhomme, M. 1979, J. Phys. B,12, 1053

HELIOSEISMIC INFERENCES OF THE SOLAR CYCLES 23 AND 24: GOLF AND VIRGO OBSERVATIONS

D. Salabert[1], R.A. García[1] and A. Jiménez[2,3]

Abstract. The Sun-as-a star helioseismic spectrophotometer GOLF and photometer VIRGO instruments onboard the SoHO spacecraft are collecting high-quality, continuous data since April 1996. We analyze here these unique datasets in order to investigate the peculiar and weak on-going solar cycle 24. As this cycle 24 is reaching its maximum, we compare its rising phase with the rising phase of the previous solar cycle 23.

Keywords: data analysis, helioseismology, activity

1 Introduction

As now very well established, the acoustic frequencies vary along the solar cycle and show high levels of correlation with the solar activity proxies. However, in this work, we find evidences of significant differences in the frequency dependence of the acoustic frequency variations between the two rising phases of cycles 23 and 24, providing insights into the related changes in magnetic field and internal structure.

2 Data and analysis

We analyzed simultaneous space-based, Sun-as-a-star helioseismic observations collected by the Global Oscillations at Low Frequency (GOLF; Gabriel et al. 1995) and the Variability of Solar Irradiance and Gravity Oscillations (VIRGO; Fröhlich et al. 1995) instruments onboard the *Solar and Heliospheric Observatory* (SoHO) spacecraft. GOLF measures the radial velocity Doppler shift - integrated over the solar surface - in the D1 and D2 Fraunhofer sodium lines at 589.6 and 589.0 nm respectively. VIRGO is composed of three Sun photometers (SPM) at 402 nm (Blue), 500 nm (Green) and 862 nm (Red). The GOLF velocity time series were obtained following García et al. (2005) and calibrated as described in Jiménez-Reyes et al. (2003), while the VIRGO photometric observations were calibrated as described in Jiménez et al. (2002). These two instruments are providing unique datasets of high-quality, continuous observations of the low-degree oscillation modes since April 1996 (i.e. since more than 18 years today) covering the solar activity cycles 23 and 24. A total of 6538 days of observations were analyzed, spanning the period from 1996 April 11 to 2014 March 5, with an overall duty cycle larger than 96%.

These two datasets were split into contiguous 730-day, 365-day, and 182.5-day sub series, each series being allowed to overlap by 182.5 days, 91.25 days, and 46.625 days respectively. The power spectrum of each sub series was fitted to estimate the $l = 0$, 1, 2, and 3 mode parameters using a standard likelihood maximization function as described in Salabert et al. (2007). Each mode component was parameterized using an asymmetric Lorentzian profile (Nigam & Kosovichev 1998). The amplitude ratios between the $l = 0, 1, 2$, and 3 modes and the m-height ratios of the $l = 2$ and 3 multiplets calculated in Salabert et al. (2011) for the GOLF and VIRGO measurements were used. The $l = 4$ and $l = 5$ were also included in the fitted profile when present in the fitted window.

[1] Laboratoire AIM, CEA/DSM-CNRS, Université Paris 7 Diderot, IRFU/SAp, Centre de Saclay, 91191 Gif-sur-Yvette, France
[2] Instituto de Astrofísica de Canarias, 38200 La Laguna, Tenerife, Spain
[3] Departemento de Astrofísica, Universidad de La Laguna, 38205 La Laguna, Tenerife, Spain

3 Temporal variations of the low-degree oscillation frequencies over 6500 days

The temporal variations of the p-mode frequencies were defined as the differences between the mode frequencies observed at different dates and reference values of the corresponding modes taken as the average over the years 1996-1997 during the minimum of cycle 22. The formal uncertainties returned from the peak-fitting analysis were used as weights in the average computation. In addition, mean values of daily measurements of the 10.7-cm radio flux, $F_{10.7}$, were obtained and used as a proxy of the solar surface activity. The frequency shifts measured at each individual angular degree, $l = 0$, 1, 2, and 3, and averaged between 2450 μHz and 3520 μHz extracted from the GOLF 365-day sub series are shown in Fig. 1. The corresponding scaled 10.7-cm radio flux is also represented by the red solid lines. The signature of the quasi-biennal oscillation (Fletcher et al. 2010) is also clearly observable in Fig. 1. The GOLF and VIRGO frequency shifts per unit of change in the 10.7-cm radio flux in nHz/RF* calculated through weighed linear regressions between these two quantities, and the associated linear correlation coefficients are given in Table 1.

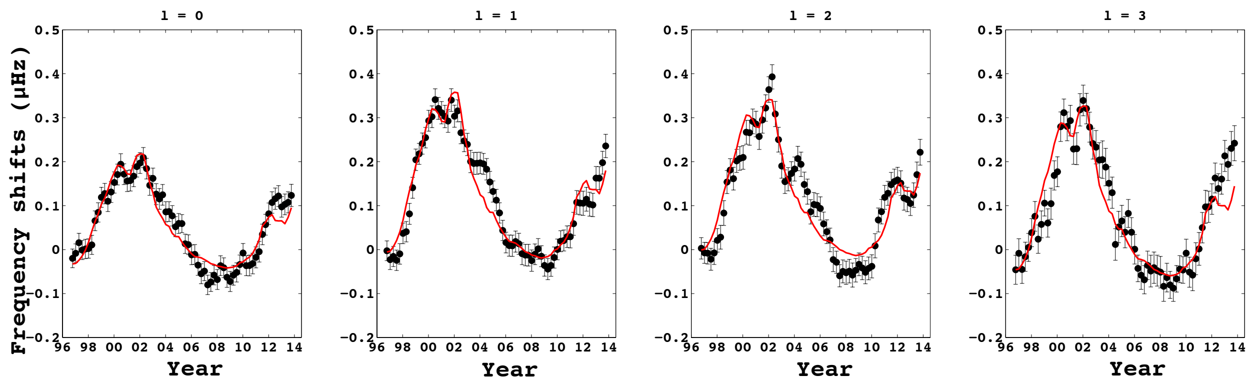

Fig. 1. Temporal variations of the frequency shifts in μHz of the individual $l = 0$, 1, 2, and 3 modes (from left to right respectively) and averaged between 2450 μHz and 3520 μHz extracted from the analysis of the 365-day GOLF spectra (black dots). The scaled 10.7-cm radio flux, $F_{10.7}$, averaged over the same 365-day timespan is shown as a proxy of the solar surface activity (solid lines).

Table 1. Variations of the frequencies shifts at each l per unit of change in the 10.7-cm radio flux (nHz/RF) and associated linear correlations, r_p, obtained from the analysis of the 365-day GOLF and VIRGO spectra. The frequency shifts were calculated between 2450 μHz and 3520 μHz. Independent points only were used.

	GOLF		VIRGO	
l	Gradient^a	r_p	Gradient^a	r_p
0	2.07 ± 0.14	0.95	2.55 ± 0.10	0.95
1	3.04 ± 0.15	0.97	3.54 ± 0.11	0.96
2	2.85 ± 0.17	0.94	2.92 ± 0.13	0.95
2	3.10 ± 0.21	0.94	-	-

[a]Gradient against the 10.7-cm radio flux in units of nHz RF^{-1} (with 1 RF = 10^{-22} J s^{-1} m^{-2} Hz^{-1}).

In the following, we studied the frequency shifts as a function of frequency during the rising phases of cycles 23 and 24. The top panels of Fig. 2 show the individual $l = 0$, 1, 2, and 3 frequency shifts as a function of frequency during the rising phases of cycles 23 (blue) and 24 (red) extracted from the GOLF observations. The 2-year periodicity was removed by applying a proper smoothing as explained in Fletcher et al. (2010). Differences in the frequency shifts are observed between the two cycles 23 and 24. First, the low-frequency part of the p-mode oscillation power spectrum, which is more sensitive to deeper sub-surface layers of the Sun, show similar shifts between the two cycles. On the other hand, in the high-frequency range of the power spectrum, where the shifts are larger, the variations of the frequency shifts are smaller during the rising phase of the solar

*The 10.7-cm radio flux has for units 1 RF = 10^{-22} J s^{-1} m^{-2} Hz^{-1}.

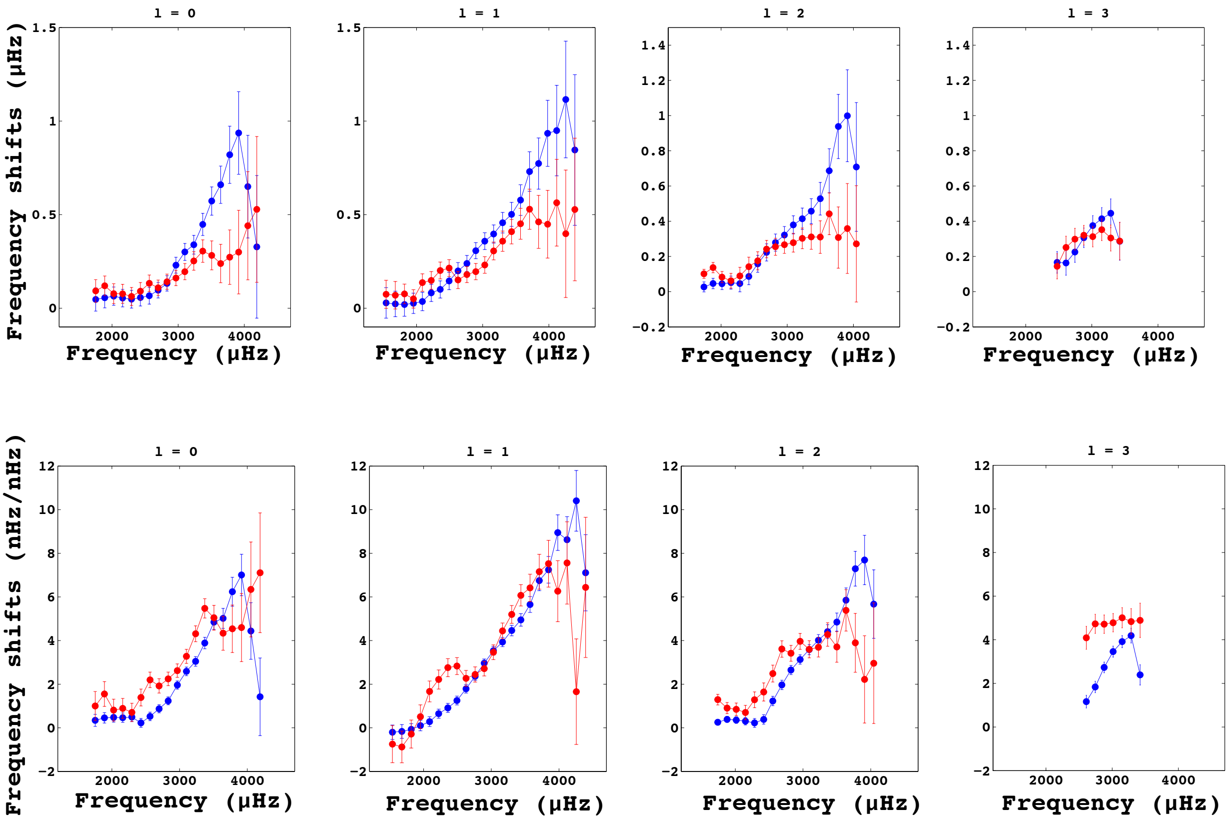

Fig. 2. Top: Frequency shifts in μHz of the individual $l = 0$, 1, 2, and 3 modes (from left to right respectively) as a function of frequency during the rising phase of the solar cycle 23 (blue dots) and the rising phase of the solar cycle 24 (red dots). **Bottom:** Same as the top panels but for the frequency shifts per unit of change in the 10.7-cm radio flux (nHz/RF).

cycle 24. As the frequency shifts at higher frequencies are highly correlated with surface activity, these smaller shifts at high frequency are consistent with the weaker surface activity observed during cycle 24. The bottom panels of Fig. 2 show the frequency shifts per unit of change in the 10.7-cm radio flux as a function of frequency during the rising phases of cycles 23 (blue) and 24 (red) extracted from the GOLF observations. The frequency variations per unit of surface activity are larger in cycle 24 than in cycle 23. The results obtained from the VIRGO data are consistent within the error bars with GOLF.

Figure 3 shows the estimated dates of the minimum of cycle 23 (2008-2009) as estimated by the $l = 1$ mode frequency shifts by measuring the minimum of their temporal variations as a function of frequency. These dates were calculated after removing the signature of the 2-year periodicity. The results extracted from the analysis of the 365-day GOLF spectra are represented in blue, while the results extracted from the analysis of the 182.5-day GOLF spectra are represented in red. The solid black line corresponds to the smoothed 182.5-day results. The horizontal green solid line corresponds to the minimum of cycle 23 measured from the smoothed 10.7-cm radio flux. The minima of the temporal variations of the mode frequency are different from the minimum estimated based on the 10.7-cm radio flux.

4 Conclusions

We analyzed more than 6500 days of radial velocity GOLF and photometric VIRGO observations. We found differences in the temporal variations of the low-degree oscillation frequencies between the two rising phases of cycles 23 and 24 with an important frequency dependence. The results obtained in this study suggest that the solar magnetic field and internal structure in the upper sub-surface layers of the Sun have changed between

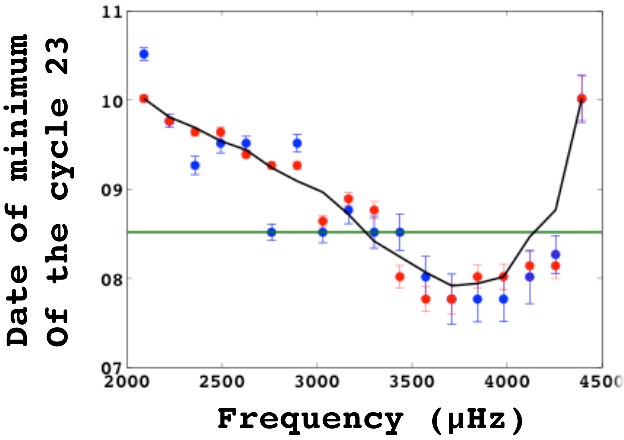

Fig. 3. Estimated dates of the minimum of the temporal variations of the $l = 1$ frequency shifts associated to solar activity during the minimum of the solar cycle 23 (2008-2009). In blue, the dates obtained from the 365-day sub series, and in red, the ones obtained from the 182.5-day sub series. The solid black line corresponds to the smoothed 182.5-day results. The horizontal green solid line corresponds to the minimum of the smoothed 10.7-cm radio flux.

cycle 23 and cycle 24. It would indicate as well that in deeper layers inside the Sun, magnetic field and internal structure are similar between cycle 23 and cycle 24. More precise localization of where the changes are taking place will need the analysis of high-degree modes.

The GOLF and VIRGO instruments onboard SoHO are a cooperative effort of many individuals, to whom we are indebted. SoHO is a project of international collaboration between ESA and NASA. D.S. and R.A.G. acknowledge the support from the CNES/GOLF grant at the SAp CEA-Saclay. The 10.7-cm solar radio flux data were obtained from the National Geophysical Data Center.

References

Fletcher, S. T., Broomhall, A.-M., Salabert, D., et al. 2010, ApJ, 718, L19

Fröhlich, C., Romero, J., Roth, H. et al. 1995, Solar Phys., 162, 101

Gabriel, A. H., Grec, G., Charra, J. et al. 1995, Solar Phys., 162, 61

García, R. A., Turck-Chièze, S., Boumier, P. et al. 2005, A&A, 442, 385

Jiménez, A., et al. 2002, Sol. Phys., 209, 247

Jiménez-Reyes, S. J., García, R. A., Jiménez, A. et al. 2003, ApJ, 595, 446

Nigam, R., & Kosovichev, A. G. 1998, ApJ, 505, L51

Salabert, D., Ballot, J., & García, R. A. 2011, A&A, 528, A25

Salabert, D., Chaplin, W. J., Elsworth, Y., New, R., & Verner, G. A. 2007, A&A, 463, 1181

SF2A 2014
J. Ballet, F. Bournaud, F. Martins, R. Monier and C. Reylé (eds)

LABORATORY DETERMINATION OF SPECTROSCOPIC DATA FOR STELLAR PHYSICS

W.-Ü L. Tchang-Brillet[1], J.-F. Wyart[1 2], Ali Meftah[1 3], N. Champion[1] and Ch. Blaess[1]

Abstract. Laboratory works on VUV emission spectra of moderately charged atomic ions aiming to obtain fundamental data needed for interpretation of observations are presented. Experimental and theoretical methods, as well as examples of studies are summarized.

1 Introduction

High resolution stellar spectra obtained by space instruments (HST/STIS, FUSE) in the far UV wavelength range need exhaustive laboratory spectroscopic data to be analyzed. In particular, improved data are necessary for complex spectra of heavy elements ions, such as moderately charged transition elements or rare earths, the presence of which were detected in chemically peculiar stars and white dwarfs. The precision on wavelengths needed for reliable identifications of species in the stellar spectra cannot be achieved by *ab initio* theoretical calculations but only by laboratory experimental measurements. For NLTE collisional-radiative modeling of stellar plasmas, a huge amount of spectroscopic and collisional data is needed, which implies the knowledge of experimental energy levels. These are derived from analysis of high resolution laboratory spectra in relation with theoretical studies of the atomic structure. The analysis also leads to a better knowledge of the quantum state wave functions, which provides better values of transition probabilities and Landé factors of the levels. Furthermore, experimental values of level energies enable improvement of calculations of photoionization cross sections or collisional excitation cross sections. In this report, we have limited the description of the experimental part to the vacuum ultra-violet (VUV) wavelength region. However, in some cases, we have to combine experimental data from different wavelength regions, either visible or infrared, produced by other authors. The theoretical method and analysis remain similar.

2 Experimental method

Several light sources are used in our laboratory for production of emission spectra of moderately charged atomic ions, depending on the ionization stages of interest. For instance, hollow cathode discharge sources operating in continuous mode produce emission of neutral atoms and singly ionized ions. In pulsed mode, they produce emission of doubly charged ions. Vacuum spark sources can produce emission of three to eight times charged ions, depending on the element constituting the anode.

For the VUV range, high resolution emission spectra are recorded on the 10.7 m normal incidence vacuum spectrograph of the Meudon Observatory (Tchang-Brillet & Azarov 2002). This high resolution instrument is unique in Europe and is registered in the ESA Ground Based Facilities (GBF) database. The instrument is equipped with a 3600 lines/mm holographic concave grating and has a linear dispersion of ~ 0.025 Å /mm operating in the 200-3000 Å wavelength region. The theoretical resolution is 150 000 (in practice $\delta\lambda \sim 0.008$Å). Two image plates or two photographic plates can be used to provide a simultaneous detection of a 200-240 Å wide wavelength range. The photo-stimulable image plates have a linear intensity response over five orders

[1] Laboratoire d'Etude du Rayonnement et de la Matière en Astrophysique (LERMA), UMR8112 du CNRS, Observatoire de Paris, Université Pierre et Marie Curie-Paris 6
[2] Laboratoire Aimé-Cotton, CNRS UPR3321, Université Paris-Sud, ENS Cachan
[3] Laboratoire de Physique et Chimie Quantique, Université Mouloud Mammeri, BP17 RP, 15000 Tizi-Ouzou, Algeria

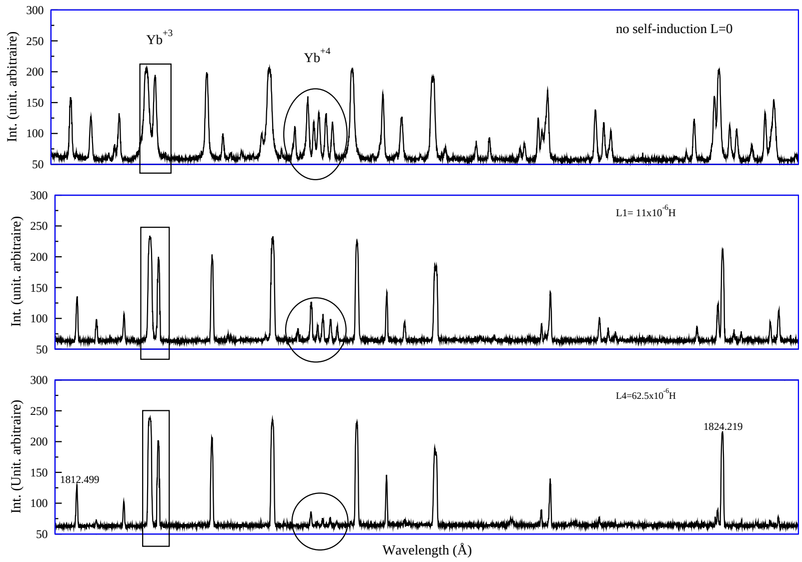

Fig. 1. Sections of spark spectra of an ytterbium electrode produced with three different discharge conditions. One can see the difference in behavior of Yb^{3+} and Yb^{4+} lines when the self-induction of the discharge circuit increases.

of magnitude and their use allows intensity measurements of spectral lines and comparison with theoretical oscillator strengths or branching ratios.

The grating instrument is complementary to high resolution Fourier Transform Spectrometry (FTS) (Tchang-Brillet & Azarov 2002). Indeed, given the absence of a transmitting device, it can be used at wavelength ranges shorter than the cut-off of the FTS beam-splitter. Moreover, its integrating operation mode allows a non-stationary or pulsed light sources, which is generally necessary for producing emission spectra of more than doubly charged ions.

3 Theoretical method

Theoretical calculations are performed using the set of Cowan's codes RCN/RCN2/RCG/RCE (Cowan 1981). In a first step, Hartree-Fock method is applied including corrections (HFR) using RCN/RCN2. Then the Hamiltonian including configuration interactions is diagonalized using RCG. In this step, the HFR energy parameters can be replaced by their scaled values. The scaling factors are provided by isoelectronic or isoionic regularities. The last code (RCE) introduces a semi-empirical step by allowing iterative least-squares fits of energy parameters, which minimize the standard deviation of calculated level energies from the experimental ones. The last iteration leads to the best calculated values of transition probabilities, Landé factors and experimentally unknown levels.

4 Analysis

The analysis consists of the derivation of energy levels from an experimental line list based on the Ritz combination principle taking into account quantum mechanical selection rules for electric dipole transitions. In practice, it is a long procedure involving manipulation of a large amount of experimental and theoretical quantities such as experimental wavelengths and intensities, calculated energies and line strengths, and going back and forth between these. This step has been greatly speeded up by using an interactive code IDEN (Azarov 1991, 1993) to visualize data. Finally, experimentally determined energy values are optimized by a general least squares fit from wave numbers of all observed lines using the LOPT code (Kramida 2010). These optimized experimental

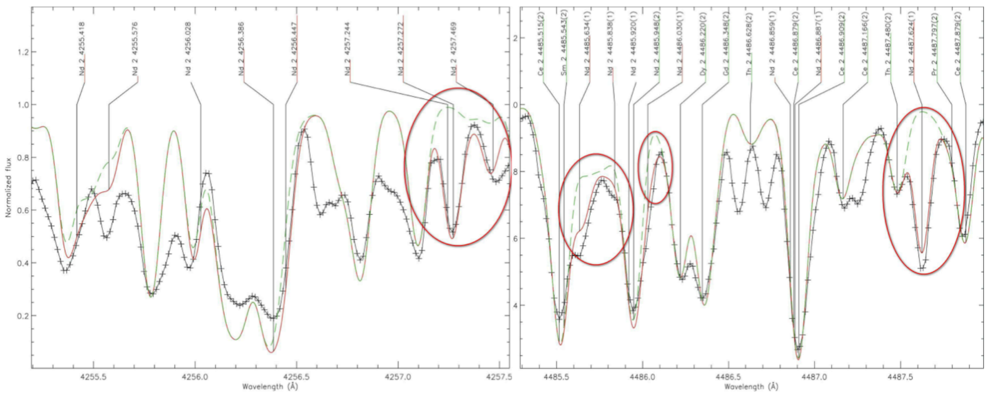

Fig. 2. Comparison between the observations (crosses), calculations with previous list of Nd II lines (dashed line) and new line list (full line)(Wyart et al 2010)

values are then used for computing Ritz wavelengths, which have reduced uncertainties compared with the directly measured wavelengths.

5 Typical results

In our laboratory, we have been working on spectra of moderately charged (II-VI) transition metal ions and rare earth element ions (lanthanides) for a longtime. The complexity of these spectra is due to the presence of incomplete d shell and f shell electrons. For rare earth ions, a systematic approach by isoelectronic or isoionic sequences must be followed to get reliable results. This allows simultaneously a critical compilation of existing data. Tables of our published data are made available online at `molat.obspm.fr` before being progressively included into databases like ADS (Kramida et al 2014) and Vienna Atomic Line Database (VALD 2014). Linelists contain experimental wavelengths and intensities, Ritz wavelengths calculated with optimized energies, calculated gf values, identifications of lower and upper levels of the transitions. Tables of energy levels contain level energies, quantum numbers, percentage compositions of levels in a given angular momenta coupling scheme and finally Landé factors. Most of the references of our previous works can be found on `molat.obspm.fr` as well as tabulated data. Works in progress concern spectra of manganese (II-V), iron and nickel ions, erbium ions Er^{2+} and Er^{3+}. The Meudon 10.7 m spectrograph is also used for studying rotationally-resolved electronic spectra of small molecules in VUV.

Figure 1 shows sections of high resolution spark spectra of ytterbium electrode, which have been used for the Yb V analysis (Meftah et al 2013). They are produced with different discharge conditions in order to differentiate lines from ionization stages.

Figure 2 shows a comparison between the spectrum of the Przybylski star (HD 101065) and two calculated spectra, one with data in VALD prior to our new analysis of the Nd II spectrum (Wyart et al 2010) and one with the newly included data. The new analysis resulted in the determination of 597 levels of the odd $4f^35d6s + 4f^35d^2 + 4f^36s^2 + 4f^46p + 5p^64f^5$ configurations and 233 levels of the even $4f^46s + 4f^45d + 4f^36s6p + 4f^35d6p$ configurations of the singly charged Nd^+ ion and it should increase the number of Nd II lines from 1287 to 5700 in VALD.

The CNRS Stellar Physics National Program (PNPS) is acknowledged for partial financial support.

References

Tchang-Brillet W-Ü L and Azarov V I, 2002, Phys. Scr., T100, 104

Cowan R D 1981, *The Theory of Atomic Structure and Spectra*, Univ. of Calif. Press, Berkeley CA

Azarov V I, 1991, Phys. Scr., 44, 528

Azarov V I, 1993, Phys. Scr., 48, 656

Kramida A E, 2010, Comput. Phys. Commun., 182, 419

Kramida, A., Ralchenko, Yu., Reader, J. and NIST ASD Team (2014). NIST Atomic Spectra Database (version 5.2). Available: http://physics.nist.gov/asd. National Institute of Standards and Technology, Gaithersburg, MD.

Vienna Atomic Line Database. Available at `http://vald.astro.uu.se`

Meftah A, Wyart J.-F., Tchang-Brillet W-Ü L, Blaess Ch, Champion N, 2013, Phys. Scr., 88, 045305

Wyart J.-F., Tchang-Brillet W-Ü L, Ryabtsev A N, Kildiyarova R R, Ryabchikova T, Illyin I, Fossati L, Kochukhov O, Poster presented at ICAMDATA 2010, Vilnus, Lithuania, September 21-24, 2010.

SF2A 2014
J. Ballet, F. Bournaud, F. Martins, R. Monier and C. Reylé (eds)

HELIUM SIGNATURE IN RED GIANT OSCILLATION SPECTRA

Vrard M.[1], Mosser B.[1] and Barban C.[1]

Abstract. The space telescopes CoRoT and *Kepler* have provided seismic data of unprecedent quality on red giants. The oscillation spectrum of these stars have shown a regular pattern called the universal oscillation pattern. These very precise data allow us to study the deviation from this regular pattern. In this work, we measure the modulation component of the radial mode frequency spacing in more than one hundred red giants and attribute the modulation to glitches due to the region of second ionisation of helium. We find a correlation between the location of this zone and the evolutionary status of the red giants. These results brings new constraints on the star interiors.

Keywords: stars : pulsations, stars : evolution

1 Introduction

Solar-like oscillations have been detected in thousands of red giants, with the CoRoT and *Kepler* missions. The radial modes discovered in these stars spectrum are p-modes forming a regular pattern called universal red giant oscillation pattern (Mosser et al. 2011). Because of sound speed discontinuities, departures from this universal pattern are observed. The aim of this work is to study these deviations called glitches which are produced by inner structure discontinuities of the star, such as the base of the convection zone or the second helium ionisation zone (Gough 1990). We use stars with an evolutionary state already determined by Mosser et al. (2012) in order to investigate the characteristics of the glitches as a function of the evolutionary status.

2 Data analysis method

2.1 Data set

Long-cadence data from *Kepler* up to the quarter Q13, corresponding to 1120 days of photometric observation were used. Original light curves were processed and corrected according to the method of García et al. (2011). We used the set of 216 stars for which Mosser et al. (2012) deduced the evolutionary status from the identification of the mixed-mode pattern. This allowed us to select spectra with high signal-to-noise ratio.

2.2 Radial mode fitting method

Pulsating red giant stars are characterized by two distinct resonant cavities, the core and the envelope, giving rise to mixed modes (e.g., Beck et al. 2011; Mosser et al. 2012). These modes behave as acoustic modes in the envelope and as gravity modes in the core. They have a complex frequency pattern. Consequently, we focused on radial modes only. A first estimate of the frequency position of radial modes is determined with the universal pattern (Mosser et al. 2011). This guess is refined by identifying nearby local maxima of the smoothed spectrum with an automated process. We then fit a Lorentzian model to nearby modes with a background component, adjusting the model described by Toutain & Appourchaux (1994), Barban et al. (2010) and Appourchaux (2011).

[1] LESIA, CNRS, Université Pierre et Marie Curie,Université Denis Diderot, Observatoire de Paris, 92195 Meudon cedex, France

2.3 Determination of the frequency differences $\Delta\nu(n)$

We calculate the local frequency separation by computing the frequency differences between consecutive radial modes. We derive the local $\Delta\nu(n)$ from the chords between adjacent modes in order to have a central value of the phase:

$$\Delta\nu(n) = \frac{\nu_{n+1,0} - \nu_{n-1,0}}{2}, \tag{2.1}$$

where n is the radial order. At the edges of the measured radial modes, we cannot use Eq. (2.1) and replace it by the frequency difference between two consecutive radial modes.

3 Measuring the glitches for red giants

The difference between the observed local large separation and the asymptotic local large separation predicted by the universal pattern is noted

$$\delta_{\rm g} = \Delta\nu(n) - \Delta\nu_{\rm UP}(n), \tag{3.1}$$

where $\Delta\nu_{\rm UP}(n)$ is the theoretical large separation.

We consider only one oscillatory component in the model used to reproduce $\delta_{\rm g}$ since the discontinuity of the second helium ionisation zone is by far the most important in red giants compared to other discontiniuties as shown by (Miglio et al. 2010). The fitted model is:

$$\delta_{\rm g} = \mathcal{A}\langle\Delta\nu\rangle \cos\left(\frac{2\pi(\nu - \nu_{\max})}{\mathcal{G}\langle\Delta\nu\rangle} + \phi\right), \tag{3.2}$$

where $\langle\Delta\nu\rangle$ is the mean value of the large frequency separation, $\mathcal{G}$ is the period of the oscillation expressed in unit of $\langle\Delta\nu\rangle$, $\mathcal{A}$ is the amplitude of the oscillation in unit of $\langle\Delta\nu\rangle$ and ϕ is the phase of the oscillation centered on $\nu_{\max}$. We used a χ^2 method to fit the three parameters. The uncertainties were extracted by the inversion of the Hessian matrix. In some of the stars we analysed, the performed fit was unsuccessful. This happens for example when the uncertainties on the frequencies are too large. We rejected such fits, when the uncertainties on the period parameter were higher than the measured value of the period.

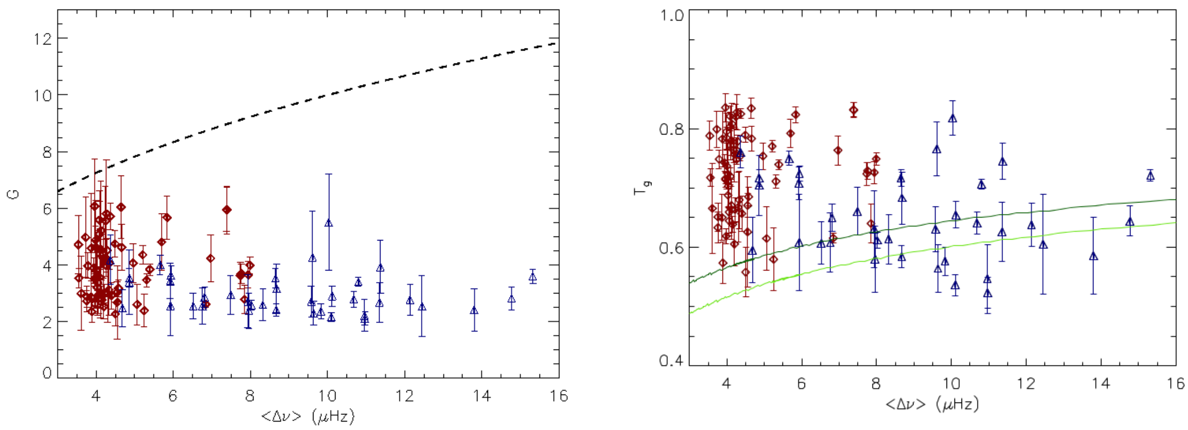

Fig. 1. Left: Dimensionless period $\mathcal{G}$ of the modulation measured as a function of the large separation. Clump stars are indicated by red diamonds and RGB stars by blue triangles. Error bars correspond to the 1σ uncertainties. The dashed black line indicates the maximum number of radial modes observable in a red giant spectrum. **Right:** Acoustic radius of the discontinuity related to the second helium ionisation zone as a function of the global large separation. Clump stars are indicated by red diamonds and RGB stars by blue triangles. Error bars correspond to the 1σ uncertainties. The light green line indicates the theoretical acoustic radius of the second helium ionisation zone for a $1M_\odot$ star during the RGB phase. The dark green line gives the same information for a $1.4M_\odot$ star.

4 Discussion

4.1 Period of the modulation

We measured the dimensionless period $\mathcal{G}$ for 107 stars. The variation of the period as a function of the large separation is shown in Fig. 1. The dimensionless period $\mathcal{G}$ is approximately constant in a large $\langle\Delta\nu\rangle$ range. The mean glitch periods are $\mathcal{G} \simeq 3.88 \pm 0.51$ for clump stars and $\mathcal{G} \simeq 2.85 \pm 0.43$ for RGB stars. Such values are similar to the periods predicted by the models for this kind of star (Broomhall et al. 2014). The period $\mathcal{G}$ is directly related to the acoustic depth of the glitch by the relation (Mazumdar et al. 2014):

$$T_g = \frac{1}{2\langle\Delta\nu\rangle}\left(1 - \frac{1}{2\mathcal{G}}\right). \tag{4.1}$$

The measured T_g are compared to results from models in Fig. 1. The models used are described in Belkacem et al. (2012).

4.2 Phase of the modulation

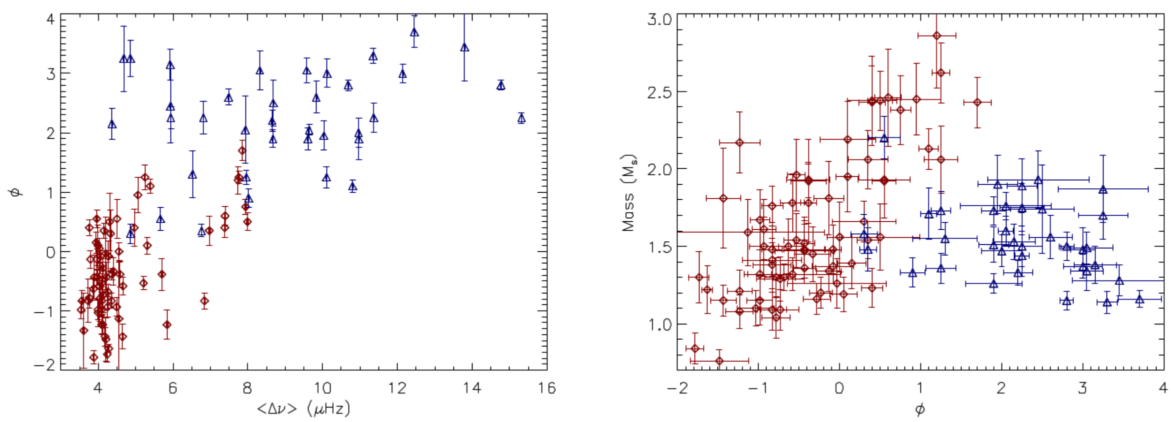

Fig. 2. Left: Phase ϕ of the modulation measured as a function of the global large separation. Clump stars are indicated by red diamonds and RGB stars by blue triangles. Error bars correspond to the 1σ uncertainties. **Right:** Stellar masses in function of the phase of the modulation. Clump stars are indicated by red diamonds and RGB stars by blue triangles. Error bars correspond to the 1σ uncertainties.

The measured phase of the modulation shows complex variation (Fig. 2). All clump stars have a phase around 0, whereas RGB stars have ϕ close to π. This phase shift between clump and RGB stars is systematically observed. To investigate the consequences of this phase difference, we consider the phase at the order corresponding to the index $n_{\max}$ of the maximum oscillation signal. Following Eq. (3.2), if the star has a phase $\simeq 0$ like clump stars, the local large separation measured will be overestimated. On the contrary, if the star has a phase $\simeq \pi$ like RGB stars, the local large separation will be slightly underestimated. This property can be used to determine the evolutionary stage of the stars. The glitch component modifies the local measurement of the large separation with a relative variation of $-0.5\,\%$ for RGB stars and $+1\,\%$ for clump stars. This translate into a change in the ε parameter ($\delta\varepsilon = -(n+\varepsilon)\,\delta\log(\Delta\nu)$), corresponding to $+0.05$ for RGB stars and -0.1 for clump stars. The difference between clump stars and RGB stars is therefore -0.15, in agreement with local measurements (e.g., Bedding et al. 2011; Kallinger et al. 2012). The difference reported by Kallinger et al. (2012) has been noted for a vast majority of red giants. We can therefore conclude that our results, reduced to a limited subset of red giants showing enough oscillation modes, can be extended to all red giants. Therefore, this work justifies the analysis made by Kallinger et al. (2012) for distinguishing RGB and clump stars. Alternatively, measuring the phase shift (Eq. 3.2) provides similar information. Based on the measured $\langle\Delta\nu\rangle$ and $\nu_{\max}$ and on the temperature of the star given by Huber et al. (2013), we deduced the approximate mass and radius of the star from the usual scaling relations (Kallinger et al. 2010; Mosser et al. 2013). We then investigated the mass dependence of the different glitch modulation parameters. Only the phase shows a clear variation with the stellar mass (Fig. 2). Phases of the clump stars have a clear mass dependence: clump stars with a high mass have a higher phase than clump stars with a lower mass. This mass dependence is not seen for RGB stars. The observed relation between the phase and the mass is clear but remains purely empirical. Its physical basis needs to be established.

5 Conclusions

In this work, we have studied the variation of the large separation, $\Delta\nu(n)$, as a function of frequencies for about 200 red giants. For most of the stars, we have found a modulation of $\Delta\nu(n)$ associated to a glitch signature due to the second helium ionisation zone. We have shown that this modulation depends on the evolutionary status of the star which represents a new way to determine the evolutionary stages of red giants. These results have been recently confirmed by theoretical work (Christensen-Dalsgaard et al. 2014).

We acknowledge the entire Kepler team, whose efforts made these results possible. Funding for this Discovery mission was provided by NASA's Science Mission Directorate.

References

Appourchaux, T. 2011, ArXiv e-prints

Barban, C., Baudin, F., Mosser, B., et al. 2010, Astronomische Nachrichten, 331, 1016

Beck, P. G., Bedding, T. R., Mosser, B., et al. 2011, Science, 332, 205

Bedding, T. R., Mosser, B., Huber, D., et al. 2011, Nature, 471, 608

Belkacem, K., Dupret, M. A., Baudin, F., et al. 2012, A&A, 540, L7

Broomhall, A.-M., Miglio, A., Montalbán, J., et al. 2014, MNRAS

Christensen-Dalsgaard, J., Silva Aguirre, V., Elsworth, Y., & Hekker, S. 2014, ArXiv e-prints

García, R. A., Hekker, S., Stello, D., et al. 2011, MNRAS, 414, L6

Gough, D. O. 1990, in Lecture Notes in Physics, Berlin Springer Verlag, Vol. 367, Progress of Seismology of the Sun and Stars, ed. Y. Osaki & H. Shibahashi, 283

Huber, D., Silva Aguirre, V., Matthews, J. M., et al. 2013, ArXiv e-prints

Kallinger, T., Hekker, S., Mosser, B., et al. 2012, A&A, 541, A51

Kallinger, T., Mosser, B., Hekker, S., et al. 2010, A&A, 522, A1

Mazumdar, A., Monteiro, M. J. P. F. G., Ballot, J., et al. 2014, ApJ, 782, 18

Miglio, A., Montalbán, J., Carrier, F., et al. 2010, A&A, 520, L6

Mosser, B., Belkacem, K., Goupil, M., et al. 2011, A&A, 525, L9

Mosser, B., Goupil, M. J., Belkacem, K., et al. 2012, A&A, 540, A143

Mosser, B., Michel, E., Belkacem, K., et al. 2013, A&A, 550, A126

Toutain, T. & Appourchaux, T. 1994, A&A, 289, 649

Author Index